

27º CONGRESSO  
DA SOCIEDADE BRASILEIRA  
DE MICROSCOPIA E  
MICROANÁLISE

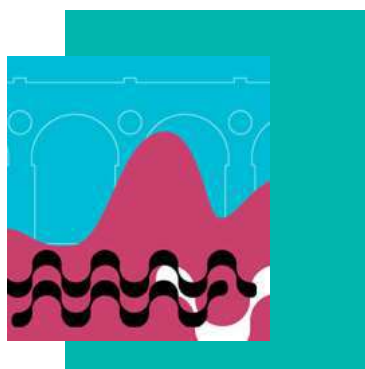
# CADERNO DE ANAIS



**RESUMOS APRESENTADOS NO  
27º CONGRESSO BRASILEIRO DE  
MICROSCOPIA E MICROANÁLISE  
DA SBMM. RIO DE JANEIRO, 2019**



# CADERNO DE ANAIS



**RESUMOS APRESENTADOS NO  
27º CONGRESSO BRASILEIRO DE  
MICROSCOPIA E MICROANÁLISE  
DA SBMM. RIO DE JANEIRO, 2017**





## **DIRETORIA DA SBMM (2018-2020)**

Presidente

**Daniel Lorscheitter Baptista (UFRGS)**

Vice-Presidente (Ciências de Materiais)

**Jefferson Bettini (LNNANO/CNPEM)**

Vice-Presidente (Ciências Biológicas)

**Marco Cesar C. Guimarães (UFES)**

Tesoureiro

**André Linhares Rossi (CBPF)**

Secretário-Geral

**Raquel Giulian (UFRGS)**

## **COMISSÃO ORGANIZADORA LOCAL**

Anderson Franzen (UEZO/RJ)

André Gomes (IBQM/UFRJ)

André Linhares Rossi (CBPF/RJ)

Bráulio Soares Archanjo (INMMETRO/RJ)

Carlos Achete (INMMETRO/RJ)

Celso B. de Sant'Anna Filho (INMMETRO/RJ)

Claudia Franca Barros (JBRJ)

Eduardo José Lopes Torres (UERJ/RJ)

Fernando Pereira de Almeida (CENABIO/UFRJ)

Guillermo Solórzano (PUC/RJ)

Kildare Rocha de Miranda (IBCCF/UFRJ)

Leonardo Salgado (JBRJ/RJ)

Luiz Henrique de Almeida (COPPE/UFRJ)

Marcia Attias (UFRJ)

Marlene Benchimol (UNIGRANRIO/RJ)

Paula Jardim (COPPE/UFRJ)

Renata Antoun Simão (COPPE/UFRJ)

Rodrigo Prioli (PUC/RJ)

Sergio Seabra (UEZO/RJ)

Sidnei Paciornik (PUC/RJ)

Suzana Corte-Real Farias (IOC/Fiocruz/RJ)

Wendell Girard-Dias (IOC/Fiocruz/RJ)

## **EDIÇÃO DOS ANAIS**

Emerson Campos Gonçalves (UFES)

## COMISSÃO CIENTÍFICA NACIONAL

### BIOLOGIA

Ana Maria Martinez (ICB/UFRJ)  
André Gomes (IBQM/UFRJ)  
Ana Claudia Guerra Araújo (CENARGEN/EMBRAPA)  
Carlos Lenz Cesar (Unicamp/SP)  
Claudia Franca Barros (JBRJ/RJ)  
Edilene Oliveira da Silva (UFPA/PA)  
Gilberto Weissmuller (IBCCF/UFRJ/RJ)  
Hernandes F. Carvalho (UNICAMP/SP)  
Kildare Miranda (IBCCF/UFRJ)  
Leonardo Tavares Salgado (JBRJ/RJ)  
Jacenir Reis dos Santos Mallet (IOC/Fiocruz/RJ)  
Marco Cesar C. Guimarães (UFES/RJ)  
Marcos Farina (ICB/UFRJ)  
Maura da Cunha (UENF/RJ)  
Maurílio José Soares (Fiocruz/PR)  
Paulo M. Bisch (IBCCF/UFRJ/RJ)  
Rodrigo Portugal (LNNANO/CNPq)  
Sonia N. Bao (UNB/DF)  
Rodrigo Portugal (LNNANO/SP)  
Rossiane Vommaro (IBCCF/UFRJ/RJ)

### MATERIAIS

Alberto Moreira Jorge Junior (UFSCar/SP)  
Ângelo Fernando Padilha (EDUSP/SP)  
Bráulio Soares Archanjo (INMETRO/RJ)  
Carlos Achete (INMETRO/RJ)  
Daniel Lorscheitter Baptista (UFRGS/RJ)  
Daniel Ugarte (UNICAMP/SP)  
Fernando Galembeck (UNICAMP/SP)  
Gloria Dulce de Almeida Soares (UFRJ/RJ)  
Guillermo Solórzano (PUC/RJ)  
Jefferson Bettini (LNNANO/SP)  
Karla Balzuweit (UFMG/MG)  
Luiz Henrique de Almeida (COPPE/UFRJ)  
Maria do Carmo Gonçalves (UNICAMP/SP)  
Paulo F. P. Fichtner (UFRGS/RS)  
Raquel Giulian (UFRGS/RS)  
Walter Botta Junior (UFSCar/SP)

### TODOS OS DIREITOS RESERVADOS.

#### Sociedade Brasileira de Microscopia e Microanálise – SBMM

Instituto de Biofísica Carlos Chagas Filho - UFRJ  
Av. Carlos Chagas Filho, 373 edifício do CCS Bloco G  
CEP 21941-902 - Rio de Janeiro - RJ Brasil

Congresso Brasileiro de Microscopia e Microanálise da SBMM (27. :  
2019 : Rio de Janeiro, RJ)

Anais do 27º Congresso Brasileiro de Microscopia e Microanálise da  
SBMM, realizado de 25 a 28 de agosto de 2019 no Rio de Janeiro/RJ  
[recurso eletrônico, PDF] – Rio de Janeiro, UFRJ, SBMM, 2017.

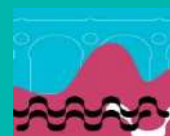
Edição digital  
Disponível em:  
ISSN –

1. Microscopia. 2. Microanálise. I. Título.



## PATROCÍNIO E APOIO





## PARTE 1

### COMUNICAÇÕES ORAIS - BIOLOGIA

Biomimetic Calcium Phosphate Films Synthesized by Pulsed Laser Deposition for Biomedical Applications Checca NR, Mello A, Rossi AM, Rossi AL	2
Automated Machine Learning Pipeline Predicts <i>Cryptococcus</i> spp. Capsular Morphotypes in Scanning Electron Microscopy Images Lopes W, Cruz GN, Vainstein MH, Vainstein MH, Schrank A	4
Structural Characterization of Poly ( $\epsilon$ -Caprolactone) Nanocapsules Through Advanced Techniques of Scanning Electron Microscopy Ramos TM, Guterres SS	6
Origin Of Multivesicular Bodies In <i>Giardia intestinalis</i> And Its Behavior During The Parasite Life Cycle Midlej V, de Souza W, Benchimol M	8
Biogenic Magnetic Nanoparticles, a Novel Tool to Treat Synaptic Deficit Diseases and Glioblastoma Vargas G, Verdan M, Correa TN, Ketzer L, Bazylnski DA, Garcia F, Romão L, Abreu FA	10
The Use Of The Myenteric Neurons of the Fish as Environmental Impact Biomarker Gonçalves ARN, Marinsek GP, Abessa DMS, Mari RB	12
Environmental Enrichment Promotes Protection Against the Dissemination of Cocal Virus in the C57BL/6 Mice Central Nervous System Freitas PSL, Lima AVL, Carvalho KGB, Diniz JAP	14
Histopathological and Ultrastructural Aspects of Cardiac Involvement in Dengue: Contributions of the Murine Model Caldas GC, Jácome FC, Rasinhas AC, Almeida ALT, Santos JPR, Pelajo Machado M, Barreto Vieira DF	16
Combined microscopy and spectroscopy techniques to characterize a fossilized feather with minimal damage to the specimen Campos APC, Carvalho RT, Straker LC, Salgado LT, Kellner AWA, Farina M	18
Time-Dependent Evaluation of Ultrastructural and Morphological Alterations Induced by 4-(5'-formyl-[2,2'-bithiophen]-5-yl)but-3-yn-1-yl acetate on Promastigote Forms of <i>Leishmania amazonensis</i> Machado RRB, Salvador DL, Oliveira AR, Serragiotto MH, Nakamura TU, Nakamura CV, Silva SO, Bidóia DL	20



The Limpet tooth revisited: matrix structure, minerals distribution and composition Werckmann J, Campos APC, Mendoza ME, Almeida F, Ersen O, Farina M	
UV-Irradiation of Oocytes for the Induction of Androgenetic Fishes. Santos MP, Nascimento NF, Evangelista MM, Nakaghi LSO, Yasui GS	<b>24</b>
Measuring Electron Beam Damage in Proteins Using Electron Energy Loss Spectroscopy de Farias MA, van Hell M, Bettini J, Portugal RV	<b>26</b>
Iron and Manganese Minerals Associated to Microalgae and Prokaryotes of the Periphyton of Doce River and Tributaries Affected by Iron Mining Tailings from Collapsed Fundão Dam (Mariana, MG) Keim CN	<b>28</b>
Morphological Changes in the Intestine of Pufferfish Due to Anthropogenic Pollution: A New Proposal for Environmental Quality Assessment Marinsek GP, Bortolotto LB, Gusso-Choueri PK, Abessa DMS, Mari RB	<b>30</b>
Measurements of the dielectric constant of a natural photonic crystal by Electric Force Microscopy Valeriano WW, Guimarães PSS, Neves BR, Rodrigues WN	<b>32</b>
Use of Tricology Associated with Electronic Microscopy in the Conservation of Genetic Resources in Sheep in Northeast of Brazil Rufino LAL, Silva KM, Nunes JVS	<b>34</b>
Studying Glycosylation Sites of Annelid Hemoglobin by Cryo-EM Mello JFR, Schatz M, Garratt RC, Portugal RV, van Heel M	<b>36</b>
Cryo-TEM Study of the Growth and Crystallization Processes of Calcium Phosphate Dalmonico G, Farina M, Rossi AL	<b>38</b>
Adaptation of Cryogenic System to a Cross Beam Scanning Electron Microscope Vieira V, Miranda K	<b>40</b>
Invasion of bacteria in intestinal tissue infected with <i>Trichuris muris</i> Oliveira DA, Nguidi PR, Rosa ACP, Lopes-Torres EJ	<b>42</b>
Behavior of osteoblasts onto topographically designed scaffolds in vitro dos Santos RS, Rougerie P, de Oliveira MMM, Anselme K, Farina M	<b>44</b>
Lack of Two Independent Physiological Regulators Impacts the Ultrastructure of <i>Cryptococcus gattii</i> Borges BS, Reis FCG, Jozefowicz LJ, Sena BAG, Castelli RF, Oliveira H, Soares Medeiros LC, Rodrigues ML	<b>46</b>
Devices produced by 3D printing for electron microscopy sample preparation Coelho LS	<b>48</b>
Scanning Electron Microscopy and Helium Ion Microscopy of the Inner Structure of <i>Trypanosoma cruzi</i> Infected Cells Fixed and Fractured by the OSMIUM-DMSO-OSMIUM Method (Fukudome and Tanaka, 1986)	<b>50</b>

Pacheco LO, Attias M, Miranda K, de Souza W

Cryoelectron Microscopy Imaging of whole cells: Preliminary results on freezing protocols applied to Protozoan Parasites **52**  
Lima A, Augusto I, Wendt C, de Souza W, Miranda K

Structural Organization of *Oscarella* (Porifera, Homoscleromorpha) Frozen and Fractured in Absolute Ethanol Observed by High Resolution Scanning Electron Microscopy **54**  
Stillitani D, Muricy G, Attias M

Chemical Modification Of Holey Carbon Support Film For Cryogenic Electron Microscopy Using 2-mercaptoethanol **56**  
Berenguel O, Serdan DC, Costa CAR, de Farias MA

## PARTE 2

### COMUNICAÇÕES ORAIS - MATERIAIS

Recent Technologies in Electron Microscopy for Modern Materials Characterization **59**  
Villaurrutia R

Morphological Study of 1D Sodium Niobate Nanostructures **61**  
Canabarro BR, Jardim PM

Mn<sub>5</sub>Si<sub>3</sub> Nanowire Composition And Crystalline Structure Resolved By TEM **63**  
Cruz ASE, Puydinger MVS, Campanelli RB, Bettini J, Pirota KR, Béron F

Effect of Size on Phase Segregation of Heusler Alloy Nanoparticles Synthesized by Pulsed Laser Deposition **65**  
Checca NR, Mello A, Rossi AL, Reis MS

Synthesis and characterization of NiFe<sub>2</sub>O<sub>4</sub> nanoparticle for removal of dyes in aqueous solution **67**  
Souza RND, Suguihiro NM, Saitovitch EMB, Alzamora M

Discrimination of Quartz and Resin using Convolutional Neural Networks in Optical Microscopy Images of Minerals **69**  
Santos R, Iglesias J, Paciornik S

Development of an Image Analysis System for Automatic Characterization of Sintering Cold Agglomerated **71**  
Santos R, Augusto K, Paciornik S, Domingues A

Application of Automated Mineralogical Mapping for Advanced Characterization of Pre-Salt Reservoir Rocks **73**  
Parizek-Silva YM, Neumann R, Ávila CA, Wense CWD

Comparing Quantitative EDS and WDS Using Microanalytical Standards and Interlaboratorial Test Samples **75**  
Balzuweit K, Flores MA, Garcia LRA, Souza MCC, Ribeiro RC

Fabrication of Lignocellulose-Based Microreactors: Copper-Functionalized Bamboo for Continuous-Flow CuAAC Click Reactions **77**  
Pandoli OG, Druval SS, Bustamante R, Khsorw G, Massi A



Hematite And Pyrite From Elba Island: From Theory To SEM/EDS Microanalysis Arrouvel C	<b>79</b>
Characterization of reduced graphene oxide thin films covered by Cu sputtering by Raman spectroscopy, scanning electron microscopy (SEM) and energy-dispersive X-ray spectroscopy (EDS) Lima AM, Silva CL, Cruz LR, Pinheiro WA	<b>81</b>
Defects Pattern on Monolayer Graphene with High Spatial Frequency Using Helium Ion Microscopy Silva WF, Medeiros HG, Archanjo BS, Almeida CA, Vasconcelos TL	<b>83</b>
STEM-EDX analysis of ion irradiation-induced precipitation in solution annealed AISI 316L alloys Timm MM, Oliviero E, Fichtner PFP	<b>85</b>
Stability of Ag and Au Nano-objects under Electron Irradiation Konrad B, Timm MM, Fabrim ZE, Fichtner PFP	<b>87</b>
Synthesis of silicon nanostructures in a quasi-order pattern induced by ion-beam Codeco CFS, Mello SLA, Magnani BF, Sant'Anna MM	<b>89</b>
Electron and Ion Microscopes as tools for materials science, nanoscience and nanometrology. Archanjo BS	<b>91</b>
Spherical Aberration-Corrected Transmission Electron Microscopy for Materials Characterization at the Brazilian Nanotechnology National Laboratory Ospina CA	<b>93</b>
Studying the Effects of Al-Doping Fe-(Hydr)Oxides on Contaminant Sorption Freitas ETF, Ciminelli VST	<b>95</b>
Fe/O Ratio Determination by EDS and EELS: Effect of Experimental Parameters Silva DS, Loureiro HC, Santos LP, Galembeck F	<b>97</b>
Analytical Electron Microscopy study of Hydrogen Reduction Synthesis of Nanoparticles of the Ternary CuNiCo Alloy System Marin EP, Brocchi EA, Solórzano IG	<b>99</b>
Plasmon-Tunable Tip Pyramid Probes for TERS Vasconcelos TL, Archanjo BS, Oliveira BS, Valaski R, Rabelo C, Achete CA, Jorio A, Cançado LG	<b>101</b>
Nanoscale Characterization of Minerals and Organic Matter in Hydrocarbon Source Rocks Lacerda DLP, Prioli R, Parizek-Silva YM, Vasquez GF	<b>103</b>
Characterization of Polymorph by AFM: Surface Properties and it Impact on Dissolution Patricio BFC, Prado LD, Gonçalves KM, Resende JALC, Rocha GM, Weissmüller G, Bisch PM, Rocha HVA	<b>105</b>

Advanced Segmentation of Metal Matrix Composite microCT Images by Deep Learning Neural Networks	<b>107</b>
Evsevleev S, Bruno G, Paciornik S	
Deep Learning Segmentation of Strain-Hardening Cement-Based Composites (SHCC) microCT Images	<b>109</b>
Lorenzoni R, Paciornik S, Curosu I, Mechtcherine V, Silva FA	
Correlative In Situ Analysis on Nanoscale Using AFM in SEM	<b>111</b>
Chourey A, Souza ER, Hummel S, Frank P, Hosseini N, Sattelkov J, Winkler R, Fantner GE, Plank H, Schwalb CH	
Structural and Morphological Characterization of BaTiO <sub>3</sub> /CoFeO <sub>4</sub> Thin Films Using Scanning and Transmission Electron Microscopies and Atomic Force Microscopy	<b>114</b>
Andrade HR, Mohallem NDS, Seara LM	
Advanced Nanoscale Orientation and Atomic Characterization of Phases in Beta Ti Alloys.	<b>116</b>
Afonso CRM, Nascente PAP, Amigó VB, Caram R	
Effect of Grain Boundary Character Distribution on $\delta$ -phase Precipitation in the Nickel-based Superalloy 718	<b>118</b>
Gallo FC, Azevedo LM, Labre C, Araújo LS, de Almeida LH	
Retained Austenite Volume Fraction in 52100 Steel Determined by EBSD and Others Correlative Techniques	<b>120</b>
Perez G, Archanjo BS, Senna CA, Kuznetsov A, Achete CA	
Combining EBSD and CL in a Geological Problem	<b>122</b>
Barbosa P, Lagoeiro L, Silva M	
Study of the growth of spicules of calcareous sponges by Transmission Electron Microscopy and Transmission Kikuchi diffraction	<b>124</b>
Werckmann J, Brodu E, Bouzi E, Rossi AL, Longuinho M, Ihiawakrim D, Klautau M, Farina M	
In-situ Electron Microscopy Observation of the Redox Process in Plasmonic Heterogeneous-Photo-Sensitive Nanoparticles	<b>125</b>
Bettini J, Scaffardi LB, Santillán MJJ, Arboleda MD, Schinca CD, Muraca D	
In-Situ TEM of Calcium Carbonate mineralization in the presence of L-Aspartic	<b>127</b>
Longuinho MM, Peña NO, Ihiawakrim D, Farina M, Rossi AL, Ersen O	
Structural Investigation of Hydrothermally Synthesized Iron Oxide Quantum dots	<b>129</b>
Mogii NVV, Verissimo NC, Kleiner CCC, Bertazzoli R	
Scanning Microwave Impedance Microscopy of 2D layered materials	<b>131</b>
Ohlberg DAA, Melo FH, Guimaraes PSSG, Medeiros-Ribeiro G	
Substrate Influencing Friction of 2D Materials	<b>133</b>
Brito TGL, Almeida CM	



The Sliding of Single Asperities in Graphene Ptak F, Almeida CM, Prioli R	135
Morphology effect on the capacitive properties of manganese oxide nanostructures prepared by pulsed laser deposition Pereira JA, Lacerda JN, Franceschini DF, Ponzio EA, Mainier FB, Xing YT	137
Characterization of Ceramic Materials Coated with Nanostructured Diamond by Microscopy Techniques Maru M, Archanjo BS, Achete CA, Perez G	139
Characterization of nanosized hydroxyapatite and hydrogel composite for biomaterials applications Santos LBF, Soares FMSS, Monteiro ES, Gomes PAMC, Elias CN	141
Ultra-High Conductive Hollow Channels Guided By Bamboo Bio-Template For Electric And Electrochemical Devices Pandoli OG, Reginaldo GN, Nathalia RO, Fingolo AC, Strauss M, Murilo S	143
Morphological Characterization of Corrosion Products of Guyed Transmission Towers Anchor Rods Dias BG, Matos TS, Bragança MOGP, Berrêdo ACS	145
Spray-forming of Al-matrix Composite Reinforced with Quasicrystals Zepon G, Silva LPM, Wolf W, Botta WJ	147
Study Of Y Addition Effect On Microstructure Of Nickel-based Alloy 718 Silveira RMS, Guimarães AV, de Almeida LH, Araújo LS, Dille J	149
Diffraction Contrast and Analytical Electron Microscopy of Multi-Phases GB Precipitation Phenomena in a Cr-Fe-Ni Alloy Spadotto JC, Burke G, Solórzano G	151

## PARTE 3

### PÔSTERES – BIOLOGIA

Morphological Analysis of the Stomach and Intestine of the Black Ray ( <i>Potamotrygon amandae</i> ) Myliobatiformes, Potamotrygonidae (Loboda & Carvalho, 2013) Aquino JB, Melo LF, Rodrigues RF, Rici REG	154
Structural Description Of Marine Turtle Fibropapilloma Melo LF, Aquino JB, Assunção MPB, Rici REG	156
Decellularization of Striated Muscle Skeletal Bovine Melo LF, Aquino JB, Rici REG	158
Characterization of Pathogenic Bacteria Adhered On the Cuticle of the Nematodes Isolated of the Bovine Ear Canal Caracciolo ME, Silva ACB, Torres EJJ	160
Morphological Characterization of Experimental Model <i>Metarhabditis blumi</i> (Nematoda: Rhabditidae) Caracciolo ME, Santos ACB, Torres EJJ	162

The Influence Of Comicronization On Particle Morphology Adauto MA, Prado LD, Patricio BFC, Rocha HVA	<b>164</b>
Antileishmanial Activity of 1,2-bis [3-(2-methyl-1,3-dioxolan-2-yl) phenyl]- ditellane Storck NC, Bandeira PT, Nakamura TU, Silva SO, Piovan L, Machado RRB, Bidóia DL, Nakamura CV, Garcia FP	<b>166</b>
Three-Dimensional Analysis Of The Biogenesis Of Hemozoin Crystals During The Intra-Erythrocytic Cycle Of <i>Plasmodium berghei</i> Azeredo A, Wendt C, Miranda K, Wendt C, de Souza W	<b>168</b>
High-resolution and Three-dimensional Analysis of Hemozoin Crystals in Human and Murine Malaria Parasites Wendt C, de Souza W, Miranda K	<b>170</b>
Morphological analysis of three-dimensional culture formation of 3D spheroids of hepatic stellate cells Rohden F, Ilha M, Giombelli MP, Guma F	<b>172</b>
Ultrastructural Characterization of A Novel Membrane Domain With Potential Function On Osmoregulation In <i>Trypanosoma cruzi</i> Augusto I, Girard-Dias W, de Souza W, Miranda K	<b>174</b>
Three-dimensional Analysis Of The Cytostome-Cytopharynx Complex In <i>Trypanosoma cruzi</i> Amastigotes And Its Function On Endocytosis Alcantara CL, de Souza W, Cunha-e-Silva NL	<b>176</b>
Morphological aspects of subpellicular microtubules of <i>Trypanosoma cruzi</i> Vidal JC, de Souza W	<b>178</b>
Three-dimensional characterization of the Contractile Vacuole Complex in <i>Trypanosoma cruzi</i> Mutants with Different Responses to Osmotic Stress Girard-Dias W, de Souza W, Miranda K	<b>180</b>
Morphological and Morphometric Evaluation of the Muscle Fibers of the Extensor Digitorum Longus and Soleus Muscles of Mice's Offspring Exposed or Not to Glyphosate Barbosa A, Oliveira MC, Kuhn C, Jerônimo LC, Balbo S, Bonfleur ML, Torrejais MM	<b>182</b>
Histoenzymology and Morphometry of the Extensor Digitorum Longus Muscle of Oophorectomized Female Rats Submitted to Vibrating Platform Treatment Barbosa A, Filho DP, Oliveira MC, Bertolini GRF, Guimarães ATB, Ribeiro LFC, Torrejais MM	<b>184</b>
Effect of Erythropoietin in the Autotransplant of Cryopreserved Cat Ovarian Tissue Félix CML, Gonçalves LP, Silva ABR, Costa MM, Lucci CM	<b>186</b>
Evaluation of Interaction Macrophages and Tumor Cells After Photodynamic Therapy Ferreira V, Godoi BH, Moraes CDGO, Silva NS, Pacheco-Soares C	<b>188</b>

Evaluation of the Environmental Quality of Three Estuaries of the São Paulo Coast Using Morphological Biomarkers in the Gills of Pufferfish Marinsek GP, Gusso-Choueri PK, Abessa DMS, Mari RB	<b>190</b>
Ultrastructural Characterization Of P-bodies In <i>Trypanosoma cruzi</i> de Almeida I, Augusto I, Girard-Dias W, de Souza W, Miranda K	<b>192</b>
Morphoquantitative Evaluation Of Two Subpopulations Of The Myenteric Neurons In Jejunum Of Golden Hamsters ( <i>Mesocricetus auratus</i> ) Infected With <i>Leishmania (Leishmania) infantum</i> Cavallone IN, Oliveira KS, Santos SK, Passero LFD, Laurenti MD, Jesus JA, Chucric TM, Mari RB	<b>194</b>
Histopathological Changes in the Central Nervous System Caused by the Juruaçá Virus in Adult Mice Cabral TS, Carvalho KGB, Quaresma JAS, Diniz JAP	<b>196</b>
Morfofunctional Aspects of Hystogenesis of Toxoplasma in Nervous System Cells Macedo J, Attias M, Portes JA, de Souza W, Moreira-Souza ACA	<b>198</b>
Histological Evaluation of Testicles After an Intratesticular Injection of Silver Nanoparticles Brito JLM, Lima VN, Azevedo RB, Lucci CM	<b>200</b>
Study of the Extensor Digitorum Longus' Connective Tissue of Obese Animals Submitted to Duodenojejunal Derivation Silva LM, Oliveira MC, Barbosa A, Ulsenheimer BH, Soares A, Balbo SL, Torrejais MM	<b>202</b>
Morphological and Morphometric Study of Neuromuscular Junctions of the Extensor Digitorum Longus Muscle of Female Oophorectomized Rats Submitted to Vibrating Platform Treatment Silva LM, Prado Filho D, Oliveira MC, Bertolini GRF, Guimarães ATB, Ribeiro LFC, Torrejais MM	<b>204</b>
Evaluation of follicular development and morphology in cat cryopreserved ovarian tissue transplanted after administration of Simvastatin Costa MM, Gonçalves LP, Silva ABR, Félix CML, Lucci CM	<b>206</b>
Effect of the Treatment with Vibrating Platform on the Morphology and Morphometry of the Extensor Digitorum Longus Muscle of Female Rats Submitted to Oophorectomy Surgery Kuhn MG, Prado Filho D, Barbosa A, Oliveira MC, Jeronimo LC, Bertolini GRF, Guimarães ATB, Ribeiro LFC, Torrejais MM	<b>208</b>
Morphometry of the Diaphragm Muscle of Obese <i>Wistar</i> Rats Submitted to Vibrating Platform Oliveira MC, Barbosa A, Soares A, Bertolini GRF, Torrejais MM, Brancalhão RMC	<b>210</b>
Quantification of Different Types of Fibers in Obese Animals Submitted to Vibrating Platform Treatment Oliveira MC, Andrade BZ, Boaretto ML, Bertolini GRF, Torrejais MM, Brancalhão RMC	<b>212</b>

Histopathological Changes In The Liver of Fish Exposed to Different Levels of Environmental Pollution	<b>214</b>
Nascimento SSN, Marinsek GP, Mari RB	
<i>Plasmodium chabaudi</i> Merozoites Evade the Nitric Oxide Microbicidal System of Macrophages: Correlation with Phosphatidylserine Exposure	<b>216</b>
Rodrigues PS, Almeida NS, Wanderley JLM, DaMatta RA, Seabra SH	
Yellow Fever Virus Modulates Energy Metabolism and Induces Cell Death of Human Megakaryoblasts	<b>218</b>
Campos SPC, Castro MG, Gomes CV, Caldeira MM, Rodrigues MF, Peçanha FLM, Kasai-Brunswic TH, Silva JL, Gomes AMO, Oliveira AC	
Dynamic of Histopathological Changes in The Intestinal Barrier of The Jejunum of Hamsters Experimentally Infected by <i>Leishmania (L.) infantum</i> .	<b>220</b>
Lima SKS, Cavallone IN, Oliveira KS, Passero LFD, Laurenti MD, Jesus JA, Chucuri TM, Mari RB	
Effects of testicular photohyperthermia on the histology of seminiferous tubules	<b>222</b>
Lima VN, Brito JLM, Nunes RB, Leite CAE, Souza PEN, Araujo MV, Bakuzis AF, Lucci CM	
Analysis of the Interaction of Type I Collagen with Two-dimensional Materials for the Development of Biomedical Nanocomposites	<b>224</b>
Brito ACF, Silva NCM, Lemos RSS, Medrado NV, Prado MC, Alvarenga ELFC, Neves BRA, Viana MM, Vasconcelos CKB, Barboza APM, Manhabosco TM	
Inedited Scanning Electron Micrographs of Cashew Plants Leaves Infected With <i>Pilgeriella anacardii</i> Von Arx and Muller	<b>226</b>
Muniz CR, Cardoso JE, Viana FMP, Lima ES, Martins MVV	
The increase of filamentous bacteria in the ileum of the mice infected by <i>Trichuris muris</i>	<b>228</b>
Carlos ECS, Oliveira DA, Torres EJJ	
The Exercise Effect on Sciatic Nerve Regeneration from Mice Previously Trained	<b>230</b>
Assis G, Laurindo RP, Santos ACR, Martinez AMB, Marques SA	
In vitro behavior and cytotoxicity evaluation of amphiphilic lipopeptides	<b>233</b>
Argüello KB, Vassiliades V	
Interaction between <i>E.coli</i> and T84 monolayer with <i>Trichuris muris</i> Excretory Secretory Products	<b>235</b>
Oliveira LTB, Oliveira DA, Rosa ACP, Lopes-Torres EJ	
Optimization of Fungal Lipase Production for Biofuels Production	<b>237</b>
Cesário LM, Pereira RFS, Pires GP, Carvalhal AF, Oliveira JP	
Analysis of the Effect of Histone Deacetylase Inhibitors against <i>Toxoplasma gondii</i> using Super-Resolution Structured Illumination Microscopy	<b>239</b>
Araujo-Silva CA, de Souza W, Martins-Duarte ES, Vommaro RC	
The Extracellular Matrix of Spleen Preserves Its Molecular and Ultrastructural Composition After the Decellularization Process	<b>241</b>

Zanardo TEC, Taufner GH, Pereira RHA, Desteffani AC, Amorim FG, Iwai LK, Nogueira BV

**Tropism Of Dengue Virus Type 4 In A BALB/c Murine Model: Experimental Infection And Analysis Of Morphological Aspects 243**

Rasinha AC, Silva MAN, Caldas GC, Jácome FC, de Almeida ALT, Leonardo R, dos Santos FB, Nunes PCG, Barth OM, Barreto Vieira DF

**Morphological Studies Of BALB/c Murine Model Tissues With Reinfection By Dengue Virus 245**

de Almeida ALT, Souza DDC, Jácome FC, Caldas GC, Silva MAN, Rasinha AC, Barth OM, Barreto Vieira DF

**Metabolic and ultrastructural renal changes in adult Wistar rats fed by a cafeteria diet 247**

dos Santos PF, de Souza DB, Torres E JL, Costa WS, Sampaio FJB, Gregorio BM

**The structure and function of glandular trichomes in *Jacquinia armillaris* (Theophrastoideae – Primulaceae) 249**

Luna BN, Freitas MF, Barros CF

**Therapeutic potential of low-cost nanocarriers produced by green synthesis: uptake of superparamagnetic iron oxide nanoparticles by macrophages and *Leishmania* 251**

Verçoza BRF, Bernardo RR, Sinnecker JP, Oliveira LAS, Rodrigues JCF

**Microscopy techniques applied to symbiont-harboring trypanosomatids: unveiling the functions of Kinetoplast Associated Proteins 254**

Gonçalves CS, Catta Preta CMC, Mottram J, Motta MCM

**Ultrastructural studies of cell cultures infected with Brazilian Zika virus 259**

Barreto-Vieira DF, Jácome FC, da Silva MAN, Caldas GC, Filippis AMB, Barth OM

**Histopathological Findings In Immunocompetent Murine Model Lung Infected With Zika Virus 262**

Bandeira DM, da Silva MAA, Rasinha AC, Caldas GC, Jácome FC, Almeida ALT, Brício RTC, da Silva JFA, Trindade GF, Barth OM, Barreto-Vieira DF

**Effect of herbicides on the physiology, morphology and cell ultrastructure of *Setaria viridis* (L.) Beauv 264**

Lelis DCC, Valença DC, Bezerra AC, Junqueira EM, Ferreira MA, Pinho C, Reinert F, Ortiz B

**In vivo antileishmanial efficacy of a topical treatment of crotoxin derived from *Crotalus durissus terrificus* venom against *Leishmania (Leishmania) amazonensis* 266**

Martins AJE, Hage AAP, Rodrigues APD, Diniz JAP, Sampaio SC, Silva EO

**Effect of copaiba oil and kojic acid association on promastigote forms of *Leishmania (Leishmania) amazonensis*. 268**

Moraes LS, Rodrigues APD, Guilhon GMSP, Silva EO

**Renal Impairment in Murine Model for Dengue 3 Infection: Histopathological, Morphometric and Ultrastructural Aspects 270**



Caldas GC, Jácome FC, Rasinhas AC, Almeida ALT, Santos JPR, Pelajo Machado M, Barreto Vieira DF

Morphological Aspects Of Aorta Of C57Bl/6 Mice Submitted To The Hyperlipidic Diet And Treated With Hexanic Extract Of *Pterodon polygalaeiflorus* **272**  
Carvalho GM, Melgar VG, Vieira AB, Nascimento ALR, Rabelo K, Ciambarella BT, Barbosa PHR, Coelho MGP, Carvalho JJ

Use of microscopy to study the biological effects induced by a novel sirtuin inhibitor on *Leishmania amazonensis* **274**  
Silva GS, Verçoza BRF, Bracher F, de Souza W, Rodrigues JCF

Spermiogenesis in an invasive *Drosophila* species in Brazil **276**  
Tonelli GSSS, Gracielle IMS, Bão SN

Fibroblast Characterization for Three Brazilian Wild Cats **278**  
Arantes LG, Tonelli GSSS, Bessler HC, Martins CF, Bão SN

A  $\mu$ ct And TD-NMR Approach To The Probing Of Negative Spaces In A Bamboo Sample **280**  
Alves H, Rodrigues E, Pandoli O, Neto R

Caracterização Morfológica dos Espermatozoides em Espécies do Gênero *Triatoma* (Insecta, Hemiptera, Reduviidae, Triatominae) **282**  
Oliveira MLR, Camara DCP, Freitas SPC, Santos-Mallet JR

Thermostability of Magnetite Magnetosomes: Implications for Fossil Record And Biotechnology **284**  
Cypriano J, Bahri M, Baazis W, Dembelé K, Leão P, Bazylinski DA, Abreu F, Ersen O, Farina M, Werckmann J

Methods for determining the concentration of green gold nanoparticles **286**  
Silva LPC, Keijok WJ, Guimarães MCC

Anti-*Sporothrix* Effect of Ibuprofen Combined with Amphotericin B **288**  
Borba-Santos LP, Rozental S

Ultrastructural Aspects of *Sporothrix brasiliensis* in feline claws **290**  
Silva AC, Borba-Santos LP, Martins BBF, Kung KDC, Monti F, de Farias MR, Rozental S

Inhibition Of Bovine Viral Diarrhea Virus by prostaglandin A<sub>1</sub> **292**  
Caldas LA, Freitas TRP, Azevedo RC, de Souza W

Occurrence of avian pox outbreaks in canary commercial breedings. Rapid diagnosis through electron transmission microscopy techniques. **294**  
Catroxo MHB, Luz LSM, Pedroso IM, Martins AMCRPF

Use of TEM to Monitor Changes in Amyloid Beta Conformations Throughout Aggregation and Identify a Non-toxic Pathway in the Presence of a Ru(II) Complex **296**  
Cali MP, Carlos RM

Ultrastructural Analysis of *Anadenanthera colubrina* (Vell.) Brenan Roots Treated with *Urochloa humidicola* (Rendle.) Morrone & Zuloaga Root Extract **298**  
Feitoza RBB, Lima RPL, Moraes LFDM, Varela RM, Macías FA, Cunha M

Study of Human Peripheral Blood Fibrocytes Interaction with <i>Leishmania (L.) amazensis</i> – an <i>in vitro</i> Analysis Pereira PRP, Macedo-Silva RM, Sousa-Vasconcelos PS, Pinho RT, Pinheiro RO, Côrte-Real S	<b>300</b>
Stereology of Mitochondria in Transmission Electron Microscopy Barbosa PHR, Carvalho JJ, Mandarin-de-Lacerda CA	<b>302</b>
Aliskiren Improves Renal Morphophysiology And Inflammation In Wistar Rats With 2K1C Renovascular Hypertension Pereira PG, Rabelo K, Silva JFR, Ciambarella BT, Argento JGC, Nascimento ALR, Vieira AB, Carvalho JJ	<b>304</b>
Carotenoid Storage Cells in <i>Bixa orellana</i> L. Louro RP, Freitas Y, Santiago LJM	<b>306</b>
Histone Desacetylase Inhibitors Affect Growth And Cell Organization Of <i>Giardia intestinalis</i> Trophozoites Verissimo RFO, Benchimol M, de Souza W, Gadelha APR	<b>308</b>
Ultrastructural Effects of Itraconazole and Metallodrugs in <i>Leishmania amazonensis</i> : SEM/TEM as Approach to Biological Studies de Macedo-Silva ST, Navarro M, de Souza W, Rodrigues JCF	<b>310</b>
Nanostructured Carbonated Hydroxyapatite Interactions with Murine Pre-osteoblasts Anjos SA, Mavropoulos E, Alves GG, Costa AM, Silva GD, Hausen MA, Spiegel CN, Mir M, Granjeiro JM, Rossi AM	<b>312</b>
The Role of a Possible Linker Histone in Chromatin Organization in <i>Toxoplasma gondii</i> Using Different Methods in TEM Klimeck TDF, Severo VR, Ávila AR, Medeiros LCS, Nardelli SC	<b>314</b>
Characterization of Giant Viruses with TEM, SEM and Cryo-EM Arantes TS, Kitten G, Ivo JC, Freitas E, Rodrigues W, Abrahão JS	<b>316</b>
Use of different microscopy approaches for the immunolocalization of costa proteins from <i>Tritrichomonas foetus</i> Bandeira PT, de Souza W	<b>318</b>
Influence of Microorganisms on Reductive Dissolution of Fe(III) in Doce River Basin after Fundão Dam failure (Mariana, MG) Santos AS, Keim CN, Sanjad PM, Cruz ACRC	<b>320</b>
Effects Of Exercise Protocols On Functional Recovery And Neuromuscular Regeneration In Animal Model Of Compressive Spinal Cord Injury Santos ACR, Laurindo RP, Pestana FM, Canedo NHS, Martinez AMB, Marques AS	<b>322</b>
A Study of Magnetic Nanoparticles Synthesis For Biological Applications Pires GP, Carvalhal AF, Cesário LM, Pereira RFS, Oliveira JP	<b>324</b>
Optimization of a Cryopreparation Protocol for Quantitative X-ray Microanalysis of Ion-Rich Compartments in <i>Trypanosoma cruzi</i> Pierre J, Girard-Dias W, de Souza W, Miranda K	<b>326</b>

Crystallographic misorientation between spicules in the skeleton of the Calcareous Sponge <i>Sycettusa hastifera</i> Coelho LS, Farina M, Klautau M, Rossi AL	328
Fiber-Like Supra-Tetrameric Assembly of Glutaminases C Investigated by Cryo-Electron Microscopy Cassago A, Quesñay JEN, van Heel M, Ambrosio ALB, Dias SM, Portugal RV	330
Structural Characterization Of The Vdac2-Bak Complex From Mitochondrial Outer Membrane By Single Particle Cryo-Electron Microscopy Borges AC, Quesñay JEN, Nagampalli RSK, Ariza AJF, Islam Z, Dias SMG, Portugal RV, Ambrosio ALB	332
Myriapoda Hemocyanin: The First 3D Reconstruction of <i>Scolopendra subspinipes subspinipes</i> and Preliminary Structural Analysis of <i>Scolopendra viridicornis</i> Riciluca KCT, Borges AC, Mello JFR, Oliveira UC, Serdan DC, Florez-Ariza A, Chaparro E, Nishiyama-Junior MY, Cassago A, Junqueira-de-Azevedo ILM, van Heel M, Silva Júnior PI, Portugal RV	334
Histological And Immunohistochemical Study on Stomach of The green iguana ( <i>Iguana iguana</i> ) Campos AOS, Brito ARR, de Luca BG, Lima MSCZ, Santos CM	336
Histological and Immunohistochemical Analysis On Oesophagus Of The Iguana ( <i>Iguana iguana</i> Linnaeus, 1758) Brito ARR, Campos AOS, de Luca BG, Lima MSCS, Santos CM	338
Histochemical and immunohistochemical analysis of the stomach and intestine of rhesus monkeys ( <i>Macaca mulata</i> ) (Cercopithecidae, Primates) de Luca BG, Abidu-Figueiredo M, Campos AOS, Brito ARR, Bastos AL, dos Santos CM	341
Establishment Of a Protocol For Cell Culture In 3D Matrix And Analysis By Confocal Microscopy Pimentel CF, Matioszek GMV, Ramos IPR, Goldenberg RCS	343
Cryofracture in the Morphological Characterization of <i>Eurytrema coelomaticum</i> (Trematoda - Digenea) Leite KG, Lopes-Torres EJ, Silva Júnior FA, Rodrigues-Silva R, Machado-Silva JR	345
3D reconstruction of embryonated eggs of <i>Trichuris muris</i> Rocha LL, Torres EJJ	347
Contribution of Three-dimensional Modeling to the Whipworm Study Lopes-Torres EJ, Rocha LL, Dias WG, Straker LC, de Souza W, Miranda KR	349
Morphometry of Nitrergic Myenteric Neurons Of The Jejunum Of Mice Fed High-Fat Diet Soares A, Beraldi EJ, Kuhn MG, Bazotte RB, Buttow NC	351
Neuroprotection In Hydrocephalic Rats, Surgically Treated Or Not: The Memantine As A Pharmacological Alternative Beggiora PS, Silva SC, Rodrigues KP, Almeida TAL, Machado HR, Lopes LS	353

Effects Of Hyperbaric Oxygen Therapy In Secondary Lesions To Experimental Hydrocephalus Associated With Surgical Treatment **355**  
 Silva SC, Feres O, Beggiora PS, Machado HR, Lopes LS

Synthesis and characterization of graphene oxide for bactericide potential evaluation **357**  
 Curti RV, Archanjo BS, Martins JL, Kuznetsov O, Araújo JR, Assis KLSC, Achete CA

## **PARTE 4**

### **PÔSTERES - MATERIAIS**

The mechanism of oxidation assisted intergranular cracking on nickel-based superalloy 718 **360**  
 Varela AV, Almeida LH

Alloy Used in Thermal Spraying – Characterization by MEV and EDS Using PyMac Software **362**  
 Guapyassu AVL, Diniz MG, Solórzano-Naranjo IG, Pimenta AR

Effects Of The Uniaxial Stretching Of Surface Treated Electrospun Polycaprolactone Mats **364**  
 Toledo ALMM, de Miranda AHV, Martinez AMB, Dias ML

Characterization of Metallic Coating with Sealant Obtained by Thermal Arc Spray Process **367**  
 Marques BB, Diniz MG

Morphological evolution of gold nanostructures electrodeposited on carbon electrodes **369**  
 Porfiro CM, Arguello J, Lavayen V, Inroga FAD

Optimization of the Three-dimensional Characterization of Iron Ore Pellets **371**  
 Souza CGP, Paciornik S, Augusto KS, Mauricio MHP

Nanostructured Starch Films **373**  
 Bernardo CN, Kling IL, Ferreira WH, Andrade CT, Simão RA

Characterization of dental implant surface roughness with light interference optical 3D profiler **375**  
 Elias CN, Soares FMS, Monteiro ES, dos Santos LFB

One-Pot Synthesis of Zinc Oxide Nanoparticles and their Characterization by Spectroscopic Methods and Scanning Electron Microscopy **377**  
 Santana CA, Lunz JN, Vasconcelos TL, Archanjo BS, Achete CA

TIG Brazing Of Metallic Glass On Carbon Steel **379**  
 Costa DA, Zúñiga A, Tercini M, Triveño C

Nanostructured Starch Composite with Lignin Nanoparticles **381**  
 Almeida E

Effect of Surface Treatment on Roughness and Morphology of titanium for dental implant **383**  
 Monteiro ES, Soares FMS, Santos LBF, Nascimento AL, Gomes PAC, Elias CN

Surface Roughness of Laser Sintered Titanium Alloys for Biomedical Application Soares FMS, Monteiro ES, Gomes PAMC, Santos LBF, Elias CN	<b>385</b>
In-Situ X-Ray MicroCT Imaging of The Microstructural Changes in Sandstones Submitted to Hydrostatic Pressures. Silva Júnior FJR, Velloso RQ, Paciornik S	<b>387</b>
SEM/EDS characterization of chrysocolla from Nova Prata do Iguaçu, State of Paraná, Brazil Garda GM, Sayeg IJ, Filgueira DA	<b>389</b>
Study of Phase Transformations in Non-Isothermal Conditions in Duplex Stainless Steel by Dilatometric Technique Freitas GCLD, Fonseca GS, Moreira LP	<b>391</b>
Solidification Microstructure Of Weld Metal Of The 316L Austenitic Stainless Steel Welding By Tig Autogenous Process Silva EMFS, Fonseca GS	<b>393</b>
Design Of Magnetic Nanoparticles: Nanorods And Nanodisc For Magnetic Hyperthermia Applications Niraula G, Sharma SK, Muruca D, Coaquira JAH, Aragon FH	<b>395</b>
Microscopic Evaluation and Fabrication Of A Metal-Ceramic Composite Firmino J, Alves H, Cavichini A, Orlando M, Lopes R	<b>397</b>
Use of EDS-SEM for fast chemical and mineralogical characterization of multiphase geological samples Matos-Pimentel HLS, Brod JA, Souza FG, Borges KOG, Carvalho JF, Oliveira CMA	<b>399</b>
Clay Minerals Identification By Chemical (Epma-Wds) And Morphological (Sem) Characteristics Matos-Pimentel HLS, Brod JA, Souza FG, Carvalho JF, Oliveira CMA	<b>401</b>
Porosity Estimative of Tablets by Backscattered Electron Images Camargo HS, Conceição EC, Gonçalves C	<b>403</b>
Silk fibroin hydrogels for potential applications in photodynamic therapy Ulloa J, Gerbelli B, Ribeiro A, Nantes-Cardoso I, Giuntini F, Alves WA	<b>405</b>
Enhanced Oil Recovery Analysis via microCT Scheffer K, Paciornik S, Carvalho MS, Méheust Y	<b>407</b>
In-situ morphology and phase modifications in Ni/Bi bi-layers induced by changing deposition order Liu LY, Xing YT, Merino ILC, Solórzano IG, Baggio-Saitovitch E	<b>409</b>
Morphological and Chemical Characterization of Sugarcane Bagasse and Straw Pellets with and without extractives using SEM/EDS. Silva LL, Palma KR	<b>411</b>
TiO <sub>2</sub> rutile doped with iron obtained by direct chlorination methods: Microanalytical characterization Cáceres LM, Brocchi E, Solórzano IG	<b>413</b>

- Microanalysis of Saddle Dolomite in Hydrothermal Breccia from Mina Rio Bonito - Campo Largo (PR, Brazil) **415**  
Camargo MHT, Ferreira AD, Duarte JP, Botelho AC, Pinto-Coelho CV, Rocha RLC, Mauricio MHP, Augusto KS, Roemers-Oliveira E
- Overcoming Challenges Associated with Microscopy Image Acquisition of Geopolymers **417**  
Paiva MDM, Gomes OFM, Moreira CR, Paiva MM, Curti RV, Archanjo BS, Neumann R, Toledo Filho RD
- Scanning Electron Microscopy - Assistant Technique In The Preparation Of Fluorescence Carbon Dots On Silica Gel **419**  
Mikhralieva A, Zaitsev V, Nazarkovsky M
- Titanium Inner Coating Of Narrow Alumina Tubes By DC Magnetron Sputtering **421**  
Bagnato OR, Defavari R, Manoel FE, Pimentel PM, Bianchi MC, Francisco FR
- Comparative study of surface treatments in polytetrafluoroethylene (PTFE) for application in Guided Bone Regeneration **423**  
Gomes PAMC, Monteiro ES, Soares FMS, Santos LBF, Elias CN
- Gunshot Residue Particles from Brazilian Ammunition Have Morphological Variation **425**  
Silva RC, Oliveira-Santos J, Souza ALM
- Synthesis and characterization of  $\text{Fe}_3\text{O}_4@\text{SiO}_2$  core-shell magnetic microparticles **427**  
Ribas VC, Arguello J, Lavayen V
- Using scanning electron microscopy to evaluate the compatibilizing effect of modified graphene oxide on poly(3-hydroxybutyrate-co-3-hydroxyvalerate)/poly(ethylene-co-vinyl acetate) blend **429**  
Ferreira WH, Silva CA, Andrade CT
- Antibacterial Films On Jarina Seeds Obtained By Plasma Jet Activation Of Copaiba Oil **431**  
Silva YF, Queiroz VM, Yoshihara NMA, Archanjo BS, Oliveira RN, Simão RA
- Enhancing Manufacturing Process of Probes for Near-Field Optical Microscopy **433**  
Oliveira BS, Vasconcelos TL, Archanjo BS, Achete CA
- Thickness Measurement of thin  $\text{HfO}_2$  films via transmission electron microscopy **436**  
Senna CA, Archanjo BS, Achete CA, Damasceno JC, Araújo JR
- Comparison Of Welded Steel Joints S355NL By FCAW With National And Imported Tubular Wire **438**  
Guedes CFP, Fonseca GS, Freitas GCLD, Santos LRL
- An Alternative of Laser Profilometry Technique to Characterization of Morphology and Roughness of a Nanofilm from  $\text{TiO}_2\text{-KOH}$  Over an Aluminium Substrate **440**  
Vaz GVA, Gianelli BF, Rodrigues GN, Sottovia L



Recognition of the Phase Penetration Index in Iron Ore Sample Using Computer Vision and Machine Learning Augusto KS, Iglesias JCA, Paciornik S, Domingues ALA	<b>442</b>
Exposure to 17 $\alpha$ -ethinylestradiol during development period alters the folliculogenesis and the frequency of interstitial gland on the ovary of senile gerbils ( <i>Meriones unguiculatus</i> ) Souza VG, Bandeira LB, Souza NCS, Marques TMM, Taboga SR, Perez APS	<b>444</b>
Plasmonic Nanoparticles as Nanosensors for Indirect of the Substrate Refractive Index Buthers EL, Vasconcelos TL, Archanjo BS	<b>446</b>
Magnetic Arrays made by Lithography from Targets of Pressed Fe <sub>3</sub> O <sub>4</sub> Nanoparticles Perez G, Saitovitch EMB, Archanjo BS, Archanjo BS, Solórzano G	<b>448</b>
Optical and structural properties of Co-doped ZnO nanoparticles Freitas MR, Mattoso N	<b>450</b>
Comparative Study between Comminutions Made in Conventional Ball Mill, Attritor Mill and Planetary Mill Aiming to Obtain Submicrometric / Nanometric Particles of Iron Oxide Martins RC, Cabral AJO	<b>452</b>
Evaluation of Images Before and After Asphalt Binder Indentations Generated In AFM. Macedo TF, Simão RA, Aragão FTS, Leite LFM	<b>454</b>
Analysis of Cracks and Coating in Iron Ore Pellets through Digital Image Processing Caldas TDP, Augusto KS, Iglesias JCA, Paciornik S, Domingues ALA	<b>456</b>
Columnar grain growth of Co <sub>2</sub> FeAl thin films for applications in spintronics Syed AR, Silva BG, Labre C, González-Chávez DE, Correa MA, Sommer RL	<b>458</b>
Use of hollow-cone and centered dark field TEM for characterization of size and morphology of TiO <sub>2</sub> nanorods produced from titanate nanotubes Pereira AF, Paciornik S, Jardim PM	<b>459</b>
Synthesis Of Fe-Fe <sub>3</sub> O <sub>4</sub> @SiO <sub>2</sub> Nanoparticles For Nanomedicine Applications Galeano-Villar B, Caraballo-Vivas R, Finotelli P, Checca NR, Garcia F	<b>461</b>
Imaging chiral spin textures in Pt/Co/Pt multilayers by using Lorentz Transmission Electron Microscopy Labre C, Dutra R, Loreto RP, Silva B G, Chavez DG, Sommer RL	<b>463</b>
Microstructural characterization of the amorphous and nanocrystalline Fe <sub>68</sub> Cr <sub>8</sub> Mo <sub>4</sub> Nb <sub>4</sub> B <sub>16</sub> alloy Coimbrão DD, Wolf W, Almeida FHP, Jorge Junior AM, Zepon G, Botta WJ	<b>465</b>
Process of Deoxidation of Superalloy Nanoparticles Through the Use of Sucrose and L-Ascorbic Acid as Additives in the Process of Chemical Co-Reduction by Borohydride Muchenski F, Tanabe A, Mattoso N	<b>467</b>

Radiation Effect on Morphology of Magnetite Nanoparticles Synthesized by Electron Beam Irradiation Tominaga FK, Jacovone RMS, Garcia RHL, Silva FRO, Sakata SK	<b>469</b>
In situ-TEM of Calcium Phosphate Crystallization and Growth in aqueous medium Dalmônico G M L, Ihiwakrim D, Ortiz N, Ersen O, Farina M, Rossi AM, Rossi AL	<b>471</b>
Multiuser Laboratory of Nanoscience and Nanotechnology For The Development Of The Brazilian Science Coelho Júnior H, Labre C, Amarante JEV, Rossi AL, Sommer RL	<b>473</b>
Combustion Synthesis and AEM Characterization of FeAl <sub>2</sub> O <sub>4</sub> Spinel Moura J, Labre C, Spadotto J, Brocchi E, Solórzano G	<b>475</b>
Structural and Morphological Studies of ZnO Nanosheets Using Graphene Oxide as Template. Lunz JN, Santana CA, Archanjo BS, Vasconcelos TL, Achete CA	<b>477</b>
Study of Small Alloy (AuAg) Nanoparticle Structure using Pair Distribution Function (PDF) derived from Precession Electron Diffraction (PED) Corrêa LM, Moreira MHM, Rodrigues V, Ugarte DM	<b>479</b>
Microstructure and superconductivity in Bi/Ni nanoparticles/thin-film hybrid systems prepared by pulsed laser deposition Liu LY, Xing YT, Merino ILC, Baggio-Saitovitch E, Franceschini DF, Solórzano IG	<b>481</b>
Synthesis and Characterization of Polymeric Nanoparticles Functionalized for Drug Delivery Applied on Osteoporosis Treatment Longuinho MM, Rossi AL, Farina M	<b>483</b>
Transmission Electron Microscopy For The Characterization of Hydroxyapatite Nanostructured From Hen's Eggshell Horta MKS, Moura FJ, Aguilar MS, Campos JB, Ramos VS, Peripolli SB, Navarro MI, Archanjo BS, Quizunda AC	<b>485</b>
Development of an antibacterial composite of calcium silicate incorporated with silver for applications in the area of bone engineering Yoshihara NM, Figueiredo A, Castro KLS, Archanjo BS, Achete CA	<b>487</b>
Stability in Culture Media for Antimicrobial Assays of Reduced Gold Nanoparticles with Extract of <i>Punica granatum</i> L. Oliveira NA	<b>489</b>
Resuspension And Flocculation Analysis Of Gold Nanoparticles Synthesized With Pomegranate Peel ( <i>Punica granatum</i> L.) Valotto RS, Monteiro FC, Keijok WJ, Guimarães MCC	<b>491</b>
Analysis of gold nanoparticles reduced with <i>Virola oleifera</i> resin and their stability in different microbiological growth mediums to possible applies antimicrobial evaluations. Marques RR, Guimaraes MCC	<b>493</b>

Synthesis, characterization and stability analysis of reduced gold nanoparticles with epigallocatechin 3-gallate in microbiological growth medium mueller hinton and cation adjusted Rodriguez SR, Diniz GP, Guimarães MCC	<b>495</b>
Hybrid hydrogels of self-assembled fluorenylmethyloxycarbonyl diphenylalanine as biomaterial matrix Vassiliades SV, Arguello KAB, Aguilar AM, Nantes-Cardoso IL, Giuntini F, Alves WA	<b>497</b>
Analysis of Precipitates of a <i>Maraging</i> 350 Steel Undergoing Thermomechanical Treatments Santana SIV, Brandao LP	<b>499</b>
Formation of Nanocrystalline Borides in Superduplex Steels with Boron Additions Processed by Rapid Solidification Berger JE, Botta WJ, Kiminami CS, Bolfarini C, Moreira AJJ, Mendes VAS	<b>501</b>
Study Osseointegration at Coating SiC With and Without TiO <sub>2</sub> in Substrat SS316L. Vieira AA, Godoi BH, Moraes CDGO, Albuquerque ALG, Silva SA, Vasconcelos G, Vieira L, Pacheco-Soares C, Silva NS	<b>503</b>
Mechanically Induced Phase Transformation in the biocompatible Ti-13Nb-13Zr Alloy Processed By High-Pressure Torsion Pérez DAGG, Mendes VAS, Lepretre JC, Roche V, Bolfarini C, Botta WJ, Jorge Junior AM	<b>505</b>
Factorial Planning Of Directed Biosynthesis Of Gold Nanoparticles Reduced And Stabilized With <i>Coffea Arabica</i> . Keijok WJ, Pereira RHA, Prado AR, Silva AR, Ribeiro J, Oliveira JP, Guimarães MCC	<b>507</b>
The Relationship Between Perpendicular Magnetic Anisotropy (PMA) of (CoFe/Pt) <sub>5</sub> Multilayers and the Crystallinity of the Buffer Layer Schmidt W, Outon L, Martins M	<b>509</b>
A Microstructural Study on Different Phases in a Heat Treated AISI-SAE 430 Ferritic Stainless Steel by SEM/EDS/EBSD Barbosa C, Cunha RPC, Gonzaga AC	<b>511</b>
Characterization of Oxides Formed in Stainless Steels Welded Joints by EBSD Technique Oliveira LG, Peripolli SB, Beltrão MAN, Carvalho LP, Pecly PHR	<b>513</b>
Evaluating the Microstructure of C-Mn Steel Weld Deposits Jorge JCF, Mendes MC, Souza LFG, Araújo LS, Bott IS, Evans GM	<b>515</b>
Evaluating the Microstructure of Steel Weld Deposits. Part 2: High Strength Steels. Jorge JCF, Mendes MC, Souza LFG, Araújo LS, Bott IS	<b>517</b>
The use of 3D Misorientation spaces in the study of phase transformation of iron oxides: a case study of Carajás Iron Formations' oxide assembly using EBSD data. Mota e Nogueira V, Barbosa PF, Mayanna S, Silva AM, Toledo CLB, Assis LC, Bracioli MC	<b>519</b>

Micro-Raman spectroscopy and Electron probe micro-analyzer techniques applied to the gemological study and identification of Paraíba tourmaline liddicoatite. Mota e Nogueira V, Fava N, Kafino CV, Lima EAM, Barbosa PF, Bracioli MC	<b>521</b>
Microstructure evaluation and lamellae spacing of the cementite from the HSLA steel DIN 38MnSiVS5 over different cooling process. Gianelli BF, Rodrigues GN, Silva MLN	<b>523</b>
Raman Spectroscopy on Twisted Bilayer Graphene Engineered by Atomic Force Microscopy França CM, Lacerda MM, Almeida CM	<b>525</b>
Raman Characterizations of Low Cost Electrochemical Sensor Made with Recycled PET and Graphite Agustini D, Santos LGM, Bergamini MF, Marcolino-Junior LH	<b>527</b>
Interface Analysis of ASME SA516-70 / Inconel 625 Bimetal Plate Obtained by Explosion Welding Employing Atomic Force Microscopy Rodrigues GN, Gianelli BF, Nossa TS	<b>529</b>
Control of the Electromechanical Properties of Transition Metal Dicalcogenides Bessa MV, Freitas WD, Neme NP, Mazzoni MSC, Matos MJS, Neves BRA, Barboza APM	<b>531</b>
Development Of Chitosan-Coated Liposomes For Octylmethoxycinnamate Encapsulation Applied In Sunscreen Formulations Castro NR, Pinto CSC, Mansur CRE, Santos EP, Campos VEB	<b>533</b>
Different Samples Preparation Method for Electron Microscopy Assisting the Comprehension of Vanadium Nanostructures. What can be seen inside the particle? Moreira CR, Pozes BB, Farias AMD	<b>534</b>
Design of ZnO structures: growth and formation mechanism determined from the correlation of morphological, structural, vibrational and optical properties Montero-Muñoz M, Ramos-Ibarra JE, Félix CML, Teodoro MD, Marques GE, Coaquira JAH	<b>536</b>
Synthesis of Supported Nickel Catalysts in Yttria-Modified by Alumina Characterized by Electron Microscopy for H <sub>2</sub> Generation Costa LOO, Gonçalves VV, Souza EJN, Silva MA, Moreira CR, Noronha FB	<b>538</b>
S(TEM) Preliminary Characterization of a Cs-P-V-W-O Mixed Pyrochlore Oxide. Licea YE, Eon JG, Werckmann J	<b>540</b>
SEM and TEM Characterization of Titanium Oxides Recovery from Tailing of Magnetite Concentration Valente AM, Brocchi EA, Solórzano G	<b>542</b>
Grain Refinement and Residual Stress in an ASTM 201LN Austenitic Stainless Steel Cold Rolled and Reversion Annealed Souza CO, Paula AS	<b>544</b>
Cryogenic Sample Preparation for Cryo-TEM of Metals by Ion Milling	<b>546</b>

Namur RS, Bettini J, Cintho OM

Cryogenic Sample Preparation for Cryo-TEM of Metals by Cryo-Ultramicrotomy **548**  
Namur RS, Bettini J, Cintho OM



Caros leitores e companheiros de pesquisa,

O mundo da microscopia é constituído por um amplo conjunto de instrumentos e metodologias de análise que evoluem de forma incessante. Estes equipamentos servem aos campos da Ciência dos Materiais, Biologia, Metalurgia, Medicina, Física, Farmácia, Geologia e Ciência Forense com inúmeras aplicações na área industrial e em empresas prestadoras de serviços.

Um rápido olhar para a história da microscopia mostra que desde os patriarcas da Nova Ciência do Século XVI até os desdobramentos da Ciência Moderna do Século XX, as reuniões científicas têm tido um papel fundamental na troca de experiências entre diferentes campos do conhecimento. Esta intensa troca tem nos conduzido neste início do século XXI a um momento de convergência de diferentes tecnologias integradas em equipamentos cada vez mais sofisticados na sua capacidade ampliada de proporcionar respostas a perguntas científicas e tecnológicas mais complexas.

**Nesse caminho, o 27º Congresso Brasileiro de Microscopia e Microanálise da SBMM buscou atrair os mais importantes pesquisadores nacionais e estrangeiros para criar um ambiente de intensa troca de experiências com estudantes, profissionais e técnicos da área de microscopia.**

Nestes anais, estão reunidos os resumos das exposições orais e dos pôsteres apresentados no 27º CSBMM. A publicação desses trabalhos tem como objetivo compartilhar os debates científicos realizados na ocasião, fomentando o estabelecimento de vínculos colaborativos entre diferentes núcleos de pesquisa e fortalecendo o compromisso da SBMM com a consolidação de uma atmosfera de constante formação de recursos humanos de alto nível no Brasil.

Desejamos um proveitosa leitura!

**Diretoria da SBMM (2018-2020)**



# PARTE 1

## COMUNICAÇÕES ORAIS - BIOLOGIA

# Biomimetic Calcium Phosphate Films Synthesized by Pulsed Laser Deposition for Biomedical Applications

N. R. Checca<sup>1</sup>, A. Mello<sup>1</sup>, A. M. Rossi<sup>1</sup> and A. L. Rossi<sup>1</sup>

<sup>1</sup>Brazilian Center for Physics Research, Rio de Janeiro, Brazil.  
nomifsc@gmail.com

Bone is a sophisticated and hierarchical structure with a complex arrangement between the organic and inorganic mineral phases (in different length scales), which directly affects its functional and physical–chemical properties [1]. Biomimetic strategies are used to improve the designs of materials as for instance producing films with nano/micro topography similar to bone aiming to obtain a microenvironment which stimulate bone tissue regeneration [2]. Roughness with values between micrometers to nanometers can be recognized by cells via cell membrane receptors and generate osteogenic differentiation [3]. The micrometer scale roughness increases the matrix protein adsorption, bone cell migration and proliferation, bone anchorage and finally osseointegration [4]. Therefore, these characteristics are desirable in the implant topography for biocompatibility and bioactivity of the biomaterial [5]. In this context, this work focuses on obtaining biomimetic surfaces composed of calcium phosphates (CPs) particles with micron/nano-topography synthesized by pulsed laser deposition (PLD). The PLD deposition combined with different gases and pressures offers a powerful platform for the synthesis of CPs films with different proprieties and free from products of chemical reactions. The ablation starts within the laser energy and the released particles undergo multiple collisions with the environment gas molecules, making possible the nucleation and growth of the particles before deposition on the substrate ('on-the-flight') [6]. The deposition of these particles, ions and clusters over the substrate of silicon produced a coating with a nano/micro topography. CaPs particles were deposited on substrate via a custom in-house equipment of pulsed laser ablation designed at the Brazilian Centre for Physics Research. The substrates were fixed at a distance of  $30 \pm 1$  mm from the target (hydroxyapatite) surface. Argon and oxygen gases were maintained at 1 Torr in the chamber. A Quantel Brilliant b Q-switched Nd:YAG laser source with 9 ns pulse duration and 10 Hz repetition rate was used and the first two harmonics of the laser with wavelength of 1064 nm and 532 nm. The particles were collect at room temperature (25 °C) by a time of 20 min. Our study focuses in the morphological, structure and composition of the surface at the micro and nanoscale by **SEM**, **DRX**, **XPS**, **FTIR**, **EDS** and **FIB-SEM** with the objective of understanding the morphology, crystallinity and phase of the particles as a function of the deposition parameters. Our results demonstrate that the surfaces exhibited micro-nano topography, specifically a mixture of spherical amorphous particles with crystalline particles as shown in FIG. 1(III). The surface between the three samples was different due to the PLD parameters used. The crystalline to amorphous phase mass proportion in G-300(Ar), IR-600(Ar) and G-300(O) was 68, 56 and 44%, respectively (FIG. 1(II)).

## REFERENCES

- [1] Furqan A. et al., *Acta Biomaterialia*. 84 (2019)1.
  - [2] Tian, Qiaomu et al., *Scientific Reports*, 6 (2019)2045.
  - [3] Sibio Shen et al., *Chemical Engineering Journal*, 339 (2018)7.
  - [4] David M. Dohan Ehrenfest et al., *Trends in Biotechnology*, 28 (2010)198.
  - [5] Rolando A. Gittens et al., *ActaBiomaterialia*, 10(2014)1742.
  - [6] N.R. Checca et al., *Materials Chemistry and Physics*, 196(2017)103.
- This research was supported by FAPERJ, CNPq and LABNANO/CBPF (Brazil).

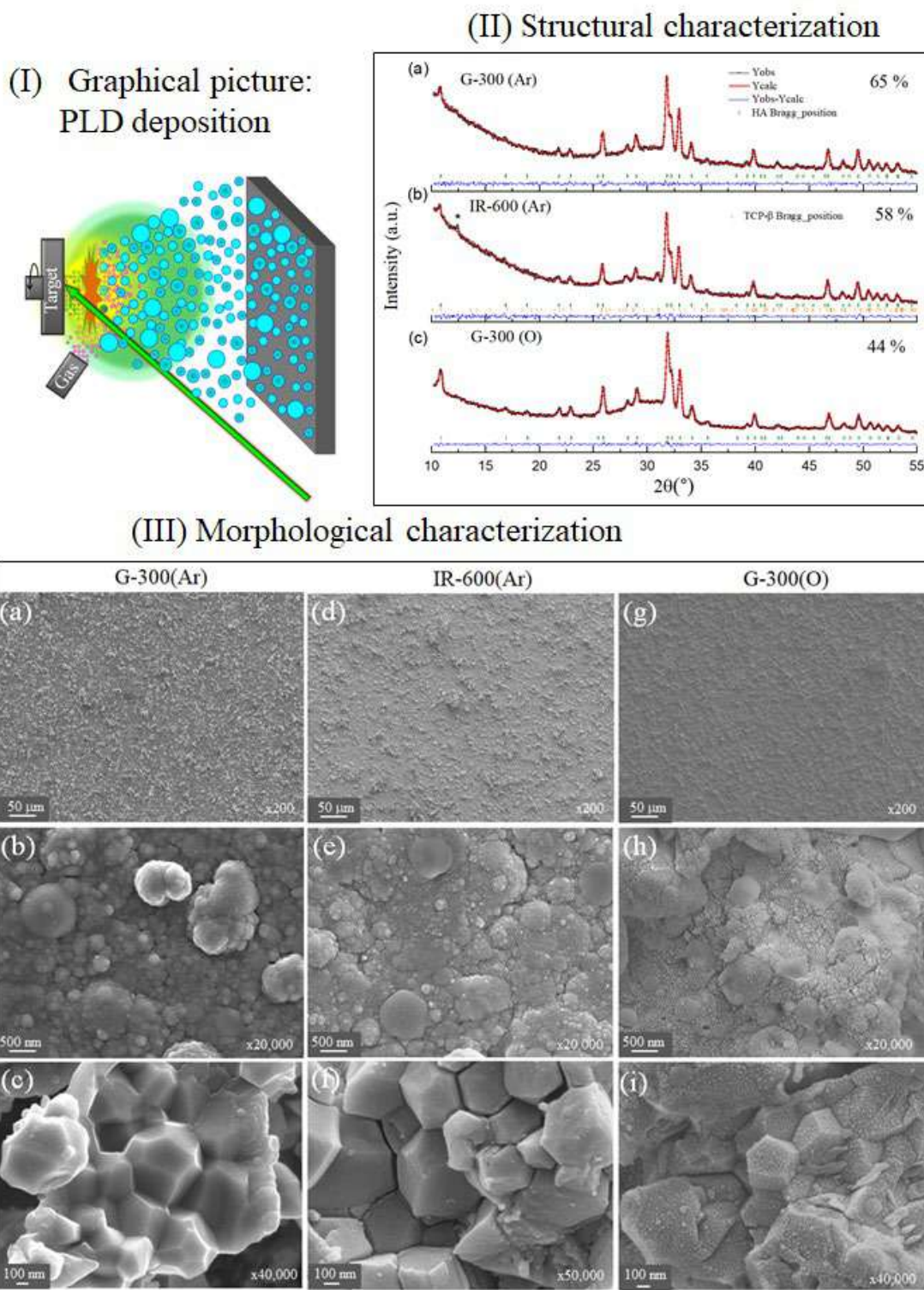


FIG. 1: (I) Graphical picture of the technique of PLD for the synthesis of particles; (II) Structural characterization of films using XRD, the diffractograms are presented with their respective adjustments with the crystalline to amorphous phase mass proportion and (III) SEM images showing the three surfaces corresponding to sample G-300(Ar), IR-600 (Ar) and G-300 (O), in different magnifications. Note: the surfaces are composed of three different morphologies: spherical particles, crystals and splashes 'type - drops'.

## Automated Machine Learning Pipeline Predicts *Cryptococcus* spp. Capsular Morphotypes in Scanning Electron Microscopy Images

William Lopes<sup>1</sup>, Giuliano N. F. Cruz<sup>2</sup>, Mendeli H. Vainstein<sup>3</sup>, Marilene H. Vainstein<sup>1</sup> and Augusto Schrank<sup>1\*</sup>

<sup>1</sup>. Centro de Biotecnologia, Universidade Federal do Rio Grande do Sul, Porto Alegre, Brazil. \*aschrank@cbiot.ufrgs.br

<sup>2</sup>. Neoprospecta, Florianópolis, Brazil.

<sup>3</sup>. Departamento de Física, Instituto de Física, Universidade Federal do Rio Grande do Sul, Porto Alegre, Brazil.

Phenotypic heterogeneity is an important trait for the development of microbial populations [1]. A deadly pathogen spread worldwide, *Cryptococcus* spp., also shows morphological characteristics strongly associated with virulence and fitness [2]. Infections caused by this yeast kill 180.000 people around the world every year [3]. Regarding *Cryptococcus* spp. pathogenicity, an important trait is capsule presence, which is well described at the molecular level and a good deal of methodologies has been applied to its description [4]. The understanding of capsular morphotypes in *Cryptococcus* spp. is currently possible through electron microscopy technologies, being essential to therapy development and description of microorganism interactions. Here, we have applied Scanning Electron Microscopy (SEM) to define four *Cryptococcus* spp. capsular morphotypes, namely Regular, Spiky, Bald, and Ghost, which are persistently seen in varying proportions among isolates (figure 1). We constructed an automated pipeline capable of (1) identifying potentially cell-associated objects in the SEM-derived images; (2) computing object-level features; and (3) classifying these objects into their corresponding classes, e.g., cell types or artifacts [5]. The machine learning approach used a Random Forest (RF) classifier whose overall accuracy reached 86% on the test dataset, with per-class specificity above 90%, and sensitivity between 66 and 94%. Additionally, the RF model indicates that structural features, e.g., object area and eccentricity, are most relevant for classification, followed by texture. Our methodology allowed automated annotation of original images, thereby enabling application in future SEM-based experiments to further describe the influence of capsular morphotypes in *Cryptococcus* spp. development and infection. Rather than providing a production-ready algorithm, our work paves the way for machine learning approaches focused on the study of clinically-relevant microbial phenotypes using electron microscopy technologies.

- [1] Weigel, W.A. and P. Dersch, *Phenotypic heterogeneity: a bacterial virulence strategy*. Microbes Infect, 2018. **20**(9-10): p. 570-577.
- [2] Wang, L. and X. Lin, *The morphotype heterogeneity in Cryptococcus neoformans*. Curr Opin Microbiol, 2015. **26**: p. 60-4.
- [3] Rajasingham, R., et al., *Global burden of disease of HIV-associated cryptococcal meningitis: an updated analysis*. Lancet Infect Dis, 2017.
- [4] Guess, T., et al., *Size Matters: Measurement of Capsule Diameter in Cryptococcus neoformans*. J Vis Exp, 2018(132).
- [5] Efron, B. and T. Hastie, *Computer Age Statistical Inference by Bradley Efron*. 2016.
- [6] This research was supported by CNPq (Brazil).



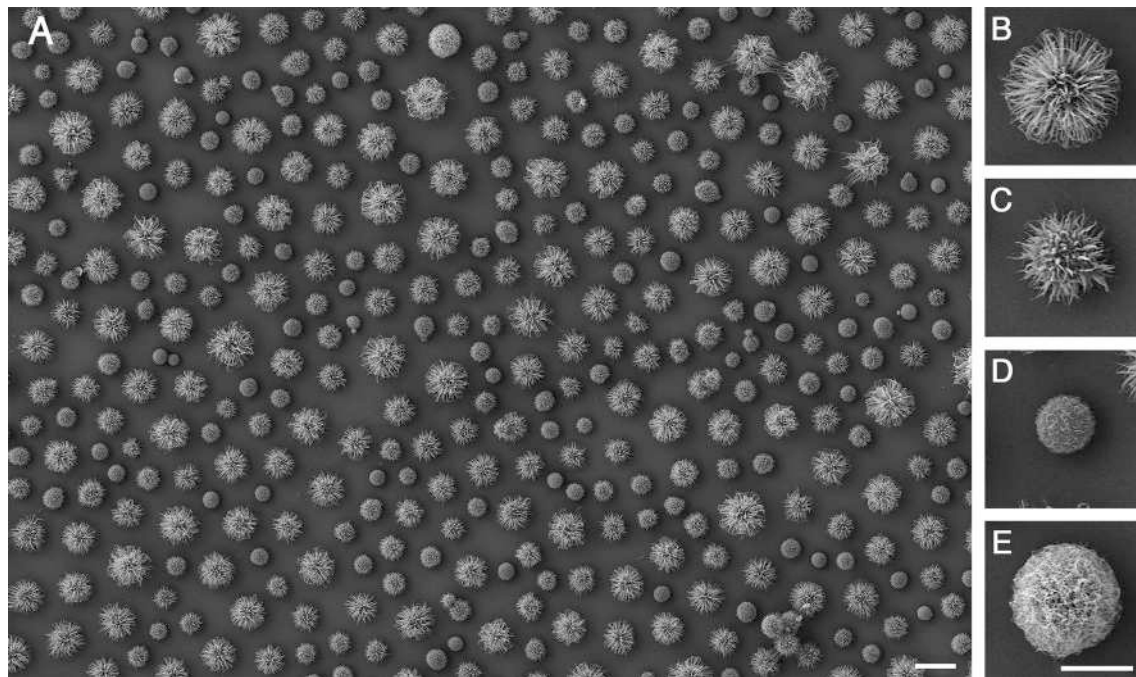


**Figure 1. Morphological diversity of *Cryptococcus* spp. capsule.** Scanning electron microscopy (SEM) of *Cryptococcus gattii* (clinical isolate). (A) SEM image showing the coexistence of different morphotypes, which were classified based on their morphological characteristics, such as: capsule abundance, thickness, size and texture. The capsular morphotypes were named: regular (Fig. 1B), spiky (Fig. 1C), bald (Fig. 1D) and ghost (Fig. 1E). Scale bars: 10  $\mu\text{m}$  (A) and 5  $\mu\text{m}$  (B-E).

# STRUCTURAL CHARACTERIZATION OF POLY ( $\epsilon$ -CAPROLACTONE) NANOCAPSULES THROUGH ADVANCED TECHNIQUES OF SCANNING ELECTRON MICROSCOPY

Thaniele Müller Ramos <sup>1\*</sup>, Silvia Stanisçuaski Guterres <sup>2</sup>

1 Pharmacy Faculty /PPGNanoFarma/UFRGS, Porto Alegre, Brazil  
(thaniele@gmail.com)

2 Pharmacy Faculty / Department of Medicines Production and Control/UFRGS, Porto Alegre, Brazil (silvia.guterres@ufrgs.br)

Polymeric nanocapsules are biomaterials and carriers of drugs widely used in the pharmaceutical and cosmetic industry. These systems are of great importance also due to the innumerable therapeutic applications, mainly for parenteral, oral or ophthalmic administration. One of the most promising areas in the use of nanocapsules is the vectorization of anticancer drugs and antibiotics. However, the nanometric size becomes a challenge for the structural characterization of this biomaterial. [1,2] In this work, techniques of scanning electron microscopy by field emission gun (FEG) and focused ion beam (FIB) [3] were used to characterize nanocapsules produced from a polyester, poly ( $\epsilon$ -caprolactone) -PCL. [4] Polymer nanocapsules suspensions were prepared by the preformed polymer interfacial deposition method (nanoprecipitation) and subsequent dried by nebulization in spray-dryer with Aerosil® 200 3% used as a drying aid. [5] The polymer nanocapsules had their particle diameter and SPAN verified by the laser diffraction technique. [6] Afterwards, they were analyzed in Auriga-Zeiss dual-beam equipment using FEG-SEM and FIB-SEM techniques.[7] For comparison, the isolated drying adjuvant was analyzed as control group using the same techniques. The nanocapsules presented spherical morphology and organization in microclusters (see example in Figure 1). Comparing with the control, it's suggested that the microclusters have silica inside and coating of polymeric nanocapsules, it was possible to see by the FIB-SEM technique (Figure 2). [8] The dual-beam equipment employed represented a very appropriate tool for characterization in improved resolution of these studied nanomaterials compared to previous studies, being possible to obtain some new data. [9] The future perspectives are to characterize other formulations of nanocapsules frequently used by our research group using FEG-SEM and FIB-SEM techniques of scanning electron microscopy, as well as to improve the results obtained in the analysis between substrate and applied pharmacological treatment.

**Keywords:** polymer nanocapsules - poly ( $\epsilon$ -caprolactone) - FEG-MEV - FIB-MEV - scanning electron microscopy

## References:

- [1] R. Singh; J. W. Lillard Jr. *Exp Mol Pathol.* 86 (3) (2009) 215.
- [2] A. R. Pohlmann et al. *Eur. J. Pharm. Science.* 16(4-5) (2002) 305.
- [3] B.A Dedavid, C.I Gomes, G. Machado. EDIPUCRS (2007).
- [4] P.P. Santos et al. *Trends in Food Sci &Tech.* 53 (2016) 23.
- [5] K.C.B. Souza et al. *Drug Dev. Ind. Pharm* 26(3) (2000) 331.
- [6] R.V Contri et al. *Int J. Nanomedicine.* 12(9) (2014) 951.
- [7] W. D Callister Jr, D. G. Rethwisch. *Ltc.* 2013.
- [8] A.R. Pohlmann et al. *Expert Opin Drug Deliv.* 10(5) (2013) 623.

[9] V. Klang et al. *Micron* 44 (2013) 45.

[10] This research was supported by Capes (Brazil). Thanks the CMM-UFRGS for the infrastructure for microscopic analysis.



Figure 1: Aggregation of several microclusters formed by PCL nanocapsules with silica drying adjuvant. Image realized by FEG-SEM in a Auriga-Zeiss microscope.

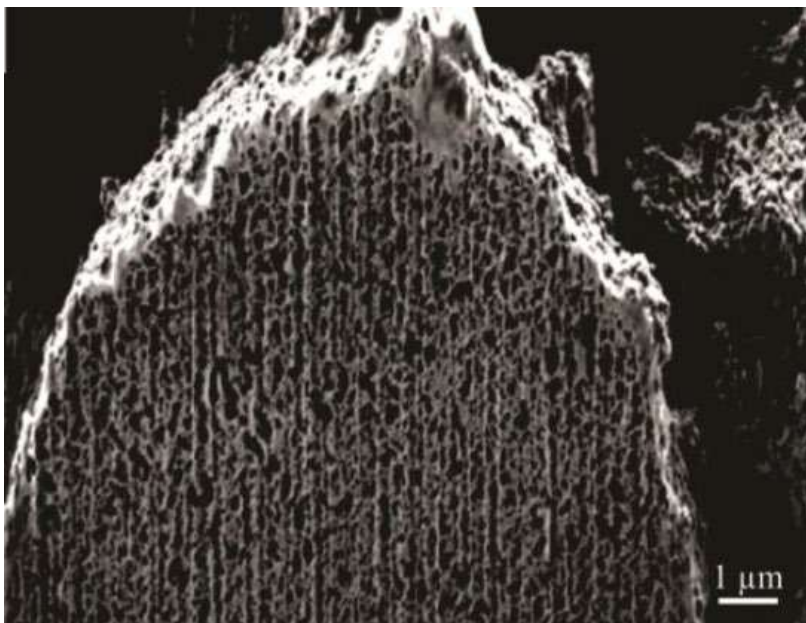


Figure 2: Tomography performed in a microcluster formed of PCL nanocapsules with silica drying adjuvant. Image realized by FIB-SEM in a Auriga-Zeiss microscope.





## Origin Of Multivesicular Bodies In *Giardia intestinalis* And Its Behavior During The Parasite Life Cycle

Victor Midlej<sup>1,2,\*</sup>, Wanderley de Souza<sup>1</sup> and Marlene Benchimol<sup>1,3</sup>

<sup>1</sup>. Laboratório de Ultraestrutura Celular Hertha Meyer, Instituto de Biofísica Carlos Chagas Filho, Instituto Nacional de Ciência e Tecnologia and Núcleo de Biologia Estrutural e Bioimagens-CENABIO, Universidade Federal do Rio de Janeiro – UFRJ, Rio de Janeiro, Brasil.

<sup>2</sup>. Instituto Oswaldo Cruz, FIOCRUZ, Rio de Janeiro – Brasil.

<sup>3</sup>. Universidade do Grande Rio-Unigranrio, Duque de Caxias, Rio de Janeiro, Brasil.

\*.vmidlej@hotmail.com

*Giardia intestinalis* is a protozoal parasite that infects mammals, including humans, by proliferating in the gastrointestinal tract causing a disease known as giardiasis. Diarrhea is the main symptom of a giardiasis infection, and transmission between different species is commonly observed, thus characterizing giardiasis as a zoonotic disease. The parasite presents an intriguing endomembrane system, which includes the endoplasmic reticulum and peripheral vesicles (PVs). Although typical lysosomes are not found, there are a number of PVs with acid phosphatase activity, which accumulate macromolecules ingested by the protozoan [1]. Recently, it was shown *G. intestinalis* releases microvesicles that contribute to parasite pathogenesis [2]. However, where these microvesicles are originated and how they are released remains unclear. In the present study we analyzed the origin of multivesicular bodies (MVB) in the PVs and its profile during encystation. To investigate the behavior of PVs during the cell cycle, *G. intestinalis* were grown in conventional medium and were induced to encyst *in vitro*. We used advanced microscopy techniques in Transmission electron microscopy (TEM), High Resolution Scanning Electron Microscopy (HR-SEM), Electron Tomography (ET) and Dual-Beam microscopy (DBM) in order to better understand the biogenesis of MVBs. A cytochemical localization of acid phosphatase was performed in both vegetative and encysting cells. ET and DBM presented MBV inside the PVs. Moreover, during the encystation process, a membrane fusion of MVBs was observed and thus characterized as an exocytosis event. We also observed exocytosis of microvesicles by TEM and HR-SEM. In conclusion, a change of PVs behavior occurs during parasite differentiation. We observed a partial translocation of acid phosphatase from peripheral vesicles to the plasma membrane and MVBs inside PVs, suggesting a possible role during parasite differentiation. We show that some PVs of vegetative trophozoites exhibited morphological characteristics of MVBs, harboring intraluminal vesicles (ILVs) with a mean diameter of 50 nm.

[1] Lanfredi-Rangel et al., J. Struct. Biol. 123 (1998) 225.

[2] Evans-Osses et al., Eur. J. Cell Biol. 96 (2017) 131.

[3] This research was supported by UFRJ, CAPES, CNPq, FAPERJ and CENABIO.

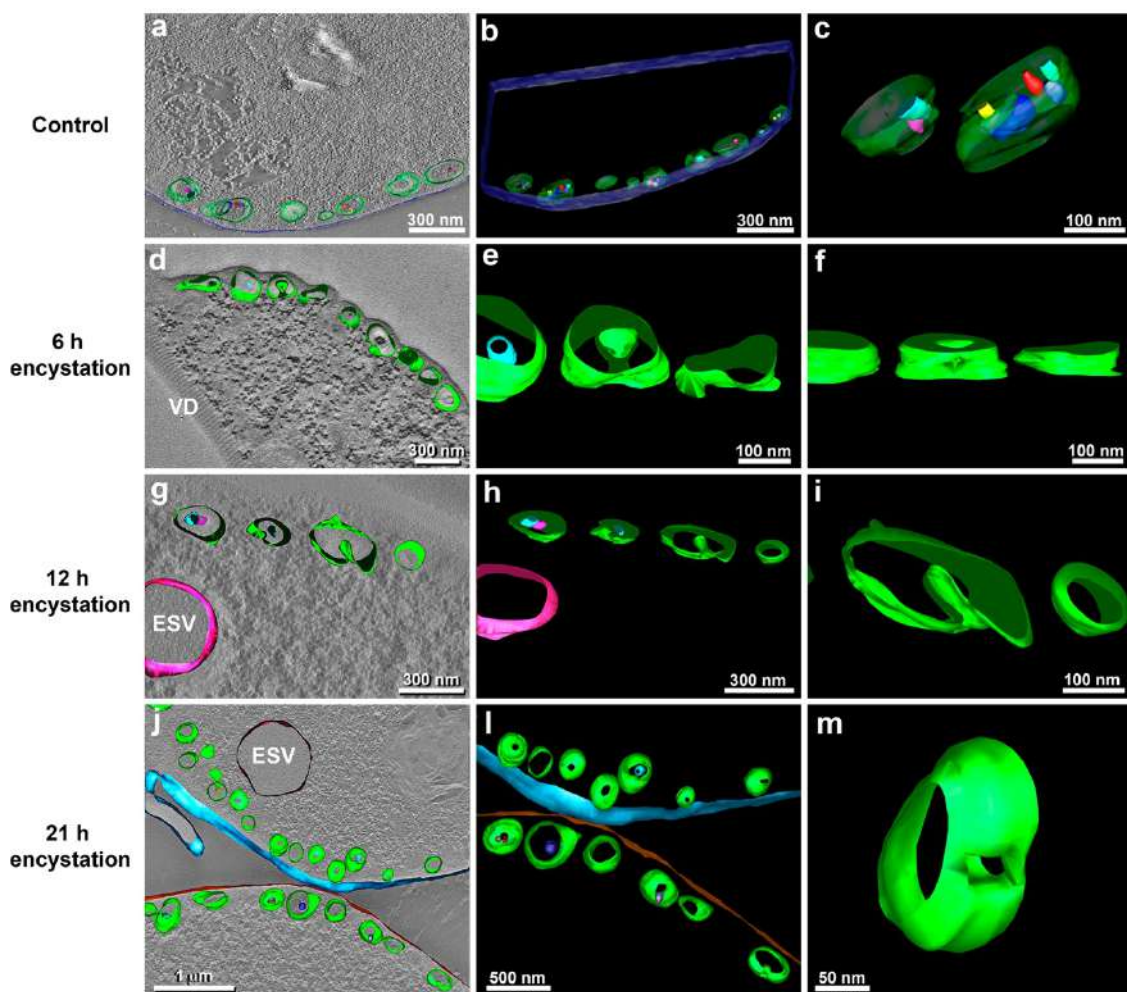


**Figure 5. Morphogenesis of *G. intestinalis* nano-vesicles during encystation.** Electron tomography of non-encysted (a–c) and encysted (d–m) parasites showing tomographic 3D reconstruction of peripheral vesicles (PVs) consisting of MVBs inside. (a–c) Vegetative trophozoites are seen presenting PVs as MVBs. Almost all PVs in this micrograph carry intraluminal vesicles (ILVs) inside (b); some PVs are harboring a number of ILVs (c). All ILVs are seen to be individually packed within MVBs. The parasites were induced to encyst *in vitro* for 6 h (d–f), 12 (g–i), and 21 h (j–m). In early stages of encystation, 6 and 12 h (d–i), it is possible to observe a connection between the PVs/MVBs' and ILVs' membranes (e and f, h and i, respectively). This type of membrane linkage can still be noted during late encystation stages, 21 h after induction (j–m). At this point, the connection of the ILV with PV/MVB membrane can also be seen (m). An overlay of tomographic virtual slices and 3D models are shown in figures a, d, g, and j. ESV, encystation specific vesicles; VD, ventral disc.

## Biogenic Magnetic Nanoparticles, a Novel Tool to Treat Synaptic Deficit Diseases and Glioblastoma

Gabriele Vargas<sup>1</sup>, M. Verdan<sup>1</sup>, T. Correa<sup>1</sup>, L. A. Ketzer<sup>2</sup>, Dennis A. Bazylnski<sup>3</sup>, Flávio Garcia<sup>4</sup>, L. Romão<sup>5</sup>, F. Abreu<sup>1\*</sup>.

<sup>1</sup> Institute of Microbiology Paulo de Góes, Federal University of Rio de Janeiro, Rio de Janeiro, Rio de Janeiro, Brazil.

<sup>2</sup> NUMPEX-Bio, Federal University of Rio de Janeiro, Duque de Caxias, Brazil.

<sup>3</sup> School of Life Sciences, University of Nevada at Las Vegas, Las Vegas, Nevada, USA.

<sup>4</sup> Brazilian Center for Physical Research, Rio de Janeiro, Rio de Janeiro, Brazil.

<sup>5</sup> Institute of Biomedical Sciences, Federal University of Rio de Janeiro, Rio de Janeiro, Rio de Janeiro Brazil.

\*fernandaaabreu@micro.ufrj.br

**Key words:** super resolution fluorescence microscopy, confocal microscopy, 3D reconstruction, magnetotactic bacteria, magnetosome, magnetic nanoparticles, neuroscience.

Nanoparticles are promising useful tools in biotechnology. In particular, magnetic nanoparticles are of great interest in Nanomedicine because they can be easily manipulated through the application of an external magnetic field [1,2]. Currently, the synthesis of most types of nanoparticles is through non-biological, chemical processes often with the generation of toxic residues and, in most cases, without the strict control of the size and shape of the synthesized magnetic nanoparticles. Magnetotactic bacteria (MTB) are capable of biomineralizing membrane-bounded magnetite or greigite nanocrystals with well-defined sizes and shapes, called magnetosomes (BM) [3]. One of the major advantages of the use of BMs is the phospholipid bilayer surrounding each nanoparticle. This structure is responsible for anchoring proteins involved in biomineralization of the BMs and creating an appropriate environment for this process. The presence of this membrane ensures that BMs are naturally biocompatible, making additional coating processes used in artificially synthesized magnetite nanoparticles unnecessary [4]. Furthermore, because of the presence of proteins in the membrane of BMs, they can be easily functionalized with different classes of molecules. Therefore, the culturing of MTB at large scale and the purification of BMs represent an environmentally friendly method to produce biocompatible, magnetic nanoparticles [4]. Functionalized BMs have already been tested as drug carriers, image contrast agents, antigen and DNA scavengers among other uses [4]. Research in this area has been focused mainly on biomedical applications, particularly, in magnetic hyperthermia and drug delivery [4]. Here we propose the use of functionalized BMs as regenerative and antitumor agents in neuroscience. The application of synthetic magnetic nanoparticles in neuroscience has showed significant advances in the area of neural regeneration and treatment of glioblastoma. Thus, we evaluated the cytotoxicity and localization of BMs after interaction with murine cortical neurons. Based on conventional cytotoxic tests and respirometry assays, BMs are not neurotoxic. Preliminary data suggest that BMs coated with poly-L-lysine are capable of stimulating the growth of neurites of cortical neurons by the increase of  $\beta$  tubulin III, a cytoskeletal marker, suggesting that BMs are involved in the modulation of neuronal arborization. Thus, BMs may represent an alternative to the use of artificially synthesized nanoparticles as potential therapeutic

approaches for synaptic deficit diseases, as Alzheimer or Parkinson. Super resolution fluorescence microscopy and 3D reconstruction using 3Dmod (IMOD Software) showed that BMs are internalized by neurons until 24 hours of incubation, without having a toxic effect on cells or modifying their metabolic rate. This result suggests that BMs are potentially good antitumor agents if used in magnetic hyperthermia therapy. In general, tumor cells internalize particles faster than normal cells, so magnetic hyperthermia therapy with BMs may selectively act on tumor cells. Our initially tests with BMs against ATCC U87 human glioblastoma model reveled that in 3 hours of interaction followed by 20 min with alternating magnetic field at 200 Gauss / 304 kHz, 15% of tumor cells was eliminated. Higher efficiency in tumor cell death will be probably be achieved by increasing the incubation time with BMs due to the increase in the internalization rate of these cells. In summary, based on their natural biocompatibility, neuronal modulation capability and magnetic properties, BMs thus represent an unprecedented tool for the development of new treatment approaches in nanomedicine.

**References:**

- [1] C.C. BERRY et al, *Frontiers Of Nanoscience*, Amsterdam Elsevier. 4 (2012) 159-180.
- [2] M.G. KRUKEMEYER et al. *J Nanomed Nanotechnol*. 6 (2015) 336.
- [3] D.A. BAZYLINSKI AND R.B. FRANKEL, *Nat Rev Microbiol*. 2 (Suppl. 3) (2004) 217-30.
- [4] G. VARGAS et al, *Molecules*. 23, (2018) 2438.

**Financial support:** FAPERJ, CAPES, CNPq.

## The Use Of The Myenteric Neurons Of The Fish As Environmental Impact Biomarker

GONÇALVES, A.R.N<sup>1\*</sup>, MARINSEK, G.P<sup>1</sup>, ABESSA, D.M.S<sup>1</sup>, MARI, R.B<sup>1</sup>

<sup>1</sup>. São Paulo State University – UNESP – Biosciences Institute – Coastal Campus, São Vicente – SP, Brasil. Email:alexandrerodrigong@hotmail.com.

The food route is one of the main routes of exposure of aquatic organisms to contaminants, mainly through the ingestion of food, water, and contaminated sediment [1,2]. In this sense, the gastrointestinal tract (GIT) and the enteric nervous system (ENS) are in direct contact with these compounds, which makes them potential biomarkers of environmental impact [3]. Based on this, the objective of this work was to verify the alterations in the ENS of the puffer fish *Sphoeroides testudineus* caused by different levels of ambient pollution. Therefore, ten animals were collected in three distinct regions as sources of contamination and public uses policies: the Juréia-Itatins Ecological Station (RA - an integral protection area), the estuarine lagoon system of Cananéia-Iguape (A1 - a marine protected area (MPA) that suffers with the presence of heavy metals) and Santos-São Vicente Estuary Complex (A2 - an extremely urbanized and industrialized area). Then the neuronal density/mm<sup>2</sup> of three myenteric neuronal subpopulations of the distal intestine (figure 1) was obtained, being: the general population, evidenced by the Giemsa technique, the metabolically active population (NADH-d<sup>+</sup>), evidenced by the NADH-dr technique and the nitrergic subpopulation (NADPH-d<sup>+</sup>), evidenced by the technique of NADPH-dr. Posteriorly, the density of the cholinergic subpopulation (NADPH-d<sup>-</sup>) was calculated using the difference between the general and nitrergic subpopulations. After the analysis, differences (ANOVA, p <0.05) were performed in relation to the densities of the observed neuronal subpopulations. Among, reductions of 20% in the general subpopulation density and 40% in the density of the NADPH-d<sup>-</sup> subpopulation compared to RA animals. Moreover, in comparison with RA animals, the density of 40% higher nitrergic neurons was observed in A2 animals. It is known that there is greater fragility of the cholinergic neurons and greater resistance of the nitrergic neurons to the stressors agents [3,4,5]. Therefore, it is suggested that the reduction of the general subpopulations and the NADPH-d<sup>-</sup> occurred by neuronal death, mainly in the cholinergic subpopulation. The increases of the density of NADPH-d<sup>+</sup> subpopulation can be explained by the increase in the expression of the nitric oxide (NO) through the phenomenon of co-localization, as a form of resistance of the myenteric neurons to the contaminants. In the comparison between the A1 and RA animals, the decreases (ANOVA, p > 0.05) in the general subpopulations and NADPH-d<sup>-</sup> densities were observed, with a 20% increase in density of the NADH-d<sup>+</sup> subpopulation, suggesting increase metabolic activity as a form of maintenance of homeostasis. Through these results, it was concluded that in different areas, with different levels of anthropic impact, different changes in myenteric neuronal plasticity were observed, indicating ENS as a good biomarker of environmental impact.

### REFERENCES

- [1] D.M. Abessa, et al.. Marine Pollution Bulletin, 2005.
- [2] V.I. Lushchak. Aquatic Toxicology, 2011.
- [3] G.P.Marinsek. Marine Pollution Bulletin, 2018.
- [4] K. Szymanska, S. Gonkowski.. Neurotoxicology, 2018.
- [5] C.G. Souza Melo, et al. Scientific Reports, 2017



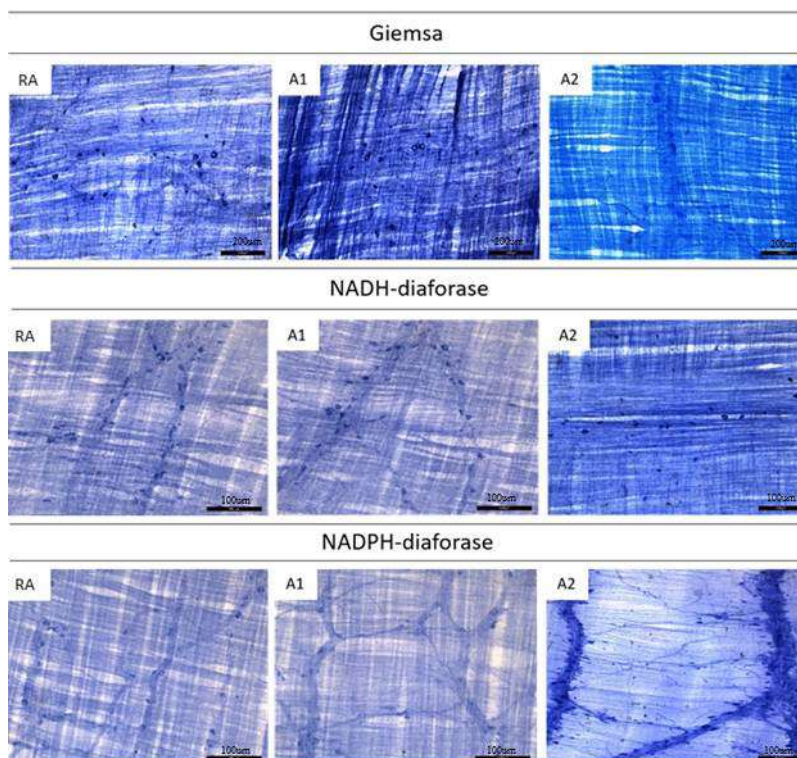


**Figure 1.** Photomicrography of the general (Giemsa), NADH-d<sup>+</sup> and NADPH-d<sup>+</sup> myenteric neurons population of the *Spherooides testudineus* collected at reference area (RA), Santos-São Vicente Estuary Complex (A1) and Lagoon System of Cananéia-Iguape (A2).

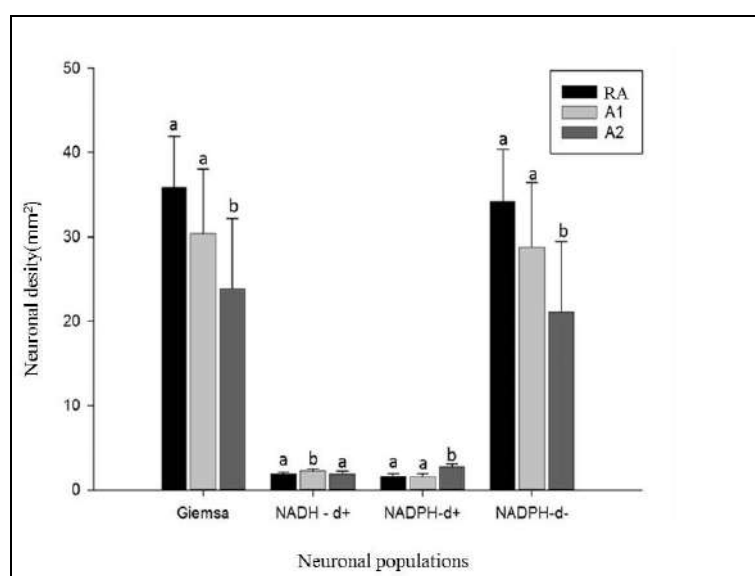


**Figure 2.** Neuronal density (mm<sup>2</sup>) of the general (Giemsa), NADH-d<sup>+</sup>, NADPH<sup>+</sup> and NADPH<sup>-</sup> populations of the *Spherooides testudineus* intestine (n=10, per site) collected at reference area (RA), Santos-São Vicente Estuary Complex (A1) and Lagoon System of Cananéia-Iguape (A2). Different letters indicate statistical difference ( $p < 0.05$ ) by the one way ANOVA test.

## **Environmental Enrichment Promotes Protection Against the Dissemination of Cocal Virus in the C57BL/6 Mice Central Nervous System**

Priscilla dos Santos Lieuthier Freitas<sup>1</sup>, Ana Victória de Lima Lima<sup>1</sup>, Karina Glazianne Barbosa Carvalho and José Antonio Picanço Diniz Júnior<sup>1\*</sup>

<sup>1</sup>. Laboratório de Microscopia Eletrônica / Instituto Evandro Chagas, Belém, Brasil.

\* E-mail to correspondence: [joseantonio@iec.pa.gov.br](mailto:joseantonio@iec.pa.gov.br)

Many studies have investigated viral diseases in the central nervous system (CNS). Arboviruses are among those that most affect the CNS. Cocal virus (VCOC) is an arbovirus responsible for vesicular stomatitis in domestic animals. In neonatal mice causes acute infection followed by death one day post-inoculation [1]. In adult mice, the virus spreads throughout the cerebral parenchyma, causing cell death due to apoptosis and necrosis, perivascular edema, hemorrhage and leukocyte infiltration [2]. Previous studies have shown that regular physical activity can induce neuroprotective effect and improve immune response [3]. Environmental enrichment consists of a combination of physical exercise, social interactions, and visuospatial and somatomotor stimuli in a cage, enriched with toys, ropes, tunnels, bridges and running wheels, which are periodically changed or moved. The aim of this work was to evaluate the influence of environmental enrichment on VCOC induced encephalitis in adult C57BL / 6 mice after intranasal inoculation. C57BL / 6 mice at 8 weeks of age were maintained in standard or enriched environment for 3 months. After this period, animals were inoculated with viral suspension or uninfected saline. On the 3<sup>rd</sup> or 6<sup>th</sup> post-inoculation days (d.p.i.), animals were perfused by intracardiac route and their brains were removed and processed for the detection of viral antigens by immunohistochemistry or processed for transmission electron microscopy analysis. The results showed that environmental enrichment reduced viral antigens dissemination in several of the infected areas (olfactory bulb, hippocampus, frontal and temporal cortex and cerebellum) when compared to animals in the standard environment in both time windows evaluated. In addition, it was possible to visualize viral particles by electron microscopy only in the olfactory bulb of animals from the standard environment at 3<sup>rd</sup> d.p.i. Our results suggest that environmental enrichment was associated with reduction of viral spread by increasing the efficiency of the immune response to VCOC infection.

[1] W. Gomes-Leal et al., Acta Tropica. 97 (2006) 126.

[2] P.S.L. Freitas. Dissertação. Biologia de Agentes Parasitários da Amazônia. UEPA, (2014) 106p.

[3] A.A Sousa et al., PLoS ONE. 6 (n.1) (2011) e15597.

[4] J. Simpson; J.P. Kelly. Behavioural Brain Research. 222 (2011) 246.

Support: Capes, Evandro Chagas Institute, (Brazil)

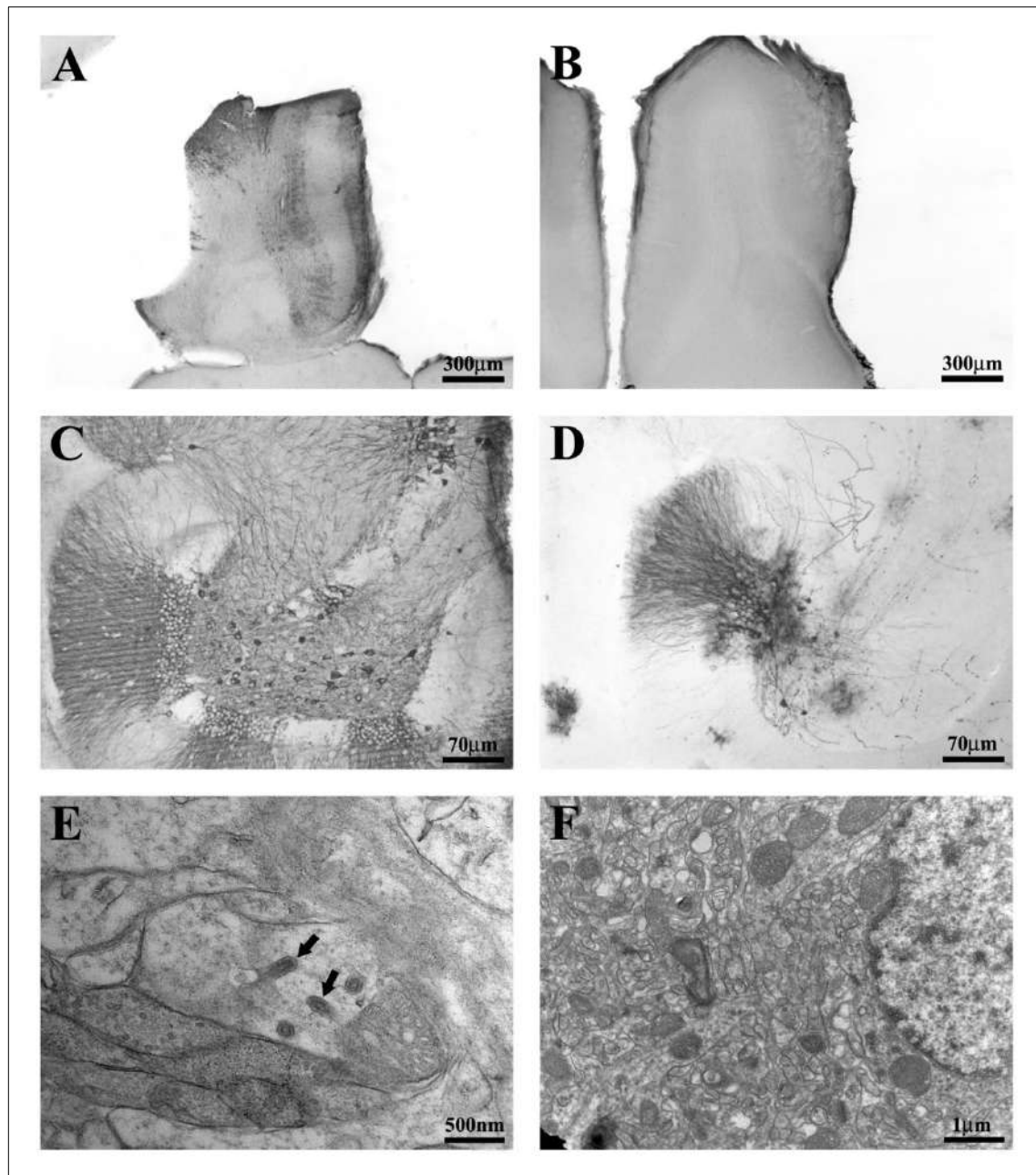


Figure 1: Photomicrography of horizontal sections of the central nervous system of control and COCAL virus infected mice. Immunolabeled sections for Coccal virus antigens (COCV) using Mouse on Mouse Elite Peroxidase Kit (A, B, C and D) and sections processed for Transmission Electron Microscopy (TEM) (E and F). Immunolabeled neurons in the olfactory bulb of standard (A) and enriched group (B) at 3rd d.p.i. Photomicrography of hippocampus section of an animal kept in the standard environment (C) and from an animal maintained in enriched environment (D) at 6th d.p.i. Presence of viral particles (arrows) in the olfactory bulb of animals from the standard environment (E) and absence of those in an individual from enriched environment (F) at 3 d.p.i.



## **Histopathological and Ultrastructural Aspects of Cardiac Involvement in Dengue: Contributions of the Murine Model**

Gabriela Cardoso Caldas<sup>1,2\*</sup>, Fernanda Cunha Jácome<sup>1</sup>, Arthur da Costa Rasinhas<sup>1</sup>, Ana Luisa Teixeira de Almeida<sup>1</sup>, João Paulo Rodrigues dos Santos<sup>2</sup>, Marcelo Pelajo Machado<sup>2</sup>, Débora Ferreira Barreto Vieira<sup>1</sup>

<sup>1</sup> Laboratório de Morfologia e Morfogênese Viral/Instituto Oswaldo Cruz, Rio de Janeiro - Brasil

<sup>2</sup> Laboratório de Patologia/Instituto Oswaldo Cruz, Rio de Janeiro – Brasil  
email for correspondence: gabrielacardosocaldas@gmail.com

The involvement of cardiac muscle tissue in dengue virus (DENV) infection, although not uncommon, is still poorly studied [1]. Clinical manifestations associated with dengue (DEN) can vary widely, ranging from asymptomatic bradycardia to fatal myocarditis [2]. The most commonly reported morphological changes from samples from human cases of DEN include degeneration of myocardial fibers, infiltration of mononuclear inflammatory cells, signs of interstitial edema, haemorrhage, neutrophil and eosinophil infiltration, and nuclear degeneration, with changes in mitochondria and presence of pycnotic nuclei [3,4,5]. Understanding the dynamics of the involvement of different organs during the course of infection is still one of the highest priorities in DEN pathophysiology studies, but the lack of an adequate experimental animal model still represents one of the main obstacles to filling the existing gaps. In this context, the main objective of this study was to verify possible histopathological and ultrastructural changes in the heart of BALB/c mice experimentally infected with DENV-3. Two-month-old, male, BALB/c mice, were intravenously infected with DENV-3 and euthanized in 72 h.p.i. The hearts were collected and processed for histopathological and ultrastructural analysis. For the histopathological analysis, heart fragments were fixed in formalin, dehydrated in ethanol, clarified in xylol and included in paraffin. Histological sections of 5 µm were stained with hematoxylin and eosin, periodic acid-Schiff and analyzed by AxioHome Carl Zeiss microscope. For the ultrastructural analysis, the samples were fixed in 2% glutaraldehyde buffered in 0.1M sodium cacodylate, post-fixed in osmium tetroxide, dehydrated in acetone and included in epoxy resin. Sections of 50 - 70 nm were contrasted with uranyl acetate and lead citrate and analyzed by TEM JEOL JEM 1011. Histopathological analysis of cardiac fragments of BALB/c mice 72 h.p.i with DENV-3 revealed well preserved areas and no relevant histopathological changes, only visual increase in endomysial cellularity and discrete cellular infiltration in the myocardium. The main ultrastructural changes observed were: infiltration of mononuclear cells and platelets in the interstitium and discrete disorganization of cardiac fibers and intercalated discs. In addition, signs of endothelial and mononuclear cell activation were observed, evidenced by cytoplasmic thickening of endothelial cells and cytoplasmic membrane extension of endothelial cells and mononuclear cells. The results show that BALB/c mice are able to present morphological changes in cardiac tissue when infected by DENV-3. However, the alterations present distinct patterns from those observed in humans and are punctual, suggesting that the cardiac compromise caused by this serotype is mild. It is necessary to compare the cardiac damage caused by different DENVs in order to know if the heart is a key organ in the pathophysiology of DEN and, if so, whether there is any relation between the infecting serotype and the intensity of the cardiac alterations.

- [1] Shivanthan *et al.*, J Infect Dev Ctries. 9 (2015) 338-46
- [2] Sheetal & Jacob. J Assoc Physicians India. 64 (2016) 30-34
- [3] Weerakoon *et al.*, BMC Research Notes. 4 (2011) 268
- [4] Miranda *et al.*, Eur Heart J Acute Cardiovasc Care. 2 (2013) 127-30
- [5] Póvoa *et al.*, PLoS One. 9 (2014) e83386 2014

This research was supported by CNPq (Brazil) and Oswaldo Cruz Institute.

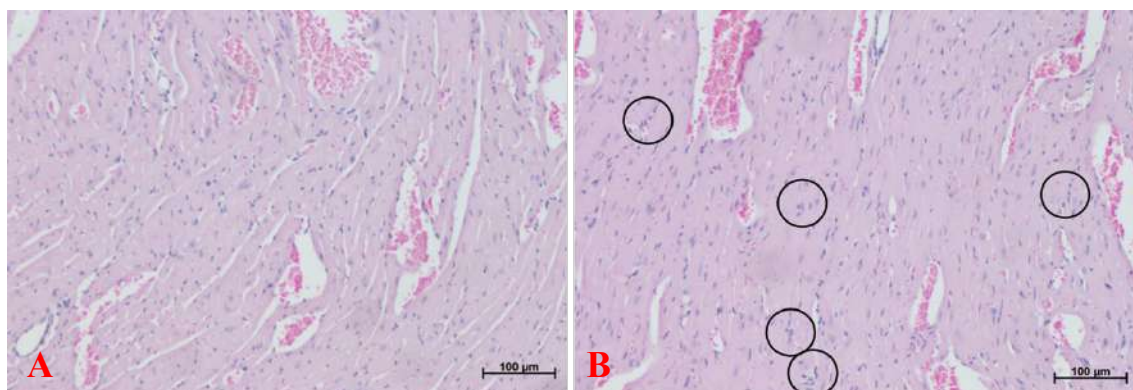


**Figure 1.** Histological sections of the heart of BALB / c mice 72h.p.i by DENV-3 stained with hematoxylin and eosin. [A] Myocardial area showing increase of cellularity in the endomysium. [B] Discrete cellular infiltrates (circles).

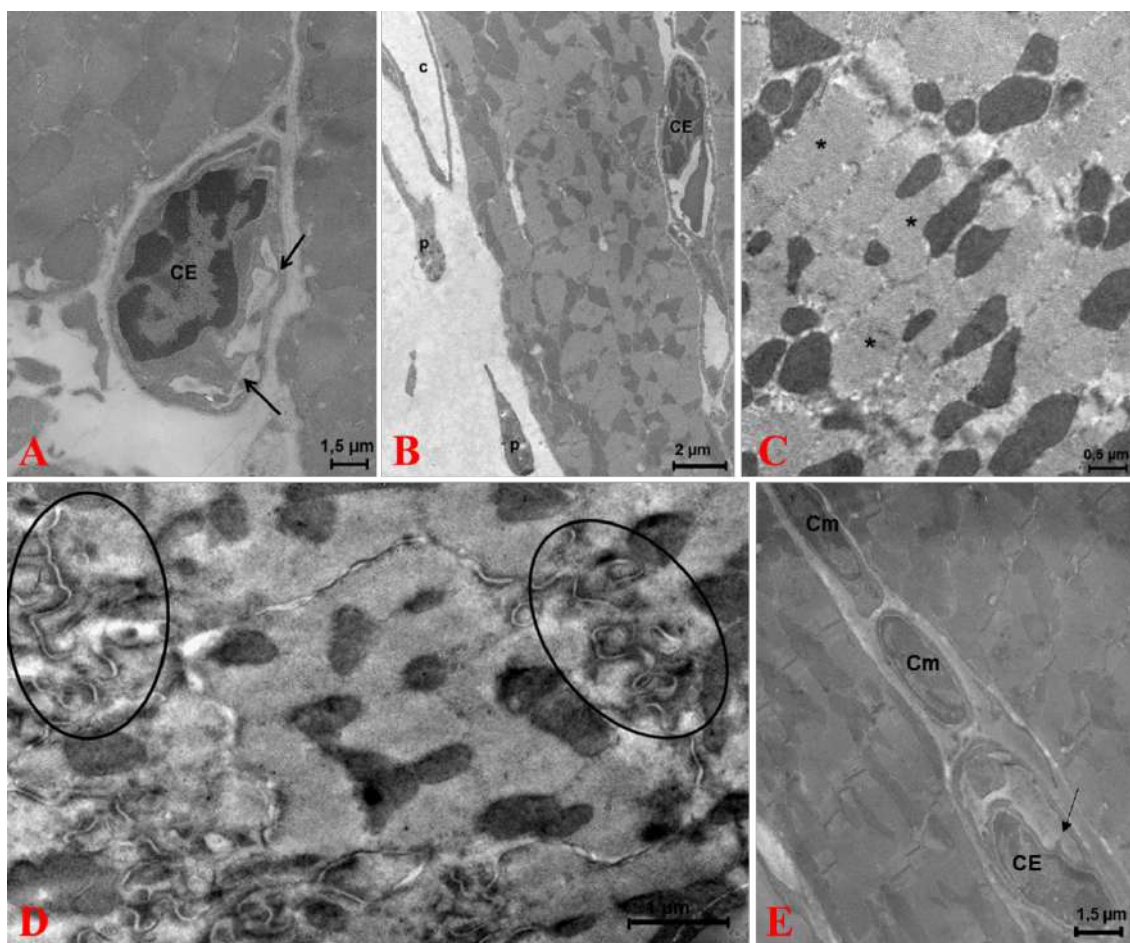


**Figure 2.** Ultrafine heart sections of BALB/c mice 72h.p.i by DENV-3. [A] Endothelial cell (CE) activation, evidenced by the emission of cytoplasmic membrane extension (arrows) and cytoplasmic thickening. [B] Platelets (p) outside the blood capillary (c). [C] Disorganization of cardiac fibers (\*). [D] Disorganization of intercalated disks (circles). [E] Presence of mononuclear cells (Cm) in the interstitium. Endothelial cell activation (CE), evidenced by the emission of cytoplasmic membrane extension (arrows).



## **Combined Microscopy and Spectroscopy Techniques to Characterize a Fossilized Feather with Minimal Damage to the Specimen**

Campos APC<sup>1</sup>, Carvalho RT<sup>2</sup>, Straker LC<sup>3</sup>, Salgado LT<sup>2</sup>, Kellner AWA<sup>4</sup> and Farina M<sup>5\*</sup>

<sup>1</sup>. Aix Marseille Université, CNRS, FSCM, CP2M, Marseille, France

<sup>2</sup>. Diretoria de Pesquisas, IPJBRJ, Rio de Janeiro, Brazil

<sup>3</sup>. Faculdade de Filosofia, Ciências e Letras de Ribeirão Preto, USP, São Paulo, Brazil

<sup>4</sup>. Departamento de Geologia e Paleontologia, Museu Nacional, Rio de Janeiro, Brazil.

<sup>5</sup>. Departamento de Histologia e Embriologia, UFRJ, Rio de Janeiro, Brazil

The study of fossil feathers has been revitalized in the last few decades and has contributed significantly to paleontological studies of dinosaurs and birds<sup>1</sup>. Specific morphological and physicochemical characteristics of the microscale structures of feathers and the protein keratin are key targets when preserved during the fossilization process<sup>2</sup>. Keratin is a fibrous protein that composes some hard tissues such as hair, nails and feathers. It is part of the intermediate filaments inside keratinocyte cells and is rich in sulfur containing amino acid cysteine<sup>3</sup>. To date, different microscopy and analytical methods have been used for the analysis and detailed characterization and classification of feathers<sup>4</sup>. However, in this work we showed that analytical optical and electron microscopies can be quick and precise methods with minimal effects on the sample during analysis. This association of different approaches on the same sample results in correlative data albeit in different length scales. Intracellular bodies called melanosomes originally present in melanocyte cells were identified with Scanning Electron Microscopy (SEM) and Transmission Electron Microscopy (TEM), and had well-defined orientation and a mean aspect ratio comparable to melanosomes extant in dark feathers. The detection of sulphur in melanosomes via Energy Dispersive Spectroscopy both in SEM and TEM shows that, along the fossilization process, sulfur (S) from the degraded keratin matrix could have been trapped inside the melanosomes. Chemical groups that make up keratin and melanin in the fossil sample were detected via FT-IR Spectroscopy and Confocal Laser Scanning Microscopy (CLSM). The use of combined analytical microscopy techniques can contribute significantly to the study of fossils generating precise results with minimum damage to the original sample.

[1] Chen et al., *Nature*, 391 (1998) 147.

[2] Vinther et al., *Bio. Lett.*, 6 (2010) 128.

[3] Love B., *Biomaterials*, Academic Press, New York, 2017.

[4] Pan t al., *PNAS*, 113(49) (2016) 900.

We thank Centro Brasileiro de Pesquisas Físicas (CBPF) and INMETRO for microscopy facilities. We also thank Lidia Agata de Sena for FEI Magellan operation. This research was supported by CNPq, CAPES and FAPERJ.



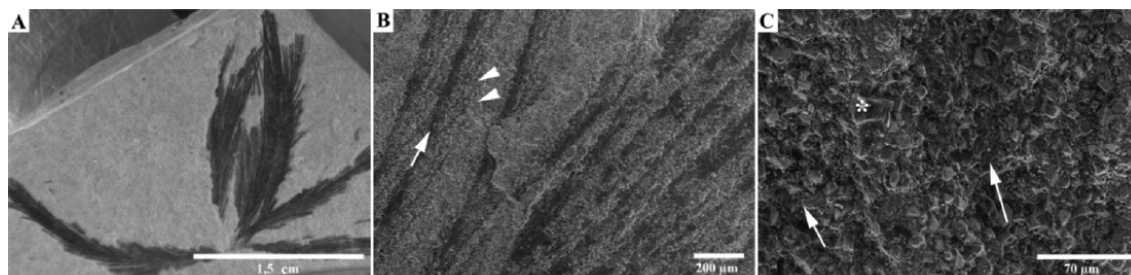


Figure 1 – General SEM view of MN 7754-V. (A) Fossilized structures within the sedimentary matrix, with clear distinction of the sample (darker regions) and its surroundings. (B) High magnifications showing the morphology of the sample, which resembles extant feather plumulaceous barbules (white arrow) with many branches that can be associated with long prong barbels (white arrow heads), (C) Higher magnification evidencing the rough surface of the sample. The fossilized material (White arrows) has less defined edges and many smaller structures than the surrounding sedimentary matrix, which contains small crystals with defined edges and a slightly smoother surface (white asterisk).

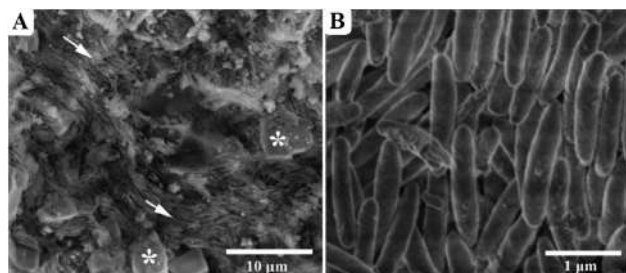


Fig. 2. SEM images from MN 7754-V. A–B) Surface topography of the sample showing microbodies with elongated appearance and curved extremities arranged in bundles, with their longer axes oriented in parallel to the direction of the bundles (white arrows in A and enhanced detail in B). Crystals with straight contours are visible in the sedimentary matrix (asterisks in A).

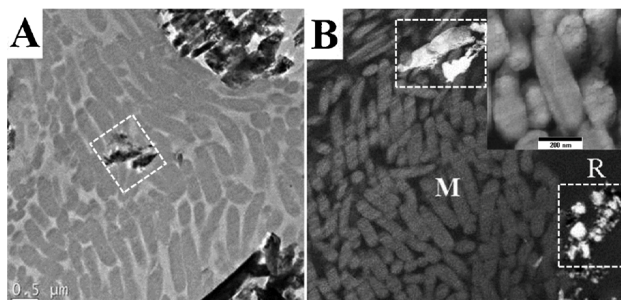


Fig. 3. Correlation between melanosomes and the surrounding matrix of MN 7754-V. Bright field TEM (A) and HAADF (B) images of tangential ultra-thin sections from a deeper region of the sample revealing not only the melanosomes (M) and the embedded resin (R), but also some fractured crystals belonging to the sedimentary rock matrix (dotted white rectangles in A and B). STEM-HAADF image (top right insert in B) of the melanosome in detail.

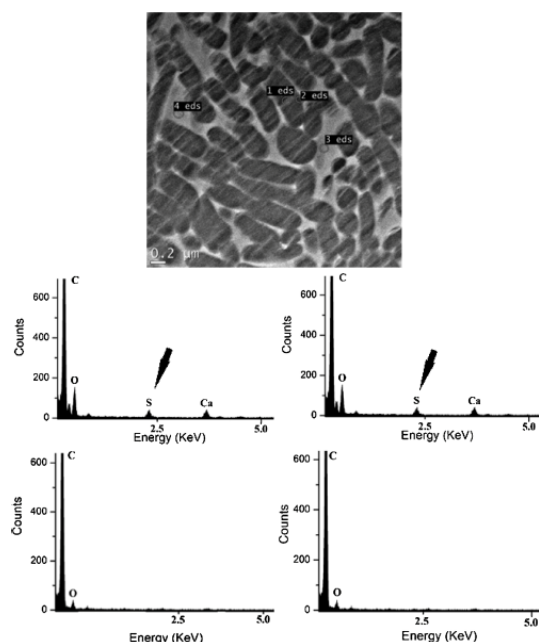


Fig. 4. Bright field TEM image of an ultra-thin section from MN 7754-V containing the melanosomes. EDS from four different regions: two from melanosomes (1,2) and two from embedding medium areas (3,4) of the sample.

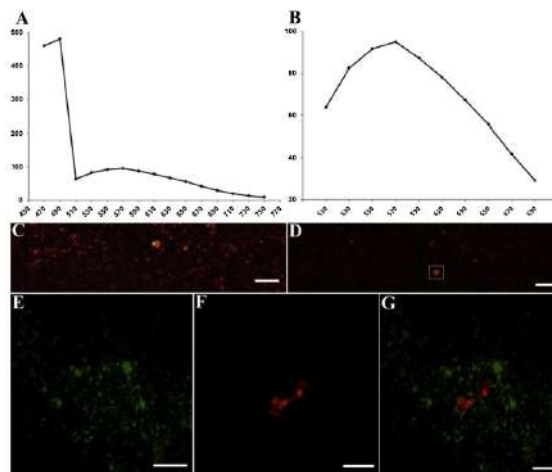


Fig. 5. Fluorescence emission spectra (x axis=intensity; y axis = wavelength in nm) showing the 490 nm peak (A) and 570 nm peak (B). Confocal microscopy mapping of the fossil region showing several parts of the material with fluorescence signals at the 490 nm peak (C) and 570 nm peak (D); scale bar=5  $\mu$ m. The 490 nm peak was associated with the sedimentary rock matrix (E) and the 570 nm peak with the melanosomes (F). Combined image of the 490 nm peak fluorescence and 570 nm peak images (G); scale bar (E, F and G)=1  $\mu$ m.

## Time-Dependent Evaluation of Ultrastructural and Morphological Alterations Induced by 4-(5'-formyl-[2,2'-bithiophen]-5-yl)but-3-yn-1-yl acetate on Promastigote Forms of *Leishmania amazonensis*

Rayanne Regina Beltrame Machado<sup>1\*</sup>, Deysiane Lima Salvador<sup>2</sup>, Aline Rufino de Oliveira<sup>2</sup>, Maria Helena Sarragiotto<sup>2</sup>, Tânia Ueda-Nakamura<sup>1</sup>, Sueli de Oliveira Silva<sup>1</sup>, Celso Vataru Nakamura<sup>1</sup> and Danielle Lazarin-Bidóia<sup>1</sup>

<sup>1</sup>Laboratório de Inovação Tecnológica no Desenvolvimento de Fármacos e Cosméticos, Departamento de Ciências Básicas da Saúde, Universidade Estadual de Maringá (UEM), Maringá, Paraná, Brazil. \*Email: [raymachado6@hotmail.com](mailto:raymachado6@hotmail.com)

<sup>2</sup>Departamento de Química, Universidade Estadual de Maringá (UEM), Maringá, Paraná, Brazil.

Leishmaniasis is a neglected disease caused by parasites of the genus *Leishmania* and widely distributed, as the regions most affected are the poorest in tropical and subtropical countries, including Brazil. Currently, the treatment is based on drugs and have shown several limitations, for example, high cost, long treatment times, high toxicity, poor efficacy, serious side effects and resistance<sup>[1,2]</sup>. Thus, is urgently needed to develop new therapeutic agents for the treatment of patients with leishmaniasis. In previous studies, our research group has already shown that the synthetic compound 4-(5'-formyl-[2,2'-bithiophen]-5-yl)but-3-yn-1-yl acetate, **ACET-1**, induced ultrastructural and morphological changes in promastigotes of *Leishmania amazonensis*, when treated with IC<sub>50</sub> (28.9 µM) for 72 h. Based on this, the aim of this study was to evaluate time-dependent on the appearance of these alterations including lipids bodies. For this, promastigote (1 x 10<sup>6</sup> cells/mL) were treated with IC<sub>50</sub> of **ACET-1** for 4, 8, 12, 24, 36, 48, 60, and 72 h at 28 °C. After, the parasites were fixed in a solution of 2.5% glutaraldehyde in 0.1 M cacodylate buffer for 24 h at 4 °C. For the scanning electron microscopy, the parasites were dehydrated in increasing concentrations of ethanol, critical point-dried in CO<sub>2</sub>, sputter-coated with gold and observed using a FEI Scios. For transmission electron microscopy, the treated parasites were fixed as described in SEM. After, the parasites were postfixed in a solution of 1% OsO<sub>4</sub>, 0.8% potassium ferricyanide and 10 mM CaCl<sub>2</sub> in 0.1 M cacodylate buffer. The samples were dehydrated in increasing acetone gradient and embedded in Polybed 812 resin. Ultrathin sections were then obtained, contrasted with uranyl acetate and lead citrate, and observed in JEOL JEM 1400. To evaluate the appearance of lipids bodies, the parasites were loaded with Nile Red and observed in confocal microscopy Zeiss LSM 5 Pascal. Our results demonstrated that **ACET-1** induced morphological and ultrastructural alterations in promastigote from 4 h of treatment, that included, reduction of the cell body, presence of autophagic vacuoles and lipid storage bodies. Alteration in plasma membrane and cytoskeleton was observed only after 8 h of treatment with **ACET-1**. These changes occurs at the molecular level<sup>[3]</sup> and thus our results support further studies for understanding the basic cellular biology of Trypanosomatids.

### References:

- [1] Murray WH, Berman JD, Davies CR, Saravia NG. The Lancet. 366, 1561-1577 (2005).
- [2] WHO. Leishmaniasis, (2018).
- [3] SILVA *et al.* Ultraestrutura de Parasitos do Gênero *Leishmania*. In: CONCEIÇÃO-SILVA, F.; ALVES, C. R. (org.). **Leishmanioses do continente americano**. Rio de Janeiro, RJ: Editora Fiocruz, 2014. cap 3, p53-71.

**Acknowledgement:** This study was supported through grants from CAPES, CNPq, FINEP, PRONEX/Fundação Araucária.

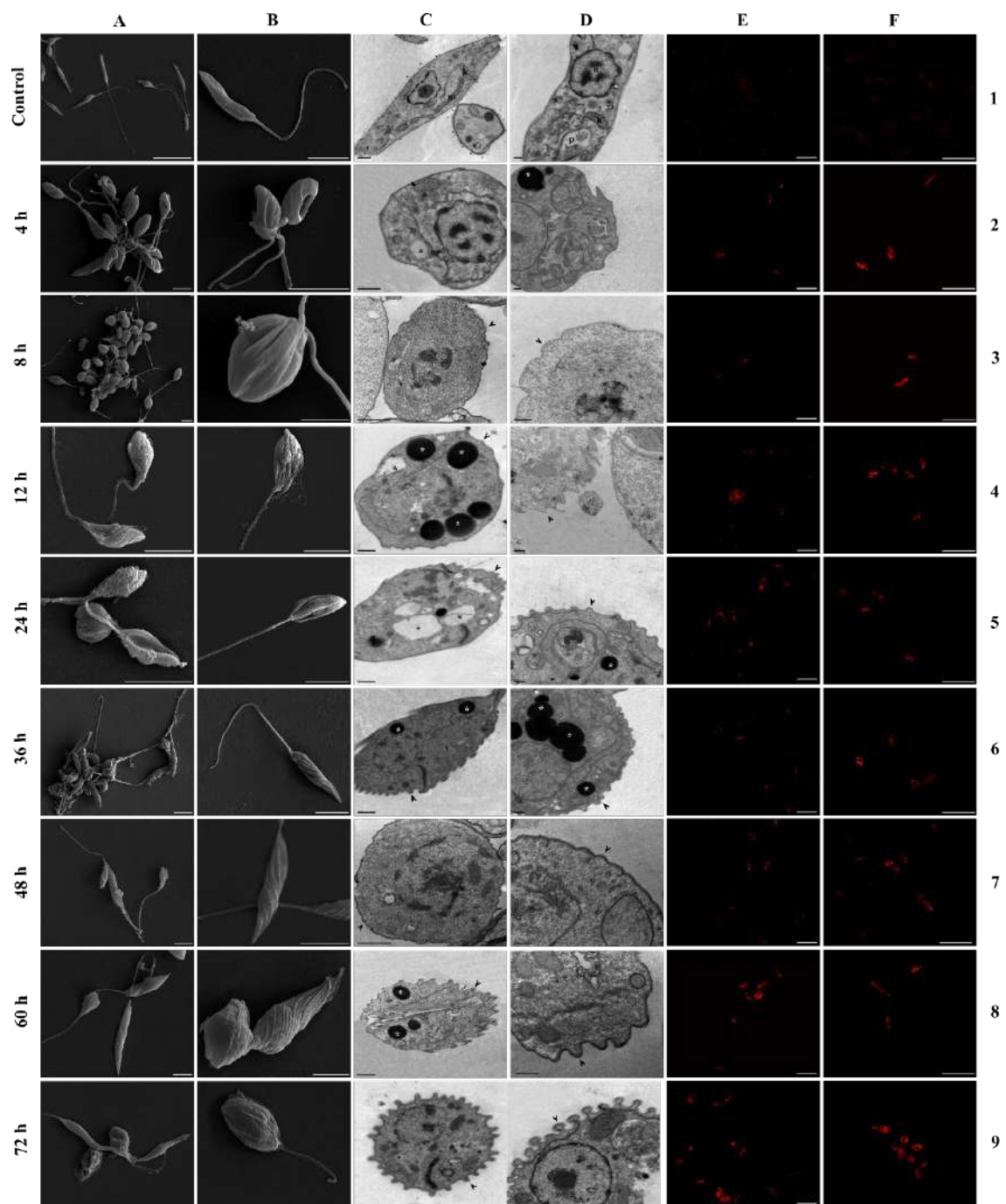


**Figure 01:** Ultrastructural and morphological alterations time-dependent in promastigote of *Leishmania amazonensis* treated with **ACET-1**. (n) nucleus; (m) mitochondrion; (k) kinetoplast; (p) flagellar pocket; (\*) white: lipid body; (\*) black: autophagic vacuole; (>) alterations in cell membrane. Bars= **5  $\mu\text{m}$** :A1-A9, B1-B2, B4-B7, B8; **2  $\mu\text{m}$** : B3, B8 **0.5  $\mu\text{m}$** : C1-C9; **0.2  $\mu\text{m}$** : D1-D9; **20  $\mu\text{m}$** : E1-E9, F1-F9;

## The Limpet tooth revisited: matrix structure, minerals distribution and composition

Jacques Werckmann<sup>1</sup>, Andrea P.C. Campos<sup>2</sup>, Martin Mendoza<sup>3</sup>, Fernando P. Almeida<sup>4</sup>  
Ovidiu Ersen<sup>5</sup> and Marcos Farina<sup>6\*</sup>

<sup>1</sup> Brazilian Center for Physics Research, CBPF, Rio de Janeiro, Brazil

<sup>2</sup> Aix-Marseille Université, CP2M, Faculté des Sciences, Campus de St Jérôme, Marseille France

<sup>3</sup> Universidad Pedagógica y Tecnológica de Colombia, Boyacá, Colombia

<sup>4</sup> National Center for Structural Biology and Bioimaging, CENABIO, UFRJ, Brazil

<sup>5</sup> Institut de Physique et Chimie des Matériaux de Strasbourg, France

<sup>6</sup> Institute of Biomedical Sciences, UFRJ, Rio de Janeiro, Brazil

\* [marcos.farina.souza@gmail.com](mailto:marcos.farina.souza@gmail.com)

### Introduction

The radula of Limpets (Mollusca: Gastropoda) contains more than one hundred rows of teeth in different stages of mineralization. In living organisms, mature mineralized teeth are used to scrape rocks to obtain food and as a consequence, new rows of teeth are formed to compensate for the eroded ones [1]. Many studies have described the general morphology of the limpet teeth and their mechanical properties [2]. Teeth have been also considered as a model for biomineralization studies particularly related to iron oxides deposition, as it is possible to follow this process from the start [3]. Mineralized tooth cusp is known to be composed of the iron oxide goethite ( $\alpha$ -FeOOH), and silica is present mainly in the base of the tooth. The organic phase is composed of chitin. The tooth matrix has a complex organization pattern in 3D. Goethite crystals are elongated along the crystallographic *c* axis and align with the chitin fibers in the tooth cusp [2] while silica composes the bottom region and start as small granules that grow and coalesce, forming a compact structure [4].

Most works until now, focused in the mineralization of goethite ( $\alpha$ -FeOOH) which is mainly responsible for the hardening of the tooth cusp, in contrast to few other works that focused in the characterization of the silica containing region, which forms the base of the mineralized tooth [4]. Although these works describe the overall morphology and elemental composition, including the silica rich regions, they do not analyze these regions at the nanoscale and do not show the inter-connection between iron oxide, silica and chitin fibers. Some aspects of this issue will be focused in this work.

### Methods

Radula from *Collisella subrugosa* limpet were fixed with glutaraldehyde in Cacodilate buffer, post fixed with osmium tetroxide, dehydrated in an acetone series and embedded in epoxi resin. Ultrathin sections were observed in a probe corrected Jeol 2100F operated in STEM mode, with an Oxford EDS analytical system.

### Results & Discussion

In this work, we focus on the organization pattern and elemental composition of the main mineral components (goethite and silica) of the tooth of the limpet *Collisella subrugosa*, and their relationship with the chitin fibers of the matrix in different regions. We show that mineralization of the silica begins as spherical granules at the base of the tooth in regions where the chitin fibers cross, and further grow, forming a glass-like material with typical conchoidal fracture, during ultrathin sectioning for analysis by TEM (Fig. 1A and insert). Differently, the iron oxides are present as elongated crystals parallel to the fibers and in close contact with them (Fig. 1B, arrows) and in some regions are embedded in



the silica (Fig. 1B). Near the tooth cusp, the iron content dominates the whole volume (Fig. 1C). We have analyzed highly mineralized cusp regions of the mature tooth and detected the presence of both silica and goethite. We show by energy dispersive X ray spectroscopy (EDS) that the matrix is completely filled by the two mineral phases (Fig. 2A), and that in some regions the two minerals are still spatially segregated (Fig. 2B and 2C). This indicates that in *C. subrugosa*, the biomineralization processes of iron and silica are independent and strictly controlled biologically.

## REFERENCES

- [1] J.A.Shaw *et al.*, *Biol Bull.* 218 (2010) 132.
- [2] P.van der Wal, H.J. Giesen and J.J. Videler, *Materials Science and Engineering C*. 7(2000)129
- [3] E.D.Sone, S.Weiner and L.Addadi, *Journal of Structural Biology* 158(2007)428.
- [4] Tsu-En Hua and Chia-Wei Li, *Zoological Studies* 46(2007)379.
- [4] Acknowledgements: CNPq and Faperj (Brazil). This work is dedicated to Renato L. S. Cruz

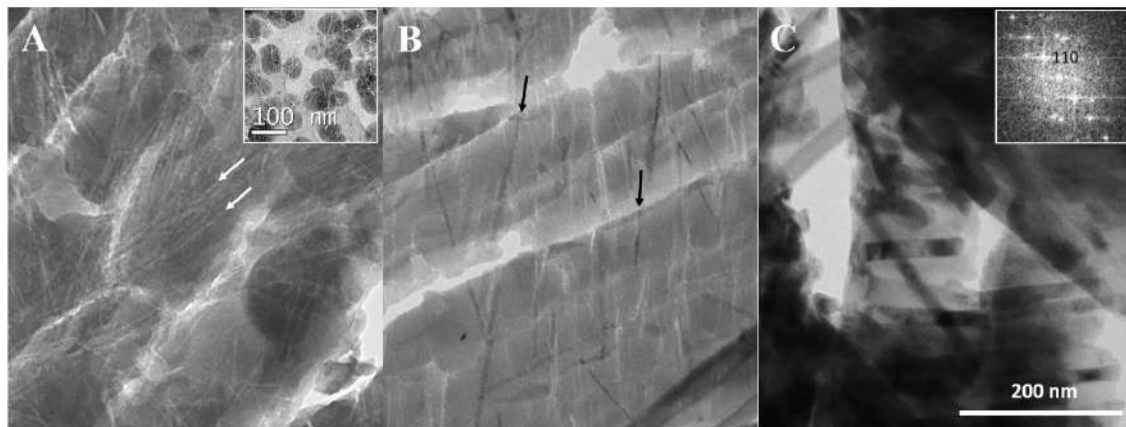


**Figure 1:** TEM images of a mineralizing limpet tooth. (A) Silica containing region of the bulk, showing conchoidal fracture and chitin fibers (white arrows). Insert: beginning of silica mineralization in the base of the tooth. Spherical particles are seen in regions where chitin cross. (B) Silica region with few elongated goethite crystals. (C) Tooth cusp with highly mineralized goethite (dark regions). Uniformly gray regions: silica. Insert: diffraction pattern of a goethite crystal. Bar: 200 nm for all images.

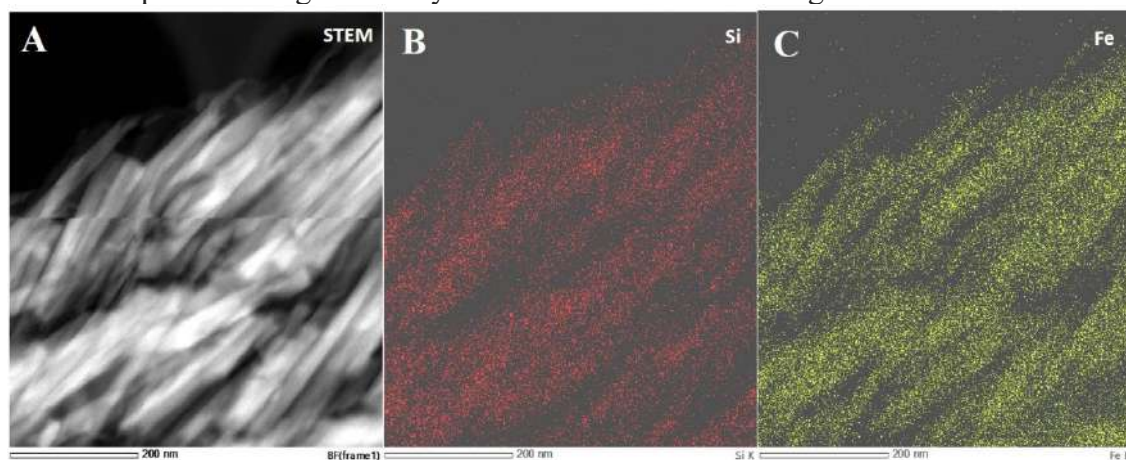


**Figure 2:** Micrographs of an ultrathin section obtained by STEM from a highly mineralized region of the tooth. (A) Densely packed goethite crystals; (B) EDS map of Si; (C) EDS map of Fe. Note that Si and Fe are not colocalized in some regions.





## UV-Irradiation of Oocytes for the Induction of Androgenetic Fishes.

Matheus Pereira dos Santos<sup>1\*</sup>, Nivaldo Ferreira do Nascimento<sup>2</sup>, Mariana Machado Evangelista<sup>3</sup>, Laura Satiko Okada Nakaghi<sup>3</sup> and George Shigueki Yasui<sup>2</sup>.

<sup>1</sup>. Professor at Universidade Federal Rural do Rio de Janeiro, Departamento de Produção Animal, Instituto de Zootecnia, Seropédica, Rio de Janeiro, Brazil. \*  
matheusps.pereira@gmail.com

<sup>2</sup>. Centro Nacional de Pesquisa e Conservação da Biodiversidade Aquática Continental. CEPTA/ICMBio, Pirassununga, São Paulo, Brazil.

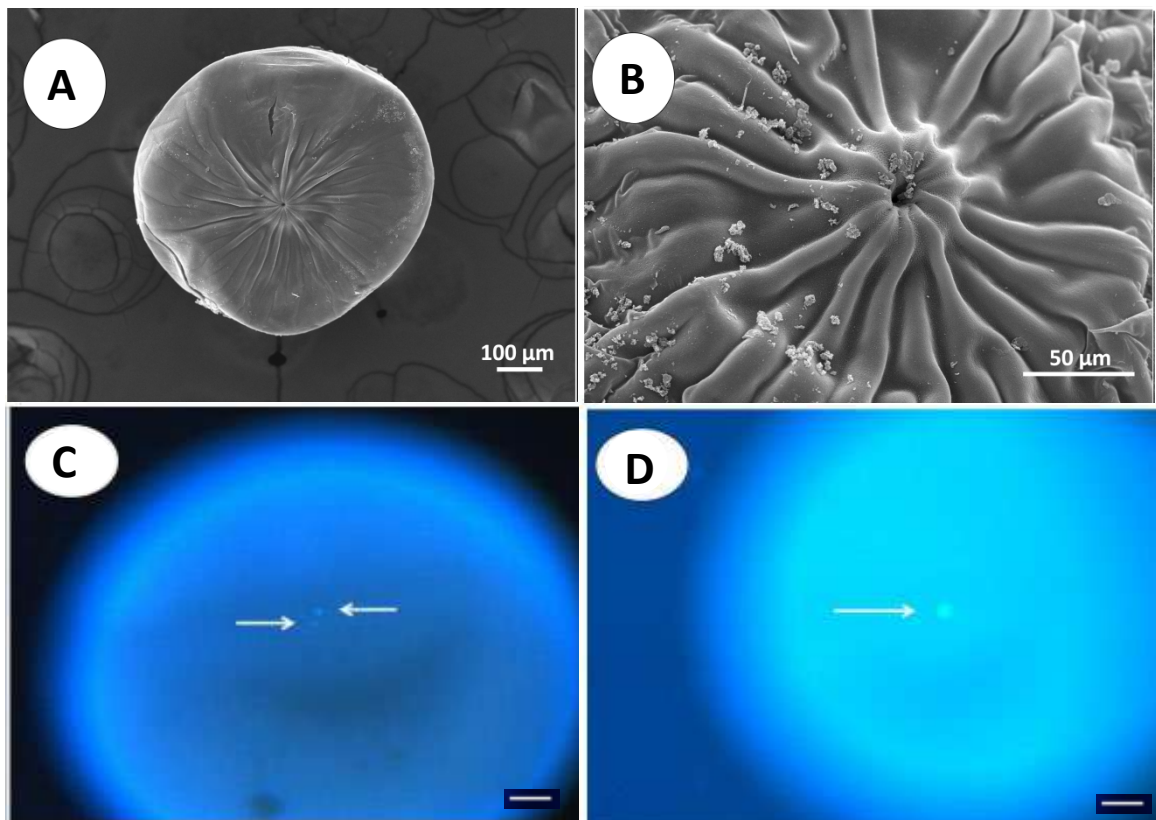
<sup>3</sup>. Centro de Aquicultura da Unesp, Jaboticabal, São Paulo, Brazil.

Aquaculture has been increasing its production potential in recent years, mainly due to the advancement of technologies in breeding systems. Among them, biotechnology applied to the reproduction of species stands out. Androgenesis, one of these techniques, represents a potential tool for use in fish production. It is a uniparental reproduction process in which the progeny receive exclusively paternal genetic material, and for this the oocytes receive sufficient UV irradiation to destroy their genetic material. A protocol for androgenesis induction by means of UV irradiation has previously been described by the present group in the *Astyanax altiparanae* species, as well as a description of the pronuclei fusion time under natural conditions [1]. Thus, the present work was conducted with the objective of elucidating if the UV irradiation of oocytes affects the pronuclei fusion time after fertilization, and may affect the later survival of the progeny. Oocyte morphology was observed by scanning electron microscopy (SEM). Samples previously fixed in Karnovsky's solution (2.5% glutaraldehyde + 2.5% paraformaldehyde) were postfixed in 1% osmium tetroxide for two hours and dehydrated in graded ethanol series. Then the samples were dried at the critical point in liquid CO<sub>2</sub> drier, mounted on stubs and coated with palladium gold ions (DENTON Vacuum Desk II) and subsequently observed and electronically scanned by electron microscopy (Jeol-JSM 5410, Akishima, Tokyo, Japan). For observation and description of pronuclei fusion, the eggs were analyzed under fluorescence microscopy at the Fish Biotechnology Laboratory of the National Center for Research and Conservation of Continental Fishes, Cepta / ICMBio, in Pirassununga. Embryos corresponding to 0 to 14 minutes post-fertilization were stained with 5 µg of fluorescent dye 4,6-diamidino-2-phenylindole dihydrochloride (DAPI, SIGMA D9542) + dPBS solution 200x mL<sup>-1</sup> (0,000005 g mL<sup>-1</sup>), diluted, analyzed and photomicrographed under a fluorescence microscope (Nikon SMZ 1500, Tokyo, Japan), with a CCD camera (Nikon DS-F1, Nikon, Tokyo, Japan), with a wavelength filter of 254 nm. The embryos were positioned with the animal pole facing the plane of observation. The analyzes were performed in triplicate, accounting for about 20 samples per replicate. To evaluate if the irradiation affected the fusion time of the pronuclei of the species, the data were compared with the results of the analysis performed by the author [1] on non-irradiated embryos of the *Astyanax altiparanae* species. The *Astyanax altiparanae* oocytes has several grooves surrounding the micropyle. The micropyle has a diameter of approximately 7.57 µm. The mean distance occupied by the grooves from the micropyle in non-hydrated oocytes is 257,111 µm. The oocyte diameter is 695,119 ± 49,5 µm. In addition, the micropyle is located in a region of projection of the oocyte, to the center of

a "ridge". The coalescence time interval of the paternal and maternal pronuclei from full fertilization to fusion was eight to ten minutes after fertilization. The induction of triploid, tetraploid, gynogenic and androgenetic individuals involves techniques that are based solely on the chronology of these events, since ploidy is conditioned to the retention or not of the extrusion of the second polar corpuscle and the deactivation of sets of paternal or maternal chromosomes [2, 3, 4]. The observation of the pronuclei by means of fluorescence microscopy showed that the irradiation of the oocytes with 90 seconds after extrusion does not affect the melting time already described for the species, making possible the application of the induction treatment of androgenetic individuals in the species.

## REFERENCES

- [1] M. P. Santos et al., Zygote. 24 (6) (2016).
- [2] M. Itono et al., J. Exp. Zool. 305 (A) (2006).
- [3] M. Itono et al., J. Exp. Zool. 307 (A) (2007).
- [4] K. Morishima et al., BMC Bio. 11 (116) (2011).
- [5] This research was supported by CNPq (Brazil).



**Observation of the oocytes before fertilization and the pronuclei in the eggs of the *Astyanax altiparanae* species irradiated by 90'.** Oocyte with chorion after hydration (A), region of the micropyle, surrounded by grooves (B), eggs with six minutes post fertilization, with fully fused pronuclei (C) and eggs with ten minutes post-fertilization (D). Arrows indicate the location of pronuclei. Scale bar: 100 μm.

# Measuring Electron Beam Damage in Proteins Using Electron Energy Loss Spectroscopy

Marcelo Alexandre de Farias<sup>1\*</sup>, Marin van Heel<sup>1</sup>, Jefferson Bettini<sup>1</sup>, Rodrigo Villares Portugal<sup>1</sup>

<sup>1</sup>Brazilian Nanotechnology National Laboratory / CNPEM, Campinas, SP, Brazil.

\*marcelo.farias@lnnano.cnpem.br

Electron beam damage in transmission electron microscopy (TEM) plays a crucial role for obtaining near-atomic resolution of proteins [1,2]. Although electron diffraction in TEM has been used as a measurement tool for beam damage of protein crystals, results obtained from this approach are primarily related to the crystal's periodicity (Bragg's diffraction) and not necessarily related to damage of the protein itself. We propose a new approach for measuring electron beam damage in proteins using electron energy-loss spectroscopy (EELS) which we believe will contribute significantly to our understanding of the beam-damage mechanism. Catalase stock solution (10 mg mL<sup>-1</sup>) was prepared in phosphate buffer (50 mM, pH 6.3) and centrifuged at 1,400 rpm, 4 °C, for 10 minutes to remove undissolved protein. 3 µL of catalase solution (80 µg mL<sup>-1</sup>) was dropped onto Cu grids (300 mesh, carbon free) coated by a 7 nm TiSi ultrathin film (in-house development) and allowed to dry. Carbon EELS spectra with total doses from 10 to 1,000 e<sup>-</sup> Å<sup>-2</sup> were acquired over an area of 300 µm<sup>2</sup> using a minimum dose system mode. The alignment of spectra was performed using the second Ti peak (464.6 eV) as a reference. The carbon-carbon bond peak (296-299 eV) was used for normalization. Results showed that carbonyl groups (C=O, 289 eV) have their EELS signal systematically decreased over accumulated radiation, while aromatic unsaturation signal (C=C, 286 eV) remained almost unchanged. These findings agree with previous reports, confirming that aromatic rings have a higher resistance to the electron beam than do carbonyl groups [3]. Our results strongly indicate that EELS can indeed be used as a tool for electron beam damage measurements in TEM with a clear specificity for different chemical groups.

Acknowledgements: CNPq, FINEP.

## References

- [1] P.N.T. Unwin, R. Henderson, J. Mol. Biol. 94 (1975) 425.
- [2] R.F. Egerton, Ultramicroscopy 127 (2013) 100–108.

[3] A. Bartesaghi, D. Matthies, S. Banerjee, A. Merk, S. Subramaniam, PNAS 32 (2015) 11709-11714.

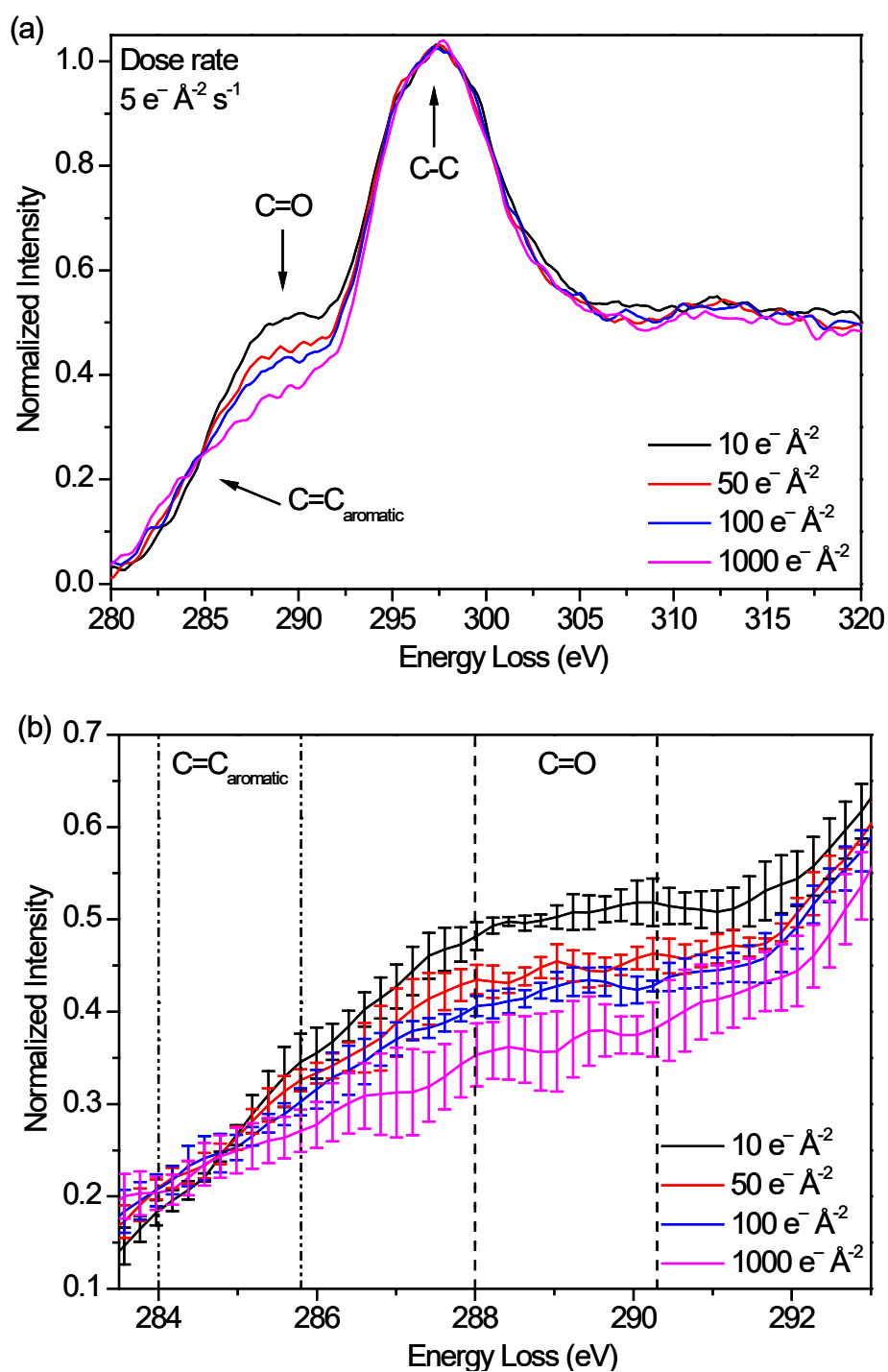


Figure 1: (a) Dependence of the carbon signal EELS spectrum of catalase on the total accumulated radiation of 10, 50, 100 and 1,000  $\text{e}^- \text{ Å}^{-2}$ . (b) The highlighted ranges of  $\text{C}=\text{C}_{\text{aromatic}}$  (dash-dotted line) and  $\text{C}=\text{O}$  (dashed line) signals.

## **Iron and Manganese Minerals Associated to Microalgae and Prokaryotes of the Periphyton of Doce River and Tributaries Affected by Iron Mining Tailings from Collapsed Fundão Dam (Mariana, MG)**

Carolina N. Keim<sup>1\*</sup>

<sup>1</sup> Instituto de Microbiologia Paulo de Góes, Universidade Federal do Rio de Janeiro – UFRJ, Rio de Janeiro, Brazil. E-mail: cnkeim@micro.ufrj.br.

On november 5, 2015, an iron mining waste dam owned by Samarco Company collapsed, releasing about 32.6 million m<sup>3</sup> of mining tailings into the environment. Tailings from Fundão Dam reached Gualaxo do Norte, Carmo, and Doce Rivers, and finally the Atlantic Ocean at Espírito Santo coast. Three years after, huge amounts of tailings remain in the sediments of Doce River and tributaries [1]. Water quality in Doce River was impaired, with dissolved Fe and Mn concentrations exceeding Brazilian legislation in several samples [2]. The periphyton influence the fate of dissolved metals in the environment through oxido-reduction reactions, mineral precipitation, and dissolution. In a previous work, we showed secondary Mn oxides containing minor amounts of Al, Ba, Ca, K and P in the periphyton grown in microcosms made with Gualaxo do Norte River water and sediments [3]. In this work, we investigate the role of periphyton in metal precipitation in Gualaxo do Norte and Doce Rivers affected by Fundão Dam tailings, and its potential to improve water quality. Field work was done in Gualaxo do Norte River at Barra Longa (MG), and Doce River in Governador Valadares (MG). Glass slides and coverslips were maintained within the river for 7-15 days to allow periphyton growth. After retrieval, samples were fixed in 2.5% glutaraldehyde in PIPES buffer 0.1M, and rinsed. For scanning electron microscopy (SEM), samples were dehydrated in etanol series, critical point dried, and gold-sputtered. For transmission electron microscopy (TEM), samples were post-fixed in OsO<sub>4</sub>, rinsed, dehydrated in etanol series, embedded in Spurr, trimmed in an ultramicrotome and put onto formvar-coated slot grids. The periphyton was dominated by prokaryotes in Gualaxo do Norte River and by microalgae in Doce River. Turbidity was very high in Gualaxo do Norte River, blocking sunlight and preventing growth of photosynthetic organisms, whereas Doce River presented more transparent waters, enabling extensive microalgae growth in the periphyton. Iron was found mainly in primary mineral particles attached to mucilage or exopolysaccharides, whereas manganese occurred in secondary minerals precipitated onto extracellular structures such as prokaryotic sheaths, filamentous algae holdfasts, and pennate diatom mucilage (Figure 1). Our results evidence the role of periphyton prokaryotes and microalgae in Mn precipitation as secondary minerals associated to extracellular structures, which could decrease dissolved Mn in water, improving water quality [4].

### **REFERÊNCIAS**

- [1] <https://www.samarco.com/rompimento-de-fundao/>
- [2] G.O. Carvalho et al., *Orbital: Electron. J. Chem.* 10 (2018) 299.
- [3] C.N. Keim et al., *Geomicrobiology Journal*, 32 (2015) 549.
- [4] We are thankful to Laboratório de Biomineralização, CENABIO-UFRJ and LABNANO-CBPF for microscopy facilities.



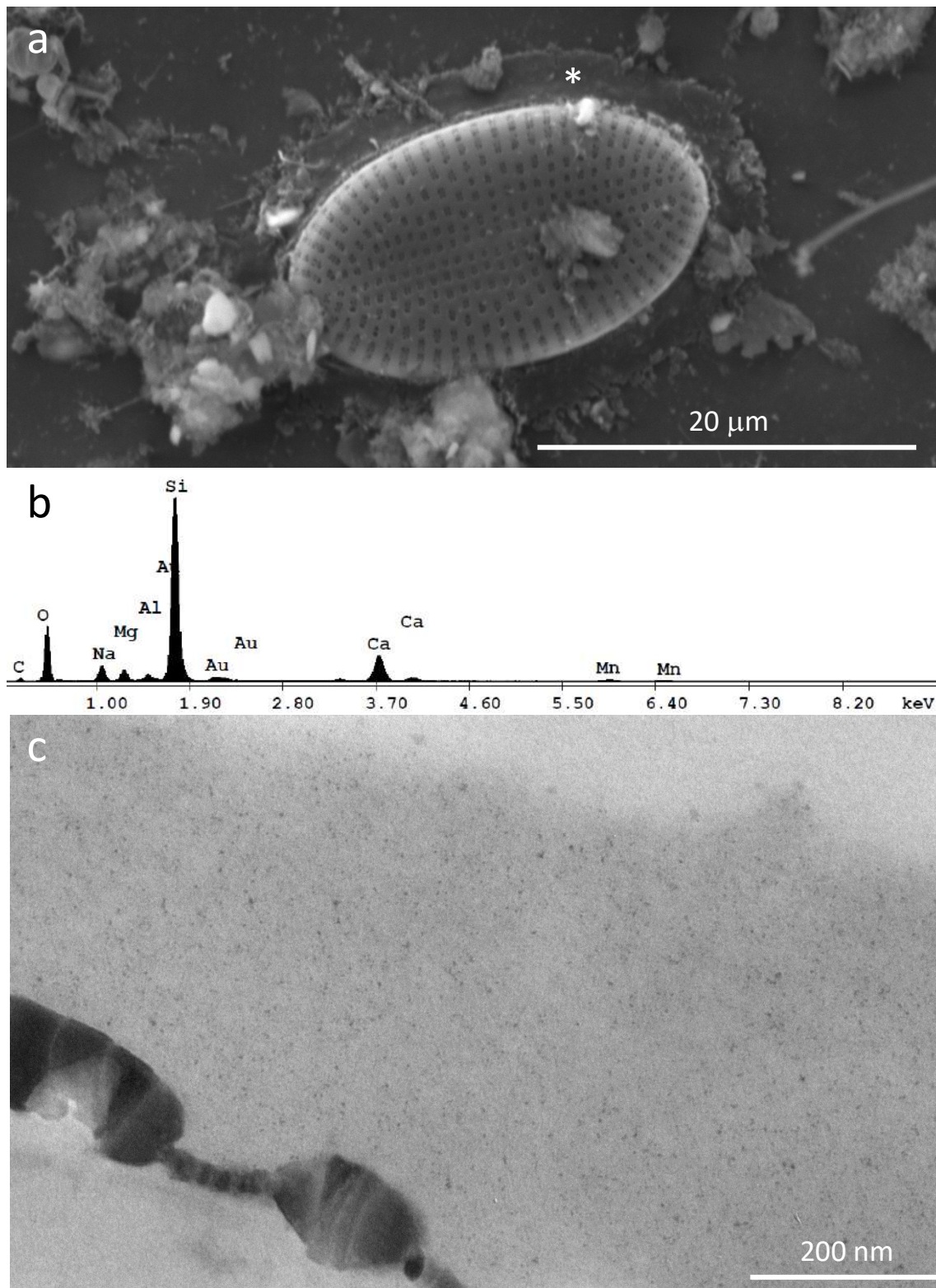


**Figure 1:** Sessile diatoms from Doce River periphyton. (a) Scanning electron microscopy image showing a diatom bound to the substrate by mucilage, along with attached mineral particles and debris. Asterisk points the site where the EDS spectrum was obtained. (b) EDS spectrum from the mucilage showing Mn peaks. O, Na, Mg, Al, Si, and Ca peaks were derived from the coverslip used as support, whereas Au came from the gold coating. (c) Transmission electron microscopy of an unstained sample showing part of the frustule (cracked structure) and the mucilage (dotted matrix). Electrone density is due to silica in the frustule and Mn in the mucilage. Note abundant Mn mineral nanoparticles in the mucilage.

## **Morphological Changes in the Intestine of Pufferfish Due to Anthropogenic Pollution: A New Proposal for Environmental Quality Assessment**

Gabriela Pustiglione Marinsek<sup>1\*</sup>, Lórihany Bogo Bortolotto<sup>1</sup>, Paloma Kachel Gusso Choueri<sup>1</sup>, Denis Moledo de Souza Abessa<sup>1</sup> and Renata de Britto Mari<sup>1</sup>

<sup>1</sup>: São Paulo University – UNESP, Bioscience Institute – IB/CLP, São Vicente, São Paulo, Brazil. \*E-mail: gabriela.marinsek@unesp.br

Anthropogenic pressure in estuarine environments has been increasing exponentially in recent years, which requires a more accentuated monitoring. The use of biomarkers is increasing in the studies that evaluate the environmental quality and the search for new models is of extreme importance for analyzes surveillance [1]. The gut contains peculiar features that make it a potential biomarker, although it is widely neglected in environmental quality studies. In addition to being responsible for the absorption of water, electrolytes and essential nutrients, this organ plays an important role in defending the body against pathogens. However, due to these characteristics this organ is also subject to constant absorption of the contaminants dissolved in the water and even accumulated in the tissues of organisms that make up the diet of the predator. In this way, this study aimed to evaluate the morphological changes in the intestine of the pufferfish in three estuaries of the coast of the São Paulo state that differed between them through the environment and anthropogenic pressures and, thus propose the use of this biomarker organ for environmental quality assessment. Ten specimens of *S. testudineus* were used in each of the evaluated regions (AR - Juréia Itatins Mosaic, A1 - Estuarine Lagoon Complex of Cananéia Iguape and A2 - Estuarine Complex of Santos - São Vicente). After collection, the distal intestine of the specimens was submitted to histological analysis and the sections were stained by the Hematoxylin-Eosin and Schiff Active Periodic techniques. For a stratigraphic measurement of the intestine ( $\mu\text{m}$ ) the 100x increase was used and for count of intraepithelial lymphocytes (IELs) and mucosecretory cells (PAS +) the increase was 1000x. All goblet cells, intraepithelial lymphocytes (IELs) and enterocytes visualized in the microscopic field were counted and subsequently subordinated to a ratio between IELs/enterocytes and goblet cells/enterocytes. The morphometric parameters evaluated showed a 20% increase in villus height and 40% in submucosa thickness ( $p < 0.05$ , ANOVA) of A2 animals, which reflected a significant increase in the total wall of this group in relation to RA and A1 ( $p < 0.05$ , ANOVA). The interface between IELs and enterocytes was increased by 45% in A1 and 60% in A2 ( $p < 0.05$ , ANOVA) when compared to RA. Goblet cell density didn't change between study regions (Figure 1). The increase in villus height of the animals captured in A2 is related to the increase in the rate of mitigation and reduction of the cellular extrusion rate, which characterizes the process of turnover; such an event may be in response to an attempt to increase the absorption surface. In addition, there is an increase in the recruitment of cells of the immune system, which can be evidenced by the increased thickness of the sheet and the increase in the ratio between the IELs/enterocytes. In this way, it is suggested that the complex mixture of contaminants found in A2 is interfering with the dynamics of the intestinal epithelium as well as causing inflammatory processes in this tissue, which compromises the homeostasis of this organ [2]. In this way, it is concluded that the intestine is subject to changes caused by the effects of contaminants and must be incorporated, along with other biomarkers, to environmental quality analyzes. In this way, it is suggested that the complex mixture of contaminants found in A2 is interfering with the dynamics of the intestinal epithelium as well as causing inflammatory processes in this tissue, which compromises the homeostasis

of this organ [2]. In this way, it is concluded that the intestine is subject to changes caused by the effects of contaminants and must be incorporated, along with other biomarkers, to environmental quality analyzes.

## REFERENCES

- [1] Cajaraville, M. P. et al., Science of the Total Environment. (2000) 295.  
[2] Brierley, S.M. et al., Nature reviews Gastroenterology & hepatology (2014) 611.

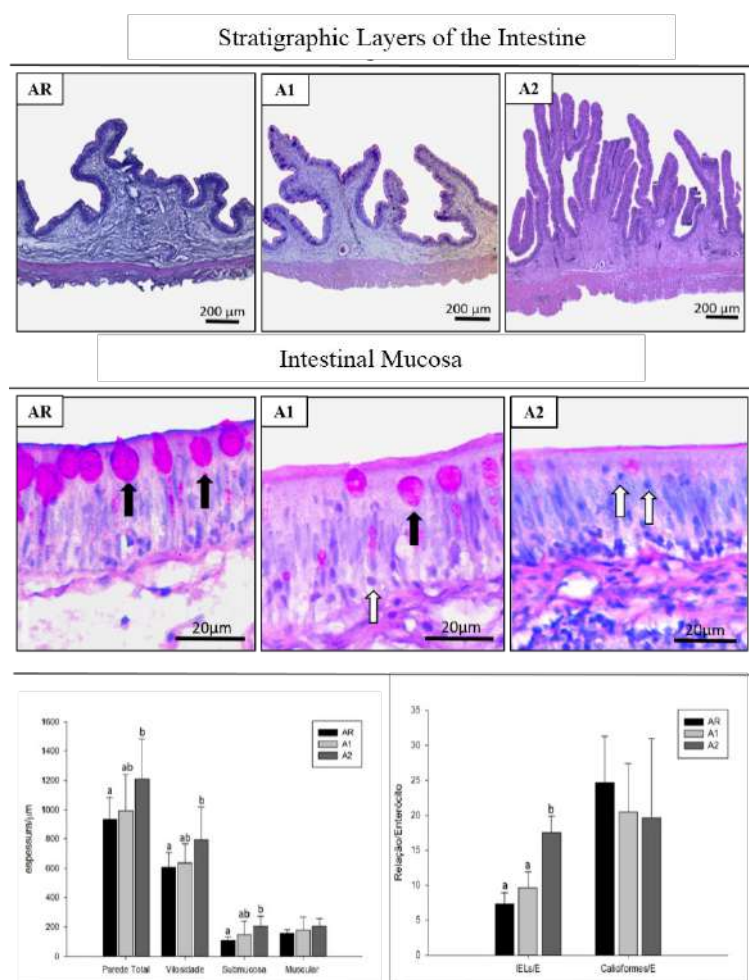


**Figure 1** - Photomicrography of the stratigraphic layers of the *Sphoeroides testudineus* intestine and graphical representation of the average of the measurements obtained in each region highlighting the difference between the collection sites (AR - Juréia Itatins Mosaic, A1 - Cananéia - Iguape Lagunar Estuarine Complex and A2 - Estuarine Complex of Santos-São Vicente). Hematoxylin-Eosin. Bar = 200µm. Below, photomicrography of the mucosal layer of the *S. testudineus* gut indicating the presence of goblet cells (white arrow) and intraepithelial lymphocytes (black arrow). Schiff's Reactive Journal (PAS) counter-stained with Hematoxylin.

\* Different letters represent statistical difference by the ANOVA test





## Measurements of the dielectric constant of a natural photonic crystal by Electric Force Microscopy

Wescley Walison Valeriano<sup>1</sup>, Paulo Sergio Soares Guimarães<sup>1</sup>,  
Bernardo Ruegger Almeida Neves<sup>1</sup>, Wagner Nunes Rodrigues<sup>1,2</sup>

<sup>1</sup> Departamento de Física, Instituto de Ciências Exatas, UFMG

<sup>2</sup> Centro de Microscopia, UFMG

In this work we studied the static dielectric properties of the strongly iridescent hind wings of the male *Chalcopteryx rutilans* damselfly [Figure 1]. We demonstrated in a previous work that such wings are photonic crystals, which colors originate from their multilayered nanometric structure [1]. A three-dimensional TOF-SIMS analysis revealed changes in Na, K, and eumelanin concentrations along the thickness of the wing, which modulated accordingly the dielectric constant of the layers (2). The dielectric constants of the layers are key to describe the wing as a photonic structure, and are also important parameters in phenomena such as the membrane permeability to ions [3].

The photonic crystal present in the studied damselfly wing is formed by layers a few nanometer thick. To obtain the local dielectric constant in each layer we used scanning probe microscopy in the electric force mode -EFM, and modeled the measured profiles with a tip-substrate interactive analytical model [4].

As a sample test, we measured the dielectric constant of a film of Al<sub>2</sub>O<sub>3</sub> [Figure 2], obtaining  $9,27 \pm 0.08$ , in excellent accordance with the found in the literature [5]. To use the EFM method, the sample needs to be less than 100 nm thick, the thinner the better. So, we embed the wing in a resin to have it mechanically supported, and a 40 nm thin layer was cut by ultramicrotomy. The obtained fragment was placed on an Au/Cr coated silicon substrate in order to have it on a smooth conductive substrate.

We prepared samples from three different color regions of the wing – blue, red and yellow/green [Figure 1]. The results show that the multilayered structures have the dielectric constant changing from  $6 \pm 1$  to  $9 \pm 1$  from layer to layer, the difference among the three colors regions being in the number and thickness of each layer [Figure 3-5]. The Na and K containing layers present the higher static dielectric constant.

The present results of the static dielectric constant of the multilayered structure of the studied damselfly wing corroborates the previous optical and microscopy studies.

### Reference

- [1] W. W. Valeriano, “Belo Horizonte Belo Horizonte,” Universidade Federal de Minas Gerais, 2015.
- [2] D. M. Carr *et al.*, “Characterization of natural photonic crystals in iridescent wings of damselfly *Chalcopteryx rutilans* by FIB/SEM, TEM, and TOF-SIMS,” *Biointerphases*, vol. 13, no. 3, p. 03B406, 2018.
- [3] T. Baştuğ and S. Kuyucak, “Role of the dielectric constants of membrane proteins and channel water in ion permeation,” *Biophys. J.*, vol. 84, no. 5, pp. 2871–2882, 2003.
- [4] C. Riedel *et al.*, “Determination of the nanoscale dielectric constant by means of a double pass method using electrostatic force microscopy,” *J. Appl. Phys.*, vol. 106, no. 2, pp. 1–6, 2009.

- [5] M. J. Biercuk, D. J. Monsma, C. M. Marcus, J. S. Backer, and R. G. Gordon, "Low-temperature atomic-layer-deposition lift-off method for microelectronic and nanoelectronic applications," *Appl. Phys. Lett.*, vol. 83, no. 12, pp. 2405–2407, 2003.

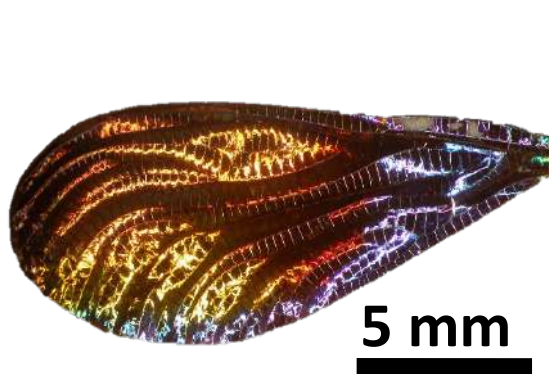


Figure 1- Damselfly *Chalcopteryx rutilans* wing.

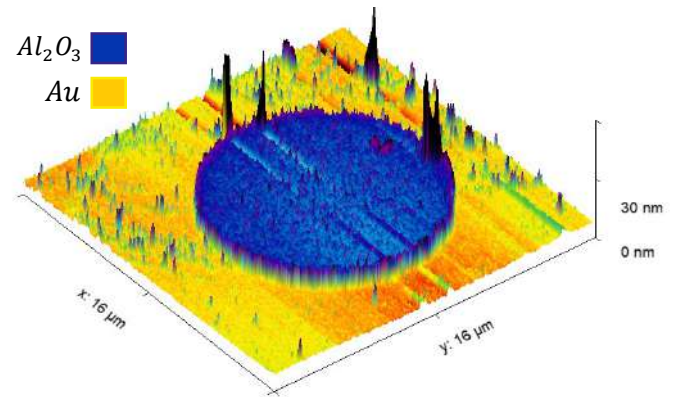


Figure 2- The test sample,  $\text{Al}_2\text{O}_3$  by ALD in a gold substrate.

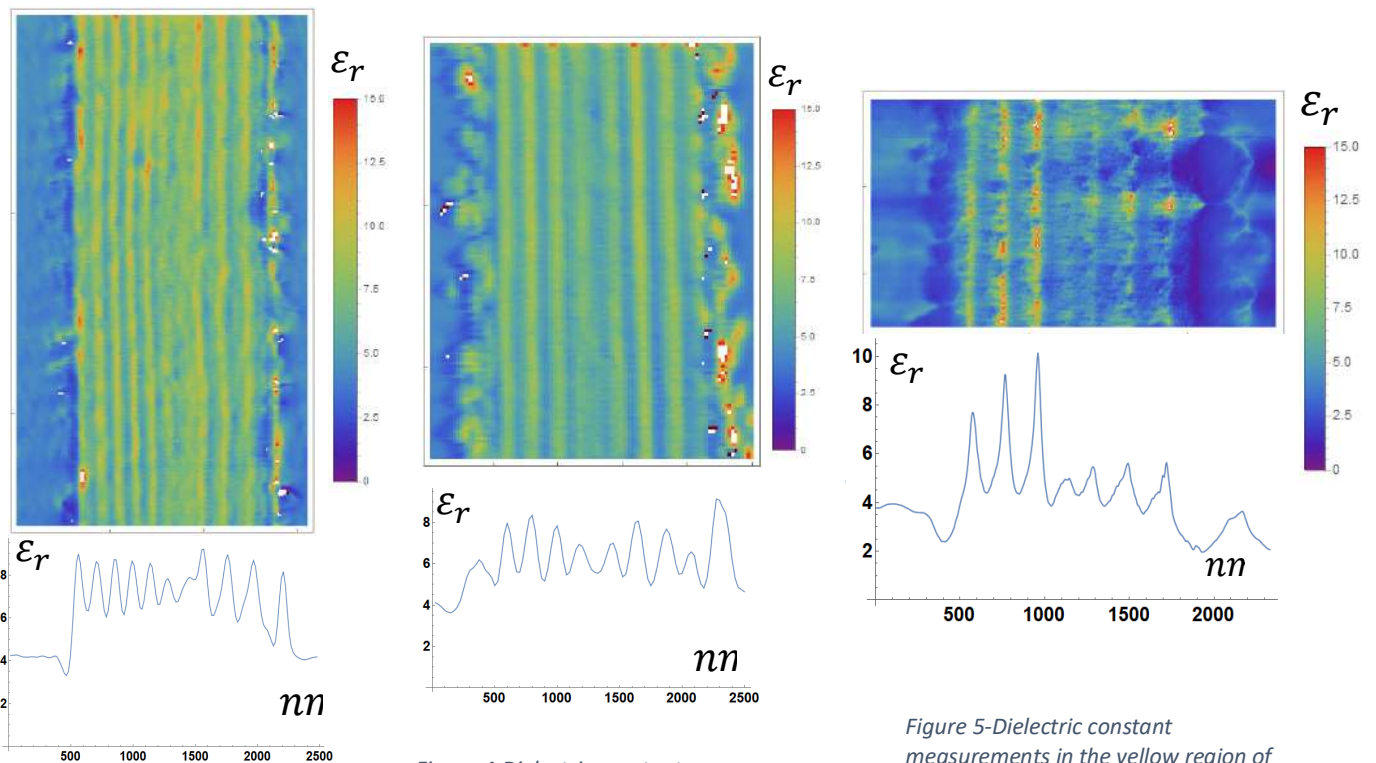


Figure 3- Dielectric constant measurements in the blue region of the wing.

Figure 4- Dielectric constant measurements in the red region of the wing.

Figure 5- Dielectric constant measurements in the yellow region of the wing.



## **Use of Trichology Associated with Electronic Microscopy in the Conservation of Genetic Resources in Sheep in Northeast of Brazil**

**Luís Alberto Linhares Rufino<sup>1</sup>, Kleibe de Moraes Silva<sup>2</sup>, João Victor Serra Nunes<sup>3</sup>.**

<sup>1</sup>Pesquisador Autônomo. \*E-mail do autor apresentador: [uadnum@gmail.com](mailto:uadnum@gmail.com)

<sup>2</sup>Embrapa Caprinos e ovinos, Sobral, Ceará, Brazil.

<sup>3</sup>Universidade Federal do Ceará, Fortaleza, Ceará, Brazil.

Morphological analysis of animal hair has been used in several situations, such as the investigation of adaptation of animals to living conditions [1]. This technique allows identifying characteristics peculiar to the species, from the analysis of the structures of the hairs, by transversal and longitudinal cuts, revealing the medullary pattern, the dimensions, the color, and generating key information that helps in the classification of the species [2]. It has contributed to programs of conservation of locally adapted breeds for the purpose of determining the genetic ancestry of animals [3]. The technique was proposed in Italy with the objective of assuring the genetic origin of these small ruminants, since products such as cheeses from local breeds have a higher added value [4]. In Brazil it was used in the characterization of the hair of the cattle breeds of Pantaneiro and Curraleiro. The study can help as a further tool for knowledge and use of animal genetic resources, generating a better identification system, as well as providing data for breeding programs and agricultural research and development [3]. The typification of the hairs makes it possible to clarify characteristics of rusticity and adaptations to adverse conditions [3]. The measurement is accurate, efficient and reliable, aiding in the interpretation of the object under study, and hence generating information, which can be used in classifying races. In this study, thirty adult sheep were used: 10 of the Morada Nova breed of white fur; 10 of the Morada Nova breed of red fur; 10 of the Somalis breed. From then, where the hairs are were removed from the left flank region in 10 points of each animal, identified and stored in small plastic bags. The material was processed for cleaning and drying, in which used Shampoo Johnson's Baby, distilled water and absolute alcohol. The samples hairs were analyzed by scanning electron microscope (INSPECT S-50 FEI) and the average cutoff widths of the hairs were measured. The results showed a general average of  $150.27 \pm 25.65 \mu\text{m}$ . The avergares obtained by genetic groups were: 148,4  $\mu\text{m}$  Morada Nova de pelagem branca; 157,2  $\mu\text{m}$  Morada Nova de pelagem vermelha; 147,6  $\mu\text{m}$  Somalis Brasileira. There was no difference between the cuticles widths of the hair between the genetic groups evaluated. Phenotypic characterization through various techniques is part of in situ conservation programs of local breeds. The use of trichology as a method, in which the analysis of the architecture of the hairs is by optical and / or electron microscopy, can serve as an alternative methodology and / or complement programs of conservation of locally adapted breeds. The technique can aid in the research and development of animal production in Brazil, conservation programs and certification processes of origin in animals of economic interest.

## REFERÊNCIAS

- [1] FARAG, M. R et al., Forensic Identification of some Wil Animal Hair using Light and Scanning Electron Microcopy. *Advances in Animal and Veterinary Sciences*, V.3, pp. 559-568, 2015.
- [2] WALLIS, R. L. A key for identification of guard hairs of some Ontario mammals. *Canadian Journal of Zoology*, Ottawa, v. 71, n.3, p. 587-591, 1993.
- [3] FELIX, G. A et al., Adaptação de metodologia: análise de microestruturas de pelos para identificação de mamíferos – Tricologia. *Comunicado Técnico–Embrapa Pantanal* 96, 6p. 2014.
- [4] FELIX, G. A et al., Trichology for identifying mammal species and breed: Its use in research and agriculture. *Arch. Zootec.* 63 ®®: 107-116, 2014.

Os autores gostariam de agradecer à Central Analítica-UFC/CT-INFRA/MCTI-SISNANO/Pró-Equipamentos CAPES.

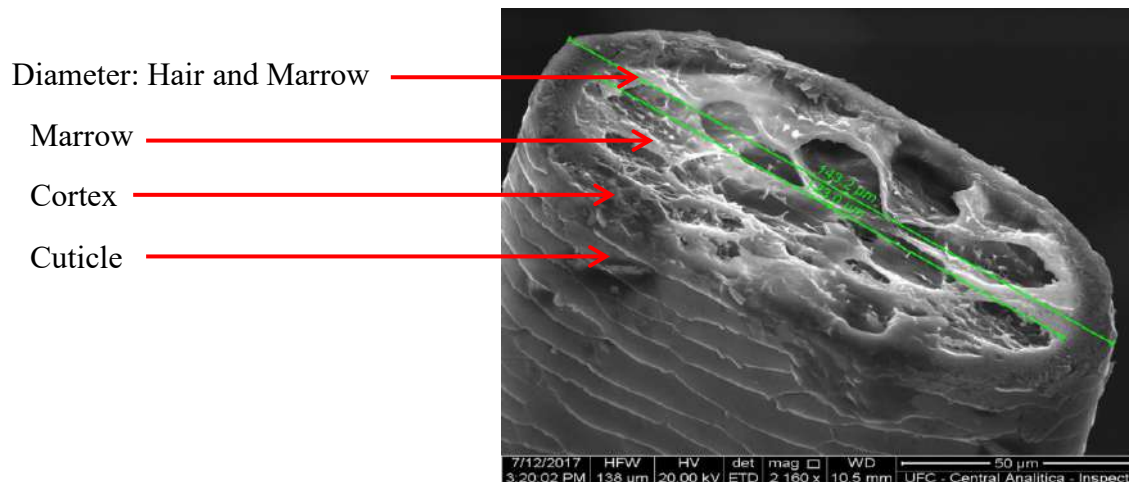


Figura 1 - Córtex e Marrow – ovino morada nova variedade branca hair

Results						
		N	Mean	Std. Error	Dif.	P-valor
overall width	SOMA	68	147,6	3,95	B	0,036
	MNB	35	148,4	4,01	AB	
	MNV	63	157,2	2,23	A	
µ width of the scales	SOMA	53	12,0	0,40	AB	0,044
	MNB	15	10,2	0,44	B	
	MNV	35	13,4	1,34	A	
µ lengths of scales	SOMA	53	62,3	2,16	A	0,0001
	MNB	15	46,7	2,70	B	
	MNV	35	46,1	1,97	B	

ANOVA *post hoc* LSD ( $P < 0,05$ )

SOMA : Somalis Brasileira

MNB: Morada Nova de pelagem branca

MNV: Morada Nova de pelagem vermelha



## Studying Glycosylation Sites of Annelid Hemoglobin by Cryo-EM

Juliana da Fonseca Rezende e Mello<sup>1</sup>, Michael Schatz<sup>2</sup>, Richard Charles Garratt<sup>3</sup>,  
Rodrigo Villares Portugal<sup>1</sup>, Marin van Heel<sup>1\*</sup>

<sup>1</sup>. Centro Nacional de Pesquisa em Energia e Materiais, Laboratório Nacional de Nanotecnologia, São Paulo, Brasil

<sup>2</sup>. Image Science Software GmbH, Berlin, Germany

<sup>3</sup>. Universidade de São Paulo, Instituto de Física de São Carlos, São Paulo, Brasil

Corresponding author: [marin.vanheel@gmail.com](mailto:marin.vanheel@gmail.com)

*Lumbricus terrestris* and many other annelid species contain erythrocrurins which are huge extracellular oxygen-carrying hemoglobin particles [1]. These giants hemoglobins packing a lot of functional units into one particle, maximizing O<sub>2</sub> transport [2]. This profile makes *L. terrestris* hemoglobin a potential blood substitute [2,3]. Instead of the number of studies discussing the hemoglobin structure, some aspects remain unclear, as the content of carbohydrate of each chain. The presence of glycosylation sites in various *L. terrestris* chains has been indicated by mass spectroscopy but has never been visualized in cryo-EM maps. Glycosylation was previously detected in *Glossoscolex paulistus* and *Lamellibrachia satsuma* hemoglobins, which structurally are similar to *L. terrestris* hemoglobin using X-ray crystallography [4, 5]. In this work we performed the evaluation of glycosylation sites in *L. terrestris* giant hemoglobin, using the atomic model fitting into the cryo-EM map. The atomic model of *L. terrestris* hemoglobin was properly fitted into its cryo-EM map and the potential glycosylation sites were predicted using the primary structure. Therefore, we performed an inspection of the predicted glycosylation sites in the cryo-EM map based on the atomic model fitting and on a clearly defined local Fourier Shell Correlation (FSC) resolution criterion. Several glycosylation sites were found and are mainly localized at the interfaces between protomers. One of the carbohydrate subunits remains clearly visible and appears more stable than the next glycans subunits. Using a new local FSC-derived metric to emphasize the relevant parts of the map in combination with model fitting (of the primary sequence) into this optimized cryo-EM map, we could directly visualize the N-glycosylation sites of *L. terrestris* hemoglobin.

[1] P. Afanasyev et al., IUCrJ, 4(5) (2017) 678-694.

[2] W.T. Chen et al., Sci. Rep., 5 (2015) 9494.

[3] D. Zimmerman et al., Bioeng Transl Med., 2(2) (2017) 212-221.

[4] J.F.R. Bachega et al., Acta Cryst., D71 (2015) 1257-1271.



- [5] N. Numoto *et al.*, *Acta Cryst*, 70 (2014) 1823-31.  
[6] This research is supported by Capes (Brazil).

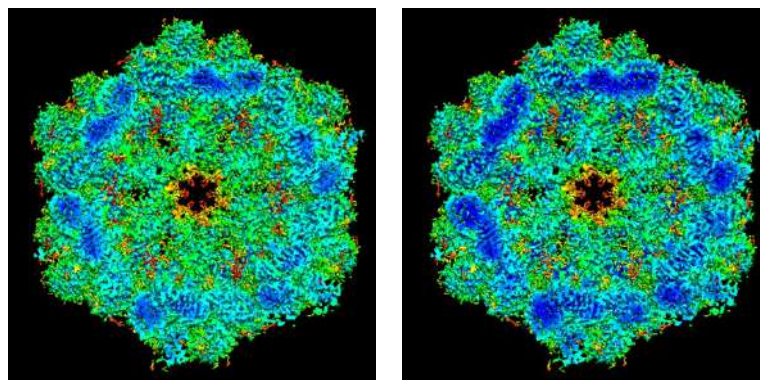


**Figure 1:** Local Resolution maps of the *L. terrestris* hemoglobin structure obtained by comparing the cryo-EM density map, with: (A) the density map created from the deposited PDB co-ordinates. (B) the density map from the deposited PDB co-ordinates after flexible fitting. The colors are scaled from red (poor correlation) to dark blue (high correlation).

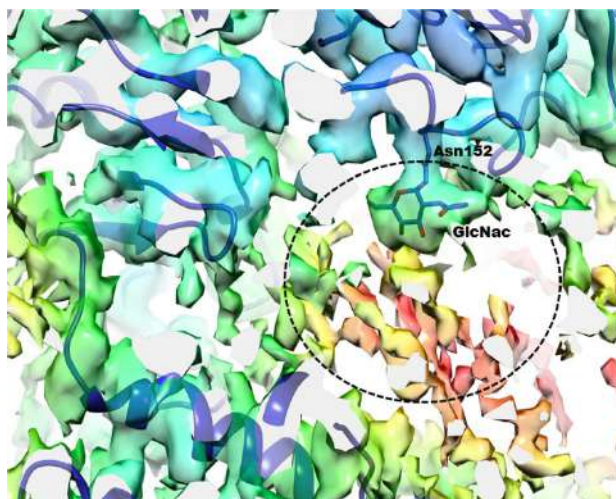


**Figure 2:** Hemoglobin map, colored using a local FSC-derived resolution metric between two independently determined cryo-EM (“half”) maps. The image is scaled from red (most flexible areas) to dark blue (highly compact rigid areas). Additional densities - not occupied by protein - suggest the presence of further sugars connected the N-acetylglucosamine (GlcNac). The detail shows the fitting of sugars to cryo-EM densities not occupied by protein.

## Cryo-TEM Study of the Growth and Crystallization Processes of Calcium Phosphate

Dalmonico G.<sup>1</sup>, Farina M.<sup>2</sup>, Rossi A.<sup>1</sup>

<sup>1</sup>. Brazilian Center for Research in Physics, Rio de Janeiro, Brazil

<sup>2</sup>. Federal University of Rio de Janeiro, Biomedical Science, Rio de Janeiro, Brazil

Calcium orthophosphates are a class of materials that attracts strong interest in many research areas in the fields of chemistry, physics, biology and medicine. They are one of the main inorganic constituents of the calcified tissues of vertebrates (bones and teeth) and can be used in bone implants due to their remarkable biocompatibility and bioactivity [1]. The synthesis of HA in a controlled manner is an important requirement for different applications and can also be used for elucidating the mechanism of mineralization in biological systems (biomineralization). In this work, the morphology and structural characteristics of calcium phosphate (CaP) nanoparticles were investigated at different steps of the synthesis process by analytical cryo-transmission electron microscopy (Cryo-TEM) in combination with other analytical techniques that need large amounts of material. The synthesis of HA was performed by dropwise addition of phosphoric acid to calcium hydroxide solution in order to obtain a final solution with a Ca/P ratio of 1.67. Calcium and phosphate ions react to form CaP and water. The whole synthesis (dropwise addition and aging) occurred over a period of 24 h. The reaction was performed at room temperature ( $\sim 25^{\circ}\text{C}$ ), and the pH was not kept constant. Samples were collected after different periods of time (5 min, 10 min, 30 min, 1 h, 2 h, 7 h, 11 h, 15 h, 19 h and 24 h) for the study of the process of HA growth and crystallization. The samples were ultrafast-frozen to be analysed by transmission electron microscopy or freeze-dried to be analysed by XPS, XRD and FTIR. We showed that the process of drying the sample, instead of analyzing the sample in vitreous ice, did not significantly alter the morphology of the nanoparticles but did induce significant changes in their crystallinity. As shown by Cryo-TEM, crystallization of the nanoparticles in the frozen hydrated state was detected only after a long period of synthesis. In the first 5 min of reaction, which corresponds to a low amount of phosphate ions in solution, we observed nanoparticles characterized by a high Ca/P ratio that transformed after 30-60 min into needle-like amorphous nanoparticles with a comparatively lower Ca/P ratio (Figure 1). The mechanism of HA formation using these chemical routes will also be discussed in the presentation regarding new paradigms of (bio)mineralization on the basis of a nonclassic mechanism of nucleation induced by nanocluster aggregation, amorphous calcium phosphate and multiple stages of crystallization [2].

[1] S. V. Dorozhkin, *Materials* (Basel), 2 (2009) 399–498.

[2] J. R. Dorvee, A. Veis, *J. Struct. Biol.*, 183 (2013) 278–303.

[3] This research was supported by CNPq and FAPERJ (Brazil).

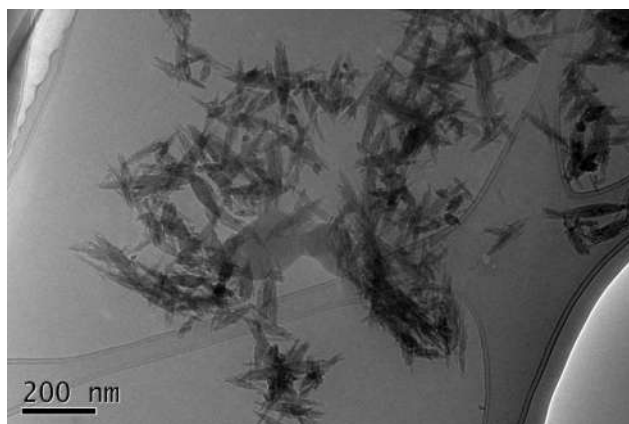


Figure 1: Cryo-TEM image of Calcium Phosphate nanoparticles after 30-60 min of synthesis.



## Adaptation of Cryogenic System to a Cross Beam Scanning Electron Microscope

Vânia Vieira<sup>2</sup>, Kildare Miranda<sup>1,2</sup>

<sup>1</sup> Instituto de Biofísica Carlos Chagas Filho, Universidade Federal do Rio de Janeiro - UFRJ

<sup>2</sup> Centro Nacional de Biologia Estrutural e Bioimagem, CCS, UFRJ, Rio de Janeiro, Brasil. E-mail: kmiranda@biof.ufrj.br

Biological electron microscopy encompasses a number of techniques that are under constant development. Some of these techniques, initially developed decades ago, have outstandingly improved allowing sample preparation and visualization in a more close-to-the-native state in microscopes now more stable and sensitive. This is the case of cryoelectron microscopy, currently applied to the structural characterization of a variety of cells and molecules and considered one of the main tools that have changed the landscape on molecular and cell biology over the past decade. This technique relies in the maintenance of the sample at low temperature inside the microscope, for which a cryostage and a cryotransfer system are required both for cryoTEM and cryoSEM. Conversion of most SEMs into cryoSEMs involves the installation of expensive systems commercially available, always tailored for the type of instrument to which they will be attached. This requires dimensional adaptations that are mostly done by the manufacturer. For this reason, adaptation of old cryosystems into new scopes is not usual. Here, we carried out an adaptation of a Leica EM VCT100 cryotransfer system to an Auriga 40 cross beam scanning electron microscopy system. For that, a number of dimensional adaptations was carried out in order to map possible pressure variation problems (flange dimension, microscope connections, cryogenic trap etc). The size and mass of heat conducting stripes vs efficiency of the system was also tested as follows: (1) 32 cm and (2) 16 cm long stripes with the same mass; and (3) 32 cm and (4) 16 cm long stripes with half of the same mass. Results showed that once the minimal mass was maintained, the predominant factor that determines the efficiency of the system is the length of the stripes, which is consistent with the Fourier Law for the heat flow (Fig 2). The sample holder was connected by stripes to a thermostatic reservoir permanently cooled with liquid nitrogen to be maintained near -150 ° C (Fig 1 – A). A low pressure cryotransfer system was adapted to the back of the microscope, allowing the sample to remain cooled throughout the process (Fig 1-B). In order to prove the efficacy of the apparatus, well-known biological models such as *Trypanosoma cruzi* which has been extensively studied through the use of cryotechniques were used [4]. The sample was frozen with High Pressure Freezing, freeze fractured and coated with a 2 nm thick platinum at 45° with rotation at a Leica BAF060. Images were obtained in a Zeiss Auriga 40 at low voltage (~2 KV), with short working distances (~1.8 mm) and the use of an in-lens SE detector. Results showed a successful application of the technique, where the general fractured aspect of the entire sample (Fig3). High resolution images of the fractured surfaces of the cell allowed the visualization of *T. cruzi* cytosome surface domain and the identification of intramembranous particles. Modifications to improve the sample holder for cryolamella preparation is currently under development.

### REFERÊNCIAS

[1] DUBOCHET, J.; MCDOWALL, A. W. Vitrification of Pure Water for Electron Microscopy. *Journal of Microscopy*, v. 124, n. 3, p. 3–4, 1981

[2] KAUFMANN, Rainer et al., Fluorescence cryo-microscopy: Current challenges and prospects. *Current Opinion in Chemical Biology*, v. 20, n. 1, p. 86–91, 2014.

[3] GIRARD-DIAS, Wendell et al. On the ultrastructural organization of trypanosoma cruzi using cryopreparation methods and electron tomography. *Histochemistry and Cell Biology*, v. 138, n. 6, p. 821–831, 2012.

This work was supported by CAPES, CNPq, FAPERJ, FINEP and Instituto Nacional de Ciência e Tecnologia em Biologia Estrutural e Bioimagem.

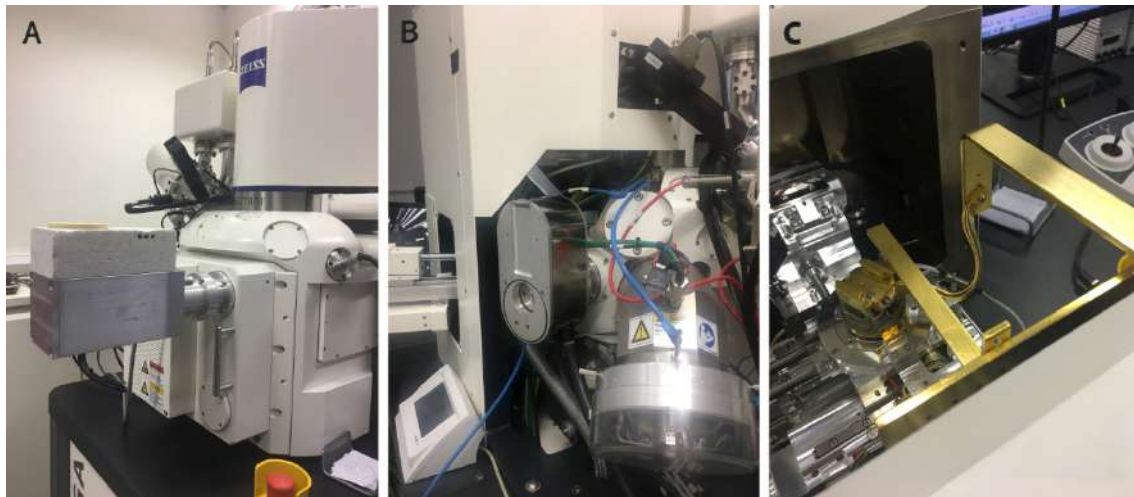


Figure 1: Cryomicroscopy apparatus (A) Outside nitrogen dewar (B) Shuttle for cryotransfer (C) Inside, cold finger and conductors stick

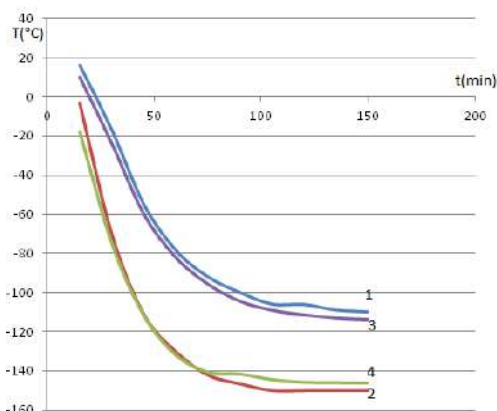


Figure 2: Temperature variation with length and mass of the stripes: 1- 32 cm long stripes weighting 32 g, 2- 16 cm long stripes weighting 32 g. 3- 32 cm long stripes weighting 16 g, 4- 16 cm long stripes weighting 16 g.

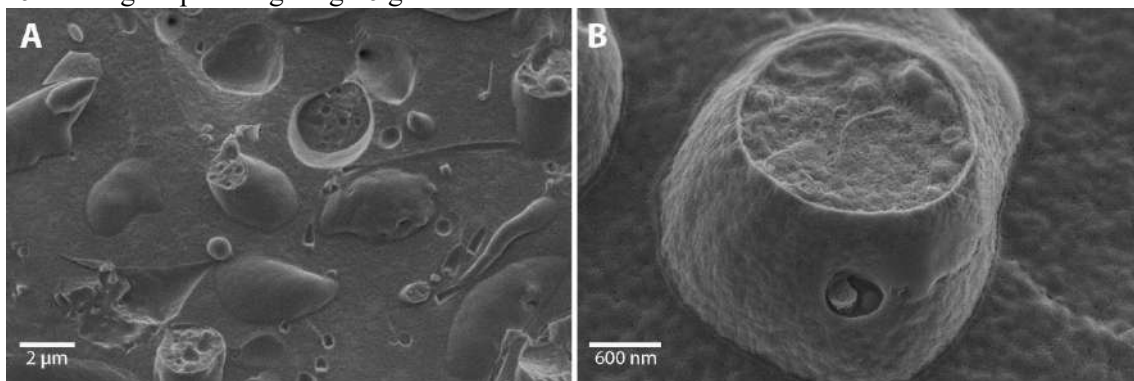


Figure 3: vitrified sample visualized in HRSEM, in-lens detector.

## Invasion of bacteria in intestinal tissue infected with *Trichuris muris*

Dayane Alvarinho de Oliveira<sup>1</sup>, Masinda P. R. Nguidi<sup>1</sup>, Ana Claudia Paula Rosas  
Ignácio<sup>2</sup> and Eduardo José Lopes Torres<sup>1,\*</sup>

<sup>1</sup>. Laboratório de Helmintologia Romero Lascasas Porto, UERJ, DMIP/ FCM, Rio de Janeiro, Brasil. \* [eduardo.torres@uerj.br](mailto:eduardo.torres@uerj.br)

<sup>2</sup>. UERJ, DMIP/ FCM, Rio de Janeiro, Brasil.

The trichuriasis is a soil transmitted helminth infection and promoted by nematodes of the genus *Trichuris* sp. *T. trichiura* species affects around 460 million people worldwide, especially in countries with basic sanitation problems associated with tropical climate [1]. *Trichuris muris* has been widely used as experimental model in mice to study the host-parasite interactions. The *Trichuris* eggs hatch in the small intestine and the larvae then migrate to the large intestine, invading the intestinal mucosa. The nematode grows and moves inside of the epithelial layer, with the anterior end remaining inserted in the host tissue and the posterior region free in the lumen, causing damages on the intestinal epithelium [2]. The aim of this work is to characterize the invasion of bacteria in the intestinal tissue infected by *T. muris* in chronic phase using bright field light microscopy, scanning electron microscopy (SEM) and fluorescence in situ hybridization (FISH). The infection was performed using the Swiss webster mice infected with 150 *T. muris* eggs and euthanized 45 days post-infection. The cecum was fixed in 4% buffered formalin, for light microscopy experiments and in Karnovsky's solution for SEM experiments. For the histological analysis the slides were stained with Giemsa, mounted with Entellan® and observed using Nikon Eclipse 80i microscope. The samples for SEM experiments were, post-fixed in osmium tetroxide, dehydrated in ethanol series, critical point dried, mounted in a metal stub, sputtered with gold and analyzed using FEI-Quanta 250. For FISH analyses fixed tissues were embedded in OCT (Tissue-Tek®), frozen in liquid nitrogen and cut in cryostat (5µm). These samples were washed with 30% formamide in the hybridization buffer, incubated in probes for eubacteria and labeling with 4,6-diamidino-2-phenylindole (DAPI). The slides were coated with N-propylgalate (Sigma / Aldrich) and observed using the Zeiss microscope. equipped with AxioImager an AxioCam RMC (Zeiss, Germany). In bright field analyses, using Giemsa stain the presence of cocci and bacilli was detected in submucosa of the infected large intestine (Figs. A and B). By SEM was possible identify the nematode inserted in to the tissue (Fig C) promoting lesions on the mucosal surface and invasive bacteria were detected in the submucosa (Fig. D). Fluorescence experiment results showed the invasive process. In control group the bacteria (green) were observed only in the mucosa surface and inside the lieberkuhn crypts (Fig E), however when the infected large intestine were analyzed, stained bacteria were identified in submucosa (Fig F). Our study contributes with a detailed description of the bacteria invasion and this understanding is fundamental to understand the clinical evolution of this infection and think about new therapeutic strategies.

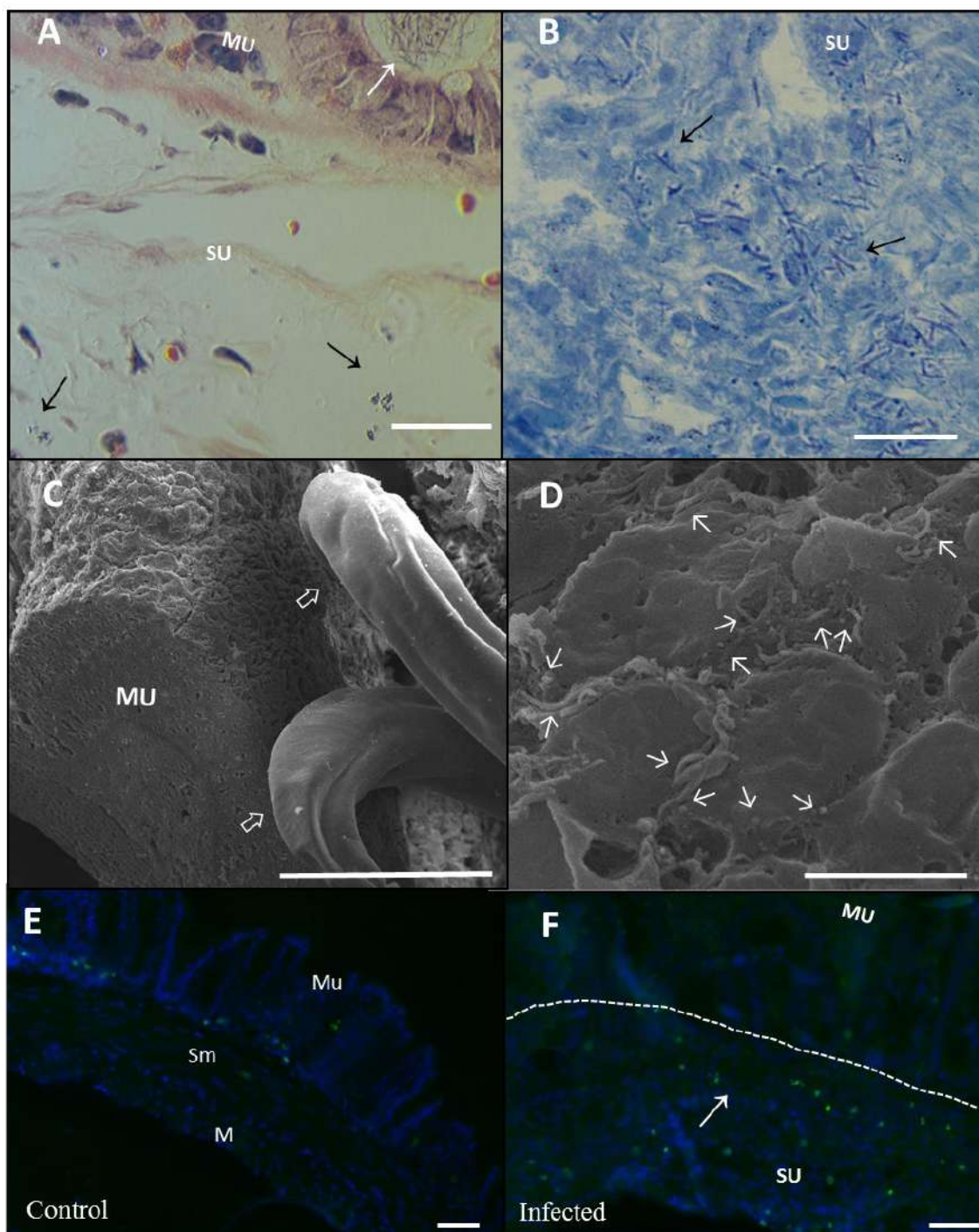
### References:

[1] Guia Prático para o Controle das Geo-helminthíases /Brasília: Ministério da Saúde, 2018. ISBN 978-85-334-2622-1il.

[2] E.J. Klementowicz et al., (2012). [https://doi: 10.1007/s00281-012-0348-2](https://doi.org/10.1007/s00281-012-0348-2).

This research was supported by CNPq, FAPERJ and Laboratorio de Biologia Celular e Magnetotaxia UFRJ (Brazil).





Legend: (A-B) Histological sections of large intestine (cecum) stained with with Giemsa, for analyses of the bacterial invasion in the submucosa layer (A) Bateria in mucosa surface (white arrow) and the submucosa with invasive coccus-shaped bacteria (black arrow). (B) A large number of the invasive bacilliform bacteria in submucosa (black arrow). (C) SEM showing the nematode inserted on the mucosa (↑) and promoting lesions. (D) SEM showing invasive bacteria in the submucosa. (E) FISH experiments showing the three layers of the uninfected tissue of the cecum and the bacteria (green) present only in mucosa. (F) FISH experiments showing infected tissue invaded by bacteria (green) in the submucosa (arrow). Abbreviations: MU – Mucosa; SU – Submucosa. Scale bar: A, B, D, E and F: 50  $\mu$ m and C: 500 $\mu$ m.



## Behavior of osteoblasts onto topographically designed scaffolds *in vitro*

Rafaela Silva dos Santos<sup>1\*</sup>, Pablo Rougerie<sup>2</sup>, Mair Machado M. de Oliveira<sup>2</sup>, Karine Anselme<sup>3</sup>, and Marcos Farina<sup>2</sup>

<sup>1</sup> Institute of Biophysics Carlos Chagas Filho, UFRJ, Rio de Janeiro, Brazil,

<sup>2</sup> Institute of Biomedical Sciences, UFRJ, Rio de Janeiro, Brazil,

<sup>3</sup> Institut de Science des Materiaux de Mulhouse, Université de Haute-Alsace, CNRS UMR 7361, Mulhouse, France

\*[rafassbio@gmail.com](mailto:rafassbio@gmail.com)

### Introduction

Topography of scaffolds can have a significant influence on cell behavior *in vitro*. Recognition of the spatial configuration of the surface can trigger different processes, such as cell adhesion, migration, proliferation, gene expression, differentiation, among others [1]. In particular, isotropic and anisotropic topographies are powerful tools to understand the mechanisms of bone matrix production by osteoblasts and develop new solutions for osteointegration involving cell/biomaterial interactions.

In living vertebrates, osteoblasts encounter curved surfaces with different local curvatures, mainly large and smooth surfaces with low curvature radius, as Howship's lacunae walls in bone tissue. It is therefore necessary to investigate the behavior of osteoblast and the bone formation on such curved topographies. In this work, we evaluated the osteoblast cell distribution, spreading and mineralization onto polymeric surfaces with periodical geometrical patterns in the order of magnitude of the cells (i.e. tenths of microns).

### Materials and Methods

Scaffolds of the polymer polydimethylsiloxane (PDMS) presenting isotropic or anisotropic surface topographies with periodical cell-scale patterns were produced and further covered with fibronectin, so that all the scaffolds had the same surface chemistry characteristics. The topographies produced presented different types of edges, from angular to sinusoidal. A second type of scaffold was also produced where concave regions simulating Howship lacunae were made with a fine drill or a needle, directly in the bottom of the culture wells where cells were seeded afterwards. The samples were fixed with glutaraldehyde, post-fixed with osmium tetroxide, dehydrated in an ethanol series and embedded in epoxy resin. Preosteoblasts (F-OST cells) obtained from rat calvaria [2] were seeded onto the surfaces produced and were induced to mineralize. Cells distribution along time over the substrates was analyzed by using light and electron microscopy. Among the several aspects analyzed were: attachment, cytoskeleton distribution (Alexa Fluor 488 phalloidin for actin filaments and Hoechst for nucleus, in a Laser scanning confocal microscope (LSCM) and organization of the biomineralized minerals of the nascent matrix (transmission electron microscopy – TEM)

### Results and Discussion

Osteoblasts (F-OST) cultivated on anisotropic PDMS surfaces composed by grooves and ridges, aligned and elongated along the elongated features of the topography and mineralized accordingly. Actin filaments and nuclei distribution confirm that the cells are anisotropically organized, influenced by the substrate topography (Fig. 1A).

To visualize the extracellular matrix produced *in vitro*, and mineralization products, cell cultures (F-OST) in the bottom of the wells was processed for TEM. Transverse sections

of the interface between the polieric substrate/cell culture region, were obtained by ultrathin sectioning. Cells were distributed in apposed layers with alternating regions rich in cells or in mineralized regions. Fig. 1B shows part of the apposed layers that appeared after 4 weeks. In this case, one cell is seen between two mineralized regions. In figure 1C it is shown a detail of the interface between the mineralized matrix (top left) and an osteoblast (bottom right). In between it is observed that collagen fibrils are also present, in layers that are crossed (arrows and dotted circle in Fig. 1C). This pattern of organization is similar to that of the bone. As a conclusion, we observed that the topography of the substrate with patterns at the micrometer scale can influence cells distribution and mineralization *in vitro*, and that culture wells can be directly used as a model for bone like tissue production including the mineralization phenotype.

### References

- [1] K. Anselme et al. Advanced Healthcare Materials (2017)1701154.
- [2] A. Balduino et al. Cell and Tissue Research 319(2005)255.
- [3] Financial support: CNPq, Faperj and CAPES brazilian agencies, and PICS - CNRS, France.

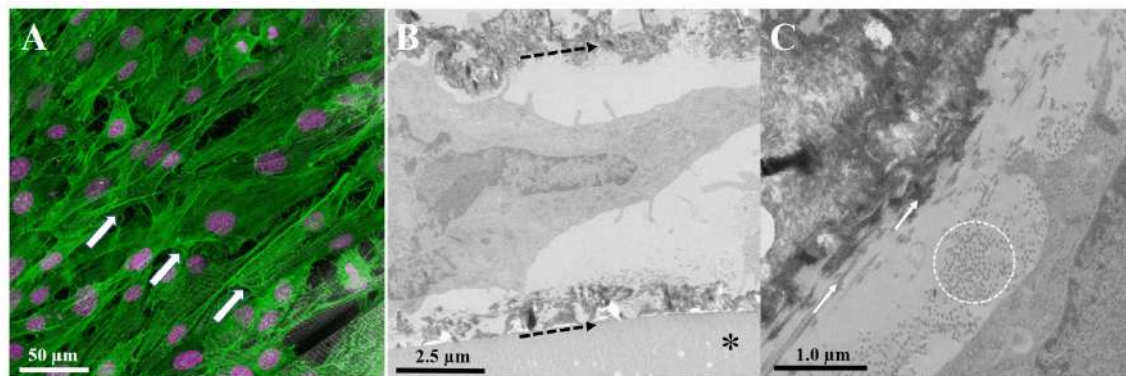


Figure 1: Laser scanning confocal microscopy (LSCM) and transmission electron microscopy images (TEM) from osteoblast cells (F-OST) grown onto different scaffolds. A) LSCM of F-OST of a confluent cell culture grown on a PDMS substrate constituted by an alternation of grooves and ridges, with straight edges, after confluence. Note the periodicity of cells distribution (white arrows) that correspond to the periodicity (50 microns) of the substrate (not seen directly); B) TEM image of a transverse section of cell culture seeded in the bottom of a culture well showing mineralization after, four weeks. Alternating patterns of cell/mineralized layers are seen (dotted arrows). C) TEM image showing three regions, from top left to bottom right: 1. mineralized region, 2. non mineralized region containing several collagen fibrils (arrows and dotted circle), 3. part of an osteoblast cell. Note that the collagen fibers in region (2) appear in lamellae that are crossed (white arrows: parallel to the plane of the figure; dotted circle: perpendicular to the plane of the figure).



## Lack of Two Independent Physiological Regulators Impacts the Ultrastructure of *Cryptococcus gattii*

Beatriz S. Borges<sup>1\*</sup>, Flavia C. G. Reis<sup>1</sup>, Luísa J. Jozefowicz<sup>1</sup>, Bianca A. G. Sena<sup>1</sup>, Rafael F. Castelli<sup>1</sup>, Haroldo Oliveira, Lia C. Soares Medeiros<sup>1</sup>, Marcio L. Rodrigues<sup>1</sup>

<sup>1</sup>Instituto Carlos Chagas, Fundação Oswaldo Cruz (Fiocruz), Curitiba, Brazil.

\*Corresponding author: beatrizsborges@hotmail.com

The yeast-like fungus *Cryptococcus gattii* is the etiological agent of cryptococcosis, one of the most lethal diseases affecting immunocompromised individuals. Currently available antifungals are expensive, toxic and associated with antimicrobial resistance. The most striking morphological feature of this pathogen is the production of a polysaccharide capsule, which is directly linked to virulence [1]. The capsule is mainly composed of glucuronoxylomannan (GXM), a highly immunodeleterious polysaccharide [2]. We have recently described two potential antifungal targets impacting GXM export, namely scramblase Aim25 and nuclear protein Nop16 [3]. In this study, we analyzed the morphological and functional aspects of mutant cells lacking expression of Aim25 or Nop16. Fungal cells were grown on solid YPD and incubated in RPMI for capsule induction. The cells were processed for scanning and transmission electron microscopy (SEM and TEM, respectively) and flow cytometry. Fungal cells prepared for TEM were processed using standard protocols. For SEM, the cells were not postfixed with osmium tetroxide 1% but were washed with 0.1 M sodium cacodylate buffer containing 0.2 M sucrose and 2 mM MgCl<sub>2</sub> [4]. To analyze potential changes in capsule formation, capsular GXM was detected by flow cytometry after staining of fungal cells with a GXM-binding monoclonal antibody. TEM revealed that *nop16Δ* mutant cells did not manifest clear ultrastructural alterations. On the other hand, mutants lacking Aim25 expression demonstrated membrane disorganization, supporting the notion that this protein is an important regulator of membrane architecture. SEM demonstrated that *aim25Δ* cells had larger capsules than the other strains analyzed in this study. This result was compatible with the detection of higher levels of extracellular GXM in cultures of *aim25Δ* cells. Further studies are required to characterize the role of Aim25 and Nop16 in fungal virulence and drug resistance. However, our results suggest that Aim25 and Nop16 can be important regulators of the physiology of *C. gattii*.

## REFERENCES

- [1] K.J. Kwon-chung *et al.*, *Cryptococcus neoformans* and *Cryptococcus gattii*, the Etiologic Agents of Cryptococcosis. Cold Spring Harb Perspect. Med, 2018.
- [2] J.C.V. Reuwsaat *et al.*, A predicted mannoprotein participates in *Cryptococcus gattii* capsular structure. mSphere, 2018.
- [3] L.S. Joffe *et al.*, The Anti-helminthic Compound Mebendazole Has Multiple Antifungal Effects against *Cryptococcus neoformans*. Front. Microbiol, 2017.
- [4] J. Rodrigues *et al.*, Lack of chitin synthase genes impacts capsular architecture and cellular physiology in *Cryptococcus neoformans*, *The Cell Surface*, 2018.
- [5] This research was supported by CNPq and Fiocruz (Brazil) .

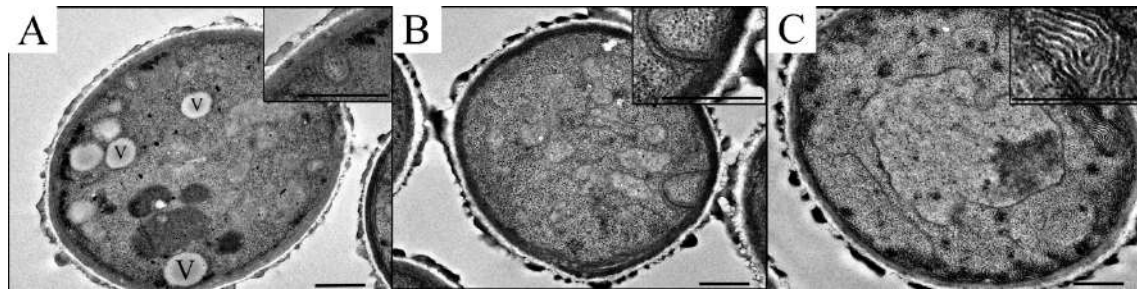


Figure 1. Transmission electron microscopy of wild-type (WT) and mutant cells (*nop16Δ* and *aim25Δ*) of *C. gattii*. A) WT cells manifested typical intracellular morphology of cryptococci, including well-defined vacuoles (V) and organized membranous compartments (inset A). B) *nop16Δ* mutant cells presented similar morphology to WT cells, including organized membranous compartments (inset B) despite of not presenting the well-defined vacuoles found in WT. C) In *aim25Δ* mutant cells, distorted membranes were abundantly detected. Phenotypic traits that were exclusive to mutant cells included a general lack of the typical cryptococcal vacuoles, highly-electron-dense membranous compartments, linearized membranes, electron-dense, stacked membranes (inset C) and atypical invaginations of the plasma membrane. Scale bars correspond to 500 nm.

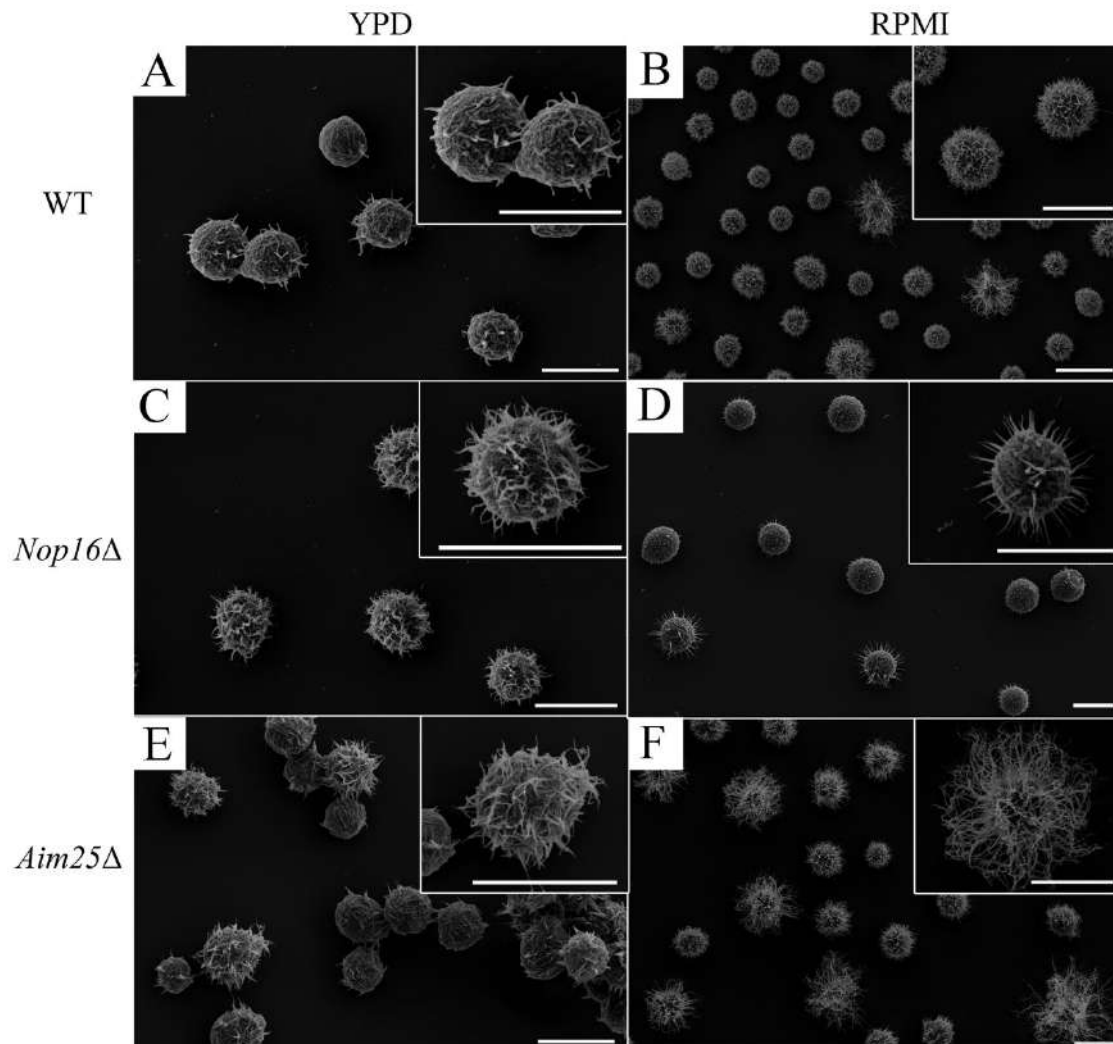


Figure 2. Scanning electron microscopy of wild-type (WT) and mutant (*nop16Δ* and *aim25Δ*) cells of *C. gattii* after growth in solid YPD (capsule repression) or incubation in RPMI (capsule induction). Insets of representative cells are shown in each general view picture. *Nop16Δ* mutants are shown in C and D with few capsule fibers, even though cells were grown in capsule induction media (RPMI). *Aim25Δ* mutants (shown in E and F) seems to have larger and more abundant capsule fibers in both growth media. Scale bars correspond to 5  $\mu$ m.

## Devices produced by 3D printing for electron microscopy sample preparation

Lia Souza Coelho<sup>1\*</sup>

<sup>1</sup>. Brazilian Center for Research in Physics, Rio de Janeiro, Brazil.  
liascoelho@gmail.com

3D printing is been used in a broad field of applications and areas and opens new horizons of possibilities in scientific works. 3D printing has been used in different areas such as: health, engineering and prototyping, food, architecture, aerospace, fashion, entertainment and education [1-3]. Rapid prototyping allows the laboratory to adjust protocols with the production of devices and supplies that facilitate analysis, reduce effort and time in material preparation. Since in Brazil most devices are imported, the use of 3D printing reduces costs and time due to lack of import taxes, low cost of 3D printing and rapid prototyping. With 3D printing of microscopy images, 3D objects can be produced for better understanding of structures and inserting people with disabilities. In the present work we used a FFF printer (Fused Filament Fabrication) with Acrylonitrile butadiene styrene (ABS) filament. The 3D modelling was produced by Fusion 360 software and sliced in the Simplify 3D software. The following devices were produced: universal support for optical microscope (MO), device to adapt blades for trimming resin blocks (Figure 1a) device for analysis and cutting of wires and fibres for MO and scanning electron microscopy (SEM) BR102016060203406 [4] and sample holder for critical point equipment (Figure 1b). Modelling and 3D printing of CaCO<sub>3</sub> crystallites imaged by transmission electron microscopy was also produced (Figure 2). All devices were tested for their efficiency and resistance. The device to adapt blades for trimming resin blocks for ultramicrotomy increased the efficiency of the pyramid preparation and provided greater comfort and safety to the technician. The sample holder for critical point equipment had a material value and print time of \$4, less than the market value of the sample holder, of \$38 (metallic material) and \$105 (resin material) without the import tax. The advantage of rapid prototyping by 3D printing is customization for different needs within the laboratory. It must be noted that in TEM images the grayscale gradient may be related to the density or diffraction contrast of the material and not necessarily to the height dimension, producing a 3D image not compatible with reality.

## REFERÊNCIAS

- [1] H. Lipson, K. Melba, FABRICATED THE NEW WORLD OF 3D PRINTING, 2013. doi:10.1017/CBO9781107415324.004.
- [2] M. Kamran, A. Saxena, A Comprehensive Study on 3D Printing Technology, MIT Int. J. Mech. Eng. (2016).
- [3] B. Redwood, F. Schöffner, B. Garret, The 3D Printing Handbook, 3D Hubs. (2017).
- [4] L.S. Coelho, C. Modesto, F. Camargo, B. Matias, BR 102016020340-6 Dispositivo e método para fixação, corte e suporte para visualização da seção transversal de fibra para microscopia, 2018.
- [5] I would like to thank Mariana Longuinho for the image of TEM.

Figure 1. Images of trim device (a) and sample holder of critical point (b).

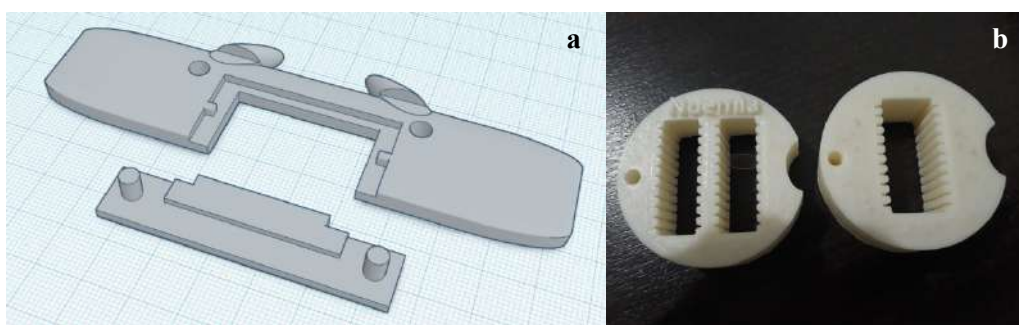
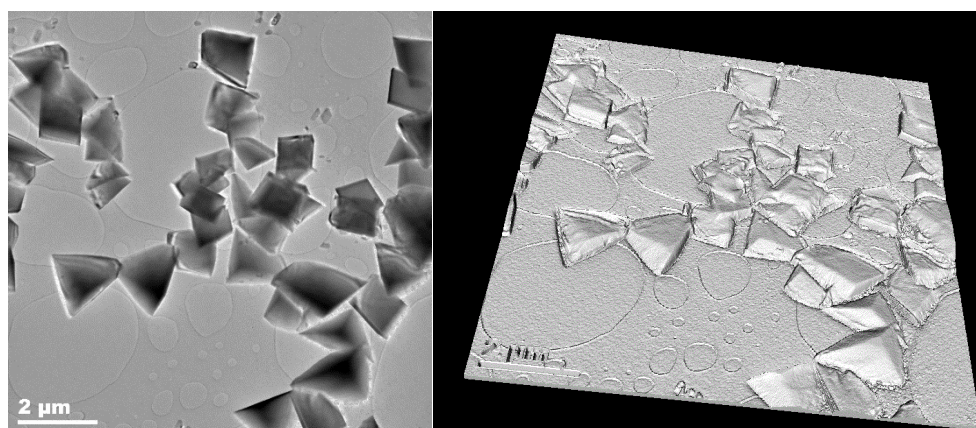


Figure 2. TEM micrograph of  $\text{CaCO}_3$  and projected image from 2D [5] to 3D.





## Scanning Electron Microscopy and Helium Ion Microscopy of the Inner Structure of *Trypanosoma cruzi* Infected Cells Fixed and Fractured by the OSMIUM-DMSO-OSMIUM Method (Fukudome and Tanaka, 1986)

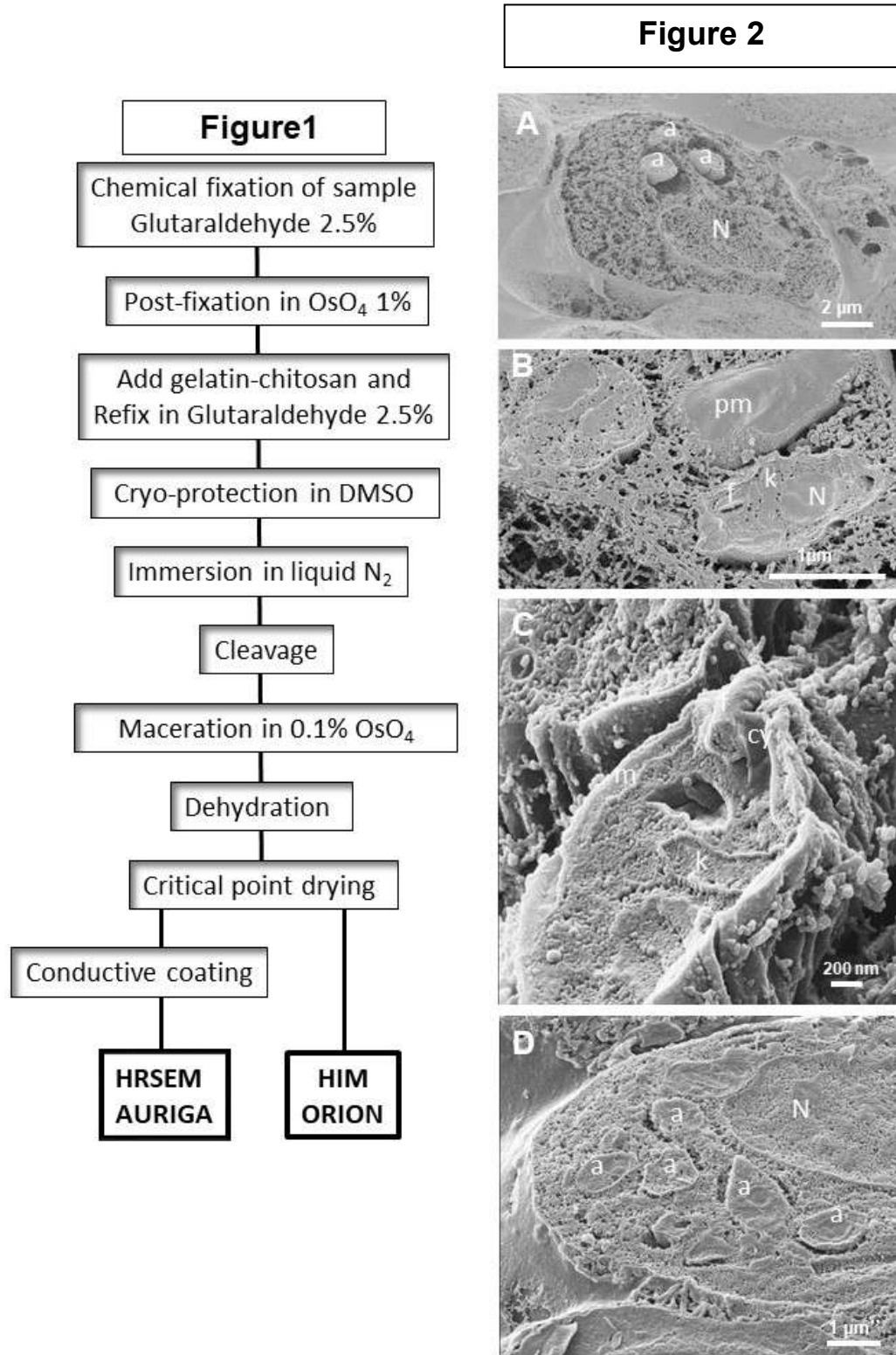
Luis Otavio da Silva Pacheco<sup>1</sup>, Márcia Attias<sup>1,2</sup>, Kildare Miranda<sup>1,2</sup>, Wanderley de Souza<sup>1,2</sup>

<sup>1</sup>Instituto de Biofísica Carlos Chagas Filho and <sup>2</sup>Centro Nacional de Biologia Estrutural e Bioimagem (CENABIO), Universidade Federal do Rio de Janeiro.

The introduction of High and Ultra High Resolution (sub-nanometer) Scanning Electron Microscopes in the laboratories stimulated the development of new techniques that allowed not only the observation of the surface of cells and tissues but also the intracellular environment. At these new levels of resolution, novel intracellular structures associated or not to organelles became visible by SEM. In this work, we have rescued the method described by Fukudome and Tanaka (1986) to investigate the intracellular development of *Trypanosoma cruzi*, the protozoan parasite that is the etiologic agent of Chagas' Disease, as well as epimastigote forms of the parasite. The method was primarily designed to be applied to free cells (as is the case of epimastigotes), but has also been applied to a monolayer of infected cells that were trypsinized before fixation, becoming unattached to the substrate and to each other. The main steps of the method included: Fixation, post fixation, embedding in a chitosan/gelatin mixture, refixation with glutaraldehyde, infiltration with DMSO for cryoprotection, freezing in liquid nitrogen, cleavage with a frozen razor blade, removal of cryoprotectant, maceration in low concentration of OsO<sub>4</sub> (0,1%), dehydration, critical point drying, conductive coating and observation by Scanning Electron Microscopy (please, see figure 1 for a flowchart of the method) (**Fig. 2A,B**). Alternatively, uncoated cells were investigated by helium ion microscopy (**Fig. 2C and D**). By using this method, we successfully exposed internal structures of the host cell infected with amastigotes (**a**) and free epimastigote (Fig. 2C) forms. Previous trypsinization of the monolayer of cells avoided the flatness of cells when adhered (**Fig. 2 A and D**). The use of a mixture of gelatin and chitosan as a matrix to hold the free cells in a pellet. Although gelatin is dissolved in the maceration process, the chitosan still holds the cells. DMSO was successfully used as cryoprotectant. The time of maceration caused an extraction of soluble components of the cytoplasm, exposing inner membranes that were cleaved. Images showed a number of filamentous structures connecting the surface of the parasite and the parasitophorous vacuole (**Fig 2. A, B and D**). Helium ion microscopy (**Fig. 2 C and D**) of uncoated samples exposed aspects of the flagellum (**f**), cystostome (**cy**), the kinetoplast (**k**), the mitochondrion (**m**) and nucleus (**N**) from parasites and host cells. Altogether, the results show the optimization of this protocol as a promising technique to be used as alternative to freeze fracturing or cryoSEM. A new set of experiments adjusting the maceration/substitution medium is currently under development in our laboratory.

Acknowledgments: CAPES, CNPq, FAPERJ, FINEP. The authors also thank the Division of Material Sciences at INMETRO for the use of the ZEISS- ORION Helium Ion Microscope.

Fukudome & Tanaka (1986). J. of Microsc. Vol 141(2):171-8 (1986)





## Cryoelectron Microscopy Imaging of whole cells: Preliminary results on freezing protocols applied to Protozoan Parasites

Adélia Lima<sup>1\*</sup>, Ingrid Augusto<sup>2</sup>, Camila Wendt<sup>2</sup>, Wanderley de Souza<sup>1,2</sup> and Kildare Miranda<sup>1,2</sup>

<sup>1</sup>. Unidade de Microscopia Avançada, Centro Nacional de Biologia Estrutural e Bioimagem, Universidade Federal do Rio de Janeiro, Rio de Janeiro, Brasil.

<sup>2</sup>. Laboratório de Ultraestrutura Celular Hertha Meyer, Instituto de Biofísica Carlos Chagas Filho, Universidade Federal do Rio de Janeiro, Rio de Janeiro, Brasil.  
adelia.belem@cenabio.ufrj.br

Artifacts generated by chemical fixation are widely known in biological electron microscopy [1]. Shrinking or swelling of cells or organelles due to osmotic changes, deformation of intracellular structures and extraction or mobilization of ions and molecules are among the major artifacts in room temperature sample preparation methods for EM. In contrast, cryopreparation methods have emerged as techniques that are able to increase the preservation cellular structures [2]. Some of the challenges in cryopreparation involve controlling the size of the ice crystals upon cryofixation [3,4], low-dose imaging (for electron cryotomography) [5] and elaboration of specific cryofixation protocols for samples of different size. In this regard, one of the main challenges in cellular cryoEM is sample thickness, especially for TEM analysis that require thin samples. A number of methods have been developed and applied (cryosectioning, cryolamella preparation and observation of thin portions of plunge frozen whole cells). In this context, a number of protozoan parasites have dimensions that allow them to be imaged as whole cells in the TEM. Nevertheless, as they differ in size and volume, optimization of freezing protocols is required to better explore the structural details gained by cryopreservation and tomographic imaging. In the present work, we show preliminary results of an optimization protocol for cryofixation of protozoan parasites by plunge freezing in liquid ethane with chamber temperature and humidity control. *Trypanosoma cruzi*, *Plasmodium chabaudi* and *Plasmodium berghei* were plunge frozen under different conditions described below (please see table 1), transferred at low temperature to the TEM and imaged under low dose conditions. Preliminary results were very promising, allowing a detailed visualization of different structures in *T. cruzi*, such as the subpellicular microtubule system, projections of the mitochondrion, kinetoplast, flagellar axoneme (Fig. 1-A) and the distribution of acidocalcisomes (Fig. 1-B). *P. chabaudi* cells showed well preserved food vacuoles containing hemozoin crystals (Fig. 2-A). In *P. berghei* cells, the dispersion of acidocalcisomes was shown in the peripheric regions of the cell (Fig. 2-B). Altogether, the results corroborate the importance of optimization of protocols for cryofixation of protozoan parasites to ensure the preservation of structures and EM imaging in a more close-to-native state. Cryoelectron tomography and 3D reconstruction of the parasites mentioned above are currently being carried out in our laboratory.

### REFERENCES

- [1] Q. Bone, E.J. Denton, J. Cell Biol. 49 (1971) 571-581.
- [2] W. Girard Dias et al., Histochem Cell Biol 138 (2012) 821-831.
- [3] J. Dubochet, A.W. McDowell, Journal of Microscopy 124 (1981) RP3-RP4.
- [4] J. Dubochet, J. Lepault, Journal de Physique Colloques 45 (1984) 85-94.

[5] P.S. Erdmann et al., Current Opinion in Colloid & Interface Science 34 (2018) 89-99.

This work was supported by Conselho Nacional de Desenvolvimento Científico e Tecnológico (CNPq), Coordenação de Aperfeiçoamento de Pesquisa de Pessoal de Ensino Superior (CAPES), Fundação de Amparo à Pesquisa do Estado do Rio de Janeiro (FAPERJ), Financiadora de Estudos e Projetos (FINEP), Instituto Nacional de Ciência e Tecnologia de Biologia Estrutural e Bioimagem (INCT-INBEB) (Brazil).

The authors are grateful for the support given by Wendell Girard Dias and Rachel Rachid.

Table 1: Conditions of plunge freezing for protozoan parasites.

Protozoan Parazites	Blotting Chamber				
	Temperature (°C)	Humidity (%)	Blot Force	Blot Time (s)	Drain Time (s)
<i>Trypanosoma cruzi</i>	30	100	4	10	1
<i>Plasmodium chabaudi</i>	30	100	7	10	2
<i>Plasmodium berghei</i>	30	100	4	15	1

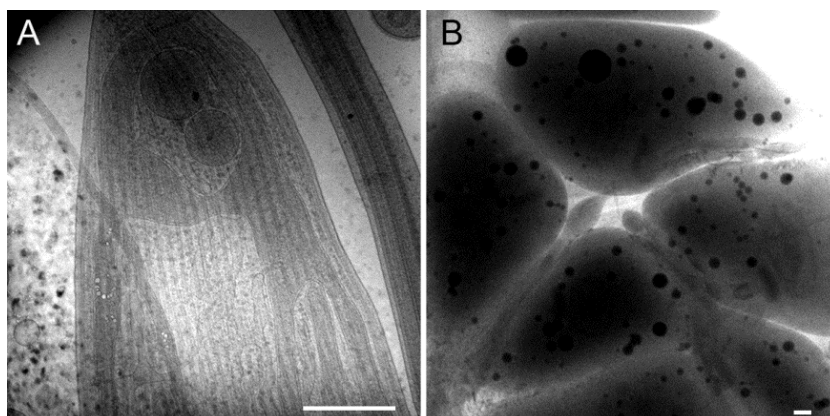


Figure 1: Two-dimensional electron cryomicroscopy images of the CL strain of the epimastigote form of *Trypanosoma cruzi*. In a) details of the subpellicular microtubule system and b) details of the acidocalcisomes. Scale bar: 500 nm.

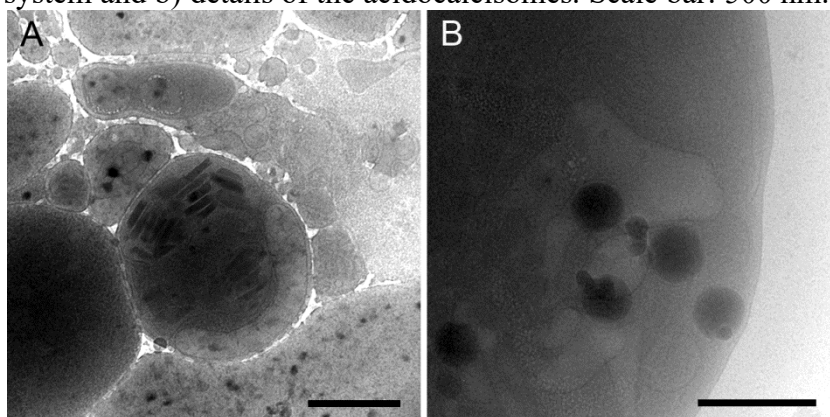


Figure 2: Two-dimensional electron cryomicroscopy images of the *Plasmodium*. In a) trophozoite form of *P. chabaudi* and the food vacuole containing hemozoin crystals and b) details of acidocalcisomes in the schizont form of *P. berghei*. Scale bar: 500 nm.

## Structural Organization of *Oscarella* (Porifera, Homoscleromorpha) Frozen and Fractured in Absolute Ethanol Observed by High Resolution Scanning Electron Microscopy

Daniele Stillitani<sup>1,2\*</sup>, Guilherme Muricy<sup>2</sup>, Márcia Attias<sup>1</sup>

<sup>1</sup>. Instituto de Biofísica Carlos Chagas Filho, Universidade Federal do Rio de Janeiro, Rio de Janeiro, Brazil.

<sup>2</sup>. Museu Nacional, Universidade Federal do Rio de Janeiro, Rio de Janeiro, Brazil.

\*dstillitani@biof.ufrj.br

*Oscarella* is a marine sponge genus belonging to the Homoscleromorpha class and is an important model in Evo-Devo [1]. Like in other sponges, the body is formed by intercommunicating cavities constituting the aquiferous systems. The surface of the sponge body (ectoderm) is covered by the pinacocyte cells and the chambers are covered by choanocyte cells. The mesohyl is composed by various types of cells and inclusions immersed in an extensive network of collagen [2,3]. Scanning Electron Microscopy (SEM) has been employed to study the ultrastructure of sponges by other authors [4]. However, modern techniques of sample preparation and high-resolution SEM (HRSEM) are bringing new data on the organization of these animals. METHODS: Samples were collected in Cabo Frio, RJ, in tide pool and islands, were fixed in glutaraldehyde 2,5 % in sodium cacodylate buffer 0.4 M and sea water 1:4:5, post fixed in OsO<sub>4</sub> diluted to 2.0 % in sea water, dehydrated in an increasing series of ethanol, frozen in liquid Nitrogen and cleaved with a cold razor blade [5]. After thawing, the fragments were dried by the critical point method and mounted on stubs, sputtered with gold or platinum and observed in Zeiss Auriga 40 (Thermo-Fisher) HRSEM at 4 mm WD and 2 kV. RESULTS AND DISCUSSION: Figure 1 shows at low magnification that the aquiferous system of *Oscarella* sp. is composed by canals (**arrowhead**) and chambers (**star**) interconnected (**arrows**). At higher magnification, shown in Figure 2, the mesohyl is seen between two layers of choanocytes (**c**) and contains vacuolar cells (**vc**) and bacteria (**b**) immersed in a collagen matrix (**cf**) that is detailed in Figure 3. Figure 4 is a view of the choanocytes in a chamber. Each choanocyte has a flagellum (**f**) centrally positioned and a collar of microvilli (**mv**) around it. At a higher magnification (Figure 5), the so-called microvilli of the collar, show various sizes and a segmentation, distinct from typical microvilli (**arrow**). In the ectoderm, the pinacocytes show a central flagellum and are juxtaposed by protuberances similar to the microvillar collar seen in the choanocytes (Figure 6). In conclusion, this technique has proven to be useful in producing a clean cleavage of the body wall of sponges, revealing, in HRSEM, new aspects of the pinacocytes and choanocytes that may lead to new interpretations of previously described structures of porifera, conducting to a better knowledge of its biology.

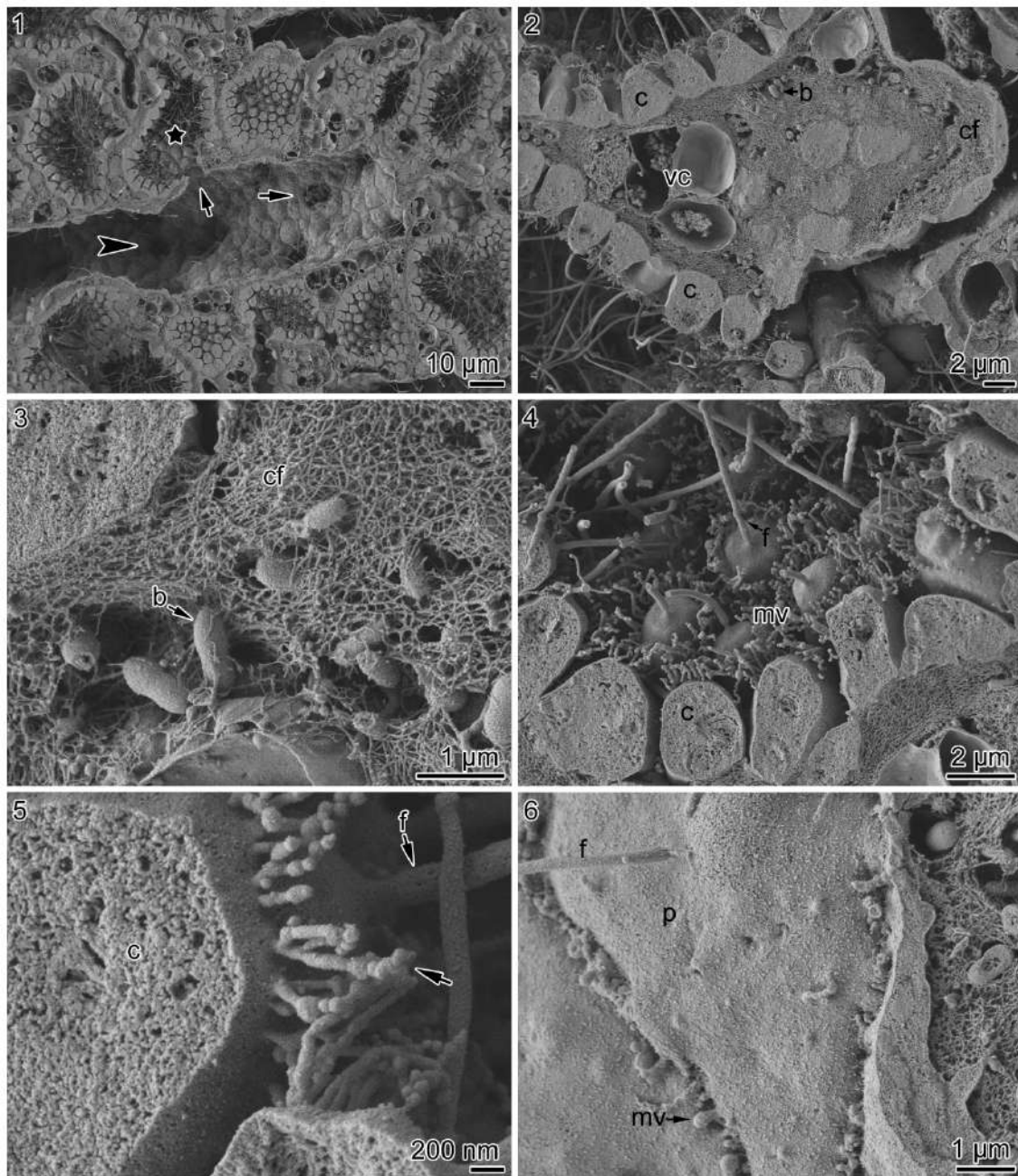
### References

- [1] Ereskovsky, A. V. et al. *BioEssays* **31**, 89–97 (2009).
- [2] Muricy, G. et al. *Can. J. Zool.* **74**, 881–896 (1996).
- [3] Ereskovsky, A. V. et al. *Cah. Biol. Mar.* **50**, 369–381 (2009).
- [4] Boury-Esnaul, N. et al. *J. Morphology* **180**, 3–17 (1984).
- [5] Taylor, J. et al. *Micros. Today* **16**, 56–59 (2008).



## Acknowledgements

To CAPES, Centro Nacional de Biologia Estrutural de Bioimagens (CENABIO), CNPq, FAPERJ and Otávio Luis Pacheco for technical assistance.



**Structural organization of *Oscarella* (Porifera, Homoscleromorpha) observed by High Resolution Scanning Electron Microscopy.** Figure 1, view of the aquiferous system with canals (**arrowhead**) and chambers (**star**) interconnected (**arrows**). Figure 2, mesohyl between two layers of choanocytes (**c**) and containing vacuolar cells (**vc**) and bacteria (**b**) immersed in a collagen fibrils matrix (**cf**). Figure 3, collagen fibrils matrix (**cf**) and bacteria (**b**). Figure 4, a view of the choanocytes in a chamber with flagellum (**f**) and collar of microvilli (**mv**). Figure 5, the so-called microvilli of the collar, showing various sizes and an unusual segmentation (**arrow**). Figure 6, pinacocytes (**p**) showing a central flagellum (**f**) and juxtaposed by protuberances similar to the microvillar collar seen in the choanocytes (**mv**).

## Chemical Modification Of Holey Carbon Support Film For Cryogenic Electron Microscopy Using 2-mercaptoethanol

Otávio Berenguel<sup>1†</sup>, Daniela C. Serdan<sup>1†</sup>, Carlos A. R. Costa<sup>1</sup>, Marcelo A. de Farias<sup>1</sup>, Rodrigo V. Portugal<sup>1\*</sup>

<sup>1</sup>. Brazilian Nanotechnology National Laboratory (LNNano), Brazilian Center for Research in Energy and Materials (CNPEM), Campinas, SP, Brazil

\* rodrigo.portugal@lnnano.cnpem.br

<sup>†</sup> Both authors equally contributed to this work

During the last decades, advances in single particle cryo-EM allow protein structure to be obtained at higher resolution than before. Nevertheless, cryo-EM is also an important technique to investigate soft materials. The sample preparation by cryo-EM involves a vitrification process that preserves the sample in a very thin layer of amorphous ice. In this technique specimens can be studied in the hydrated state preserving their native structure [1]. An efficient application of this technique requires the particles to be dispersed and randomly oriented throughout the ice layer inside the holes of a carbon support film. Protein partitioning in random orientations in the holes can be difficult to achieve, mainly for biological specimens that have strongly preference for the carbon support film used. Chemical modifications of holey carbon support film for cryo-EM, producing a self-assembled monolayer (SAM), has already been shown to be an effective method to maximize the grid wettability while allowing the best dispersion of the particles across the ice. The aim of this work is to develop a simple and accessible methodology for most biochemistry laboratories, requiring a commonly available reactant, the 2-mercaptoethanol. The workflow is presented at Figure 1. In this work, we demonstrated that gold coated C-flat grids (ca. 13 nm thickness measured through atomic force microscopy technique – Figure 2) with 2-mercaptoethanol yields a hydrophilic surface to holey carbon cryo-EM supports. Besides increasing the grid wettability, cryo-EM images confirm the success to drive partitioning of liposomes that have a strong affinity by the carbon surface into the grid holes (Figure 3). In fact, the use of a hydrophilic SAM is a viable way to mitigate the specimen adhesion to the carbon surface. This approach may enable structure determination of macromolecular targets that suffer from high affinity to the holey carbon support film. The authors would like to thank the LNNano for the use of facility, the Conselho Nacional de Desenvolvimento Científico e Tecnológico (CNPq) for the financial support and Monica Pickholz (Universidad de Buenos Aires) for kindly donating the samples used in this work.

- [1] C.J. Russo, L.A. Passmore, Progress towards an optimal specimen support for electron cryomicroscopy, *Curr. Opin. Struct. Biol.* 37 (2016) 81–89. doi:10.1016/j.sbi.2015.12.007.

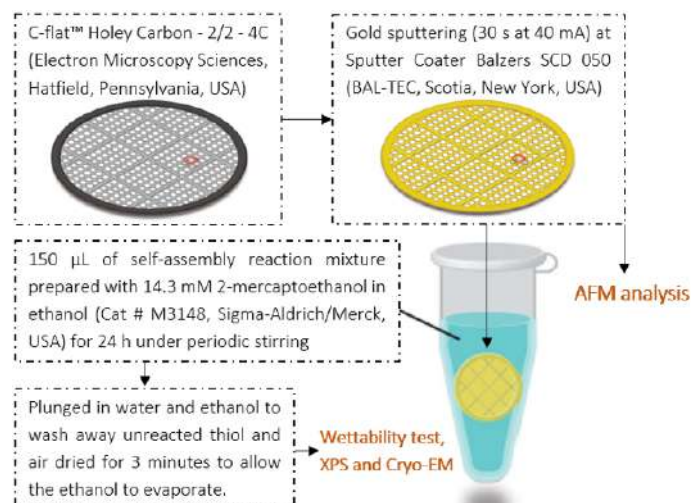


**Figure 1.** Schematic illustration of chemical modification of a C-flat grid using 2-mercaptoethanol.

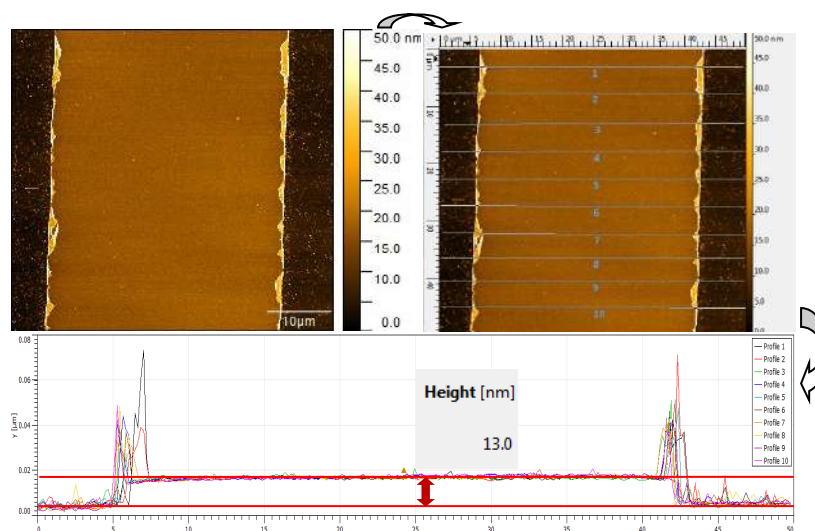


**Figure 2.** AFM image of the scan, whose medium is deposited gold and ends, silicon. The graph calculates thickness by means of two horizontal lines.

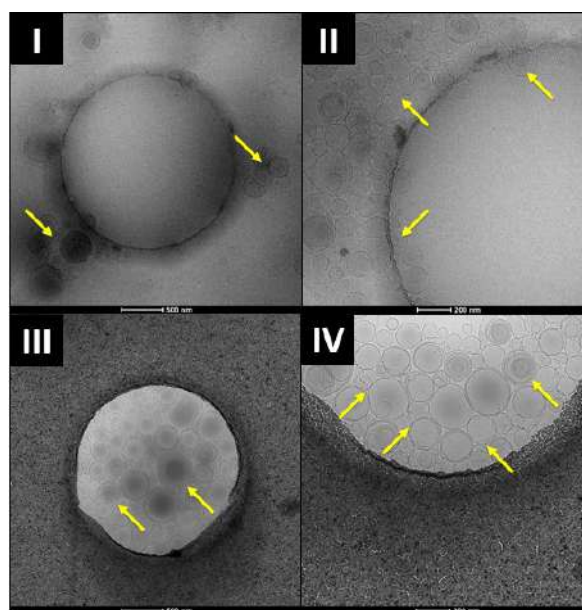


**Figure 3.** Cryo-EM images of liposomes in a C-flat grid (I and II) and in a SAM C-flat grid prepared with 2-mercaptoethanol (III and IV). The yellow arrows highlights some liposomes.



# PARTE 2

## COMUNICAÇÕES ORAIS - MATERIAIS



## **Recent Technologies In Electron Microscopy for Modern Materials Characterization**

Rafael Villaurrutia<sup>1</sup>

<sup>1</sup>ThermoFisher Scientific, México,

New possibilities for the application of focused electrons are being revealed for atomic-scale materials characterization. While advances in materials science demand advances in electron microscopy techniques, the electron microscopy technologies evolution demand more challenges to push their limits. The availability of functional and modern materials has provided ideal samples and challenges for entirely describing the structure of such materials. Correctors for the parasitic lens aberrations that otherwise limit resolution, new electron sources for increasing the signals, new and more detectors for analysis, have opened new possibilities of study for the new generation of nanomaterials and devices. Scanning transmission electron microscopy (STEM) technique has undergone significant advances in recent years, allowing electron beams to be produced with a spot size well below 1 Å, sufficient to resolve inter-atomic spacings in most crystal structures. This is revolutionising our understanding of new devices, heterostructures and nanoparticles. This includes qualitative analysis of structures with picometer precision, mapping of electric polarization at the unit cell scale, mapping of chemistry on an atom-by-atom basis and crystallographic orientations (Figure 1). Nonetheless, the electron microscopy evolution has been noticeable not just in scanning transmission electron microscopy, but as well in the whole range of techniques which have become complementary between them. This includes the scanning electron microscopy and focused ion beam. It is necessary to be aware of the evolution of each technique in order to have the whole picture in the characterization of new materials. In this talk we highlight the recent advances of the main techniques in electron microscopy with applications in modern materials.

[1] I. MacLaren et al., Adv. Funct. Mater. 22 (2012).

[2] M.U. Farooq et al. Journal of Microscopy, 230 (2008) 445.

[3] This research was supported by Thermofisher Scientific.

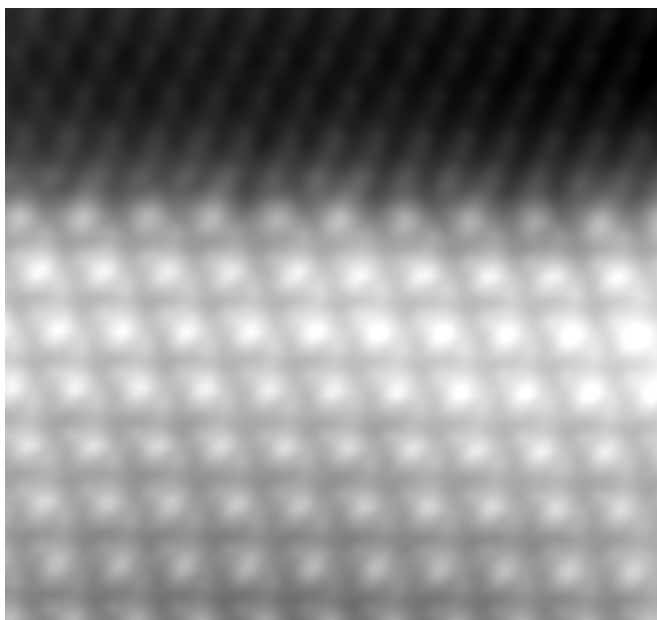


Figure 1: ZrO<sub>2</sub>/Ni Interface showing atomic details of oxygen vacancies.

## Morphological Study of 1D Sodium Niobate Nanostructures

Beatriz Rodrigues Canabarro<sup>1\*</sup>, Paula Mendes Jardim<sup>1</sup>

<sup>1</sup>. Department of Metallurgical and Materials Engineering, Federal University of Rio de Janeiro (COPPE/UFRJ), Rio de Janeiro, Brazil.

\*canabarro@metalmat.ufrj.br

Sodium niobate ( $\text{NaNbO}_3$ ) has gained scientific attention due to its properties as semiconductivity, piezoelectricity, and photoactivity, that combined can be used as a piezo phototronic device [1]. Motivated by the potential efficiency improvement, this material can be synthesized in the nanoscale by alkali hydrothermal route followed by heat treatment at  $550^\circ\text{C}$  in a vacuum furnace [2,3]. In this study, it was used metallic niobium as a substrate and also as a precursor, that reacting with NaOH generates the oriented growth of sodium niobate nanocrystals [4]. In order to use this system composed by a nanostructured layer of  $\text{NaNbO}_3$  supported on metallic niobium as a possible piezo phototronic device, it is necessary to understand its nanostructure organization. Morphological properties of sodium niobate nanostructure were obtained with scanning transmission electron microscopy (STEM), with an acceleration voltage of 300kV and high angular dark field (HAADF) detector, and electron tomography, varying the tilt angle of the sample holder in steps of  $2^\circ$  from  $-70^\circ$  to  $70^\circ$ . The results revealed the formation of 1D nanostructured orthorhombic perovskite  $\text{NaNbO}_3$  ( $P2_1ma$ ) with the formation of facets at the surface, exposing the crystallographic planes (1-1-1), (031) and (120) (Figure 1). Electron tomography analyses showed that the dimensions and morphology (nanowires or nanoribbons) of the 1D nanocrystals could change depending on the synthesis conditions. It was observed the presence of nanoribbons in the sample obtained with more severe synthesis conditions ( $[\text{NaOH}]=0.75\text{M}$ ,  $120^\circ\text{C}$ , 12h) (Figure 2), while it was observed a combination of nanowires and nanoribbons with mild conditions ( $[\text{NaOH}]=0.50\text{M}$ ,  $80^\circ\text{C}$ , 24h) (Figure 3). In conclusion, it was possible to identify the presence of different sodium niobate nanostructure morphologies, synthesized with different alkali hydrothermal route conditions, applying the method of electron tomography with STEM mode.

### REFERENCES

- [1] K. Huang, *et al.* Inorg. Chem. Front. 2 (2015) 965.
- [2] Y. Chang, *et al.* Mater. Res. Bull. 44 (2009) 538.
- [3] Y. Özeren, *et al.* Adv. Powder Technol. 25 (2014) 1825.
- [4] B.R. Canabarro, *et al.*, Adv. Mater. Sci. Eng. 2018 (2018) 1.
- [5] This research was supported by CAPES (Brazil).
- [6] Electronic Microscopy Laboratory (LME) from Nanotechnology National (LNNano), CNPEM, for their support with the equipment (Titan Cubed Themis – FEI).

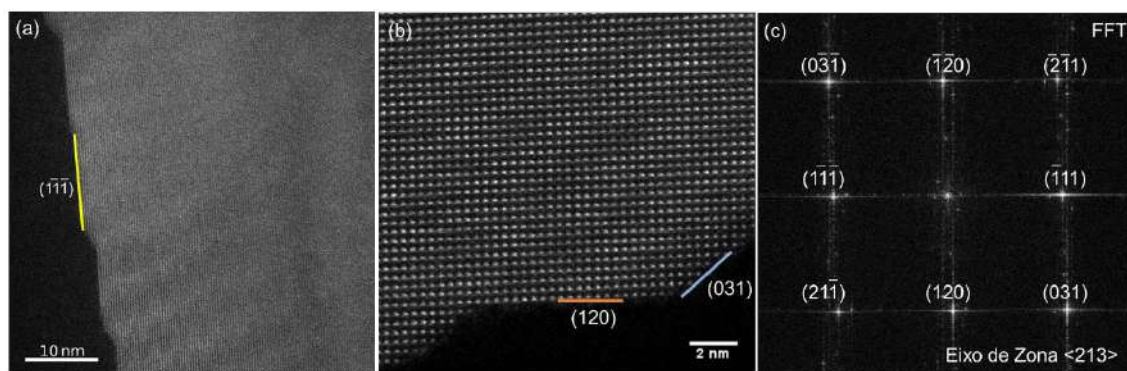


Figure 1 – HRSTEM images of the sample ( $[\text{NaOH}] = 0.75\text{M}$ ,  $120^\circ\text{C}$ , 12h) oriented in the zone axis  $\langle 213 \rangle$  showing the facets planes (1-1-1) (a) and (120) and (031) (b), and corresponding image FFT (c).

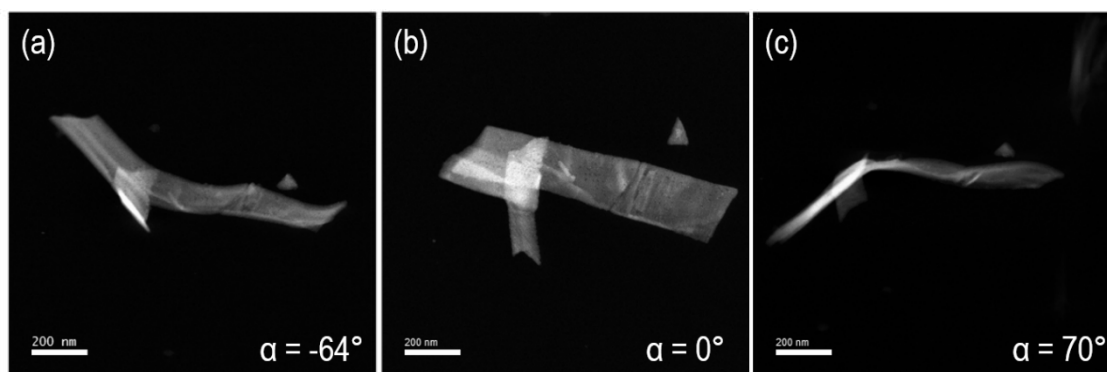


Figure 2 – STEM images of the sample ( $[\text{NaOH}] = 0.75\text{M}$ ,  $120^\circ\text{C}$ , 12h) in three different holder tilt angle ( $\alpha$ )  $-64^\circ$  (a),  $0^\circ$  (b) e  $70^\circ$  (c).

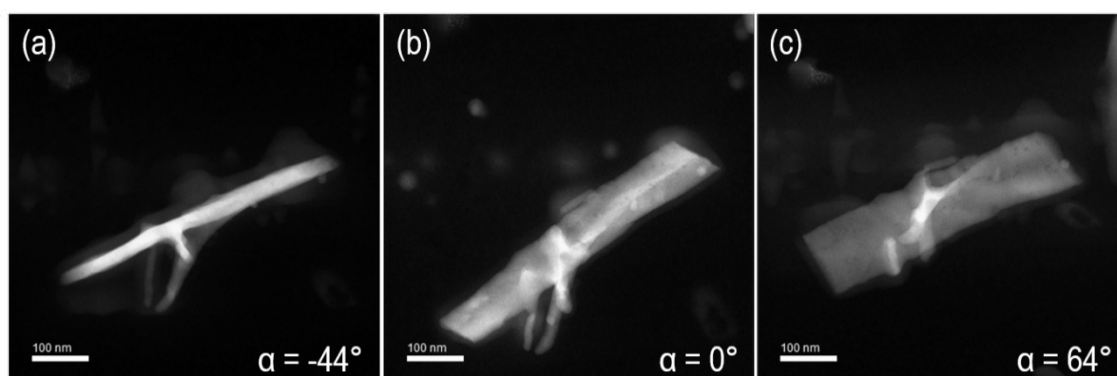


Figure 3 – STEM images of the sample ( $[\text{NaOH}] = 0.50\text{M}$ ,  $80^\circ\text{C}$ , 24h) in three different holder tilt angle ( $\alpha$ )  $-44^\circ$  (a),  $0^\circ$  (b) e  $64^\circ$  (c).

## Mn<sub>5</sub>Si<sub>3</sub> Nanowire Composition And Crystalline Structure Resolved By TEM

Alexsandro dos Santos Evangelista da Cruz<sup>1\*</sup>, Marcos Vinicius dos Santos Puydinger<sup>1</sup>,  
Raul Back Campanelli<sup>1</sup>, Jefferson Bettini<sup>2</sup>, Kleber Roberto Pirota<sup>1</sup>, Fanny Béron<sup>1</sup>

<sup>1</sup>Institute of Physics Gleb Wataghin, State University of Campinas (UNICAMP),  
Campinas, Brazil.

<sup>2</sup> Brazilian Nanotechnology National Laboratory, (CNPEN), Campinas, Brazil.

alex.asec@gmail.com

Over the last decades there has been a growing interest in producing new materials for spintronics applications in order to achieve a faster and higher density of magnetic data storage in non-volatile memories. In this sense, new storage devices might rely on antiferromagnetic materials due to their typical frequency resonance ( $\sim$  THz) higher than the current ones based on ferromagnetic materials [1]. In addition, since the racetrack memory proposed by S. Parkin and co-workers [2], which promised revolutionizing the magnetic storage industry, magnetic nanowires are believed to be an adequate geometry for future device generation. Therefore, new attempts to produce magnetic nanowires are required. In this context, this work reports the first production of Mn<sub>5</sub>Si<sub>3</sub> nanowires by metallic flux nanonucleation method (MFNN) [3]. This recent technique relies on using a flux, which is a metal with a low melting point in comparison with the desired compound, which will act as a solvent. A thermal ramp is required in order to melt together the compound and the flux. In this case, we used Ga as flux, with a stoichiometry weighted ratio of 20 : 1 : 1, with respect to Mn and Si. A nanoporous anodic aluminum oxide with a honeycomb-like structure have been used as template, to induce the nanowire nucleation. Both materials and template were put in a crucible to be carried onto an oven. At first the oven was heated up to 1200 °C and kept at this temperature for 15 h before cooling down to 700 °C at a rate of 2 °C/h. Figure 1 shows a high resolution transmission electron microscopy (HRTEM) image of an isolated nanowire. In the nanowire region we can see the atomic planes in specific directions suggesting a non-polycrystalline material. The nanowire is surrounded by an amorphous layer, which might be related to a surface oxidation. Figure 2 shows X – rays dispersive spectroscopy map probed by TEM. As can be seen through a tod images, our compound exhibits the Mn and Si elements, as expected as well as Ga and O. In the e to h color mixture images, we can observe that the obtained nanowire is probably coaxial-like with a core of Mn-Si and a shell of SiO<sub>2</sub> and GaO<sub>2</sub>. Electron diffraction through TEM (Figure 3a) shows a single crystal-like pattern, which is an indicative of the good crystalline quality obtained by MFNN. Indexing the experimental and the simulated data (Figure 3b), we can conclude that the desired crystalline phase Mn:Si = 5:3 was successfully achieved.

### REFERENCES

- [1] T . Jungwirth et al., Nature Physics. 14 (2016) 200.
- [2] S. S. P. Parkin et al, Science 320 (2008) 190
- [3] K. O. Moura, et al, Sci. Rep. 6 (2016) 28364
- [4] This research was supported by CNPq, CAPES, FAPESP (Project # 2017/10581-1) (Brazil) as well as LNNano (CNPEN) and CCSNano (UNICAMP) staff.



Therefore, MFNN has found to be a cheap alternative method to grow different types of intermetallic nanowires with a high crystalline quality.

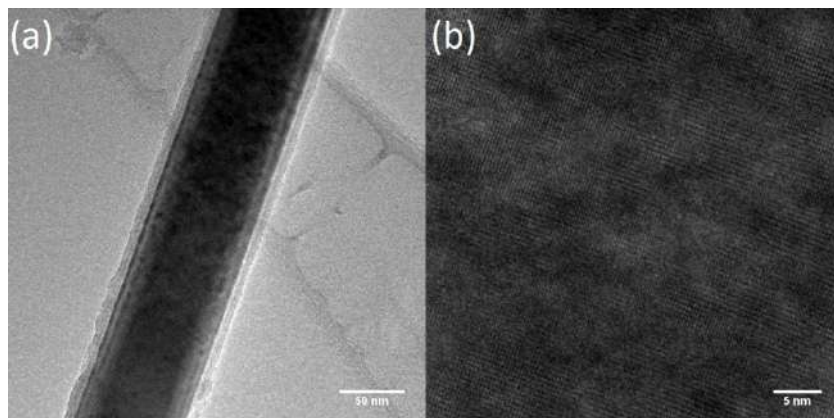


**Figure 1: (a) HRTEM image (b) magnification inside the nanowire**

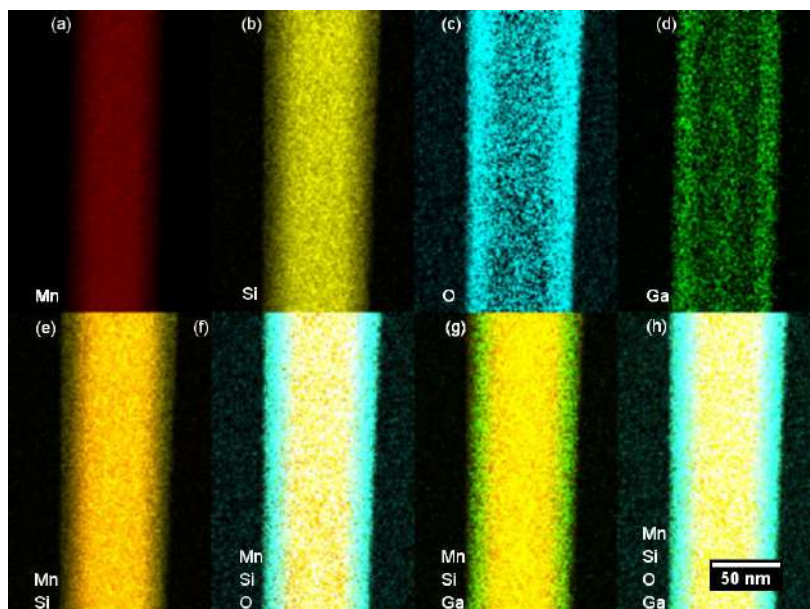


**Figure 2 :  $\text{Mn}_5\text{Si}_3$  nanowire X-ray dispersive spectroscopy map**

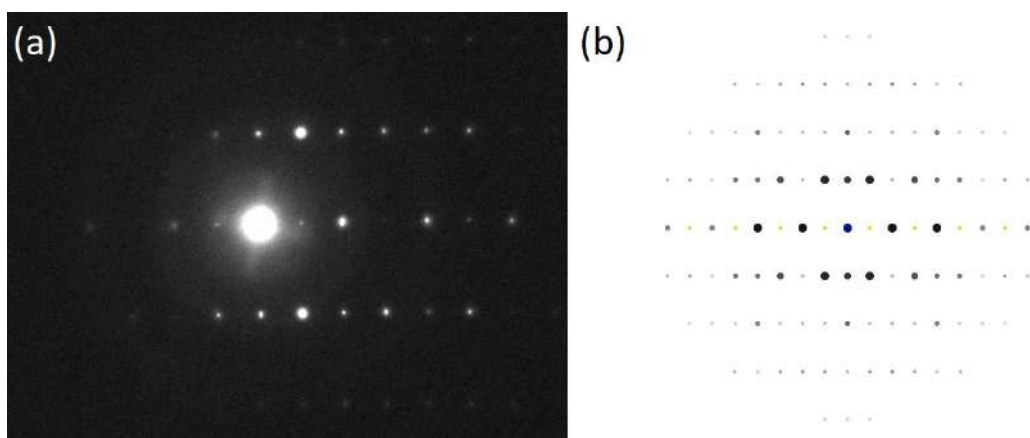


**Figure 3:  $\text{Mn}_5\text{Si}_3$  nanowire experimental (a) and simulated (b) electron diffraction pattern.**

## Effect of Size on Phase Segregation of Heusler Alloys Nanoparticles Synthesized by Pulsed Laser Deposition

N. R. Checca<sup>1</sup>, A. Mello<sup>1</sup>, A. L. Rossi<sup>1</sup> and M.S. Reis<sup>2</sup>

<sup>1</sup>Brazilian Center for Physics Research, Rio de Janeiro, Brazil.

<sup>2</sup>Instituto de Física, Universidade Federal Fluminense, Niteroi-RJ, Brazil.  
nomifsc@gmail.com

Full Heusler alloys (FHA) are well known to either crystallize in a cubic structure (Cu<sub>2</sub>MnAl-type), or present tetragonal distortions. Both structure types present interesting properties, like half-metallicity, room temperature magnetic memory shape effect and/or remarkable magnetocaloric effect, mainly ruled by strong magnetostructural coupling [1]. FHA with cubic structure (L2<sub>1</sub>- phase) are of the form X<sub>2</sub>YZ, where X and Y are d-block elements and Z is a p-block element [2]. In this context, our study focuses on the structural, chemical and magnetic properties of these alloys in reduced dimensions (nanoparticles). In this scale, these nano-alloys emerge as a new class of multifunctional materials. Heusler nanoparticles are considered to exhibit different magnetic properties and reduced spin polarization compared to those in the bulk since a larger fraction of atoms are placed at surfaces. On the other hand, in this nanometric regime we observed that the alloys exhibit phase separation i.e., formation of precipitates showing a core shell morphology. This morphology is extremely interesting on its own both from a fundamental as well as from a technological standpoint. The investigation in Atomic-Scale of the nano-alloys is of primary interest for a full understanding of the magnetic properties. The ternary nanoparticles were produced starting from a full Heusler alloy targets made by arc melting method under inert (argon) gas atmosphere. For this work, the Ni<sub>2</sub>MnGa and Co<sub>2</sub>FeSi nanoparticles were deposited using the pulsed laser deposition (PLD) method, using a Nd:YAG laser with the wavelength  $\lambda=1064$  nm. In order to prevent oxidation issues, the chamber was pumped down to a base pressure of  $10^{-6}$  Torr. For the deposition, argon was used as the inert gas with a continuous flux in a constant pressure of 1 Torr inside the chamber. Two types of substrates were used to collect the nanoparticles: i) carbon coated grids for TEM and HR-TEM imaging, EDS, EELS and SAED and ii) Si (100) substrate for magnetic (SQUID) and structural (GIXRD) measurements. In FIG 1 we show the results of system Ni<sub>2</sub>MnGa deposited with a wavelength of 1064nm and 200mJ per pulse. The XRD analysis shows a cubic structure, although the FFT analyzes of the HRTEM images show an orthorhombic structure (Pnnn) corresponding to the martensitic phase of these shape memory alloys. The magnetic measurements show a dramatic decrease of saturation magnetization of the nanoparticles in compared to bulk. The chemical analyzes by EDS exhibit a concentration of Ni atoms in the particle nucleus. This behavior of segregation of the atoms is observed in the other nano-alloy.

### REFERENCES

[1] Checca, N.R. et al., Materials and Design. 143 (2018) 268.

[2] T. Kanomata, Y. et al., Phys. Rev. B 82 (2010) 144415.

This research was supported by FAPERJ, CNPq and LABNANO/CBPF (Brazil).

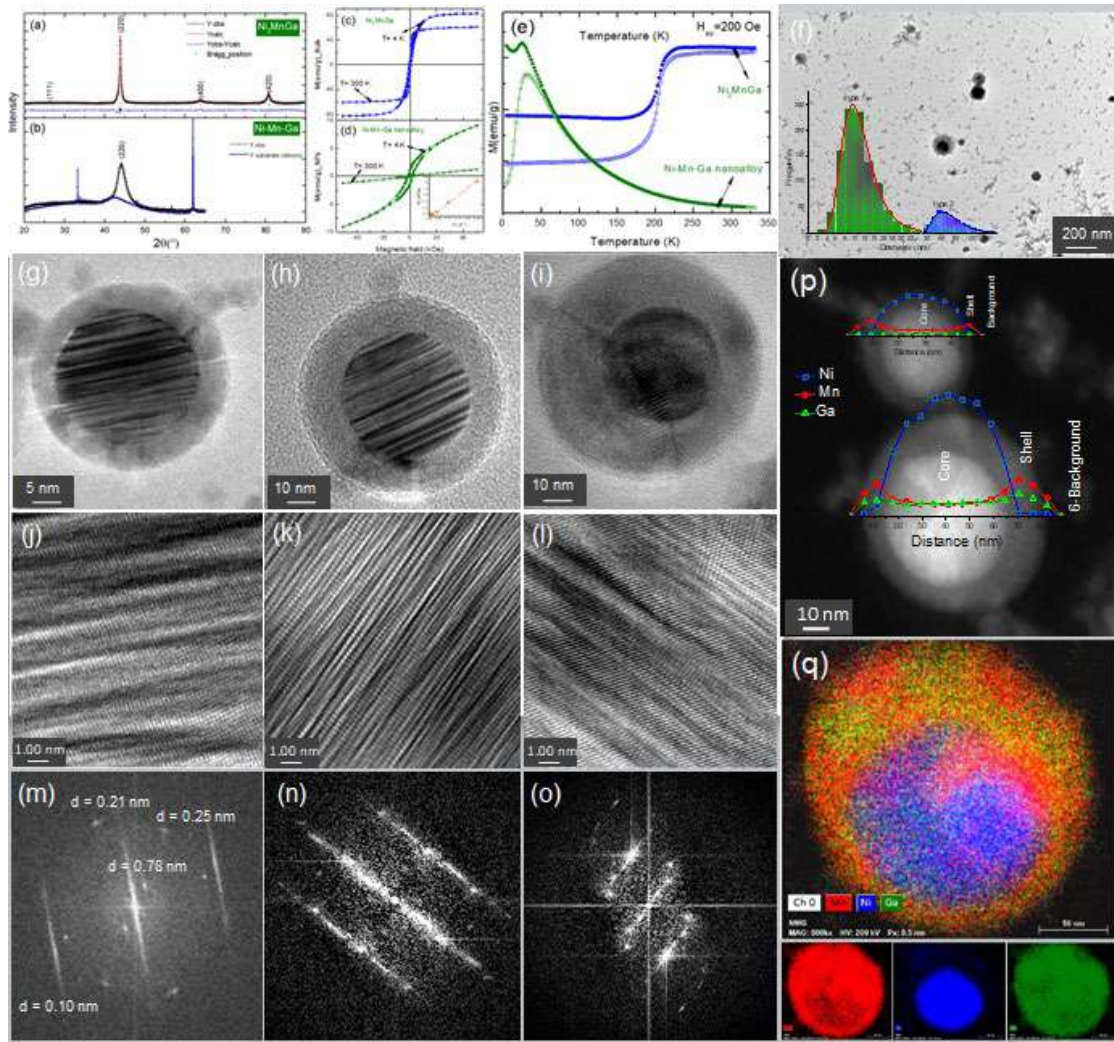


**FIG 1:** show the results of system  $\text{Ni}_2\text{MnGa}$  deposited with a wavelength of 1064nm and 200mJ per pulse. (a)DRX Bulk, (b) DRX Nanoparticle, (c) MxH bulk, (d) MxH nanoparticle, (e) MxT, (f) size distribution (g-o) Images of the core / shell particles with their respective high resolutions and FFT indicating the martensitic phase  $\text{Pnnn}$  and (p-q) chemical analyzes by EDS that exhibit a concentration of Ni atoms in the nanoparticles nucleus.

## Synthesis and characterization of $\text{NiFe}_2\text{O}_4$ nanoparticle for removal of dyes in aqueous solution

R. N. D. Souza<sup>1\*</sup>, N. M. Suguhiro<sup>1</sup>, E. M. Baggio-Saitovitch<sup>2</sup>, M. Alzamora<sup>1</sup>

<sup>1</sup>Universidade Federal do Rio de Janeiro (UFRJ), Rio de Janeiro- Brazil

<sup>2</sup>Centro Brasileiro de Pesquisas Físicas (CBPF), Rio de Janeiro-Brazil

\*nascimentorafael42@gmail.com

Dyes are usually present in the effluent water of several industries, including textile, leather, paper, rubber, plastics, printing, cosmetics, pharmaceuticals and food industries. They contribute to water toxicity and represent an increasing danger for the environment, humans and animals. Dyes are generally resistant to light, water, oxidizing agents and many chemicals and therefore difficult to degrade once released into the aquatic systems[1].

Aiming to acting for dye removal,  $\text{NiFe}_2\text{O}_4$  nanoparticles (NPs) have been prepared by solvothermal method, using Iron(III) and Ni(II) acetylacetonate, in a solution with benzilacool. The synthesized compound had its crystalline structure characterized by X-ray Diffraction (XRD) and Transmission Electron Microscopy (TEM), its magnetic properties were evaluated by magnetic hysteresis and Mossbauer spectroscopy of  $^{57}\text{Fe}$  as a function of temperature, and its morphology and stability by scanning electron microscopy (SEM). The adsorption capacity of the methyl orange dye was evaluated by Uv-Vis spectroscopy.

The crystalline structure of the material was confirmed by the Rietveld refinement of the XRD pattern as being of the spinel type with lattice parameter 8,35 Å, close to bulk reference[2]. Using the Scherrer relation at the most intense peak of the XRD pattern we obtained an average crystallite size of 9 nm. TEM analysis confirmed the presence of nanoparticles of spherical morphology, shown in figure 1, with an average size of 7.45 nm. Low-temperature Mössbauer spectra were fitted considered two six lines, indicate that all iron ions are in the magnetically ordered state, and their values of isomer shifts (IS) are typical of  $\text{Fe}^{3+}$  ions. Combined the IS and the hyperfine magnetic field values obtained it is possible to associated this two site a tetrahedral (A) and octahedral [B] site of the spinel structure of Ni-ferrite. The cation distribution of the sample was estimated by the intensity of the Mössbauer components as  $(\text{Ni}_{0.17}\text{Fe}_{0.83})[\text{Ni}_{0.83}\text{Fe}_{1.17}]\text{O}_3$  corresponding a partial inverted spinel structure with inversion degree of 0.83. At room temperature the spectrum consists of the broad line, such behavior of the spectra could be associated to superparamagnetic relaxation of the iron magnetic moments. The superparamagnetic behavior is also confirmed by M vs H curves at room temperature, the coercivity field was only observed below 25 K while measurement M Vs. T show that blocking temperature is approximately 50 K [3]. Methyl orange adsorption tests were carried out in aqueous solution in presence of Ni-ferrite Nps. The best adsorption capacity, 73%, was obtained after 15 minutes of reaction, showing us the efficient this material.

However, analyzes SEM revealed that the NPs has low stability, entering the process of agglomeration, shown by figure 2a. In this figure it is possible to notice the formation of



aggregates of NPs, as the process evolves, the NPs begin to coalesce and create well defined faces, shown in figure 2b. We believe that the addition of nickel in the ferrite caused the surface energy of the NPs to increase, decreasing their stability, causing the coalescing process. The current focus of the research is functionalization of the surface of the NPs in order to avoid the agglomeration, improving dyes adsorption.

#### References:

- [1]García, Elizabeth, et al. *Materials* 7.12 (2014): 8037-8057.
- [2]R.M Cornell et al. John Wiley & Sons, 2003.
- [3]N. S. Gajbhiye et al. In *Hyperfine Interactions*, p 99–102. Springer, 2002

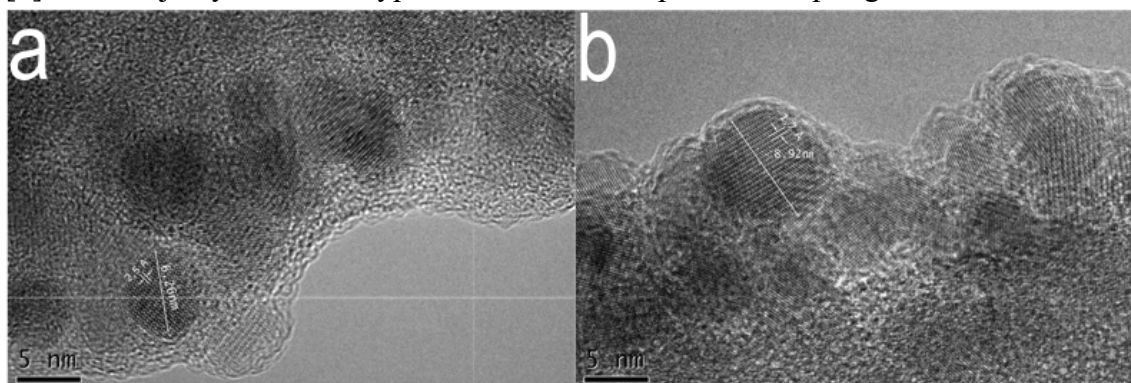


Figure 1: MET images of the  $\text{NiFe}_2\text{O}_4$  NP, a) shows a NP of 6.26 nm and a spacing between the fringes of 2.5 Å, b) shows a NP of 8.92 nm and a distance between the fringes of 1.7 Å

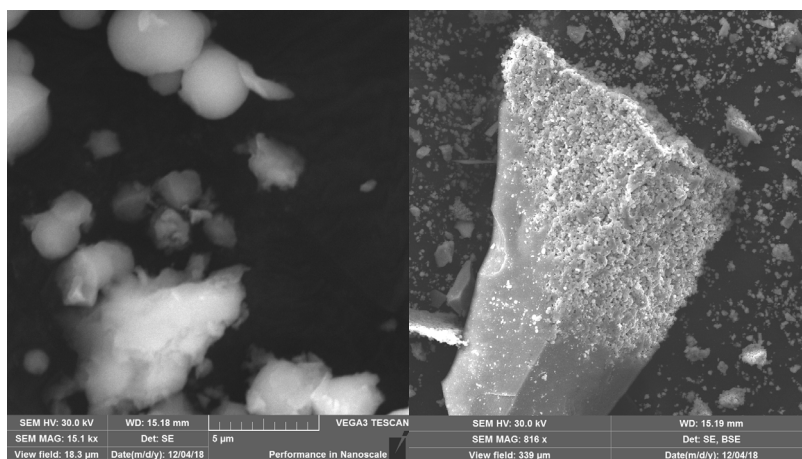


Figure 2: SEM images of  $\text{NiFe}_2\text{O}_4$ , a) shows the process of aggregation of NPs and formation of the first clusters, b) shows the evolution of the coalescing process of the initial clusters and the creation of faces in the structure



## **Discrimination of Quartz and Resin using Convolutional Neural Networks in Optical Microscopy Images of Minerals**

Julio César Álvarez Iglesias<sup>1</sup>, Richard Bryan Magalhaes Santos<sup>1\*</sup> and Sidnei Paciornik<sup>1</sup>

<sup>1</sup>. Dept. of Chemical and Materials Engineering (DEQM), PUC-Rio, Rio de Janeiro, Brazil

\*rbryan2008@hotmail.com

The final quality of the iron ore in mineral processing is tied to the efficiency of its beneficiation process, which can be optimized when the composition of the iron ore is known. Manual methods have been proposed and developed to analyze the composition of iron ore samples and, therefore, guide the beneficiation process. One of the most traditional techniques applied to this problem is Reflected Light Optical Microscopy (RLOM) which has a contrast based on the difference of reflectance of the materials. Unfortunately, the mounting resin commercially available mounting resins have a tendency to get mixed with the quartz phase, as both have a very similar reflectance. The quartz can be problematic, as it has a very wide tonal range. It can be as light as the resin and even as dark as some of the other phases. Therefore, besides being difficult to differentiate from the resin, it also ends up hindering the identification of other phases. Due to the aforementioned reasons, it is a well-known problem that it's not possible to analyze and segment the quartz phase apart from the other major phases, for example: hematite, goethite and magnetite, by RLOM. One of the more recent and promising developments in the field of image analysis are Convolutional Neural Networks (CNNs) [1], which themselves are a branch of machine learning that have been able to match and sometimes even outperform humans, [2],[3],[4]. It is feasible to apply them to this problem, for a human operator, once trained to do so, can easily distinguish between quartz and resin in a given image. However, for a CNN to be able to learn how to solve the problem it is necessary to build a large and representative databank. Our databank consists of 1747 images of resin and 1745 images of quartz for the training set and 442 images of each class for the test set. The Convolutional Neural Network (CNN) achieved, once trained, success rates above 95%, which proves that CNNs can indeed solve this classic problem.

### **REFERENCES**

- [1] Shokri, R., Shmatikov, V., In: 22nd ACM SIGSAC Conference on Computer and Communications Security, pp 1310-1321.
- [2] Ciresan et al., In IEEE International Conference on Computer Vision and Pattern Recognition, pp. 3642-3649.
- [3] Azimi et al., Scientific reports 8 (1), 2128.
- [4] Masci et al., In: International Joint Conference on Neural Networks, pp 1-6.
- [5] This research was supported by CNPq, CAPES and FAPERJ.

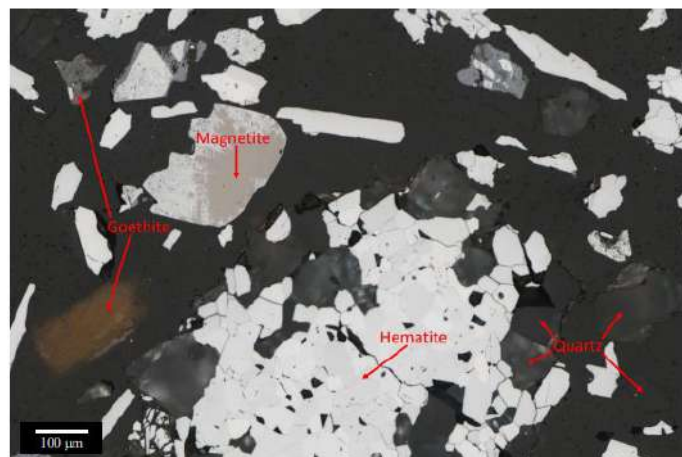


Figure 1- A typical iron ore RLOM image with its most common phases identified.

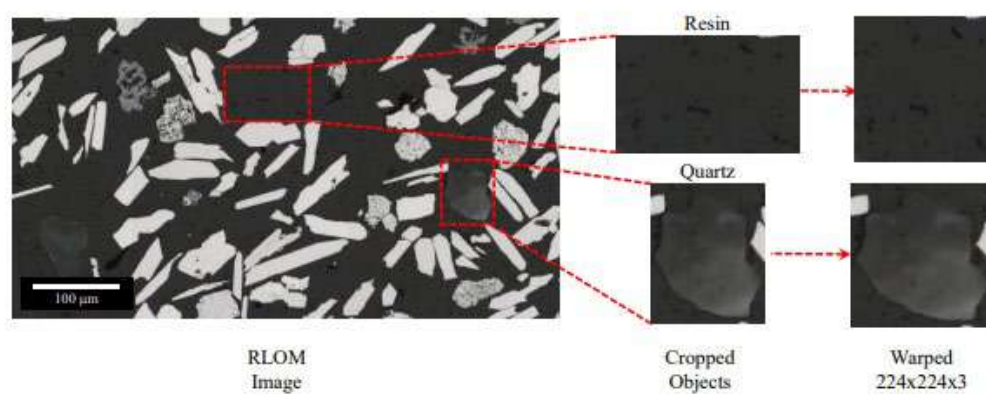


Figure 2 –Databank preparation.

Table 1- Confusion matrix of trained CNN applied to the entire training set.

	Resin	Quartz
Resin	1727	20
Quartz	73	1672



## Development of an Image Analysis System for Automatic Characterization of Sintering Cold Agglomerated

Richard Bryan Magalhaes Santos<sup>1\*</sup>, Karen Soares Augusto<sup>1</sup>, Sidnei Paciornik<sup>1</sup>  
and Alei Leite Alcantara Domingues<sup>2</sup>

<sup>1</sup>. Dept. of Chemical and Materials Engineering (DEQM), PUC-Rio, Rio de Janeiro, Brazil

<sup>2</sup>. CTF/VALE, Nova Lima, Minas Gerais, Brazil  
\*rbryan2008@hotmail.com

Due to the fine nature of some iron ore particles, they cannot be used in reduction furnaces directly, requiring an agglomeration processes, such as pelletizing or sintering. In the sintering process, which is the focus of this work, the fines must first undertake a micro-agglomeration stage. In this stage, there is the formation of 3 typical structures for a cold agglomerated: quasiparticles (cores + adherent layers), micropellets, and non-agglomerated particles. It is known that many of the characteristics and properties of the sinter are a function of the structure of the pre-heat treatment cold agglomerated [1]. Due to the subjectivity and the time it takes for a human operator to analyze optical microscopy images of the material (Figure 1A) and count the numbers of each structure while estimating their size and shape, the development of a routine capable of automatic analysis and more accurate and consistent measures would allow for a better understanding of the relations between the structure of the cold agglomerated and the final sinter. The routine was developed in the free software FIJI [2], and made use of more unusual and sophisticated morphological functions, such as: Morphological Reconstruction [3] and Local Thickness [4]. It is capable of identifying the particles of different granulometry that compose the sample, and classify them in the 3 classes aforementioned (Figure 1B), while also calculating the class percentage (Table 1) and shape factors like average circularity (Table 1), average thickness of the quasiparticles outer layer by two different methods (weighted by area and by number) (Figure 1C) (Table 2), identify the different mineral phases in the quasiparticles (Figure 1D) and quantify them (Table 3). The routine can be run upon mosaic images, which can contain thousands of particles depending on the sample granulometry. The developed routine is in regular use in CTF/Vale, allowing a fully automatic characterization.

### REFERENCES

- [1] Vieira C. B., Avaliação técnica de minérios de ferro para sinterização nas siderúrgicas e minerações brasileiras: uma análise crítica, REM: R. Esc. Minas, Ouro Preto, 56(2): 97-102, abr. jun. 2003.
- [2] Fiji: an open-source platform for biological-image analysis. Nature Methods. 9 (2012).
- [3] Legland, D. et al. (2016), MorphoLibJ: integrated library and plugins for mathematical morphology with ImageJ, Bioinformatics (Oxford Univ Press) 32(22): 3532-3534 (on Google Scholar).
- [4] Hildebrand, T; Rüesgsegger, P. A new method for the model-independent assessment of thickness in three-dimensional images”, Journal of Microscopy, 185 (1996) 67-75.
- [5] This research was supported by CNPq, CAPES and FAPERJ.

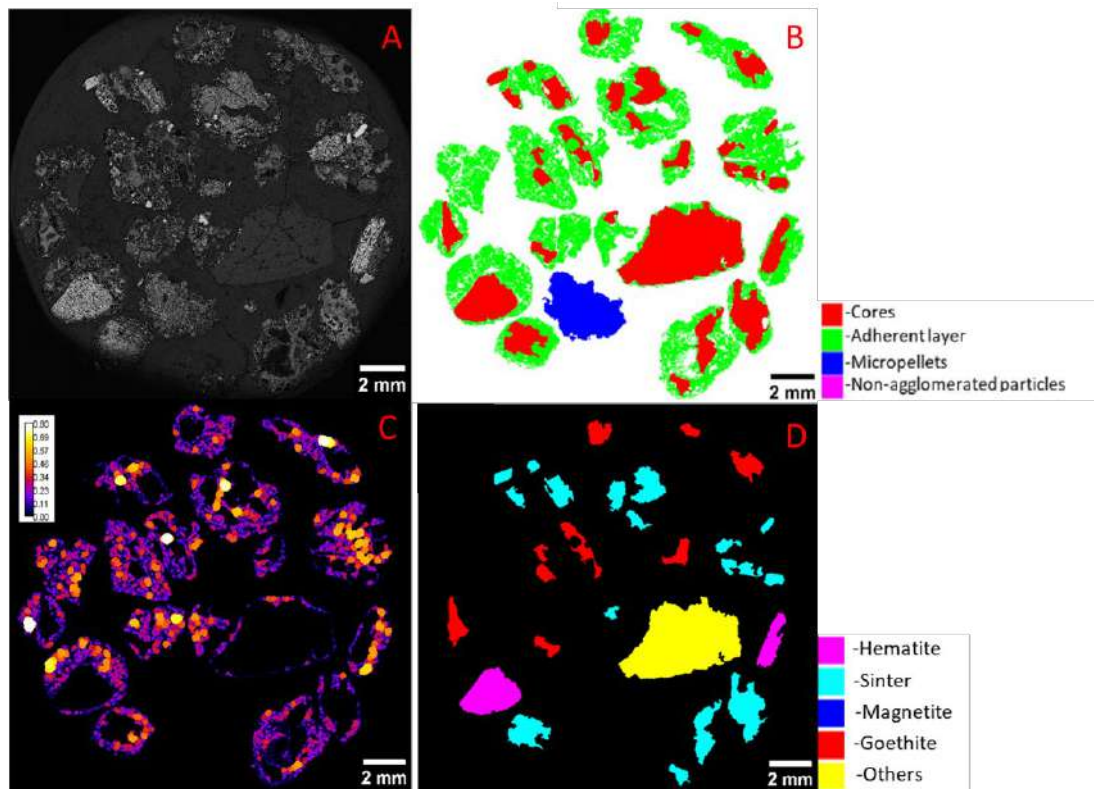


Figure 1- A typical iron ore cold agglomerated RLOM image (A). Classification of the different structures quasiparticles (cores + adherent layers), micropellets, and non-agglomerated particles (B). Local Thickness map for the adherent layer of the quasiparticles (C). Classification of the different phases in the quasiparticles' cores (D).

Table 1 – Area fraction, average circularity and their standard deviations for the 3 particle classes for the image in Figure 1 B.

	Fração de Área(%)	Circularidade	Desvio padrão
Quasipartículas	94,09	0,66	0,19
Micropelotas	5,91	0,65	0,00
Não aglomeradas	0,00	-	-

Table 1 – Mean thickness of the AL of the QP's by 2 different methods.

Mean thickness of the adherent layer	
Area weighted	0,251 mm
Number weighted	0,249 mm

Table 3 – Percentage of the different phases in the cores of the quasiparticles.

	Area Fraction (%)
Hematite	13,85
Sinter	35,73
Goethite	16,54
Magnetite	-
Others	33,89

## Application of Automated Mineralogical Mapping for Advanced Characterization of Pre-Salt Reservoir Rocks

Yaro Moisés Parizek-Silva<sup>1,3\*</sup>, Reiner Neumann<sup>2,3</sup>, Ciro Alexandre Ávila<sup>3</sup> and Camila Wense Dias dos Anjos<sup>1</sup>

<sup>1</sup>. PETROBRAS-CENPES, Rio de Janeiro, Brasil. \*yaro@petrobras.com.br

<sup>2</sup>. CETEM-SCT, Rio de Janeiro, Brasil.

<sup>3</sup>. Postgraduate Program in Geosciences, National Museum, UFRJ, Rio de Janeiro Brasil.

Despite being target of many researches since their discovery, the Aptian reservoirs of pre-salt section (Santos Basin, Brazil) still demand advances in characterization studies. These rocks are predominantly composed by carbonates [1] and the knowledge about the mineralogy is impactful for studies of reservoir quality and for the construction of geological models. Mineralogical maps obtained by scanning electron microscopy (SEM) of petrographic thin sections can represent a progress in the characterization of these rocks, providing quantitative and visual mineralogical data, in high resolution without destroying the sample [2]. The aim of this work was to validate advanced techniques of automated mineralogical mapping in order to optimize the acquisition of mineralogy and porosity data in carbonate rocks samples. The technique was applied in 59 pre-salt rocks samples, using QEMSCAN (Quantitative Evaluation of Minerals by Electron Microscopy) and the results were compared with those acquired by X-ray diffraction (XRD), optical petrography, electron microprobe, inorganic geochemistry and conventional petrophysics analysis (Figure 1). The resolution of 10  $\mu\text{m}$  for the mapping was the most appropriate for the characterization of the mineral phases with a reasonable time of data acquisition. Calcite, dolomite and quartz were the most abundant minerals found in the samples and the following constituents occur in lower proportions: strontianite, dawsonite, magnesite, phyllosilicates, feldspars, pyrite, barite, apatite, goyazite, cryolite and fluorite. It was also possible to identify and quantify non-stoichiometric carbonates (magnesium calcite and calcium dolomite) and the porosity. The occurrence, associations and distribution of each constituents were detailed, helping in the construction of hypotheses for the syngenetic and diagenetic processes. Comparing to established mineralogy, chemical and porosity determination methods, the applied automated mineralogical mapping proved to be consistent and valid (Figure 1). In addition, the mineralogical maps exhibited good visual quality, showing the spatial distribution of the minerals, emphasizing textures and structures often difficult to characterize by other techniques (Figure 2). Finally, the mineralogical characterization is essential for the evolution of the knowledge about the rocks of the pre-salt reservoirs. In this context, the mineralogical mapping proved to be a valuable tool to obtain more accurate and advanced results.

### References

- [1] J.L.P. Moreira et al., Bacia de Santos. Bol. de Geoc. Petrobras, 15 (2007).
- [2] Y.M. Parizek-Silva, Métodos Avançados para Caracterização de Mineralogia, Porosidade e de Parâmetros Petrofísicos em Reservatórios Carbonáticos, Dissert. MSc., UFRJ, Rio de Janeiro (2019).



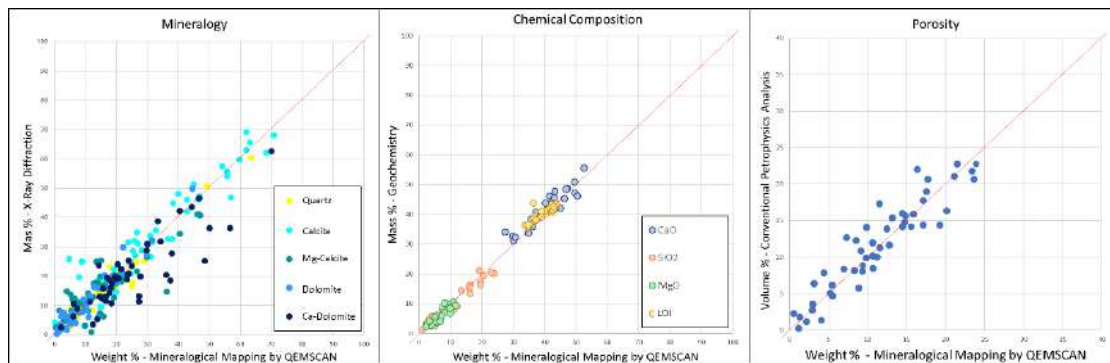


Figure 1: Comparison of mineralogical, chemical and porosity results obtained by mineralogical mapping and by conventional techniques. Graph analysis indicates good data correlation and the few outliers are mainly related to sampling issues; A - Comparison of mineralogy obtained by mapping and XRD. B - Comparison of chemical composition obtained by mapping and geochemistry (ICP-OES). Comparison of pores quantification by mapping and conventional petrophysics analysis.

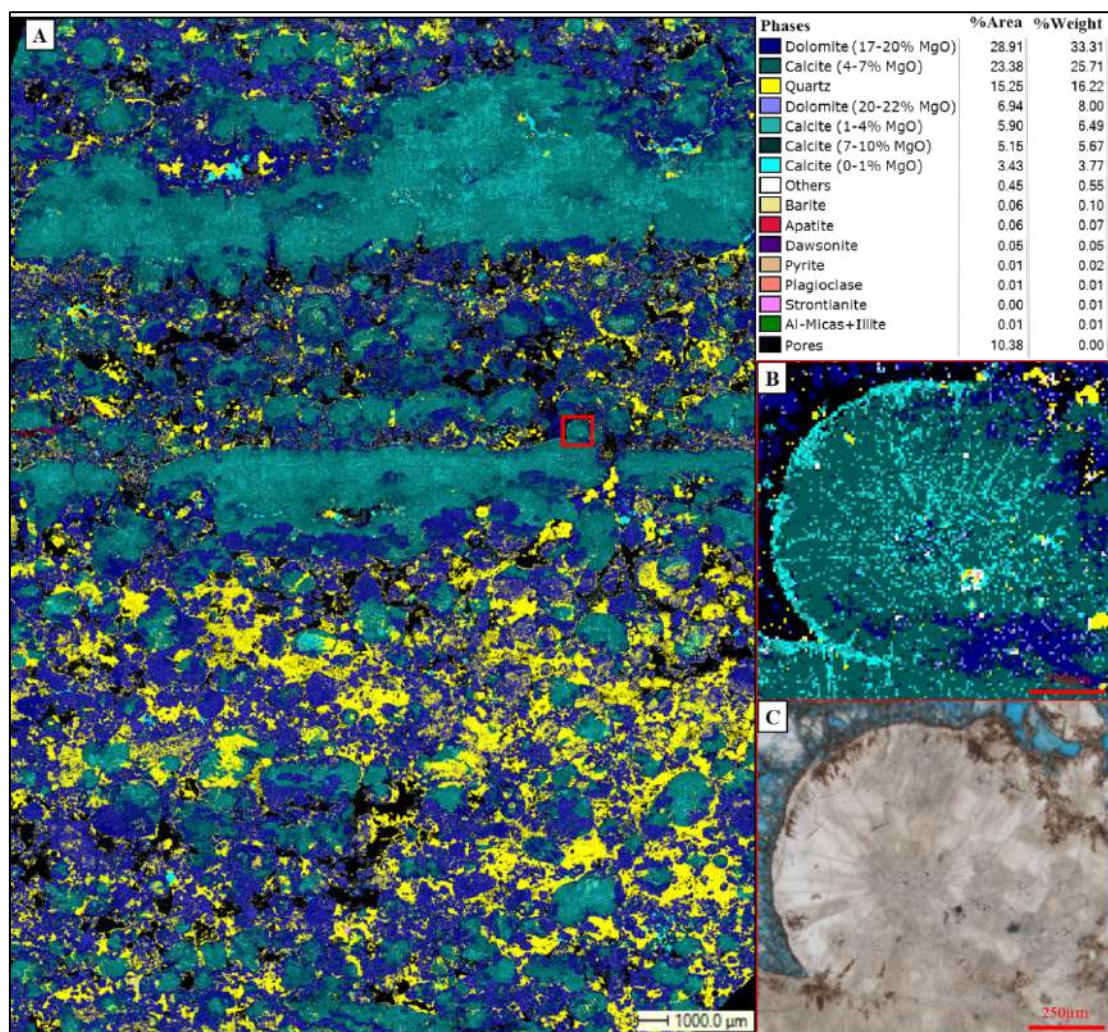


Figure 2: A - Mineralogical map (resolution: 5  $\mu$ m) showing distribution of all identified phases. In the upper right is the color legend of the phases and the respective quantifications. The rock's lamination is highlighted and it is possible to see the dolomite and quartz cements. B - Detail of the red area marked on the general map (A) showing the distribution of the calcite varieties within the spherulite. C - Optical microscope photomicrograph of same area shown in B (transmitted light and parallel polarizers).



## Comparing Quantitative EDS and WDS Using Microanalytical Standards and Interlaboratorial Test Samples

Karla Balzuweit<sup>\*1,2</sup>, Márcio deAlmeida Flores<sup>2</sup>, Luis A. R. Garcia<sup>2</sup> and Marcelo C. C. Souza<sup>2</sup>, Rilberte C. Ribeiro<sup>2</sup>

<sup>1</sup>. Departamento de Física/ Instituto de Ciências Exatas / Universidade Federal de Minas Gerais, Belo Horizonte, Brasil

<sup>2</sup>. Centro de Microscopia da Universidade Federal de Minas Gerais, Belo Horizonte, Brasil

Historically electron microprobe (EPMA) with wavelength dispersive spectrometers (WDS) is a worldwide accepted microanalytical tool opposed to scanning electron microscopy (SEM) with energy dispersive spectrometers (EDS) [1,2]. EPMA quantitative analysis imply in high, constant and stable current, in the order of nA or tenth's of nA, as well as the use of microanalytical standards for comparison, which can become quite time consuming. SEM's were mainly imaging tools with pA current which varies significantly with magnification, or with qualitative elemental identification. However, in the last years SEM's have grown more versatile and stable, as well as the new silicon drift detectors (SDD-EDS), where much higher count rates are possible enabling better peak to background ratios, allowing a more quantitative approach [3]. Additionally, the need for faster and more reliable analysis spurred the current investigation. Four distinct microanalytical standards and two interlaboratorial test samples were analyzed on a Jeol 8900JXA microprobe with 4 WDS and 3 SEM's with Bruker SDD-EDS spectrometers, namely a thermoionic Jeol 6360LV, a Quanta200 FEG and a Quanta3D FEG dual FIB from FEI. Conditions varied slightly, but energy calibration was always performed immediately before each measurement, spot mode, high count rates and point spectra were used in each dataset. Standard and standardless ZAF matrix correction procedures were used to analyze each spectra, and the data of EPMA and the SEM's were compared. The figure below shows the data of a interlaboratorial test sample measured with EPMA and the Quanta3D dual FIB FEG, showing a quite surprising agreement, even for trace elements as silicon and vanadium. Results of all 6 samples will be shown and discussed. EPMA error bars were around 3 times smaller than SEM EDS's and the results were quite encouraging, except where peak overlap was present in such a way that did not allow using a different line.

### REFERÊNCIAS

- [1] S.J.B. Reed, Electron microprobe analysis, Cambridge University Press, 1993.
- [2] J.I. Goldstein et al., Scanning Electron Microscopy and X-ray Microanalysis, Plenum, New York, 1992.
- [3] D.E Newbury et al., Scanning, 35 (3) (2013) 141.
- [4] This research was supported by Centro de Microscopia da UFMG, CNPq, FINEP and FAPEMIG (Brazil).



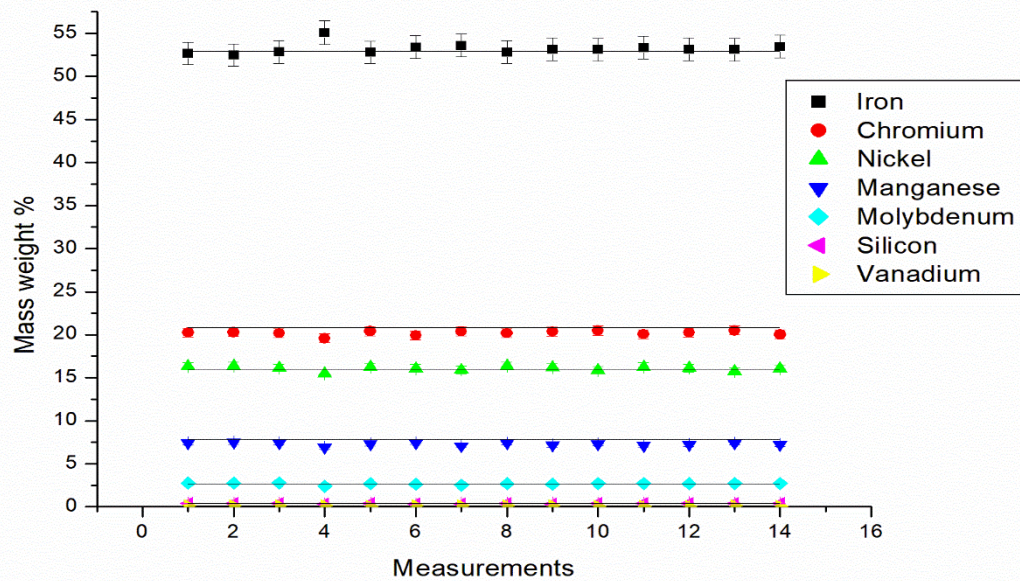


Chart comparing EPMA and EDS-SEM measurements: the solid line represent the EPMA measurements; 14 SEM-EDS measured points and their respective error bars for each element, showing a quite surprising agreement.

## Fabrication of Lignocellulose-Based Microreactors: Copper-Functionalized Bamboo for Continuous-Flow CuAAC Click Reactions

Omar Ginoble Pandoli<sup>1\*</sup>, Druval Santos de Sa<sup>1</sup>, Rodrigo Bustamante<sup>1</sup>,  
Khosrow Ghavami<sup>2</sup> and Alessandro Massi<sup>3</sup>

<sup>1</sup>. Departamento de Química, PUC-RIO, Rio de Janeiro, Brasil.

<sup>2</sup>. Departamento de Engenharia Civil, PUC-RIO, Rio de Janeiro, Brasil.

<sup>3</sup>. Dipartimento di Scienze Chimiche e Farmaceutiche, Università di Ferrara, Italia.

\*email: [omarpandoli@puc-rio.br](mailto:omarpandoli@puc-rio.br)

The research on bio-microfluidics has shown to be promising for the application of biomaterials and biomimetic analogues as microfluidic devices (MDs), mainly for biosensing and biomedical studies.[1] The plants are one of the best sources to create advanced materials, specifically biopolymers (cellulose, hemicellulose and lignin), which might be employed as the structural basis of functional MDs, such as paper-based microfluidic devices (PμDs),[2] with some advantages compared to the common systems manufactured from elastomers, thermoplastic, glass and metals. Plant-derived microfluidic systems have never been applied to synthetic processes for the production of target molecules, according to available publications.[3] Microreactor technology (MRT) is targeting process intensification through the design of size-controlled microfluidic reactors with large surface-area-to-volume ratio to induce diffusion mixing of the reagents and fast dissipation of heat.[4] MRT provides benefits in terms of reaction selectivity, yield, sustainability, and scalability of reaction by numbering-up approach. Moreover, an important aspect is the reproducibility and low-cost production of MDs to establish a scalable fabrication technology for the potential industrial and academic market. This paper presents the results of an investigation related to the lignocellulose-based microreactors (LμRs), fabricated from vegetal resources, namely bamboo culms, which are effectively operated to conduct environmentally benign chemical processes, expanding the toolbox of available microfluidic reactors for organic synthesis. In the present investigation the hydrophilic micro-sized channels of bamboo have been doped with copper ions to run copper(I)-catalyzed 1,3-dipolar cycloadditions (CuAACs) for the continuous-flow synthesis of model 1,2,3-triazole derivatives in aqueous medium (Figure 1). In this work, the rapid, cost-effective prototyping of the disclosed copper-functionalized lignocellulosic microreactor (Cu-LμR) also is described together with a detailed microanalysis (Figures 2-3) of the bamboo-based biocomposite material.[5]

[1] P. Domachuk et al., *Advanced Materials* 22 (2010) 249.

[2] D.M. Cate et al., *Analytical Chemistry*. 87 (2015) 19.

[3] M.Z.C. Hatit et al., *Nature Communications* 9 (2018) 1.

[4] O.G. Pandoli, et al., *Journal of Photochemistry and Photobiology A* 364 (2018) 59.

[5] O.G. Pandoli, et al., *ACS Sustainable Chemistry & Engineering* 7 (2019) 3267.

[6] The authors are grateful for the financial support from the Serrapilheira Institute (grant number Serra-1709-17482) and the LNNano/CNPq. O.P. thanks FAPERJ-Brazil for the JCNE fellowship (E-26/203.281/2016).

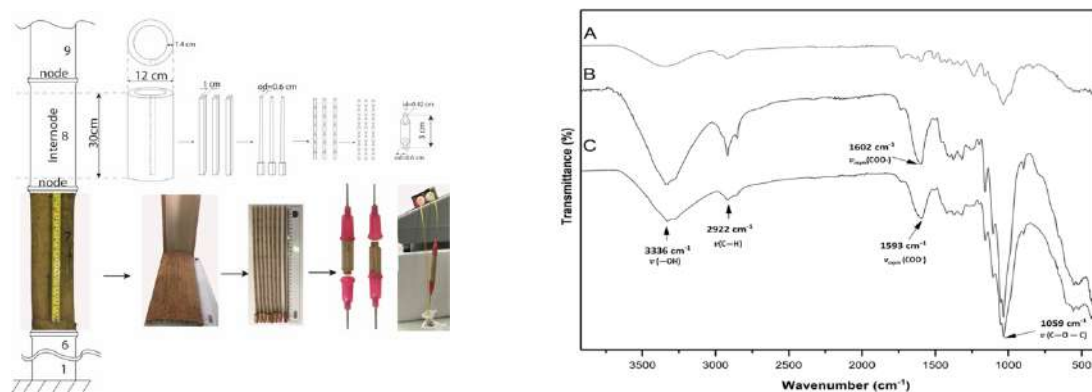


**Figure 1.** (left) Fabrication of lignocellulose-based microreactors (LμRs) from bamboo. (Right) FT-IR-ATR spectra for sliced bamboo (A) LμR, (B) LμR oxidized with TEMPO and (C) Cu-LμR.

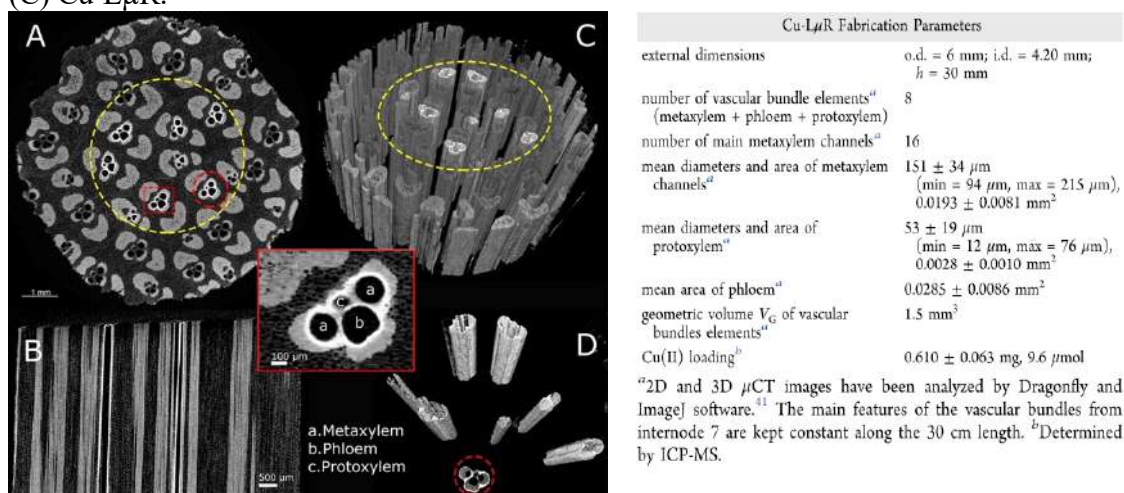


**Figure 2.** μCT images of copper-functionalized lignocellulosic microreactor (Cu-LμR): transversal and longitudinal cross sections of bamboo culm (A-B); 3D image with and without the vegetal biomass (C-D). Dotted circular yellow line with internal diameter of 4.2 mm corresponds to the internal area of flow injection. Insight of the metal depositions onto microchannels (metaxylem, phloem, protoxylem) are highlighted with red lines. Copper deposition of about 21 μm thickness.

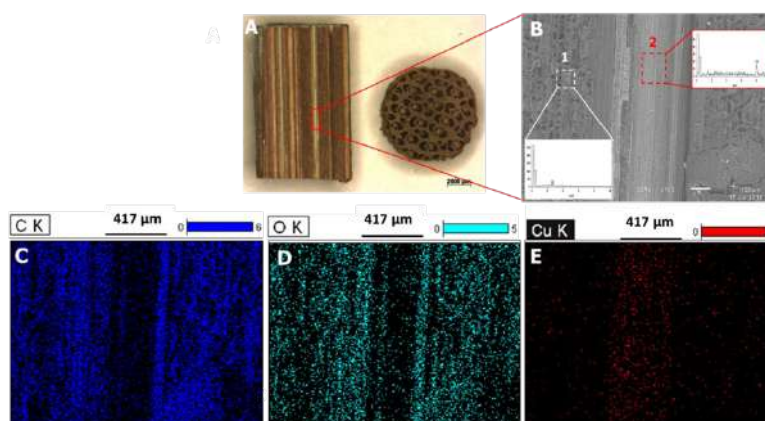


**Figure 3.** Optical image (A), SEM image (B) and EDS maps spectroscopy (C-D) of a longitudinal section of a Cu-LμB vascular bundles. SEM image shows a fused channel with a diameter approximately of 417 μm. EDS maps identify the distribution of C, O, and Cu outside and inside the walls of the channel.



# Hematite And Pyrite From Elba Island: From Theory To SEM/EDS Microanalysis

Corinne Arrouvel

UFSCar - DFQM/CCTS, Campus Sorocaba, Sorocaba, SP, Brazil.

Natural pyrite  $\text{FeS}_2$  exposes commonly three types of surfaces  $\{001\}$ ,  $\{111\}$  and  $\{210\}$  at the origin of the cubical, bi-pyramidal and pyritohedral shapes respectively or a combination of them. A recent study using force field methods details the structure and the stability of a wide range of surfaces, distinguishing the kinetic growth from the thermodynamic growth of pyrite and the observed  $\langle 001 \rangle$  striations onto  $(hk0)/(h00)$  surfaces[1]. So far, the 'negative' orientation of the striations onto pyritohedral surfaces, minerals from Japan that have been reported by Endo and Sunagawa[2], is rare and has not been solved. Lately, we found samples of pyrite from Elba, growing with magnetic hematite, revealing the same peculiar orientation. A comparative study with other pyrite minerals is also undertaken to clarify the geological conditions influencing the crystal growth.

The samples have been cleaned with isopropanol and grounded in an agate mortar for X-Ray Diffraction, XRD patterns were obtained using a PANalytical X'Pert Pro X-ray diffractometer with a  $\text{CuK}\alpha 1$  radiation source (wavelength  $\lambda$  of  $1.5406 \text{ \AA}$ ) and operating at 40 kV with a current of 40 mA. The sample holder was a silicon zero-background. Raw samples were examined on a JEOL JSM 7100F FE-SEM with FEG source of electrons at an acceleration voltage of 15 kV for all measurements. The elemental composition of the nanocrystals was determined using energy dispersive X-ray spectroscopy (EDS) Oxford (SDD de  $80 \text{ mm}^2$ ).

SEM image analyses combined with theoretical simulations (using METADISE software) demonstrate that the striations are along the  $\langle 001 \rangle$  directions of the unexpected (120) surface on pyrite samples from Elba. Actually, the (120) and the (210) surfaces have different terminations. Indeed, the (210) surface is S-terminated with a surface energy of  $1.65 \text{ J m}^{-2}$  under vacuum while the (120) is slightly less stable, Fe-terminated with a surface energy of  $1.68 \text{ J m}^{-2}$  (unpublished results). In addition to common impurities (e.g. Cu, Ni, Co, Si, Al), small peaks in EDS spectra correspond to rare earth elements (REE) at low concentrations ( $\text{At}\% 0.1 < C < 0.5$  for Er, Ho and Tb). Sulfur/iron-rich environments, impurities are factors influencing morphologies. REE have been recently discovered in Japan and identified in Elba basalts[3]. That might explain the stabilization of the (120) surface of the so-called 'negative' pyrite.

## REFERENCES

- [1] C. Arrouvel and J.-G. Eon, Materials Research, 22(1) (2019) e20171140.
- [2] Y. Endo and I. Sunagawa, American Mineralogist, 58 (1973) 930.
- [3] E. Saccani and G. Principi, Mineralogy and Petrology, 110 (2016) 713.

## ACKNOWLEDGMENT

C. Arrouvel thanks CBPF (Labnano and MatMult) for the use of equipment SEM-XRD. She is particularly grateful to Elisabeth Lieutaud for her search on 'negative' pyrite and Krijn and his late wife Petra Tommel for donating pyrite and hematite from their collection.

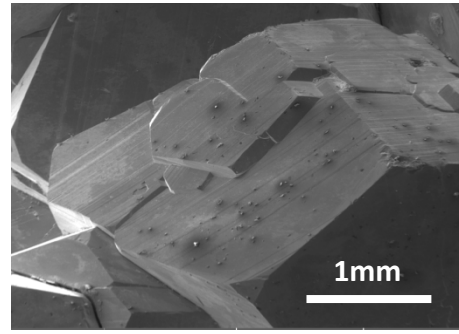
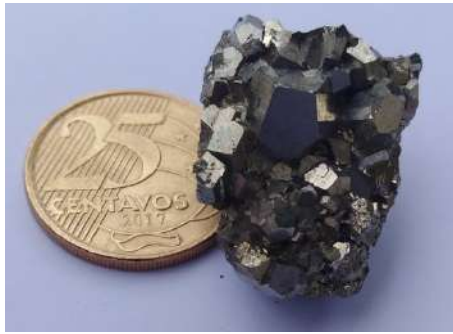


**Figure:** Photography image and SEM image of pyrite  $\text{FeS}_2$  from Elba island.

## Characterization of reduced graphene oxide thin films covered by Cu sputtering by Raman spectroscopy, scanning electron microscopy (SEM) and energy-dispersive X-ray spectroscopy (EDS)

Andreza Menezes Lima<sup>1\*</sup>, Cilene Labre Alves da Silva<sup>2</sup>, Leila Rosa de Oliveira Cruz<sup>1</sup>  
and Wagner Anacleto Pinheiro<sup>1</sup>

<sup>1</sup>. Instituto Militar de Engenharia - Department of Materials Engineering, Praça General Tibúrcio, 80 – Rio de Janeiro, Brasil

<sup>2</sup>. Centro Brasileiro de Pesquisas Físicas, Rua Doutor Xavier Sigaud, 150 – Rio de Janeiro, Brasil

Thin films of reduced graphene oxide can be applied in many technological fields, the exceptional electronical properties of graphene made these films good candidates to integrate solar cells, batteries, supercapacitors and others [1]. The instability of the dispersion and the difficult to generate continuous, low resistive and high-quality films still are an impediment to production in large scale and industry applications. Raman, SEM and EDS are simple and nondestructive characterizations methods that can be used to understand the properties of these films [2]. Raman spectroscopy is one of the most important analyses to prove that films are really constituted of graphene oxide, because the spectrum shows the appearing of D and G band, that are features bands of carbon-based materials [3]. In addition, SEM images and EDS are important to verified morphology, uniformity and continuity. In this work, from GO e rGO dispersions, rGO films was produced by spray coating method [4], reduced in a controlled hydrogen atmosphere oven and then copper was sputtered during 20 seconds over the surface of the films, to improve the link between the graphene flakes, in order to reduce electrical resistance. Raman spectroscopy from rGO films exhibited the D ( $1354\text{ cm}^{-1}$ ) and G ( $1586\text{ cm}^{-1}$ ) bands in both cases; in the sample with Cu sputtering, it was possible to verify Raman bands of  $\text{Cu}_2\text{O}$ , in  $214\text{ cm}^{-1}$  and  $284\text{ cm}^{-1}$  [5]. By the SEM image analysis, it was possible to conclude that the films were continuous and uniforms in most of its extension. Wrinkles and folds were observed, proving the presence of graphene flakes. Comparing the EDS analysis between the samples with and without copper, it was possible to verify the effectiveness of sputtering process, working as a bridge among the rGO flakes. The Cu sputtering was responsible for a reduction from  $5323\text{ }\Omega/\square$  to  $4947\text{ }\Omega/\square$  in the sheet resistance of the films, this subtle effect probably was caused by the electrical resistance of the contact.

### REFERENCES

- [1] Y. Tong et al., Austin J. Nanomed. Nanotechnol., 1 (2013) 1003.
- [2] A. Pruna et al., J. Nanopart. Res., 15 (2013) 1605.
- [3] Y. Zhu et al., Adv. Mater., 22 (2010) 3906.
- [4] V. Pham et al., Carbon, 48 (2010) 1945.
- [5] M. Patwary et al., Thin Solid Films, 675 (2019) 59.

### ACKNOWLEDGEMENTS

The authors would like to thank CAPES and FAPERJ for the financial support.

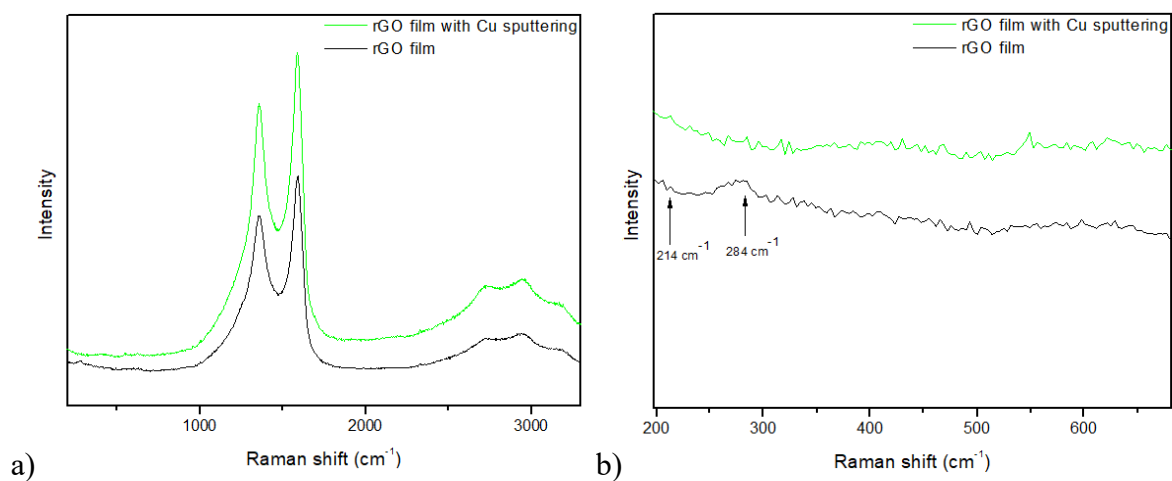


Figure 1 – Raman spectroscopy of rGO films.

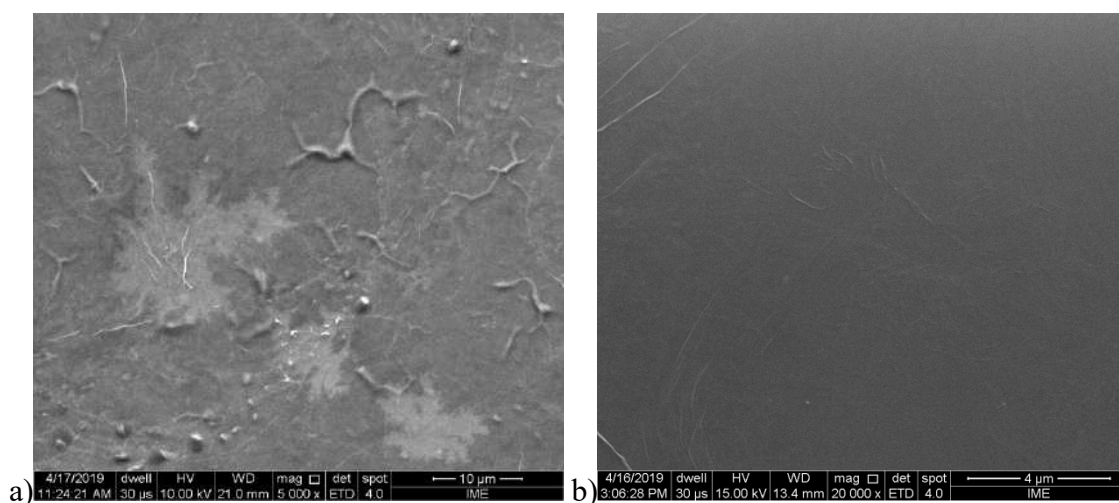


Figure 2 – SEM microscopy of a) rGO film, b) rGO film with Cu sputtering.

Table 1 – EDS results in wt%.

	rGO film	rGO film + Cu sputtering
<b>C</b>	14,2%	10,6%
<b>O</b>	85,1%	86%
<b>S</b>	0,8%	0,2%
<b>Cu</b>	0%	3,6%

## Defects Pattern on Monolayer Graphene with High Spatial Frequency Using Helium Ion Microscopy

William F. da Silva<sup>1\*</sup>, Helton G. Medeiros<sup>1</sup>, Bráulio S. Archanjo<sup>1</sup>, Clara M. Almeida<sup>1</sup> and Thiago L. Vasconcelos<sup>1</sup>.

<sup>1</sup>. National Institute of Metrology, Quality and Technology (INMETRO), Materials Metrology Division (Dimat), RJ-Brazil

E-mail: williamsilvakse@gmail.com

Recently, two-dimensional materials has attracted attention due to its disruptive technologies applications in optics, electronics, spintronics and several other areas [1]. With the objective of manipulate these materials and generate new properties from them, techniques such as electron beam or ion beam lithography have been employed, enabling structural modifications such as the creation of patterns and punctual defects. Among such lithography techniques, helium-ion microscopy (HIM) stands out, in which a focused beam of helium ions is used to generate images and sample milling with high spatial resolution, higher than that achieved by scanning electron microscopy and focused gallium ion beam, respectively [2]. Since it utilize He-ion as source and generates emission of secondary electrons along the analyses, this HIM always generates a positive charge accumulation on the surface of the sample during the imaging. Thus, this equipment is capable to add an electrons flow for each scanning line in order to neutralize the total charge in the sample, which allows the scanning of insulating materials without the necessity of doing any type of treatment. Due to this characteristic, this technique is very interesting for analysis of biological materials and visualization of samples supported by insulating materials, such as glass. As an example, it can generate monolayer graphene images with high contrast in a unique way (Fig. 1a). In this work, a pattern of line defects was introduced on a graphene monolayer, wherein such line defects present spatial frequency ranging from 1 to 30 cycles/ $\mu\text{m}$ . This standard was developed aiming its usage as a reference material for tip-enhanced Raman spectroscopy (TERS). TERS is a new optical technique capable to generating Raman spectroscopic images with spatial resolution beyond 20 nm, even using wavelength laser in the visible spectrum. This high resolution achieved is about 20x higher than the spatial resolution limit defined by diffraction effects [3]. The graphene sample was initially obtained through mechanical exfoliation over glass substrate and later analyzed by Raman spectroscopy and atomic force microscopy (AFM) in order to search for monolayers and investigate possible surface contamination. The pattern of defect lines was created by HIM over graphene monolayer and analyzed by Raman, AFM and TERS spectroscopy techniques. With this investigation, it was possible to determine the best He ion dose ( $1.06\text{E} + 16$  ions /  $\text{cm}^2$ ) for which it shows the lower line thickness ( $\sim 10$  nm of FWHM) and optimum surface defects density, i.e., high intensity of the Raman D band with no amorphization and low important defects in the regions between lines. The defects lines and spatial frequency obtained in the generated pattern are consistent with the higher TERS, and, therefore, suitable to its destination as TERS standard.



## REFERENCES

- [1] A.K. Geim, I.V. Grigorieva, *Nature* 499 (2013) 419.
- [2] D.C. Bell, M.C. Lemme, et al., *Nanotechnology* 20 (2009) 455301.
- [3] T.L. Vasconcelos, B.S. Archanjo, L.G. Cançado, et al., *ACS Nano* 9 (2015) 6297.
- [4] This research was supported by CNPq (Brazil) and Inmetro.

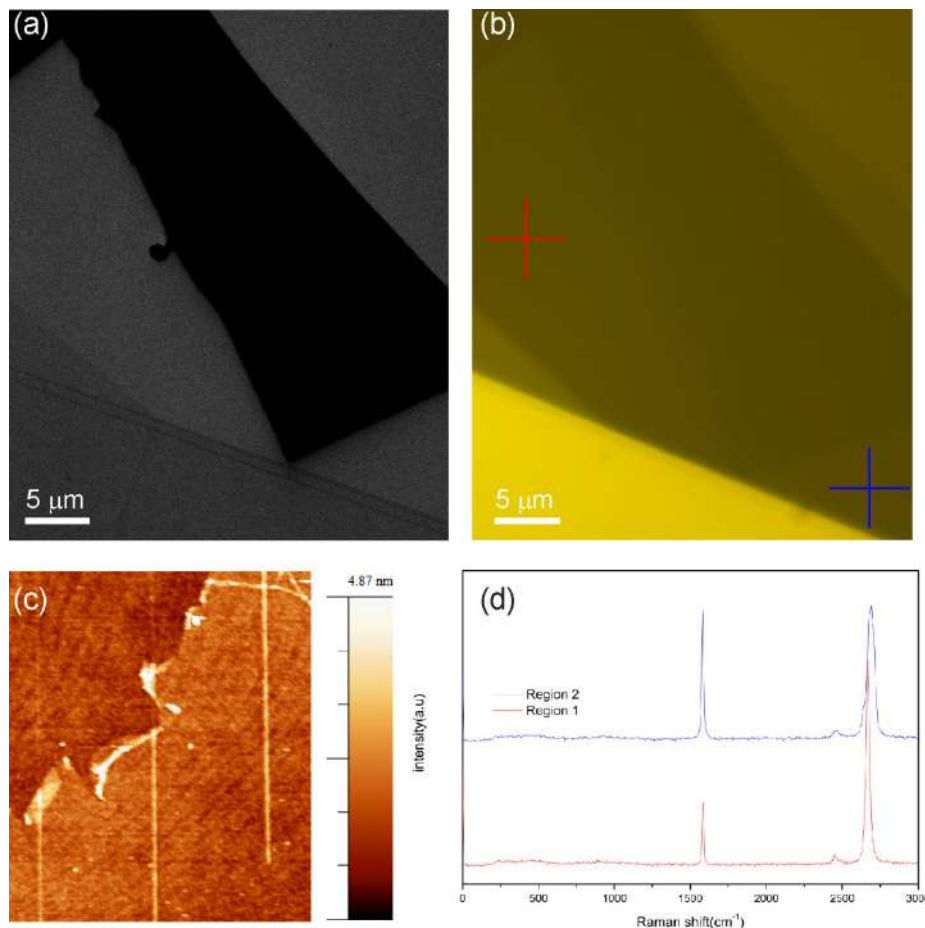


Figure 1: Graphene monolayer sample exfoliated over glass substrate imaged by HIM (a) and by conventional optical microscopy (b). The regions containing monolayer graphene (red cross) and bilayer graphene (blue cross) were identified by Raman spectroscopy (d). In (c), AFM topographic image of a monolayer graphene containing defect lines with different doses.



## **STEM-EDX analysis of ion irradiation-induced precipitation in solution annealed AISI 316L alloys**

Mariana M. Timm<sup>1,2,\*</sup>, Erwan Oliviero<sup>2,3</sup>, Paulo F. P. Fichtner<sup>1,4</sup>

<sup>1</sup> Instituto de Física, Universidade Federal do Rio Grande do Sul, Porto Alegre, RS, Brazil

<sup>2</sup> MEA, Université de Montpellier, Montpellier, France

<sup>3</sup> ICGM, CNRS-Université de Montpellier, France

<sup>4</sup> Escola de Engenharia, Universidade Federal do Rio Grande do Sul, Porto Alegre, RS, Brazil

\*e-mail: mariana.timm@ufrgs.br

Ion irradiation experiments give important insight on the mechanisms that govern the nucleation and growth of defects in materials exposed to a nuclear environment. A thorough understanding of the composition and microstructure of these defects is needed since the irradiation damage and fission products can affect in different ways phase stability of the matrix and its mechanical properties. In this contribution, we report on the influence of the ion mass on the formation of precipitate and the growth of bubble systems produced during Au and Ag ion irradiation to the same dpa level in a solution annealed stainless steel AISI 316L target. Mechanically polished AISI 316L samples were room temperature implanted with Ar ions and subsequently irradiated with 5 MeV Au ions and with 3.5 MeV Ag ions reaching fluences equivalent to 40 dpa in samples kept at 550 °C. The samples were analyzed via plan-view TEM and STEM-EDX using a JEOL JEM 2200FS operating at 200 kV. STEM-EDX analyses were obtained with a spot size of 0.7 nm and acquisition times from 200 to 740 s. The formation of a dense system of Ar bubbles and large precipitates is observed in both samples (Figure 1). The EDX analysis shows that the precipitates formed during the irradiations are rich in Cr (Figure 2). The results are discussed considering that the number of vacancies produced by single ions (i.e. the density of the collision cascade) influences the point defect fluxes governing the formation of the precipitates and the growth of the bubbles. The evolution of the precipitate system is also discussed considering the diffusion controlled supply of C atoms from the matrix and the efficiency of the Ar bubbles as vacancy traps.

### **Acknowledgements:**

The authors would like to acknowledge the use of the facilities from the Ion Implantation Laboratory, UFRGS. This study was financed by the Conselho Nacional de Desenvolvimento Científico e Tecnológico (CNPq), Brazil.

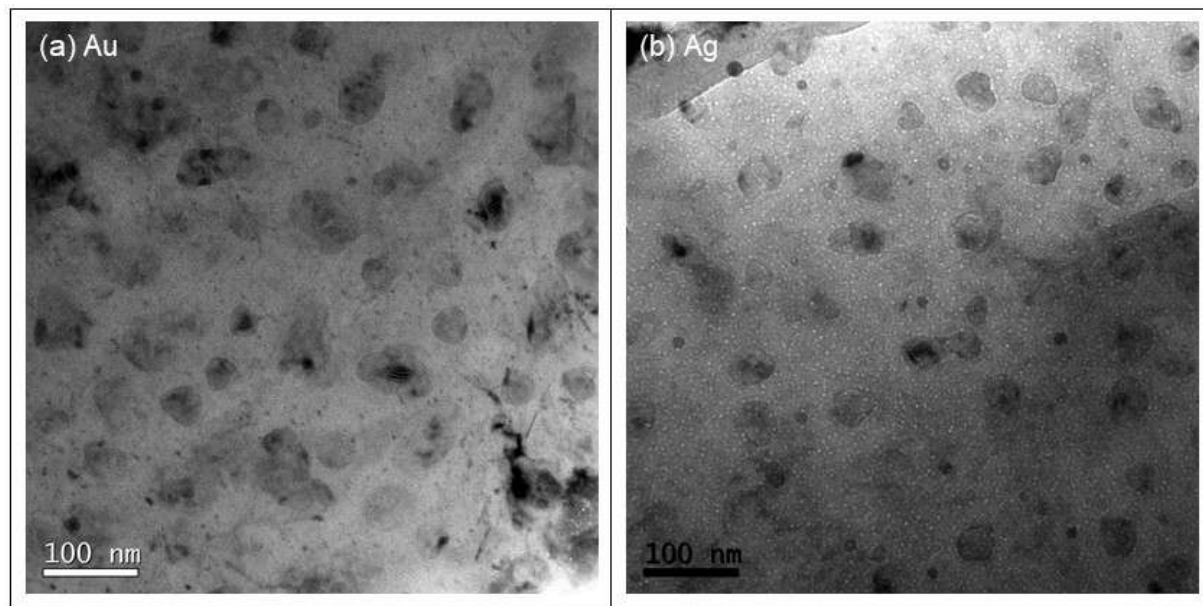


Figure 1: TEM micrographs of the Ar-implanted AISI 316L samples irradiated with (a) 5 MeV Au and (b) 3.5 MeV Ag ions to a fluence of 40 dpa

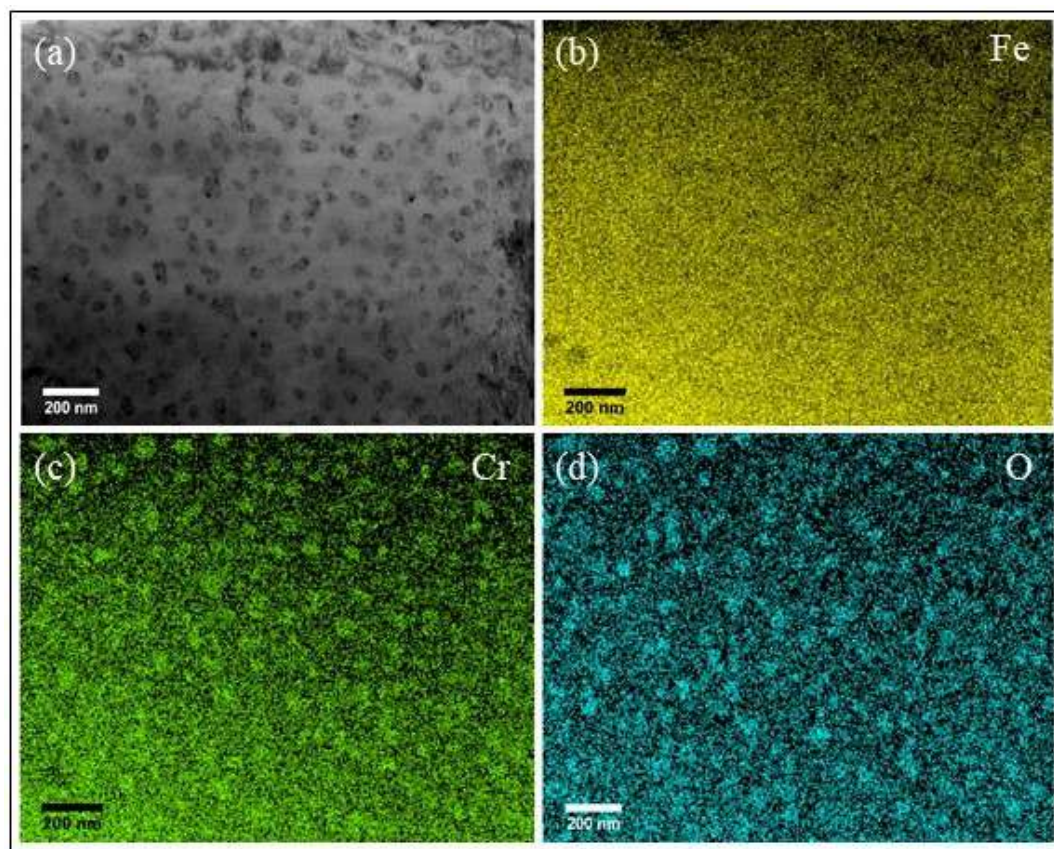


Figure 2: (a) Plan-view bright field STEM image showing the precipitates in Ar-implanted AISI 316L sample irradiated with 5 MeV Au ions. (b) EDX elemental map of Fe, (c) Cr and (d) O

## Stability of Ag and Au Nano-objects under Electron Irradiation

Bárbara Konrad<sup>1\*</sup>, Mariana M. Timm<sup>2</sup>, Zacarias E. Fabrim<sup>1</sup> and Paulo F. P. Fichtner<sup>1,2,3</sup>

<sup>1</sup>. Programa de Pós-Graduação em Ciência dos Materiais, Instituto de Física, Universidade Federal do Rio Grande do Sul, Porto Alegre, Brasil.

<sup>2</sup>. Programa de Pós-Graduação em Física, Instituto de Física, Universidade Federal do Rio Grande do Sul, Porto Alegre, Brasil.

<sup>3</sup>. Escola de Engenharia/Instituto de Física, Universidade Federal do Rio Grande do Sul, Porto Alegre, Brasil.

\* barbara.konrad@inf.ufrgs.br

The formation and/or modification nano-objects (NOs) have attracted academic and technological interest due to distinct application possibilities [1]. It is known that NOs show size-dependent properties, which are generally different from their bulk counterpart [2]. Electron irradiation provides a way to obtain, modify and manipulate these materials [3], but the understanding of the electron interactions with matter at the nanoscale still needs to be refined. This work presents a study on the formation and stability of Ag and Au NOs submitted to electron irradiation at energies of 120, 160 e 200 keV. The NOs were prepared either via magnetron sputtering onto 50 nm thick Si<sub>3</sub>N<sub>4</sub> self-standing membranes, or via direct ion implantation onto 100 nm thick films supported by a Si substrate, and characterized by Rutherford Backscatter Spectrometry (RBS) and Transmission Electronic Microscopy (TEM). The irradiations were realized in the same microscope used for characterization, which allowed real-time observation of the effects caused by irradiation. The obtained results show that the irradiation promotes: i) nucleation and growth of Au NPs in implanted samples; ii) spherization of Au NOs on deposited membranes; and iii) spherization and/or sputtering of Ag NOs (Fig. 1). A detailed observation of the beam energy effects on the Ag samples show: i) 120 keV – spherization of NOs produced by deposition; ii) 160 keV – spherization and partial loss of deposited metal; and iii) 200 keV – complete destruction of the NOs in the deposited sample and removal of the implanted Ag content in ion implanted samples. The observed phenomena are discussed in terms of electron induced surface diffusion and sputtering processes produced by elastic collisions [4]. Based on the beam energy dependence of the displacement cross sections (Fig. 2), a model is proposed to describe how the number of atoms  $N$  in a NO depends on the electron beam fluence  $\Phi$  (Eq. 1),

$$N(\Phi) = N_0 - k \int A(\Phi) d\Phi. \quad (1)$$

In this expression,  $N_0 = \rho_v V$  is the NO initial number of atoms,  $\rho_v^{Ag} = 58,47 \text{ at/nm}^3$ ,  $k \equiv \sigma \rho_s / e$  with  $\sigma$  the displacement cross-section,  $\rho_s^{Ag} = 11,42 \text{ at/nm}^2$  and  $e = 1,6\text{E-}19 \text{ C}$ ,  $A(\Phi)$  is the area projected by the NOs and  $\Phi$  is the irradiation fluence. We estimate a displacement energy  $E_d^{Ag} = 3,25 \pm 0,28 \text{ eV}$  for Ag. This energy value can be treated as a fundamental parameter for Ag NOs, since, from universal relations, other physical quantities can be determined as a function of  $E_d$  [5].

### ACKNOWLEDGEMENTS

For financial support from CAPES (Brazil) and support from Center for Microscopy and Microanalysis (UFRGS), Ion Implantation Laboratory (UFRGS) and Laboratory of Nanometric Conformation (UFRGS).



## REFERENCES

- [1] K. W. Han et al. Applied Physics Letters, 99 (2011) 247.
- [2] J. Park and J. Lee. Calphad. 32 (2008) 135.
- [3] M. M. Timm et al. Journal of Applied Physics, 122 (2017) 165301.
- [4] R. F. Egerton et al. Ultramicroscopy, 110 (2010) 991.
- [5] S. C. Vanithakumari and K. K. Nanda. Physics Letters A, 372 (2008) 6930.

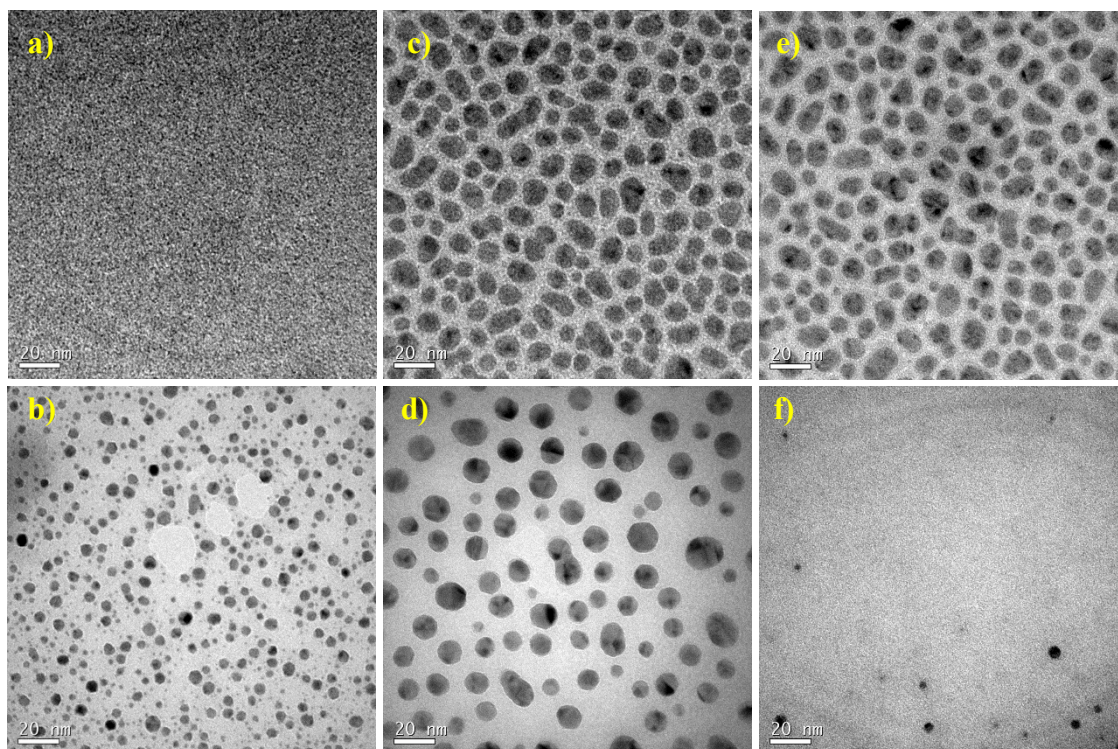


Fig. 1) Transmission electron micrographs of (a) Au ion implanted sample; (b) 200 keV electron irradiation of (a) region,  $\phi = 3,71E10^5$  C/cm<sup>2</sup>; (c) and (e) Ag deposited samples; (d) 120 keV irradiation of (c) region,  $\phi = 1,80E10^5$  C/cm<sup>2</sup>; and (f) 200 keV irradiation of (f) region,  $\phi = 1,76E10^5$  C/cm<sup>2</sup>.

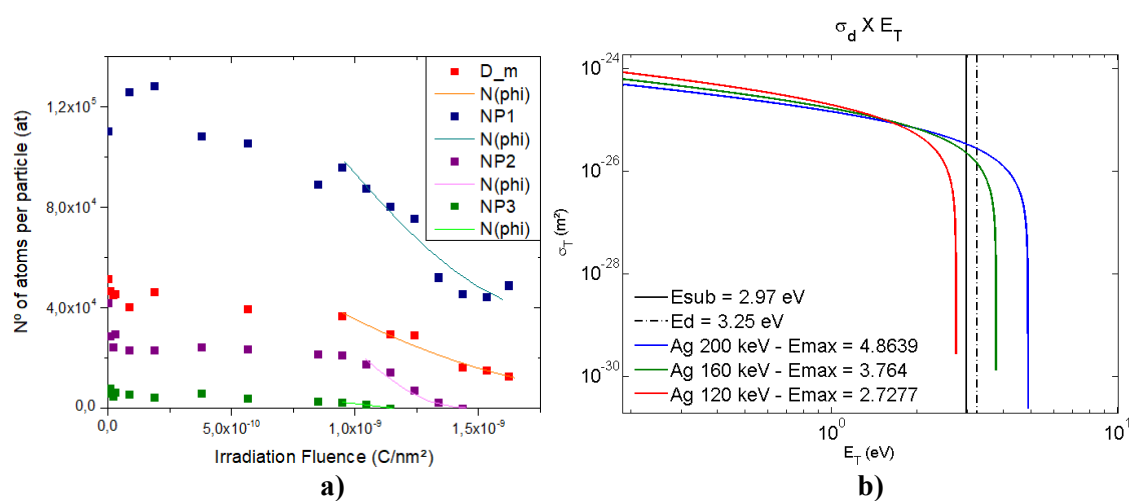


Fig. 2) (a) Ag atoms loss for three NOs and average system diameter ( $D_m$ ) at 160 keV irradiation energy beam and respective  $N(\phi)$  fittings; (b) Ag displacement cross-sections for the three work energies, maximum energy transferred for each energy, Ag sublimation energy and the displacement energy determined in this work.





## Synthesis of silicon nanostructures in a quasi-order pattern induced by ion-beam

Camilla F. Codeço<sup>1\*</sup>, Sérgio L. A. Mello<sup>2</sup>, Bárbara F. Magnani<sup>3</sup> and Marcelo M. Sant'Anna<sup>4</sup>

<sup>1</sup>. Instituto de Física, Universidade Federal do Rio de Janeiro, Rio de Janeiro, Brazil/  
Laboratório Nacional de Luz Síncrotron, CNPEM, Campinas, São Paulo.

<sup>2</sup>. Departamento de Física, Universidade Federal de Viçosa, Viçosa, Brazil.

<sup>3</sup>. Instituto de Física, Universidade de São Paulo, São Carlos, Brazil

<sup>4</sup>. Instituto de Física, Universidade Federal do Rio de Janeiro, Rio de Janeiro, Brazil.

[\\*camilla@if.ufrj.br](mailto:camilla@if.ufrj.br)

The synthesis of Si nanopatterns is an important topic in physics research given the many different possible applications of this material, like photovoltaic cells [1] and microelectronic devices [2], just to mention a few. The possibilities become more interesting if we consider the synthesis of structures self-organized in a quasi-ordered pattern [3]. There are many techniques for the synthesis of nanostructures. In this work we explore the ion beam sputtering technique obtained from the use of an electrostatic ion accelerator of Tandem type [4]. We present experimental results for the changes in metallic layers (Au/Ti) that cover a Si wafer after this system was irradiated by Cs<sup>+</sup> ion beam of 2 keV energy. By atomic force microscopy we observed that the irradiation process induces a reorganization in a surface atoms that can culminate with the nanostructure synthesis. We identify that the surface passes for different steps from the beginning of irradiation until the end. The novelty of this work is the possibility to follow steps of the surface evolution. These steps reveal at least three stages in which the surface goes through different configurations starting with a dewetting-like pattern (Fig1) followed by a combination of holes and mounds (inset of Fig3) and culminating in the end with the appearance of nanodots (Fig2). In all stages we showed that the structures formed follow a quasi-order pattern (Fig3) and in the last stage the formed nanodots can be described by the Bradley-Shipman model [5].

[1] A. Polman, *Plasmonics Applied*, Science. 322, 868 (2008).

[2] M. Reimann, M. Manninen, *Rev. Mod. Phys.*, 74, 1283 (2002).

[3] S. Yu, C. Wang, Y. Zhang, B. Dong, Z. Jiang, X. Chen, W. Chen, C. Sun, *Scientific Reports*, 7, 3752, (2016).

[4] S. L. A. Mello, C. F. S. Codeço, B. F. Magnani, M.M.Sant'Anna, *Rev. Sci. Instrum*, 87, 063305 (2016).

[5] R. M. Bradley, P. D. Shipman, *Physics Review Letters*, 105, 145501 (2010).

[6] This research was supported by CNPq (Brazil)

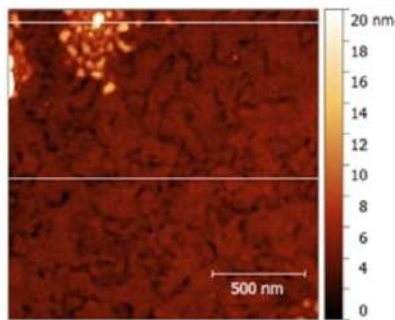


Fig1: AFM image of surface (Au/Ti/Si) after the irradiation by  $\text{Cs}^+$  of 2 keV shows the dewetting pattern with some gold remains.

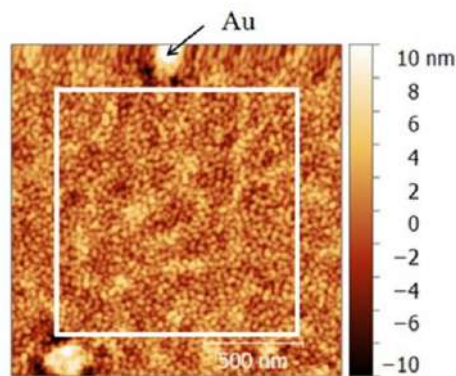


Fig2: AFM image of silicon surface after the irradiation by  $\text{Cs}^+$  of 2 keV shows the nanodots pattern.

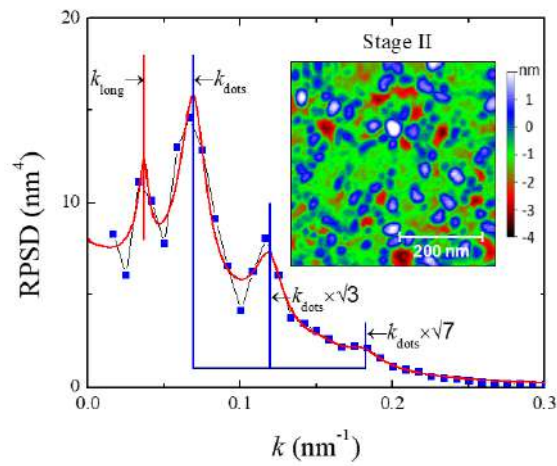


Fig3: RPSD analysis for stage II AFM image (inset) and its corresponding RPSD spectrum that shows a quasi-order pattern. AFM image shows a surface composed with mounds (white color) and holes (red color)

## **Electron and Ion Microscopes as tools for materials science, nanoscience and nanometrology.**

B. S. Archanjo\*, T. L. Vasconcelos and C. A. Achete

Divisão de Metrologia de Materiais, Instituto Nacional de Metrologia, Qualidade e Tecnologia (INMETRO), Duque de Caxias-RJ, 25250-020, Brasil;

Materials science and nanoscience research is frequently pushing the characterization need to smaller scales in order to further understand and manipulate nature behavior. Chemical and physical processes at the nanoscale often determine the properties of material and new functionalities. Therefore, these widely established fields of knowledge enable nanotechnology products to be present in our lives. Unfortunately, visible light cannot resolve objects in the nanoscale, therefore electron microscopes work as our eyes and in many cases, they also work as our hands, allowing us to see and manipulate the nature in very tiny scales. Due to the impact of nanotechnology in our day life, the development of nanometrology in the nanoscale is required to the progress of nanotechnology. In this context, electron microscopy and related techniques are essential to both, the characterization of nanoobjects and assistance in the development of new characterization techniques. Some of those new techniques might enable the analyses of nature with visible light at nanoscale with spatial resolution better than diffraction limit [1-3]. In this talk, we are going to present the fundamentals of materials metrology and nanometrology including a few applied examples. In addition, the use of transmission electron microscopy (TEM), electron energy loss spectroscopy (EELS) and helium ion microscopy (HIM) in the development of new techniques [1-3] and the modification and characterization of carbon-based materials [4,5] will be discussed.

### References

- [1] T. L. Vasconcelos, B. S. Archanjo et. al, Tuning localized surface plasmon resonance in scanning near-field optical microscopy probes, *ACS Nano* 9, 6297 (2015)
- [2] B. S. Archanjo et. al, Plasmon 3D Electron Tomography and Local Electric-Field Enhancement of Engineered Plasmonic Nanoantennas, *ACS Photonics* 5, 2834 (2018)
- [3] T. L. Vasconcelos, B. S. Archanjo et. al, Plasmon-Tunable Tip Pyramids: Monopole Nanoantennas for Near-Field Scanning Optical Microscopy, *Advanced Optical Materials* 1800528 (2018).
- [4] B. S. Archanjo et. Al, Graphene nanoribbon superlattices fabricated via He ion lithography, *Applied Physics Letters* 104, 193114 (2014)
- [5] Martin E Mendoza, B. S. Archanjo et al. Revealing lattice disorder, oxygen incorporation and pore formation in laser induced two-photon oxidized graphene *Carbon* 143, 720 (2019)

**Acknowledgments:** The Authors would like to acknowledge the funding agencies CNPQ, FAPERJ and FINEP and also the students, researchers and technicians involved in these works.

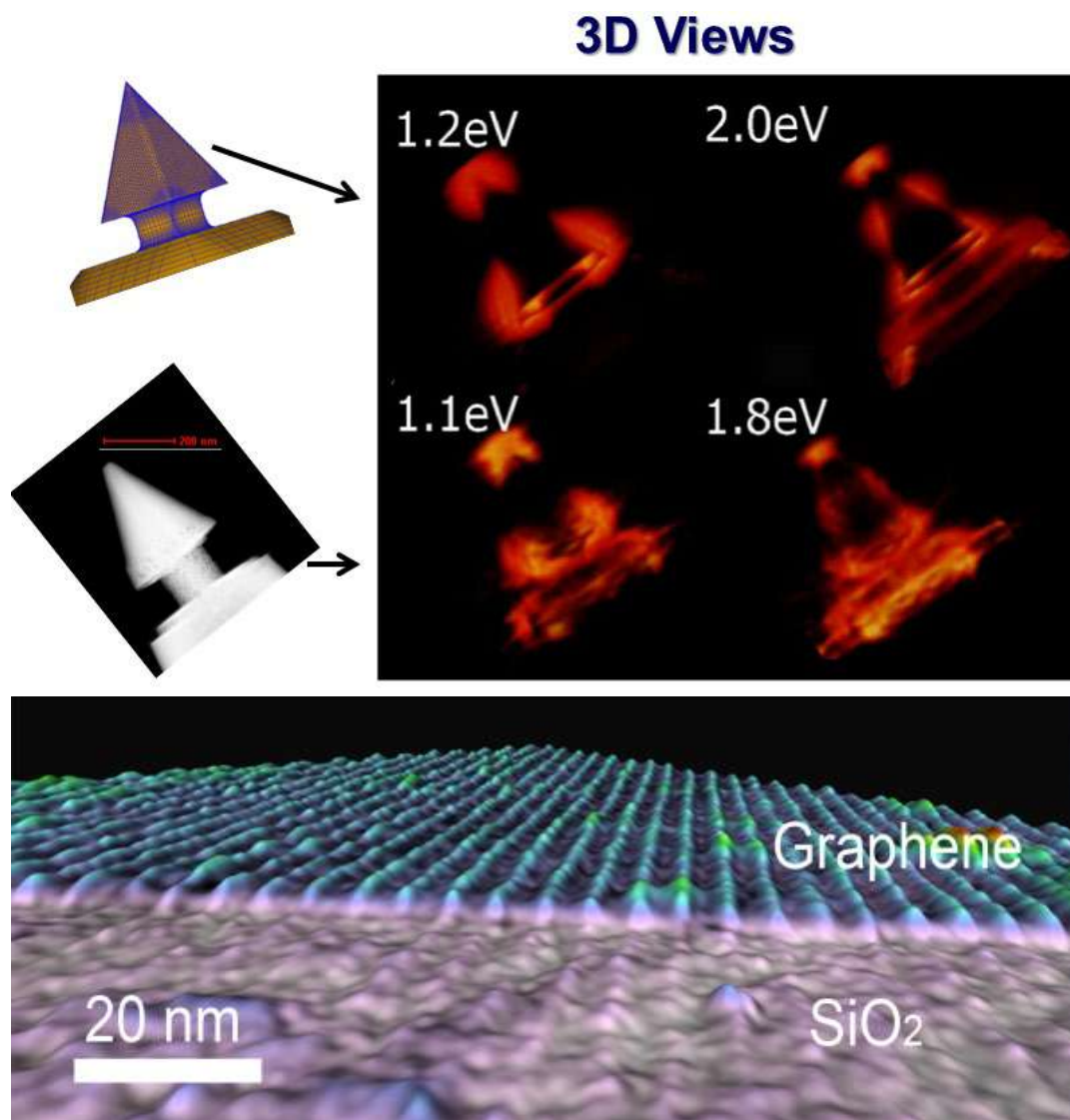


**Figure 1** - Surface mesh of the simulated nanoantenna (top left) fabricated via HIM and a STEM image of the HIM fabricated nanoantenna (bottom left). In the right it is shown the 3D reconstructed EELS images of the plasmon modes from simulated and fabricated nanoantennas. In the bottom part of the figure HIM nanopatterned lines in graphene at sub 10 nm resolution is shown.

## Spherical Aberration-Corrected Transmission Electron Microscopy for Materials Characterization at the Brazilian Nanotechnology National Laboratory

C. A. Ospina <sup>1\*</sup>

<sup>1</sup>. Brazilian Nanotechnology National Laboratory, Brazilian Center for Research in Energy and Materials, Campinas, Brazil.

\* carlos.ospina@lnnano.cnpem.br

Transmission Electron Microscopy (TEM) is a powerful conjunction of various imaging, diffraction and spectroscopic techniques in a single equipment. The point resolution typically achieved in TEM analyzes is of the order of sub-nanometers. Using correction systems for compensating intrinsic spherical aberration of lenses improves this resolution even further, in one order of magnitude [1, 2]. A better resolution allows the identification of physicochemical features of samples inaccessible for uncorrected microscopes, while enhancing the understanding of the cyclic relationship of processing-structure-functionalities. The Brazilian Nanotechnology National Laboratory of the Brazilian Center for Research in Energy and Materials, in Campinas, provides to the scientific community the use of the Titan Cubed Themis, with probe and image correctors, to apply characterization techniques with sub-ångström resolution. Equipped with a Schottky Field Emission Gun, monochromator and four detectors for Energy-Dispersive X-Ray Spectroscopy (EDX) analyses, this microscope is one of the most advanced open facilities for structural and compositional analyzes of materials at low (80 kV) and high tensions (300 kV). One representative example of applying sub-ångström resolution for chemical analysis is the characterization of GaAs structures. Unstrained GaAs structures were grown in a home-build Molecular Beam Epitaxy (MBE) system and sample lamellas were prepared by Focused Ion Beam (FIB) on the Helios NanoLab 660 DualBeam microscope [3]. After the published analyzes, the installation of the double aberration-corrected microscope allowed evidencing the separation of the Gallium and Arsenic atomic columns, as well as the elemental identification of each one of the columns along the [101] zone axis. Figure 1 shows an overlay of the Spectrum Image (SI) in High-Angle Annular Dark-Field (HAADF) and Gallium (in red color) and Arsenic (in green) maps after processing the SI. Another important application is the characterization of crystallographic defects, bringing light on its effects in the surroundings with greater precision. Analyzes performed at 300 kV in Scanning TEM (probe or STEM) mode on the epitaxial growth of ferroelectric BaTiO<sub>3</sub> thin films on a SrTiO<sub>3</sub> substrate showed the existence of misfit dislocations at the beginning of the piezoelectric film [4]. Figure 2a shows a HAADF – HR-STEM image of the FIB sample prepared parallel to the growth direction of the film [100]. By Geometrical Phase Analyses (GPA) was possible to measure the lattice distortions around the dislocation and the interface and obtain the strain fields as shown in Figures 2b and 2c.

[1] M. Haider et al., *Ultramicroscopy*, 75 (1998) 53.

[2] O.L. Krivanek, *Ultramicroscopy*, 78 (1999) 1.

[3] S.F.C. da Silva et al., *Nanoscale Research Letters*, 12 (2017) 61.

[4] F.R. Estrada et al., *Ferroelectrics*, Accepted.

[5] SisNANO financed the Titan Cubed Themis at LNNano.



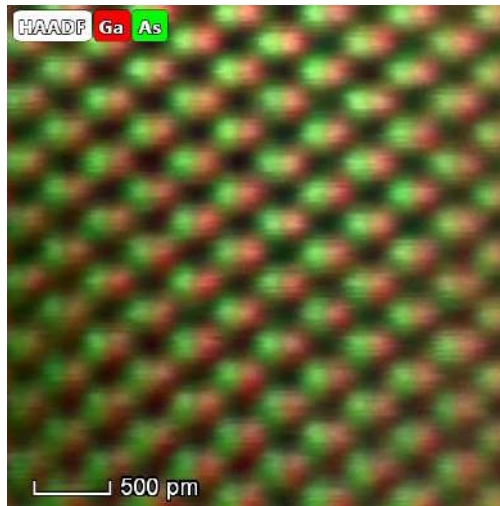


**Figure 1:** Overlapping of Energy-Dispersive X-Ray Spectrum Image of Gallium Arsenite semiconductor and Ga (red) and As (green) maps acquired in HAADF at 300 kV.

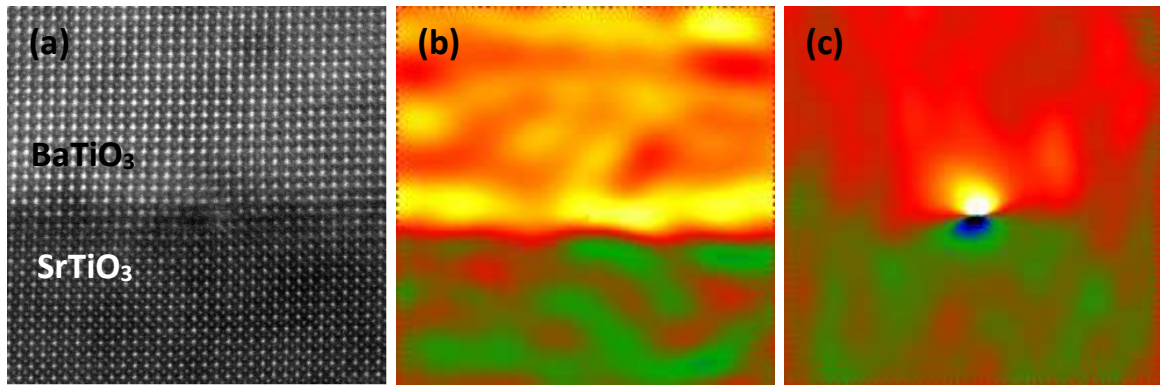


**Figure 2:** (a) HAADF-HRSTEM image of the BaTiO<sub>3</sub> / SrTiO<sub>3</sub> interface. (b-c)  $\epsilon_{xx}$  and  $\epsilon_{yy}$  strain maps of image (a). The color scale in (b-c) goes from -10% (blue) to +10% (white), through green (0%), red (+1.5%) and yellow (+4.5%). [From ref. [4], and reproduced with permission of F.R. Estrada.]

## Studying the Effects of Al-Doping Fe-(Hydr)Oxides on Contaminant Sorption

Erico T. F. Freitas<sup>1\*</sup>, Virginia S. T. Ciminelli<sup>2</sup>

<sup>1</sup> UFMG / Centro de Microscopia, Belo Horizonte, Brazil

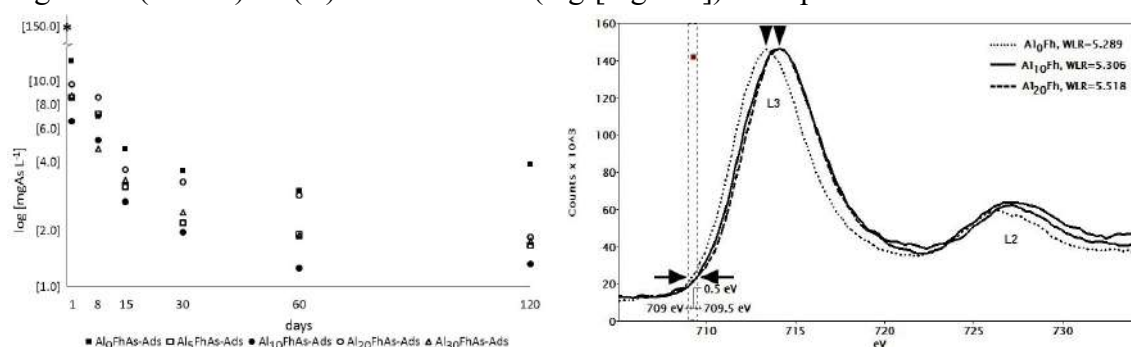
<sup>2</sup> UFMG / Depto. de Engenharia Metalúrgica e de Materiais, Belo Horizonte, Brazil

### Abstract

Nanostructured iron (hydr)oxides show high efficient capacity for contaminant uptake from wastewater [1, 2, 3, 4, 5, 6], and several attempts have been made to enhance the arsenic (As) adsorption capacity of Fe-oxides either synthesized from fresh or Fe-rich waste materials [4, 7, 8, 9, 10]. As aluminum is ubiquitous in natural environment and as well as in acid mine drainage water, the understanding of its role in As uptake by Al-containing Fe-(hydr)oxides is crucial to develop remediation technologies for As immobilization by such mixed phases. Therefore, the combination of Al and Fe in adsorption and co-precipitation experiments for water treatment has opened a discussion on the role of Al in arsenic uptake by such bi-metal (hydr)oxides. The effects of Al on As sorption behavior onto Al-Fe-(hydr)oxides is scarcely studied, specially the fate of As upon ageing its host phases. In this work we present TEM results of a study on the effects of Al-for-Fe substitution in ferrihydrite (Fh), which might highlight the behavior of As(V) adsorption onto Al-Fh. Series of Al-free and Al-containing Fh samples were produced from mixed iron and aluminum nitrate solutions, at circumneutral pH and room temperature, in the absence and presence of As(V), following a modified procedure of Schwertmann and Cornell [11]. The initial Al/(Al+Fe) molar ratios (R) varied from 0 to 30% mol mol<sup>-1</sup>. The suspensions of the samples were left ageing at 30 °C for up to 120 days, and sampling at different times for analysis. The ICP-OES data showed that As(V) content in solution decreased for all Fh suspensions upon ageing, from 150.28 to 12.61 mg L<sup>-1</sup> for Al-free Fh, after 1 day ageing, and down to 3.96 mg L<sup>-1</sup> at day 120. For Al-Fh samples, the As(V) concentration upon ageing was even lower, from 150.28 down to 1.30 mg L<sup>-1</sup> in the course of the experiments (Figure 1). The maximum Al-for-Fe substitution in Fh was shown to be around 21% mol mol<sup>-1</sup>, based on the energy dispersive X-ray spectroscopy (EDX) analysis, and the As/(Al+Fe) molar ratio between 0.062 – 0.075. Electron energy-loss spectroscopy (EELS) analysis at the Fe L<sub>2,3</sub> ionization edge of the series of Fh without As suggested the Al-doping Fh promotes an increasing in the average charge density surrounding Fe atoms due to a screening effect, which might be related to the relatively larger As-uptake by Al-Fh precipitates. The EELS measurements were performed in STEM mode using a LaB6-TEM Tecnai G2-20 SuperTwin at 200kV coupled with a GIF Quantum SE system at the Center of Microscopy/UFMG. The EELS data of Fh precipitates (Figure 1) show a chemical shift of Fe L<sub>2,3</sub>-edge towards higher energy-loses for Al-Fh compared to pure Fh. The energy shift of about 0.5 eV is shown at the spectra onset energies for Al<sub>0</sub>Fh (709.00 ± 0.25 eV) and for Al<sub>10,20</sub>Fh samples (709.50 ± 0.25 eV). The error on the onset energy was considered as the observed spectra shift of 0.25 eV by double checking the zero-loss peak (ZLP) right before and after the acquisition of the EEL core loss spectra in each measurement. This chemical shift suggests a relative higher charge density surrounding Fe atoms in Al-Fh. It is also evidenced by the increasing of the Fe L<sub>2,3</sub> white-line ratios (WLR) with the increasing of substituted Al in ferrihydrite. The WLR were measured by taken the integral intensity ratio of the L<sub>3</sub> (2p<sub>3/2</sub> → 3d) and L<sub>2</sub> (2p<sub>1/2</sub> → 3d) excitation peaks of the Fe L<sub>2,3</sub>-edge.

The script Measure EELS Peak Intensity was used to measure the Fe- $L_{2,3}$  peaks [12]. The chemical shift and the changing in the WLR have been ascribed to a changing in the oxidation state of transition metals [13, 14, 15], but it is unlike that Fe has an average higher oxidation state in the Al-Fh system as there would be need a high electronegative ion to stabilize Fe(IV). The observed changing in the electronic density of Fe might be caused by a screening effect, a displacement of some electrons from Fe towards Al atoms in the lattice due to the higher electrostatic potential of Al(III) compared to Fe(III), thus giving to Fe atoms a relative higher positive charge density. The increased charge surrounding Fe in the Al-Fh may have contributed to enhance As uptake respectively to Al-free Fh, as observed from the chemical analysis. Further investigations have been carried out in our group to understand the actual role of Al in these systems as well as the incorporation of As into the structure of the crystalline products upon aging Fh, which will highlight the As partitioning and its immobilization in environmental samples.

Figure 1: (At left) As(V) concentration (log [mg L<sup>-1</sup>]) in supernatants recovered from



suspensions of samples Al<sub>R</sub>Fh-As. R stands for the initial Al/(Al+Fe) molar ratio in the precipitates. The “star” point at day 0 is the As concentration added to each suspension. (At right) EEL spectra of samples Al<sub>0</sub>Fh, Al<sub>10</sub>Fh, and Al<sub>20</sub>Fh at day 120, showing the (white-lines) L<sub>3</sub> (2p<sub>3/2</sub> → 3d) and L<sub>2</sub> (2p<sub>1/2</sub> → 3d) excitation peaks of the Fe L<sub>2,3</sub>-edge. The white-line ratios (WLR) of Fe L<sub>2,3</sub> peaks are shown at the legend.

## References:

- [1] E. Smith et al., *Adv. Agron.* 64 (1998) 149-195.
  - [2] P.L. Smedley, D.G. Kinniburgh, *Appl. Geochemistry* 17:5 (2002) 517-568.
  - [3] M. Hua et al., *J. Hazard. Mater.* 211-212 (2012) 317-331.
  - [4] I. Carabante et al., *Ind. Eng. Chem. Res.* 53 (2014) 12689-12696.
  - [5] A.S. Adeleye et al., *Chem. Eng. J.* 286 (2016) 640-662.
  - [6] S. Lata, S.R. Samadder, *J. Environ. Manage.* 166 (2016) 387-406.
  - [7] W. Tang et al., *J. Hazard. Mater.* 192:1 (2011) 131-138.
  - [8] I. Akin et al., *J. Hazard. Mater.* 235-236 (2012) 62-68.
  - [9] C.Y. Cao et al., *Langmuir* 28:9 (2012) 4573-4579.
  - [10] L. Feng et al., *J. Hazard. Mater.* 217-218 (2012): 439-446.
  - [11] U. Schwertmann, R.M. Cornell, *Iron Oxides in the Laboratory*. 2nd Edition. Weinheim, Germany, 2000.
  - [12] D.R.G. Mitchell, B. Schaffer, *Ultramicroscopy* 103:4 (2005) 319-332.
  - [13] C. Colliex et al., *Phys. Rev. B*, 44:20 (1991) 11402-11411.
  - [14] R.F. Egerton, *Reports Prog. Phys.* 72:1 (2008) 016502.
  - [15] H. Tan et al., *Ultramicroscopy* 116 (2012) 24-33.
- This research was supported by INCT-Aqua – Recursos Minerais e Biodiversidade.

## Fe/O Ratio Determination by EDS and EELS: Effect of Experimental Parameters

Douglas Soares da Silva<sup>1\*</sup>, Hugo Campos Loureiro<sup>1</sup>, Leandra Pereira dos Santos<sup>1</sup> and Fernando Galembeck<sup>1</sup>.

<sup>1</sup>. Instituto de Química/Unicamp, Campinas/SP, Brasil.

Nanoanalysis in electron microscopes is an important tool in materials science since it may reveal correlations between morphology and chemical/physical properties together with data on local sample composition. Quantification of chemical composition and oxidation state in metal transition oxides, such as iron and titanium, may be performed using EELS[1,2] or EDS[3]. This study compares the calculated Fe/O atomic ratio obtained for a 99.999% pure iron-III oxide ( $\text{Fe}_2\text{O}_3$  - Aldrich), depending on two important microscope operation parameters: the acceleration voltage in SEM/EDS and objective aperture (OA), as well as on the Fourier-Log deconvolution (FLD) of the TEM/EELS signal. A Schottky emission FEI/Quanta 250 SEM equipped with an Oxford Instruments X-Max<sup>N</sup> 50 mm<sup>2</sup> detector was used to evaluate EDS data and a Zeiss/Libra 120 *in-column* “ $\Omega$ ” spectrometer TEM with a LaB<sub>6</sub> filament operated at 120 kV was used for EELS analyses. The iTEM/Olympus software was used for data acquisition, deconvolution and calculation of the relevant edge cross-sections. The SEM sample was examined without a conductive coating since no charging effects were observed. Removing OA during EELS experiments leads to a ca 50% deviation for the Fe/O ratio obtained, compared to the nominal value of 0.67. Otherwise, the use of any OA reduces these errors to below 15%. The Fourier-Log treatment of EELS spectra did not promote any significant change in the calculated values when using OA (fig. 2, a), because the inelastic  $t/\lambda$  parameter was  $(0.30 \pm 0.05)$ , which limits multiple scattering effects. A 60  $\mu\text{m}$  OA produces 0.66 for Fe/O ratio, in spite of the limited collection semiangle (10 mrad) allowed by this aperture. The EDS results strongly depends on the acceleration voltage (fig. 2, b) and the most accurate ratios were obtained using 5 kV and  $\text{O}_{\text{K}\alpha}$  and  $\text{Fe}_{\text{L}}$  lines, mainly because of the better adequacy of these lines to the incident beam energy. Summing up, this work verifies the risk of “automatic” analyses, showing how accurate values may be obtained using suitable procedures.

[1] C. Colliex, T. Manoubi and C. Ortiz, Physical Review B, 44 (20) (1991) 11402.

[2] R.F. Egerton, Electron Energy-Loss Spectroscopy in the Electron Microscope, Springer, New York, 2011.

[3] J.I. Goldstein et al., Scanning Electron Microscopy and X-ray Microanalysis, Springer, New York, 2003.

This work was supported through INCT/INOMAT (National Institute for Complex Functional Materials) financed by grant #2014/50906-9, São Paulo Research Foundation (FAPESP) and grant #465452/2014-0, National Council for Scientific and Technological Development (CNPq/MCTIC).

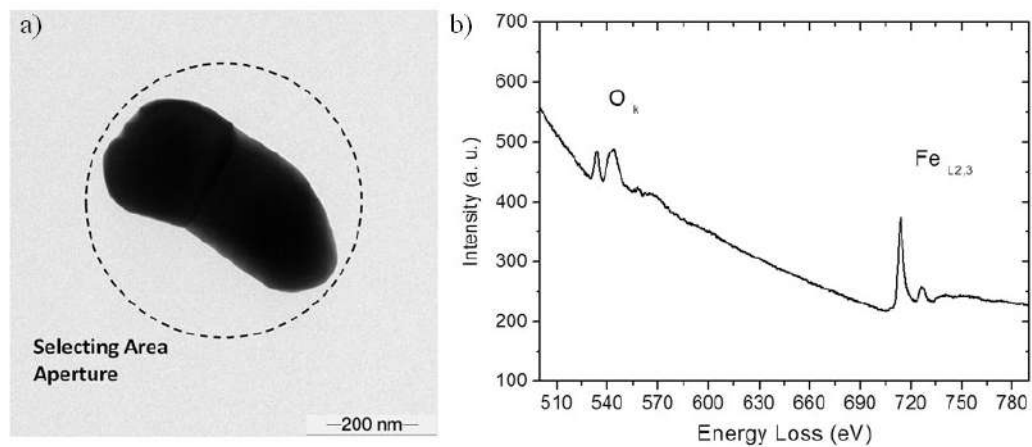


Figure 1 – a) Iron oxide particle with the selected area utilized for EELS and b) the energy loss spectrum.

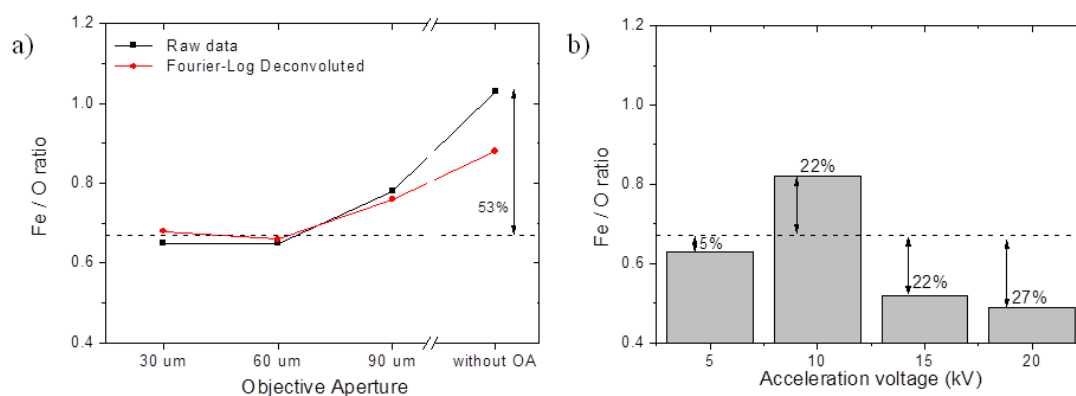


Figure 2 – a) Fe/O atomic ratio as a function of objective aperture diameter in TEM/EELS and the application of Fourier-Log deconvolution and b) the Fe/O atomic ratio by SEM/EDS.



## Analytical Electron Microscopy study of Hydrogen Reduction Synthesis of Nanoparticles of the Ternary CuNiCo Alloy System

Marin EP<sup>1</sup>, Brocchi EA<sup>1</sup>, Solorzano IG<sup>1</sup>

<sup>1</sup> Pontificia Universidade Catolica de Rio de Janeiro, Department of Chemical engineering and Material, RJ, Brazil

It is well recognized that the wide technological interest on metals and alloys is further increased if they are nanostructured. In the literature it is currently found several proposed chemical synthesis methodologies in order to obtain different kind of Nano particulate materials [1, 2]. Within this subject, the main objective of this work were obtaining a CuNiCo polycrystalline alloy by an alternative procedure, capable of generating nanostructured grains, followed by its preliminary characterization. The first part was carried out by dividing the process into two steps: the first one was the thermal decomposition of a nitrate solution [Cu(NO<sub>3</sub>)<sub>2</sub>, Ni(NO<sub>3</sub>)<sub>2</sub> and Co(NO<sub>3</sub>)<sub>3</sub>] aiming to obtain a homogeneous co-formed metal oxides mixture. In the second step, these oxides are heated up to a desired temperature and kept in a reductive flow of hydrogen, leaving the CuNiCo alloy as final product. The applied reduction temperatures were in the range between 300°C and 900°C.

The materials obtained after each step were characterized by Scanning Electron Microscopy (SEM), transmission electron microscopy (TEM), and Energy Dispersive X-Ray Detector (EDS). As result of the first step, it was found that Cu, Ni, Co and O were homogeneously distributed (Fig. 1). After the reduction process, it was obtained material which presented different shape and particle size, this due on the applied temperatures; it was evident the thermal activation effect on particle coarsening upon reduction. Also, it was changed the alloys composition (Cu-64wt%Ni-24wt%Co, Cu-64wt%Ni-12wt%Co and Cu-80wt%Ni-10wt%Co) at the same temperature (600°C) showing that the Cu-rich mixture, with a lower melting point, had undergone a pronounced particle coarsening than the other mixtures (Fig. 2). The alloys analysis revealed robust particles and the corresponding diffraction patterns allowed to observe the development of defect structure and nano scale precipitation contrast (Fig. 3). After the polished, the Ni-rich three metallic pellet exhibited individual grains, which were removed leaving some holes on the surface. EDS elemental mapping of a Ni-rich tri-metallic pellet, in which Co oxide grains was developed on the pellet surface, a line scan of the sample confirmed that the particles are constituted by Co oxide (Fig. 4).

*Keywords:* nanoparticles, CuNiCo alloys, chemical synthesis.

### Acknowledgments

The authors are grateful to LabNano (CBPF) for same characterizations and also to CAPES, CNPq and FAPERJ for financial support and scholarships.

### References

- [1] S. Pané, E. Gómez, E. Vallés. Journal of Electroanalytical Chemistry 596 (2) (2006) 87–94.
- [2] E. A. Brocchi, F. J. Moura, D. W. de Macedo. Mineral Processing and Extractive Metallurgy 118 (1) (2009) 249 35–39.

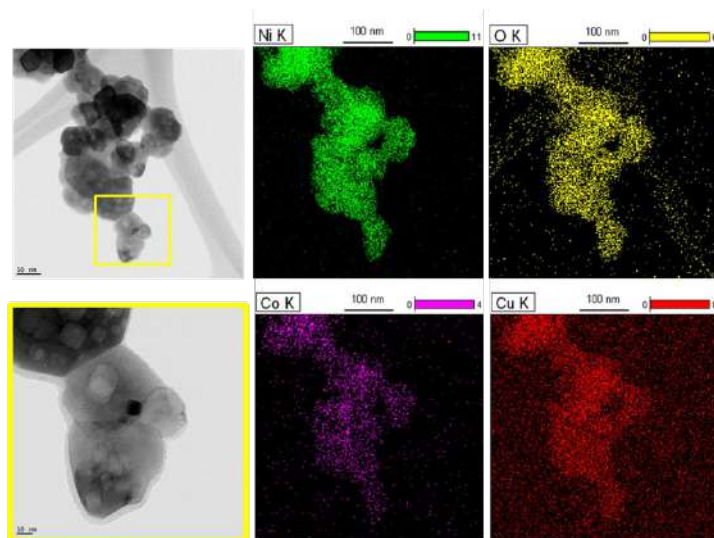


Figure 1. Secondary electron SEM images and EDS analysis of co-formed metal oxides at 500 °C.

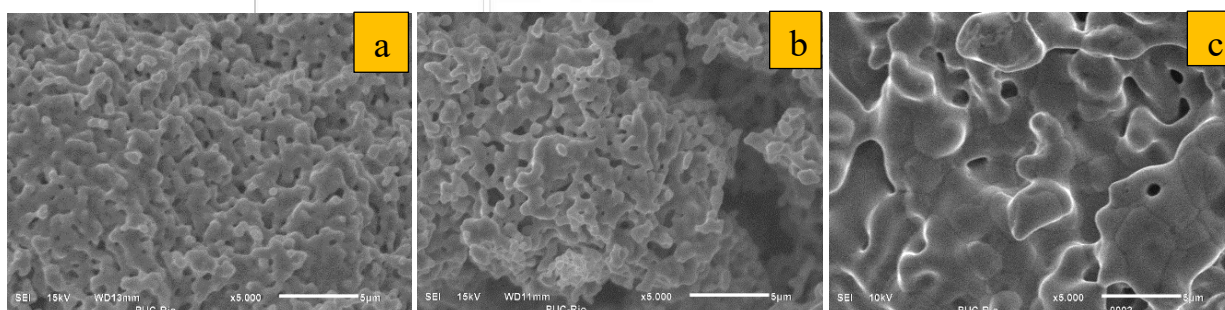


Figure 2. Secondary electron SEM images of trimetallic powder varying the composition a) Cu-64wt%Ni-24wt%Co and b) Cu-80wt%Ni-10wt%Co and c) Cu-64wt%Ni-12wt%Co at 600°C.

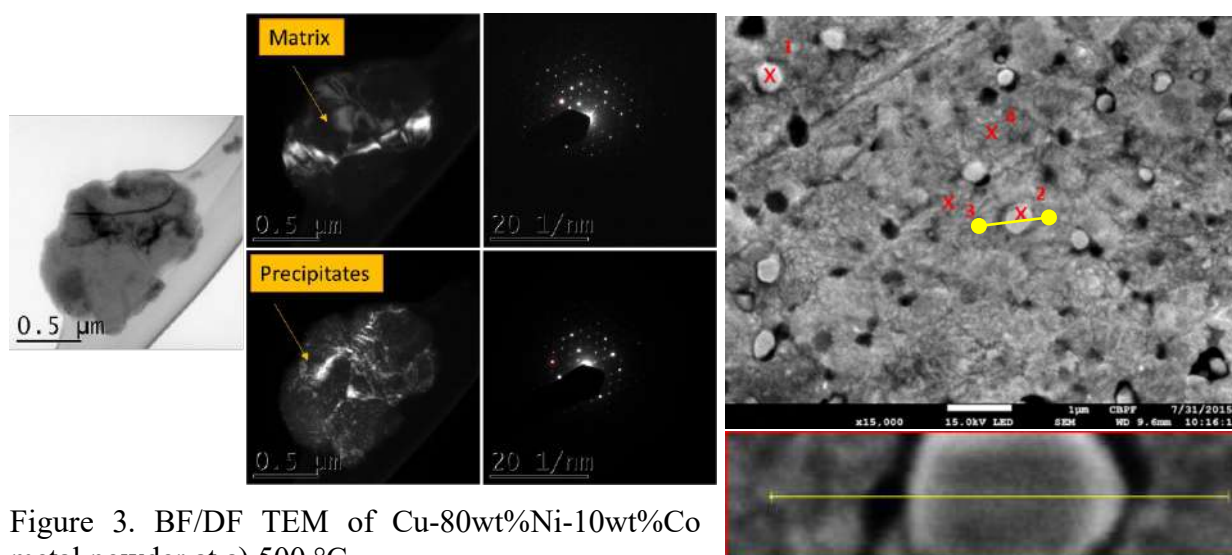
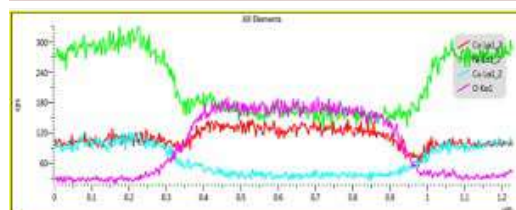


Figure 3. BF/DF TEM of Cu-80wt%Ni-10wt%Co metal powder at a) 500 °C.

Figure 4. Secondary electron SEM-FEG images and a line scan through the highlighted particle of Cu-80wt%Ni-10wt%Co trimetallic alloy pellet showing elemental distribution across the particle and matrix.





## Plasmon-Tunable Tip Pyramid Probes for TERS

Thiago L. Vasconcelos<sup>1\*</sup>, Bráulio S. Archanjo<sup>1</sup>, Bruno S. Oliveira<sup>1</sup>, Rogerio Valaski<sup>1</sup>,  
Cassiano Rabelo<sup>2</sup>, Carlos A. Achete<sup>1</sup>, Ado Jorio<sup>2</sup> and Luiz Gustavo Cançado<sup>2</sup>

<sup>1</sup> National Institute of Metrology, Quality and Technology (INMETRO), Materials Metrology Division (Dimat), RJ-Brazil.

<sup>2</sup> Federal University of Minas Gerais (UFMG), Physics Department, MG-Brazil.

E-mail: tlvasconcelos@inmetro.gov.br

Reproducibility on fabrication of tip-enhanced Raman spectroscopy (TERS) probes which generates high signal enhancement and spatial resolution beyond 20 nm is the main issue not only to provide reliability on TERS analyses but also to provide tools for the development of TERS metrology. The usage of template-stripe technique on fabrication of gold pyramids TERS probes is the most promising way to solve the fabrication reproducibility issue [1]. However, the pyramidal-like probe produced by this process does not show plasmon confinement at Nano scale and consequently does not support localized surface plasmon resonance (LSPR) on the visible spectrum range. Excitation of LSPR is crucial to generate high field enhancement on the tip apex vicinity, as we showed in our previous work [2]. In this work, we introduce a modified template-stripe technique to fabricate high optical efficiency TERS probes with full reproducibility on its morphology and signal enhancement [3]. The plasmon tunable-tip pyramids (PTTP) probes are composed of a micropyramidal body with a nanopyramidal end whose lateral dimension can be scaled to fine-tune LSPR monopole modes. The monopole character of the nanoantennas is revealed by electron energy loss spectroscopy (EELS) into a transmission electron microscope, and their efficiency as well as its reproducibility are tested in TERS experiments performed on single-layer graphene and single-walled carbon nanotubes. We acquired enhancements of the G' Raman band on the range of 23 fold, which is around 6 times greater than the enhancement produced by a conventional gold pyramid and it is the higher signal enhancement over graphene sample we found on the literature.

### REFERENCES

- [1] T. W. Johnson et al., ACS Nano 6 (2012) 9168.
- [2] T.L. Vasconcelos et al., ACS Nano 9 (2015) 6297.
- [3] T.L. Vasconcelos et al., Adv. Optical Mater. 6 (2018) 1800528.
- [4] This research was supported by Inmetro, Faperj, and CNPq (Brazil).

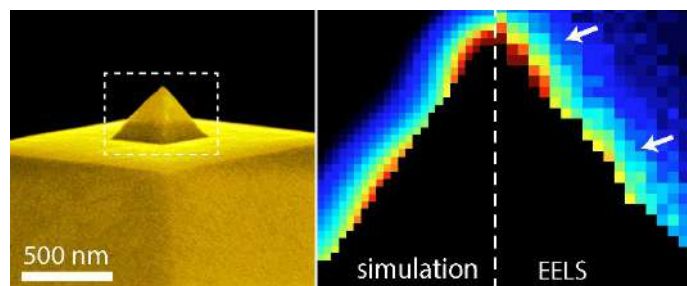


Figure 1: At left, an artificial colored scanning electron microscopy image of a gold PTPP probe. The white dashed quadrant highlights the nanopyramid structure, with 490 nm of lateral length, where its plasmon features were analyzed by EELS. The simulation and experimental EELS map at 1.7 eV (right quadrant) show only two hotspots, marked by white arrows, localized at the tip apex and at halfway from the apex to the base, which indicates a monopole second mode LSPR. The same procedure were also made on a 350 nm gold nanopyramid for both modes in order to create a scaling relation between the size of the nanopyramid and the monopole second mode LSPR wavelength.

## Nanoscale Characterization of Minerals and Organic Matter in Hydrocarbon Source Rocks

D. L. P. de Lacerda<sup>1,2</sup>, R. Prioli<sup>1</sup>, Y. M. Parizek-Silva<sup>2</sup>, G. F. Vasquez<sup>2</sup>

<sup>1</sup> Departamento de Física, Pontifícia Universidade Católica do Rio de Janeiro, Marquês de São Vicente 225, Rio de Janeiro, 22453-900, Brazil

<sup>2</sup> Centro de Pesquisas Leopoldo Aurélio Miguez de Mello (CENPES), Petrobras, Av. Horácio de Macedo 950, Cidade Universitária, Rio de Janeiro, 21941-915, Brazil

Hydrocarbon Source Rocks usually are fine-grained, sedimentary rocks composed by a variety minerals and organic components[1]. Because of its texture, the characterization of this type of rock is not trivial and requires the use of advanced tools. Friction characteristics of Ca- and Mg-rich carbonate films on dolomite and Cd-rich carbonate films on calcite surfaces have been used for mapping surface composition [2,3]. Friction forces for characterization of minerals, organic matter and pores on shales have been previously addressed by Javadpour [4]. In this work, immature kerogen shale sample from the Assistência Member, Irati Formation in the Paraná Basin, Brazil, were studied with a combination of high-resolution atomic force microscopy (AFM) and scanning electron microscopy (SEM). The shale fragment were embedded in an epoxy-resin, manually grinded and polished. Bright-field optical micrographs (BF) were used for identification of same areas of interest in both AFM and SEM microscopes. The samples were brought to AFM for characterization in contact mode with topography, error, lateral force forward and lateral force backward images were simultaneously acquired. Backscattering electron detector (BSE) images were used to characterize the microstructure. Energy dispersive x-ray spectroscopy (EDS) were used to evaluate mineralogical composition of the sample at the same region previously observed by the optical and AFM microscopes. Small geometric distortions introduced by the scanning were processed on the open source image analysis software Fiji [5], which were also used for colocalize AFM and SEM images. The SEM-AFM colocalization are shown on figure 1 together with friction distribution on selected minerals and the dependence between friction and normal force. Friction between the microscope tip was observed to be higher for organic matter, followed by mica, quartz and pyrite. The friction forces, thus, increases with the decrease of the elastic modulus. The results show that when combined with scanning electron microscopy, friction data contributes to the geochemical, morphological, and mechanical characterization of individual minerals and organic matter with a wide range of elastic modulus, varying in two orders of magnitude.

### REFERENCES

- [1] A. C. Aplin, J. H. S. Macquaker, AAPG Bulletin 95 (12) (2011) 2031–2059
- [2] X. Hu, P. Cubillas, S. R. Higgins, Langmuir 26 (7) (2010) 4769–4775
- [3] P. Cubillas, S. R. Higgins, Geochemical Transactions 10 (1) (2009) 7
- [4] F. Javadpour, M. Moravvej Farshi, M. Amrein, Journal of Canadian Petroleum Technology 51 (04) (2012) 236–243.
- [5] J. Schindelin, et al., Nature Methods 9 (7) (2012) 676–682.



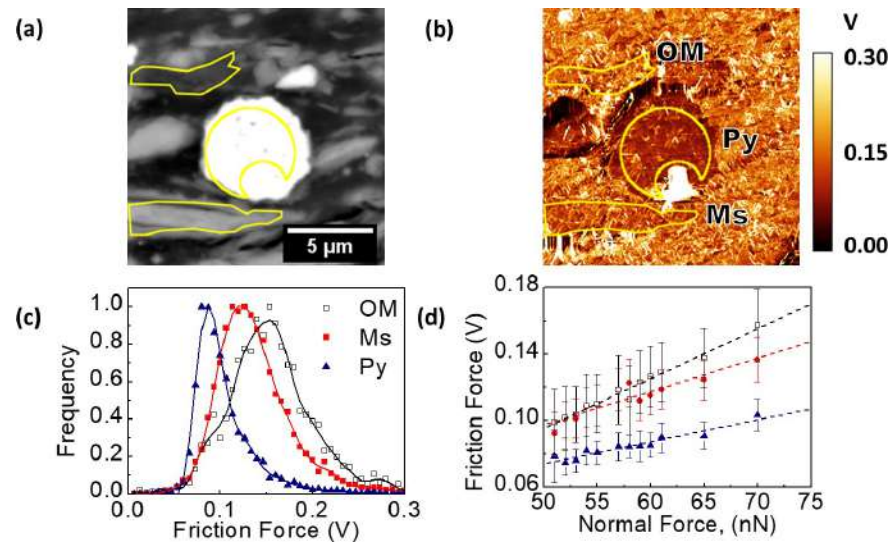


**Figure 1:** Selection of specific regions for organic matter (OM), pyrite (Py) and muscovite (Ms) in the SEM image (a). The overlap of the AOIs contours on the FF image in (b). In (c), the friction force distribution at a constant normal load of 70nN and in (d), friction forces as a function of normal load for OM, Py and Ms are shown in open squares, blue triangles and red squares, respectively.

## Characterization of Polymorph by AFM: Surface Properties and its Impact on Dissolution

B. F. C. Patricio<sup>1,2</sup>, L. D. Prado<sup>1</sup>, K. M. Gonçalves<sup>1</sup>, J. A. L. C. Resende<sup>3</sup>, G. M. Rocha<sup>2</sup>, G. Weissmüller<sup>2</sup>, P. M. Bisch<sup>2</sup>, H. V. A. Rocha<sup>1</sup>

<sup>1</sup>Laboratório de Micro e Nanotecnologia, Farmanguinhos / Fiocruz, Rio de Janeiro, Brazil.

<sup>2</sup> Laboratório de Física Biológica, Instituto de Biofísica Carlos Chagas Filho, Universidade Federal do Rio de Janeiro, Rio de Janeiro, Brazil.

<sup>3</sup>Instituto de Ciências Exatas e da Terra, Universidade Federal do Mato Grosso, Mato Grosso, Brazil

Currently, it is possible to increase the understanding of the physicochemical properties of drug systems and determine its single particle adhesive interactions with the atomic force microscopy (AFM) [1]. The producing of high-resolution images of surface morphology and the measurements of forces with spatial resolution enables the study of drug polymorphs, particle size, shape and crystallinity [1, 2]. These parameters have a direct impact on the bulk properties of materials that influence on powder properties, flowability and compression process [2]. In addition, poorly water-soluble drugs have low bioavailability and poor oral absorption, so they are a challenge for the pharmaceutical industry [3]. The use of polymorphs is a way to achieve appropriate bioavailability and has been extensively studied and depending on the groups exposed on the surface their dissolution can be changed [3]. Carvedilol, a  $\beta$ -blocker drug is used to treat hypertension, shows poor water solubility and is known to exhibit polymorphism. This drug presents three polymorphs (I, II and III) with solved structures [4]. The goal of this work is to evaluate and characterize the polymorphous II and III of the drug carvedilol (CAR) and its dissolution. PFQNM<sup>®</sup> mode AFM images of planes (0 1 1) and (1 0 -1) polymorph III and plane (0 0 1) polymorph II morphology, adhesion, and DMT modulus were acquired. The polymorph II plane (0 0 1) of CAR presented flat terraces separated by steps of 1,5 nm. It is comparable to the interplanar spacing and along the a-axis by the single crystal XRD analysis. For the AFM nanoindentation measurements, it was done 100 force curve on the surface of the crystal planes and the value of the elasticity and adhesion was obtained (Figure 1). Furthermore, it was evaluated the dissolution the polymorph II plane (0 0 1) in the pH of 6.8 and 4.5. The results to the (0 0 1) plane indicate that the dissolution occurred on the surface by the recession of the molecular steps (1.5 nm) in both media (Figure 2). The AFM allowed characterizing the physical-chemical properties of the surface of the planes of the polymorph of Carvedilol. It also allowed the study of the dissolution mechanism of it.

[1] P. Russell et al., *Microscopy and analysis* 49, (2000) 5.

[2] V. Wakins, et al., *Pharmaceutical Research* 31. (2014) 160.

[3] H. G. Brittain, *Polymorphism in pharmaceutical solids*. New York: Marcel Dekker, 1999.

[4] L. D. Prado et al., *Cryst Eng Comm* 16, (2014), 3168.

[5] This research was supported by CNPq (Brazil), Capes (Brazil), FAPERJ (Brazil).

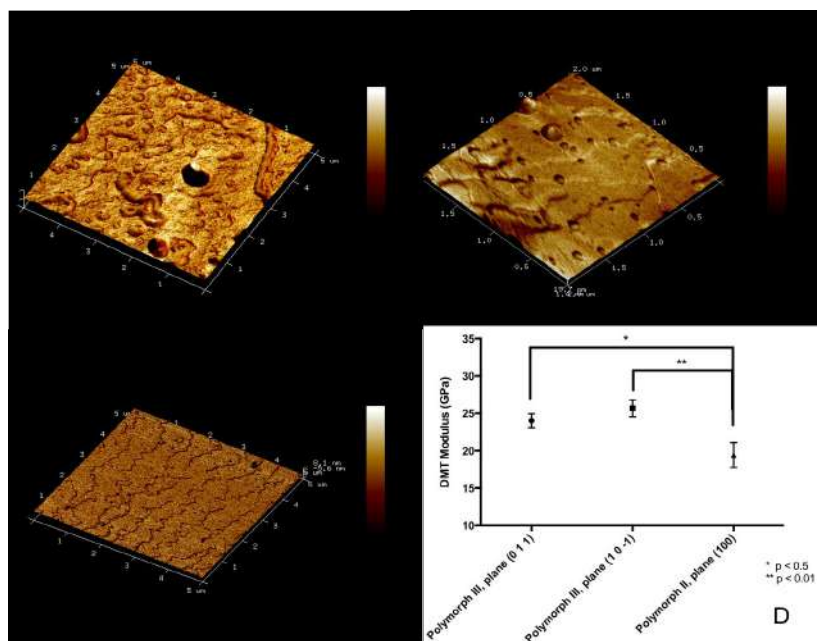


Figure 1: 5  $\mu\text{m}$  x 5  $\mu\text{m}$  tridimensional DMT modulus images obtained by AFM from carvedilol polymorph III plane (0 1 1) (A), polymorph III plane (1 0 -1) (B) and polymorph II plane (1 0 0) (C). Dimension Icon (Bruker, EUA), in PFQNM mode with cantilever OTESPA. Resolution of 512 x 512. DMT modulus of the planes of the polymorphs of carvedilol measured by the force curves (n=9 crystals /plane). Test One-Way ANOVA, Dunnett's post-test (\*\*p<0,01, \*\*\*p<0,001).

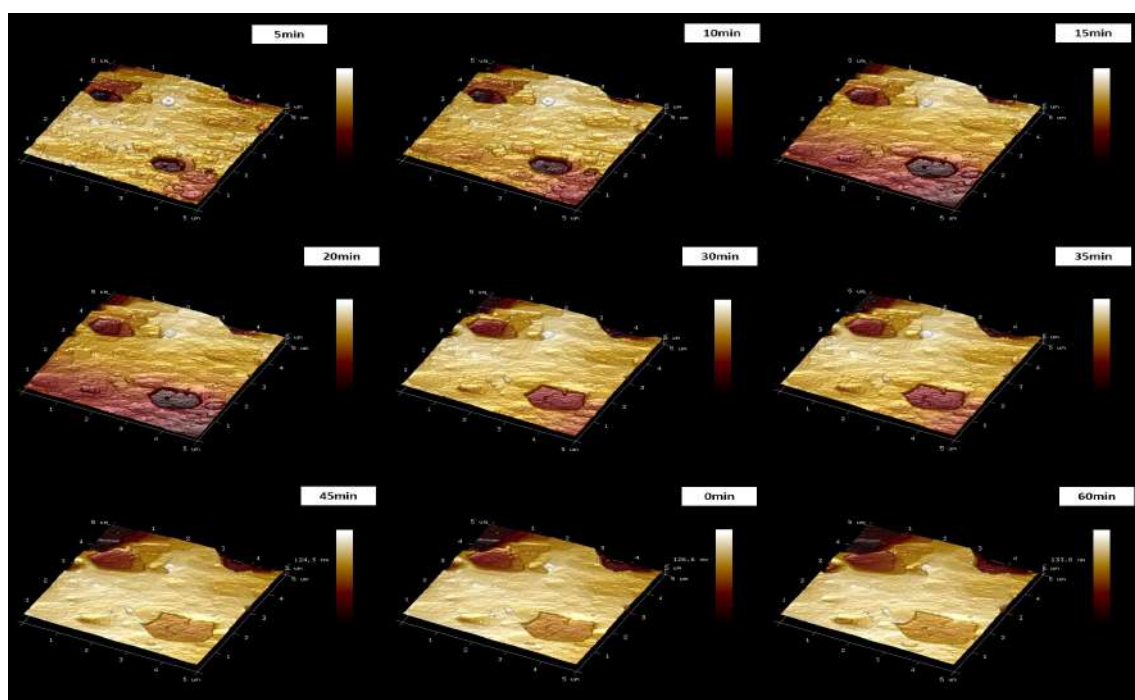


Figure 2: 5  $\mu\text{m}$  x 5  $\mu\text{m}$  images obtained by AFM from carvedilol polymorph II, plane (1 0 0) surface in phosphate buffer pH6,8. Dimension Fast Scan (Bruker, EUA), in Tapping fluid mode with cantilever Fast Scan-B. Resolution of 256 x 256 pixels and a scan rate of 10 Hz.

# Advanced Segmentation of Metal Matrix Composite microCT Images by Deep Learning Neural Networks

Sergei Evsevlev<sup>1</sup>, Giovanni Bruno<sup>1</sup>, Sidnei Paciornik<sup>2\*</sup>

<sup>1</sup> Division 8.5 - Micro-NDT – BAM, Berlin, Germany

<sup>2</sup> Department of Chemical and Materials Engineering – PUC-Rio, Rio de Janeiro, Brazil  
[\\*sidnei@puc-rio.br](mailto:sidnei@puc-rio.br)

One of the most difficult steps in image analysis for Materials Science is segmentation. Traditionally, objects would be discriminated by their intensity, contour or texture. However, there are many situations in which none of these approaches work (Figure 1) and, importantly, it is difficult to extrapolate from one problem to another. Moreover, there is no analytical or general way to decide the best segmentation method. It is always a trial and error situation. Deep Learning (DL) Convolutional Neural Networks (CNN) bring a new perspective to this problem. Using as input data the individual pixel/voxel intensities, the CNN automatically extracts discriminating features and can converge to a set of classes/objects given a reasonable training set. The training, which also serves as ground truth, is typically defined as regions of each object/class manually outlined by the user. This is the most work intensive step. However, once the network produces a reliable segmentation, in principle it can be directly applied to similar images with no further effort. This approach was used to segment a 5-phase Metal Matrix Composite (MMC) imaged by synchrotron microCT. Even though the phases can be discriminated in SEM images, a 2D approach is not enough to describe the microstructure. On the other hand, the limited contrast in the microCT images precludes a simple intensity-based segmentation (Figure 1, center, right). Initial results (Figure 2 and Table 1) using the so-called U-Net network architecture were very promising [1, 2]. Fibers and other phases were automatically segmented with good agreement with the ground truth, defined by manual thresholding. Different training strategies involving data augmentation were tested. These results raise several questions about the best strategy for using DL CNN's in image segmentation. Is there an ideal CNN architecture? How large must the training set be? Which parameters should be included in the data augmentation procedure? How should we proceed from 2D to 3D training set creation? What is required in terms of network architecture and GPU capabilities to obtain true 3D segmentation?

## References

- [1] Ronneberger, O. et al. MICCAI 2015 v9351, p. 234–241 (2015).
- [2] Nature Methods v16, p. 67–70 (2019).
- [3] The support of CNPq, CAPES and FAPERJ are gratefully acknowledged.



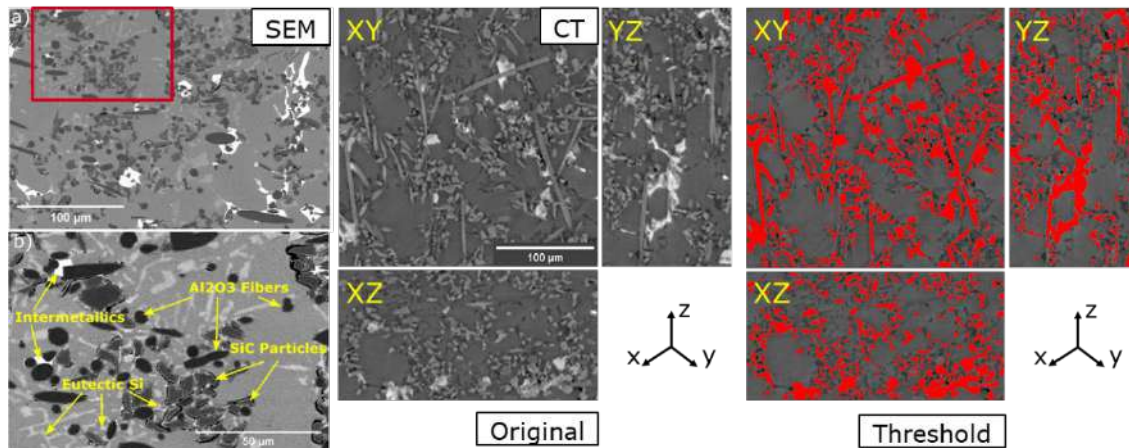


Figure 1 – 5-phase MMC. Left: 2D SEM images (all phases can be discriminated). Center: 2D sections of microCT 3D images. Right: Threshold segmentation (most phases cannot be discriminated).

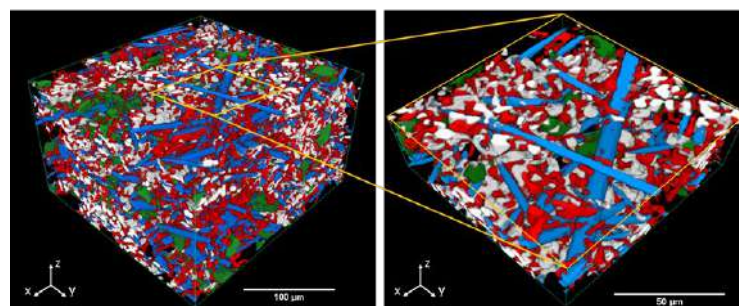
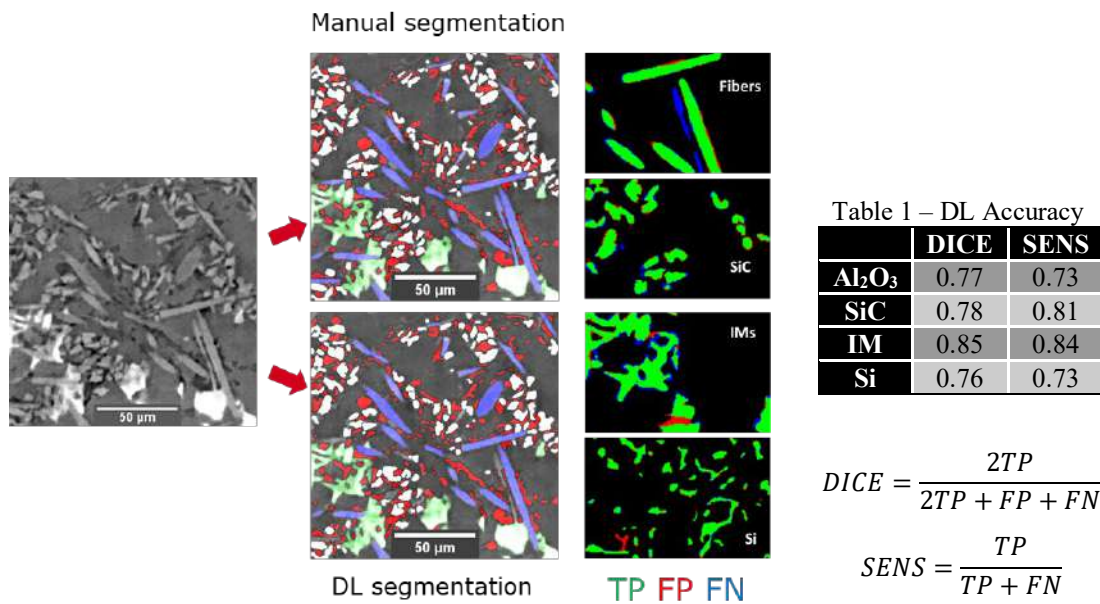


Figure 2 – Deep Learning segmentation results. All phases can be discriminated. TP = True Positive. FP = False Positive. FN = False Negative.



## Deep Learning Segmentation of Strain-Hardening Cement-Based Composites (SHCC) microCT Images

Renata Lorenzoni<sup>1\*</sup>, Iurie Curosu<sup>2</sup>, Sidnei Paciornik<sup>1</sup>, Viktor Mechtcherine<sup>2</sup> and Flavio A. Silva<sup>3</sup>

<sup>1</sup> Department of Chemical and Materials Engineering, PUC-Rio, Rio de Janeiro, Brazil

<sup>2</sup> Institute of Construction Materials, Technische Universität Dresden, Germany

<sup>3</sup> Department of Civil and Environmental Engineering, PUC-Rio, Rio de Janeiro, Brazil  
e-mail: renata\_lorenzoni@hotmail.com

Strain-hardening cement-based composites (SHCC) represent a distinct type of fiber reinforced concretes that yield controlled multiple cracking when subject to increasing tensile loading [1]. Considering the multi-phase constitutive nature of SHCC's and the decisive influence of their micromechanics on the overall material behavior, appropriate methods are necessary for the representation of their micro-structure. In this respect, micro-computed tomography (microCT) is an efficient non-destructive technique which can bring this information. For this, appropriate segmentation techniques must be applied. However, given the small scale of analysis and the typical resolution of common computed tomography, as well as the small differences among the material constituents in terms of density and x-ray absorption, the application of common segmentation techniques to SHCC is ineffective. In this scenario, Deep Learning (DL) neural networks are a novel method with high potential for accurate and efficient segmentation of complex micro-structures. In this work, DL was used within the Dragonfly software platform. Two different SHCCs were analyzed, representing typical compositions for their strength classes and that have been mechanically investigated by the author in previous works [2]. The first one, used for training the DL network (Figure 1), was made with high-strength SHCC matrix (M2) and polyethylene fibers (PE). The second SHCC was made with normal-strength matrix (M1) and polyvinyl alcohol fibers (PVA), and was used to check the transfer learning ability of the trained network to other images/samples. The main difference between the images is that in M1-PVA the sand was not distinguishable in the matrix, as in M2-PE. The contrast of the images was also quite different due to the different densities of the matrices. Thus, image pre-processing was performed to normalize the M1-PVA histogram according to M2-PE histogram (Figure 2). Once this was done, the network trained with M2-PE and applied to M1-PVA worked well (Figure 3), proving that the same training can be applied for the automatic segmentation of other similar images. The obtained results are highly promising and quantitatively in accordance with the composition of the analyzed samples.

The authors would like to acknowledge the financial support offered by agencies CNPq, CAPES and FAPERJ, as well as by the German Academic Exchange Service – DAAD.

- [1] V. C. Li, "On Engineered Cementitious Composites (ECC) A Review of the Material and Its Applications," *J. Adv. Concr. Technol.*, vol. 1, no. 3, pp. 215–230, 2003.
- [2] I. Curosu, V. Mechtcherine, and O. Millon, "Effect of fiber properties and matrix composition on the tensile behavior of strain-hardening cement-based composites (SHCCs) subject to impact loading," *Cem. Concr. Res.*, vol. 82, pp. 23–35, 2016.

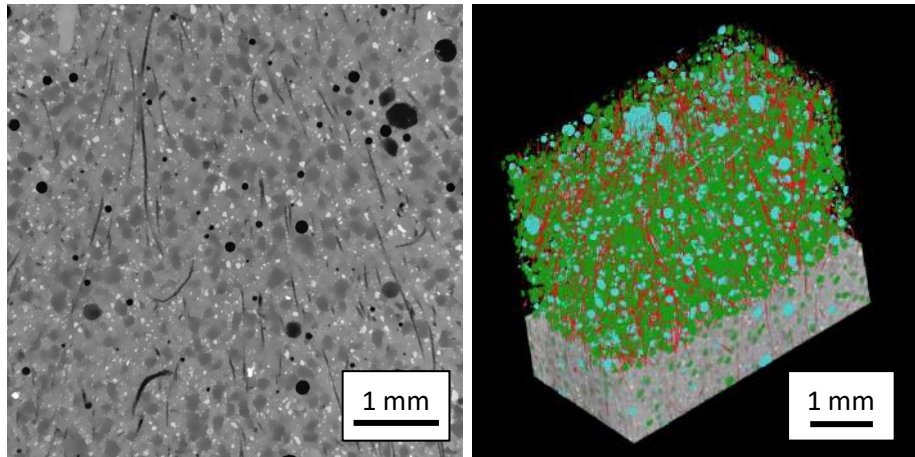


Figure 1. M2-PE: original 2D image (left) and segmented 3D pores (blue), fibers (red) and sand (green) by deep learning.

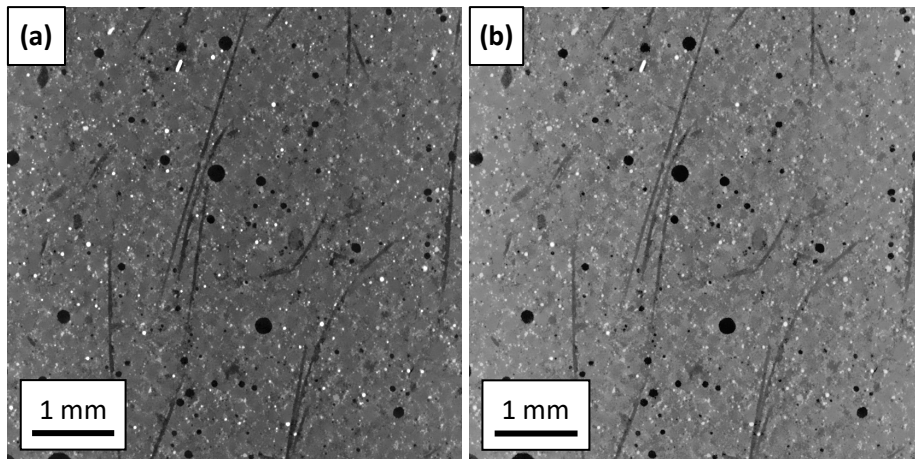


Figure 2. Histogram matching: (a) original M1-PVA image and (b) same layer after histogram matching based on a M2-PE reference image.

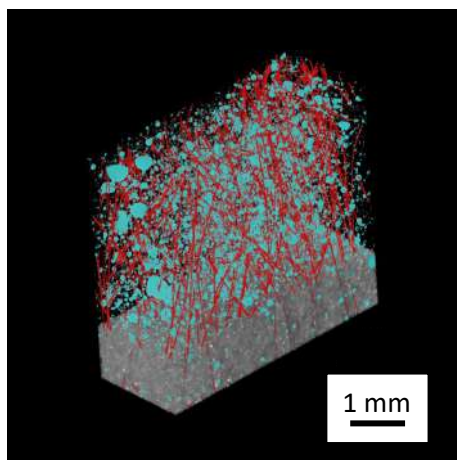


Figure 3. Segmented 3D pores (blue) and fibers (red) in M1-PVA image using deep learning network trained with M2-PE data.



## Correlative In Situ Analysis on Nanoscale Using AFM in SEM

A. Chourey<sup>1\*</sup>, E. R. Souza<sup>2</sup>, S. Hummel<sup>3</sup>, P. Frank<sup>3</sup>, N. Hosseini<sup>4</sup>, J. Sattelkov<sup>5</sup>, R. Winkler<sup>5</sup>, G.E. Fantner<sup>4</sup>, H. Plank<sup>5</sup> and C.H. Schwalb<sup>3</sup>

<sup>1</sup> Quantum Design Inc., San Diego, USA.

<sup>2</sup> Quantum Design Latin America, Campinas – SP, Brazil.

<sup>3</sup> GETec Microscopy GmbH, Vienna, Austria.

<sup>4</sup> Laboratory for Bio- and Nano-Instrumentation, Institute for Bioengineering, EPFL, Switzerland.

<sup>5</sup> Institute for Electron Microscopy and Nanoanalysis, Graz University of Technology, Austria.

Correlative in situ microscopy has gained immense importance for studying nanoscale materials, especially with combination of scanning electron microscopy (SEM) and atomic force microscopy (AFM). This correlative in situ microscopy technique enables ease of correlation of 2D lateral SEM image with high precision 3D topographical AFM image. In this work, we present a novel AFM, AFSEM, which uses self-sensing cantilevers and can be easily integrated and aligned into high-vacuum environment of almost any scanning electron microscope (SEM) or other host system (e.g. dual beam microscopes. FIB systems). It allows direct in-situ AFM measurements using functionalized tips and correlate data with information gained using multiple detectors in SEM. Therefore, SEM imaging, chemical information by EDX, and crystallographic information using EBSD is correlated with real 3D topography, phase information, mechanical, electrical, and magnetic properties by AFM. Furthermore, due to ease of alignment of AFSEM in SEM, measurements could also be correlated, for standard additions like tensile stages, nano-indenters or nano-manipulators

We will present a variety of case studies which highlight advantages of correlative in-situ analysis for different materials. We show results for in-situ electrical characterization of nanostructures by combining SEM and conductive AFM measurements for dose-dependent conductivity measurements of nanogranular Pt(C) structures after focused electron beam induced processing. In addition, we will demonstrate the analysis of bone tissue and show how the SEM allows to quickly identify the area of interest, in this case the lacunae on the surface of the bone structure (Figure 2a). The AFM then provides the real 3D topography inside the lacunae and enables the detailed analysis of the collagen fibers within the lacunae area. Finally, we show results for Nano mechanics of free standing nanowire, examples of characterization of magnetic materials, failure mechanical analysis by in-situ tensile stress measurements of metal wires or polymer structures.



Based on the broad variety of applications and characterization of different materials and devices, we anticipate correlative in situ analysis using AFSEM to be one of the driving characterization tools for the future.

- [1] D. Yablon, P. Werten, M. Winhold and C.H. Schwalb, *Microscopy and Analysis* 31(2) 14-18 (2017).
- [2] J. Kreith, T. Strunz, E.J. Fantner, G.E. Fantner and M.J. Cordill, *Rev. Sci. Instr.* 88 053704 (2017).

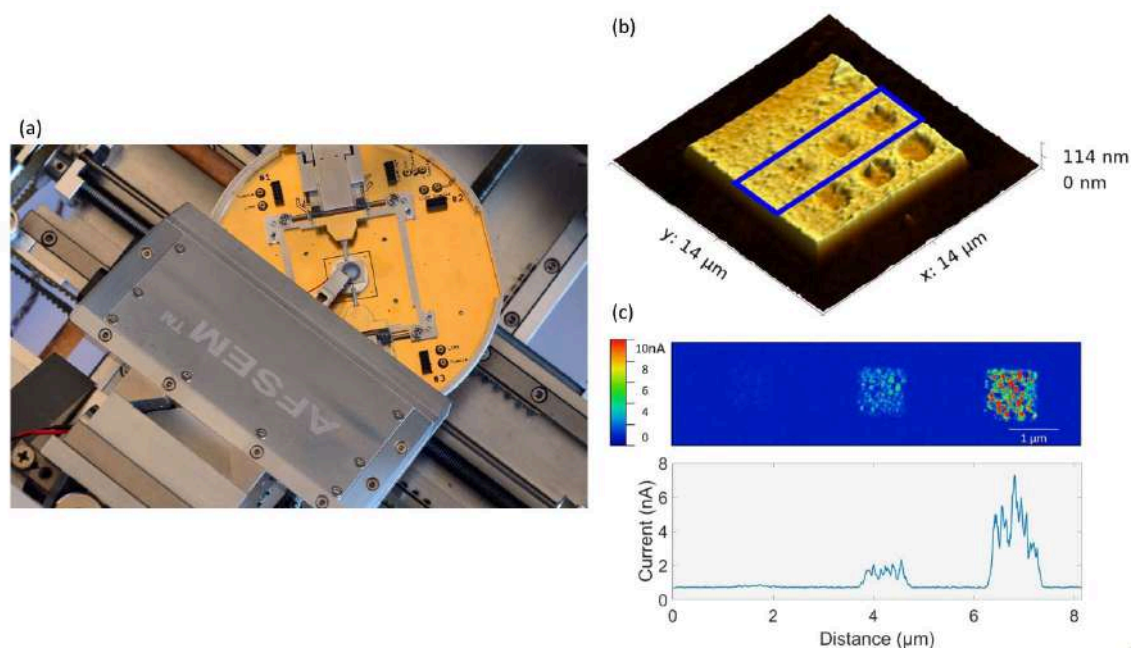


Figure 1. (a) AFSEM integration inside SEM in combination with a nanomanipulator setup (b) In-situ AFM topography of nanogranular Pt(C) structure prepared by focused electron beam induced deposition (c) In-situ conductive AFM measurement of nanogranular Pt(C) structure.

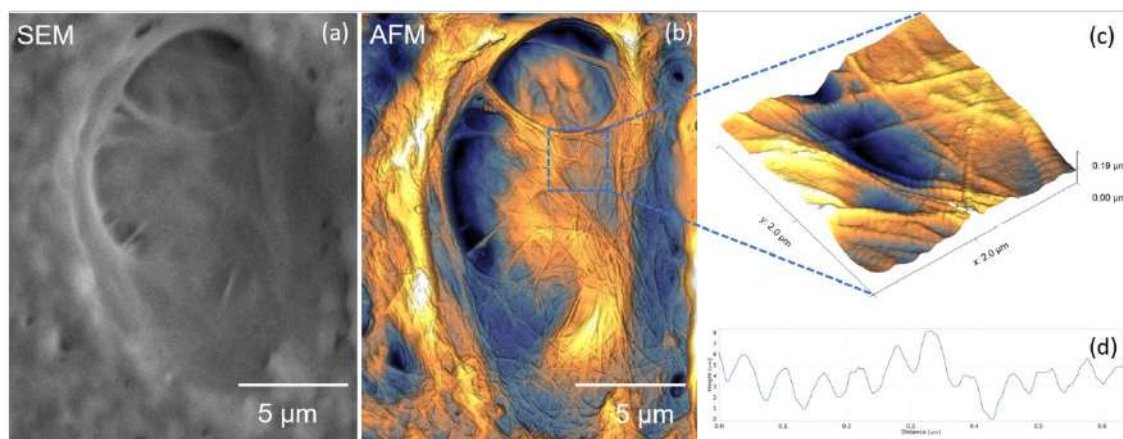


Figure 2. (a) SEM image of lacunae structure on a bone tissue surface. (b) Correlative in-situ AFM image of lacunae structure. (c) High-resolution AFM image of collagen fibers inside the lacunae. (d) Cross section of collagen fiber surface structure.



## Structural and Morphological Characterization of BaTiO<sub>3</sub>/CoFeO<sub>4</sub> Thin Films Using Scanning and Transmission Electron Microscopies and Atomic Force Microscopy

Helen Rose C. S. Andrade<sup>1\*</sup>, Nelcy D. S. Mohallem<sup>2</sup> and Luciana M. Seara<sup>3</sup>

<sup>1</sup>. Afiliação do primeiro autor, incluindo Departamento/Instituto, Diamantina e Brazil.

<sup>2</sup>. Centro de Microscopia/UFMG/ Belo Horizonte/Minas Gerais.

<sup>3</sup>. Centro de Microscopia/UFMG/ Belo Horizonte/Minas Gerais

Nanocomposite thin films formed by ferrimagnetic and ferroelectric materials present magnetoelectric coupling phenomenon, characteristic of multiferroic materials. The magnetoelectric behavior of these composites is dependent on their microstructure and of the coupling interaction across the ferromagnetic–ferroelectric interface [1]. These nanocomposites have a variety of applications in tunable microwave devices using electric control of spin wave propagation or new magnetic memories in which the magnetic response is controlled by electric field.

The sol-gel process has been an efficient method to produce this kind of thin film, since a good control of the sample morphology, texture, structure, and chemical composition can be attained by careful monitoring in the physical-chemistry parameters of the precursor solution and of the deposition process [2,3]. In this work, transparent and homogeneous thin films of BaTiO<sub>3</sub> interleaved with CoFe<sub>2</sub>O<sub>4</sub> were deposited onto clean silicon substrates by sol-gel method using dip-coating process. The precursor solutions were prepared using Ti alkoxide and barium acetate to obtain the BaTiO<sub>3</sub> and Fe alkoxide and Co nitrate to obtain the CoFe<sub>2</sub>O<sub>4</sub> thin films. The films were dried in air after each dipping and heated at 900 °C for 1 hour to convert the amorphous films into crystalline ones. The samples were characterized by low angle X-ray diffraction (XRD), scanning electron microscopy (SEM), high resolution transmission electron microscopy (HRTEM) and atomic force microscopy (AFM). Their multiferroic properties was tested with success, using magnetic and electric force microscopy.

### REFERÊNCIAS

- [1] G. Liu, C-W Nan, N. Cai and Y H Lin, *J. Appl. Phys.* **95**, 2660 (2004).
- [2] C. J. Brinker, *The Physics and Chemistry of Sol-Gel Processing*, Academic Press, San Diego, 1990.
- [3] H. C. S. Andrade, L. M. Seara, N. D. S. Mohallem, *Mater. Res. Soc. Symp. Proc.*, **1368** (2011), Materials Research Society.

This research was supported by CNPq, FAPEMIG and CAPES (Brazil).

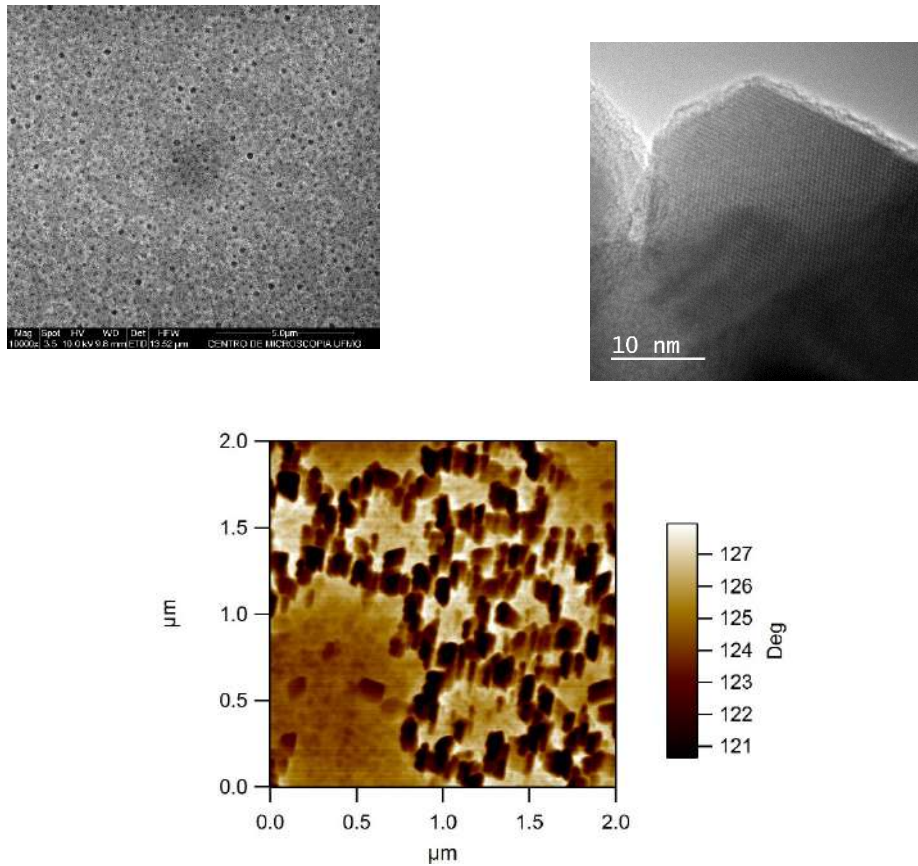


Figure 1 – Scanning electron microscopy, high resolution transmission electron microscopy and atomic force microscopy of the BaTiO<sub>3</sub>/CoFeO<sub>4</sub> thin film

## Advanced Nanoscale Orientation and Atomic Characterization of Phases in Beta Ti Alloys

C.R.M. Afonso<sup>1</sup>, P.A.P. Nascente<sup>1</sup>, V. Amigo<sup>2</sup>, R. Caram<sup>3</sup>

<sup>1</sup>Department of Materials Engineering (DEMa), Universidade Federal de São Carlos (UFSCar), CEP 13565-905, São Carlos – SP, Brazil

<sup>2</sup>Universitat Politècnica de València (UPV), 46022, Valencia, Spain

<sup>3</sup> Universidade Estadual de Campinas (Dema/FEM/UNICAMP), Campinas, SP, Brazil

Nanocrystalline materials are constantly been developed and the need for its characterization is always advancing in order to fulfill the requirements of the resulting nanostructured phases and complex precipitates in sub-micron scale interfaces with variation of composition. Characterization of nanocrystalline materials in this work was realized using X-ray diffraction (XRD), scanning electron microscopy with field emission gun (SEM-FEG) coupled with energy dispersive spectroscopy (EDS) and electron backscattered diffraction (EBSD). In order to improve resolution for the characterization of nanoscale phases it was used TEM analysis together with associated techniques: STEM-EDS, HRTEM. The distribution of phases and grain orientation maps were determined with an Automatic Crystal Orientation Mapping (ACOM) system installed in a JEOL JEM 2100F (TEM/STEM) 200kV with field emission gun (FEG). A ASTAR<sup>TM</sup> NanoMegas system was used for ACOM diffraction data acquisition [1,2]. Usually the step sizes (resolution) adopted in ASTAR mapping starts in 1 nm to 10 nm, and cover areas through the sample from 100 x 100 pixels (nm<sup>2</sup>) up to 700 x 700 pixels (μm<sup>2</sup>). Crystallographic mapping through ASTAR technique was able to characterize and identify submicron down to nanometric β-Ti (bcc) nanoscale thin film grains Ti<sub>85</sub>Nb<sub>15</sub>, Ti<sub>80</sub>Nb<sub>20</sub>, Ti<sub>70</sub>Nb<sub>30</sub> and Ti<sub>60</sub>Nb<sub>40</sub> (%at) coatings (Fig. 1), becoming a very useful tool for characterization of β-Ti alloys. Other metallic materials cases were analyzed, such as interfaces in welding explosion of high strength steel with super duplex steel and Inconel 625 Ni alloy, thin films, automated GMAW-P welding of Al 5083 alloy, laser clad Ni- and Fe-based BMG coatings, in its interfaces, nanostructured grains and intermetallic phases. Using STEM analysis in nano and atomic scale combined with EDS scale of β Ti-13Mo-2Fe alloy sample after annealing can map elements in nanoscale ω phase distribution through the β Ti matrix (Fig. 2.a to 2.d), and through high resolution STEM (HR-STEM) image (Fig. 2.e to 2.h) mapping in detail, atomic scale phase separation of β'+β regions.

**Keywords:** Nanocrystalline alloys; advanced characterization; crystallographic orientation mapping; intermetallic phases.

[1] F. Sun, J.Y. Zhang, M. Marteleur, C. Brozek, E.F. Rauch, M. Veron, P. Vermaut, P.J. Jacques and F. Prima, *Scripta Mater* **94**, 17 (2015).

[2] E. David Gonzalez, Conrado R.M. Afonso, Pedro A.P. Nascente. Nanostructural characterization of sputter deposited Ti-Nb coatings by automated crystallographic orientation mapping. *Thin Solid Films*, **661**, 92 (2018).



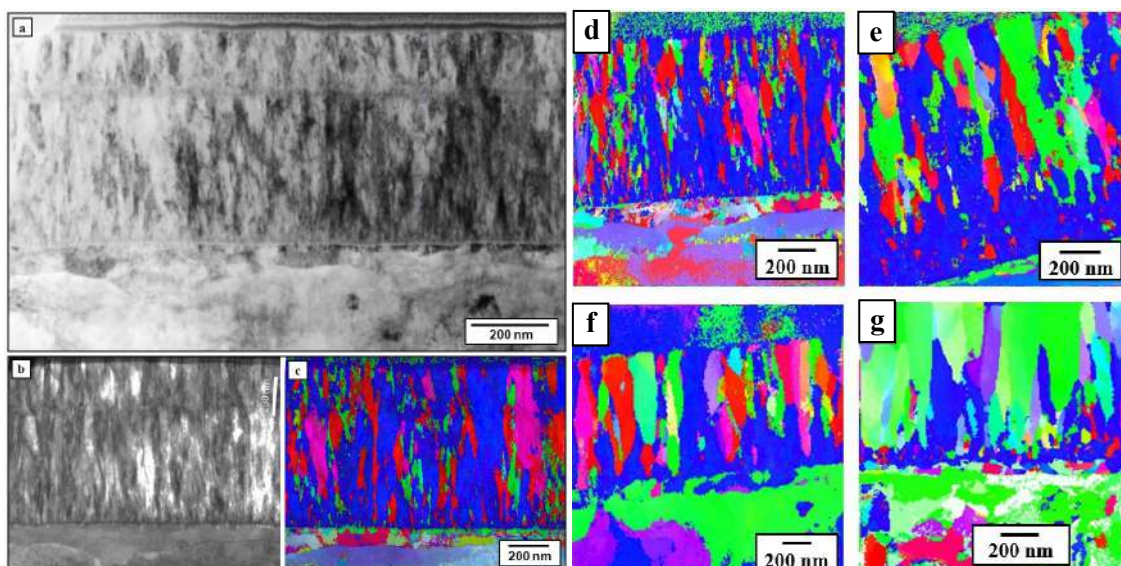


**Fig. 1.** Automatic Crystal Orientation Mapping (ACOM) STEM-BF image (a) of FIB sample cross section of 1  $\mu\text{m}$  thick Thin Film of  $\text{Ti}_{85}\text{Nb}_{15}$  (%at) alloy over Stainless Steel (SS) substrate. Crystallographic orientation mappings obtained by ACOM showing inverse pole figure coloring for the Z-axis for (d)  $\text{Ti}_{85}\text{Nb}_{15}$ , (e)  $\text{Ti}_{80}\text{Nb}_{20}$ , (f)  $\text{Ti}_{70}\text{Nb}_{30}$ , and (g)  $\text{Ti}_{60}\text{Nb}_{40}$  (%at) coatings. The Z-axis is perpendicular to the film growth direction (y-axis).

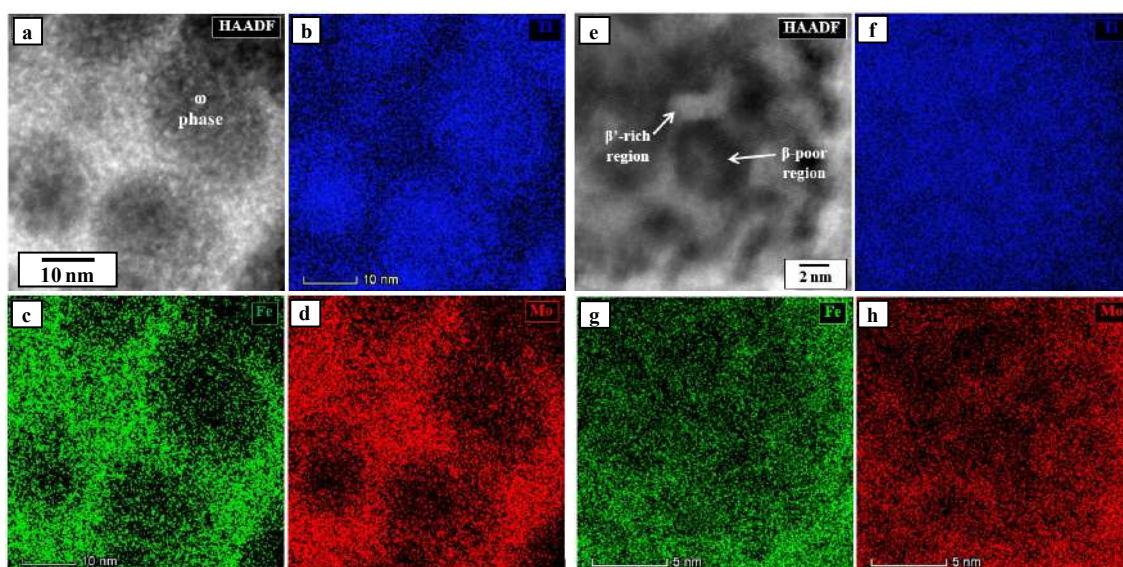


**Fig. 2** – STEM analysis of Ti-13Mo-2Fe alloy sample after annealing showing a) HAADF (Z-contrast) image of nanoscale  $\omega$  phase distribution through the  $\beta$  Ti matrix. Respective X-ray elemental mapping through EDS (ChemiStem) of b) Ti-K (blue) c) Fe-K (green) and c) Mo-K (red) showing Ti-rich omega ( $\omega$ ) precipitates and Mo and Fe-rich segregation through  $\beta$ -Ti matrix. e) High resolution STEM (HR-STEM) image in detail showing atomic scale phase separation of  $\beta'$ + $\beta$  regions distribution through the  $\beta$ -Ti matrix. X-ray mappings through EDS of f) Ti-K g) Fe-K and h) Mo-K showing Ti-rich  $\beta$ -poor region (darker) and Mo and Fe-rich  $\beta'$ -rich region (brighter).

## Effect of Grain Boundary Character Distribution on $\delta$ -phase Precipitation in the Nickel-based Superalloy 718

Flávia da Cruz Gallo<sup>1\*</sup>, Luiz Maurício Barreto de Azevedo<sup>1</sup>, Cilene Labre<sup>2</sup>, Leonardo Sales Araújo<sup>1</sup>, Luiz Henrique de Almeida<sup>1</sup>

<sup>1</sup>Programa de Engenharia Metalúrgica e de Materiais – UFRJ, Rio de Janeiro, Brasil,

<sup>2</sup>Centro Brasileiro de Pesquisas Físicas (CBPF), Rio de Janeiro, Brazil.

\*[flaviagallo@globo.com](mailto:flaviagallo@globo.com)

Hot rolled Ni-based superalloy 718 sheets were investigated in terms of  $\delta$ -phase ( $\text{Ni}_3\text{Nb}$ ) intergranular precipitation. The role of  $\delta$ -phase can be beneficial or detrimental to alloy's properties, depending on its morphology, volume fraction and distribution [1,2]. Volume fraction of  $\delta$ -phase shall be controlled, since it occurs at the expense of the hardening phase  $\gamma''$ [3]. Manipulation of grain boundary character distribution (GBCD) through thermomechanical processing is used to improve Ni-based superalloys properties [4], aiming to increase the fraction of special low energy low-CSL boundaries ( $\Sigma < 29$ ), and consequently affecting interfacial energy distribution and intergranular related phenomena [5,6]. Previous studies on the effect of GBCD in intergranular phase precipitation were focused on carbides and the way their morphology and distribution affect intergranular failure related phenomena [7,8]. However,  $\delta$ -phase precipitation and its correlation to CSL boundaries have not been addressed. A hot rolled (HR) sheet was submitted to heat treatments comprising solution annealing at  $\delta$ -phase super-solvus temperature ( $1050^\circ\text{C}/30\text{min}$ ) and aging at  $900^\circ\text{C}$  for various time intervals (HR-2 to 24h). The phase composition and distribution as well as the GBCD was examined in a JEOL 7100F FEG-SEM equipped with electron backscatter diffraction (EBSD) detector and energy dispersive spectroscopy (EDS). The MATLAB open source extension MTEX (version 5.1.1) was used to process EBSD data. The aging temperature resulted in precipitates with needle-like morphology, as can be seen in SEM/BSE images presented in Fig.1(a) and 2, for samples HR-2h and 6h respectively. Fig.1(b) also shows EDS maps of the inhomogeneous network of intergranular needle-like  $\delta$ -phase. EBSD was used for phase indexation by kikuchi patterns, as can be seen in phase map shown in Fig.3(a) for HR-24h sample. Fig.3(b) shows the inverse pole figure (IPF) generated based on orientation mapping. Quantification of  $\delta$ -phase area fraction and length fraction of  $\Sigma^{3n}$  are presented in Fig.4(a) and (b). Fig.4(c) presents the quantitative analysis of preferable precipitation sites for  $\delta$ -phase in alloy 718. The objective of this study was to provide some preliminary systematic correlation between  $\delta$ -phase intergranular precipitation and GBCD in a hot rolled sheet of superalloy 718. Based on the results summarized in Fig.4(c) it can be concluded that high energy HABs and non-special TJs (0CSL and 1CSL) are preferable precipitation sites for  $\delta$ -phase in alloy 718 at all studied conditions.

### REFERENCES

- [1] A. Niang, Institut National Polytechnique de Toulouse (INP Toulouse), 2010.
- [2] M.A. Medeiros, et al., Mater. Sci. Eng. A. 726 (2018) 187–193.
- [3] M. Sundararaman, et al., Metall. Trans. A. 19 (1988) 453–465.
- [4] V. Randle, Acta Mater. 47 (1999) 4187–4196.
- [5] V. Randle, G. Owen, Acta Mater. 54 (2006) 1777–1783.
- [6] T. Watanabe, Mater. Sci. Eng. A. 176 (1994) 39–49.
- [7] X. Dong, et al., J. Mater. Sci. Technol. 28 (2012) 1031–1038.
- [8] A. Telang, et al., J. Nucl. Mater. 505 (2018) 276–288.

This research was supported by CAPES (Brazil).



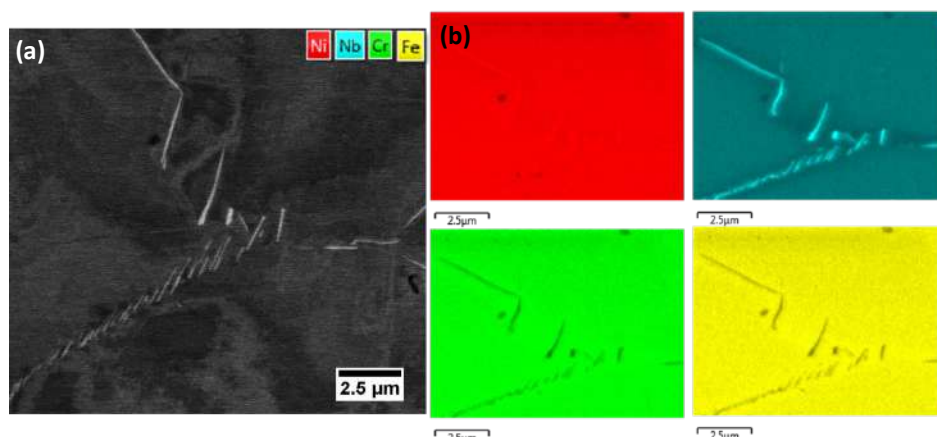


Figure 1 – (a) SEM/BSE image of a triple junction in sample HR-2h and (b) EDS maps of the same region, showing Ni, Nb, Cr and Fe distribution.

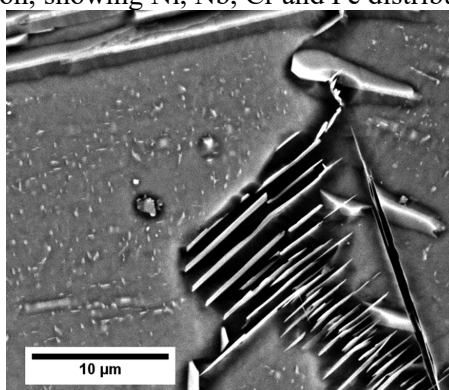


Figure 2 – SEM/BSE image of sample HR-6h, showing a grain boundary with a colony of  $\delta$ -phase needles.

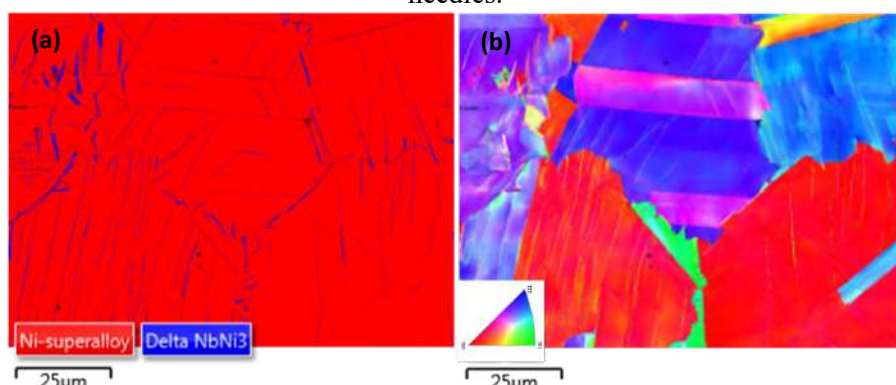


Figure 3 – EBSD data of HR-24h sample showing (a) phase map and (b) inverse pole figure (IPF).

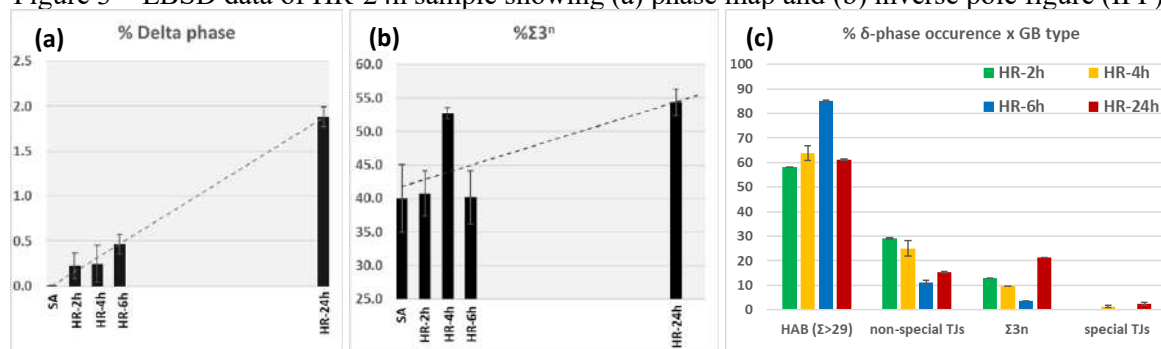


Figure 4 – (a) Area fraction of  $\delta$ -phase (%) and (b) length fraction of  $\Sigma 3^n$  CSL boundaries ( $\Sigma 3 + \Sigma 9 + \Sigma 27$ ) (%) plotted as a function of aging time; and (c) frequency of occurrence of  $\delta$ -phase precipitation (%) plotted as a function of GB type (random HABs and low-CSL  $\Sigma 3^n$ ) and TJs group (non-special TJs: 0CSL and 1CSL; special TJs: 2CSL and 3CSL).

## Retained Austenite Volume Fraction in 52100 Steel Determined by EBSD and Others Correlative Techniques

Geronimo Perez\*, Bráulio Soares Archanjo, Carlos Alberto Senna, Alexei Kuznetsov and Carlos Alberto Achete

Divisão de Metrologia de Materiais, Instituto Nacional de Metrologia, Qualidade e Tecnologia (INMETRO), Duque de Caxias-RJ, 25250-020, Brasil;

The retained austenite is a well-known microstructural component of quenched steels that may cause adverse effects, positive or negative, in the properties and performance depending on the steel type. The correct determination of retained austenite fraction is one of the most sought metrological tasks in the metalworking industry manufacturers and consumers of carbon steel. In this work we determined retained austenite fractions and other secondary phases by combining electron backscatter diffraction (EBSD), dispersive X-ray spectroscopy (EDS), transmission electron microscopy (TEM), X-ray diffraction (XRD) and vibrating sample magnetometer (VSM) on samples of AISI 52100 steel with different volume fractions of retained austenite. AISI 52100 steel were quenched from different temperatures, 760 °C up to 920 °C in oil at 60 °C. EBSD combined to EDS revealed to be extremely sensitive to identify different phases. The electron backscatter diffraction (EBSD) is able to identify with great precision each phase present in the analyzed material [1, 2]. The EBSD phase maps show clearly the difference on the microstructure between the samples quenched from different temperatures. The sample quenched from 760 °C (Figure 1a) exhibits a high amount of cementite particles fraction and low austenite fraction, on the other hand, the sample quenched from 920 °C shows a high austenite fraction and low number of cementite particles (Figure 1b). In the TEM images of Figure 2 the difference on microstructure between the sample quenched from 760 °C and from 920 °C is clearly seen. In Figure 2a is possible to observe cementite particles with diameters around 500 nm, while the quenched sample (Figure 2b) shows a typical ripple structure of martensite.

[1] M. Calcagnotto et al., Mater. Sci. Eng., A 527 (2010) 2738-2746.

[2] K. Yvell, et al.; Mater. Char. 135 (2018) 228-237.

[3] This research was supported by CNPq (Brazil).

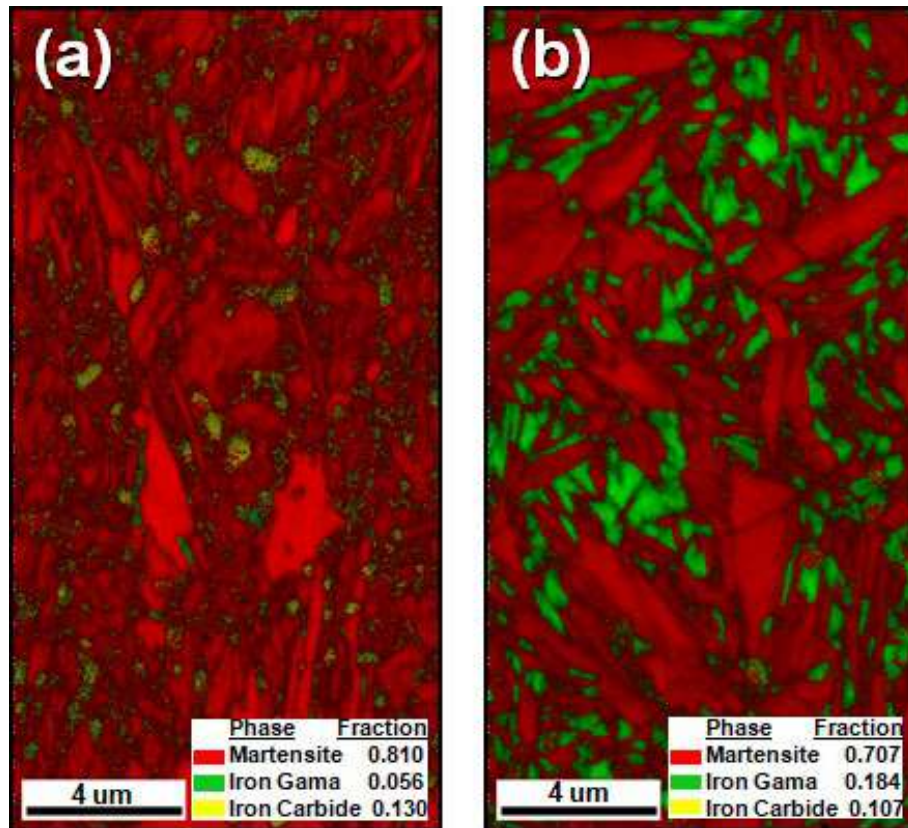


Figure 1 - EBSD phase maps of quenched samples: (a) quenched from 760 °C and (b) quenched from 920 °C.

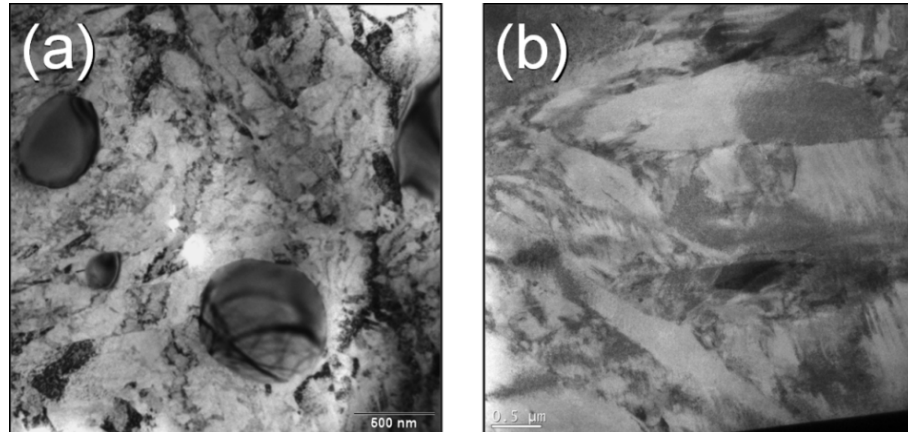


Figure 2 - TEM images of AISI 52100 steel samples: (a) quenched from 760 °C, (b) quenched from 920 °C.

## Combining EBSD and CL in a Geological Problem

Paola Barbosa<sup>1\*</sup>, Leonardo Lagoeiro<sup>2</sup> and Mateus Silva<sup>2</sup>

<sup>1</sup>. Universidade de Brasília, Instituto de Geociências, Brasília, Brazil.

<sup>2</sup>. Universidade Federal do Paraná, Departamento de Geologia, Curitiba, Brazil.

Kinematic indicators, including certain strain fringes, represent an important group of structures related to the progressive deformation in rocks. The evolution of these fibrous textures can be explained by the combination of multiple mechanisms of deformation and fluid flow, mainly controlled by the orientation of the strain field and the morphology of the grains. In general, the observations are done with an optical microscope and compared with computational models of growth. This work proposes a combination between crystallographic and cathodoluminescence data obtained in rocks from banded iron formations of Iron Quadrangle, Brazil representing an example of how complementary analytical techniques can be useful to understand geological problems. The chosen sample exhibits a strain fringe structure of quartz around a clast of magnetite partially transformed into goethite and hematite. Through the crystallographic data it was possible to identify the grain boundary morphology and domains of low deformation areas. On the other hand, the cathodoluminescence signal evidenced the occurrence of grains with higher concentration of crystalline defects (Fig.1). With this work [1], we would like to disseminate the use of a simple but powerful technique in Geosciences. Further studies of electron diffraction via the transmission electron microscope are necessary to understand the formation of crystallographic defects and lattice substitutions in quartz. But in case of rocks, this is not so straightforward mainly due to the size of the grains and of the entire structure. The sample preparation is complicated for minerals and the representativeness of the data are often questioned. So, the EBSD is a suitable technique for rocks because the relationship of crystallographic texture between grains in space are relevant and because we can collect data from large areas. Nevertheless, the sensitivity of CL to lattice defects in general when compared to the variations of the data of electron backscattering diffraction patterns is higher. So we have decided to combine two techniques that can be used in bulk analyses, along the same microstructure, working as a complementary strategy of studies in rocks. We think that this work is really relevant because shows to Geoscientists who work most of the time only with light microscopy that it is possible to study many different grains from a large structure combining different well-known techniques and preserving the relationship between grains and the global rock microstructure.

[1] This research was supported by Brazilian Science Foundations FAPEMIG (CRA - APQ-02969-14), FAP-DF (0193.001526/2017) and CNPq (443725/2014-4, 305257/2014-5, 406849/2016-1).



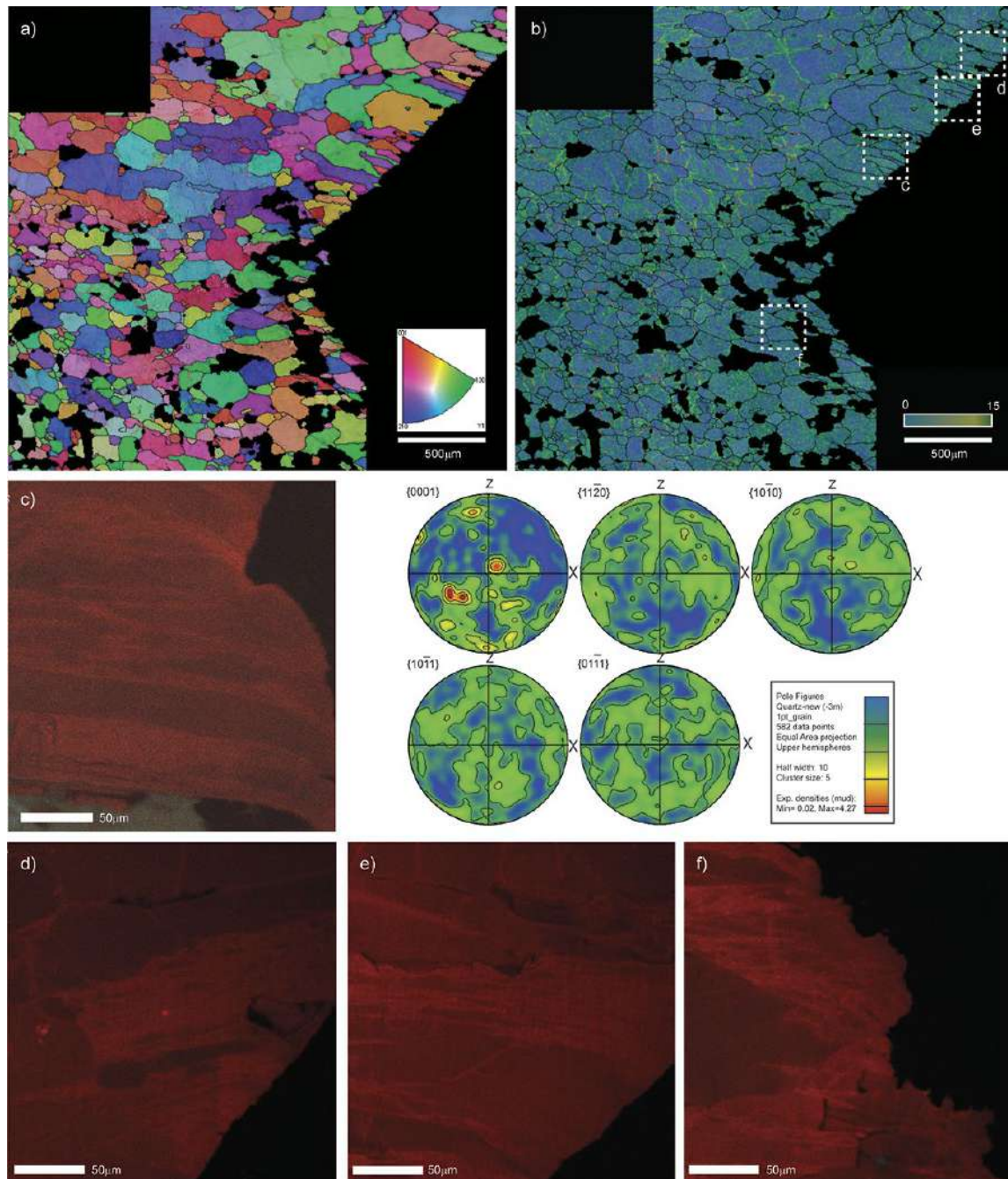


Figure 1: Crystallographic preferred orientation (CPO) of 582 quartz grains around the magnetite clast. a) Inverse pole figure image of half pressure shadow, where different colors represent distinct crystallographic orientation of quartz grains. According to the pole figures of basal (0001), prismatic (11-20) and (10-10) and rhomb planes of quartz (10-11) and (01-11), it is not possible to observe a clear CPO controlled by the clast. b) The blue areas of the image reveal the areas of lower misorientation angles, while the green and yellow areas reveals mainly boundaries and areas of crystalline defects. c) to f) Comparing the misorientation image and the cathodoluminescence images of the red square area, it is interesting to observe that the CL images reveal more details about boundaries and possible defects regions.



## Study of the growth of spicules of calcareous sponges by Transmission Electron Microscopy and Transmission Kikuchi diffraction

Jacques Werckmann<sup>1\*</sup>, Etienne Brodu<sup>2</sup>, Emmanuel Bouzi<sup>2</sup>, André Rossi<sup>1</sup>, Marianne Longuinho<sup>1</sup>, Dris Ihiawakrim<sup>3</sup>, Michelle Klautau<sup>4</sup>, Marcos Farina<sup>5</sup>

<sup>1</sup>Centro Brasileiro de Pesquisas Fisicas Rio de Janeiro Brazil

<sup>2</sup>LEM3 Université de Lorraine Metz France

<sup>3</sup>IPCMS CNRS Université de Strasbourg France

<sup>4</sup>Instituto de Biologia UFRJ Rio de Janeiro Brazil

<sup>5</sup>Instituto de Ciências Biomédicas UFRJ

j.werckmann@gmail.com

The sponges appeared 500 millions years ago at the beginning of the Cambrian explosion. The sponges are the first multicellular organisms synthesizing minerals. Sponges are organisms without circulatory, digestive and nervous system. Its cylindrical body is essentially composed of collagen in which is entangled spicules of calcite or silica, which gives them a three-dimensional structure. There are several types of spicules that are distributed according to a determined spatial order [1]. In the case of the calcareous sponges that we studied, the spicules consist of calcite. The spicules are growing within an extracellular space, sealed by septate junctions between the membranes of sclerocytes, and are surrounded by an organic sheath that is secreted by the sclerocytes. Each spicules is formed by two (diactines), six (triactines, or seven (tetractines) sclerocytes, In our work we are interested in triactine spicules. The nucleation and growth of the spicules is under the strict control of the biological through the intermediary of sclerocytes and proteins. Spicule are in the form of single crystals as shown by polarized light microscopy and transmission electron microscopy from diffraction patterns. Paradoxically, the fracture of the spicules generated by a mechanical force has a conchoïdal shape, whereas the single crystals of calcite fracture along well-defined {104} cleavage planes. To bring elements of understanding to the particular mechanical properties of the spicules, and the mechanism of their growth, we have studied their ultrastructure and their structure at nanoscale, by High Resolution Transmission Electron Microscopy (HRTEM) and Transmission Kikuchi Diffraction TKD. The results show that the particular properties of the spicules can be explained on the one hand by the presence of porosity and on the other hand that the ultrastructure of the spicules consists of nanograins of about ten nanometers very weakly disoriented. This allows us to formulate the hypothesis of a catalytic growth of nanograins that are deposited almost epitaxially on the spicule in formation. This mechanism is controlled by specific protein.

[1] A. Rossi et al. Journal of Structural Biology 196(2016) 164-172

Acknowledgements: This work was supported by CNPq, FAPERJ, and the international associated laboratory “AEMB” between the CNRS (France) and UFRJ (Brazil)

## In-situ Electron Microscopy Observation of the Redox Process in Plasmonic Heterogeneous-Photo-Sensitive Nanoparticles

Jefferson Bettini<sup>1\*</sup>, Lucia B. Scaffardi<sup>2,3</sup>, Jesica M. J. Santillán<sup>2</sup>, David Muñetón Arboleda<sup>2</sup>, Daniel C. Schinca<sup>2,3</sup> and Diego Muraca<sup>4</sup>

1. Electron Microscopy Laboratory, Brazilian National Nanotechnology Laboratory/CNPEM.
2. Centro de Investigaciones Ópticas (CIOp) (CONICET La Plata-CIC-UNLP), Gonnet, La Plata, Buenos Aires, Argentina.
3. Departamento de Ciencias Básicas, Facultad de Ingeniería, UNLP, La Plata, Buenos Aires, Argentina.
4. Instituto de Física ‘Gleb Wataghin’, Universidade Estadual de Campinas, Campinas, Brazil.

\* [jefferson.bettini@lnnano.cnpem.br](mailto:jefferson.bettini@lnnano.cnpem.br)

Catalytic properties observed by in-situ transmission electron microscopy may provide a unique understanding of the involved processes due to the resolution attained with this technique [1]. This understanding is essential for the development of catalysts, which in turn are of fundamental importance for energy and environmental technologies [2]. Effects of intense electron probes, that depend on the induced surface diffusion or sputtering mechanisms, were reported using field-emission transmission electron microscope [3]. However, when in-situ transmission electron microscopy is performed on a nanosystem composed by NPs with a specific configuration and an electron-beam sensitive material, the interaction between them can give rise to new phenomena. In this way, we report the experimental and direct observation of photo-sensitive material with catalytic properties composed of metallic silver NPs (Ag-NPs) and silver chloride nanoparticle (AgCl-NP). The electron beam interaction with this system configuration, in fact, shows somewhat unexpected behavior, such as the evolution of AgCl-NP composed initially of a majority of amorphous phase with a minor crystalline phase and possible chlorine nanobubbles moving inside the AgCl-NP as shown in figure 1. When the thickness of AgCl-NP reaches a critical point, this structure breaks up in the edge and shows up a crystalline AgCl phase with fast-growing and fast-dissociation of their atomic planes. We also observed fast-nucleation and fast-dissociation of small silver NP (more than once) on the crystalline AgCl phase, as shown in figure 2. This new NP nucleation involves an ultrafast mass transport, that is correlated with specific places in the originals Ag-NPs and, when the small NP dissolves, the observed correlation persists. Finally, any portion of the smallest silver NPs in contact with AgCl is partially or entirely dissolved, and the major one grows significantly. In summary, we report by in-situ electron microscopy observation different stages and new phenomena of the dynamical redox process in plasmonic heterogeneous-photo-sensitive nanoparticles.

[1] Tao, F. F., et al, Science 331, (2011) 171.

[2] Yoshida, H., et al, Science 335, (2012) 317.

[3] Egerton, R. F., et al. Microsc. Microanal. 12, (2006) 65.

This work was Granted by PIP 0280 of CONICET, MINCyT-PME 2006-00018, 11/I197, Facultad de Ingeniería of Universidad Nacional de La Plata, Argentina. Fabrication of NPs by Ultrafast Pulse Laser Ablation was carried out at CIOp (CONICET, CICBA, and UNLP), La Plata.

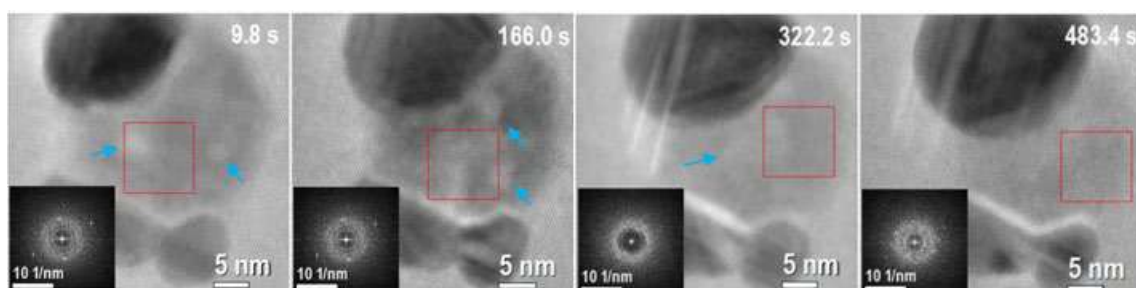


Fig. 1 - This figure corresponds to different times of a movie at the initial stage of the reaction with 3 Ag NPs and in between them AgCl NP. The corresponding times are shown on each image. Darkest contrasts correspond to the Ag NP, whereas less dark contrast corresponds to the AgCl phase. The insets inside of each figure correspond to a fast Fourier transform (FFT) of the region inside the red box for each frame. The FFTs show weak spots indicating the existence of a minority crystalline phase with a majority of the amorphous phase. Two-nanometer sized nanobubbles (brighter contrast) are present on the system within the AgCl-NP at 9.8 s. Blue arrows indicate places with presence of nanobubbles.

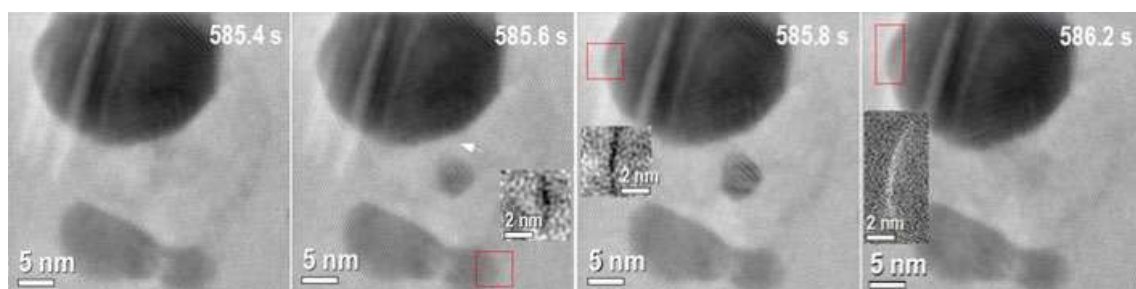


Fig. 2 - Time sequence of the reaction for 0.8 seconds of a Movie. The corresponding times are shown on each image. 585.4 s: shows the initial condition of the time sequence with three original silver NPs and a small silver nanoparticle formed on the AgCl, between the Ag NPs. 585.6 s: small Ag-NP is formed, dark contrast on the small box evidence mass loss from the Ag-NP at the bottom right denoted by the red box. The mass difference was obtained by subtraction of figure at 585.6 s from 585.4 s. White arrow shows another place with different mass before and after the nanoparticle formation. 585.8 s: small formed nanoparticle increases its size, dark contrast on the small box evidence mass loss on the Ag-NP at the top left denoted by the red box. The mass difference was obtained by subtraction of figure at 585.8 s from 585.6 s. 586.2: small formed nanoparticle is completed dissolved, bright contrast on the small box evidences mass gain on the Ag-NP at the up left denoted by the red box. The mass difference was obtained by subtraction of figure at 586.2 s from 585.8 s.

## In-Situ TEM of Calcium Carbonate mineralization in the presence of L-Aspartic

Mariana Moreira Longuinho<sup>1,4\*</sup>, Nathaly Ortiz Peña<sup>2</sup>, Dris Ihiawakrim<sup>2</sup>, Marcos Farina<sup>3</sup>, André Linhares Rossi<sup>4</sup> and Ovidiu Ersen<sup>2</sup>

<sup>1</sup> Institute of Biophysics Carlos Chagas Filho, Federal University of Rio de Janeiro, Rio de Janeiro, Brazil,

<sup>2</sup> Institut de Physique et Chimie des Matériaux de Strasbourg, Strasbourg, France,

<sup>3</sup> Institute of Biomedical Sciences, Federal University of Rio de Janeiro, Rio de Janeiro, Brazil,

<sup>4</sup> Condensed Material, Applied Physics and Nanoscience Coordination, Brazilian Center for Physics Research, Rio de Janeiro, Brazil.

\*mariana.longuinho@gmail.com

Biomimetic syntheses are widely studied for the development of new materials for pharmaceutical purposes, tissue regeneration and for the understanding of biomineralization processes [1]. A better comprehension on how mineralization occurs in biological environment allow the synthesis of materials with special properties, which ensure the reliability of the production [1]. Among the biominerals, calcium carbonate ( $\text{CaCO}_3$ ) is the most abundant in nature, being present in primitive to complex organism like the ear otoliths in humans. Therefore,  $\text{CaCO}_3$  mineral is of great interest for fundamental studies as a model for nucleation, growth and crystallization [2]–[4]. A great challenge in the biomineralization field is the understanding of the initial stages of crystallization, since the formation of a critical nucleus occurs in a short period and in the molecular level. This impede the direct observation of the process in routine analytical imaging techniques [2], [5]. To overcome this limitation, *in situ* techniques allow the observation of crystallization from solution, in real time like morphological changes, crystallinity and structural dynamic. More specific, the *in situ* Transmission Electron Microscopy (*in situ*-TEM) enables acquisition of images and videos at Angstrom resolution, chemical and structural information during the development of mineral phase [6]. The present work aims to understand how organic molecules, specifically aminoacids, influence  $\text{CaCO}_3$  biomineralization. As described in the literature, there are specific proteins directly related to the biomineralization and are capable of influencing the structure and kinetic of  $\text{CaCO}_3$  crystallization due to polarity, electrophilicity and presence of sulfate or phosphate groups [1], [7]–[9]. The experiment was carried out by mixing  $\text{CaCl}_2$  and  $\text{Na}_2\text{CO}_3$  solutions, with and without l-aspartic acid, and then the mixture was dropped in a chip of *in situ* sample holder (Protochips) and analyzed in a JEOL-2100F TEM. Preliminary results show a region more electron dense, probably with accumulation of ions where crystalline nuclei are formed. However, most of them undergoes dissolution before reaching a critical size (70 to 120 nm) in the samples without addition of the amino acid (Figure 1). The dissolution may have happened because of the higher energy of the system leading to instability or because of the energy of the electron beam during the analysis. In the experiment containing l-aspartic acid, it was also possible to observe crystals with calcite-like morphology and organic vesicular-like structures containing crystalline material. The existence of nanocrystals inside vesicular structures suggests that the amino acid can accumulate ions inside these structures, inducing the precipitation of crystals (Figure 2). Such phenomena is described in micron and millimeter scale using polymers and polypeptides as polymer induced liquid phase (PILP)



[10], however, never described for small molecules like aminoacids forming nanoscale crystals. Further studies will be carried out to better understand this mechanism.

## REFERENCES

- [1] D. C. Green *et al.*, *Cryst. Growth Des.* 16 (2016) 5174.
- [2] A. Dey *et al.*, *Nat Mater* 9 (2010) 1010.
- [3] M. Hariharan, N. Varghese, A. B. Cherian, P. V Sreenivasan, and J. Paul, *Int. J. Sci. Reaserch Publ.* 4 (2014) 1.
- [4] L. Štajner *et al.*, *J. Cryst. Growth* 486 (2018) 71.
- [5] J. Tao, M. H. Nielsen, and J. J. De Yoreo, *Curr. Opin. Colloid Interface Sci.* 34 (2018) 74.
- [6] A. Dey, G. de With, and N. A. J. M. Sommerdijk, *Chem. Soc. Rev.* 39 (2010) 397.
- [7] B. J. Aizenberg, G. Lambert, L. Addadi, and S. Weiner, *Adv. Mater.* 8 (1996) 222.
- [8] S. Bentov, S. Weil, L. Glazer, A. Sagi, and A. Berman, *J. Struct. Biol.*, 171 (2010) 207.
- [9] C. L. Freeman, J. H. Harding, D. Quigley, and P. M. Rodger, *Angew. Chemie - Int. Ed.* 49 (2010) 5135.
- [10] L. B. Gower and D. J. Odom, *J. Cryst. Growth* 210 (2000) 719.
- [11] This research was supported by CNPq (Brazil) and CNRS (France).

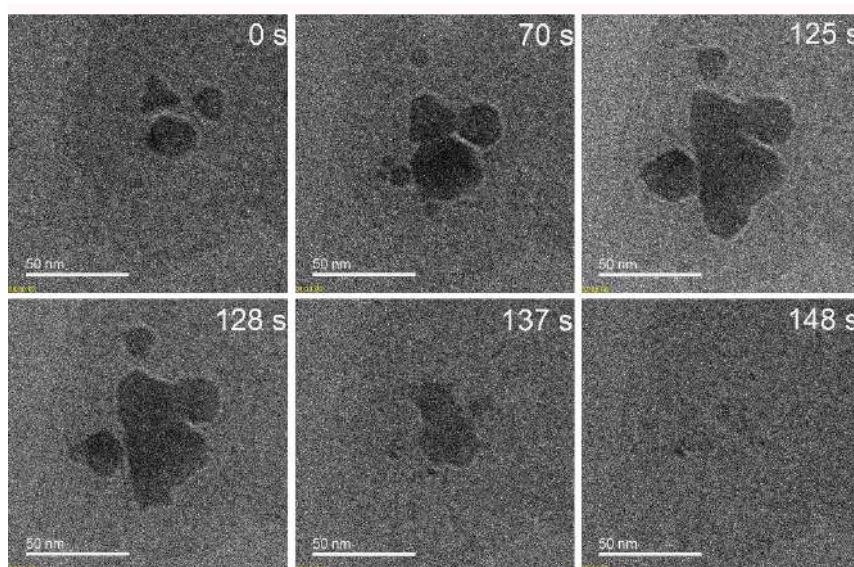


**Figure 1:** Frames of the video recorded during the *in situ*-TEM experiments of  $\text{CaCO}_3$  synthesis without additives. Flow = 10  $\mu\text{l}/\text{min}$ .

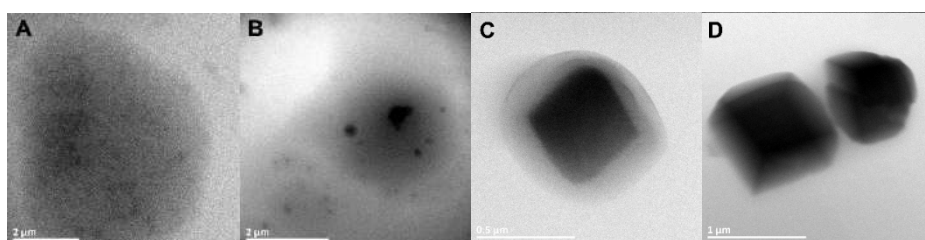


**Figure 2:** Micrographs obtained during the *in situ*-TEM static experiment of  $\text{CaCO}_3$  synthesis with L-aspartic acid in the medium.



# Structural Investigation of Hydrothermally Synthesized Iron Oxide Quantum dots

Naga V. V. Mogili<sup>1\*</sup>, Nathália C. Verissimo<sup>1,2</sup>, Cinthia C.C. Kleiner<sup>1,2</sup>, Rodnei Bertazzoli<sup>1,2</sup>

<sup>1</sup> Brazilian Nanotechnology National Laboratory, LNNano/CNPem, Campinas, Brazil

<sup>2</sup> Department of Manufacturing and Materials Engineering, University of Campinas, UNICAMP, 13083e860, Campinas, SP, Brazil.

Email: [vishnu.mogili@lnnano.cnpem.br](mailto:vishnu.mogili@lnnano.cnpem.br)

## INTRODUCTION

Iron is one of the most abundant elements in the earth's crust. Among its forms, the most known crystalline phases are Magnetite ( $\text{Fe}_3\text{O}_4$ ), Maghemite ( $\gamma\text{-Fe}_2\text{O}_3$ ) and Hematite ( $\alpha\text{-Fe}_2\text{O}_3$ ). Of those oxides, maghemite stands out due to its specific structure, distinct luminescent and magnetic properties. The application of these nanoparticles is widely used in magnetic resonance imaging forming a new class of materials for bioimaging. Our interest here is to evaluate the efficiency of Fe-O bonds of  $\gamma\text{-Fe}_2\text{O}_3$  quantum dots synthesized by hydrothermal approach, understand the oxidation state and possibly the local coordination of the atomic species. In this regard, Parallel Electron Energy Loss Spectroscopy (EELS) attached to a Field Emission Gun (FEG) Transmission Electron Microscope was used. Specifically, the oxidation states were determined based on the Oxygen K and Iron L ionization edge spectra that were acquired in one single EELS energy resolution.

## MATERIALS AND METHODS

The quantum dots used in this work were produced by hydrothermal synthesis with an addition of PEG 4000 and oleic acid as surfactants and placed in a Parr reactor for 3 hours at 140°C and 2 bar pressure. Further the particles were sonicated in acetone and drop casted over thin film carbon-coated, copper mesh grids for TEM characterizations. EELS spectra obtained from these synthesized quantum dots were compared to Magnetite standard sample purchased from Sigma-Aldrich. TEM characterizations were performed using JEOL 2100F FEG TEM fitted with Tridiem Gatan Imaging Filter (GIF) having 2048 channels. In order to reduce the electron dose on the quantum dots, all the energy loss spectra were acquired in diffraction mode with a collection angle of 6.05 mrad and an energy dispersion of 0.2 eV per channel positioned at 490eV.

## RESULTS AND CONCLUDING REMARKS

Figure-1 shows the STEM HAADF image of a well distributed quantum dots obtained from the hydrothermal synthesis process. After measuring over 3500 discrete particles, the size distribution appears to be around 1.4nm ( $\pm 0.2$ ) in diameter. For understanding oxidation state of these particles, enough counts in EELS spectrum are required. So various EELS spectra were recorded from a small agglomeration of quantum dots. Figure-2 illustrates one such spectra in which typical core-loss features related to oxygen K and iron  $\text{L}_{2,3}$  ionization edges superposed over a continuously decreasing background is visible. To estimate Fe/O concentration ratio, initially a power law type background,  $f(E) = AE^{-\lambda}$  where  $E$  is the energy loss,  $A$  and  $\lambda$  are the fitting parameters

are fitted below each edge and the calculated background is subtracted from the recorded spectrum [1]. Further by applying hydrogenic and Hartree-Slater type cross sections for Fe  $L_{2,3}$  and O K edges respectively, the absolute quantification of Fe/O is determined. This approach was applied for both standard Magnetite sample and synthesized quantum dots and Fe/O ratio is  $0.74 \pm 0.02$  (Magnetite) and  $0.68 \pm 0.05$  (quantum dots). On comparison to literature values [2], there is a good agreement and it can be understood that the synthesized quantum dots possess  $\gamma\text{-Fe}_2\text{O}_3$  structure.

## REFERENCES

- [1] R.F. Egerton, *Electron Energy Loss Spectroscopy in the Electron Microscope*, 2<sup>nd</sup> edition, Plenum, New York, 1996.
- [2] C. Colliex et al., *Phys Rev B*, 44 (1991) 11402.
- [3] This research was supported by FAPESP, FINEP, CNPq (INCT program) and CAPES (Brazil).

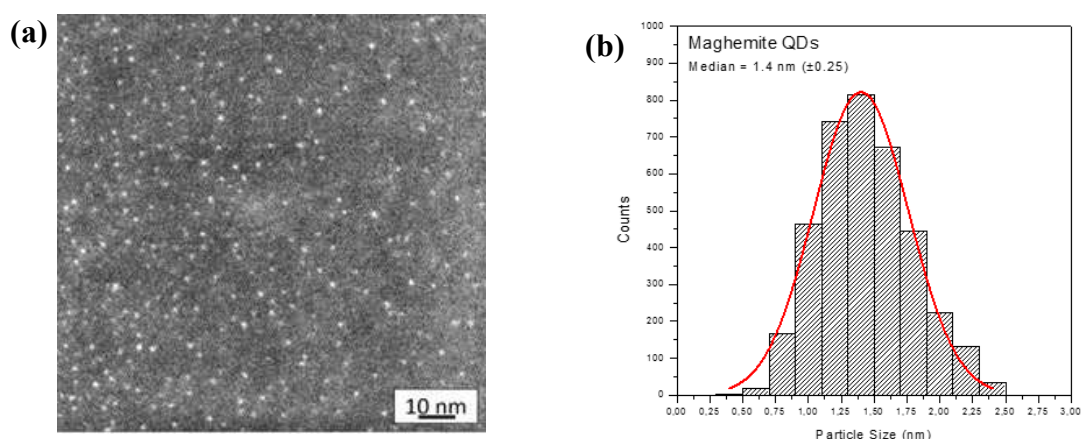


Figure-1: (a) STEM-High Angle Annular Dark Field image of quantum dots and (b) related size distribution histogram

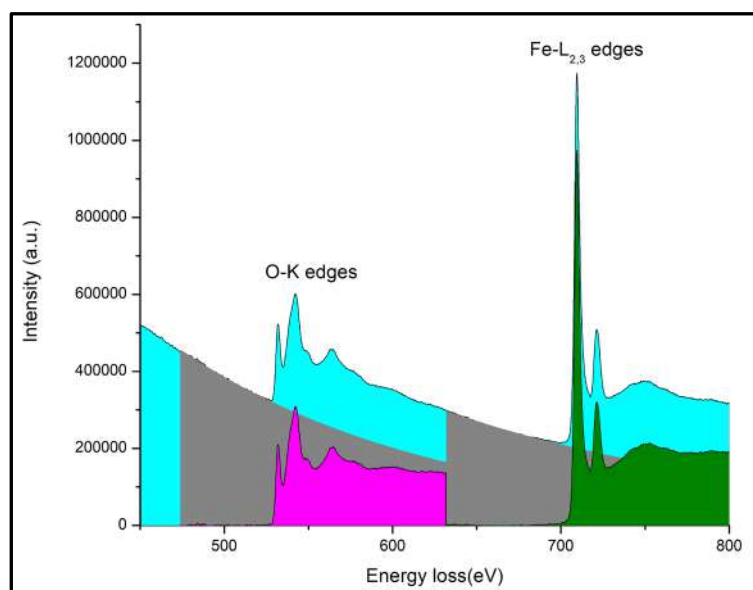


Figure-2: Typical EELS spectrum obtained from an agglomeration of quantum dots illustrating O-K and Fe- $L_{2,3}$  ionization edges after background subtraction

## Scanning Microwave Impedance Microscopy of 2D layered materials

Douglas A.A. Ohlberg<sup>1\*</sup>, Henrique Melo<sup>2</sup>, Paulo S. S. Guimarães and G. Medeiros-Ribeiro<sup>3\*\*</sup>

<sup>1</sup>. Centro de Microscopia, Universidade Federal de Minas Gerais, Belo Horizonte, Brazil

<sup>2</sup>. Dept. de Física, Universidade Federal de Minas Gerais, Belo Horizonte, Brazil

<sup>3</sup>. Dept. de Ciência da Computação, Universidade Federal de Minas Gerais, Belo Horizonte, Brazil

\*[calypete@comcast.net](mailto:calypete@comcast.net); \*\*[gilberto@dcc.ufmg.br](mailto:gilberto@dcc.ufmg.br)

Capacitance voltage experiments are one of the primary tools for the development of Metal-Oxide-Semiconductor technology and has been employed over the past decades in the semiconductor industry, providing answers ranging from oxide characterization, dopant profiling and band-offsets [1]. Additionally, capacitance measurements can provide a wealth of information on nanostructured systems. One of the key concepts that is instrumental to evaluate nanosystems is that of quantum capacitance. Quantum capacitance can be derived and expressed in terms of the local electronic density of states at the Fermi Level, which can be modulated by an external bias, by the so-called Capacitance-Voltage (CV) spectroscopy technique. By sweeping an external bias, spectroscopic information can be derived such as in quantum dots [2], and it has been shown recently that the electronic structure of graphene layers can be unveiled as well [3]. Here we use spatially resolved capacitance spectroscopy to investigate the electronic properties of MoS<sub>2</sub> and graphene 2D layered systems in a variety of configurations: isolated single layers, isolated multi-layers, and heterojunctions between single layers. We utilized the recently developed scanning Microwave Impedance Microscopy technique (sMIM) [4] to examine the Graphene:MoS<sub>2</sub> system. CVD-deposited and exfoliated MoS<sub>2</sub> has been recently investigated by sMIM [5], where carrier concentrations varied according to the number of layers. Nevertheless, there were numerous issues that could account for the charging effects such as interfacial impurities, strain, disorder and charge transfer. Our results demonstrate the one can spatially resolve permittivity, conductivity, capacitance and charge localization in the 2D structures. In particular, for a multilayer MoS<sub>2</sub> we observed charge accumulation, whereas for single layer MoS<sub>2</sub> the CV spectra is devoid of any observable charging effect. When contrasting single graphene layers with graphite flakes, for the former we see the indication of the Dirac point shifted from 0 eV, perhaps due to adjacent doping/charges, whereas for the latter we observed a featureless spectrum. Finally, for a single layer graphene: single layer MoS<sub>2</sub> heterostructure, we see a shift in the Dirac point with respect to the single layer graphene, indicating a charge transfer between layers. In summary, we demonstrate a wealth of information that can be extracted in sMIM experiments and in conjunction with modelling may allow one to infer band diagrams and band offsets in 2D systems.

### REFERENCES

- [1] see E. H. Nicollian; J. R. Brews, MOS (Metal Oxide Semiconductor) Physics and Technology (1982) and references therein.
- [2] G. Medeiros-Ribeiro, D. Leonard, and P.M. Petroff, Appl. Phys. Lett, **66**, 1767 (1995).
- [3] G. L. Yua et al., PNAS, **110**, 3282 (2013).
- [4] see, for example, K. Lai et al., Rev. Sci. Instruments, **78**, 063702 (2007).
- [5] L. Lei et al., Journal of Physics Comm., **2**, 025013 (2018).

[6] This research was supported by CNPq and FINEP (Brazil).

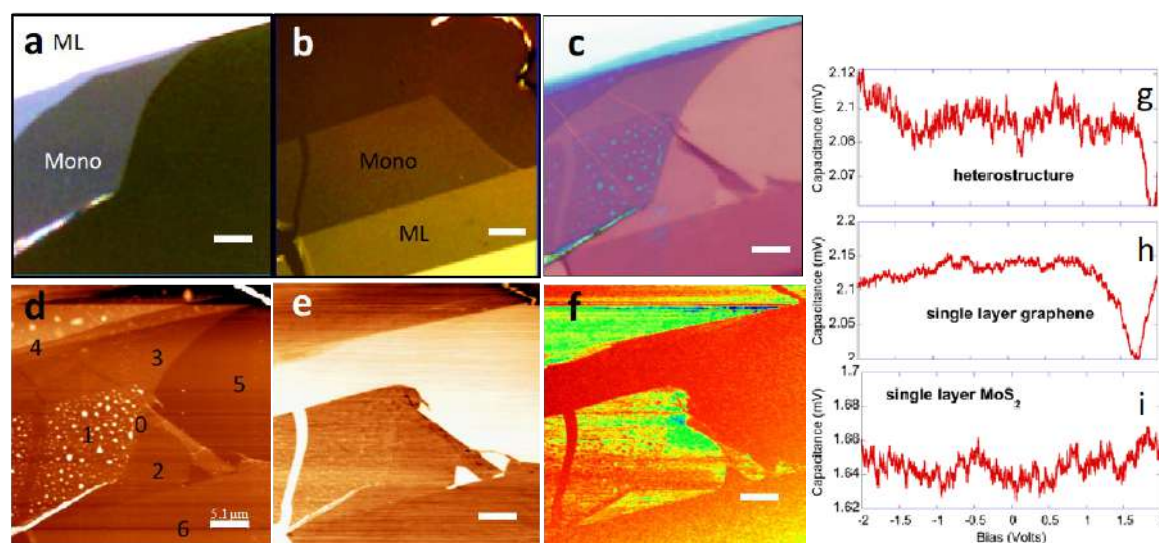


Figure 1: a) optical image of exfoliated MoS<sub>2</sub> before transfer; b) optical image of exfoliated graphene before transfer; c) Optical image of combined MoS<sub>2</sub>/Graphene heterostructure after transfer; d) Corresponding AFM topo image; e) permittivity maps of the same region, exhibiting the different contrast mechanisms of each layer; f) dC/dV at 0 bias showing charge redistribution over a surface (blue – high concentration, red, low or negligible charge); g, h, i) Capacitance Voltage traces taken at spots 1, 2, and 3 (see fig. 1d), corresponding to heterostructure, single layer graphene, and single layer MoS<sub>2</sub>, respectively. Bar corresponds to 5  $\mu$ m, and color in the images keyed to refractive index contrast (a-c), height with bright corresponding to taller features (d), permittivity amplitude, with dark being larger values (e), and dC/dC amplitude which is proportional to charge, with blue as largest concentration.



## Substrate Influencing Friction of 2D Materials

Brito, T.G-L.\*<sup>1,2</sup>, Almeida, C.M.<sup>2</sup>

<sup>1</sup>Universidade Federal do Rio de Janeiro, Rio de Janeiro, 25245-390, Brazil

<sup>2</sup>Materials Metrology Division, National Institute of Metrology, Quality and Technology (Inmetro), Rio de Janeiro, 25250-020, Brazil

\* tglbrito@colaborador.inmetro.gov.br

Special attention has been given on the use of 2D materials as solid lubricants for controlling friction and wear at interfaces. Frictional properties of 2D materials, like graphene, have been shown to be highly dependent on numerous factors, such as thickness, speed of the sliding contact, crystallographic direction [1], strain and roughness [2]. The supporting substrate plays a critical role in the frictional response of 2D materials. The interaction between 2D materials and substrate in addition with the interaction between 2D materials and a sliding contact leads to a scenario with different energy dissipation processes that are not well understood [3]. The purpose of this study is to investigate the dependence of friction of 2D materials with surface roughness, modifying the supported substrate. Friction was evaluated between a single asperity tip of nanometer size and a graphene (Fig. 1b) and graphene oxide (GO) (Fig. 1a) deposited onto MICA and silicon oxide (SiO<sub>2</sub>) substrates. Graphene were micromechanically exfoliated into the substrates with a scotch-tape. GO diluted in aqueous solution was dripped onto substrates. Topographical and tribological measurements were performed with Atomic Force Microscope (AFM) in ambient conditions. Raman spectroscopy was used to identify the numbers of graphene layers. The friction and surface roughness of monolayer materials are highly dependent on the substrate. It was observed that friction in monolayers is higher when substrate roughness is higher, that is, friction of graphene onto SiO<sub>2</sub> is higher than onto MICA. Friction forces in graphene decrease while increase the number of layers (Fig. 2a), for both studied substrates. This dependence was not observed for GO layers, independently of the substrate. Roughness of graphene follows substrate roughness for the first 40 layers, than it behaves like graphite, without the influence of substrate on frictional properties (Fig. 2b). The friction change linearly with the normal load revealing different angular coefficient according with the number of layers and the substrate. This study contributes to understand the factors that influence friction in graphene and graphene oxide, the next generation of solid lubricant in nanotechnology.

### References

- [1] C. M. Almeida et al., Scientific Rep. 6 (2016) 31569.
- [2] Chun Hung Liu et al., Nature 462 (7271) (2009) 339-341.
- [3] Meagan B. Elinski et al., J. of Physics D: Applied Physics 50 (2017) 103003.

### Acknowledgments

This research was supported by FAPERJ, Rio de Janeiro, Brazil. Authors would like to thank Raphael Verdan for supplying graphene oxide samples.



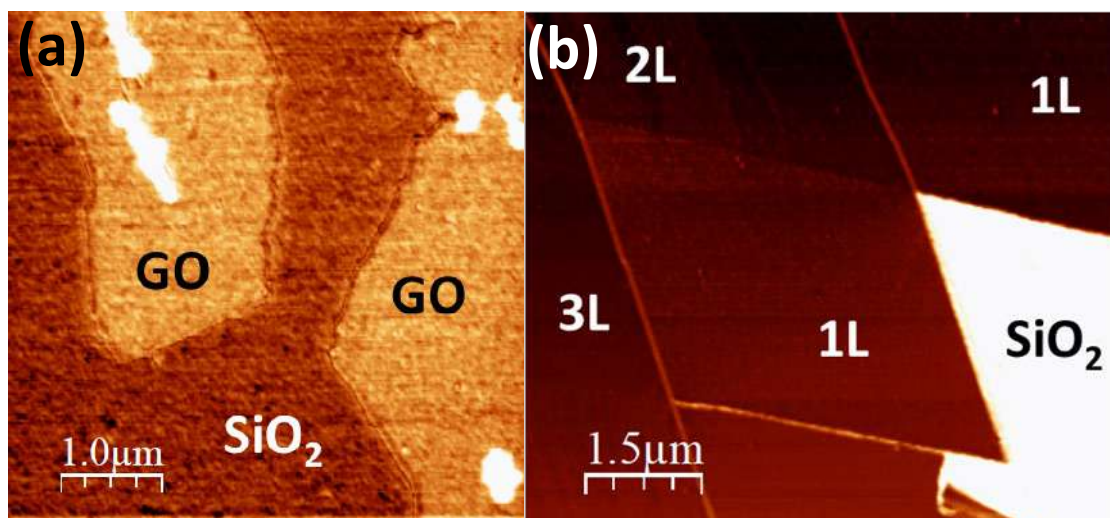


Figure 1. Friction force images obtained with AFM. In (a) Graphene Oxide (GO) monolayer deposited onto SiO<sub>2</sub> showing that friction in GO is higher than in the substrate. In (b) friction image of graphene monolayer (1L), bilayer (2L) and trilayer (3L) onto SiO<sub>2</sub>. It can be observed that friction in graphene is lower than friction of SiO<sub>2</sub>.

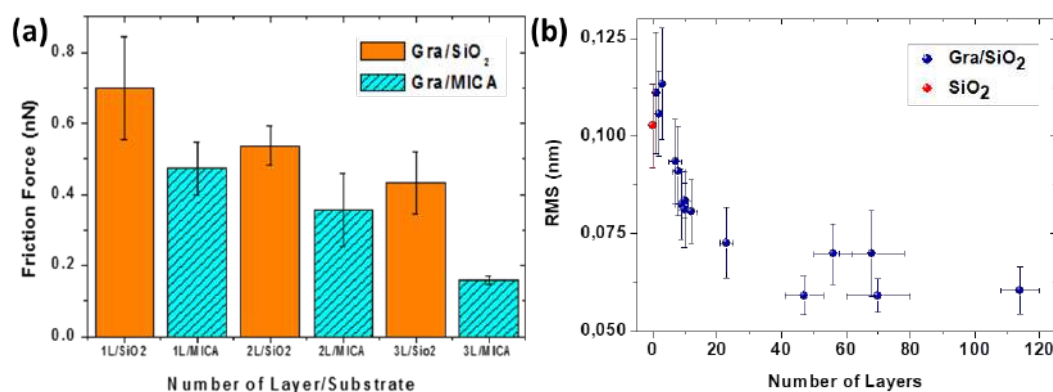


Figure 2. (a) Dependence of friction in graphene with the number of layers deposited onto SiO<sub>2</sub> (orange) and onto MICA (blue). (b) The Root Mean Square (RMS) of graphene onto SiO<sub>2</sub> as a function of number of layers (blue circles). The red circle shows the RMS of the substrate.

## The Sliding of Single Asperities in Graphene

Felipe Ptak<sup>1\*</sup>, Clara M. Almeida<sup>2</sup> and R. Prioli<sup>1</sup>

<sup>1</sup>. Departamento de Física, Pontifícia Universidade Católica, Marques de São Vicente 225, Rio de Janeiro, 22453-900, Brazil

<sup>2</sup>. Divisão de Metrologia de Materiais, Instituto Nacional de Metrologia, Normalização e Qualidade Industrial (INMETRO), Av. Nossa Senhora das Graças 50, Duque de Caxias, Rio de Janeiro, 25250-020, Brazil

In recent years, graphene and other low-dimensional materials have been widely studied due to its prominent properties and potential applications. One possibility is to use it as a solid lubricant and coating material [1], making the study of graphene tribology relevant. On the nanoscale, friction is often measured by an atomic force microscope (AFM) and modeled by the Prandtl-Tomlinson (PT) model [2, 3] characterized by the stick-slip motion. The sliding speed is considered an important parameter in tribology [4], as it may reveal important aspects on the friction mechanisms of a system. In this work, the influence of sliding speed between a silicon tip, considered as a single asperity, and graphene sheets was measured with the use of an AFM. Friction forces were measured on mechanically exfoliated graphene flakes with AFM. We found that friction decreases as the number of layers increase, and sliding speed are more relevant for monolayer than multilayer graphene. Figure 1a shows an AFM topography of a graphene flake containing various layers. A friction map of the same region showing higher friction for single layer graphene and lower friction for multilayer graphene is shown in Figure 1b. Corresponding friction histograms for single and multilayer graphene are depicted in Figures 1c and 1d, respectively. With the PT model, we were able to extract and estimate important parameters in the friction mechanism, such as the potential barrier  $\Delta V$  involved in a slip event and frequencies at which such slip event occurs. As a conclusion, we note that the friction process could be facilitated with an appropriate set of cantilever parameters.

### References

- [1] K.-S. Kim et al., ACS Nano 5 (2011) 5107.
- [2] L. Prandtl, Angew. Math. Mec. 8 (1928) 85.
- [3] G.A.A. Tomlinson, Phil. Mag. 7 (1929) 905.
- [4] E. Riedo et al., Phys. Rev. Lett. 91 (2003) 084502.
- [5] This research was supported by the Brazilian funding agencies CAPES, CNPq and FAPERJ.

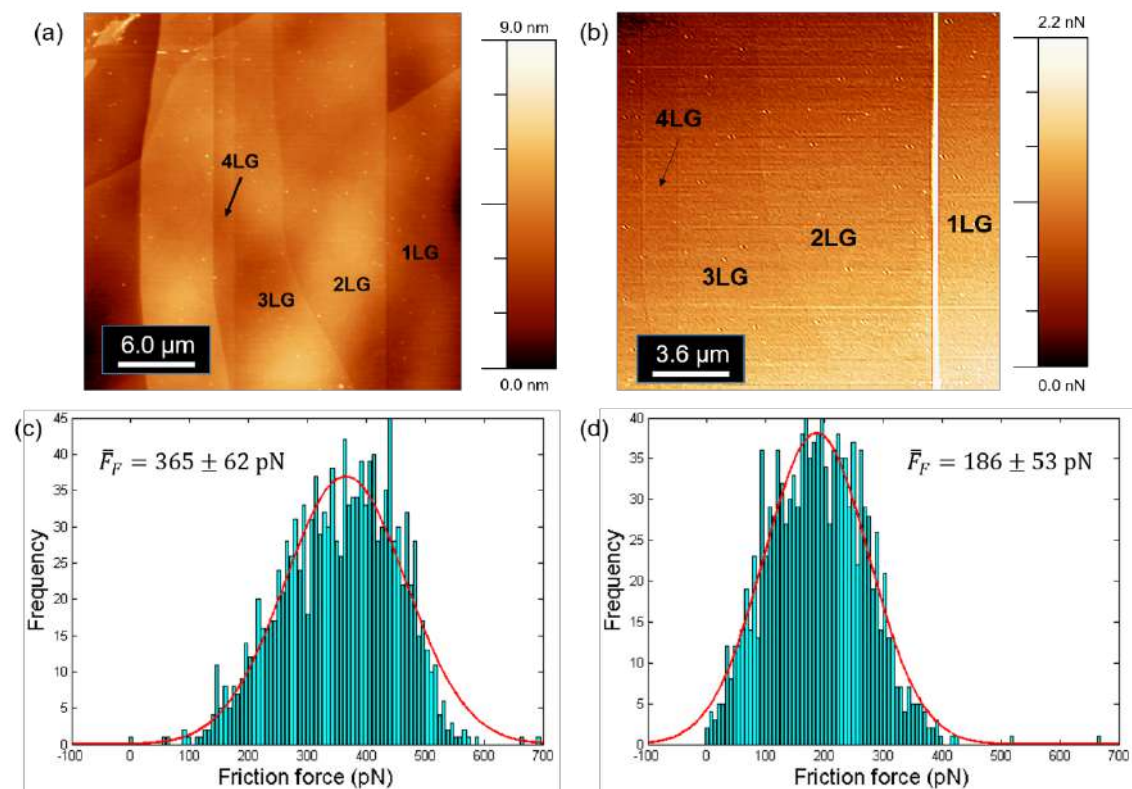


Figure 1: (a) Topography image of a graphene flake with multiple layers; (b) Friction map of the same flake; (c) Friction histogram for monolayer graphene; (d) Friction histogram for multilayer graphene.

## Morphology effect on the capacitive properties of manganese oxide nanostructures prepared by pulsed laser deposition

J. de Araújo Pereira<sup>1</sup>, J. N. Lacerda<sup>1</sup>, D. F. Franceschini<sup>1,2</sup>, E. A. Ponzio<sup>1,3</sup>, F. B. Mainier<sup>1</sup>, Yutao Xing<sup>1,2\*</sup>

1. Departamento de Engenharia Química e de Petróleo, Universidade Federal Fluminense, Niterói, 24210-346, Brasil

2. Instituto de Física, Universidade Federal Fluminense, Niterói, 24210-346, Brasil

3. Instituto de Química, Universidade Federal Fluminense, Niterói, 24020-141, Brasil

Supercapacitors are an interesting type of energy storage device with desirable properties as long life-time, high power density, faster charge/discharge rate and environmental friendliness [1]. The use of manganese oxide (MO) has been frequently reported due to the high energy storage capacity, abundance in nature and low cost [2,3]. MO does not possess fast protonic diffusion in bulk form, and thus the pseudo-capacitance is primarily contributed by surface reactions. Therefore the morphology of the MO electrodes plays an important role in performance of a supercapacitor. However, there is no report yet on the pure morphology effect due to the difficulty of a controlled morphology modification. In this work we prepared manganese oxide nanostructures by pulsed laser deposition (PLD), using metallic Mn target at room temperature and in different pressures of O<sub>2</sub> atmosphere. After deposition, all the samples are heat-treated at 300°C for 90 minutes in air in order to improve the mechanical bonding properties. The morphology of the MO nanofoam was investigated by field-emission scanning electron microscopy and results are shown in figure 1. With the increase of gas pressures in the chamber, the deposited samples show a gradually morphology change from dense film (pressure: 0.10 Torr), agglomerated nanoparticles with cracks (0.50 torr), low dense agglomerated nanoparticles (1.0 Torr) to very low dense foam-like nanostructure (2.0 Torr). Raman spectroscopy indicates that all the samples have the same chemical composition. The capacitive properties of the deposited samples were tested by Cyclic Voltammetry using an electrochemical workstation in a 0.1 M Na<sub>2</sub>SO<sub>4</sub> aqueous solution. The mass of the material deposited on the substrate was determined by a quartz crystal balance mounted in the PLD chamber. The specific capacitances (C<sub>s</sub>) of the samples are shown in figure 2. Since all the samples have the same chemical composition and the only difference among the samples is the morphology, the different C<sub>s</sub> values in figure 2 for different samples are of a pure morphology effect. One can see that although samples prepared in 2.0 Torr O<sub>2</sub> has lowest density, it does not have highest C<sub>s</sub> in all the scan rates. With very slow scan rate, the sample prepared in 0,50 Torr shows highest C<sub>s</sub> with a value close to 1000 F/g. The sample prepared at 1.0 Torr has highest C<sub>s</sub> values in the other scan rates. The results indicate that it is not always good to increase the porosity of the MO electrodes for the application in supercapacitors [4].

\*xy@id.uff.br

[1] D. P. Dubal, O. Ayyad, V. Ruiz, and P. Gmez-Romero, Chem. Soc. Rev. 44, (2015) 1777.

[2] A. Gonzlez, E. Goikolea, J. A. Barrena, and R. Mysyk, Renew. Sust. Energ. Rev. 58, (2016) 1189.

[3] W. Wei, X. Cui, W. Chen, and D. G. Ivey, Chem. Soc. Rev. 40, (2011) 1697.

[4] This research was supported by CNPq, FAPERJ and CAPES (Brazil). The authors thank LaMAR/CAIPE at UFF for usage of the facilities.

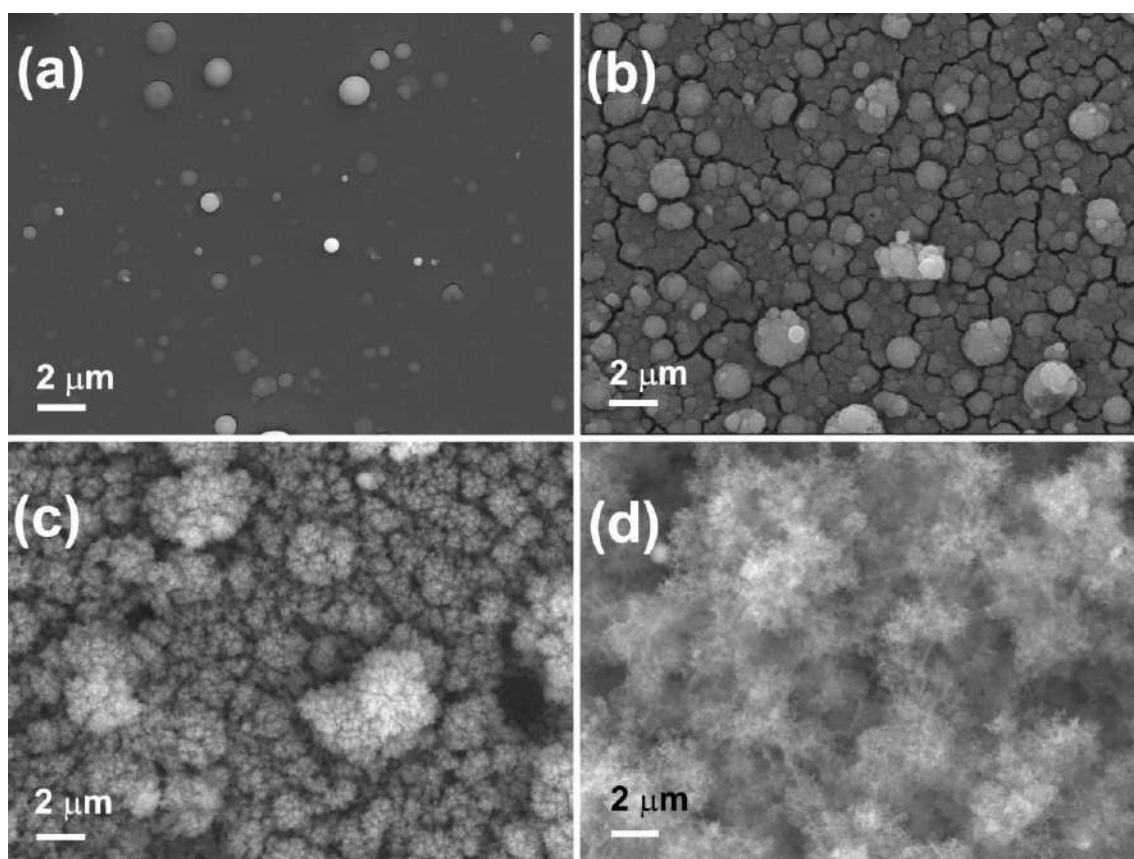


Figure 1. SEM images of manganese oxide nanostructures prepared in (a) 0.10 Torr, (b) 0.50 Torr, (c) 1.0 Torr and (d) 2.0 Torr  $O_2$ .

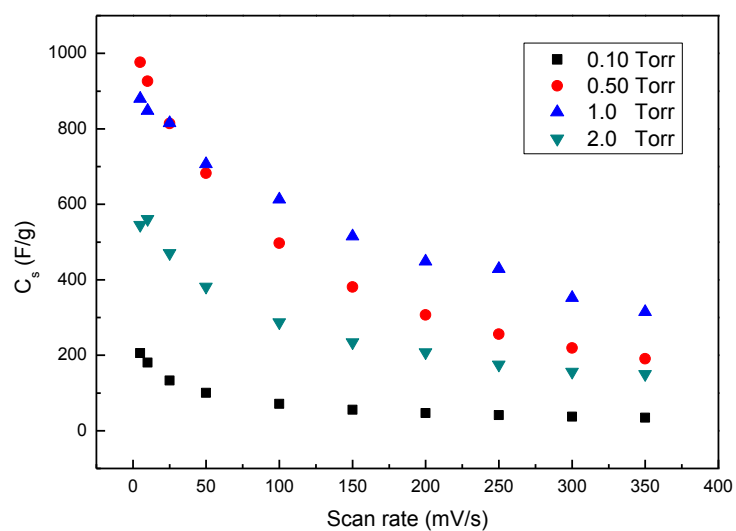


Figure 2. Specific capacitance of the manganese oxide electrodes as a function of voltage scan rates.



## **Characterization of Ceramic Materials Coated with Nanostructured Diamond by Microscopy Techniques**

Rodrigo Pinto de Souza\*, Marcia Maru, Braulio Archanjo, Carlos Achete, Geronimo Perez

Divisão de Metrologia de Materiais, Instituto Nacional de Metrologia, Qualidade e Tecnologia (INMETRO), Duque de Caxias-RJ, 25250-020, Brasil;

Diamond film coating technologies have gained strength in recent years in the field of materials engineering and metallurgy, providing materials with increased mechanical properties of interest promoting greater hardness combined with good thermal conductivity and corrosion resistance. The Materials Metrology Division (Dimat) is equipped with a FEI Company's Helios NanoLab 650 dual-beam (SEM) scanning electron microscope, which was used throughout this project. This equipment has a coupled focussed ion beam (FIB) which has high grinding power capable of producing cross section analysis and preparing samples for transmission electron microscopy (TEM). The chemical vapor deposition (CVD) technique used in diamond film synthesis is done by a reactor operating at 2300 °C in CH<sub>4</sub>/H<sub>2</sub> atmosphere, with specific deposition parameters (pressure, temperature, filaments distance). The deposition was made at the University of Aveiro, with films grown with thicknesses of 10 to 30 µm. A friction wear test was performed on Si<sub>3</sub>N<sub>4</sub> samples coated of diamond with to generate different regions of wear, in different environments, with a frequency of 1 Hz, totaling 14,400 oscillation cycles. Surface diamond wear was analyzed by SEM (Figure 1), as well as the characterization of the coated film nanostructure, combined with cross section analysis by FIB. The preparation process consisted of ionic wear of a small rectangular area of approximately 10 to 20 µm in length. Based on the analysis, it was possible to identify the crystalline structures and their state, in different regions of the sample. Figure 2 shows a cross-section analysis of the diamond layer showing the presence of micro and nanocrystalline diamond (MCD and NCD).

- [1] F.A. Almeida et al., Mater. Sci. Eng., (2007) 1443–1447.
- [2] C.S. Abreu et al., Surf. Coat. Techn. 200 (2006) 6235–623.
- [3] C.S. Abreu et al., Diam. Relat. Mater. 15 (2006) 739-744.
- [4] This research was supported by FAPERJ (Brazil).

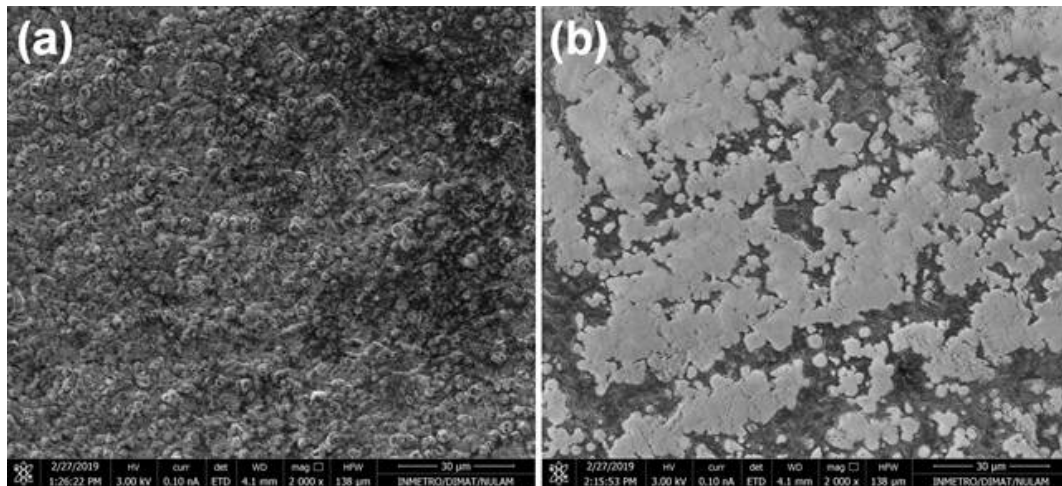


Figure 1 - SEM images of the diamond coat surface: (a) virgin region and (b) worn out area.

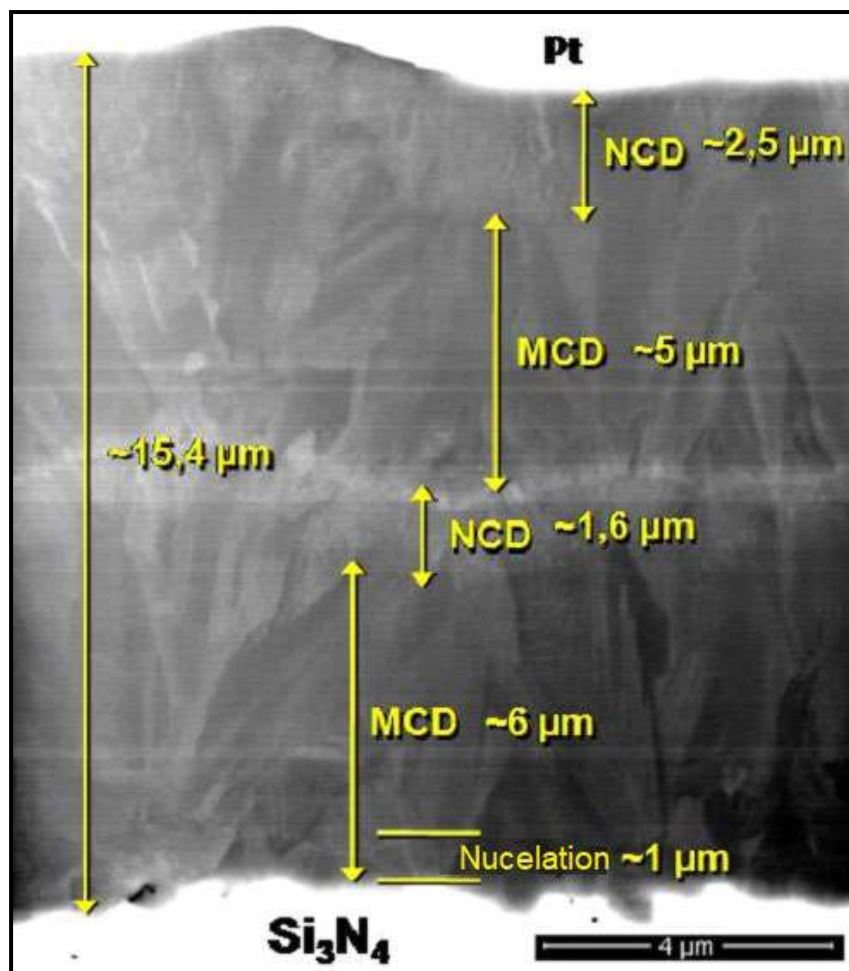


Figure 2 - Cross section analysis of the diamond layer showing a presence of micro and nanocrystalline diamond (MCD and NCD).

## Characterization Of Nanosized Hydroxyapatite And Hydrogel Composite For Biomaterials Applications

Luíza Braga Ferreira dos Santos<sup>1\*</sup>, Francielly M de S Soares<sup>1</sup>, Emília dos Santos Monteiro<sup>1</sup>, Paula Anastácia Moraes Cairo Gomes<sup>1</sup>, Carlos Nelson Elias<sup>1</sup>

<sup>1</sup> Instituto Militar de Engenharia, Seção de Engenharia de Materiais – SE8, Rio de Janeiro, Brasil. luizabraga\_f@hotmail.com

Nowadays, the methodology for cartilage repairing and bone tissue fail filling is the use of synthetic biomaterials in the form of particles or hydrogels. The use of hydrogels has demonstrated great potential for use as three-dimensional biomimetic scaffolds, owing to their high water content, similar to the natural extracellular matrix (ECM). Another application is for porous scaffold for cell transplantation and proliferation. The hydrogels has low invasive properties and ability to match irregular defects. There is possible to manipulate a big number of proper using different procedures of hydrogels synthesis [1, 2]. PNIPAAm is a remarkable smart hydrogel, which changes its structure with heating. In the present work, two hydrogels (HN1.0.3 and HN1.1.3) were synthesized utilizing the same reagents (MBA (N,N-methylenebis(acrylamide)) as crosslinker and NMB (Sodium Metabisulfite) with APS (Ammonium Persulfate) as active reagents with addition of 30% w/w of nano hydroxyapatite [1]. The difference between HN1.1.3 and HN1.0.3 was the synthesis processes. The HN1.1.3 was synthesized by magnetic agitation, while for the HN1.0.3 was not used the agitation system [3]. The Infrared analysis showed that both the composites have the same functional groups. The hydrogels were analyzed in the SEM (Field Emission Gun FEI QUANTA FEG 250 - FEI Corporation, Hillsboro, Oregon, USA). Figure 1a and 2a show that HN1.0.3 has more porous and cavities than HN1.1.3. The semi-quantitative chemical analysis was performed with EDS using a Bruker detector, controlled by the Quantax CrystAlign Software, coupled to the SEM (FEG Quanta FEG 250). The element mapping (Fig 1B and 2B) demonstrated that the HN1.0.3 has more homogeneous calcium distribution on the surface than HN1.1.3. (Figure 3) showed. The EDS spectrum reveals the elemental chemical composition on the hydrogel surface. Figure 3 shows that the HN1.0.3 has more calcium concentration than HN1.1.3, corroborating with the mapping result. Based on the experimental is concluded that changing synthesis parameter is possible to increase the calcium amount on the surface, so as to the number of cavities and porous presents. The morphology is essential for the interaction between the scaffold and the cells.

### REFERENCES

- [1] Ahmed, E. M.. Hydrogel: Preparation, characterization, and applications: A review. *Journal Of Advanced Research* (2015) 105.
- [2] F. You, X. Chen, D. M. L Cooper, T. Chang, B. F. Eames. Homogeneous hydroxyapatite/alginate composite hydrogel promotes calcified cartilage matrix deposition with potential for three-dimensional bioprinting. *Biofabrication*, 2018, 11(1), 015015.
- [3] M. A. HAQ; Y. Su; D. Wang. Mechanical properties of PNIPAM based hydrogels: A review. *Materials Science And Engineering: C* (2017) 842.



## ACKNOWLEDGMENT

This research was supported by CAPES, CNPq, FAPERJ and FINEP.

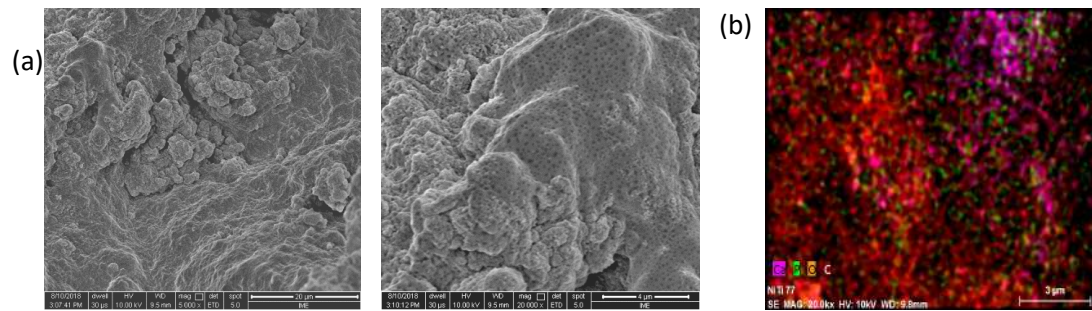


Figure 1: (a) SEM morphology of HN1.1.3 with magnification of 5.000x (left side) and 20.000x (right side). (b) chemical composition mapping of the biocomposite with identification of the distribution of calcium (pink), phosphorus (green), oxygen (orange) and carbon (red). Increase of 10,000x.

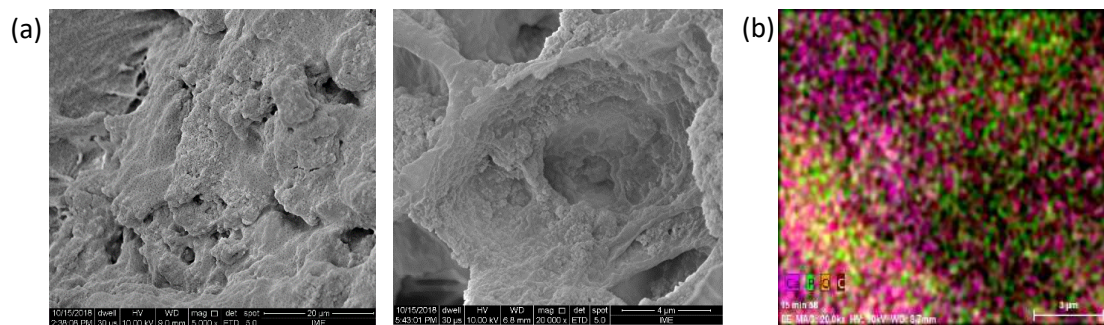


Figure 2: (a) SEM morphology of HN1.0.3 with magnification of 5.000x (left side) and 20.000x (right side). (b) chemical composition mapping of the biocomposite with identification of the distribution of calcium (pink), phosphorus (green), oxygen (orange) and carbon (red). Increase of 10,000x.

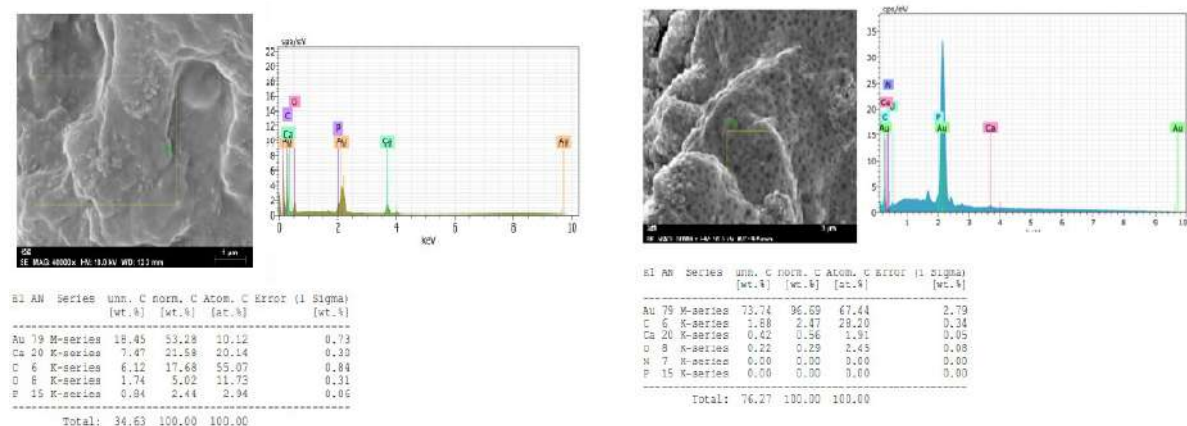


Figure 3: EDS spectrum, chemical composition table and composite particle in the region where the analysis was performed. (a) HN1.0.3 EDS analyses. (b) HN1.1.3 EDS analyses.



## Ultra-High Conductive Hollow Channels Guided By Bamboo Bio-Template For Electric And Electrochemical Devices

Omar Ginoble Pandoli<sup>1\*</sup>, Reginaldo Gomes neto<sup>2</sup>, Nathalia Rodrigues de Oliveira<sup>2</sup>, Ana Claudia Fingolo<sup>2</sup>, Mathias Strauss<sup>2</sup> and Murilo Santhiago<sup>2</sup>

<sup>1</sup>. Departamento de Química, PUC-RIO, Rio de Janeiro, Brasil.

<sup>2</sup>. Laboratório Nacional de Nanotecnologia, LNNano/CNPEM, Campinas, Brasil.

\*email: omarpandoli@puc-rio.br

The fabrication of well-aligned arrays of microfluidic channels is very challenging using conventional microfabrication processes. Nature is unique on creating complex hierarchical architectures, for instance, some wood-derived materials have aligned channels that offers the possibility to add new functions to biological templates, necessities for green electronic, biological devices and energy applications.[1] In order to explore novel hierarchical architectures, biological structures have been used as bio-templates for the fabrication of functional biodevices. Understanding the complexity of living systems, its anisotropic structures, as well as incorporation of metal ions,[2] metal-organic framework (MOF),[3] conductive organic polymers[4] and nanomaterials[5,6] to increase or add new functionalities to plants, is important to promote plant science and bio-nanotechnology devices. Herein, in this work, we developed for the first time a room temperature fast prototyping method to fabricate ultrahigh conductive arrays of conductive microchannels using bamboo matrix as bio-template. Considering its lightweight and strengthened mechanical properties, bamboo is the best candidate to be explored as a lignocellulosic natural resource for a scalable production of eco-friendly, sustainable, low cost and portable electronic and electrochemical biodevices. Our method consists of flowing silver ink through the array of microchannels in bamboo *Dendrocalamus Giganteus* and removing the excess of ink by flowing nitrogen. X-rays microtomography, EDS and MEV were used to characterize the formation of hollow conductive channels of bamboo specimen (Figure 1). We achieved a regioselective coating of the bamboo vascular bundles with a conductivity of  $9.3 (\pm 4.0) \times 10^5 \text{ S m}^{-1}$  ( $\sigma_1$ ), which is the highest value reported so far for tracks along the vascular network of wood-derived materials. Moreover, the hollow conductive channels enabled the fabrication of unprecedented electronic and electrochemical bamboo-based devices that we call “bambootronic” technology. As a proof-of-concept we will present 3D electrical circuits, multi-channel microfluidic heater, and fully integrated carbon-based electrochemical cell using carbon black nanostructures (Figure 2).

### References

- [1] H. Zhu et al., Chemical Reviews 116 (2016) 9305.
- [2] O.G. Pandoli et al., ACS Sustainable Chemistry & Engineering 7 (2019) 3267.
- [3] J.J. Richardson et al., Small 14 (2018) 1.
- [4] R. Gabrielsson et al., Science Advances 1 (2015) 150.
- [5] O.G. Pandoli et al., Journal of Coatings Technology and Research. 1 (2019) 1.
- [6] S.M. Faltermeier et al., Nature Materials 13 (2014) 400.
- [7] The authors are grateful for the financial support from the Serrapilheira Institute (grant number Serra-1709-17482) and the LNNano/CNPEM. O.P. thanks FAPERJ-Brazil for the JCNE fellowship (E-26/203.281/2016).



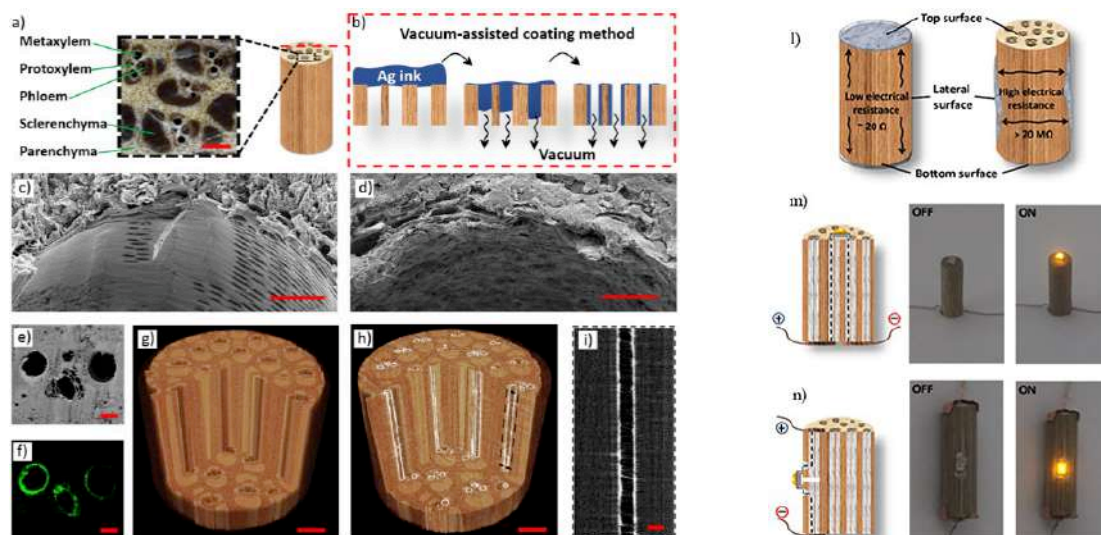


**Figure 1.** a) Optical and schematic images of bamboo and its main structures [scale bar is 500  $\mu\text{m}$ ]. b) Scheme of the Ag-coating method for hollow conductive channels fabrication. c) SEM images of metaxylem channel with its free surface pits and d) with internal metal coated surface [scale bars are 20  $\mu\text{m}$ ]. (e-f) SEM image of the top face of bamboo and its respective Ag mapping using EDS [scale bars are 100  $\mu\text{m}$ ]. g-h) X-rays microtomography ( $\mu\text{CT}$ ) 3D images of bamboo template before and after silver coating [scale bars are 500  $\mu\text{m}$ ]. i) 2D  $\mu\text{CT}$  magnification of single vascular channel with internal wall metal deposition (thickness  $10.3 \pm 2.2 \mu\text{m}$ ) [scale bar is 100  $\mu\text{m}$ ]. l-n) 3D electrical circuits with high conductivity ( $9.3 \times 10^5 \text{ S m}^{-1}$ ) by means of regioselective Ag coating.

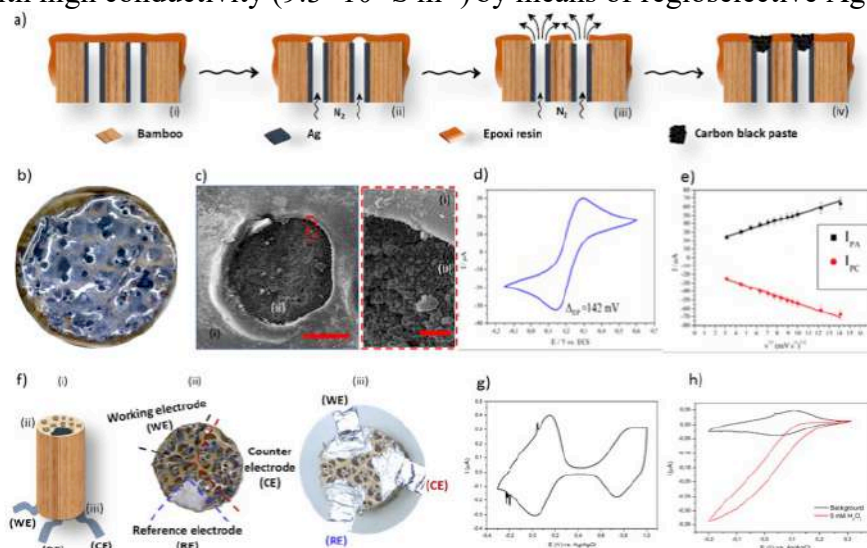


**Figure 2.** a) Schematic fabrication process of the carbon-based electrode. b) Optical image of the bamboo bottom-face modified with carbon black paste with several carbon microelectrodes; c) SEM image and relative insight of the cover epoxy resin onto bamboo bottom-face (i) and packed carbon black paste into an individual microchannel (ii) [scale bars are 50 and 5  $\mu\text{m}$ , respectively]. d) Cyclic voltammograms using a modified bamboo as working electrode. e) Graph of peak current vs.  $V^{-1/2}$ ; f) Schematic layout of bamboo-based electrochemical cell with working, counter and reference electrodes fully integrated in one single bamboo specimen: (i) top (ii) and bottom surface (iii) illustrating the electrodes and electrical contacts, respectively. g) Cyclic voltammogram of the bamboo-based electrochemical cell modified with prussian blue. h) Cyclic voltammograms in the absence and presence of hydrogen peroxide.

## Morphological Characterization of Corrosion Products of Guyed Transmission Towers Anchor Rods

Bruna G. Dias<sup>1\*</sup>, Tiago S. de Matos<sup>1</sup>, Mariana O. G. P. Bragança<sup>2</sup> and Alessandro Cesar de Sousa Berrêdo<sup>3</sup>

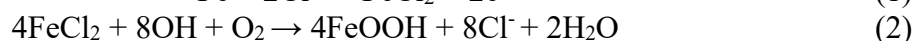
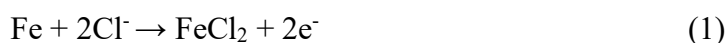
<sup>1</sup>. Lactec, Federal Univesity of Paraná /UFPR, Curitiba - Brazil

\*bruna.dias@lactec.org.br

<sup>2</sup>. Lactec, Curitiba - Brazil

<sup>3</sup>. Transmissora Aliança de Energia Elétrica S.A. –TAESA, Rio de Janeiro – Brazil

Metal structures become subject to soil corrosion when buried, due to physical-chemical interactions between the material and the environment to which it is exposed that may result in its deterioration. It is estimated that around 4% of GDP of several countries are direct costs with corrosion (i.e. preventing corrosion and maintaining or replacing lost materials). The soil corrosivity are related with different properties, such as, presence of sulfate and chloride ions, oxygen concentration, resistivity, total acidity, among others <sup>[1]</sup>. The corrosion process usually starts on the material surface and can affect its performance. Thus, the morphological study of corrosion products and their characterization helps to understand this process. Fragments of corroded galvanized steel anchor rods, removed from the field after maintenance were analyzed without prior treatment (in nature) by Scanning Electron Microscopy (SEM-FEG) and Energy Dispersion Spectroscopy (EDS). Several scientific articles mention the characterization of steel corrosion products, and iron oxyhydroxides (lepidocrocite, goethite and akaganite) and iron oxides (magnetite and maghemite) are frequently found. From the results of the analysis, different morphologies were observed and the extent of corrosion throughout the fragment, the morphologies found correspond to the lepidocrocite, akaganite and goethite minerals. The lepidocrocite was characterized by different morphologies, such as laminar and globular formations shown in Figure 1. Goethite, on the other hand, was easily found in acicular forms (needles), as can be observed in Figure 2 (a). The morphology of the corrosion product assessed may also depend on the magnification used in the SEM for observation, this may occur since the composition of the rust layer will depend on the conditions of the medium and the exposure time and mixtures of phases, because the corrosive process is not homogeneous. Moreover, lepidocrocite is considered a primary corrosion product, and can be transformed in more stable products, e.g. goethite <sup>[2]</sup>. Another morphology found, was the rod type, observed in Figure 2 (b), being this a formation of akaganite. High chloride contents were found in the rust composition, described in Table 1. These ions, provided from the soil, can act as a catalyst and can accelerate the oxyhydroxides formation and corrosive process, according reaction presented in Equations 1 and 2 <sup>[3]</sup>.



### ACKNOWLEDGEMENTS

The authors are grateful for the infrastructure and support in human resources and funding to TAESA, P&D 5012-0045 / 2016, ANEEL, LACTEC, CNPq Law 8010/90 (LI 15 / 2187214-1, LI 14 / 4695814- 5, LI14 / 3410726-9), P&D COPEL 6491-0301 / 2013, CNPq / PIBIT grant DT, process 302672 / 2016-8, and the Federal University of Paraná - PIPE / UFPR.

The variety of morphologies found represents the complexity of soil corrosivity, since it depends on several factors. The analysis performed are important to understand the corrosion mechanism and select materials with best performance for this environment to extend the structure service life. Other techniques, such as X-ray diffraction (XRD) and Raman Spectroscopy are complementary and additional research should be conducted.

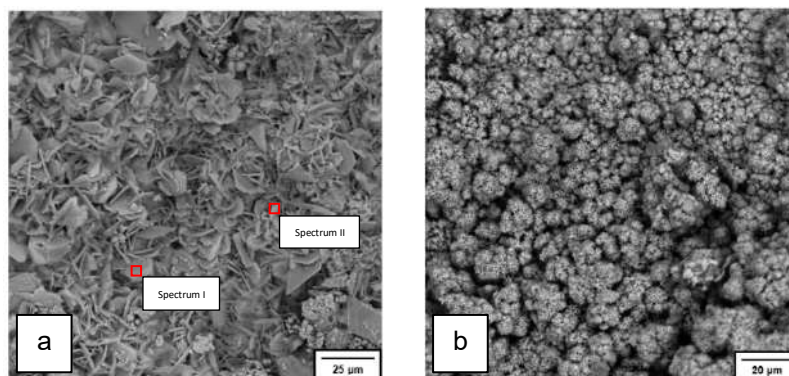


Figure 1: Laminar formation of lepidocrocite (a). Globular formation of lepidocrocite (b). The result of the EDS analysis of the demarcated areas is shown in table I.

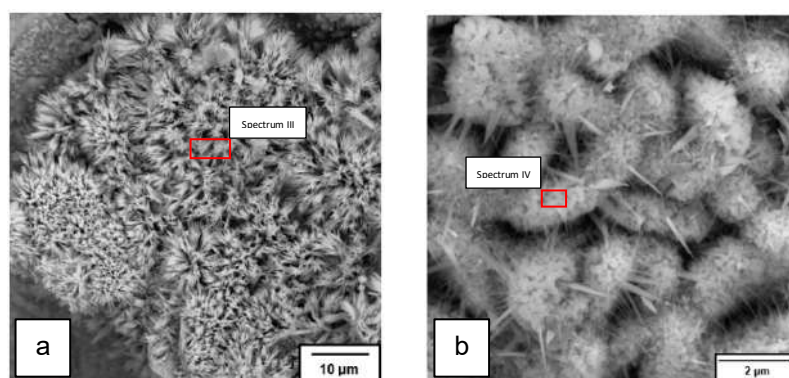


Figure 2: Corrosion product micrograph. Formation of goethite needles (a). Formation of rod type of akaganeite (b). The result of the EDS analysis of the demarcated area is shown in table I.

Spectrum	O	Fe	Cl	C
I	39,1	47,1	8,4	5,4
II	39,7	44,4	8,8	7,1
III	45,9	51,5	1,8	-
IV	48,9	42,6	2,8	5,7

Table 1: Data from the EDS spectra in different regions of the corroded fragment, all results are given in “weight %”.

## REFERENCES

- [1] ROBERGE, Pierre R. Corrosion Engineering: Principles and Practice. 1. ed. McGraw-Hill Education, 2008.
- [2] J. Alcantara, B. Chico, J. Simancas, I. Díaz, D. de la Fuente, and M. Morcillo, Materials Characterization **118**, 65–78, 2016.
- [3] Xin Zhang, Kui Xiao, Chaofang Dong, Junsheng Wu, Xiaogang Li, Yizhong Huang, Engineering Failure Analysis **18**, 1981–1989, 2011.

## Spray-forming of Al-matrix Composite Reinforced with Quasicrystals

Guilherme Zepon<sup>1</sup>, Luiz Paulo Mendonça e Silva<sup>2</sup>, Witor Wolf<sup>3</sup>, Walter José Botta<sup>1</sup>.

<sup>1</sup>Departamento de Engenharia de Universidade Federal de São Carlos, São Carlos-SP, Brasil.

<sup>2</sup>Programa de Pós-graduação em Engenharia Metalúrgica, de Materiais e Minas, Universidade Federal de Minas Gerais, Belo Horizonte-MG, Brasil.

<sup>3</sup>Departamento de Engenharia Metalúrgica e de Materiais, Universidade Federal de Minas Gerais, Belo Horizonte-MG, Brasil.

\* corresponding author e-mail: [zepon@ufscar.br](mailto:zepon@ufscar.br)

Since their discovery by Shechtman et al. [1], quasicrystals (QCs) have drawn attention due to their peculiar atomic structure, which do not follow traditional laws of crystallography, and to their physical properties such as high hardness, low thermal conductivity, low friction coefficient and wear resistance [2]. One of the main drawbacks of these materials is their inherent brittleness, which restrains the fields of application that they could be used for. One way of overcoming this problem is by fabricating composites, e.g. Al-matrix composites, so the brittleness of the QC phase can be balanced with a ductile Al matrix. Most of the fabrication of such composites are based on rapidly solidification or powder metallurgy methods [3, 4]. Recently the composition range of formation of the decagonal Al-Cu-Fe-Cr QC was revealed [5] and it was shown that, unlike most stable QC-forming systems, this phase forms over a large portion of the quaternary system, with Al content up to 79% [6]. This opened a new possibility of fabrication of these composites using solidification techniques followed by appropriate thermal treatments to achieve equilibrium conditions [6]. The spray-forming process can result in microstructures close to the equilibrium of a given metallic alloy, due to its solidification features [7]. In this sense, we have applied this fabrication technique in a QC-forming alloy of atomic composition  $\text{Al}_{85}\text{Cu}_6\text{Fe}_3\text{Cr}_6$ , that was appropriately designed to produce a microstructure based on Al-FCC and QC phase formation. The 1.5 Kg sample was fabricated using commercially pure metals and its phase formation was analyzed by XRD, SEM and TEM. Figure 1 shows the XRD pattern of the as-sprayed alloy, showing that it consists of Al-FCC, decagonal-QC and  $\omega\text{-Al}_7\text{Cu}_2\text{Fe}$ . It is impossible to distinguish the XRD pattern of the QC and its orthorhombic approximant (which can form depending on the processing conditions), so electron diffraction patterns are necessary to confirm the QC phase (Fig. 2). Figure 2 shows SEM and TEM images of the as-sprayed sample, and reveals the 3-phase microstructure, with the QC phase being the major phase, followed by Al-FCC and a small amount of the tetragonal  $\omega\text{-Al}_7\text{Cu}_2\text{Fe}$ . This is the first time a relatively large sample (mass above 1 Kg) of Al-matrix composite reinforced with QCs could be processed directly from the liquid phase and this opens a great deal of possibilities for industrial application of these materials, for example, as tribological protective materials.

### References

- [1] D. Shechtman, I. Blech, Physical Review Letters 53(20) (1984) 1951-1954.
- [2] J.-M. Dubois, Chemical Society Reviews 41(20) (2012) 6760-6760.



- [3] G.Y. Koga, A.M.B.e. Silva, W. Wolf, C.S. Kiminami, C. Bolfarini, W.J. Botta, *Journal of Materials Research and Technology* (2019).
- [4] W. Wolf, L.C. Rodriguez Aliaga, D.N. Travessa, C.R. Moreira Afonso, C. Bolfarini, C.S. Kiminami, W.J. Botta, *Materials Research-Ibero-American Journal of Materials* 19 (2016) 74-79.
- [5] W. Wolf, S.A. Kube, S. Sohn, Y. Xie, J.J. Cha, B.E. Scanley, C.S. Kiminami, C. Bolfarini, W.J. Botta, J. Schroers, *Scientific Reports* 9(1) (2019).
- [6] W. Wolf, C. S. Kiminami C. Bolfarini, W.J. Botta, to be published.
- [7] G. Zepon, N. Ellendt, V. Uhlenwinkel, C. Bolfarini, *Metallurgical and Materials Transactions A: Physical Metallurgy and Materials Science* 47(2) (2016) 842-851.

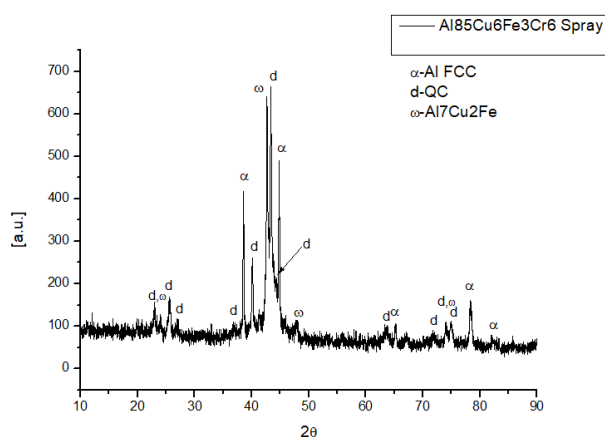


Figure 1. XRD pattern of the as-sprayed sample.

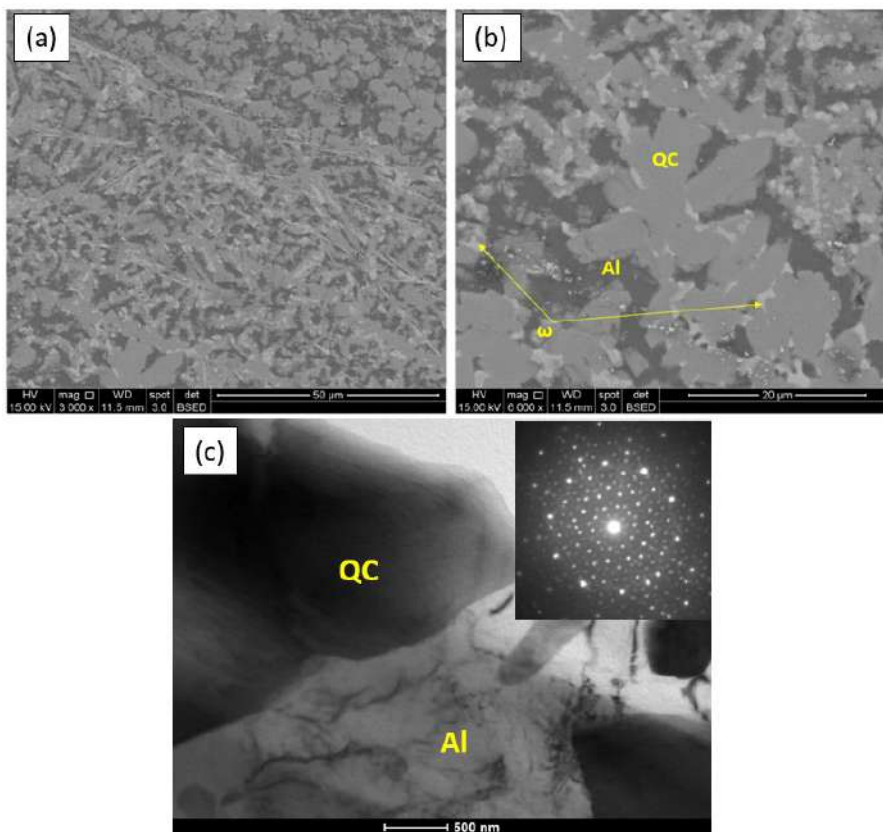


Figure 2. (a and b) SEM-BSE micrographs of the as-sprayed alloys. (c) TEM bright-field micrograph of the same alloy with the SAED pattern of the QC particle in the inset, displaying ten-fold rotational symmetry.



## Study Of Y Addition Effect On Microstructure Of Nickel-based Alloy 718

Rosa Maria Sales da Silvera<sup>1,\*</sup>, Alessandra Vieira Guimarães<sup>1</sup>, Jean Dille<sup>2</sup>, Leonardo Sales Araujo<sup>1</sup> and Luiz Henrique de Almeida<sup>1</sup>

<sup>1</sup> PEMM/COPPE/UFRJ, C.P.: 68505, Rio de Janeiro, R.J. 21945-970, Brazil

<sup>2</sup> SME/ULB, C.P.: 194/03, Av. F. D. Roosevelt 50, B-1050 Brussels, Belgium

\* [rosasilveira@metalmat.ufrj.br](mailto:rosasilveira@metalmat.ufrj.br)

The nickel-based alloy 718 is widely used in the petrochemical, nuclear and aerospace industries, due its great performance at high temperatures, up to 650°C, combining properties such as high mechanical strength, high corrosion and oxidation resistance, good conformability and weldability [1]. However, the need to improve its performance motivates researches for the continuous innovation of this alloy. Thus, the use of rare earth as modifying alloying elements has been considered in the last years for the development of superalloys [2]. Among them, yttrium (Y) is a prominent element, due to its higher availability, compared to other rare earths elements and, especially, for its positive contribution to properties of superalloys. Studies about Y addition on austenitic alloys and different nickel-based alloys showed that Y improved the tensile strength and oxidation and corrosion resistance, besides its desulfurizing effect on Ni alloys and a markable effect on carbides fragmentation [3–5]. However, excessive Y contents causes a reduction in its mechanical properties, thanks to the formation of Y-rich phases that grows at the expense of Y available in solid solution and also serve like preferential sites for crack nucleation [6]. The potential influence of the Y addition in Ni alloys and the limited number of works about its effect on microstructure, especially on alloy 718, motivated this research subject. Thus, the present work evaluated the effect of the variation of Y content on the microstructure of forged and solution annealed alloy 718. A reference 718 alloy (A) and two alloys with different Y contents (B and C) were analyzed. Their chemical composition is shown on Table 1. The alloys were melted in a vacuum induction furnace, homogenized at high temperature and hot-forged to round bars. Then, the alloys were submitted to a solution heat treatment at 1030°C for 1 hour, followed by quenching in water. A Jeol 7100FT scanning electron microscope on backscattering electrons mode and a FEI Titan G2 80-200 transmission electron microscope (TEM) with EDAX EDS, were employed to investigate the microstructure and identify yttrium-rich phases. The results were compared with thermodynamic calculations made with the ThermoCalc© software. The Y addition strongly contributed to MC carbide fragmentation. It was observed that the higher yttrium content, the smaller is the carbide mean size, causing a reduction up to 78% for alloy C, compared with the reference alloy. Additionally, Y contributed to reduce the occurrence of carbides strings, typical of alloy 718, that tends to align according the forging direction. Yttrium-rich particles were also observed next to MC carbides, Figure 1. EDS analysis showed Ni-Y and Y-O particles on alloys B and C. Besides, Y sulphides were also detected on alloy C. Thermodynamic simulations of stable phases formed for the compositions of alloys B and C, showed that  $\text{Ni}_6\text{Al}_2\text{Y}_3$ ,  $\text{Ni}_{17}\text{Y}_2$  and  $\text{Y}_2\text{O}_3$  are predicted to occur, Figure 2. These phases are consistent with Li *et al*, that identified the phase  $\text{Ni}_{17}\text{Y}_2$  in 16Mo-7Cr-4Fe nickel-based superalloy, containing 0.05-0.43wt.%. Zhou *et al* detected  $\text{Ni}_6\text{Al}_2\text{Y}_3$  in a nickel-alloy with 6 wt% Al and 0.014-0.041% of Y, as well. TEM/EDS analyses showed that, based on the high Ni/Y ratio, the  $\text{Ni}_{17}\text{Y}_2$  phase is predominant, showing also that a minor Al content can be dissolved in the particle, Figure 3.

## REFERENCES

- [1] R.J. Smith et al., *Aircr. Eng. Aerosp. Technol.* 73 (2001) 138–147.
- [2] K. Di Xu et al., *Rare Met.* 33 (2014) 111–126.
- [3] X. Jiawen et al., *Rare Met. Mater. Eng.* 45 (2016) 1413–1418.
- [4] P.J. Zhou et al., *Scr. Mater.* 57 (2007) 643–646.
- [5] F.C. Nunes et al., *Mater. Charact.* 58 (2007) 132–142.
- [6] X.L. Li et al., *Mater. Charact.* 95 (2014) 171–179.

The authors would like to thank CNPq (Brazil) for the financial support and Villares Metals. S.A. for supplying the alloys for this research.

Table 1 – Chemical composition of alloys (wt.%).

Alloy	Ni	Cr	Fe	Mo	Nb	Al	Ti	C	S	O	N	Y
A	52.7	17.81	19.71	2.90	5.10	0.518	0.972	0.026	0.0040	0.0042	0.0110	0.000
B	52.5	17.80	20.05	2.90	4.99	0.519	0.980	0.023	0.0016	0.0020	0.0055	0.052
C	51.4	17.62	20.69	2.91	5.01	0.549	0.966	0.024	0.0010	0.0012	0.0060	0.613

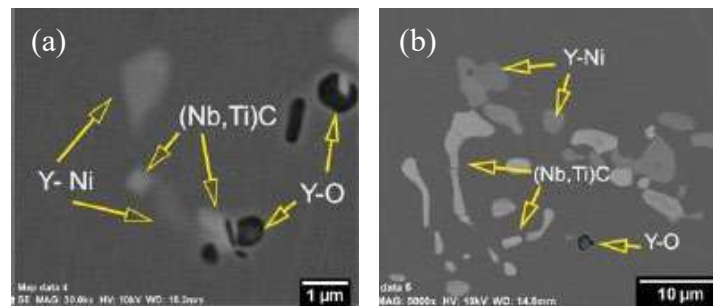


Figure 1 – SEM images showing the identified phases on alloys B (a) and C (b).

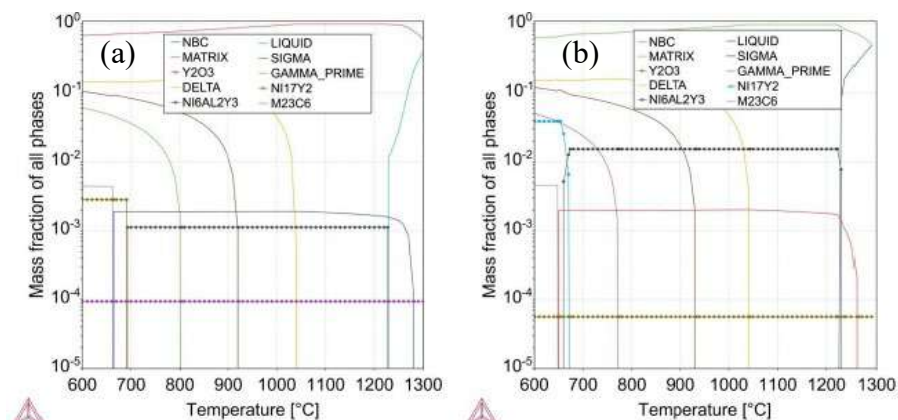


Figure 2 – Thermodynamic simulation of stable phases formed for alloys B (a) and C (b) composition.

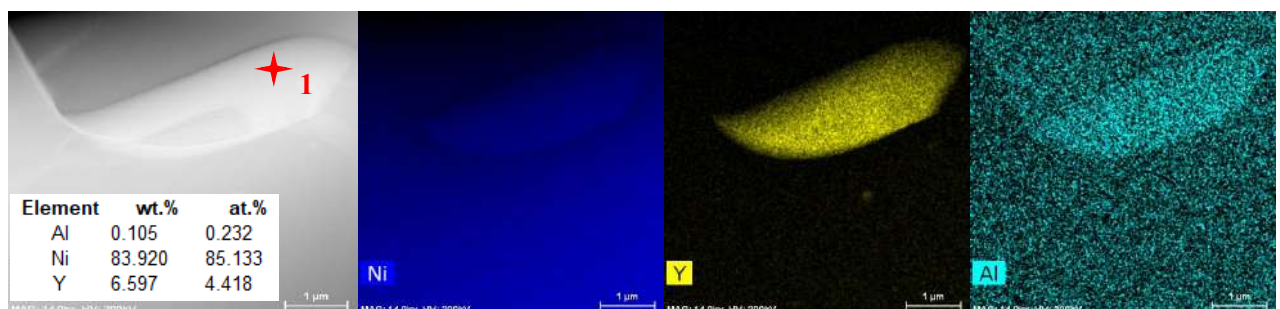


Figure 3 – EDS mapping showing Ni-Al-Y particle and a semi-quantitative analysis of this elements detected on point 1.

## Diffraction Contrast and Analytical Electron Microscopy of Multi-Phases GB Precipitation Phenomena in a Cr-Fe-Ni Alloy

J.C. Spadotto<sup>1\*</sup>, M.G. Burke<sup>2</sup>, I.G. Solórzano<sup>1</sup>

<sup>1</sup> Department of Chemical and Materials Engineering, PUC-Rio, Brazil

<sup>2</sup> Material Performance Centre, University of Manchester, Manchester, UK

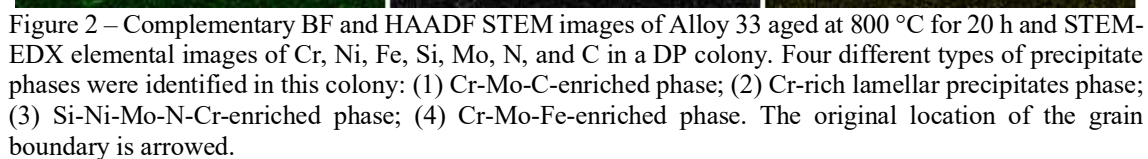
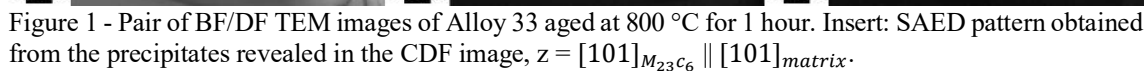
\*Corresponding author: [julioespadotto@gmail.com](mailto:julioespadotto@gmail.com)

Grain boundary (GB) phenomena, including precipitation processes, diffusion-induced GB migration (DIGM) and discontinuous reactions are of increasing interest. From the practical point of view, the phenomena demand to be well understood in order to prevent undesirable effects on mechanical and corrosion properties of structural alloys. Such effects occurring in alloys used in high-performance industries are reported in the literature [1][2]. An interesting GB phenomenon observed in such structural alloys is the discontinuous precipitation (DP) reaction involving concurrent precipitation and GB migration in which the DIGM phenomenon may operate as the precursor of the DP [3]. Basically, DP reaction is a GB diffusion-controlled phenomenon driven by migrating GB, which acts as fast diffusivity path under action of chemical and capillary forces, leaving behind a regularly spaced array of lamellar or rod-type equilibrium precipitates growing cooperatively from the supersaturated matrix. In this context, the present investigation deals with phase identification of precipitates resulting from GB phenomena in Alloy 33 (austenitic matrix and nominal composition (wt. %) 33Cr-32Fe-31Ni-1.6Mo-0.6Cu-0.4N). In order to understand the DP behavior upon direct isothermally aging at 800 °C, an experimental study has been conducted using scanning electron microscopy (SEM), scanning/transmission electron microscopy (STEM/TEM) together with X-ray energy dispersive spectroscopy (XEDS). Detailed microstructural and microcompositional data were acquired using an FEI Talos F200A with Super X (4 SDDs) and X-FEG for high sensitivity STEM-EDX spectrum imaging of electron-transparent thin-foil specimens. The bright-field (BF)-TEM image in Figure 1a shows a GB that has migrated into the adjacent FCC grain upon aging at 800 °C for 1 h. The centered dark-field (CDF)-TEM image in Figure 1b shows that the depleted matrix of the DP colony maintains the same crystal orientation of the parent matrix. From both the SAED pattern (shown in the insert) and XEDS analyses, GB precipitates shown in the CDF-TEM image (Figure 1c) were identified as FCC Cr-rich  $M_{23}C_6$ -carbide. Figure 2 shows BF/HAADF STEM images of Alloy 33 aged at 800 °C for 20 h displaying a DP colony with a classical lamellar morphology. Discrete precipitates were observed to have decorated the original GB position of the DP colony, in addition to lamellar precipitates that had nucleated adjacent to GB and grown parallel to each other behind the advancing GB. From XED elemental maps shown in this figure and SAED patterns, the existence of 4 different precipitates was confirmed as follows: (1) Cr-Mo-C-enriched phases at the original GB position identified as  $M_{23}C_6$ -carbide; (2) Cr-rich lamellar precipitates identified as  $\alpha$ -Cr phase (BCC structure), (3) Si-Ni-Mo-N-Cr-enriched phase identified as  $\eta$ -phase (diamond-cubic structure), and (4) Cr-Fe-Mo-enriched phase located at DP reaction-front, identified as  $\sigma$ -phase (tetragonal structure) [4]. Further detailed analysis concerning precipitation phenomena in Alloy 33 is to be published in the near future.

### References:

- [1] M. G. Burke et al., *Ultramicroscopy*, vol. 176, pp. 46–51, 2017.
- [2] B. Langelier et al., *Acta Materialia*, vol. 131, pp. 280–295, 2017.
- [3] I. G. Solórzano and M. F. S. Lopes, *Phase Transform.* **87**, pp. 242–245, 1988.
- [4] The authors are grateful to support of LabNano-CBPF and CNPq, Brazil.





# PARTE 3

## PÔSTERES - BIOLOGIA



## **Morphological Analysis of the Stomach and Intestine of the Black Ray (*Potamotrygon amandae*) Myliobatiformes, Potamotrygonidae (Loboda & Carvalho, 2013)**

Júlia Bastos de Aquino<sup>1</sup> \*, Luana Félix de Melo<sup>1</sup>, Rosângela Felipe Rodrigues<sup>2</sup>, Rose Eli Grassi Rici<sup>1</sup>

1 - University of São Paulo, Faculty of Veterinary Medicine and Animal Science, Department of Anatomy of Domestic and Wild Animals. São Paulo Brazil.

2- State University of São Paulo Júlio de Mesquita Filho (UNESP) / Faculty of Veterinary Medicine. Aracatuba, SP, Brazil

Corresponding author: [julianato@usp.br](mailto:julianato@usp.br)

The Black Ray belonging to the Potamotrygonidae family is the only group within this class in which all species are adapted exclusively to freshwater. The *Potamotrygon amandae* streak has a geographic distribution originally described throughout the Paraná-Paraguay basin [1] [2], and currently in the Countries: Argentina, Brazil, Bolivia and Paraguay. *Potamotrygon* species have been captured in the Amazon River system and exported as ornamental fish to the international market [3]. This species has recently been cataloged having morphological and physiological specializations for life in this type of environment, still quite incomplete, because it is difficult due to the scarcity of information, being many species poorly described, due to lack of adequate material, presence of great variation and color overlap, different forms and morphometries among species [4]. The study of Streaks of the family Potamotrygonidae is relevant, considering that these are of great ecological and economic importance and have been explored as a source of food in the Amazon Basin, mainly by riverside. The study of the stomach and intestine in this species allows knowledge in the description of how its adaptation occurred in fresh water. So our study aimed to analyze the morphology through light microscopy (ML) and scanning electron microscopy (SEM) techniques. Microscopically, it observed a rough surface in the stomach region in the stomach, in the sequence they diminish until they become longitudinal folds entering the intestine, in the region of intersection (pyloric sphincter). The intestine presents a spiral shape, already described as a spiral valve. At the end of the intestine, rectum, the mucosa becomes again pleated tapering to the cloaca. The findings are consistent with the function of each compartment. The stomach presents a rough region, characterized by the presence of the glands to aid digestion, the intestine has a spiral region for greater contact surface for greater absorption of nutrients, ions and water and finally the rectum where water absorption and fecal release occurs.

## References:

- [1] D. Garrone-Neto, V. Haddad Jr., M. J. A. Vilela and V. S. Uieda. Record of occurrence of two species of potamotrygonids in the Upper Paraná River region and some considerations about their biology. *Biota Neotropica* 7 (1): 1-4, 2007.
- [2] T. S. Loboda and M. R. de Carvalho. Systematic revision of the *Potamotrygon motoro* (Müller & Henle, 1841) species complex in the Paraná-Paraguay basin, with description of two new ocellated species (Chondrichthyes: Myliobatiformes: Potamotrygonidae). *Neotropical Ichthyology* 11 (4): 693-737, 2013.
- [3] W. P. Duncan, S. O. Inomata and M. N. Ferdinand. Trade in freshwater in the region of the middle Rio Negro, state of Amazonas, Brazil. *Brazilian Journal of Fisheries Engineering* 5 (2): 13-22, 2010.
- [4] M.R. Carvalho, N.R. Lovejoy, R.S. Rosa . Family Potamotrygonidae (river stingrays). In: *Check List of the Freshwater Fishes of South and Central America* (eds Reis RE, Kullander SO, Ferraris Jr. CJ), Edipucrs, Porto Alegre, pp. 22-28, 2003.

Acknowledgments: To the financial support of CAPES. To the Center of Advanced Diagnostic by Image - FMVZ USP.

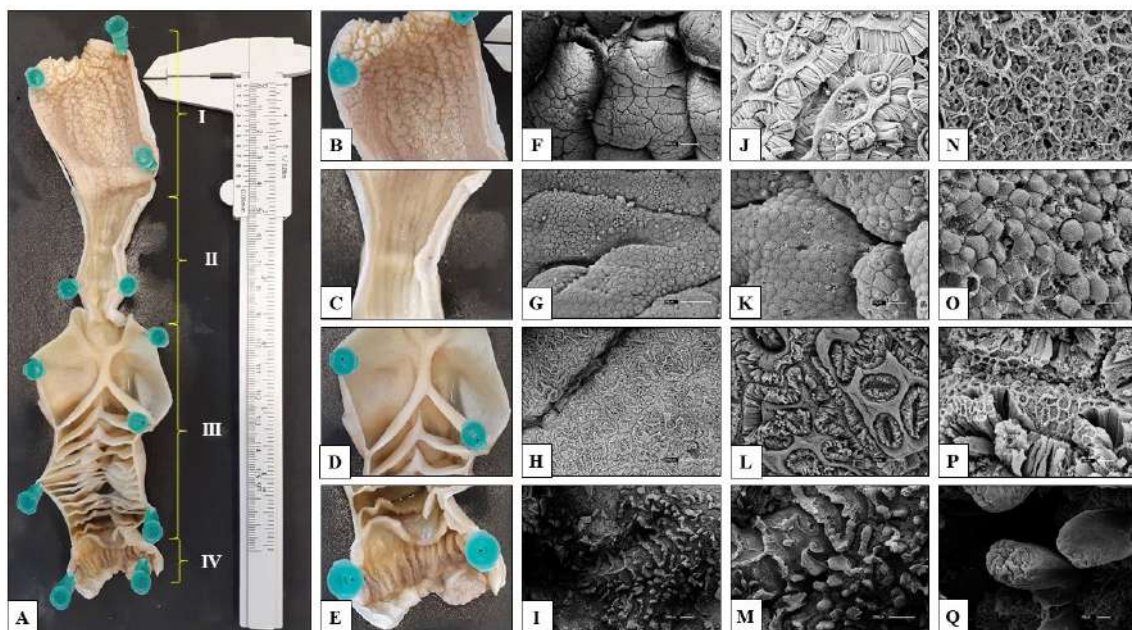


Figure 1: Photomacrography (A): demonstrating in I the stomach (B), II the pyloric sphincter (C), III valve intestine (D), and IV the rectum (E). Scanning electron microscopy (SEM) analysis demonstrating the glandular stomach (FJN), the pyloric sphincter with the pleated mucosa intersecting the stomach and intestine (GKO), the spiral valve to increase the contact surface for nutrient absorption (HLP ), and rectum with pleated mucosa with mucosa for water absorption and secretion of mucus for excretion.



## Structural Description Of Marine Turtle Fibropapilloma

Luana Félix de Melo<sup>1\*</sup>, Julia Bastos de Aquino<sup>1</sup>, Marcos Paulo Batista de Assunção<sup>1</sup>,  
Rose Eli Grassi Ricci<sup>1</sup>

1 - University of São Paulo, Faculty of Veterinary Medicine and Animal Science, Department of Anatomy of Domestic and Wild Animals. São Paulo Brazil.

Corresponding author: [luanafelix@usp.br](mailto:luanafelix@usp.br)

Fibropapillomatosis is a debilitating disease causing morbidity and mortality in marine chelonians, which can cause fibromas, papillomas and fiberoptic skin and visceral fibropapillomas [1], although it is considered a benign disease [2], is debilitating and potentially fatal for turtles because they make it difficult the survival of the turtles, causing wasting (thinness and loss of excessive body mass), difficulty in swimming, locomotion, breathing and feeding [3]. Being pointed as one of the main causes of reduction of the population of green turtles, because they hardly reach the adult stage, thus, do not contribute to the continuity of the species [4]. It is common for individuals affected by this disease to be infested by ectoparasites [5], causing inflammation with an aggressive hyperplastic response, which contributes to tumor growth [6] [7]. Although its etiology has not been fully elucidated, the strong involvement of an alpha-herpes virus is known, but the influence of other factors such as parasites, genetics, chemical carcinogens, contaminants, immunosuppression and ultraviolet radiation may be important in the disease [8] [9] [10] [11]. The aim of this study was to characterize the fibropapilloma found in three specimens of green turtles (*C. mydas*) by light microscopy and scanning electron microscopy. Macroscopically no pattern of tumor appearance was observed, being random, mostly in the soft tissue of the skin around the neck, tail base, cervical region, inguinal, axillary and hull base, presenting in several sizes and in different aspects regarding its external appearance. The presence of ectoparasites and their eggs spread in small populations throughout the individuals were also observed. In the microscopic analyzes the tumors present a hyperplastic stromal proliferation and epidermal proliferation, covered by keratin, with some invaginations of the keratinocytes, thus allowing the keratin grow inside the tumor forming large circular spirals, increasing the size of the fibropapilloma. This amount of dead tissues (keratin) within the tumor suggests a tumor death in a manner not yet elucidated.

### References:

- [1] A.A. Aguirre & P.L. Lutz. Marine turtles as sentinels of ecosystem health: is fibropapillomatosis an indicator? *EcoHealth*, 1 (3), 275-283. 2004.
- [2] C.J. Limpus, D.J., Limpus, K.E., Arthur, C.J., Parmenter. Monitoring of green turtle population dynamics in Shoalwater Bay: 2000-2004. Research Publication No. 83, Great Barrier Reef Marine Park Authority Research Publication Series, Townsville. 2005.
- [3] P.H. Cubas, C. Baptistotte. Chelonia (tarataruga, tortoise, turtle, jabuti). In: Z.S. Buckets; J.C.R. Silva; J.L. Catão-Dias (eds.), *Wildlife Treaty*. São Paulo, Roca, p. 108-110. 2007.
- [4] S. Rossi. Study of the impact of fibropapillomatosis on *Chelonia mydas* Linnaeus, 1758 (Testudines, Cheloniidae). Master's Dissertation in Sciences, Faculty of Veterinary Medicine and Animal Science, University of São Paulo, São Paulo. 104p. 2007.
- [5] E.R. Matushima, A. Longatto Filho, C. Di Loretto, C.T. Kanamura, I.L. Sinhorini, B. Gallo, C. Baptistolle. Cutaneous papillomas of green turtles: a morphological, ultrastructural and immunohistochemical study in Brazilian specimens, 2001.
- [6] T.M. Norton, E.R. Jacobson, J.P. Sundberg. Cutaneous fibropapillomas and renal myxofibroma in a green turtle, *Chelonia mydas*. *Journal of Wildlife Diseases* 26: 265-270. nineteen ninety



- [7] L.H. Herbst, E.R. Jacobson, P.A. Klein, G.H. Balazs, R. Moretti, T. Brown, et al. Comparative pathology and pathogenesis of spontaneous and experimentally induced fibropapillomas of green turtles (*Chelonia mydas*). *Veterinary Pathology* 36: 551-564. 1998.
- [8] Y.A. Lu, Y. Wang, A.A. Aguirre, Z.S. Zhao, C.Y. Liu, V.R. Nerurkar, R. Yanagihara. RT-PCR detection of the expression of the polymerase gene of a novel reptilian herpesvirus in tumor tissues of green turtles with fibropapilloma. *Arch Virol* 148: 1155-1163. 2003.
- [9] E.R. Matushima. Fibropapillomas in sea turtles: histological, immunohistochemical and ultrastructural aspects. São Paulo-SP. Habilitation Thesis. University of São Paulo, São Paulo, 113 p. 2003.
- [10] A. Ene, M. Su, S. Lemaire, C. Rose, S. Schaff, R. Moretti, J. Lenz, L.H. Herbst. Distribution of chelonid fibropapillomatosis associated herpesvirus variants in Florida: molecular genetic evidence for infection of turtles following recruitment to neritic developmental habitats. *Journal of Wildlife Diseases*, 41 (3), pp. 489-497, 2005.
- [11] R.J. Greenblatt, S.L. Quackenbush, R. N. Casey, J. Rovnak, G.H. Balazs, T.M. Work, J.W. Casey, C.A. Sutton. Genomic variation of the fibropapilloma-associated marine turtle herpesvirus across seven geographic areas and three host species. *Journal of Virology*, 79: 1125-1132. 2005.

Agradecimentos: Ao apoio financeiro da CAPES. Ao Centro de Avançado de Diagnóstico por Imagem – FMVZ USP.

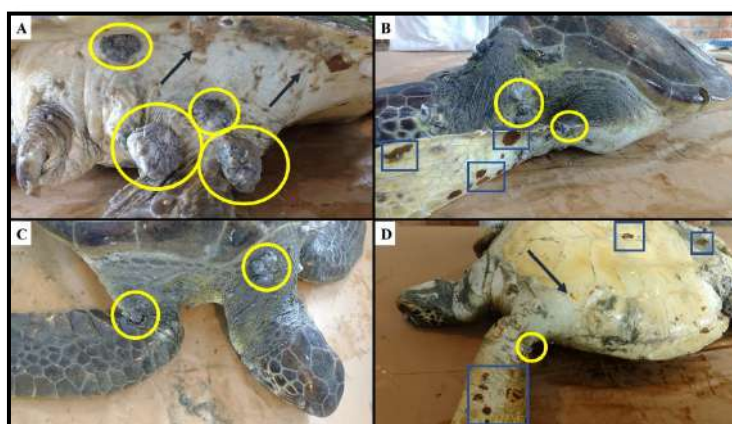


Figure 1: Macroscopic analysis of the arrangement of fibropapillomas found in *Chelonia mydas* specimens circled in yellow, ectoparasites by arrows, and eggs marked by blue squares.

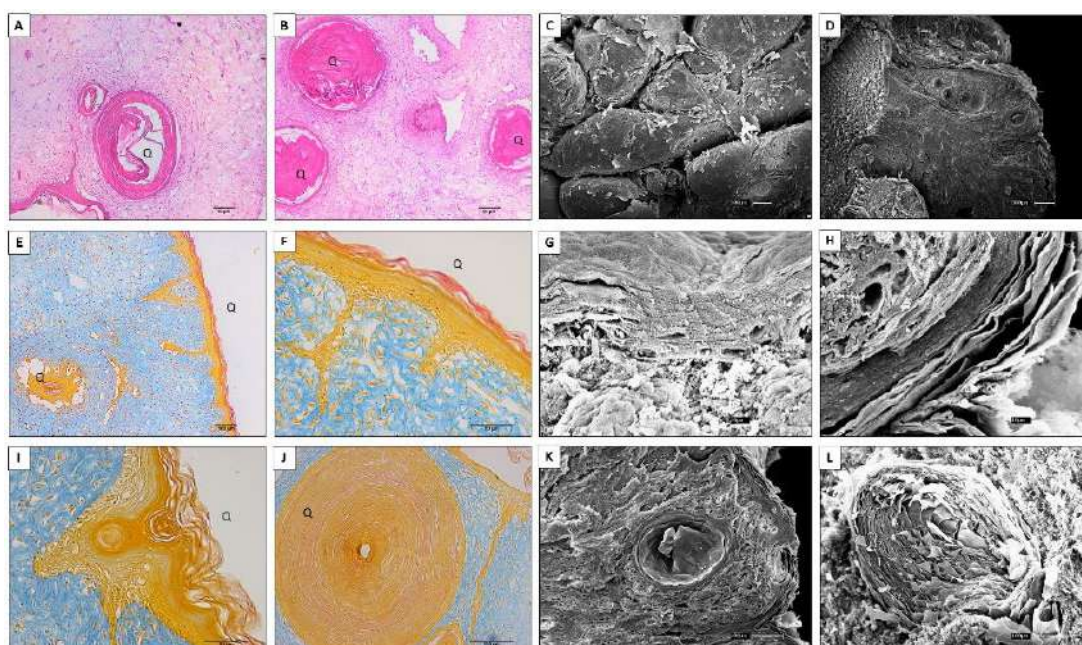


Figure 2: Photomicroscopy of fibropapillomas, revealing keratinocyte invagination, causing keratin (Q) to grow inside the tumor forming large circular spirals. Light microscopy images: AB stained in HE, EFIJ stained in Mallory. Scanning electron microscopy images CDGHKL.



## Decellularization of Striated Muscle Skeletal Bovine

Luana Félix de Melo<sup>1\*</sup>, Julia Bastos de Aquino<sup>1</sup>, Rose Eli Grassi Ricci<sup>1</sup>

1 - University of São Paulo, Faculty of Veterinary Medicine and Animal Science, Department of Anatomy of Domestic and Wild Animals. São Paulo Brazil.

Corresponding author: [luanafelix@usp.br](mailto:luanafelix@usp.br)

Muscle tissue constitutes on average 40% of the body mass and 53 to 64% of the carcass. The animal organism has more than 600 muscles that vary enormously in size, shape and function. These, in turn, consist of different types of fibers that present different physicochemical characteristics and frequency of occurrence of each type depending on genetics, nutrition, sex, age, anatomical region, among other environmental factors [1]. The concept of tissue engineering is an interdisciplinary field that applies principles of engineering, molecular biology, clinical sciences, physics, and chemistry to the development of biological substitutes that can maintain, restore, or enhance the function of organs and tissues. This new science is based on three pillars: cells, biocompatible matrixes and bioactive molecules responsible for the morphogenic signals [2]. In order for tissue engineering to be a viable therapeutical option in tissue regeneration, three-dimensional structures of cellular support and tissue growth are required [3]. Cell structures (scaffolds) are three-dimensional structures that provide a microenvironment capable of allowing cell adhesion and migration. These should present physical, chemical and biological characteristics favorable to cell growth and differentiation, as well as microporosities to allow the connectivity between the graft and the adjacent tissue, facilitating the transport of nutrients and the elimination of products of cellular metabolism [4]. The integration of gene therapy, tissue engineering and biomaterials present the potential to create synthetic environments that provide the signals needed to promote the formation of functional tissues. The objective of this study was to study the extracellular matrix (ECM) comparing in natura and decellularized muscle tissues using detergents such as SDS 2% to remove cells, leaving only their framework. The analyzes were performed using scanning electron microscopy (SEM) and light microscopy (ML). The findings confirm the cellular absence confirmed by DAP, preserving the extracellular matrix, as well as its components such as collagens I, III and IV through the staining of polarized picrossiriin, fibronectin, elastin and glycosaminoglycans through PAS (periodic acid-Schiff). Thus, it can be confirmed that this ECM can be used as a framework for tissue recrystallization.

### Reference:

- [1] H. Amthor, *et al.* A molecular mechanism enabling continuous embryonic muscle growth - a balance between proliferation and differentiation. *Development*, v.126, n.5, p.1041-1053, 1999.
- [2] R. Langer; J.P. Vacanti. *Tissue engineering*. Science, Washington, v.260, n5110, p.920-6 May14. 1993.
- [3] M. Nakashima, *Tissue engineering in endodontics*. *AustEndod J*, Melbourne, v.31, n.3, p.111-3 Dec. 2005.
- [4] Sachlos, E.; Czernuska, J.T. Making tissue engineering scaffolds work. Review: the application of solid free form fabrication technology to the production of tissue engineering scaffolds. *Eur Cell Matter*, Glasgow, v.5, p. 29-39; discussion 39-40 Jun 30.2003.
- [5] M. Nakashima, A. Akamine. The application of tissue engineering to regeneration of pulp and dentin in endodontics. *J Endod*, Baltimore, v.31, n.10, p.711-8 Oct. 2005.

**Acknowledgments:** To the financial support of CAPES. To the Center of Advanced Diagnostic by Image - FMVZ USP.



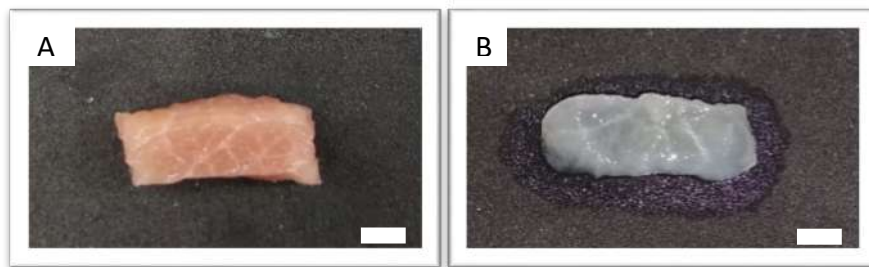


Figure 1: Photomacrography of the bovine femoral biceps muscle before (A) and after the decellularization process (B). Bar = 1cm.

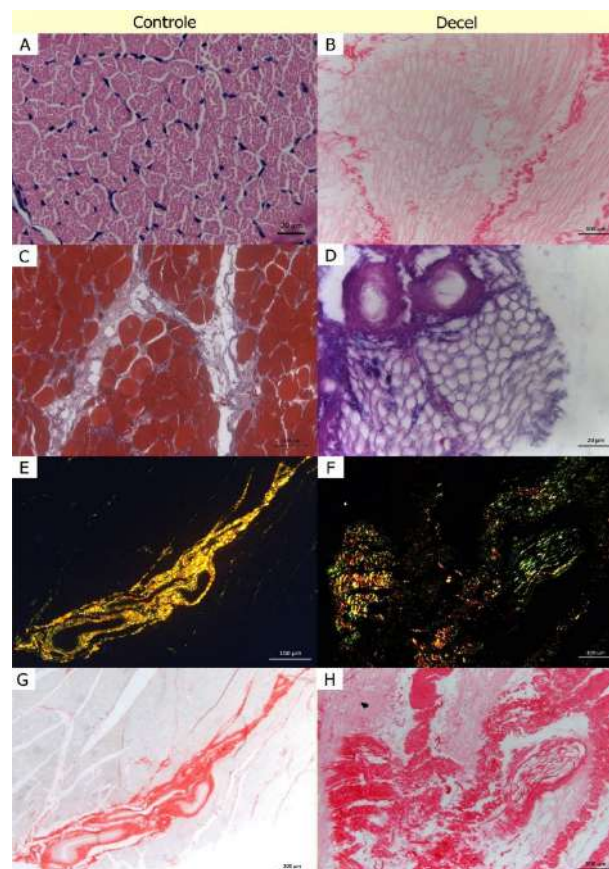


Figure 2: Photomicrography of the techniques used comparing control and decellularized tissue. A and B: HE staining. C and D: Masson trichrome staining. E and F: Polarized picrosirius staining. G and H: coloring of picrosirius, obtained through the light microscope (ML).

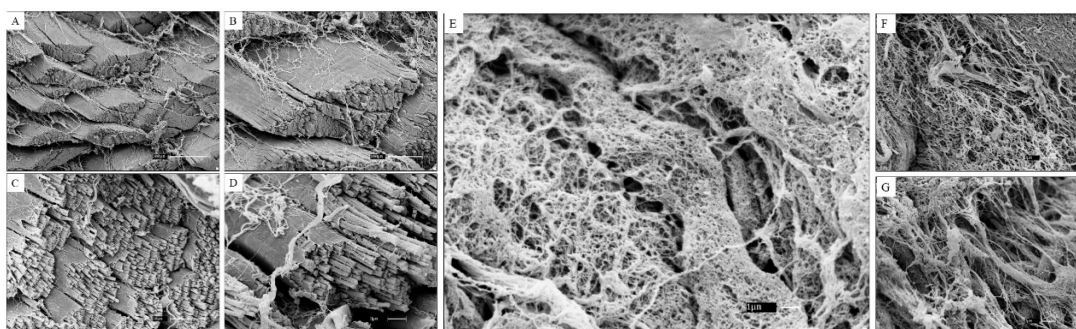


Figure 3: Scanning Electron Microscopy Photomicrography comparing the in natura muscular tissues (ABCD), and the decellularized tissues (EFG).

## Characterization of Pathogenic Bacteria Adhered On the Cuticle of the Nematodes Isolated of the Bovine Ear Canal

Makoto Enoki Caracciolo<sup>1</sup>, Ander Castello Branco Santos<sup>1,2</sup> and Eduardo José Lopes Torres<sup>1\*</sup>

<sup>1</sup>. Laboratório de Helminologia Romero Lascasas Porto (LHRLP), FCM-UERJ, RJ. Brasil.

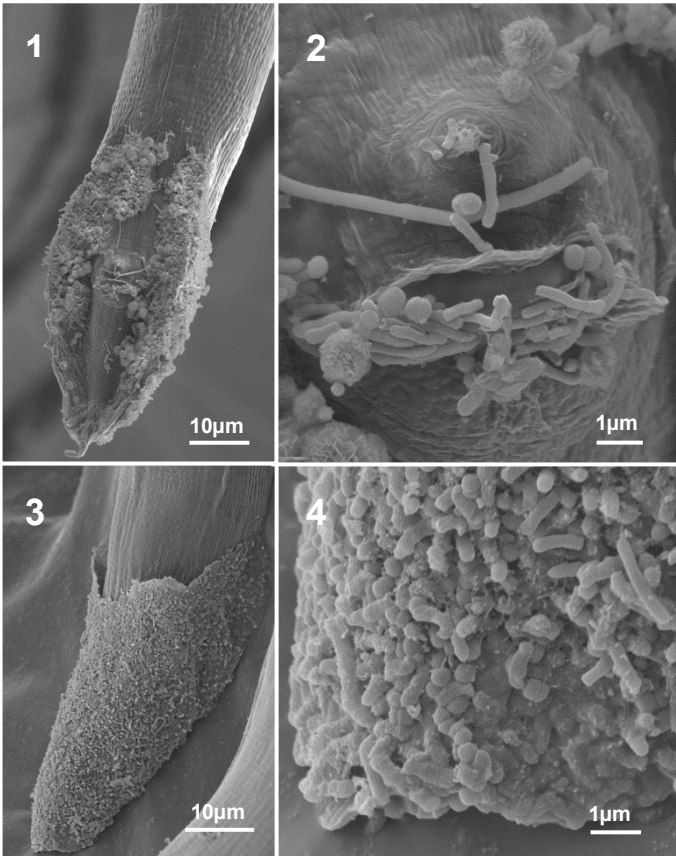
<sup>2</sup>. Universidade Estácio de Sá, RJ. Brasil.

\* E-mail: lopestorresej@gmail.com

The parasitic otitis presents veterinary impact due to infection caused by nematodes and bacteria species associated. This infection resulting in an intense inflammatory process, which may affect both the external and internal ear and has been reported in hot and humid countries [1]. Clinical signs of otitis caused by rhabditiforms nematodes initially include apathy and repetitive movement of the head and the aggravation of infection can lead to damage in the central nervous system of the animal, causing dysfunction or paralysis of the facial and vestibulocochlear nerves as well as meningitis can be occur [2]. In Brazil the *Metarhabditis* species have been described as being responsible for creating the parasitic otitis in Gir cattle (*Bos taurus indicus*) [3] [4] and associated with the translocation of microorganisms and their products. The main objective of this work was to identify the pathological bacterial species associated with the nematodes present in the auricular pavilion of cattle from the Gir breed from farms located in states of three different regions of Brazil (Southeast, Center West and North). The nematodes recovered were washed using PBS (Phosphate Buffer Saline), fixed with Karnovsky's solution, adhered on glass coverslips, post-fixed in osmium tetroxide, dehydrated in ethanol series, critical point dried, mounted in a metal stub, sputtered with gold and analyzed using a field emission scanning electron microscope MEV ZEISS Auriga 600 Compact, FEI-Quanta 250 and Jeol JSM-7100F. Our results identified two species *M. freitasi* (Fig. 1-2) and *M. costai* (Fig. 3-4) and five species of the pathological bacteria in cattle infected with nematodes (Tab. 1). These bacteria species were described with the ability to form biofilm and in this samples were identified bacteria groups adhered on the nematode cuticle, in posterior end of both species (Fig. 5 e 6), suggesting the formation of biofilms and the action of the parasites as carriers. The biofilm is associated with the pathological and antibiotic resistance increase of the bacteria and is possible that the nematode presence can be contributed in this infection process.

### REFERENCES

- [1] P. V. B. Leite et al. *Pesq. Veterinária Brasileira*. 32 (2012) 855.
- [2] E. R., Duarte et al. *Vet. Med. B Infect. Dis. Vet. Public. Health*. 51 (2004) 1.
- [3] W. Jr. Martins *Mem. do Inst. Oswaldo Cruz*. 80 (1985) 11.
- [4] J. S. Barbosa et al. *Pesq. Vet. Bras*. 36 (2016) 605.
- [5] This research was supported by CNPq (Brazil) and FAPERJ (Brazil).



Conventional SEM of nematodes adult male. Measure in micrometers (µm). **Fig. 1** – Posterior end of male *M. freitasi*, showing adhered bacteria on bursa cuticle; **Fig. 2** – Detail of Male *M. freitasi* Cloaca with bacteria adhered on cuticle; **Fig. 3** – Posterior region of *M. costai* showing bacteria completely adhering bursa surface; **Fig. 4** – Posterior end of male *M. costai*, showing adhered bacteria on bursa cuticle.

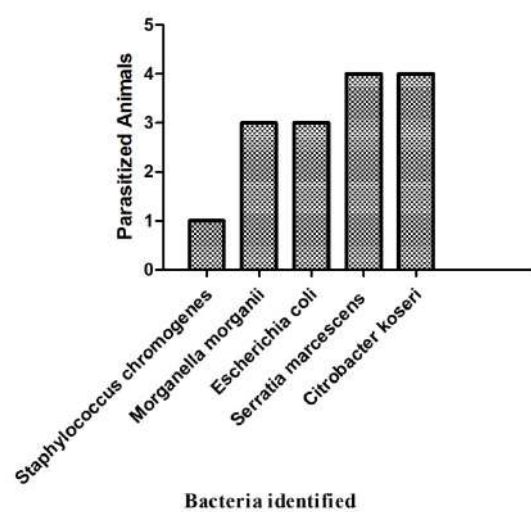


**Table 1-** Bacteria identified from parasitized Gir cattle (*Bos taurus indicus*).

## Morphological Characterization of Experimental Model *Metarhabditis blumi* (Nematoda: Rhabditidae)

Makoto Enoki Caracciolo<sup>1</sup>, Ander Castello Branco Santos<sup>2</sup> and Eduardo José Lopes Torres<sup>1</sup> \*

<sup>1</sup>. Laboratório de Helmintologia Romero Lascasa Porto (LHRLP), FCM-UERJ, RJ, Brasil. \*lopestorresej@gmail.com

<sup>2</sup>. Universidade Estácio de Sá, RJ, Brasil.

The nematode *Metarhabditis blumi* was recently reported in cases of parasitic otitis in Gir (*bos taurus indicus*) cattle. However, the authors did not present any morphological data, only the molecular characterization [1], [2]. This nematode had only been described in soil samples and by light microscopy [3]. The aim of this study is ultrastructural characterization of *M. blumi* using scanning electron microscopy (SEM) a nematode cultivated in our laboratory as experimental model for bovine otitis study. In addition, the species identification was performed using molecular tools. Nematodes were washed in PBS solution and chemically fixed by immersion in Karnovsky's, adhered on glass coverslips, post-fixed in osmium tetroxide, dehydrated in ethanol series, critical point dried, mounted in a metal stub, sputtered with gold and analyzed using the field emission scanning electron microscopies MEV ZEISS Auriga 600 Compact and Jeol JSM-7100F. The results using SEM was possible to detailed the anterior end of male and female, including a triangular morphology of oral opening with three lips, one dorsal and two lateroventral. The dorsal are ornamented with four cephalic papillae and the two lateroventral with two papillae and one amphid each (Fig. 1). Females present the vulva with two simple lips with a cuticular structure surrounding these lips and two cuticular folds in the lateral of the opening (Fig. 2). In posterior end, the anus is identified and on the lateral faces was possible to identify a pair of phasmids (Fig. 3). The copulatory bursa is distinguished in the posterior region of males, present a cuticular dilatation and is ornamented with x cloacal papillae and was possible to identify a pair of spicules tip arrow-shaped (Fig. 5). On the internal face of the bursa is possible to observe a pair of phasmids, close to the region of the tail appendix projection (Fig. 6). By the molecular analysis of 28S rDNA, ITS and cox2 molecular targets, clearly demonstrated the species identification of *M. blumi*. The SEM results associated with molecular experiments allowed advances in integrative taxonomic identification of *M. blumi*, presenting a detailed and more complete description of this species. Our results can be contribute in bovine otitis diagnosis and in advances of this species as experimental model in parasitology and other research areas.

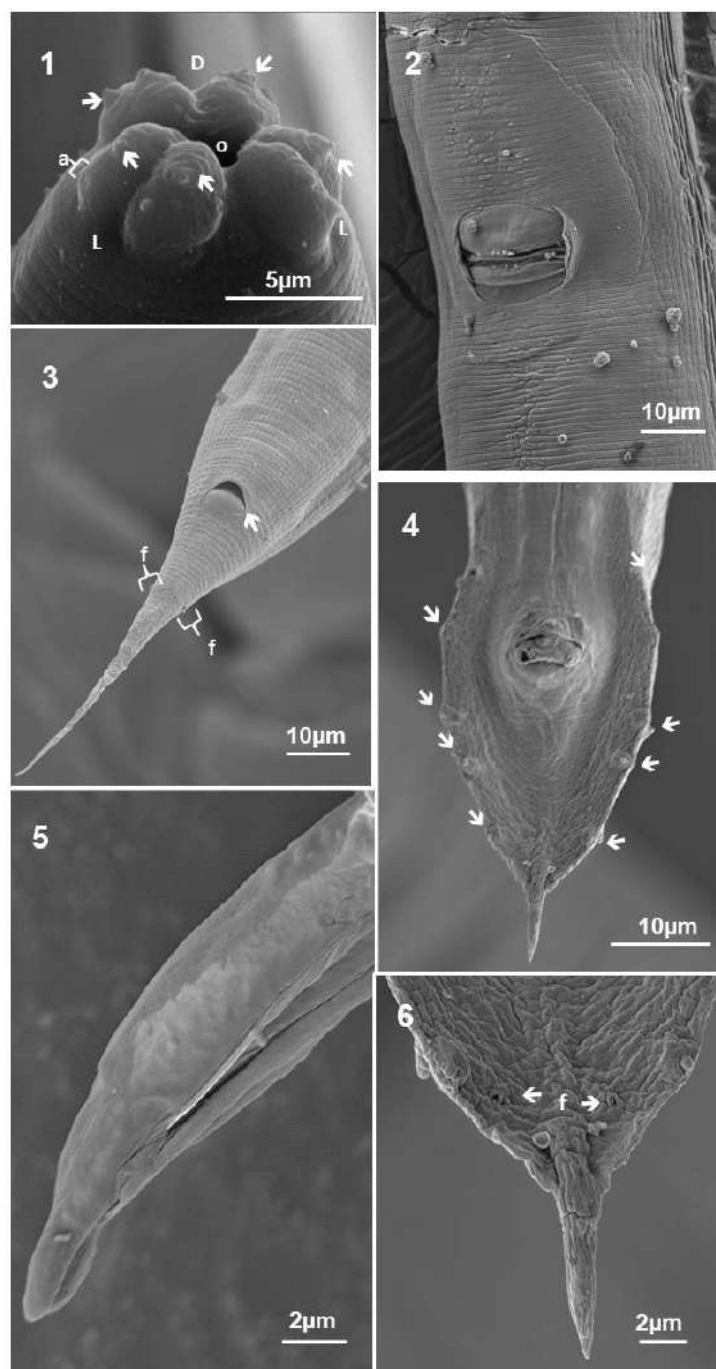
[1] P. V. B. Leite et al. *Veterinary Parasitology*. 214 (2015) 184.

[2] J. S. Barbosa et al. *Pesq. Vet. Bras.* 36 (2016) 605.

[3] W. Sudhaus. *Nematologica*. 22 (1974) 49.

[4] This research was supported by FAPERJ (Brazil) and CNPq (Brazil).





Legends: Conventional SEM of nematodes adult male. Measure in micrometers ( $\mu\text{m}$ ) **Fig. 1** - Anterior end of *M. blumi*, showing the oral opening (o), two latero-ventral lips (L) and dorsal lip (D) and cephalic papillae ( $\rightarrow$ ) and amphid (a); **Fig. 2** – Middle region of female *M. blumi* showing vulva opening; **Fig. 3** – Posterior region of female *M. blumi*, showing anus ( $\rightarrow$ ) and phasmids (f); **Fig. 4** – Posterior region of male *M. blumi* showing bursa and genitals papillae; **Fig. 5** – Detail of male *M. blumi* espicule, showing the arrow shape end; **Fig. 6** – Posterior end of male *M. blumi*, showing phasmids (f).



## The Influence Of Comicronization On Particle Morphology

Mariana de Andrade Adauto Costa<sup>1\*</sup>, Livia Deris Prado<sup>1</sup>, Beatriz Ferreira de Carvalho Patricio<sup>1</sup>, Helvécio Vinícius Antunes Rocha<sup>1</sup>

<sup>1</sup>Laboratório de Micro e Nanotecnologia – Farmanguinhos, FIOCRUZ, Rio de Janeiro, Brazil.

\*e-mail: mariana.adauto@hotmail.com

Glibenclamide, also known as glyburide, is a second generation sulfonylurea drug indicated for the treatment of diabetes type II. It is a drug poorly soluble in water. It is classified as Class II, according to the Biopharmaceutics Classification System, which consists of drugs of low water solubility and high permeability, showing variable absorption and oral bioavailability between the individuals. Therefore, the bioavailability and *in vivo* behavior of the drug are dependent on its dissolution rate [1]. Knowing that smaller particles and some excipients can facilitate higher dissolution rates, nine different excipients (sodium lauryl sulfate (SLS), manitol, lactose monohydrate spray dried, lactose monohydrate mesh 200, hydroxypropylcellulose (HPC), hydroxypropylmethylcellulose E5 (HPMC E5), Lutrol F68, microcrystalline cellulose 102, polyvinylpyrrolidone K30 (PVP K30)) were co-micronized (air jet milling) with glibenclamide in three different proportions, drug to excipients 1:0.25:0.25; 1:0.25; 1:0.5. They were respectively divided in three groups 1, 2 and 3. The samples were analyzed by X-ray powder diffraction, scanning electron microscopy (SEM), and dissolution. The X-ray diffraction results indicated that after the co-micronization process the polymorph of glibenclamide stay the same. The SEM images were important to observe the roughness of the surface of the particles, the agglomerate form, irregular crystals in different sizes and if the process was successful [2]. The samples presented smaller particles compared to the raw material and had higher dissolution efficiency (DE). When comparing between the samples, some present agglomerate or was not fully micronized, exhibiting a lower dissolution profile compared to others, as observed with the sample co-micronized with HPMC E5 (in group 2). However, SEM images of sample with lactose monohydrate SD (group 1) present a homogeneous sample, indicating a better co-micronization process. It also present a DE above 80. Since almost all of the co-micronized samples had higher DE than the raw material, we can confirm that reducing particles size can increase efficiency and SEM images are important to control the efficiency of the process. In conclusion, this work indicate that the method of co-micronized process enhance the dissolution of low solubility drugs.

### Refêrencias:

- [1] Bachhav, Y.G.; Patravale, V.B. SMEDDS of Glyburide Formulation, In Vitro Evaluation, and Stability Studies. *AAPS Pharmaceutical Science Technology*, v. 10 (2), p. 482–487, 2009.
- [2] Neto, S.A.L.; *Preparação e Caracterização Analítica de Dispersões Sólidas e Cristalinas de Glibenclamida, Obtidas Através de Secagem por Aspersão*. PhD Thesis. Universidade Federal da Paraíba. 102p. 2012.
- [3] This research was supported by CNPq (Brazil), FAPERJ (Brazil), Universidade Federal Fluminense – UFF (Brazil) e Centro de Tecnologia Mineral – CETEM (Brazil).

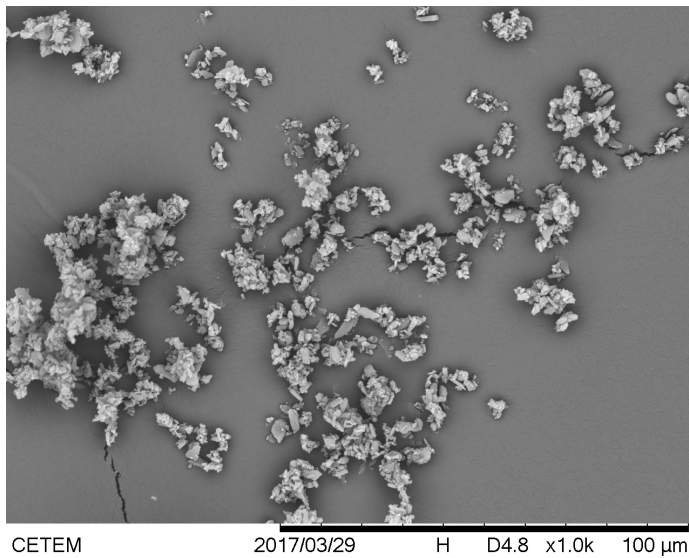


Figure 1: Scanning electron microscopy, amplification 1.000X, glibenclamide and lactose monohydrate SD comicronized, proportion from group 1.

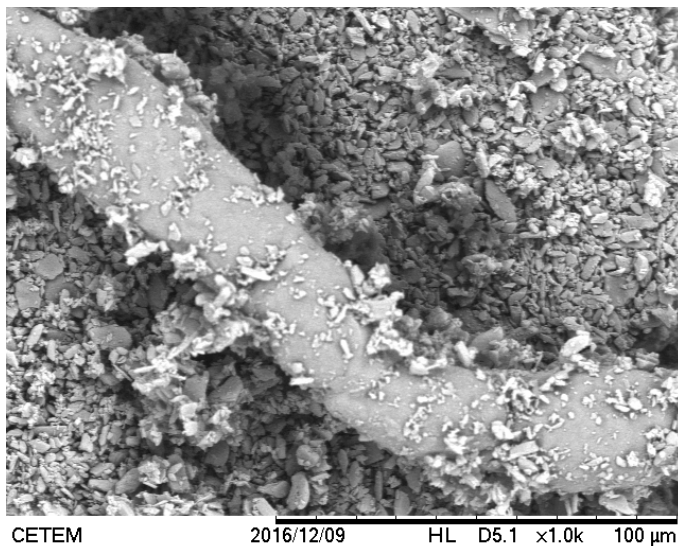


Figure 2: Scanning electron microscopy, amplification 1.000X, glibenclamide and HPMC E5 comicronized, proportion from group 1.

## Antileishmanial Activity of 1,2-bis [3-(2-methyl-1,3-dioxolan-2-yl) phenyl]-ditellane

Natália Storck Ceroni<sup>1</sup>, Pamela T. Bandeira<sup>2</sup>, Tânia Ueda-Nakamura<sup>1</sup>, Sueli de Oliveira Silva<sup>1</sup>, Leandro Piovan<sup>2</sup>, Rayanne Regina Beltrame Machado<sup>1</sup>, Danielle Lazarin Bidóia<sup>1</sup>, Celso Vataru Nakamura<sup>1</sup> and Francielle Pelegrin Garcia<sup>1</sup>

<sup>1</sup> Laboratório de Inovação Tecnológica no Desenvolvimento de Fármacos e Cosméticos, Universidade Estadual de Maringá, Maringá Brasil  
nattistorck@hotmail.com

<sup>2</sup> Departamento de Química, Universidade Federal do Paraná, Curitiba, Brasil

*Leishmania* is a protozoan parasite that is transmitted by bite of phlebotomine sandflies and is the causative agent of a range of diseases, collectively known as leishmaniasis, which affect over 150 million people worldwide <sup>[1]</sup>. Leishmaniasis is endemic in at least 98 tropical and temperate countries, both developed and developing, and it is considered to be a neglected tropical disease <sup>[2]</sup>. One of the species that causes cutaneous leishmaniasis is *Leishmania amazonensis*, characterized by a non-contagious skin lesion infection. Amphotericin B and miltefosine (or hexadecyl-phosphocholine), antifungal and antitumor originally drugs, respectively, have been used as second line drugs to treat leishmaniasis <sup>[3]</sup>, however they present many limitations including development of resistance and various toxicities <sup>[4]</sup>. Thus, the relevance of research in new potential drugs is easily justified. The aim of this study was to evaluate the *in vitro* activity against *L. amazonensis* promastigotes and cytotoxicity potential in J774.A1 macrophages of the ditelluride 1,2-bis [3-(2-methyl-1,3-dioxolan-2-yl) phenyl]-ditellane, **LQ 6** (Fig. 1), previously synthesized <sup>[2]</sup>. For this, the antiproliferative effect against promastigotes was evaluated by directly counting free-living parasites in Neubauer's chamber, after 72 h of treatment with different concentrations of **LQ 6**. Additionally, cytotoxic activity against macrophages were also performed with **LQ 6**, and after 48 h of treatment, MTT method was used to determine CC<sub>50</sub> value. The results obtained are shown in Table 1. Finally, scanning electron microscopy (SEM) was used to analyze morphology of parasites treated with IC<sub>50</sub> and 2 times IC<sub>50</sub> values of **LQ 6**. Briefly, after 72 h treatment, samples were fixed in glutaraldehyde, dehydrated in increasing concentrations of ethanol, critical point dried in CO<sub>2</sub>, coated with gold and observed in FEI SCIOS microscope. **LQ 6** exhibited an interesting activity and selectivity against promastigotes. Moreover, SEM photomicrographs (Fig. 2) revealed altered size and shape of treated parasites including rounding and reduction of cellular body and membrane damages with exposure of intracellular content of parasites. **LQ 6** showed to be a promising substance as a future antiprotozoal agent. Further studies are currently underway to elucidate its mechanism of action.

### References

- <sup>[1]</sup> P.KAYE, et al. **Nature Reviews Microbiology**. 9 (2011), 604.
- <sup>[2]</sup> P.T. BANDEIRA, et al. **ACS Med. Chem. Lett.** 10 (2019), 806.
- <sup>[3]</sup> D.B SCARIOT. et al. **Frontiers in microbiology**. 8 (2017), 255.
- <sup>[4]</sup> M. Banerjee, et al. **Eur J Med Chem.** 55 (2012) 449.

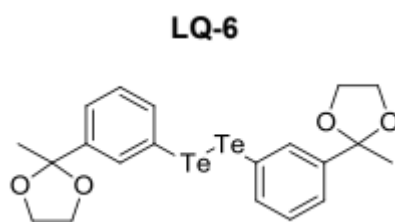


**Figure 1** 1,2-bis [3- (2-methyl-1,3-dioxolan-2-yl) phenyl]- ditellane

**Table 1** Evaluation of the antiproliferative and cytotoxic activity of 1,2-bis [3- (2-methyl-1,3-dioxolan-2-yl) phenyl] ditellane against *L. amazonensis*

Substance	Promastigote IC <sub>50</sub> <sup>1</sup> (μM)	Macrophages <i>J774.A1</i> CC <sub>50</sub> <sup>2</sup> (μM)
<b>LQ-6</b>	0.165 ± 0.002	3.8 ± 0.2
<b>SI (CC<sub>50</sub>/IC<sub>50</sub>)</b>	23.03	

<sup>1</sup> inhibitory concentration of 50% of parasites

<sup>2</sup> cytotoxic concentration of 50% of macrophages

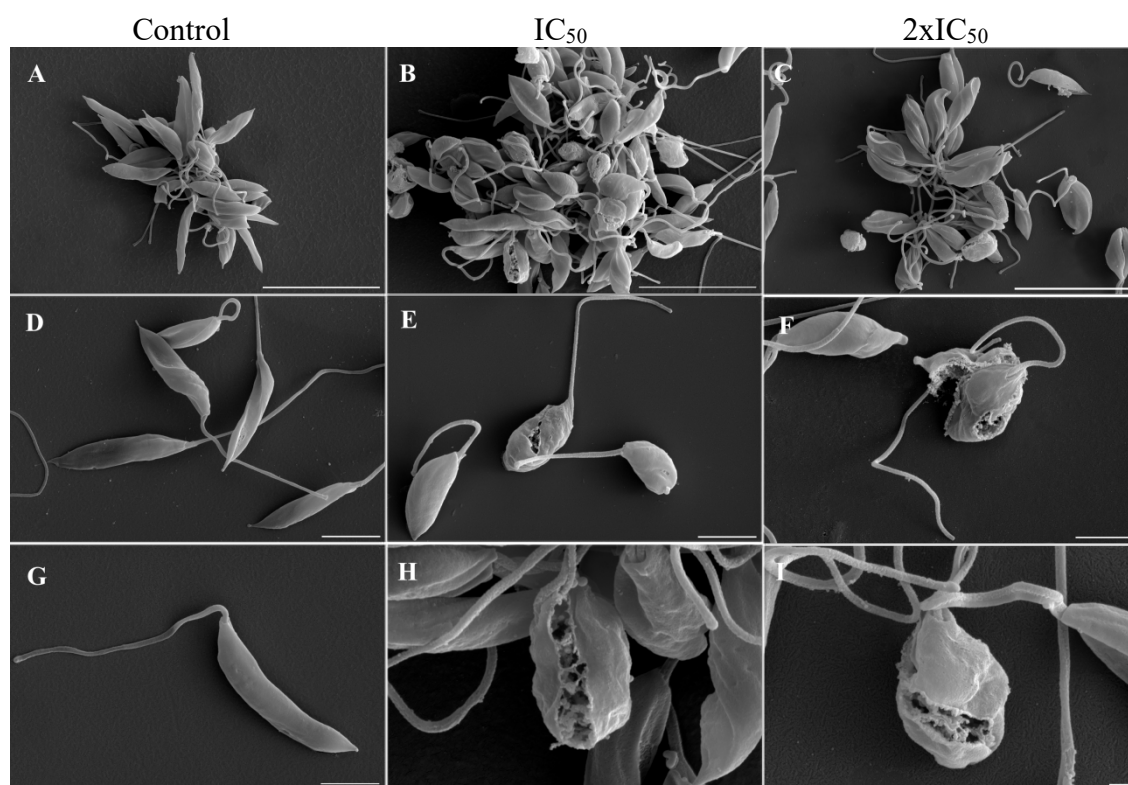


**Figure 2:** Scanning electron microscopy images of promastigote forms of *L. amazonensis* cultivated in the absence (column 1) or presence of **LQ-6** at concentrations of 0.165 μM (column 2) and 0.33 μM (column 3) for 72 h. Scale bar 10 μm (A-D), 5 μm (E-G) and 2 μm (H-I).

## Three-Dimensional Analysis Of The Biogenesis Of Hemozoin Crystals During The Intra-Erythrocytic Cycle Of *Plasmodium berghei*

Azeredo, A.<sup>1\*</sup>, Wendt, C.<sup>1</sup>, De Souza, W.<sup>1</sup> and Miranda, K.<sup>1</sup>

<sup>1</sup> Laboratório de Ultraestrutura Celular Hertha Meyer, Instituto de Biofísica Carlos Chagas Filho and Centro Nacional de Biologia Estrutural e Bioimagem – Universidade Federal do Rio de Janeiro, Rio de Janeiro, Brazil.

\*E-mail: [pereiraalineazr@gmail.com](mailto:pereiraalineazr@gmail.com)

Malaria is a parasitic disease that is among the most serious problems of global public health, responsible for more than a million deaths per year. Mortality and morbidity of this disease results from the *Plasmodium spp.* asexual cycle inside red blood cells. It has already been described that during its intraerythrocytic cycle the parasite internalizes a large part of the red blood cell cytoplasm. Internalized hemoglobin is directed to the food vacuole, where a proteolytic cleavage of hemoglobin occurs to yield free heme and amino acids. In order to avoid free heme toxicity, this molecule is stored in the form of a crystalline polymer, named hemozoin crystal. This mechanism is essential for parasite development, representing an important target for the development of antimalarial drugs. Hemoglobin uptake and catabolism have been described in different *Plasmodium* species, specially in *P. falciparum*, which is responsible for most of the deaths associated to malaria in humans. Nevertheless, little is known about this mechanism in *P. berghei*, an important murine model commonly used in the study of malaria. In this work we studied the mechanism of hemozoin nucleation in the different stages of the intra-erythrocytic cycle of the rodent parasite *Plasmodium berghei* by means of transmission electron tomography of cryofixed and freeze substituted cells. Cryofixation of samples generally provided a better preservation of the cells and their hemozoin crystals (figure 1). The three-dimensional dispersion of hemozoin crystals within the food vacuole and the cytoplasm of the parasite was revealed by electron tomography (figure 2). Results showed that large amounts of hemoglobin are internalized in the early stages after invasion (ring stage and early trophozoite), whereas in late stages (trophozoite), assembly of several vesicles containing hemoglobin spread through the parasite cytoplasm were observed. Small food vacuoles concentrated near the membrane of the parasite were also frequently seen. Taking together, these results provide new insights on the mechanisms of hemoglobin uptake and degradation in rodent malaria parasites.

This work was supported by CNPq, FAPERJ, FINEP, CAPES (Brazil) and Instituto Nacional de Ciência e Tecnologia de Biologia Estrutural e Bioimagem.



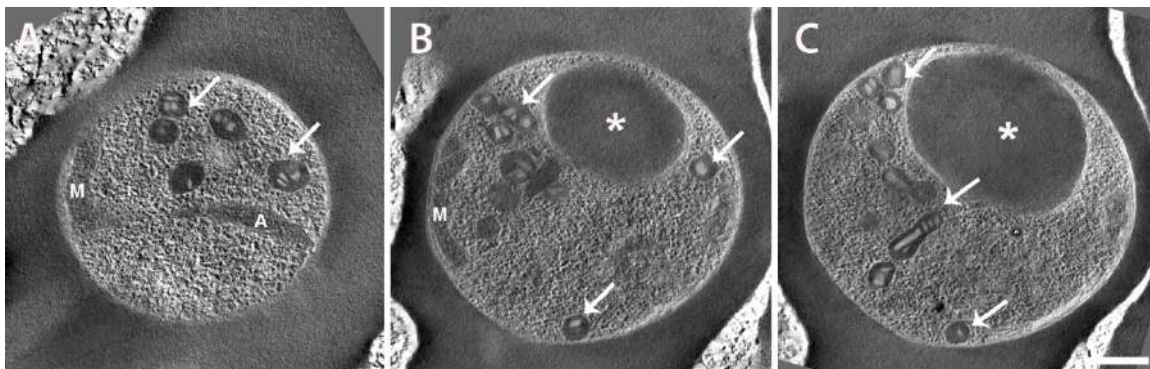


Figure 1: Serial electron tomogram of an early trophozoite (A-C) form of *P. berghei* submitted to high pressure freezing and freeze substitution. The morphology of several cell components could be observed through the different Z-sections, including hemozoin crystals (arrows) and a large hemoglobin vacuole (asterisk). M: mitochondria, A: apicoplast. Scale bar: 300nm

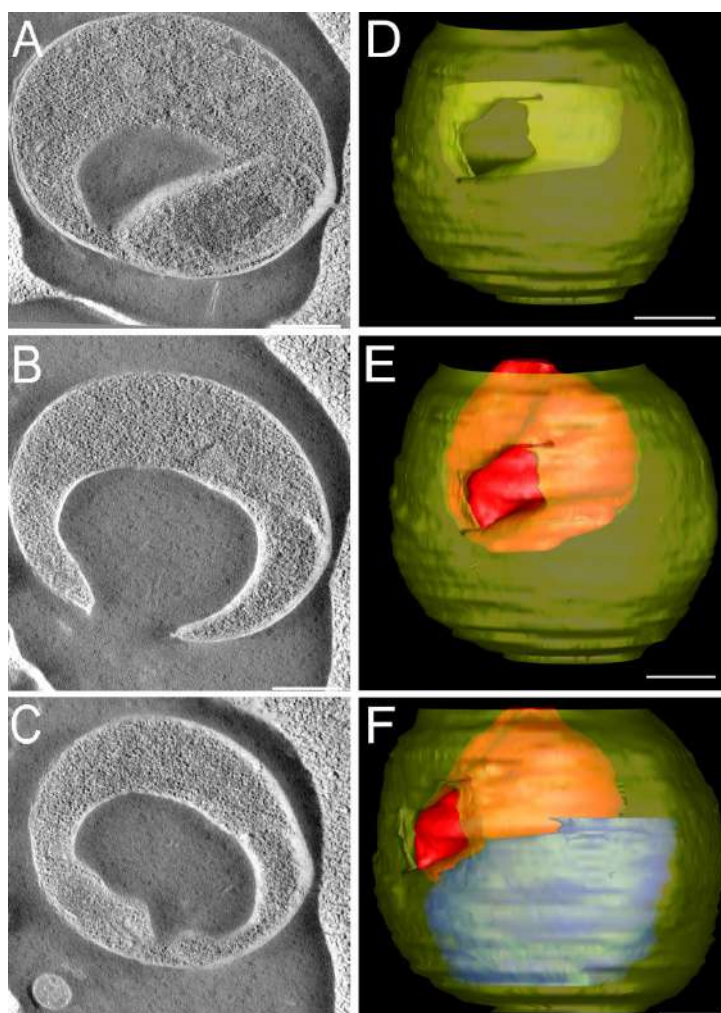


Figure 2: Serial section electron tomography of a ring stage of *P. berghei* submitted to high pressure freezing and freeze substitution. Hemoglobin uptake by the big gulp mechanism can be observed through the different Z-sections (A – C). 3D reconstruction allowed a better visualization of hemoglobin uptake mechanism (D – F). Yellow: membrane; red: hemoglobin vacuole; blue: nucleus. Scale bar: 300nm (A-C), 400nm (D-F).

## High-resolution and Three-dimensional Analysis of Hemozoin Crystals in Human and Murine Malaria Parasites

Wendt, C.<sup>1</sup>, de Souza, W.<sup>1</sup> and Miranda, K.<sup>1</sup>

<sup>1</sup> Laboratório de Ultraestrutura Celular Hertha Meyer, Instituto de Biofísica Carlos Chagas Filho and Centro Nacional de Ciência e Tecnologia em Biologia Estrutural e Bioimagem – Universidade Federal do Rio de Janeiro, Rio de Janeiro, Brazil.

Malaria is a disease caused by protozoan parasites from the genus *Plasmodium* with the highest impact on public health in endemic areas. Morbidity and mortality of this disease results from the asexual replication of *Plasmodium* in the erythrocyte of the mammalian host. In the course of its intraerythrocytic development, malaria parasites incorporate massive amounts of the host cell cytoplasm. Internalized hemoglobin is digested in a compartment with acidic pH termed the food vacuole, producing aminoacids and others by products, namely heme. Due to its toxic effects, free heme is immobilized and stored in a crystal form known as hemozoin. This mechanism is essential to parasite development and represents a physiological step used as target for many antimalarial drugs. So far, most of the studies regarding hemozoin crystal structure were obtained by the analysis of the hemozoin crystal synthetic analogue,  $\beta$ -hematin. In this work we used different microscopy approaches to analyze *P. chabaudi* hemozoin crystals. Initially, hemozoin crystals were observed inside the food vacuole of late stage (schizont) parasite by STEM-tomography (figure 1), revealing its dispersion inside the organelle. Isolated hemozoin crystals were observed by high resolution scanning electron microscopy and compared with hemozoin crystals from *Plasmodium berghei*, another murine model of malaria, and *Plasmodium falciparum*, a model of human malaria (figure 2). Hemozoin crystals observed in the different *Plasmodium* species presented a regular rectangular morphology, with modest size differences between murine and human malaria species. Furthermore, hemozoin crystals were observed in parasites that were previously treated with chloroquine, an antimalarial drug that interfere in hemozoin crystals nucleation. Serial section transmission electron microscopy revealed parasites with larger food vacuoles and small hemozoin crystals located near the food vacuole membrane (figure 3). Altogether, these results provide new insights on hemozoin crystal morphology, as well as the effect of antimalarial drugs in the process of hemozoin crystal nucleation in rodent malaria.

This work was supported by CNPq, FAPERJ, FINEP, CAPES (Brazil) and Instituto Nacional de Biologia Estrutural e Bioimagem

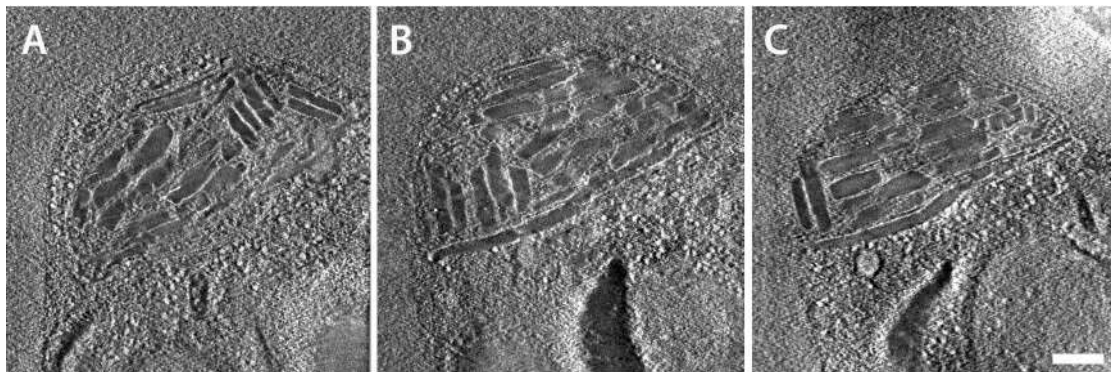


Figure 1: Serial section scanning transmission electron tomography of a food vacuole observed in the schizont form of *P. chabaudi* submitted to high pressure freezing and freeze substitution. Hemozoin crystal morphology, as well as its dispersion inside the food vacuole can be observed through the different Z-sections. Scale bar: 200nm

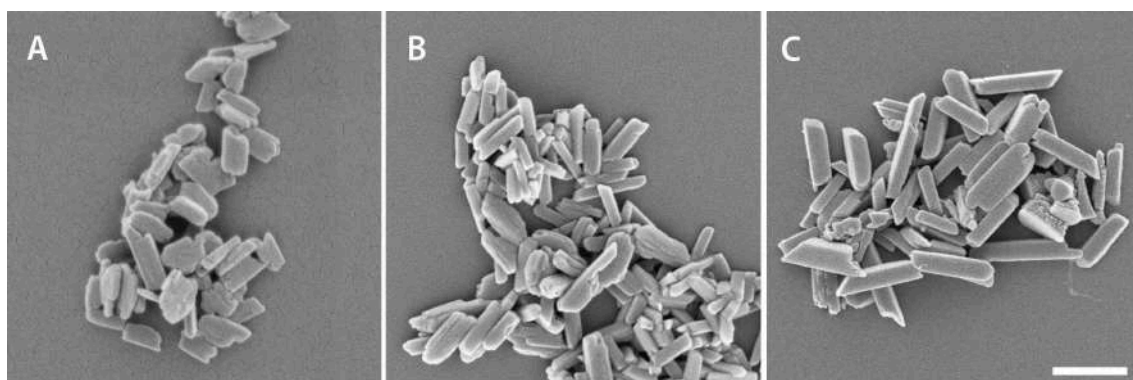


Figure 2: Hemozoin crystals isolate from *P. chabaudi* (A), *P. berghei* (B) and *P. falciparum* (C) were observed by high resolution scanning electron microscopy. Hemozoin crystal morphology observed in the three species was very similar, differing slightly in size dimensions. Scale bar: 200nm.

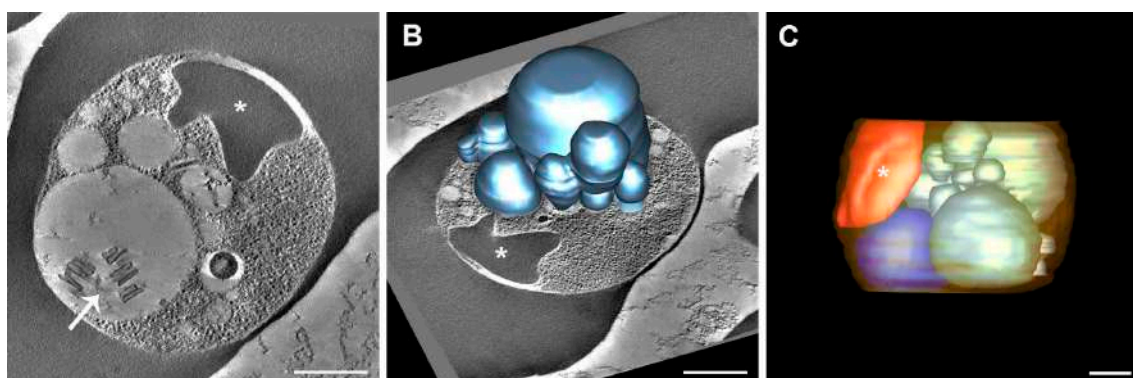


Figure 3: 3D reconstruction of a *P. chabaudi* trophozoite treated with chloroquine. Large food vacuoles were observed with small hemozoin crystals located close to the membrane (A, arrow). The food vacuole occupied most of the cell volume, being also observed a hemoglobin vacuole (asterisk). Red: hemoglobin vacuole; light blue: food vacuole; dark blue: nucleus. Scale bar: 300nm.



## Morphological analysis of three-dimensional culture formation of 3D spheroids of hepatic stellate cells

Francieli Rohden<sup>1,2\*</sup>, Mariana Ilha<sup>1</sup>, Mariana Pies Giombelli<sup>1</sup>, Fátima Guma<sup>1,2</sup>

<sup>1</sup> Universidade Federal do Rio Grande do Sul - UFRGS

<sup>2</sup> Centro de Microscopia e Microanálise, CMM - UFRGS

Three-dimensional spheroid (3D) cultures of cells have the potential to revolutionize *in vitro* studies. This is because the tissue has a microenvironment that includes extracellular matrix and the neighboring cells, being fundamental for the form, function and for the control of the growth and development of the tissues [1]. 3D cell culture models have gained considerable attention as they have the potential to promote levels of cell differentiation and tissue organization in which it is not found in conventional two-dimensional (2D) [2]. With this, 3D culture models are being developed for studies of various pathologies and toxicological studies involving liver, and other organs [3]. Found in liver space, hepatic stellate cells (HSCs) are intralobular connective tissue cells, presenting a quiescent phenotype with storage of vitamin A in lipid droplets. Importantly, they participate in extracellular matrix homeostasis of the liver, repair, regeneration and fibrosis. In response to damage, they activate myofibroblasts, characterized by increased proliferation, expression of pericellular matrix proteins and secretion of extracellular matrix proteins [3,4]. The GRX is representative lineage of HSCs [5]. **Objective:** to evaluate the morphology of the 3D spheroid culture of the GRX line and the ultrastructure of the cells of the periphery and the center of this culture. **Method:** GRX cells were plated on 1% agarose U-bottom plates for 24 h until spheroid formation. For analysis of the external morphology was performed by scanning electron microscopy, SEM (Jeol JSM 6060). Ultrastructural analysis was performed with the use of transmission electron microscopy, MET (Jeol JEM 1200 EXII). **Results:** Through the analysis of the images by SEM, were observed a great interaction between the cells composed by the spheroid. It is also possible to identify a large amount of extracellular matrix giving rise to the cellular spheroid (Fig 01). In the images of MET, the differences in the cell morphologies of the periphery and the center of the cellular spheroids are visible. The peripheral cells present fusiform morphology and a large amount of autophagosomes (Fig 02 and 03). However, the cells at the center of the spheroids are more "rounded" with large amounts of lipid droplets and autophagosomes (Fig 02). **Conclusion:** Spheroid cultures (3D) have been increasingly used for their similarity with *in vivo* models. SEM images showed a large cell-cell contact and the existence of extracellular matrix production that binds these cells to one another. On the other hand, the TEM images showed a difference in cellular morphology between the peripheral and central cells. The differential of the 3D culture is to allow the cells to explore the three dimensions of the space, thus increasing the interaction with the microenvironment and between the cells.

[1] Zuzana Koledova. 2017. DOI 10.1007/978-1-4939-7021-6\_1

[2] Dongeun Huh, *et al.* 2011. DOI:10.1016/j.tcb.2011.09.005

[3] Sophie A. Lelièvre, *et al.* 2017. DOI:10.1016/j.tiv.2017.03.012.

[4] Linshan Shang, *et al.* 2018. DOI: doi.org/10.1007/s00535-017-1404-4

[5] Borojovic, *et al.* 1985. DOI: 10.1007/BF02623469

**Figure 01**

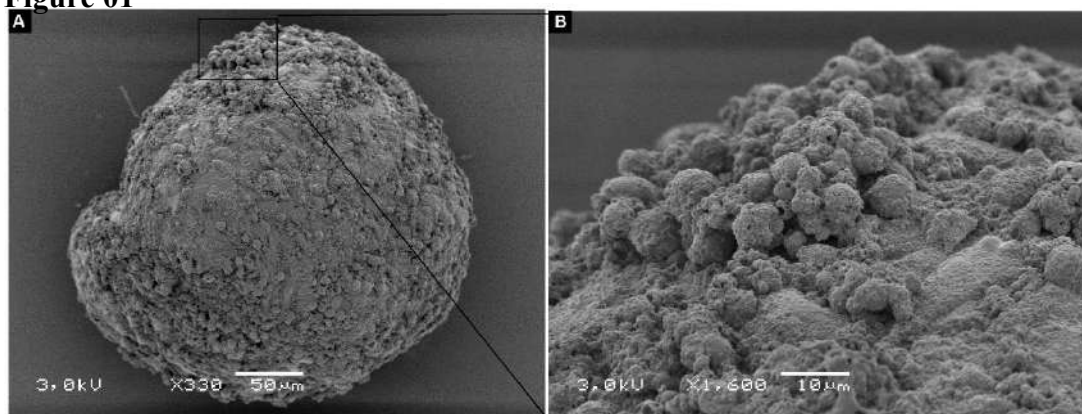


**Figure 01:** It presents the external morphology acquired by SEM. A: presents the whole spheroid. B: In the detail, it is possible observed a great interaction between the cells of the spheroid and the large amount of extracellular matrix.

**Figure 02**

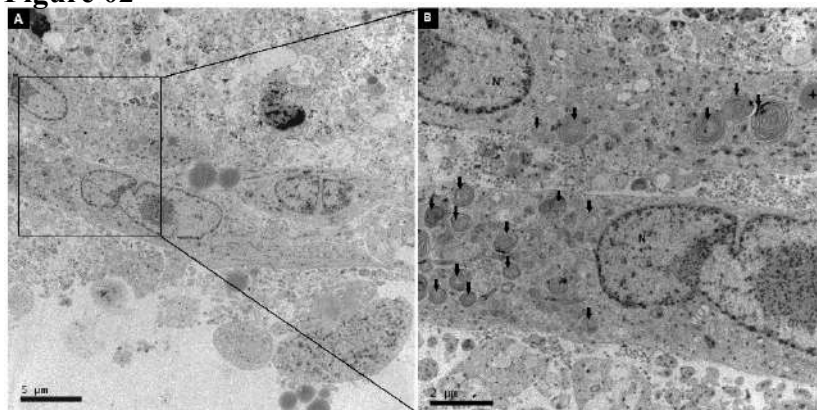


**Figure 02:** It presents the ultrastructure of the cells that components the outer face of the spheroid. A: Dynamic image, where we can observe the fusiform structure of peripheral cells. B: In the detail, we were able to identify a large amount of auto phagosomes (black arrow) and lipid droplets (black star). Magnifications of 4K and 10K, respectively.

**Figure 03**

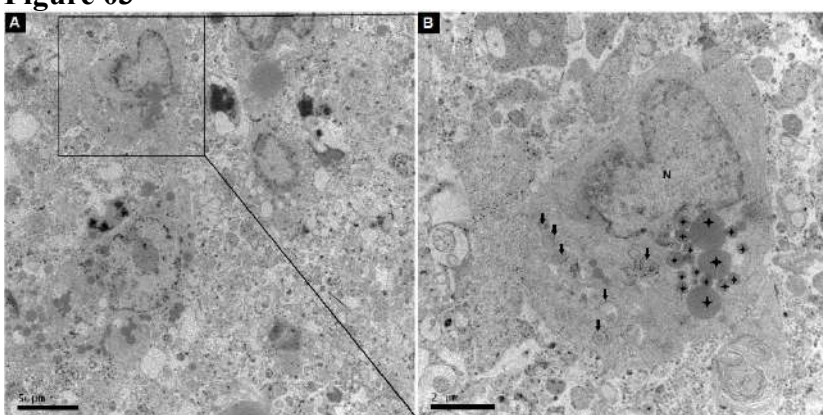


**Figure 03:** It presents the ultrastructure of the cells that components the internal portion of the spheroid. A: Dynamic image, where we can observe we can observe the rounded morphology of the cells. B: In the detail, we were able to identify a large amount of auto phagosomes (black arrow) and many lipid droplets (black star). Magnifications of 4K and 10K, respectively.



## Ultrastructural Characterization of A Novel Membrane Domain With Potential Function On Osmoregulation In *Trypanosoma cruzi*

Ingrid Augusto<sup>1,3</sup>, Wendell Girard Dias<sup>2</sup>, Wanderley de Souza<sup>1,3</sup> and Kildare Miranda<sup>1,3\*</sup>

<sup>1</sup>. Laboratório de Ultraestrutura Celular Hertha Meyer, Instituto de Biofísica Carlos Chagas Filho, Universidade Federal do Rio de Janeiro, RJ, Brazil.

<sup>2</sup>. Fundação Oswaldo Cruz, Rio de Janeiro, Brazil.

<sup>3</sup>. Centro Nacional de Biologia Estrutural e Bioimagem, Universidade Federal do Rio de Janeiro, Rio de Janeiro, Brazil.

\*kmiranda@biof.ufrj.br.

Chagas is an endemic neglected disease caused by the protozoan parasite *Trypanosoma cruzi*. Infection with *T. cruzi* affects 7 million people worldwide and cause about 7.000 deaths per year [1]. The current treatment is based on the use of Benznidazoles and Nifurtimox, which present high toxicity and resistance. Understanding the biology of *T. cruzi* is important for the rational development of more effective drugs. During the course of infection, the parasite faces several changes in the physicochemical properties of the extracellular milieu when alternating between invertebrate and mammalian hosts [2]. To cope with such changes, *T. cruzi* possess a precise osmoregulatory system that involves acidic organelles rich in calcium, polyphosphates and other cations, named acidocalcisomes, and the contractile vacuole complex (CVC), an organized structure formed by a central vacuole surrounded by a set of vesicles and tubules (the spongione), responsible for uptake and release of water during osmotic stress [3]. The CVC is always localized in a region close to flagellar pocket, where the efflux of the accumulated water may occur by unknown mechanisms. Previous works suggest the presence of a structure between the CVC and the flagellar pocket that would act as a water exit site during osmoregulation named adhesion plaque (AP), whose structure has never been described in detail [4]. Here, we investigated the structure of the adhesion plaque in *T. cruzi*, using wild type and mutant epimastigotes (TcVps34) that present super-efficient responses to hyposmotic stress. Samples were submitted to (1) freeze-fracturing and (2) high-pressure freezing, followed by freezing substitution and visualized by different three-dimensional electron microscopy methods, such as electron tomography and dual beam scanning electron microscopy. Results showed an irregular shape in the AP and thickness variations along its extension (Fig. 1), making the membranes of the central vacuole and flagellar pocket parallel and planar (Fig 1A and 2). Several filaments (6-8 nm thick) were also observed connecting both flagellar pocket and vacuole membranes, forming a dense filamentous network (Fig. 3). The presence of two APs in cells during mitosis was also observed, suggesting a synchronous organization with the CVC during cell division (Fig. 4). Despite dramatic differences on both CVC systems of wild type and TcVps34 parasites, results showed no significant differences in the general structure of their adhesion plaque. In addition, no pores or continuity of CVC and flagellar pocket membranes were observed on the plaque region. Altogether the results provide evidence for a novel subcellular domain attaching CVC to the flagellar pocket with potential functional role in the osmoregulation system of *T. cruzi*. This research was supported by CNPq, CAPES, FAPERJ, and FINEP.

[1] WHO, Wkly Epidemiol Rec. 6 (2015); [2] V. Jimenez, Res Microbiol. 165 (3) (2014); [3] P. Rohloff et al, J Biol Chem. 279 (50) (2004); [4] W. Girard-Dias et al., Histochem Cell Biol. 138 (6) (2012).

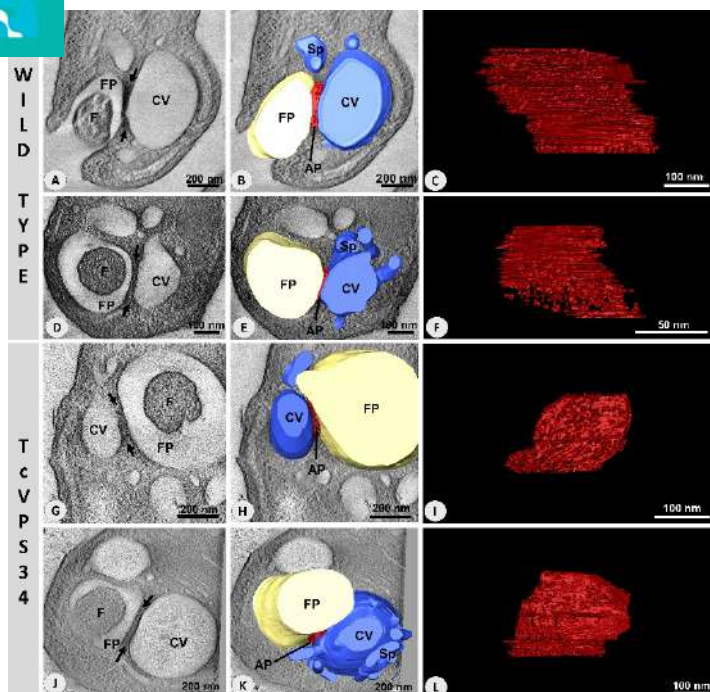


**Figure 1. Overview of tomograms and three-dimensional models of adhesion plaque in wild-type and mutants overexpressing TcVps34 cells group.** First column (A, D, G, J): virtual sections of reconstructed cells showing the electron dense region of the adhesion plaque (arrows). Second column (B, E, H, K): the top view of 3D models showing the CVC attached to the flagellar pocket by the AP. Third column (C, F, I, L): front view of the adhesion plaque (3D models), displaying different shapes. CV - contractile vacuole; Sp - spongiome; FP - flagellar pocket; F - flagellum; AP - adhesion plaque

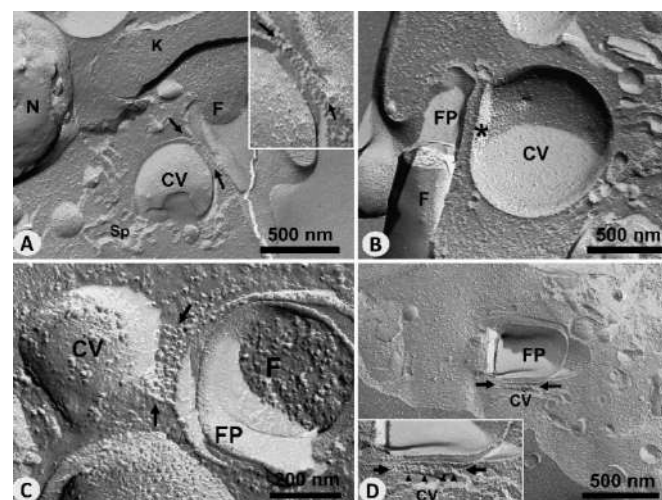


**Figure 2. Freeze fracture of wild-type (WT) and mutant TcVps34 cells.** (A) Arrows show a set of IMP's in adhesion plaque. (B) asterisk points to parallelism of the flagellar pocket and CVC membranes. (C) Row organization of IMPs in the plaque region. (D) central vacuole in lamellar shape connected to the flagellar pocket by the adhesion plaque. CV - central vacuole; Sp - Spongiome; FP - flagellar pocket; F - flagellum; K - kinetoplast; N-nucleus.

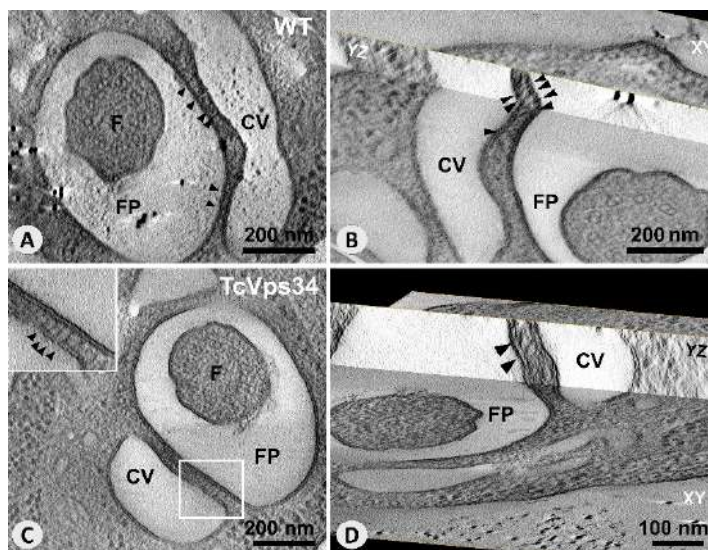


**Figure 3. Filaments observed in the region of adhesion plaque in wild-type (WT) cells and mutant TcVps34.** (A) and (C) the filaments are pointed by arrowheads. (B) and (D) show filaments with different orientations in YZ plane. CV - contractile vacuole; FP - flagellar pocket; F - flagellum.

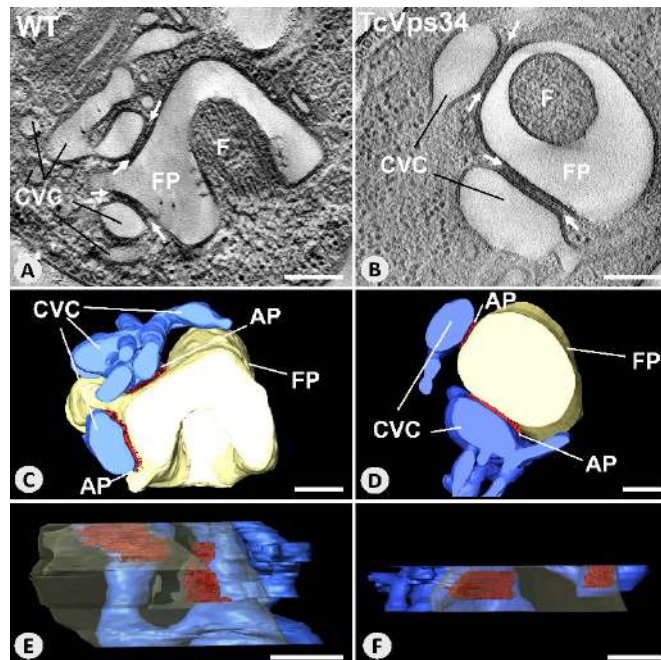


**Figure 4. Wild-type (WT) and mutant (TcVps34) cells with the presence of two adhesion plaques.** (A) and (B) Electron tomography of wild-type cell and mutant TcVps34, respectively (arrows point to adhesion plaque); (C) - (F) Three-dimensional models highlighting the contractile vacuole complex anchored in more than one region to the flagellar pocket. CVC - contractile vacuole complex; FP - flagellar pocket; F - flagellum; AP - adhesion plaque. Scale bar = 200 nm.

## Three-dimensional Analysis Of The Cytostome-Cytopharynx Complex In *Trypanosoma cruzi* Amastigotes And Its Function On Endocytosis

Carolina de L. Alcantara<sup>1,2\*</sup>, Wanderley de Souza<sup>1,2</sup> and Narcisa L da Cunha-e-Silva<sup>1,2</sup>

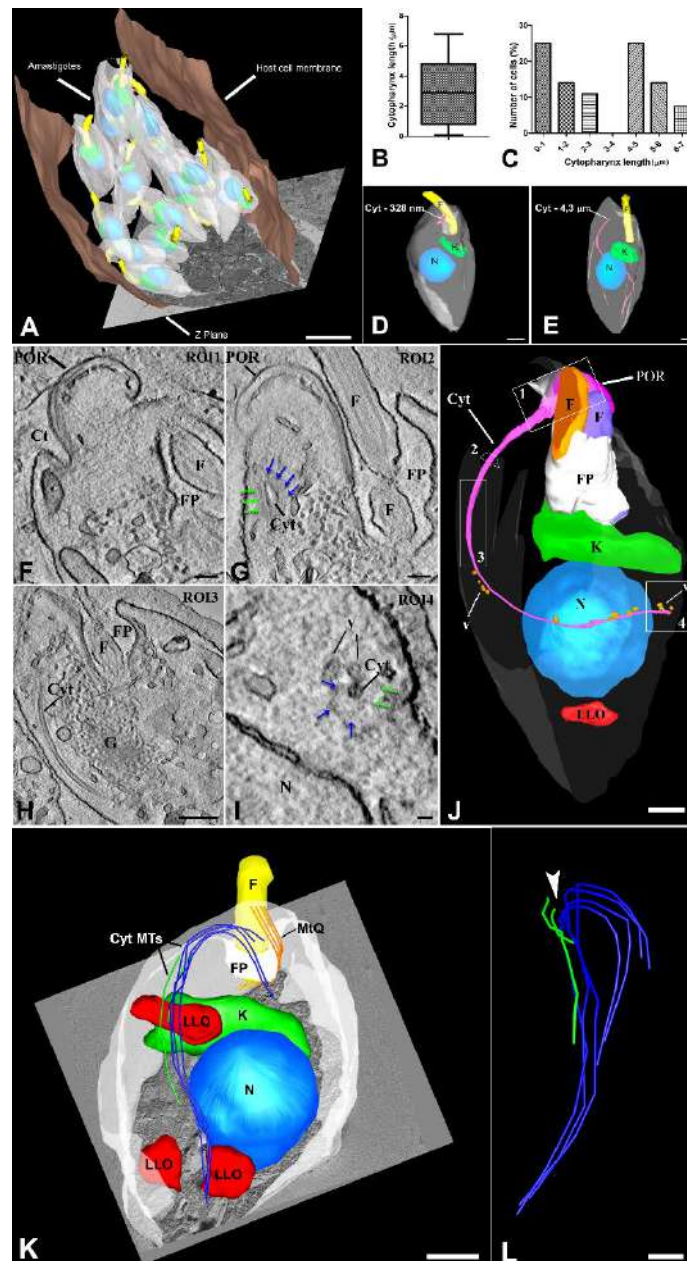
<sup>1</sup> Instituto de Biofísica Carlos Chagas Filho, Universidade Federal do Rio de Janeiro, Rio de Janeiro 21941-902, Brazil. <sup>2</sup> Instituto Nacional de Biologia Estrutural Bioimagem, INBEB. \*alcantara@biof.ufrj.br

*Trypanosoma cruzi* is a protozoan parasite that causes Chagas' disease. During its life cycle, the parasite presents two proliferative forms: epimastigotes are extracellular forms, present in the midgut of the insect vector; amastigotes are intracellular forms, present in the cytoplasm of vertebrate host cells. In epimastigotes, endocytosis is well characterized and occurs through a specialized membrane domain called cytostome-cytopharynx complex<sup>1</sup>. The cytostome opens near the flagellar pocket and invaginates deeply forming the cytopharynx, which is supported by a special set of microtubules, disposed as a gutter<sup>2</sup>. Amastigotes also possess a cytostome-cytopharynx complex, however the participation on endocytosis of these forms have not been elucidated. Extracellular amastigotes can be obtained from the supernatant of infected cells or from *in vitro* amastigogenesis and are capable to establishing and maintaining infection *in vivo* and *in vitro*<sup>3</sup>. It has been shown in the literature that intracellular amastigotes and extracellular amastigotes present differences in their surface proteins<sup>4</sup>. In this work, we analyzed and compared the ultrastructure of the cytostome-cytopharynx complex of intracellular amastigotes, within their host cells, and extracellular amastigotes, obtained from the supernatant of infected cells. Three-days infected cells or six-days culture supernatant were processed for TEM and observed using FIB-SEM in slice and view mode. With the serial images obtained we analyzed the shape and length of the cytopharynx in the population and observed that while intracellular amastigotes had a long (~3µm) helical shape cytopharynx, like that of epimastigotes, extracellular amastigotes lacked this structure. By serial electron tomography we could confirm that in extracellular amastigotes the cytostome-cytopharynx membrane domain was not present but the accompanying microtubules were maintained in their length and arrangement. We also compared the endocytic ability of intracellular amastigotes, obtained through cell lysis, with that of extracellular amastigotes using fluorescent endocytic tracers and observed that while ~50% of isolated intracellular amastigotes can uptake the tracer, 100% of the extracellular amastigotes cannot. After isolation through host cell lysis, intracellular amastigotes undergo ultrastructural modifications in the cytostome-cytopharynx complex, leading to an impairment of the endocytic ability. Those observations are new evidences of structural and functional differences between intra and extracellular *T. cruzi* amastigotes.

### REFERENCES

- [1] I. Porto-Carreiro et al., Eur J Cell Biol, 79 (2000) 858.
- [2] C. L. Alcantara et al., J Cell Sci, 127 (2014) 2227.
- [3] V. Ley et al., J Exp Med, 168 (1988) 649.
- [4] E. O. Silva et al., Parasitol Res, 84 (1998) 257.
- [4] This research was supported by CNPq and CAPES (Brazil).





**(A-E) Intracellular amastigote's cytopharynx length.** Three days-infected cultures were processed for TEM and imaged in a FIB-SEM microscope. (A) 3D reconstruction of the FIB-SEM series acquired, showing the reconstructed amastigotes inside its host cell. (B) After reconstruction, we measured the cytopharynx length of 27 entire amastigotes. The cytopharynx length varied among the amastigotes, with a mean of 3  $\mu\text{m}$ . (C) Frequency distribution of the cytopharynx length among the reconstructed amastigotes showed that the cytopharynx can assume very different lengths, from a few nanometers to micrometers. Half of the amastigotes analyzed possessed a cytopharynx with less than 1  $\mu\text{m}$  (25%) or between 4-5  $\mu\text{m}$  (25%). (D-E) 3D reconstructions of amastigotes with the more representative cytopharynx lengths. Bars: A-E, 500 nm. **(F-J) The ultrastructure of intracellular amastigote's cytopharynx.** Three days-infected cultures were processed for TEM and imaged by Serial Electron Tomography. (F-I) Virtual images of the serial tomogram obtained from an amastigote inside its host cell. (F) Shows the region of the cytostome (Ct) opening, that is continuous with the preoral ridge (POR). (G) A transversal section of the cytopharynx (Cyt) shows the triplet and quartet accompanying microtubules (arrows). (H) A longitudinal section of the cytopharynx showing its proximity to the Golgi complex (GC). (I) Vesicles (v) are present aligned to the cytopharynx naked side - without microtubules (arrows) - of the cytopharynx. (J) 3D reconstruction of the amastigote highlighting the ROIs (1-4) corresponding to the images in F-I. Bars: F-I, 200 nm; J, 500 nm. **(K-L) Extracellular amastigotes lack a cytostome-cytopharynx.** Extracellular amastigotes were collected from the supernatant of infected cultures, processed for TEM and imaged by Serial Electron Tomography. (K) Three-dimensional reconstruction of an extracellular amastigote. We did not observe the presence of neither the cytostome nor the cytopharynx, only the accompanying microtubules (green and blue tubes-Cyt mts) could be observed. (L) The number and disposition of the microtubules were maintained, extending to the posterior of the cell. The arrowhead points to the site where the cytostome should appear but it was not observed in these forms. Bars: K, 500 nm; L, 100 nm. Cytopharynx (pink), Flagellar pocket (white), Kinetoplast (green), Nucleus (blue) and Lysosome-like organelle (LLO-red)



## Morphological Aspects of Subpellicular Microtubules of *Trypanosoma cruzi*

Juliana Cunha Vidal<sup>1\*</sup> and Wanderley de Souza<sup>1,2</sup>

<sup>1</sup>Laboratório de Ultraestrutura Celular Hertha Meyer, Instituto de Biofísica Carlos Chagas Filho, UFRJ- Rio de Janeiro -Brasil.

<sup>2</sup>Instituto Nacional de Ciência e Tecnologia de Biologia Estrutural e Bioimagem – INBEB- Rio de Janeiro - Brasil.

*Trypanosoma cruzi* is a protozoan parasite and exhibits unique features, which differ them significantly from their mammalian host. Among them, the subpellicular microtubules (SPMT) that follows the helical pattern along the long axis of the cell body organized in a highly ordered array of stable microtubules placed beneath the plasma membrane, absent in flagellar pocket and cytostome-cytopharynx complex [1]. The parasite's life cycle involves symmetrical division and different developmental transitional stages. The maintaining and establishment of cell shape is a fundamental role of cytoskeleton and provides interesting models for cellular biology studies [2]. The morphological knowledge of SPMT during *T. cruzi* life cycle is limited. To analyze this array of microtubules, tridimensional reconstruction were performed using electron microscopy tomography and focused ion beam-scanning electron microscopy (FIB-SEM). The observations shows that epimastigotes has approximately 60 SPMT, among them, the microtubules next to flagellar pocket are extremely shorter or half-length when compared to others SPMT. Besides this, the helicoidally pattern is held. In conclusion, shorter length microtubules may represent the first evidence that biogenesis of SPMT occurs next to flagellar pocket. At the present time, analysis of SPMT during mitosis and metacyclogenesis are being made and also analysis of the posterior region of cell body to elucidate how SPMT are joined together firmly. These studies can reveal ultrastructural details about the maintenance of cell shape even during its complex life cycle. This work was supported by CNPq, FAPERJ, CAPES and INBEB.

[1] Meyer H, De Souza W. Electron microscopic study of *Trypanosoma cruzi* periplast in tissue cultures. I. Number and arrangement of the peripheral microtubules in the various forms of the parasite's life cycle. The Journal of Protozoology. 1976; 23 (3):385–90.

[2] Vidal JC and De Souza W (2017) Morphological and functional aspects of cytoskeleton of trypanosomatids. Cytoskeleton – Structure, Dynamics, Function and Disease. doi: 10.5772/66859.

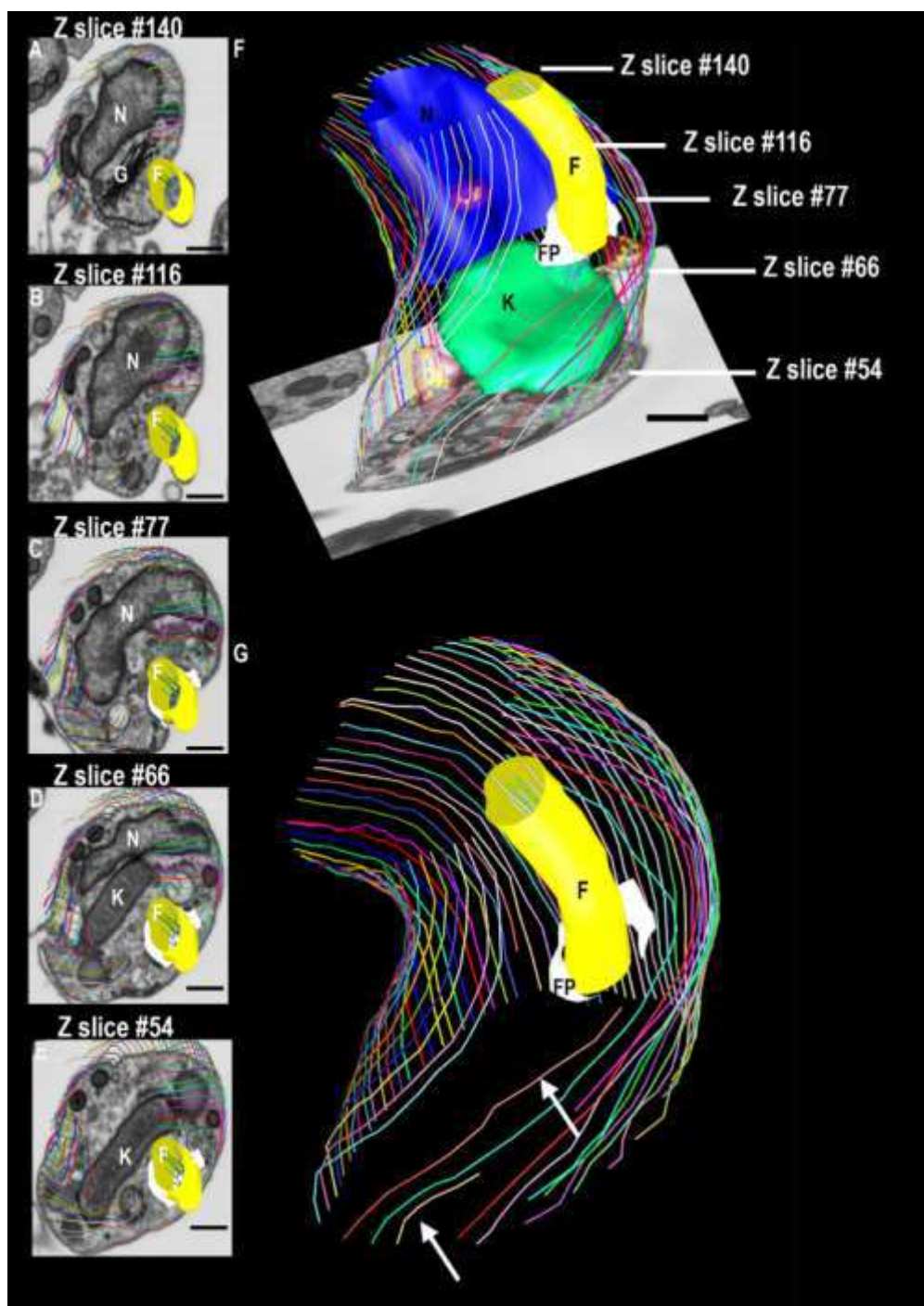


**Figure 1:** A-E) Sequence of FIB-SEM images of a cell showing different portions of the cell body and SPMT. F) A 3D model of the cell shown in A-E. The model shows the anterior region of *T. cruzi* (z-slice#140 to 54). Near to the flagellar pocket region (portion lacking SPMT) was possible to observe shorter length microtubules (z-slice#66 to #54). G) Omission of some structures to highlight some shorter length SPMT was emphasizing with arrows. Nucleus (N), blue; Kinetoplast (K), green; Flagellum (F), yellow; Flagellar pocket (FP), white. Bars: 200nm

## Three-dimensional characterization of the Contractile Vacuole Complex in *Trypanosoma cruzi* Mutants with Different Responses to Osmotic Stress

Wendell Girard-Dias<sup>1,2</sup>, Wanderley De Souza<sup>1</sup> and Kildare Miranda<sup>1\*</sup>

1. Laboratório de Ultraestrutura Celular Hertha Meyer, Instituto de Biofísica Carlos Chagas Filho and Centro Nacional de Biologia Estrutural e Bioimagem / Universidade Federal do Rio de Janeiro, Rio de Janeiro, Brazil.

2. Plataforma de Microscopia Eletrônica Rudolf Barth, Instituto Oswaldo Cruz / Fiocruz, Rio de Janeiro, Brazil.

\* [kmiranda@biof.ufrj.br](mailto:kmiranda@biof.ufrj.br)

*Trypanosoma cruzi*, the etiologic agent of Chagas disease, is a protozoan that has a complex life cycle that involves different hosts. During the course of infection, the parasite faces different environments where extreme variations in the concentration of ions and osmolytes in the extracellular milieu are found. To cope with these fluctuations, the parasite has developed adaptation mechanisms that involve signaling pathways and remodeling of parasite organelles, as the contractile vacuole complex (CVC) and acidocalcisomes [1]. The CVC of some trypanosomatids is formed by several tubules and vesicles forming a multi-tubular structure named spongiome, connected to a central vacuole located near the flagellar pocket [2]. Our group showed using cryotechniques that the vacuole of *T. cruzi* is positioned docked to a specific domain of the flagellar pocket, presenting an electron dense aspect, and associated with a spongiome. The tubules of the spongiome connect to the contractile vacuole preferentially in a region opposite to the kinetoplast and parallel to the flagellum, suggesting that this structure has a polarized organization [3]. However, the structural modifications that take place in the CVC during events of fluid expelling have not been yet fully characterized in *T. cruzi*. Thus, the aim of this work was to study the morphology of the CVC during their pulsation cycle and the influence of enzymes involved in the osmotic control, using as tools mutants of *T. cruzi* that overexpress these enzymes, a phosphatidylinositol 3-kinase (TcVps34) [4] and a phosphodiesterase C2 (TcrPDEC2) [5], resulting in parasites with different patterns of response to hyposmotic shock (superefficient response and sub-efficient response, respectively). The samples were processed by high-pressure freezing followed by freeze-substitution and observed by advanced methods of three-dimensional electron microscopy such as electron tomography and dual beam scanning electron microscopy. The results showed major structural changes in the phenotype of the CVC in mutants compared to the wild type parasites, such as increase in the volume of the central vacuole in superefficient cells and decrease in the sub-efficient ones, as observed in quantitative data extracted from 3D models of the CVC (figure 1, C, F and I). As well, a fragmentation of the tubules of spongiome was observed in cells with a compromised response (figure 1). These results allowed the identification of structural phenotypes of the CVC that justify the physiological phenotype for this essential asset for osmotic control in *T. cruzi*. Altogether, the results suggest that the spatial organization of CVC is defined by specific domains of the spongiome and the contractile vacuole, which may be modulated during events of regulatory volume decrease in *T. cruzi*.

### References:

- [1] P. Rohloff and R. Docampo, 2008. Exp. Parasitol., 118: 17-24.
- [2] J. C. Linder and L. A. Staehelin, 1977. J. Ultrastruc. Res., 60: 246-262.

- [3] Girard-Dias et al, 2012. Histochem cell biol., 138(6):821-31.  
[4] Schoijet et al, 2008. J. Biol. Chem., 283: 31541-31550.  
[5] Schoijet et al, 2010. Mol. Microbiol., 79: 50-62.  
[6] This work was supported by CNPq, FAPERJ, CAPES and FINEP (Brazil)

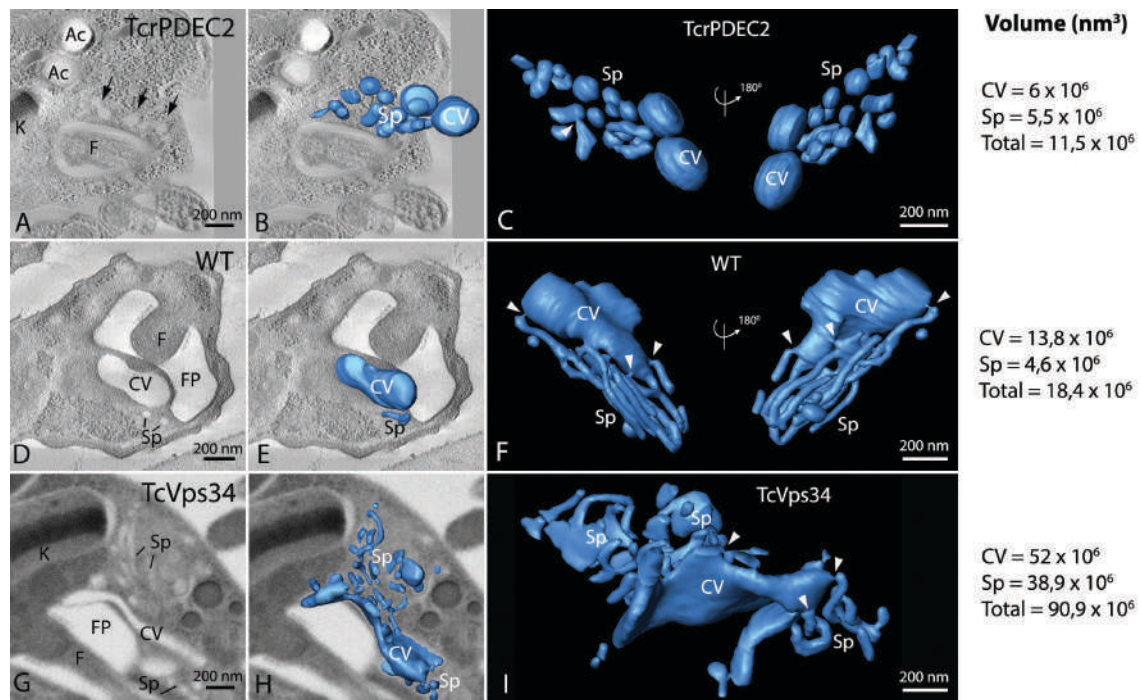


**Figure 1.** Three-dimensional organization of the CVC of *T. cruzi* at systole phase in wild type (WT) cells (A-C) and mutants overexpressing the enzymes TcrPDEC2 (D-F) and TcVps34 (G-I). Note the fragmented aspect of the spongiome in TcrPDEC2 mutants (A-C), which are less efficient cell in volume recovery, while in TcVps34 mutants, which are more efficient in volume recovery, the spongiome is a dense network and the contractile vacuole enlarged, both compared with WT cells. Quantitative data of contractile vacuole and spongiome volume, extracted from 3D models is also showed (C, F and I). Ac (acidocalcisome), F (flagellum), Sp (spongiome), CV (contractile vacuole), FP (flagellar pocket) and K (kinetoplast).



## **Morphological and Morphometric Evaluation of the Muscle Fibers of the Extensor Digitorum Longus and Soleus Muscles of Mice's Offspring Exposed or Not to Glyphosate**

Ariadne Barbosa<sup>1\*</sup>, Mylena De Campos Oliveira<sup>1</sup>, Camila Kuhn<sup>1</sup>, Lésle Cazetta Jerônimo<sup>1</sup>, Sandra Balbo<sup>2</sup>, Maria Lucia Bonfleur<sup>2</sup> and Marcia Miranda Torrejais<sup>1</sup>

<sup>1</sup>. Universidade Estadual do Oeste do Paraná-UNIOESTE, LABEM, Cascavel, Brazil

<sup>2</sup>. Universidade Estadual do Oeste do Paraná-UNIOESTE, LAFEM, Cascavel, Brazil

\*ariadne\_barbosa@hotmail.com

In Brazil, there is a high consumption of pesticides [1], which is reflected as a major public health problem due to several cases of population's intoxication by the exposure to these components [2]. Organophosphates are the most commonly used pesticides in agriculture and glyphosate is a part of this group [1,3]. It is known that organophosphates promote the inhibition of the enzyme acetylcholinesterase (AChE) [4], degeneration of muscle fibers [5] and impaired motor function in exposed mice's offspring [6]. In contrast, it is not known which effect is promoted by the exposure of glyphosate in the morphology and morphometry of the neuromuscular junctions (NMJs) of the exposed mice's offspring, justifying the accomplishment of this work. All the procedures adopted were submitted and approved by the Ethics Committee in the Use of Animals (CEUA) of Unioeste on 09/16/2016. Twelve female mice of lineage C57BL/6 were used, which, after pregnancy detection, were separated into CTL group, receiving only water and GF group, which received water with 0.5% glyphosate during pregnancy and lactation. After weaning, male offspring were separated into two groups (n=8): CTL-F1, from mothers who received only water and GLY-F1 from mothers exposed to glyphosate. Both groups received standard diet during the whole experiment. At the age of 150 days the mice were euthanized, and the extensor digitorum longus (EDL) and soleus (SOL) muscles were collected and their left antimeres were stored and fixed in Karnovsky, which later were cut longitudinally with a stainless steel blade and submitted to Nonspecific Esterase technique [7]. The material obtained with the technique was photo documented and used for the measurements of area, smaller diameter and larger diameter of NMJs. Groups CTL-F1 and GLY-F1 presented elliptic, oval and round NMJs in both EDL and SOL muscles (Figure 1A, 1B, 1C and 1D). Regarding the measurements of area, larger diameter and smaller diameter did not present significant differences between the GLY-F1 and CTL-F1 groups in the JNMs of the EDL and SOL muscles (Figure 1E, 1F and 1G), demonstrating that the exposure to the pesticide glyphosate did not promote changes in the NMJs of the exposed mice's offspring.

[1] Brazil, Pesticides in the context of the single health system. 2016

[2] V. G. Barth & A.C.B. Biazon. Rev. Sau. Biol. 10 (2010).

[3] D. B. Jesus e Vale et al., Convibra (2017).

[4] E. R. Barboza et al., Mov. Disord.. 10 (2018).

[5] J. E. Bright., Hum. Exp. Toxicol. 10 (1991).

[6] J. M. Spyker & D. L. Avery. J. Toxicol. Environ. Health. 3 (1977).

[7] M. J. Karnovsky. J. Cell Biol

[8] This research was supported by CAPES (Brazil).

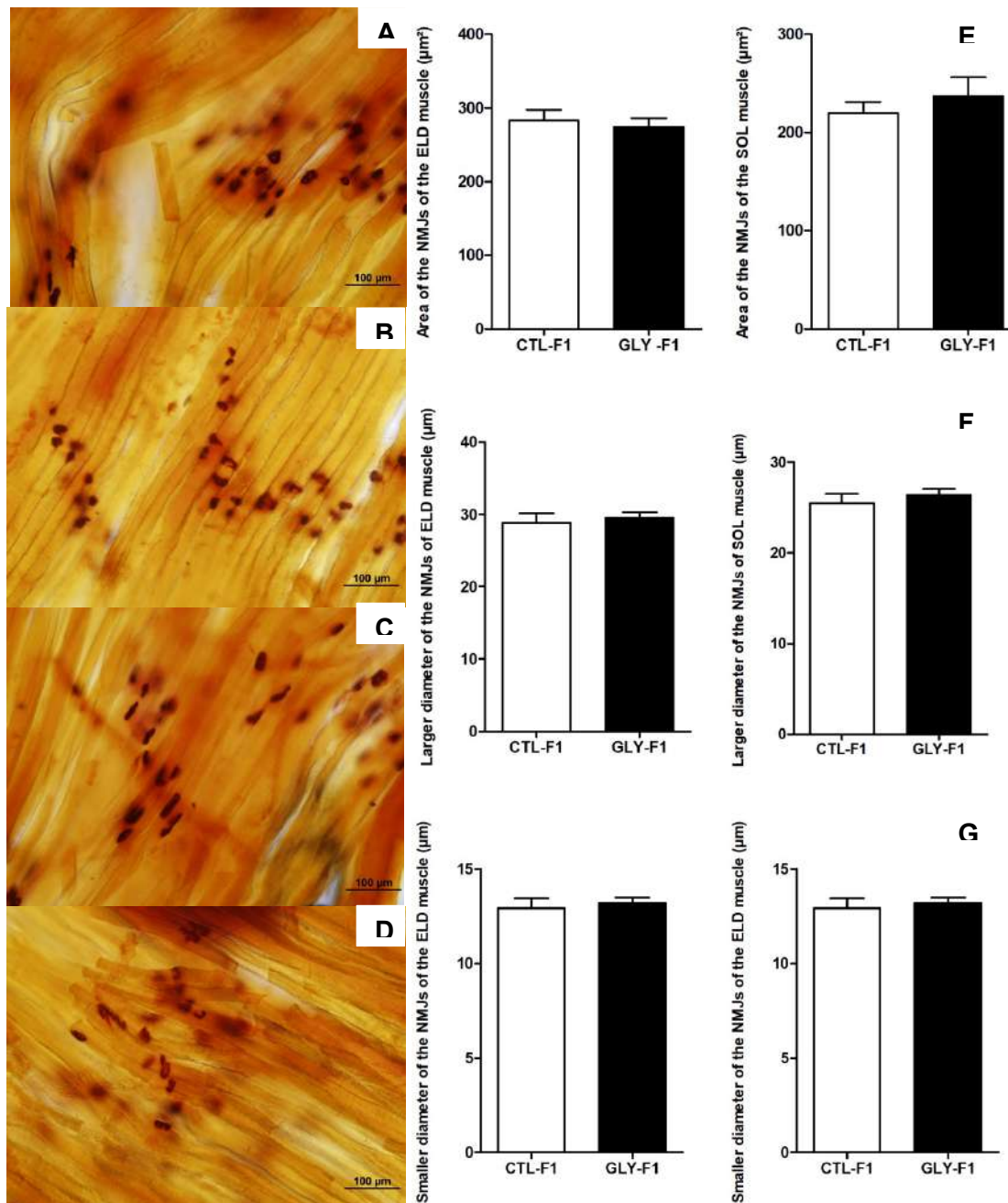


**Figure 1-** Photomicrographs of the neuromuscular junctions (NMJs) of the extensor digitorum longus (EDL) and soleus (SOL) muscle. In **A**: NMJs of the EDL muscle of animals from CTL-F1 group and **B**: NMJs of the EDL muscle of animals from GLY-F1 group. **C**: NMJs of the SOL muscle of CTL-F1 group and **D**: NMJs of the SOL muscle of GLY-F1 group. **E**, **F** e **G**: area, larger diameter and smaller diameter of the NMJs of the EDL and SOL muscles, respectively.

## Histoenzymology and Morphometry of the Extensor Digitorum Longus Muscle of Oophorectomized Female Rats Submitted to Vibrating Platform Treatment

Ariadne Barbosa<sup>1\*</sup>, Dinei Prado Filho<sup>1</sup>, Mylena de Campos Oliveira<sup>1</sup>, Gladson Ricardo Flor Bertolini<sup>1</sup>, Ana Tereza Bittencourt Guimarães<sup>1</sup>, Lucinéia de Fátima Chasko Ribeiro<sup>1</sup>, Marcia Miranda Torrejais<sup>1</sup>

<sup>1</sup>Universidade Estadual do Oeste do Paraná - UNIOESTE - Campus of Cascavel - Parana - Brazil

\*ariadne\_barbosa@hotmail.com

Mechanical vibration by vibrating platform (VP) has been used to gain strength and muscle mass in animal models of oophorectomy<sup>1</sup>. The present study investigated the counting of muscle fiber types of the extensor digitorum longus (EDL) of oophorectomized female rats treated with VP. All the procedures adopted were submitted and approved by the Ethics Committee in the Use of Animals (CEUA) of Unioeste on 08/24/2016 [2]. Sixty-two Wistar rats were randomized into two groups: Pseudo-oophorectomy (GP) and Oophorectomy (GO). After a 60-day postoperative period the animals were separated into eight subgroups: non-submitted to VP treatment in four (GP4 and GO4) and eight (GP8 and GO8) weeks and treated with VP for four (GPP4 and GOP4) and eight (GPP8 and GOP8) weeks. The treatment was performed on VP, 60 Hz frequency for 10 minutes, three times a week. The EDL muscle was collected, frozen in liquid nitrogen and cross-sectioned in a cryostat and submitted to histoenzymologic NADH-TR technique. In order to count the different types of fiber, three images (200x) of each were captured. The three-way ANOVA was used to analyze the data. The NADH-TR reaction evidenced the presence of the three types of muscle fibers (I, Ila and I Ib), showing random distribution of fibers in all groups studied (Figure 1). However, when analyzing the type I fibers count, there is a reduction for the oophorectomized (GO4, GOP4, GO8 e GOP8) ( $\bar{x}=69,354 \pm 11,82$ ) groups in relation to the pseudo-oophorectomized (GP4, GPP4, GP8 e GPP8) ( $\bar{x}=78,413 \pm 14,23$ ) groups. Regarding the Ila fibers, in the four-week period, the groups GO4 ( $\bar{x}= 65.8 \pm 23.1$ ) and GOP4 ( $\bar{x}= 61.1 \pm 11.0$ ) ( $\bar{x}= 61.642 \pm 15.96$ ) had a reduction in relation to the groups pseudo-oophorectomy GP4 ( $\bar{x}= 84.7 \pm 17.3$ ) and GPP4 ( $\bar{x}= 79.2 \pm 17.9$ ). In the eight-week period, groups GO8 ( $\bar{x}= 72.3 \pm 18.0$ ) and GOP8 ( $\bar{x}= 81.6 \pm 16.4$ ) showed an increase in the amount of muscle fibers of type Ila when compared with oophorectomized female rats in the period of four weeks GO4 ( $\bar{x}= 65.8 \pm 23.1$ ) and GOP4 ( $\bar{x}= 61.1 \pm 11.0$ ) ( $\bar{x}= 61.642 \pm 15.96$ ). By analyzing type I Ib fibers, there was an increase in muscle fiber counts in the groups that did not undergo VP treatment in the eight-week period GP8 ( $\bar{x}= 119.9 \pm 29.0$ ) and GO8 ( $\bar{x}= 116.9 \pm 18.8$ ) when compared with those who did not perform VP in the four-week period GP4 ( $\bar{x}= 105.6 \pm 15.2$ ) and GO4 ( $\bar{x}= 94.2 \pm 11.6$ ) (Table 1). Oophorectomy reduced type I fiber counts, decreased type Ila fiber counts over a four-week period, increased over eight-week period, increased I Ib fiber counts over the eight-week period in relation to the four-week period, without any interference from VP treatment.

## REFERENCES

- [1] M. Komrakova et al., *Calcif. Tissue Int.* 99 (Suppl. 4) (2016) 408.  
 [2] This research was supported by Araucaria Foundation (Brazil).

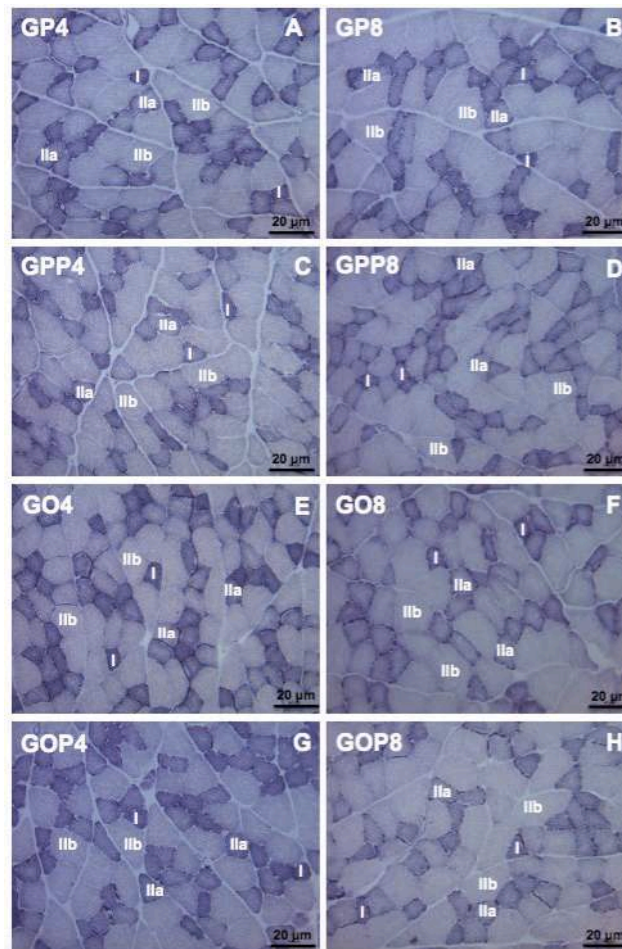


**Figure 1-** Photomicrographs of female Wistar rats' EDL muscle, cross-section of muscle fibers. NADH-TR reaction. **A:** Group Pseudo-oophorectomy four weeks (GP4) and **B:** Group Pseudo-oophorectomy eight weeks (GP8). **C and D:** Pseudo-platform groups treated in four (GPP4) and eight (GPP8) weeks, respectively. **E and F:** Groups Oophorectomy four (GO4) and eight (GO8) weeks. **G and H:** Oophorectomy-platform groups treated in four (GOP4) and eight (GOP8) weeks. Type I fibers presenting strong reaction and smaller muscle fibers cross-sectional area (CSA). Type IIa fibers with reaction and intermediate CSA. Type IIb fibers, higher CSA and poor reaction to NADH-TR.

**Table 1-** Values expressed as the average  $\pm$  standard deviation of type I, type IIa and type IIb muscle fiber counts of the groups GP (pseudo-oophorectomy), GPP (pseudo-platform), GO (oophorectomy) and GOP (oophorectomy-platform), in the periods of four and eight weeks.

GROUPS	Type I <sup>*</sup>	Type IIa <sup>Ø</sup>	Type IIb <sup>†</sup>
GO4	75,3 $\pm$ 11,0 <sup>a</sup>	65,8 $\pm$ 23,1 <sup>a</sup>	94,2 $\pm$ 11,6 <sup>a</sup>
GO8	67,9 $\pm$ 15,2 <sup>a</sup>	72,3 $\pm$ 18,0 <sup>b</sup>	116,9 $\pm$ 18,8 <sup>b</sup>
GOP4	71,4 $\pm$ 7,0 <sup>a</sup>	61,1 $\pm$ 11,0 <sup>a</sup>	99,9 $\pm$ 15,8 <sup>a</sup>
GOP8	63,6 $\pm$ 11,6 <sup>a</sup>	81,6 $\pm$ 16,4 <sup>b</sup>	99,5 $\pm$ 14,3 <sup>a</sup>
GP4	76,8 $\pm$ 21,7 <sup>b</sup>	84,7 $\pm$ 17,3 <sup>b</sup>	105,6 $\pm$ 15,2 <sup>a</sup>
GP8	78,3 $\pm$ 13,0 <sup>b</sup>	72,5 $\pm$ 12,0 <sup>b</sup>	119,9 $\pm$ 29,0 <sup>b</sup>
GPP4	80,9 $\pm$ 9,5 <sup>b</sup>	79,2 $\pm$ 17,9 <sup>b</sup>	124,5 $\pm$ 18,6 <sup>a</sup>
GPP8	77,2 $\pm$ 13,8 <sup>b</sup>	81,6 $\pm$ 15,0 <sup>b</sup>	110,3 $\pm$ 26,9 <sup>a</sup>

<sup>\*</sup> letters indicate the simple effect of surgery.

<sup>Ø</sup> letters indicate the interaction of time effects and surgery.

<sup>†</sup> letters indicate the interaction of treatment effects and time.



## Effect of Erythropoietin in the Autotransplant of Cryopreserved Cat Ovarian Tissue

Cecibel M. L. Félix<sup>1</sup>, Liudimila P. Gonçalves<sup>1</sup>, Ana Bárbara R. Silva<sup>2</sup>, Marcella M. Costa<sup>1</sup> and Carolina M. Lucci<sup>1\*</sup>

<sup>1</sup>. Laboratory of Animal Reproduction and endocrinology, Department of Physiological Sciences, Biological Sciences Institute, University of Brasília, Brasília-DF, Brazil.

<sup>2</sup>. Faculty of Agronomy and Veterinary Medicine, University of Brasília, Brasília-DF, Brazil.

\*Corresponding author.

E-mail address: [carollucci@gmail.com](mailto:carollucci@gmail.com)

Ovarian tissue cryopreservation and transplantation are methods that allow the conservation of female gametes [1, 2]. However, in the process of transplantation there is an initial period of ischemia, which affects the survival and development of the follicles, which is especially deleterious for cryopreserved tissues [3]. The objective of the present study is to evaluate the effect of erythropoietin (EPO) in cryopreserved cat ovarian tissue autografted to a peripheral site. Five adult cats (n=5) were used. Four of them were treated with EPO (500 UI/Kg/day, Sc) during seven days (three days before, on the same day and three days after the ovariohysterectomy), and the other one cat received no medication. All cats were submitted to ovariohysterectomy and small pieces of ovarian tissue were taken and cryopreserved (slow freezing with 1.5M DMSO). After 3 days, the ovarian tissue pieces were thawed and transplanted to the subcutaneous tissue of the dorsal neck of the same cat (autografting). The grafts were removed after 7, 14, 21, 28, 49 and 63 days, processed for histology and stained with hematoxylin-eosin and Gomori trichrome. The number of morphologically normal follicles after cryopreservation of ovarian tissue showed a significant reduction in both non-treated and EPO-treated animals. On Day 7 post-transplantation, the percentages of morphologically normal primordial follicles were 45.1 % (32/71) in the non-treated animal and 86% (54/63) in the EPO-treated group. From Day 14 onwards, very few follicles were found in the transplanted tissue. However, on days 28, 49 and 63 post-transplantation, a few morphologically normal follicles were still observed [Table 1]. The EPO-treated group showed follicle-like structures in all post-transplant days evaluated, and in greater numbers compared to the non-treated animal. The inflammatory process was lower in the EPO-treated group on days 7 and 14 post-transplantation. Blood vessels were observed every day after transplantation, but on days 7, 24 and 63 post-transplantation the EPO-treated group showed more blood vessels in the transplanted tissue. The EPO-treated group had a lower area of fibrosis in the ovarian cortex on day 7, 49 and 63 post-transplantation [Fig. 1]. In conclusion, EPO allowed a better follicular survival and greater vascularization, together with smaller area of fibrosis on Day 7 post-transplantation. However, massive follicular loss still happened on the cryopreserved tissue transplantation after 7 days post-transplant. CEUA the University of Brasília - 74º/2017. The authors acknowledge the Brazilian financial support by CAPES, CNPq and FAPDF (Brazil).

### REFERÊNCIAS

- [1] R.A. Anderson et al., Human Reproduction Open. (2017) 1–9.
- [2] E.C.R. Leonel et al., Theriogenology. 105 (2018) 97–106.
- [3] P. Bosch et al., Theriogenology. 61 (2004) 581-594.

Table 1. Number (summation) of primordial follicles and growing follicles, and percentage of morphologically normal (calculated from the summation) found in fresh tissue (D0-Fresh) and cryopreserved tissue before (D0-Cryo) and after transplantation in the control animal (Non-treated) and in the EPO-treated group.

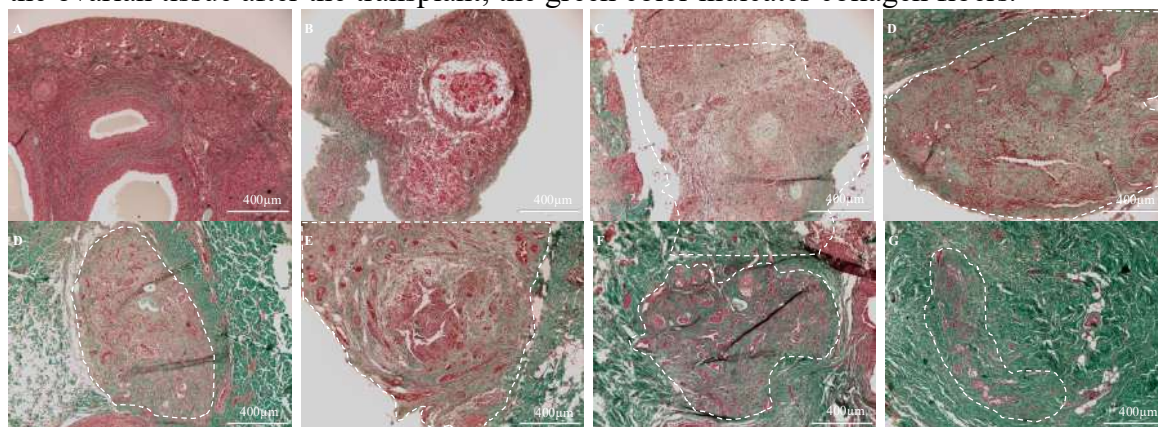
Treatment	Day	Primordial follicles			Growing follicles			Preantral follicles (Primordial + Growing)		
		Total	MN	% MN	Total	MN	% MN	Total	MN	% MN
<b>Control Animal (non-treated)</b>	D0 – Fresh	1644	1325	80.6 <sup>A</sup>	25	24	96.0 <sup>A</sup>	1669	1349	80.8 <sup>A</sup>
	D0 – Cryo	935	242	25.9 <sup>B</sup>	15	10	66.7 <sup>B</sup>	950	252	26.5 <sup>B</sup>
	D7	71	32	45.1 <sup>C</sup>	4	0	-	75	32	42.7 <sup>C</sup>
	D14	0	0	-	0	0	-	0	0	-
	D28	13	6	46.1 <sup>D</sup>	0	0	-	13	6	46.1 <sup>D</sup>
	D49	0	0	-	0	0	-	0	0	-
	D63	14	8	57.1 <sup>E</sup>	0	0	-	14	8	57.1 <sup>E</sup>
<b>EPO-treated Group</b>	D0 – Fresh	10942	9521	87 <sup>A</sup>	244	177	72 <sup>A*</sup>	11186	9698	87 <sup>A</sup>
	D0 – Cryo	11001	3557	33 <sup>B</sup>	224	117	52 <sup>B*</sup>	11225	3674	33 <sup>B</sup>
	D7	63	54	86 <sup>A*</sup>	1	0	0 <sup>C</sup>	64	54	84 <sup>C*</sup>
	D14	0	0	-	1	1	100 <sup>D</sup>	1	1	100 <sup>D</sup>
	D21	1	0	0 <sup>C</sup>	0	0	-	1	0	0 <sup>E</sup>
	D28	1	1	100 <sup>D*</sup>	0	0	-	1	1	100 <sup>D*</sup>
	D49	8	8	100 <sup>D</sup>	1	0	0 <sup>C</sup>	9	8	89 <sup>AC</sup>
	D63	0	0	-	0	0	-	0	0	-

EPO = erythropoietin; N: total number, MN: morphologically normal.

ABCDE: Values with different letters in the same column are significantly different within the same treatment group ( $P < 0.05$ ). Chi-square test.

\*: Indicates significant difference between treatment groups within the same day post-transplantation ( $P < 0.05$ ). Chi-square test.

Fig. 1. Histology of ovarian tissue (EPO-treated group) with Gomori trichomic staining. (A) fresh ovarian tissue; (B) cryopreserved ovarian tissue prior to transplantation; days 7 (C), 14 (D), 21 (E), 28 (F), 49 (G) and 63 (H) post-transplantation. The dotted lines delimit the ovarian tissue after the transplant; the green color indicates collagen fibers.



## EVALUATION OF INTERACTION MACROPHAGES AND TUMOR CELLS AFTER PHOTODYNAMIC THERAPY

Vanessa Ferreira<sup>1</sup>, Bruno H. Godoi<sup>1</sup>, Carlos D. G. O. Moraes<sup>1</sup>, Newton S. Silva<sup>1</sup>,  
Cristina Pacheco-Soares<sup>1</sup>.

<sup>1</sup>. Universidade do Vale do Paraíba - UNIVAP, São José dos Campos - SP, Brazil

Despite the therapeutic advances in cancer treatment, conventional therapies in general do not present satisfactory results because they do not treat the disease in the long term. Some studies have already described that when photodynamic therapy (PDT) is given in both normal and tumor tissue, an acute inflammatory process occurs that will stimulate the production of inflammatory cytokines and interleukins [1]. These substances will promote the migration of neutrophils and macrophages into the region of tumor cells promoting tumoricidal activity [2]. The present work evaluated the interaction of macrophages with tumor cells submitted to PDT. HEp-2 cells (laryngeal carcinoma) were organized into 4 groups: PDT; LED; photosensitizing and untreated. Cells were incubated with 5  $\mu$ M photosensitizer, Tetrasulfonate Aluminum Phthalocyanine (AlPcS4) for 1 h at 37 ° C in 5% CO<sub>2</sub> atmosphere. For irradiation, cells were maintained in PBS and irradiated with Irrad-LED 660nm (Biopdi®) 25mW / cm<sup>2</sup>, with 200s exposure. After the photodynamic treatment, RAW 264.7 macrophages were added on HEp-2 cells, and cultures incubated for 24h. After this time the cells were washed and fixed in 4% [v / v] paraformaldehyde in 0.1 M phosphate buffer) for 40 min, and dehydrated in a gradual series of acetone (50-100% / 15 min each), dried with Hexamethyldisilazane and analyzed on scanning electron microscope Zeiss EVO MA10. The analysis of scanning photomicrographs demonstrates the interaction of RAW 264.7 macrophages with HEp-2 cells in the control, phthalocyanine and LED groups. However, when we analyzed the PDT group, we observed the presence of a single type of cell that suggests that they are macrophages. The macrophages in the PDT group began their spreading process. We can conclude that macrophages interact with HEp-2 cells in all groups, but in the PDT group a stimulus for more intense phagocytic activity occurs.

### REFERENCES

- [1] S O Gollnick, et al. British journal of cancer vol. 88 (11) (2003): 1772-9.
- [2] Hwang, H.S., Shin, H., Han, J. et al. Journal of Pharmaceutical Investigation (2018) 48: 143.

[3] This research was supported by FAPESP (process nº 16/17984-1) CNPq -Brazil (process nº 305920/2017-0).

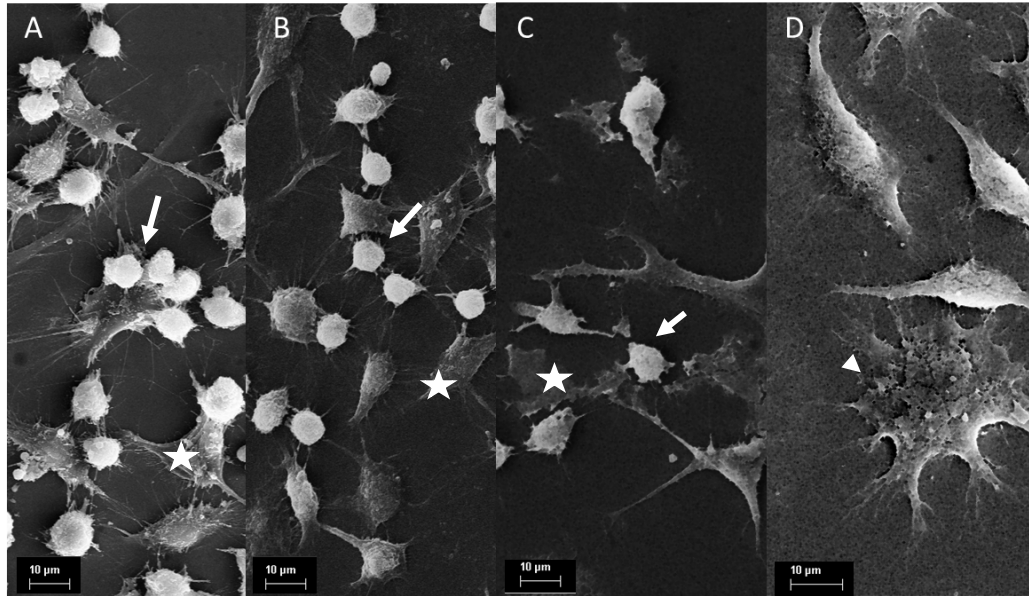


**Figure 1:** HEp-2 cells post PDT interacting with macrophages RAW 264.7. A - Control group, arrow indicates macrophages, star indicates HEp-2 cells. B - Phthalocyanine group, arrow indicates macrophages, star indicates HEp-2 cells. C - Group LED, arrow indicates macrophages, star indicates HEp-2 cells. 500X. D - PDT group, arrowhead indicates macrophages. 750X.



## Evaluation of the Environmental Quality of Three Estuaries of the São Paulo Coast Using Morphological Biomarkers in the Gills of Pufferfish

Gabriela Pustiglione Marinsek<sup>1\*</sup>, Paloma Kachel Gusso Choueri<sup>1</sup>, Denis Moledo de Souza Abessa<sup>1</sup> and Renata de Britto Mari<sup>1</sup>

<sup>1</sup>. São Paulo State University- UNESP, Bioscience Institute, São Vicente (SP), Brazil.

\*E-mail: gabriela.marinsek@unesp.br

The increasing anthropogenic activity in coastal environments has aroused great interest related to the conservation of biodiversity. In this way, this study aimed to evaluate the quality of three estuaries located on the coast of the state of São Paulo, which are different for anthropogenic impacts and conservation policies. The specimens of *Sphoeroides testudineus* were collected in the Juréia-Itatins Mosaic (AR), at the Lagoon estuarine Complex of Cananéia Iguape (A1) and at the Santos-São Vicente Estuary Complex (A2) and were submitted to morphological and biochemical biomarkers evaluation in the gills. For this purpose, the samples were collected and destined for histological processing, where the slides obtained were stained with the hematoxylin eosin (HE) technique and analyzed histopathologically according to the protocol proposed by Bernet; and the enzymatic activity analysis (GPx and GST) using a spectrophotometer (340 and 415 nm respectively). The analyzed gills of animals collected in RA were morphologically normal with occasional occurrences of circulatory and inflammatory pathologies. The highest histopathological index occurred in A2 followed by A1, where inflammatory, progressive and regressive lesions such as presence of leukocyte infiltration, hyperplasia, degeneration and lamellar fusion could be observed (Figure 1). As for the enzymatic kinetics, GPx activity increased by about 30% in A2 when compared to the other regions ( $p < 0.001$ , ANOVA). In general, as much as the gills of *S. testudineus* have demonstrated that A1 is characterized as an estuary with intermediate environmental quality since there was only an increase in the activity of GST, an enzyme to combat oxidative stress. Such a change demonstrates that there are toxic compounds in this region that are causing oxidative damage in this tissue, but it still able to combat them. However, in A2, the damage found was more severe, since in addition to alterations in the enzymatic defense system, there were damages at the tissue level that will rarely be reversed. The gills participate in numerous important functions in fish such as respiration, osmoregulation and excretion, being constantly in contact with contaminants dissolved in water [1]. Histopathological lesions in this sense can be interpreted mainly as a result of acute contamination. Thus, the highest histopathological index in the gills of the animals collected in Santo- São Vicente Estuary can be explained due to a range of stressors available in the high dosage as high concentrations of nutrients, polychlorinated biphenyls, polycyclic hydrocarbons, surfactants, and illicit drugs that are discharged in the estuary daily [2,3]. In this way, it is concluded from the evaluation of the gills of *S. testudineus* that A1 is an environment that suffers from the presence of contaminants that cause oxidative damage to the tissue. However, in A2 the concentration of such contaminants, or even the diversity of them have been causing oxidative and tissue damage in the organisms that inhabit this region.

## REFERENCES

- [1] Mazon, A. F. et al. Brazilian Journal of Biology. 2002.621-631.
- [2] Hortellani, M.A. et al. Química Nova. 2008. 10 - 19.
- [3] Pereira, C. D. S. et al. Science of the Total Environment. 2016. 148-154.

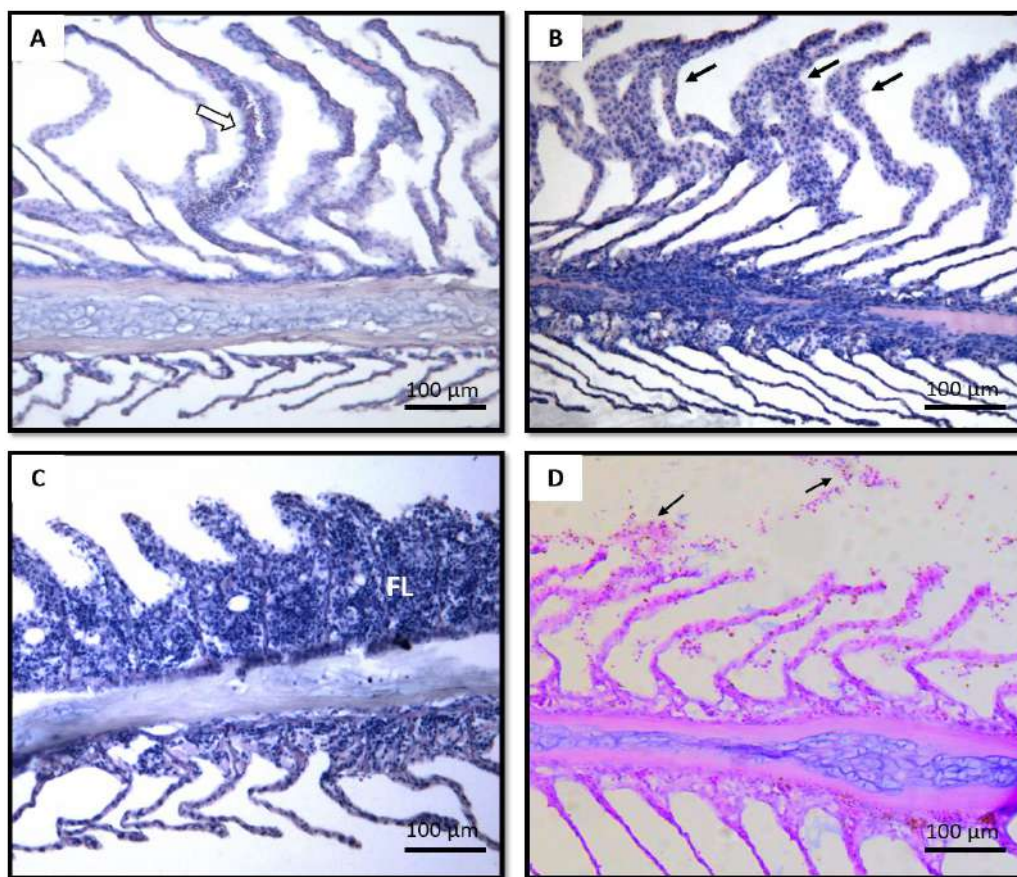


Figure 1. Most relevant histopathological lesions found in the *Spherooides testudineus* gills collected in the Juréia – Itatins mosaic (AR), in the Lagunar Estuarine Complex of Cananéia - Iguape (A1) and in the Estuarine Complex of Santos - São Vicente (A2). A: Lymphocyte infiltration (white arrow), B: lamellar hyperplasia (thin arrows), C: Lamellar fusion (FL) and D: epithelial detachment (arrows). Hematoxylin-Eosin (HE).

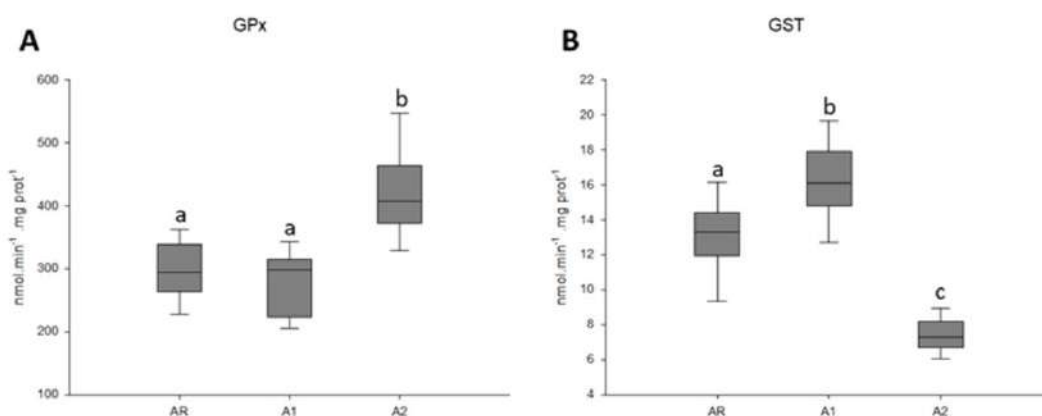


Figure 2. Graphical representation of the activities of Glutathione Peroxidase (GPx) and Glutathione S-transferase (GST) enzymes evaluated in the *Spherooides testudineus* gills collected in the Lagunar Estuarine Complex of Cananéia - Iguape (A1) and in the Estuarine Complex of Santos - São Vicente (A2).

## Ultrastructural Characterization Of P-bodies In *Trypanosoma cruzi*

Ingrid de Almeida <sup>1\*</sup>, Ingrid Augusto <sup>1</sup>, Wendell Girard-Dias <sup>3</sup>, Wanderley de Souza <sup>1</sup>  
and Kildare Miranda <sup>1,2</sup>

<sup>1</sup>. Laboratório de Ultraestrutura Celular Hertha Meyer, Instituto de Biofísica Carlos Chagas Filho, Universidade Federal do Rio de Janeiro, RJ, Brazil.

<sup>2</sup>. Centro Nacional de Biologia Estrutural e Bioimagem, Universidade Federal do Rio de Janeiro, Rio de Janeiro, Brazil.

<sup>3</sup>. Fundação Oswaldo Cruz, Instituto Oswaldo Cruz, Rio de Janeiro, Brazil.

The regulation of gene expression in trypanosomatids is mostly done post-transcriptionally, through mechanisms that control the stability and access the translation machinery of mature messenger RNA (mRNA) [1]. The protozoan *Trypanosoma cruzi* (*T. cruzi*) has untranslated cytoplasmic mRNAs which binds to proteins forming ribonucleoprotein complexes named Processing bodies (P-bodies) [1]. The P-bodies work basically through three mechanisms activated upon physiological stress: degradation, storage and translation of the mRNA [1]. Immunolocalization experiments using antibodies against the existing TcDHH1 protein in P-bodies show punctate labeling all over the cell cytoplasm, a typical pattern of membrane-enveloped compartments. However, the subcellular localization and structural organization of P-bodies in *T. cruzi* are still unknown. Artifacts generated during sample preparation chemical fixation (CF) for electron microscopy may lead to organelle deformation due to osmotic changes and extraction of contents, potentially causing the disintegration of P-bodies. To elucidate the intracellular distribution and structural organization of P-bodies in *T. cruzi*, fluorescence microscopy experiments using antibodies against the TcDHH1 protein (a functional part of the P-bodies) were carried out to optimize cultivation conditions that induce an increase in the number of P-bodies. We compared parasites under two conditions: with and without starvation. Quantification of P-bodies was carried out under both conditions. Approximately 23% of epimastigotes under normal nutritional conditions were labeled, whereas 56% of cells under starvation presented P-bodies, as is previously shown [1]. To improve the resolution of fluorescence images obtained, we used deconvolution microscopy (Fig.1). In order to obtain a better preservation of cell structure for electron microscopy, high pressure freezing and freeze substitution (0.1% glutaraldehyde, 2% osmium, 1% water) was also carried out. Unlike *T. cruzi* chemically fixed cells, where the ribosomes are randomly distributed through the cytoplasm, cryofixed cells showed a distinct pattern of ribosome organization, forming clusters in different locations of the cell body or lining the surface of some organelles such as the reservosomes (Fig.2), being potential candidates for P-bodies at the ultrastructural level [2]. Correlative microscopy experiments using super resolution fluoresce microscopy and electron tomography are currently being carried out to elucidate the fine structure of P-bodies and establish a potential morphofunctional connection with other *T. cruzi* organelles, thus contributing to a better understanding of the basic (cell) biology of these parasites. This work was supported by CNPq, CAPES, FAPERJ, and FINEP.

## REFERENCES

[1] F.B. Holetz, et al. FEBS J 2010; [2] W. Girard-Dias, et al. Histochem. Cell Biol. (2012).

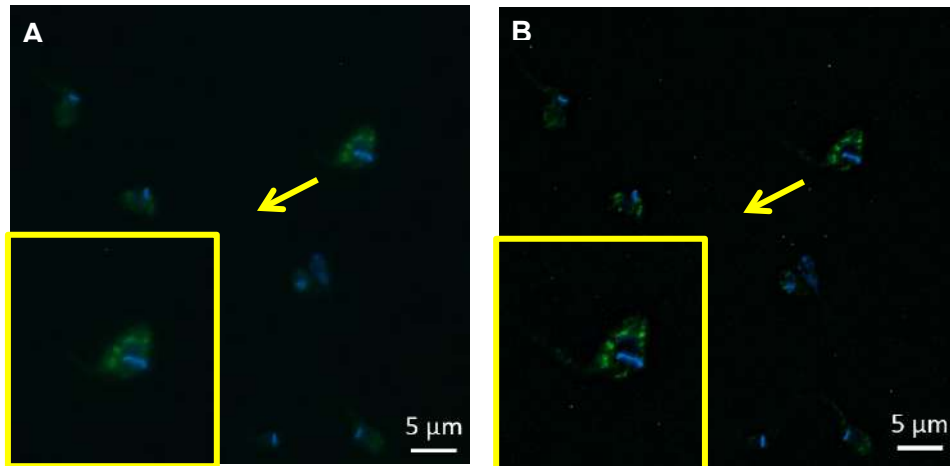


Fig.1. Comparison of (A) conventional and (B) deconvolution immunolocalization of TcDhh1 in cells under starvation incubated with antiserum against TcDhh1 with 1:50 concentration.

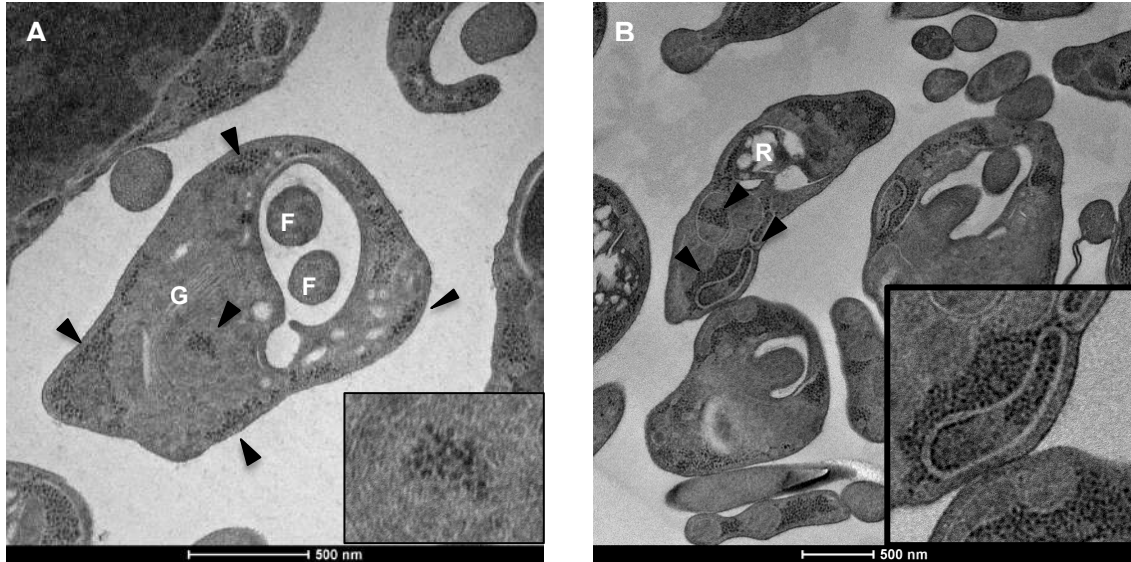


Fig.2. Transmission electron microscopy images of cryofixed epimastigote forms of *T. cruzi*. (A, B) Several clusters of ribosomes (A, inset) lining to the surface of organelles (B, inset) or the inner face of the cell plasma membrane (arrows) are seen. *R* - reservosomes, *G* - golgi apparatus, *F* - flagellum.



## **Morphoquantitative Evaluation Of Two Subpopulations Of The Myenteric Neurons In Jejunum Of Golden Hamsters (*Mesocricetus auratus*) Infected With *Leishmania (Leishmania) infantum***

CAVALLONE, Italo Novais<sup>1\*</sup>, OLIVEIRA, Karine Soares<sup>1</sup>, LIMA, Sarah Kymberly Santos<sup>1</sup>, PASSERO, Luiz Felipe Domingues<sup>1</sup>, LAURENTI, Márcia Dalastra<sup>2</sup>, JESUS, Jéssica Adriana<sup>2</sup>, CHUCRI, Thaís Martins<sup>1</sup> and MARI, Renata de Britto<sup>1</sup>

<sup>1</sup>Laboratory of Animal Morphophysiology, São Paulo State University - UNESP, Bioscience Institute, São Vicente, Brazil. <sup>2</sup>Laboratory of Pathology and Infectious Diseases, Department of Pathology/FMUSP, São Paulo, Brasil.

\*E-mail: id.cavallone@gmail.com

Visceral leishmaniasis is a growing zoonosis due to the disorderly occupation of urban regions, deforestation and synanthropic habits of wild animals, strongly related to precarious sanitation conditions [1]. Among the signs and symptoms of this disease are changes in the gastrointestinal tract (GIT) such as vomiting, diarrhea, which provoke the thought that the infection compromises the enteric nervous system, responsible for the control of GIT functions [2,3]. The objective of this study was to evaluate the plasticity of jejunum myenteric neurons of golden hamsters (*Mesocricetus auratus*) infected of *Leishmania (Leishmania) infantum*. Three experimental groups (n = 5) of hamsters were infected intraperitoneally with  $2 \times 10^7$  promastigotes of *L. (L.) infantum* (GE) and three other groups were also inoculated with physiological solution (GC). The groups were euthanized after 30, 60 and 90 days of infection, the jejunum were collected and destined to the NADPH-d (nitrergic population) and NADH-d (metabolically active population) techniques. The whole mount preparation were used for analysis of neuron/ganglion density and cell profile. In the quantitative analysis (figure 1) of nitrergic neurons a significant increase ( $p < 0.05$ ) of this subpopulation was observed at 30 days of infection (acute period) and a significant reduction ( $p < 0.05$ ) at 90 days (chronic period), whereas the metabolically active neurons showed an expressive increase ( $p < 0.05$ ) in the acute and intermediate (60 days) followed by a significant reduction ( $p < 0.05$ ) at 90 days. In the morphological analysis (figure 2) of the nitrergic population, the neurons presented a significant reduction ( $p < 0.05$ ) in the area of the cellular profile in all the observed experimental periods, as the NADH-dp subpopulation occurred a decrease ( $p < 0.05$ ) at 60 days, followed by an increase ( $p < 0.05$ ) at 90 days. Nitrogenic subpopulation increases under the influence of the immune system due to the antiparasitic and neuroprotective properties of the neurotransmitter nitric oxide, which makes this subpopulation resistant to cell death [4]. The changes in the two subpopulations evaluated indicate that the neural metabolism reflects changes in the nitrergic subpopulation.

[1] C.M.F. Gontijo et al. Rev. Bras. Epidemiol. (2004).

[2] A.C. Pastorino et al. Jornal de Pediatria (2002).

[3] J.B. Furness. Oxford: Blackwell Publishing (2006).

[4] S.L. Vicentino-vieira et al. Exp Parasitol (2015)

[5] This research was supported by São Paulo Research Foundation – FAPESP (processes 2018/06778-7)

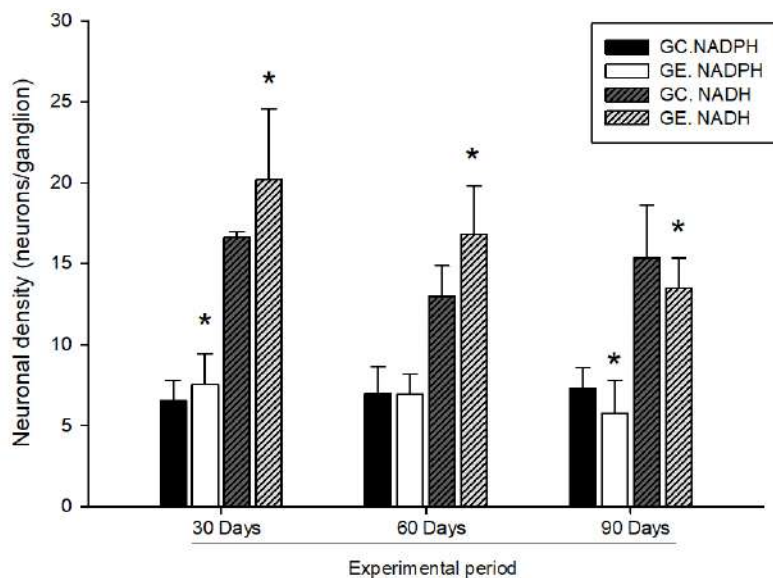


Figure 1: Neuronal density (neuron/ganglion) of the NADPH-dp and NADH-dp myenteric neurons subpopulations. GC - control group; GE - experimental group. \*Asterisk on experimental groups indicates significant difference with their respective control groups.

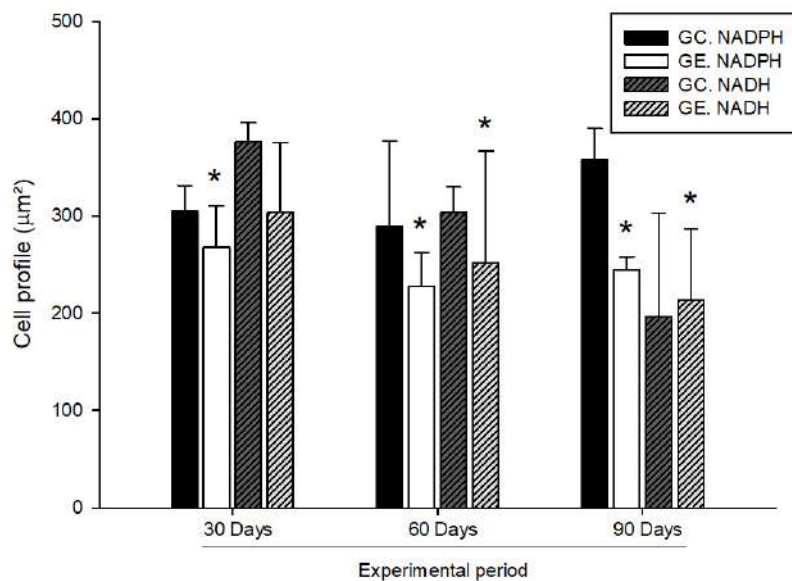


Figure 2: Cellular profile ( $\mu\text{m}^2$ ) of the NADPH-dp and NADH-dp myenteric neurons subpopulations. GC - control group; GE - experimental group. \*Asterisk on experimental bars indicates significant difference with their respective control groups.

## **Histopathological Changes in the Central Nervous System Caused by the Juruaça Virus in Adult Mice**

Tatyane da Silva Cabral<sup>1</sup>, Karina Glazianne Barbosa Carvalho<sup>1</sup>, Juarez Antônio Simões Quaresma<sup>2</sup> and José Antônio Picanço Diniz Junior<sup>1\*</sup>

<sup>1</sup>. Instituto Evandro Chagas/Laboratório de Microscopia Eletrônica, Belém, PA, Brasil.

<sup>2</sup>. Instituto Evandro Chagas/Seção de Patologia, Ananindeua, PA, Brasil.

\* E-mail to correspondence: [joseantonio@iec.pa.gov.br](mailto:joseantonio@iec.pa.gov.br)

The Juruaça virus was isolated from viscera of a bat captured in the Porto Trombetas region in 1982, in the municipality of Oriximiná, Pará. Newborn mice of the Swiss albino and BALB/c strains when inoculated intracerebrally (ic) or intranasally (in) showed signs indicative of an acute disease characterized by progressive lesions mainly in the Central Nervous System (CNS), but also in other organs [1,2]. However, the neuropathology caused by the Juruaça virus in adult mice remains to be described in detail. In this work we described in young adult mice the histopathological changes associated with Juruaça virus antigens in the CNS, following inoculation of viral suspension in the nostrils. For this, 31-day-old female BALB/c mice had their nostrils instilled with viral suspension once a day for three consecutive days. After identification of clinical signs, CNS samples were processed for histopathological analysis and detection of viral antigens by immunohistochemistry. Among the infected animals, three experimental groups were formed based on the intensity of infection signs: infected group without clinical signs (G1); infected group with moderate clinical signs (G2); infected group with severe clinical signs (G3) and these groups were compared with each other and with the uninfected control group (CG). There were discrete histopathological changes in G1 and conspicuous neuropathological alterations in G2 and G3 groups. Among these, we found areas of moderate congestion, including reactive nuclei and neuronal cell bodies with chromatolysis and pyknoses, moderate to severe edema, and meningeal edema and moderate mononuclear infiltration. Virus antigens were observed in the putamen, ventricular wall, choroid plexus, diencephalon, but mainly in temporal cortex, midbrain, cerebellum and spinal cord (Figure 1). These findings suggest that the Juruaça virus may induce encephalopathy in young adult mice of the BALB/c strain after repeated intranasal inoculation.

### References

- [1] ARAÚJO, T. P. 2006. 123 f. Dissertação (Mestrado em Patologia das Doenças Tropicais)-Universidade Federal do Pará, Belém, 2006.
- [2] FERREIRA, N. C. 2013. 134 f. Dissertação (Mestrado em Neurociências e Biologia Celular)-Universidade Federal do Pará, Belém, 2013.

Financial support: FAPESPA, IEC/SVS/MS



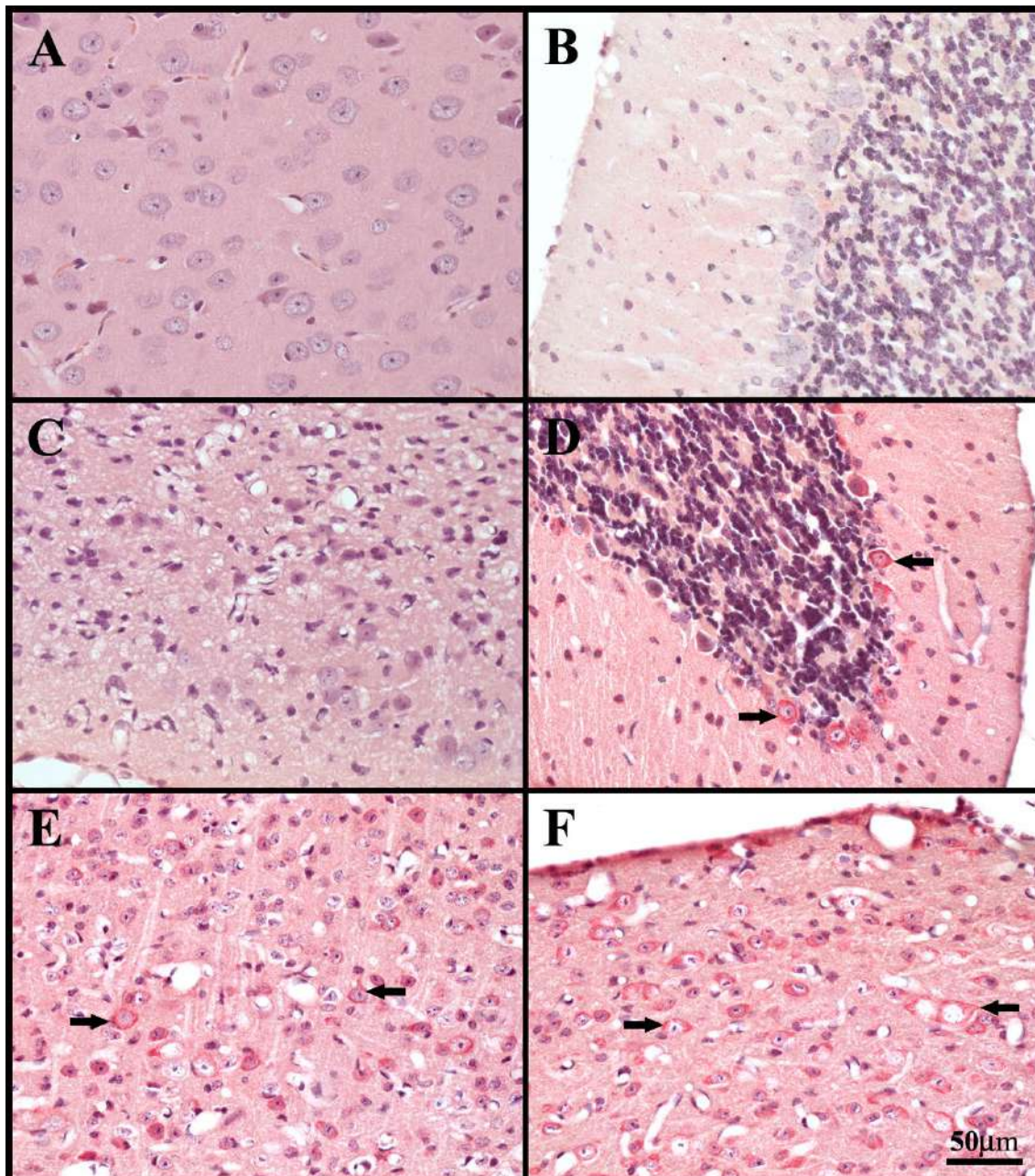


Figure1: Photomicrography's of parasagittal section of central nervous system, hematoxylin/eosin stained (A and C) and immunolabeled sections for Juruaça virus antigens, using HistoMark Red Phosphatase Substrate Kit and counterstained with hematoxylin (B, D, E and F). Immunostained neurons (arrows) in the cerebellum (D); temporal cortex (E) and anterior portion of the spinal cord (F). Notice control uninfected (A) and infected edematous (C) HE stained cortical sections. Scale bar: 50µm.



## MORFOFUNCTIONAL ASPECTS OF HYSTOGENESIS OF TOXOPLASMA IN NERVOUS SYSTEM CELLS

Macedo, J.<sup>1,2</sup>, Moreira-Souza, A.C.A.<sup>2</sup>, Portes, J.A.<sup>2</sup>, De Souza, W.<sup>2,3</sup>, Attias, M.<sup>2,3</sup>

1- Instituto Federal de Educação, Ciência e Tecnologia do Rio de Janeiro, IFRJ. 2- Instituto de Biofísica Carlos Chagas Filho, Universidade Federal do Rio de Janeiro. 3- Centro Nacional de Biologia Estrutural de Bioimagem, Universidade Federal do Rio de Janeiro

*Toxoplasma gondii*, the agent of toxoplasmosis, is an obligate intracellular protozoan that infects a broad spectrum of cells of homeothermic vertebrates. Toxoplasmosis causes severe pathology to immunosuppressed hosts or to the fetuses, and immunocompetent individuals may be affected by ocular toxoplasmosis. During acute infection, there are forms of rapid replication: the tachyzoites; and the bradyzoites are forms of resistance characteristic of the chronic phase. Atypical strains of *T. gondii* are present in the Latin America (Robert-Gangneux and Dardé, 2012). The EGS strain was isolated from amniotic fluid in Minas Gerais and has a type I / III profile of virulence, which combines features of the acute condition with ability to form tissue cysts (Ferreira et al., 2006). The chronic phase of the disease is related to the central nervous system (Skariah et al., 2010). Parasites of the EGS strain expressing stage-specific fluorescence (Paredes-Santos et al., 2016) are tools in the study of cystogenesis and were used to study the cystogenesis of the EGS strain in primary cell cultures of the murine nervous system. Methods: Newborn Swiss mice had the brains isolated for cortex removal, which was dissociated in DMEM medium, centrifuged (400g, 3min) and the pellet generated was resuspended and cultured. After 3 weeks, when microglia and astrocytes prevailed in the cell monolayer, they were plated and 24 hours later, they were infected with *T. gondii* of the EGS strain for conventional light microscopy, immunofluorescence or electron microscopy experiments. The appearance of *T. gondii* cysts was followed in an interval of 24 to 96 hours of infection, fixed with 4% nascent formaldehyde and processed for conventional light microscopy or immunofluorescence using the *Dolichos biflorus* lectin (DBA-FITC) as the cyst wall marker. For ultrastructural analysis, the cells were grown in bottles, infected and processed for analysis by electron microscopy. The production of reactive oxygen species (ROS) and nitric oxide (NO) in response to *T. gondii* infection were also analyzed. At 48h after infection, astrocytes appears to be more activated, and clusters of parasites similar to tissue cysts begin to appear, indicating the onset of cystogenesis, but labeling of cyst wall by DBA-FITC was not seen. This is more evident at 96 hpi, with specific labeling for DBA within astrocytes. As for the activation profile of these cells, measured through the production of ROS and NO, it was observed that the production of ROS occurred at 48h of infection, while NO production was not detected in any of the evaluated times. Thus, we concluded that the activated profile observed at 48h cells after infection has the participation of ROS, and that this mediator is related to cystogenesis of *Toxoplasma gondii*.

Acknowledgements: CNPq, FAPERJ, CAPES, FINEP. CEUA-UFRJ.

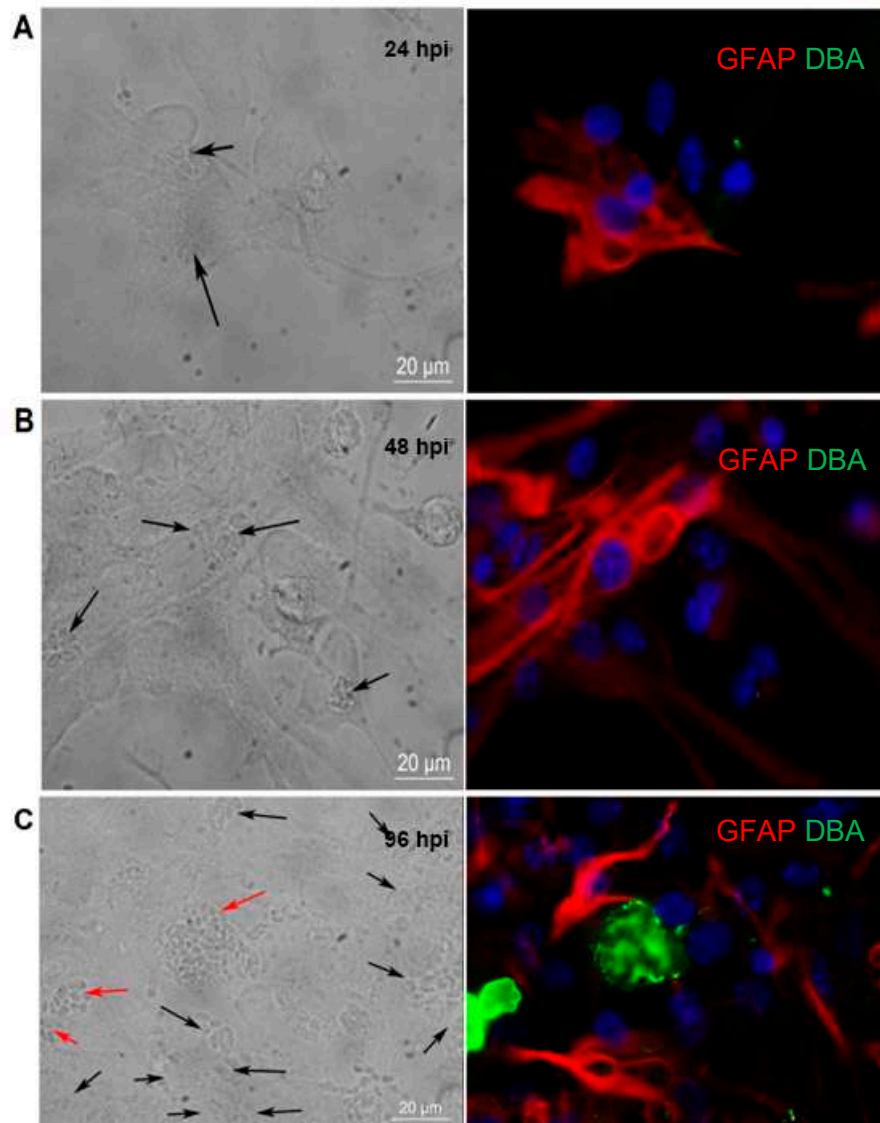
#### References:

Ferreira, A.D.M., Vitor, R.W. Gazzinelli, R.T., and Melo, M.N. (2006) . Infect. Genet. Evol. 6, 22–31.

Paredes-Santos, T.C., Tomita, T., Yan Fen, M., de Souza, W., Attias, M., Vommaro, R.C., and Weiss, L.M. (2016). Microbes Infect. 18.

Robert-Gangneux, F., and Dardé, M.-L. (2012). Clin. Microbiol. Rev. 25, 264–296.

Skariah, S., McIntyre, M.K., and Mordue, D.G. (2010). Parasitol. Res. 107, 253–260.



Primary cultures of astrocytes and microglia infected with the EGS strain of *T. gondii* for (A) 24, (B) 48 and (C) 96h. Parasitophorous vacuoles (black arrows) and tissue cysts (red arrows). Only 96hpi cyst wall labeling by DBA-FITC is seen (C). Astrocytes are labeled red, nuclei labeled with Hoechst (blue).

## Histological Evaluation of Testicles After an Intratesticular Injection of Silver Nanoparticles

Juliana L. M. Brito<sup>1\*</sup>, Vanessa N. Lima<sup>1</sup>, Ricardo B. Azevedo<sup>2</sup> and Carolina M. Lucci<sup>1</sup>

<sup>1</sup>. Department of Physiological Sciences, Institute of Biological Sciences, University of Brasília, Brasília/DF, Brazil

<sup>2</sup>. Department of Genetic and Morphology, Institute of Biological Sciences, University of Brasília, Brasília/DF, Brazil

Correspondence e-mail: julianalis.brito@gmail.com

Silver nanoparticles (AgNP) are among the most popular nanomaterials [1], due to their antibacterial action, as well as toxic effects caused by Ag<sup>+</sup> released from the nanoparticles [4]. Studies have already shown that AgNP can cause DNA damage on germ cells, decrease sperm counts, and promote morphometric changes in seminiferous tubules [5,6], decreases spermatogonia proliferation [7,8] and increase germ cells apoptosis [9] when intravenously administered. The aim of this study is to evaluate the effects of an intratesticular injection of silver nanoparticles (AgNP) on reproductive parameters, aiming at the development of a potential nanotechnological neutering agent. The animals were randomly divided into three groups: 1) Animals without any manipulation (Control group – N=4), 2) animals receiving an intratesticular injection of saline solution (Sham group – N=4) and 3) animals receiving an intratesticular injection of AgNP solution (AgNP group – N=20). Animals from AgNP group received an injection of 220µL of AgNP solution (0.46µg Ag/mL) in each testicle, and groups of 5 animals were killed 7, 14, 28 and 56 days after the injection. The left epididymis was used to collect the spermatozoa for motility and morphology evaluations. Both testicles and the right epididymis were fixed for histological analysis. The percentage of motile sperm was significantly reduced ( $P<0.05$ , Tukey test) in AgNP-D7 group (9%) in comparison to Control (73%), AgNP-D14 (86%), AgNP-D28 (68%) and AgNP-D56 groups (90%). The AgNP-D7 group also present a significant decrease ( $P<0.05$ , Tukey test) in the percentage of morphologically normal spermatozoa (33%) compared to control (58%) and sham (50%) groups. This decrease in the percentage of normal sperm on AgNP-D7 group was accompanied by a significant increase ( $P<0.05$ ) on the percentage of sperm with abnormal morphology of sperm head (20%) and mid piece (11%). The histological analysis of the testicles (Figure 1) allowed the identification of all germline cells in the seminiferous tubules in both control, sham and treated groups. In AgNP-D7, AgNP-D14 and AgNP-D28 it is possible to notice that the architecture of the seminiferous tubule is normal, although there are some debris in the lumen and few spermatozoa could be seen.

### REFERÊNCIAS

- [1] M.E. Vance et al., Beilstein J Nanotechnol. 6 (2015) 1769-1780.
- [2] J.S. Kim et al., Nanomedicine. 3 (2007) 95-101.
- [3] K. Dziendzikowska et al., J. Appl. Toxicol. (2012) 1-9.
- [4] J. Gromadzka-Ostrowska et al., Toxicol Lett. 214 (2012) 251-258.
- [5] L. Braydich-Stolle et al., Toxicol Sci. 88 (Suppl. 2) (2005) 412-419.
- [6] L.K. Braydich-Stolle et al., Toxicol Sci. 116 (Suppl. 2) (2010) 577-589.
- [7] T.X. Garcia et al., Reprod Toxicol. 45 (2014) 59-70.
- [8] This research was supported by CNPq (Brazil), Capes (Brazil), INCT (Brazil).



Histological analysis of the epididymis (Figure 2) showed that AgNP-D7 group did not present spermatozoa inside the tubules, whereas in AgNP-D14 and AgNP-D28 groups some spermatozoa are visible together with some debris. In AgNP-D56 group spermatozoa are visible within the epididymis, as well as in the Control and Sham groups. In conclusion, some acute and severe toxic effect in sperm cells were observed following intratesticular injection of AgNP. However, this effect was reversible, not capable to neuter the treated animals. Considering the temporary effect of the intratesticular injection of AgNP, testicular AgNP injection could be further studied to serve as a temporary male contraceptive method. CEUA-UnB - n° 102854/2015. Financial support by CNPq (Brazil), Capes (Brazil), INCT (Brazil).

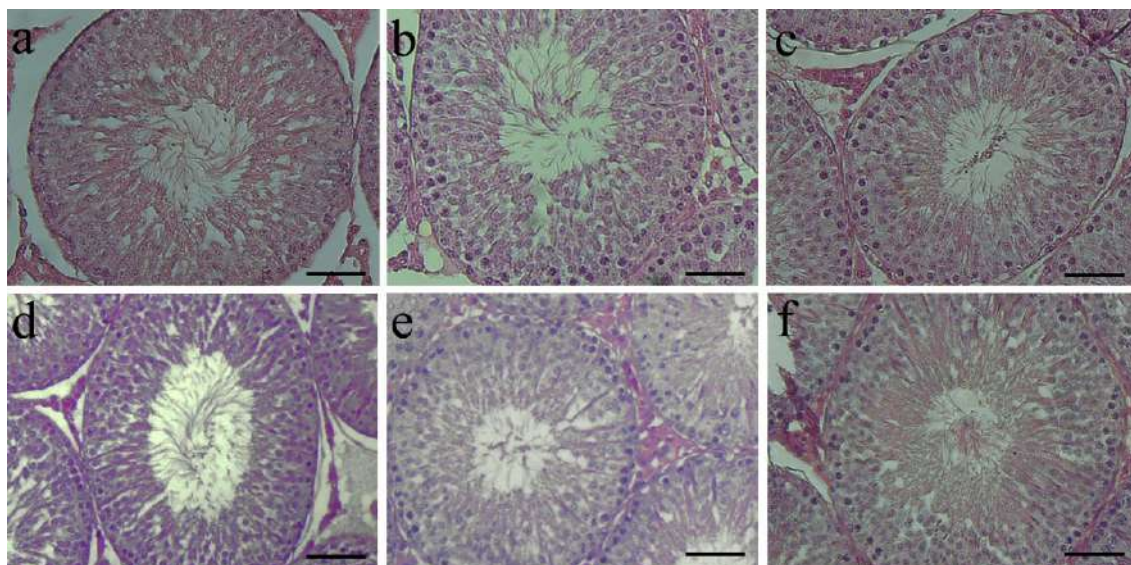


**Figure 1:** Representative micrographs of seminiferous tubules from each group. Control group (a); Sham group (b); AgNP-D7 (c); AgNP-D14 (d); AgNP-28 (e); AgNP-D56 (f). Bars = 10 $\mu$ m.

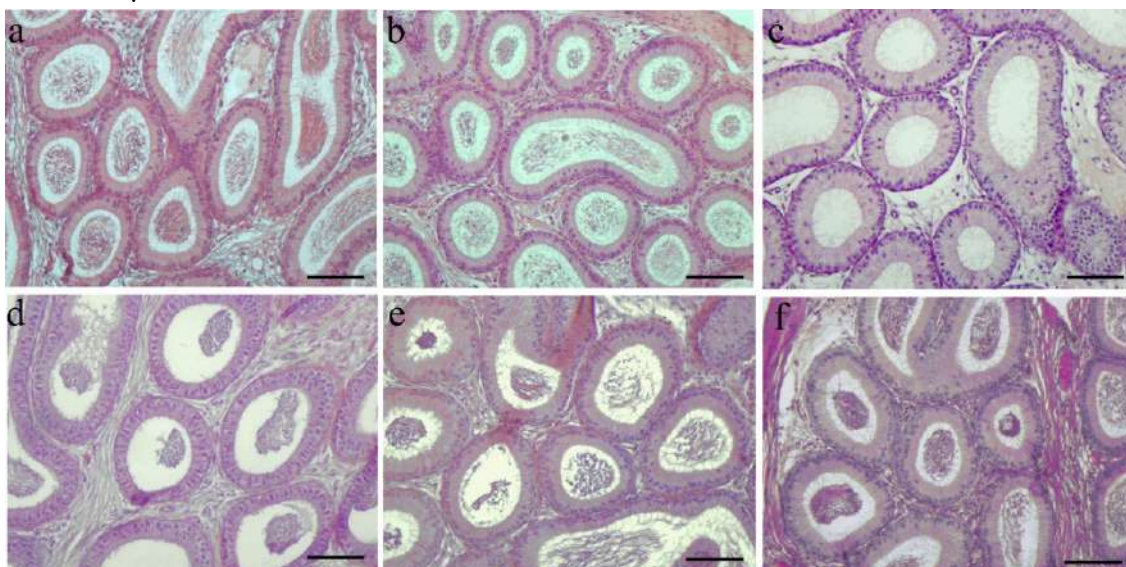


**Figure 2:** Representative micrographs of epididymis from each group. Control group (a); Sham group (b); AgNP-D7 (c); AgNP-D14 (d); AgNP-28 (e); AgNP-D56 (f). Bars = 10 $\mu$ m.



## Study of the Extensor Digitorum Longus' Connective Tissue of Obese Animals Submitted to Duodenojejunal Derivation

Leticia Massochim da Silva<sup>1\*</sup>, Mylena de Campos Oliveira<sup>1</sup>, Ariadne Barbosa<sup>1</sup>, Bruna Hart Ulsenheimer<sup>1</sup>, Angélica Soares<sup>1</sup>, Sandra Lucinei Balbo<sup>1</sup>, Marcia Miranda Torrejais<sup>1</sup>.

<sup>1</sup>. Universidade Estadual do Oeste do Paraná – UNIOESTE, Campus of Cascavel – Parana, Brazil.

\* massochimleticia@gmail.com

Obesity can be defined as the accumulation of adipose tissue in the individual and is the main risk factor for various chronic and musculoskeletal diseases [1,2]. Bariatric surgery is used as one of the options to reverse obesity, one of the models being the duodenojejunal bypass (DJB), characterized as a disabsorptive procedure [3]. One of the tissues that can be affected is the connective tissue, which in the muscle tissue is responsible for transmitting muscle's contraction force to tendons and bones [4], keeping the fibers attached and also conducting blood vessels [5]. Due to the few studies investigating the relationship between obesity and DJB surgery on the skeletal striated muscle, the present work aimed to investigate the percentage of connective tissue in the extensor digitorum longus (EDL) muscle in obese animals induced by cafeteria diet and submitted or not to DJB. All the procedures adopted were submitted and approved by the Ethics Committee in the Use of Animals (CEUA / UNIOESTE, nº 8709). Eighteen 8-week-old Wistar rats were randomly divided into two groups: control (CTL; n=6), which received standard diet and water *ad libitum* and cafeteria group (CAF; n = 12) which received cafeteria diet and soda *ad libitum*. After 10 weeks consuming the cafeteria diet, the obese animals of the CAF group were divided into two groups: cafeteria group submitted to false operation (CAF FO; n=6) and cafeteria group submitted to duodenojejunal bypass (CAF DJB; n=6), which continued to receive cafeteria diet for another eight weeks. At 26 weeks of age, the animals were euthanized and the EDL muscle was collected. The right antimere muscle was fixed in formaldehyde (10%) and submitted to cross sections (7 µm thickness) in a microtome. The obtained sections were stained with Masson's trichrome and photo documented to analyze the connective tissue, which was performed through the percentage in pixels, through 10 microscopic fields per animal (objective of 40x). Statistical analysis was performed using analysis of variance test ANOVA and Tukey post-test ( $p < 0.05$ ). The connective tissue collagen was predominantly in the perimysium (Figure 1A, 1B and 1C), which involves the fascicles. When evaluating the percentage of intramuscular collagen, the three study groups (CTL, CAF FO and CAF DJB) showed similarity in their data ( $p = 0.8061$ ) (Figure 1D). The results showed that obesity induced by cafeteria diet and the bariatric surgery do not interfere in the intramuscular collagen percentage of the studied muscle.

### REFERENCES

- [1] F.B.C. Pimenta et al., *Frontiers in Psychology* 6 (2015).
- [2] D. Aune et al., *Brazilian Journal of Microbiology* 353 (2016).
- [3] C. Hu et al., *Obesity Surgery* 23 (2013).
- [4] S.M. Dal-Pai et al., *R. Bras. Zootec.* 36 (2007).
- [5] G.J. Tortora et al., *Princípios de Anatomia Humana*, Guanabara Koogan, Rio de Janeiro, 2013.

[6] This research was supported by Araucaria Foundation (Brazil).

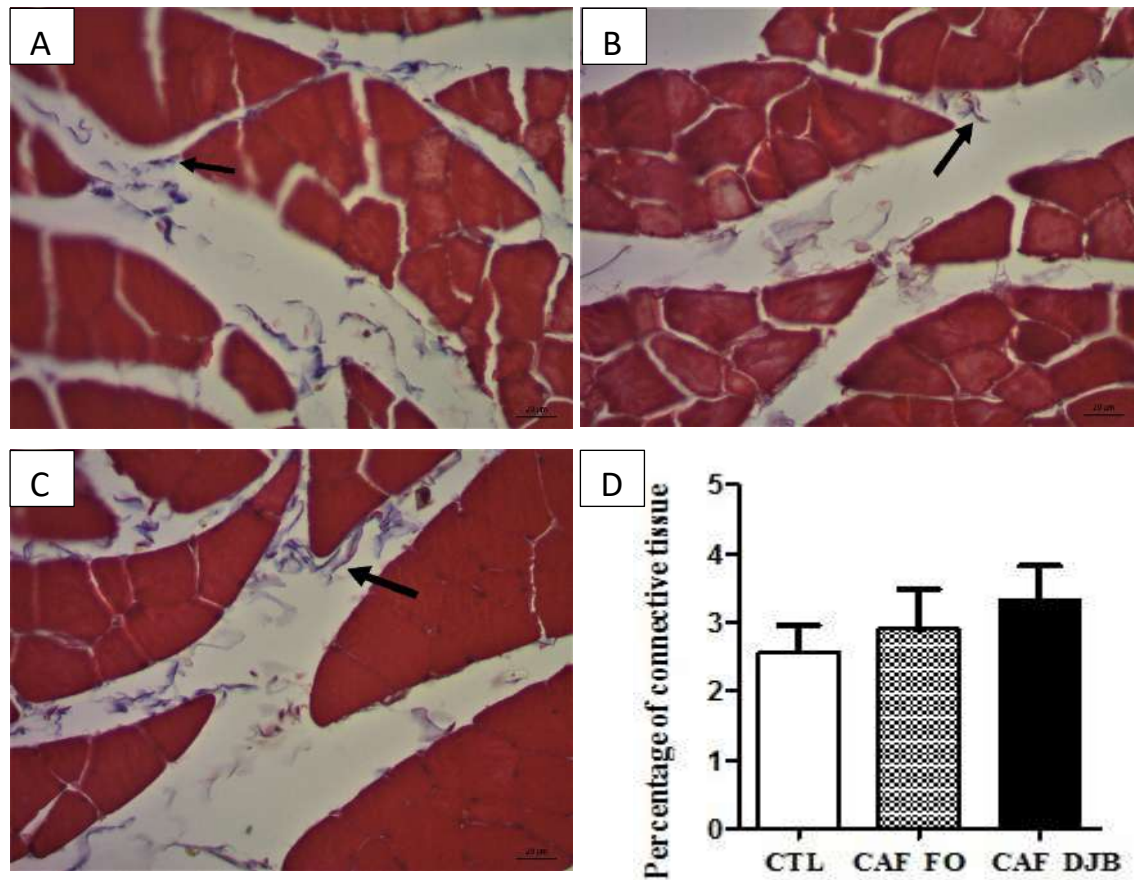


**Figure 1** – Photomicrographs of the EDL muscle of 17-week-old Wistar rats. Cross section. **A, B and C:** Perimysium (arrow) of control groups (CTL), cafeteria submitted to false operation (CAF FO) and cafeteria submitted to duodenojejunal bypass (CAF DJB), respectively. Masson's trichrome. **D:** Data on the percentage of connective tissue percentage of CTL, CAF FO and CAF DJB groups. Values expressed as the average  $\pm$  standard deviation. Different letters mean significant differences. Analysis of variance test ANOVA ( $p < 0.05$ ).

## **Morphological and Morphometric Study of Neuromuscular Junctions of the Extensor Digitorum Longus Muscle of Female Oophorectomized Rats Submitted to Vibrating Platform Treatment**

Letícia Massochim da Silva<sup>1\*</sup>, Dinei Prado Filho<sup>1</sup>, Mylena de Campos Oliveira<sup>1</sup>, Gladson Ricardo Flor Bertolini<sup>1</sup>, Ana Tereza Bittencourt Guimarães<sup>1</sup>, Lucineia de Fatima Chasko Ribeiro<sup>1</sup>, Marcia Miranda Torrejais<sup>1</sup>

<sup>1</sup>Universidade Estadual do Oeste do Paraná - UNIOESTE - Campus of Cascavel - Parana - Brazil

\*massochimleticia@gmail.com

Exercise, in general, and mechanical signals from the vibrating platform (VP), in particular, help to improve the neuromuscular symptoms of aging and possibly other neurodegenerative disorders, improving muscle<sup>1</sup> function. The present study investigated the neuromuscular junction morphometry (NJMs) of the extensor digitorum longus (EDL) of female oophorectomized rats treated with VP. All the procedures adopted were submitted and approved by the Ethics Committee in the Use of Animals (CEUA / UNIOESTE, 08/24/2016). Sixty-two female Wistar Rats were randomized into two groups: Pseudo-oophorectomy (GP) and Oophorectomy (GO). After a 60-day postoperative period, the animals were submitted to therapeutic interventions and separated into eight subgroups: non-treated with VP in four (GP4 and GO4) and eight (GP8 and GO8) weeks and treated with VP for four (GPP4 and GOP4) and eight (GPP8 and GOP8) weeks. The treatment was performed on VP, 60 Hz frequency for 10 minutes, three times a week. The EDL muscle was collected, fixed in Karnovsky and sectioned in longitudinal cuts, being submitted to Nonspecific Esterase reaction. To measure the area, 100 NJMs were analyzed from microscopic images (200x) of each animal. Data were analyzed by the three-way ANOVA statistical test. The NJMs of the EDL muscle presented classical plaque-like morphology, with oval, round or elliptical shape. Variations in shape, such as open junctions, irregular or compact shapes characterized the polymorphism of these structures in all groups studied (Figure 1). Analyzing the morphometry of NJMs, it was verified that the groups GO4 ( $\bar{x} = 304,243 \pm 10,4$ ) and GPP4 ( $\bar{x} = 346,149 \pm 11,3$ ) had an increased area of NJMs in relation to group GP4 ( $\bar{x} = 286,018 \pm 11,8$ ). On the other hand, group GOP4 ( $\bar{x} = 344,213 \pm 4,8$ ) presented a similarity in the NJMs area in relation to group GPP4. In the eight-week period, group GO8 ( $\bar{x} = 274.024 \pm 12.9$ ) showed a reduction in the area of the NJMs in relation to group GP8 ( $\bar{x} = 292,767 \pm 11,2$ ) and group GPP8 ( $\bar{x} = 358,622 \pm 5,4$ ) showed an increase in area of NJMs in relation to GP8. Group GOP8 ( $\bar{x} = 349,153 \pm 15.8$ ) presented similarity to group GPP8 (Figure 2). The results show a significant effect of the vibrating platform in the area of NJMs in the first four weeks of treatment, since oophorectomy surgery provided a reduction in the area of NJMs in the eight-week period. Therefore, VP is effective in restoring the neuromuscular symptoms resulting from oophorectomy.

### **REFERENCES**

- [1] G. Mettlach et al., J. Biomech. 47 (Suppl. 1) (2014) 1.
- [2] This research was supported by Araucaria Foundation (Brazil).

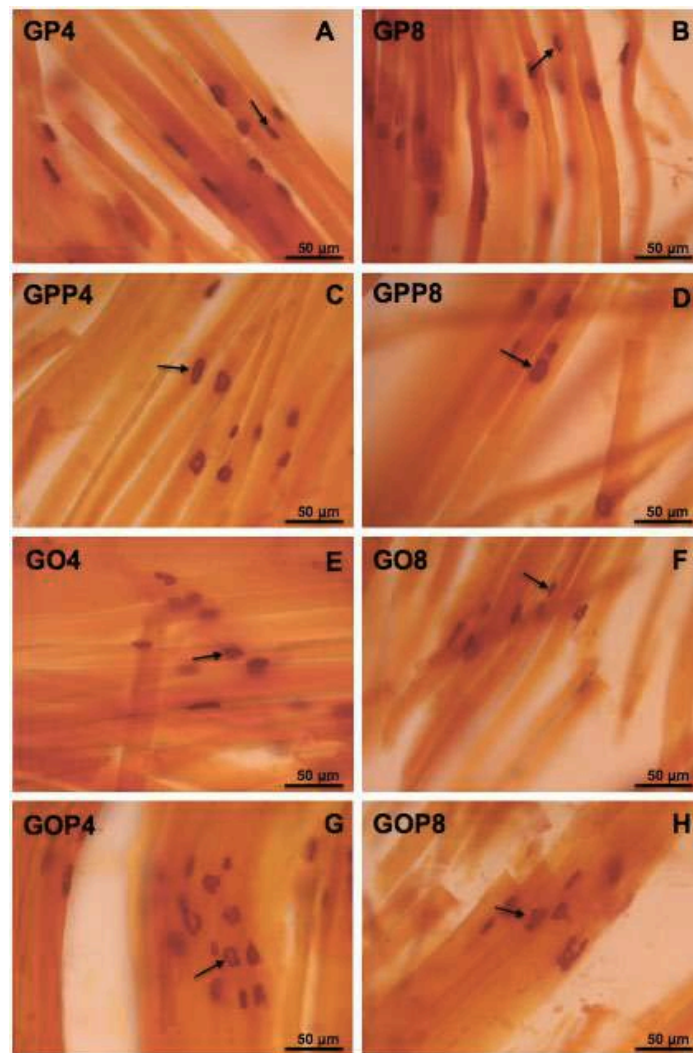


**Figure 1-** Photomicrographs of the neuromuscular junctions of the EDL muscle of female Wistar rats after Nonspecific Esterase Reaction in longitudinal cut. **A:** Pseudo oophorectomy group four weeks (GP4) and **B:** Pseudo oophorectomy group eight weeks (GP8). **C** and **D:** Pseudo platform groups treated in four (GPP4) and eight (GPP8) weeks, respectively. **E** and **F:** Oophorectomy groups four (GO4) and eight (GO8) weeks. **G** and **H:** Oophorectomy-platform groups treated in four (GOP4) and eight (GOP8) weeks. Arrows represent the neuromuscular junctions.

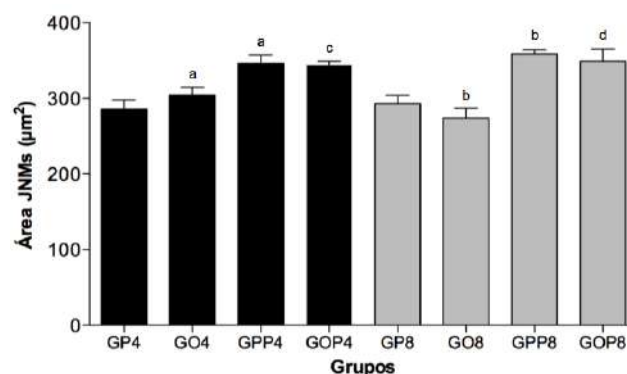


**Figure 2-** Bar chart showing average  $\pm$  standard deviation of the NJMs area of the EDL muscle of the studied groups of female Wistar rats. <sup>a</sup> the statistical difference in relation to GP4. <sup>b</sup> statistical difference in relation to GP8. <sup>c</sup> similarity to GPP4. <sup>d</sup> similarity to GPP8.



## **Evaluation of follicular development and morphology in cat cryopreserved ovarian tissue transplanted after administration of Simvastatin**

Marcella M. Costa<sup>1\*</sup>, Liudmilla P. Gonçalves<sup>1</sup>, Ana Bárbara R. Silva<sup>2</sup>, Cecibel M.L. Félix<sup>1</sup> and Carolina M. Lucci<sup>1</sup>

<sup>1</sup> Laboratory of Animal Reproduction and endocrinology, Department of Physiological Sciences, Biological Sciences Institute, University of Brasília, Brasília-DF, Brazil.

<sup>2</sup> Faculty of Agronomy and Veterinary Medicine, University of Brasília, Brasília-DF, Brazil.

\*Correspondence e-mail: [costa.motta@gmail.com](mailto:costa.motta@gmail.com)

Cryopreservation of ovarian tissue is a strategy for fertility preservation already used in humans which may be of great interest for endangered species, such as wild felines [1]. Previous studies of our group confirmed the success of heterotopic transplantation of fresh ovarian tissue in domestic cats, with development of antral follicles from 28 to 63 days post-transplant [2]. In contrast, other studies with cryopreserved ovarian tissue demonstrated a marked reduction in the number of follicles already seven days after transplantation [3]. Simvastatin is widely used to improve reperfusion and minimize ischemic damage in transplantation of different organs, including ovarian tissue [4]. In view of this, the present study aimed to evaluate the follicular morphology and development in cryopreserved ovarian tissue autotransplanted to cats who received Simvastatin. Each animal received Simvastatin (5 mg/Kg) orally four hours before OSH. Ovary of the four cats were divided into eight fragments, one of which was immediately fixed (Fresh Control) and the rest cryopreserved (slow freezing with 1.5 M DMSO). After thawing, a fragment was immediately fixed as a cryopreservation control (Cryo Control), and the remaining six fragments were transplanted to the subcutaneous tissue of the donor cat (autotransplant). The transplanted ovarian tissue fragments were recovered on days 7, 14, 21, 28, 49 and 63 post-transplantation and processed for light microscopy. All follicles were counted and classified according to the developmental stage as primordial or growing (Figure 1A and B), and as morphologically normal or degenerate. Gomori trichomic was used to analyze fibrosis in samples of ovarian tissue. For the assessment of fibrosis, a subjective evaluation was used to quantify the area of connective tissue (fibrosis) in the transplanted ovarian tissue. The percentage of morphologically normal follicles (MNF) was analyzed by the Chi-square test. The total number and percentage of morphologically normal primordial and growing follicles are shown in Table 1. Although the average percentages of morphologically normal primordial and growing follicles remain stable or even increase significantly in some days, the absolute number of follicles suffered a progressive and sharp fall after transplantation. The most common types of degeneration observed were follicles with oocytes fully or partially detached from the cells and follicles with retracted oocytes (Figure 1C).

[1] C Wiedemann et al., *Reprod Dom Anim* 47 (Suppl. 6), (2012) 300-304.

[2] E.C.R. Leonel et al., *Theriogenology* 105 (2018) 97-106.

[3] J.M.V. Vilela, Repository of the University of Brasilia (2016).

[4] J. Lee et al., *Theriogenology* 83 (2015) 285–293

Moreover, there was an increase in the area of fibrosis as time progressed after transplantation (Table 2). Comparing our results with a previous work of our group [4], the administration of Simvastatin did not improve follicular survival and development after transplantation of cryopreserved cat ovarian tissue, and severe follicular depletion was still observed. Further studies are necessary to solve the problem the loss of follicles after cryopreservation and transplantation of cat ovarian tissue.

This research was supported by CAPES and CNPq.

CEUA: n° 66718/2016.

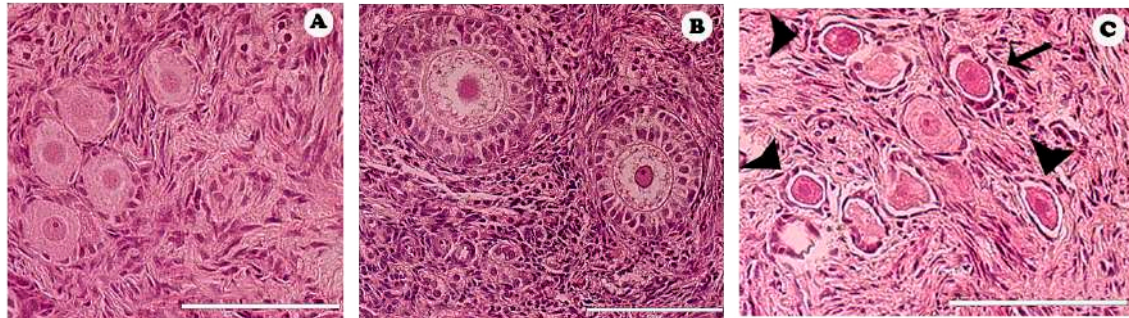


**Figure 1.** A) morphologically normal primordial follicles. B) morphologically normal growing follicles. C) degenerated follicles. Arrowhead: follicles with oocytes totally detached from granulosa cells. Black arrow: follicle with retracted oocyte. Bars = 100 µm.

**Table 1.** Total number and mean percentage ( $\pm$  SD) of morphologically normal (MN) follicles in the fresh and cryopreserved control tissue and to D7, D14, D21, D28, D49 and D63 after transplantation.

	Primordial Follicles			Growing Follicles		
	Total	n° MN	% MN	Total	n° MN	% MN
Fresh Control	7350	6966	94,2 $\pm$ 2,1 <sup>A</sup>	351	342	97,4 $\pm$ 1,2 <sup>A</sup>
Cryo Control	3804	2446	60,3 $\pm$ 13,6 <sup>Ba</sup>	243	96	41,4 $\pm$ 11,0 <sup>Ba</sup>
D7	91	32	48,8 $\pm$ 46,5 <sup>a</sup>	3	1	11,1 $\pm$ 19,2 <sup>b</sup>
D14	67	49	67,7 $\pm$ 10,9 <sup>a</sup>	3	2	50,0 $\pm$ 70,7 <sup>a</sup>
D21	17	14	80,0 $\pm$ 0,0 <sup>b</sup>	1	1	100 $\pm$ 0,0 <sup>c</sup>
D28	24	13	56,5 $\pm$ 0,0 <sup>a</sup>	0	0	0,0 $\pm$ 0,0 <sup>d</sup>
D49	19	11	61,5 $\pm$ 0,0 <sup>a</sup>	0	0	0,0 $\pm$ 0,0 <sup>d</sup>
D63	8	0	0,0 $\pm$ 0,0 <sup>c</sup>	0	0	0,0 $\pm$ 0,0 <sup>d</sup>

A-B: Different letters in the same column indicate significant difference between the Control groups ( $P < 0.05$ ).

a-d: Different letters in the same column indicate significant difference ( $P < 0.05$ ).

**Table 2.** Classification of the area of connective tissue (fibrosis) in the days after transplantation in the groups with and without Simvastatin.

Fresh Control	Cryo Control	D7	D14	D21	D28	D49	D63
+	+	++	+++	+++	++++	+++	++++

+ - 0-20% of ovarian tissue occupied by conjunctive tissue

++ - 20-40% of ovarian tissue occupied by conjunctive tissue

+++ - 40-60% of ovarian tissue occupied by conjunctive tissue

++++ - 60-80% of ovarian tissue occupied by conjunctive tissue

+++++ - 80-100% of ovarian tissue occupied by conjunctive tissue

## **Effect of the Treatment with Vibrating Platform on the Morphology and Morphometry of the Extensor Digitorum Longus Muscle of Female Rats Submitted to Oophorectomy Surgery**

Mikael Gerson Kuhn<sup>1\*</sup>, Dinei Prado Filho<sup>1</sup>, Ariadne Barbosa<sup>1</sup>, Mylena de Campos Oliveira<sup>1</sup>, Lésle Cazzetta Jerônimo<sup>1</sup>, Gladson Ricardo Flor Bertolini<sup>1</sup>, Ana Tereza Bittencourt Guimarães<sup>1</sup>, Lucineia de Fatima Chasko Ribeiro<sup>1</sup>, Marcia Miranda Torrejais<sup>1</sup>

<sup>1</sup>Universidade Estadual do Oeste do Paraná - UNIOESTE - Campus of Cascavel - Parana - Brazil

\*mikaelsingerson@hotmail.com

Changes in skeletal muscle are observed after menopause, due to hormonal decline, leading to mass and muscle strength deficits, and the vibrating platform (VP) has been used as a way of treatment<sup>1</sup>. This study investigated the muscle fibers' morphometry of the extensor digitorum longus (EDL) of oophorectomized female rats treated with VP. Sixty-two Wistar rats were randomized into two groups: Pseudo-oophorectomy (GP) and Oophorectomy (GO). All the procedures adopted were submitted and approved by the Ethics Committee on Animal Use (CEUA), on 2016/08/24. After a 60-day postoperative interval the female rats were separated into eight subgroups: non-treated with VP in four (GP4 and GO4) and eight (GP8 and GO8) weeks and treated with PV for four (GPP4 and GOP4) and eight (GPP8 and GOP8) weeks. The treatment was performed on VP, 60 Hz frequency for 10 minutes, three times a week. The EDL muscle was collected, frozen in liquid nitrogen and cross-sectioned in a cryostat. The sections were stained with Hematoxylin-Eosin. To measure the cross-sectional area (CSA) and nuclei count, 10 images (400x) of each animal were captured. Data were analyzed by the three-way ANOVA statistical test. The EDL muscle showed similarity in the morphological pattern, with preserved skeletal muscle fibers organized in fascicles, which presented polygonal aspect and peripheral nuclei in all groups, however, an increase in the CSA of the EDL muscle of oophorectomized groups was observed in relation to the pseudo-oophorectomized groups (Figure 1). Analyzing the CSA's morphometry of the fibers, there was a significant difference in the simple effect of the surgery factor. Female rats that underwent oophorectomy (GO4, GO8, GOP4 and GOP8) ( $\bar{x}=1345.043 \pm 169.70$ ) showed an increase in CSA when compared to female rats that did not undergo surgery (GP4, GP8, GPP4 and GPP8) ( $\bar{x}=1196,506 \pm 189.00$ ) regardless of treatment and time. Regarding the nuclei count, significant differences were observed only in the simple effect of the surgery factor. The groups that underwent oophorectomy (GO4, GO8, GOP4 and GOP8) ( $\bar{x}=267,000 \pm 35.30$ ) presented smaller numbers of nuclei when compared to the pseudo-oophorectomy groups (GP4, GP8, GPP4 and GPP8) ( $\bar{x}=287,367 \pm 34,91$ ) (Table 1). Oophorectomy increased muscle fibers' CSA and reduced nuclei count without any interference from vibrating platform treatment and treatment time.

## **REFERENCES**

- [1] E. K. Stuermer et al., *Calcif. Tissue Int.* 87 (Supl. 2) (2010) 168.
- [2] This research was supported by Araucaria Foundation (Brazil).

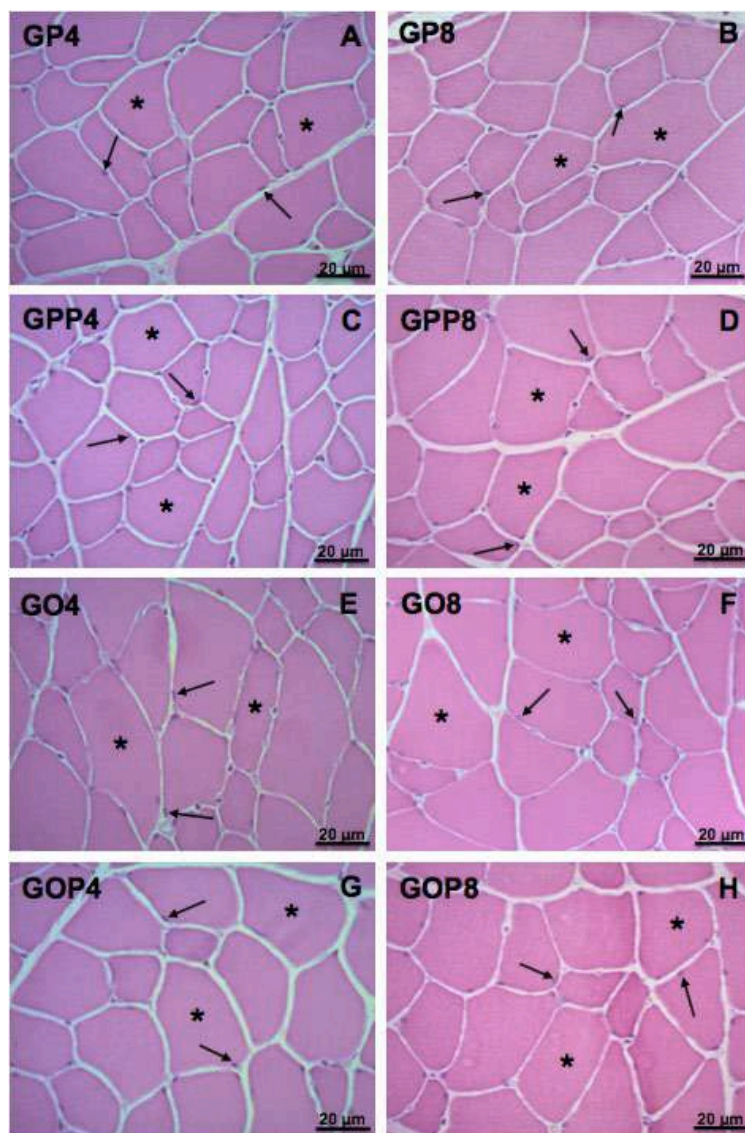


**Figure 1-** Photomicrographs of female Wistar rats' extensor digitorum longus muscles, cross section, Hematoxylin and Eosin. **A:** Group Pseudo-oophorectomy four weeks (GP4) and **B:** Group Pseudo-oophorectomy eight weeks (GP8). **C and D:** Pseudo-oophorectomy groups treated in four (GPP4) and 8 (GPP8) weeks, respectively. **E and F:** Groups Oophorectomy four (GO4) and eight (GO8) weeks. **G and H:** Oophorectomy groups treated in four (GOP4) and eight (GOP8) weeks. General morphology with peripheral nuclei (arrow) and muscle fibers (\*).

**Table 1-** Values expressed by the average  $\pm$  standard deviation of the muscle fibers' cross-sectional area and number of nuclei of the GP (pseudo-oophorectomy), GPP (pseudo-platform), GO (oophorectomy) and GOP (oophorectomy-platform) groups, in the periods of four and eight weeks.

GROUPS	Area ( $\mu\text{m}^2$ )*	Nº. Nuclei*
GO4	1380,8 $\pm$ 173,2 <sup>a</sup>	264,6 $\pm$ 39,7 <sup>a</sup>
GO8	1295,9 $\pm$ 179,9 <sup>a</sup>	270,2 $\pm$ 35,5 <sup>a</sup>
GOP4	1333,3 $\pm$ 106,9 <sup>a</sup>	269,0 $\pm$ 31,0 <sup>a</sup>
GOP8	1370,5 $\pm$ 220,5 <sup>a</sup>	264,1 $\pm$ 41,1 <sup>a</sup>
GP4	1159,4 $\pm$ 164,8 <sup>b</sup>	297,3 $\pm$ 24,9 <sup>b</sup>
GP8	1156,4 $\pm$ 194,6 <sup>b</sup>	282,7 $\pm$ 42,2 <sup>b</sup>
GPP4	1154,1 $\pm$ 116,1 <sup>b</sup>	298,1 $\pm$ 33,5 <sup>b</sup>
GPP8	1327,9 $\pm$ 243,5 <sup>b</sup>	270,4 $\pm$ 36,7 <sup>b</sup>

\* the letters indicate the simple effect of surgery.





## **Morphometry of the Diaphragm Muscle of Obese *Wistar* Rats Submitted to Vibrating Platform**

Mylena de Campos Oliveira<sup>1\*</sup>, Ariadne Barbosa<sup>1</sup>, Angelica Soares<sup>1</sup>, Gladson Ricardo Flor Bertolini<sup>1</sup>, Marcia Miranda Torrejais<sup>1</sup>, Rose Meire Costa Brancalhão<sup>1</sup>.

<sup>1</sup>Universidade Estadual do Oeste do Paraná - UNIOESTE, Campus of Cascavel - Parana, Brazil.

\* mylenac.oliveira@hotmail.com

Obesity is characterized by the accumulation of body fat, resulting in several health problems, such as musculoskeletal and respiratory disorders [1,2]. The practice of physical exercises is a way of treatment [1] and due to the wide use of the vibrating platform and the few studies that evaluate their results in obese people and also the morphology of muscle tissue [3], this study aimed to investigate the effects of the vibrating platform on the morphometry of obese rats' diaphragm muscle induced by monosodium glutamate (MSG). All procedures involving the use of animals were submitted and approved by the Ethics Committee in the Use of Animals (CEUA) of Unioeste (number 08/18). Twenty-eight animals were randomized into four groups: control (CG); obese (GO); trained in vibrating platform (GCP) and obese trained in vibrating platform (GOP). The induction of obesity in the GO and GOP animals were performed in the first five days of life, through the administration of MSG. At the age of 70 days the GCP and GOP animals started the vibrating platform training protocol, at a frequency of 60 Hz and a 2-millimeter amplitude, three times a week, for 10 minutes over a period of eight weeks [4]. At the end of the experimental period, at 130 days of age, the animals were euthanized and the diaphragm muscle was collected. The right antimere of this muscle was frozen in liquid nitrogen, submitted to cross sections (7  $\mu$ m thick) in a cryostat chamber and stained with Hematoxylin-Eosin (HE). The laminae were photo documented and used for the analysis of the cross-sectional area, larger diameter and smaller diameter of muscle fibers, using 10 microscopic fields per animal (objective 40x). Statistical analyses were performed using the two-way analysis of variance test ANOVA, with Bonferroni post-test ( $p < 0.05$ ). The muscle fibers presented preserved general architecture, organized in fascicles in all the studied groups (Figures 1A, 1B, 1C and 1D). In the analyzes of the cross-sectional area, larger and smaller diameters of muscle fibers, the groups with obese animals (GO and GOP) showed a reduction in these parameters, being 25% in the area and 13% in the larger and smaller diameters when compared to the control groups (GC and GCP). On the other hand, comparing the groups that trained with vibrating platform (GCP and GOP) with the untrained groups (CG and GO), there were no significant differences in any of the evaluated parameters (Figures 1E, 1F, and 1G). The results showed that the vibrating platform had no significant interference in the evaluated parameters and that obesity causes changes in morphological muscle characteristics, which may be detrimental to the function of this muscle.

### REFERENCES

- [1] F.B. Bernardes et al., RBONE. 3 (2009).
- [2] U. El-Khani et al., Obesity Surgery. 24 (2014).
- [3] V. Gilsan et al., JBMR. 21 (2006).
- [4] M.M. Butezloff et al., Acta Cirurgica Brasileira. 30 (2015).

[5] This research was supported by CAPES (Brazil).

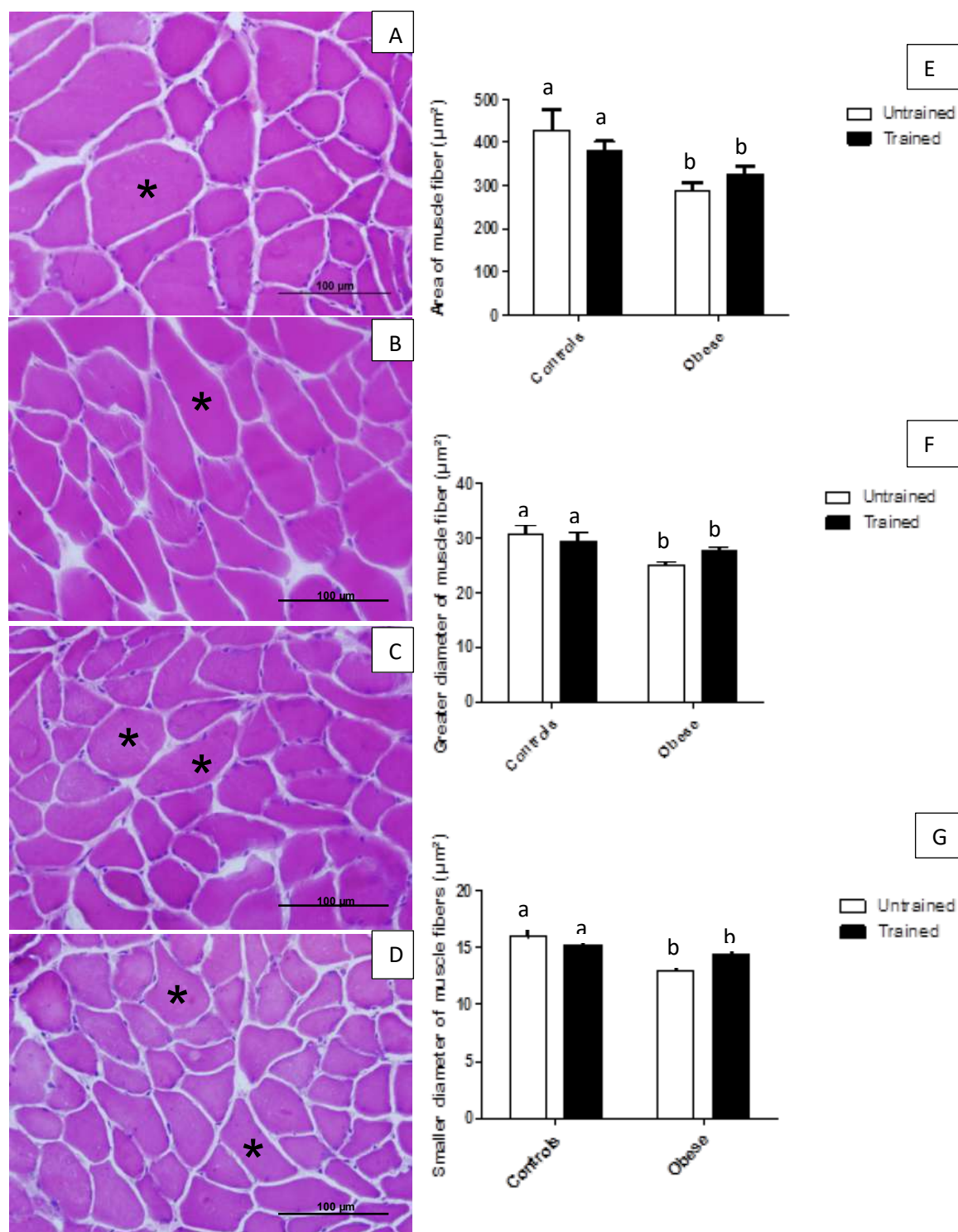


**Figure 1** – Photomicrographs of Wistar rats' diaphragm muscle. Cross section. HE. **A, B, C and D:** Organization of muscle fibers (asterisks) in fascicles, of groups control (GC), submitted to vibrating platform (GCP), obese (GO) and obese submitted to vibrating platform (GOP), respectively. **E, F and G:** Data of the cross-sectional area, larger diameter and smaller diameter in the CG, GCP, GO and GOP groups, respectively. Values expressed as the average  $\pm$  standard deviation. Different letters indicate significant differences. Analysis of variance test ANOVA ( $p < 0.05$ ).

## Quantification of Different Types of Fibers in Obese Animals Submitted to Vibrating Platform Treatment

Mylena de Campos Oliveira<sup>1\*</sup>, Barbara Zanardini de Andrade<sup>1</sup>, Mariana Laís Boaretto<sup>1</sup>,  
Gladson Ricardo Flor Bertolini<sup>1</sup>, Marcia Miranda Torrejais<sup>1</sup>, Rose Meire Costa  
Brancalhão<sup>1</sup>.

<sup>1</sup>Universidade Estadual do Oeste do Paraná - UNIOESTE, Campus of Cascavel - Parana, Brazil.

\* mylenac.oliveira@hotmail.com

Diaphragm muscle is presented as the most important muscle of breathing [1], presenting remarkable plasticity, being able to undergo remodeling by various stimuli, such as obesity or physical activities [2]. Vibrating platform has been widely used, however, little is known about its effects on animals and also on muscle morphology [3]. Thus, this work's objective was to evaluate the effect of the vibrating platform on the diaphragm muscle's muscle fibers in an obesity model. All procedures involving the use of animals were submitted and approved by the Ethics Committee in the Use of Animals (CEUA) of Unioeste (number 08/18). Newborn Wistar rats were initially separated into: control group (CG; n = 14) and obese group (GO; n = 14); which in the first five days of life, for obesity induction, received the administration of MSG. At 70 days of age, the groups were subdivided into four; control (GC; n=7), trained on vibrating platform (GCP; n=7), obese (GO; n=7) and obese trained on vibrating platform (GOP; n=7), where the GCP and GOP animals started the training protocol with vibrating platform, at a frequency of 60 Hz and an amplitude of two millimeters, three times a week for 10 minutes, in a period of eight weeks [4]. At the end of the experimental period, at 130 days of age, the animals were euthanized and the diaphragm muscle was collected. The right antimer of this muscle was frozen in liquid nitrogen, submitted to cross sections (7 µm thick) in a cryostat chamber and submitted to the NADH-TR reaction. This material was photo documented and used to quantify the different types of fibers through four microscopic fields per animal (objective 20x). Statistical analyzes were performed using the two-way analysis of variance test ANOVA, with Bonferroni post-test ( $p < 0.05$ ). The muscle fibers were classified according to the proposal of Brooke and Kaiser [5]. The NADH-TR reaction showed muscle fibers of types I (with small diameter and intense oxidative activity), IIA (with intermediate diameter and moderate oxidative activity) and IIB (with large diameter and low oxidative activity) in all the studied groups (Figures 1A, 1B, 1C and 1D). When the different types of fibers were quantified, type I and type IIA did not present significant differences in any of the analyzed groups, while type IIB fibers showed a reduction of 21% in groups trained with vibrating platform (GCP and GOP) when compared to (GC and GO), with no significant differences in the comparisons between the obese groups (GO and GOP) and control groups (CG and GCP) (Figures 1E, 1F, and 1G). With these results, we conclude that vibrating platform training reduces the amount of type IIB fibers without interference in other fibers, and that obesity has no effect on the number of different types of fibers present in this muscle.

### REFERENCES

- [1] T.B. Lessa et al., Pesquisa Veterinária Brasileira. 32. (2012).
- [2] M.S. Denies et al., Physiological Reports. 2 (2014).

- [3] V. Gilsan et al., JBMR. 21 (2006).  
[4] M.M. Butezloff et al., Acta Cirurgica Brasileira. 30 (2015).  
[5] M.H. Brooke & K.K. Kaiser, J. Histochem. Cytochem. 18 (1970).  
[6] This research was supported by CAPES (Brazil).

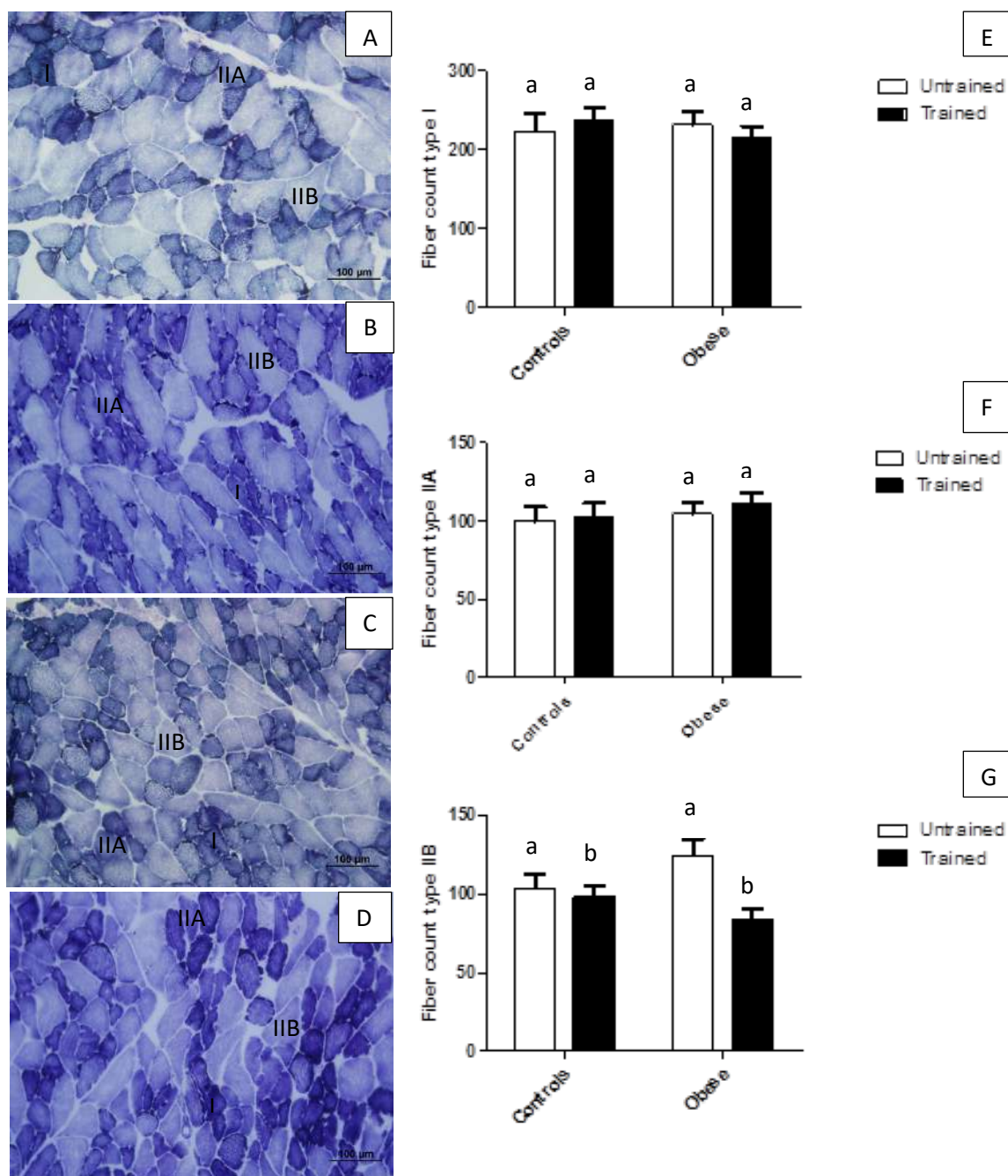


**Figure 1** – Photomicrographs of Wistar rats' the diaphragm muscle. Cross section. NADH-TR reaction. **A, B, C and D:** muscle types I, IIA and IIB, from groups control (GC), submitted to vibrating platform (GCP), obese (GO) and obese submitted to vibrating platform (GOP), respectively. **E, F and G:** Data on the amount of different fiber types in the animals of the GC, GCP, GO and GOP groups, respectively. Values expressed as the average  $\pm$  standard deviation. Different letters indicate significant differences. Analysis of variance test ANOVA ( $p < 0.05$ ).



## Histopathological Changes In The Liver of Fish Exposed to Different Levels of Environmental Pollution

Nathalia Sales Soares do Nascimento<sup>1\*</sup>, Gabriela Pustiglione Marinsek<sup>1</sup>, Renata de Britto Mari<sup>1</sup>

<sup>1</sup>Laboratory of Animal Morphophysiology (LABMA), São Paulo State University - UNESP, Bioscience Institute, São Vicente, Brazil. \*e-mail: nathassn@hotmail.com

Over the years, a direct relationship has been created between the exploitation of natural resources by anthropogenic actions and the amount of waste released into ecosystems. Since coastal regions are rich in the availability of natural resources, they are considered the main affected ecosystems. To identify and evaluate the various human-caused impacts, biomarkers of environmental contamination are used, which evaluate the health of the organisms included in this environment. Thus, the objective of this study was to perform biomonitoring through histopathological analyzes of the puffer fish liver, in three estuaries off the São Paulo coast, with different levels of anthropic interference. Twenty specimens of the puffer fish *Sphoeroides testudineus* were collected in three estuaries of the São Paulo Coast: Rio Verde - Juréia (used as the reference area), Cananéia (impacted area 1 – A1) and Santos - São Vicente, cited in the literature as a pollutant soup (impacted area 2 – A2). The animals were transferred to laboratories, and after 24hrs of acclimation, they were euthanized in benzocaine at 50ppm (Ethics Committee/UNESP n. 08/2018) for recording weight, length and liver samples for microscopic analysis. These samples were submitted to histological processing, stained in H.E. and evaluated histopathologically according to Bernet et al. (1999)<sup>2</sup>. The biometry of the specimens did not present a significant difference between the three study areas. However, the hepatosomatic index and the histopathological score<sup>2</sup> differed between the areas ( $p < 0.001$ , ANOVA), being significantly higher in A1, followed by A2. The A1 region presented lymphocyte infiltration, fibrillar inclusions, necrosis, and cell hypertrophy, as well as the smallest number of hepatocytes, whereas in A2, pathologies such as cholestasis, steatosis and melanomacrophagic centers were found. The animals collected in A1 presented pathologies classified as late and severe<sup>2</sup>. Although it is an area of environmental protection, Cananéia was the stage of mining activities until the end of the sec. XX, which may have favored the occurrence of lesions in the liver of the animals of this region, since the presence of heavy metals in the waters of the estuary has been reported<sup>1</sup>. Liver changes may be related to the processes of bioaccumulation<sup>1</sup>, since the species used has bentofagic habits. The pathologies reported in A2 are characterized as a less severe or immediate response<sup>2</sup>, possibly due to the presence of organic contaminants, which may be affecting other routes of exposure. In this way, the liver proved to be a good biomarker<sup>3</sup>, however, it is suggested that biomonitoring studies use several classes of biomarkers and organs, in order to avoid mistaken reports<sup>3</sup>.

### REFERENCES

- [1] ABDALLA, R. P. et al. Comparative Biochemistry and Physiology Part C: Toxicology & Pharmacology, v. 215, p. 33-40, 2019.
- [2] BERNET, D. et al. Journal of fish diseases, v. 22, n. 1, p. 25-34, 1999.
- [3] VIEIRA, C. E. D. et. al. Science of The Total Environment, v. 666, p. 508-524, 2019.
- [4] This research was supported by São Paulo Research Foundation – FAPESP (processes n. 2014/07793-9-5).

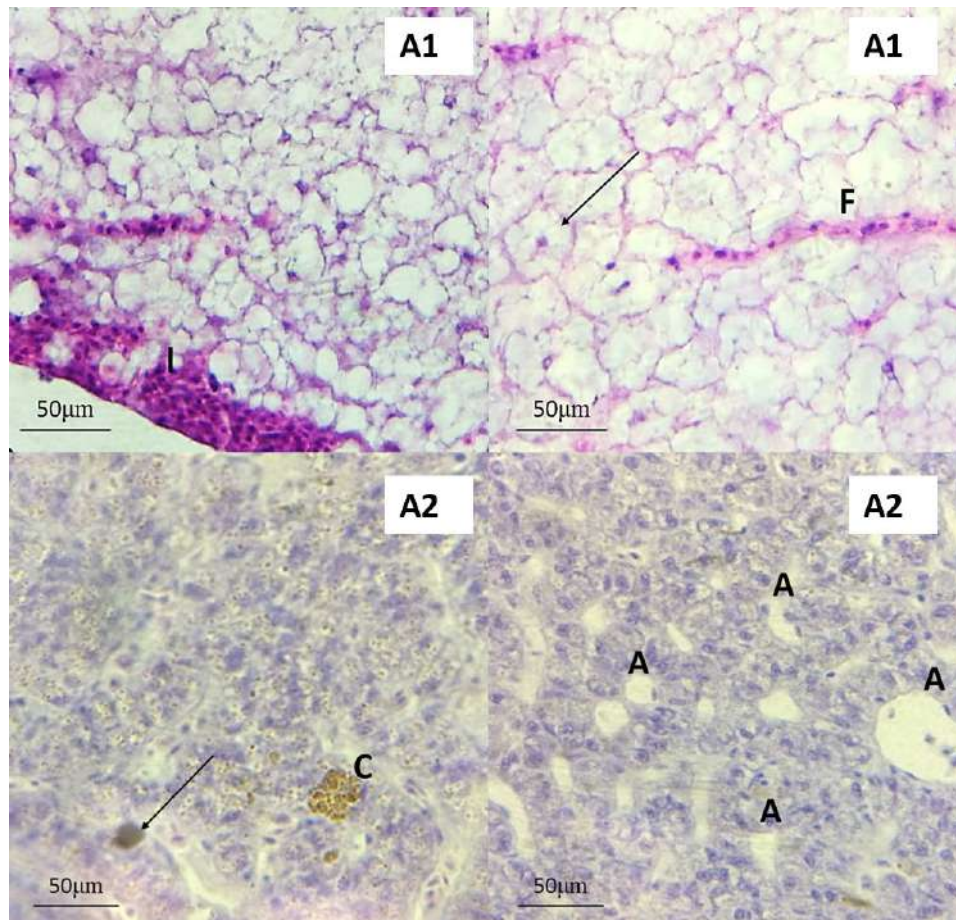


Figure 1 - Photomicrography evidencing the histopathological changes in the puffer fish liver of Cananéia (A1) and Santos-São Vicente (A2). The pathologies found in A1 are shown in the upper images: Cell hypertrophy (arrow); Leukocyte Infiltration (I); Fibrillary inclusions (F). In the inferior images the pathologies found in A2: Cholestasis (arrow); Melanomorphagic centers (C); Steatosis (A).

## ***Plasmodium chabaudi* Merozoites Evade the Nitric Oxide Microbicidal System of Macrophages: Correlation with Phosphatidylserine Exposure**

Pedro Souto Rodrigues<sup>1,3</sup>, Natália de Souza Almeida<sup>1</sup>, João Luiz Mendes Wanderley<sup>2</sup>, Renato Augusto DaMatta<sup>1\*</sup> and Sergio Henrique Seabra<sup>3\*</sup>  
\*seabrash@gmail.com, renato@uenf.br

<sup>1</sup>. Universidade Estadual do Norte Fluminense Darcy Ribeiro, Laboratório de Biologia Celular e Tecidual, Campos dos Goytacazes, Brasil.

<sup>2</sup>. Universidade Federal do Rio de Janeiro, Laboratório de Imunoparasitologia, Macaé, Brasil.

<sup>3</sup>. Centro Universitário Estadual da Zona Oeste, Laboratório de Tecnologia em Bioquímica e Microscopia, Rio de Janeiro, Brasil.

Malaria is one of the most prolific parasitic diseases in tropical countries [1]. The disease cycle shows distinct forms and the biology of the cell interactions is still not entirely understood [2]. The infection of mice by *Plasmodium chabaudi* is one of the closest models to the human disease caused by *P. falciparum* [3]. Not a lot is known about the interaction of *P. chabaudi* with macrophages. Phosphatidylserine (PS), a phospholipid found in the plasma membrane of cells, may be exposed, and causes lower production of Nitric Oxide (NO) in activated macrophages [4]. Since *Leishmania* spp. [5], *Toxoplasma gondii* [6] and *Trypanosoma cruzi* [7] expose PS generating anti-inflammatory response, we verified if *P. chabaudi* merozoites expose this phospholipid and reduce NO production of macrophages. We adapted a protocol to obtain merozoites from infected red blood cells and evaluated the PS exposure in this infectious form. Activated murine peritoneal macrophages were infected with merozoites to analyze parasite development and NO production. Collected merozoites were analyzed directly or after filtering (3.0 µm). Filtration removed leukocytes from the merozoite preparation and resulted in higher homogeneity of events by flow cytometry. We produced an anti-merozoite antibody for the detection of merozoites inside macrophages, evaluated the expression of inducible nitric oxide synthase (iNOS) and verified lysosomal fusion to vacuoles containing parasite by labeling lysosomal-associated membrane protein 1 (LAMP-1). About 50% of the *P. chabaudi* merozoites population exposed PS. The interaction of merozoites with macrophages for 24 and 48 h caused reduction of NO production. Merozoites were capable of infecting about 80% of the macrophages after 2 h of interaction and this infection remained after 24 and 48 h. Such results were compatible with the fluorescence microscopy that showed merozoite localization (Figure 1A and 1B) with lower iNOS expression in infected macrophages after 24 h of interaction (Figure 1C, D and E). In addition, little lysosomal fusion to merozoites containing vacuoles were observed in activated macrophages after 6 h of interaction (Figure 1F, G and H). In conclusion, *P. chabaudi* merozoites realize “apoptotic mimicry”, reinforcing the hypothesis that such evasive mechanism is common to parasitic protozoa that interact with macrophages. The PS exposure seems to have fundamental role in the parasitic protozoa infective process.

### References:

[1] R. W. Snow et al., The global distribution of clinical episodes of *Plasmodium falciparum* malaria. Nature., 2014.

- [2] J.S. Richards et al., The future for blood-stage vaccines against malaria. *Immunol. Cell. Biol.*, 2009.
- [3] J. Cox et al., *Plasmodium chabaudi*: a rodent malaria model for in-vivo and in-vitro cytoadherence of malaria parasites in the absence of knobs. *Parasite Immunol.*, 1987.
- [4] V.A. Fadok et al., Exposure of phosphatidylserine on the surface of apoptotic lymphocytes triggers specific recognition and removal by macrophages. *J. Immunol.*, 1992.
- [5] J.M.F. Balanco et al., Apoptotic mimicry by an obligate intracellular parasite downregulates microbicidal activity. *Curr. Biol.*, 2001.
- [6] T.A. Dos Santos et al., Phosphatidylserine exposure by *Toxoplasma gondii* is fundamental to balance the immune response granting survival of the parasite and of the host. *PLoS One*, 2011.
- [7] R.A. DaMatta et al., *Trypanosoma cruzi* exposes phosphatidylserine as an evasion mechanism. *FEMS Microbiol. Lett.*, 2007.

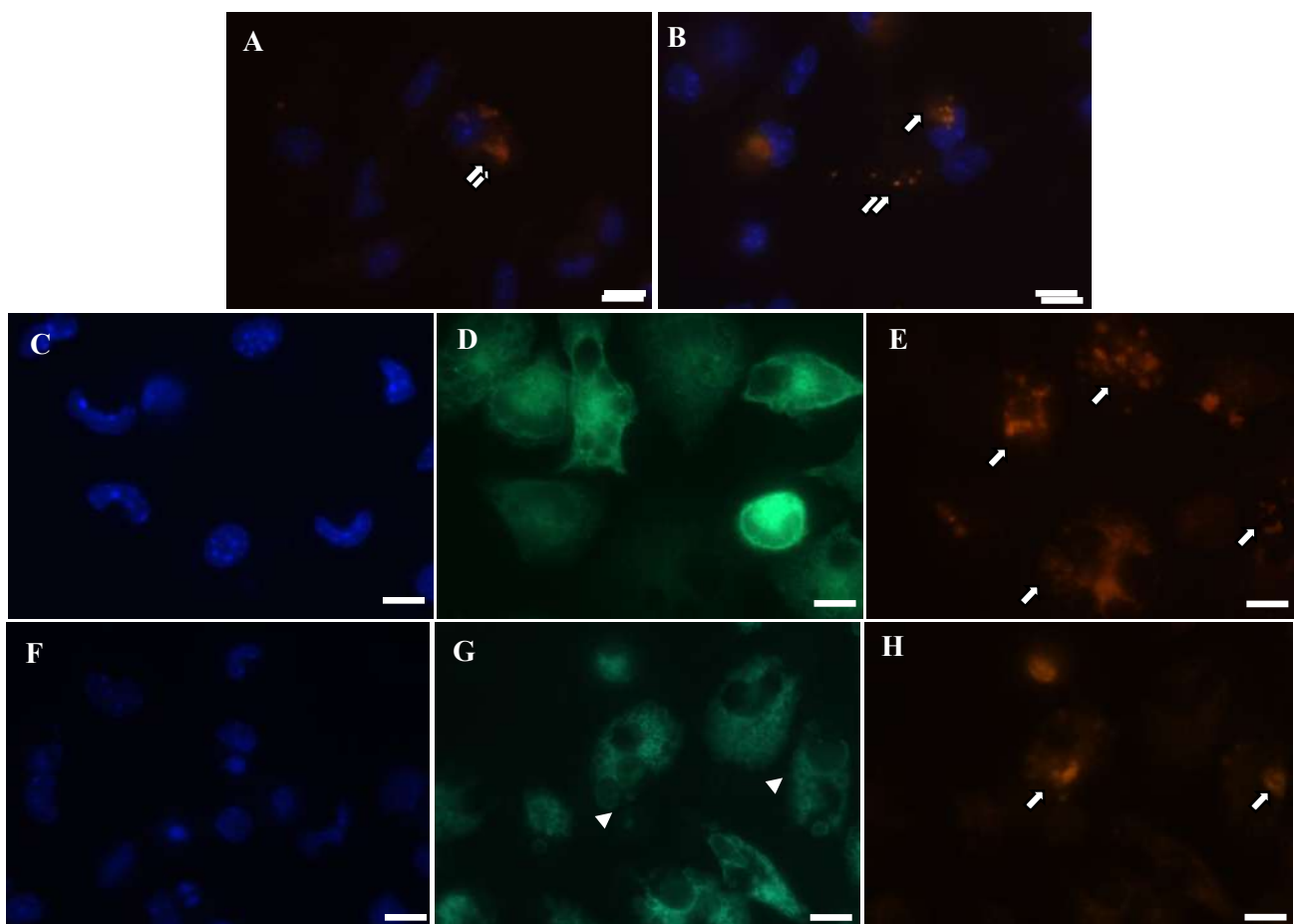


Figure 1. Analysis of the infection between merozoites of *P. chabaudi* and activated peritoneal macrophages from mice. We tested the antibody we produced in dilutions of 1:500 (A) and 1:1000 (B) in a 1:5 infection ratio for 2 h. Parasites in red (A and B - arrows). Later we evaluated the expression of the iNOS (D) in infected cells (merozoites in E) after 24 h (C-E). Note lower iNOS expression in infected macrophages. Then we evaluated the occurrence of lysosomal fusion to the parasite containing vacuole by labeling LAMP-1 (G - arrowheads) (F-H). C and F – DAPI, D – iNOS, G – LAMP-1, E and H – Merozoites.



## YELLOW FEVER VIRUS MODULATES ENERGY METABOLISM AND INDUCES CELL DEATH OF HUMAN MEGAKARYOBLASTS

Campos, S.P.C.<sup>1</sup>; Castro, M. G. <sup>1</sup>; Gomes, C.V. <sup>1</sup>; Caldeira, M.M. <sup>1</sup>; Rodrigues, M.F.<sup>2</sup>; Peçanha, F.L.M. <sup>4</sup>; Kasai-Brunswick, T.H.<sup>5</sup>; Silva, J.L. <sup>3</sup>; Gomes, A.M.O. <sup>1</sup> & Oliveira, A.C. <sup>1</sup>

<sup>1</sup> Laboratório de Biologia Estrutural de Vírus - IBqM/UFRJ

<sup>2</sup> Laboratório de Biologia Molecular do Câncer - IBqM/UFRJ

<sup>3</sup> Laboratório de Termodinâmica de Proteínas e Estruturas Virais Gregorio Weber – IBqM/UFRJ

<sup>4</sup> Laboratório de Adaptações Metabólicas – IBqM/UFRJ

<sup>5</sup> Centro Nacional de Biologia Estrutural e Bioimagem – CANABIO/UFRJ

**INTRODUCTION:** Yellow Fever Virus (YFV) causes yellow fever and has great importance in Africa and South America. Viral infections can induce cell death and metabolic disfunctions, which could be related to the pathogenesis. Yellow fever can lead to thrombocytopenia, that correlates to the frequent hemorrhagic events, characterizing the disease severity. Megakaryoblasts are responsible for platelet production and a modulation of viability and metabolism of these cells during YFV infection can be related to the thrombocytopenia. **OBJECTIVES:** Investigate cell death and metabolic alterations in human megakaryoblasts infected by YFV. **MATERIALS AND METHODS:** We infected MEG-01 cells with YFV 17DD, using a MOI of 1 and detected infection through fluorescent confocal microscopy. Cell death was assessed through trypan blue exclusion, flow cytometry and confocal fluorescence microscopy. Mitochondrial physiology was assessed by high-resolution respirometry and the Bound/Free NADH ratio by Fluorescence Lifetime Imaging Microscopy. We measured lactate release by spectrophotometry. **DISCUSSION AND RESULTS:** We detected intracellular viral proteins since 24h post infection (p.i.) and observed YFV-induced cell death since 120h p.i.. Using TUNEL assay and Annexin V assay, we observed YFV-induced apoptosis by regular nuclear fragmentation and phosphatidylserine exposure since 120h p.i., with caspase 3/7 activation with a peak on 96h p.i.. Through respirometry, we observed reduction on routine and ATP coupled respiration on infected cells 144h p.i., compared to controls. By analyzing the Free/Bound NADH ratio, we observed a decreased free NADH fraction 72h p.i. on infected cells, indicating a more oxidative profile compared to the control cells. We also detected an increased lactate release by infected cells until 96h p.i.. **CONCLUSION:** Our data suggest that YFV replicates and induces apoptosis on MEG-01 cells. YFV can modulate mitochondrial physiology, by reducing cell routine and coupled respiration. Our results also suggest that infection leads to a more oxidative profile, through NADH metabolism and increased lactate release on MEG-01 cells.

**Keywords:** Megakaryoblasts, Yellow Fever Virus, Metabolism

**Supported by:** CNPq, Capes, FAPERJ, INCT-INBEB

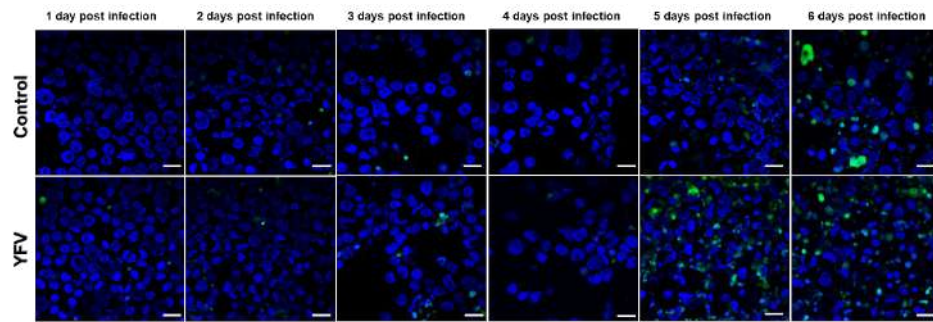


**Figure 5 – Apoptosis Detection.** Apoptotic nuclear fragmentation was detected using TUNEL assay (DeadEnd Promega). The nuclear probe Hoechst 33258 (Blue) was used to stain cell nucleus. Nucleotide conjugated to FITC (Green) were used to mark regular nuclear fragmentation. The images were obtained using fluorescence microscopy (LSM 510 Meta Confocal Scope) and EC Plan-Neofluar 40x/1.30 Oil DIC M27 (Zeiss Inc.) objective lens. MEG-01 cells were infected with YFV 17DD using a multiplicity of infection of 1 (MOI:1) and analyzed 1 to 6 days post infection. Bars represent a 20  $\mu$ m distance.

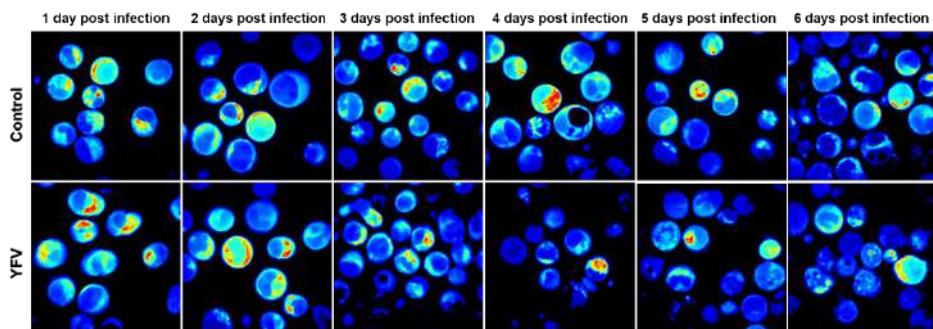


**Figure 9 – NADH Autofluorescence of MEG-01 Cells.** Two-photon fluorescence microscopy intensity images showing NADH fluorescence of MEG-01 cells excited at 740 nm during different days of infection. MEG-01 cells were infected with a MOI of 1. The images were obtained on a two-photon microscope (Nikon Eclipse TE2000-U) and Plan-Apochromat 60x/1.20 water immersion objective lens (Nikon). Data were acquired on VistaVision software and Alba Film instrument (ISS). Data were analyzed on SimFCS software developed at the Laboratory for Fluorescence Dynamics, University of California at Irvine.

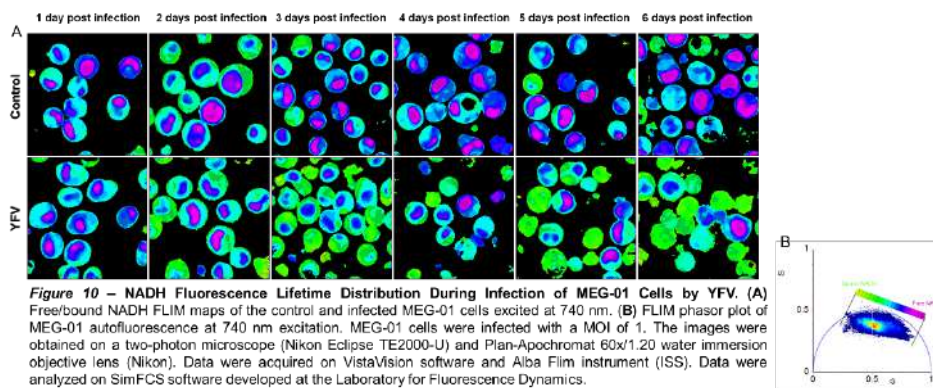


**Figure 10 – NADH Fluorescence Lifetime Distribution During Infection of MEG-01 Cells by YFV.** (A) Free-bound NADH FLIM maps of the control and infected MEG-01 cells excited at 740 nm. (B) FLIM phasor plot of MEG-01 autofluorescence at 740 nm excitation. MEG-01 cells were infected with a MOI of 1. The images were obtained on a two-photon microscope (Nikon Eclipse TE2000-U) and Plan-Apochromat 60x/1.20 water immersion objective lens (Nikon). Data were acquired on VistaVision software and Alba Film instrument (ISS). Data were analyzed on SimFCS software developed at the Laboratory for Fluorescence Dynamics.

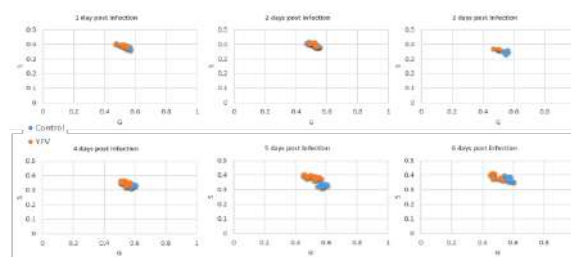


**Figure 11 – NADH Fluorescence Lifetime Distribution During Infection of MEG-01 Cells by YFV.** The graphs represent the average coordinates of S and G on Phasor Plot of image pixels of each field of view of each condition. The plots represent a total of 15 fields of view for each condition, on a total of 3 independent experiments. The images were obtained on a two-photon microscope (Nikon Eclipse TE2000-U) and Plan-Apochromat 60x/1.20 water immersion objective lens (Nikon). Data were acquired on VistaVision software and Alba Film instrument (ISS). Data were analyzed on SimFCS software developed at the Laboratory for Fluorescence Dynamics.

## Dynamic of Histopathological Changes in The Intestinal Barrier of The Jejunum of Hamsters Experimentally Infected by *Leishmania (L.) infantum*.

LIMA, Sarah Kymberly Santos<sup>1\*</sup>, Cavallone, Italo Novais<sup>1</sup>, OLIVEIRA, Karine Soares<sup>1</sup>, PASSERO, Luiz Felipe Domingues<sup>1</sup>, LAURENTI, Márcia Dalastra<sup>2</sup>, JESUS, Jéssica Adriana<sup>2</sup>, CHUCRI, Thaís Martins<sup>1</sup> and MARI, Renata de Britto<sup>1</sup>

<sup>1</sup>Laboratory of Animal Morphophysiology, São Paulo State University - UNESP, Bioscience Institute, São Vicente, Brazil.

<sup>2</sup>Laboratory of Pathology and Infectious Diseases, Department of Pathology/FMUSP, São Paulo, Brazil.

\*E-mail: sarah\_melchert@hotmail.com

Visceral leishmaniasis is a systemic infectious disease of great importance for public health, which when untreated can lead to death in 90% of the cases [1]. As the disease evaluates, symptoms such as hepatosplenomegaly, fever, weight loss, anemia, leukopenia, peripheral edema, manifest themselves. In the gastrointestinal tract (GIT), studies described intense parasitism, which by causing inflammation can progress to severe ulcerations, intestinal hemorrhage, diarrhea and vomiting. All these symptoms are related to intestinal dysfunctions [2]. Based on that, our objective was to analyze the morphometrics changes of villus, crypts, and intraepithelial lymphocytes (IELs) of golden hamster's jejunum infected with *Leishmania (L.) infantum* at 30, 60 and 90 days of infection. Thirty-three male golden hamsters *Mesocricetus auratus* were divided into experimental group (EG) which was infected intraperitoneally with 2x10<sup>7</sup> promastigotes and control group (CG) which received PBS solution in the same amount. After the periods of 30, 60 and 90 days of infection, the animals were euthanized for collection of the small intestine. Fragments of the jejunum were submitted to histological technique with staining in HE for morphometrics analysis and disclosure of IELs. As result we saw that all periods of infection for the crypts and villus were statistically significant (p<0,05, t-student teste) (figure 1). At 30 days of infection we observed an increase on the depth of crypts and increase of the villus. At 60 and 90 days it was observed atrophy of crypts and villus. For the IELs results, we saw the significant (p<0,05, t-student test) increase of population on 30 and 60 days of infection, and the non-significant increase of population on 90 days. The hypertrophy of villus and crypts in addition with the increase of IELs migration could be an immunological response typical of acute infections [3], passing to intermediate and chronic period of infection it was seen that the intensity of IELs migration is decreasing, until it is no longer significant on 90 days. These results and the atrophy of villus and crypts are typical of chronic infections, showing that the immune tolerance is already established in the intestine [4].

[1] WHO, WORLD HEALTH ORGANIZATION. Health topics: Leishmaniasis, 2017.

[2] DE SOUSA SILVA et al. Revista da Universidade Vale do Rio Verde, 2018.

[3] TREVIZAN, Aline Rosa et al. Experimental Parasitology, 2016.

[4] DA SILVA, M. J. et al. Revista Brasileira de Parasitologia Veterinária, 2010.

[5] This research was supported by São Paulo Research Foundation – FAPESP (processes n. 2018/04869-5).

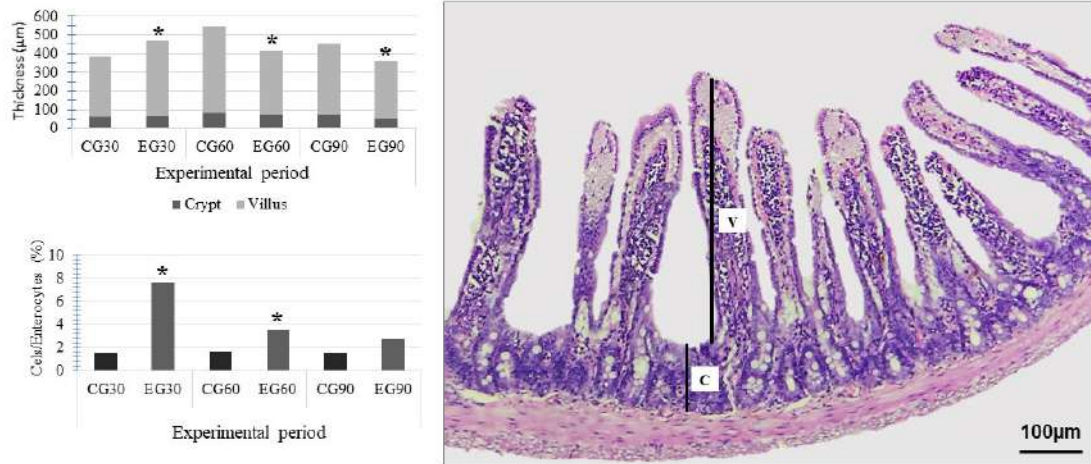


Figure 1. Graphic of villus and crypts thickness (μm) comparisons and percentual quotient (%) between IELs and enterocytes between control (CG) and experimental (EG) groups in 30, 60 and 90 days of infection. \* Results statistically significant ( $p < 0,05$ ). Photomicrography (100μm) of intestine simulating a mensuration scheme of villus and crypts.





## Effects of testicular photohyperthermia on the histology of seminiferous tubules

Vanessa N. Lima<sup>1\*</sup>, Juliana L. M. Brito<sup>1</sup>, Rodrigo B. Nunes<sup>2</sup>, Carlos A. E. Leite<sup>2</sup>, Paulo E. N. Souza<sup>2</sup>; Marcus V. Araujo<sup>3</sup>; Andris F. Bakuzis<sup>3</sup>; Carolina M. Lucci<sup>1</sup>

<sup>1</sup>. Department of Physiological Sciences, Institute of Biological Sciences, University of Brasília, Brasília/DF, Brazil.

<sup>2</sup>. Institute of Physics, University of Brasilia, Brasilia/DF, Brazil.

<sup>3</sup>. Institute of Physics, Federal University of Goiás, Goiânia/GO, Brazil.

\* Corresponding e-mail: [vanessanicolaudelima@gmail.com](mailto:vanessanicolaudelima@gmail.com)

Considering the elevated number of stray animals with a high reproductive rate [1, 2] and knowing that sperm production is affected by temperatures equal or higher than the body temperature [3, 4], the use of photohyperthermia (PHT), producing heat in the testicular region may be an alternative method for male neutering. This study aimed to evaluate the effect of testicular photohyperthermia on the morphology of seminiferous tubules. Twenty Wistar rats (16 weeks old) were used. PHT treatment consisted in injecting 150µL of magnetic fluid in the testicle and LED irradiating the testicle until the temperature reached 45 °C, which was kept for 15 minutes. Twenty-five testicles were subjected to this PHT treatment (PHT group). Four testicles received only the intratesticular injection of 150µL of magnetic fluid (MNP group), and 11 testicles were subjected to LED irradiation alone (LED group). Animals were euthanized 7, 28 or 56 days after treatment. After euthanasia both testicles were fixed for histomorphological analysis. The LED group (Figure 1A) presented intact seminiferous tubules with the presence of all the cells of the germinative lineage. The MNP group (Figure 1B) presented some damage in the tissue, with an amorphous infiltrate within the seminiferous tubules, probably due to a toxic effect of the magnetic fluid. Seven days after PHT (Figure 1C) most seminiferous tubules presented only Sertoli cells and spermatogonia, and nanoparticles were visible in the interstitial space. On Day 28 after PHT most seminiferous tubules showed a disorganized epithelium, sometimes with swollen cells filling the lumen and sometimes with only Sertoli cells and spermatogonia (Figure 1D), and agglomerations of nanoparticles were visible in the interstitial space. However, at the periphery of the testis some tubules still preserved their normal morphology, with seminiferous epithelium showing all germinative cell types (Figure 1E). Coincidentally, no nanoparticles were visible in the interstitium around normal seminiferous tubules. On Day 56 after PHT (Figure 1F), testis morphology was completely damaged. Seminiferous tubules presented a very thin and disorganized epithelium, with vacuolated cells. Aggregates of nanoparticles were still seen in the interstitial tissue.

[1] Hughes, J., & Macdonald, D. W. *Biological Conservation*, 157 (2013) 341–351.

[2] Olson, P., & Johnston, S. *Journal of the American Veterinary Medical Association* 202(6) (1993) 921–8.

[3] Kastelic, J. P., et al., *Animal Reproduction Science*, 45 (1997) 255–261.

[4] Hansen, P. J. *Philosophical Transactions of the Royal Society B: Biological Sciences*, 364 (2009) 3341–3350.

In conclusion, the use of photohyperthermia associated with intratesticular injection of magnetic fluid was shown to be efficient to impair fertility in male Wistar rats in the short term (56 days). However, the effect was not complete, probably because the magnetic fluid was not homogeneously distributed within the testis. Further studies are needed in order to improve the method and obtain a complete neutering effect. (CEUA/UnB/Protocol#75/2017). Financial support by CAPES, CNPq and FAPDF (Brazil).

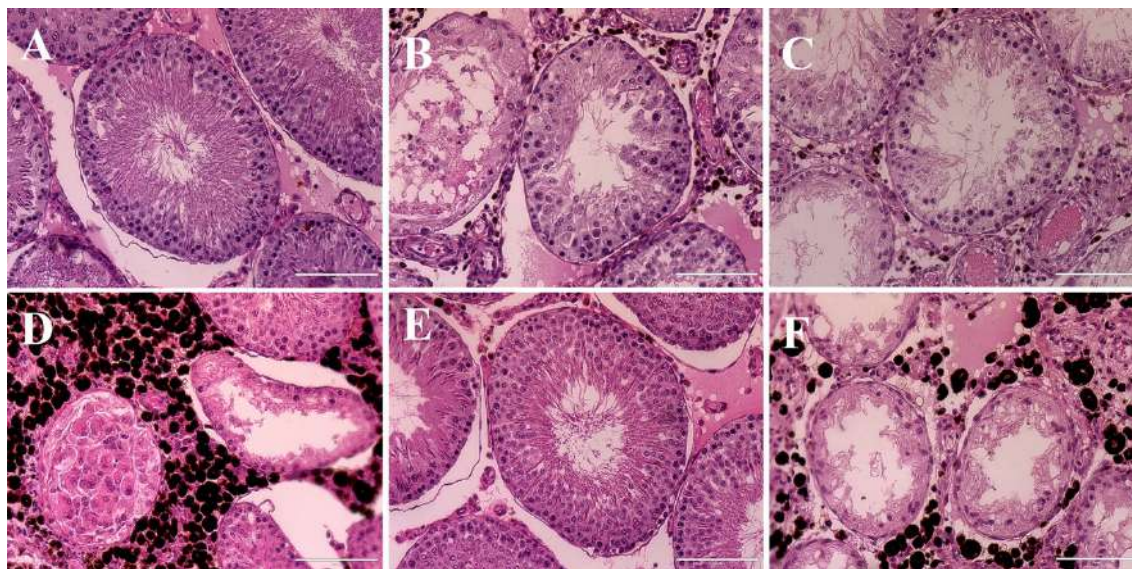


**Figure 1:** Micrographs of seminiferous tubules from different treatment groups. (A) LED group: Seminiferous tubules with all cells of the germinative lineage identified, with spermatozoa in the lumen. (B) MNP group: Left, damaged seminiferous tubule with amorphous infiltrate in the lumen. Right, morphologically normal seminiferous tubule. (C) Day 7 after PHT: Seminiferous tubule with only spermatogonia and Sertoli cells. (D) Day 28 after PHT: Left, seminiferous tubule with swollen cells filling the lumen. Right, seminiferous tubule with only spermatogonia and Sertoli cells. Presence of nanoparticles in the interstitial space. (E) Intact tubule at the periphery of the testis. No visible nanoparticles are present. (F) Day 56 after PHT: Tubules of central region of the testis, presenting a very thin and disorganized epithelium, with vacuolated cells. Presence of nanoparticles in the interstitial space. Bars = 100  $\mu$ m

## **Analysis Of The Interaction Of Type I Collagen With Two-dimensional Materials For The Development Of Biomedical Nanocomposites**

A. C. F. Brito<sup>1\*</sup>, N. C. M. Silva<sup>2</sup>, R. S. S. Lemos<sup>2</sup>, M. C. Prado<sup>3</sup>, E. L. F. C. Alvarenga<sup>4</sup>, B. R. A. Neves<sup>5</sup>, C. K. B. Vasconcelos<sup>2</sup>, M. M. Viana<sup>6</sup>, A. P. M. Barboza<sup>3</sup> and T. M. Manhabosco<sup>3</sup>

<sup>1</sup>. Universidade Federal de Ouro Preto, REDEMAT/ Escola de Minas, Ouro Preto, Brazil.

<sup>2</sup>. Pontifícia Universidade Católica de Minas Gerais, Departamento de Engenharia Química, Belo Horizonte, Brazil.

<sup>3</sup>. Universidade Federal de Ouro Preto, Departamento de Física/ Instituto de Ciências Exatas e Biológicas, Ouro Preto, Brazil.

<sup>4</sup>. Universidade Federal de São João del-Rei, Departamento de Ciências Naturais, São João del-Rei, Brazil.

<sup>5</sup>. Universidade Federal de Minas Gerais, Departamento de Física, Belo Horizonte, Brazil.

<sup>6</sup>. Universidade Federal de Minas Gerais, Departamento de Química, Belo Horizonte, Brazil.

\* annacarolinnabrito@gmail.com

Advances in bioengineering allowed the improvement of biomaterials from materials at most tolerated by the organism to bioactive materials capable of influencing biological processes towards tissue regeneration. Type I collagen is a biodegradable biopolymer, biocompatible and susceptible to chemical modifications. The nanostructured talc is a two dimensional material that presents monolayers with resistance to rupture and modulus of elasticity with values close to the graphene records, in addition to flexural stiffness thirty times greater than it similar [1]. In order to develop biocompatible composites with superior mechanical properties, we studied the interaction between the type I bovine collagen matrix and nanostructured reinforcement phases (talc from soapstone and graphene oxide). Aqueous phase exfoliation methods were performed using different solvents in order to optimize the nanostructured talc, with an average thickness of less than 10 nanometers in homogenous dispersion of sodium cholate. Graphene oxide was obtained from flakes graphite by using modified Hummers' method and characterized using Fourier-transform infrared spectroscopy, thermogravimetric analysis, scanning electron microscopy and X-ray diffraction [2]. Samples containing different concentrations of diluted and neutralized type I collagen were analyzed by atomic force microscopy (AFM) to evaluate the fibers morphology and the interactions: collagen - nanostructured talc and collagen - graphene oxide. AFM images of samples with different collagen concentrations showed that 2.0 mg.mL<sup>-1</sup> is an adequate concentration for the implementation of the reinforcement phases. Initial tests on 1:1 v/v composites of collagen and nanostructured talc indicate that the presence of talc did not significantly modify the morphology of collagen fibers. Similar results were obtained for the 1:1 v/v graphene oxide/collagen nanocomposites.



- [1] A. B. Alencar et al., 2D Materials 2 (2015) 015004.  
[2] D. C. Marcano et al., ACS Nano 4 (2010) 4806-4814.  
[3] This research was supported by CNPq (Brazil), CAPES (Brazil), FAPEMIG - Grant TEC - RED-00282-16 (Brazil).

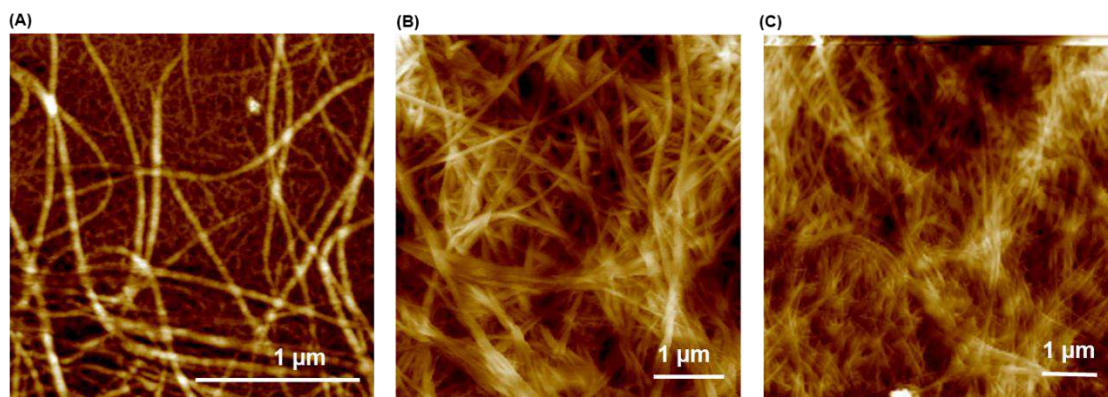


Figure 1. AFM topography images (intermittent contact mode) of diluted and neutralized type I collagen samples at concentrations of (A) 2 mg.mL<sup>-1</sup> (B) 1 mg.mL<sup>-1</sup> and (C) 0.5 mg.mL<sup>-1</sup>, respectively, deposited on glass substrate

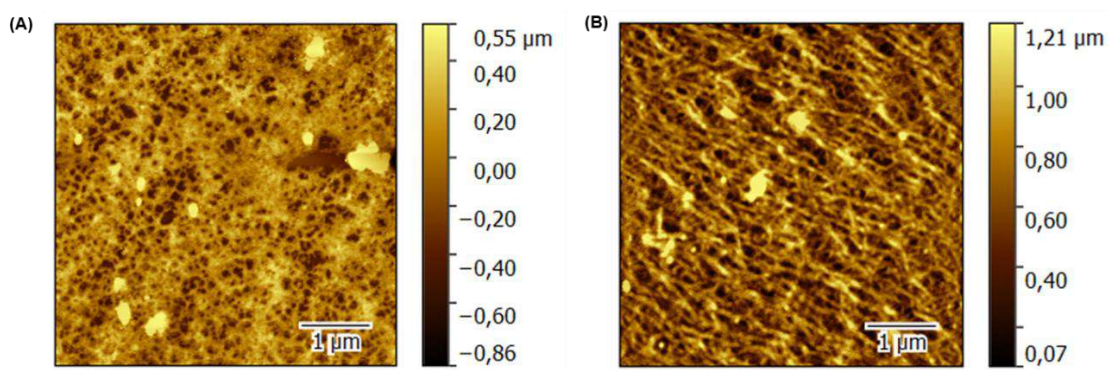


Figure 2. AFM topography images (intermittent contact mode) of composite collagen + dispersion containing nanostructured talc (1:1 v/v) samples at concentrations of (A) 6 mg.mL<sup>-1</sup> and (B) 1 mg.mL<sup>-1</sup> sodium cholate, respectively, deposited on glass substrate



## Inedited Scanning Electron Micrographs of Cashew Plants Leaves Infected With *Pilgeriella anacardii* Von Arx and Muller

Celli Rodrigues Muniz<sup>1\*</sup>, José Emilson Cardoso<sup>1</sup>, Francisco Marto Pinto Viana<sup>1</sup>,  
Eduarda da Silva Lima<sup>1</sup> and Marlon Vagner Valentim Martins<sup>1</sup>

<sup>1</sup>. Embrapa Agroindústria Tropical, Fortaleza, Brazil.

Black mold, caused by the obligate parasite fungus *Pilgeriella anacardii* Von Arx and Muller, is an important foliar disease of cashew (*Anacardium occidentale* L.) in coastal zones of Northeastern Brazil. The pathogen grows profusely on the lower surface of leaves showing a black layer of mycelium, hence the common name of the disease [1]. Fungus growth is profuse and may impair physiological metabolism, leading to chlorotic spots on the upper surface of leaves, reducing eventually fruits production [3]. Since dark colonies with a velvet-like appearance are clearly visualized on abaxial surface of leaves, it was believed that the fungus would had grown only on these surfaces. Although the high significance of this disease for the cashew crop, microscopic images of the fungus infecting the cashew plants leaves were never performed, neither scanning electron microscopy (SEM), remaining, therefore, a gap on this issue. This work aimed to show, for the very first time, SEM of leaves of cashew plants infected with Black Mold from both surfaces, abaxial and adaxial, to elucidate its microstructural features in vivo. Samples of diseased leaves from different plants, reared at the Experimental Research Station of Embrapa in Pacajus, Ceará, Brazil, were collected and processed for SEM, according to [4]. Longitudinal and transverse sections were obtained from abaxial and adaxial surfaces. Images of abaxial surfaces are presented in FIGURE 1. Magnifications ranging from 197 to 7.500 x were carried out. Mycelial and asexual spores of the fungus colonized large areas of the leaf surface. Growth is continuous and profuse, blocking the stomata openings. Mycelium is thick and large, varying from straight to curved branches. Conidiogenesis was examined under higher magnification and conidia maturation initiates as spherical shapes, evolving to barreled ones, as they become older. Surprisingly, adaxial surfaces presented a few colonies (FIGURE 2A), which are not visible by naked eye. Transversal sections also show the fungus within mesophyll (FIGURE 2B), indicating that infection occurs widely internally, being responsible for the serious damage imposed to the physiology of the leaf tissues. The use of chemical agents (fungicides and systemic acquired resistance (SAR)) and biological are therefore, a logical approach to control the fungus, as asserted by [1; 2; 5].

### REFERENCES

- [1] FREIRE, F. C. O. Controle químico do mofo-preto (*Diploidium anacardiacearum* Bat. & Cav.). Revista Brasileira de Fruticultura, v. 13, p. 53-55, 1991.
- [2] FREIRE, F. C. O. Mycoparasitism of the cashew black mould agente by *Acremonium* sp. Agrotrópica, v. 11, n.1, p.25-30, 1999.
- [3] Cardoso JE, Felipe EM, Cavalcante MJB, Freire FCO, Cavalcanti JJV (2000) Precipitação pluvial e progresso da antracnose e do mofo-preto-do-cajueiro (*Anacardium occidentale* L.). Summa Phytopathologica 26:413-416.
- [4] BOZZOLA, J. J.; RUSSELL, L. D. Electron Microscopy: principles and techniques for biologists. Boston: Jones and Bartlett, 1999. 670 p.
- [5] VIANA, F. M. P.; LIMA, J. S.; LIMA, F. A.; CARDOSO, J. E. Control of cashew black mould by acibenzolar-S-methyl. Tropical Plant Pathology, v. 37, p. 354-357, 2012.

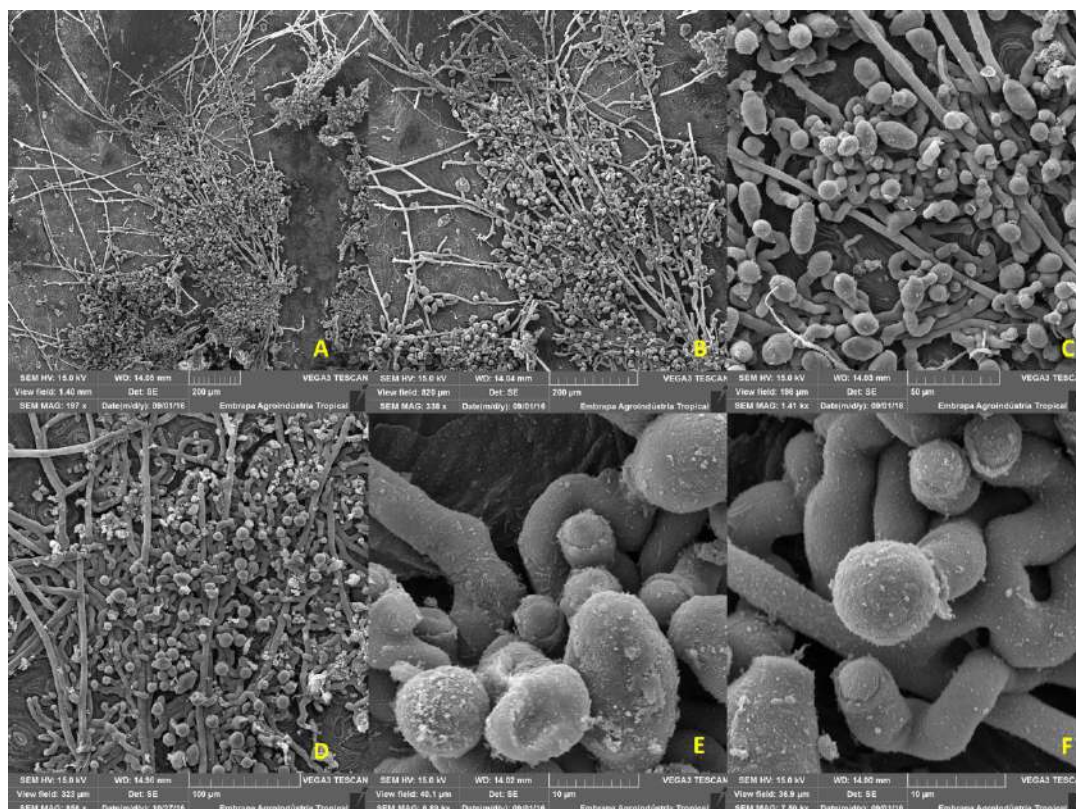


FIGURE 1 – Scanning Electron micrographs of abaxial surface of cashew plants leaves infected with *Pilgeriella anacardii* Von Arx and Muller. (A) Larger area of the abaxial surface as seen under lower magnification (197x) enhancing the profuse distribution of the mycelium. (B) Mycelium under a higher magnification (338x). Few unobstructed stomata are seen. (C and D) Mycelium and Conidiophores more detailed (1.410 and 856x). (E and F) Conidiogenesis process.

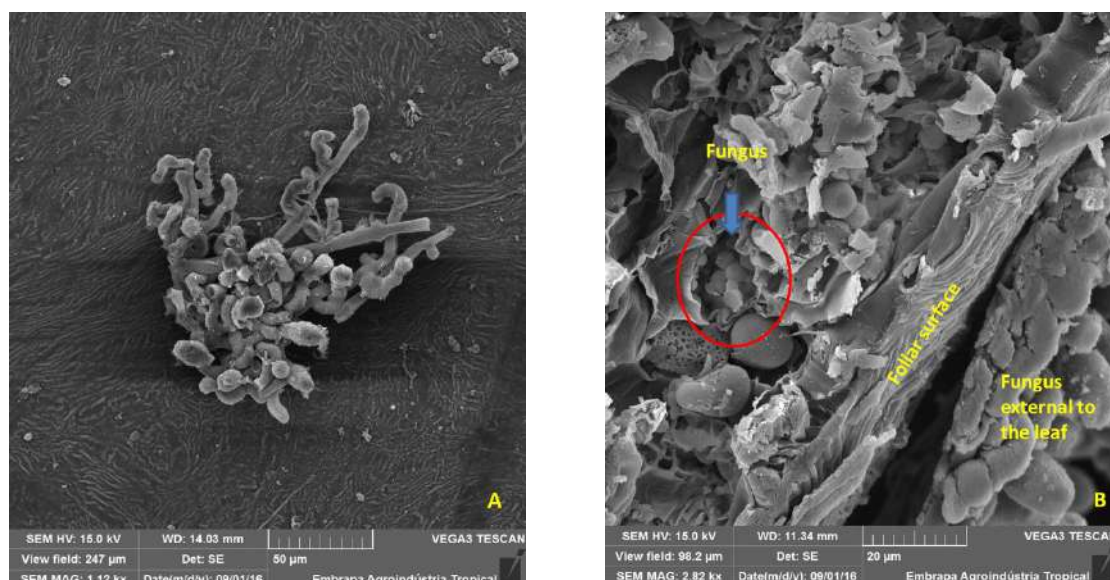


FIGURE 2 - Scanning Electron micrographs of adaxial surface and inner tissues of cashew plants leaves infected with *Pilgeriella anacardii* Von Arx and Muller. A. Leaf adaxial surface showing small colony of the fungus. Magnification of 1.120x. B. Transversal section of the infected leaf showing the fungus within parenchyma cell. Magnification of 2.820x.

## **The increase of filamentous bacteria in the ileum of the mice infected by *Trichuris muris***

Eduarda Cristina da Silva Carlos<sup>1</sup>, Dayane Alvarinho de Oliveira<sup>1</sup>, Eduardo José Lopes-Torres<sup>1,\*</sup>

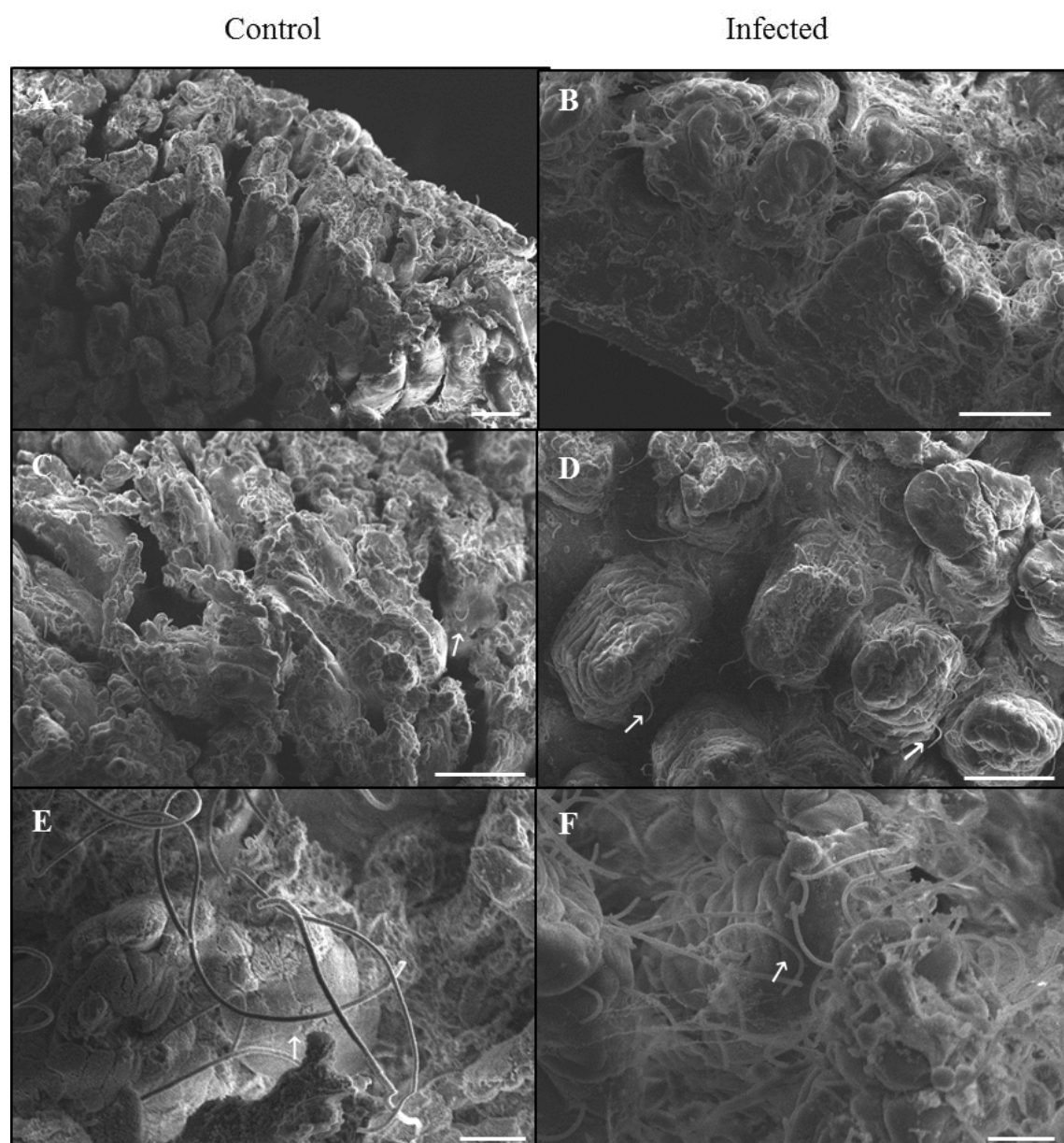
<sup>1</sup> Laboratório de Helmintologia Romero Lascasas Porto, UERJ, DMIP/ FCM, Rio de Janeiro, Brasil. \*eduardo.torres@uerj.br

Whipworms are of the genus *Trichuris* Roederer, 1791, are distributed worldwide and comprise nematode species that parasitize humans and other mammals. The human infection is caused by *T. trichiura* and affects 700 million people worldwide, especially children [1]. These nematodes invade the intestinal mucosa of the host (cecum), causing mucosa alteration and imbalance of the microbiota. The intestine present microorganisms and the microbiota is made up of tens of trillions of bacteria, including at least 1000 different species [2]. This infection promotes an increase in the diversity of species and in abundance of intestinal bacteria in mice, and based on these results, the aim of this work is to investigate the bacterial colonization in different region of the intestine (ileum) using scanning electron microscopy (SEM). Control and infected tissues of the mice were fixed in Karnovsky's solution, post-fixed in osmium tetroxide, dehydrated in ethanol series, critical point dried, mounted in a metal stub, sputtered with gold and analyzed using JEOL, JSM-6510LV. In our results we observed the surface mucosa of the control ileum, showing the villi without visible modifications (Fig A). In infected tissues, we observed, in a cross-section of the intestine, a large number of filamentous bacteria on the surface (Fig B). Using SEM images in high magnification, it was possible to identify the filamentous bacteria in the mucosa of the ileum (Fig. C and E), however when we analyzed the infected tissues, was possible to identify a large number of these bacteria on the surface of the ileum (Fig. D and F). Based on these results, we conclude that the infection may influence in the increased colonization of filamentous bacteria in the ileum, a different intestinal region of the nematode infection. We suggested that the infection promote an intestinal change not only at the site of the parasite, however it is possible that the parasitism promotes more extensive changes in the digestive system.

[1] Bethony, J., Brooker, S., Albonico, M., Geiger, S.M., Loukas, A., Diemert, D., Hotez, P.J. 2006. Soil-transmitted helminth infections: ascariasis, trichuriasis, and hookworm. *Lancet* 367, 1521–1532.

[2] Filippo Pedrinola et al., Microbiota, intestine and health, *Endocrinology and Metabology*. (2019).





Legend: Fragment of ileum tissue analyzed using scanning electron microscopy (SEM). A, C, and E: Control group. B, D and F: infected group. (A) Ileum mucosa showing the intestinal villi without changes and was not possible to identify bacteria colonization. (B) In a cross section of the tissue was possible identify filamentous bacteria. (C and E) Hight magnification enabled the observation of the filamentous bacteria on the mucosa surface (D and F) In infected tissue was possible identify a large number of the filamentous bacteria on the surface of the ileum. Scales bar: A - D: 50  $\mu$ m; E and F: 10 $\mu$ m.



## THE EXERCISE EFFECT ON SCIATIC NERVE REGENERATION FROM MICE PREVIOUSLY TRAINED.

<sup>1</sup>Assis G.\*; <sup>2</sup>Laurindo, R. P.; <sup>1</sup>Santos, A.C.R.; <sup>1,2</sup>Martinez, A.M. B; <sup>1,3</sup> Marques, S.A.

<sup>1</sup>Departament of Pathological Anatomy, Medical School, Federal University of Rio de Janeiro <sup>2</sup> Institute of Biomedical Sciences, Federal University of Rio de Janeiro; <sup>3</sup> Departament of Neurobiology, Institute of Biology, Federal Fluminense University; Brazil. [\\*givanildes.assis@hotmail.com](mailto:givanildes.assis@hotmail.com)

Sciatic nerve lesion is the most frequent lower extremities injury around the world [1]. Although the peripheral nervous system can regenerate after injury, the functional deficits are maintained, particularly when the lesion is distant from the target [2, 3]. The exercise stimulates the plasticity, to speed up the budding of the motor neuron, and decrease the reinnervation latency time [4]. This study aimed to evaluate if the exercise promotes similar regeneration in sedentary and previously trained animals. In this work (CEUA-UFF: 589/2014), we studied 4 groups (n=6/Group): PTT (trained previously, injured and exercised after), LTT (exercised after injury) LST (just injured) and CST (control without injury or exercise). We used young male C57BL/6 mice (weight of 19-25g), anesthetized (Ketamine and xylazine, i.p.) submitted to proximal sciatic nerve crushing with a curve forceps during 1 minute. PTT group starts the treadmill training (two 30 minutes cycles with a 10 minutes pause between them, in a 10m/min speed) 10 days before surgery. Injured groups started treadmill training 3 days after surgery. And the treadmill training (10m/min), started 3 days after injury, in two sequential cycles of 30min, with a pause of 10min between them, for 10 days in a row. Functional analyses (Electronic von Frey test; Pinprick and Sciatic Functional Index - SFI) were made before to surgery (normality pattern), 1 and 14th days after surgery when the electroneuromyography (ENMG) from gastrocnemius muscles and sciatic nerve morphological analyses were carried out. ANOVA and Bonferroni test were used to statistical analyses, and we plotted the mean±EPM. All injured groups showed a loss to the sensitivity on the withdraw reflex when compared to CST (0.380±0.022), but the trained groups (PTT 0.545±0.008, and LTT 0.650±0.028) showed improvement in tactile stimulus detection 14 days after injury by Electronic von Frey test. The PTT group showed a significant difference when compared with the LST group (p<0.05). Moreover the PTT group no-showed a significant difference compared with the non-injured group (CST) indicating better sensitivity recovery them the other injured groups. Painful sensitivity assessment no-showed significant differences between the groups (PTT 4.50±0.28; LTT 4.75±0.25 and CST 5.0±0.0) by the pinprick test. The injured groups showed lower negative values on the first day after injury by SFI, indicating that the nerve injured procedure was corrected. At 14 days after injury, the PTT group (-28.21±10.64, p<0.05) presented better recovery when compared to the LTT (3.50±13.62, p<0.05) and LST. This better performance of the PTT is in accord by ENMG results, that shows compound muscle action potential (CMAP) with higher amplitude (PTT 6.438±0.276. LTT 2.693±0.946, p<0.05); and lower latency (PTT 0.001±0.022; LTT 0.145±0.336, p<0.05). Also, these functional data combined with the morphological analyses, from the semithin cross-sections, showing better nerve cytoarchitecture organization and myelin nerve fibers preserved suggest that exercise can optimize nerve regeneration and recovery of neuromotor function. And previously exercised individuals present better use of this therapy.

## References

- [1] IJHEMA-PAASSEN, J., JANSEN, K., GRAMSBERGEN, A., E MEEK, M.F., (2004) Transection of peripheral nerves, bridging strategies and effect evaluation. *Biomat.*, 25(9), 1583-1592.
- [2] LUNDBORG, G., RICHARD, P. (2003). Bunge memorial lecture. Nerve injury and repair – a challenge to the plastic brain. *J. peripher. Nerv. Syst.* 8209-226.
- [3] KANDEL, E.; SCHWARTZ, J.; JESSEL, T.; SIEGELBAUM, S.; HUDSPETH, A. *Princípios de Neurociências*. 5 Edição. Ed. Artmed, 2014
- [4] ILHA, J., CENTENARO, L.A., CUNHA, N. B., DE SOUZA, D. F., JAEGER, M., DO NASCIMENTO, P.S., KOLLING, J., BEM, J., MARCUZZO, S., WYSE, A. T. S., GOTTFRIED, C., ACHAVAL, M. The Beneficial Effects of Treadmill Step Training on Activity- Dependent Synaptic and Cellular Plasticity Markers After Complete Spinal Cord Injury *Neurochem Res.*, 36:1046–1055, 2011.
- [5] NAVARRO, X.; ALLODI, I; UDINA, E. A neural plasticity after peripheral nerve injury and regeneration. *Prog. Neurobiol.* 82(4):163-201,2007.

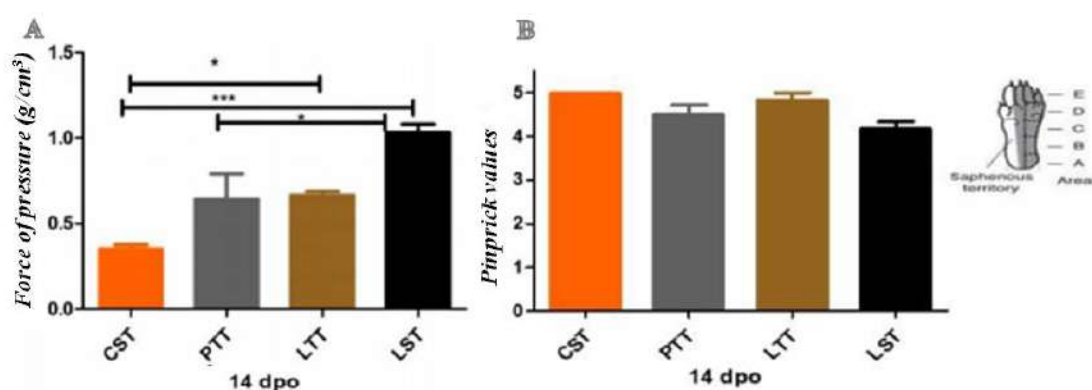


Figure 1: Mechanical and painful sensitivity assessment. (A) ; PTT and LTT groups showed improvement in tactile stimulus detection (n=6) 14 days after injury by Electronic von Frey test. The PTT group showed a significant difference when compared with the LST group. PTT group no-showed a significant difference compared with the non-injured group (CST). (B) The groups no-showed a significant difference by the pinprick test. dpo= days after surgery. \*p<0.05, \*\*\*p<0.001.

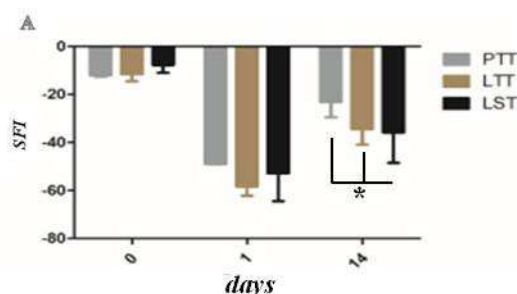


Figure 2: Sciatic Functional Index evaluation. Bar graph showing the comparative evolution of sciatic nerve function through the analyzed time. The groups showed lower negative values on the first day after surgery, indicating the nerve injured. At 14 days, the animals exhibiting some locomotor recovery.

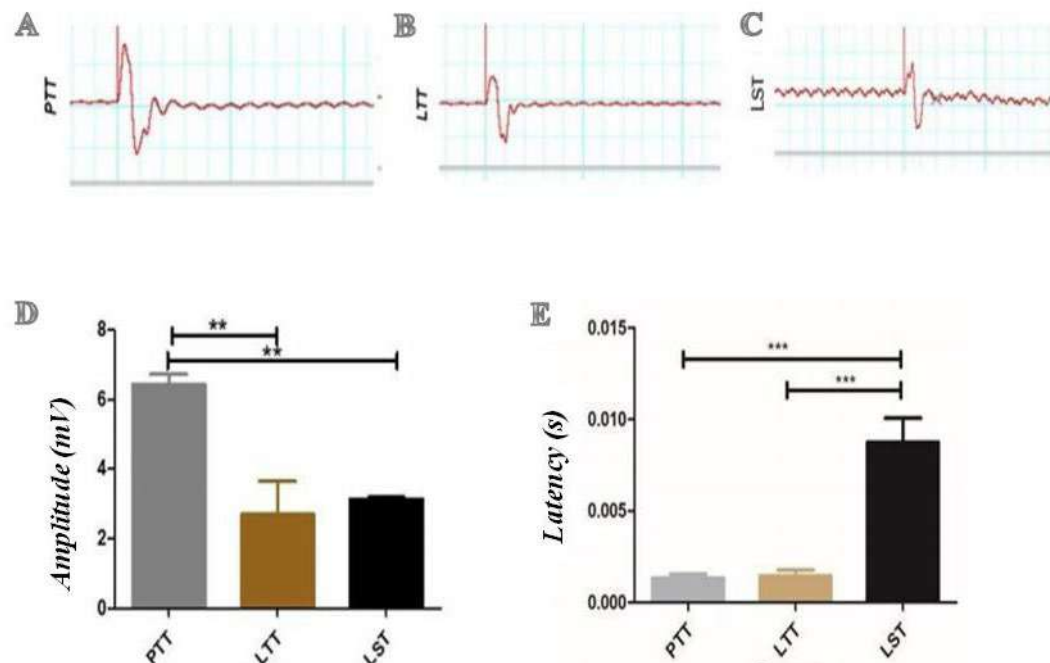


Figure 3: Pre-trained group showed better muscle activation. (A, B and C) Representative examples of electroneuromyography (ENMG) traces of the compound muscle action potential of gastrocnemius muscle after sciatic nerve stimulation obtained in PTT (A), LTT (B) and LST (C) groups, at 14 days after surgery. Bar graphs show the amplitude (D) and latency (E) of the responses. Statistical analysis: one-way ANOVA and Post-test Tukey's. Values represent mean  $\pm$  SEM. (n=6 each group) \*  $p<0.05$ , \*\*\*  $p<0.001$ .

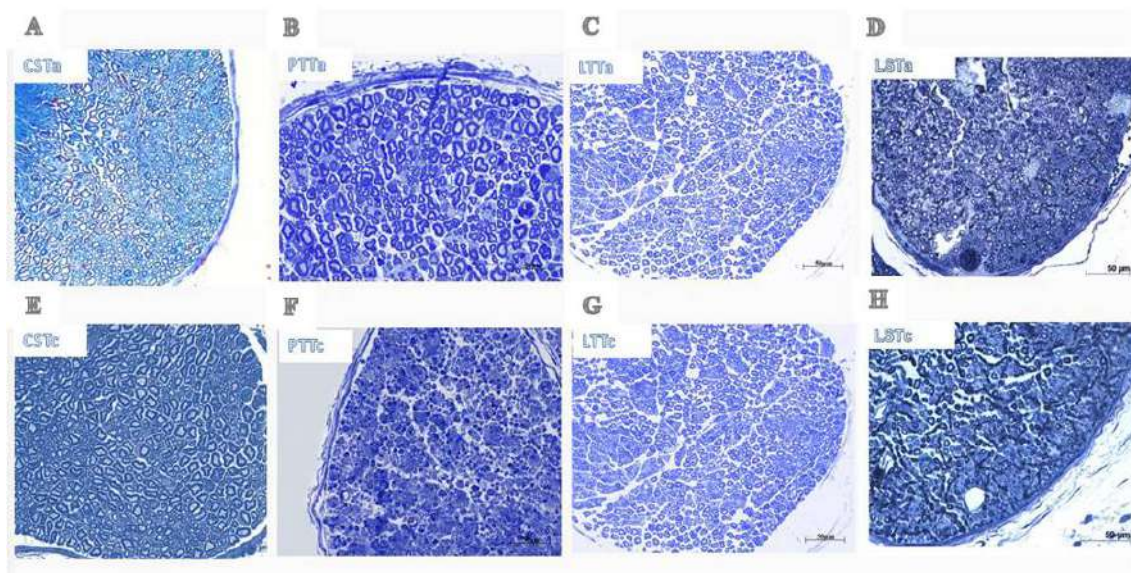


Figure 4: Sciatic nerve regeneration. Semithin cross-section of regenerating sciatic nerve from proximal (A-D) and distal (E-H) to the lesion, at 14 days after injury, stained with toluidine blue.

## In vitro behavior and cytotoxicity evaluation of amphiphilic lipopeptides

Karina A. B. Argüello<sup>1</sup>, S. Valeria Vassiliades<sup>1</sup>, Andrea M. Aguilar<sup>2</sup>, Iseli Laurenço Nantes<sup>1</sup>, Wendel A. Alves<sup>1\*</sup>

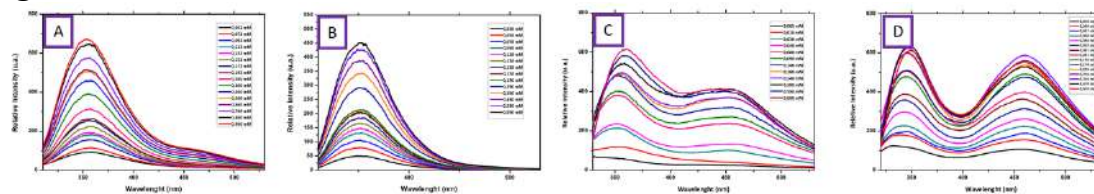
<sup>1</sup>Center for Natural and Human Sciences, Federal University of ABC (UFABC);

<sup>2</sup>Federal University of São Paulo, (UNIFESP).

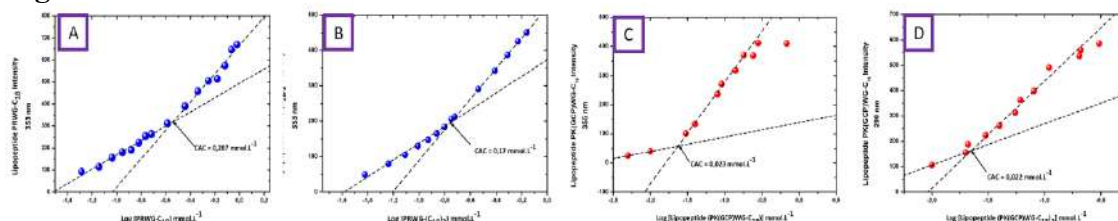
### Abstract

We have prepared four lipopeptides PRWG-(C<sub>18</sub>), PRWG-(C<sub>18</sub>)<sub>2</sub>, PK(GCP)WG-C<sub>18</sub>, and PK(GCP)WG-(C<sub>18</sub>)<sub>2</sub>. The lipopeptides PRWG-C<sub>18</sub> and PRWG-(C<sub>18</sub>)<sub>2</sub> have in its structure the amino acids L-proline (P), L-arginine (R), L-tryptophan (W), and L-glycine (G). The amino acids L-proline (P), L-Lysine (K), were functionalized with the artificial amino acid guanidiniocarbonyl pyrrole (GCP) and L-tryptophan (W) in the lipopeptides PK(GCP)WG-C<sub>18</sub>, and PK(GCP)WG-(C<sub>18</sub>)<sub>2</sub>, amino acid glycine was coupled in every lipopeptide as a spacer to confer greater mobility to the double chain aliphatic of 18 carbon atoms. The preparation of this lipopeptide consisted of three stages, the coupling between the amino acid Boc-glycine and the dioctadecylamine, the synthesis of the tripeptide PRW and PK(GCP)WG in solid phase through a series of coupling reactions using the Fmoc-strategy and finally the coupling between the tripeptide with the amino acid glycine bounded to the double aliphatic chain [1]. The coupling of these peptides with molecules such as lipids and polymers provides certain advantages as potential drug carriers in the selective release of bioactive, as high encapsulation efficiency, high bioavailability, and low toxicity. Fluorescence spectrophotometry studies (Figure 1) were carried out to determine the critical aggregation concentration (CAC) (Figure 2), to evaluate self-organization processes, based on the relative intensity of the tryptophan emission at 350 nm. The cytotoxicity of this compound was evaluated in HEK293 cells using the MTT assay [3-(4,5-dimethylthiazol-2-yl)-2,5-diphenyltetrazolium bromide] [2], whose IC<sub>50</sub> values demonstrate that for PRWG-C<sub>18</sub> and PRWG-(C<sub>18</sub>)<sub>2</sub> were below the CAC and for PK(GCP)WG-C<sub>18</sub> and PK (GCP)WG-(C<sub>18</sub>)<sub>2</sub> were above their estimated CAC values (Figure 3). Fluorescence microscopy studies were carried out to determine the behavior of the material, observing a change in the appearance of the nucleus between the control, the minimal concentration and the highest concentration which agrees with the cell viability studies (Figure 4). This study shows that the change in the peptide sequence influences the polymorphism and self-organization of the material, which in turn determines the viability of these materials. According to the different results presented, it is demonstrated that the materials PRWG-(C<sub>18</sub>), PRWG-(C<sub>18</sub>)<sub>2</sub> can be used in their molecular forms and tested for other types of cell lineages, however, lipopeptides PK(GCP)WG-C<sub>18</sub>, and PK(GCP)WG-(C<sub>18</sub>)<sub>2</sub> are promising materials since they can be used as transporters of drugs in their molecular form as self-organized.

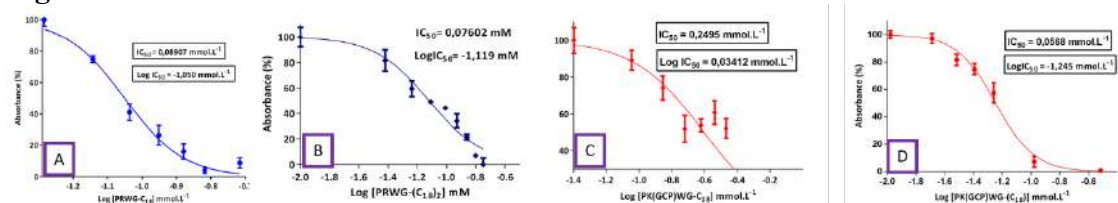


**Figure 1.**

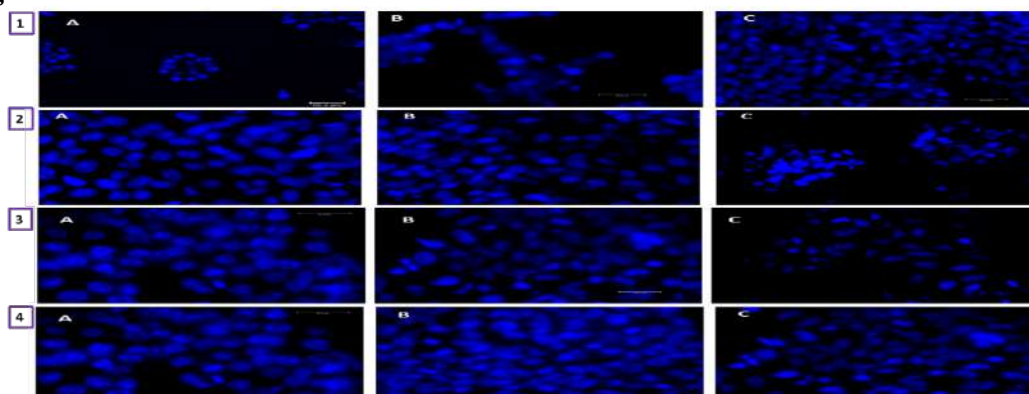
Fluorescence spectrophotometry studies were carried out to evaluate the aggregation processes of each material through the estimation of the CAC. Each lipopeptide solution was illuminated at 290 nm corresponding to the excitation wavelength of tryptophan, and these data show a peak at 350 nm, which is characteristic of this amino acid.

**Figure 2.**

These graphs show the tryptophan-based emission as a function of the log lipopeptide concentration. The intersection between the fitted straight lines provided the estimate of the CAC.

**Figure 3.**

The values obtained from  $IC_{50}$  for PRWG-(C<sub>18</sub>), PRWG-(C<sub>18</sub>)<sub>2</sub> are below the CAC, which shows that these materials have cytotoxicity above estimate. For lipopeptides, PK(GCP)WG-C<sub>18</sub>, and PK(GCP)WG-(C<sub>18</sub>)<sub>2</sub> the  $IC_{50}$  values are above the CAC, being materials with low cytotoxicity both in their molecular and self-organized forms.

**Figure 4.**

HEK293 cells were incubated for 24 hours and labeled with Hoechst 33342, observing a change in the appearance of the nucleus. Three images were taken for each material, being a) control b) minimum concentration below  $IC_{50}$  and c) above  $IC_{50}$ . These results are consistent with cell viability studies, were observed levels above  $IC_{50}$  values; the cell came to enter a pyknotic nucleus or cellular apoptosis.

- [1] B. Soares Miranda and W. Alves Andrade, "Synthesis and characterization of lipopeptidic nanostructures: Application as Catalysts in Aldol Reaction in Aqueous Medium," Federal University of ABC, 2017.
- [2] J. Yang, A. Bahreman, G. Daudey, J. Bussmann, R. C. L. Olsthoorn, and A. Kros, "Drug Delivery via Cell Membrane Fusion Using Lipopeptide Modified Liposomes," *Acs Cent. Sci.*, vol. 2, no. 9, pp. 621–630, 2016.

This research was supported by FAPESP, CNPq, INCTBio and CAPES

## Interaction between *E. coli* and T84 monolayer with *Trichuris muris* Excretory Secretory Products

Larissa Trotta Barroso de Oliveira<sup>1</sup>, Dayane Alvarinho de Oliveira<sup>1</sup>, Ana Claudia P. Rosas<sup>2</sup>  
Eduardo José Lopes-Torres<sup>1,\*</sup>

<sup>1</sup> Laboratório de Helmentologia Romero Lascasas Porto, UERJ, DMIP/ FCM, Rio de Janeiro, Brasil

<sup>2</sup> UERJ, DMIP/ FCM, Rio de Janeiro, Brasil

\* eduardo.torres@uerj.br

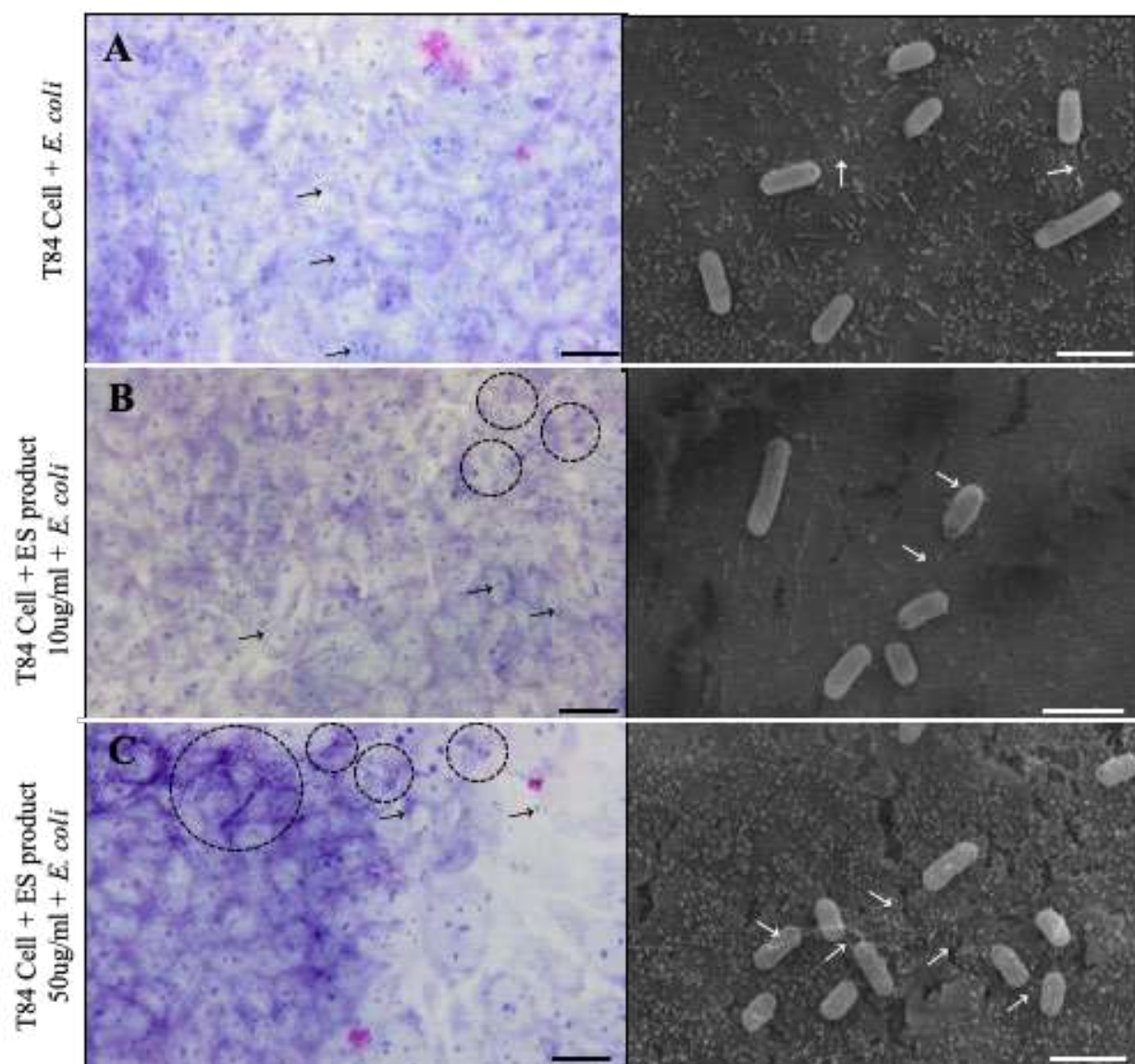
Trichuriasis is a disease caused by nematodes common in poorer countries with impact on human and veterinary health. *Trichuris trichiura* is the species that infects humans and the transmission is promoted by the ingestion of embryonated eggs. The success of the infection is associated to the modulation of the host's inflammatory response by the excretory-secretory (ES) products released by the nematodes in the intestinal tissue. *T. muris* infection promotes tissue damage that contributes to the bacteria invasion and this parasitism causes a microbiota imbalance, promoting an increase in species diversity and in the abundance of intestinal bacteria in mice [1, 2]. *T. muris* is a nematode model used in the study of gastrointestinal infection and T84 is a colon adenocarcinoma cell that forms a polarized monolayer, commonly used in studies associated with the intestinal tissue [3]. In this study, we are investigating the influences of the *T. muris* ES product in the intestinal colonization of the *E. coli* in using *in vitro* experiments with T84 cells monolayer. The monolayer T84 was submitted to different conditions using the 24-well cell culture plates. *Escherichia coli* 042 strains with T84 monolayer interaction was used as control group, the experiments was performed with monolayer, bacteria and ES product in two concentrations (10 and 50ug/ml) for 3 hours. Subsequently the samples were processed for Light Microscopy (LM), fixed in methanol, stained with Giemsa and observed using Olympus BX53 microscope attached with the Olympus SC100 digital camera. For the Scanning Electron Microscopy (SEM), the samples were fixed with Karnovsky solution, post-fixed in osmium tetroxide, dehydrated in ethanol series, critical point dried, mounted in a metal stub, sputtered with gold and analyzed using Jeol JSM-6510LV. LM results showed that the ES product promotes an increase in the number of bacteria associated with the monolayer and using the SEM was possible to identify fiber-like structures connecting bacteria with bacteria and bacteria to the T84 cell monolayer (Fig. A-C). These results suggested that the ES product influences in the bacteria adhesion on the tissue and it is possible that these fiber-like structures may be precursors of the biofilm. These *in vitro* results corroborate with observed *in vivo*, when we performed the identification of the microbiota of the infected mice and identified an increase of the species in intestinal colonization. These increase can be promoted by the chemical environmental changes of the intestine promoted by the nematode ES products.

[1] OLIVEIRA, D.A. Alterações no tecido intestinal e o envolvimento de bactérias na fase crônica da infecção de *Trichuris muris* em camundongos. 2017. 49 f.

[2] TRITTEN, L. et al. Excretory/secretory products from the gastrointestinal nematode *Trichuris muris*, 2017.

[3] DEVRIESE, S. et al. T84 monolayers are superior to Caco-2 as a model system of colonocytes, 2017.

[4] This research was supported by CNPq and FAPERJ (Brazil).



Legend: Light (bright field) and scanning electron microscopy of the T84 cell monolayer interaction with *E. coli*. A - Control group: Is possible identify bacteria on the monolayer (black arrow) and fiber-like structures; B - *Trichuris muris* ES product (10 µg/ml): In this experiment we identified an increase of the bacteria on the monolayer (black arrow and dotted circle) and the SEM images shows the increase in the fiber-like structures; and C - *Trichuris muris* ES product (50 µg/ml): These results show a large number of the bacteria colonies (black arrow and dotted circle) and the fiber-like structures increased on the bacteria, promoting a strongly interaction of the bacteria with the monolayer. Scale bar: A, C and E: 20 µm; B, D and C: 2µm.



## Optimization of Fungal Lipase Production for Biofuels Production

Letícia Miranda Cesário<sup>1</sup>, Rafael Freitas Santos Pereira<sup>1</sup>, Giovanna Pinto Pires<sup>1</sup>, André Fraga Carvalhal<sup>1</sup>, Jairo Pinto de Oliveira<sup>1\*</sup>

<sup>1</sup>Federal University of Espírito Santo, Department of Biology, Alegre, Brazil

\* jairo.oliveira@ufes.br

Biocatalysis is a promising field when it comes to expansion of technologies that deal with high aggregated value compounds [1]. Lipases (triacylglycerol hydrolase ester, EC 3.1.1.3) are enzymes that catalyze the breakdown of fats and oils releasing fatty acids, diglycerides, monoglycerides and glycerol. They also catalyzed reactions such as the esterification, transesterification and interesterification, which makes them great interest for biodiesel production [2]. Lipases are from of different sources and consequently have different properties suitable for the process. Current research studied the optimization of lipases' yield process (*Aspergillus niger* e *Aspergillus sp.*) by analyzing variables that exerce influence on the process, such as temperature and percentage of inductor in the xxx, as demonstrated by full factorial design 3<sup>2</sup>. In order to obtain the aforementioned lipases, it was required six days of fungal culture (which had formerly been set), in minimum medium with different concentrations of inductor (soy oil) and temperatures — according to experimental design. The fungal isolates were characterized by scanning electron microscopy (SEM-JEOL1600LV), while the lipases' extraction was performed with sodium acetate; the cultures, per se, were then filtered and centrifuged, being subsequently used for partial characterization of the raw enzyme. Lipase activity was quantified utilizing standard spectrophotometric method by reducing synthetic substrate p-nitrophenyl palmitate (pNPP) and, also, Bradford method, for the quantification of total proteins. In the end, it was possible to see the fast fungal growth under the conditions studied by SEM images, showing conidia and spores. Results of factorial design indicate ideal conditions for the production of lipases, favoring the application of these enzymes as catalysts in the biodiesel transesterification process.

## REFERÊNCIAS

- [1] Demirjian, D. C. et al., Biocatalysis- From discovery To Application 1999, 200, 1.
- [2] Pinotti, LM et al. Waste and Biomass Valorization. 2018, 9, p293-299. Doi : 10.1007/s12649-016-9776.



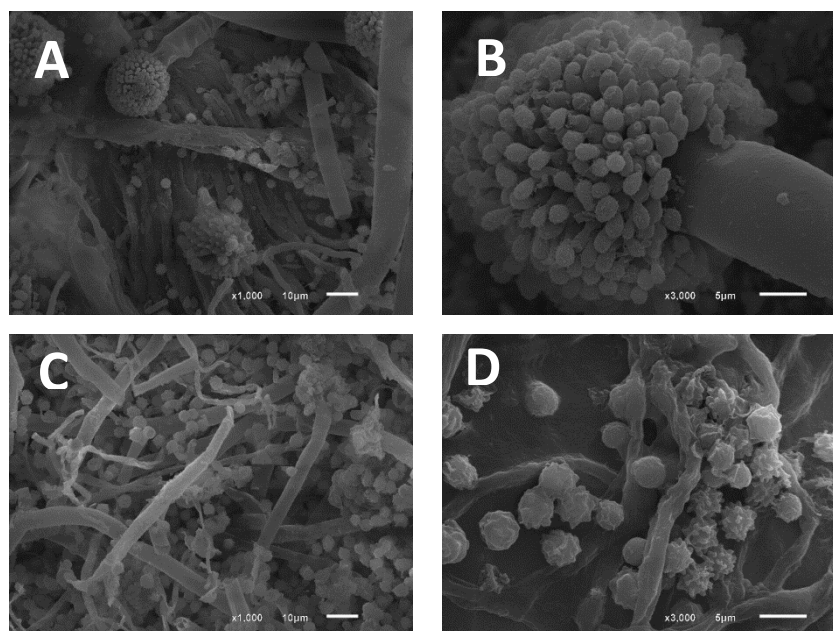


**Figure 1.** Scanning electron microscopy (SEM) images showing the filaments (hyphae) that form the conidia and spherical bodies (vegetative spores) in *Aspergillus niger* (A, B) and *Aspergillus sp.* (C, D)

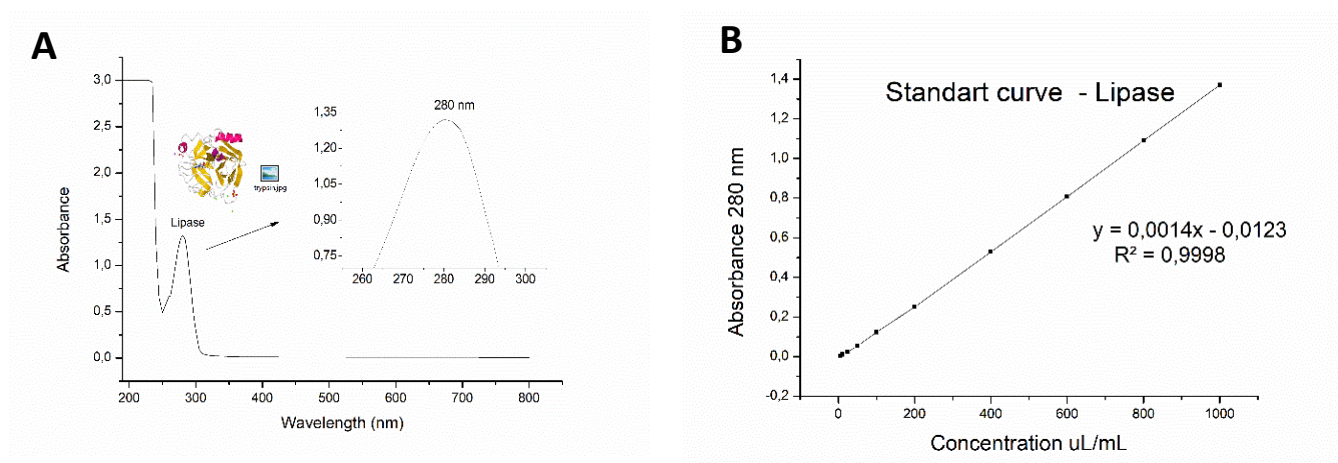


**Figure 2.** Lipase UV-Vis Spectrum (A) and Standard Curve for Protein Dosage (B).

**Table 1.** Factorial Design Matrix 3<sup>2</sup> for lipase production of fungal isolates

Run	[Inductor] (%)	Temperature (°C)
1	2 (-)	28 (-)
2	2 (-)	32 (0)
3	2 (-)	36 (+)
4	6 (0)	28 (-)
5	6 (0)	32 (0)
6	6 (0)	36 (+)
7	10 (+)	28 (-)
8	10 (+)	32 (0)
9	10 (+)	36 (+)
10	6 (0)	32 (0)
11	6 (0)	32 (0)

## Analysis of the Effect of Histone Deacetylase Inhibitors against *Toxoplasma gondii* using Super-Resolution Structured Illumination Microscopy

Carlla Assis Araujo-Silva<sup>1,2</sup>, Wanderley de Souza<sup>1,2</sup>, Erica dos Santos Martins-Duarte<sup>3</sup>,  
Rossiane Claudia Vommaro<sup>\*1,2</sup>

1. Instituto de Biofísica Carlos Chagas Filho – Universidade Federal do Rio de Janeiro
2. Instituto Nacional de Ciência e Tecnologia em Biologia Estrutural e Bioimagens e Centro Nacional de Biologia Estrutural e Bioimagens, UFRJ, Brasil
3. Universidade Federal De Minas Gerais, Brasil.

\* [vommaro@biof.ufrj.br](mailto:vommaro@biof.ufrj.br)

Super-Resolution Structured Illumination Microscopy (SR-SIM) was applied in this work to analyze the effects of two inhibitors of histone deacetylase - Tubastatin A (TST) and Hydroxamic Acid Suberoylanilide (SAHA) [1] against *T. gondii* in vitro. *T. gondii* is a protozoan parasite that can cause hydrocephalus, uveitis, motor and neurological delay in newborns, and encephalitis in immune compromised individuals. The treatment is restricted to an association of pyrimethamine and sulfadiazine, which are related to side effects and appearance of allergy. The search for new therapeutic alternatives becomes critical. LLC-MK<sub>2</sub> epithelial cells were infected with tachyzoites of *T. gondii* RH strain and treated with TST and SAHA for 48 hours. Both compounds were active against *T. gondii* and presented IC<sub>50</sub> in the nanomolar range. Cytotoxicity assay by MTS showed TST and SAHA were high selective for *T. gondii*. Infected fibroblasts (NDHF) were incubated with anti-SAG-1 (surface antigen), anti-Centrin-1 (centrosome) and anti-IMC (internal membrane complex) followed by incubation with secondary antibodies conjugated with Alexa 488, 546, 568 or 647. Nuclear probe, Hoechst 33342 was also used. Samples prepared for immunofluorescence were subjected to SR-SIM in an ELYRA PS.1 microscope (Carl Zeiss). Z-stacks of high-resolution image frames were collected in 5 rotations by utilizing an alpha Plan-Apochromat 63×/1.46 oil DIC M27ELYRA objective. Images were reconstructed using a structured illumination algorithm in the ZEN software (Blackedition, 2012). Fluorescence microscopy using anti-SAG-1 and anti-Centrin-1 showed that control parasites presented only one centrosome and formed characteristic rosettes (Figure 1). Treatment of tachyzoites with 1 µM TST for 24h induced the formation of a rounded mass of parasites presenting several centrosomes (Figure 1, arrowheads) and disruption of the budding process of daughter cells (Figure 1). After treatment with 0.1 µM SAHA, the effect was even more drastic. The presence of masses of damaged parasites showing disorganized centrosome division (Figure 1, arrowheads) and miss localization of this structure, at the parasite periphery, were evident (Figure 1). Fluorescence microscopy using anti-IMC confirmed that both compounds induced interruption of the daughter cell budding process. leading to parasite proliferation arrest. These results indicate SR-SIM as a powerful tool to analyze the effect of drugs on protozoa membranes and organelles and TST and SAHA are potential new chemotherapeutic agents to toxoplasmosis.

### REFERÊNCIA:

- [1] Bougdour A et al., J Exp Med. 13;206(4) (2009) 953.

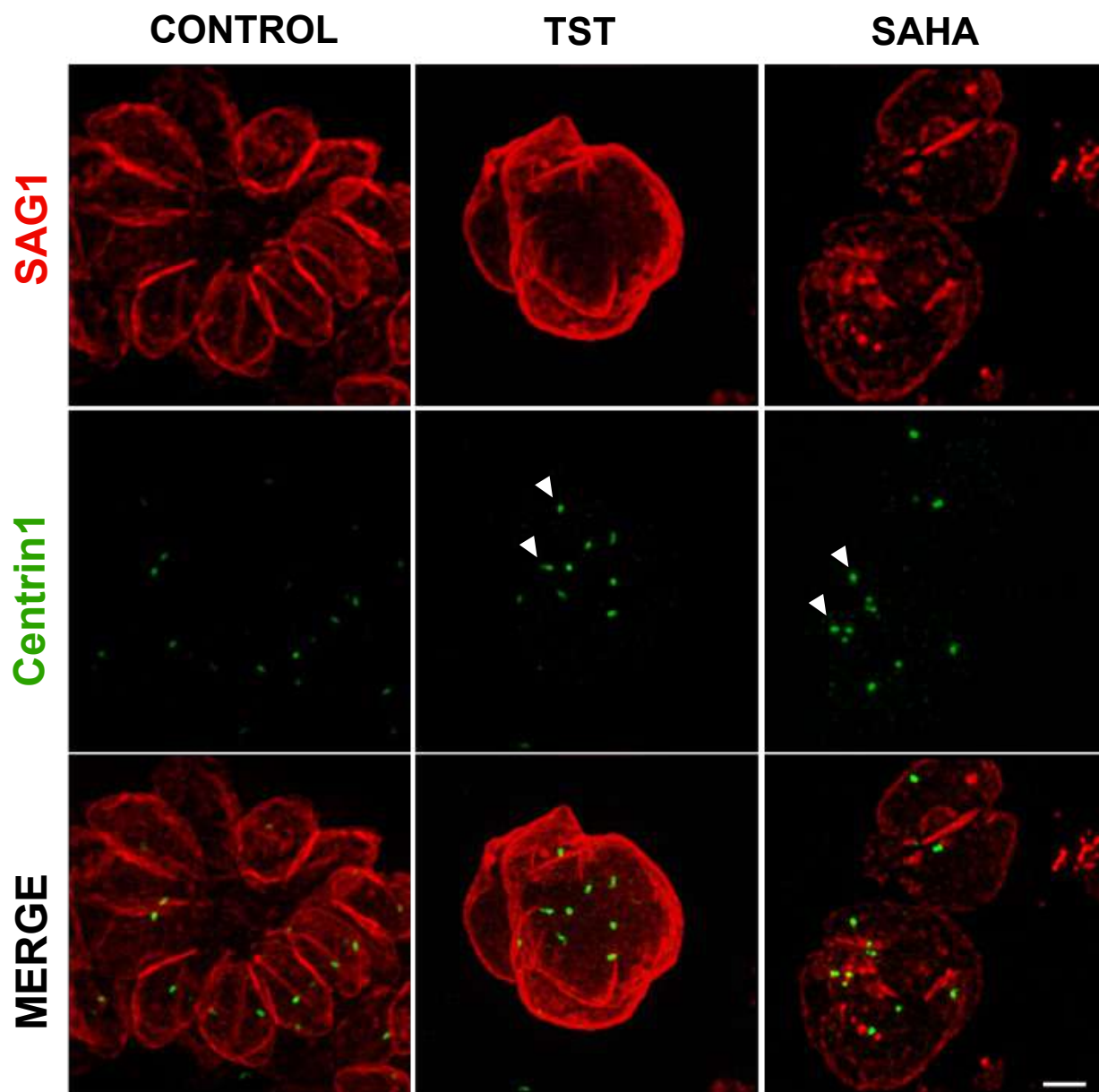


Figure 1- 3D SR-SIM projection of NDHF cells treated with 1 $\mu$ M TST and 0.1 $\mu$ M SAHA for 24h. A formation of masses of damaged parasites can be clearly identified in the treated infected. Centrosomes appeared disorganized in the giant mass of parasite although their shape seem to remain intact even with the altered cell location. Scale bar = 2 $\mu$ m.

## THE EXTRACELLULAR MATRIX OF SPLEEN PRESERVES ITS MOLECULAR AND ULTRASTRUCTURAL COMPOSITION AFTER THE DECELLULARIZATION PROCESS

Tadeu Ériton Caliman Zanardo<sup>1,2\*</sup>, Gabriel Henrique Tauffner<sup>2</sup>, Rayssa Helena Arruda Pereira<sup>2</sup>, Afrânio Côgo Desteffani<sup>1</sup>, Fernanda Gobbi Amorim<sup>1</sup>, Leo Kei Iwai<sup>3</sup> and Breno Valentim Nogueira<sup>1</sup>

<sup>1</sup>. Department of Morphology, CCS, Federal University of Espírito Santo (UFES), Vitória, Brazil

<sup>2</sup>. Postgraduate Program in Biotechnology/RENORBIO - Focal Point UFES, Vitória, Brazil

<sup>3</sup>. Laboratory of Proteomics and Mass Spectrometry-Special Laboratory of Applied Toxinology LETA, Instituto Butantan, São Paulo, Brazil

*e-mail para correspondência:* [tadeucz@hotmail.com](mailto:tadeucz@hotmail.com)

**INTRODUCTION:** The spleen presents functions ranging from filtration of aged erythrocytes to the immune response. Its absence or dysfunction may lead to increased susceptibility to infections, thromboembolism and cancer. Thus, we use the decellularization process to create a splenic scaffold, which can be used to restore the major functions of this organ. **OBJECTIVE:** Characterize the splenic scaffold after the decellularization process. **METHODS:** Detergents such as sodium dodecyl sulfate (SDS) (9 hours) and triton x-100 (30 minutes) were perfused through the splenic artery of rats (CEUA-UFES n° 42/2016; n = 26). The scaffold created was evaluated with hematoxylin and eosin (HE), residual DNA quantification, scanning and transmission electron microscopy and proteomic analysis. In the statistical analysis, Student's *t*-test was used, with  $p < 0.05$ . **RESULTS:** At the end of the decellularization process, the organ maintained its 3D structure, becoming completely translucent (**Figure 1**). Histological analysis by HE revealed the absence of cells, corroborating with the result of residual DNA quantification, with 99% reduction (Native:  $4068 \pm 522.8$  vs. Decellularized:  $51.2 \pm 13.1$  ng/mg of dry weight) (**Figure 2**). Through the ultrastructural analysis, the absence of cells can be confirmed, as well as the maintenance of the structure of the white pulp, red pulp and the marginal zone (**Figure 3**). In total, 411 proteins were identified by the proteomic analysis, of which 339 were related to cellular content and 72 to splenic matrissome. The proportional analysis of the cellular protein and matrissome contents varied before and after the decellularization process, with enrichment of matrissome proteins, from 83:17% in the native tissue to 63:37% in the decellularized (cell contents:matrissome, respectively) 405 were present in native tissues and 135 in decellularized tissues, of which 129 were identified in native and decellularized tissues. Concerning the matrissome constituent proteins, 69 were present in the native and 50 were present in the decellularized, with 47 shared by both (72% retention in matrissome protein content). The proteins of the collagen subtypes obtained the highest maintenance rate with 100% preservation, while the extracellular matrix regulatory proteins were shown to be the most sensitive, with a maintenance rate of about 25% when compared to the native tissue (**Figure 4**). **CONCLUSION:** The present decellularization process promoted efficient removal in the DNA content and preservation of the main components of the extracellular matrix. Such scaffold is promissory for reconstruction of the spleen with the patient's own cells by tissue bioengineering. **FINANCIAL SUPPORT:** CAPES (1675447); FAPES (0606/2015; 239/2016; 526/2018); CNPq (439439/2018-3; 315017/2018-0).



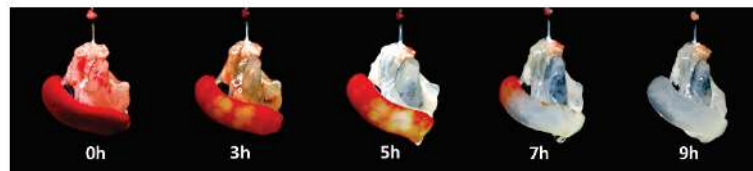


**FIGURE 1:** Representative images of the process of splenic decellularization over the 9 hours of decellularization with 0.1% SDS.

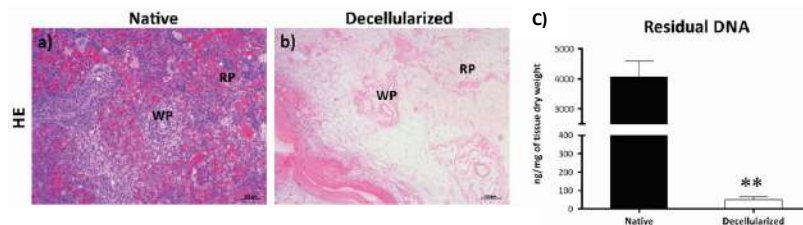


**FIGURE 2:** Representative images of native spleen and decellularized scaffold stained by HE, showing the presence of cells with their nuclei in the native (2a) and their absence with maintenance of the extracellular matrix in the decellularized scaffold (2b). The bar graph shows the difference in residual DNA content between the native spleen and the scaffold (2c). **WP:** White Pulp; **RP:** Red Pulp; **ng/mg:** nanograms/milligram;

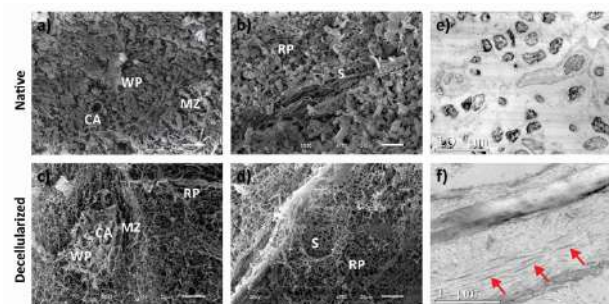


**FIGURE 3:** Ultrastructural analysis of the splenic scaffold. Scanning electron micrographs showing the removal of all cells and their debris by maintaining the main components of the splenic parenchyma as in native tissue (3a) and after decellularization of the scaffold (3c). There was good preservation of the ultrastructure of the large caliber vessels, with the sinusoids of the red pulp maintaining its basement membrane fenestrated as in the native organ (3b) after decellularization (3d). Likewise, transmission electron microscopy analysis demonstrated the absence of cells in the framework differently from the native organ (3e and f), in addition to maintenance of the main components of the extracellular matrix, mainly collagen fibers (red arrows) (3f). **CA:** Central Artery; **WP:** White Pulp; **MZ:** Marginal Zone; **S:** Sinusoids; **nm:** nanometers; **SD:** standard deviation;

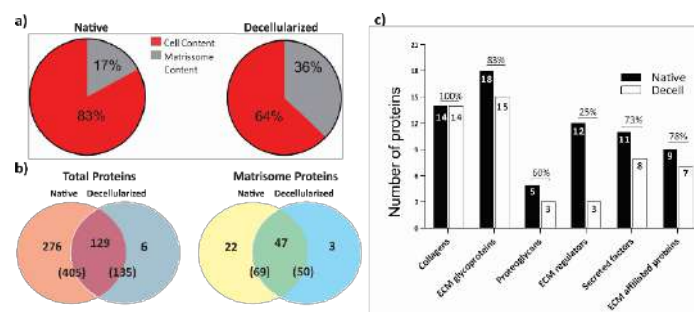


**FIGURE 4:** Cell and matrissome contents before and after the process of decellularization of the spleen. Percent composition relative to cellular and matrissome proteins content in native and decellularized tissue (a). Venn diagram showing the amount of total and matrissome proteins shared between native and decellularized tissues (b). Bar graph showing the number of proteins and percentage maintenance rate per class between native and decellularized tissues (c).

## **Tropism Of Dengue Virus Type 4 In A BALB/c Murine Model: Experimental Infection And Analysis Of Morphological Aspects**

A. C. Rasinhas<sup>a\*</sup>, M. A. N. da Silva<sup>a</sup>, G. C. Caldas<sup>a</sup>, F. C. Jácome<sup>a</sup>, A. L. T. de Almeida<sup>a</sup>, R. Leonardo<sup>a</sup>, F. B. dos Santos<sup>b</sup>, P. C. G. Nunes<sup>b</sup>, O. M. Barth<sup>a</sup>, D. F. Barreto Vieira<sup>a</sup>

<sup>a</sup>Laboratory of Morphology and Viral Morphogenesis, Instituto Oswaldo Cruz, Fiocruz, Avenida Brasil 4365, 21040-900, Rio de Janeiro, RJ, Brazil

<sup>b</sup>Laboratory of Viral Immunology, Instituto Oswaldo Cruz, Fiocruz, Avenida Brasil 4365, 21040-900, Rio de Janeiro, RJ, Brazil

\*Corresponding author at: Laboratory of Morphology and Viral Morphogenesis, Instituto Oswaldo Cruz, Fiocruz, Avenida Brasil 4365, 21040-900, Rio de Janeiro, RJ, Brazil

E-mail address: tukabr@gmail.com

Dengue is an emerging human disease, caused by the arthropod-borne virus named Dengue Virus (DENV). DENV is categorized in 4 genetically distinct individual serotypes (DENV-1 through -4), which do not confer cross immunity. According to the Centers for Disease Control around 2.5 billion people live in areas where there is risk of dengue transmission [1]. Ever since its introduction in the Brazilian territory, in 1981, DENV-4 has remained absent from the national epidemiological scene for almost 25 years, until its reintroduction in 2010 [2]. To this day, the mechanisms associated with the immunopathogenesis of DENV are not yet fully understood. This is mostly due to the absence of an experimental animal model that adequately replicates the DENV infection as it is observed in humans [3]. This simple fact brings about the greatest difficulty faced when studying the interaction between virus and host, as well as the development and production of effective drugs and vaccines against DENV [4]. Currently proposed models utilize immunodeficient animals, very invasive inoculation routes, and neuroadapted viral inocula, conditions that do not reproduce the disease progression as it happens in human cases [5]. The present study aims to analyze the potential tropism of DENV-4 for hepatic, pulmonary and cardiac tissue and evaluate the morphological and ultrastructural alterations caused by the virus in said organs. To achieve this goal, immunocompetent mice of the BALB/c line were inoculated via intravenous route with non neuroadapted doses of DENV-4 isolated from human case. Alterations observed in the analyzed tissue presented similar profile to that shown in human cases of Dengue, with intense presence of activated inflammatory cells, wide areas of hemorrhage, and alterations in the intercalated disc structure. Particular findings, such as the vast presence of inflammatory cells in cardiac tissue, and alterations on the intercalated disc's morphology – alterations not commonly described in heart – suggest that DENV-4 could have a stronger affinity with this organ.

[1] CDC. Atlanta: Centers for Disease Control and Prevention. 2019.

[2] R. M. Nogueira et al., Mem Inst Oswaldo Cruz. 106 (2011) 255-6.

[3] C. Simmons et al., N Engl J Med. 366 (2012) 1423-1432.

[4] R. Oliveira et al., Mem Inst Oswaldo Cruz. 111 (2016) 378-384.

[5] S. Zompi et al., Viruses. 4 (2012) 62-82.

[6] This research was supported by CNPq and Instituto Oswaldo Cruz, Fiocruz.

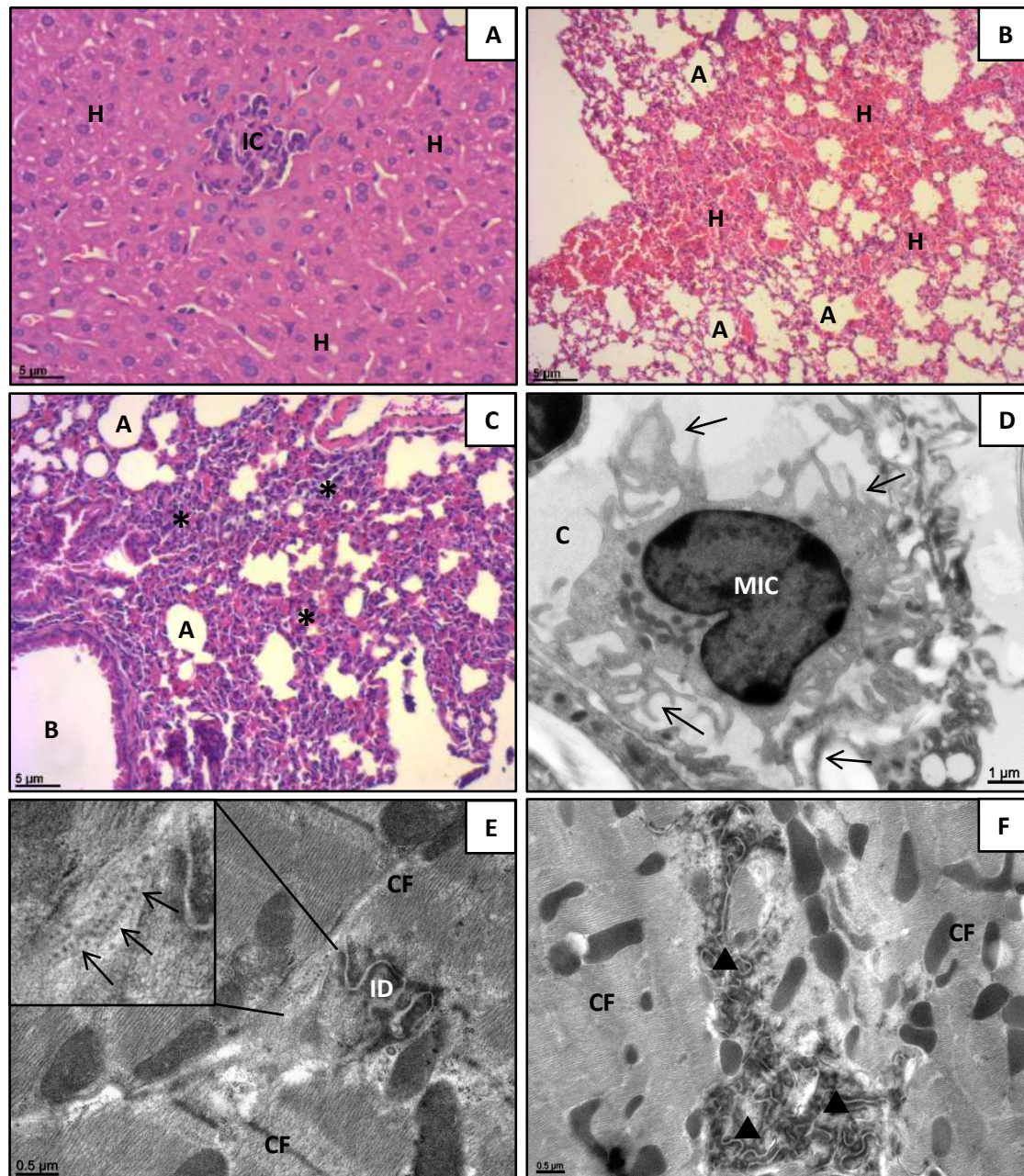


**Figure 1:** Organ samples of DENV-4 infected BALB/c mice. **(A)** Liver sample, stained with hematoxylin and eosin, observed in a bright field microscope. Presence of inflammatory infiltrate (IC) among the hepatocytes (H), 20x. **(B)** Lung sample, stained with hematoxylin and eosin, observed in a bright field microscope. Areas of pulmonary hemorrhage (H) close to alveoli (A). 5x. **(C)** Lung sample, stained with hematoxylin and eosin, observed in a bright field microscope. Thickening of the interalveolar septa (\*); Alveolus (A); bronchiole (B). 10x. **(D)** Lung sample, positive stained, observed in an electron transmission microscope. Mononuclear inflammatory cell (MIC) presenting filopodia (arrow) inside a capillary (C). 12.000x. **(E)** Heart sample, positive stained, observed in an electron transmission microscope. Dengue virus-like particles (arrows) in cardiomyocyte cytoplasm (inset), next to intercalated disc (ID) and cardiac fibers (CF). 30.000x. **(F)** Heart sample, positive stained, observed in an electron transmission microscope. Intense intercalated disk disorganization (▲) close to cardiac Fibers (CF). 20.000x.



## Morphological studies of BALB/c murine model tissues with reinfection by dengue virus

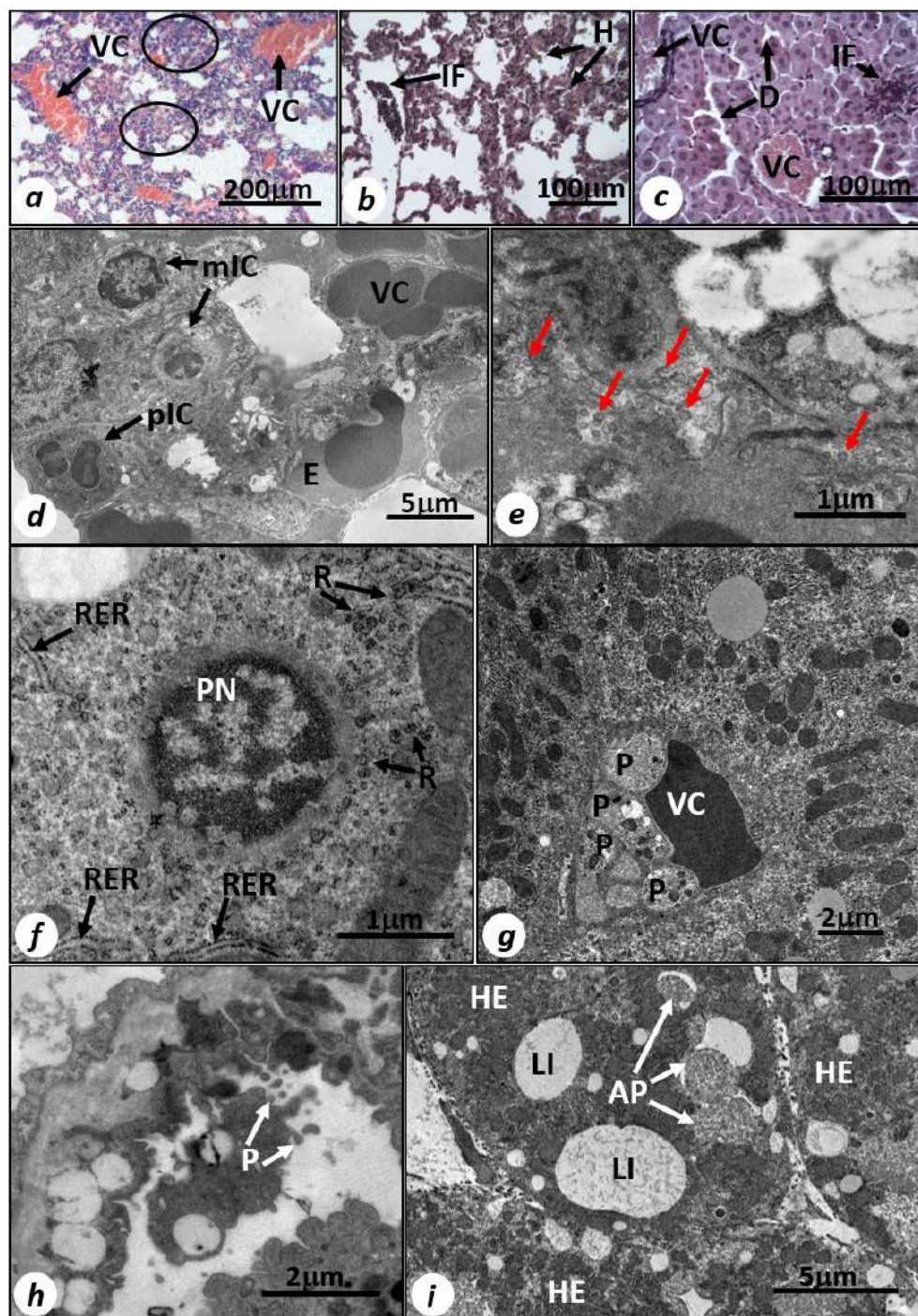
Ana Luisa Teixeira de Almeida<sup>1</sup>, Gabriela Cardoso Caldas<sup>1</sup>, Marcos Alexandre Nunes da Silva<sup>1</sup>, Fernanda Cunha Jácome<sup>1</sup>, Arthur da Costa Rasinhas<sup>1</sup>, Ortrud Monika Barth<sup>1</sup>, Debora Ferreira Barreto Vieira<sup>1</sup>

<sup>1</sup>- Laboratório de Morfologia e Morfogênese Viral, Instituto Oswaldo Cruz – Fundação Oswaldo Cruz, Rio de Janeiro – Brazil.

Dengue virus (DENV), members of the *Flaviviridae* family, occurs as four antigenically distinct serotypes (DENV-1, -2, -3, -4) [1]. Dengue (DEN), disease caused by DENV, is a leading cause of illness and death in the tropics and subtropics [2]. One of the major challenges regarding DEN studies in humans and the development of vaccines and drugs is the lack of an appropriate experimental animal model that reproduces an infection similar to DEN human cases, including Dengue Hemorrhagic Fever and Dengue Shock Syndrome [3]. Patients with secondary infection by a serotype heterologous present higher probability of the disease evolving to the hemorrhagic form [4]. The susceptibility of murine model to DENV has been reported in many studies. However, these models use neonatal or immunosuppressed mice, if not, they resort to intracerebral inoculation, an invasive route, or infection with neuroadapted virus strains [5]. This present study demonstrates morphological alterations in lungs and liver of immunocompetent mice with secondary infection. The BALB/c mice were infected by the intravenous route with non-neuroadapted DENV samples (DENV-1: primary infection, with dose of 10.000 TCID<sub>50</sub>/0.1 ml, and DENV-2 or DENV-3: secondary infection, with doses of 20.000 TCID<sub>50</sub>/0.1 ml and 125.000 TCID<sub>50</sub>/0.1 ml respectively). The titers of the samples of DENV-1: 106.23TCID<sub>50</sub>/0.1ml, DENV-2: 106.66TCID<sub>50</sub>/0.1ml and DENV-3: 107.23TCID<sub>50</sub>/0.1ml were calculated by the Reed & Muench method [6]. Euthanasia occurred 72 hours after reinfection. For histological studies, the lung samples were fixed in Carson Millonig Formalin, embedded in paraffin and stained with hematoxylin and eosin. For ultrastructural studies, the specimen were fixed by perfusion and immersion and contrasted with uranyl acetate and lead citrate. In the lung, analysis by phase contrast light and transmission electron microscopy revealed interstitial pneumonia, vascular congestion, presence of red blood cells in the alveolar spaces, inflammatory cells, platelets and edema in the capillaries. In the liver, steatosis, vascular congestion, inflammatory infiltrate, dilation of sinusoidal capillaries, thickening of rough endoplasmic reticulum and signs of autophagy and apoptosis were present. Morphological alterations observed were similar to those observed in DEN human cases and in murine model studies for primary DENV infection and confirm the susceptibility of BALB/c mice to DENV secondary infection by a serotype heterologous with non-neuroadapted strains [7].

- [1] R. C. Reiner et al. PLoS Negl. Trop. Dis. (2016), 10(5).
- [2] S. Bhatt et al. Nature. (2013), 496(7446): 504-7.
- [3] D. J. Gubler. Trends Microbiol. (2002); 10(2):100-3.
- [4] S. B. Halstead. Yale J Biol Med. (1970); 42: 350-352.
- [5] C.G Raut et al. Acta Virol. (1996); 40(3): 143-6.
- [6] R. H Reed; H. Muench. Am J Hyg. (1938); 27: 493-497.
- [7] This research was supported by CNPq (Brazil).





Histopathological and ultrastructural aspects of lung and liver of BALB/c mice in secondary infection with dengue virus serotype 2 (D2) or serotype 3 (D3). Histological sections: **(a)** Lung – D2. Vascular congestion (VC); thickening of septa (area). **(b)** Lung – D3. Inflammatory infiltrate (IF); haemorrhage (H). **(c)** Liver – D3. Vascular congestion (VC); inflammatory infiltrate (IF); dilation of sinusoidal capillaries (D). Ultrathin sections: **(d)** Lung – D2. Mononuclear (mIC) and polymorphonuclear inflammatory (pIC) cells; vascular congestion (VC); edema (E). **(e)** Lung – D2. Pinocytotic vesicles (red arrows). **(f)** Liver – D3. Thickening of rough endoplasmic reticulum (RER); ribosomes (R); pyknotic nuclei (PN). **(g)** Liver – D3. Platelets (P); vascular congestion (VC). **(h)** Lung – D3. Activated platelet (P) emitting extensions of cytoplasm (arrows). **(i)** Liver – D2. Hepatocyte (HE); lysosome (LI); autophagosome (AP).

## **Metabolic And Ultrastructural Renal Changes In Adult Wistar Rats Fed By A Cafeteria Diet**

Priscila Fernandes dos Santos<sup>1</sup>, Diogo Benchimol de Souza<sup>1</sup>, Eduardo José Lopes Torres<sup>2</sup>, Waldemar Silva Costa<sup>1</sup>, Francisco José Barcellos Sampaio<sup>1</sup> and Bianca Martins Gregorio<sup>1\*</sup>

<sup>1</sup>Urogenital Research Unit, Department of Anatomy, Roberto Alcântara Gomes Institute of Biology, Rio de Janeiro, Brazil.

<sup>2</sup>Department of Microbiology, Immunology and Parasitology, Biomedical Center, Rio de Janeiro, Brazil.

\*Author for correspondence: Bianca Martins Gregorio (bmgregorio.uerj@gmail.com)

Researches involving experimental models and nutrition have been widely carried out in order to clarify the pathophysiology of several non-transmissible chronic degenerative diseases. Among the most used diets is the cafeteria diet, which is highly energetic and palatable [1]. High protein and high-fat diets are correlate positively with the occurrence of glomerular damage [2,3]. However, there is little discussion of the effects of the association between lipids and simple carbohydrates (cafeteria diet) on the ultrastructure of the kidneys. The aim of this study was to evaluate, by quantitative and qualitative methods, the glomerular ultrastructure of Wistar rats fed with a cafeteria diet. Male Wistar rats were divided into two groups at 21 days of age: control (C, n = 10) and diet cafeteria (CAF, n = 8). The animals were followed up until five months of age (euthanasia). Here, blood, kidneys and fat deposits (epididymal, retroperitoneal and subcutaneous) were removed for future analysis. Data were analyzed by Student's t test and  $P < 0.05$  was considered significant. The cafeteria diet promoted glucose intolerance, hyperglycemia ( $P < 0.0001$ ) and increased deposits of retroperitoneal fat ( $P < 0.005$ ). Scanning electron microscopy analyzes showed that the length of the foot process was similar in both groups. The quantitative analyzes obtained by transmission electron microscopy revealed that the cafeteria diet reduced the thickness of the glomerular basement membrane ( $P < 0.05$ ). The intake of lipids and simple carbohydrates were associated with alteration in glomerulus ultrastructure. However, more studies are needed to evaluate not only the components of the glomerular filtration barrier, but also renal physiology.

### Referências:

[1] F.A. De Oliveira et al., Asian J Androl, 21 (2019) 201.



[2] T.H. Hostetter et al., J Am Soc Nephrol, 12 (2001) 1315.

[3] J.Y. Chen et al., J Endocrinol, 231 (2016) 109.

Figure 1: Microscopic images of glomerulus of rats by scanning electron microscopy. We observed that the foot processes (P) length were similar in animals from from C (A) and CAF (B) groups. Both images were obtained at a magnification of 27Kx (approximately) and a beam acceleration voltage of 2kV.

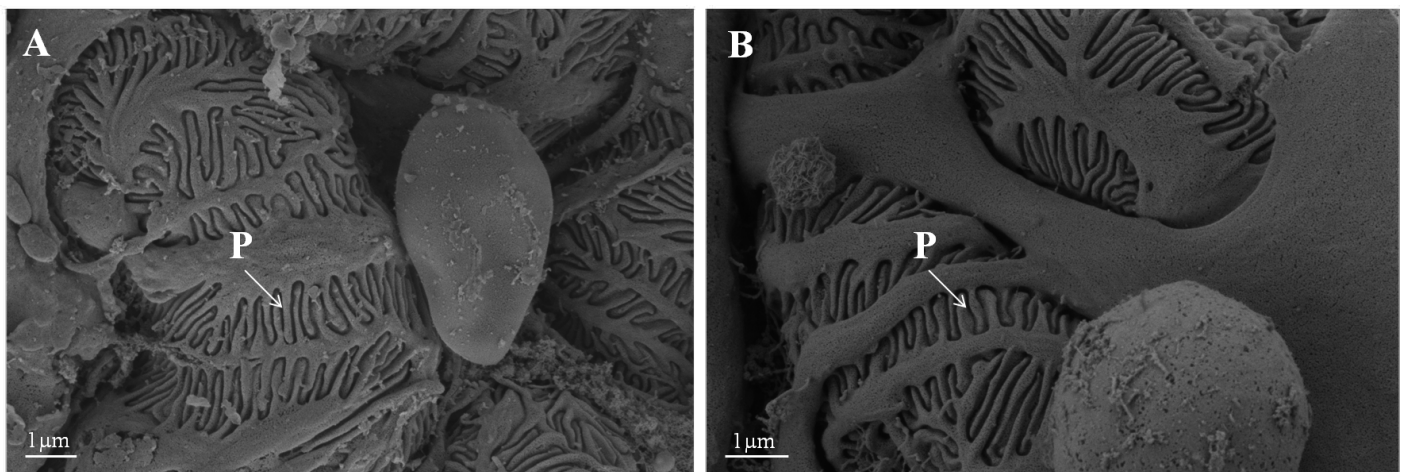
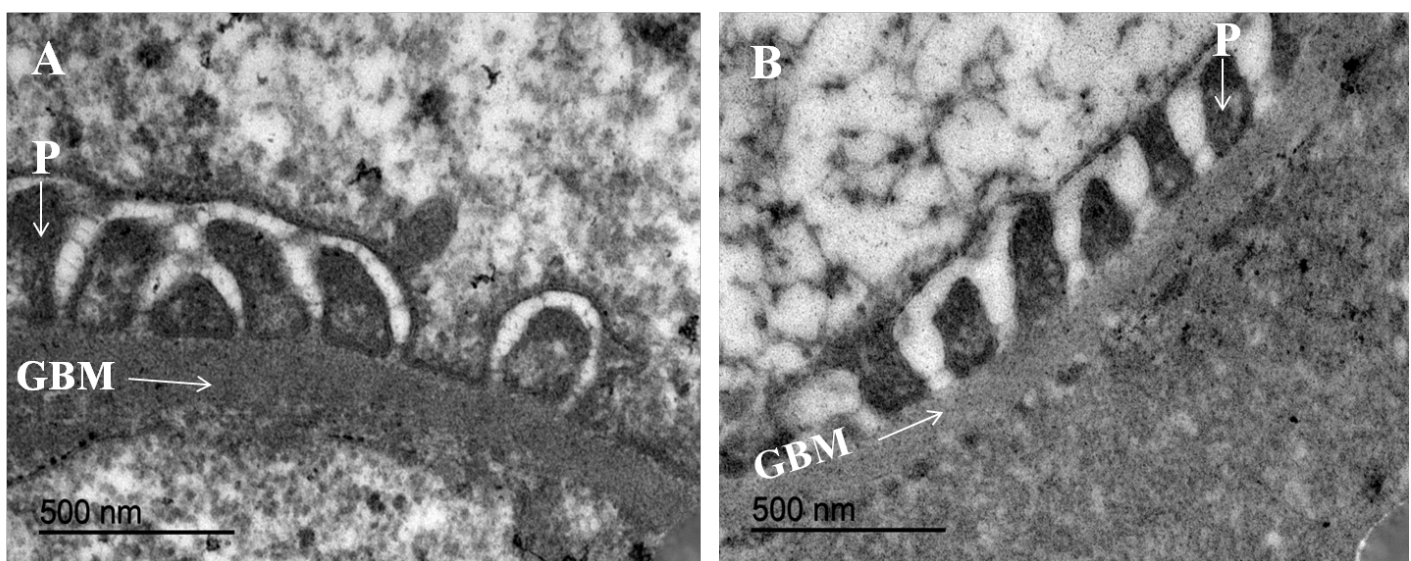


Figure 2: Transmission electron microscopy images of glomerular filtration barrier components: glomerular basement membrane (GBM) and foot processes (P). In image A (C group), we noticed that the GBM thickness is higher when compared to the animals fed with CAF diet (B). This diet also showed a tendency to reduce the foot process length (P) in relation to the C group. Both images were obtained at a magnification of 50Kx and a beam acceleration voltage of 80kV.



## The structure and function of glandular trichomes in *Jacquinia armillaris* (Theophrastoideae – Primulaceae)

Bruna Nunes de Luna<sup>1\*</sup>, Maria de Fátima Freitas<sup>1</sup> and Claudia Franca Barros<sup>1</sup>

<sup>1</sup>. Instituto de Pesquisas Jardim Botânico do Rio de Janeiro, Diretoria de Pesquisas, Rio de Janeiro, Brazil. [\\*brunaluna@jbrj.gov.br](mailto:*brunaluna@jbrj.gov.br)

The pantropical family Primulaceae presents about 2.500 species in 58 genera. Within the four subfamilies circumscribed in this family [1], three of them present halophyte species: Myrsinoideae, Theophrastoideae and Primuloideae. One of its well-known halophyte species is the mangrove tree *Aegiceras corniculatum* (L.) Blanco (Myrsinoideae) [2]. Recently, Luna et al. [3] indicated the need of further ultrastructural and physiological studies to clarify if the glandular trichomes in *Jacquinia armillaris* Jacq. (Theophrastoideae) are salt glands due to their morpho-anatomical resemblance with those from Primulaceae [4] and to their occurrence in sandbank environments that are constantly subjected to saline stress [5]. Considering the above-mentioned premises, in the present study we intended to investigate if the glandular trichomes in the leaves of *J. armillaris* are salt glands. For this, fully developed leaves were collected and fixed in a solution of 2.5% GA and 4.0% PA buffered with 0.05 mol·L<sup>-1</sup> sodium cacodylate buffer, pH 7.2 and processed following the standard protocols for light microscopy, LSCM, TEM and SEM. The qualitative analysis and the distributional map of the secretion produced by the glandular trichomes were performed in fresh fully developed leaf samples using LVSEM coupled to an X-ray detector. The glandular trichomes are sunken in both adaxial and abaxial epidermis (Fig. 1A) and are composed by a basal cell, a stalk cell and a multicellular head with 20-30 cells (Figs. 1B, C). A thin cuticle covers the outer periclinal walls of the head cells, and detaches from the cell wall forming a sub-cuticular chamber (Fig. 1D). The anticlinal walls of the stalk cells are covered by a thick cuticle (Fig. 1D, E), which is probably related to the restriction of the secretion coming from the mesophyll to the basal cell to the symplastic pathway through plasmodesmata (Fig. 1F). Under TEM, the stalk cell is subdivided in two portions: one that present large vacuoles and several plasmodesmata communicating it with the basal cell (Fig. E); and other that is adjacent to the secretory head cells and presents a cytoplasm rich in mitochondria, plastids with plastoglobules and many endoplasmic reticulum elements (Fig. 1F). The former portion is connected to the secretory head cell via several plasmodesmata (Fig. 1F). The secretory head cells have a dense cytoplasm with numerous mitochondria, and plastids (Fig. 1G). X-ray spectrums of the glandular trichome exudate are shown in Fig. 1H. They indicate that the secretion contains Na (Fig. 1J), Cl (Fig. 1K) and Ca (Fig. 1L). Altogether, the gathered results supports the hypothesis that the glandular trichomes in *J. armillaris* are in fact salt glands that acts eliminating salt from the plant tissues.

[1] P.F. Stevens, Angiosperm Phylogeny Website, 2001 (onwards).

[2] S. Cardale & C.D. Field, *Planta*, 3 (1971) 183–191.

[3] B.N. de Luna et al., *Botany*, 97: 1 (2018) 35–51.

[4] M.N. Grigore & C. Toma, *Anatomical Adaptations of Halophytes*, Springer, 2017.

[5] B. Stahl, *Brittonia*, 44: 1 (1992) 54–60.

[6] This research was supported by CAPES, FAPERJ and CNPq (153892/2018-8) (Brazil).



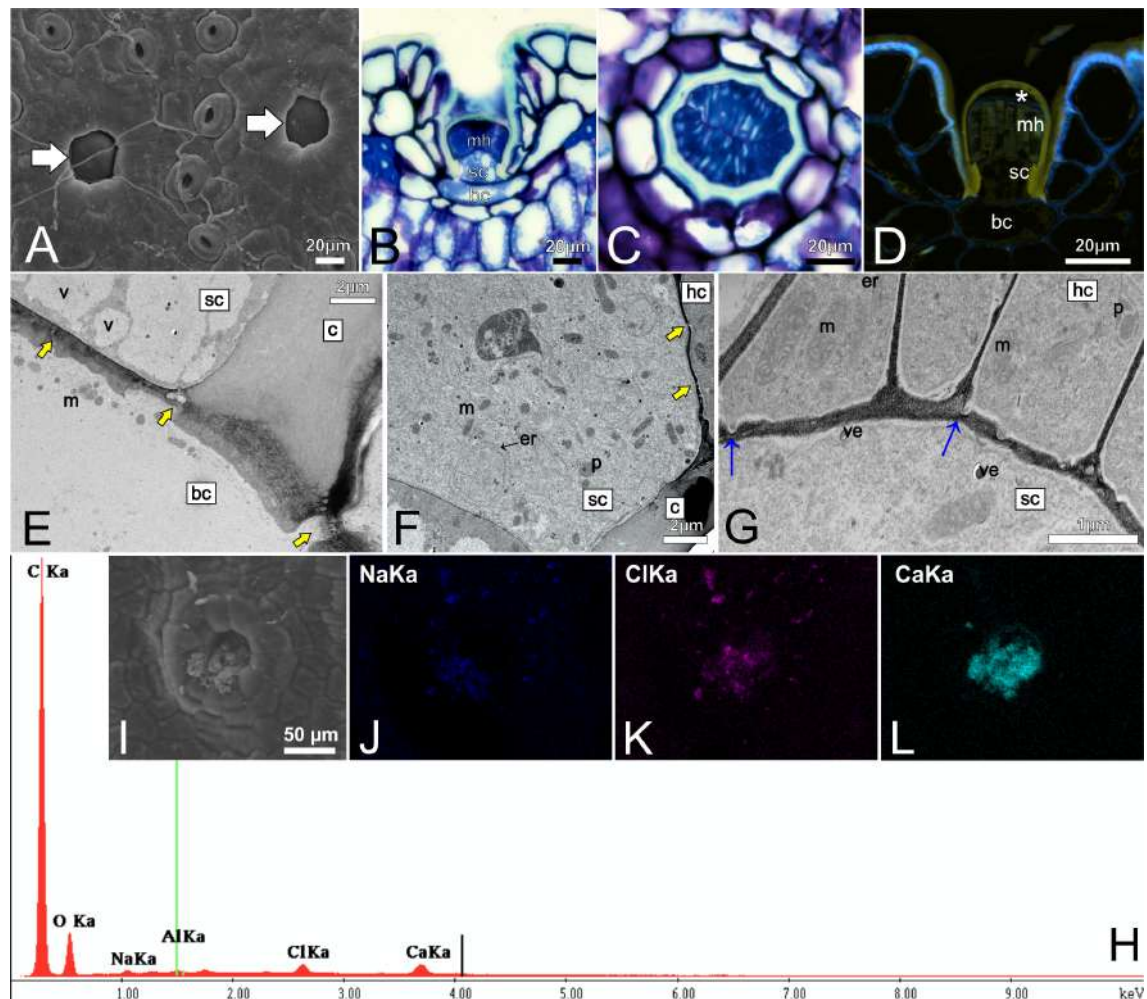


**Figure 1** – Glandular trichomes in the leaves of *Jacquinia armillaris*. A – SEM; B and C – Light microscopy, stained with Toluidine blue; D – Confocal microscopy, stained with Auramin O, Calcofluor and DAPI; E-G – TEM; H – Microanalysis spectrum; I – LVSEM; J-K and L – X-ray microanalysis. A – Sunken glandular trichomes in the abaxial epidermis (arrows). B – Transversal section of the trichome showing the basal cell (bc), the stalk cell (sc) and the multicellular head (mh). C – Paradermal section of the trichome showing the multicellular head. D – Transversal section of the trichome showing the detached cuticle forming a sub-cuticular chamber (\*). E – Plasmodemata (yellow arrow) communicating the basal cell (bc) and stalk cell (sc). Note the thick cuticle (c) in the anticlinal wall of the stalk cell. F – Upper portion of the stalk cell showing the dense cytoplasm with numerous mitochondria, endoplasmic reticulum and plastids. Note the plasmodemata (yellow arrow) connecting the stalk cell to the head secretory cell (hc). G – Detail of the secretory head cells (hc) showing mitochondria, plastids and endoplasmic reticulum. Blue arrows indicate the vesicles passing through the cell wall. Notes: er = endoplasmic reticulum; m = mitochondria; p = plastid; v = vacuole; ve = vesicle

## Therapeutic potential of low-cost nanocarriers produced by green synthesis: uptake of superparamagnetic iron oxide nanoparticles by macrophages and *Leishmania*

Verçoza, B. R. F.<sup>1,2</sup>, Bernardo, R.R.<sup>1,3</sup>, Sinnecker, J.P.<sup>4</sup>, Oliveira, L.A.S.<sup>1,3</sup> and Rodrigues, J.C.F.<sup>1,2</sup>

<sup>1</sup>Núcleo Multidisciplinar de Pesquisas em Biologia, NUMPEX-Bio, Campus Prof. Geraldo Cidade, Universidade Federal do Rio de Janeiro, Duque de Caxias, RJ, Brazil.

<sup>2</sup>Instituto Nacional de Ciência e Tecnologia de Biologia Estrutural e Bioimagem, Rio de Janeiro, Brazil.

<sup>3</sup>Núcleo Multidisciplinar de Pesquisas em Nanotecnologia, NUMPEX-Nano, Campus Prof. Geraldo Cidade, Universidade Federal do Rio de Janeiro, Duque de Caxias, RJ, Brazil.

<sup>4</sup>Centro Brasileiro de Pesquisas Físicas, Rio de Janeiro, RJ, Brazil.

Nowadays, there are a significant number of disorders affecting the human society, some of them are devastating, such as caused by different microorganisms, where the treatment has several drawbacks and reduced attention from the pharmaceutical companies. Thus, there is an urgent need for new therapeutic regimens trying to develop more alternatives for the treatment these diseases. One interesting, novel and promising therapeutic application is based on the use of magnetic nanomaterials for magnetic hyperthermia therapy [1,2]. In the scenario of infections caused by microorganisms, macrophages are important cells of the innate immune response system and one of the first lines of defense against microbial infections, since they phagocytize pathogens. However, different intracellular parasites such as *Leishmania sp.*, *Mycobacterium sp.*, and several viruses have the ability to evade macrophages defense mechanisms, and thereby proliferate as intracellular pathogens, giving the continuity to the replicative cycle that allows the disease progression [3–8]. Although widely studied, leishmaniasis continues to be a public health problem worldwide affecting around 12 million people in 98 countries [9] being classified by the World Health Organization (WHO) as one of the most important neglected diseases [10]. The first choice treatment for these parasites is based on the use of pentavalent antimonials and in cases of resistance on amphotericin B, pentadimidine or miltefosine. Nonetheless, the undesirable side effects of these drugs and the reports of drug-resistant parasites throughout the world demonstrate the necessity to development new safety treatment. In this context, the present study aims to characterize physically the low-cost nanoparticles seeking their application in magnetic hyperthermia, as well as to evaluate the ability of macrophages and *Leishmania* to internalize these nanoparticles and determine their toxicity. For this, different techniques were used: X-ray diffraction, FTIR, magnetization, optical microscopy, scanning and transmission electron microscopy, and cellular viability analysis by MTS / PMS. The results revealed that the superparamagnetic iron oxide nanoparticles (SPIONs) synthesized were made of magnetite, presenting a spherical structure with approximately 4 nm of diameter and a superparamagnetic behavior. Biological assays show that SPIONs were internalized by both cell types used in this study, including the intracellular amastigote forms of *Leishmania* cultivated within macrophages. SPIONs also showed low toxicity to macrophages and did not inhibit the growth of promastigote forms, however, they had a powerful antiproliferative effect against *L. amazonensis* intracellular amastigotes. All these results together indicated that SPIONs are promising candidates for a new therapy to treat leishmaniasis based on magnetic hyperthermia.

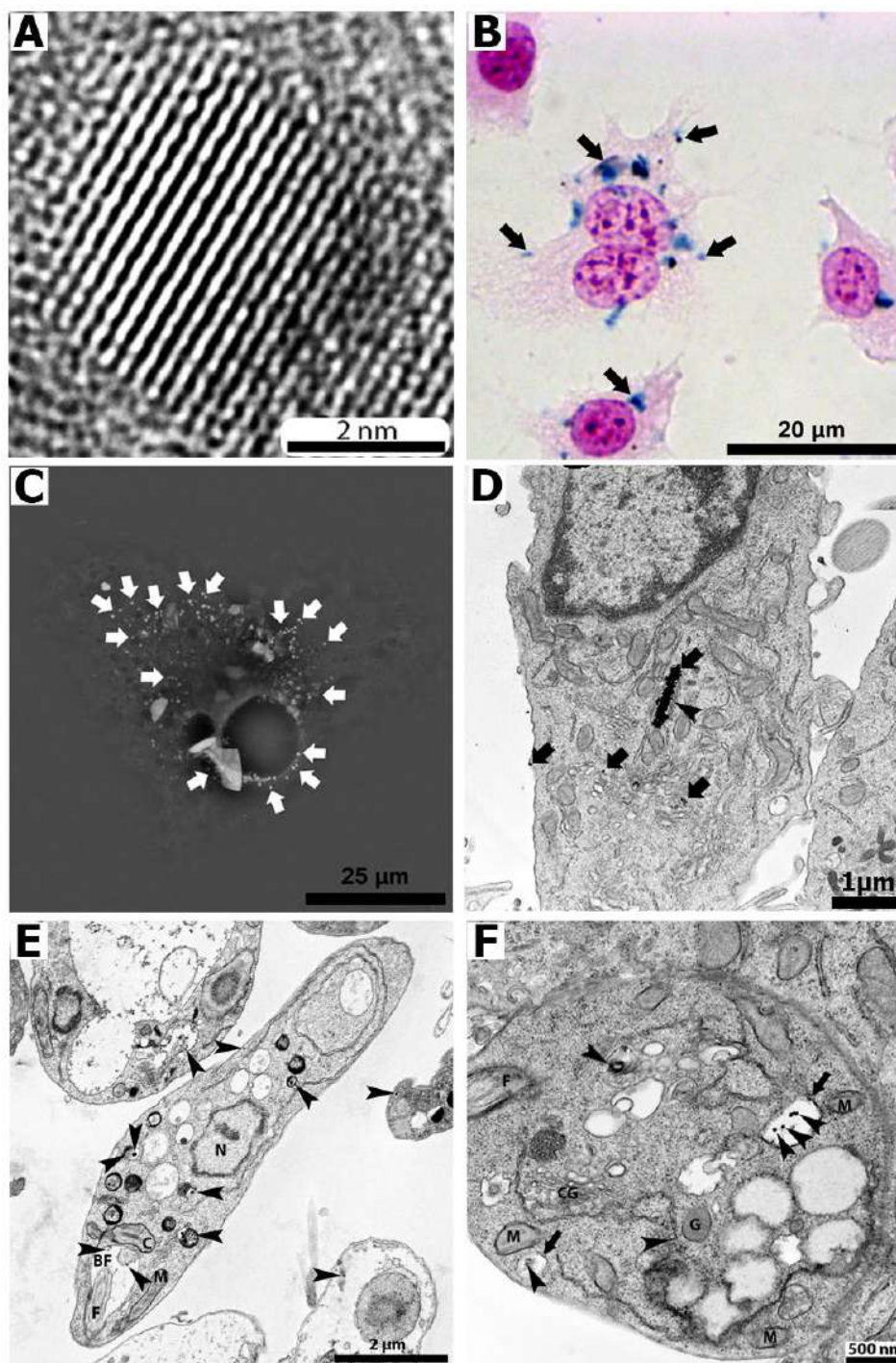


Figure – **A** - HRTEM image of SPIONs showing a spherical morphology and an approximate size of 4 nm. **B** - High digital magnification of prussian blue staining of macrophages treated with 100  $\mu\text{g/mL}$  of SPIONs for 24 h showing the characteristic blue marking of the cytoplasmic iron deposit (arrows). **C** - Macrophage treated with 100  $\mu\text{g/mL}$  of SPIONs for 24 h observed by detection of backscattered electron (BSE) showing the presence of an electronlucent aggregate (arrows). **D** - STEM-IN-SEM of macrophage treated with 100  $\mu\text{g/mL}$  of SPIONs for 24 h showing electrondense aggregates of nanoparticles (arrows) surrounded by membrane (arrowheads). **E** - STEM-IN-SEM of *Leishmania promastigotes* promastigotes treated with 100  $\mu\text{g/mL}$  of SPIONs for 24 h showing the electrondense aggregates of nanoparticles (arrowheads). **F** - TEM of *L. amazonensis* amastigotes treated with 100  $\mu\text{g/mL}$  of SPIONs for 24 h showing electrondense aggregates of nanoparticles (arrows) surrounded by membrane (arrowheads). N, nucleus; n, nucleolus; M, mitochondrion; K, kinetoplast; FP, flagellar pocket; F, flagellum; PV, parasitic vacuole;

## References

- [1] Maier-Hauff K, Ulrich F, Nestler D *et al.* *J. Neurooncol.* 103(2), 317-324 (2011).
- [2] Yang Y, Wang F, Zheng K *et al.* *PLoS One* 12, e0177049 (2017).
- [3] von Stebut E, Tenzer S. *Int. J. Med. Microbiol.* 308(1), 206-214 (2018).
- [4] Reiling N, Homolka S, Kohl TA *et al.* *Int. J. Med. Microbiol.* 308(1), 118-128 (2018).
- [5] Scollard DM, Truman RW, Ebenezer GJ. *Clin. Dermatol.* 33(1), 46–54 (2015).
- [6] Cianciotto NP. *Int. J. Med. Microbiol.* 291(5), 331-343 (2001).
- [7] Cline TD, Beck D, Bianchini E. *J. Gen. Virol.* 98(10), 2401-2412 (2017).
- [8] Ray NB, Ewalt LC, Lodmell DL. *J. Virol.* 69(2), 764-772 (1995).
- [9] KATO, H. *et al.* *Int J Environ Res Public Health*, v. 7, n. 3, p. 814-26, Mar 2010.
- [10] DE MENEZES, J. P. *et al.* *Biomed Res Int*, v. 2015, p. 815023, 2015.



## Microscopy techniques applied to symbiont-harboring trypanosomatids: unveiling the functions of Kinetoplast Associated Proteins

Camila Silva Gonçalves<sup>1,2\*</sup>, Carolina Moura Costa Catta Preta<sup>2,3</sup>, Jeremy Mottram<sup>3</sup> and Maria Cristina Machado Motta<sup>2</sup>

<sup>1</sup>. Centro Nacional de Biologia Estrutural e Bioimagem, IBCCF - UFRJ, RJ, Brasil.

<sup>2</sup>. Laboratório de Ultraestrutura Celular Hertha Meyer, IBCCF- UFRJ, RJ, Brasil.

<sup>3</sup>. Centre for Immunology and Infection, University of York, York, United Kingdom.

\*camilabiof@gmail.com

In this study different microscopy techniques were used to study *Angomonas deanei* (Fig. 1), a trypanosomatid protozoan that co-evolves in a mutualistic way with a symbiotic bacterium, that divides in synchronicity with other host cell structures [1,2]. Trypanosomatids contain unusual structures, as the kinetoplast, the portion of the single branched mitochondrion that contains the kDNA, a network composed by thousands of topologically interlocked DNA circles (minicircles and maxicircles) [3]. The kDNA presents an unique and intriguing array that varies according to trypanosomatid species and stages of development [4]. Such variations on the network arrangement are related to the presence of histone like-proteins that associate to kDNA and are known as KAPs (Kinetoplast Associated Proteins). Furthermore, such proteins neutralize the negatively charged kDNA, thus influencing the activity of mitochondrial enzymes involved in DNA replication, transcription and repair. In *A. deanei* the kDNA fibers are disposed in a looser arrangement that fullfills the matrix of the trapezoid shape kinetoplast [5] (Fig. 1A), thus facilitating the identification of kDNA alterations after using compounds that target KAPS [6]. In this work we used microscopy techniques to investigate *A. deanei* cells that had *kap4* or *kap7* genes deleted by CRISPRCas9 system. The Transmission Electron Microscopy (MET) showed that KAP4 and KAP7 hemi-knockout cells, as well as KAP4 double knockout cells presented alterations on the kDNA network, that was seen densely packed especially in the region facing the basal body (brackets) (Fig. 2). Ultrastructural analysis by Scanning Electron Microscopy (SEM) showed that the knockout cells presented a reduced length of the cell body and flagellum when compared to control protozoa (Fig. 3). Interestingly, Fluorescent Microscopy (FM) images of protozoa labeled with DAPI revealed that in knockout cells the symbiotic division was impaired, generating filamentous bacterium. This can be related to the fact that in such protozoa the kinetoplast division does not occurs, generating cells with atypical number of structures (Fig 4 B and C). Quantification of protozoa observed by FM showed that symbiont filamentation occurred in approximately 11% of the KAP4 hemi-knockout cells, 24% of the KAP4 double knockout cells and 37% of the KAP 7 hemi-knockout cells (Fig. 4D) . Taken together, our data obtained by different microscopy techniques indicate that KAPs present important roles in kDNA arrangement and segregation, as well as for kinetoplast division. Our results also reinforce the idea that the symbiont division is synchronized with the replication of other host cell structures.

## REFERÊNCIAS:

- [1] Motta MCM, Martins ACA, *et al.*, PLoS ONE, 8(4): e6020, 2013.
- [2] Catta-Preta CM, Brum FL, *et al.*, Front. Microbiol. 6:520, 2015.
- [3] Lukes J, Guilbride DL, Votýpka J *et al.*, Eukaryot Cell., Aug;1(4):495-502, 2002.
- [4] Cavalcanti DP, Shimada MK, *et al.*, BMC microbiology, v. 9, p. 120, 2009.
- [5] de Souza SS, Catta-Preta CM, *et al.*, PLoS ONE 12(11): e0187516, 2017.
- [6] Cavalcanti DP, Fragoso, S. P. *et al.*, Parasitology Research, v. 94, p. 439-448, 2004.

This research was supported by CNPq (Brazil), FAPERJ, CAPES.

Acknowledgements to CENABIO.

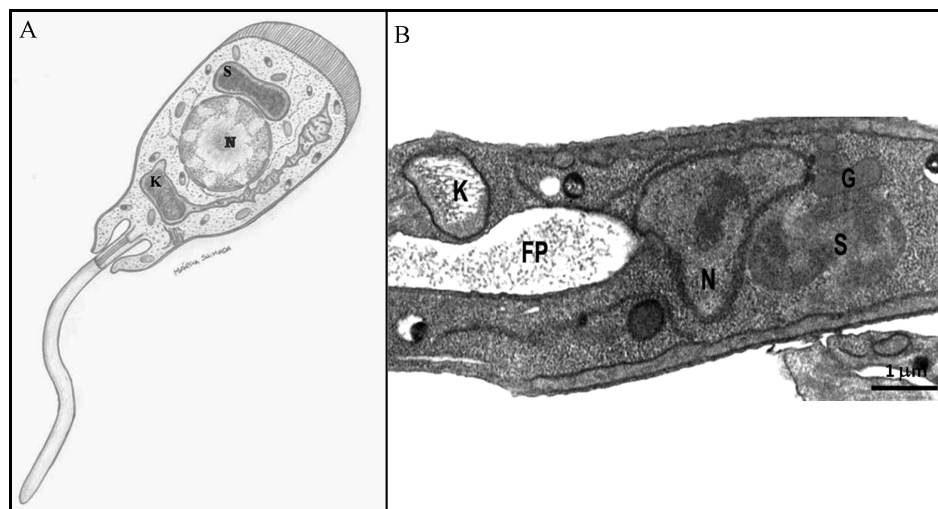


**Figure 1:** A- Schematic drawing of the *Angomonas deanei* showing the coanomastigote shape. The symbiont (S) is seen in close association with the host cell nucleus (N) and the kinetoplast (K) is located in the anterior end of the cell body (Designed by Márcia Shimada). B- TEM of a typical *A. deanei* cell (Motta *et al.*, 2010). N-nucleus, K-kinetoplast, S- symbiont, G- glycosome, FP-flagellar pocket.

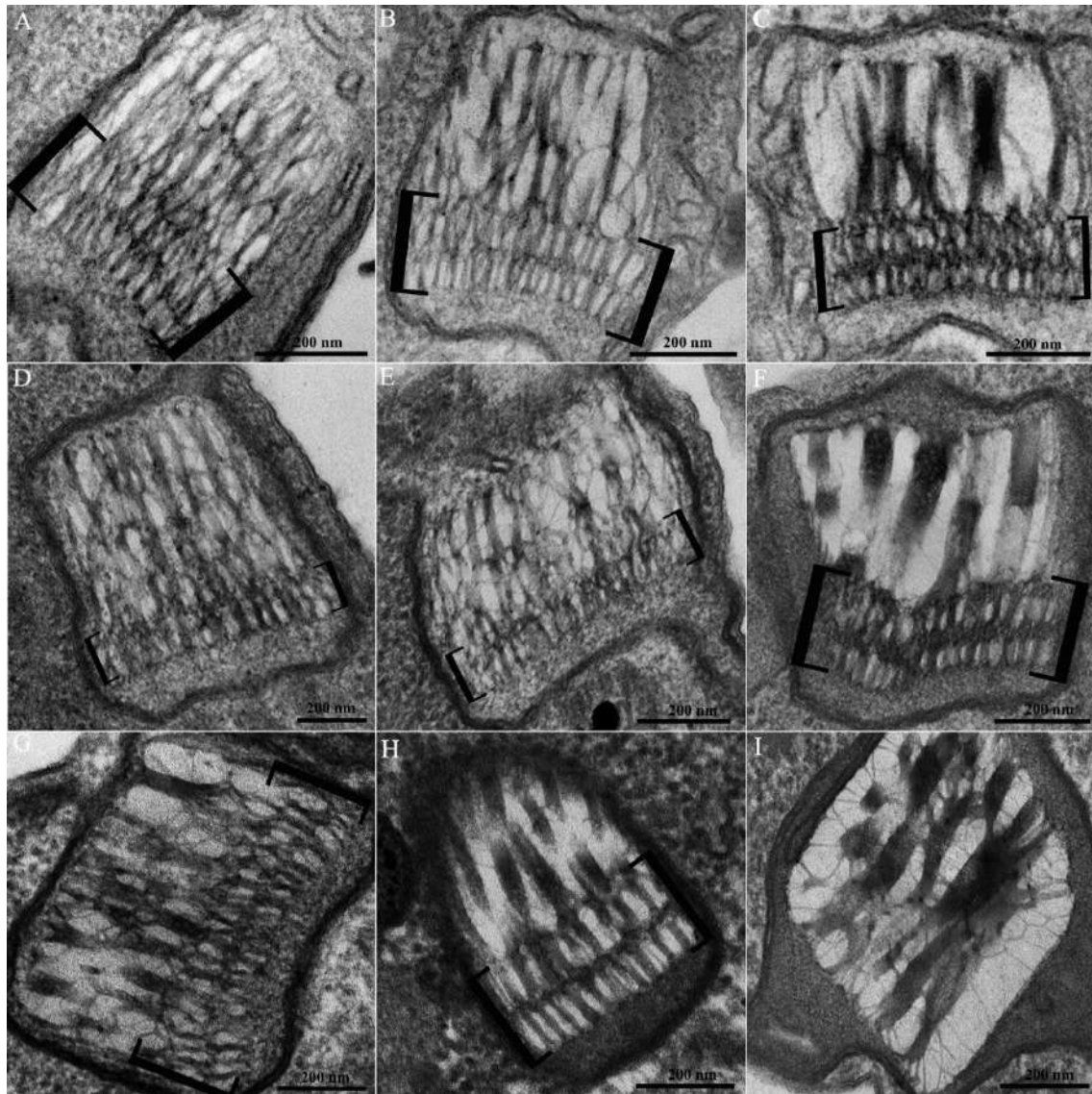


**Figure 2:** Ultrastructural analyses of the *Angomonas deanei* kDNA by TEM. A- wild type cell, B and C- KAP4 hemi-knockout cells, D to F- KAP4 double knockout cells, G to I - KAP7 hemi-knockout cells.

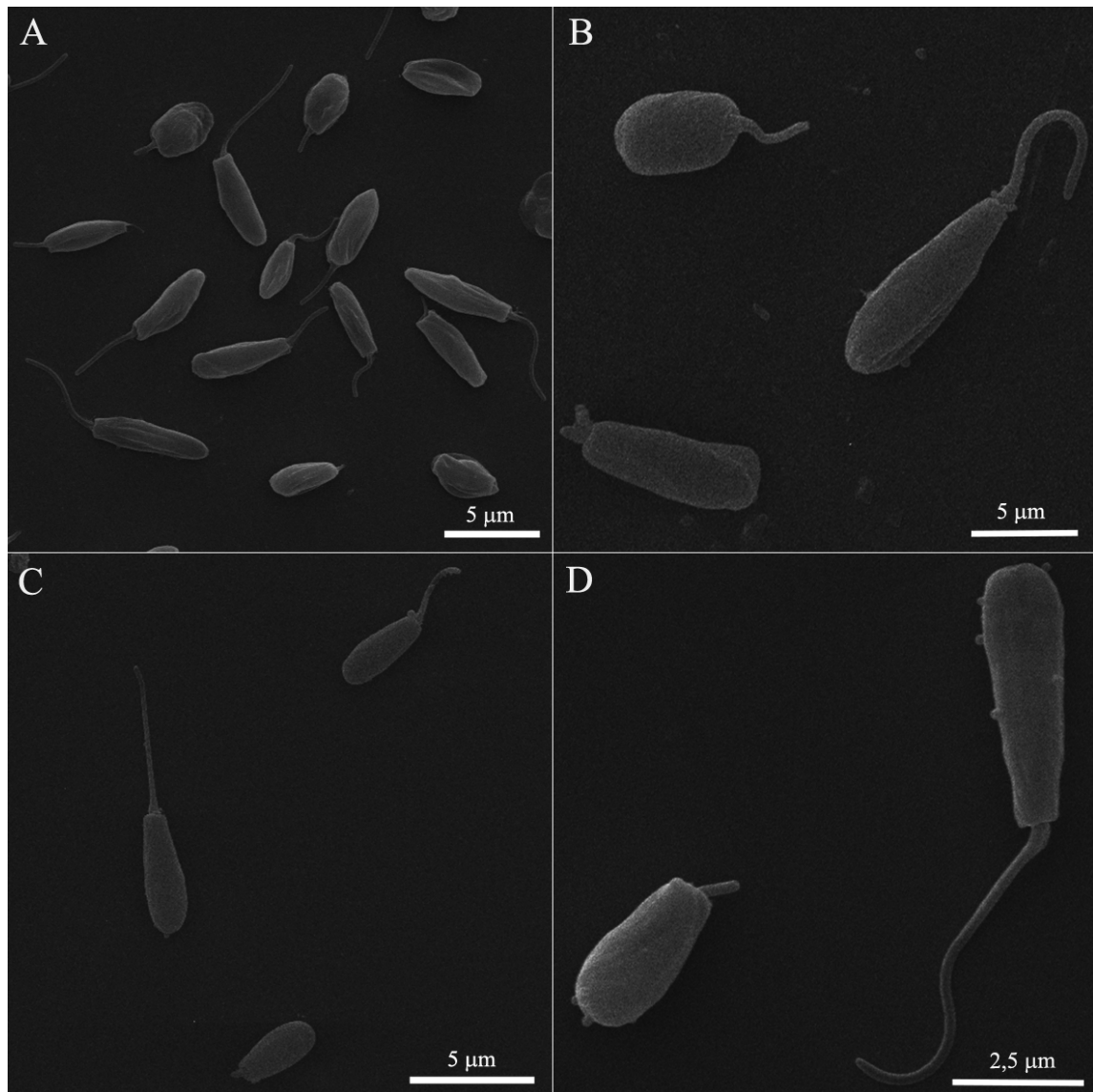


**Figure 3:** Analyses by SEM of *Angomonas deanei* . A- wild type cells, B - KAP 4 hemi-knockout cells, C - KAP4 double knockout cells, D - KAP7 hemi- knockout cells.



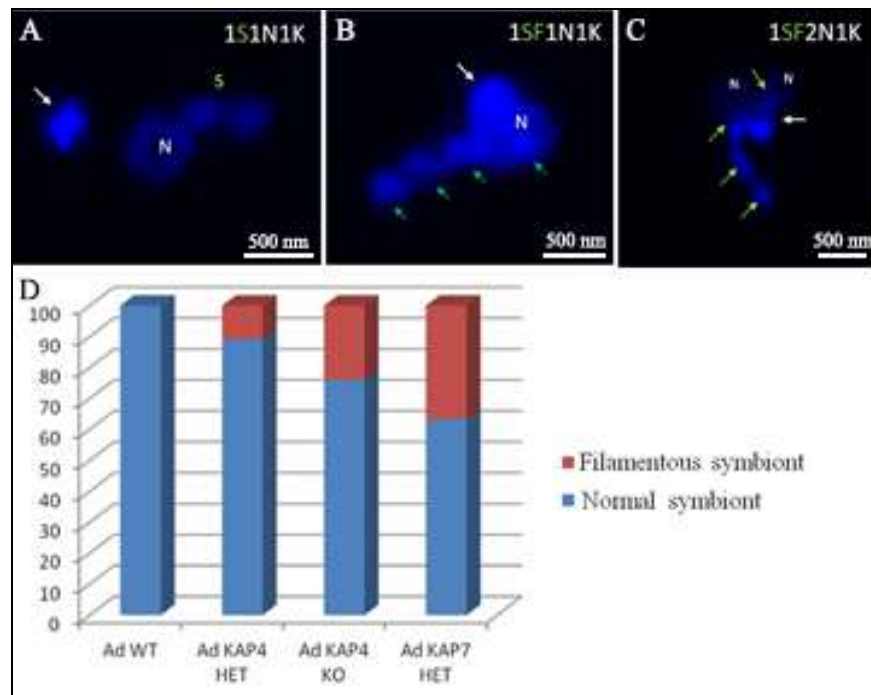


**Figure 4:** Analyses by FM of DAPI labeled cells, showing typical (A) or atypical (B and C) cellular patterns of KAP4 double knockout cells. Usually protozoa present one nucleus (N), one kinetoplast (K) and one symbiont (S) as seen in Fig. 4A. In knockout cells, it was observed protozoa containing filamentous symbiont, showing that the bacterium division was impaired (Fig. 4B). Cells with two nuclei, one kinetoplast and one filamentous symbiont (fs) were also observed (Fig. 4C). This indicates kinetoplast division impairment, since this structure divides before the nucleus. D- Quantification of cells observed by FM, considering the shape of the symbiont: normal or filamentous.

## Ultrastructural studies of cell cultures infected with Brazilian Zika virus

D.F. Barreto-Vieira<sup>1\*</sup>, F. C. Jácome<sup>1</sup>, M. A. N. da Silva<sup>1</sup>, G. C. Caldas<sup>1</sup>, A. M. B. de Filippis<sup>2</sup>, O. M. Barth<sup>1</sup>

<sup>1</sup>Laboratório de Morfologia e Morfogênese Viral, Instituto Oswaldo Cruz, Fiocruz, Avenida Brasil 4365, 21040-900, Rio de Janeiro, RJ, Brazil

<sup>2</sup>Laboratório de Flavivírus, Instituto Oswaldo Cruz, Fiocruz, Avenida Brasil 4365, 21040-900, Rio de Janeiro, RJ, Brazil

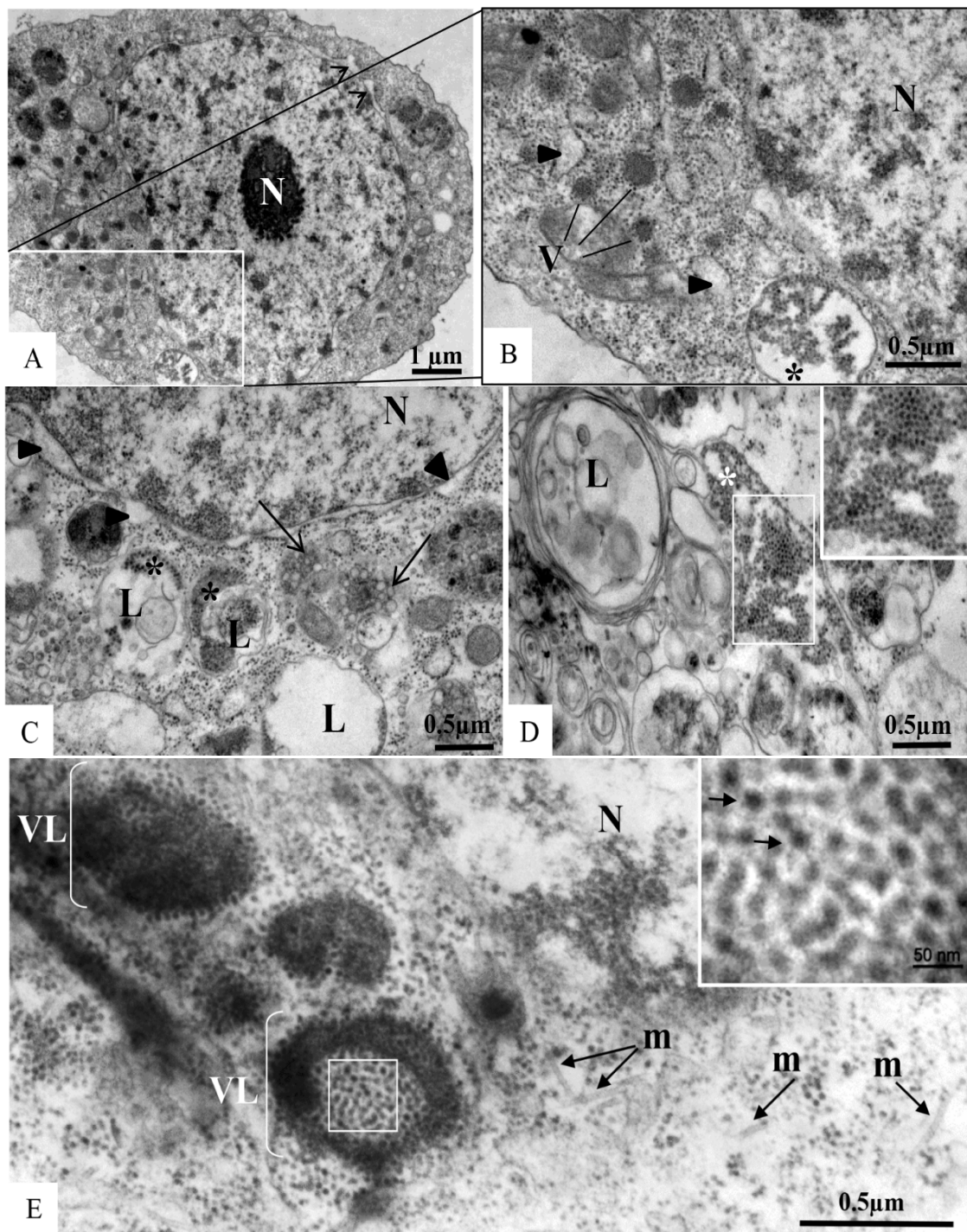
\*Corresponding author at: Laboratório de Morfologia e Morfogênese Viral, Instituto Oswaldo Cruz, Fiocruz, Avenida Brasil 4365, 21040-900, Rio de Janeiro, RJ, Brazil  
E-mail address: barreto@ioc.fiocruz.br

Zika virus (ZIKV) is a member of the flavivirus genus, and its genome is approximately 10.8 kilobases of positive-strand RNA enclosed in a capsid and surrounded by a membrane [1,2]. Studies on the replication dynamics of ZIKV are scarce, which limits the development of antiviral agents and vaccines directed against ZIKV. In this study, *Aedes albopictus* mosquito lineage cells (C6/36 cells) and African green monkey kidney epithelial cells (Vero cells) were inoculated with a ZIKV sample isolated from a Brazilian patient, and the infection was characterized by immunofluorescence staining, phase contrast light microscopy, real-time RT-PCR and fixed in glutaraldehyde 1% in cacodylate buffer for ultrastructural analyses by transmission electron microscopy. The infection was observed in both cell lineages, and ZIKV particles were observed inside lysosomes, the rough endoplasmic reticulum and viroplasm-like structures. The susceptibility of C6/36 and Vero cells to ZIKV infection was demonstrated. Moreover, this study showed that part of the replicative cycle may occur within viroplasm-like structures, which has not been previously demonstrated in other flaviviruses. The susceptibility of C6/36 and Vero cells to infection with a ZIKV sample isolated from a Brazilian patient was confirmed in the present study. In addition, the dynamics of ZIKV replication were investigated and presented as different from what is commonly observed during replication by other flaviviruses, since part of the replication cycle of this virus can occur in viroplasm-like structures. Further studies are necessary to investigate the relationship between viroplasm-like structures and ZIKV replication dynamics. The data presented in this study are important for use in the development of model systems to evaluate therapeutic approaches.

[1] Dick GWA, Kitchen SF, Haddow AJ. Zika virus. I. Isolations and serological specificity. *Trans R Soc Trop Med Hyg.* 1952; 46:509–520.

[2] Altman, LK (3 July 2007). "Little-Known Virus Challenges a Far-Flung Health System". *The New York Times*.

This research was supported by CNPq and Instituto Oswaldo Cruz, Fiocruz.



**Figures A-D:** C6/36 cells infected with ZIKV analyzed by transmission electron microscopy (TEM) at different time points post-infection (A-B: 48 hr p.i., C-D: 72 hr p.i.). Several large

viroplasm-like perinuclear compartments (V) (A-B) and ZIKV particles (\*) measuring approximately 40-50 nm in diameter in the endoplasmic reticulum cisternae (RER) (A, B) and in lysosomes (L) (C-D) were observed. Nucleocapsids were observed inside the RER (D). Thickening of the nuclear membrane and rough endoplasmic reticulum cisternae (rER) (black head arrow) (C), numerous lysosomes (L) (C, D) and vesicular compartments associated with rER (arrow) (C) measuring approximately 100 nm in diameter were observed. Nucleus (N). **Figure E:** Vero cell monolayers infected with ZIKV analyzed by TEM at 48 hr p.i. Several large viroplasm-like perinuclear compartments (VL) containing ZIKV particles in the lumen (arrow) were observed. Microtubules (m), nucleus (N).



## Histopathological Findings In Immunocompetent Murine Model Lung Infected With Zika Virus

Derick Mendes Bandeira<sup>1\*</sup>, Marcos Antonio Alvino da Silva<sup>1</sup>, Arthur da Costa Rasinhas<sup>1</sup>, Gabriela Cardoso Caldas<sup>1</sup>, Fernanda Cunha Jácome<sup>1</sup>, Ana Luisa Teixeira de Almeida<sup>1</sup>, Renata Tourinho Cantinho Brício<sup>2</sup>, Juliana Fernandes Amorim da Silva<sup>2</sup>, Gisela Freitas Trindade<sup>2</sup>, Ortrud Monika Barth<sup>1</sup>, Debora Ferreira Barreto Vieira<sup>1</sup>

<sup>1</sup> Laboratório de Morfologia e Morfogênese Viral, Instituto Oswaldo Cruz, Rio de Janeiro, Brazil.

<sup>2</sup> Laboratório de Tecnologia Viroológica, Biomanguinhos, Rio de Janeiro, Brazil.

\* Corresponding author e-mail: derick\_mendes@live.com

Most of the Zika virus (ZIKV) research was conducted from 2015, the year of the epidemic in which the association between the virus infection and the microcephaly and Guillain-Barré syndrome was discovered. As most of the data is extremely recent, many questions remain unanswered. The objective of this study is to quantify the viral load in different tissues and to evaluate evidences of lung tissue injury in BALB/c mice experimentally inoculated with ZIKV through the technique of light field microscopy. Two-month-old male BALB/c mice were inoculated with 100µL of Zika virus (at the titration of  $10^4$ ) diluted in L-15 medium. For the qRT-PCR, the animals were divided into three-point kinetics, with five animals each: three days after infection (DAI), seven DAI and fourteen DAI. These groups labels refer to how much time after the inoculation of the virus the euthanasia of the animals was done. Five animals inoculated with L-15 medium alone were used as negative controls. Saliva samples were collected with swab wet in L-15 medium; urine samples were collected from spontaneous urination or puncture of the bladder; and serum samples were obtained by cardiac puncture. The animal's organs were conditioned in 1.5mL plastic tubes with 500µL of L-15 medium, macerated and centrifuged to obtain the supernatant. Then, the extraction of RNA from the samples was done with the Qiaamp viral RNA minikit, following the manufacturer's instructions. For the quantification, we used the ZDC kit (Biomanguinhos), following the manufacturer's instructions as well. For the analysis by light field microscopy, the animals were divided in the same way as those destined for the qRT-PCR. The lungs were fixed in 50% alcohol, paraffin embedded, sectioned and stained with hematoxylin and eosin. Viral RNA was recovered from a heart sample (3DAI), two muscle samples (3DAI) and nine spleen samples (four in 3DAI, three in 7DAI and two in 14DAI). Despite the fact that viral RNA was not recovered in the lung, the histopathological analysis in this organ reveled some alterations as: thickening of the alveolar septum, compensatory alveolar dilatation, presence of inflammatory infiltrate, alveolar collapse, rupture of the bronchiole's epithelium from the underlying tissues, hemorrhage, edema and congestion of the blood vessels. These results show that, despite the undeniable relevance of molecular techniques, the exclusive use of qRT-PCR would exclude any suspicion of lung damage, causing the loss of many significant data that a deeper histopathological investigation could bring. Thus, it is concluded that the use of light field microscopy is an extremely valuable tool for understanding the pathogenesis of ZIKV infection, increasing the sensitivity of the analyzes.

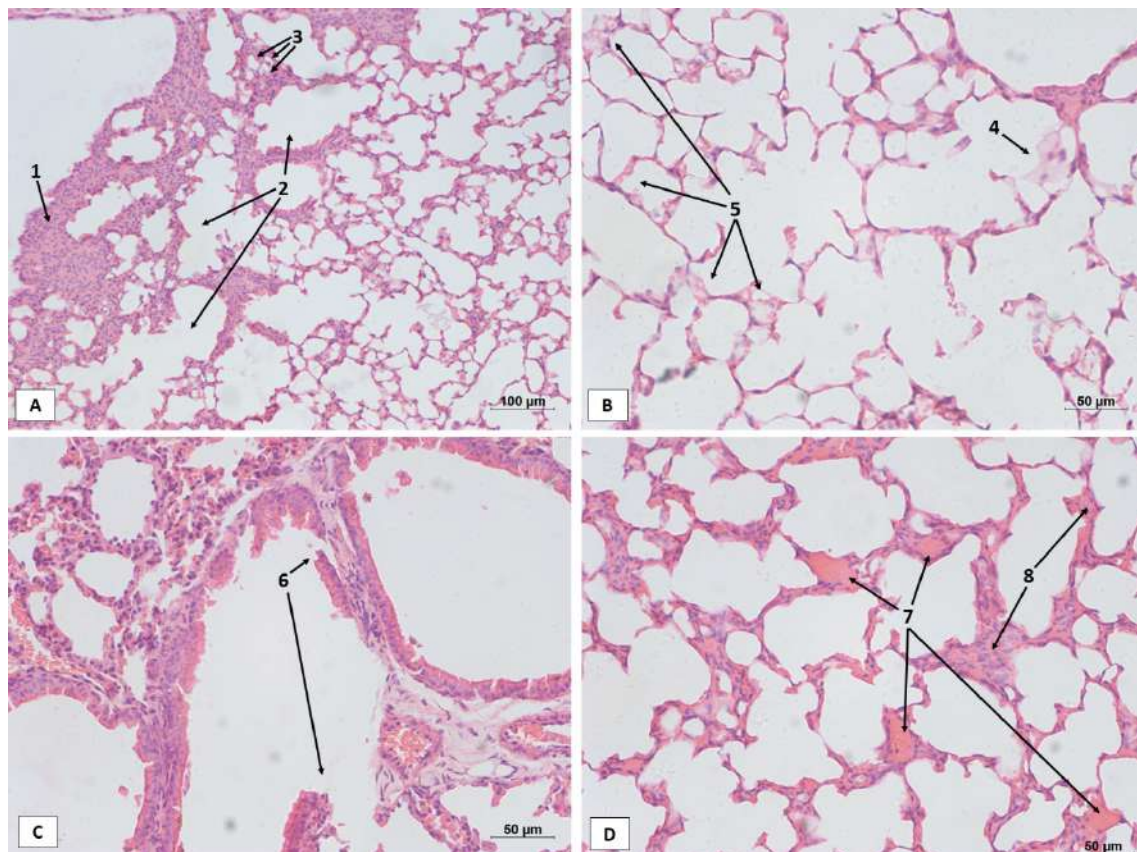


**Figure 1.** Histopathological alterations in lung tissue of BALB/c mice infected by Zika virus. [A.] 1. Presence of inflammatory infiltrate; 2. Compensatory alveolar dilatation; 3. Alveolar collapse. [B.] 4. Edema; 5. Erythrocytes outside the blood vessels as an evidence of hemorrhage. [C.] 6. Rupture of the bronchiole's epithelium from the underlying tissues. [D.] 7. Congestion of many blood vessels in a same microscope field; 8. Thickening of the alveolar septum.

## Effect of herbicides on the physiology, morphology and cell ultrastructure of *Setaria viridis* (L.) Beauv

Lelis DCC <sup>1,2\*</sup>, Valença DC <sup>1,2\*</sup>, Mendes AC <sup>1,2</sup>, Junqueira NE <sup>1,2</sup>, Ferreira MA <sup>3</sup>, Pinho C<sup>4</sup>, Reinert F <sup>2</sup> and Ortiz B <sup>2,5</sup>

<sup>1</sup>Pós-graduação em Biotecnologia Vegetal e Bioprocessos, Centro de Ciências da Saúde, Decania, Universidade Federal do Rio de Janeiro

<sup>2</sup>Laboratório de Fisiologia Vegetal, Instituto de Biologia, Departamento de Botânica, Centro de Ciências da Saúde, Universidade Federal do Rio de Janeiro,

<sup>3</sup>Laboratório de Genética Molecular Vegetal, Instituto de Biologia, Departamento de Genética, Centro de Ciências da Saúde, Universidade Federal do Rio de Janeiro,

<sup>4</sup>Departamento de Fitotecnia, Instituto de Agronomia, Universidade Federal Rural do Rio de Janeiro,

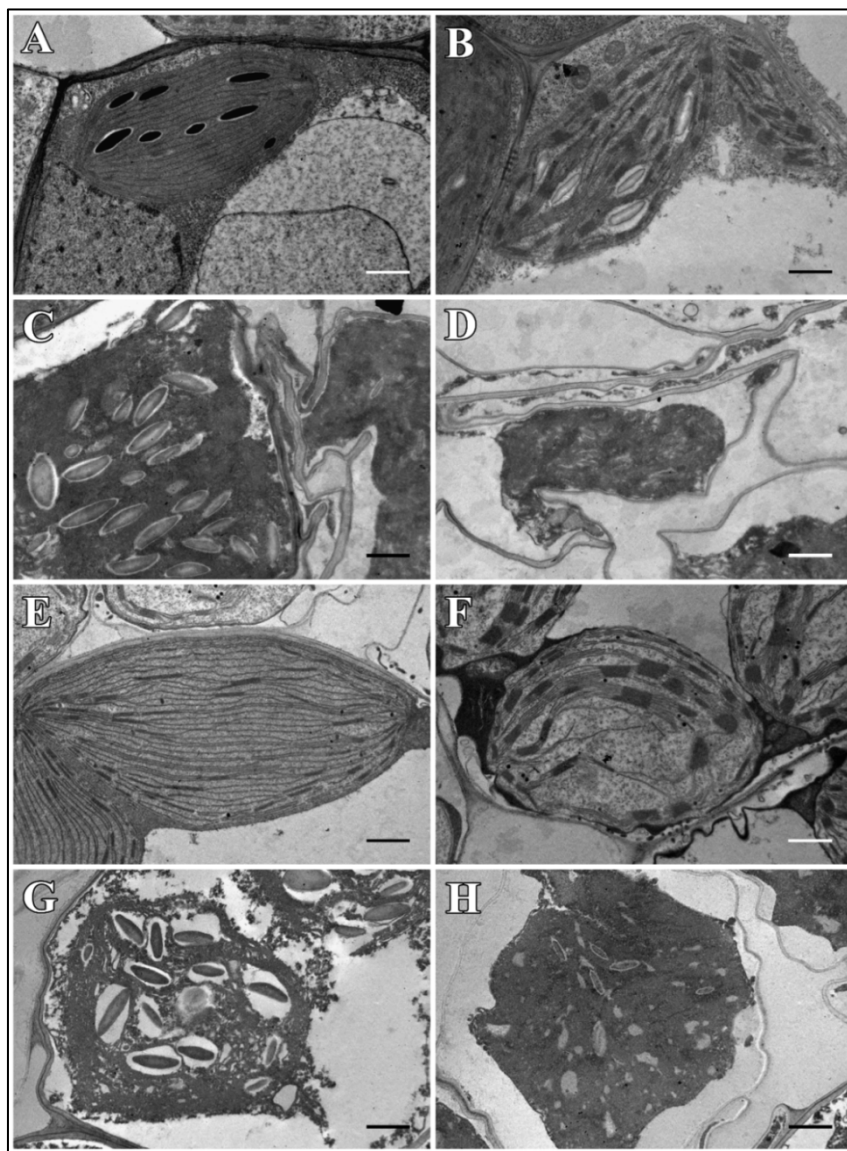
<sup>5</sup>Núcleo de Pesquisa Multidisciplinar, Campus Duque de Caxias, Universidade Federal do Rio de Janeiro

\*lelis.dcc@gmail.com

\*engagri@hotmail.com

*Setaria viridis* is one of the major agricultural weeds worldwide and belongs to same Panicoideae clade of several major feed, fuel, and bioenergy grasses, as maize (*Zea mays*), sorghum (*Sorghum bicolor*) and sugarcane (*Saccharum officinarum*) <sup>[1]</sup>. It has been used in scientific studies as a genetic model of grasses with C<sub>4</sub> photosynthetic metabolism due to its small genome (~ 515 Mb), a short life cycle (~ 60 days) and small stature (10-40cm) <sup>[1]</sup>. It is unknown whether this genetic diversity is correlated with variability in important adaptive traits such as herbicide resistance. Herbicides are commonly used in agriculture, and most studies seek to evaluate the influence of herbicides on plant physiology and metabolism <sup>[2,3]</sup>. The objective of this study was to analyze the effects of the herbicides paraquat, diuron and its combination (paraquat+diuron) on transient fluorescence, leaf anatomy, foliar surface and cell ultrastructure after 24h and 96h herbicide application. Leaf sections of the middle third were fixed with Karnovsky's solution, dehydrated in increasing ethanolic series, postfixed with osmium tetroxide and included in Spurr resin <sup>[4]</sup>. Paraquat and paraquat + diuron caused a drastic reduction in photosynthesis from 2 hours after application ( $F_v/F_m < 0.2$ ). The anatomical analysis of the leaf cross sections evidenced a retraction of the epidermal and mesophyll cells in all 24 hours after application treatments. On the leaf surface, the epidermal cells crinkled and withered. Only paraquat significantly altered the area and width of the stomata. Paraquat and paraquat + diuron caused degradation of the thylakoid and grana membranes of the bundle sheath and mesophyll chloroplasts. In contrast, the chloroplasts of the diuron treatment maintained the ultrastructure of the preserved stromal thylakoid membranes and grana. In 96 hours after application diuron affected the size of all cells of the leaf tissue causing the reduction of leaf thickness. In the analysis of the leaf surface an apparent corrosion in the epidermis and some fractures were observed. In addition, the presence of the silica bodies became more evident. In 96 hours after application the chloroplasts of bundle sheath and mesophyll cells had degradation of the thylakoid membrane and grana. The results showed the potential of *S. viridis* as a model and contribute to elucidate the effects of paraquat and diuron on photosynthesis, anatomy, morphology and plant cell ultrastructure of C<sub>4</sub> plants.

- [1] T.P. BRUTNELL et al., *Setaria viridis*: a model for C4 photosynthesis. *The Plant cell*, v. 22, n. 8, p. 2537–2544, 2010.
- [2] L. M. CASANO et al., Leaf age- and paraquat concentration-dependent effects on the levels of enzymes protecting against photooxidative stress. *Plant Science*, v. 149, n. 1, p. 13–22, 1999.
- [3] C.P. DE SOUSA et al., Photosynthesis of soybean under the action of a photosystem II-inhibiting herbicide. *Acta Physiologiae Plantarum*, v. 36, n. 11, p. 3051–3062, 2014
- [4] A. R. A. SPURR, Low-viscosity epoxy resin embedding medium for electron microscopy. *Journal of Ultrastructure Research*, v. 26, n. 1–2, p. 31–43, 1969.
- [5] This research was supported by CAPES (Brazil).



Effect on chloroplast ultrastructure after 24h application of herbicides. Chloroplast of bundle sheath cells (A-G); Chloroplast of mesophyll cells (B-F). Control (A, B); paraquat (C,D.); diuron (E, F) paraquat + diuron (G, H); Scale bar 1  $\mu$ m.



## **In vivo antileishmanial efficacy of a topical treatment of crotoxin derived from *Crotalus durissus terrificus* venom against *Leishmania (Leishmania) amazonensis***

MARTINS, A.J.E.<sup>1</sup>; HAGE, A.A.P.<sup>1</sup>; RODRIGUES, A.P.D.<sup>2</sup>; DINIZ, J.A.P.<sup>2</sup>, SAMPAIO, S.C.<sup>3</sup>; SILVA, E.O.<sup>1\*</sup>

<sup>1</sup>. Federal University of Pará, Institute of Biological Sciences, Laboratory of Structural Biology, Belém, Pará, Brazil.

<sup>2</sup>. Laboratory of Electron Microscopy, Evandro Chagas Institute, Department of Health Surveillance, Ministry of Health, Belém, Pará, Brazil;

<sup>3</sup>. Butantan, São Paulo - SP

\* Corresponding author: edilene@ufpa.br

Leishmaniasis are neglected emerging diseases in 98 countries caused by several species of protozoa of the genus *Leishmania* [1]. The treatment of tegumentar leishmaniasis is limited due to the several side effects and the development of protozoan parasites resistance against the drugs used [2]. Thus, search for new medicaments from natural origin and efficacy against the parasite without toxicity are needed. In this context, animal venoms and its purified compounds are known to exhibit a variety of pharmacological activities [3]. In the present study it was evaluated the effects of crotoxin (CTX), the predominant toxin in *Crotalus durissus terrificus* snake venom, on experimental cutaneous leishmaniasis caused by *Leishmania (Leishmania) amazonensis*. Animals (eight-week-old female BALB-c mice) were infected with 10<sup>6</sup> of *L. (L.) amazonensis* promastigotes during the stationary growth phase. The treatment was initiated after five weeks of infection and the CTX formulation was applied topically to all lesions once daily for 30 days. Control groups were also maintained in parallel. After the treatment, animals were euthanized and tissues from lesions were processed for different microscopy methods. For histopathological analysis, fragments of the lesion were fixed in paraformaldehyde 10% and included in paraffin. Subsequently, sections (5µm) were stained with hematoxylin and eosin and examined with an AxioScope A1 Zeiss. For transmission electron microscopy (TEM), tissues from lesions were fixed, post-fixed, dehydrated in graded acetone and embedded in epoxy resin. Ultrathin sections obtained were examined with a Zeiss 906E TEM. For scanning electron microscopy (SEM), tissues were fixed, dehydrated in graded ethanol, frozen using liquid nitrogen, fractured and, after thawing, critical-point dried. Samples were examined with a LEO 1450VP SEM. Histopathological analysis showed CTX was able to decrease parasitic load; ultrastructural analysis showed morphological alterations in the intracellular amastigotes in the tissues of treated animals and the presence of vesicles in host cell. In conclusion, our results suggest that treatment with CTX may be a possible topical therapy against tegumentar leishmaniasis.

[1] WHO. The Special Programme for Research and Training in Tropical Diseases. Leishmaniasis: Disease information. (2010)

[2] D. O. Santos, et al., Leishmaniasis treatment—a challenge that remains: a review. Parasitology research, v. 103, n. 1, (2008) 1-10

[3] D. F. Cardoso, I. Mota, Effect of *Crotalus* venom on the humoral and cellular immune response. Toxicon, v. 35, n. 4, (1997). 607-612

[4] This research was supported by CNPq, INBEB, UFPA, FAPESPA,

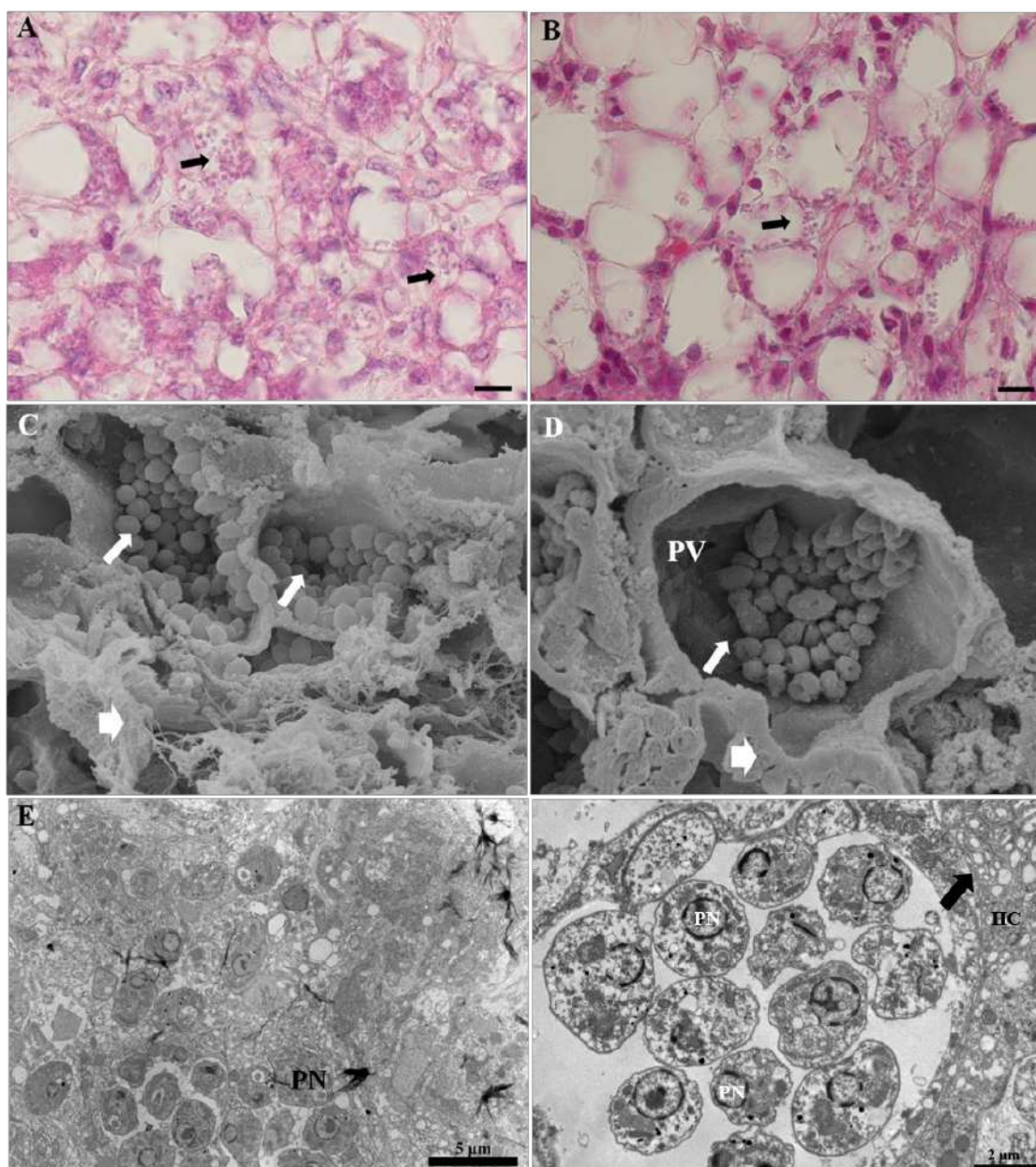


**Figure 1: Histopathological and ultrastructural analysis of skin lesion from *L. (L.) amazonensis*-infected animals untreated and treated with CTX-topical formulation.**

(A-B) Light microscopy. A – Untreated group showed large amount of amastigotes in the parasitophorous vacuoles (arrows). B - Group treated with 0.096 µg/ml of CTX showed reduced number of amastigotes (C-D) Scanning Electron Microscopy. C- Untreated group showed rounded amastigotes (arrow) and tissue disruption (large arrow). D - Group treated with 0.096 µg/ml CTX showed amastigotes with elongated body and morphological alterations in the amastigote cell body (large arrow-Parasitophorous vacuole membrane). (E-F) Transmission electron microscopy. E – Untreated group showed typical morphology of amastigotes in the infected tissue. F - Group treated with 0.096 µg/ml CTX showed ultrastructural alterations in the amastigote cytoplasm and presence of vesicles in the host cell (arrow), indicative of cellular activation. PV – Parasitophorous vacuole; PN - Parasite nucleus; HC – Host Cell. Bars: A - 10µm; B - 10µm; E- 5µm; F - 2µm.

## Effect of copaiba oil and kojic acid association on promastigote forms of *Leishmania (Leishmania) amazonensis*.

Lienne S de Moraes<sup>1,2</sup>, Ana Paula D Rodrigues<sup>2,3</sup>, Giselle M S Guilhon<sup>4</sup> and Edilene O Silva<sup>1,2,\*</sup>.

<sup>1</sup>Federal University of Pará, Institute of Biological Sciences, Laboratory of Structural Biology, Belém, Pará, Brazil.

<sup>2</sup>National Institute of Science and Technology in Structural Biology and Bioimaging, Rio de Janeiro, Rio de Janeiro, Brazil.

<sup>3</sup>Laboratory of Electron Microscopy, Evandro Chagas Institute, Department of Health Surveillance, Ministry of Health, Belém, Pará, Brazil.

<sup>4</sup>Federal University of Pará, Institute of Exact and Natural Sciences, Belém, Pará, Brazil

\* Corresponding author: edilene@ufpa.br

Leishmaniasis is a complex of anthroponozoonotic diseases distributed worldwide, caused by protozoa of the genus *Leishmania*. These parasites are responsible for promoting infections such as Cutaneous Leishmaniasis, (CL) Mucocutaneous Leishmaniasis (MCL) and Visceral Leishmaniasis (VL). The main chemotherapeutics used in the treatment of these diseases are pentavalent antimonials (Glucantime<sup>®</sup>), Miltefosine and Amphotericin B [1]. These drugs are effective, but they have a high cost and toxicity. The search for new substances, which are economically viable and act on the protozoan without causing damage to the host cell, becomes necessary. As an alternative sources of new substances against leishmaniasis, copaiba oil (CO) and kojic acid (KA) have been described as potent antileishmanial agents [2,3]. Therefore, we herein demonstrate for the first time the *in vitro* action of the CO and KA association on the promastigote form of the protozoan *Leishmania (L.) amazonensis*. The promastigotes were treated with 30 µg/mL OC and 50 µg/mL AK by 72 hours. Morphological analysis of the treated cells were determined by light microscopy (LM), scanning electron microscopy (SEM) and transmission electron microscopy (TEM). The results showed that CO+KA caused morphological changes in promastigote forms when compared to the control group (without treatment). Alterations of promastigotes forms with atypical cell division were observed by LM and MEV. Analysis by MET demonstrated that the treatment with association induced kinetoplast alteration and disruption of the cellular body. Analysis of cell viability by MTT method showed that this association presented no cytotoxic effects against murine macrophages. In conclusion, these results show that association between CO and KA can be a promising leishmanicidal agent.

### REFERENCES

- [1] B.S.MCGWIRE, et al. Leishmaniasis: clinical syndromes and treatment. **Oxford Journal of Medicine**. V. 107, n. 1, p. 7-14, 2014.
- [2] AO. SANTOS, et al. Copaiba Oil: An Alternative to Development of New Drugs against Leishmaniasis. **Evidence-Based Complementary and Alternative Medicine**. V. 2012, 2011.
- [3] A.P.D. RODRIGUES, et al. A Novel Function for Kojic Acid, a Secondary Metabolite from *Aspergillus Fungi*, as Antileishmanial Agent. **Plos One**. V. 9, p. e91259, 2014.
- [4] This research was supported by INBEB, CNPq and CAPES.



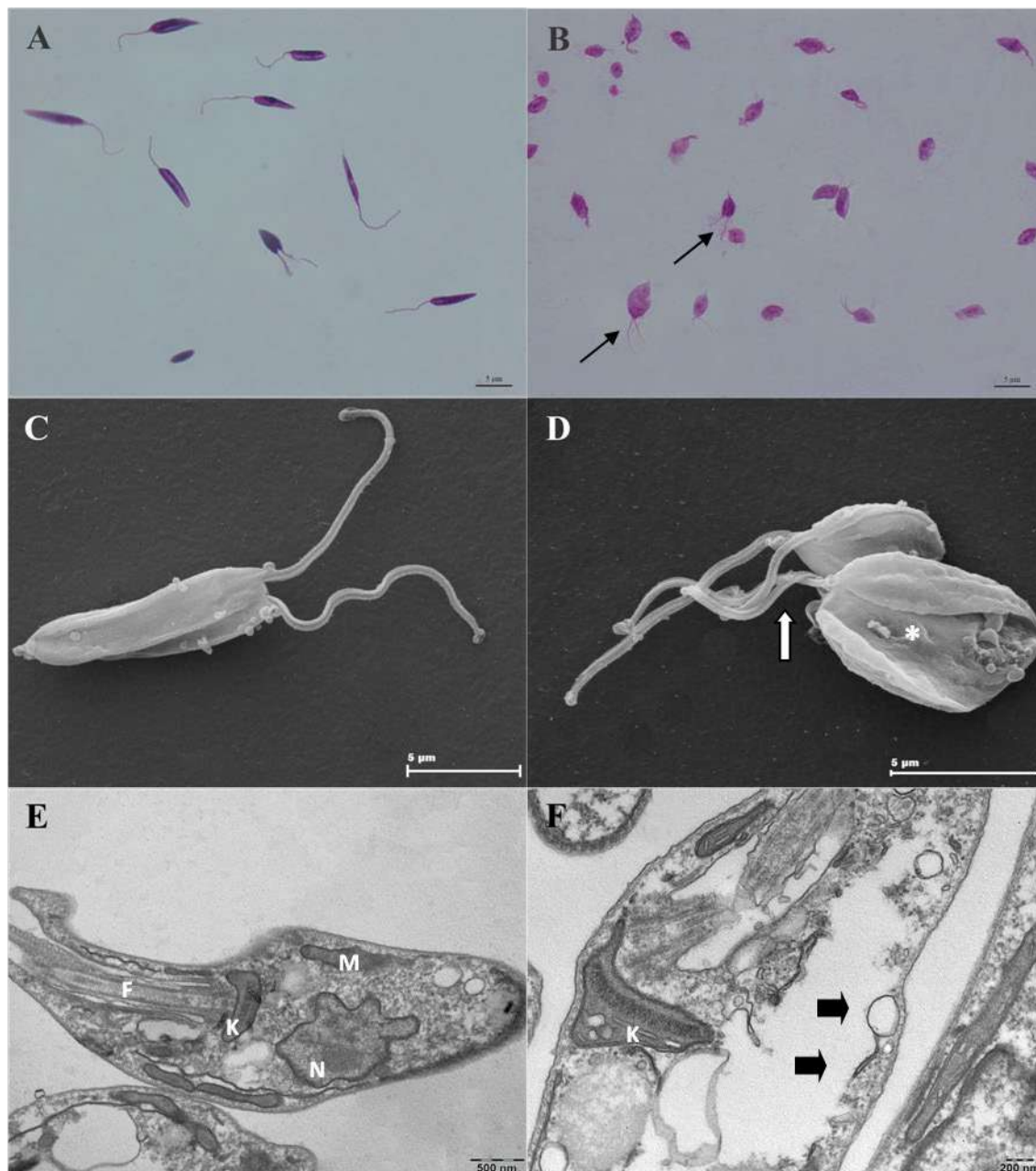


**Figure 1:** Morphological alterations in promastigotes forms after treatment with copaiba oil and kojic acid association. (A-B) Light microscopy. A- General view of untreated promastigotes. B- Treated parasites. Note promastigotes forms with atypical division, presenting multiple flagella (arrows). (C-D) Scanning electron microscopy (SEM). C- Untreated promastigotes with normal morphology, evidencing promastigotes in cell division; D- Treated Promastigotes. Observe promastigotes with apparent atypical cell division, presenting more than two flagellum (arrow) and reduction in the parasite body (\*). (E-F) Transmission electron microscopy (TEM). E- Promastigotes without treatment showing the characteristic structure of parasite. F- Treated promastigotes. Observe disruption of the flagellum (F) and cell body (arrows) and alterations in kinetoplast shape. F-Flagellum; K- kinetoplast; M- mitochondria; N- nucleus.



## **Renal Impairment in Murine Model for Dengue 3 Infection: Histopathological, Morphometric and Ultrastructural Aspects**

Gabriela Cardoso Caldas<sup>1,2\*</sup>, Fernanda Cunha Jácome<sup>1</sup>, Arthur da Costa Rasinhas<sup>1</sup>, Ana Luisa Teixeira de Almeida<sup>1</sup>, João Paulo Rodrigues dos Santos<sup>2</sup>, Marcelo Pelajo Machado<sup>2</sup>, Débora Ferreira Barreto Vieira<sup>1</sup>

<sup>1</sup>. Laboratório de Morfologia e Morfogênese Viral/Instituto Oswaldo Cruz, Rio de Janeiro - Brasil

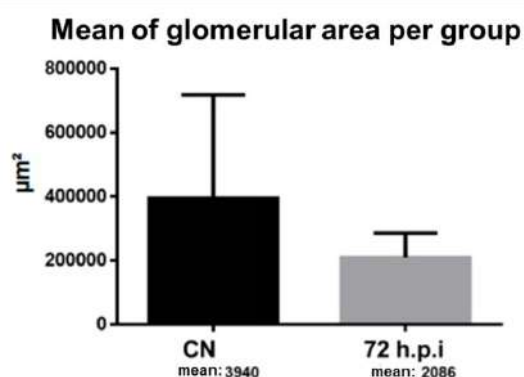
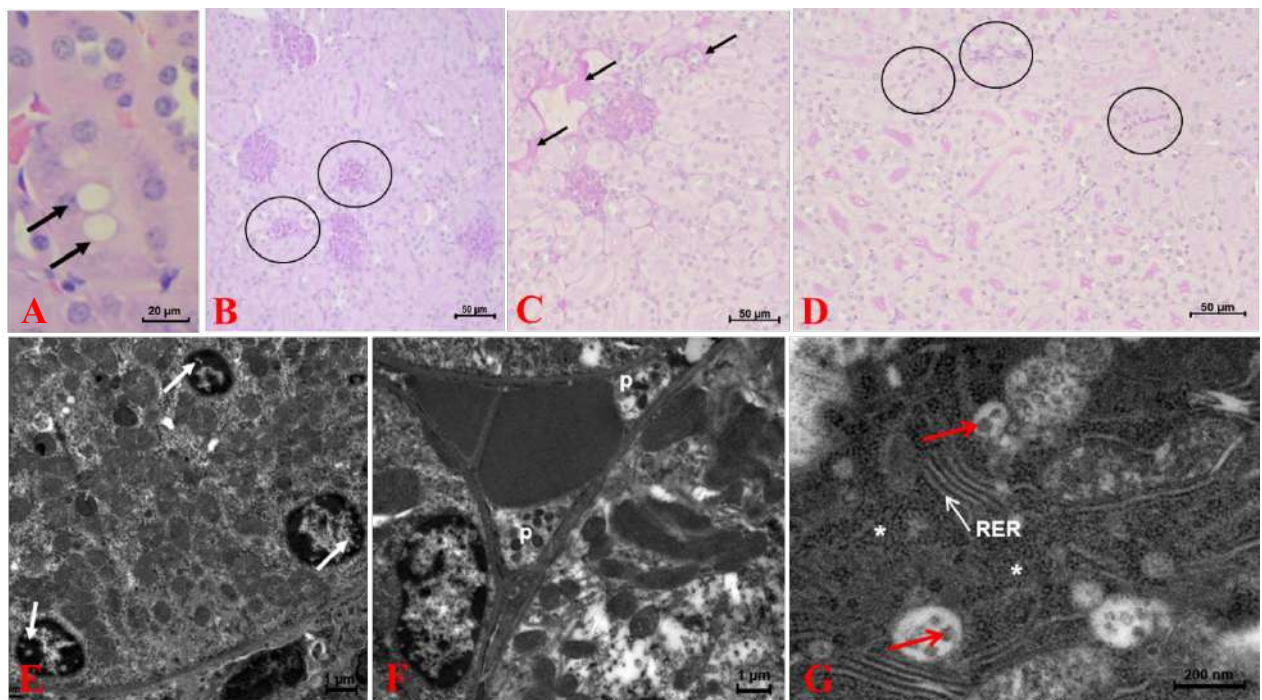
<sup>2</sup>. Laboratório de Patologia/Instituto Oswaldo Cruz, Rio de Janeiro – Brasil  
email for correspondence: gabrielacardosocaldas@gmail.com

Dengue (DEN) is considered the arbovirose of major importance in the world and presents a systemic character, in which several organs and physiological systems are affected. Several forms of renal impairment have been identified in patients with DEN [1,2]. Acute renal failure (ARF) is a potential complication of severe DEN and, although poorly studied, has a high mortality rate [3,4]. Several mechanisms have been proposed to explain the etiopathogenesis of ARF induced by DENV infection, including direct virus action, hemodynamic instability, rhabdomyolysis, haemolysis and acute glomerular injury [5]. In this context, the establishment of an experimental animal model that presents renal impairment in a similar way to that observed in human cases of DEN is extremely relevant to better understand the involvement of the kidneys during the course of DENV infection. The main goal of this study was verifying possible macroscopic, histopathological, histomorphometric and ultrastructural changes in the kidneys of BALB/c mice experimentally infected with DENV-3. Two-month-old, male, BALB/c mice were intravenously infected with DENV-3 and euthanized in 72 h.p.i. The kidneys were collected, weighed and processed for histopathological and ultrastructural analysis. For the histopathological analyzes, the renal fragments were fixed in formalin, dehydrated in ethanol, clarified in xylol and included in paraffin. Histological sections of 5 µm were stained with hematoxylin and eosin, periodic acid-Schiff and analyzed by AxioHome Carl Zeiss microscope. Histomorphometric analyzes were conducted using ImageJ software. For the ultrastructural analyzes, the samples were fixed in 2% glutaraldehyde buffered in 0.1M sodium cacodylate, post-fixed in osmium tetroxide, dehydrated in acetone and included in epoxy resin. Sections of 50 - 70 nm were contrasted with uranyl acetate and lead citrate and analyzed by TEM JEOL JEM 1011. Histopathological analysis of kidneys 72h.p.i. by DENV-3 revealed the presence of cytoplasmic inclusions in proximal convoluted tubule epithelial cells and glomerular atrophy, with a deranged mesangial structure and absence of the Bowman's capsule. Areas showing mitotic figures in tubular cells, signs of congestion with presence of transudate and cells infiltrated in the interstitium were also observed. Ultrastructural analysis revealed the presence of mononuclear cells in the interstitium and in capillaries, platelet adhesion to the endothelium, vascular congestion foci, signs of cellular degeneration, characterized by the presence of pycnotic nuclei and nuclear degeneration of interstitial cells. Signs of intense protein synthesis activity in the interstitial cell were observed, evidenced by the thickening of the rough endoplasmic reticulum and the presence of innumerable electron-dense ribosomes. In this same field, it was also observed the presence of similar particles in morphology and diameter to DENV. Histomorphometric analysis revealed that 72 h.p.i mice by DENV-3 had a lower glomerular area than the uninfected mice. A statistically significant increase in mouse kidney weight was observed 72 h.p.i in relation to the control group, which may be a consequence of the exudate present in the interstitium. From the results obtained, it is concluded that the BALB/c mouse is a relevant model to

analyze renal involvement in the course of DENV infection, presenting important morphological alterations that may be a consequence of the direct viral action and the host immune response and which indicate that the kidneys may play a central role in the pathophysiology of DEN.

- [1] Lizarraga & Nayer, J. of Nephropath. 3 (2014) 57–62
- [2] Oliveira & Burdmann, Clin Kidney J. 8 (2015) 681-685.
- [3] Horvath, McBride & Hanna, Dengue Bull. 23 (1999) 24–29
- [4] Lombardi *et al.*, Semin Nephrol. 28 (2008) 320–329
- [5] Lima & Nogueira, Semin Nephrol. 28 (2008) 409–415

This research was supported by CNPq (Brazil) and Oswaldo Cruz Institute.



contrasted with uranyl acetate and lead citrate. [E] Signs of degeneration of contorted tubule cells, characterized by the presence of pycnotic nuclei (arrows) [F] Platelets (p) adhered to the endothelium. [G] Intense cell protein activity of the proximal contorted tubule, evidenced by the thickening of rough endoplasmic reticulum (RER) (arrows) and areas with numerous electrondense ribosomes (\*). Particles similar in morphology and diameter to the DENV (red arrows) inside the membranous compartment in the cytoplasm. [H] Mean of the glomerular area per analyzed experimental group.

## Morphological Aspects Of Aorta Of C57Bl/6 Mice Submitted To The Hyperlipidic Diet And Treated With Hexanic Extract Of *Pterodon polygalaeflorus*

Gabriella Melo Carvalho<sup>1</sup>, Vicky Goldbach Melgar<sup>1</sup>, Jorge José de Carvalho<sup>1\*</sup>, Ana Lucia Rosa Nascimento<sup>1</sup>, Pedro Henrique Reis Barbosa<sup>1</sup>, Marsen Garcia Pinto Coelho<sup>2</sup>, Aline Bonfim Vieira<sup>3</sup>

<sup>1</sup>: Laboratory of Ultrastructure and Tecidual Biology, University of the State of Rio de Janeiro, Rio de Janeiro, Rj, Brazil. \*Corresponding author: [jjcarv@gmail.com](mailto:jjcarv@gmail.com)

<sup>2</sup>: Laboratory of Biochemistry, University of the State of Rio de Janeiro, Rio de Janeiro, Rj, Brazil.

<sup>3</sup>: Ross University School of Veterinary Medicine.

Obesity has become a worldwide epidemic disease, which can lead to metabolic syndrome. Because it has a multifactorial characteristic, it can lead to the development of cardiovascular disease and insulin resistance [1-4]. Among cardiovascular diseases, atherosclerosis is a major cause of myocardial infarction in obese individuals. Several authors point out the importance of the use of herbal medicines in the treatment of chronic diseases, among them obesity [5]. Phytotherapy derived from *Pterodon polygaleoforus* (sucupira), has different properties, such as antineoplastic, analgesic and mainly, anti-inflammatory, allowing this herbal medicine to become a potential treatment for obesity [6-7]. Thus, the aim of this project is to evaluate the effect of the hexanic extract of *Pterodon polygaleoforus* on the aorta of C57Bl/6 mice in the obesity model with high fat diet. The experiment was performed over 18 weeks with 32 C57Bl/6 mice, at 3 months of age. The animals were divided into 4 groups: control (SC), treated control (SC-SU), High Fat (HF) and treated High Fat (HF-SU). SC and HF received water by oral gavage and SC-SU and HF-SU received sucupira extract (50 mg/kg). The body mass was measured weekly. After euthanasia, plasma was collected for biochemical analysis. The aorta was dissected, fixed, processed and cut for histopathological analysis (HE and Gomori Trichrome techniques). Ultrastructural analysis (TEM) and cell immunostaining (immunoperoxidase and Immunofluorescence) were performed to with the the inflammatory process knowledge caused by the obesity model and the sucupira's ability to reverse this process. Animals fed with HF diet had an increase in body mass, as well as plasma levels of triglycerides and cholesterol. Morphological analysis showed that in HF group there is more abundant extracellular matrix, with fragmentation of elastic laminae and increase of subendothelial smooth muscle cells. In the ultrastructural analysis, the HF group presented smooth muscle cell migration and few mitochondria. Corroborating with the previous data, we observed in these animals, increased distribution of smooth muscle  $\alpha$ -Actin, TNF- $\alpha$  and cytochrome C and reduction of PGC1 $\alpha$ . Treatment with sucupira extract was able to reduce body mass, cholesterol levels, expression of smooth muscle  $\alpha$ -Actin, TNF- $\alpha$  and cytochrome C, and increased PGC1 $\alpha$  expression. The morphological and ultrastructural analysis showed a beneficial effect of the treatment, in the reorganization of the elastic laminae and reduction of the subendothelial smooth muscle cells, smaller vesicles, many mitochondria and elastic lamellae more electron dense. Taken together, our results indicate that treatment with sucupira extract induces beneficial effects in the aorta of obese mice, making this compound a potential drug for the treatment of obesity.

[1]Cohen-Cole E, Fletcher JM. Is obesity contagious? Social networks vs. environmental factors in the obesity epidemic. J Health Econ (2008); 27: 1382-1387



- [2]Hardy LL, Mhrshahi S, Gale J, Nguyen B, Baur LA, O'Hara BJ. Translational research: are community-based child obesity treatment programs scalable? BMC Public Health (2015);15:652.
- [3]Kahn R, Buse J, Ferrannini E, Stern M. The metabolic time for a critical appraisal. Joint statement from the American Diabetes Association and the European Association for the Study of Diabetes. Diabetes Care. (2005); 28:2289-304.
- [4]Daoud, E., Scheede-Bergdahl, C., Bergdahl, A. Effects of Dietary Macronutrients on Plasma Lipid Levels and the Consequence for Cardiovascular Disease. Journal of Cardiovascular Development and Disease, (2014), 1, 201-213
- [5]Vieira, LG. O uso de fitoterápicos e plantas medicinais por pacientes diabéticos. 2017. 68 f. Dissertação (graduação de farmácia), Universidade de Brasília, Brasília. 2017.
- [6]Luciano M de Jr, Eduardo B de Almeida Jr. Metabolic Effect of an Oriental Herbal Medicine on Obesity and Its Comorbidities with Transcriptional Responses in Diet-Induced Obese Mice. 2017
- [7]Spindola HM et al. Atividade antinociceptiva do óleo das sementes de *Pterodon pubescens* Benth (Leguminosae – Papilionoidea), 2006. Dissertação (Mestrado) – Faculdade de Odontologia de Piracicaba, da Universidade Estadual de Campinas, para obtenção do título de Mestre em Odontologia. Área de Farmacologia, Anestesiologia e Terapêutica, Piracicaba, (2006).

## FIGURES

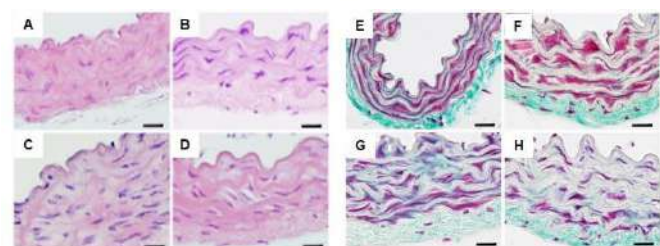
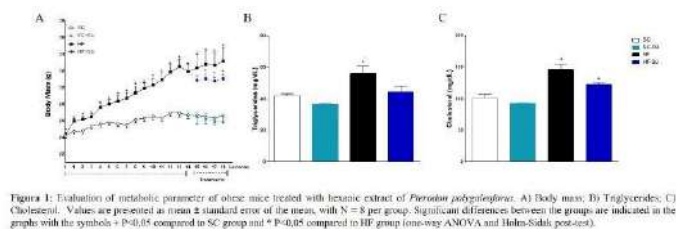


**Figure 2:** Photomicrographs of aorta sections of the different groups, stained with HE (panels A to D) and Gomori Trichrome (Panels E to H) technique. (A, E) Control group (SC); (B, F) and control group treated with Sucupira (SC-SU); (C, G) Control High Fat group (HF); (D, H) High Fat group treated with sucupira (HF-SU). Calibration bar 20µm.

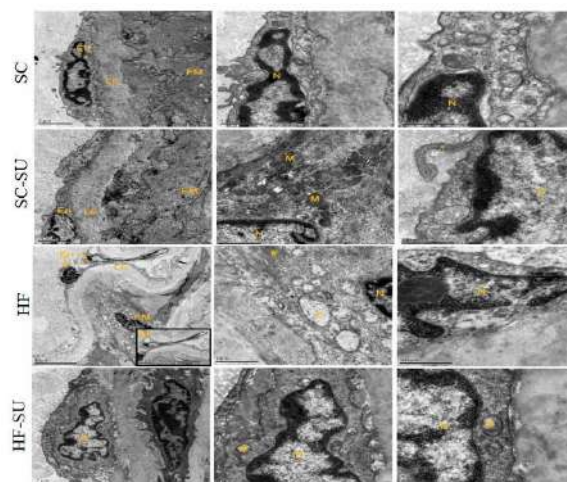


**Figure 4:** Ultrastructural analysis of aorta in mice obesity model treated with hexanic extract of *Pterodon polygaleifolius*. LE- elastic lamina, endothelium, N- nucleus, M- mitochondria, FM- muscle fiber, # -myofilaments, \* pseudopod. Calibration bar 20 µm.

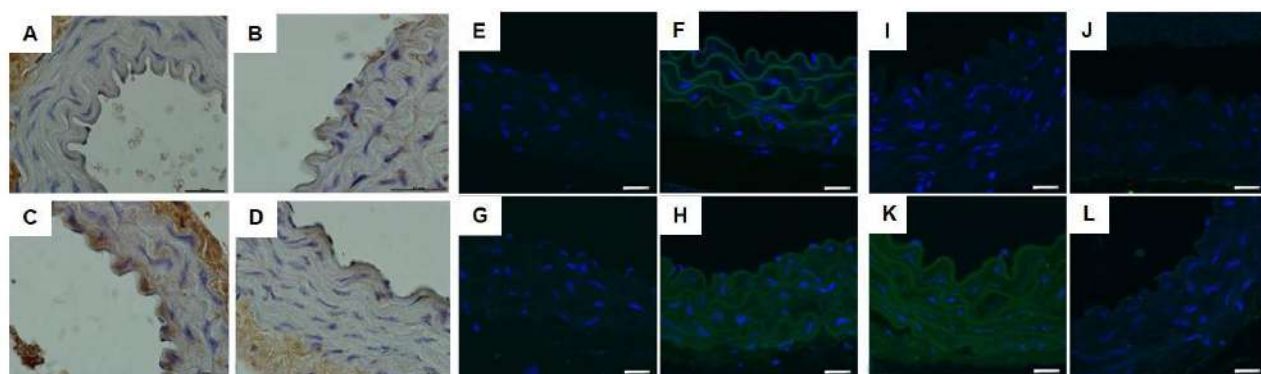


**Figure 3:** Evaluation of Intracellular Mechanism of obese mice treated with hexanic extract of *Pterodon polygaleifolius*. Panels A to D refers to the immunostaining of TNF- $\alpha$  in the aorta of the C57BL/6 mice; Panels E to H refers to Immunofluorescence for the protein indicative of mitochondrial PGC1- $\alpha$  biogenesis. In green, the immunostaining for PGC1- $\alpha$ . In blue, marking with DAPI, evidencing the nucleus and Panels I to L refers to evaluation of programmed cell death by immunofluorescence for Cytochrome C. In green, the immunostaining for Citochrome C. In blue, DAPI labeling, evidencing the nucleus. (A, E, I) Control group (SC); (B, F, J) and control group treated with Sucupira (SC-SU); (C, G, K) Control High Fat group (HF); (D, H, L) High Fat group treated with sucupira (HF-SU). Calibration bar: 25µm to TNF- $\alpha$  and 20µm to PGC1- $\alpha$  and Cytochrome C.



## Use of microscopy to study the biological effects induced by a novel sirtuin inhibitor on *Leishmania amazonensis*

Silva, G.S.<sup>1,2\*</sup>, Verçoza, B.R.F.<sup>1,2,3</sup>, Bracher, F.<sup>4</sup>, De Souza, W.<sup>2</sup> and Rodrigues, J.C.F.<sup>1,2,3</sup>

<sup>1</sup> Núcleo Multidisciplinar de Pesquisas em Biologia, NUMPEX-Bio, Campus Prof. Geraldo Cidade, Universidade Federal do Rio de Janeiro, Duque de Caxias, RJ, Brazil.

<sup>2</sup> Instituto de Biofísica Carlos Chagas Filho, UFRJ, Brasil

<sup>3</sup> Instituto Nacional de Ciência e Tecnologia de Biologia Estrutural e Bioimagem, Rio de Janeiro, Brazil.

<sup>4</sup> Department of Pharmacy, Center for Drug Research, Ludwig-Maximilians-University, Munich, Germany

Leishmaniasis is a disease caused by protozoan parasites of *Leishmania* genus distributed worldwide [1]. The clinical manifestations of leishmaniasis depend on the host immune system and the parasite species. Then, there are cutaneous, mucocutaneous and visceral leishmaniasis, which has important economic and social impact and should be fatal if not treated. However, there are some problems in chemotherapy, such as high toxicity rates, high cost and the routes for drug administration. Therefore, this disease needs attention for the identification of new chemotherapeutic targets, which are less toxic and more accessible to patients [2]. In this scenario, class III deacetylase histones (sirtuins) are proteins present in some cellular compartments, such as the nucleus, mitochondria and cytosol. The sirtuins can act in several cell signaling pathways, energetic metabolism, cytoskeletal dynamics and gene transcription [3]. In addition, there are 7 sirtuins (SIRT1-7) in humans and only one sirtuin, SIRT-2, was found in *Leishmania* with 46% similarity [4]. The present study evaluated the effects of NIH119, a novel sirtuin inhibitor, in the growth, morphology, ultrastructure and cell cycle of *Leishmania amazonensis* promastigotes and intracellular amastigotes. Promastigotes were significantly affected by the treatment, presenting an IC<sub>50</sub> value of 457 nM at 48 h of exposure to the compound. NIH119 was also active against intracellular amastigotes. Optical microscopy and scanning electron microscopy revealed changes in the cell body morphology of the promastigotes. Immunofluorescence microscopy indicated possible abnormal chromatin condensation and increase in the number of lipid bodies, which was also observed by transmission electron microscopy. Furthermore, images also indicated presence of several small vesicles inside the flagellar pocket, indicating a possible increase in the secretory pathway. Cell cycle analysis by flow cytometry revealed a significant effect between 24 and 48 h of treatment, which resulted in an increase in number of promastigotes in super/G2 phase with a concomitant decrease in G0/G1 phase, indicating a cell cycle arrest at cytokinesis. Taken together, all the results obtained here indicated sirtuins as a promising target for the development of new chemotherapeutic agents against leishmaniasis.

## REFERENCES

- [1] Rodrigues, J. C. F., Godinho, J. L. P., & de Souza, W. (2014). In *Proteins and Proteomics of Leishmania and Trypanosoma* (pp. 1-42). Springer, Dordrecht.
- [2] PACE, David. *Journal of Infection*, v. 69, sup. 1, p. S10-S18, 2014.

- [3] Religa, A. A., & Waters, A. P. (2012). *Molecular and biochemical parasitology*, 185(2), 71-88.
- [4] Mittal, N., Muthuswami, R., & Madhubala, R. (2017). *PLoS neglected tropical diseases*, 11(5), e0005590.
- [5] This research was supported by CNPq (Brazil).

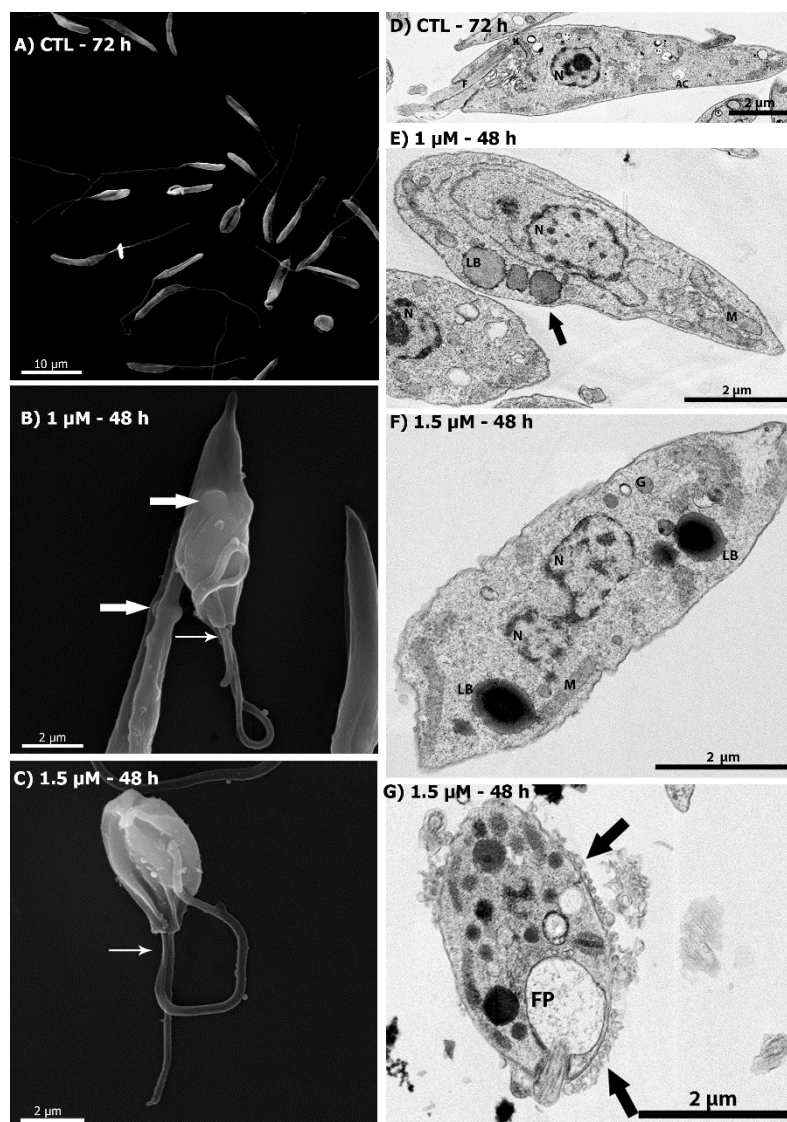


**Fig.** Scanning electron microscopy (A-C) and ultrathin sections (D-G) of *Leishmania amazonensis* promastigotes. (A) Control parasites after 72 h of growth. (B) Parasites treated with 1 μM and (C) 1.5 μM NIH119 for 48 h. Some images indicated that the treatment with NIH119 induced a significant swelling of the medial region of the cell body where the nucleus is located (B), however, we also observed promastigotes presenting a smaller and rounded cell body (C). Alterations in the flagellum (small arrow) and presence of membrane protrusions (arrow) were also observed. (D) Control parasites after 72 h of growth. (E) Parasites treated with 1 μM and (F, G) 1.5 μM NIH119 for 48 h. NIH119 induced different ultrastructural alterations such as: 1) increase in the number of lipid bodies; 2) abnormal chromatin condensation and 3) possible presence of vesicles (arrows) close to membrane and in the flagellar pocket. Nucleus (N), flagellar pocket (FP), kinetoplast (K), mitochondria (M), lipid body (LB), flagellum (F).



## Spermiogenesis in an invasive *Drosophila* species in Brazil

Guilherme S. S. S. Tonelli<sup>1\*</sup>, Ingrid M. S. Gracielle<sup>1</sup>, Sônia Nair Bão<sup>1</sup>

<sup>1</sup>. Laboratório de Microscopia Eletrônica, Departamento de Biologia Celular, Instituto de Ciências Biológicas, Universidade de Brasília, Brasil.\*E-mail: Guistonelli@gmail.com

It is commonly accepted that spermatozoon ultrastructure reveals taxonomic and phylogenetic relationships amongst species. Scientists consider possible to determine the phylum (and in some cases, species) of a male specimen just by examining the bearer's spermatozoa morphology [1]. Such relationships concerning phylogeny and ultrastructural variation, however, are not tested thoroughly in *Drosophila*. Considering the importance of those flies as a model for the study of several fields, it could be useful to understand the relationship between sperm cells and evolution. The main difficulty remains the fact that *Drosophilidae* is a vast group comprising more than a thousand species. This study aims to describe for the first time the morphology of *D. nasuta* spermatozoa, invasive species to Neotropical region recently reported in Brazil [2], and might as well cooperate in descriptive efforts to further elucidate above mentioned questions. Specimens were submitted to cold lethargy and dissected. Testis were photographed fresh in a Leica M205C stereomicroscope. For Transmission Electron Microscopy (TEM), after overnight fixation in Karnovsky (2% glutaraldehyde, 2% paraformaldehyde, 5 mM CaCl<sub>2</sub>, 3% sucrose, 0.1 M sodium cacodylate buffer, pH 7.2) and subsequent post-fixation in osmium tetroxide 2% and potassium ferrocyanide 1.6% in sodium cacodylate buffer 0.2M. Samples were stained in uranyl acetate 0.5% and dehydrated in acetone gradual series (30%-100%) before being embedded into Spurr resin. Ultra-thin sections were contrasted with uranyl acetate and analyzed under JEOL-1011. For Scanning Electron Microscopy (SEM) (Jeol-7001), after fixation in Karnovsky, testis were cut open on a coverslip covered with poly-L-lisine, post-fixed, dehydrated in acetone, submitted to a critical dryer and metal coated with platinum. Spermiogenesis occurs into a pair of testicles composed of four spirals (Fig.1), limited from the outside by a two cell layer rich in tracheoblasts (Fig. 2). Each cyst is delimited by cystic envelope cells, and inside them, 64 spermatozoa mature displayed side by side (Fig.3). Envelope cells are rich in mitochondria and endoplasmic reticulum (Fig. 4). Cytoplasmic bridges are noted in early spermiogenic stages in spermatozoa. The tail is flanked by two mitochondrial derivatives, the smaller is oval and the major is triangular and contains paracrystalline material on its core. The shape of such derivatives vary wildly in drosophilids. Axoneme presents the standard 9 + 9 + 2 microtubules (Fig. 5). Compared to other species, *D. nasuta* contains a limited number of spermatozoa per cyst, we understand this as indicative of a highly efficient differentiation process for this species. Considering the morphological variation in drosophilids, species-specificity is likely not only contained in the genetic material of sperm cells but just as well on their ultrastructure. Spermatozoa are highly adapted to survive in males (including gonadal maturation time vs cell complexity theoretical ratios and storage conditions) and be effective on fecundation events (highly complex situations with overwhelming pressures over cell viability).

[1] Jamieson, B. The Ultrastructure and Phylogeny of Insect Spermatozoa. Cambridge University Press. 1987

[2] Vilela, C. V. e Goñi B. Revista Brasileira de Entomologia. 59 346–350. 2015

This research was supported by UnB, CNPq, CAPES, FAP-DF and FINEP



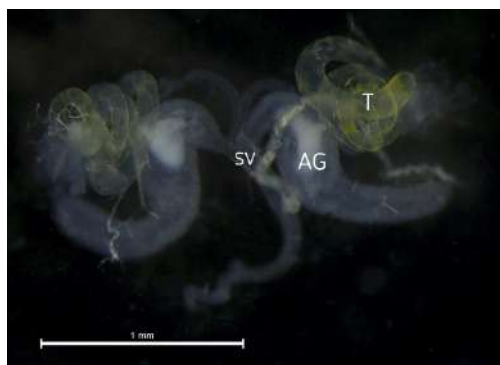


Figure 1. Reproductive system.  
Abbreviations: Seminal vesicle (SV);  
Accessory Gland (AG); Testis (T).

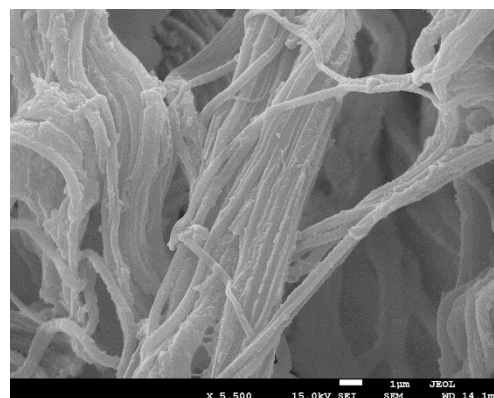


Figure 2. Scanning Electron  
Microscopy of spermatozoa inside a  
ruptured cyst.

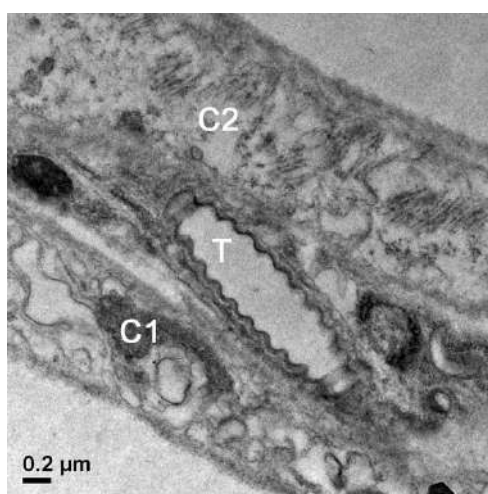


Figure 3. Testicular wall.  
Abbreviations: Cell of the outermost  
layer (C1); Cell of the innermost  
layer (C2); Tracheoblast (T).

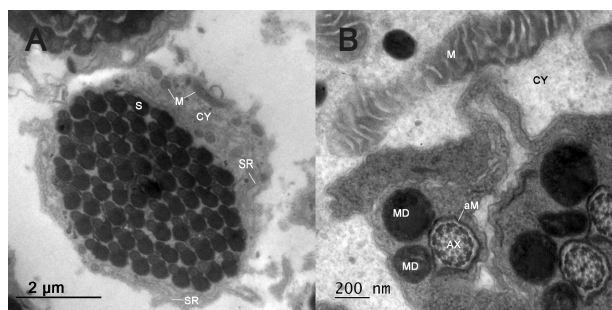


Figure 4. Transverse sections. Cyst containing  
64 cells (A). Presence of mitochondria in cystic  
cells (B). Abbreviations: Spermatozoon (S);  
Mitochondria (M); Cystic Cell (CY);  
Mitochondrial Derivative (MD); Axoneme  
(AX); Smooth Endoplasmic Reticulum (SR);  
Membrane of the Axoneme (aM).

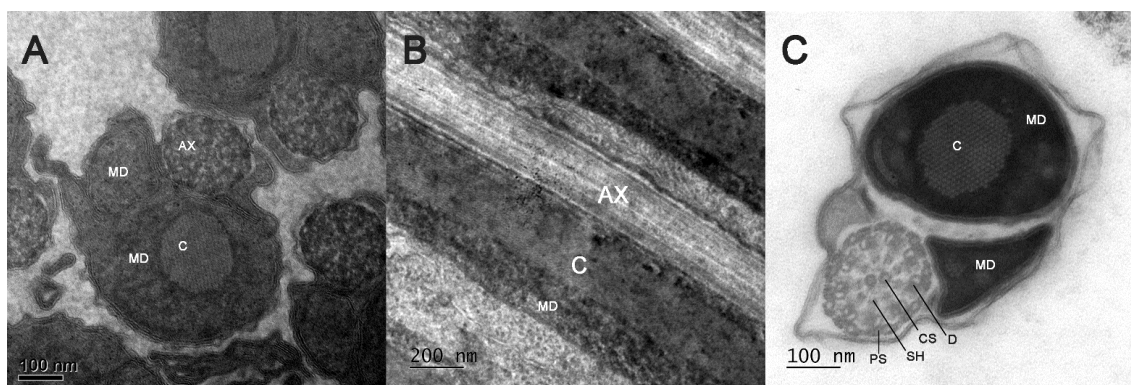


Figure 5. Sections of the Tail. Transverse section of crystalline material being deposited  
in the major mitochondrial derivative (A), longitudinal section of the tail (B) and cross  
section of mature spermatozoon (C). Abbreviations: Mitochondrial Derivative (MD);  
Axoneme (AX); Paracrystalline material (C); Peripheral Singlet (PS); Spoke Head (SH);  
Central Singlets (CS); Doublets (D).



## FIBROBLAST CHARACTERIZATION FOR THREE BRAZILIAN WILD CATS

Letícia Gobbi Arantes<sup>1</sup>, Guilherme S. S. S. Tonelli<sup>1</sup>, Heidi Christina Bessler<sup>2</sup>,  
Carlos Frederico Martins<sup>2</sup>, Sônia Nair Bão<sup>1</sup>

<sup>1</sup> Laboratório de Microscopia Eletrônica, Departamento de Biologia Celular, Instituto de Ciências Biológicas, Universidade de Brasília. \*E-mail: [le.gobbi@gmail.com](mailto:le.gobbi@gmail.com)

<sup>2</sup> Laboratório de Reprodução Animal do Centro de Transferência de Tecnologia em Raças Zebuínas de Aptidão Leiteira (CTZL)- EMBRAPA

Germplasm banks overcome barriers of time and space, promoting the possibility of storage of genetic material for generations to come. On what concerns wild species, such banks are an efficient way of reducing loss of genetic diversity, aiding species conservation efforts[1]. Cats are of key importance to wildlife conservation. The Fundação Jardim Zoológico de Brasília maintains a germplasm bank as integrating part of an ongoing conservation program. Cells used in this research were obtained from this bank. Fibroblasts are the most commonly used cell in cryopreservation as it is easily obtained. Also, this cell type is extremely appropriate for SCNT [2]. Fibroblasts of *Leopardus colocolo*, *Leopardus tigrinus* and *Panthera onca* were characterized, after thawing (approved under UnBDOC nº 66706/2016). Cells were cultured on Petri dishes added 2mL of DMEM before being analyzed under Light Microscopy. For Transmission Electron Microscopy (TEM), cells were fixed overnight on Karnovsky (2% paraformaldehyde and 2% glutaraldehyde diluted in 0.1M sodium cacodylate buffer, pH 7.2) and post-fixed on osmium tetroxide 2%, potassium ferricyanide 1.6% in sodium cacodylate buffer 0.2 M, for one hour. For TEM, in bloc contrast was made using uranyl acetate 0.5% for two hours followed by gradual dehydration on acetone and further infiltration of Spurr resin. Ultrathin sections were contrasted with uranyl acetate and lead citrate before analysis on Jeol-1011 80kv. For Scanning Electron Microscopy (SEM), after fixation, post-fixation and dehydration, samples were submitted to Critical Point Drying and metal coating. The three species present morphological variation. *L.colocolo* cells are fusiform and highly ramificated (Fig.1). *L. tigrinus* cells are more spherical, with short ramifications (Fig.2). *P. onca* cells are fusiform and presents long ramifications (Fig.3). In conformity to literature [3] fibroblasts of the three species presented irregular cytoplasmic prolongations, big nucleus and oval shape, also, nucleoles are present (Figs.1,3). Cytoplasm presented endoplasmic reticulum. The Golgi complex was hardly noted in samples, even though this organelle is usually present on fibroblasts[3]. Mitochondria were also hardly noted in the samples, apart from *L. colocolo* (Fig.1). Cells presented several secretion granules and vacuoles, indicating intense cell activity. *L. tigrinus* presented greater membrane expansions. Morphology is a great indicative of whether the cryopreservation protocols used in germoplasm banks are successful or not. This study aims to facilitate the establishment of future cryopreservation protocols and possibly SCNT procedures for wild Brazilian Cats.

[1] Machado, LC. et al. Pesqui. Vet. Bras, São Paulo, v. 1, n. 36, p.61-66 2016

[2] Leon-Quinto, Trinidad, et al. Anim Reprod Sci (112), 347-361. 2009

[3] Srirama, G.; Bligliardi, P.L.; Bligliardi-QI, M. Eur. J. Cell. Biol. European, p. 483-512. 2015

[4] UnB, FAP, FINEP, CNPQ and CAPES for financial support.

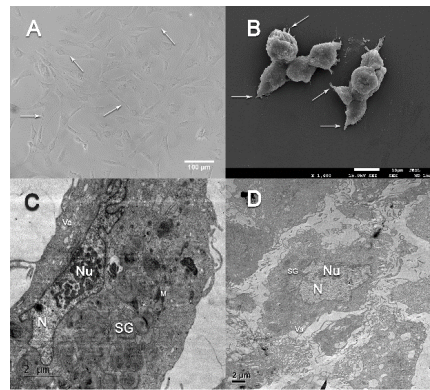


Figure 1. *L. colocolo* cells seen in Light Microscopy (A), Scanning Electron Microscopy (B) and Transmission Electron Microscopy (C,D). Cells ramifications are indicated by arrows. Abbreviations: Nucleus (N), Nucleole, (Nu), Vacuoles (Va), Secretion Granules (SG), Mitochondria (M).

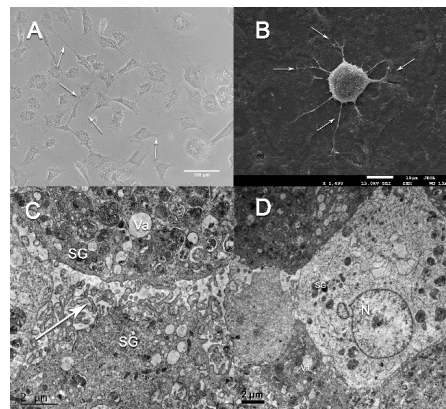


Figure 2. *L. tigrinus* cells seen in Light Microscopy (A), Scanning Electron Microscopy (B) and Transmission Electron Microscopy (C,D). Cells ramifications are indicated by arrows. Abbreviations: Nucleus (N), Nucleole (Nu), Vacuoles (Va), Secretion Granules (SG).

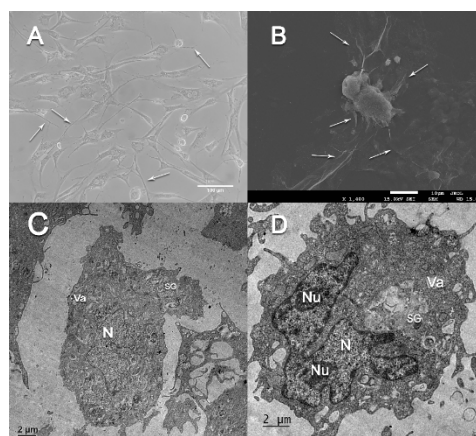


Figure 3. *P. onca* cells seen in Light Microscopy (A), Scanning Electron Microscopy (B) and Transmission Electron Microscopy (C,D). Cells ramifications are indicated by arrows. Abbreviations: Nucleus (N), Nucleole (Nu), Vacuoles (Va), Secretion Granules (SG).

# A $\mu$ CT And TD-NMR Approach To The Probing Of Negative Spaces In A Bamboo Sample

\*Haimon Alves<sup>1</sup>, Elton Rodrigues<sup>2</sup>, Omar Pandoli<sup>2</sup>, Roberto Neto<sup>2</sup>

<sup>1</sup>. Physics Institute, UERJ, Rio de Janeiro, Brasil [alveshaimon@gmail.com](mailto:alveshaimon@gmail.com)

<sup>2</sup>. Chemistry Department, PUC-RJ, Rio de Janeiro, Brasil

## Abstract

Bamboo (*Dendrocalamus giganteus*) is a widely cultivated plant that holds in its anatomy micrometer-sized vascular channels and cellular structures that allows the efficient circulation of water and nutrients, endowing the organism with a remarkably fast growth. The mentioned microstructures can be harvested, as demonstrated recently, as a natural template for microfluidics applications in chemical synthesis. Thus, it became of interest the knowledge of the kinetics of the imbibition and spatial distribution of fluid inside the vascular channels and other structures inside the bamboo plant. Here, we employed a combination of X-ray microtomography ( $\mu$ CT) and proton time-domain NMR (TD-NMR) to identify, measure and investigate the negative spaces embedded in the plant tissue.

## Method

### *3D X-ray microtomography (3D $\mu$ CT)*

The 3D images of bamboo samples were obtained using a Bruker Skyscan microtomograph 1173 as to visualize and quantify the 3D structure. The experimental parameters for all samples were: Pixel size 5  $\mu$ m; 50 kV Voltage; 8 W Power; 1.0 s of exposure time and 1440 projections.

### *TD-NMR measurements*

All measurements were performed on a MARAN Ultra (Oxford Instruments®) low-resolution NMR spectrometer operating at 0.54 T (23 MHz, proton Larmor frequency) equipped with a 18 mm diameter probe at  $30 \pm 1^\circ\text{C}$ . The  $90^\circ$  (p90) RF pulse was calibrated to 7.5  $\mu$ s and the  $180^\circ$  (p180) pulse was calibrated to 15  $\mu$ s. Coil dead time and filter stabilization time were set to 6.0 and 3.0  $\mu$ s, respectively. We employed a CPMG pulse sequence with  $\tau = 300 \mu$ s and about 2048 echoes. The intensity of the first echo as a function of time was employed in this study to determine the kinetic parameters discussed below.

## Results

### *Image processing and analysis of $\mu$ CT images*

The  $\mu$ CT images were processed using the CTan© software (version 1.18.8.0, Bruker, 2018), and Avizo© software (version 9.0.1, FEI, 2018). Image post-processing was done to reduce noise and average the intensities on the image. Regions of interest were defined to reduce computational requirements.

We investigated the molecular mobility of some probe fluids (namely water) while confined inside the plant's cellular and vascular environments (Figure 1). The results were better analyzed and interpreted with the aid of the quali-quantitative data provided by the processing of the  $\mu$ CT images. We were able to ascribe two main fluid molecules populations to spaces observed directly via  $\mu$ CT, thus constricting our interpretation to physically meaningful explanations.

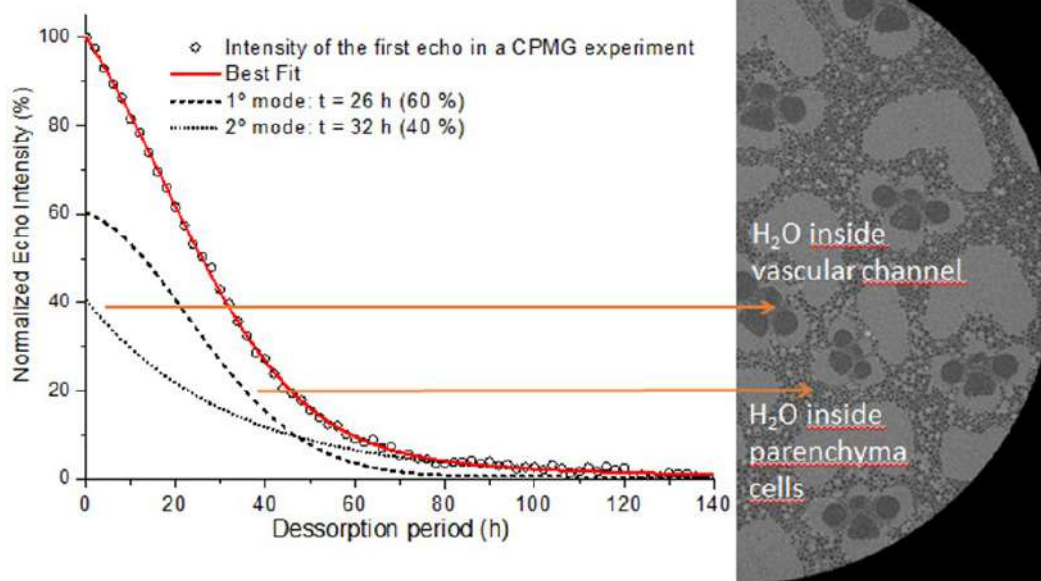


Figure 1: TD-NMR data of a CPMG experiment in a bamboo sample can be tentatively correlated with physical, rational spaces inside the sample.

### Conclusion

Results obtained via the TD-NMR experiments, using a CPMG pulse sequence to investigate the molecular mobility of some probe fluids (namely water) while confined inside the plant's cellular and vascular environments, were better analyzed and interpreted with the aid of the quali-quantitative data provided by the processing of the  $\mu$ CT images. We were able to ascribe two main fluid molecules populations to spaces observed directly via  $\mu$ CT, thus constricting our interpretation to physically meaningful explanations.

### References:

- [1] Elton Rodrigues, Roberto Neto, Pedro Sebastião, Maria Tavares, "Real-time monitoring by proton relaxometry of radical polymerization reactions of acrylamide in aqueous solution", *Polym Int*, vol 67 (6) (2018) 675-686.
- [2] Druval Santos de Sá, Rodrigo de Andrade Bustamante, Carlos Eduardo Rodrigues Rocha, Verônica Diniz da Silva, Elton Jorge da Rocha Rodrigues, Camilla Djenne Buarque Müller, Khosrow Ghavami, Alessandro Massi, Omar Ginoble Pandoli "Fabrication of Lignocellulose-Based Microreactors: Copper-Functionalized Bamboo for Continuous-Flow CuAAC Click Reactions", *ACS Sustainable Chem. Eng.*, vol 7(3) (2019) 3267-3273.
- [3] Ginoble Pandoli, O., Martins, R.S., De Toni, K.L.G. et al. *J Coat Technol Res* (2019).



## Caracterização Morfológica dos Espermatozoides em Espécies do Gênero *Triatoma* (Insecta, Hemiptera, Reduviidae, Triatominae)

Maria Luiza Ribeiro de Oliveira<sup>1</sup>, Daniel Cardoso Portela Camara<sup>2</sup>, Simone Patrícia Carneiro de Freitas<sup>1\*</sup> and Jacenir Reis Santos-Mallet<sup>1,3</sup>

<sup>1</sup>. Laboratório Interdisciplinar de Vigilância Entomológica em Díptera e Hemiptera, Instituto Oswaldo Cruz, Fiocruz, Rio de Janeiro, Brasil.

<sup>2</sup>. Laboratório de Mosquitos Transmissores de Hematozoários, Instituto Oswaldo Cruz, Fiocruz, Rio de Janeiro, Brasil.

<sup>3</sup>. Escritório Regional Fiocruz Piauí, Teresina, Brasil.

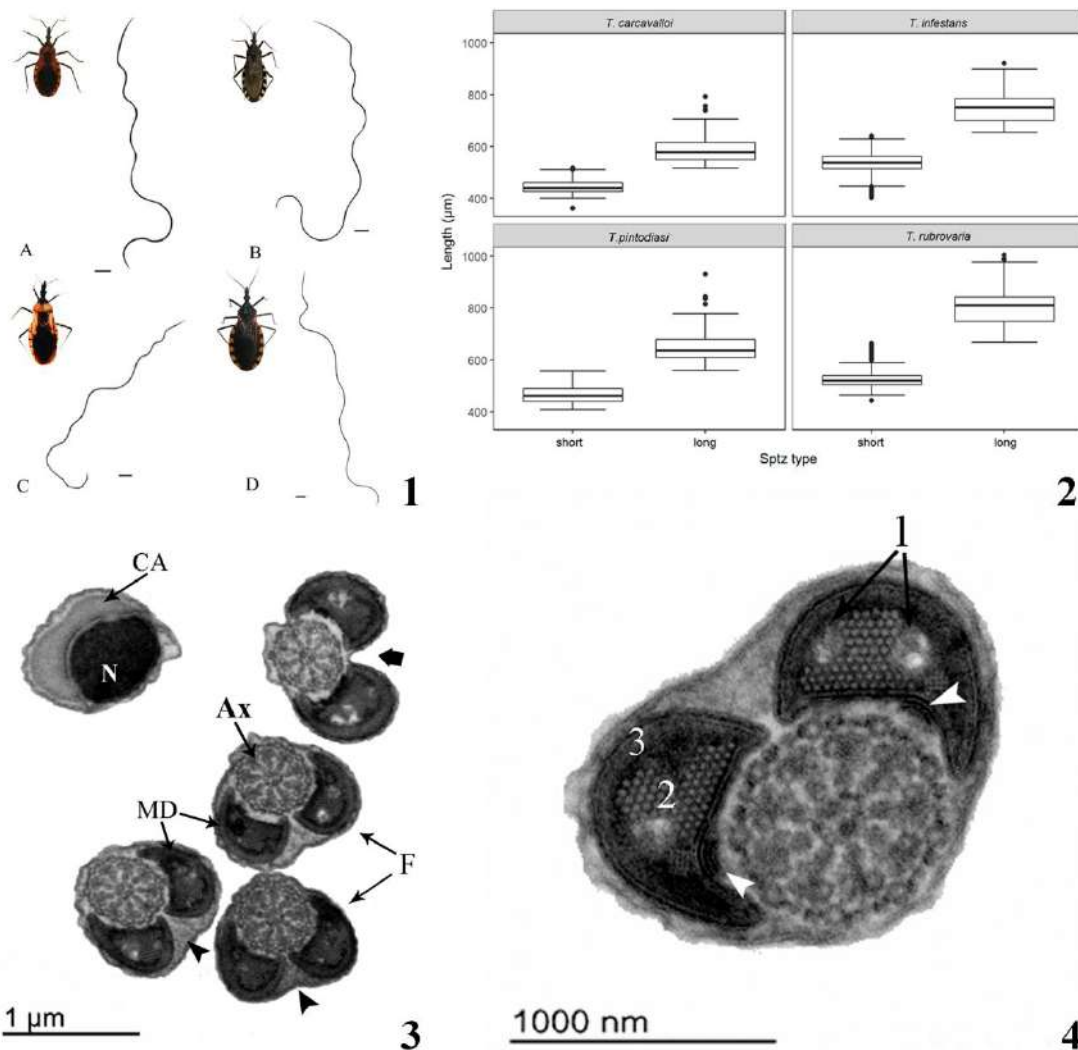
\* sfreitas2@gmail.com

Spermatozoa are among the most diverse cell types, and their morphologies often provide data that can be used to reliably evaluate phylogenetic relationships [1]. They can also help to clarify the nature of ‘specific complexes’, which are common among triatomines [2]. In the present study, we evaluated the copulation behavior of *Triatoma rubrovaria* Blanchard 1843 (Hemiptera: Reduviidae: Triatominae) and the structural morphology of sperm from *T. carcavalloei* Jurberg Rocha & Lent, 1998, *T. infestans* Klug, 1834, *T. pintodiasi* Jurberg Cunha & Rocha, 2013, and *T. rubrovaria* (Fig. 1). Copulatory behavior was described from the moment males and females genitalia joined until they separated. Insemination was confirmed by the presence of a spermatophore in the female’s bursa copulatrix. To measure their sperm, males were dissected and their seminal vesicles were removed, squashed on glass slides, and then spread, fixed, and observed under a photomicroscope. The images obtained were analyzed to measure the sperm. Seminal vesicles were also prepared for transmission electron microscopy. We performed K-means clustering separately for each species to group their sperm based on morphology. The differences in spermatozoa length among species of Triatominae, sperm types, and the interaction between species and sperm type were assessed with a two-way analysis of variance (ANOVA). The copulation time in *T. rubrovaria* was 3 to 5 min, which was sufficiently long for spermatophore transfer. All taxa showed polymorphic (short and long) sperm, with significant differences in the lengths of sperm among taxa (Fig. 2). Using electron microscopy, the sperm cells of the four taxa examined were found to have similar ultrastructural morphology: two or three crystalline bodies in the mitochondrial derivatives, and bridges attaching mitochondrial derivatives to the axoneme (Fig. 3 and 4), confirming the hypothesized synapomorphies of sperm within the suborder Heteroptera (Hemiptera).

[1] B.G.M Jamieson, Cambridge University Press, Cambridge, MA (1987).

[2] A.F. Baffa et al., Med. Vet. Entomol. 31 (2017) 192–199.

[3] This research was supported by Rudolph Barth Electron Microscopy Platform, IOC, Fiocruz and CAPES (Brazil).



Figures: [1] Schematic drawings of the sperm of members of the *Triatoma rubrovaria* subcomplex, including (A) *Triatoma carcavalloei*, (B) *Triatoma infestans*, (C) *Triatoma pintodiasi*, and (D) *Triatoma rubrovaria* (scale bars = 10  $\mu\text{m}$ ). [2] Boxplots of the measurements made of the sperm of the four species examined, divided up according to K-means clustering results. [3] Electromicrograph of *T. carcavalloei* sperm in cross-section. Ax: axial filament; CA: centriole adjunct; F: flagellum; MD: mitochondrial derivatives; N: nucleus; arrowhead: electron-dense area; arrow: region of the flagellum not connected to the centriole. [4] Electromicrograph of *T. rubrovaria* sperm in cross-section. The axoneme and the three regions of the mitochondrial derivatives are highlighted: (1) two electron-dense areas, (2) the area containing crystalline material, and (3) the peripheral crystalline area. Arrowheads indicate bridges between the microtubules and the mitochondrial derivatives.

## Thermostability of Magnetite Magnetosomes: Implications for Fossil Record And Biotechnology

Jefferson Cypriano<sup>1\*</sup>, Mounib Bahri<sup>2</sup>, Walid Baazis<sup>2</sup>, Kassioyé Dembelé<sup>2</sup>, Pedro Leão<sup>1</sup>, Dennis A. Bazylinski<sup>3</sup>, Fernanda Abreu<sup>1</sup>, Ovidiu Ersen<sup>2</sup>, Marcos Farina<sup>4</sup> and Jacques Werckmann<sup>4,5</sup>

<sup>1</sup> Instituto de Microbiologia Paulo de Góes, Universidade Federal do Rio de Janeiro, Brazil

<sup>2</sup> Institut de Physique et Chimie des Matériaux de Strasbourg, Strasbourg, France

<sup>3</sup> School of Life Sciences, University of Nevada at Las Vegas, Las Vegas, USA

<sup>4</sup> Instituto de Ciências Biomédicas, Universidade Federal do Rio de Janeiro, Brazil

<sup>5</sup> Centro Brasileiro de Pesquisas Físicas, Rio de Janeiro, Brazil

[Jeffcy@micro.ufrj.br](mailto:Jeffcy@micro.ufrj.br)

Biomineralization is a process in which organism concentrate metal ions and synthesize crystalline structures [1, 2]. One group of organisms capable of biomineralization is the magnetotactic bacteria (MTB), the prokaryotic cells that respond to magnetic fields due to the presence of iron-rich intracellular nano-particles called magnetosomes. Each magnetosome is composed of magnetite ( $\text{Fe}_3\text{O}_4$ ) or greigite ( $\text{Fe}_3\text{S}_4$ ) crystals enveloped by a biological membrane [3]. Because of the stability of these particles in the environment after cell death, they contribute to sediment magnetization and may represent fossil record of ancient microbial ecosystems [4]. Due to their uniform size and shape, external lipid bilayer and unique magnetic properties, magnetosomes have been studied as tools for biotechnological application [5]. Therefore, the characterization of chemical changes of magnetosomes in harsh conditions is an important issue in biotechnological and paleogeography fields. Here we evaluated the magnetosomes thermostability in a temperature range between 150 and 500 °C subjected to oxidizing conditions using *in situ* conventional / scanning transmission electron microscopy, EDS and EELS. The results showed that magnetosome crystals are stable and structurally unaffected in temperatures up to 300 °C. When heated to temperatures between 300 and 500 °C, structural damage was observed in the magnetosomes crystalline structure. The electron energy loss near edge structure (ELNES) spectrum of magnetosome damaged areas indicated a change in the oxygen / iron ratio. This study shows that magnetosomes are thermostable in temperatures up to 300 °C and displays novel tools to investigate biogenic nanomaterials and potentially, their relation with environmental changes along geological periods.

### References:

- [1] Sogin, ML et al., Proc Natl Acad Sci USA 103 (2006) 12115–12120.
- [2] Pedrós-Alió, C, Ann ver Mar Sci 4 (2012) 449–466.
- [3] Lefèvre CT and Bazylinski DA, Microbiol Mol Biol Rev. 77(3) (2013) 497-526.
- [4] Kopp and Kirschvink, Earth-Science Rev. 86 (2008) 42–61.
- [5] Vargas et al., Molecules 23 (2018) 1–25.

We thank Unidade de Microscopia Multiusuário Padrón-Lins (UNIMICRO), UFRJ and Institut de Physique et Chimie des Matériaux de Strasbourg (IPCMS) for electron microscopy facilities; This work was supported by the Brazilian agencies CNPq, CAPES and FAPERJ.

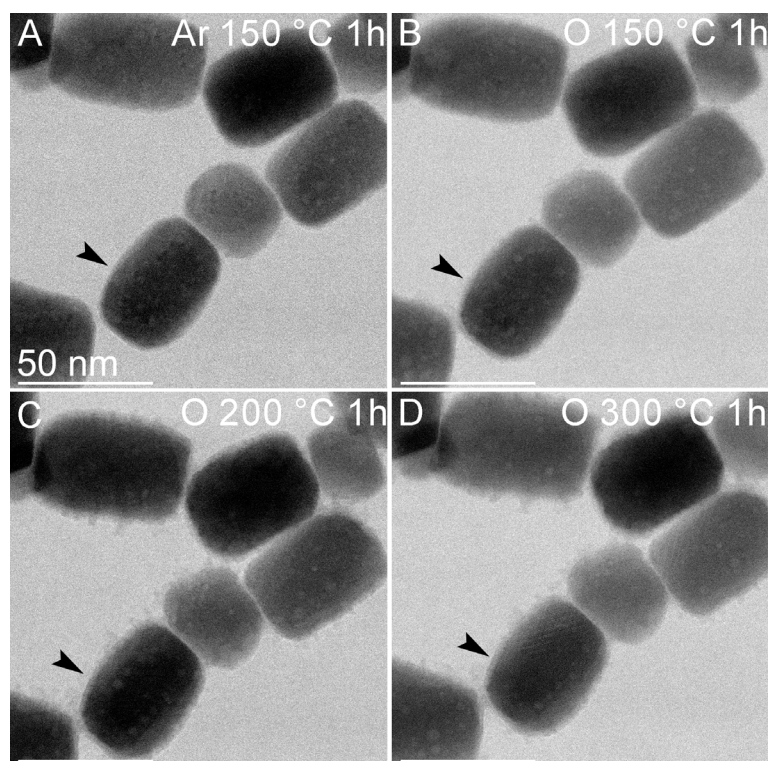


Figure 1. Evaluation of the thermostability of magnetosomes by BF-STEM. (A) Magnetosomes subjected to 150°C for 1 hour in an argon (Ar) atmosphere. (B) Magnetosomes subjected to 150°C for 1 hour in an O<sub>2</sub> atmosphere. (C) Magnetosomes subjected to 200°C for 1 hour in an O<sub>2</sub> atmosphere. (D) Magnetosomes subjected to 300°C for 1 hour in an O<sub>2</sub> atmosphere. The arrowheads in A-D were included for comparison of the thicknesses of the magnetosome membranes. Images show that membranes are apparent in (A-D) and present a non-uniform aspect around the magnetite crystal (arrows).

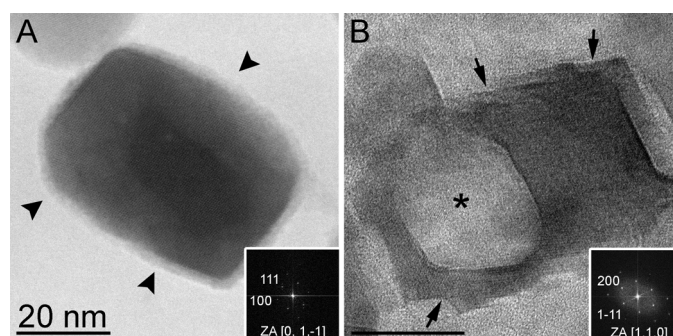


Figure 2. HRTEM images of magnetosomes after *in situ* heating experiment when subjected to 300°C and 500°C exposed to O<sub>2</sub>. (A) High-resolution-TEM image showing crystal structure after 300°C exposed to O<sub>2</sub>, without alteration and the presence of a membrane (arrowheads). Inset: FFT from the image displaying distances and angles compatible with theoretical magnetite structure. (B) Image of a magnetosome after heating to 500°C and exposed to O<sub>2</sub>, displaying a large cavity (asterisk) and border defects (arrows). Inset: FFT from the image-compatible with magnetite or maghemite, based on magnetite cubic pattern with 8.396 Å unit cell parameter and structure of maghemite derived from magnetite structure.





## Methods for determining the concentration of green gold nanoparticles

Laryssa Pinheiro Costa Silva<sup>1</sup>, Wanderson Juvencio Keijok<sup>2</sup> and Marco Cesar Cunegundes Guimarães<sup>3\*</sup>

<sup>1,2,3</sup>. Federal University of Espírito Santo, Department of Morphological Sciences, Vitória, Brazil.

\*marco.guimaraes@ufes.br

There is great interest in the quantification of nanoparticles from their applications in nanobiotechnological processes.<sup>1</sup> Traditionally, characterization methods for metal nanoparticles have included: dynamic light scattering (DLS); transmission electron microscopy (TEM); and inductively coupled plasma mass spectroscopy (ICP-MS). Some authors use the optical properties of spherical AuNPs in aqueous solutions to calculate for nanoparticle concentration and diameter, from UV-vis spectra.<sup>3</sup> This work want to evaluate which technique would present higher fidelity of the results of the nanoparticle concentration when compared to the technique considered gold standard (ICP-MS) and lower cost of sample preparation and analysis. The gold nanoparticles used for this analysis were synthesized using  $2.5 \times 10^{-4}$  mol/L solution of tetrachlorouronic acid (HAuCl<sub>4</sub>) and a 17% Epigallocatechin -3-gallate (EGCG), the ratio 3:1. To calculate the diameter of the AuNPs, images obtained by MET were used. The concentration of gold present in the nanoparticles was verified using ICP-MS. Three methods of calculation were used for the concentration of AuNp's: Method 1 of Haiss et al. 2007; Method 2 of Gadogbe et al. 2013 and Method 3, of Wang et al 2014. It was observed that the concentration of nanoparticles obtained by the method 2 and 3 calculations was 1.72 nM and the concentration obtained in method 1 was 1.94 nM. This difference could have occurred because in the method 1, the partition coefficient of nanoparticles synthesized is note the same for NP-EGCG. It's important to highlight that the results obtained by the ICP-MS analysis showed that the concentration of gold present in the nanoparticle solution is very close to the concentration of gold initially used. Thus, for the calculation of gold nanoparticles synthesized from EGCG it is possible to use the equations suggested by Gadogbe et al. 2013 and Wang et al 2014 and consider that all the gold used in the reaction was consumed.

### REFERENCES

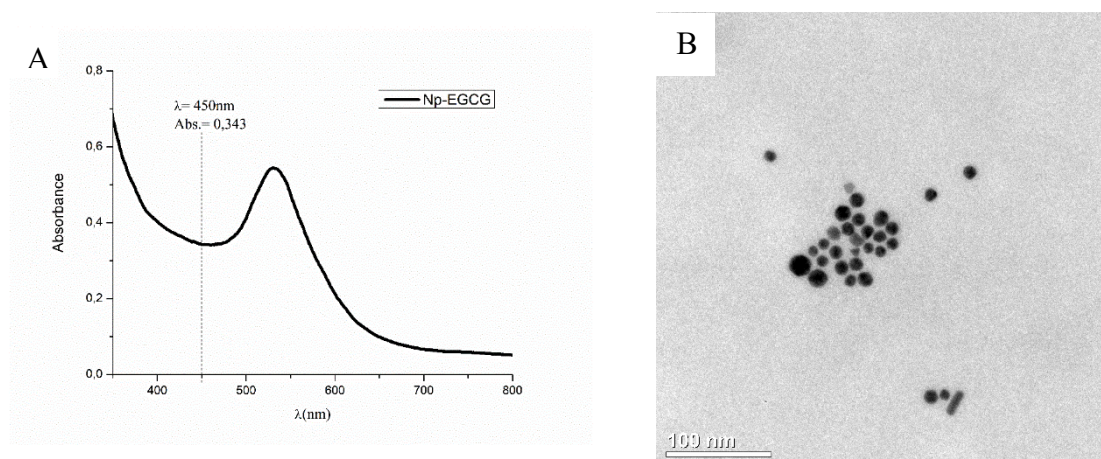
- [1] R. Allabashi et al., J. Nanopart. Res. 11 (2009) 2003.
- [2] D.R. Wilson et al., Methods Mol Biol. 1570 (2007) 31.
- [3] W. Haiss et al., Anal. Chem. 79 (2007) 4215.
- [4] M. Gadogbe et al., Anal. Bioanal. Chem. 405 (2013) 413.
- [5] Wang et al., Chin. Sci. Bull. 59 (2014) 1816.
- [6] This research was supported by CNPq (Brazil), Ministry of Science and Technology, the Ministry of Science and Technology and Foundation Support Research and Innovation of Espírito Santo. This work used the equipment facilities at the Laboratory of Cellular Ultrastructure Carlos Alberto Redins and the Laboratory of Biomolecular Analysis (LABIOM) at Federal University of Espírito Santo.

**Table 1.** Values for the calculation of concentration of gold nanoparticles of Epigallocatechin-3-gallate (Np-EGCG).

Np-EGCG	
Abs 450	0,343
Diameter (nm)	14,54
$\epsilon_{450}$ (Haiss et al. 2007)	$1,76 \times 10^8$
Au [mg/L]	32,327
Au [mol/L]	$1,641 \times 10^{-4}$

**Table 2.** Values obtained from the concentration of gold nanoparticles of Epigallocatechin-3-gallate (Np-EGCG) from the equations suggested by the authors studied.

Np-EGCG [nM]	
Haiss et al. 2007	1,94
Godagbe et al. 2013	1,72
Wang et al.2014	1,72

**Figure 1. a)** UV-Vis spectrum of Np-EGCG. **b)** Image of the Np-EGCG obtained by transmission electron microscopy (TEM).

## Anti-*Sporothrix* Effect of Ibuprofen Combined with Amphotericin B

Borba-Santos, L.P.<sup>1\*</sup>, Rozental, S.<sup>1</sup>

<sup>1</sup>. Laboratório de Biologia Celular de Fungos, Instituto de Biofísica Carlos Chagas Filho, Universidade Federal do Rio de Janeiro, Rio de Janeiro, Brazil.

\*luanaborba@biof.ufrj.br

The *Sporothrix* genus includes important human pathogens that cause sporotrichosis - neglected endemic mycoses with limited therapeutic options. The first-line treatment against human sporotrichosis is itraconazole, while amphotericin B is the only option to treat severe disease (as pulmonary, meningitis or disseminated manifestations). In this study, we evaluate the anti-*Sporothrix* effect of ibuprofen, an anti-inflammatory drug commonly used as antipyretic and analgesic medication. We determined the *in vitro* efficacy of ibuprofen alone and in combination with itraconazole and amphotericin B against *Sporothrix brasiliensis* and *Sporothrix schenckii*, the main etiological agents of sporotrichosis in Brazil and Latin America, respectively. Minimum inhibitory concentration (MIC) of ibuprofen alone and combined with amphotericin B or itraconazole was determined against pathogenic yeast phase, using reference isolates and clinical strains. For scanning electron microscopy (SEM) visualization, *S. schenckii* yeasts of a clinical isolate were treated with synergic concentrations of ibuprofen and amphotericin B, washed in PBS and fixed in 2.5% glutaraldehyde and 4% formaldehyde in 0.1 M cacodylate buffer. Cells were washed in cacodylate buffer, adhered to poly-L-lysine-coated glass coverslips, dehydrated in a graded ethanol series, critical-point-dried in CO<sub>2</sub> and coated with gold. Images were obtained in a FEI Quanta 250 scanning electron microscope (FEI Company, USA). As a single agent, ibuprofen inhibited *Sporothrix* growth with a median MIC value of 256 µg/ml. The best synergistic effect was obtained when *Sporothrix* spp. was co-incubated with ibuprofen and amphotericin B, mainly against *S. schenckii*. The fourteen strains tested exhibited reduction in the amphotericin B MIC after co-incubation with ibuprofen and eight isolates exhibited synergism (Fractional Inhibitory Concentration Index  $\leq 0.5$ ). SEM analysis revealed that yeast-hyphae conversion was observed in untreated and treated cultures (Figure 1). However, hyphae and conidia of treated cultures exhibited altered morphology (Figure 1 D, F and H). The changes were more expressive after treatment with ibuprofen/amphotericin B combination, where a chlamydospore structure was observed (Figure 1 H, arrow). In summary, we demonstrated that ibuprofen, an anti-inflammatory drug, increases the *in vitro* activity of amphotericin B against *S. brasiliensis* and, mainly, *S. schenckii*. This relevant synergistic activity highlights the importance of expanding studies about clinical evaluation of this combined therapy, that may improve the treatment of human sporotrichosis in situation where amphotericin B is the only option.

This research was supported by CAPES, CNPq and FAPERJ (Brazil).

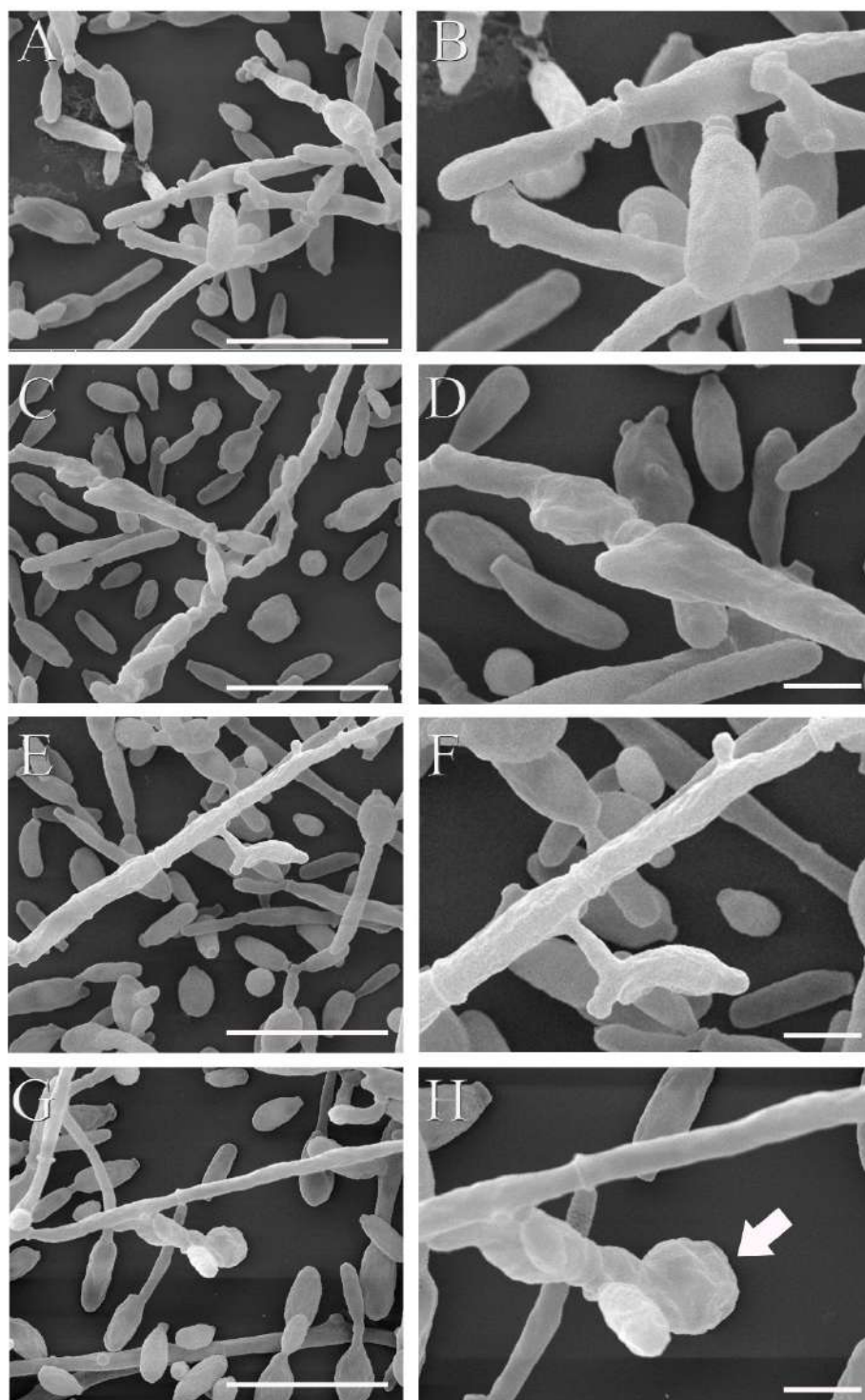


**Figure 1.** Ultrastructural alteration of *Sporothrix schenckii* on exposure to synergistic combination of ibuprofen and amphotericin B, evaluated by scanning electron microscopy. Untreated cells exhibit yeasts (A) and hyphae (B) with normal morphology, while samples treated for 48 h with 0.001 µg/ml amphotericin B (C, D) or 128 ibuprofen µg/ml (E, F) show hyphae and conidia with alterations (D, F). Exposure to ibuprofen/amphotericin B combination induced a chlamydospore structure (H, arrow). Bars: A, C, E, G: 10 µm; B, D, F, H: 2 µm.



## Ultrastructural Aspects of *Sporothrix brasiliensis* in feline claws

Alice Carvalho da Silva<sup>1</sup>, Luana P. Borba-Santos<sup>1\*</sup>, Beatriz Bastos Fonseca<sup>1</sup>, Kung Darh Chi Kung<sup>2</sup>, Fabiana Monti<sup>2</sup>, Marconi Rodrigues de Farias<sup>2</sup> and Sonia Rozental<sup>1</sup>.

<sup>1</sup> Laboratório de Biologia Celular de Fungos, Instituto de Biofísica Carlos Chagas Filho, Universidade Federal do Rio de Janeiro, Rio de Janeiro, Brazil.

<sup>2</sup> Escola de Ciências da Vida, Pontifícia Universidade Católica do Paraná, Curitiba, Brazil.

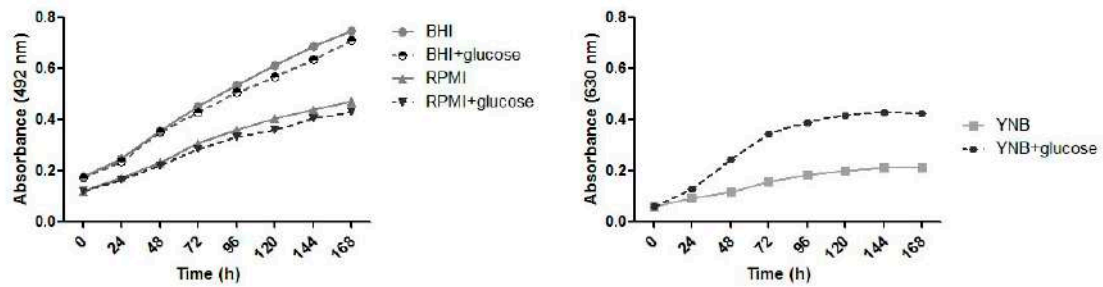
\*luanaborba@biof.ufrj.br

Sporotrichosis is a serious public health problem in Brazil. Cat-transmitted sporotrichosis has been related in most cases of human and animal disease in country and *Sporothrix brasiliensis* is the etiological agent. This zoonotic transmission occurs through scratches and bites from infected cats. The objective of our study was evaluate the *ex vivo* growth of *S. brasiliensis* on feline claws. Firstly, yeasts of feline-borne isolate SBG44 was cultivated by 7 days in brain heart infusion (BHI) broth and  $1 \times 10^6$  ufc/ml was incubated with BHI, RPMI 1640 or YNB media, supplemented or not with 2% glucose. The growth was evaluated by 7 days according spectrophotometric reading. Then, the medium with worse growth was selected and used to incubated yeasts with feline claws (previously sterilized) to analyze by scanning electron microscopy. Fungal cells were incubated by 6 days with claws and the following procedures were performed: (i) cells were fixed in 2.5% glutaraldehyde and 4% formaldehyde in 0.1M cacodylate buffer; (ii) post-fixed in 1% osmium tetroxide in 0.1M cacodylate buffer containing 1.25% potassium ferrocyanide and 5 mM  $\text{CaCl}_2$  for 30 min; (iii) dehydrated in a series of ethanol solutions of increasing concentrations (30, 50, 70, 90, 100%) for 15 min at each step; (iv) critical-point-dried in  $\text{CO}_2$ ; and (v) coated with gold. Images were obtained in a FEI Quanta 250 scanning electron microscope (FEI Company, USA). After 7 days, the lower growth was observed when *S. brasiliensis* was incubated in YNB medium (**Figure 1 i**). However, *S. brasiliensis* showed a considerable growth when it was incubated in YNB medium with feline claws (**Figure 1 ii**). Although yeasts have been add in claws, yeast-hyphae conversion occurred after 6 days (**Figure 1 ii B and C**). *S. brasiliensis* has adhered to keratin fragments and invade the claw (**Figure 1 ii C**). In conclusion, *S. brasiliensis* was able to grow in a poor nutrient medium in the presence of feline claws. It is possible that fungus has degraded the claw to obtain nutrients and further experiments are required to confirm this hypothesis.

This research was supported by CAPES, FAPERJ and CNPq (Brazil).

(i)

## Growth kinetics



(ii)

## Growth in YNB

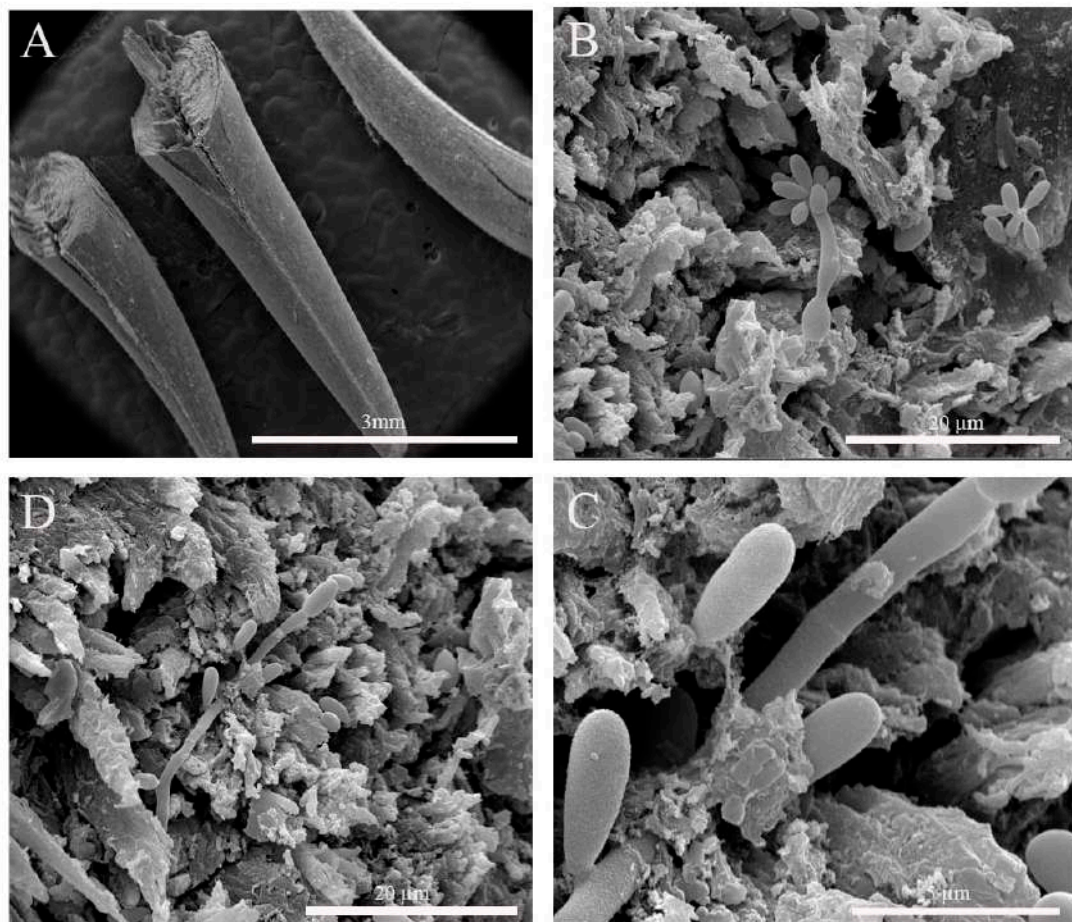


**Figure 1.** (i) Kinetics plots showing growth of *Sporothrix brasiliensis* at different media. (ii) Micrograph of *Sporothrix brasiliensis* grown in the feline claws. Bars: A: 3 mm, B, C: 20 μm and D: 5 μm.



## **Inhibition Of Bovine Viral Diarrhea Virus Replication By Prostaglandin A<sub>1</sub>**

Lúcio Ayres Caldas<sup>1\*</sup>, Tânia Rosária Pereira Freitas<sup>2</sup>, Renata Campos Azevedo<sup>3</sup> and Wanderley de Souza<sup>1</sup>

<sup>1</sup>. Universidade Federal do Rio de Janeiro, Instituto de Biofísica Carlos Chagas Filho, Rio de Janeiro, RJ, Brazil. Email: [lucio@biof.ufrj.br](mailto:lucio@biof.ufrj.br)

<sup>2</sup>. Ministério da Agricultura, Pecuária e Abastecimento, Laboratório Nacional Agropecuário – LANAGRO – MG, Pedro Leopoldo, MG, Brazil

<sup>3</sup>. Universidade Federal do Rio de Janeiro, Instituto de Microbiologia Professor Paulo de Góes, Rio de Janeiro, RJ, Brazil

Bovine viral diarrhea virus is an insidious, complex and ubiquitous pathogen that belongs to the *Flaviviridae* family, *Pestivirus* genus. This virus can affect cattle of all breeds and all ages, as well as others domestic and wild ruminants, causing acute disease in livestock and leading to economic losses. In pregnant cows, BVDV can reach the fetus and cause abortion, stillbirth or teratogenic defects. Alternatively, calves can give birth to immunotolerant and persistently infected calves that are considered reservoirs of the virus [1,2]. Prostaglandin A<sub>1</sub> is a natural eicosanoid secreted by a variety of human tissues and capable of causing profound and diverse physiological effects at very low concentrations, and was previously shown to block the replication of a wide variety of RNA and DNA viruses [3,4]. In the present work we demonstrate that Prostaglandin A<sub>1</sub> inhibits bovine viral diarrhea virus replication in Madin-Darby bovine kidney cells (94% inhibition using 5 µg/mL). Light and transmission electron microscopy of infected cells were used to investigate the morphological alterations in the infected cell showing that the virus-induced vacuolization persists even when this inhibition (94%) of viral production is achieved. Ruthenium red was added to the transmission electron microscopy fixation and post-fixation solutions (as well as to the intermediate washes), in order to situate the virus-induced vacuoles. This procedure was also performed during *en face* sectioning, avoiding removal of the cells from the substratum, which could disrupt and disorient their architecture. Finally, we demonstrated that the prevention of this vacuolization occurs only at higher concentrations of Prostaglandin A<sub>1</sub> (10 µg/mL). These results suggest that the vacuolization triggered by the Bovine viral diarrhea virus infection is not crucial to viral replication [5].

### **REFERÊNCIAS**

- [1] P. Nettleton, Bovine viral diarrhoea virus: biology, diagnosis and control. *Vet Rec.* 172(17) (2013) 447–448.
- [2] A. Meyling et al., Epidemiology of bovine virus diarrhoea virus. *Rev Sci Tech.*;9(1) (1990)75–93.
- [3] T.R. Freitas, et al., Prostaglandin A<sub>1</sub> inhibits replication of classical swine fever virus. *Mem Inst Oswaldo Cruz.*;93(6) (1998) 815–818.
- [4] M.G. Santoro MG. Antiviral activity of cyclopentenone prostanooids. *Trends Microbiol.*;5(7) (1997) 276–281.
- [5] This research was supported by Pronametro/INMETRO (Brazil).



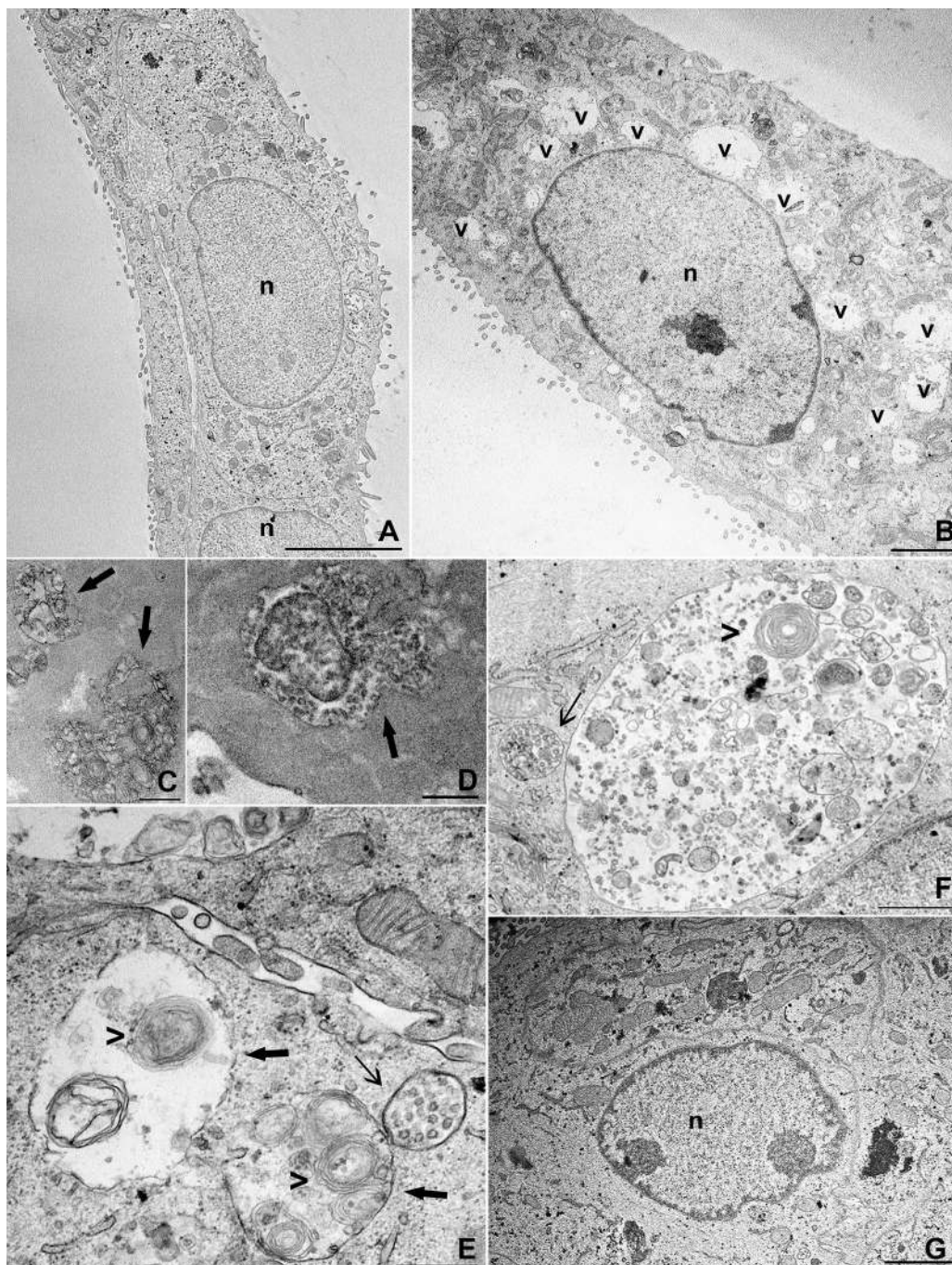


Figure 1. TEM analysis of BVDV-infected cells treated with PGA<sub>1</sub>. Infected and non-infected MDBK cells were treated with PGA<sub>1</sub> for 36 h, and then processed for routine TEM. Vacuoles (v) were rare or absent in the majority of sections from non-infected cells (A), but were abundant in BVDV-infected cells not treated with PGA<sub>1</sub> (B). Many of these structures exhibited extracellular content, as shown by ruthenium red labeling (arrows) in traditional (C) and en face (D) sections. Treatment with 1 µg/mL (E) or 2.5 µg/mL (F) PGA<sub>1</sub> could not prevent BVDV-induced vacuolization in infected cells, which had large vacuoles (arrows) with multilamellar structures (arrowheads), and often surrounded by smaller vesicles-containing vacuoles (thin arrows). (G) Treatment with 10 g/mL PGA<sub>1</sub>, however, dramatically reduced virus-induced vacuolization. n, nucleus. Scale bars: (A) 5 µm; (B, G) 2 µm; (C, E) 500 nm; (D, F) 1 µm.



## Occurrence of avian pox outbreaks in canary commercial breedings. Rapid diagnosis through electron transmission microscopy techniques.

M.H.B. Catroxo<sup>1\*</sup>, L.S.M. Luz<sup>1</sup>, I.M. Pedroso,<sup>1</sup> A.M.C.R.P.F. Martins<sup>1</sup>

<sup>1\*</sup> Electron Microscopy Laboratory, Biological Institute, São Paulo, SP, Brazil

Canary breeding is a practice that has become increasingly profitable and widespread in Brazil and plays a fundamental role in preservation of species. The yellow color of the Belgian lineage is the most popular, but the search for new and different tonalities, size, genetic improvement, besides presentation in exhibitions and preservation, are the breeder's objectives [1]. Avian pox is one of the major viral diseases that affects canaries and due to its rapid spread, can decimate the entire breeding, causing great economic damages to breeders [2]. *Canaripoxvirus* species belongs to the *Poxviridae* family and *Avipoxvirus* genus [3]. Transmission involves insects, aerosols, or contaminated food and water [2]. Three forms characterize the disease, the cutaneous, represented by nodular skin lesions [4], diphtheric, where fibrinous lesions occur in the mucosa of the tongue, pharynx and larynx and septicemic characterized by high mortality [6]. From 2017 to 2018, three avian pox outbreaks occurred in intensive breeding of canaries, located in São Paulo, SP, Brazil, with an average of 200 canaries. Initially 50 to 100 birds died and 50 became ill. The birds had symptoms and clinical signs of progressive emaciation and death within a few days of evolution. A total of 12 canaries, 8 months old, were sent to Biological Institute of São Paulo, SP, Brazil, for research on viral agents. Necropsy showed the presence of the nodular lesions with blood on the legs, feet, beaks and around the eyes that were collected and processed by the techniques of negative staining (rapid preparation), immunoelectron microscopy, and immunocytochemistry. In the negative staining, the clinical samples were suspended in phosphate buffer 0.1 M and pH 7.0, placed in contact with metallic grids and negatively stained at 2% ammonium molybdate [6]. In the immunoelectron microscopy technique, the screens were incubated with a virus-specific antibody and with viral suspension drops. Upon the screens were contrasted at 2% ammonium molybdate [6]. At the immunocytochemistry technique [7], the screens were placed in contact with viral suspension and with primary polyclonal antibody drops. After the screens were incubated in protein A drops in association with 10 nm gold particles (secondary antibody) and contrasted at 2% ammonium molybdate. By means of the negative staining technique, avipoxvirus particles, ovoid, were visualized in all samples of nodular lesions, showing irregular distribution of the tubules on the outer membrane, some enveloped, measuring on average 350X250nm in diameter. The presence of aggregates formed by the antigen-antibody interaction characterized the positive result for avian pox obtained in the immunoelectron microscopy technique. In the immunocytochemistry technique the antigen-antibody reaction was strongly enhanced by the dense particles of colloidal gold on poxviruses. The application of the techniques was paramount for the diagnosis of avian pox and the immediate adoption of prophylactic measures and control of the disease in the canary breedings.

### References

- [1] F.M. Hosken, A.C. Silveira, Criação de Canários de Cor, Aprenda Fácil, Viçosa, MG, 2001.
- [2] C. van Riper et al., The Auk. 119 (4) (2002) 929.
- [3] ICTV, Virus Taxonomy. Available in: <https://talk.ictvonline.org/taxonomy/>
- [4] M.H.B. Catroxo et al., Int. J. Morphol. 27 (2) (2009) 577.
- [5] B.W. Ritchie et al., Avian Medicine: Principles and application, Wingers Publishing Inc., Florida, 1994.
- [6] M.A. Hayat, S.E. Miller. Negative Staining, Mc. Graw-Hill Publ. Company, New York, 1990.
- [7] S. Knutton, Methods Enzymol, 253 (1995) 145.

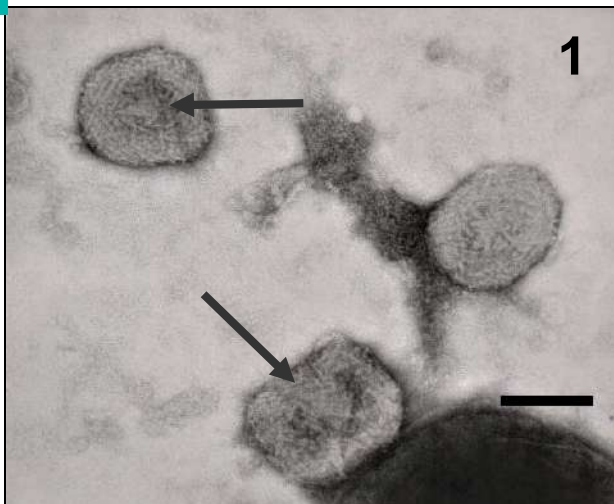


Fig. 1 - Negatively stained avipoxvirus particles, ovoide, showing irregular distribution of the tubules on the outer membrane (arrows). Bar: 190 nm.

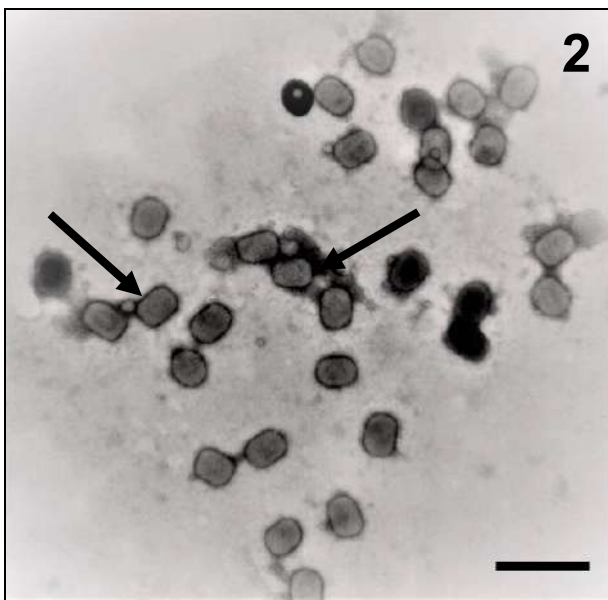
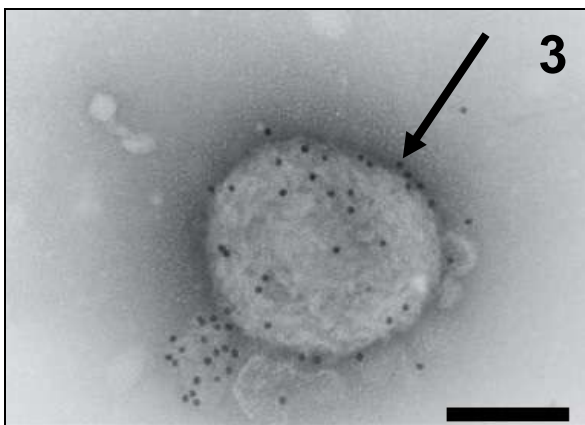


Fig. 2: In the immunoelectron microscopy technique the avipoxvirus particles were aggregated by antigen-antibody interaction (arrows). Bar: 690 nm.



Figs. 3, 4: Antigen-antibody interaction strongly enhanced by the dense gold particles over the avipoxvirus (arrow). Observe enveloped particles in fig. 4 (minor arrow). Bar fig. 3: 160 nm; Bar fig. 4: 200 nm.

## Use of TEM to Monitor Changes in Amyloid Beta Conformations Throughout Aggregation and Identify a Non-toxic Pathway in the Presence of a Ru(II) Complex

Mariana P. Cali<sup>1\*</sup>, Rose M. Carlos<sup>1</sup>

<sup>1</sup> Universidade Federal de São Carlos, Department of Chemistry, São Carlos/SP, Brazil

The A $\beta$  peptides formed via the amyloidogenic pathway of APP proteolysis can misfold and assemble through a series of conformational modifications and metastable oligomers to form deposits of insoluble amyloid fibrils[1]. Hypothesis for the contribution of A $\beta$  aggregates in the AD pathology include the presence of mature fibrils and, more recently, pores-like oligomeric structures.[2] However, the precise mechanism of A $\beta$  aggregation and toxicity has not yet been fully understood. Undoubtedly, the elucidation of conformational changes of A $\beta$  in detail and the identification of toxic species generated in the course of aggregation are essential to develop a more selective and effective therapy for amylogenic diseases. However, strategies to follow and identify the conformational changes in the early stages of A $\beta$  aggregation must be very sensitive.

Here we show that the luminescent and non-toxic metal complex *cis*-[Ru(phen)<sub>2</sub>(Apy)<sub>2</sub>]<sup>2+</sup> developed in our lab, not only maps the conformational changes of A $\beta$  in detail through luminescent lifetime images, but also changes the mechanism of A $\beta$  aggregation to a non-toxic pathway where the pore-like structures are replaced by micelle-like conformations, depending on the concentration. We investigated the conformational changes and toxicity of the species generated during the course of aggregation of different amyloid fragments - A $\beta$ <sub>1-40</sub>, A $\beta$ <sub>1-28</sub>, A $\beta$ <sub>11-22</sub> and A $\beta$ <sub>29-40</sub> - and the role of our complex on their self-assembly and toxicity. In the presence of our complex the A $\beta$ <sub>1-40</sub> peptide showed globular instead of pore-like structures, which are formed in higher predominance in early stages of self-assembly and coexist at longer incubation periods amongst protofibrils and mature fibril plaques, Figure 1. For A $\beta$ <sub>1-28</sub>, oligomeric micelle-like aggregates dominate the course of aggregation. They remain the prevalent specie through to the final stages of aggregation, whereas long, extended and twisted structures were predominant for A $\beta$ <sub>11-22</sub>. A $\beta$ <sub>29-40</sub> aggregates in a similar manner to A $\beta$ <sub>1-40</sub>. Our experiments indicate that only the full length peptide A $\beta$ <sub>1-40</sub> is toxic to PC12 cells and the toxicity depends on aggregation of the step investigated: the oligomeric pore-like structures generated in the beginning of aggregation of A $\beta$ <sub>1-40</sub> are toxic whereas the mature fibrils are not. Thus the toxicity of A $\beta$ <sub>1-40</sub> depends on a specific interaction between the 3 constituents fragments: A $\beta$ <sub>1-28</sub>, A $\beta$ <sub>11-22</sub> and A $\beta$ <sub>29-40</sub>.

Notably, the luminescent complex changes the aggregation process of A $\beta$ <sub>1-40</sub> to a new and non-toxic pathway, with formation of oligomeric micelle-like structures and belt-like fibrils in contrast to pore-like oligomers and twisted fibrils in the absence of complex.

[1] G.Paroni et al., Understanding the Amyloid Hypothesis in Alzheimer's Disease. 2019, 68, 493-510.

[2] E.N.Cline et al., The Amyloid- $\beta$  Oligomer Hypothesis : Beginning of the Third Decade, 64 (2018) S567-S610.

*Acknowledgments:* The Brazilian National Laboratory of Nanotechnology (LNNano) is acknowledged for the TEM microscopy experiments (processes TEM-20515/TEM-21480/ME-22280). We thank FAPESP (2017/00839-1), CNPq and CAPES for the funding.

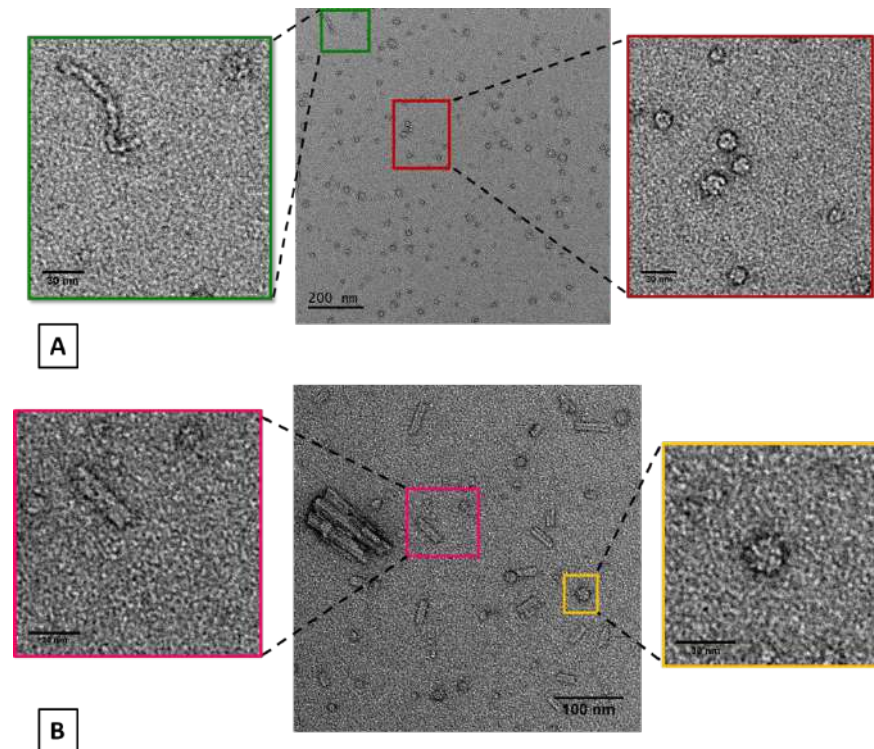


**Figure 1:** (A) Negative staining TEM images of Aβ<sub>1-40</sub> (B) Incubation of Aβ<sub>1-40</sub> with the complex (1:1).

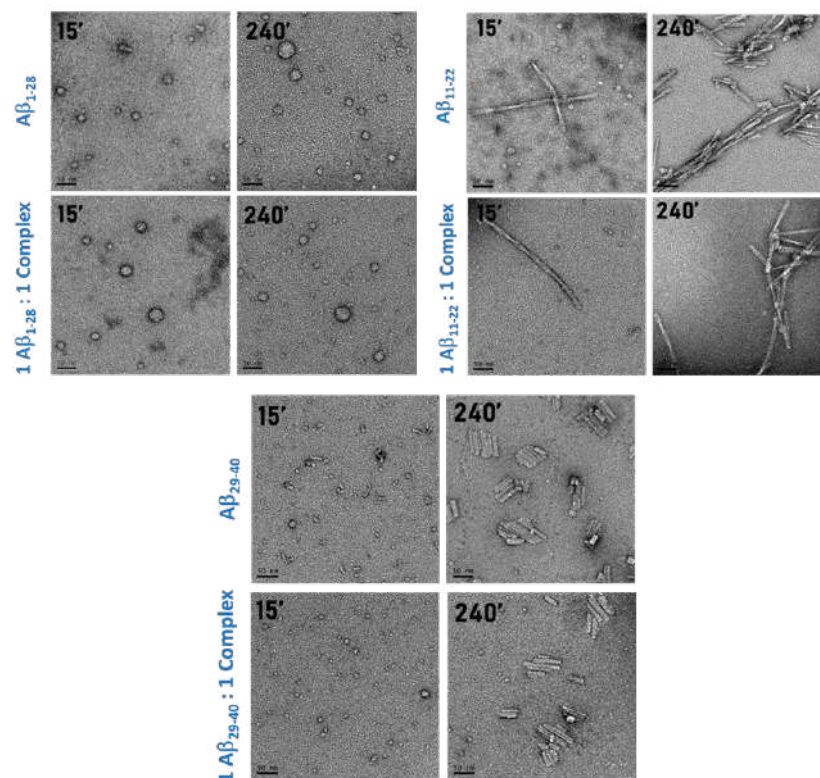


**Figure 2:** Negative staining TEM images Aβ<sub>1-28</sub>, Aβ<sub>11-22</sub> and Aβ<sub>29-40</sub> in the absence of the complex at 15 and 240 min of incubation in the absence and presence of the complex in a 1:1 Aβ<sub>1-28</sub> to complex ratio.



## Ultrastructural Analysis of *Anadenanthera colubrina* (Vell.) Brenan Roots Treated with *Urochloa humidicola* (Rendle.) Morrone & Zuloaga Root Extract

Rodrigo Barbosa Braga Feitoza<sup>1\*</sup>, Helena Regina Pinto Lima<sup>2</sup>, Luiz Fernando Duarte de Moraes<sup>3</sup>, Rosa María Varela<sup>4</sup>, Francisco Antonio Macías<sup>4</sup>, Maura Da Cunha<sup>1</sup>

<sup>1</sup>Universidade Estadual do Norte Fluminense Darcy Ribeiro, Centro de Biociências e Biotecnologia, Laboratório de Biologia Celular e Tecidual, Campos dos Goytacazes, Brazil. rfeitoza@pq.uenf.br.

<sup>2</sup>Universidade Federal Rural do Rio De Janeiro, Instituto de Ciências Biológicas e da Saúde, Departamento de Botânica, Seropédica, Brazil.

<sup>3</sup>Embrapa Agrobiologia, Seropédica, Brazil.

<sup>4</sup>Universidad de Cádiz, Facultad de Ciencias, Departamento de Química Orgánica, Puerto Real, Spain.

The grass *Urochloa humidicola* (Rendle) Morrone & Zuloaga was introduced in Brazil as a pasture crop. However, introduced exotic species may establish themselves as invaders, which affects either ecologic or agronomic issues [1]. Distinct special metabolites from this species, such as phenolic acids and saponins, have been recognized as phytotoxic compounds since they hamper development of other plants [2]. This work aimed to test the phytotoxicity of *U. humidicola* root extracts, and to evaluate possible ultrastructural effects on the Atlantic Forest-native *Anadenanthera colubrina* (Vell.) Brenan roots. Firstly, *U. humidicola* roots were collected, dried, grounded, and extracted by different solvents: water (crude aqueous extract - CAE), ethyl acetate (REA), acetone (RAc) and methanol (RMe and RMS). Such extracts were diluted to 200, 400 and 800 ppm and tested in a wheat coleoptile assay, conducted in assay tubes in dark. After 24 h, coleoptiles were measured and compared to control (water). The most inhibitory extract was tested against *A. colubrina* seeds at the same dilutions, and compared to control (water) and to the herbicide Logran. After 10 days of bioassay, root samples were fixed and processed for transmission electron microscopy (TEM, Jeol JEM 1400 Plus)) [3]. After the wheat coleoptile assay, aqueous extracts inhibited coleoptile length by less than 30%, whereas REA inhibition varied between 50-90%, and RAc and methanol extracts inhibited between 24-67%. RAE successfully inhibited both *A. colubrina* seed germination and early development after all tested concentrations. Control root cells of *A. colubrina*, 0.5 cm from root tip, appeared turgid, and exhibited one large vacuole, abundant mitochondria with unaffected cristae, and conspicuous nucleus and nucleolus. After RAE treatment at 800 ppm, cellular wastes were found stored in the vacuole. Moreover, smaller vacuoles were found next to larger ones, indicating vacuolization. After either RAE or Logran treatments, vacuoles also stored globular osmiophylic-dense content, and nucleus exhibited degraded chromatin. This inhibitory effect may be related to production of distinct phytotoxic compounds, in example, the saponin dioscin, and phenols *p*-coumaric acid and catechin-7-O-glucoside, which were already detected in *U. humidicola*.

[1] R.M. Callaway et al., Front. Ecol Environ. 2 (8) (2004) 436.

[2] FA Einhellig, In FA Macías et al. (Eds.), Allelopathy: chemistry and mode of action of allelochemicals (2004).

[3] ES Reynolds, J. Cell Biol. 17 (1963) 208-212.

[4] This research was supported by CNPq, CAPES, FAPERJ, AGEVAP (Brazil).

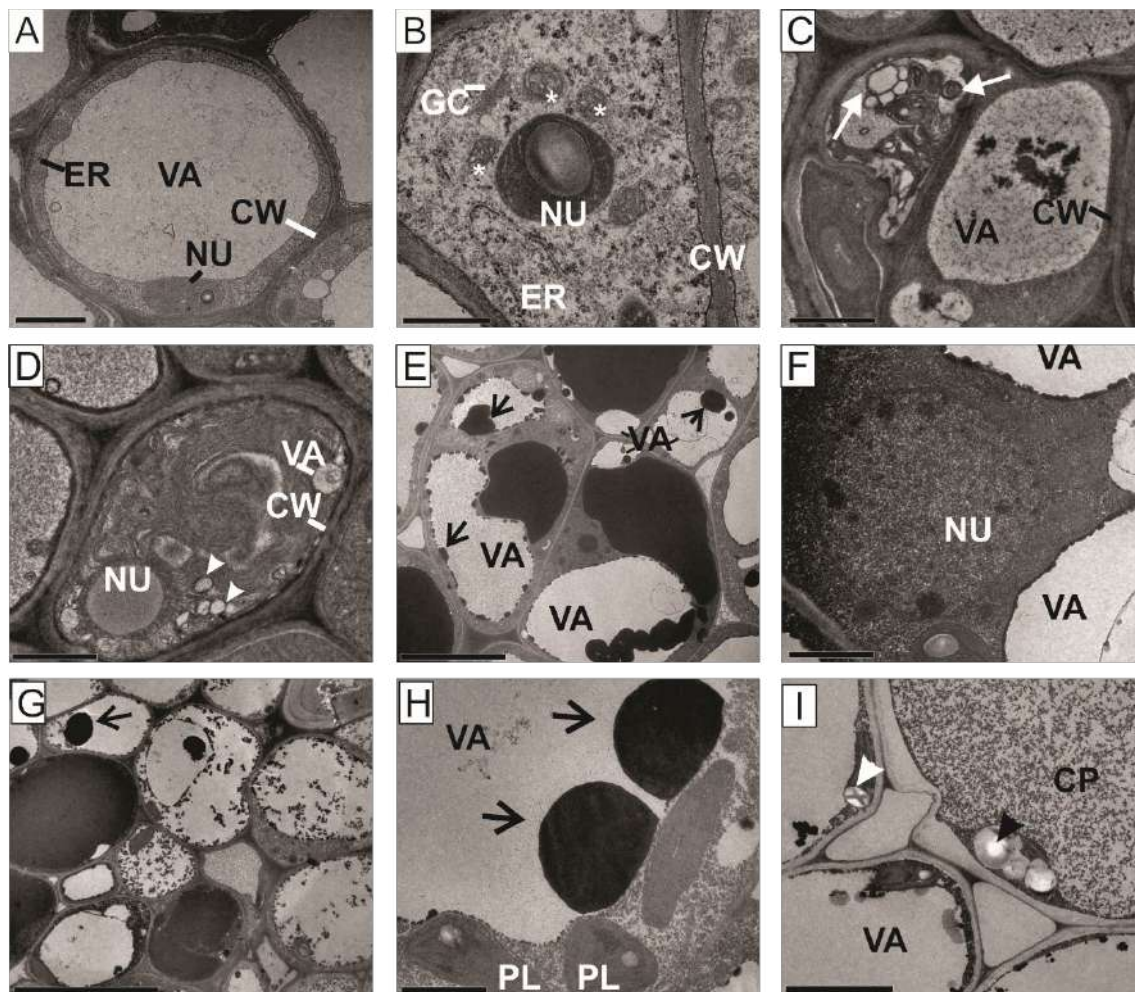


Figure 1. *Anadenanthera colubrina* root cells, 0.5 cm from root tip, as observed in Transmission Electron Microscopy (TEM). (A-B) Control. (A) Parenchyma cell exhibiting large vacuole and conspicuous nucleus. (B) Phloem cell, indicating intact organelles, and nucleus with distinct nucleolus. (\*) Indicates mitochondria with intact cristae. (C-D) *Urochloa humidicola* root ethyl acetate extract (REA), 800 ppm. (C) General aspect of phloem cells. Note osmiophylic-dense deposits in the center of the vacuole, and cellular wastes (→). (D) Degraded organelles in cytoplasm, small vacuole, indistinct nucleolus, and starch grains (▶). (E-F) REA, 200 ppm. (E) Central cylinder cells. Note osmiophylic-dense content next to vacuole membrane (→), or occupying the whole vacuole. (F) Detail of nucleus with degraded chromatin. (G-H) Logran, 800 ppm. (G) General aspect of central cylinder cells. (H) Osmiophylic-dense deposits in vacuoles (→). (I) Logran, 200 ppm. Note granules cytoplasm and starch grains (▶). CP = cytoplasm, CW = cell wall, ER = endoplasmic reticulum, GC = Golgi complex, NU = nucleus, PL = plastid, VA = vacuole. Bars: A, C, D, E, F, H = 2  $\mu$ m; B = 1  $\mu$ m; E, G = 10  $\mu$ m; I = 5  $\mu$ m.



## Study of Human Peripheral Blood Fibrocytes Interaction with *Leishmania (L.) amazonensis* – an *in vitro* Analysis

Pereira, PRP<sup>1</sup>, Macedo-Silva, RM<sup>2</sup>, Sousa-Vasconcelos, PS<sup>3</sup>, Pinho, RT<sup>3</sup>,  
Pinheiro, RO<sup>4</sup>, Côrte-Real, S<sup>1\*</sup>.

<sup>1</sup>. Laboratory of Structural Biology, Oswaldo Cruz Institute/Fiocruz, Rio de Janeiro-Brasil.

<sup>2</sup>. Rudolf Barth Electron Microscopy Platform, Oswaldo Cruz Institute/ Fiocruz, Rio de Janeiro-Brasil.

<sup>3</sup>. Laboratory of Clinical Immunology, Oswaldo Cruz Institute/ Fiocruz, Rio de Janeiro-Brasil.

4 - Laboratory of Hanseniasis, Oswaldo Cruz Institute/ Fiocruz, Rio de Janeiro-Brasil.

\*E-mail: scrif@ioc.fiocruz.br

Leishmaniasis is an infectious disease caused by protozoan of the genus *Leishmania*. After transmission of the parasite by the insect vector in the mammalian host dermis, resident and inflammatory cells are attracted to the site of infection. Among these cells are fibrocytes, hematopoietic cells that express CD45 pan-leukocyte protein and produce extracellular matrix proteins [1]. Studies have showed the fibrocytes participation in different pathological processes [2] and fibrocytes of BALB/c mice in interacting with *Leishmania (L.) amazonensis* (*L. amazonensis*) [3]. However, there are no studies on the role of human fibrocytes in leishmaniasis. So, we analysed, *in vitro*, the interaction of human fibrocytes with *L. a* promastigote. Primary cultures were established and from the 15th day, fibrocytes were infected and analyzed. Phenotypic characterization of the human fibrocytes was performed by fluorescence microscopy through two assays using the identification of three main markers: CD45 (pan-leukocyte protein), collagen type I (matrix protein) and HSP-47 (heat shock protein involved in the synthesis of collagen type I and present specifically in the endoplasmic reticulum of the cells producing this protein). In ultrastructural analysis by scanning (Jeol JSM-6390LV) and transmission electron microscopy (Jeol JEM-1011), we observed that the fibrocytes emit cytoplasmic projections that rolled up the parasites favoring phagocytosis. After 15 days of interaction, fibrocytes were susceptible to infection by *L. amazonensis*, as we observed the differentiation of promastigotes into amastigotes, as well as their multiplication within parasitophorous vacuoles. From the analysis of the production of the inflammatory chemical mediators, we verified that fibrocytes respond to the infection with the production of pro and anti-inflammatory cytokines during the times established in this study, making favorable the conditions for the establishment of the infection. These results allow us to suggest that human fibrocytes may serve as host cells in the initial response and the development of cutaneous leishmaniasis because parasites of the *Leishmania* genus modulates the response of human fibrocytes, multiplies, breaks the cell, and is released to infect other types cells or the fibrocyte itself.

### REFERENCES:

- [1] Bucala et al., *Mol. Med.* 1 (1994) 71.
- [2] Grab et al. *Trends in Parasitology* (2004) 1: 12.
- [3] Macedo-Silva, R.M. et al. *Mem. Inst. Oswaldo Cruz.* (2014) 109(1):61-9.
- [4] This research was supported by Instituto Oswaldo Cruz (IOC)/ Fiocruz, Rudolf Barth Electron Microscopy Platform/Fiocruz and CAPES (Brazil).



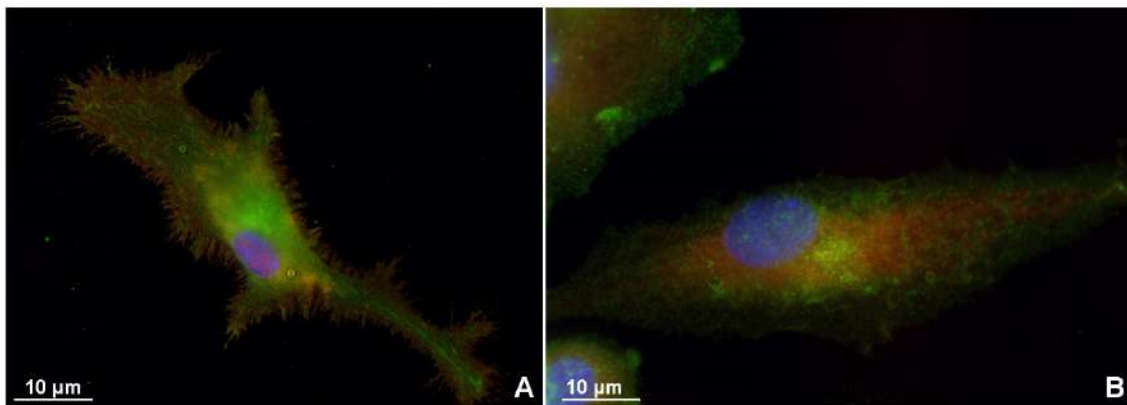


Figure 1 (A-B): Phenotypic characterization of the primary culture of human fibrocyte using double marker performed by fluorescence microscope A: double marking using the 4',6-diamidino-2-phenylindole DAPI (blue), CD45 Alexa Fluor 594 (red) and anti-colágeno tipo I Alexa Fluor 488 (green); B: double marking using the 4',6-diamidino-2-phenylindole DAPI (blue), CD45 Alexa Fluor 488 (green) and HSP-47 Alexa Fluor 594 (red).

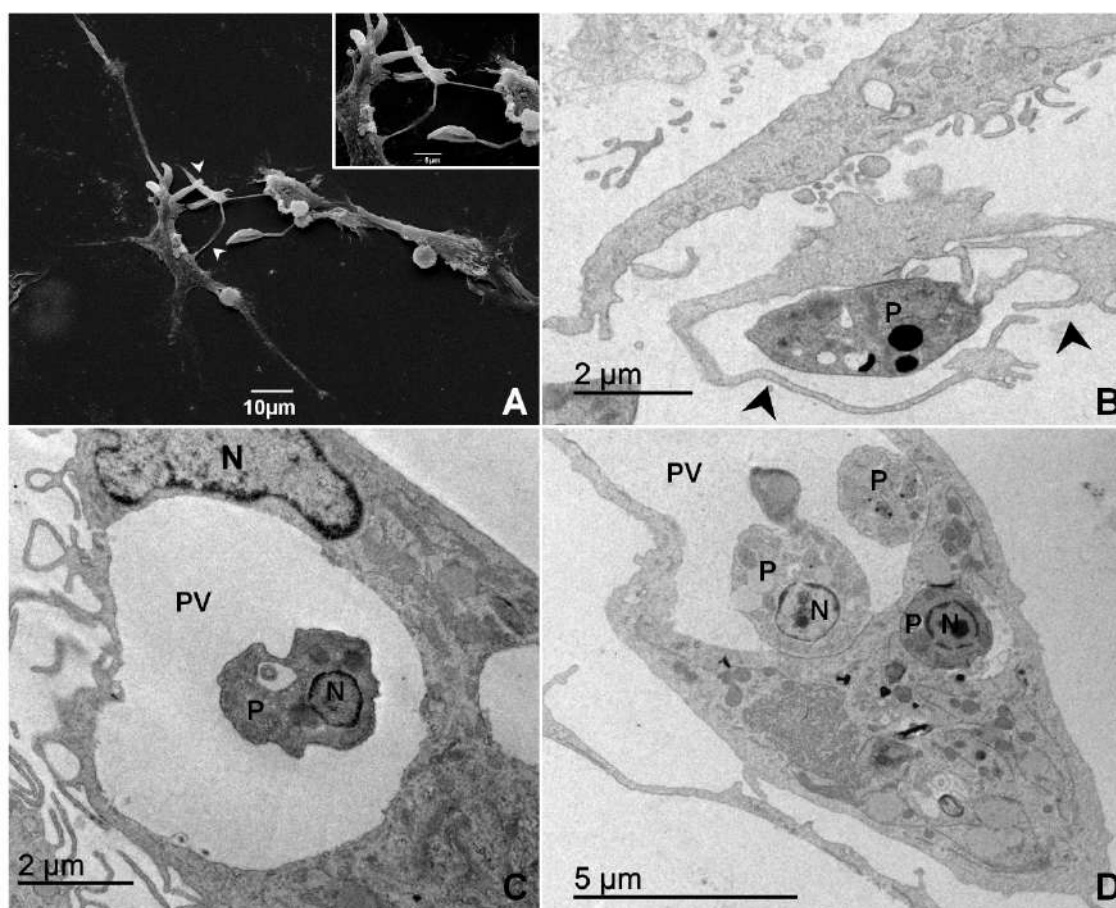


Figure 2 (A-D): Ultrastructural analysis of the interaction with fibrocyte and *Leishmania* (*L.*) *amazonensis* by scanning (Jeol JSM-6390LV) and transmission electron microscopy (Jeol JEM-1011). A: The first endocytosis stages, 30 minutes, of the parasite by flagellum with the participation of fibrocyte cellular extension (arrow head); B: participation of fibrocyte cellular extension in the first hour (arrow head); C: differentiation for amastigote after 24h; D: multiplication within parasitophorous vacuoles (PV) after 72h.



## Stereology of Mitochondria in Transmission Electron Microscopy

Pedro Henrique Reis Barbosa<sup>1,2\*</sup>, Jorge José de Carvalho<sup>2</sup>, and Carlos A. Mandarim-de-Lacerda<sup>1</sup>

- <sup>1</sup>. Laboratory of Morphometry, Metabolism, and Cardiovascular Diseases, Institute of Biology, State University of Rio de Janeiro, Rio de Janeiro, Brazil;
- <sup>2</sup>. Laboratory of Ultrastructure and Tissue Biology, Institute of Biology, State University of Rio de Janeiro, Rio de Janeiro, Brazil.

\*Corresponding author: [barbosaphr@outlook.com](mailto:barbosaphr@outlook.com)

Mitochondria (m) are responsible for the energy availability of cells, and their analysis is indicated in studies related to metabolism and oxidative stress, for example. The direct measurement of mitochondria (morphometry) is biased because of the section obliquity and position relative to the mitochondria length (non-equatorial cut). Therefore, stereology is an appropriate technique to evaluate mitochondria. However, before beginning the study, it is necessary to consider the premises to obtain random and uniform samples to be analyzed stereologically [1]. It is essential that the mitochondria have the chance to appear in all the possibilities of cut and orientation in the micrographs. The number of micrographs to be analyzed will depend on the distribution and occupation of mitochondria in the cell [2]. After this is resolved, a proposal is the estimation of the following stereological data: volume density ( $V_v$ ), surface density ( $S_v$ ), and mean cross-sectional area ( $A$ ). Overlapping a known test area at each micrograph (Fig. 1), the density by area of mitochondria is estimated ( $N_{AT}$ ).  $V_v$  [m] can easily be estimated by *point-counting* ( $V_v = P_p/P_T$ ;  $P_p$  are the points hitting the structure,  $P_T$  are the number of points of the test system).  $S_v$  is estimated overlaying a test-line ( $L_T$ ) on the micrographs and counting the intersections of the lines ( $I$ ) with the outer membrane (om), inner membrane (im), and crests (c), thus,  $S_v$  [om],  $S_v$  [im],  $S_v$  [c] ( $S_v = 2I / L_T$ ).  $A$  [m] is obtained as the ratio:  $A = V_v / 2N_{AT}$  [3].

### REFERENCES

1. Mandarim-de-Lacerda CA, Del Sol M. Tips for studies with quantitative morphology (morphometry and stereology). *Int J Morphol* 2017;35:1482-94.
2. Mandarim-de-Lacerda CA. Morphometry and stereology in transmission electron microscopy. In: De Souza W, editor. *Técnicas de microscopia eletrônica aplicadas às ciências biológicas*. 3rd ed. Rio de Janeiro: SBMM; 2011. p. 423.
3. Mandarim-de-Lacerda CA. Stereological tools in biomedical research. *An Acad Bras Cienc* 2003;75:469-86.

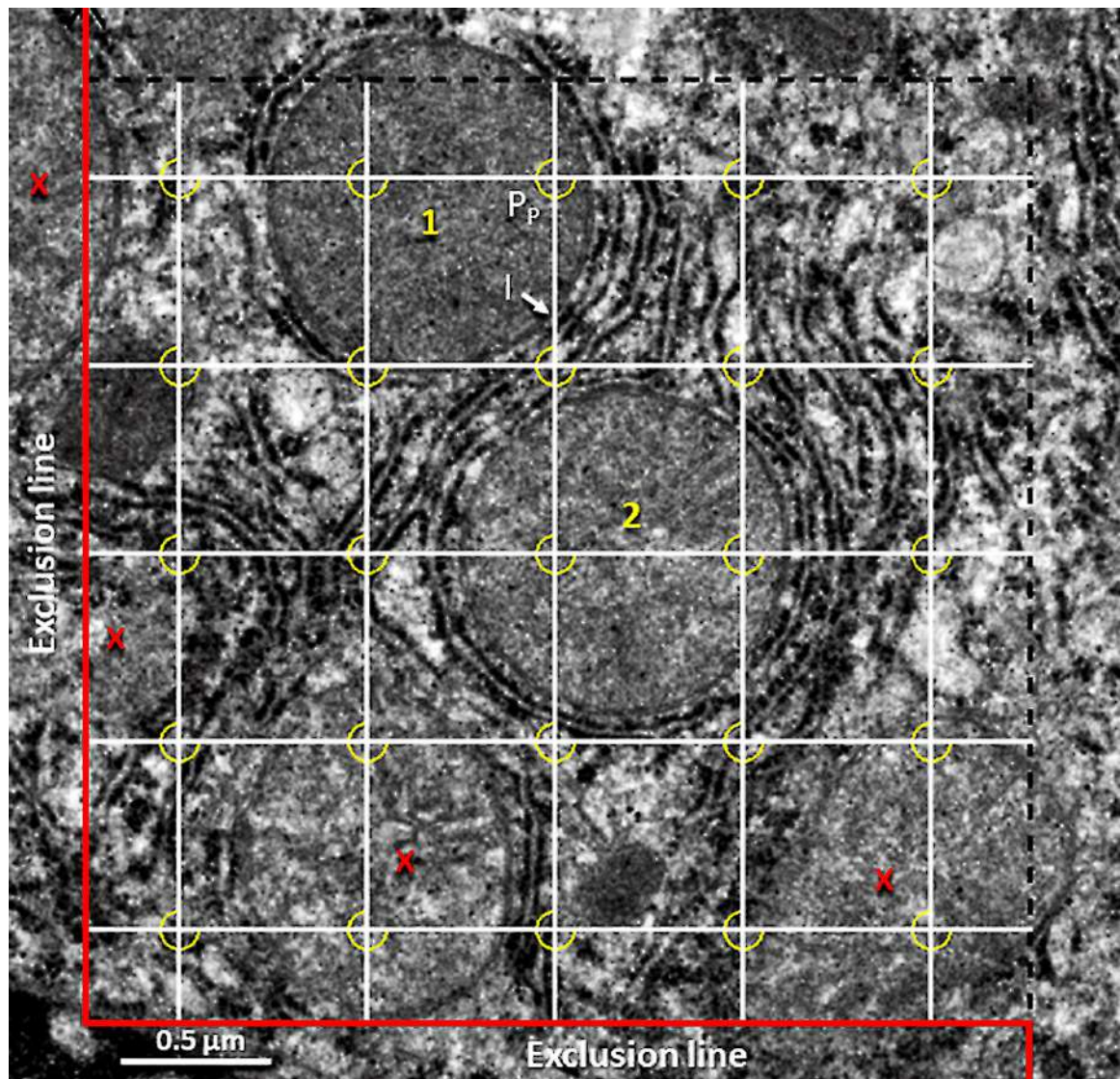


Figure 1 - Electron micrograph with superimposition of the test system. Thus, here there are two available mitochondria in the test area (the others cannot be considered since it touches the exclusion lines in red). It should also be counted the test points on the mitochondria (yellow circles,  $P_p$ ) and the intersections of the test line with the mitochondria (I).

## **Aliskiren Improves Renal Morphophysiology And Inflammation In Wistar Rats With 2K1C Renovascular Hypertension**

Priscila G. Pereira<sup>1</sup>, Kíssila Rabelo<sup>1</sup>, Jemima F. R. da Silva<sup>1</sup>, Bianca T. Ciambarella<sup>1</sup>, Juliana G. C. Argento<sup>1</sup>, Ana L. R. Nascimento<sup>1</sup>, Aline B. Vieira<sup>2</sup>, Jorge J. de Carvalho<sup>1\*</sup>

<sup>1</sup> Laboratory of Ultrastructure and Tecidual Biology, Institute of Biology, State University of Rio de Janeiro, RJ, Brazil.

<sup>2</sup> Ross University School of Veterinary Medicine. Biomedical Department, Basseterre, Saint Kitts.

\*Corresponding author e-mail address: [jjcarv@gmail.com](mailto:jjcarv@gmail.com).

Hypertension is characterized by persistent elevated blood pressure levels, which is one of the leading causes of death worldwide [1]. Renovascular hypertension represents the most common causes of secondary hypertension, and its progress is associated with overactivation of the renin angiotensin aldosterone system (RAAS), causing systemic and local changes [2, 3, 4]. Aliskiren is a renin-inhibiting drug that optimizes RAAS suppression [5, 6]. In this sense, the objective of the present study was to analyze the morphophysiology of the left kidney in Wistar rats with renovascular hypertension (model of Goldblatt 2K-1C) after the treatment with Aliskiren [7]. Parameters such as systolic blood pressure, urinary creatinine and protein excretion were analyzed. Besides that, the histopathology of the renal cortex was investigated by light microscopy, in the HE and Picro Sirius Red stainings techniques. Tissue inflammation was observed through the labeling of different pro and anti-inflammatory cytokines by immunoperoxidase technique, also quantified. The ultrastructural alterations in renal cells were analyzed by transmission electron microscopy. All quantifications were performed in Image Pro Plus 7.0 software. Our results showed that hypertensive animals treated with Aliskiren presented lower blood pressure and reestablishment of renal function with lower levels of urinary proteins and increased creatinine levels. In addition, remodeling of the morphological changes imposed by renovascular hypertension, through the reduction of fibrosis and expression of renin, laminin and pro-inflammatory cytokines, such as TNF- $\alpha$ , TGF- $\beta$  and IL-6, as well as restoration of integrity of the glomerular filtration barrier and increased levels of IL-10, an anti-inflammatory cytokine. Therefore, our findings suggest that the treatment with Aliskiren has renoprotective effect acting on the improvement of the morphology, physiology and pathology of the renal cortex of animals with renovascular hypertension.

[1] Sociedade Brasileira de Cardiologia. VI Diretrizes Brasileiras de Hipertensão. Arq Bras Cardiol. 2010; 95 (1 supl.1): 1-51.

[2] Pullalarevu R, Akbar G, Teehan G. Secondary hypertension, issues in diagnosis and treatment. Prim Care. 2014 41(4): 749-64.

[3] Matavelli LC, Huang J, Siragy HM. Angiotensin at receptor stimulation inhibits early renal inflammation in renovascular hypertension. Hypertension 2011;57:308–313.

[4] Oliveira-Sales EB, Boim MA. Mesenchymal stem cells and chronic renal artery stenosis. Am J Physiol Renal Physiol. 2016; 310(1):F6-9.

[5] Riccioni G, Vitulano N, D'orazio N, Bellocchi F. Aliskiren, the first approved renin inhibitor: Clinical application and safety in the treatment of hypertension. Adv Ther. 2009 Jul; 26(7):700-10.

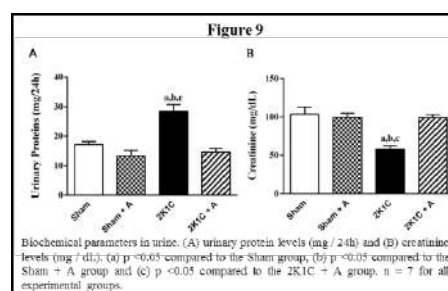
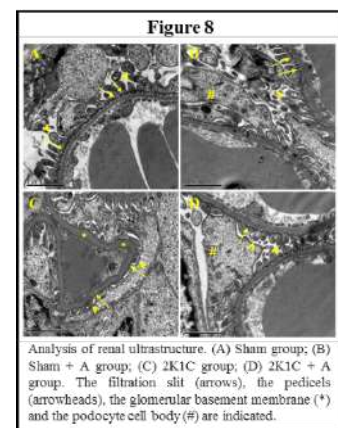
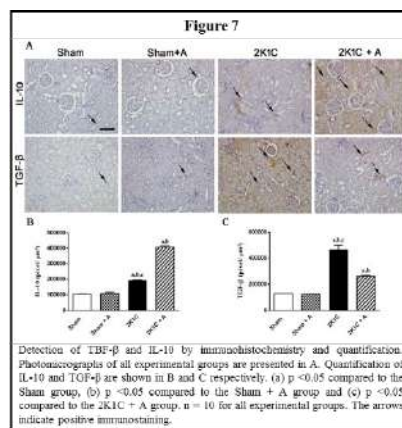
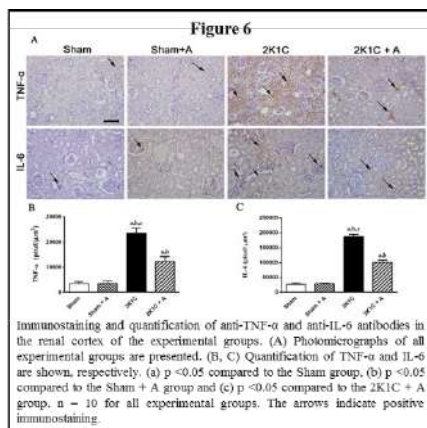
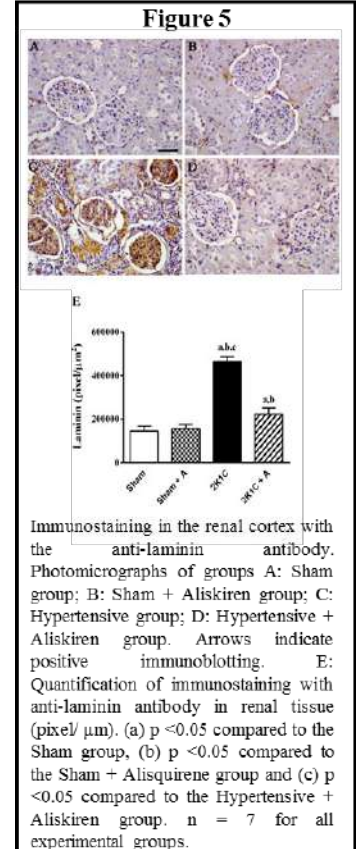
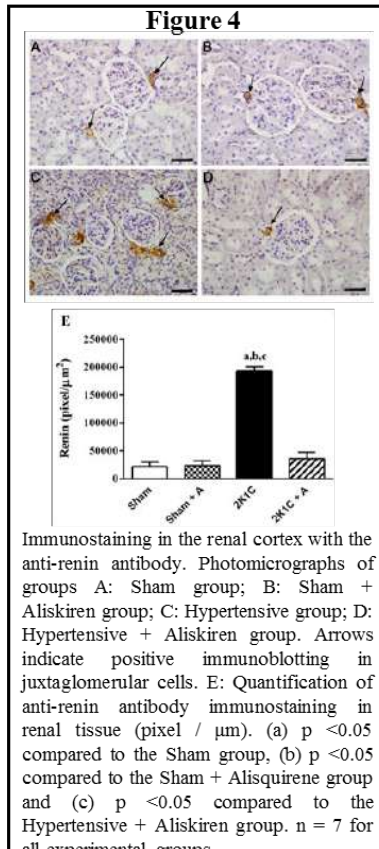
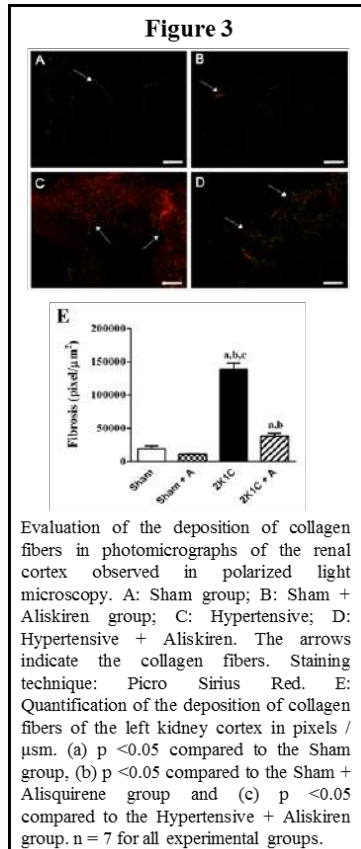
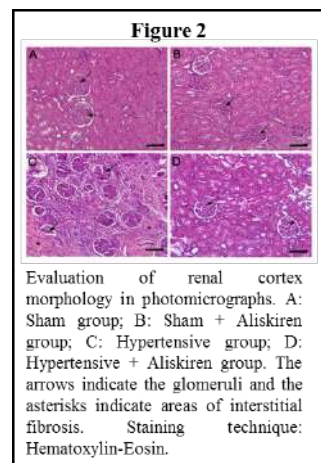
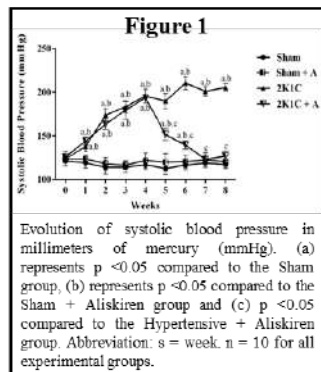
[6] Friedrich S, Schmieder RE. Review of direct renin inhibition by aliskiren. Journal of the Renin-Angiotensin- Aldosterone System. 2013; 14(3): 193–196.

[7] Goldblatt H, Lynch J, Hanzal RF, Summerville WW. Studies on experimental hypertension: I. The production of persistente elevation of systolic blood pressure by means of renal ischemia. J Exp Med. 1934. 28;59(3):347-79.



[8] This research was supported by FAPERJ and CNPq (Brazil).

## FIGURES







## Carotenoid Storage Cells in *Bixa orellana* L.

Louro, RP<sup>1\*</sup>, Freitas, YG<sup>1,2</sup>, Santiago, LJM<sup>2</sup>

1-Laboratório de Ultraestrutura Vegetal, Departamento de Botânica, Instituto de Biologia, Universidade Federal do Rio de Janeiro, Bloco A Avenida Carlos Chagas Filho, 373. Centro de Ciências da Saúde (CCS), Cidade Universitária, Rio de Janeiro, RJ, Brazil, CEP: 21941-902 \*E-mail for correspondence: louro@biologia.ufrj.br

2-L. J. M. Santiago Laboratório de Biodiversidade e Biotecnologia, Departamento de Botânica, Instituto de Biociências, Universidade Federal do Estado do Rio de Janeiro, Rio de Janeiro, Av. Pasteur 458, S. 301, Urca, Rio de Janeiro, RJ, Brazil CEP: 22290-240

*Bixa orellana* L. (Bixaceae), also known as urucum in Brazil, is a native shrub of Central and South America [1] cultivated in tropical areas worldwide. The aril of urucum seeds accumulate the carotenoids bixin and norbixin, important pigments, which are utilized in the food and pharmaceutical industries. These pigments are stored in specialized cells denominated carotenoid storage cells – CSC [2]. Studies have been carried out on chemical and deposition of these compounds [2,3] and seed coats and endosperm cells [4,5]. However, the cellular biology on seed development in CSCs remains poorly known with relation to carotenoids synthesis. With this purpose, in this study the aril of the urucum seeds will be analyzed on transmission electron microscopy, focused ion beam-scanning electron microscope (FIB-SEM) and confocal microscopy. For the studies in TEM, samples were examined with a Morgagni 286 transmission microscope, the tomographic datasets were obtained using Zeiss Auriga 40 dual beam microscope and the fluorescence analyses was obtained in Zeiss Elyra confocal microscope. The results demonstrated that the aril was formed by an outer epidermal cell layer with large specialized cells (CSC) (Figs 1. A and B). The confocal analysis demonstrated that the content of these cells was mainly autofluorescence between 400 - 440 nm (Fig 1. E) which corresponded to bixin, localized in both, cytoplasm and vacuole. The ultrastructural analyses (Figs 1. C, D and F) evidenced that the formation of these pigments occurs inside of the chromoplast. These substances were transported outside of the chromoplast and may fused one to each other, inside or outside of the chromoplast, forming a larger electron dense structure widely dispersed in the cytoplasm. During the formation of CSCs, the pigments are transported from the cytoplasm towards the vacuole, passing through the tonoplast, being storage in the central region of the vacuole. Three different deposition types can be seen in the vacuole, small droplets highly electron dense, large droplets electron dense and a crystalline structure. Studies are still necessary to understand the biological processes involved in the formation and targeting of the pigments, as well as to identify these different deposits found in the vacuole.

### References

- [1] Venugopalan A, Giridhar P, Ravishankar GA (2011) Ind J Fund Appl Life Sci 1: 9-3
- [2] Louro, R. P., & Santiago, L. J. M. (2015). Protoplasma, 253(1), 77–86.
- [3] Scotter MJ, Lesley AW, Appleton GP, Castle L (1998) J Agr Food Chem 46:1031–1038
- [4] Amaral LIV, de Pereira MFDA, Cortelazzo AL (2001) Acta Bot Bras 15:125–132
- [5] Amaral LIV, Cortelazzo AL, Buckeridge MS, Pereira LAR, de Pereira M, FDA (2009) Trees 23: 287–293

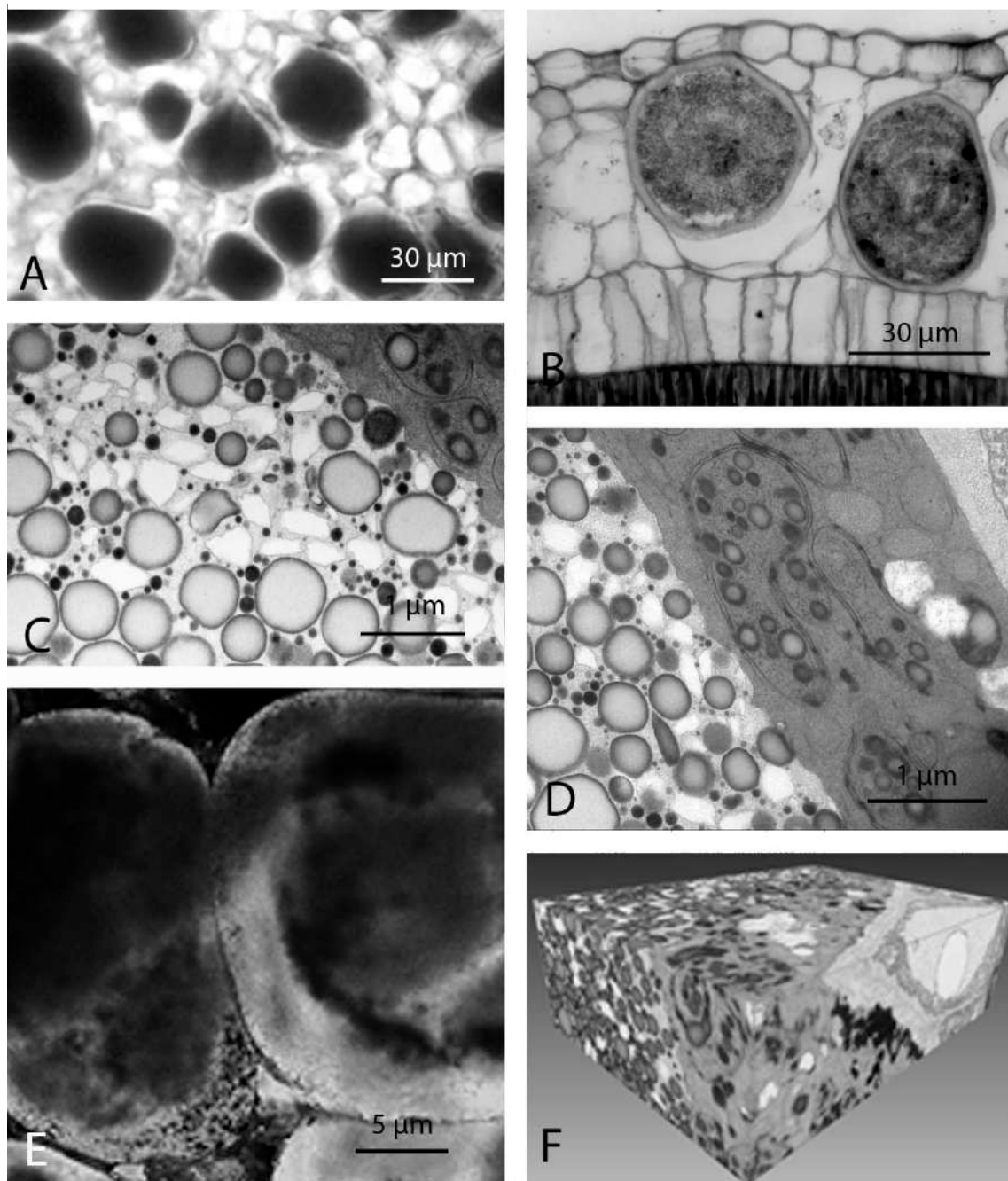


**Figure 1. Characterization of carotenoid storage cell (CSC) in *Bixa orellana* L. seed.** A, Paradermic view of the aril showing the CSCs. B, Cross section of the aril. C, Detail of the CSC vacuole. D, Detail of the CSC cytoplasm showing chromoplasts. E. Paradermic view observed in confocal microscope. F, 3D model obtained in FIB-SEM microscope

## Histone Desacetylase Inhibitors Affect Growth And Cell Organization Of *Giardia intestinalis* Trophozoites

Roberta Verissimo F. de Oliveira<sup>1,4\*</sup>, Marlene Benchimol<sup>2, 4</sup>, Wanderley de Souza<sup>2, 3</sup>, Ana Paula Rocha Gadelha<sup>1, 4</sup>

<sup>1</sup>Diretoria de Metrologia Aplicada a Ciências da Vida, Instituto Nacional de Metrologia, Qualidade e Tecnologia, Rio de Janeiro, Brasil;

<sup>2</sup>Instituto de Biofísica Carlos Chagas Filho, Universidade Federal do Rio de Janeiro, Rio de Janeiro, Brasil;

<sup>3</sup>Instituto Nacional de Ciência e Tecnologia em Biologia Estrutural e Bioimagens e Centro Nacional de Biologia Estrutural e Bioimagens, Universidade Federal do Rio de Janeiro, Rio de Janeiro, Brasil;

<sup>4</sup>Universidade do Grande Rio, Unigranrio, Duque de Caxias, Rio de Janeiro, Brazil;  
[roberta.verisfran@gmail.com](mailto:roberta.verisfran@gmail.com)\*

*Giardiasis* is an intestinal disease that affected approximately 200 million people annually. It is caused by the parasitic protozoan *Giardia intestinalis*, which presents two morphological stages during its life cycle, the cyst and the trophozoites [1]. For over five decades, giardiasis treatment was based in nitro compounds, but resistance and failure to these drugs have been related. In this context, the need to develop new approaches to the chemotherapy of giardiasis is widely recognized [2]. Epigenetic mechanisms as acetylation and deacetylation of histone proteins have become target of several studies in *Giardia* because they are associated with different cellular processes. Histone acetylation is controlled by the activity of histone acetylases (HATs) and deacetylation of histone deacetylases (HDACs), which promote chromatin condensation and gene silencing. Class I HDACs have been found in various parasitic protozoa (including *G. intestinalis*) where they were associated with antigenic variation regulation, proliferation and cell differentiation [3, 4]. In view of the biological role, inhibitors of histone deacetylases may become interesting alternatives for the treatment of parasitic diseases. In this study, morphological analyses were used to understand the effects of class I HDACs inhibitors, named KV-30 and KV-46, on *Giardia intestinalis* growth and cell organization. These inhibitors decreased the trophozoites proliferation and viability at 24, 48 and 72 h of incubation. Scanning electron microscopy analysis revealed membrane surface alterations and flagella internalization. Transmission electron microscopy analyses showed that trophozoites treated with KV-30 at concentration of 1  $\mu$ M presented myelinic figures and large vacuoles in the cytoplasm. Flow cytometer assays indicated a higher number of parasites in G0/G1 phase after incubation with the inhibitors. Further biochemical and other microscopy assays are under performance to better understand the activity/mechanism of action of these drugs. Taken together, these data show that class I HDACs inhibitors have significant effects against *G. intestinalis* trophozoites growth and in its structural organization suggesting that histone deacetylation pathway should be explored.

[1] Benchimol M., 2005. The nuclei of *Giardia lamblia*--new ultrastructural observations. Arch Microbiol., 183, 160-8. [2] Bezagio RC, Colli CM, Romera LI, Ferreira EC, Falavigna-Guilherme AL, Gomes ML., 2017. Synergistic effects of fenbendazole and metronidazole against *Giardia muris* in Swiss mice naturally infected. Parasitol Res., 116, 939-944. [3] Pedro G.Carranza., Pablo R.Gargantiniab., César G.Pruccaa., AlessandroTorria., AliciaSauraab., StaffanSvård., Hugo D.Lujan., 2016. The International Journal of Biochemistry & Cell Biology. Int J Biochem Cell Biol, 8, 32-43. [4] Yee, J., Lau, W., Ritter, H., Delpont, D., Page, M., Adam, R.D., Müller, M., Wu, G., 2007. Core Histones genes of *Giardia intestinalis*: genomic organization, promoter structure and expression. BMC Molecular Biology, 10, 8-26.

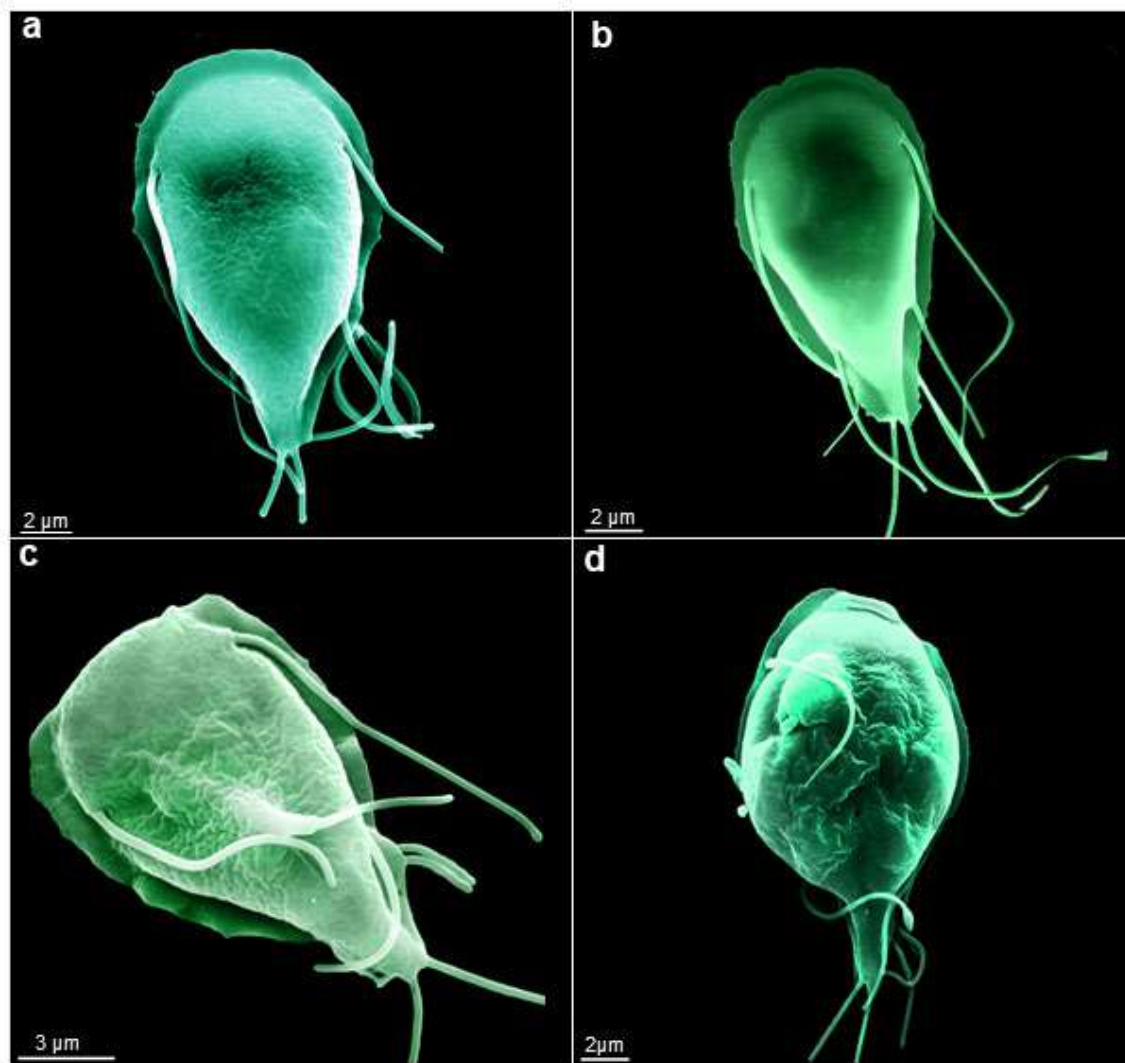


**Figure 1:** (a) Dorsal surface of *G. intestinalis* trophozoites as seen by scanning electron microscopy. (b) Parasites culture after incubation with DMSO. (c) and (d). Trophozoites exposed to KV-30 at concentration of 10 μM. It is possible to observe flagella internalization (c) and protrusions of the dorsal surface (d) of the cell.



## Ultrastructural Effects of Itraconazole and Metallodrugs in *Leishmania amazonensis*: SEM/TEM as Approach to Biological Studies

De Macedo-Silva, ST<sup>1\*</sup>, Navarro, M<sup>3</sup>, de Souza, W<sup>2</sup> and Rodrigues, JCF<sup>2,4</sup>

<sup>1</sup>. Unidade de Microscopia Avançada, CENABIO, UFRJ, Rio de Janeiro, Brazil.

<sup>2</sup>. Instituto de Biofísica Carlos Chagas Filho, UFRJ, Rio de Janeiro, Brazil.

<sup>3</sup>. Departamento de Química, ICE, UFJF, Juiz de Fora, Brazil.

<sup>4</sup>. Núcleo Multidisciplinar de Pesquisa em Biologia, UFRJ, Duque de Caxias, Brazil.

\*email address: sara@cenabio.ufrj.br

Leishmaniasis are among the most prevalent neglected tropical diseases and are endemic in 98 countries. The available treatments are unsatisfactory due to toxicity, limited efficacy, cost and administration. Thus, there is an urgent need for developing of new compounds to treat leishmaniasis. Trypanosomatids have an essential requirement for ergosterol and other 24-alkyl sterols, which are absent in mammalian cells. The inhibition of ergosterol biosynthesis (EB) has been recognized as a promising target for the development of new chemotherapeutic agents. In previous works, our group showed that itraconazole (ITZ), a well-known antifungal drug, is a potent inhibitor of EB in *Leishmania amazonensis*, leading to ultrastructural alterations that resulted in cell death of parasites [1, 2]. Moreover, well-designed metallodrugs could be candidates to antileishmanial agents since transition metal (Pt, Au, Ag, Zn) complexes have been approved as successful drugs to treat human diseases [3]. Thus, the aim of this work was to investigate the effects of new zinc-ITZ complexes against *L. amazonensis*. For biological investigation, scanning and transmission electron microscopy were widely applied. Control and treated parasites were fixed in 2.5% glutaraldehyde in 0.1 M cacodylate buffer (pH 7.2), and postfixed in a solution containing 1% OsO<sub>4</sub>, 1.25% potassium ferrocyanide and 0.1 M cacodylate buffer, pH 7.2. For transmission electron microscopy (TEM), cells were dehydrated in acetone, and embedded in Epon. Ultrathin sections were stained with uranyl acetate and lead citrate and observed under a FEI Tecnai Spirit electron microscope. For scanning electron microscopy (SEM), cells were dehydrated in ethanol, critical point-dried, mounted on stubs, sputtered with thin gold layer, and observed under a FEI Quanta 250 [2]. ITZ produced a marked reduction in the viability of *L. amazonensis* promastigotes, resulting in an IC<sub>50</sub> value of 44 nM, however the new complexes were more active, with IC<sub>50</sub> values of 4 nM and 1.6 nM, for Zn(ITZ)<sub>2</sub>Cl<sub>2</sub> and Zn(ITZ)<sub>2</sub>(OH)<sub>2</sub>, respectively. Against intracellular amastigotes, the antiproliferative effects of the treatments was very potent, resulting in IC<sub>50</sub> values of 145.38 nM, 0.118 nM, and 33.07 nM for ITZ, Zn(ITZ)<sub>2</sub>Cl<sub>2</sub> and Zn(ITZ)<sub>2</sub>(OH)<sub>2</sub>, respectively (Table 1). SEM and TEM revealed several alterations in *L. amazonensis* promastigotes. By SEM, when promastigotes were treated with 0.5 µM ITZ, Zn(ITZ)<sub>2</sub>Cl<sub>2</sub> and Zn(ITZ)<sub>2</sub>(OH)<sub>2</sub> for 48 h, they appeared rounded and swollen, sometimes presenting more than two flagella (Figure 1). By TEM, several alterations were observed after treatment, such as: intense mitochondrial swelling followed by its disorganization, presence of lipid bodies; and presence of vacuoles similar to autophagosomes, some of them containing small vesicles and membrane profiles. Images also indicated a close association between these vacuoles and organelles as the nucleus (Figure 2). In conclusion, zinc-ITZ-complexes resulted in several ultrastructural alterations that could

lead the parasites to cell death, confirming the potent effect of the new chemical identities. Changes in the integrity of plasma membrane and mitochondria could be explained by decrease of their 24-alkyl sterols. The strategy of combining zinc with ITZ was efficient to enhance ITZ activity, because zinc-ITZ-complexes were more active than azole. Moreover, the use of SEM and TEM are excellent approaches for biological investigation. Ultrastructural changes could suggest the mechanism of action of several new compounds.

[1] de Macedo-Silva ST et al., PLoS One 8 (2013) e83247.

[2] de Macedo-Silva ST et al., Antimicrob Agents Chemother 59 (2015) 6402.

[3] Wee HA & Dyson PJ. Eur J Inorg Chem (2006) 4003.

**Table 1: Antiproliferative effects in *Leishmania amazonensis* intracellular amastigotes.<sup>a</sup>**

Compounds	IC <sub>50</sub> 72h (nM)	CC <sub>50</sub> 72h (nM)	Selective Index (SI)
	Intracellular amastigotes	Peritoneal macrophages	CC <sub>50</sub> /IC <sub>50</sub>
ITZ	145.38	15.000	103.17
Zn(ITZ) <sub>2</sub> Cl <sub>2</sub>	0.118	600	5084
ZN(ITZ) <sub>2</sub> (OH) <sub>2</sub>	33.07	800	24.19

<sup>a</sup>Parasites were treated with different concentrations for 72 h to evaluate the growth inhibition. The inhibitors were added after 24 h of growth.

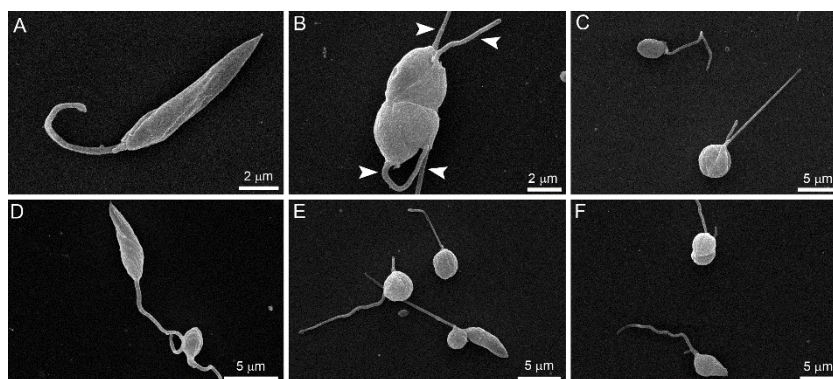


**Figure 1.** Scanning electron microscopy of *L. amazonensis* promastigotes. (A) Control parasites after 72 h of growth; (B, C) 0.5 μM Itraconazole (ITZ); (D) 0.5 μM Zn(ITZ)<sub>2</sub>Cl<sub>2</sub>; and (E, F) 0.5 μM Zn(ITZ)<sub>2</sub>(OH)<sub>2</sub>. Treatment induced significant alterations in the shape of cell bodies; the parasites presented swollen and rounded (B-F), some of them with a long flagellum, sometimes with more than two flagella (B, arrowhead).

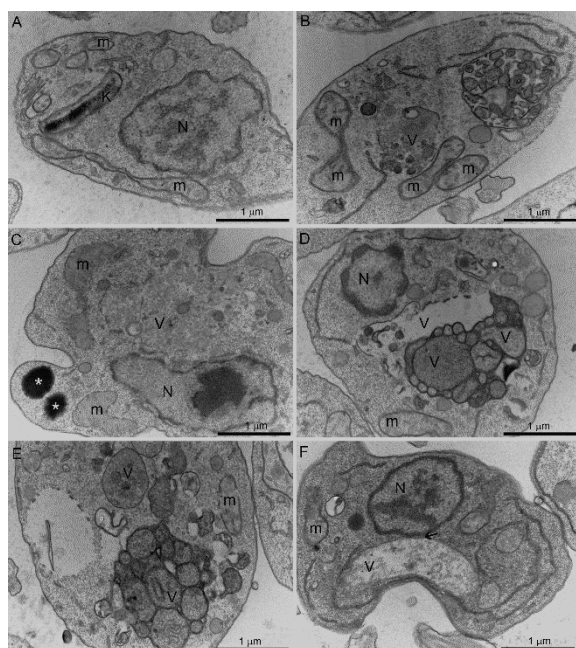


**Figure 2.** Transmission electron microscopy of *L. amazonensis* promastigotes control (A) and treated with 0.5 μM itraconazole (ITZ) (B, C), 0.5 μM Zn(ITZ)<sub>2</sub>Cl<sub>2</sub> (D, E), or 0.5 μM Zn(ITZ)<sub>2</sub>(OH)<sub>2</sub> (F). Several alterations were observed, such as intense disorganization and swelling of the mitochondrion (B, C, E), the presence of lipid bodies (C), and the appearance of vacuoles similar to autophagosomes close to organelles such as nucleus (F, arrow).

## Nanostructured Carbonated Hydroxyapatite Interactions with Murine Pre-osteoblasts

Suzana Azevedo dos Anjos<sup>1</sup>, Elena Mavropoulos<sup>1\*</sup>, Gutemberg G. Alves<sup>2</sup>, Andrea M. Costa<sup>1</sup>, Gisele Dornelas da Silva<sup>3</sup>, Moema de Alencar Hausen<sup>4</sup>, Carolina N. Spiegel<sup>2</sup>, Mirta Mir<sup>5</sup>, José M. Granjeiro<sup>6</sup>, Alexandre M. Rossi<sup>1</sup>

<sup>1</sup>. Department of Condensed Matter, Applied Physics and Nanoscience, Brazilian Center for Physics Research, Urca, Rio de Janeiro, Brazil

<sup>2</sup>. Department of Cellular and Molecular Biology, Institute of Biology, Universidade Federal Fluminense, Niterói, Rio de Janeiro, Brazil

<sup>3</sup>. Post-Graduation Program in Science & Biotechnology, Universidade Federal Fluminense, Niterói, Rio de Janeiro, Brazil

<sup>4</sup>. Biomaterial's Laboratory, Faculty of Medical Sciences, Pontifical Catholic University of São Paulo, Sorocaba, São Paulo, Brazil

<sup>5</sup>. Federal University of Alfenas, Exact Sciences Institute (ICEx) MG-Brasil, Alfenas, Brazil

<sup>6</sup>. National Institute of Metrology, Duque de Caxias, Rio de Janeiro, Brazil

\* Corresponding author. E-mail: [elena@cbpf.br](mailto:elena@cbpf.br)

Synthetic HA is a nanostructured biomaterial for bone treatment constituted of nanoparticles (NPs), which present high specific surface area and interactions with biological systems at the cellular level [1]. The incorporation of carbonate into HA changes physicochemical properties of the material, leading to a low crystallinity, increasing its dissolution rate and allowing the release of nanoparticles into tissues, with possible effects on cell viability [2]. In order to assess such effects in vitro, in this study, murine pre-osteoblasts (MC3T3-E1) were exposed to suspensions with high levels of carbonated apatite nanoparticles with intermediary crystallinity (synthesized at 37°C, nCHA37) and assessed their effects on cell morphology, viability, proliferation and NPs internalization by the cells. nCHA37 powder was synthesized from calcium nitrate tetra hydrate, ammonium di-hydrogen phosphate and ammonium carbonate extra pure (Merck) salts dissolved in aqueous solutions and maintained at 37°C for 2 hours/ pH =13.0. The dried powder was ground and sieved, and suspended in culture media (alpha-MEM) at a 100mg/mL ratio. Zeta-potential revealed aggregates with 0.99±0.36 micrometers, with a mean particle size of 117±26 nm (Rietveld analysis). A viability/cytotoxicity assay using calcein-AM and ethidium homodimer-1 (EthD-1) was used to quantify viable cells after 24h exposure to this suspension with an Axio A1 Observer Fluorescence Microscope, revealing the absence of cytotoxicity (Figure 1), and without significant alterations in the release of pro-inflammatory surface interactions with nCHA aggregates, and evidence of internalization (Figure 2). Indeed, Transmission Electron Microscopy (JEOL JEAM-1011 Electronic Transmission Microscope) confirmed the presence of nanoparticles and smaller aggregates internalized inside membranous organelles in exposed cells. These results indicate that nCHA37 nanoparticles strongly interact with bone cells without affecting cell viability.

- [1] K. Fox et al. *ChemPhysChem*, 13(10) (2012) 2495–2506.  
 [2] S. dos Anjos et al. *J Biomed Mater Res.* (2019) 1–12.  
 [3] Authors acknowledge the technical assistance from Ana Lucia Rosa Nascimento, the Platform of Electron Microscopy at FIOCRUZ, and the financial support of the Brazilian agencies CNPq, CAPES, and FAPERJ.

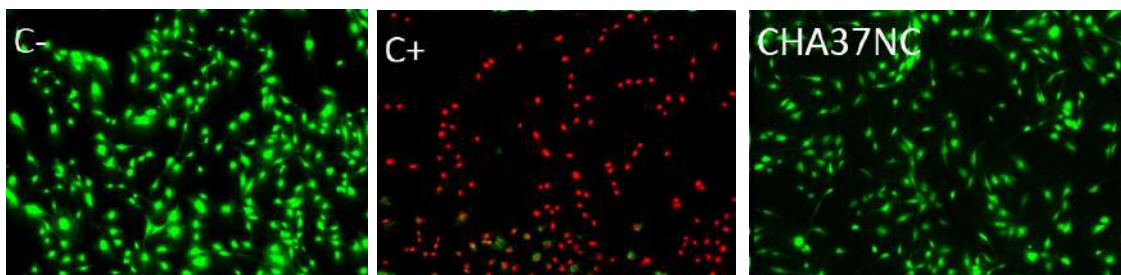


Figure 1. Cell viability after exposure to nanoparticle suspensions of CHA37, culture media (negative control, C-) or latex extracts (positive cytotoxic control, C+). Cells were stained with a live dead assay kit, where green staining indicates viable cells, and red staining indicates dead cells. Images obtained with 10x magnification.

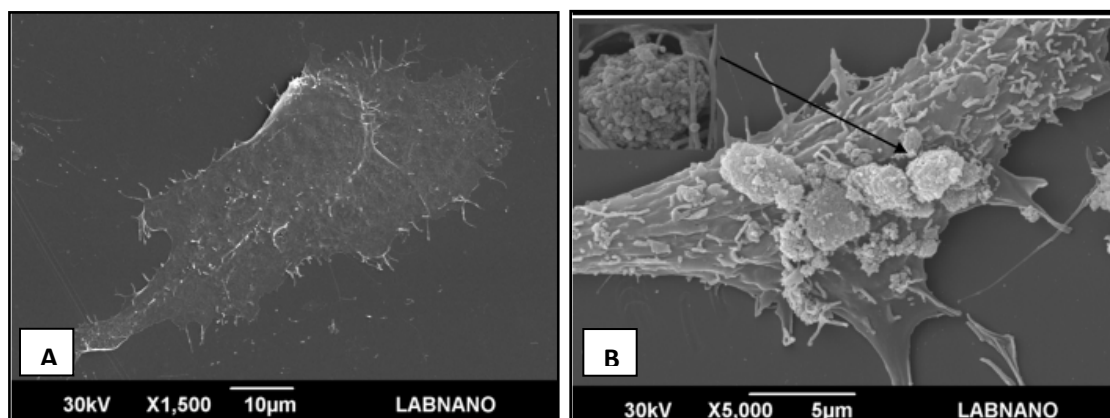


Figure 2. SEM micrographs showing the general morphology of MC3T3-E1 cells after 24 hours exposure to nCHA37 suspensions.



## The role of a possible linker histone in chromatin organization in *Toxoplasma gondii* using different methods in TEM

Tabata D'Maiella Freitas Klimeck<sup>1\*</sup>, Vanessa Rossini Severo<sup>1\*</sup>, Andréa Rodrigues Ávila<sup>1</sup>, Lia Carolina Soares Medeiros<sup>1</sup> and Sheila Cristina Nardelli<sup>1</sup>

1. Instituto Carlos Chagas, Fundação Oswaldo Cruz (FIOCRUZ), Curitiba, Paraná, Brasil

\* tabata.klimeck@gmail.com / vanessarsevero@gmail.com

The chromatin compaction levels are regulated mainly by histones and their post-translational modifications (PTMs). In *Toxoplasma gondii*, the histone H1 or linker histone has not been identified. In other eukaryotes, H1 acts linking nucleosomes and its absence could interfere with the chromatin condensation. Our group performed the knockout of a small and basic protein from *Toxoplasma* similar to H1-like of bacteria. Transmission electron microscopy was used to compare the structure of the nucleus and the chromatin organization in mutants with TgH1-like deleted (*Δtgh1-like*) and control parasites (RH *ΔhxgprtΔku80*). For the first analysis, tachyzoites were fixed in 2.5% glutaraldehyde, post-fixed using 1% osmium tetroxide followed by a series of dehydration process using different acetone concentrations and finally embedded in EMBED-812 EMNEDDING KIT (Direct Replacement of Epon -812) resin. Thin sections (70 nm) were stained with 5% uranyl acetate and lead citrate [1]. Chromatin states were poorly stained using this method and it was not possible to evaluate the differences in chromatin architecture. The *in bloc*o protocol was performed with uranyl acetate since it stains a variety of cellular components, mainly nucleic acids (DNA). Tachyzoites were fixed in 2.5% glutaraldehyde, post-fixed in 1% osmium tetroxide and the sample was immersed in 2% uranyl acetate in water for 2h at 4 ° C protected from the light. The samples were dehydrated using a series of different acetone concentrations and embedded in EMBED-812 EMNEDDING KIT (Direct Replacement of Epon-812) resin. Thin sections (70 nm) were stained with lead citrate [1]. This protocol also showed a poorly stained chromatin making it impossible to analyse the differences between the parasite lines. Next, we used ethanolic phosphotungstic acid (PTA) [2], commonly used for detection of basic proteins since in alcoholic medium it binds mainly in lysine, arginine and histidine [1,3]. Samples were fixed in 2.5% glutaraldehyde followed by dehydration process by a series of ethanol concentrations and embedded in EMBED-812 EMNEDDING KIT (Direct Replacement of Epon-812) resin. Thin sections (70 nm) were stained with lead citrate. Using PTA staining was possible to distinguish the distinct chromatin states highlighting the differences between mutants and control parasites. The *Δtgh1-like* parasites showed more heterochromatin-like structure at nuclei periphery, observed by the electron density regions. Control parasites also showed high-condensed regions at the periphery but in contrast to *Δtgh1-like* parasites, those regions become diffuse towards the nucleus center, suggesting a role of TgH1-like in chromatin organization in *Toxoplasma*.

## REFERENCES

- [1] W. Souza et al., Técnicas de Microscopia Eletrônica Aplicadas às Ciências Biológicas, 3ª edição, Sociedade Brasileira de Microscopia, Rio de Janeiro, 2007.
- [2] M. Gordon; K. G. Bensc, J. Ultrastruct, Res 24:33-50, 1978.

[3] W. Souza; T. Souto-Padrón, Ultrastructural Localization of Basic Proteins on the Conoid, Rhoptries and Micronemes of *Toxoplasma gondii*, *Z. Parasitenkd.* (56, 123-129), 1978.

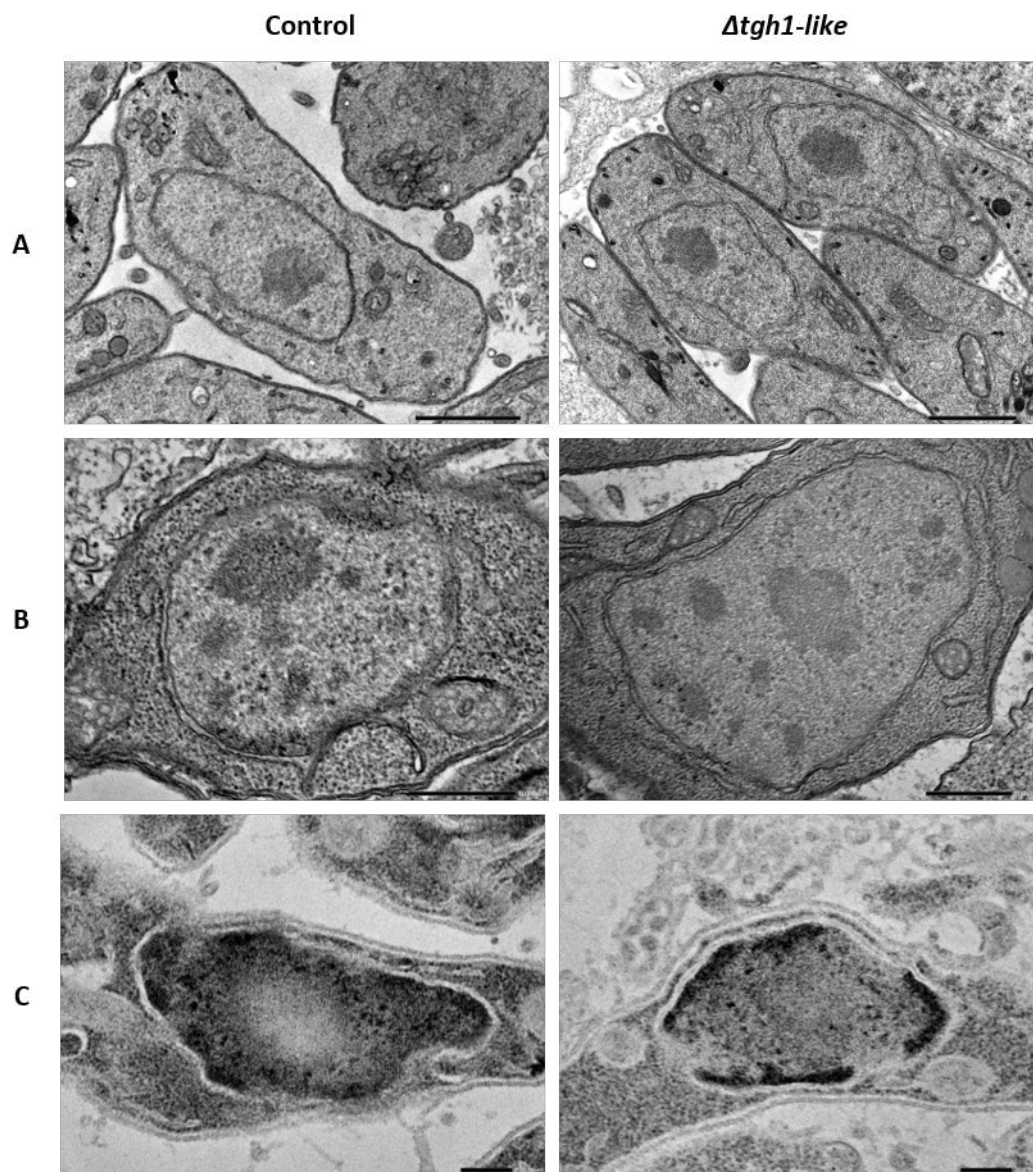


Fig. 1. A) Control and *Δtgh1-like* parasites were fixed in 2.5% glutaraldehyde, post-fixed in 1% osmium tetroxide and after dehydration were embedded in EMBed-812 resin. x 15.000 B) Uranyl acetate *In bloco* blocking protocol was performed, fixed in 2.5% glutaraldehyde, post-fixed in 1% osmium tetroxide and samples were immersed in 2% uranyl acetate in water for 2h, after dehydration samples were embedded in EMBed-812 resin. x 30.000 C) Parasites were fixed in 2.5% glutaraldehyde, dehydration through a series of different alcohol concentrations, and incubated during 2 h at room temperature in 2% phosphotungstic acid in absolute ethanol and embedded in EMBed-812 resin. x 30.000

## Characterization of Giant Viruses with TEM, SEM and Cryo-EM

Thalita Souza Arantes<sup>1\*</sup>, Gregory Kitten<sup>1</sup>, Janine Costa Ivo<sup>1</sup>, Érico Freitas<sup>1</sup>, Wagner Rodrigues Nunes<sup>1</sup>, Jônatas Santos Abrahão<sup>2</sup>

1. Centro de Microscopia, Universidade Federal de Minas Gerais, Belo Horizonte, Brazil.
2. Instituto de Ciências Biológicas, Universidade Federal de Minas Gerais, Belo Horizonte, Brazil.

\*tsararantes@gmail.com

Giant viruses are an important and unique group of viruses whose first representative was discovered in 2003. The *Acanthameba polyphaga mimivirus* (APMV) was isolated from water collected in a cooling tower for air conditioning in the British city of Bradford [1]. APMV captured the attention of the scientific community for two reasons: (a) because of its large size, with dimensions greater than some bacteria, and (b) since it contained genes never before identified in other viruses [1]. Since the discovery of APMV, many other giant viruses have been isolated from different sources and localizations utilizing various protocols of isolation [2,3]. Here, our aim was to utilize transmission electron microscopy (TEM), scanning electron microscopy (SEM) and cryo-electron microscopy (Cryo-EM) to analyze the replication cycle and structural features of three isolated giant viruses: mimivirus, marseillevirus and tupanvirus. The analysis of the replication cycle was performed using TEM analysis of amoeba cells infected with each of the viruses. Structure analyses were carried out using SEM and Cryo-EM analysis of purified viral particles. Based on the images obtained from these techniques, it was possible to elucidate some steps of the replication cycle of these giant viruses. The results revealed that marseillevirus is able to form a giant vesicle, which is/are able to stimulate amoebal phagocytosis. In addition, we observed the presence of an internal membrane in the capsid and alternative routes of viral penetration. In relation to mimiviruses, it was possible to better understand some processes which have not yet been well-elucidated in viruses, such as morphogenesis of viral particles and the formation of an area called the fibril acquisition area. Finally, EM techniques allowed the structural characterization of the tupanvirus, one of the largest virus isolated to date, containing particles with a size of ~1.2 - 2.3  $\mu\text{m}$ . In addition, it was possible to understand some stages of the replication cycle of this virus: penetration, morphogenesis and release of viral particles. Thus, in the context of giant viruses, the use of electron microscopy techniques are essential for the understanding of the ultrastructure of these viruses, information which is indispensable for characterization of their replication cycle.

### REFERENCES

- [1] La Scola et al., Science. 299 (2003) 2033
- [2] Arantes et al., JVI. 90 (2016) 99
- [3] Abrahão et al., Nature Communication. 9 (2018) 749

Financial support: CAPES, CNPq, FINEP, FAPEMIG.



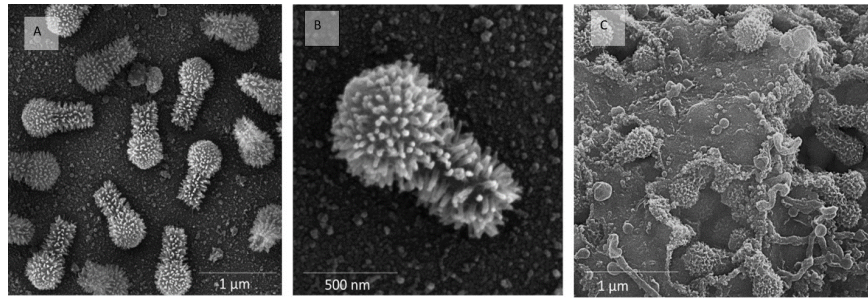


Figure 1: A and B) Scanning Electron Microscopy (SEM) images of purified particles of tupanvirus. C) SEM images of amoeba cells infected with tupanvirus.

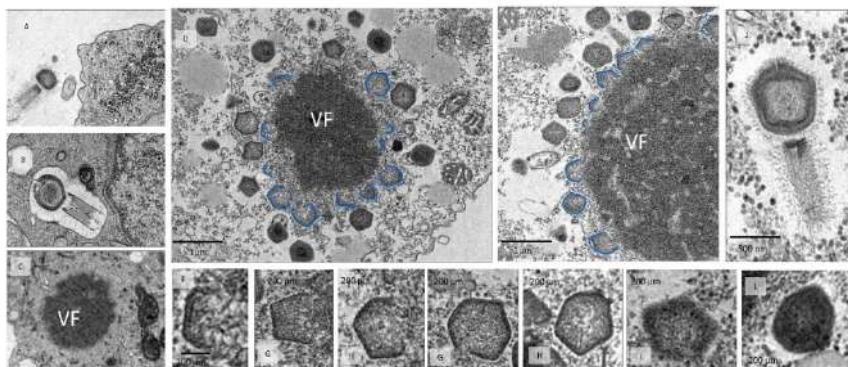


Figure 2: Transmission electron microscopy (TEM) represented the steps of the replication cycle of tupanvirus.

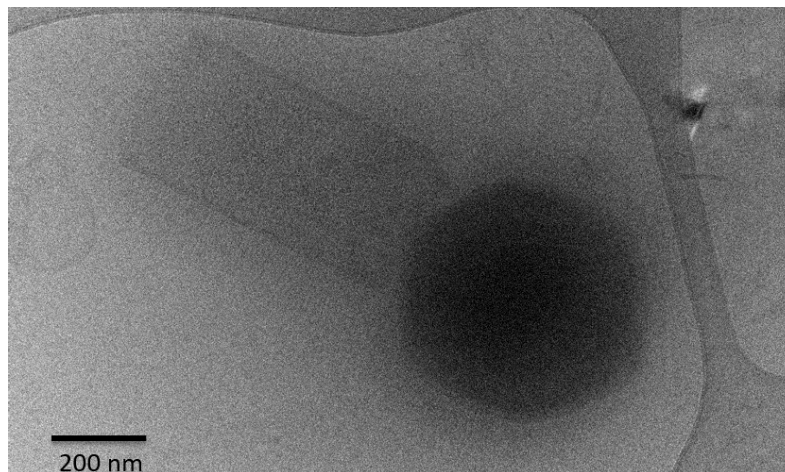


Figure 3: Cryo microscopy of purified particles of tupanvirus.



## Use Of Different Microscopy Approaches For The Immunolocalization Of Costa Proteins From *Tritrichomonas foetus*

Paula Terra Bandeira<sup>1\*</sup>, Wanderley de Souza<sup>1</sup>

<sup>1</sup> Universidade Federal do Rio de Janeiro, Instituto de Biofísica Carlos Chagas Filho, Rio de Janeiro, Brasil. paulaterrabandeira@gmail.com

The costa of *Tritrichomonas foetus* is a prominent striated fiber, composed of a complex filament ensemble and globular structures, that is connected to the recurrent flagellum through a filament network [1]. This peculiar structure, although part of the cellular cytoskeleton, differs in many aspects from filaments usually found in the muscle, cilia, flagella or other structures containing microtubules, and is, until now, still not fully characterized. In previous studies from our group, using proteomic analysis of enriched costa fractions, it were identified 44 hypothetic proteins without conserved domains [1, 2]. Trough bioinformatics analysis, the protein 11810 was selected for the production of specific polyclonal antibodies to proceed with its immunolocalization in the isolated costa. Thus, this study aimed to use a differential array of microscopy techniques to help confirm the presence and assess the potential distribution of this protein in the costa. To achieve this, *T. foetus*'s costa was isolated by cell fractionation and the specific localization of 11810 was evaluated by immunofluorescence and immunocytochemistry. The observation by conventional immunofluorescence, as an initial investigation, revealed the antibody localization throughout the whole costa structure. In order to obtain an enhanced overview, the costa was then observed by super-resolution microscopy, confirming the presence of the 11810 protein in all the structure, and furthermore it provided the indication of a regular pattern of this protein in the whole structure, suggesting an abundant distribution of this protein in the costa. To deepen the analysis of the 11810 protein localization in the costa, immunocytochemistry was performed and analyzed by negative staining and Tokuyasu frozen sections. Both techniques confirmed the distributed localization of the 11810 throughout costa's structure. However, more studies to further characterize the specific localizations of this protein in the distinct regions that compose the costa, as also with other candidate proteins as well, are still in progress. Nonetheless, this present data could assist in determining also the functional role of this protein in the assembled costa and therefore better understand the organization and function of this structure in unicellular organisms.

[1] de Andrade Rosa et al., Biol Cell 109 (2017) 6.

[2] Benchimol et al., Genome Announc.5 (2017) 16.

[3] This research was supported by Finep, CNPq, CAPES and FAPERJ.

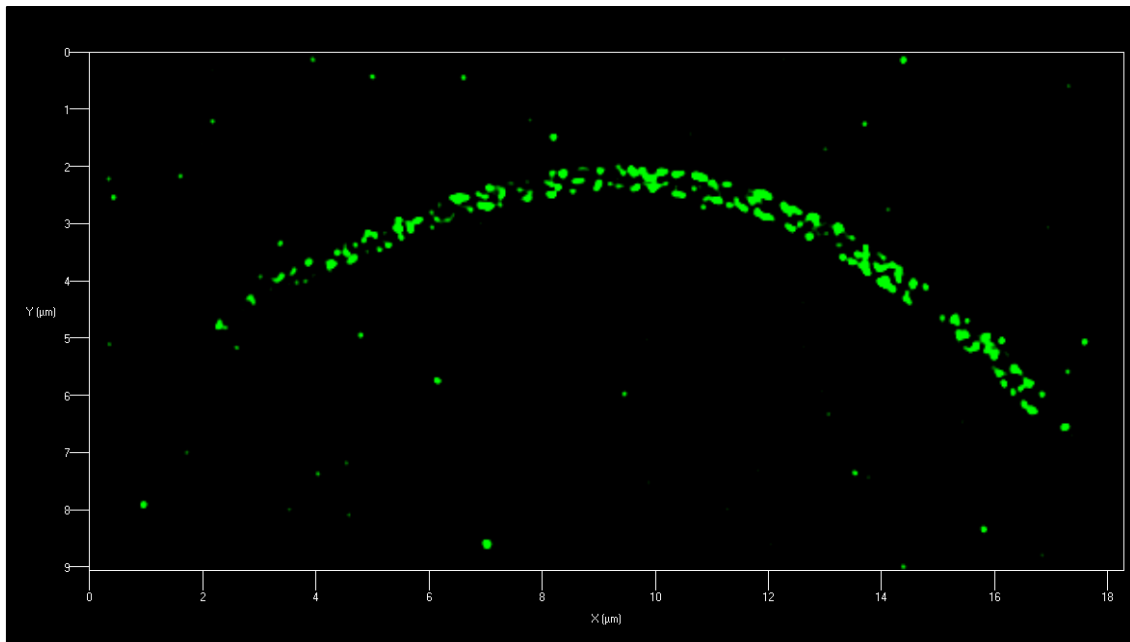


Image 1: **Immunofluorescence of costa from *Tritrichomonas foetus***. The costa was isolated and immunolabeled with polyclonal antibodies against the 11810 protein. Note that this protein is distributed all along the structure in a regular pattern. Image acquired with ELYRA PS.1 microscope using SIM mode.

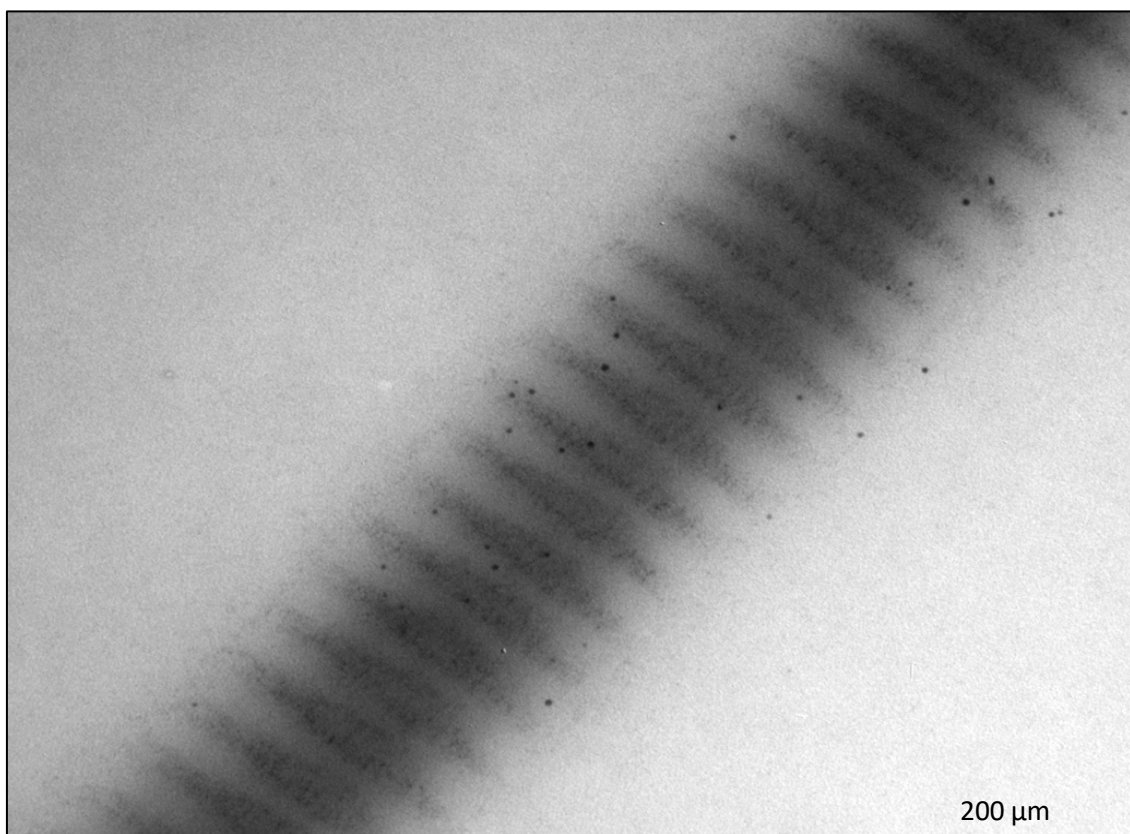


Image 2: **Negative staining of costa from *Tritrichomonas foetus***. The costa was isolated and immunolabeled with polyclonal antibody against the 11810 protein, confirming its presence in the structure. Image obtained with JEOL 1200 EX microscope.

## **Influence of Microorganisms on Reductive Dissolution of Fe(III) in Doce River Basin after Fundão Dam failure (Mariana, MG)**

Alex Silva Santos<sup>1\*</sup>, Pedro de Moura Sanjad<sup>1</sup>, Ana Caroline Ribeiro da Cruz<sup>1</sup>, and Carolina N. Keim<sup>1</sup>

<sup>1</sup>. Instituto de Microbiologia Paulo de Góes, Universidade Federal do Rio de Janeiro (UFRJ), Rio de Janeiro, Brasil. alexssantos25@outlook.com

The biogeochemical cycle of iron (Fe) comprises alternation between Fe(II), the most soluble form, and Fe(III), the least soluble. In aerobic environments, Fe(II) is oxidized to Fe(III) by O<sub>2</sub>, followed by precipitation. In anaerobic environments, reduction of Fe(III) to Fe(II) is mostly mediated by heterotrophic microorganisms, both fermenters and dissimilatory Fe-reducing microorganisms [1]. On November 5, 2015, Fundão Dam failed in Mariana (MG), releasing about 30 million m<sup>3</sup> of iron mining tailings into Doce River and tributaries [2]. Long term consequences may include microbial reduction of Fe(III) oxides coupled to oxidation of organic matter. Besides Fe, toxic species of As, Cd, Mn, Pb, Zn and other elements could be mobilized. In this work, we evaluate the influence of organic matter and microorganisms on the reduction of Fe(III) from the sediments of Doce River and affected tributaries, producing Fe(II). In addition, we evaluate the release of other chemical elements to the aqueous phase. For this purpose, we collected water and sediment samples in Doce and Gualaxo do Norte Rivers, and prepared anaerobic microcosms and enrichment cultures. Fe(II) concentrations in the liquid phase were measured with ferrozine. All experimental microcosms with added organic matter showed higher concentrations of Fe(II) as compared to both controls without addition of organic matter and dead controls, showing the role of organic matter and microorganisms in the reductive dissolution of Fe (Figure 1). Glucose led to higher concentrations of Fe(II) in the liquid phase as compared to acetate, which could indicate participation of fermenting microorganisms. Fe(II) concentrations showed good correlation to added organics for each type of organic substrate used (Figure 1). Manganese was also mobilized, reaching concentrations about ten times lower than iron. In enrichment cultures for dissimilatory Fe-reducing microorganisms, there was microbial growth and increase of Fe(II) concentrations over the weeks. X-ray diffraction showed that most of the amorphous Fe oxide used as Fe(III) source was converted to magnetite (FeO·Fe<sub>2</sub>O<sub>3</sub>). Cultures 170 days old contained isometric crystals about 30 nm in length, distinct from the elongated nanoparticles observed in controls (Figure 2). Our results show that native microorganisms are able to couple organic matter degradation to Fe(III) reduction to Fe(II), which may remain soluble or precipitate in secondary minerals as magnetite. We propose that control of organic matter input into Doce River and tributaries could reduce mobilization of Fe, Mn, and other toxic metal species, improving water quality [3].

### **REFERENCES**

- [1] K.A. Weber et al., Nature Rev. Microbiol. 4 (2006) 752.
- [2] <https://www.samarco.com/rompimento-de-fundao/>
- [3] We are thankful to CENABIO-UFRJ for microscopy facilities, and CNPq for financial support of A.S. Santos.

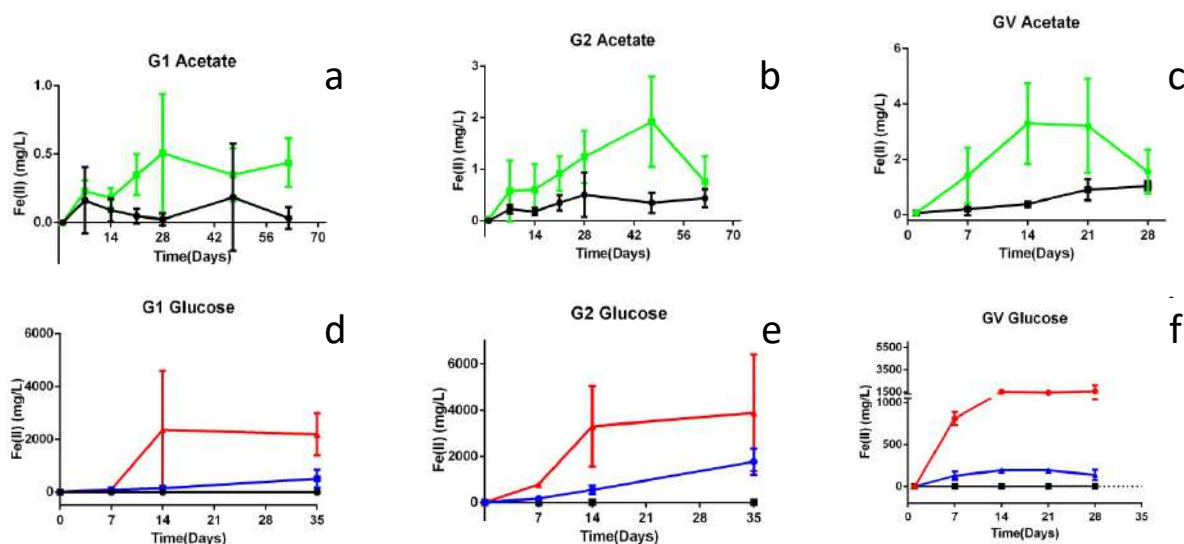


**Figure 1:** Fe(II) concentrations over time in microcosms made from river water and sediments containing (a-c) acetate 6.8 g/L or (d-f) glucose 3 g/L (blue) or 15 g/L (red), as compared to living controls without added organics (black). Microcosms were constructed with samples from (a-b) Gualaxo do Norte River not reached by Fundão Dam tailings (G1), (c-d) Gualaxo do Norte River highly impacted by Fundão Dam tailings (G2), and (e-f) Doce River affected by tailings (GV). Bars indicate standard deviation.

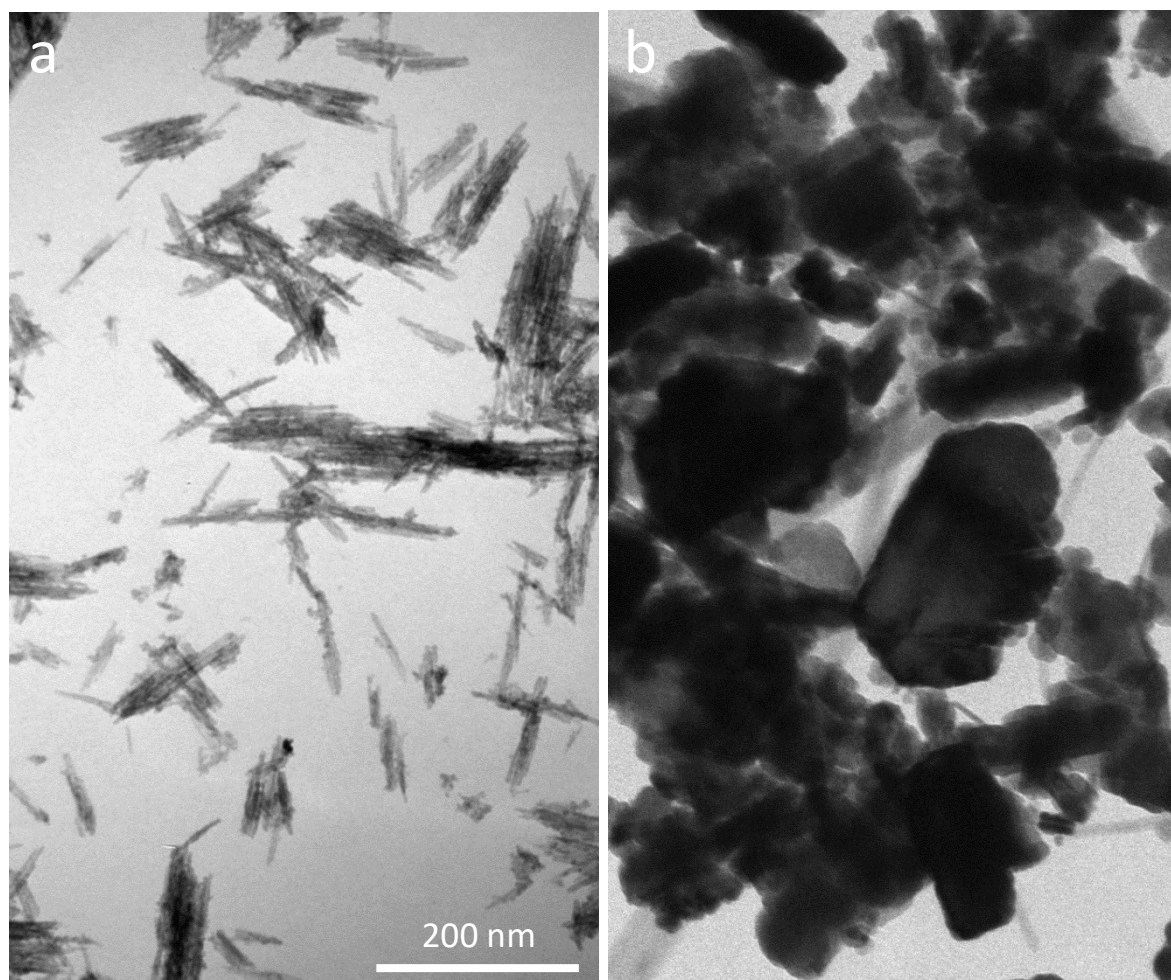


**Figure 2:** Transmission electron microscopy of the solid phase of enrichment cultures. (a) Control (dead) cultures showing amorphous minerals used as Fe(III) source. (b) Solid phase of enrichment cultures composed mainly of magnetite (FeO·Fe<sub>2</sub>O<sub>3</sub>).



## EFFECTS OF EXERCISE PROTOCOLS ON FUNCTIONAL RECOVERY AND NEUROMUSCULAR REGENERATION IN ANIMAL MODEL OF COMPRESSIVE SPINAL CORD INJURY

Anne Caroline Rodrigues dos Santos<sup>1</sup>, Renata Pereira Laurindo<sup>1</sup>, Nathalie Henriques Silva Canedo<sup>2</sup>, Fernanda Marques Pestana<sup>1</sup>, Ana Maria Blanco Martinez<sup>1</sup> and Suelen Adriani Marques<sup>1,3</sup>

<sup>1</sup>. Laboratório de Neurodegeneração e Reparo, Hospital Clementino Fraga Filho, Faculdade de Medicina, Departamento de Patologia, Universidade Federal do Rio de Janeiro, Rio de Janeiro, Brasil.

<sup>2</sup>. Faculdade de Medicina, Departamento de Patologia, Universidade Federal do Rio de Janeiro, Rio de Janeiro, Brasil.

<sup>3</sup>. Laboratório de Regeneração Neural e Função – Departamento de Neurobiologia, Instituto de Biologia, Universidade Federal Fluminense, Rio de Janeiro, Brasil.

e-mail: arsants@gmail.com

Traumatic spinal cord injury promotes sensory and motor deficits that impair functional performance; physical rehabilitation is the only established therapeutic reality in the human clinical set. This study aimed to evaluate the effect of exercise protocols with different intensity on functional recovery, and neuromuscular regeneration in a mice model of compressive spinal cord injury. We used young female C57BL/6 mice, submitted to spinal cord extradural compression (vascular clip, 30g / 10 seconds compression) after T9 laminectomy. This study was developed in 2 phases, and 5 groups were analyzed: SHAM (laminectomy only); SCI (injured, without treadmill training); TMT1 (injured, treadmill trained for 10min), TMT2 (injured, treadmill trained for two 10-minute cycles, with a 10-min pause between them), and TMT3 (injured, treadmill trained during 28 days with the TMT2 protocol and, after that period, with the TMT1 protocol). The 8-weeks treadmill training starting 7 days after injury and performed 3 times a week. Functional evaluations (Basso Mouse Scale - BMS, Ladder Walking Test - LWT, Rotarod, digital analgesimeter, n=6/group) were assessed weekly, and electroneuromyography was made 8 weeks after injury. After perfusion, morphological evaluations were performed. SHAM group did not show alteration after injury and was used as a normal pattern. In the first stage, we compared the results of TMT1 and TMT2 groups and, although the TMT2 showed earlier functional recovery, TMT1 group was better than TMT2 during the chronic phase of the injury, as seen by functional and morphometric analyses. In stage two, we compared TMT1 protocol with TMT3, a combination of TMT2 and TMT1 protocols. The best results in terms of regeneration, functional recovery and muscle plasticity were observed in the TMT3 group. We concluded that, the intensity of the exercise can modulate the quality of the regenerative response, and if this intensity is adjusted according to the clinical phase of the injury, the results can be further improved.

### REFERENCES

- [1] M. ARDESTANI, et al. Neurorehabilitation and Neural Repair, vol. 33, 1, Jan. 2019.
- [2] S. COBIANCHI, S. Current neuropharmacology, 15(4), 495-518. 2017.
- [3] J. HOULE. et al., Ann. N. Y. Acad. Sci ISSN0077-8923. 2013.[5] S. A. MARQUES et al. Journal of Neuroscience Methods 15: 177, 183-93. 2009.

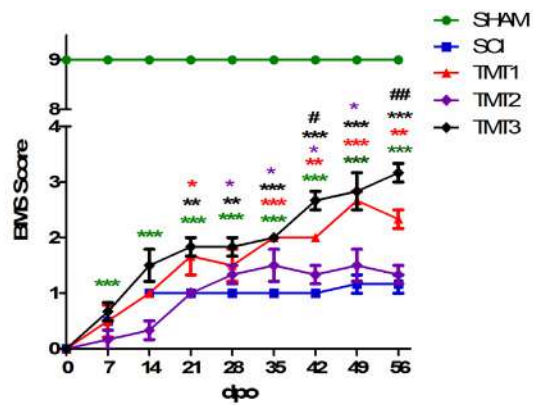


Figure 1 –Comparative BMS assessment up to 8 weeks after 21 dpo the treated groups showed a higher significant difference in relation to the SCI group. Also, the TMT3 group showed a significant difference when compared to TMT1 after 42 dpo.

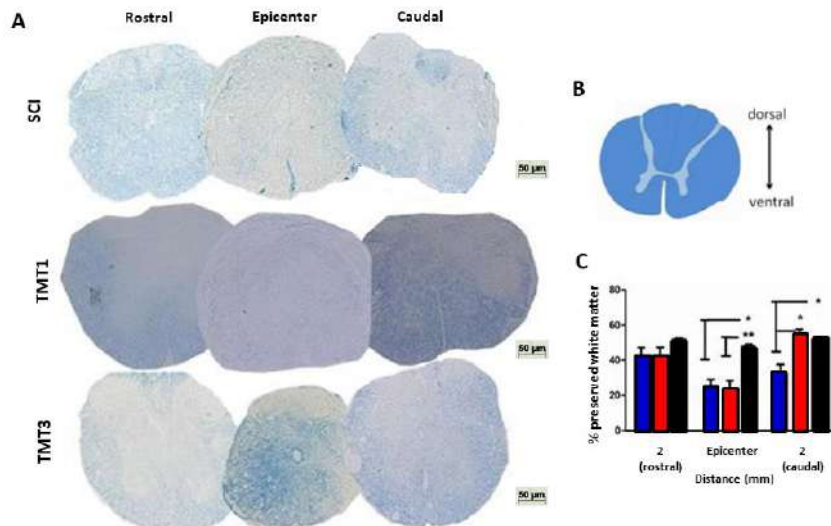


Figure 2 - Analysis of preserved white matter. (A) Spinal cord cross-sections, stained with Luxol Fast Blue (LFB), 8 weeks after injury. (B) schematic view of the quantified area. (C) Bars graphs showing the white matter area quantification.

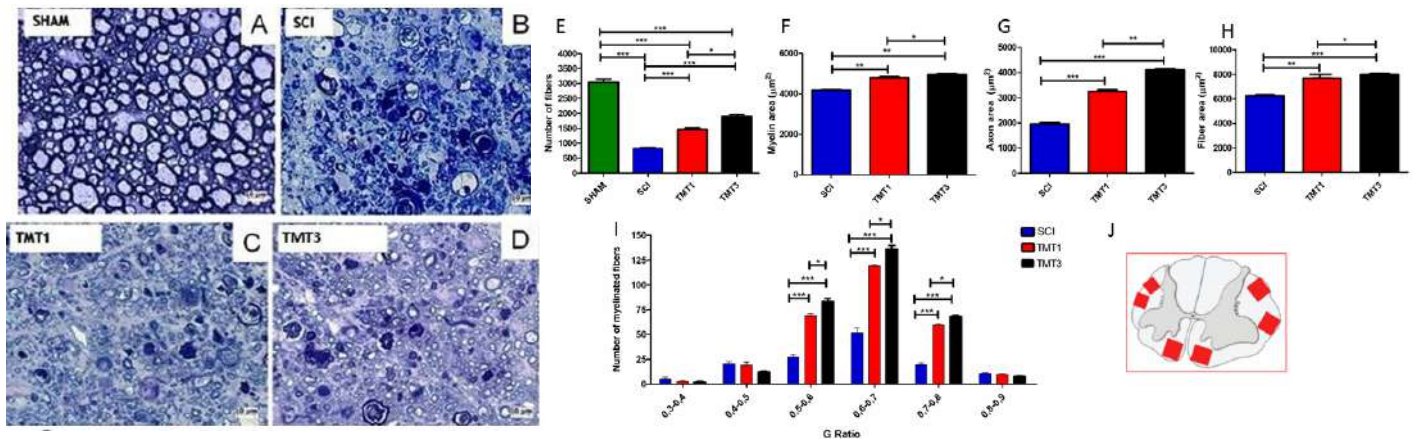


Figure 4 - Qualitative analysis of the spinal cord. A-D - Cross-sections stained with toluidine blue, 56 days after injury, showing the organization of cytoarchitecture and preservation of myelinated nerve fibers in the studied groups. E - Quantification of the number of myelin fibers. Morphometric analysis of the spinal cord. (F) Myelin area; (G) Axon area; (H) Nerve fiber area. (I) Stratification by ranges of G ratio values. All groups exhibited most fibers in the range of 0.5-0.8 µm. The TMTs groups show a shift from the graph to the left, exhibiting more fibers in the range of 0.5-0.8. In figure 4J, representative scheme of the areas analyzed.

## A Study of Magnetic Nanoparticles Synthesis For Biological Applications

Giovanna Pinto Pires<sup>1</sup>, André Fraga Carvalhal<sup>1</sup>, Letícia Miranda Cesário<sup>1</sup>, Rafael Freitas Santos Pereira<sup>1</sup> and Jairo Pinto de Oliveira<sup>1\*</sup>

<sup>1</sup>Federal University of Espírito Santo, Department of Biology, Alegre, Brazil

Nanotechnology has become a resource, nowadays, to a wide variety of applications, such as process engineering, biodetection of pathogens, tissue engineering, enzyme immobilization, and many more [1, 2]. Due to magnetic iron oxides' ( $\text{Fe}_3\text{O}_4$  and  $\gamma\text{-Fe}_2\text{O}_3$ ) low toxicity levels, easy separation process and superparamagnetic properties, much attention has been directed at them [3], though its high reactivity and effortless degradation under certain conditions makes it unstable and difficult to deal with when working in nanoscale [2]. Thus, a study about the magnetic nanoparticles (MNPs) themselves and their properties, as well as an optimization of their synthesis process, takes place. Therefore, this work's main goal was to optimize monodispersive magnetic iron nanoparticles through factorial experiments, as the influence of time, molar ratio and temperature of the synthesis process were all assessed. Iron Chloride II and III ( $\text{FeCl}_2$  and  $\text{FeCl}_3$ , respectively) were chosen as the metallic precursors, along with sodium hydroxide for the alkaline solution. The synthesized nanomaterials had their properties characterized by infrared radiation (IR) — (FT-MIR FTLA 2000 Bomem) —, x-ray diffraction (XRD) — Difractômetro D8 – ADVANCE (BRUKER – AXS) —, scanning electron microscopy (SEM) — (SEM-JEOL1600LV) —, and, at last, their elementary composition was confirmed by energy-dispersive X-ray spectroscopy (EDS), utilizing detector Bruker XFlash 6/10. The IR analysis showed that hematite ( $\text{Fe}_2\text{O}_3$ ) is characterized by the bands 443, 589 and  $632\text{ cm}^{-1}$ , which is related to the vibrational modes Fe-O. The XRD analysis presented characteristic pattern, indicating the actual yield of highly pure  $\text{Fe}_2\text{O}_3$  (FeNPs), besides its spinel structure. Additionally, MEV images exhibited a uniform, monodispersive pattern, while EDS confirmed the presence of the elements Fe and O.

### REFERÊNCIAS

- [1] SALATA, Oleg V. Applications of nanoparticles in biology and medicine. **Journal of nanobiotechnology**, v. 2, n. 1, p. 3, 2004.
- [2] BILAL, Muhammad et al. Magnetic nanoparticles as versatile carriers for enzymes immobilization: A review. **International journal of biological macromolecules**, 2018.
- [3] ALI, Attarad et al. Synthesis, characterization, applications, and challenges of iron oxide nanoparticles. **Nanotechnology, science and applications**, v. 9, p. 49, 2016.



Figure 1. SEM (scanning electron microscope) image of the FeNPs.

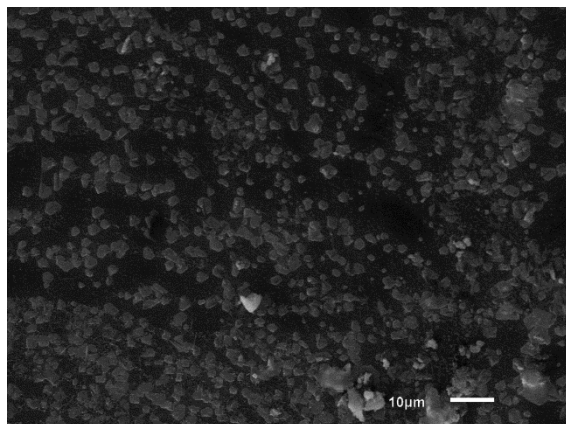


Figure 2. FeNPs' EDS (energy-dispersive X-ray spectroscopy).

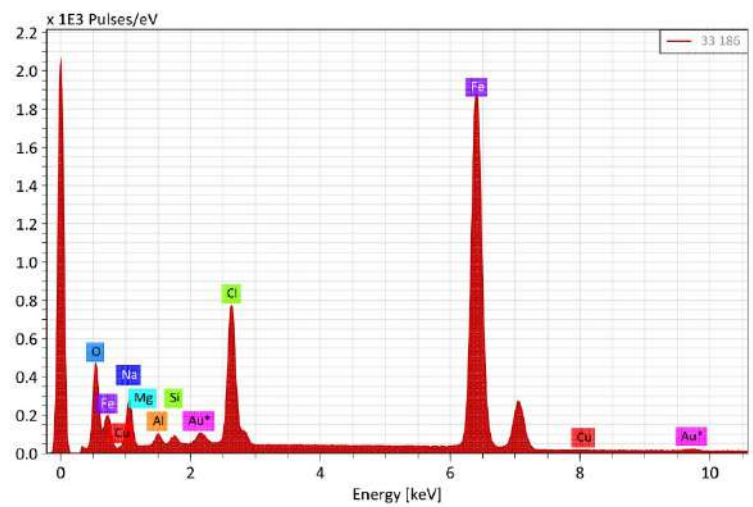


Figure 3. XRD (X-ray diffraction) of the FeNPs.

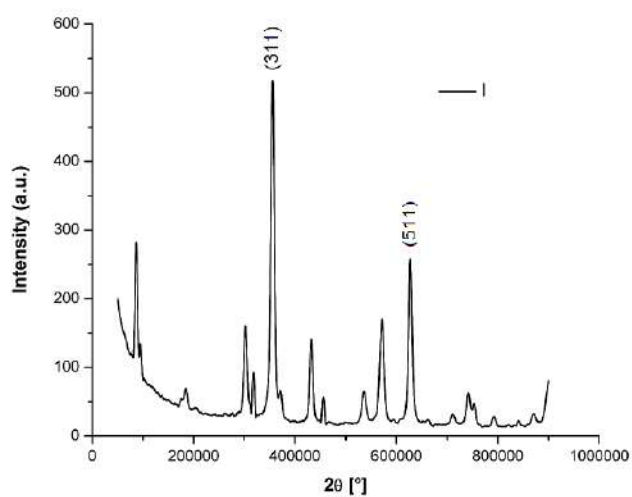
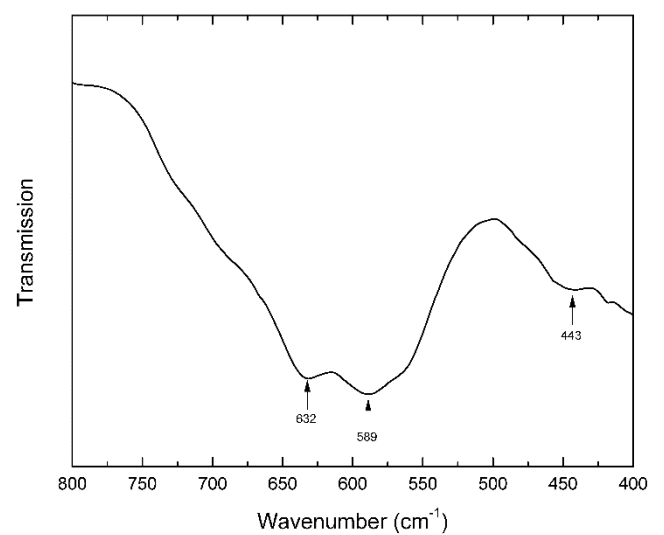


Figure 4. IR (Infrared radiation) analysis of the FeNPs..





## Optimization of a Cryopreparation Protocol for Quantitative X-ray Microanalysis of Ion-Rich Compartments in *Trypanosoma cruzi*

Jean Pierre<sup>1</sup>, Wendell Girard-Dias<sup>1,2</sup>, Wanderley de Souza<sup>1</sup> and Kildare Miranda<sup>1\*</sup>

1. Laboratório de Ultraestrutura Celular e Microscopia Hertha Meyer, Instituto de Biofísica Carlos Chagas Filho and Centro Nacional de Biologia Estrutural e Bioimagem – Universidade Federal do Rio de Janeiro, Rio de Janeiro, Brazil.
2. Plataforma de Microscopia Eletrônica Rudolf Barth, Instituto Oswaldo Cruz – Fiocruz, Brazil.

[kmiranda@biof.ufrj.br](mailto:kmiranda@biof.ufrj.br)

Ions are of vital importance to cells. They are involved in different cellular processes such as control of enzymatic reactions, cell signaling, controlling of pH, among other functions. The study of ion mobilization in cells and tissues is therefore important for the understanding of different cellular processes, including those involved in infection and intracellular survival in protozoan parasites.. X-ray microanalysis is a well known technique used to identify and quantify the elemental composition in samples of different origin (biological and non-biological specimens) [1]. Although powerful as a research tool in electron microscopy, when it comes to biological samples (cells and tissues) this technique has been mostly applied as a qualitative method due to (1) limitations in sample preparation methods, that usually require the use of cryotechniques due to mobilization or extraction diffusible ions with room temperature methods, and (2) the lack of appropriate standards to calibrate the instruments and provide a reference value for quantitative analysis. In this work, we optimized a protocol for sample preparation and calibration of an X-ray microanalysis system for quantification of ions in *T. cruzi*. We focused on ion-rich organelles - acidocalcisomes - which contain different ions such as phosphorus, calcium, magnesium, potassium, sodium and zinc and for this reason, are excellent models to study ion composition *in situ* [2]. Cells as well as standards containing different ions at known concentrations where cryofixed either by high pressure freezing or by plunge freezing and 120 nm thick frozen sections were obtained using cryoultramicrotomy. Sections were then frozen-dried under high vacuum at -190 °C for 2 hours. X-ray microanalysis was performed using the same conditions for cells and standards and the elemental concentration was determined using the Hall method [3]. Preliminary results (figure 1) showed that the concentration of potassium and iron in acidocalcisomes were 0.052 mmoles and 0.189 mmoles / kg dry mass, respectively. Elemental mapping showed that the elements were restricted to the matrix of the acidocalcisomes (Fig.1, C-E). Given the importance of the acidocalcisomes for the cellular viability of *T. cruzi*, the understanding of the dynamics involved in ion mobilization of these structures may help the development of new drugs for the treatment of Chagas disease. Thus, optimization of a protocol for quantification of ions in single cells that could be applied to other biological models may contribute for scientific development in this field.

### References:

- [1]. Warley, Alice. Development and comparison of the methods for quantitative electron probe X-ray microanalysis analysis of thin specimens and their application to biological material. Journal Microscopy., 261:177-184, 2016.

- [2]. Miranda. Kildare. de et al. The fine structure of acidocalcisomes in *Trypanosome cruzi*. Parasitol Res. 86:373-384, 2000.
- [3]. Hall, T. A.; Gupta, B.L. Quantification for the X-ray microanalysis of cryosections. Journal Microscopy. 126:333-345, 1982.
- [4]. This work was supported by CNPq, FAPERJ, FINEP, CAPES (Brazil) and Instituto Nacional de Ciência e Tecnologia de Biologia Estrutural e Bioimagem.

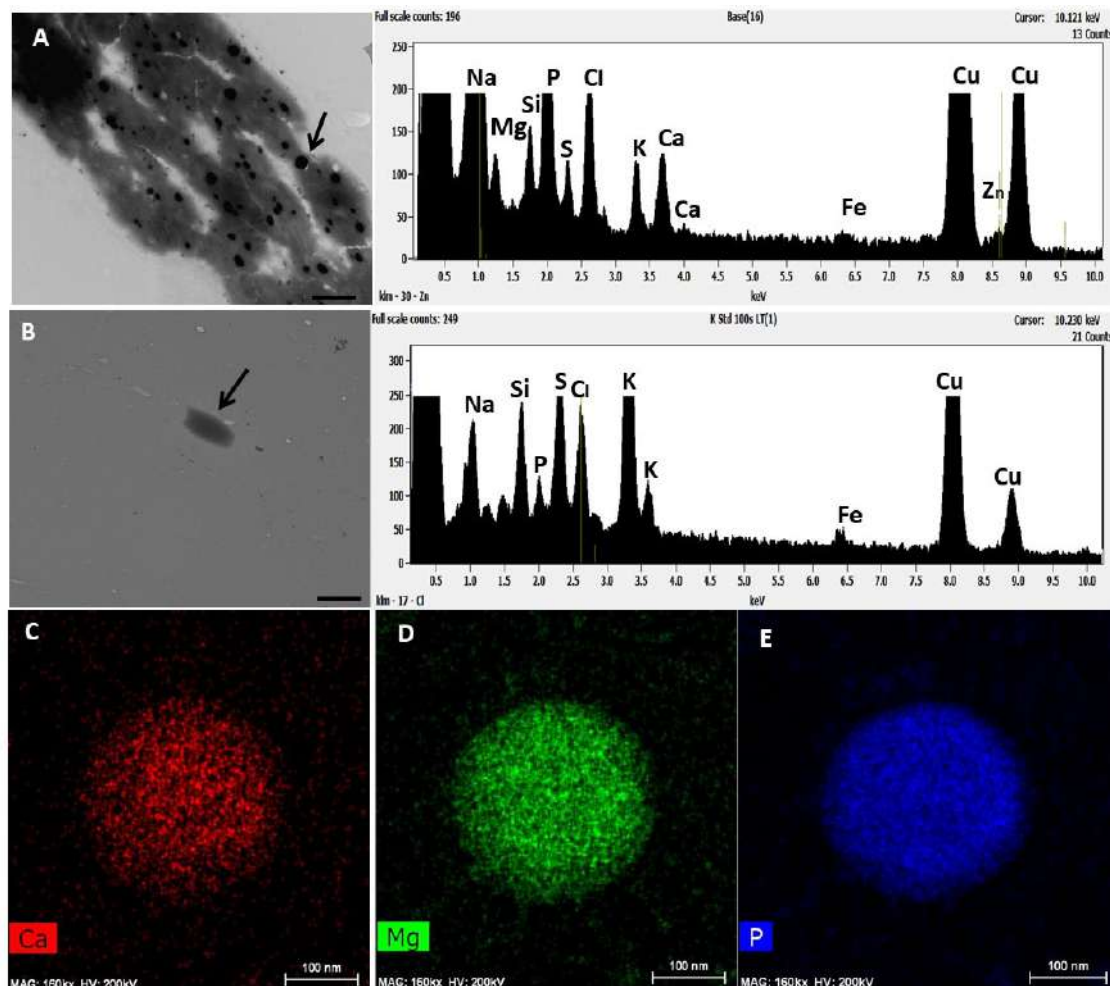


Figure 1. Representative images of the cell profile of *T. cruzi* (A) with their respective acidocalcisomes (electron dense organelles). The x-ray spectrum acquired at an acidocalcisome (arrows) is shown, (B). Image of a fraction of a potassium standard. (C),(D) and (E) Elemental mapping of acidocalcisomes showing the elements immobilized at the matrix of the acidocalcisomes. Scale bars: 2  $\mu$ m in A, 10  $\mu$ m in B, 100 nm in C, D and E.

## Crystallographic Misorientation Between Spicules in The Skeleton of the Calcareous Sponge *Sycettusa hastifera*

Lia Souza Coelho<sup>1\*</sup>, Marcos Farina<sup>2</sup>, Michelle Klautau<sup>3</sup>, Andre Linhares Rossi<sup>1</sup>

<sup>1</sup>. Centro Brasileiro de Pesquisas Físicas, Rio de Janeiro, Brasil.

<sup>2</sup>. Universidade Federal do Rio de Janeiro, Instituto de Ciências Biomédica, Rio de Janeiro, Brasil.

<sup>3</sup>. Universidade Federal do Rio de Janeiro, Instituto de Biologia, Rio de Janeiro, Brasil.

The skeleton of calcareous sponges (phylum Porifera, class Calcarea) is formed by Mg-calcite spicules ranging from approximately 10 to 2000  $\mu\text{m}$  in length and usually composed of two, three or four (rarely five) conics rays joined at the base [1,2]. One individual spicule behaves as a monocrystal (trigonal system) with only few degrees of misorientation ( $<1^\circ$ ) [1,3]. The species *Sycettusa hastifera* belong to the subclass Calcaronea. In this subclass the unpaired actine of tri and tetractine spicules is elongated approximately in the [211] direction. The crystallographic direction of the actines are conserved through the evolution of the classes. In the class Calcinea, the actines are elongated in the {210} directions. The spicules normally have a specific position in the body of the sponge (cormus) and are used as a taxonomic character. *S. hastifera* has triactine and tetractine spicules in the cortical, subcortical, subatrial and atrial regions of the choanosome of the sponge. In this work, the crystallographic misorientations between spicules in the cortex, subcortical, subatrial and atrial regions were identified in different transversal sections of the tubular structure of the sponge (base, middle and top of the sponge tube) and in different area of each section of the tube. The aim of this study is to relate the misorientation between spicules with the process of growth of the sponge skeleton and the resistance proprieties of the aquiferous system tubes. Samples from *S. hastifera* were collected in Arraial do Cabo city, Rio de Janeiro, Brazil. The sponges were dehydrated with increasing concentrations of ethanol and infiltrated with epoxy resin. The sponge embedded in resin was cut transversally to the tube direction using a diamond saw. Transversal sections of the sponge were polished with alumina 1 $\mu\text{m}$  and then coated with a thin carbon layer. Electron Backscatter Diffraction (EBSD) were performed in a Scanning Electron Microscope Jeol 7100FT equipped with an Oxford EBSD detector [4]. Kikuchi line patterns were recorded using Aztec and Channel 5 softwares. Each transversal section was divided into four areas (1, 2, 3 and 4) from where cortical, subcortical, subatrial and atrial spicules were studied. Stereographic projections were

generated to study misorientation between spicules. Spicule types were identified using an inverted optical microscope. The subcortical spicules were the less oriented spicule type from *S. hastifera*. The absence of a preferential orientation may be related with the existence of pseudotriactine spicules which present similar morphology but different crystallographic orientation compared to a conventional triactine. All spicule types in the middle section of the sponge tube were more well oriented than in the base of the sponge. This result is related with the process of growth of the sponge tube. The transversal section of the sponge tube had an oval symmetry. The areas of the section superposed to the larger diameter presented spicules more well oriented compared to the areas in the smaller diameter of the tube. The same spicule type may have different orientation in different area. The spicule orientation in the cormus of *S. hastifera* present more or less misorientation depending on the transversal section of the sponge tube (base, middle or top), the spicule type and the area of the transversal section.

## REFERÊNCIAS

- [1] M. Manuel et al., Class Calcarea Bowerbank, 1864.
- [2] A.L. Rossi et al., Journal of Structural Biology, 2 (2016) 164.
- [3] A.L. Rossi, Acta Biomaterialia. 10 (2014) 3875–3884.
- [4] This research was supported by LabNano (Brazil).





## Fiber-Like Supra-Tetrameric Assembly of Glutaminases C Investigated by Cryo-Electron Microscopy

Alexandre Cassago<sup>1</sup>, Jose Edwin N. Quesnay<sup>2</sup>, Marin van Heel<sup>1</sup>, Andre LB Ambrosio<sup>2\*</sup>, Sandra MG Dias<sup>3\*</sup> and Rodrigo V Portugal<sup>1\*</sup>

<sup>1</sup> Brazilian Nanotechnology National Laboratory – LNNano – CNPEM

<sup>2</sup> Physics Institute of São Carlos – IFSC – USP

<sup>3</sup> Brazilian Biosciences National Laboratory – LNBio – CNPEM

\* [andre@ifsc.usp.br](mailto:andre@ifsc.usp.br)

\* [sandra.dias@lnbio.cnpem.br](mailto:sandra.dias@lnbio.cnpem.br)

\* [rodrigo.portugal@lnnano.cnpem.br](mailto:rodrigo.portugal@lnnano.cnpem.br)

Glutaminases are enzymes involved in the glutamine metabolism, an important anaplerotic source for the TCA cycle of highly proliferative cancer cells [1-3]. The phosphate dependent transition between enzymatically inert dimers into catalytically-capable tetramers has long been the accepted mechanism for the glutaminase activation [4]. We have already demonstrated that activated Glutaminase C (GAC), in the presence of inorganic phosphate, self-assembles into a helical, fiber-like double-stranded oligomer. We have also proposed a molecular model, consisting of seven tetramer copies per turn per strand interacting via the N-terminal domains [5] and also demonstrated a direct correlation between the tendency to self-assemble and the activity levels of GAC [4-5]. Indeed, BPTES (Bis-2-(5-phenylacetamido-1,3,4-thiadiazol-2-yl) ethyl sulfide), a known glutaminase inhibitor, completely disrupted the higher order oligomer, explaining its allosteric mechanism of inhibition via tetramer stabilization [6-9]. We are now pursuing the structure of this polymer by cryo-electron microscopy. Recombinant GAC was expressed in *Escherichia coli* and purified to the homogeneity in the presence of 20 mM of inorganic phosphate. Quantifoil holey carbon grids were prepared after glow discharged using a Vitrobot Mark IV (Thermo Fisher). Data acquisition was performed in a Talos Arctica operating at 200 kV and recorded on a Ceta CMOS and Falcon 3EC directed electron detector (Thermo Fisher). As expected, GAC prepared with inorganic phosphate was organized in a long fiber-like structure, resembling the double helical structure previously modeled by us (REF [5] and Figure 1). Our goal is to understand the basis of increased glutaminase activity dictated by the polymer formation [10].

[1] R.J. DeBerardinis et al., Cell Metabolism Rev. 7 (2008) 11-20.

[2] O. Warburg, Science 123 (1956) 309-314.

[3] R.J. DeBerardinis et al., Curr. Opin. Genet. Dev. 18 (2008) 54-61.

[4] A. Cassago et al., PNAS 109 (2012) 1092–1097.

[5] AP. Ferreira et al., JBC 288 (2013) 28009–28020.

[6] MM. Robinson et al., Biochem. J. 406 (2007) 407–414.

[7] B. DeLaBarre et al., Biochemistry 50 (2011) 10764–10770.

[8] K. Thangavelu et al., PNAS 109 (2012) 7705–7710.

[9] WP. Katt et al., Mol Cancer Ther 11 (2012) 1269–1278.

[10] This research was supported by FAPESP-2015/25832-4; FAPESP 2017/15340-2 (Brazil).

Acknowledgment: Cryo-EM facility at LNNano/CNPEM – Brazil.

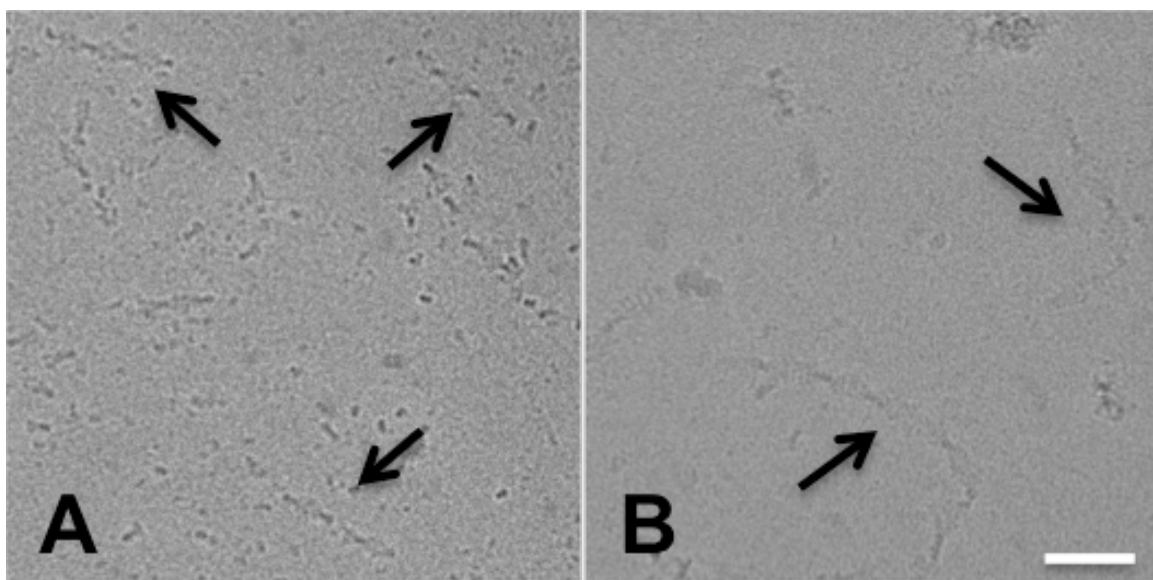


**Figure 1-** Cryo-Electron Microscopy images of the fiber-like Glutaminase C in the presence of inorganic phosphate (Black arrows). A- Image acquired in Ceta CMOS camera; B- Image acquired in Falcon 3EC directed electron detector. Scale bar indicates 50 nm.

## Structural Characterization Of The Vdac2-Bak Complex From Mitochondrial Outer Membrane By Single Particle Cryo-Electron Microscopy

Antonio Carlos Borges<sup>1;2</sup>, José Edwin Neciosup Quesñay<sup>2</sup>, Raghavendra Sashi Krishna Nagampalli<sup>2</sup>, Alfredo Jose Florez Ariza<sup>1</sup>; Zeyaul Islam<sup>2</sup>, Sandra Martha Gomes Dias<sup>2</sup>, Rodrigo Villares Portugal<sup>1\*</sup>, Andre Luis Berteli Ambrosio<sup>3\*</sup>

1. Brazilian Nanotechnology National Laboratory / Brazilian Center for Research in Energy and Materials (LNNano/CNPEM), Campinas, Brazil.
2. Brazilian Biosciences National Laboratory / Brazilian Center for Research in Energy and Materials (LNBio/CNPEM), Campinas, Brazil.
3. São Carlos Institute of Physics / University of São Paulo (IFSC/USP), São Carlos, Brazil.

Also known as mitochondrial porins, VDACs (voltage-dependent anion-selective channel) are the most abundant membrane integral proteins found in the outer membrane of the mitochondria and considered a new target for the action of anti-cancer drugs [1;2]. Bak (Bcl-2 homologous antagonist / killer) belongs to the pro-apoptotic members of the Bcl-2 protein family and is constitutively integrated into the mitochondrial outer membrane. In healthy cells, VDAC2 and Bak are linked in a complex and Bak is inactivated or repressed. The mechanism of formation and dissociation of the VDAC2-Bak complex is closely related to the mitochondrial pathway of apoptosis [3]. The present work aims to establish basis for the structural investigation of the complex formed by VDAC2-Bak and obtaining structural information by Single-Particle Cryo-Electron Microscopy (Cryo-EM). Optimizations performed in the assays for overexpression in *S.cerevisiae* yeast produced results with high level of target membrane protein expression. Three different approaches were used for the extraction and purification of VDAC2-GFP: sorting by detergents, nanodiscs and SMALPs. With SMALPs, the result of the extraction and purification allowed to obtain the best samples so far. Images obtained by the techniques of negative staining and cryomicroscopy allowed to observe nanodiscs and SMALPs of VDAC2-GFP. It was possible to observe that the dimensions are compatible with those expected for both nanodiscs and SMALPs. Preliminary processing of collected images indicates the structure obtained resembles the crystallographic structure of VDAC1. The next steps will allow us to obtain more concentrated samples of particles and to test these conditions for the VDAC2-Bak complex. Obtaining structural complex model will contribute to elucidate how Bak interacts structurally with VDAC2, paving the way for future studies to use the complex as a therapeutic target.

- [1] Yagoda, N. et al (2007) 'RAS-RAF-MEK-dependent oxidative cell death involving voltage-dependent anion channels', *Nature*, 447(7146), pp. 865-869.
- [2] Shoshan-Barmatz, V. and Mizrachi, D. (2012) 'VDAC1: from structure to cancer therapy.', *Frontiers in oncology*, 2(November), p. 164.
- [3] Ma, S. et al (2013) 'Assembly of the bak apoptotic pore: A critical role for the bak protein $\alpha$ 6 helix in the multimerization of homodimers during apoptosis', *Journal of Biological Chemistry*, 288(36), pp. 26027-26038.
- [4] This research was supported by FAPESP (2016/14350-1) (Brazil).

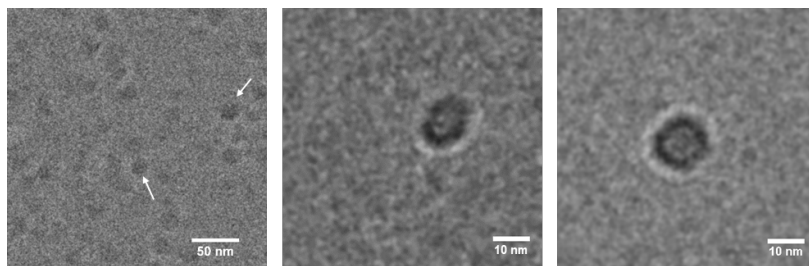


Figure 1. Cryo-Electron microscopy of nanodiscs. Images of nanodiscs in vitreous ice obtained by the Cryo-EM technique. In the first image, the white arrows indicate the nanodiscs in the vitreous ice. The other two images show isolated particles in higher magnification and different orientations. Transmission electron microscopy images were obtained from Thermo Scientific™ Talos F200C Microscope.

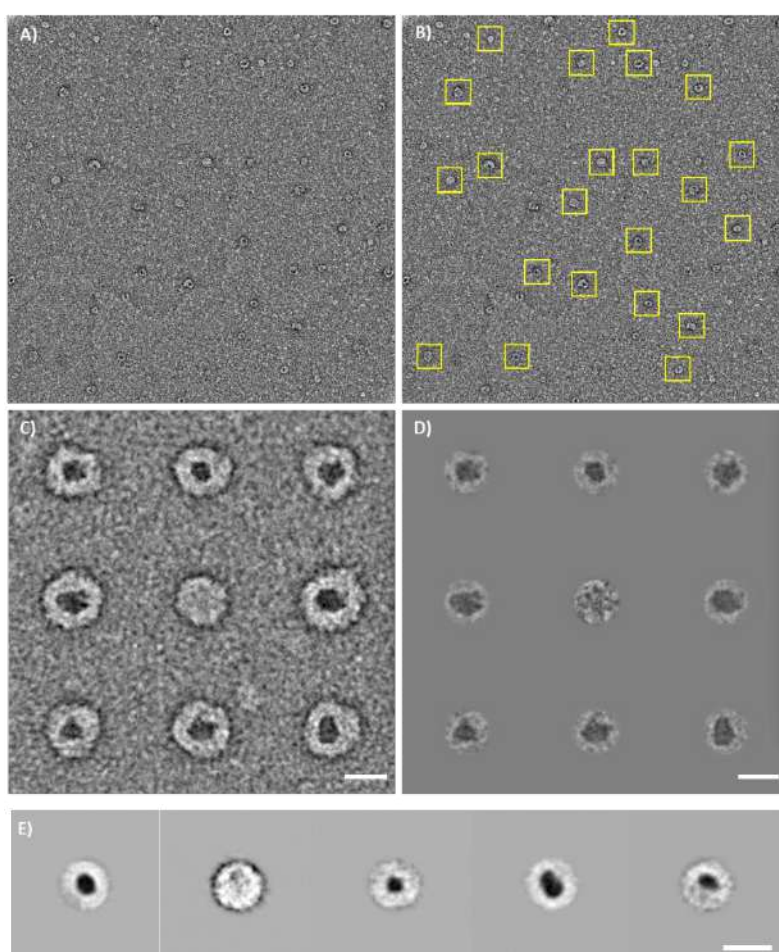


Figure 2. Preliminary image processing of VDAC2-GFP SMALPs. A) Dispersed VDAC2-GFP SMALPs particles. B) Picking the particles that correspond to SMALPs within the yellow squares. C) A total of 1903 SMALP particles were selected by picking. D) Mask on the selected particles, leaving exposed only the region around the protein inserted in the membrane. E) Examples of classes formed by various particles (~ 10 particles / class). Transmission electron microscopy images were obtained from Thermo Scientific™ Talos F200C Microscope. The Imagic 4D v.180316 software was used in particle processing. The scale bars correspond to 20nm.



## Myriapoda Hemocyanin: The First 3D Reconstruction of *Scolopendra subspinipes subspinipes* And Preliminary Structural Analysis of *Scolopendra viridicornis*

Riciluca KCT<sup>1,2,§</sup>, Borges AC<sup>1,§</sup>, Mello JFR<sup>1</sup>, Oliveira UC<sup>2</sup>, Serdan DC<sup>1</sup>, Florez-Ariza A<sup>1</sup>, Chaparro E<sup>2,3</sup>, Nishiyama Jr M<sup>2</sup>, Cassago A<sup>1</sup>, Junqueira-de-Azevedo ILM<sup>2</sup>, van Heel M<sup>1</sup>, Silva Jr PI<sup>2,†</sup>, Portugal RV<sup>1,‡</sup>

<sup>1</sup>Laboratório Nacional de Nanotecnologia, Campinas, Brasil.

<sup>2</sup>Leta CeTICS/CEPID – Instituto Butantan, São Paulo, Brasil

<sup>3</sup>Interunidades em Biotecnologia - Universidade de São Paulo, São Paulo, Brasil

§ Both authors contributed equally to this work.

Corresponding authors: † [pisjr@usp.br](mailto:pisjr@usp.br); ‡ [rodrigo.portugal@lnnano.cnpem.br](mailto:rodrigo.portugal@lnnano.cnpem.br)

Hemocyanins (Hc) are copper-containing, respiratory proteins that do not occur in blood cells, but are found freely dissolved in the hemolymph [1–3]. The basic structure of arthropod hemocyanin is hexameric in nature and is usually found as single or multiple hexamers (2x6-mer to 8x6-mer) [1]. Very little is known about hemocyanins in the Myriapoda subphylum [4]. We here present the quaternary structure of the hemocyanin of *Scolopendra subspinipes subspinipes*, an introduced centipede of humid coastal area, and *Scolopendra viridicornis*, a Brazilian native centipede that occur in dry areas. Negatively stained specimens were prepared applying 3 µl sample (36 µg/ml and 25 µg/ml respectively) on a pre-charged grid, dried using a filter paper and stained with a uranyl acetate 2%. Images were recorded using a Talos F200C, operating at 200 kV (Ceta camera). The hemocyanin of *S. subspinipes subspinipes* [4] was found to have a 3x6-mer quaternary structure, as observed in *Polydesmus angustus* hemocyanin. The hemocyanin of *S. viridicornis*, in contrast, was found to have a 6x6-mer quaternary structure, such as was observed in *Scutigera coleoptrata* [5]. This difference may be related to the evolution of trachea system, which would reduce the need for oxygen accumulation and influence the oligomerization and thus the size of the complex. The analysis of the transcriptome of *S. subspinipes subspinipes* reveals the presence of two distinct subunits of Hc and six of Prophenoloxidase (PPO) in the 75-kDa range. The final model was obtained by single particle analysis from ~6000 particles (247 class-averages) of *S. subspinipes subspinipes*. The subunits were modelled by homology, and docked into the (~17Å resolution) EM reconstruction by rigid body fitting. Studies with Chelicerata showed that PPO activity are exclusively associated to the Hcs. This study indicates that *Scolopendra* may have different proteins performing the oxygen transport (Hc) and the PPO function [6].

- [1] Van Holde KE, Miller KI, Decker H. J. Biol. Chem.(2001)
- [2] Decker H, Jaenicke E. 2004 Dev. Comp. Immunol. (2004)
- [3] Coates CJ, Nairn J. Dev. Comp. Immunol. (2014)
- [4] Pick C, Scherbaum S, Hegedüs E, Meyer A, Saur M, Neumann R, Markl J, Burmester T. FEBS J. (2014)
- [5] Markl J, Moeller A, Martin AG, Rheinbay J, Gebauer W, Depoix F. J. Mol. Biol. (2009)
- [6] This research was supported by CAPES-Brazil.

**Acknowledgment:** We thank LNNano/CNPq for the access to the EM facility, LETA/Butantan Institute for biochemistry and molecular analysis, CAPES, CNPq, FAPESP for financial support.

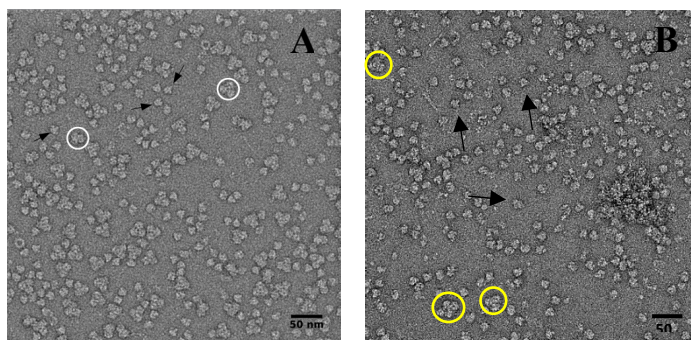


Figure 01. TEM imaging of negatively stained hemocyanin. A patch from one of the original 4096 x 4096 pixels collected micrographs. Some different projections views of the ternary complex are marked by white circles (3x6-mer) and yellow circle (6x6-mer) while small individual particles, possible part of some dissociated high-order complexes, are pointed by black arrows. (A) Hemocyanin of *Scolopendra subspinipes subspinipes* (B) Hemocyanin of *Scolopendra viridicornis*. Scale bar is shown.

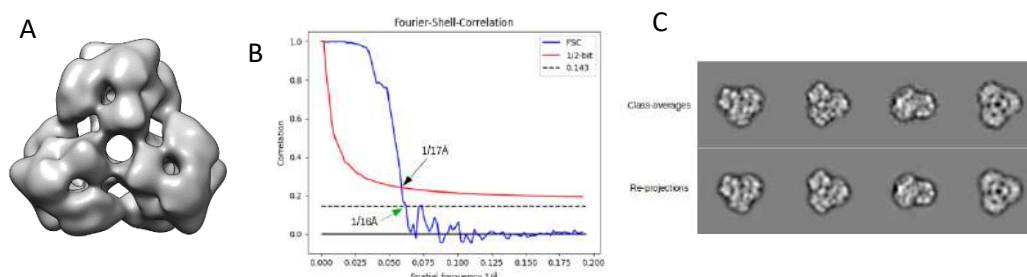


Figure 02. Single particle analysis, 3D reconstruction and FSC. (A) One view of the EM reconstruction of 3x6-mer complex (contour level 0.4  $\sigma$ ). (B) Fourier-Shell-Correlation (FSC) with 1/2-bit and 0.143 criterion indicating the resolution of the EM model at 17 Å (black arrow) and 16 Å (green-arrow), respectively. The final 3D density map was low-pass filtered at 17 Å according to the estimated resolution and hide-dust tool of Chimera software was used to suppress densities not-connected to the EM model, to finally be shown in (A). (C) Representative 2D class-averages (top row) and their corresponding 2D re-projections (bottom row) used in the final three-dimensional reconstruction.

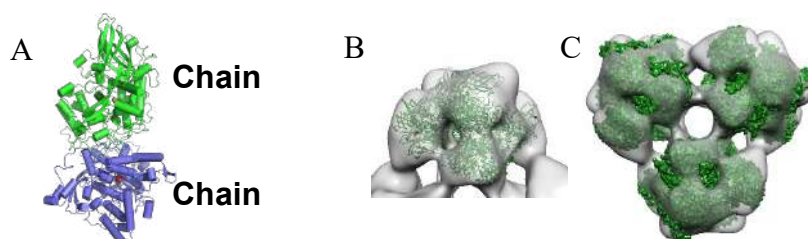


Figure 03. (A) Molecular docking between chains A and B (tight dimer) of *Scolopendra subspinipes subspinipes* (B) Rigid body fitting of 3 dimers generating the hexameric structure. (C) Each hexamer was fitted individually into the map generating the 3x6 oligomer of hemocyanin.

## Histological And Immunohistochemical Study on Stomach of The green iguana (*Iguana iguana*)

Amanda Oliveira Serra-Campos<sup>1\*</sup>, Amanda Ribeiro Ricardo Brito<sup>1</sup>, Beatriz Gouveia De Luca<sup>3</sup>, Mauro Sérgio Cruz Souza Lima<sup>2</sup> and Clarice Machado-Santos<sup>1</sup>

<sup>1</sup>. Laboratório de ensino e pesquisa em Histologia e Embriologia Comparada (LEPHEC), Departamento De Morfologia, Universidade Federal Fluminense, Niterói, RJ, Brasil

<sup>2</sup>. Laboratório de Herpetologia, CAFS/Universidade Federal do Piauí, Floriano, PI, Brasil.

\*e-mail: [camposamanda@id.uff.br](mailto:camposamanda@id.uff.br)

The *Iguana iguana* belongs to the Squamata Order, Iguanidae Family widely distributed throughout Latin America. Morphological studies on the structure of the digestive tube of this animal are essential for the comprehension of its lifestyle and your physiological aspects. In the stomach, somatostatin (SS) can be an important physiological regulator of gastric acid secretion both directly, by acting on the parietal cell, and indirectly, by regulating gastrin secretion. The Serotonin (5-HT) has a strong effect on the regulation of digestive functions and is widely distributed in the gastric epithelium. In light of this, the work aims was to describe the histological and histochemical structure of the I. iguana and verify the occurrence and distribution of serotonin and somatostatin secretory cells providing data on the enteroendocrine cells of this species for comparative purposes with other reptiles. Five iguanas of both sexes were collected in the Barão do Grajaú-MA, license Sisbio 54501-2. The stomach fragments were fixed in 10% Formaldehyde and embedded in paraffin. The slides were stained by the techniques of Hematoxylin-eosin (HE) and Gomori trichrome (GT), Periodic acid- Schiff (PAS) and Alcian Blue (AB). In Immunohistochemistry, for the Antigen retrieval the slides were immersed in citrate buffer at pH 6, in a water bath at 96 °C for 45 min. They were then incubated overnight at 4°C with rabbit polyclonal anti-serotonin diluted to 1:8000 and anti-somatostatin diluted to 1:300. Digital images of the stained slides were obtained using a Leica ICC50 HD camera mounted on Leica DM 500 microscope. The lining epithelium of the mucosa layer throughout the entire stomach is simple columnar with strong PAS and AB positivity. The lamina propria has an abundance of simple tubular gastric glands. These glands have a predominance of oxynticopeptic cells. The cranial stomach muscular layer has bundles of smooth muscle fibers in two directions, while the middle and caudal regions consist of only one layer of smooth fibers. 5-HT cells were observed in all portions of the stomach and somatostatin secretory cells were only observed in the caudal region near the intestine. In reptiles, variations in terms of the stomach shape, distribution of the mucus secretions and pattern in the delivery of the enteroendocrine cells in the GIT demonstrate an adaptive response, which occurs interspecifically.

### REFERÊNCIAS

- [1] Troyer, K. Structure and Function of the Digestive Tract of a Herbivorous Lizard *Iguana iguana*. *Physiological Zoology*, 1984, 57(1), 1–8.
- [2] Schonhoff, S. E., Giel-Moloney, M., & Leiter, A. B. Minireview: Development and differentiation of gut endocrine cells. *Endocrinology*, 2004, 145(6), 2639–2644.
- [3] Chiba T, Yamada T. Gut somatostatin. In: Walsh JH, Dockray GJ (editors): *Gut Peptides: Biochemistry and Physiology*. New York: Raven, 1994, pp. 123–145.

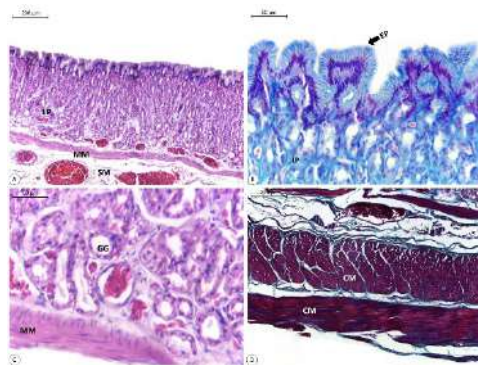


**Figure 1.** Cranial region of stomach of *I. iguana*. (a,b)The epithelium lining is simple columnar mucous (EP) with positive histochemical reactions for AB (pH 2.5). (c) Observed that the lamina propria (LP) is constituted by gastric glands (GG) formed basically by oxynticopeptic cells. (a,c) The muscularis mucosa (MM) and Submucosa is present (SM). (d) Muscular layer (CM): internal longitudinal and external circular. A: (H&E), B: (AB) C: (H&E), D: (TG).

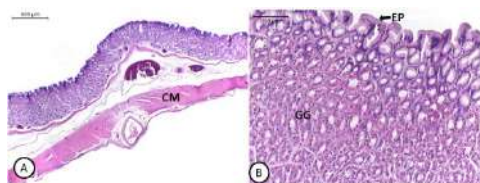


**Figure 2.** Middle region of stomach of *I. iguana*. (a,b) Observed that the lamina propria (LP) is constituted by gastric glands (GG) formed basically by oxynticopeptic cells. The epithelium lining is simple columnar mucous (EP). (b) Muscular layer (CM): one layer of longitudinal fibers. A,B: (H&E).

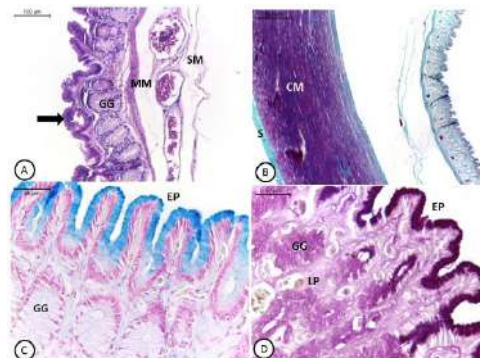


**Figure 3.** Caudal region of stomach of *I. iguana*. (a) Observed that the lamina propria (LP) is constituted by gastric glands (GG) formed basically for mucous neck cells (GG). (c,d) The epithelium lining is simple columnar mucous (EP) with positive histochemical reactions for AB (pH 2.5) and positive reaction for PAS. (b) Muscular layer (CM): one layer oriented circularly and notably thicker (b). (a) The muscularis mucosa (MM). (a) Submucosa (SM). (b) Serosa (S). A: (H&E), B: (TG) C: (AB), D: (PAS).

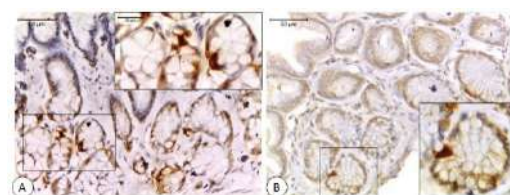


**Figure 4.** Light micrograph of the stomach of *I. iguana*. (a) Serotonin-positive cells in the caudal region. (b) Somatostatin-positive cells in the caudal region.



## Histological and Immunohistochemical Analysis On Oesophagus Of The Iguana (*Iguana iguana* Linnaeus, 1758)

Amanda Ribeiro Ricardo Brito<sup>1\*</sup>, Amanda Oliveira Serra-Campos<sup>1</sup>, Beatriz Gouvea De Luca<sup>1</sup>, Mauro Sérgio Cruz Souza Lima<sup>2</sup>, Clarice Machado-Santos<sup>1</sup>

<sup>1</sup>. Laboratório de ensino e pesquisa em Histologia e Embriologia Comparada (LEPHEC), Departamento De Morfologia, Universidade Federal Fluminense, Niterói, RJ, Brasil.

<sup>2</sup>. Laboratório de Herpetologia, CAFS/Universidade Federal do Piauí, Floriano, PI, Brasil.

\*e-mail: [amandabrito@id.uff.br](mailto:amandabrito@id.uff.br)

**Introduction.** The Common Green Iguana (*I. iguana*) is arboreal and primarily herbivorous, being able to consume animal protein like snails and insects that occur on vegetation, probably incidentally. Histological knowledge about reptile's gastrointestinal tract is an essential tool for the understanding of their biology as well as a prerequisite for the implementation of conservation and management projects. In light of this, the work aims was to describe the histological and histochemical structure of oesophagus the *I. iguana* and verify the occurrence and distribution of serotonin secretory cells through a specific immunohistochemical method, providing data on the enteroendocrine cells of this species for comparative purposes with other reptiles. **Methods.** For light microscopic studies, five iguanas of both sexes were used. The specimens were collected in the Barão do Grajaú-MA, license Sisbio 54501-2. After necropsy, fragments were fixed in 10% buffered formaldehyde and sent to LEPHEC and processed according to the standard histological techniques for paraffin embedding. The slide were stained with hematoxylin-eosin (HE), Alcian blue (AB) at pH 2.5 and periodic acid Schiff (PAS). In Immunohistochemistry, for the Antigen retrieval the slides were immersed in citrate buffer at pH 6, in a water bath at 96 °C for 45 min. They were then incubated overnight at 4°C with rabbit polyclonal anti-serotonin 1:8000. Digital images of the stained slides were obtained using a Leica ICC50 HD camera mounted on Leica DM 500 microscope. **Results.** The esophagus is a structure with a thin walled tube extending from the pharynx to the stomach. The mucosa layer had three components: (1) a superficial epithelium; (2) an underlying loose connective tissue (lamina propria), and (3) a relatively thin layer of smooth muscle (muscularis mucosae) (Fig. 1). A ciliated columnar pseudostratified epithelium with goblet cells overlaid a lamina propria of loose connective tissue (Fig 2). The goblet cells were abundant nonciliated cells; its apical portion contained mucus secretion which showed affinity for AB (Fig 3). The PAS Showed selective affinity for only a few of those epithelium muco secretory cells (Fig. 4). The lamina propria of loose connective tissue is rich in blood vessels and exocrine glands are absents. The submucosal layer contains a network of collagenous and elastic fibers and many small blood vessels. The muscularis consists of both inner circular and outer longitudinal layers of smooth muscle only. The outermost layer, the serosa, is a very thin sheet of loose connective tissue covered by mesothelium and has some blood vessels and nerves. The serotonin immunoreactive cells were found randomly scattered at the base of the epithelium in all portions of the oesophagus of the iguana (fig. 5,6). **Conclusion.** The histological and immunohistochemical study on the oesophagus of the iguana reveals distinct characteristics for the specie, even though it follows the general structure of the organ composed by layer of mucosa, submucosa, muscular and adventitia/serosa vertebrate pattern. REFERENCES

[1] Hirth, H. F. . Some Apects of the Natural History of Iguana iguana on a Tropical Strand. *Ecology Hollingsworth* (1963) 44(3): 613-615.

[2] El-Salhy, M., Wilander, E., & Lundqvist, M. (). Comparative Studies Of Serotonin-Like Immunoreactive Cells in the Digestive Tract of Vertebrates; *Biomedical Research* (1985) 6(6), 371–375.

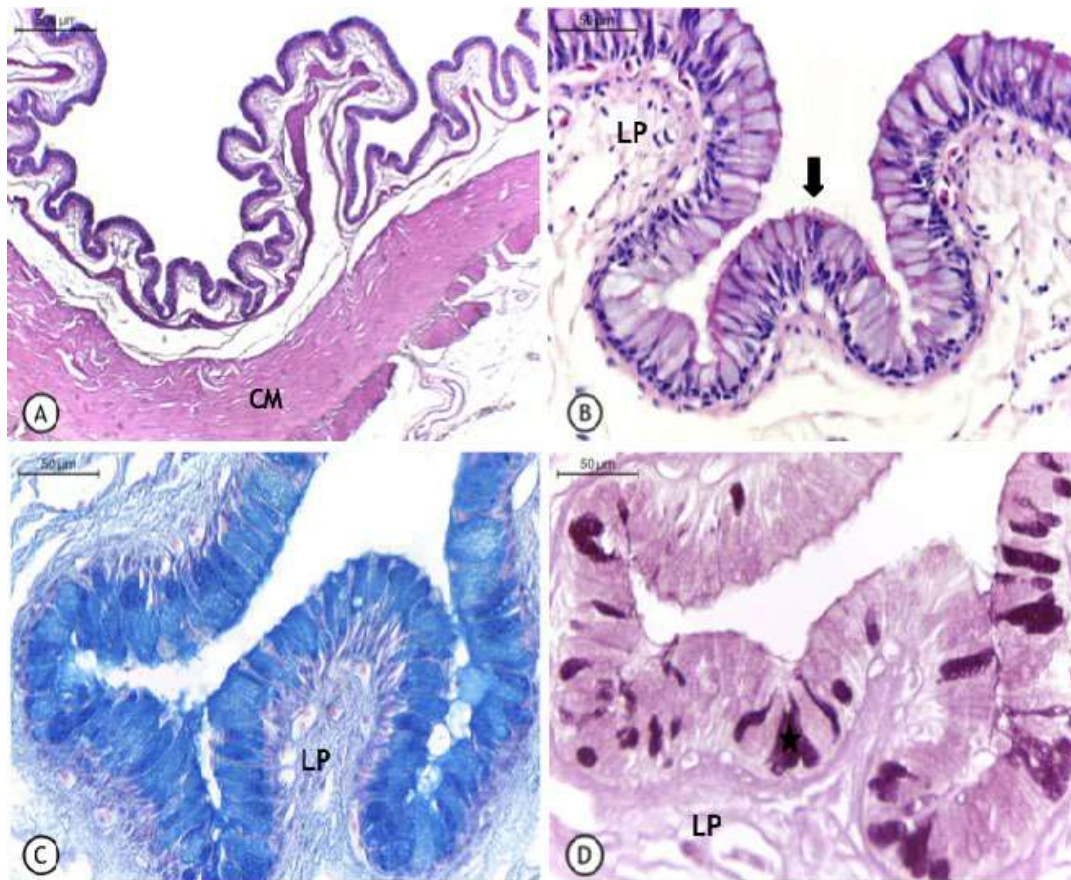


Figure 1- Light micrograph of the esophageal wall, showing the mucosa and submucosa layers. (A and B) The muscularis (CM) is subdivided into the inner circular and outer longitudinal layers of smooth muscle. (C and D) The mucosa layer is composed of ciliated columnar pseudostratified epithelium (↓), lamina propria and muscularis mucosa with goblet cells(\*) overlies with positive histochemical reactions for PAS and AB (pH 2.5). The lamina propria (LP) está presente. Note numerous cilia (↓). A: (H&E), B: (H&E), C: (AB), D: (PAS).

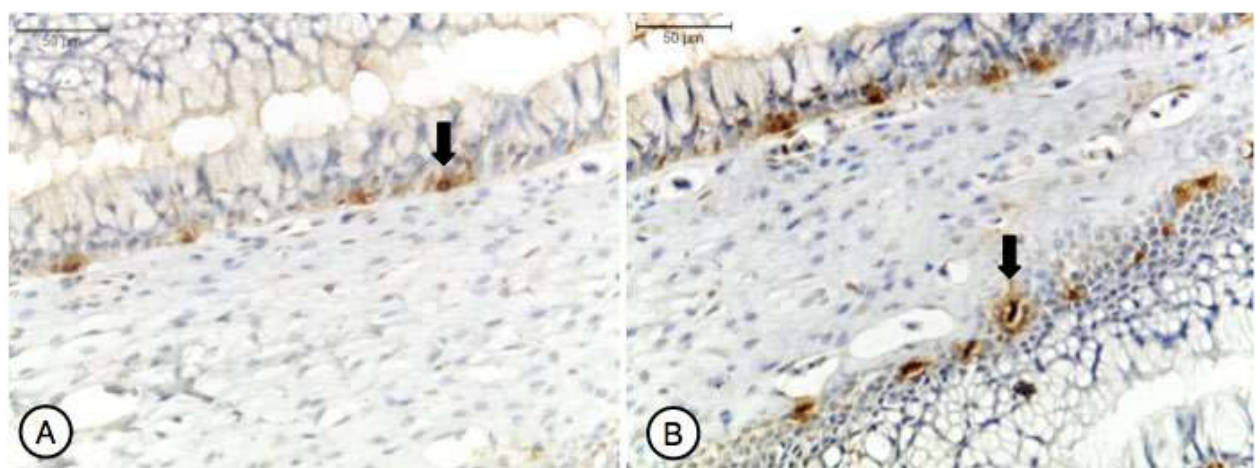




Figure 2. Light micrograph of the esophagus of *I. iguana*.(A,B)  
positive cells randomly scattered at the base of the epithelium (↓)

Serotonin-

## **Histochemical and immunohistochemical analysis of the stomach and intestine of rhesus monkeys (*Macaca mulata*) (Cercopithecidae, Primates)**

\*Beatriz Gouvêa de Luca<sup>1</sup>, Marcelo Abidu-Figueiredo<sup>2</sup>, Amanda Oliveira Serra Campos<sup>1</sup>, Amanda Ribeiro Ricardo Brito<sup>1</sup>, Ana Luiza Bastos, Clarice Machado Dos Santos<sup>1</sup>,

1. Universidade Federal Fluminense, Departamento De Morfologia, Niterói, RJ, Brasil.
2. Universidade Federal Rural do Rio de Janeiro, Programa de Pós-graduação em Medicina Veterinária, Seropédica, RJ, Brasil.

\*e-mail: bluca@id.uff.br

The anatomical, physiological and nutritional aspects between humans and primates allows comparative studies in the área of gastroenterology[1]. Histological structures of the rhesus monkey stomach and intestine were analyzed using histochemical and immunohistochemical techniques for serotonin (5-HT) secretory enteroendocrine cells in the cardiac, fundic, body and pylorus regions and in the duodenum. The fragments were fixed in 10% formaldehyde and processed for paraffin inclusion. The slides were stained with hematoxylin and eosin, alcian blue, PAS [2,3] and immunohistochemistry with anti-5HT. The region of the cardia presents deep gastric pits, associated to branched tubular glands rich in basophilic cells. Serotonin secreting cells were observed throughout the gland. The mucosa presents the simple cylindrical epithelium mucosecretor PAS + and AB +. The fundus region presents smaller gastric pits, the surface of which is covered by the same PAS + and AB + epithelium and well developed gastric glands, formed by parietal and chief cells. In the region of the body the lamina propria presents glands in lesser quantity and makes the connective tissue loose evident

### **REFERENCES**

- [1] JUSTIN D. VIDAL et al, Evaluation of the Cynomolgus Monkey Stomach: Recommendations for Standard Sampling Procedures in Nonclinical Safety Studies, 2008
- [2] LILLIE RD et al Histopathologic Technique and Practical Histochemistry, 1976
- [3] KIERNAN JA, Histological and Histochemical Methods - Theory and Practice. Frankfurt, 1990

### **ACKNOWLEDGMENTS**

To CNPq/PIBIC for the founding of the research project and to the laboratory fellow Laboratório de Ensino e Pesquisa em Histologia e Embriologia Comparada for the support during the project execution.



In this region the serotonin immunoreactive cells were predominant in the colon and base of the gastric glands. The pylorus region has deep pits and short gastric glands, represented basically by the presence of mucosecretory cells. Serotonin immunoreactive cells are scarce, being observed at the base of the pyloric gland. The duodenum presented villi coated with simple cylindrical epithelium with striated plain and goblet cells reactive to PAS + and AB + staining. Serotonin secreting cells are present in both the lining epithelium and the intestinal mucosal glands. Similarities can be observed in the morphology and distribution of serotonin-secreting cells along the gastrointestinal tract of rhesus monkeys and humans, and this study may contribute to research on the physiological and pathological aspects of the primate and human digestive system.

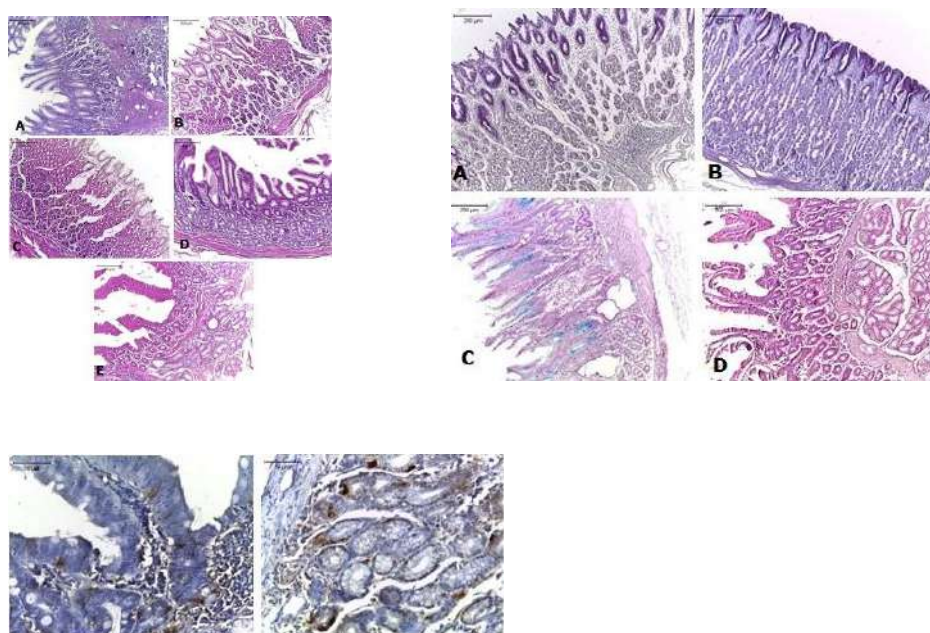


Figure 1: Photomicrograph of the stomach and intestine of Rhesus Monkey. A: Region of the Cárdia. B: Fund Region. C: Region of the Body. D: Piloro Region

Figure 2: Photomicrographs of regions of the stomach and intestine of Rhesus monkey in different stains. A and B: Shiff Period (PAS). C and D: Alcian Blue (AB)

Figure 3: Photomicrography of gastric mucosa sections submitted to immunohistochemistry. The presence of serotonin immunoreactive cells can be observed



## **Establishment Of a Protocol For Cell Culture In 3D Matrix And Analysis By Confocal Microscopy**

Cibele Ferreira Pimentel<sup>1\*</sup>, Grasiella M. Ventura Matioszek<sup>3</sup>, Isalira Peroba Rezende Ramos<sup>1,2</sup>, Regina Coeli Dos S. Goldenberg<sup>1</sup>

- 1.Laboratory of Cellular and Molecular Cardiology, IBCCF /UFRJ, Rio de Janeiro- Brazil.
- 2.National Center of Structural Biology and Bioimaging, CENABIO/UFRJ, Rio de Janeiro- Brazil.
- 3.Confocal Microscopy Multiusers Unity, ICB/ UFRJ, Rio de Janeiro-Brazil.

**ABSTRACT:** The primary culture of hepatocytes is a challenge for in vitro culture. The cells undergo stress due to the isolation processes, which may alter the results obtained. Its functional and proliferative potential in vitro is reduced. A widely used culture model for in vitro studies are liver cells derived from a Hepatocellular Carcinoma, the HepG2 [1]. Thus, this project proposed the development of a 3D culture protocol for HepG2 cells, to mimic the hepatic framework. The morphological characteristics of the hepatocyte cell line was analyzed by confocal microscopy, a well established technic to 3D analyses. HepG2 was grown on plastic 24 well culture plates, without matrix (2D control), on (ON) and inside (IN) of collagen I matrices (1.0 mg / mL in amount of final solution of 100  $\mu$ L). The proteins phalloidin, collagen I and vinculin were stained by fluorescence assay and evaluated by confocal microscopy after the 48 and 96 hours. The results showed that HepG2-2D maintained their morphology in clusters while HepG2-3D-ON and HepG2-3D-IN were dispersed. At 48 and 96 hours the cells in the 3D: ON / IN matrix presented many filopodia, suggesting a better interaction capacity between the HepG2 and the collagen I matrix in relation to the 2D control (figures 1A-F). To quantify these filopodia, a statistical graph was made (figure 1G). In the 3D-IN condition there was a better distribution of the cells along the Z axis of the matrix, filling the 3 space planes x, y and z (figure 2C) in relation to the 2D control (figure 2A) and the 3D-ON condition (figure 2B). In the 3D-ON / 3D-IN conditions the cells had a differentiated expression of vinculin, as well as morphological differences in the tensile fibers of actin microfilaments of the cellular cytoskeleton, in relation to the 2D condition. In conclusion, the culture of HepG2 within the collagen I matrix was successfully obtained [2]. Confocal microscopy was effective in the analysis of the morphological characteristics of HepG2 cells in the culture conditions and times evaluated [3,4].

[1] FUKUDA, T. et al. Isolation and expansion of human pluripotent stem cell-derived hepatic progenitor cells by growth factor defined serum-free culture conditions. *Experimental Cell Research*, v. 352, n.2, p. 333-345. 2017.

[2] PAMPALONI, F; REYNAUD, EG; STELZER, EH. The third dimension bridges the gap between cell culture and live tissue. *Nature Reviews Molecular Cell Biology* 8, 839-845, 2007.

[3] DE SOUZA, W. et al. *Microscopia Óptica: Fundamentos e Aplicações às Ciências Biomédicas*, 1a. ed. SBMM, 2010.

[4] DIASPRO, A; FARETTA, M e SAPUPPO, P. *Confocal Microscopy*. Leica Microsystems, 2008.

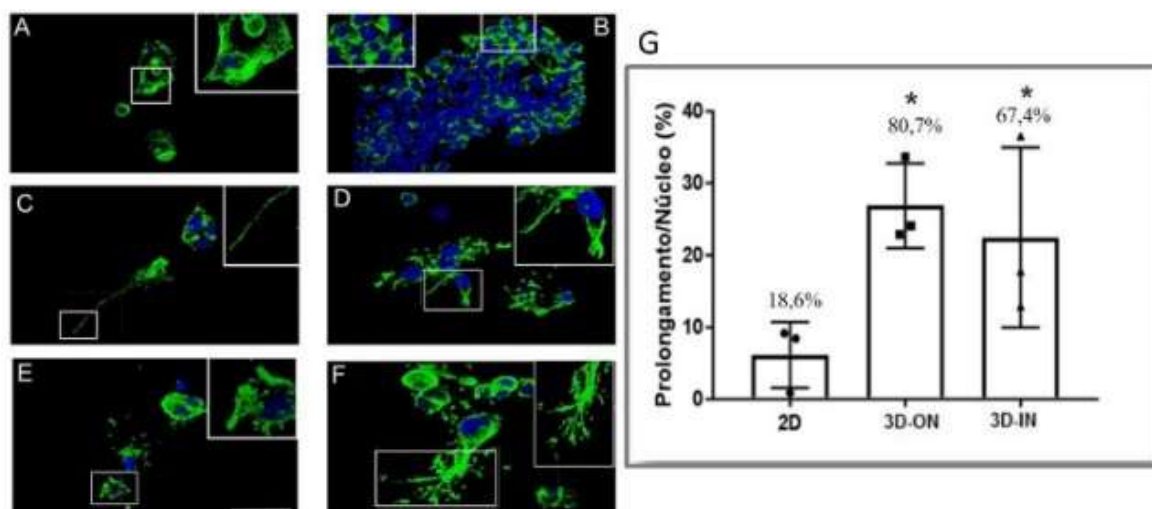


**Figure 1: Confocal microscopy of the morphological characteristics of the cells:** HepG2-2D (figures A, B), HepG2-3D-ON (figures C, D) and HepG2-3D-IN (E, F) at 48 and 96 hours, respectively. Labels for phalloidin (actin microfilament marker - green) and DAPI (blue). Obj 63x. Scale bar 20  $\mu$ m. In figure 2G, the abscissa axis is the 2D, 3D-ON and 3D-IN conditions and in the coordinate axis the ratio of the number of extensions per nucleus (%).\* (p < 0.05 GraphPad Prism® version 7.0).

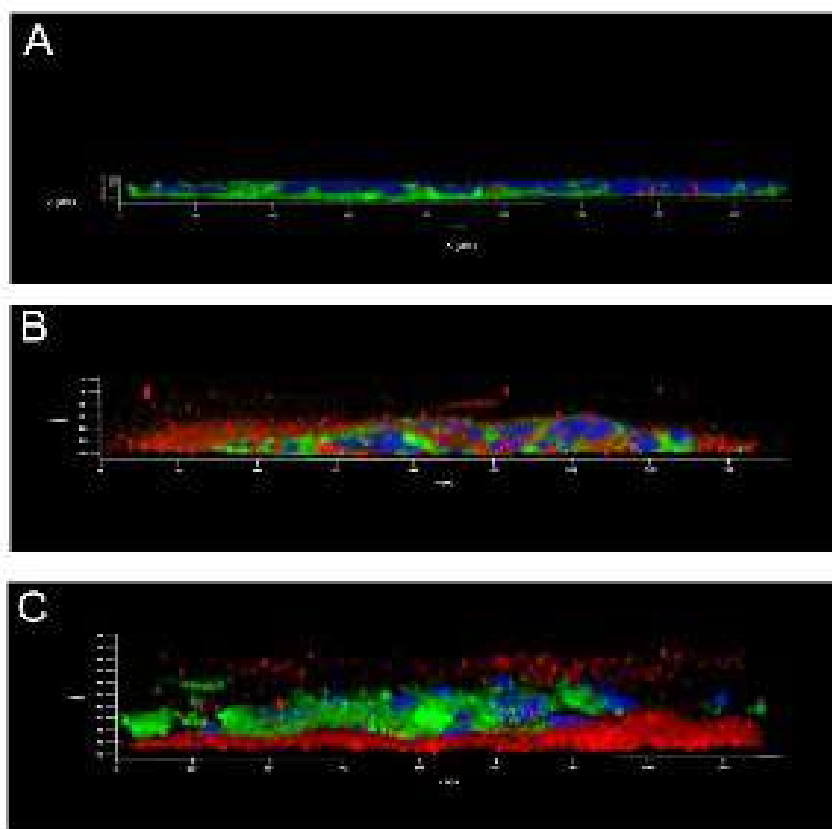


**Figure 2: Confocal microscopy of the Z-axis distribution of the cells:** (A) HepG2-2D, (B) HepG2-3D-ON and (C) HepG2-3D-IN at 48 hours. Labels for phalloidin (actin microfilament marker - green), collagen I (red) and DAPI (blue). Obj 40x. Scale bar 50  $\mu$ m.

## Cryofracture in the Morphological Characterization of *Eurytrema coelomaticum* (Trematoda - Digenea)

Karine Gomes Leite<sup>1\*</sup>, Eduardo José Lopes-Torres<sup>1</sup>, Fidelis Antônio da Silva Júnior<sup>2</sup>,  
Rosângela Rodrigues-Silva<sup>3</sup>, José Roberto Machado-Silva<sup>1</sup>.

<sup>1</sup> Laboratório de Helminologia Romero Lascasas Porto, FCM-UERJ, RJ, Brasil.

<sup>2</sup> Faculdade de Ciências Biológicas e da Saúde, UFVJM, MG, Brasil.

<sup>3</sup> Laboratório de Helmintos Parasitos de Vertebrados, IOC - FIOCRUZ, RJ, Brasil.

\*Corresponding author: karine.leite88@gmail.com

*Eurytrema coelomaticum* is an etiological agent of bovine eurytrematosis with economic and veterinary importance. In spite of studies of egg and larval stages for this species using advanced microscopy techniques [1][2][3], studies of adult worm morphology are classically made using light microscopy [4][5]. Scanning electron microscopy (SEM) has been a key tool in the advancement of morphological helminths studies. However, SEM is typically limited to the observation of the surface of samples. To expose the internal structures, a method of cryofracture was introduced in the 70's [6]. The present investigation was designed to aggregate new structural information in *E. coelomaticum* adult worms collected from the pancreatic ducts of cattle (*Bos taurus*) from slaughterhouses at Campo Belo, MG and Barra Mansa, RJ. Following previous methodology [7] the samples fixed in AFA were dehydrated in graded ethanol series (70–100% GL) for 20 minutes at each step; for cryofracture, the samples were packed in Parafilm<sup>®</sup> and frozen by immersion in liquid nitrogen. The frozen samples were placed on the metal block and fractured in different positions using a single-edged blade (EMS<sup>®</sup>). Subsequently, the samples were stored in absolute ethanol and dried at critical-point in CO<sub>2</sub> liquid; mounted on metallic stubs and coated with gold (20–25 nm). Finally, the samples were examined using the scanning electron microscope Jeol/EO1.0 in high vacuum mode. The cryofracture experiments enabled a detailed characterization of the parasite body, showing the muscular layer with longitudinal and transverse fibers, the syncytial layer with cubic crystals proteins inclusions emerging on the tegument and internal view with cells arranged in a dense parenchyma (Fig. 1-2). Both oral and ventral sucker presents a complex arrangement of muscle radial fibers and parenchymal cells (Fig. 3 a-b, 4 a-b). Regarding the reproductive apparatus, spermatozoa were present inside the testis (Fig. 5-6), also the seminal receptacle contained numerous spermatozoa and the ovary filled by oocytes followed by the ootype and Mehlis' gland (Fig. 7). Inside the uterus, many operculated eggs (Fig. 8), fractured eggs in intrauterine mucus showed the blastomeres and the developed embryo (Fig. 9). The collection samples fixed in AFA can be explored using this strategy, providing a detailed characterization of the external and internal structures complementing and amplifying the morphofunctional comprehension of *E. coelomaticum*.

[1] J. Pinheiro et al., Vet. Parasitol. 182:201-212 (2011).

[2] J. Pinheiro et al., Parasitol. Res. 111:1437-1445 (2012).

[3] J. Pinheiro et al., Helminthologia. 52; 3: 244–251 (2015).

[4] L. Travassos. Monografia do Instituto Oswaldo Cruz. 2:1-357 (1944).

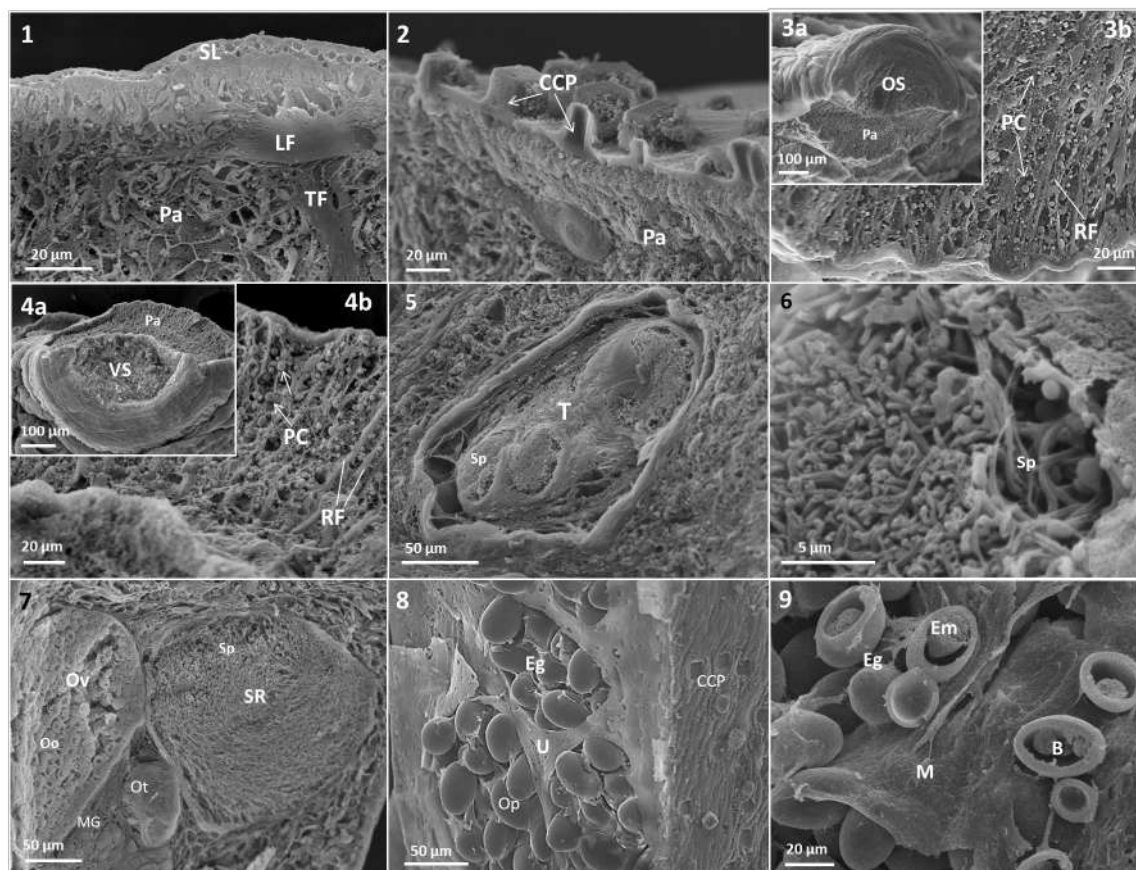
[5] L. Travassos et al., Mem. Inst. Oswaldo Cruz. 67:1-886 (1969).

[6] G. H. Haggis. Scanning Electron Microscopy. 97-104 (1970).

[7] A.F. Adnet et al., Microsc. Microanal. 19:1470-1474 (2013).

This research was supported by CNPq, CAPES and FAPERJ (Brazil).





Legend: *E. coelomaticum* structural organization by SEM - cryofracture. 1. Tegument of the body showing the syncytial layer (SL), muscular fibers, transverse (TF) and longitudinal (LF) and parenchyma (Pa); 2. Tegument with cubic crystal proteins (CCP) in cut; 3a. Oral sucker (OS) showing the parenchyma (Pa); 3b. Detail of oral sucker with parenchymal cells (PC) and radial fibers (RF). 4a. Ventral sucker (VS) showing the parenchyma (Pa); 4b. Detail of ventral sucker with parenchymal cells (PC) and radial fibers (RF); 5. Testis (T) with spermatozoa (Sp); 6. Detail of the spermatozoa (Sp) of the testis; 7. ovary (Ov) showing oocytes (Oo), seminal receptacle (SR) containing spermatozoa (Sp), ootype (Ot) and Mehlis' gland (MG). 8. Uterus (U) with many eggs (Eg) with operculum (Op). 9. Fractured eggs (Eg) inserted in intrauterine mucus (M) exhibiting blastomeres (B) and embryo (Em).



### 3D reconstruction of embryonated eggs of *Trichuris muris*

Ludmila Rocha Lima<sup>1</sup> and Eduardo José Lopes Torres<sup>1</sup> \*

<sup>1</sup>. Laboratório de Helminologia Romero Lascasa Porto (LHRLP), FCM-UERJ, RJ, Brasil.

\*lopestorresej@gmail.com

Soil-transmitted helminths are neglected diseases promoted by nematodes and are associated with soil contacted and their development is dependent of temperature and humidity. According to WHO 2019[1], is estimated that 1.5 billion people are infected with these parasites. They are diseases associated with social and climatic characteristics, affecting mainly children. The last national survey of schistosomiasis and soil-transmitted helminthiasis prevalence data show that the trichuriasis present an approximately 5% infected in Brazil [2]. The trichuriasis is a disease that affects several mammals with human health and veterinary impact. *Trichuris muris* species is used as an experimental model for trichuriasis. The life cycle begins with the ingestion of embryonated eggs and finalize with a unembryonated egg elimination by host feces. The egg shell present three layers using light microscopy [3]. The aim of this work is the ultrastructural characterization of the embryonated eggs and of the L1 larva of *Trichuris muris* chemically fixed using by light microscopy tools Fixed samples were stained with calcein and DAPI and analyzed using fluorescence, confocal and super resolution microscopies. The results showed the three egg-shell layers formed by trilaminar layer (vitelline, chitin and lipid layers) (Fig 1A- inset). Was possible to identify the larval esophagus and germinative cells concentrated in the larva posterior region (Fig. 1A). Based on fluorescence microscopy, the calcein showed high affinity for polar plugs and DAPI enabled the L1 cells characterization (Fig. 1B). Through the image series obtained by confocal experiments, we performed the reconstruction and modeling of germ cells, enabled a quantification and resulting in approximately 151 cells in each larva (Fig. 1D-F). In unembryonated egg we identified 208 embryonic cells (Fig. G-I). Our results shows that the embryonic process that triggered the formation of L1 larvae resulting a number cell reduction in embryonated eggs when compared to unembryonated eggs. The larval hatching of L1 larvae is viable by the association of egg-shell fragility in polar plugs region and the internal force promoted by the larvae.

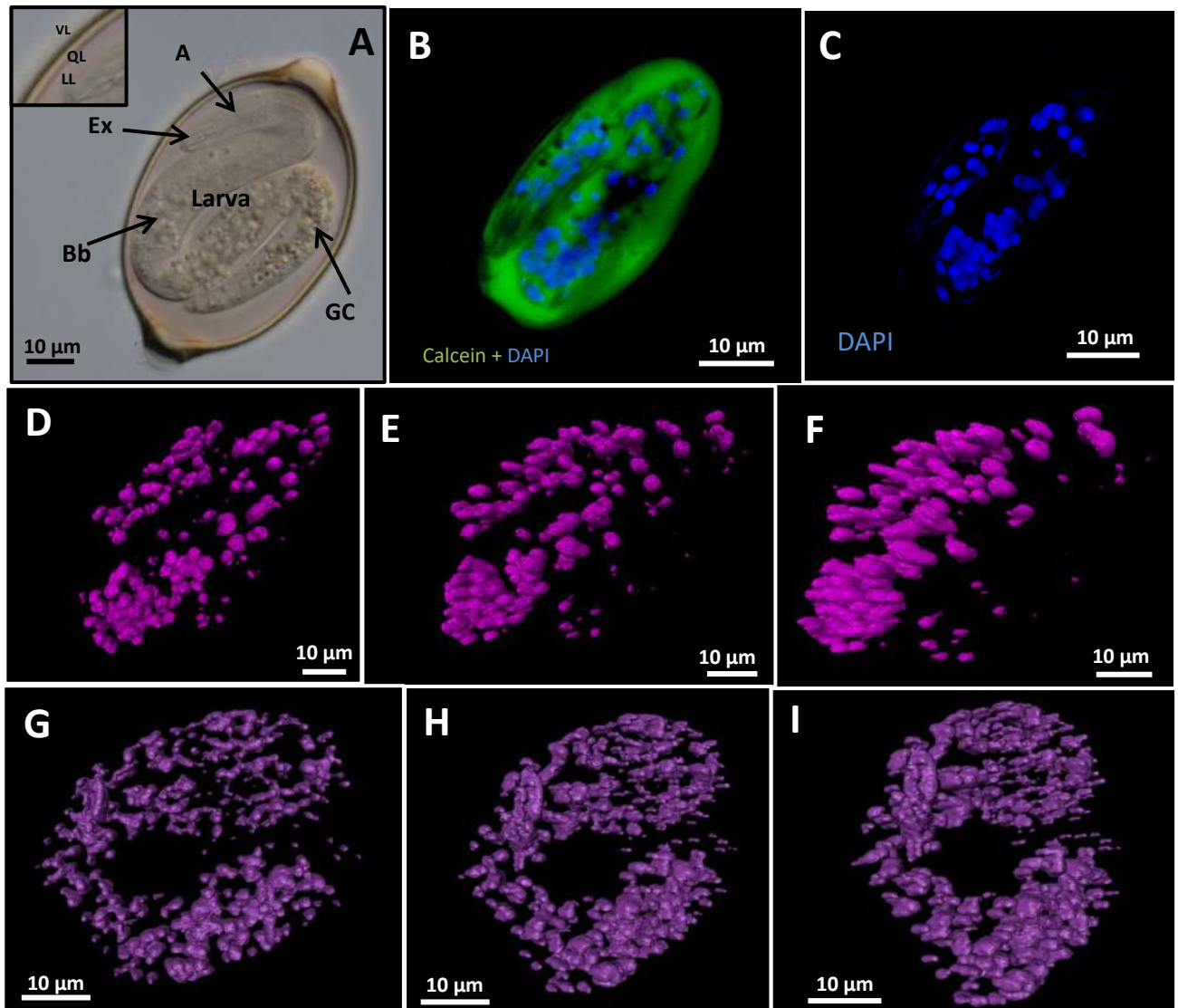
[1]WHO, W.H.O. Helmintiasis transmitidas por el suelo , 2019

[2] KATZ, N. Inquérito Nacional de Prevalência da Esquistossomose mansoni e Geohelmintoses.2018.

[3] PRESTON, C. M.; JENKINS, T.. Parasitology, v. 89, (1984) 263.

[4] This research was supported by CNPq (Brazil) and FAPERJ (Brazil).

Keywords: *Trichuris muris*. Egg. Confocal. 3D.



Legends: A – Normarski microscopy (DIC): Embryonated egg anterior region (A) showing the esophagus (Ex) of the larvae, posterior region with germ cells (GC) and bacillary band (Bb); Detail: Egg shell layers: Vitelline layer (VL), Chitin layer (CL) and Lipidic layer (VL); B – C : Confocal microscopy: B: Double staining (Calcein + DAPI); D-F: Reconstruction and modeling of germ cells in the embryonated egg; G-I: Reconstruction and modeling of germ cells in the non embryonated egg

## Contribution of Three-dimensional Modeling to the Whipworm Study

Eduardo J. Lopes-Torres<sup>1\*</sup>, Ludmila Rocha<sup>1</sup>, Wendell Girard-Dias<sup>5</sup>, Lorian C. Straker<sup>3,4</sup>, Wanderley de Souza<sup>2,3</sup> and Kildare R. Miranda<sup>2,3</sup>

<sup>1</sup>Laboratório de Helminologia Romero Lascasa Porto (LHRLP), FCM-UERJ, RJ. Brasil, <sup>2</sup>Laboratório de Ultraestrutura Celular Hertha Meyer, IBCCF-UFRJ, <sup>3</sup>Centro Nacional de Biologia Estrutural e Bioimagem (CENABIO) - UFRJ, <sup>4</sup>Laboratório de Evolução e Biologia Interativa, FFCLRP-USP and <sup>5</sup>Instituto Oswaldo Cruz-Fiocruz.

\*e-mail: eduardo.torres@uerj.com

Whipworms, genus *Trichuris* Roederer, 1791, have worldwide distribution [1] and comprise nematode species that parasitize humans and other mammals. The *T. trichiura* infect an estimated 700 million people worldwide [2]. These nematodes invade the intestinal mucosa of the host, particularly the cecum, causing colitis, anemia and *Trichuris* dysentery syndrome. The transmission is promoted by the ingestion of embryonated eggs and the infection success is associated to the modulation of the host's inflammatory response by the bacillary gland secretion. Whipworms present a unique strategy in forming an intra-tissue niche in the intestine promoted by its ~50.000 bacillary glands found in the anterior region of these nematodes [3]. The structural organization of eggs, adult worms and tissue interaction have been investigated with different microscopy techniques, mainly confocal, scanning (SEM) and transmission electron microscopy (TEM). The 3D modeling process is a strategy with a great potential to amplify the comprehension of the nematodes and the pathophysiology development besides, it has not been widely explored in this field. Chemical (CF) and Cryofixation/freeze substitution (FS) samples associated with different microscopies and 3D modeling can promote advances in helminthology. In the present work, we used light microscopy (bright field, confocal and lightsheet), SEM, TEM, FIB, Micro-CT and 3D modelling to analyze the eggs, bacillary glands and the tissue alterations promoted by *Trichuris muris* inserted in the host tissue. We characterized the L1 larva, eggshell structure and the larva germ cell organization. The 3D modeling of the germ cells allowed to study the spatial distribution and quantification of these cells in the larva body (Fig. A-D). In the adult worm, we find that the bacillary glands of the anterior region show, within its structure, a large volume at the lamellar zone. TEM thin section of cryofixed bacillary glands showed its secretory content in the chamber and projected through the cuticular pore (Fig. E-F). FIB-SEM of this material was reconstructed and the 3D model of the bacillary gland shows the lamellar zone with a lacunar aspect. The model with membrane transparency allow visualization of the lamellar zone morphology with tubular and bag-like structures (Fig. G-I). Lightsheet and Micro-CT experiments allow large volume analyses and 3D modeling of the nematode inserted in the tissue and the alterations on the mucosa surface (Fig. J-L). Our results showed that 3D model analysis provide new insights to the structural organization of the different structures in *T. muris*, opening the possibility to the analyses of other nematodes, helminths and tissues. 3D models provide information of the volume study, hence, a better understanding of the structures in three-dimensional complexity. The application of cryotechniques, 3D reconstruction and 3D modeling open new perspectives for the morphology and the host-parasite interaction fields.

### REFERENCES

- [1] Cafrune, M.M., Aguirre, D.H., Rickard, L.G., 1999. Recovery of *Trichuris tenuis* Chandler, 1930, from camelids (*Lama glama* and *Vicugna vicugna*) in Argentina. *J. Parasitol.* 85, 961-962.
- [2] Bethony, J., Brooker, S., Albonico, M., Geiger, S.M., Loukas, A., Diemert, D., Hotez, P.J. 2006. Soil-transmitted helminth infections: ascariasis, trichuriasis, and hookworm. *Lancet* 367, 1521-1532.



[3] Tilney, L.G., Connelly P.S., Guild, G.M., Vranich K.A., Artis, D. 2005. Adaptation of a nematode parasite to living within the mammalian epithelium. J. Exp. Zool. A Comp. Exp. Biol. 303, 927–945

**ACKNOWLEDGMENTS:** CENABIO-UFRJ, CDB-FFCLRP-USP, CAPES, FAPERJ, FINEP and CNPq.

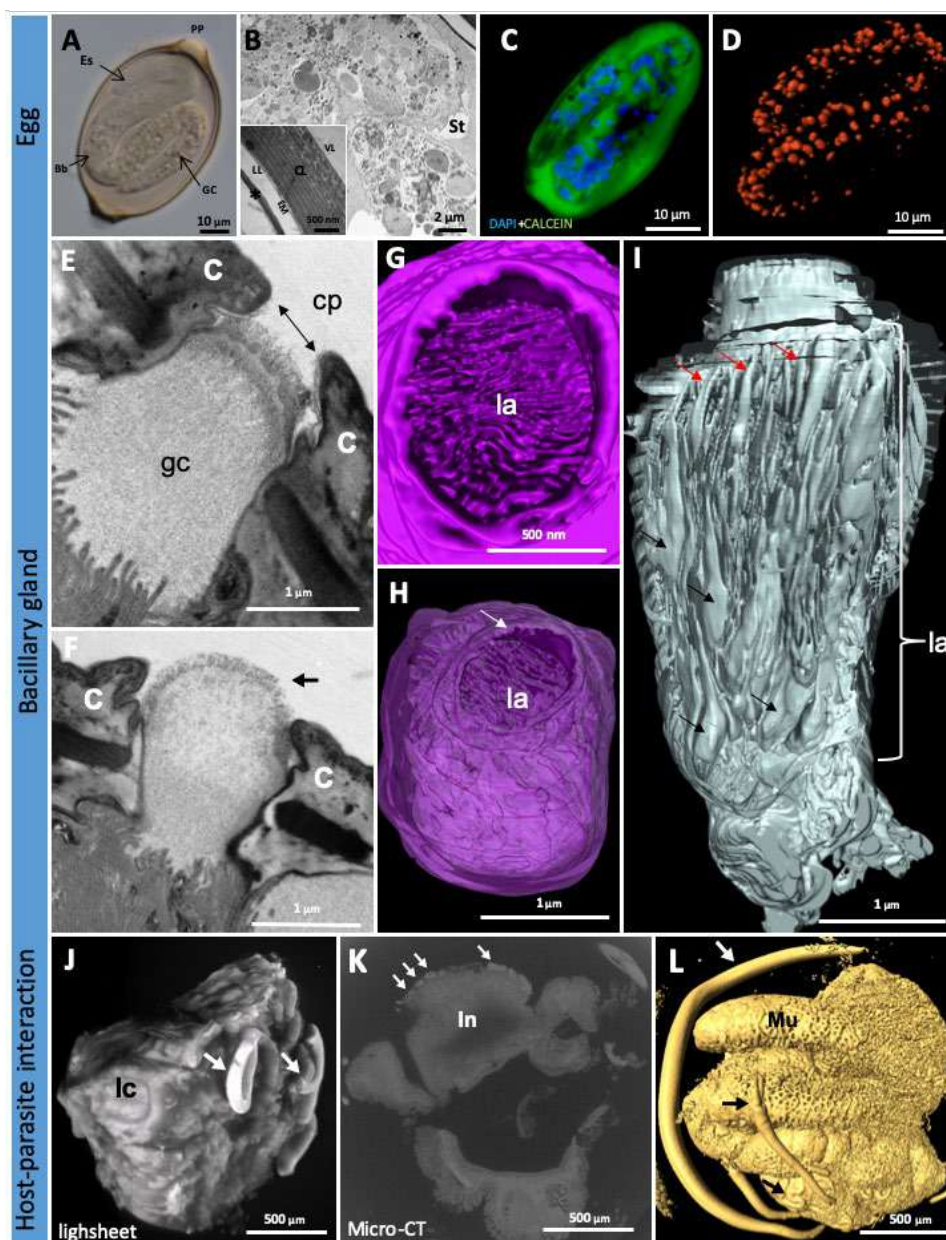


**Fig. 1 - *Trichuris muris* structures:** **Fig. A-D EGG:** (A) Bright field showing the polar plug (PP), larva L1 with esophagus (Es) and germ cells (GC) associated with the formation of the bacillary band (Bb) and digestive system. (B) TEM showing in detail the germ cells, larva stylet (St). Inset: Detail of the eggshell layers (VL: Vitelline, CL: Cuticulin and LL: Lipid), extraembryonic membrane (EM) and permeability layer (asterisk). (C) Confocal image showing larva germ cells (blue) and egg content (green). (D) Modeling of the L1 stage germ cells; **Fig. E-I BACILLARY GLAND:** (E-F) TEM of the bacillary glands showing the pore (cp) in the cuticle (C) and the secretory product in glandular chamber (gc) and in secretion process (arrow). (G-I) Modeling of the gland showing the lamellar zone structure (la), cuticular pore (arrow) and the membrane organization of the lamellar zone showing tubular structures (red arrows) and bag-like structures (black arrows); **Fig. J-L HOST-PARASITE INTERACTION:** (J) Model of the large intestine infected obtained by lightsheet experiments, showing the nematode (arrow) and the lieberkuhn crypts (lc). (K) Micro-CT slice image showing a section of the large intestine with nematode inserted (arrows) in the intestinal tissue (In). (L) Model of the intestine showing a mucosa surface (Mu), posterior region of the nematode (white arrow) and the anterior inserted into the tissue (black arrows).

## Morphometry of Nitrergic Myenteric Neurons Of The Jejunum Of Mice Fed High-Fat Diet

Angelica Soares<sup>1\*</sup>, Evandro José Beraldi<sup>2</sup>, Mikael Gerson Kuhn<sup>3</sup>, Roberto Barbosa Bazotte<sup>4</sup>, and Nilza Cristina Buttow<sup>5</sup>

<sup>1</sup>. Center of Medical and Pharmaceutical Sciences/State University of the West of Paraná, Cascavel, Brazil. \*angelica.soares@gmail.com

<sup>2</sup>. Center of Health Sciences/ State University of the West of Paraná, Francisco Beltrão, Brazil.

<sup>3</sup>. Center of Biological and Health Sciences/ State University of the West of Paraná, Cascavel, Brazil.

<sup>4</sup>. Department of Pharmacology and Therapeutics/State University of Maringá, Maringá, Brazil.

<sup>5</sup>. Department of Morphological Sciences/State University of Maringá, Maringá, Brazil.

The greater intake of foods that are rich in fat is considered one of the causes of the increasing rates of obesity [1]. Obesity is a challenge for global public health, particularly with regard to the association with chronic diseases such as cardiovascular disease, diabetes, cancer [2], and alterations in the gastrointestinal motility [3,4]. The pathogenesis of gastrointestinal alterations might involve changes in enteric nervous system, which is essential for determining the patterns of movement of the gastrointestinal tract [5]. The present study evaluated the effects of a high-fat diet (HFD) in the morphometry of the nitrergic (nNOS-IR) subpopulation in the myenteric plexus of the jejunum of mice. Male Swiss mice, 42 days old, were fed standard rodent chow (CON group) or HFD (OB group), for 17 weeks. All of the procedures were approved by the Ethics Committee on Animal Experiments at the State University of Maringá (protocol 032/2009; approval 075/2009). The HFD (Table 1) was prepared using lard in a composition that was previously used [6] and based on the AIN-93G purified diet [7]. Samples of the jejunum were fixed in a solution of 4% buffered paraformaldehyde (pH 7.4), opened at the mesenteric border, washed with 0.1 M phosphate-buffered saline (PBS; pH 7.4), and microdissected under a stereomicroscope to obtain whole-mounts of the muscular tunic by removing the mucosa and submucosa. The whole-mounts containing the myenteric plexus were subjected to immunofluorescence technique to label the subpopulation of neurons that express neuronal nitric oxide synthase (nNOS-IR), using anti-nNOS primary antibody (dilution 1:500; Zimed) and anti-rabbit IgG FITC secondary antibody (dilution 1:500; Santa Cruz Biotechnology). The analyzes were performed in images randomly captured of the whole-mounts on the histological slides, with an AxioCam MRC high-resolution camera (Carl Zeiss) coupled to an Axioshop Plus fluorescence microscope (Carl Zeiss) with a 20x objective lens. The area of 100 neuronal cell bodies per animal was measured using Image Pro Plus software (v. 4.5, Media Cybernetics). Measurements were made in nNOS-IR neurons where it was possible to clearly see the limits of the cell body. The results were analyzed by Student's t test or an equivalent nonparametric test using Prism 5.01 software (GraphPad); values of  $p < 0.05$  were considered statistically significant. The HFD increased body weight and visceral fat of the OB group (Table 2). The length of the small intestine and the areas of neuronal cell bodies of the nNOS-IR subpopulation (Figure 1) did not change with the HFD consumption (Table 2). In conclusion, although the high-fat diet for 17 weeks promoted obesity in the animals, the neuronal profile of the nitrergic myenteric subpopulation of the jejunum

was maintained. The data provide a basis for further studies to clarify the influence of HFD in the intestinal motility.

## REFERENCES

- [1] G.A. Bray, Am. J. Clin. Nutr. 93 (2011) 481.
- [2] World Health Organization, <https://www.who.int/topics/obesity/en/> (2019).
- [3] K.A. Boyd et al., Am. J. Physiol. Gastrointest. Liver. Physiol. 284 (2003) G188.
- [4] B.G. Nezami et al., Gastroenterology. 146 (2014) 473.
- [5] J.B. Furness, The enteric nervous system, Malden, 2006.
- [6] D.P. Arçari et al., Obesity (Silver Spring). 17 (2009) 2127.
- [7] P.G. Reeves, J. Nutr. 127 (Suppl 5) (1997) 838S.
- [8] This research was supported by CAPES (Brazil).

Table 1. Nutritional composition of the standard chow and high-fat diet (HFD).

	Standard chow	HFD
	g/100 g	
Protein	22	20
Carbohydrate	55	35
Total fat	4	35
Fiber	7	5
Micronutrients	12	5
Kcal/Kg	3773	5358

Table 2. Body weight, visceral fat weight, length of the small intestine, and cell bodies areas of nNOS-IR myenteric neurons of the jejunum of mice fed standard rodent chow (CON group) and high-fat diet (OB group).

	CON	OB
Body weight (g)	49.2 ± 2.18	59.6 ± 2.54*
Visceral fat (g)	2.94 ± 0.67	5.13 ± 0.47*
Length of the small intestine (cm)	57.1 ± 1.08	53.4 ± 1.44
Area of nNOS-IR neurons (μm <sup>2</sup> )	172.8 ± 1.92	173.8 ± 1.95

Results are expressed as the mean ± SEM (n = 5). \* Significant difference compared to the CON group (p<0.05).

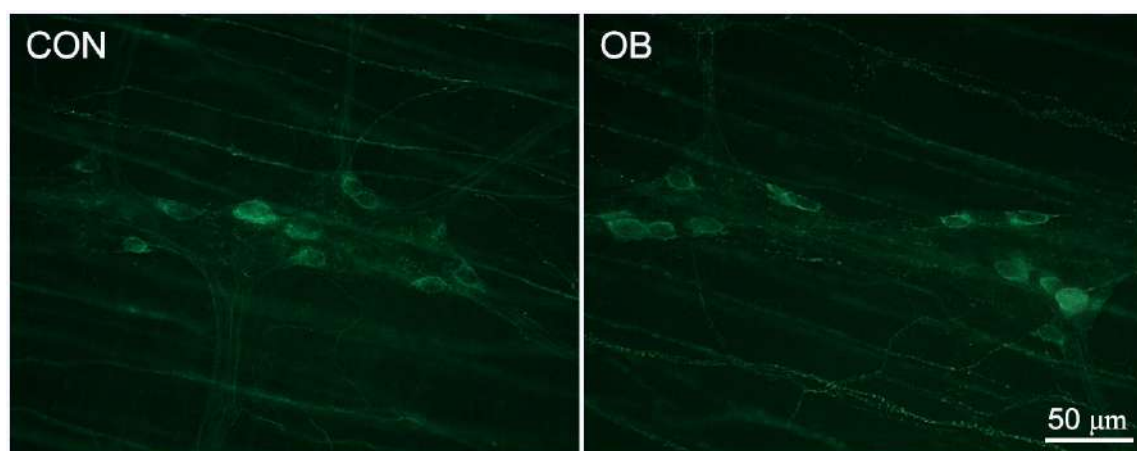


Figure 1. Micrographs of nNOS-IR neurons in the myenteric plexus of the jejunum of mice fed standard rodent chow (CON group) and high-fat diet (OB group).

## Neuroprotection In Hydrocephalic Rats, Surgically Treated Or Not: The Memantine As A Pharmacological Alternative

Pâmella da Silva Beggiora<sup>1\*</sup>, Stephanya Covas da Silva <sup>1</sup>, Karine Pereira Rodrigues<sup>2</sup>,  
Timóteo Abrantes de Lacerda Almeida<sup>1</sup>, Hélio Rubens Machado<sup>1</sup> and Luiza da Silva  
Lopes<sup>1</sup>.

<sup>1</sup>. Department of Surgery and Anatomy, Ribeirão Preto Medical School, University of São Paulo, Ribeirão Preto, Brazil

E-mail of the corresponding author: pambeggiora@usp.br

<sup>2</sup>. Postgraduate program in Physical Education and Sport, School of Physical Education and Sports of Ribeirão Preto, University of São Paulo, Ribeirão Preto, Brazil

Hydrocephalus is an imbalance in the flow or absorption of cerebrospinal fluid, resulting in a dilation of the ventricular system [1,2]. The treatment of hydrocephalus usually used is surgical (ventriculoperitoneal shunt), but not all patients can undergo surgical treatment immediately after diagnosis [3,4]. With this, neuroprotective measures have been tested in order to minimize the tissue lesions involved [5]. Memantine is a non-competitive N-methyl-D-aspartate (NMDA) receptor antagonist, which revealed neuroprotective action in Alzheimer's disease [6]. The aim of this study was to evaluate the neuroprotective response of Memantine in animals treated with or without a shunt. Male Wistar rats were submitted to hydrocephalus by intracisternal injection of kaolin, divided into five groups: control (n = 10), hydrocephalus without treatment (n = 10), hydrocephalus treated with intraperitoneal Memantine (20mg / kg / day) (n = 10), hydrocephalus treated with shunt (n = 10), hydrocephalus treated with shunt plus Memantine (n = 10). To evaluate the treatment, behavior tests (open field, automatic activity monitor, water maze and object recognition), histological and immunohistochemical studies were performed. The treatment with Memantine resulted in a significant improvement in sensorimotor development (p <0.05), greater agility and exploration of the environment, preservation of spatial and recognition memory, and greater learning ability (p <0.05). Reduced astrocytic reaction in the cortex and germ matrix (p <0.05) by GFAP immunolabeling. It is concluded that Memantine offers beneficial effects to the structures that have been affected by the ventricular increase and can be considered an adjuvant therapy to the surgical treatment of hydrocephalus. Ethics Committee Approval: 96/2016. This research was supported by Coordenação de Aperfeiçoamento de Pessoal de Nível Superior (CAPES) and Fundação de Amparo à Pesquisa do Estado de São Paulo (FAPESP) grant number 2016/11212-7. (Brazil).

### REFERENCES

- [1] F. E. OLOPADE et al., The relationship between ventricular dilatation, neuropathological and neurobehavioural changes in hydrocephalic rats. *Fluids Barriers CNS*, 9 (2012), 19.
- [2] M.R. DEL BIGLIO et al., Hydrocephalus – Pathology. In: CHOUX, M., DI ROCCO, C. AL, E. *Pediatric Neurosurgery*, London, Churchill Livingstone (1999), 217-36.



- [3] J. J. FACURE, Ventriculo-peritoneal shunt with valve in the treatment of childhood hydrocephalus. *Arq Neuropsiquiatr*, 30 (1972), 8-29.
- [4] E. HOPPE-HIRSCH et al. Late outcome of the surgical treatment of hydrocephalus. *Childs Nerv Syst*, 14 (1998), 97-9.
- [5] M. R. DEL BIGIODI CURZIO et al., Nonsurgical therapy for hydrocephalus: a comprehensive and critical review. *Fluids Barriers CNS*, 13 (2016), 3.
- [6] E. SCARPINI et al., Treatment of Alzheimer's disease: current status and new perspectives. *Lancet Neurology*, 2 (2003), 539-47.

## Figures

GFAP immunostained of the cortex and germ matrix slides of the in rat brain

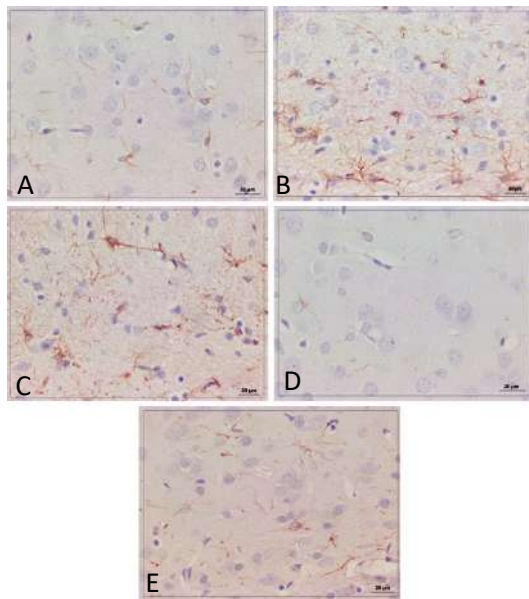


**Figure 1:** Photomicrographs of CTx immunohistochemical evaluation. It is observed that the astrocytic reaction of HTS and H animals are more coarse. However, the HTM animals showed almost no astrocytic reaction and the HTSM group was similar to the C group, presenting resting astrocytes with fine and delicate extensions. C - controls (A), Untreated H (B), HTS - hydrocephalic treated with shunt (C), HTM - hydrocephalic treated with Memantine (D) and HTSM- hydrocephalic treated with shunt and Memantine (E). . Objective magnification  $\times 40$ . Scale bar =  $20\mu\text{m}$ .

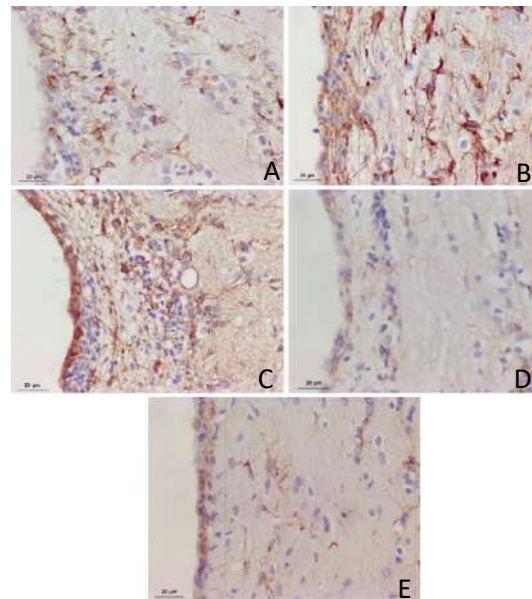


**Figure 2:** Photomicrographs of GFAP immunostained slides of deep cortex in rat brain. C control (A), H hydrocephalic without treatment (B), HTS hydrocephalic rats treated with shunt (C), HTM hydrocephalic rats treated with Memantine (D), and HTSM hydrocephalic rats treated with shunt and Memantine (E). It is observed that the astrocytic reaction in the HTS and H groups is coarser. The HTM group shows almost no reaction. The HTSM group is like group C, presenting astrocytes with fine and delicate extension. Objective magnification  $\times 40$ . Scale bar =  $20\mu\text{m}$ .

## Effects Of Hyperbaric Oxygen Therapy In Secondary Lesions To Experimental Hydrocephalus Associated With Surgical Treatment

Stephanya C Silva<sup>1\*</sup>, Omar Feres<sup>1</sup>, Pâmella S Beggiora<sup>1</sup>, Hédio R Machado<sup>1</sup> and Luíza S Lopes<sup>1</sup>

<sup>1</sup>. Department of Surgery and Anatomy, Ribeirão Preto Medical School, University of São Paulo, Ribeirão Preto, Brazil

E-mail of the corresponding author: tetecovas@usp.br

**Introduction:** Hydrocephalus represents the accumulation of cerebrospinal fluid (CSF) in the cerebral ventricles. Progressive increase in CSF occurs due to an imbalance between CSF production and reabsorption, which leads to enlargement of ventricular cavities [1]. The increase of the CSF promotes various damages to the nervous tissue with cerebral hypoxia/ischemia the most important factor involved [2]. Hyperbaric oxygen therapy (HBOT) promotes the improvement of O<sub>2</sub> supply to tissues, and associated with surgical treatment, may further reduce the damage caused by hydrocephalus [3]. **Methods:** Seven-day-old Wistar Hannover rats were submitted to hydrocephalus by intracisternal injection of 15% kaolin in the cisterna magna. Were divided into five groups: control (n=10), untreated hydrocephalic (n=10), hydrocephalic treated with HBOT (n=10) (3ATA/2h/day), hydrocephalus with shunt (n=10), hydrocephalus with shunt plus HBOT (n=10). HBOT sessions were performed for 21 days. Behavioral tests (open field, Morris aquatic labyrinth) and imaging exam by cranial ultrasonography were performed. After 21 days, the animals were euthanized, and the brain removed for immunohistochemical studies. **Results:** The hyperbaric treatment associated with CSF surgery appears to reduce ventricular enlargement, as seen by ultrasound examinations. The animals improved the behavioral performance (p=0.0001), greater agility and greater exploration of the environment (p=0.0001). They also presented greater preservation of spatial memory and learning capacity. The astrocytic activity was significantly reduced (p=0,0001), highlighted by GFAP immunolabeling. **Conclusions:** The results suggest that the hyperbaric treatment associated with the surgery improved the behavioral performance, offered benefits to the structures affected by the ventricular increase and a decrease of the ventricular size was observed. Thus, HBOT can be considered an adjuvant therapy for the surgical treatment of hydrocephalus.

This research was supported by Coordenação de Aperfeiçoamento de Pessoal de Nível Superior (CAPES) and Fundação de Amparo à Pesquisa do Estado de São Paulo (FAPESP) grant number 2016/11212-7. (Brazil).

### REFERENCES

- [1] J. P. McAllister et al., Pathophysiology of congenital and neonatal hydrocephalus. *Seminars in Fetal and Neonatal Medicine*, 17 (2012), 285-294.
- [2] M. R. Del Biggio et al., Chronic Hydrocephalus in Rats and Humans: White Matter Loss and Behavior Changes. *Ann Neurol*, 53 (2003), 337-346.
- [3] S. C. da Silva et al., Hyperbaric oxygen therapy reduces astrogliosis and helps to recovery brain damage in hydrocephalic young rats. *Childs Nerv Syst*, 34 (2018) 1125-1134.

## GFAP immunostained slides of the corpus callosum in rat brain

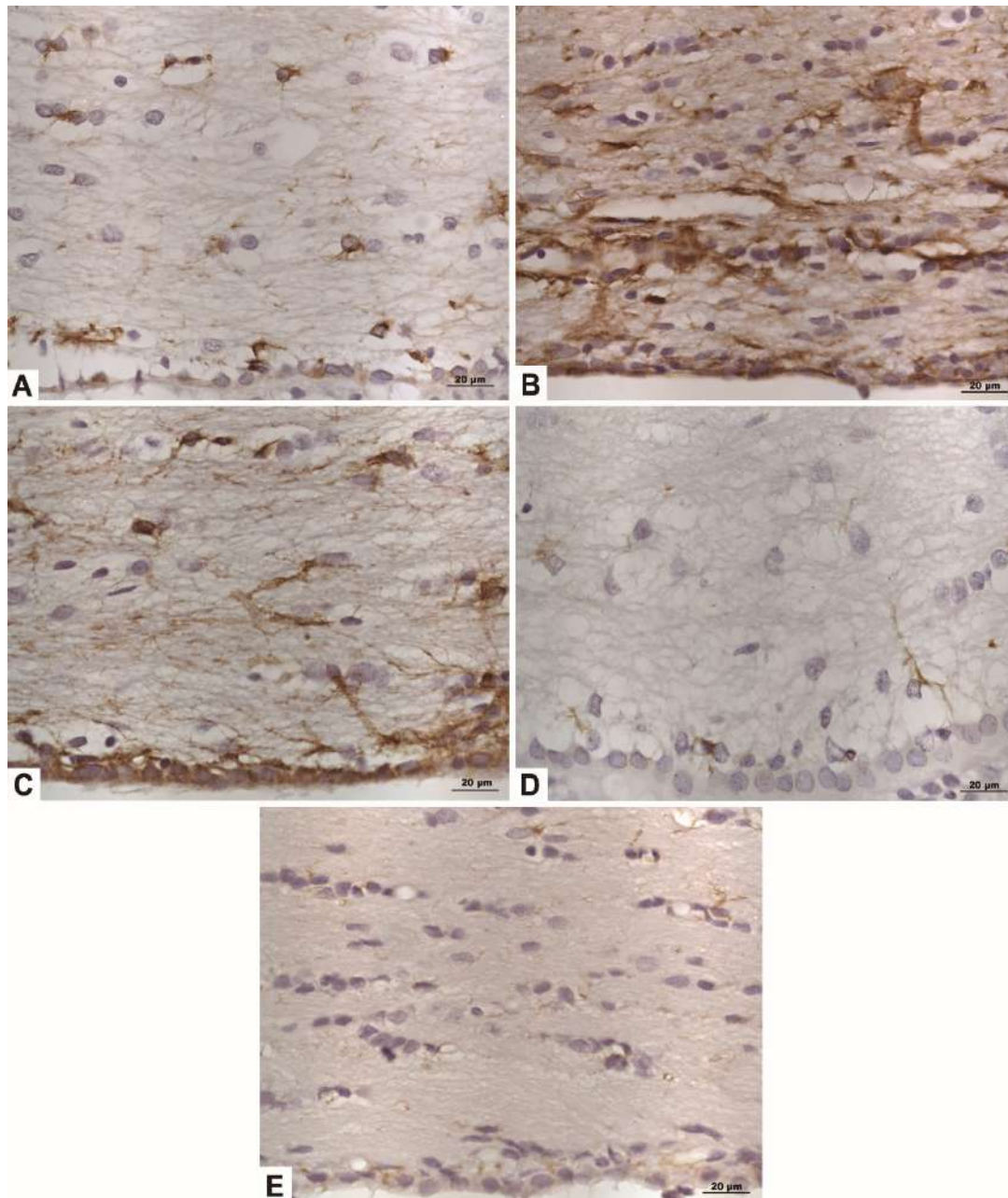


**Figure 1:** Photomicrographs of GFAP immunostained slides of the corpus callosum in rat brain. (A) control (C), (B) hydrocephalic without treatment (H), (C) hydrocephalic treated with shunt (HTS), (D) hydrocephalic treated with hyperbaric oxygen therapy (HBOT), and (E) hydrocephalic treated with shunt plus hyperbaric oxygen therapy (HTOS). It is observed that the animals of the HBOT and HTOS groups have resting astrocytes with thin extensions and are similar with group C. In the HTS group, a greater presence of astrocytic reaction is observed, as well as in the group HNT. Objective magnification  $\times 40$ . Scale bar = 20 $\mu$ m.

## Synthesis and characterization of graphene oxide for bactericide potential evaluation

Raphael Verdan Curti<sup>1</sup>, Bráulio Soares Archanjo<sup>1</sup>, Juliana Lopes Martins<sup>2</sup>, Oleksii Kuznetsov<sup>1</sup>, Joyce Rodrigues Araújo<sup>1</sup>, Kelly Leite dos Santos Castro Assis, Carlos Alberto Achete<sup>1</sup>.

1. Instituto Nacional de Metrologia, Qualidade e Tecnologia – DIMAT, Duque de Caxias, Brazil.
2. <sup>1</sup>. Instituto Nacional de Metrologia, Qualidade e Tecnologia – LABIO, Duque de Caxias, Brazil.

Graphene and its derivatives such as graphene oxide (GO) are currently widely studied materials in the world given their potential in several areas of knowledge. Among these potentialities we can highlight their antimicrobial potential recently demonstrated in the literature. In this work, we will use the chemical route to obtain GO and test its antimicrobial potential. The research on the interaction of GO with human and bacterial cells [1, 2] has promoted efforts to discover potentialities of the material in the biotechnology and biomedical areas [3-5]. The observation of a destructive interaction between the GO and the bacterial membranes motivated the search for an understanding of the phenomena involved in this process and opened up new opportunities for the application of GO. After the chemical synthesis of the GO the graphene sheets acquire functional groups of oxygen, improving its dispersity and reactivity. In this work, GO was obtained using the methodology proposed by Hummers, however varying the concentration of potassium permanganate to obtain three different materials. GO and *E. coli* cells were characterized by scanning electron microscopy (SEM) (Fig. 1 a-i) and Helion ion microscopy (HIM) (Fig. 2 a-b). X-ray diffraction, Raman spectroscopy and X-ray photoelectron spectroscopy were used to chemical and structural characterization of GO. GO produced here were submitted to sterility test for the detection of microorganisms, and we have found that these materials were already sterile after synthesis, an important step to find trusted results in bactericidal test. In the bactericidal test we have found that the GO concentration of 160 µg/mL or higher provided positive results, reducing the bacteria growth up to 90%.

**Keywords:** Hummers Synthesis, graphene oxide, bactericidal potential

### REFERENCE LIST

- [1] O. Akhavan, E. Ghaderi, Toxicity of Graphene and Graphene Oxide Nanowalls Against Bacteria, *ACS Nano* 4(10) (2010) 5731-5736.
- [2] M. Mazaheri, O. Akhavan, A. Simchi, Flexible bactericidal graphene oxide–chitosan layers for stem cell proliferation, *Applied Surface Science* 301(0) (2014) 456-462.
- [3] K. Krishnamoorthy, M. Veerapandian, L.-H. Zhang, K. Yun, S.J. Kim, Antibacterial Efficiency of Graphene Nanosheets against Pathogenic Bacteria via Lipid Peroxidation, *The Journal of Physical Chemistry C* 116(32) (2012) 17280-17287.
- [4] O. Akhavan, E. Ghaderi, *Escherichia coli* bacteria reduce graphene oxide to bactericidal graphene in a self-limiting manner, *Carbon* 50(5) (2012) 1853-1860.
- [5] J. Campos-Delgado, K.L.S. Castro, J.G. Munguia-Lopez, A.K. González, M.E. Mendoza, B. Fragneaud, R. Verdan, J.R. Araujo, F.J. González, H. Navarro-Contreras, I.N. Pérez-Maldonado, A.d. León-Rodríguez, C.A. Achete, Effect of graphene oxide on



bacteria and peripheral blood mononuclear cells, Journal of Applied Biomaterials & Functional Materials 14(4) (2016) 0.

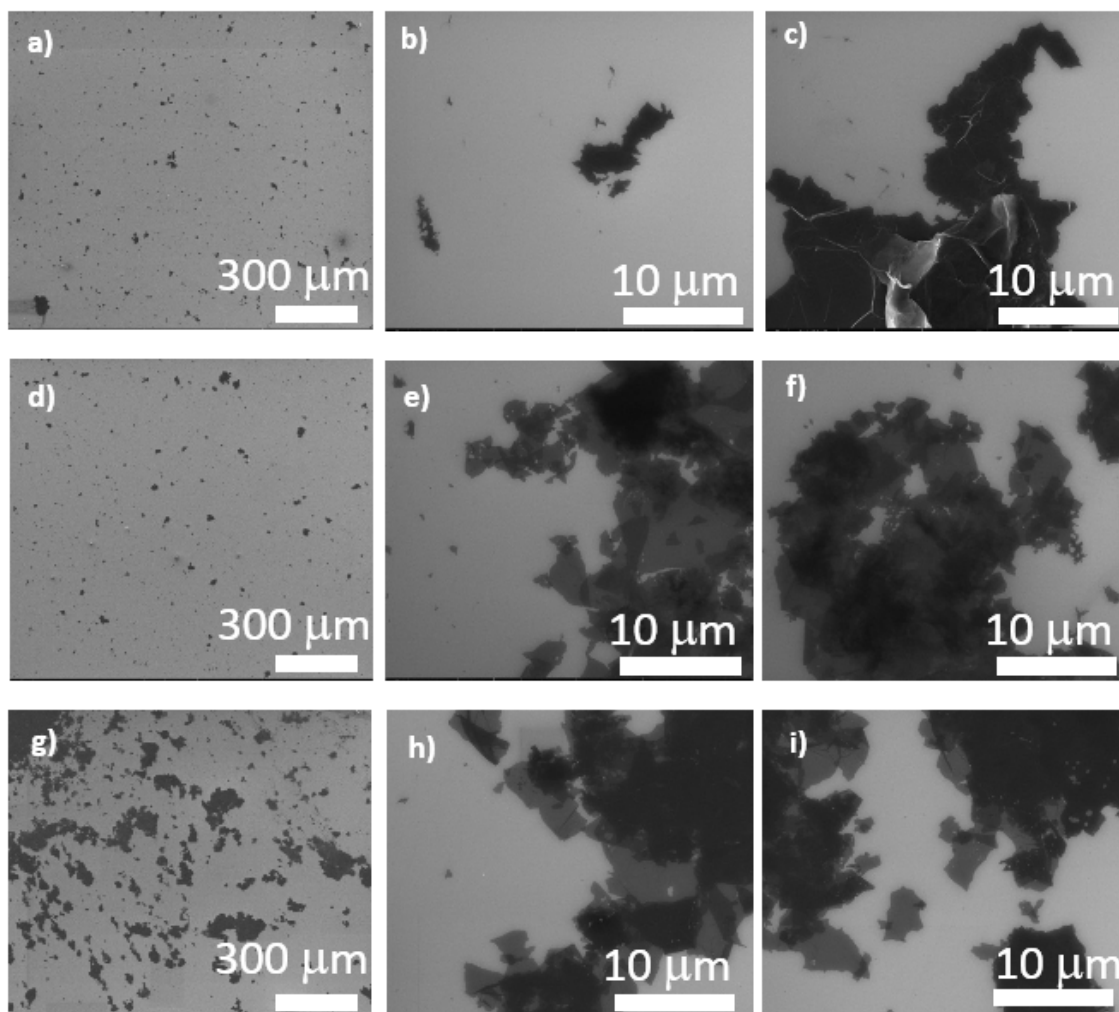


Fig. 2 – Scanning electron microscopy of graphene oxide in different concentrations of potassium permanganate; 1 g (a-c), 3 g (d-f) and 6 g (g-i).

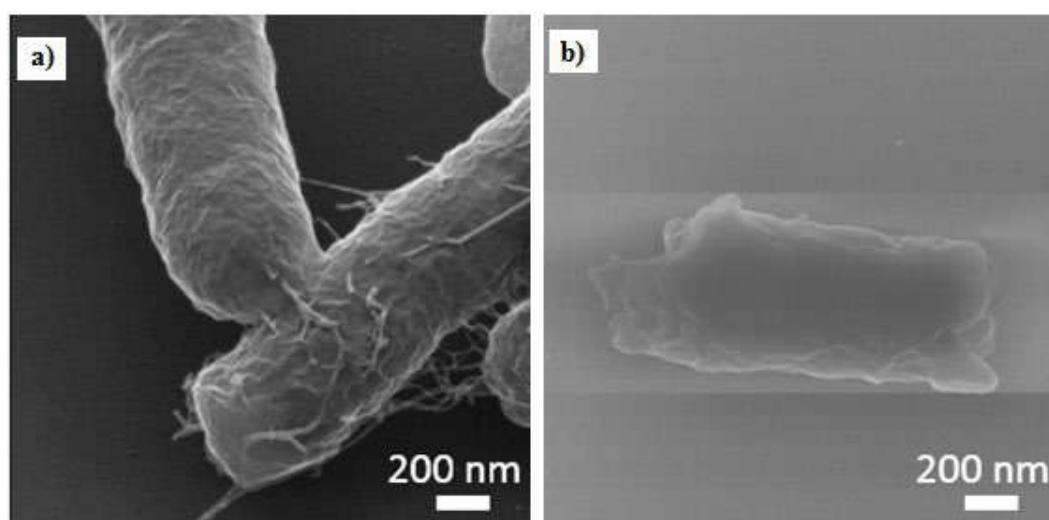


Fig. 1 – a) E. coli cell before contact with graphene oxide, b) E. coli cell after contact with graphene oxide.



DOI:  
ISSN:

# PARTE 4

## PÔSTERES - MATERIAIS

## The Mechanism of Oxidation Assisted Intergranular Cracking on Nickel-Based Superalloy 718

Amanda Varela<sup>1\*</sup>, Luiz Henrique de Almeida<sup>1</sup>

<sup>1</sup>- Programa de Engenharia Metalúrgica e de Materiais/UFRJ, Rio de Janeiro, Brasil.

\*amandavarela@poli.ufrj.br

Alloy 718 is a precipitation-hardened nickel-based superalloy of major technological importance especially in the aerospace industry, which implicates on regular exposure to elevated temperatures and oxidizing environments [1]. Its remarkable performance relies on the slow kinetic precipitation of the metastable phase  $\gamma''$  ( $\text{Ni}_3\text{Nb}$ ). However, its service temperature is limited at about 650°C due to  $\gamma''$  instability and also the oxidation assisted intergranular cracking (OAIC) manifestation. The latter leads to a dramatic decrease in ductility [1]. Niobium, representing around 5% at of Alloy 718, is also a MC-type carbide former and it is known for its oxygen affinity. Therefore, several studies have pointed out the NbC (or (Nb,Ti)C) primary role on the OAIC mechanism [2,3]. It is reported that, at high temperatures and in the presence of oxygen, intergranular NbC decomposes to form a brittle oxide,  $\text{Nb}_2\text{O}_5$ , on the grain boundaries [2,3]. The stresses of service would ultimately lead to an intergranular fracture. Although there is evidence of the niobium surface enrichment in the given conditions to form the oxide, there is no confirmation of the NbC as its source or characterization of this  $\text{Nb}_2\text{O}_5$  formation [4]. Driven by some contradictions in the literature, this work makes an effort towards the understanding of this phenomenon by hot tensile testing and image characterization by SEM. The samples were primarily solution annealed at 1050°C for 1h. For the tests between 650 and 900°C, the surface fractures revealed partial or total intergranular crack propagation, indicating the OAIC interval, as it is shown in Figure 1. Figure 2 presents some of the longitudinal sections of this interval, showing many secondary cracks in low magnification, except for the lowest ductility temperature at 850°C. At this condition, they emerged in the last 120 seconds according to interrupted tests, revealing a much faster kinetic than the reported NbC decomposition times, which exceeds 8h [4]. Since this catalytic reaction is closely related to the temperature of fastest precipitation rate of the  $\gamma''$  strengthening phase, it suggests its critical role. It was previously reported that Nb atoms cluster together to form the alloy's intergranular precipitate within 120 seconds [5]. Furthermore, the samples were overaged at 800 and 900°C for 32h. These specimens had nearly all Nb available for precipitation consumed in the form of  $\delta$  phase, the most stable form of  $\text{Ni}_3\text{Nb}$ , and they were tested at 850°C. Compared to the previous condition, there was an increase in ductility. Figure 3 shows the image of a sample aged at 900°C and its respective EDS mapping for niobium and titanium, confirming major niobium-rich precipitation together with (Nb,Ti)C carbides. Table 1 presents the elongation parameter increasing. Therefore, it is suggested that the OAIC mechanism might have in the boundary driven segregation of niobium, prior to the precipitation, the primary source of its embrittlement.

### REFERENCES

- [1] A. de Vasconcelos Varela et al., J. Mater. Res. Technol., 7 (2018) 319-325.
- [2] M. Gao et al., Superalloys 718, 625, 706 and var. derivatives, TMS (1994) 581-592.
- [3] M. Rezende et al., J. Alloy. Compd., 643 (2015) S256-S259.
- [4] A. de Vasconcelos Varela, (2017). UFRJ, Rio de Janeiro, Brazil.
- [5] T. Alam et al., Mater. Sci. Eng., 527 (2010) 7770-7774.

This research was supported by CNPq (Brazil).

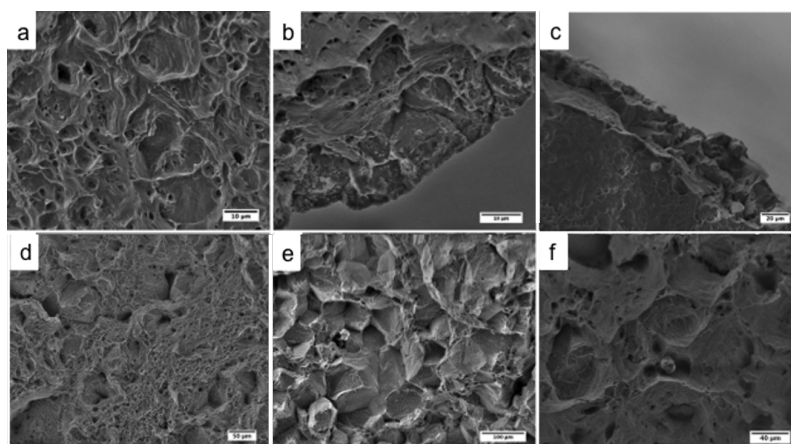


Figure 1 – SEM/SE images of the fracture surfaces of solution annealed samples tested at (a) 600, (b) 650, (c) 670, (d) 700, (e) 850 and (f) 900°C. The fractures reveal a change in the fracture mode, going from 100% ductile at 600°C to 100% brittle at 850°C and recovering ductility at 900°C.

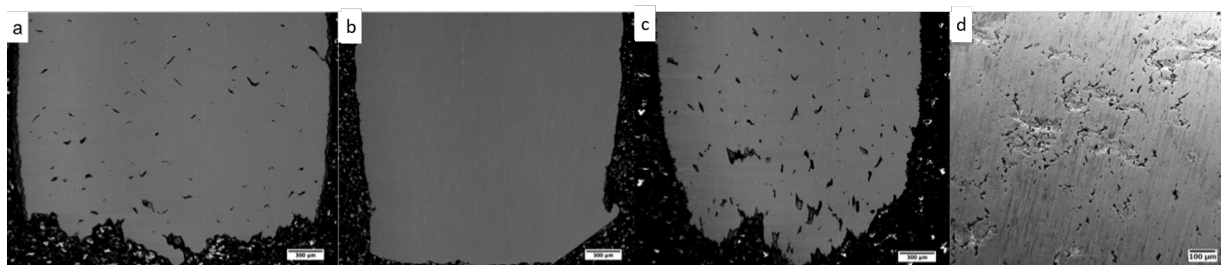


Figure 2 – SEM/BSE images of the longitudinal sections of solution annealed samples tested at (a) 650, (b) 850, (c) 900°C and (d) the image for the interrupted test at 850°C at 94% of its total elongation.

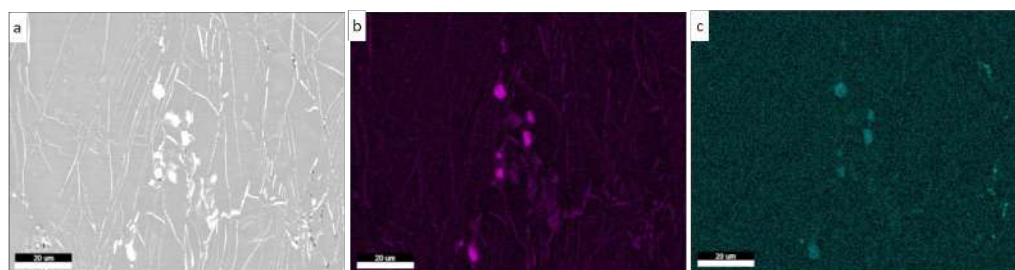


Figure 3 – (a) SEM/BSE image of the sample aged at 900°C for 32h and tested at 850°C and its respective EDS mapping for (b) niobium and (c) titanium, showing the Nb-rich precipitation at the boundaries and (Nb,Ti)C carbides.

Table 1 – Ductility parameter of total elongation (%) for the samples tested at 850°C.

Test temperature (°C)	Heat Treatment	Elongation (%)
850	Solution Annealed (1050°C/1h)	20,4
	Overaged (800°C/32h)	32,3
	Overaged (900°C/32h)	30,1



## **Alloy Used in Thermal Spraying – Characterization by MEV and EDS Using PyMac Software**

Ananda Velloso Lara Guapyassu<sup>1</sup>, Marilia Garcia Diniz<sup>1</sup>, Ivan Guillermo Solórzano Naranjo<sup>2</sup> and André Rocha Pimenta<sup>3\*</sup>

<sup>1</sup>. State University of Rio de Janeiro, PPG-EM/UERJ, Rio de Janeiro, Brazil.

<sup>2</sup>. Pontifical Catholic University of Rio de Janeiro, PUC-Rio, Rio de Janeiro, Brazil.

<sup>3</sup>. Federal Institute of Rio de Janeiro, Laboratory of Computer Instrumentation and Simulation, Campus Paracambi, Paracambi, Brazil. \* rochapimenta@gmail.com

The thermal spraying techniques are good processes for coating components fabricated from non-noble metals, with better performance materials [1 – 2]. The erosion of coal ash is a common problem in boilers [3], which can be solved using hard materials deposited with thermal spraying. The aim of present work was to characterize the microstructure of experimental alloy used to coat steel carbon tube of boilers. Carbon steel plate was prepared by shot peening treatment. Stainless steel alloy (1.6 Si; 29 Cr; 1.65 Mn; 3.75 B; wt.%) was used in thermal spraying process to coat the plate. Cross-section specimen was prepared by metallography techniques. Scanning electron microscopy (MEV - Hitachi TM3000) using backscattered electron (BSE) imaging and with energy dispersive spectroscopy analysis system (EDS - Bruker XFlash MIN SVE) were used to characterize the microstructure. The results of EDS was analyzed by Quantax end PyMac softwares. BSE images results (Figure 01) shows the secondary phases and a few quantity of defects. Unfused particles, porosity, oxides end crack were identified. EDS results showed a matrix composed of Cr, Fe, Mn and Si, and two types of secondary phases, one rich in Cr and another rich in iron. Were identified aluminum oxide at the interface between the coating and the plate, it is possible to state that there were inclusions during the shot peening. EDS results also showed that oxides were aluminum and silicon oxides. In a conventional analysis of EDS results it is not possible to identify the presence of Mn, because the alloy have a few quantity of Mn in comparison with Fe and Cr, and the Mn K $\alpha$  is to close Cr K $\beta$  (5.900 eV and 5.947 eV, respectively), and Mn k $\beta$  is to close the Fe K $\alpha$  (6.492 eV and 6.405 eV, respectively). Results of PyMac software (Figure 02) fit the theoretical (red) and experimental (black) curves, Figure 02 shows the fits with and without Mn. It is possible to observe that when the simulation does not use Mn, there is a right shift of the theoretical curve in relation to the experimental one, being possible to verify the Mn presence.

[1] T. Lindner, M. Lobel, T. Lampke. Metals. 8 (2018).

[2] S.H. Liu et al., Surface & Coatings Technology. 337 (2018) 241-249.

[3] V.H. Hidalgo et al., Wear. 247 (2001) 214-222.

This research was supported by FAPERJ (E-26/290.066/2018), IFRJ (PIBICT / PROCENCIA), and VGK company.

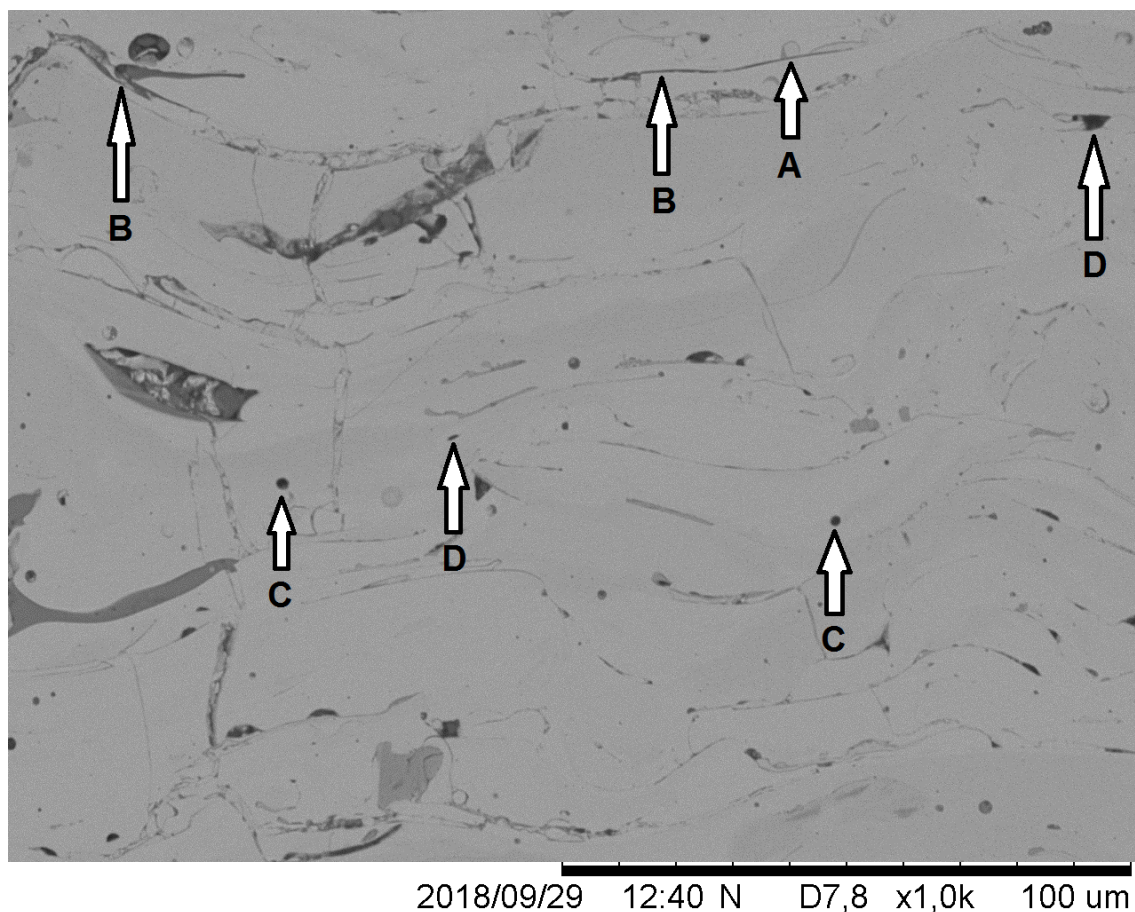


Figure 01 – Characterization by BES MEV (A - Unfused particles; B – crack; C – Porosity; D – oxides).

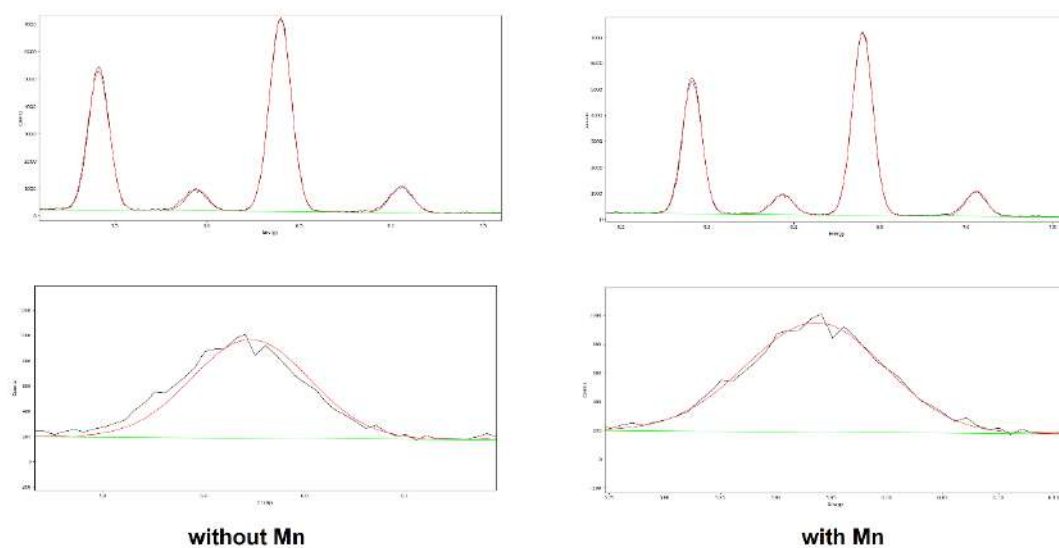


Figure 02 – Mn analysis using PyMac software.

## EFFECTS OF THE UNIAXIAL STRETCHING OF SURFACE TREATED ELECTROSPUN POLYCAPROLACTONE MATS

Anna Lecticia Martinez Martinez Toledo<sup>1,2\*</sup>, Arthur Henrique Vidigal de Miranda<sup>1</sup>, Ana Maria Blanco Martinez<sup>2</sup> and Marcos Lopes Dias<sup>1</sup>

<sup>1</sup>. Laboratório de Catálise para Polimerização, Reciclagem e Polímeros Biodegradáveis, Instituto de Macromoléculas Eloisa Mano/UFRJ, Rio de Janeiro, Brasil.

<sup>2</sup>. Laboratório de Neurodegeneração e Reparo, Hospital Universitário Clementino Fraga Filho/UFRJ, Rio de Janeiro, Brasil.

Electrospinning is a trending technique that yields nanofibers with a high surface area to volume ratio and intra/inter fiber-porosity. It has been applied to different polymers in areas such as tissue engineering, nanosensors and thin films because of its versatility [1]. One of the most common electrospun polymers is poly( $\epsilon$ -caprolactone) (PCL), a biodegradable semi-crystalline aliphatic polyester, because of its cost, biocompatibility, biodegradability and mechanical properties. This polymer also has a large amount of ester groups (-COO-) that can be modified with diamines to yield -NH<sub>2</sub> functional groups, which in turn might grant a better biocompatibility [2,3]. The study of the mechanical properties on nanofibers is an important step due to their structure and the unique response of the fibrillar materials. Therefore, we studied the mechanical properties of four different electrospun PCL mats after the treatment with three different diamines. The use of those diamines - hexamethylenediamine (PCL-HMD), ethylenediamine (PCL-EtDA) and 2,2'-(ethylenedioxy)bis(ethylamine) (PCL-EDEA) resulted in altered contact angles (Figure 1) and different Young's Modulus after an uniaxial stretch of the films, which can be seen in Figure 2. However, only the PCL-HMD sample showed statistically significant difference ( $p < 0,05$ ) in comparison with the neat PCL sample. This result can be related to a higher penetration of this particular diamine in the bulk of the polymer [3,4], hence decreasing its stiffness due to some level of decay of molecular weight caused by the degradation of amorphous regions [5]. From the Scanning Electron Microscopy (SEM) (Figure 3) it is possible to see the fibers before and after the uniaxial stretch. While only few fibers appear to be ruptured, the majority of the fibers appears to be reorganized and aligned. This is related with the force distribution over random fibers, since prior to the rupture the fibers will rotate, align and separate from each other [6]. The fibers also present a high aspect ratio [7] and the PCL has an elastic nature, contributing to this outcome [8]. No significant statistical difference was found in the fiber diameter post-stretch when compared with the non-stretched fibers, although the separation of the fiber bundle and the alignment can be seen. The authors conclude that the use of diamines, even though can influence the hydrophilicity of the samples, it mostly does not affect the bulk properties, and the HMD was able to penetrate further, decreasing the stiffness of the mats.

### REFERENCES

- [1] A. Haider et al., *Arabian J. Chem.*, 8 (2018) 1165.
- [2] E. Malikmammadov et al., *J. Biomater. Sci., Polym. Ed.*, 29 (2018), 863.
- [3] Y. Zhu et al., *Biomacromolecules*, 3 (2002), 1312.
- [4] J. Shen et al., *Biomaterials*, 25 (2004), 423.
- [5] K. Fukatsu, *J. Appl. Polym. Sci.*, 42 (1992), 2037.
- [6] S. Ramakrishna et al., *Biotechnol. Bioeng.*, 110 (2013), 2775.

- [7] S.-C. Wong et al., Polymer, 49 (2008), 4713.  
[8] X. J. Loh et al, Chem.Soc.Rev., 47 (2018), 4545

#### ACKNOWLEDGEMENTS

The authors would like to thank CAPES and CNPq for the financial grant.

PÁGINA 2

Figure 1. Static Contact Angle of the fibers.

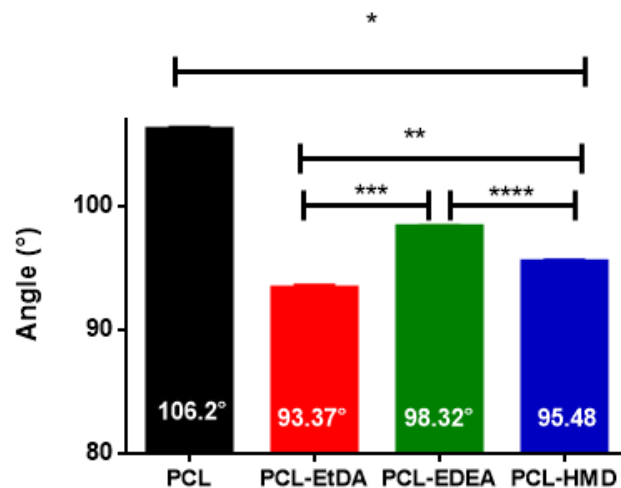


Figure 2. Comparison between the Young Modulus of the nanofibers pre- and post-treatment with diamines.

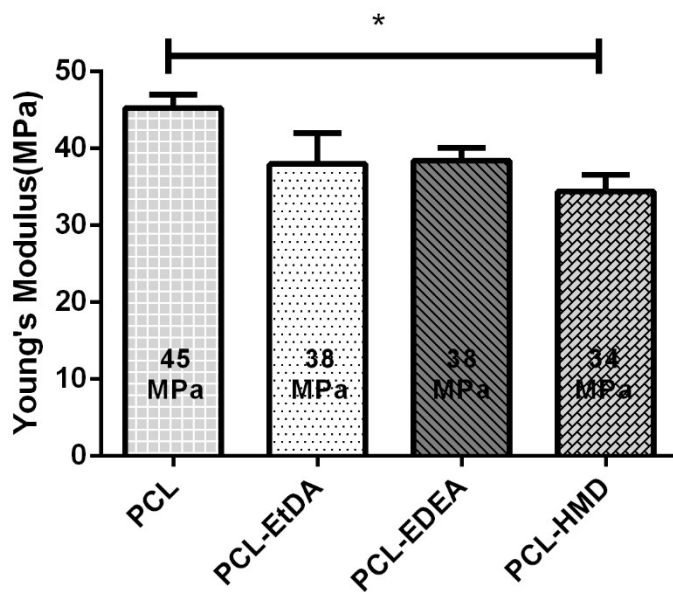
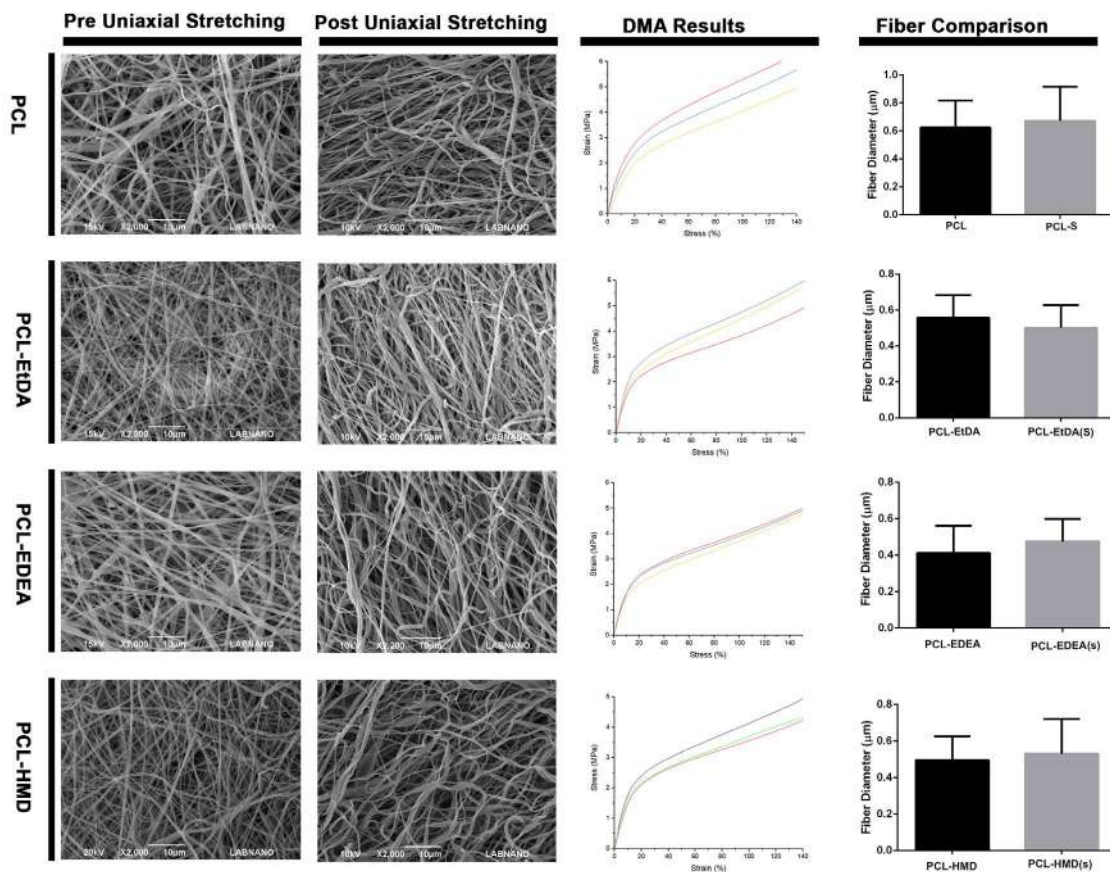






Figure 3. SEM images, stress-strain curves and fiber diameter of nanofibers pre- and post-treated with diamines, before and after uniaxial stretching.



## Characterization of Metallic Coating with Sealant Obtained by Thermal Arc Spray Process

Bianca Barroso Marques<sup>1\*</sup>, Marília Garcia Diniz<sup>1</sup>

1. Mechanical Engineering Postgraduate Program, Rio de Janeiro State University, Rio de Janeiro, Brazil.

\* Email: bianca\_bmarques@yahoo.com.br

A modern and very effective method for corrosion prevention has been the coating application, usually metallic, by Thermal Arc Spray Process [1]. The Thermal Arc Spray Process is a low cost and high productivity technique, however it produces coatings with high surface roughness values and some porosity [2, 3]. The surface finish type and the defects presence (pores, cracks and oxide clusters) will affect the metal coatings corrosion resistance, and the use of sealants that penetrate in the defects may decrease the surface porosity and increase the coatings action in base material protection [4]. This work objectived the characterize of a metallic coating thermally sprayed by electric arc and covered with silicone resin sealant with alumina pigmentation. Surface roughness measurements were carried out, were made too semi-quantitative chemical analysis by Energy Dispersive Spectroscopy (EDS) of sprayed layer and of sealant applied and sealant layer thickness measurements on images obtained by Scanning Electron Microscopy (SEM) using the Image J software (FIJI). The chemical composition of the consumable used for spraying and the coating chemical composition detected by EDS are shown in Table 1 and are fully compatible. Boron is not identified by EDS because of your low atomic weight. The coating with sealant presented an average roughness of 51  $\mu\text{m}$ . Figure 1 exemplifies the spectrum obtained by EDS of the sprayed layer area where was verified the high aluminum and silicon indices confirming the presence of the sealant (Figure 2). The sealant layer thickness found was around 20 $\mu\text{m}$ , 40% less than specified by the manufacturer (almost 50  $\mu\text{m}$ ). For operational performance evaluation, samples of this Thermal Arc Spray coating-sealant system are being tested in a gas boiler of a pharmaceutical industry in Rio de Janeiro, Brazil.

### REFERENCES

- [1] V.R. BRITO, Caracterização de Revestimentos Metálicos Aspergidos Termicamente por Arco Elétrico, Masters Dissertation, Mechanical Engineering and Materials Technology Postgraduate Program, Technological Education Federal Center Celso Suckow da Fonseca, Rio de Janeiro, Brazil, 2010.
- [2] C.C. BERNDT et.al, Handbook of Thermal Spray Technology, ASM International, 2004.
- [3] M.M. COSSENZA, Caracterização de Revestimento Metálico à Base de Ferro-Cromo-Nióbio Obtido por Aspersão Térmica para Tubos de Caldeiras que Operam a Carvão Mineral, Masters Dissertation, Mechanical Engineering Postgraduate Program, Rio de Janeiro State University, Rio de Janeiro, Brazil, 2018.
- [4] SULZER, Technical Information, "An Introduction to Thermal Spray", 2013.

This study was financed in part by the Coordenação de Aperfeiçoamento de Pessoal de Nível Superior – Brazil (CAPES) – Finance Code 001.

Table 1. Quantitative chemical composition of consumable used in the Thermal Arc Spray Process and semi quantitative coating chemical composition found by EDS technique.

Chemical composition (% weight)								
Consumable used	Cr	Nb	Ni	B	Al	Mn	Si	Fe
	13.20	6.00	5.50	4.20	2.00	1.30	1.20	balance
Arc spray coating	Cr	Nb	Ni	B	Al	Mn	Si	Fe
	14.53	8.72	5.28	-	1.88	0.72	1.67	balance

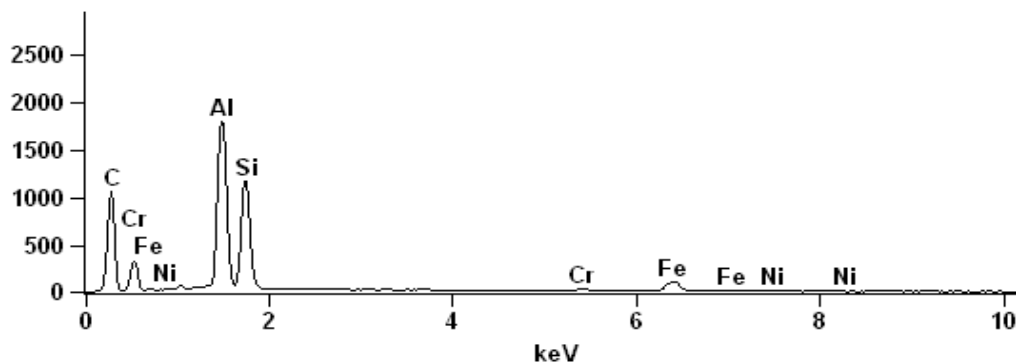


Figure 1. Energy spectrum characteristic of coating region analyzed in Figure 2.

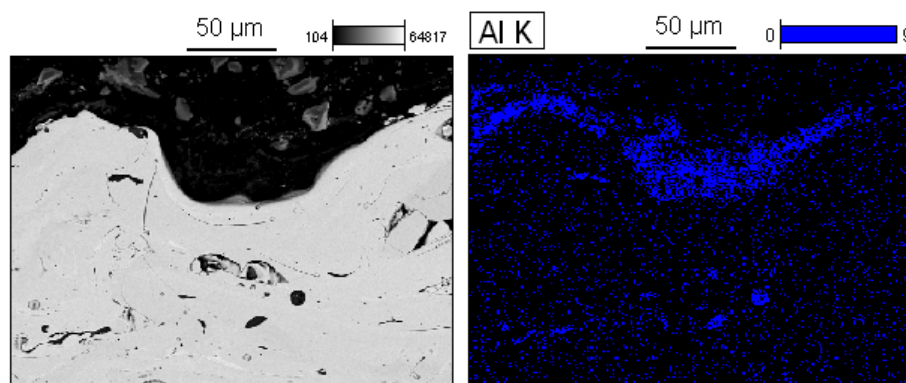


Figure 2. Sealant area analysed by EDS technique. Significant presence of Aluminium were revealed in the region with sealant.

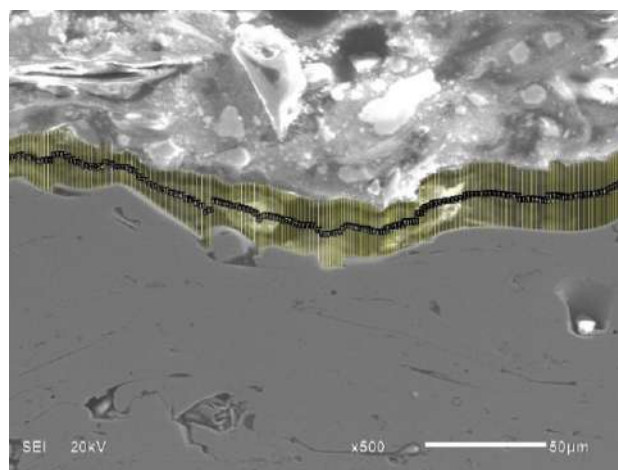


Figure 3. Sealant thickness measurement using the FIJI software.

## Morphological evolution of gold nanostructures electrodeposited on carbon electrodes

Caio de Mello Porfiro<sup>1</sup>, Filomeno A. D. Inroga<sup>2</sup>, Vladimir Lavayen<sup>1</sup> and Jacqueline Arguello<sup>1\*</sup>

<sup>1</sup>Inorganic Chemistry Department, Institute of Chemistry, Universidade Federal do Rio Grande do Sul, Porto Alegre, Brazil.

<sup>2</sup>Universidade Pedagógica de Moçambique, Maputo, Mozambique.

\* jacqueline.arguello@ufrgs.br

Gold nanostructures have continuously been the focus of attention due to their wide range of applications in electronics [1], biomedicine [2], sensing [3], and catalysis [4]. Their unique size- and shape-dependent properties make them promising candidates for the design and fabrication of highly active electrochemical platforms. Among several synthetic methodologies reported in the literature, electrochemical deposition is a fast, easy-to-handle and inexpensive bottom-up method, where the size and morphology can be controlled by simply changing the concentration of the gold precursor, the electrodeposition time, or the applied potential [5]. In this work, gold was electrochemically deposited on screen-printed carbon electrodes (SPCE) under potentiostatic conditions, by applying a constant potential of  $-0.6$  V during interval times of 150, 400 and 600 seconds, and the growth evolution was investigated by scanning electron microscopy (SEM) and cyclic voltammetry. The experiment was carried out in a solution consisted of 0.1 M  $\text{Na}_2\text{SO}_4$  and 30 mM  $\text{HAuCl}_4$ , using an Autolab potentiostat (PGSTAT128N, Metrohm). The scanning electron microscopy images were recorded using a Zeiss AURIGA FIB-SEM and JEOL JSM 6060 microscopes. After the first 150 s of reaction time, most of the structures adopted irregular shapes made up of agglomerates of nanoparticles. Some of these structures already have a vertical growth tendency, being the initial portion of the stems. As the reaction proceeds, at 400 seconds, it was possible to observe the elongation of the stems. By increasing the reaction time to 600 seconds, lateral branches emerge symmetrically from the central stem giving the appearance of leaves, as shown in Fig. 1. The angle between the branches, measured using the ImageJ software, is  $\sim 70^\circ$ , which is very close to the values reported for a preferential growth along the direction [111] of the face-centered cubic (fcc) structure of gold. The cyclic voltammetry measurements revealed the significantly increased of the electrode surface area of SPCE after the electrodeposition as confirmed by the electrochemical response of 1.0 mM ferricyanide.

[1] L. Gonzalez-Garcia, *Procedia Engineer.* 141 (2016) 152

[2] A. F. Versiani et al., *Future Virol.* 11(4) (2016) 293

[3] Shao Su et al., *Small* 12 (28) (2016) 3794

[4] L. Wang et al., *Nat. Commun.* 6 (2015) 6957

[5] W. Ye et al., *J. Phys. Chem. C* 114 (2010) 15617

This research was supported by CNPq (Brazil), INCTBio, PROPESQ-UFRGS, CMM-UFRGS.



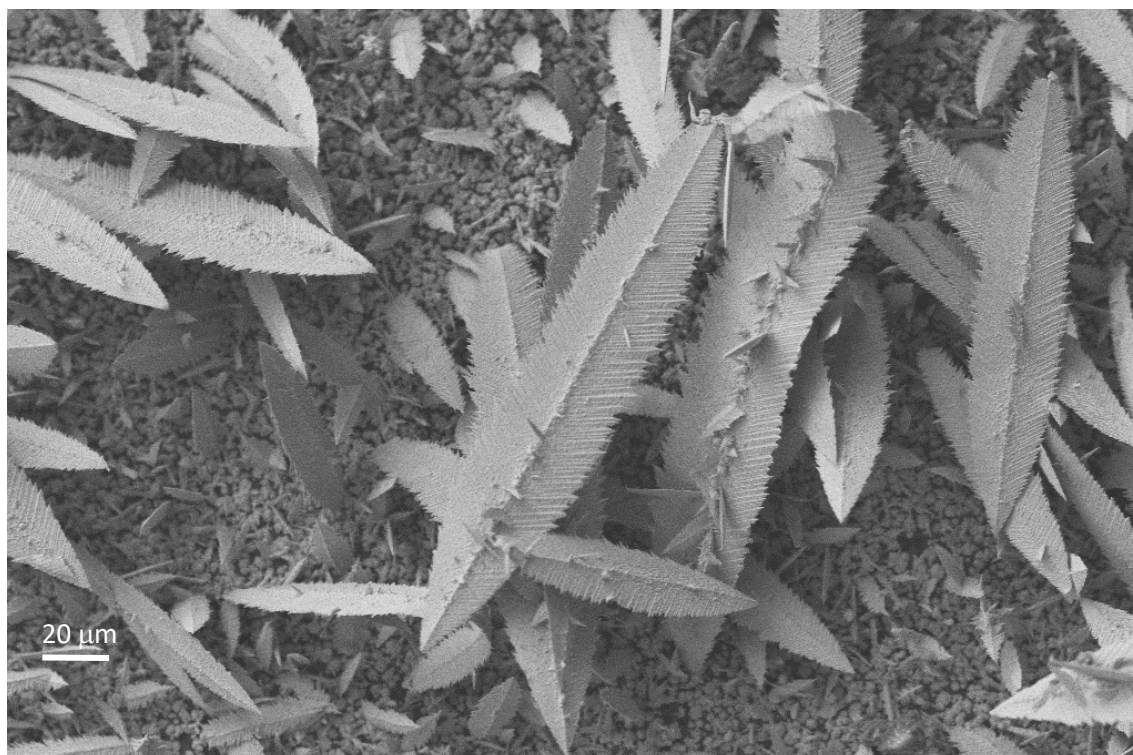


**Fig. 1.** SEM image of the leaf-like gold structures obtained under constant potential electrolysis at  $-0.6\text{V}$  for 600 s.



## Optimization of the Three-dimensional Characterization of Iron Ore Pellets

Camila Gomes Peçanha de Souza<sup>1\*</sup>, Sidnei Paciornik<sup>1</sup>, Karen Soares Augusto<sup>1</sup>, Marcos Henrique de Pinho Mauricio<sup>1</sup>.

<sup>1</sup>. Dept. of Chemical and Materials Engineering (DEQM), PUC-Rio, Rio de Janeiro, Brazil

\*camilagpsouza@gmail.com

Porosity and pore space arrangement are essential for heat transfer and the reduction process of iron ore pellets in steelworks. Therefore, the pellet microstructural characterization becomes important for the quality control of the final product, steel, helping in the understanding of its behavior in the blast furnaces. Currently, the most used techniques for characterization are optical microscopy, which offers only two-dimensional results and thus does not accurately represent the reality; and mercury intrusion porosimetry that evaluates only pores connected to the surface, and uses mercury, which is highly harmful to human health. Moreover, these are destructive techniques. This work proposes to optimize a methodology of 3D characterization of porosity in pellets using x-ray microtomography (microCT). This is a non-destructive technique that provides 3D information, but presents limitations related to the time of analysis and spatial resolution. A wide range of resolutions was tested: 7.6  $\mu\text{m}$ ; 4  $\mu\text{m}$ ; 2  $\mu\text{m}$ ; 1  $\mu\text{m}$ , and different sample volumes: the whole pellet; a cylindrical sub volume spanning the original diameter; and an octant - the variation of the sample volume was aimed at solving the previously detected limitations of the technique. As can be seen in the graph of figure 1, the determination of the threshold is also important because it causes great impact in the porosity measurement. Open and closed porosity was also measured by a new developed methodology. In the results obtained for the whole pellet, the percentage of open and closed porosity in relation to the total pores was 55.84% and 44.16%, respectively. In order to understand how the porosity varies along the same pellet, the pellet was analyzed by dividing it into 3 parts: a central disc and the two remaining caps. Figure 2 shows the porosity in the different regions of the whole pellet with a resolution of 7.6  $\mu\text{m}$ , where it is noticeable that the center of the pellet is more porous and the caps have a similar behavior. Thus, the acquisition methodology was optimized, reaching a reduction of analysis time - 3 hours for the analysis of an entire pellet, compared with the previously achieved acquisition time of 18 hours. It was confirmed that the resolution had a great impact on the porosity characterization, evidenced by the great difference between the porosities measured at the different resolutions reached (table 1): 14.83% for 7.6  $\mu\text{m}$ , 23.69% for 4  $\mu\text{m}$  and 26.75% for 2  $\mu\text{m}$ .

### REFERENCES

- [1] Augusto, S. K., Paciornik, S. Materials Research. 21. 10.1590/1980-5373-mr-2017-0621. (2018).
- [2] Castellanos, R. M. et al. Metallurgy and materials, v. 71, n. 2, p. 209–215, 2018.
- [3] Gonzalez, R. C., et al., Digital Image Processing Using MATLAB. Third New Jersey: Prentice Hall, 2004.
- [4] Iglesias, J. C. Á., et al. Journal of Materials Research and Technology, v. 7, n. 3, p. 376–380, 2018.
- [5] This research was supported by CNPq, CAPES and FAPERJ.

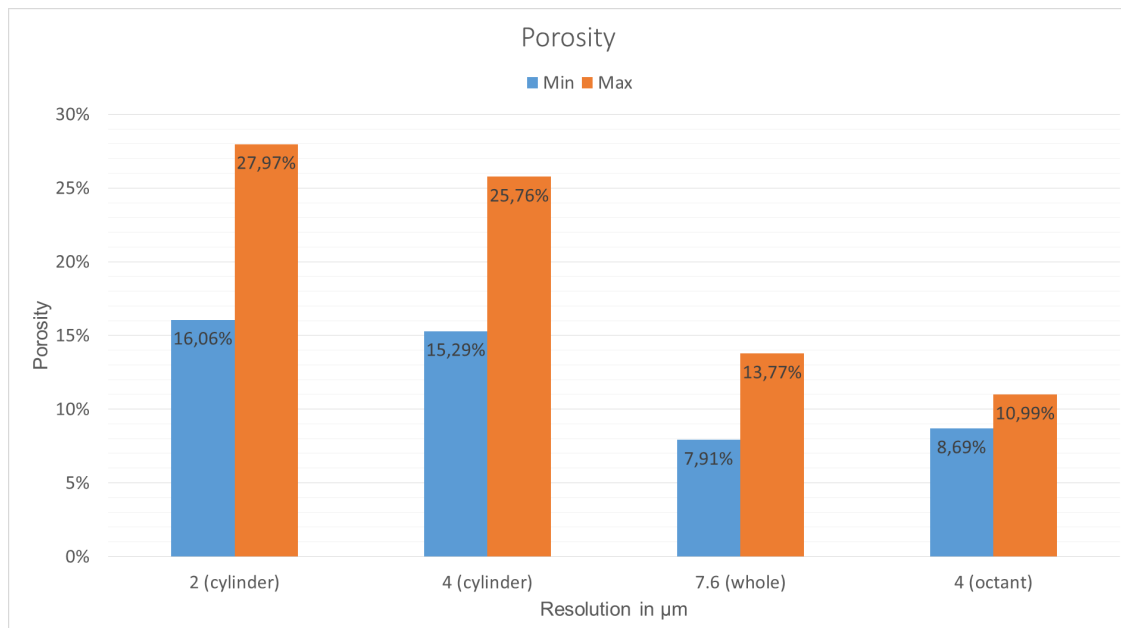


Figure 1: Influence of segmentation thresholds on measured porosity for different microCT resolutions: 2; 4 and 7.6  $\mu\text{m}$ .

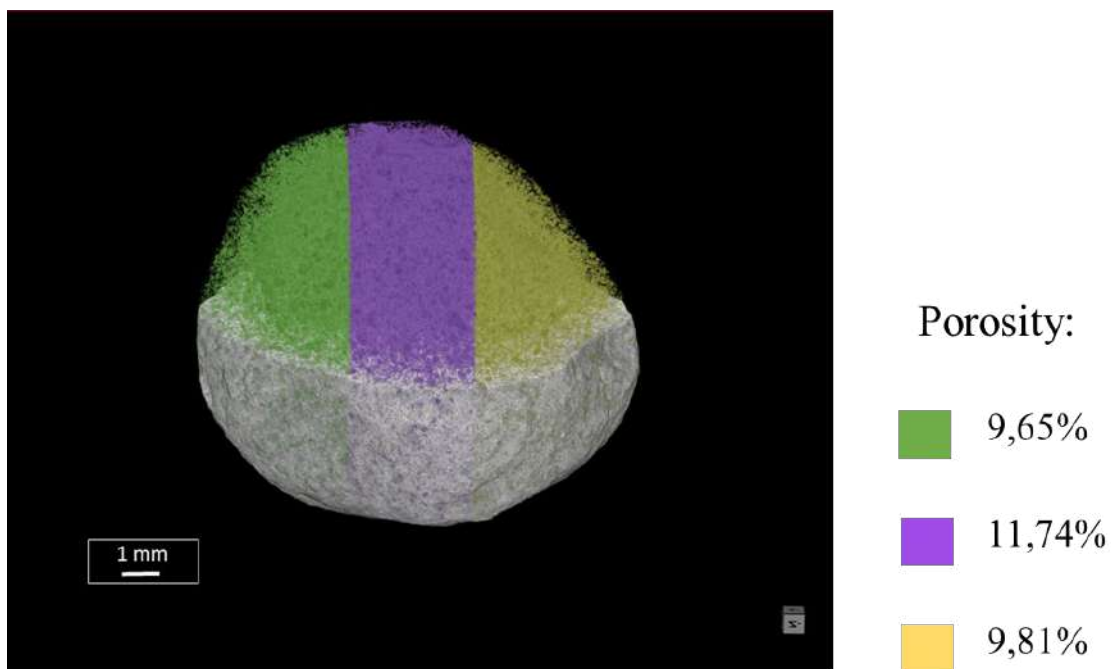


Figure 2: Porosity in different regions: green, purple and yellow.

Table 1 - Comparison of porosity with different volumes and resolutions.

Type of Volume	Resolution ( $\mu\text{m}$ )	Porosity (%)
Subvolume (cylinder)	7.6	14.83
	4.0	23.69
	2.0	26.75
Whole	7.6	10.70



## Nanostructured Starch Films

Camilla<sup>1\*</sup>, Isabelle<sup>2</sup>, Willian<sup>3</sup>, Cristina<sup>4</sup> and Renata<sup>5</sup>

<sup>1</sup>. Bernardo, Department of Metallurgical and Materials Engineering, UFRJ, Rio de Janeiro, Brazil

<sup>2</sup>. Kling, Department of Metallurgical and Materials Engineering, UFRJ, Rio de Janeiro, Brazil

<sup>3</sup>. Ferreira, Instituto de Macromoléculas Eloisa Mano, UFRJ, Rio de Janeiro, Brazil

<sup>4</sup>. Andrade, Instituto de Macromoléculas Eloisa Mano, UFRJ, Rio de Janeiro, Brazil

<sup>5</sup>. Simão, Department of Metallurgical and Materials Engineering, UFRJ, Brazil

\*(camilla\_nb@metalmat.ufrj.br).

Starch is an excellent option to substitute plastic due to its versatility, low cost and availability in the nature compared with other biodegradable polymeric materials [1], [2]. Thermoplastic starch (TPS) is composed by a blend of starch and a plasticizer mixture. Amide nanoparticles [3], [4] have been incorporated to amide films to improve not only its hydrophilic, thermal, mechanics properties (like improvement of the storage module and lost of elasticity), but also to slow up its ageing. This article aims to produce starch films with glycerol and starch nanoparticles. The nanoparticles were obtained through the nanoprecipitation method using addition of non-solvent. Films structure, morphology and mechanicals properties were studied by contact angle, Atomic Force Microscopy (AFM) and scanning electron microscopy (SEM). The films were prepared following the procedure described in the literature [5] and an extra addition of glycerol plasticizer. 10.7 grams (g) of starch and 6.2 g of glycerol were weighted and added to the reactor with 200 mL of distilled water. The reactional mixture was submitted to a mechanical shaker of 400 rotations per minute (rpm) and oil bath heating controlled between 70 and 80 °C. Once the gelatinization started, the mixture was kept under heat during the time required to obtain each film. Subsequently the starch solution was taken out of the oil bath heating and 200 mL of ethanol was dropwise added still stirring the mixture. If necessary, the same volume of ethanol was added again under the same conditions when the reactional mixture was at a temperature equal or lower than 30 °C [6]. Thereafter, the mixture was taken out of the shaker and it was kept resting. After that 30 mL of particles were collected with a Pasteur pipette from the bottom of the reactor and they were transferred to a 50 mL becker. Finally, the content of the becker was transferred to a Petri dish and it was put in a hothouse on 50°C for 24 hours. Table 1 shows the type of films produced according to the variable conditions. Then, the films produced were analyzed by SEM. The Figure 1 (a) shows that the MEV of the film SAG60WC indicates a rough surface due to the absence of plasticizer [3]. It is possible to observe the addition of plasticizer made the surface smoother and more even, as shown in the Figure 1 (b) and (c). On Figure 1 (b) the SPG60WC film has a lot of nanoparticles evenly distributed on the surface [2]. These particles seem very bright. Figure 1 (c) exhibits the SEM of SPG60W film, which presents dispersed nanoparticles that are not so bright as the ones observed in Figure 1 (b), and this maybe due to their adherence to the polymeric matrix as they can easily diffuse in the hot polymeric solution [6]. Figure 1 (c) shows the rough surface of SPG30WC film. On this one the amount of starch granules is higher than than on the others films because the gelatinization time of 30 minutes was not enough to transform the granular amide to viscoelastic paste [7].



## REFERÊNCIAS

- [1] Q. Sun, T. Xi, L. Xiong, Plos One, 9 (2014) 1.
- [2] H. Fan, N. Ji, M. Zhao, L. Xiong, Q. Sun, 92 (2016) 865.
- [3] A. Shin, L. Wang, D. Li, B. Adhikari, Carbohydrate Polymers, 96 (2013) 593.
- [4] A. Shin, L. Wang, D. Li, B. Adhikari, Carbohydrate Polymers, 96 (2013) 602.
- [5] I. Lima, Instituto Alberto Luiz Coimbra de pós-graduação e pesquisa em engenharia, Universidade Federal do Rio de Janeiro, Brasil (2018).
- [6] X. Ma, R. Jian, P. R. Chang, J. Yu, Biomacromolecules, 9 (2008) 3314.
- [7] R. Parker, S. G. Ring, Journal of Cereal Science, 34 (2001) 1.
- [8] This research was supported by CAPES (Brazil).

Table 1 - Conditions of the films produced.

Symbol	Glycerol	Time of gelatinization (min)	Addition of ethanol
SAG60WC	absent	60	Hot and cold
SPG60WC	present	60	Hot and cold
SPG60W	present	60	Hot
SPG30WC	present	30	Hot and cold

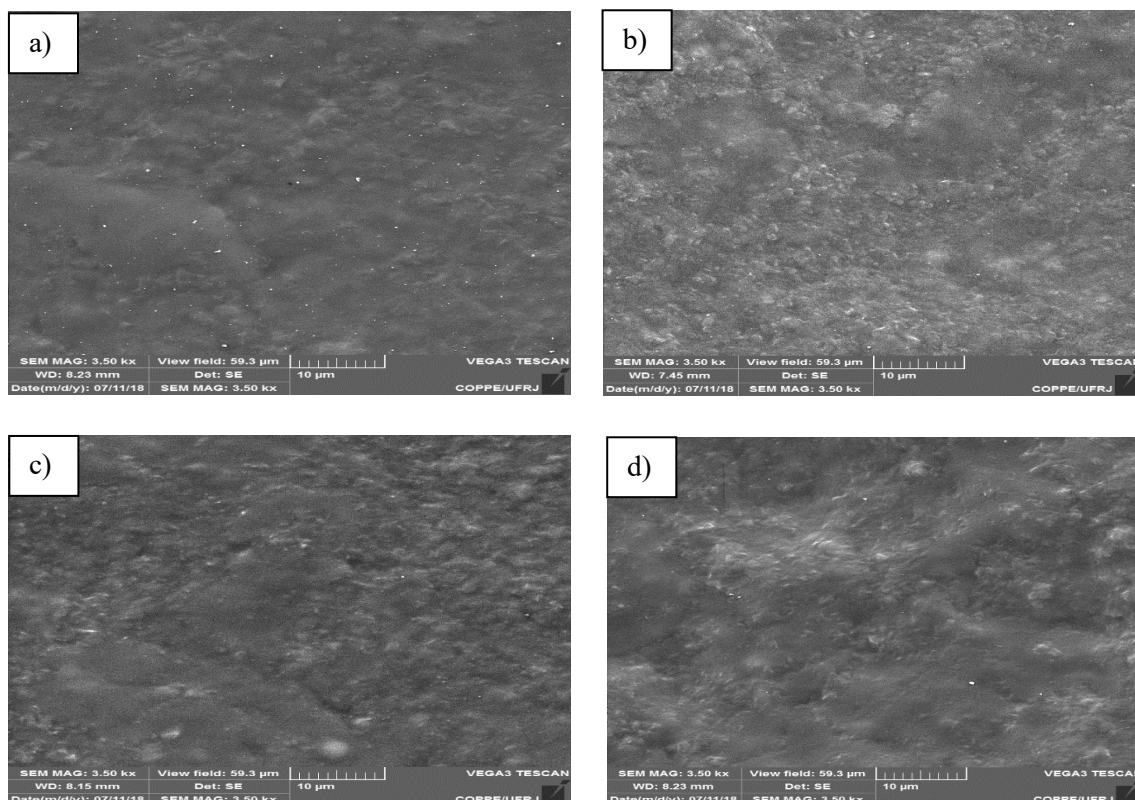


Figure 1 – SEM image of the films: a) SAG60WC, b) SPG60WC, c) SPG60W and d) SPG30WC.

## Characterization of dental implant surface roughness with light interference optical 3D profiler

Carlos Nelson Elias<sup>1\*</sup>, Francielly Moura de Souza Soares<sup>1</sup>, Emília dos Santos Monteiro<sup>1</sup>, Luiza Braga Ferreira dos Santos<sup>1</sup>

<sup>1</sup>. Instituto Militar de Engenharia. Materials Sci Departament. Rio de Janeiro, RJ, Brazil.

Dental implants surface morphology influences the osseointegration and the success rate of clinical results. Several techniques including acid etching, particle blasting, and anodizing have been used in order to change the surface roughness and improve titanium dental implant surfaces biological properties [1]. Micro and nano roughness are important surface features, since mesenchymal cells adhesion, proliferation and differentiation are sensitive to this implant surface characteristic [2]. Meanwhile osteoblasts involved in osseointegration have better adherence in rough titanium surfaces, cells responsible for soft tissue sealing (fibroblasts) have higher adhesion rates into smooth surfaces [3]. The effects of sub-micron topography and microtopography on bone bonding and interfacial stability of endosseous implants is very important. Normally, the dental implants surfaces are characterized only with SEM analysis. Due the screw shape is very difficult the surface roughness measurement. The solution is using of disc with the same dental implant surface treatment and measurement the roughness with contact profiler. Some papers available in the literature present the values of only one parameters of the roughness of the implants and suggest the use of the Ra value without presenting an explanation for the choice of this parameter [2]. In the present work, dental implant surface roughness was measured with 3D optical surface profiler and the surface morphology was analyzed by scanning electron microscope (SEM). This manuscript is based on the influence of temperature and time on acid etching toward commercially pure titanium surfaces roughness for biomedical purposes as implantable devices. Dental implants etched at two temperatures (35 and 40°C) for 25 and 30 min. The surface morphology was observed using a SEM FEI Quanta FEG 250 (FEI, Hillsboro, Oregon-USA). The roughness parameters were measured in an optical 3D surface profiler NewView 7100 (ZYGO Corporation, Middlefield, CT-USA). This instrument let us measure parameters without specimens contact utilizing a light interference phenomena. Using a laser as collimated light source, interference patterns are generated by light emitted directly by the source and those reflected by the surface. With obtained data, the equipment software generates a 3D image of the surface, associating it to superficial roughness parameters. This instrument advantage among others is that it's possible to measure roughness without need of physical contact with the surface and allow damage to the material. Another advantage of this profiler is the low time needed to acquire data, knowing that it only takes a brief emission of light from the source to conclude measure, which is done in a large area sections with nanometric accuracy. Analysis is concluded in a few seconds. The following roughness parameters were determined: Ra, PV, Rms, peak size, valley depth, Rz and Srmax. Figure 1 and 2 show the surface morphologies of analyzed dental implants. It can be seen that the surface is homogeneous with uniformly distributed microcavities. It is not possible to quantify the difference among the surfaces. Figure 3 shows the 3D image from 3D profiler. Table 1 shows the roughness parameters. The results show that the roughness increased with temperature and time of etching. The highest roughness was found after surface treatment at 40°C during 30 minutes.

## REFERÊNCIAS

- [1] C.N. Elias et al., J Materials Technology 8 (2019) 1060.  
 [2] Y.T. Sul, C. Johansson, T. Albrektsson. Int J of Prosthodontics, 19 (2006) 319.  
 [3] C. Eriksson, J. Lausmaa, H. Nygren. Biomaterials. 22 (2001) 1987.  
 [4] This research was supported by CNPq, CAPES and FAPERJ (Brazil).

Table 1: Dental implant surfaces roughness.

Temperature (°C)	Time (min)	Ra (μm)	PV (μm)	Rms (μm)	Peak (μm)	Valley (μm)	Rz (μm)	Srmax (μm)
35	25	0,46	45,95	0,65	22,69	-23,26	24,07	32,00
35	30	0,75	36,95	1,07	19,37	-17,58	25,81	27,31
40	25	0,75	27,87	0,99	10,07	-17,81	18,67	27,87
40	30	1,10	54,59	1,62	32,22	-22,37	48,56	51,03

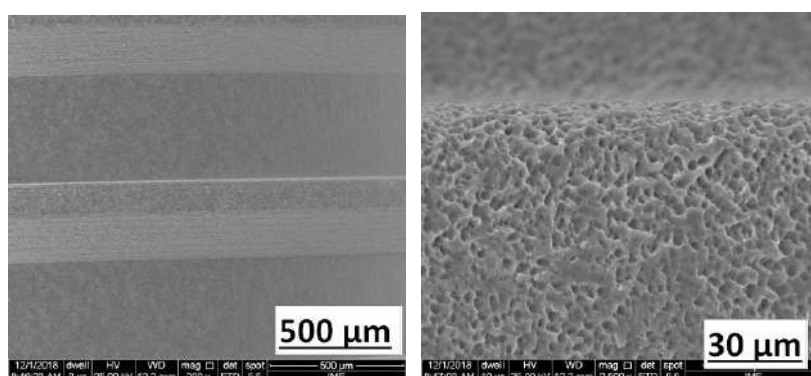


Figure 1: Ti dental implant surface morphology after acid etching at 35°C and 25 min.

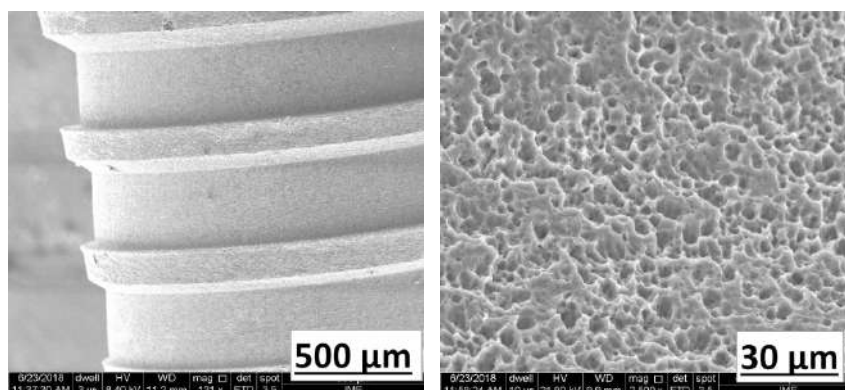


Figure 2: Ti dental implant surface morphology after acid etching at 40°C, 30 min.

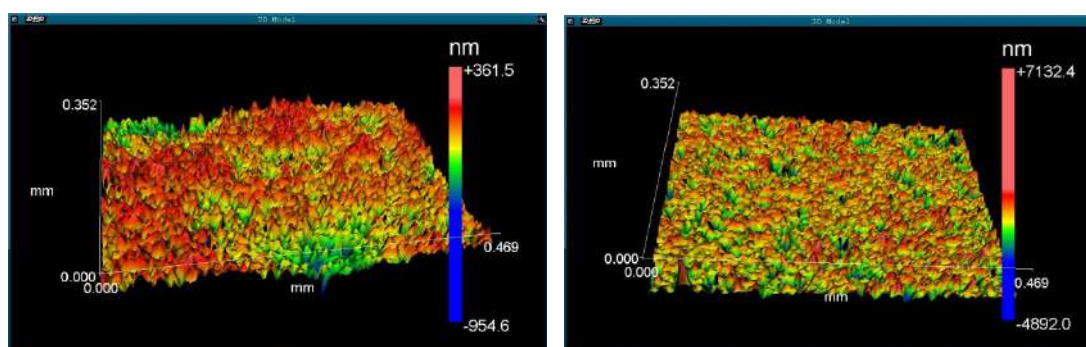


Figure 3: 3D image of the roughness obtained by interferometry. Acid etching surface treatment: left side: 35°C and 25 min; right side 40°C, 30 min.

## One-Pot Synthesis of Zinc Oxide Nanoparticles and their Characterization by Spectroscopic Methods and Scanning Electron Microscopy

Santana C.A.<sup>1\*</sup>, Lunz J.N.<sup>1</sup>, Vasconcelos T.L.<sup>1</sup>, Archanjo B.S.<sup>1</sup> and Achete C.A.<sup>1</sup>

<sup>1</sup>. Instituto Nacional de Metrologia, Qualidade e Tecnologia, Diretoria de Metrologia Científica, Divisão de Metrologia de Materiais, Xerém – Brasil.

\* casantana@colaborador.inmetro.gov.br

Zinc oxide (ZnO) is a covalent solid with high ionic character, which crystallizes in cubic form (zinc blende or rocksalt) and in hexagonal form (wurtzite). At room temperature, wurtzite is the thermodynamically stable phase, while the zinc blende phase is stable if grown on cubic substrate and the rocksalt one is obtained under high pressure condition.<sup>[1]</sup> The literature reports a diversified range of technological applications to materials based on nanostructured zinc oxide particles: UV light-emitting diodes, solar cells, electrochemical and gas sensors, anodes of batteries, catalysts, among others.<sup>[2 – 5]</sup> Its versatility is attributed to the differentiated mechanical, magnetic, chemical, electrical and optical properties presented by the material, such as its broad band gap of 3.37 eV and large exciton binding energy equal to 0.06 eV.<sup>[3]</sup> These properties and therefore the performance in the desired application are directly related to the size and morphology of the synthesized particles. This work aims to present the initial results of a simple synthesis for the development of ZnO nanosheets using a one-pot controlled precipitation methodology in strongly alkaline medium, at room temperature, from zinc acetate dihydrate and ethanol P.A. as raw materials. The product obtained was deposited on silicon substrate (1 cm<sup>2</sup>) and the process was monitored for two settling times - 4 h and 24 h - and then conducted to thermal treatment at 600 °C and 1000 °C in order to enquire informations regarding crystallinity, morphology and depth. For this, the synthetic process was characterized by a range of techniques, such as: Fourier Transform Infrared (FT-IR) Spectroscopy, UV-Vis Spectroscopy, Raman Spectroscopy, Scanning Electron Microscopy (SEM) as well as Atomic Force Microscopy (AFM). These analyzes prove the formation of the oxide particles in morphology close to the one of interest. Furthermore, they show that the increase in temperature, in spite of favoring the crystallinity, intensifies the depth and the densification of the material, changing the shape of the same, which acquires rounded edges. Modifications in the synthesis route as well as the use of templates in nanosheet shapes will be investigated as alternative ways of obtaining the ZnO nanosheets; those will be tested in promising areas in the technological fields of photocatalytic sensors and lithium battery anodes.

### REFERENCES

- [1] H. Morkoç ; Ü. Özgür, Zinc Oxide: Fundamentals, Materials and Device Technology, 2009.
- [2] D.G. Tong et al., Materials Letters, 70 (2012) 94 – 97.
- [3] S. Boudjadar et al. International Journal of Nanoscience, 9 (2010) 585 – 590.
- [4] C. Mayrinck et al. Revista Virtual de Química, 6 (2014) 1185 – 1204.
- [5] S. Jurablu et al. Journal of Sciences, 26 (2015) 281 – 285.
- [6] H. Zhao et al., Angew. Chem. Int. Ed. 56 (2017) 8766 –8770.
- [7] The authors acknowledge the financial support from the Brazilian Agencies CNPq and FAPERJ.



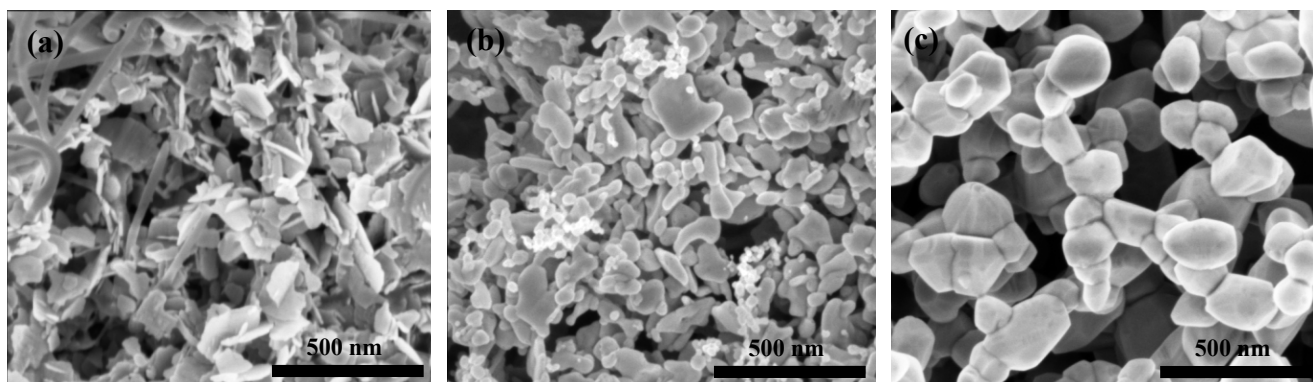


Figure 1. SEM micrographs of a 4 hours deposition process: (a) without thermal treatment, (b) treated at 600 °C and (c) treated at 1000 °C.

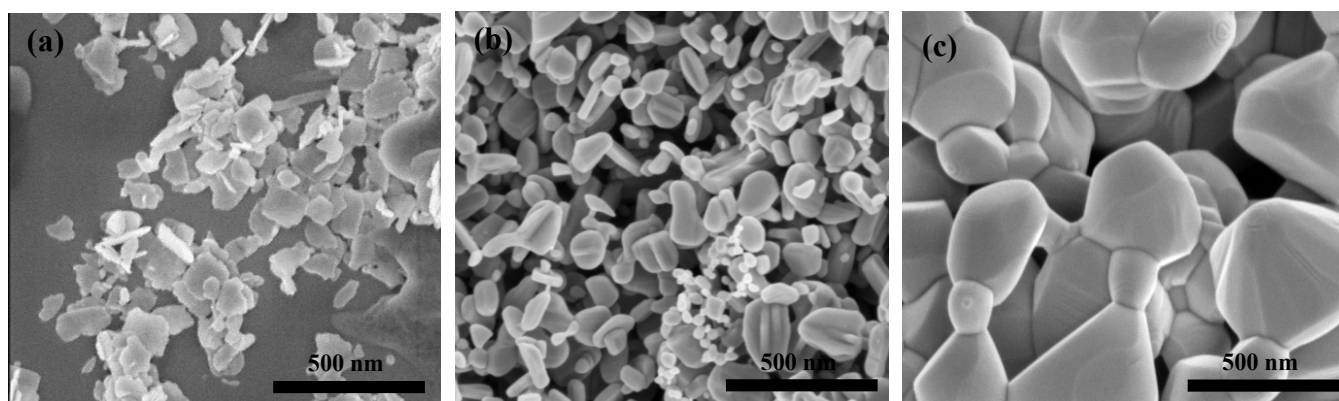


Figure 2. SEM micrographs of a 24 hours deposition process: (a) without thermal treatment, (b) treated at 600 °C and (c) treated at 1000 °C.

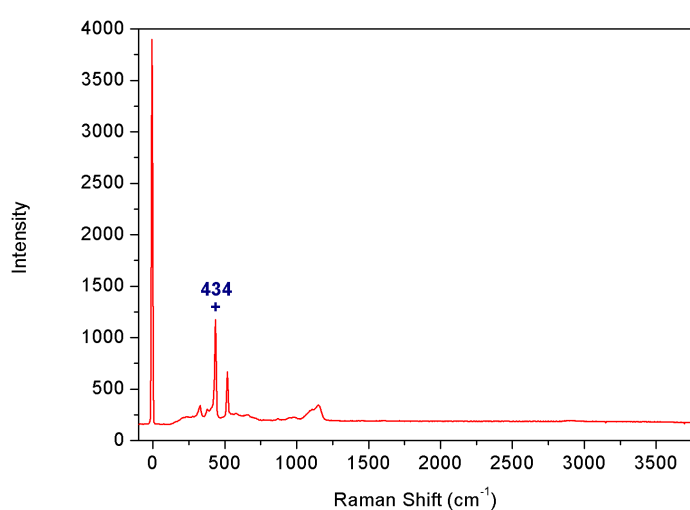


Figure 3. Raman Spectra of 24 h deposition process treated at 1000 °C.

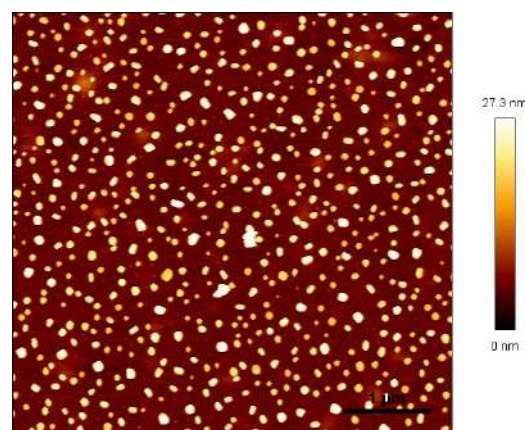


Figure 4. AFM Spectra of 4 h deposition process treated at 600 °C.

## TIG Brazing Of Metallic Glass On Carbon Steel

Dênis de Almeida Costa<sup>1\*</sup>, Alejandro Zúñiga<sup>1</sup>, Marcela Tercini<sup>1</sup> and Carlos Triveño Rios<sup>1</sup>.

<sup>1</sup>Engineering, Modeling and Applied Social Sciences Center (CECS), Federal University of ABC (UFABC), Santo André, Brazil. \*denis.costa@ufabc.edu.br.

Metallic Glasses have interesting properties for various application fields, however, like most products derived from basic scientific research, such alloys have still few applications [1] and, one way to expand their use is through the union with conventional crystalline alloys. In this work a TIG brazing procedure was developed for deposition of the Cu<sub>47.5</sub>Zr<sub>47.5</sub>Al<sub>5</sub> Bulk Metallic Glass (BMG) alloy on AISI 1020 carbon steel. After brazing, the alloy transformation kinetics were modeled by Kolmogorov-Johnson-Mehl-Avrami [2] and the thermal cycle of the brazing by the Rosenthal model [3]. The union obtained between BMG and carbon steel was characterized with Scanning Electron Microscopy (SEM) with back-scattered electrons and Energy Dispersive Spectroscopy (EDS). The SEM microscopy of the deposited metal shown in figure 1 reveals the existence of a dark matrix with a substructure of dendritic format, this configuration results from the solidification with cooling rate below the critical rate and is typical for the alloy studied [4]. The volumetric fraction of the crystalline phase was measured on ImageJ software [5] and the result was 70% of crystalline phase. The EDS analysis provided the maps of figure 2, in this image it is possible to identify that the amorphous phase is rich in Cu and Al while the crystalline phase is rich in Zr. With these data it is concluded that the TIG brazing process resulted in a deposit of BMG composite, a material with improved ductility and toughness by combination of amorphous matrix with secondary crystalline phase [6].

[1] M. F. Ashby, A. L. Greer, Metallic glasses as structural materials, *Scripta Materialia*, v. 54, n. 3, p. 321–326, 2006.

[2] D. R. Uhlmann, A kinetic treatment of glass formation, *Journal of Non-Crystalline Solids*, v. 7, n. 4, p. 337–348, 1972.

[3] S. Kou, *Welding Metallurgy*, 2<sup>a</sup>, Hoboken, Wiley-Interscience, 2003.

[4] S. Pauly et al., Microstructural heterogeneities governing the deformation of Cu<sub>47.5</sub>Zr<sub>47.5</sub>Al<sub>5</sub> bulk metallic glass composites, *Acta Materialia*, v. 57, n. 18, p. 5445–5453, 2009.

[5] ImageJ, Available in: <<https://imagej.nih.gov/ij/>>, Access on: May 23, 2019.

[6] M. Ferry et al., Recent developments in ductile bulk metallic glass composites, *MRS Communications*, v. 3, n. 1, p. 1–12, 2013.

This research was supported by National Council for Scientific and Technological Development – CNPq (process number: 481355/2013-8), Multiuser Experimental Center (CEM-UFABC) and UFABC (Brazil).



Figure 1: SEM of structure obtained in deposited metal.

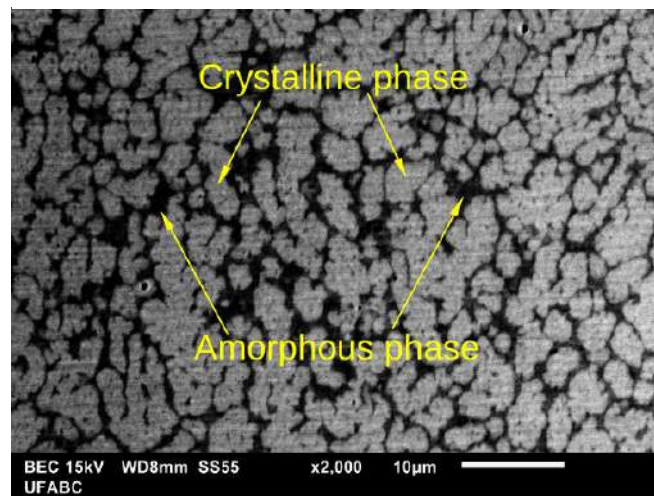
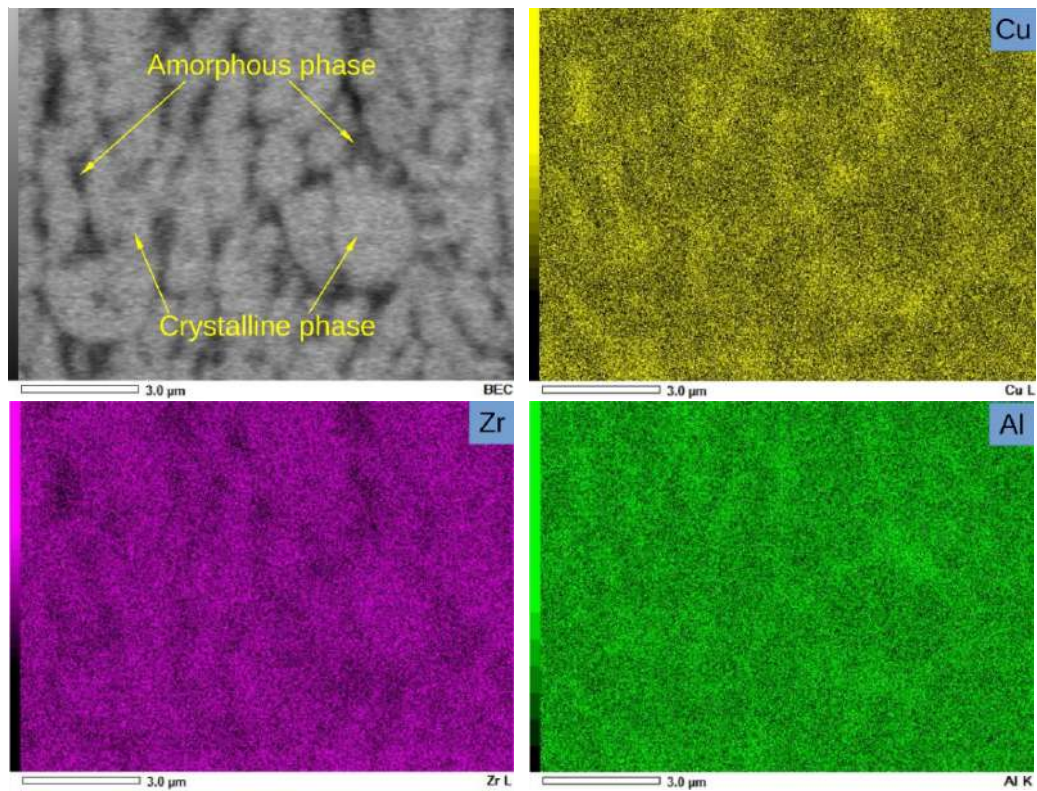


Figure 2: EDS Map Structure.





## Nanostructured Starch Composite with Lignin Nanoparticles

Eduardo Genner F. Almeida<sup>1\*</sup>, Renata A. Simão<sup>2</sup>

<sup>1</sup>. Nanotechnology Engineering Program/COPPE, UFRJ, Rio de Janeiro-Brazil

<sup>2</sup>. Nanotechnology Engineering Program/COPPE, UFRJ, Rio de Janeiro-Brazil

Recently, environmental pollution due to packaging derived from petroleum has become a serious problem. Thus, the development of new biodegradable nanocomposite materials has attracted significant attention. These products consist of a biodegradable polymer matrix reinforced with a material nanoscale, which improves the mechanical, thermal, optical and physicochemical properties compared to the pure polymer matrix<sup>[1]</sup>. The aim of this work was to produce lignin nanoparticles and disperse them on starch influence of lignin nanoparticles on the mechanical properties of nanocomposites based on starch.

The pH change method described by Frangville<sup>[2]</sup> et al., 2012 was used, with minor modification, for the synthesis of lignin nanoparticles. In this case only the dialysis was not done. The starch films were produced by the technique of solvent evaporation (*casting*) based on mixtures containing starch (5g), glycerol (3.1g) and distilled water (200g). The solution was heated for 1 h at 90 °C. After cooling, lignin nanoparticles were added to the solution in amounts of 1, 2 and 3 wt%. The solutions were then stirred for 3h. 30 ml of each solution was withdrawn and placed in Petri dishes. The films were dried at 50 °C for 24h.

Nanostructured starch films were characterized by Scanning Electron Microscope (SEM), Atomic Force Microscopy (AFM) and tensile tests. Figure 1a obtained through AFM and Figure 1b by SEM indicates lignin nanoparticles with average sizes in the order of 200 nm or less. Figure 2 shows a good dispersion of the nanoparticles in the film matrix. It is necessary that there is interaction between the reinforcement and the matrix, because if there is no such interaction the composite tends to have poor mechanical properties when compared to the pure polymers. In this case, since starch and lignin are two natural polymers, there is no need to make a compatibilization between them. Besides the advantage of improving the mechanical and barrier properties it is possible to even add new properties to the film, making the material suitable for various applications, such as for packaging, for example.

The tensile tests (Figure 3) indicate differences for the control film (without lignin) and with the incorporation of lignin nanoparticles. In Figure 4, where the starch films were reinforced with lignin nanoparticles synthesized through the pH change, the results show that the addition of 1% of nanoparticles in the films increased both the tensile values and the elongation at break, whereas for higher concentrations of nanoparticles these values decreased. The stress tests make it clear that the incorporation of lignin nanoparticles in the starch films improves their mechanical properties. It is a very interesting result for future applications of this material as packaging, for example.

### REFERENCES

- [1] Thiellemans S. *et al.*, CarbPolym. 143 (2016) 310.
- [2] Frangville C. *et al.*, ChemPhysChem. 13, (2012) 4235.
- [3] This research was supported by FAPERJ (Brazil).



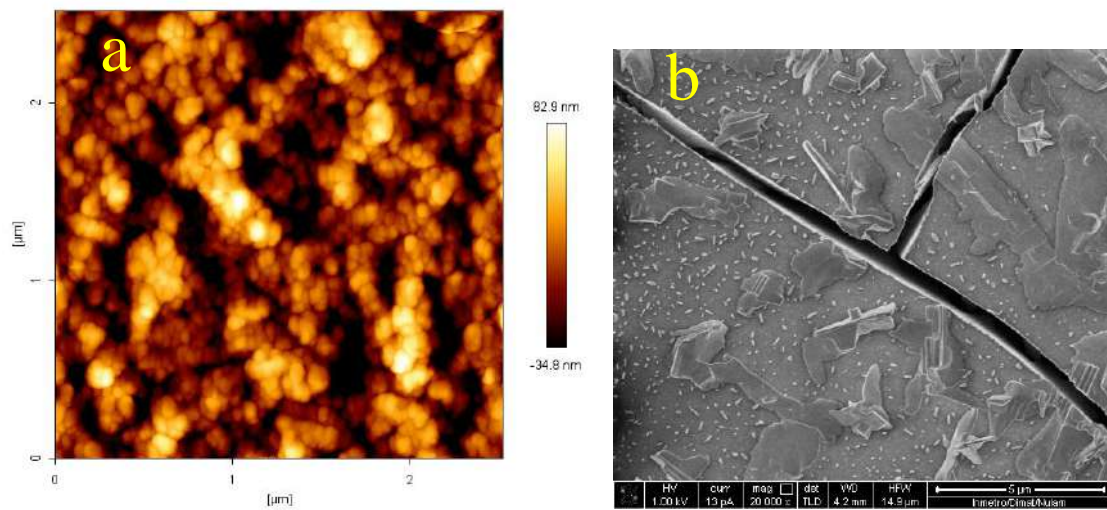


Figure 1: AFM and SEM of the lignin nanoparticles

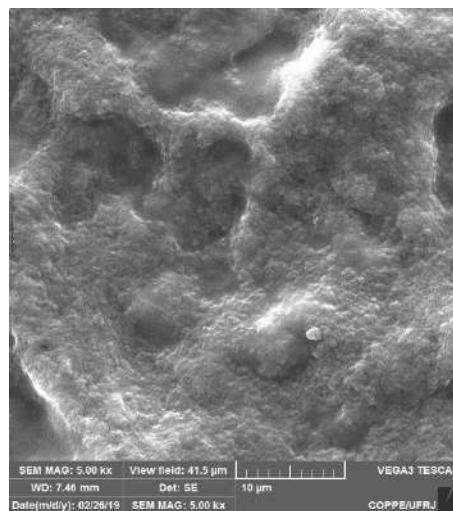


Figure 2 - Starch film reinforced with 1% lignin nanoparticles

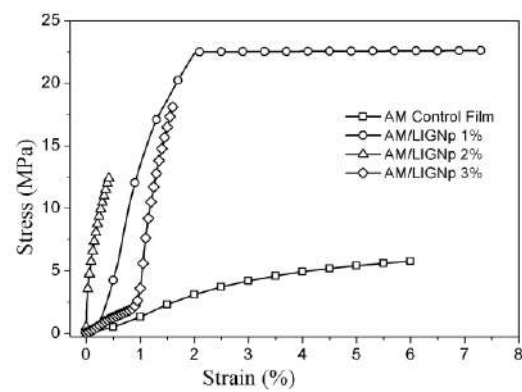


Figure 3 – Tensile curves versus strain for films with lignin NPs.

## Effect of Surface Treatment on Roughness and Morphology of titanium for dental implant

Emília dos Santos Monteiro<sup>1\*</sup>, Francielly M de S Soares<sup>1</sup>, Luíza B. F. dos Santos<sup>2</sup>, Ana Lúcia Nascimento<sup>1</sup>, Paula Anastácia C. Gomes<sup>1</sup>, Carlos Nelson Elias<sup>1</sup>

<sup>1</sup>. Instituto Militar de Engenharia, Seção de Engenharia de Materiais – SE8, Rio de Janeiro, Brasil. emimonteiro@yahoo.com.br

<sup>2</sup>. Universidade Federal de Minas Gerais, Seção de Engenharia de Minas, Metalúrgica e Materiais, Minas Gerais, Brasil.

Unalloyed titanium and its alloys are the most materials used as dental implants owing to its excellent mechanical properties, biocompatibility, and high resistance to corrosion. It has been done a lot of investigations about the biocompatibility of titanium linking to its surface. Parameters such as morphology, roughness, thickness and type of oxide layer, topography, and surface energy can be modified to ensure better interactions with the bone tissue, i.e, to allow the osseointegration process to occur [1, 2]. Osseointegration is an important parameter to evaluate the success of an implant since it is in this process that the stability is ensured through a connection between the bone and the implant. Osseointegration can only occur if there is cell adhesion on surface of the biomaterial [3]. Both roughness and morphology will influence the proliferation and differentiation of cells in osteoblasts, i.e., bone growth on implant. The surface properties depend on the type of surface modification performed on the implant. For instance, at the unalloyed titanium, the surface modification increases the oxide layer thickness, provides isotropic surface roughness, changes surface energy, modifies morphology, and topography [4]. Herein, surface features were analyzed by roughness and scanning electronic microscopy using implants with machined surface, acid etched surface (commercially named as Porous<sup>®</sup>, Conexão Sistemas e Prótese, Arujá, SP, Brazil) and anodized surface (commercially named as Actives<sup>®</sup>, Conexão Sistemas e Prótese, Arujá, SP, Brazil). Surface roughness parameter were measured by NewViewTM 7100 (Zygo Company, Middlefield, CT 06455, USA) light interferometer (profilometer). The roughness average (Ra), valley depth value (PV), root mean square value of roughness (rms), peak-to-valley roughness (Rz), and three lowest local minimums (R3z) were calculated. Surface morphology was observed on a scanning electron microscope Field Emission Gun FEI QUANTA FEG 250 (FEI Corporate, Hillsboro, Oregon, USA). The mean of the titanium dental implant machined, anodized, and acid etching surface roughness parameters are displayed in Table 1. As one shown, the surface treatment significantly increased the roughness. Fig.1a shows machined implant without surface treatment, in Fig.1b is shown acid etched surface, which one observed an isotropic surface. Fig.1c it was represented the anodized surface, as we can see, there are various cavities. Fig.1 also shows a representative surface morphology of the implants obtained by interferometry.

### KNOWLEGMENT

This research was supported by CNPq, FAPERJ and Finep.

## REFERENCES

- [1] C.N. Elias, L. Meirelles, Expert Rev. Med. Devices 7 2 (2010) 241–256.  
 [2] R. Adell, U. Lekholm, B. Rockler, P.-I. Branemark. Int. J. Oral Surg. 10 (1981) 387-416.  
 [3] C.N. Elias, F. A. Rocha, A. L. Nascimento. P. G. Coelho. Journal of the mechanical behavior of biomedical materials 16 (2012) 169-180.  
 [4] D. J. Fernandes, R.G. Marques, C.N. Elias, J Mater Sci: Mater Med (2017) 28:164.

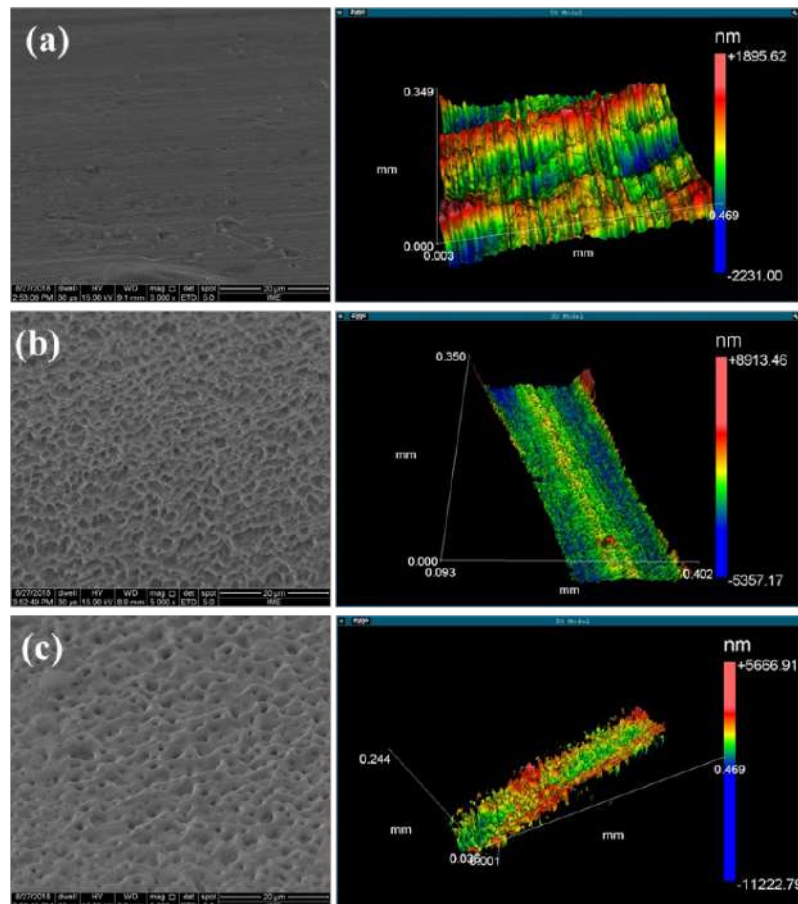


Figure 1. Surface morphology and roughness of dental implants. (a) Machined, (b) Acid etched and (c) Anodized.

Table 1. Roughness of the dental implants.

	Ra	PV	rms	Rz	R3z
<b>Machined</b>	0.463	14561	0.617	10256.45	10339.10
<b>Acid Etched</b>	1.051	16.937	1.392	12804.95	12725.53
<b>Anodized</b>	1.626	30.829	2.303	26598.28	25518.87

Ra: Roughness average; rms: Root mean square value of roughness; PV: Valley depth value; Rz: Peak-to-valley roughness; R3z: Three lowest local minimums.

## Surface Roughness of Laser Sintered Titanium Alloys for Biomedical Applications

Francielly Moura de Souza Soares<sup>1\*</sup>, Emília dos Santos Monteiro<sup>1</sup>, Luíza Braga dos Santos<sup>2</sup>, Paula Anastácia Cairo Gomes<sup>1</sup> and Carlos Nelson Elias<sup>1</sup>.

<sup>1</sup> Instituto Militar de Engenharia, Laboratório de Materiais, Rio de Janeiro, Brasil.  
mourafrancielly@outlook.com

<sup>2</sup> Universidade Federal de Minas Gerais, Seção de Engenharia de Minas, Metalúrgica e Materiais, Minas Gerais, Brasil.

Commercially pure Ti and Ti alloys are the main metal for medical device applications. In the last decade the industry developed the methodology 3D laser sintering process. This process employs the basic concepts of additive manufacturing to produce parts with different shapes and sizes. With additive manufacturing it is possible to obtain the products in final shape without the need for large finishes [1-4]. Medical device manufactured from Ti alloys (ASTM grade 5) has good osseointegration, but surface roughness influence the treatment success because the medical device surface roughness influences the interaction of the cells and the osseointegration of titanium. The titanium with rough surface presents higher osseointegration than those with smooth surface. The titanium surface rougher has better adhesion of osteoblastic cells than smooth surface. Therefore, over the years surface treatments have been developed to improve cellular adhesion, thus increasing the roughness. The surface treatments can be done by blasting, acid etching, plasma spray, and electrochemical treatment [5]. However, it is important that the new additive manufacturing methodologies allow obtaining surface with roughness and morphology suitable for the adhesion of the cells. The objective of the present work is to compare the surface morphology and roughness of Ti G5 discs produced by additive manufacturing by laser sintering. Scanning electron microscopy images were done using a MEV FEI Quanta FEG250 with. The roughness was evaluated with an optical profilometer Zygo 7100 Profilometer (Zygo Co, Middlefield, CT). This equipment allows accurate three-dimensional roughness measurement using the interferometric technique. Figure 1 shows the surface morphology of machined and 3D sintered samples. Figure 2 shows the discs morphologies obtained in the profilometer. Table 1 shows the surface roughness parameters. The scanning electron microscopy images and the 3D images obtained in the profilometer showed that the surface morphology and roughness were different. The surface of sintered laser titanium has higher roughness than titanium acid etching. The acquired roughness parameter values (Table 1) corroborate the SEM image and profilometer (Tables 1 and 2).

### REFERENCES

- [1] F. J. Gil et al., Journal of Mat. Science: Mat. in Med. 23 (2012) 885-890.
- [2] N. Kahraman et al., Inter. Journal of Imp. Eng. 34 (2007) 1423-1432.
- [3] L. Thijs et al., Acta Mat. 58 (2010) 3303-3312.
- [4] T. Chiu et al., Electroch. Acta, 279 (2018) 143-151.
- [5] C.N. Elias, Revista Matéria, 15(2010) 140-144.

### ACKNOWLEDGMENT

This research was supported by CAPES, CNPq, FAPERJ and Finep. The authors are grateful to M3 Health Indústria e Comércio de Produtos Médicos, Odontológicos e Correlatos Ltda for providing the sintered samples.



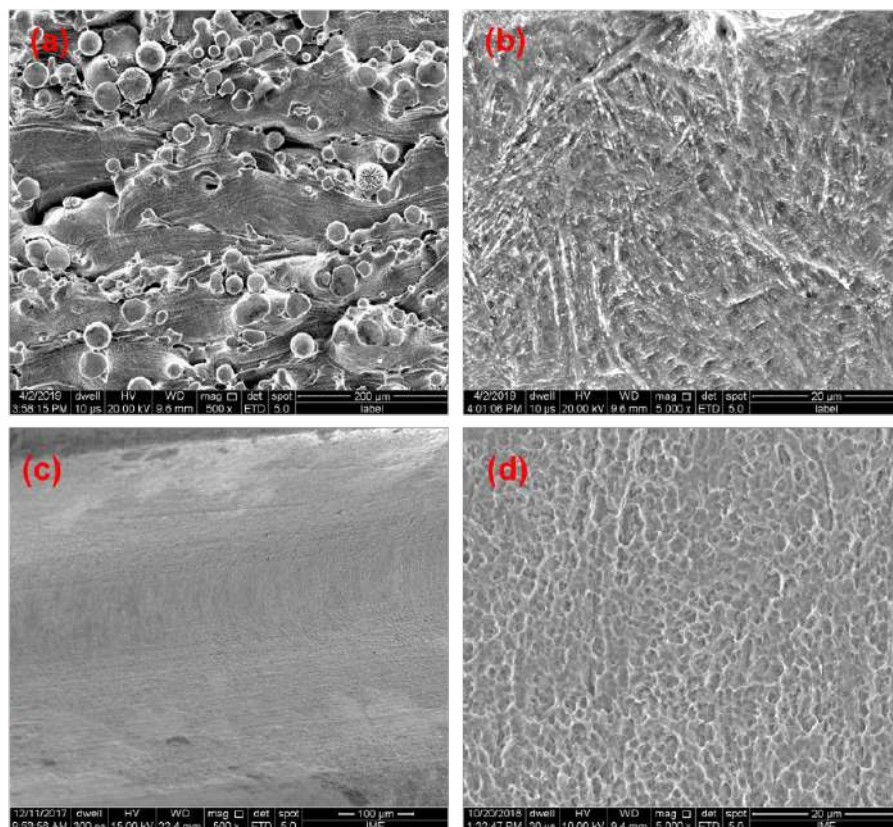


Figure 1. Scanning electron microscopy of the different surface morphologies at different magnifications (a) Sintered sample surface (500x); (b) Sintered surface (5000X); (c) Surface after acid etching (500x) and (d) Surface after acid etching (5000X).

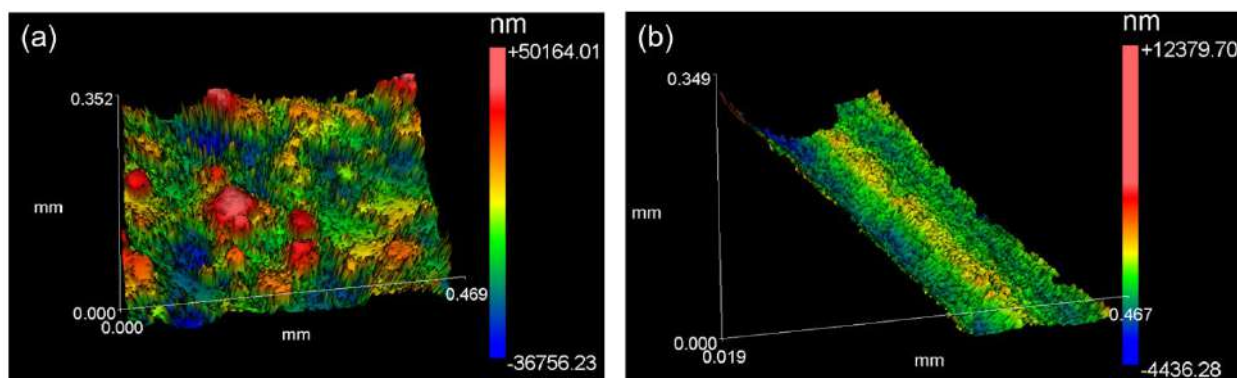


Figure 2. 3D surface morphology obtained in the Zygo profilometer.(a) Sintered surface and (b) Acid etched Surface.

Table 1. Surface roughness parameter of the titanium alloys produced by laser sintering.

Surface	Ra (µm)
As sintered	12,976 ± 0,63
After acid etching	1,417 ± 0,43

## In-Situ X-Ray MicroCT Imaging of The Microstructural Changes in Sandstones Submitted to Hydrostatic Pressures.

SILVA JUNIOR, Francisco José Rodrigues da<sup>1\*</sup>, VELLOSO, Raquel Q.<sup>2</sup> and PACIORNIK, S.<sup>1</sup>

<sup>1</sup>. Dept. of Chemical and Materials Engineering (DEQM), PUC-Rio, Rio de Janeiro, Brazil

<sup>2</sup>. Dept. of Civil Engineering (CIV), PUC-Rio, Rio de Janeiro, Brazil

\*Corresponding author, [fjphb@hotmail.com](mailto:fjphb@hotmail.com)

In the oil industry, problems such as mechanical damage reduce the porosity and permeability of a rock formation, reducing the productivity and injectivity of wells in oil and gas production systems [1]. During the well drilling there is a change in the state of the stress in its surroundings, causing a deformation in the rock that can induce a significant loss of porosity [2, 3]. In this work we study the influence of mechanical damage on the porosity of sandstone rocks by means of x-ray microtomography (microCT) coupled to a cell developed for in situ application of hydrostatic stress. A sandstone sample of 8 mm in diameter was scanned under 3 conditions: without load, after application of 3300 psi hydrostatic stress and after unloading. The cell allowed the load variations to be performed without removing the sample from the tomograph, allowing a quantitative comparison between the 3D images in the 3 conditions. Data such as total porosity, variation of the porous area in each layer, volume and shape of the pores were obtained. Image processing steps illustrated in Fig. 1 were fundamental for the calculation of the sandstone porosity. Thus, porosity values of 23.16% were obtained for the sandstone without pressure, 21.48% for the sandstone with pressure of 3300 PSI and 21.56% for the decompressed sandstone. It is noted by Fig. 2 that the volumes of the solids of the three conditions are substantially the same, indicating that the comparison between the three conditions is consistent. After compression, the pore volume distribution became narrower, dropping from a maximum value of  $\approx 7 \times 10^6 \mu\text{m}^3$  to  $\approx 5.5 \times 10^6 \mu\text{m}^3$ . In addition, there was a reduction in the number of larger pores, leading to a higher concentration of pores of smaller volume. After the decompression, there is not much difference in relation to the compressed sample, although the larger pores have a slightly larger volume.

### REFERENCES

- [1] Yang, Y., Zhang, W., Gao, Y., Wan, Y., Su, Y., An, S., Sun, H., Zhang, L., Zhao, J., Liu, L., Liu, P., Liu, Z., Li, A., Yao, J., 2016. Influence of stress sensitivity on microscopic pore structure and fluid flow in porous media. J. Nat. Gas Sci. Eng. <https://doi.org/10.1016/j.jngse.2016.09.061>
- [2] Saenger, E.H., Lebedev, M., Uribe, D., Osorno, M., Vialle, S., Duda, M., Iglauer, S., Steeb, H., 2016. Analysis of high-resolution X-ray computed tomography images of Bentheim sandstone under elevated confining pressures. Geophys. Prospect. <https://doi.org/10.1111/1365-2478.12400>
- [3] Schindler, M., Prasad, M., 2016. Micro X-ray CT imaging of sediments under confining pressure, in: SEG Technical Program Expanded Abstracts 2016. <https://doi.org/10.1190/segam2016-13966227.1>
- [4] This research was supported by Petrobras, CNPq, CAPES and FAPERJ.

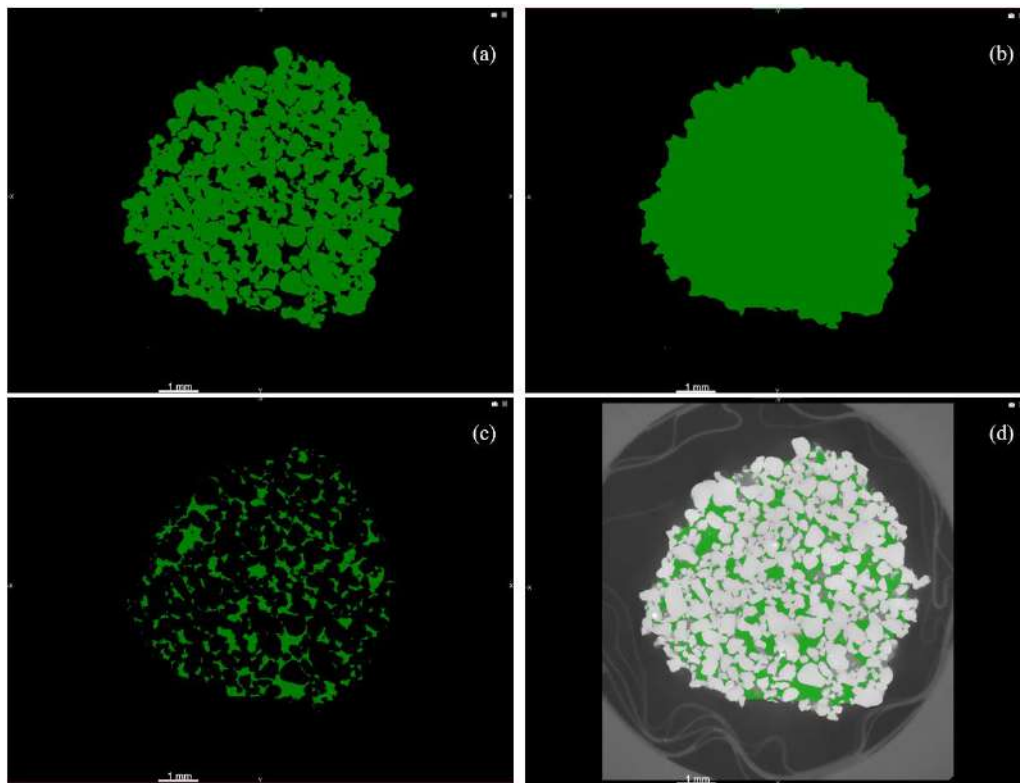


Fig. 1 - Segmentation of the solid phase (a), Filling of pores (b), Identification of pores by subtraction (c), result of subtraction in relation to whole sample (d).

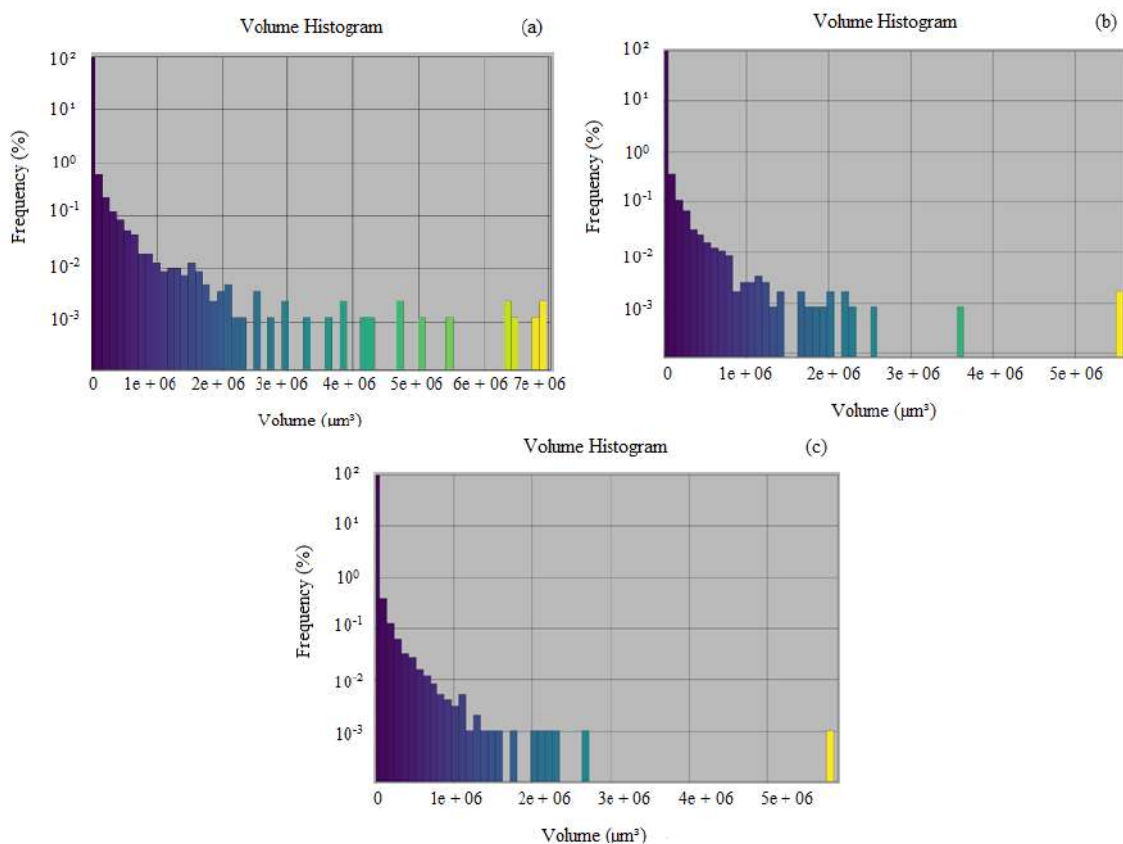


Fig. 2 - Distribution of pore volumes (a) Sandstone without pressure; (B) Sandstone with 3300 PSI pressure; (c) Sandstone with decompression.

## SEM/EDS characterization of chrysocolla from Nova Prata do Iguaçu, State of Paraná, Brazil

Gianna Maria Garda<sup>1\*</sup>, Isaac Jamil Sayeg<sup>2</sup> and Diego Arruda Filgueira<sup>3</sup>

<sup>1</sup> Dept. of Mineralogy and Geotectonics/ IGc-USP – Geosciences Institute of São Paulo University, São Paulo, Brazil. E-mail: giagarda@usp.br.

<sup>2</sup> Scanning Electron Microscopy Laboratory/IGc-USP, São Paulo, Brazil.

<sup>3</sup> LiGeA Graduate student/IGc-USP, São Paulo, Brazil.

Chrysocolla is a hydrated copper silicate that usually occurs as a gelatinous precipitate or a hydrogel containing 12.2 to 18.8 wt.% of water. Some authors consider chrysocolla an assemblage of, *e.g.* spertiniite [Cu(OH)<sub>2</sub>], silica, and water [1], instead of a mineral *sensu stricto*. Intense chemical weathering of copper deposits causes silica mobilization and precipitation and formation of chrysocolla, copper oxides and carbonates [2]. In Nova Prata do Iguaçu (NPI – State of Paraná, Southern Brazil), chrysocolla is found covering vesicles, fractures, and secondary minerals of weathered basaltic rocks mineralized with native copper [3]. In order to better characterize weathering products, a Leo 4401 scanning electron microscope (SEM/EDS) was used in this study. The difficulty in analyzing hydrated materials with SEM/EDS lies in the fact that hydrogen and hydroxyl cannot be analyzed by this method and some rules-of-thumb have to be designed in order to identify and characterize them via *in situ* chemical analysis. Figure 1A shows a back-scattered electron (BSE) image of the area of sample NPI-06 analyzed by SEM/EDS (inset in Fig. 1). For a better identification of the analyzed spots, Figure 1B shows a photomicrograph of the same area of Figure 1A, in which native copper (center-down) and blue and orange chrysocolla (center-up) can be distinguished by their colors. The yellow numbers in both figures mark the spots analyzed by SEM/EDS (operating conditions: 20 KV; 100-second acquisition time; carbon-coated sample NPI-06). The data were processed via the INCA software. Table 1 presents the ranges of Al, Si, Fe, Cu and O contents in wt. % (not normalized to 100 wt.%) for the analyzed spots. Figure 2 shows a graph of Si (wt.%) versus Cu (wt.%), in which native copper (~90-100 wt.% Cu; Si ~0 wt.%) and oxidized copper (80 wt.% Cu; 23 wt.% O) are distinguished from malachite (hydrated Cu carbonate: 53-55 wt.% Cu; Al and Si ~0 wt.%) and chrysocolla. The calculation of the structural formula of chrysocolla according to [4]: (Cu<sub>2-x</sub>Al<sub>x</sub>)HSi<sub>2</sub>O<sub>5</sub>(OH)<sub>4</sub>·nH<sub>2</sub>O, where  $x < 1$ , resulted in oxygen atoms per formula unit (O pfu in Table 1) varying from 6.7 to 8.8, which are distinct from the value obtained for malachite (4.1 O pfu). Variations in chrysocolla colors correspond to varying Cu pfu, being 2.0 Cu pfu characteristic of blue chrysocolla and 1.5-1.8 Cu pfu of orange chrysocolla. Aluminum (0.2-0.5 Al pfu) and to a lesser extent iron (0.06-0.1 Fe pfu) replace copper in orange chrysocolla. Taking into account the proportions Cu: Si or (Cu+Al+Fe):Si of 2:2 given by the structural formula, as shown in Table 1, there is an excess of Si in both blue and orange chrysocolla, varying from 0.3 to 0.8 Si pfu, which is interpreted as amorphous silica or cryptocrystalline quartz associated with chrysocolla, previously identified in X-ray diffractograms of NPI samples.

### REFERENCES

- [1] F. Farges et al., 13th International Conference On X-Ray Absorption Fine Structure, Proceedings, 882 (2006) 223.
- [2] M.J. Crane et al., Records of the Australian Museum, 53 (2001) 49.



- [3] Garda et al., Acta Microscópica 26, Supplement B (2017) 288.  
 [4] R.L. Frost et al., Thermochimica Acta, 545 (2012) 157.

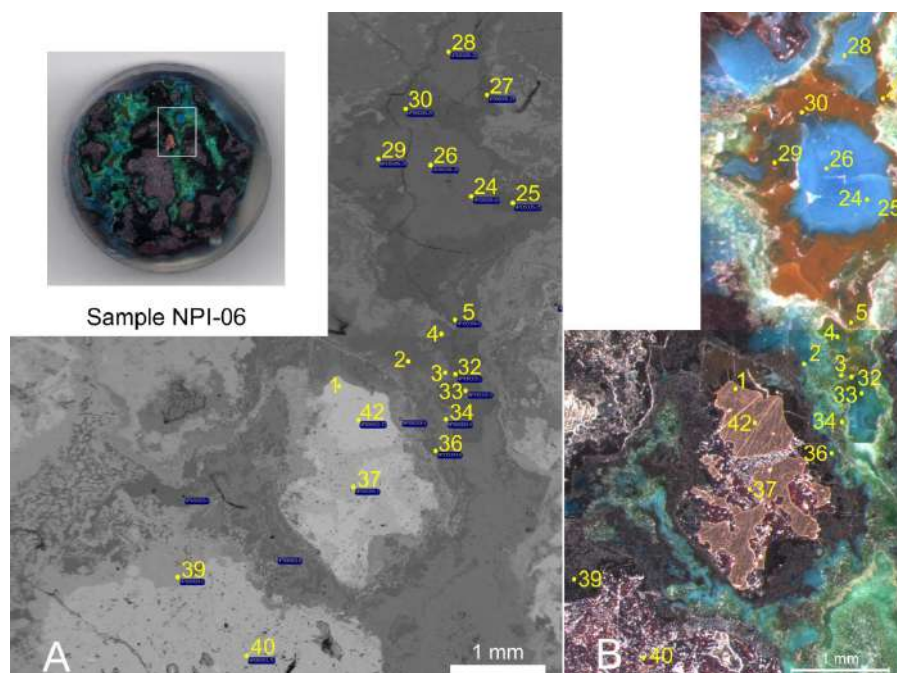


Figure 1. BSE image (A) and photomicrograph (B) of the area marked with a rectangle in the inset. Numbers in yellow signal the spots analyzed by SEM/EDS.

Table 1. Ranges of Al, Si, Fe, Cu and O contents (wt. %) and atoms per formula unit (pfu) for the spots analyzed by SEM/EDS (see Fig. 1).

	orange chrysocolla	blue chrysocolla	malachite	oxydized copper	native copper
analysis #	32; 27; 30; 5; 25	33; 36; 2; 4; 28; 26; 24; 29	34; 3	39	37; 1; 42; 40
Al wt. %	1.6-4.3	—	—	—	0-0.2
Si wt. %	18.3-26.7	18.2-27.0	(0.15)	(1.6)	—
Fe wt. %	0.9-3.0	—	—	—	—
Cu wt. %	28.6-38.5	34.1-47.2	53.0-55.0	80.0	90.0 to ~100
O wt. %	29.3-45.6	28.8-46.4	27.5-29.0	23.0	1.3-10.4
Al pfu	0.2-0.5	—	—	—	—
Si pfu	2.5-2.8	2.3-2.6	—	—	—
Fe pfu	0.06-0.1	—	—	—	—
Cu pfu	1.5-1.8	2.0	2.0	2.0	2.0
O pfu	7.2-8.8	6.7-7.9	4.1	2.3	0.1-0.9

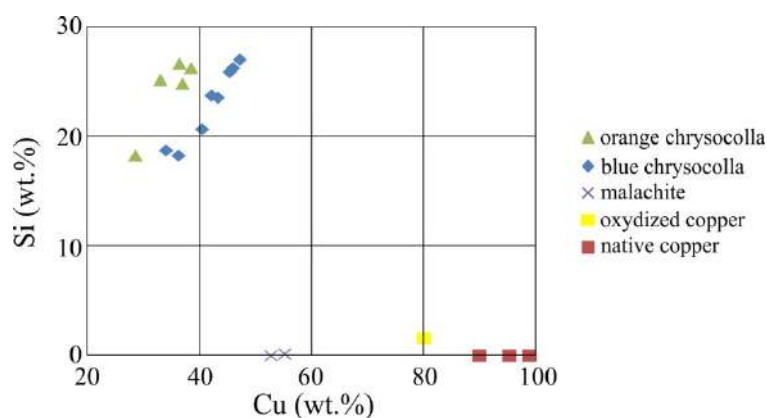


Figure 2. Graph Si (wt.%) versus Cu (wt.%) for the spots marked in yellow in Figure 1.

## Study of Phase Transformations in Non-Isothermal Conditions in Duplex Stainless Steel by Dilatometric Technique

Gabrielle Cristine Lemos Duarte Freitas<sup>1\*</sup>, Gláucio Soares da Fonseca<sup>2</sup> and Luciano Pessanha Moreira<sup>3</sup>

<sup>1</sup>. Universidade Federal Fluminense, Programa de Pós-Graduação em Engenharia Metalúrgica da Escola de Engenharia Industrial Metalúrgica de Volta Redonda, Volta Redonda, Brazil. e-mail: gabriellecristine@id.uff.br

<sup>2</sup>. Universidade Federal Fluminense, Programa de Pós-Graduação em Engenharia Metalúrgica da Escola de Engenharia Industrial Metalúrgica de Volta Redonda, Volta Redonda, Brazil. e-mail: glaucio@metal.eeimvr.uff.br

<sup>3</sup>. Universidade Federal Fluminense, Programa de Pós-Graduação em Engenharia Metalúrgica da Escola de Engenharia Industrial Metalúrgica de Volta Redonda, Volta Redonda, Brazil. e-mail: luciano.moreira@metal.eeimvr.uff.br

Duplex stainless steels are a class of materials that are characterized by a biphasic microstructure of both ferrite ( $\alpha$ ) and austenite ( $\gamma$ ) volumetric fractions, which give this class of steels excellent mechanical and anticorrosive properties [1]. Due to this variety of properties, this group of materials is applied on a large scale in the chemical and petrochemical industries, offshore, steel, food and power generation plants [2]. Much of the research associated with this classification of steel is related to phase transformations at high temperatures, since in this condition deleterious compounds are formed, damaging the previously mentioned properties [3]. Kim et. al developed studies evaluating the phase transformation kinetics found in duplex stainless steels CD3MN and superduplex CD3MWCuN through isothermal and non-isothermal cooling cycles, constructing time-temperature-transformation (TTT) curves and continuous cooling curves (CCT) [4]. Rivolta et. al applied differential thermal analysis techniques in order to understand the microstructural evolution in a F55 grade duplex stainless steel, using cycles with varying heating rates [5]. The aim of this present work is evaluating phase transformations present in non-isothermal cooling cycles in a SAF 2205 duplex stainless steel. Through the Gleeble 3500<sup>®</sup> thermomechanical simulator five samples are homogenized at 1100 °C to 30 min and later contemplate cooling rates of 5°C/min, 4 °C/min, 3°C/min, 2°C/min and 1°C/min. Through the image processing, the characterization of the phases was obtained by secondary electron beams (SEM) and backscattered electrons (SEM-BSE). Note that in the first method only topography analysis is possible, not being accessible the distinction of phases presents in the samples. According to Figure 1, the precipitation of chi ( $\chi$ ) phase was found by MEV-BSE at the 5 °C / min cooling rate. In the other rates, the presence of sigma ( $\sigma$ ) and chi ( $\chi$ ) phases were identified, as shown in Figure 2. Note that the  $\chi$  phase precipitates preferentially in the grain boundaries of ferrite-ferrite, since the sigma phase has its precipitation in the ferrite-austenite interfaces [1]. The chemical compositions of these phases were determined by energy dispersive spectroscopy (SEM-EDS). The  $\chi$  phase present in the samples has a weight average percentage of chromium, molybdenum and nickel of 24.58%, 10.53% and 2.95%. While the  $\sigma$  phase identifies the average percentage by weight of chromium and molybdenum and nickel of 27.08%, 5.90% and 3.30%, respectively. The compositions at extreme cooling rates are shown in Table 1.

## REFERENCES

- [1] D.M. Escriba, E. Materna-Morris, R.L. Plaut, A.F. Padilha, “Chi-phase precipitation in a duplex stainless steel”, *Materials Characterization*, vol. 60, n°11, p. 1214-1219, 2009.
- [2] G.S. Fonseca, P.M. Oliveira, M.G. Diniz, D.V. Bubnoff and J.A. Castro, “Sigma Phase in Superduplex Stainless Steel: Formation, Kinetics and Microstructural Path”, *Materials Research*, vol. 20, n° 1, p. 249-255, 2017.
- [3] I. Calliari, M. Zanesco and E. Ramous, “Influence of isothermal aging on secondary phases precipitation and toughness of a duplex stainless steel SAF 2205”, *Journal of Materials Science*, vol. 41, n° 22, p. 7643–7649, 2006.
- [4] Y.-J. Kim, L.S. Chumbley and B. Gleeson, “Continuous Cooling Transformation in Cast Duplex Stainless Steels CD3MN and CD3MWCuN”, *Journal of Materials Engineering and Performance*, vol. 17, n° 2, p. 234-239, 2007.
- [5] B. Rivolta, R. Gerosa and F. Tavasci, “The dilatometric technique for studying sigma phase precipitation kinetics in F55 steel grade”, *Journal of Thermal Analysis and Calorimetry*, vol. 132, n° 2, p. 869–877, 2018.

## ACKNOWLEDGMENTS

To the Brazilian agencies for the promotion of research (CNPq, CAPES and FAPERJ) for the financial support granted.

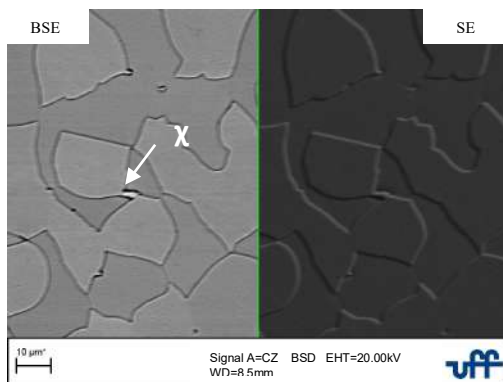


**Figure 1.** Comparative image of MEV-SE and MEV-BSE of sample with cooling rate of 5 °C / min with evidence of chi phase.

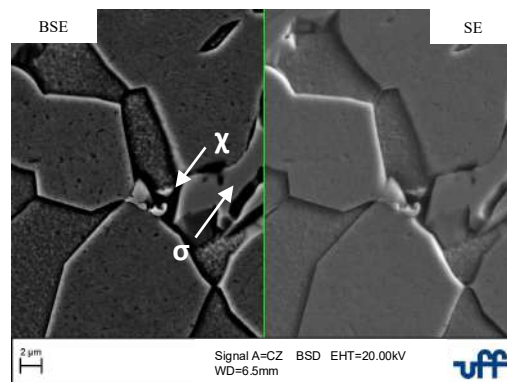


**Figure 2.** Comparative image of MEV-SE and MEV-BSE of sample with cooling rate of 1 °C / min with evidence of chi and sigma phase.

**Table 1.** Contents of principal metallic elements in austenite, ferrite,  $\sigma$ - and  $\chi$ -phases as determined by energy-dispersive X-ray spectroscopy in duplex stainless steel (wt.%).

Elements (wt%)	Cooling rates (°C/min)	$\alpha$	$\gamma$	$\chi$	$\sigma$
Cr	5	23,29± 0,16	19,95± 0,78	24,15± 1,29	-
	1	22,96± 0,40	20,16± 0,33	24,31± 0,63	28,49± 1,53
Mo	5	4,52± 0,16	2,30± 0,23	10,70± 0,67	-
	1	4,8± 0,00	2,42± 0,06	13,07± 1,01	6,50± 0,42
Ni	5	3,58± 0,20	5,65± 0,04	3,10± 0,37	-
	1	3,17± 0,06	5,75± 0,12	2,56± 0,13	3,01± 0,24

## **SOLIDIFICATION MICROSTRUCTURE OF WELD METAL OF THE 316L AUSTENITIC STAINLESS STEEL WELDING BY TIG AUTOGENOUS PROCESS**

Erica Marcelino Freitas de Souza Silva<sup>1\*</sup>, Glaucio Soares da Fonseca<sup>2</sup>

<sup>1</sup>. Graduate Program on Metallurgical Engineering, Federal Fluminense University - Volta Redonda, Rio de Janeiro, Brazil, <sup>2</sup>, Federal Fluminense University Mechanical Engineer Department- Graduate Program on Metallurgical Engineering - Volta Redonda, Rio de Janeiro, Brazil. ericauffmetal@gmail.com

Austenitic Stainless Steels (ASS) are formulated and thermo-mechanically processed such that the microstructure is primarily austenite [1]. However on the welding process, is also known that the presence of ferrite is requirement in some amount on the weld deposits of austenitics to prevent solidification cracking [2], since this one is of the major problems related to welding of this alloys, because it can lead to failure. The propose of this paper was to investigate the delta ferrite existence on the weld microstructure of a ASS 316L tube, welded by TIG autógenous process, using for such investigation the scanning electronic microscopy (SEM) and energy-dispersive spectroscopy (EDS) technique. A mapping of the weld zone quantified 17.1 % Cr (Wt%) and 10.1 Ni (Wt%), meaning that the material solidified on the FA mode, in other words, the delta ferrite is present on the microstructure, the solification occurs as ferrite primary and it has eskeletal morphology. Specific analysis of the skeletal phase measured  $19,8\text{Cr} \pm 1.4$  (wt%), meaning be in fact, delta ferrite since presente hight percentage of Chromium and low content of Nickel. Same solidification mode was found to 316L for Kozuh et al., 2009 [3]. The delta ferrite can be beneficial or melefic depending on the place, volumétric fraction and the alloy application [2] With the aid of ImageJ software the ferrite volumétric fraction found on the weld zone was  $9\% \pm 2$ , being within the expected for this alloy. This amount, according the literature, is enough to prevent solidification crackings [4]. Therefore for the 316L the delta ferrite did not cause microstructures problems, upside down, brought benefits for it in terms of preservation of microstructure after welding, since no solidification cracks were observed.

### **Acknowledgment,**

This study was financed in part by the Coordenação de Aperfeiçoamento de Pessoal de Nível Superior - Brasil (CAPES) - Finance Code 001.

---

[1] LIPPOLD, John C.; KOTECKI, Damian J., Welding metallurgy and weldability of stainless steels, Hoboken, NJ: John Wiley, 2005.

[2] PASSOS, Douglas de Oliveira; OTUBO, Jorge, A influência da ferrita delta em aços inoxidáveis austeníticos forjados, Rem: Revista Escola de Minas, v. 63, n. 1, p. 57–63, 2010.

[3] KOŽUH, S; GOJIC, M; KOSEC, L, Mechanical properties and microstructure of austenitic stainless steel after welding and post-weld heat treatment, Kovove Mater., p. 10, 2009.

[4] LIPPOLD, J C; SAVAGE, Vv F, Solidification of Austenitic Stainless Steel Weldments Part I- A Proposed Mechanism, p. 362s–374s, 1979.



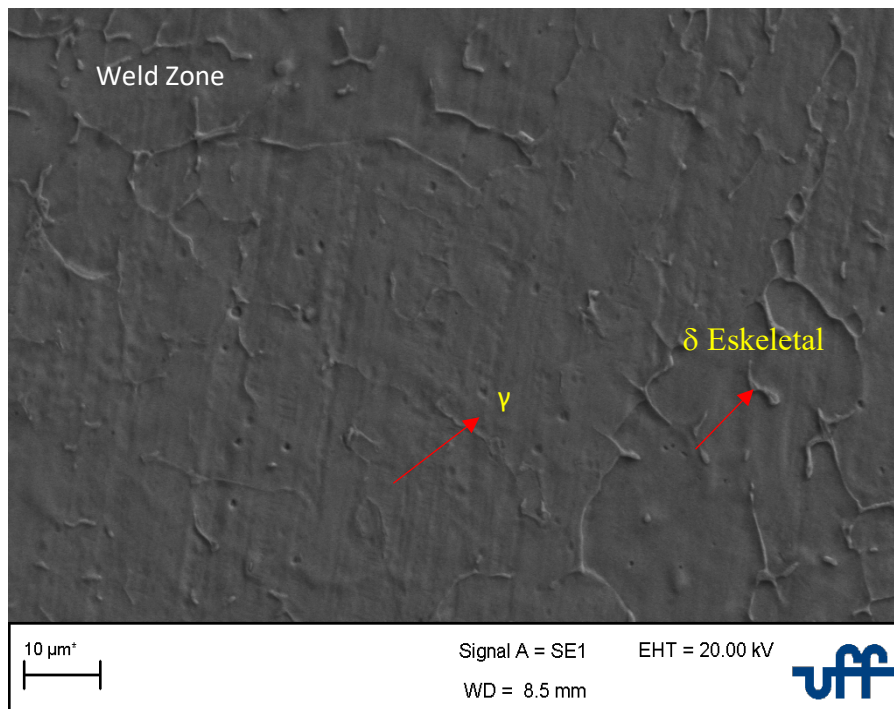


Figure 1: SEM micrograph of the 316L weld zone showing delta ferrite and austenite phases.

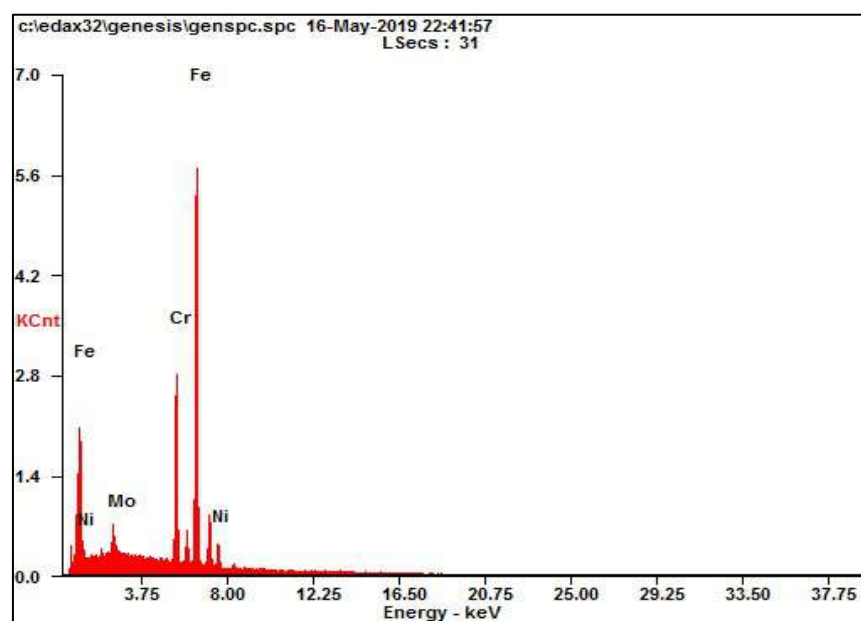


Figure 2: Spectrum of the SEM/DES technique performed in the ferrite delta phase.

Table 1: Delta Ferrite analysis

Element	Wt %
Fe	69.5±1
Cr	19.8±1.4
Ni	7.0±1.2
Mo	3.8±0.7

## Design Of Magnetic Nanoparticles: Nanorods And Nanodisc For Magnetic Hyperthermia Applications

Gopal Niraula,<sup>1\*</sup> Diego Muruca,<sup>2</sup> F.H. Aragon,<sup>3</sup> J.A.H. Coaquira,<sup>3</sup> S.K. Sharma,<sup>1</sup>

<sup>1</sup> Pos-Graduate Department of Physics, Federal University of Maranhao, Sao Luis, Brasil

<sup>2</sup> Institute of Physics “Gleb Wataghin” (IFGW), University of Campinas, Campinas, Brasil

<sup>3</sup> Institute of Physics, University of Brasilia, Brasilia, Brasil

\*gopalniraula891@gmail.com

### **ABSTRACT**

Iron oxide (IO) based nanoparticles (for instance hematite, magnetite etc.) have been widely used in biomedical applications because of their size-dependent tuneable magnetic properties, which enable the formation of stable suspensions. Small-sized IO nanoparticles can exhibit superparamagnetic (SPM) behaviour with very weak magnetic interactions and good dispersion; when an external field is applied, they will undergo transition from a SPM state to a ferrimagnetic (FiM) state. This typical feature together with other properties such as a large surface area and high biocompatibility makes them promising nano-magnets for highly sensitive magnetic resonance imaging, targeted drug delivery and biological sensing. In currently available superparamagnetic (SPM) IO nanoparticles, the difficulty of striking a balance between having a good suspension and improved magnetic properties presents a challenging obstacle for the development of high-performance magnetic nanoparticle based diagnostics and therapeutics. Although small superparamagnetic iron oxide nanoparticles under low fields have been favored (linear response theory regime), these nanoparticles present a series of limitations, including relatively low heating efficiency (specific absorption rate or SAR), that need to be overcome to make magnetic hyperthermia an efficient clinical application. There are large number of studies focused on single domain nanoparticles by designing and optimizing their size, shape, and surface coating to maximize the SAR value but insufficient heat generation by such IO nanoparticle is major problem. However, ferromagnetic nanoparticles have higher heat generation via hysteresis loss having certain remanence which may lead to undesired agglomeration due to strong magnetic dipole–dipole interactions. In application point of view, design of ferro/ferrimagnetic iron oxide nanoparticles improving agglomerations with low remanence is very important for performance. Iron oxide nanodiscs possess a ferrimagnetic vortex-domain structure, in which magnetization is circumferential to the ring without stray fields. This unique magnetic structure endows the ferrimagnetic vortex-

domain nanodiscs (FVIOs) with negligible remanence and coercivity that can greatly reduce dipole–dipole interactions and enable a good colloidal stability, with having a much higher saturation magnetization and large hysteresis loop in comparison with superparamagnetic iron oxide nanoparticles (SPIOs) and hence exhibit better heating performance for magnetic hyperthermia application than SPIOs. Therefore, with this goal, we synthesized the iron-oxide nanodiscs above single domain for magnetic hyperthermia applications. In this scenario, we will present the synthesis of iron oxide based nanoparticles by microwave assisted hydrothermal route with emphasize on the size/shape tenability by varying the ratio of sodium phosphate to sodium sulphate and keeping other parameters same. In this work, the different morphology (nanotubes, nanorods and finally nanodiscs, for example) of iron oxide nanoparticles with variation of phosphate and sulfate ratio have been presented, and interesting thing is nanoparticles morphology are contradicted with previous result proposed by Jia et al[1]. The comparative study based on morphology, size, phase composition; crystallinity, core and surface composition and hence magnetic properties by using different techniques SEM measurement, X-ray diffraction, Reitveld analysis, Mossbauer spectroscopy, FTIR spectroscopy and SQUID Quantum design etc. has been investigated. Finally, we will present the heating effect of differently shaped iron oxide nanoparticles by comparing with the existing literature on superparamagnetic nanoparticles for magnetic hyperthermia applications.

**Key Words:** Ferrimagnetic iron oxide nanoparticles, magnetic hyperthermia

#### REFERENCES:

- [1] Jia C-J, Sun L-D, Luo F, Han X-D, Heyderman LJ, Yan Z-G, Yan C-H, Zheng K, Zhang Z, Takano M, Hayashi N, Eltschka M, Kläui M, Rüdiger U, Kasama T, Cervera-Gontard L, Dunin-Borkowski RE, Tzvetkov G, Raabe J (2008) Large-Scale Synthesis of Single-Crystalline Iron Oxide Magnetic Nanorings. *J Am Chem Soc* 130:16968–16977 . doi: 10.1021/ja805152t

[2] Figures:

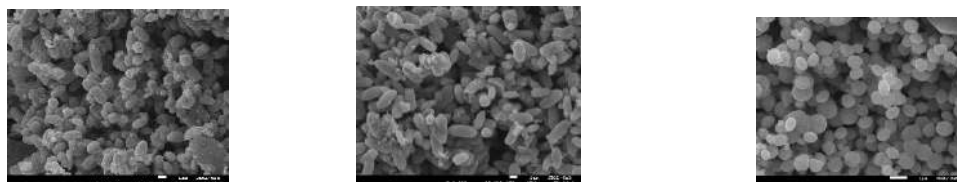


Figure1: SEM image of nanotubes, nanorods and nanodisc structure

**ACKNOWLEDGMENTS:** We highly acknowledged Coordination of Improvement of Higher Education Personnel (CAPES), Brasil for its support in this research work.

## Microscopic Evaluation and Fabrication Of A Metal-Ceramic Composite

Haimon Alves<sup>1\*</sup>, José Firmino<sup>2</sup>, Arthur Cavichini<sup>3</sup>, Marcos Orlando<sup>3</sup>, Ricardo Lopes<sup>4</sup>

<sup>1</sup>. Physics Institute, UERJ, RJ, Brasil. [alveshaimon@gmail.com](mailto:alveshaimon@gmail.com)

<sup>2</sup>. Mechanical Engineering Program, IFES, ES, Brasil.

<sup>3</sup>. Physics Department, UFES, ES, Brasil

<sup>4</sup>. Nuclear Engineering Department, UFRJ, RJ, Brasil

### INTRODUCTION

Austenitic steel 316L (S31603) has high resistance to general corrosion [1,2]. However, the steel in question has no magnetic response according to the manufacturer. Double Perovskites, in turn, have been of great interest recently because of their wide range of properties [3]. Among them, the  $\text{Sr}_2\text{CrReO}_6$  compound is one of the most outstanding due to its properties: conductive and ferromagnetic at room temperature. However, the double perovskites in general present some type of degradation. The production of a composite that is resistant to corrosion and has a magnetic response may be of interest for the production of structural devices, such as actuators and magnetic sensors that need to be immersed in extreme environments. It is intended to combine mechanical and chemical properties of the 316L steel with the magnetic properties of the SYCRO to obtain controllable magnetic properties in the composition and working temperature range for applications in chemically and thermally aggressive environments.

### EXPERIMENTAL SETUP

AISI 316L / SYCRO composite sintering was performed by solid state diffusion. The ceramic compound SYCRO was obtained by a method described by Orlando et al. [4]. Scanning Electron Microscopy (SEM) and Dispersive Energy Spectroscopy (EDS) were made with the purpose of observing the microstructure and chemical composition of the composite. SEM measurements were performed on a Zeiss machine, model EVO MA10, equipped with an X-MaxN detector from Oxford Instruments. X-ray diffraction (XRD) measurements were performed on a conventional Bruker D8 Advance X-ray machine. The length used was  $\lambda = 1.5418 \text{ \AA}$  with a pitch of  $0.02^\circ$  in a range of  $15^\circ - 100^\circ$ . Rietveld refinement was performed using the software FullProf Suite. Magnetic susceptibility a.c. at room temperature were performed on the composite. X-ray computed microtomography ( $\mu\text{CT}$ ) was performed to analyze the 3D distribution of particles and defects in the sample. The measurement parameters used were: energy of 130 kV and current of 61  $\mu\text{A}$ ; pixel size of 6  $\mu\text{m}$ ;  $0.5^\circ$  angular pitch; number of 5 frames for each projection and 0.50 mm Copper filter

### RESULTS

The composite formed by 316L steel with 10% of  $\text{Sr}_{1.8}\text{Y}_{0.2}\text{CrReO}_6$  (SYCRO) double perovskite was successfully sintered using Top Down nanotechnology associated with powder metallurgy. SEM images (fig.1) showed that the SYCRO nanoparticles were deposited on the steel surface homogeneously. The scattering spectra of the images confirmed the presence of the Sr and Re elements scattered homogeneously on the surface of the composite, which corroborates the images observed by SEM. X-ray microtomography (fig.2) showed a solid build, with few pores and cracks, and a 3D distribution of the main components. X-ray diffraction measurements showed that SYCRO particles were embedded in the 316L steel matrix. Magnetic susceptibility a.c. showed that the composite has ferromagnetism and  $T_c$  close to that found in the literature for the ceramic composite  $\text{Sr}_{1.8}\text{Y}_{0.2}\text{CrReO}_6$ , which certifies that the sintering of the composite was obtained successfully.



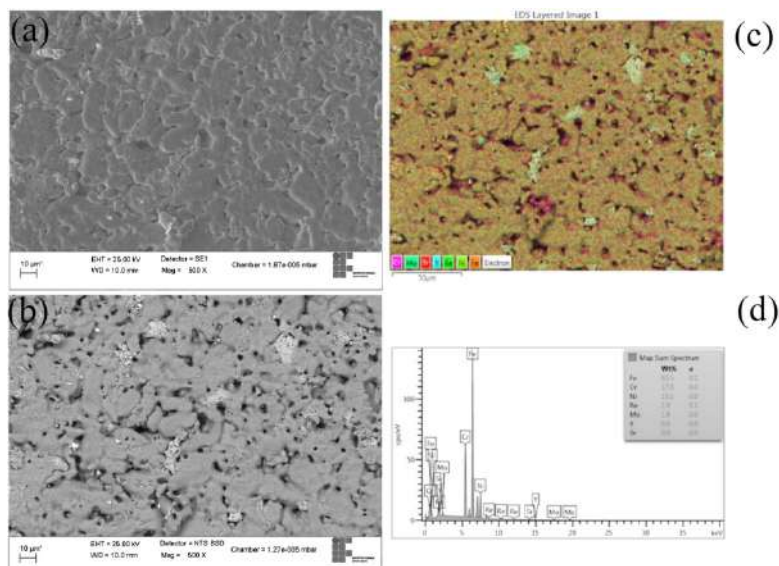


Figure 1: 316L / SYCRO Composite Scanning Electron Microscopy Images. (a) Image of secondary electrons in 500 X. (b) Image of backscattered electrons in 500 X. (c) Map of dispersive energy spectroscopy in 500 X and dispersion spectrum (d).

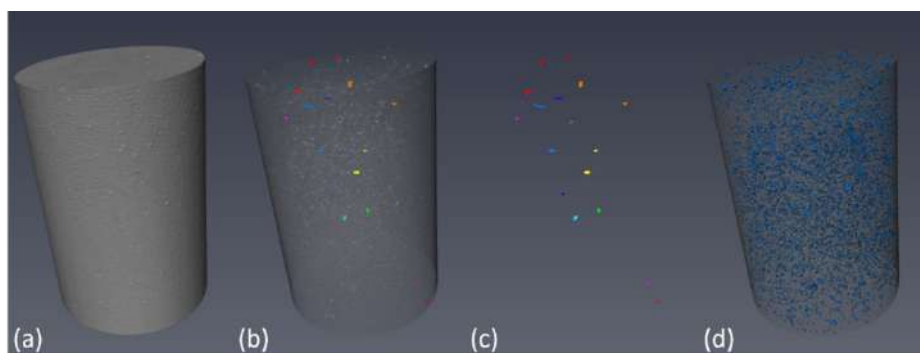


Figure 2: 3D images of original  $\mu$ CT (a); (b) pore and crack, with sample volume edge; (c) voids and cracks only; (d) segmentation of higher density structures

## CONCLUSIONS

This work indicates opportunities for the production of new composites that can be elaborated from this idea for several other applications: biomaterials, microheaters, sensors and magnetic actuators to be used even in chemically aggressive environments

## REFERENCES

- [1] Plaut RL, Herrera C, Escriba DM, Rios PR, Padilha AF., A Short Review on Wrought Austenitic Stainless Steels at High Temperatures: Processing, Microstructure, Properties and Performance, Materials Research. 10 (2007) 453-460.
- [2] Ruiz A, Timke T, van de Sande A, Heftrich T, Novotny R, Austin T, Corrosion and microstructural analysis data for AISI 316L and AISI 347H stainless steels after exposure to a supercritical water environment., Data in Brief. 7(2016) 1341-1348.
- [3] Vasala S, Karppinen M.,  $A_2B'B''O_6$  perovskites: A review., Progress in Solid State Chemistry., 43 (2015) 1-36.
- [4] Orlando MTD, Cavichini AS, Depianti JB, Passamai JL, Rocha JR, Salvador JF, Orlando CGP., Effects of yttrium doping in ordered double perovskite  $Sr_2CrReO_6$ ., Journal of Alloys and Compounds., 687 (2016) 463-469.

## USE OF EDS-SEM FOR FAST CHEMICAL AND MINERALOGICAL CHARACTERIZATION OF MULTIPHASE GEOLOGICAL SAMPLES

Hannah L. S. Matos-Pimentel<sup>1\*</sup>, José Affonso Brod<sup>1</sup>, Flávia Gomes de Souza<sup>1</sup>, Karolina de Oliveira Gonçalves Borges<sup>1</sup>, Jesiel Freitas Carvalho<sup>1</sup>, Cecília Maria Alves de Oliveira<sup>1</sup>.

<sup>1</sup>Centro Regional para o Desenvolvimento Tecnológico e Inovação (CRTI), Universidade Federal de Goiás (UFG), Goiânia – Brazil. hannah.matos@gmail.com

The most common techniques for mineral characterization are X-ray diffraction (XRD), X-Ray Fluorescence (XRF), and inductively coupled plasma-atomic emission spectroscopy (ICP-AES) and -mass spectroscopy (ICP-MS) [1, 2]. Here we demonstrate that map area analysis of energy dispersive X-ray spectroscopy (EDS) by scanning electron microscope (SEM) can be used as a fast, non-destructive, semi-quantitative tool that correlates well with the results of more traditional techniques. Mineral Liberation Analysis (MLA) is a well-known application of SEM backscattered-electron image (BEI) combined with EDS point analysis to obtain, among various other parameters, the modal composition in rock or ore samples [3]. However, sample preparation and data acquisition in MLA are expensive and time-consuming [4]. An adequate, semi-quantitative determination of the chemical composition of an ore or rock powder can be achieved with minimal preparation and quick EDS analysis. Samples of ground rock were split, homogenized, and sprinkled onto a double-face adhesive carbon strip, then mounted on a brass stub. The method does not require any polishing or metal coating. The analyses were carried out in a JEOL JSM-IT300LV SEM under 40 Pa and 15 kV accelerating voltage. EDS spectra of 3x4 mm mapping areas were obtained with a 80 mm<sup>2</sup> Oxford Instruments X-MaxN EDS detector. Each such area was called a Quant Map, reconstructed from the combined chemical information from each pixel [5]. The Quant Map spectra were obtained without calibration, and normalized to 100%. Three maps were averaged for each sample. Scanning time was set at ten minutes, since we observed no significant changes after 5 minutes collections (figure 1). Four rock types were analyzed: muscovite-biotite schist, chlorite-schist, limestone and shale Figure 2 illustrates the combination of an EDS map, where to each element is attributed a different color, and a backscattering electron image. The results were compared with the chemical composition both obtained directly by XRF and derived from XRD/Rietveld modelling (figure 3). Except for MgO, the analyzed oxides show consistently good 1:1 correlation. Although MgO results can be variably affected by sample topography [6], the reason for the observed MgO behavior is not clear and currently under investigation.

- [1] H.E. Jamieson et al., Mineralogical characterization of mine waste, Applied Geochemistry, 2015.
- [2] A.M. Brinatti et al., Mineralogical characterization of a highly-weathered soil by the Rietveld method, Scientia Agricola, 2010.
- [3] P. Zhang et al., MLA-based sphalerite flotation optimization: Two-stage roughing, Powder Technology, 2019.
- [4] C. Xu et al., Process mineralogy of Weishan rare earth ore by MLA, Journal of Rare Earths, 2019.
- [5] Oxford Instruments, Aztec 3.0 – User Manual, 40 -41p, 2010.

[6] H.L.S. Matos-Pimentel et al., Effect of Surface Irregularity in the SEM-EDS Analysis of Ca-Mg Carbonates, In: XXVI Congresso da Sociedade Brasileira de Microscopia e Microanálise – CSBMM 2017, Buzios-RJ, 2017.

The authors would like to thank ANP and PETROBRAS for funding and to CRTI and UFG for access to analytical facilities.

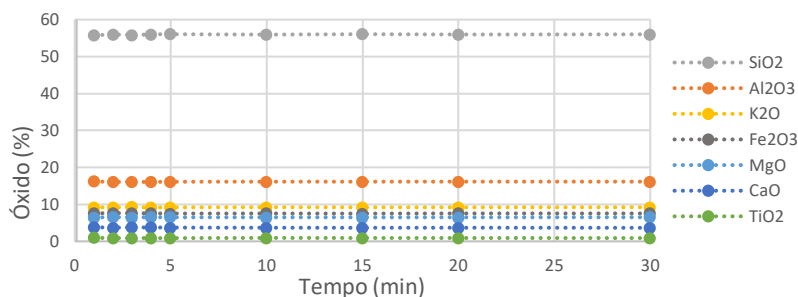


Figure 1 – Changes in concentration (oxide %) of Map Quant in function of time.

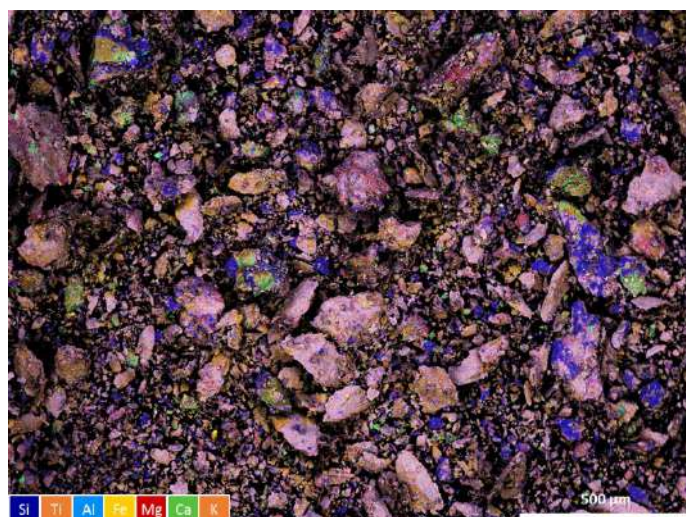


Figure 2 – Image of EDS compositional map where each color indicates a chemical element and its spatial distribution.

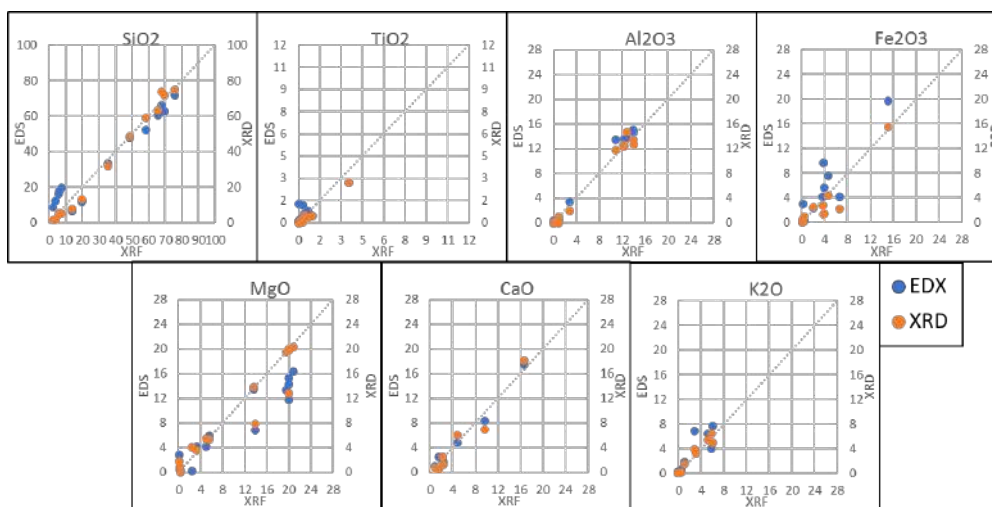


Figure 3 – Correlation of different analytical techniques (EDS and XRD with XRF).

## CLAY MINERALS IDENTIFICATION BY CHEMICAL (EPMA-WDS) AND MORPHOLOGICAL (SEM) CHARACTERISTICS

Hannah L. S. Matos-Pimentel<sup>1\*</sup>, José Affonso Brod<sup>1</sup>, Flávia Gomes de Souza<sup>1</sup>, Jesiel Freitas Carvalho<sup>1</sup>, Cecília Maria Alves de Oliveira<sup>1</sup>.

<sup>1</sup>Centro Regional para o Desenvolvimento Tecnológico e Inovação (CRTI), Universidade Federal de Goiás (UFG), Goiânia – Brazil. hannah.matos@gmail.com

Clay minerals are often studied because of their complex and unique structures and their use for information about mineralogical and geological processes [1]. Also, the characterization of clay minerals is useful to modelling petroleum reservoir [2]. However, because of composition and structural variation, preferred orientation and numerous diversities of clay minerals it is difficult to identify and separate the different phases in the same group [1,3]. X-ray diffraction (XRD) is the most used technique for quantitative clay minerals analysis, scanning electron microscopy (SEM) and transmission electron microscopy (TEM) are used for morphological characterization due to variation of crystal sizes of clay minerals (micrometer to nanometer scale). Other techniques include Fourier transform infrared spectroscopy (FTIR), thermal analysis and X-ray fluorescence spectrometry (XRF) [4]. Moreover, electron probe microanalysis (EPMA) with wavelength-dispersive spectrometry (WDS) is able to produce quantitative spot analysis without sample damage and using a small beam diameter (1  $\mu\text{m}$ ) [5]. In this study, Sepiolite, Palygorskite, Saponite and Kerolite/Stevensite were identified using morphological characteristics seen by FEG-SEM (JEOL JSM-7100F) and chemical analysis by were carried out in an EPMA-WDS (JEOL JXA-8230) under 15 kV with 20 nA of current and spot of 10  $\mu\text{m}$ . The analyses were confirmed by XRF and XRD. Morphologically, Sepiolite and Palygorskite are fibrous ( $\sim 100$  nm in thickness), Kerolite/Stevensite has an irregular flake morphology and saponite forms lath-like plates with fine fibers (figure 1). The chemical analyses by XRF and WDS are not sufficient to separate these phases because clay minerals can have similar chemistry (figure 2). In some cases, natural samples are composed of different clay phases and the total analysis by XRF shows just an average value. EPMA-WDS can give a clearer picture, because it is possible to analyze an isolated grain or a small area with a reduced spot. If the samples are interesterified, they can be extremely complex to identify by XRD. Also, morphology or chemistry alone are not enough to identify and separate these clay minerals, so we use a combination of electronic images and ternary diagrams of the stoichiometric ratio of cations Si and Al (tetrahedral site - IV): and Mg (octahedral site - VI), to confirm these phases (figure 3).

[1].X. Zhou et al, XRD-based quantitative analysis of clay minerals using reference intensity ratios, mineral intensity factors, Rietveld, and full pattern summation methods : A critical review, Solid Earth Sciences, v. 3, 2018, p.16-29.

[2] S. Hillier, Accurate quantitative analysis of clay and other minerals in sandstones by XRD: comparison of a Rietveld and a reference intensity ratio (RIR) method and the importance of sample preparation, Clay Minerals, 2000, v. 35, p. 291-302.

[3] G. Jozanikohan et al, Quantitative analysis of the clay minerals in the Shurijeh Reservoir Formation using combined X-ray analytical techniques, Russian Geology and Geophysics, v. 57, 2016, p.1048-1063.

[4] F. Bergaya and G. Lagaly, Critical Assessment of Analytical Techniques of Clays and



Clay Minerals, in: Handbook of Clay Science, 2nd Ed., Elsevier, Amsterdam, 2013, v. 5A, p. 25-26, 275-276.

[5] B. Velde, Note: Electron Microprobe Analysis of clay minerals, Clay Minerals, 1984, v. 19, p.243-247.

The authors would like to thank ANP and PETROBRAS for funding and to CRTI and UFG for access to analytical facilities.

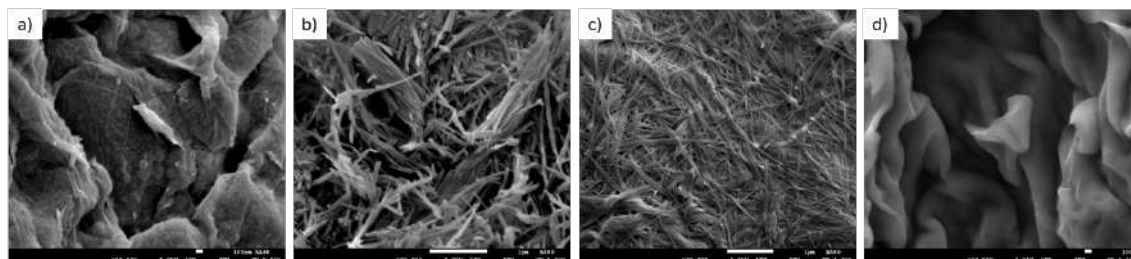


Figure 1 –FEG-SEM images of a) saponite, b) sepiolite, c) palygorskite and d) kerolite-stevensite and their morphological differences.

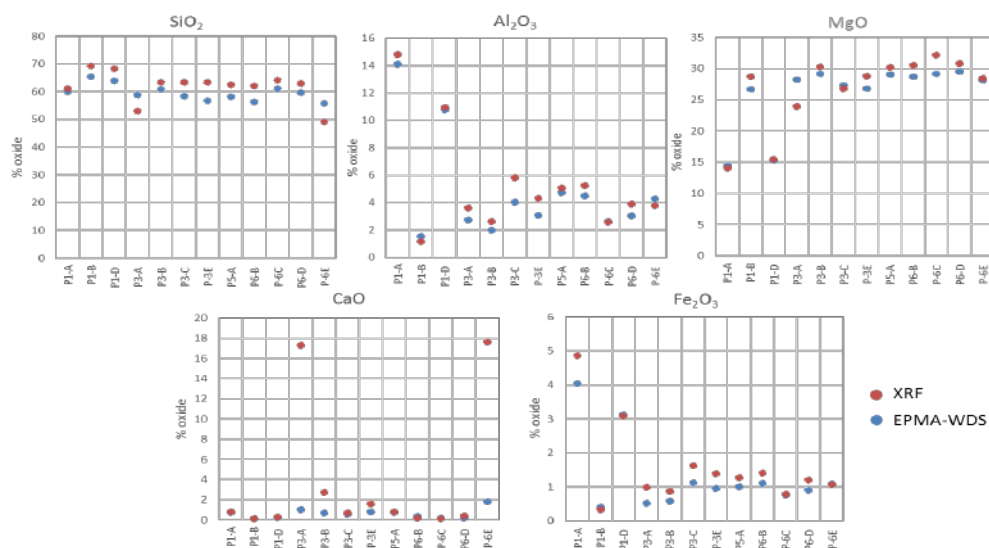


Figure 2 – Chemical analysis by XRF and EPMA-WDS.

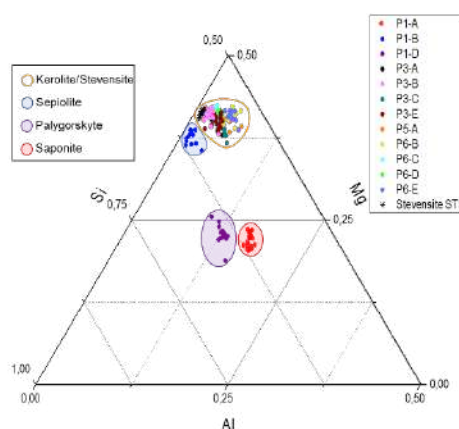


Figure 3 – Ternary diagram showing the separation stoichiometry ratio  $^{(IV)}\text{Si} + \text{Al}$  (*a.p.f.u*)  $\times$   $^{(VI)}\text{Mg}$  (*a.p.f.u*) of saponite (red), palygorskite (purple), sepiolite (dark blue) and the possible kerolite-stevensite samples (orange).

## Porosity Estimative of Tablets by Backscattered Electron Images

Camargo, Henrique<sup>1\*</sup>, Conceição Edemilson<sup>2</sup> and Gonçalves, Cristhiane<sup>3</sup>

<sup>1</sup>. Federal University of Goiás, Faculty of Pharmacy/Goiânia- Brazil.

<sup>2</sup>. Federal University of Goiás, Faculty of Pharmacy /Goiânia- Brazil.

<sup>3</sup>. Federal University of Goiás, Institute of Physics /Goiânia- Brazil

The therapeutic action of a drug is directly linked to the time it will be bioavailable for absorption. Thus, studying the factors that influence this bioavailability is extremely important, in order to ensure the effectiveness of the therapy[1]. One of these factors that alter the time of drug availability is the porosity of the tablet. This work aims to study the porosity of propranolol 40mg tablets by processing a set of backscattered electron images obtained from the tablets.

For the study, 40 mg propranolol hydrochloride tablets, submitted to the process of deposition of a conductive film and analyzed to a scanning electron microscope (SEM), JEOL 6610. Backscattered electron images were recorded with a voltage of 15 KV and a magnification of 350x. The images were acquired on the surface of the tablet and on its fracture. The degree of porosity was the value through an algorithm built using MATLAB® software.

Each one of these images is represented by a two-dimensional array, from a grayscale which pixels assumed 0-255 values, equivalent to its gray level. Once 0 value and 255 values correspond to the regions of darkest and highest brightness respectively. Therefore, the input image that was in grayscale (Figure 1) is converted into a binary image (Figure 2), where the dark regions represent the pores of the sample. The threshold level was obtained by Otsu's method [2]. The methodology was used for all images obtained from the sample, external surface and inner part (fracture). The data obtained were statistically treated in order to estimate the porosity of the propranolol 40 mg tablet.

### REFERENCES

- [1] Yassin, S., Goodwin, D. J., Anderson, A., Sibik, J., Wilson, D., Gladden, L., & Zeitler, J. The Disintegration Process in Microcrystalline Cellulose Based Tablets I.: Influence of Temperature, Porosity and Superdisintegrants. *Journal of Pharmaceutical Sciences*, 104 3440-3450.; 2015
- [2] GONZALEZ, R. C., Woods, R. E. "Digital Image Processing". Addison-Wesley Publishing Company, INC., 2001.

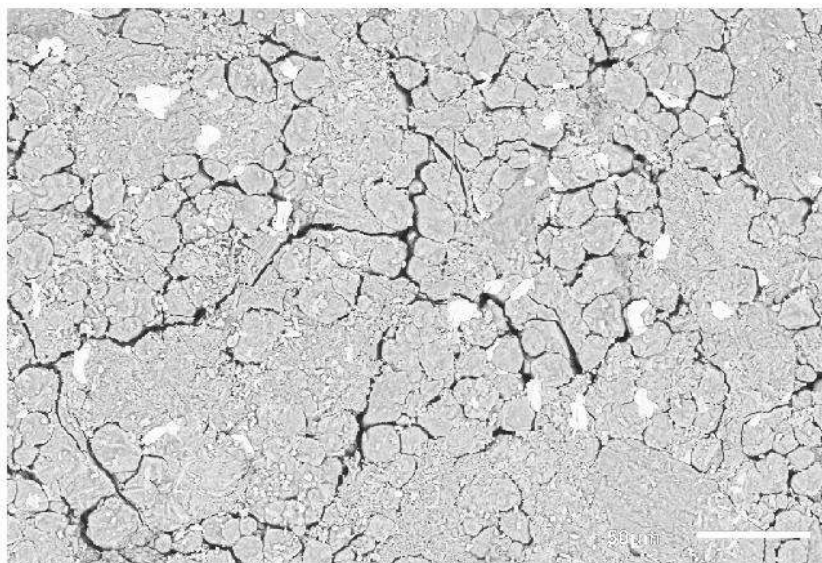


Figure 1 - Scanning Electron Microscopy Image by backscattered electrons

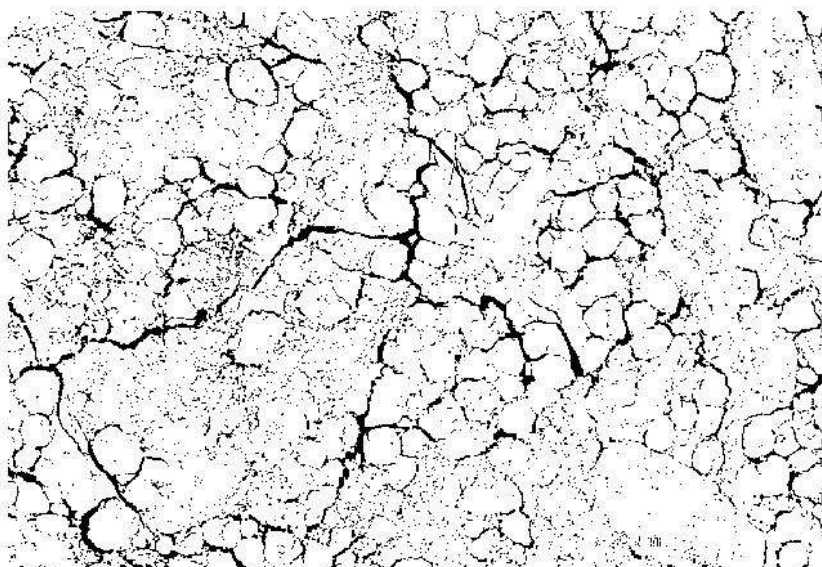


Figure 2 - Binary image corresponding to Figure 1, where the dark spots represent the pores.



## Silk fibroin hydrogels for potential applications in photodynamic therapy

**Jose Eduardo U. Rojas<sup>1</sup> (PG), Barbara B. Gerbelli<sup>1</sup> (PG), Anderson O. Ribeiro<sup>1</sup> (PQ), Iseli L. Nantes-Cardoso<sup>1</sup> (PQ), Francesca Giuntini<sup>2</sup> (PQ), Wendel A. Alves<sup>1\*</sup> (PQ)**

[joecullo@hotmail.com](mailto:joecullo@hotmail.com); [wendel.alves@ufabc.edu](mailto:wendel.alves@ufabc.edu)

<sup>1</sup>*Centro de Ciências Naturais e Humanas, Universidade Federal do ABC, 09210-580, Santo André, Brazil;* <sup>2</sup>*School of Pharmacy and Biomolecular Sciences, Liverpool John Moores University, Byrom Street, Liverpool, L3 3AF, UK.*

**Keywords:** *Porphyrin, fibroin, hydrogels, photodynamic therapy, crosslinking, rheology, singlet oxygen.*

### Abstract

The objective is to show the ability of hybrid porphyrin-fibroin hydrogels to generate singlet oxygen after gelification. Silk fibroin hydrogels demonstrate a distinct efficacy as matrices for incorporation of new functional molecules to the application in photodynamic therapy and photothermal therapy. In this study, we prepared translucent hydrogels with different concentrations of silk fibroin, extracted from raw silk fibers, and used them as a matrix to incorporate the photosensitizer 5-(4-aminophenyl)-10,15,20-tris-(4-sulphonatophenyl) porphyrin trisodium for application in photodynamic therapy (PDT). The hydrogels obtained were characterized by rheology, spectro- photometry, and scattering techniques to elucidate the factors involved in the formation of the hydrogel, and to characterize the behavior of silk fibroin (SF) after incorporating of the porphyrin to the matrix. The rheology results demonstrated that the SF hydrogels had a shear thinning behavior. In addition, we were able to verify that the structure of the material was able to be recovered over time after shear deformation. The encapsulation of porphyrins in hydrogels leads to the formation of self-assembled peptide nanostructures that prevent porphyrin aggregation, thereby greatly increasing the generation of singlet oxygen. Also, our findings suggest that porphyrin can diffuse out of the hydrogel and permeate the outer skin layers. This evidence suggests that SF hydrogels could be used as porphyrin encapsulation and as a drug carrier for the sustained release of photosensitizers for PDT<sup>[1]</sup>.

### References

- (1) Rojas, J. E. U.; Gerbelli, B. B.; Ribeiro, A. O.; Nantes-Cardoso, I. L.; Giuntini, F.; Alves, W. A. *Silk. Biopolymers* **2018**.

### Acknowledgements

This work was supported by FAPESP (grant nos. 2015/24018-1, 2014/18527-8 and 2017/02317-2) and CNPq (grant no. 302923/2015-2). INCT in Bioanalytics (FAPESP grant no. 2014/50867-3 and CNPq grant no. 465389/2014-7) are gratefully acknowledged for their grants. J.E.U.R. is grateful to CAPES for a doctoral fellowship. B.B.G. acknowledges FAPESP (project number 2018/05888-3) for a post- doctoral fellowship. FG acknowledges the FAPESP (project number 2014/50972-1) for a Newton Mobility grant. The staff at LNNano and LNLS are gratefully recognized for invaluable help and access to the SEM and SAXS facilities, respectively. Dr. Emerson Rodrigo da Silva (Biophysics Dept, UNIFESP) is kindly acknowledged for providing access and assistance during the circular dichroism experiments. The authors are grateful to the Multiuser Central Facilities at UFABC.



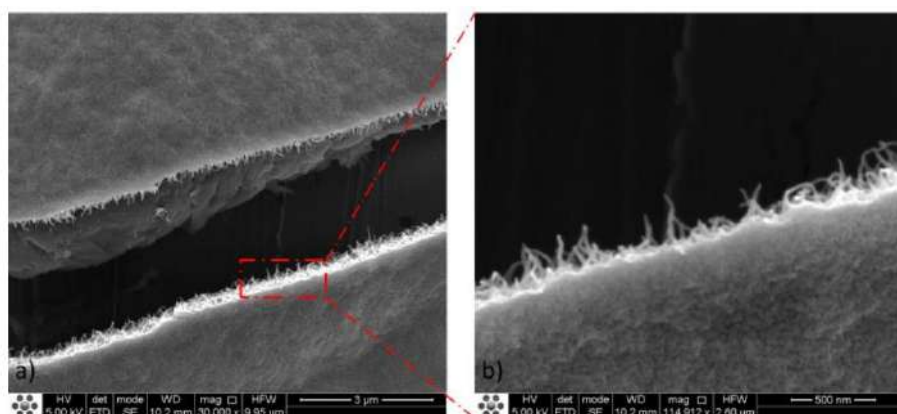


**Fig. 1-** SEM cross-section images of dry films formed from 7.5 mg mL<sup>-1</sup> SF. The results of the SEM analysis demonstrated the presence of interconnected fibers that form the structure of the fibroin film and hydrogels. The diameter of the fibers was approximately 37 to 40 nm.

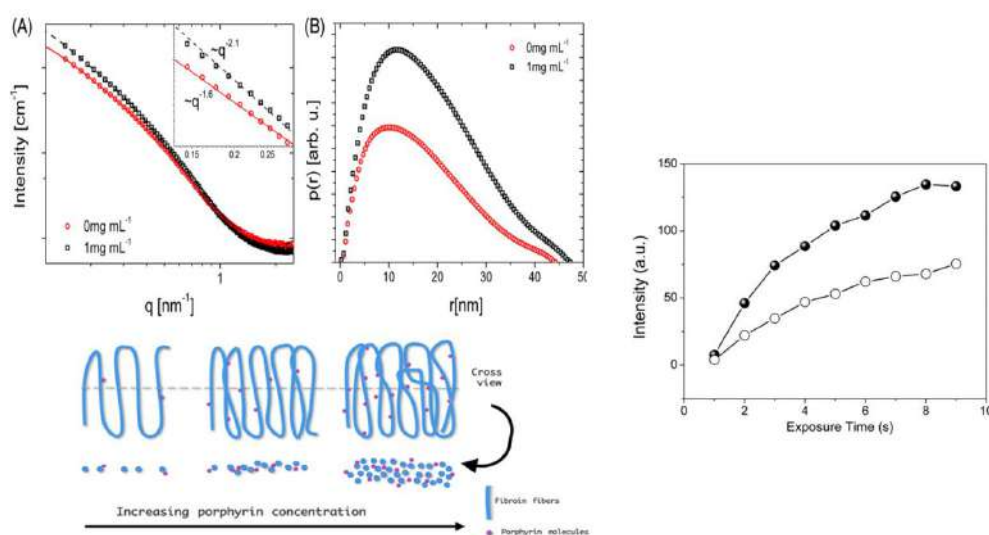


**Fig. 2-** (left) Fibroin/porphyrin hydrogels SAXS profiles of fibroin hydrogel with (black open symbols) and without (red circle symbols) porphyrin. and Schematic images (2D and 3D view) illustrating that increasing concentrations of porphyrin causes an increase of the radius of the fibroin fibers in the hydrogel. (Right) kinetic curve of generation of reactive oxygen species by using singlet oxygen sensor green (SOSG; Life Technologies, Carlsbad, CA) as the fluorescent probe for hybrid hydrogel (•) and porphyrin solution (o).



## Enhanced Oil Recovery Analysis via microCT

Kamila Scheffer Carlos<sup>1\*</sup>, Sidnei Paciornik<sup>1</sup>, Marcio da Silveira Carvalho<sup>2</sup>  
and Yves Méheust<sup>3</sup>

<sup>1</sup> Dept. of Chemical and Materials Engineering (DEQM), PUC-Rio, Rio de Janeiro, Brazil

<sup>2</sup> Dept. of Mechanical Engineering (DEM), PUC-Rio, Rio de Janeiro, Brazil

<sup>3</sup> Geosciences Rennes, Université Rennes 1, Rennes, France

[\\*kamila@lmmmp.mec.puc-rio.br](mailto:kamila@lmmmp.mec.puc-rio.br)

Enhanced oil recovery (EOR) methods are used to increase oil recovery from reservoirs beyond the limits of primary (5-10%) and secondary (15-45%) method [1]. The principle is to use emulsions to block pores in the porous rock that would otherwise allow the recovery fluid (typically water) to flow freely, leaving immobilized oil ganglia behind [2]. In the present work the microscopic behavior of EOR methods were tested and optimized in synthetic media, emulating porosity and permeability of real oil-bearing rocks [3, 4]. Such a medium was produced with sintered bi-disperse glass beads and microCT images (4  $\mu\text{m}$  voxel size) were acquired at different stages of fluid motion through the medium. Synthetic seawater with or without oil-water emulsion was used to recover oil previously saturating the pores, corresponding, respectively, to EOR and secondary methods. As water and oil present similar low x-ray absorption, the water was doped with KI to increase absorption and allow discrimination between the 2 fluids. Thus, 3D images showing the glass beads, doped water and residual oil presented a 3-modal pixel intensity histogram (Fig. 1a). After denoising with a non-local means filter (Fig. 1b), the images were segmented by manual thresholding (Fig. 1c) and the distribution of residual oil ganglia (Fig. 1d) was visualized, quantified and compared in the different stages (Fig. 2). Automatic 3D image registration was used to directly compare the oil ganglia after secondary recovery and EOR. Probability density functions of volumes ( $10^4$  ganglia spanning 8 orders of magnitude) show well-defined exponential behaviors for the displacement of oil by water, while the use of emulsions provides better recovery efficiency with larger numbers of larger ganglia.

## REFERENCES

- [1] ENGELKE, B., CARVALHO, M. S. and ALVARADO, V. Energy and Fuels, 27:1967–1973, 2013.
- [2] GUILLEN, V. R., CARVALHO, M. S. and ALVARADO, V. Transport in Porous Media, 1:197–206, 2012.
- [3] TIANSHOU, M. and PING, C. Petroleum Exploration and Development, 41:249–256, 2014.
- [4] FEALI, M. et al. SPE Reservoir Evaluation & Engineering, 15:706–711, 2012.
- [5] This research was supported by CNPq, CAPES and FAPERJ.

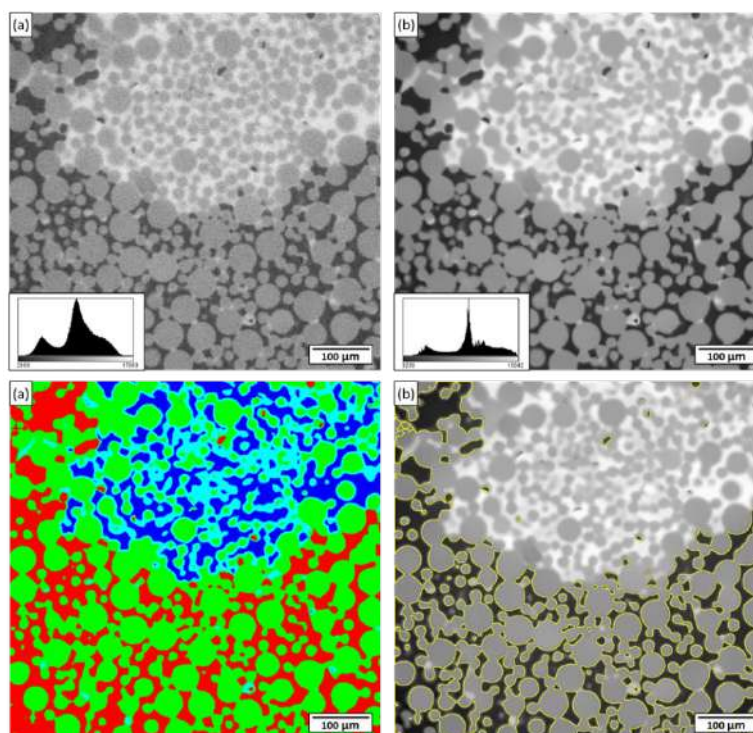


Figure 1 – Image processing sequence. a) One layer of the microCT image of the synthetic medium. Water is bright, glass is grey and oil is dark. b) Noise reduction with NLM filter. c) 3-phase segmentation. d) Residual oil ganglia outlined in yellow.

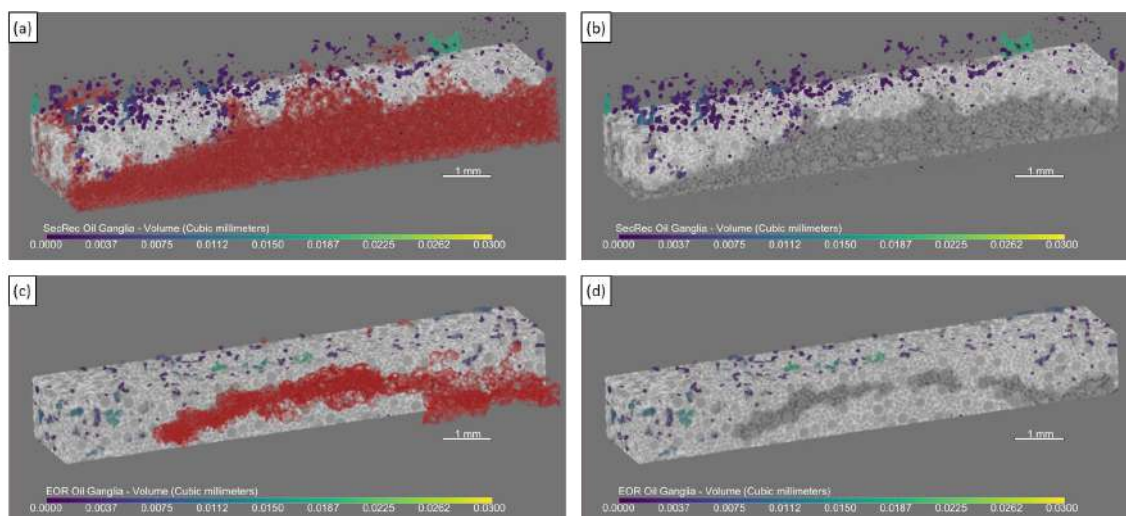


Figure 2 – 3D visualization and quantification of residual oil ganglia, color-coded by volume. Top row – Secondary recovery. Bottom row – EOR. a, c). The largest connected ganglion is shown in red. b, d) Largest ganglion hidden to reveal the remaining distribution.

## In-situ morphology and phase modifications in Ni/Bi bi-layers induced by changing deposition order

L.Y. Liu<sup>1\*</sup>, Y. T. Xing<sup>2</sup>, I. L.C. Merino<sup>1</sup>, I. G. Solórzano<sup>3</sup> and E. Baggio-Saitovitch<sup>1</sup>,

<sup>1</sup> COMAN, Centro Brasileiro de Pesquisas Físicas, Rio de Janeiro 22290-180, Brasil

<sup>2</sup> Laboratório de Microscopia Eletrônica de Alta Resolução, Centro de Caracterização Avançada para Indústria de Petróleo (LaMAR/CAIPE), Universidade Federal Fluminense, Niterói, 24210-346, Brasil

<sup>3</sup> DEQM, Pontifícia Universidade Católica do Rio de Janeiro, Rio de Janeiro, Brasil

\*lyliu.xing@gmail.com

Recently the Bi-Ni bi-layers attracted much attention of researchers due to the interesting superconducting properties in this system. The crystalline bismuth (Bi) and nickel (Ni) are not superconducting down to 50 mK [1]. However, if one deposit a Ni layer on top of a rhombohedral Bi layer or vice versa, the bi-layer becomes a superconductor [2]. There were many different interpretations, but no agreement has been reached up to date [3]. Our previous results show that Bi reacted with Ni spontaneously and forms BiNi and Bi<sub>3</sub>Ni during sample preparation by pulsed laser deposition (PLD) at room temperature [4]. The reaction is due to the higher energy of the atoms in PLD than other preparation methods. The possibility of spontaneous reaction between Ni and Bi is still an open question in other preparing techniques. In this work we studied Ni-Bi bi-layers prepared by sputtering at room temperature. Two samples, namely Bi<sub>40</sub>Ni<sub>4</sub> and Ni<sub>4</sub>Bi<sub>40</sub>, with 40 nm of Bi and 4 nm of Ni have been obtained with different deposition order. The morphology of the samples has been investigated by high resolution scanning electron microscopy (SEM) and high resolution transmission electron microscopy (HRTEM). From the SEM results (Fig. 1) one can see that Bi<sub>40</sub>Ni<sub>4</sub> sample has much less bright points on the surface than the Ni<sub>4</sub>Bi<sub>40</sub>. The high magnification images shows that the bright point on the surface are nanocrystals. HRTEM study confirmed that they are Bi<sub>3</sub>Ni nanoparticles. The cross-section images reveal that the first sample is still a flat layer and the second sample has a very thin continuous layer and most of the materials are formed Bi<sub>3</sub>Ni nanoparticles. A pure 4 nm Ni sample and 40 nm Bi sample has been prepared and both of them have very flat surfaces. It indicates that the reaction occurred spontaneously during sample preparation and the reaction rate depends on the deposition order. Depositing first Ni and then Bi leads to much more Bi<sub>3</sub>Ni nanoparticles. Both of the samples are superconducting with  $T_c \sim 4.0$  K [5].

### References:

- [1] Behnia, et al. Signatures of electron fractionalization in ultra-quantum bismuth. *Science*, 317(5845):1729– 1731, 2007.
- [2] Esaki et al. Study of electronic band structures by tunneling spectroscopy: Bismuth. *Phys. Rev. Lett.*, 14:902–904, May 1965.
- [3] Gong et al. Possible p-wave superconductivity in epitaxial Bi/Ni bilayers. *Chinese Physics Letters*, 32(6):067402, 2015.
- [4] Liu, et al. Superconductivity in Bi/Ni bilayer system: Clear role of superconducting phases found at Bi/Ni interface. *Physical Review Materials* 2, 014601, 2018.
- [5] This research was supported by CNPq, FAPERJ and CAPES (Brazil). The authors thank LaMAR/CAIPE at UFF and LABNANO at CBPF for use of the facilities.



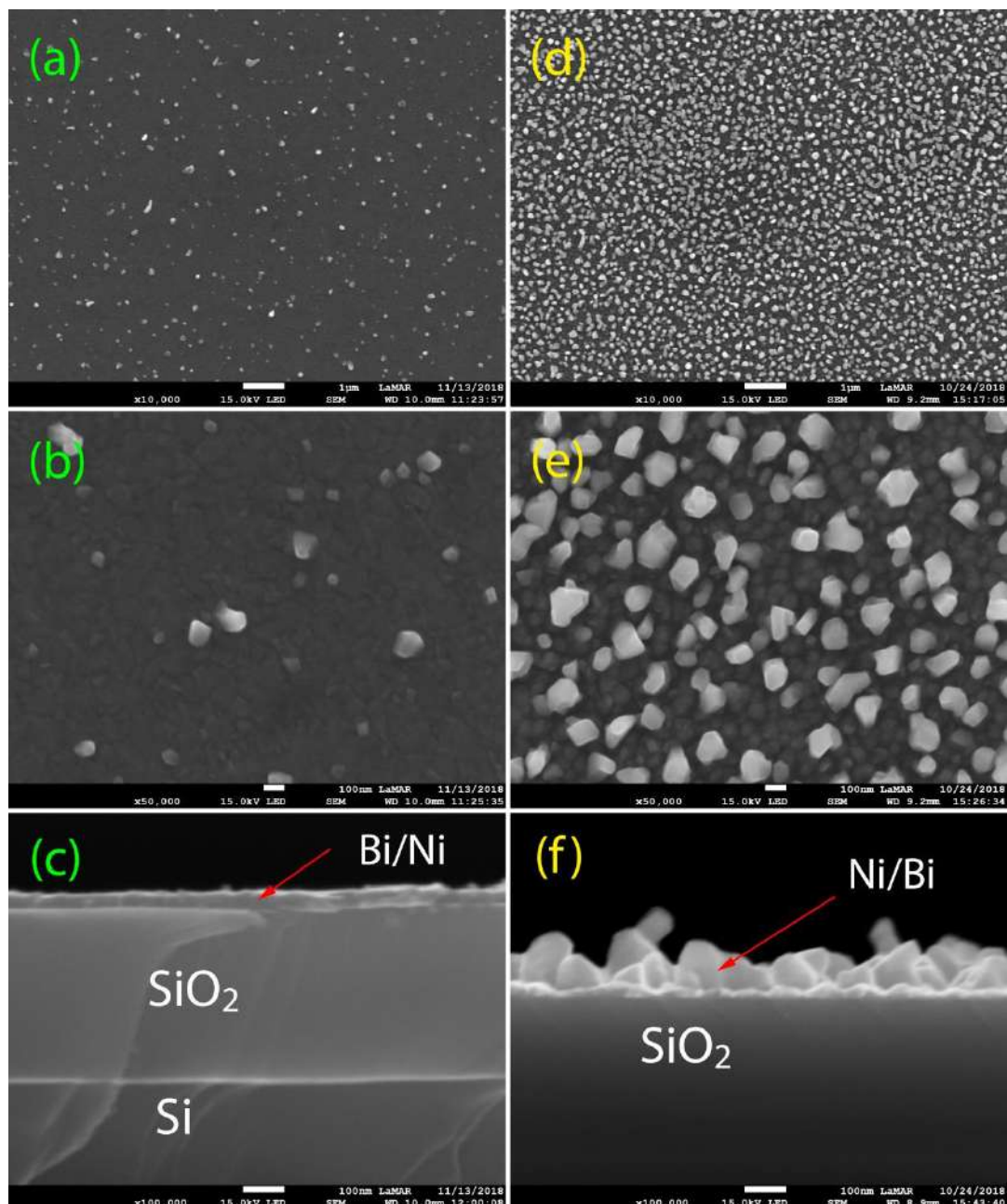


Figure 1. (a) Low magnification, (b) high magnification and (c) cross-section SEM images of Bi-Ni bi-layers with the deposition of Bi first and then Ni. (d) Low magnification, (e) high magnification and (f) cross-section SEM images of Ni-Bi bi-layers with the deposition of Ni first and then Bi.

## Morphological and Chemical Characterization of Sugarcane Bagasse and Straw Pellets with and without extractives using SEM/EDS

Silva, L. L.<sup>1\*</sup> and Palma, K. R.<sup>1</sup>

<sup>1</sup>UNICAMP, School of Chemical Engineering, Campinas, Brazil. \*lils@unicamp.br

### TEXT:

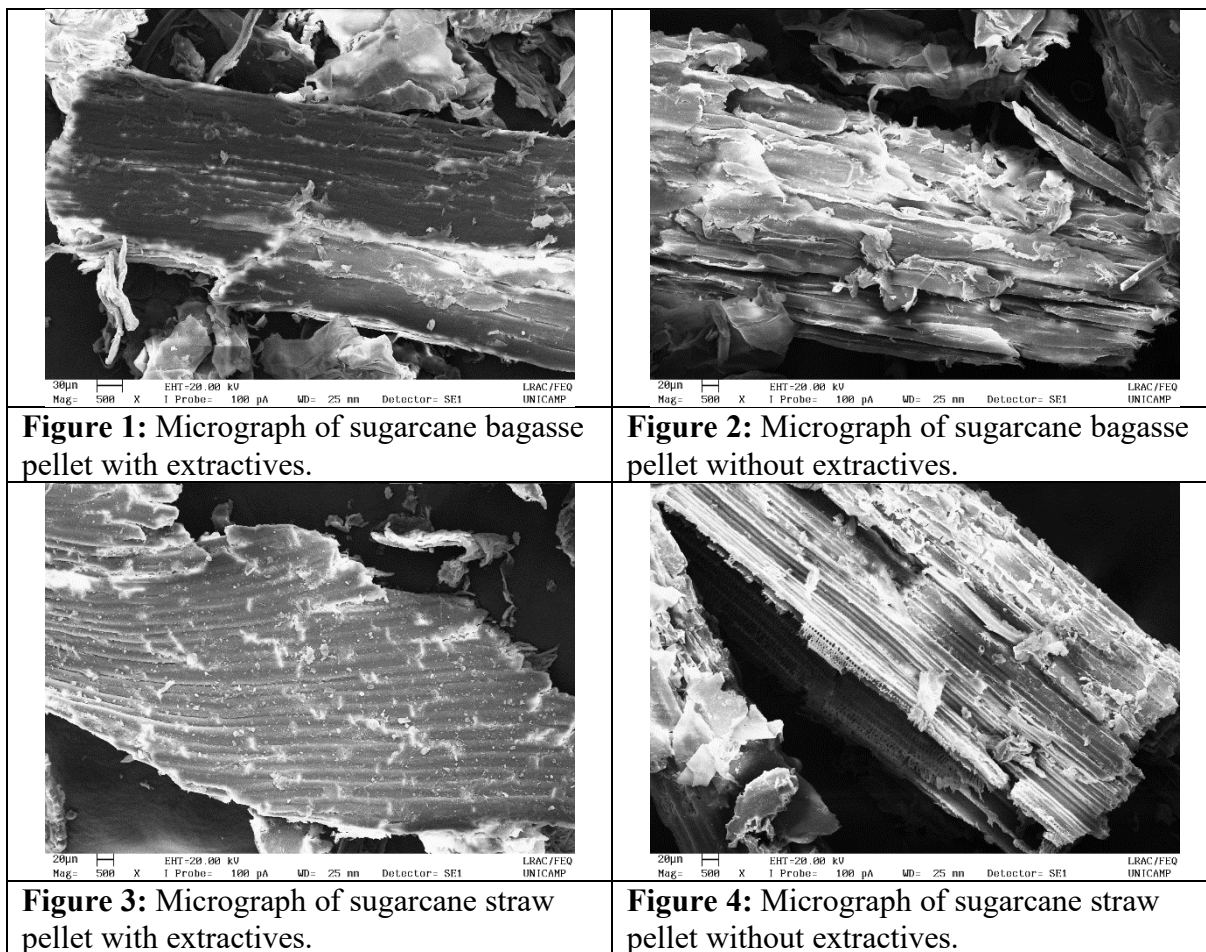
Residues from sugarcane cultivation and from the sugar and alcohol production, bagasse and straw, have been considered a biomass with great potential to energy generation, therefore the study of their structural composition, immediate and proximate analysis are fundamental to knowledge of their fuel properties. Vegetable biomass is formed through photosynthesis reactions that produce plant fibers forming the natural polymers, including cellulose, hemicellulose and lignin. The vegetable fibers are constructed by the cellulose maintained by a matrix of lignin and hemicellulose, also by extractives and inorganic components [1], extractives are non-structured nonpolymer composition of biomass that could affect structural analysis and they need to be removed prior experimentation [2]. Samples of sugarcane bagasse and straw pellets were used in this study, for the structural analysis the samples were grounded in a knife mill (Marconi), separated in 0.84 mm sieves, their moisture was known and the extraction following NREL method [3], that is a two step extraction process, was performed in soxhlet system initially by ethanol/cyclohexane (1:1), to remove the organic soluble material, followed by water to remove water soluble material, the whole process for removal of the extractives lasted for about a week. The aim of this work was to study possible morphological and chemical differences in the interest biomass after the extractive removal process. Scanning Electron Microscopy (Leo 440i Zeiss) and Elementary Analysis by EDS (Oxford) were used to characterize chemical and morphologically the sugarcane bagasse and straw pellets before and after the process of organic and water extraction. The images to morphological observations show that the fibers of the biomass underwent slight modifications and the chemical analyses show that the potassium salts present initially were removed, being this more pronounced in the sugarcane straw pellets.

### REFERENCES

- [1] R. Silva et al, Química Nova 32 (vol. 3) (2009) 661-671.
- [2] NREL/TP-510-42618, 2012.
- [3] NREL/TP-510-42619, 2008.

## RESULTS

The micrographs obtained for morphology evaluation are presented in Figures 1 to 4.



The results obtained with the elemental microanalysis are summarized in Table 01.

**Table 01:** Elemental microanalysis of sugarcane bagasse and straw pellets.

Element	Sugarcane bagasse pellets		Sugarcane straw pellets	
	With extractives	Without extractives	With extractives	Without extractives
C*	47,47	44,98	41,90	45,37
O*	51,92	54,18	53,10	53,38
Mg	-	-	0,19	-
Al	0,17	0,27	0,86	0,30
Si	0,26	0,28	1,62	0,54
Cl	-	0,02	0,20	-
S	-	-	0,15	-
P	-	0,02	-	-
K	0,11	-	0,65	-
Ca	0,05	0,20	0,42	0,21
Fe	0,03	0,05	0,91	0,21
Average data standardized at 100% and expressed as mass %				
(*) Not properly quantified by the EDS detector.				



## **TiO<sub>2</sub> rutile doped with iron obtained by direct chlorination methods: Microanalytical characterization**

\*L.M.Cáceres<sup>1</sup>, E. Brocchi<sup>2</sup>, I.G. Solorzano<sup>3</sup>

\*<[ludymargaritacm@gmail.com](mailto:ludymargaritacm@gmail.com)>

Department of Chemical and Materials Engineering, PUC-Rio, Rio de Janeiro, Brazil.

The properties of TiO<sub>2</sub> as photo catalyst are well known [1]. However, for specific applications it is required to achieve a higher spectral sensitivity. For scale production, therefore, it is highly convenient to, develop processes where, starting from raw TiO<sub>2</sub>, a material with improved spectral properties can be obtained [2]. On the other hand, it is also known that chlorination processes is quite efficiently used in the chemical treatment of low grade minerals aiming at obtaining highly graded materials. Over the course of our chlorination studies it was found that, when processing ilmenite at high temperatures, it is possible to obtain, as a solid granular product, structures rich in titanium oxides doped with iron. Given the nature of the precursor mineral it is possible that in the resulting structure there are substitutions coming from aluminosilicates present in the raw material. Both the raw material used for this study and the resulting product were analyzed by means of X ray diffraction (XRD), scanning electron microscopy (SEM), operating in both secondary electrons (SE) and Back scattered electrons (BSE) and X Ray fluorescence (FRX) techniques. A typical XRD spectrum of the raw material is shown in Figure 1, display the dominance of Ilmenite mineral. Figures 2 and 3 are BSE-SEM and SE-SEM images of the row material. With this objective in mind, the viability of the process was analyzed, with the support of previous thermodynamic calculations, to evaluate both the selectivity of the chlorination process with the iron and titanium oxides of the ore, as well as the temperatures suitable for processing it. As a result, a material rich in titanium oxides was obtained (Fig. 4) with the presence of iron in the structure. It was observed that the majority of iron ions are inserted in the crystalline structure of TiO<sub>2</sub> in the rutile phase, presumably occupying some of the Titanium sites or located in the interstices of the crystalline network [3]. So one may expected to obtain greater activity in the UV-Visible region [4], upon obtaining changes in both the morphology and crystalline structure/defects of the material. In the set of Figures below, we present the evidence of the changes in the morphology of the mineral structure throughout the chlorination reaction, as well as in the subsequent calcination. During the chlorination, a selective attack to the iron oxides was noticed, as expected from thermodynamic predictions, however, even in the final structure, remnants are observed that give rise to the effect of doping.

### References:

- [1] P. Wang. et. al. Journal of Alloys and Compounds, Vol 780, (2019), (Pg 660-670)
- [2] M. Castañeda-Juárez, et. al. Journal of Photochemistry and Photobiology A: Chemistry, Vol. 380. (2019), 111834
- [3] C. E. Rodriguez Torres, et. At. Physica B, Vol. 354, (2004), (Pg. 67–70)
- [4] S.Wang et. al. Applied Surface Science. Vol. 263, (2012), (Pg 260-265).

### Acknowledgements

The authors are grateful to Labnano-CBPF, Rio de Janeiro, for access to the electron microscopes and to CAPES and CNPq (Brazil) for financial support



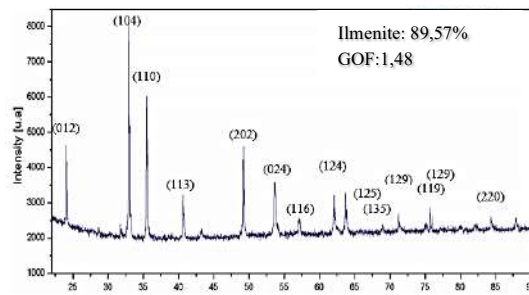


**Figure 1.** XRD spectrum of the raw material

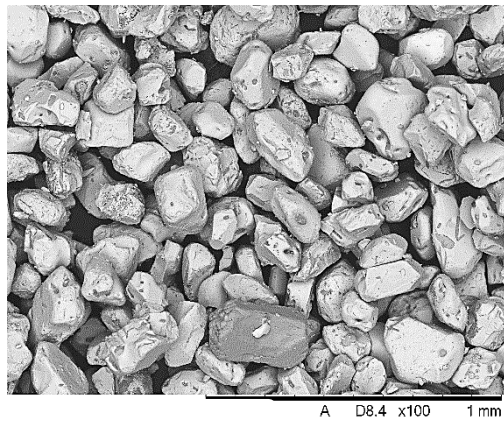


**Figure 2.** BSE-SEM of the raw material.

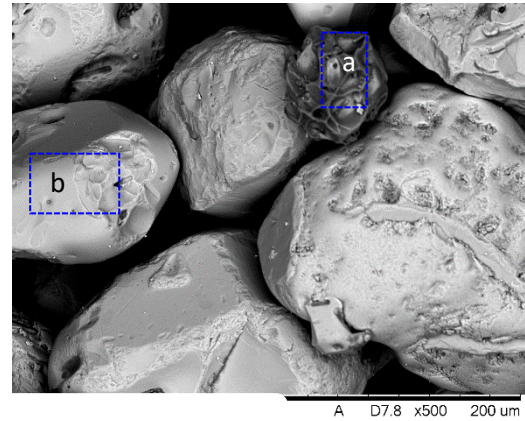


**Figure 3.** SE -SEM of the raw material, a) particles rich in Ti, b) particles rich in Si.

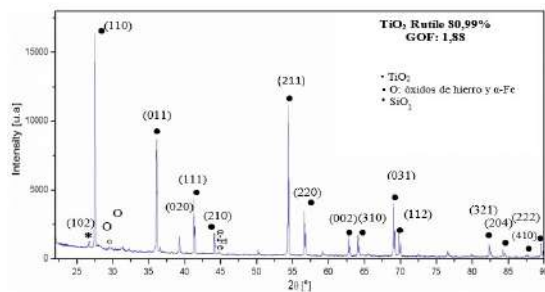


**Figure 4.** XDR of the material obtained

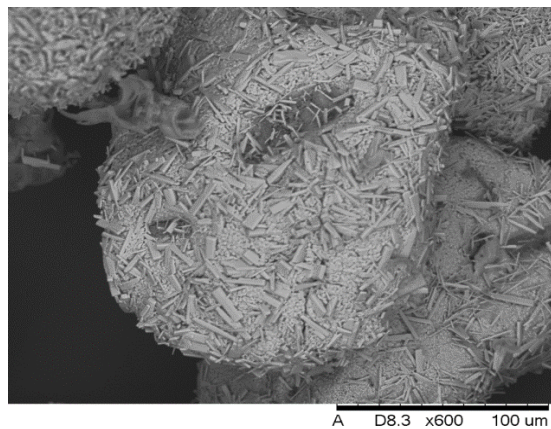


**Figure 5a.** SE-SEM of the material obtained,



**Figure 5b.** SE-SEM of the material obtained

**Table 1.** FRX results of the raw material.

FeO (%)	Fe <sub>2</sub> O <sub>3</sub> (%)	TiO <sub>2</sub> (%)	SiO <sub>2</sub> (%)
58,57		32,66	5,14

**Table 2.** FRX of the material obtained

FeO (%)	Fe <sub>2</sub> O <sub>3</sub> (%)	TiO <sub>2</sub> (%)	SiO <sub>2</sub> (%)
17,45		74,10	7,23

## Microanalysis of Saddle Dolomite in Hydrothermal Breccia from Mina Rio Bonito - Campo Largo (PR-Brazil)

Murilo Henrique T. Camargo<sup>1\*</sup>, André Davi Ferreira<sup>1</sup>, Janaína P. Duarte<sup>1</sup>, Alberto C. Botelho<sup>1</sup>, Cristina V. Pinto-Coelho<sup>1</sup>, Rafaela Larissa da Cunha Rocha<sup>1</sup>, Marcos Henrique de Pinho Mauricio<sup>2</sup>, Karen Soares Augusto<sup>2</sup>, Eduardo Roemers-Oliveira<sup>3</sup>

<sup>1</sup>Dept. of Geology/Universidade Federal do Paraná (UFPR), Curitiba, Brazil.

<sup>2</sup>Dept. of Chemical and Materials Engineering/PUC-Rio, Rio de Janeiro, Brazil.

<sup>3</sup>PETROBRAS

\*muriloht.mc@gmail.com

Hydrothermal dolomitization associated with fracturing and brecciation is widely cited in the literature as the generative of discontinuity in rocks, contributing to the fluid percolation and hydrocarbons migration. In this context, saddle dolomite (SD)<sup>[1]</sup> of hydrothermal breccia in Rio Bonito Quarry (Campo Largo - PR) was analyzed using different analytical techniques as an analog study of dolomitized and brecciated carbonate reservoirs. The dolomitic breccia (Fig.1A) is composed of fragments of marble, cemented by distinct textural types of carbonates, being the SD the last phase void-filling. Under the optical microscope, it shows spearhead shape, turbid axial zone and exsolution of goethite on the cleavage surfaces (Fig.1B). Scanning electron microscopy in backscattered electron (SEM-BSE) imaging shows core-edge structures, where the core is divided into the inner core and the outer core; in the transition to the edge, it's possible to notice intracrystalline porosity. Analysis in optical cathodoluminescence (CL) (Fig.1D) shows dark red color in weakly luminescent edges and outer and inner cores with intense orange to reddish orange luminescence, arranged roughly alternate, coinciding with the presence of calcite; the zoning in the outer core coincide with portions in the crystal where there is exsolution of goethite. The CL spectrum shows an emission band of 637nm, with strong intensity (6.000cps), indicating the presence of Fe<sup>3+</sup> [2]. The porosity in dolomitic breccias is classified as of vuggy type, with enlarged pores and larger cavities associated with SD. A 3D characterization of breccia blocks was performed using the X-ray microtomography ( $\mu$ CT) followed by a sequence of digital image processing (Fig.1F). This analysis allowed to estimate the total porosity between 0.41 to 1.03% of the volume, where the highest value is associated with SD. The space opened by the hydraulic fracturing allied to dolomitizing fluids functioned as an important geological scenario for the generation of secondary porosity.

### REFERENCES

- [1] J. Warren, Dolomite : occurrence, evolution and economically important associations, *Earth Science Reviews*, 52 (2000), p. 1–81.
- [2] C.M. MacRae & Wilson N. C., *Luminescence database I-minerals and materials. Microscopy and Microanalysis*, 14 (2008), p. 184-204.
- [3] This research was funded by PETROBRAS (Grant ID 0050.0101319.16.9)/ANP.
- [4] The authors also would like to thank Companhia de Cimentos Itambé and DEGEOL / LAMIR / CME-UFPR for the support.



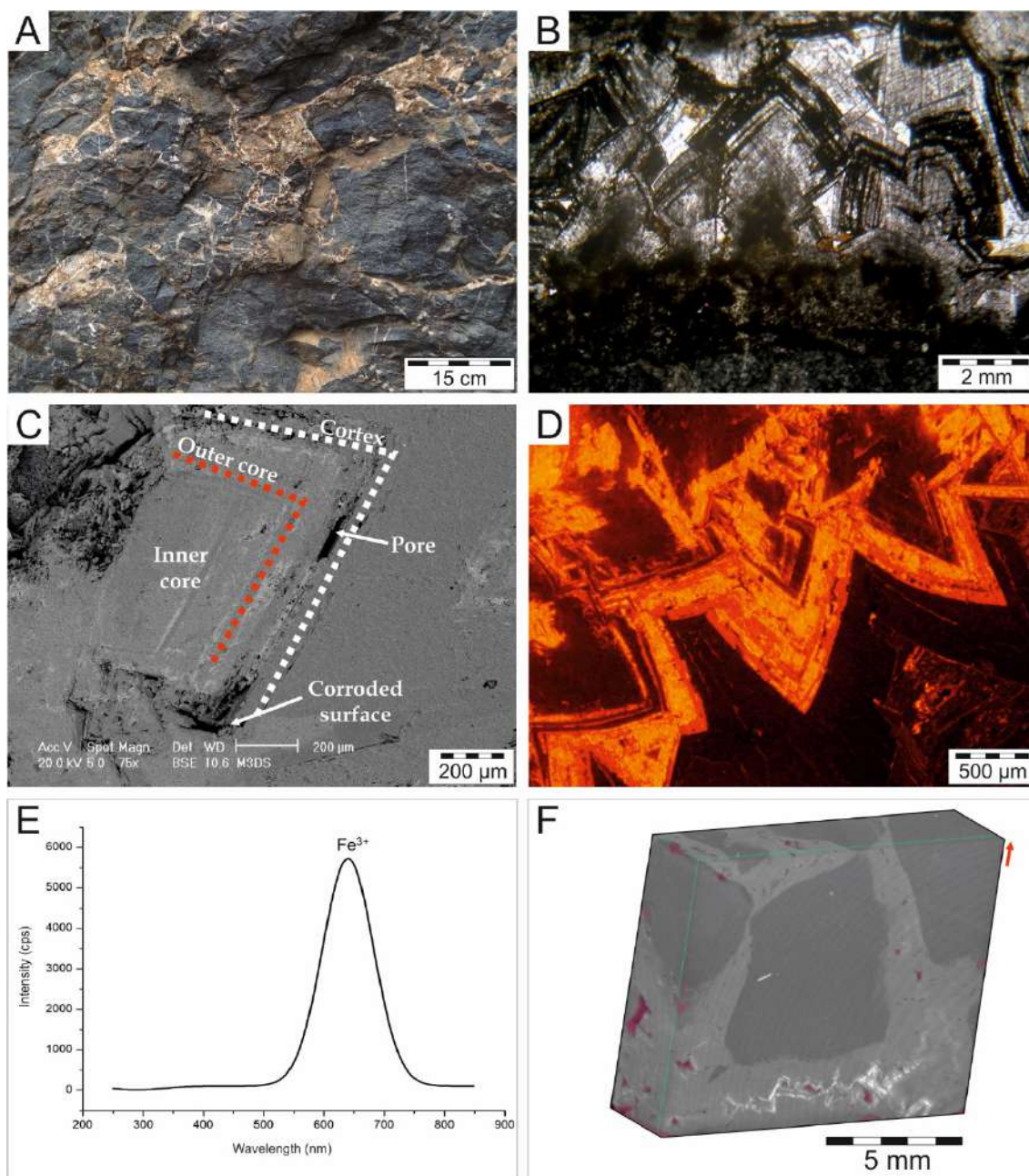


Figure 1 - (A) Macroscopic aspect of dolomitic breccia with marble fragments. (B) Saddle dolomite with characteristic spearhead shape, turbid aspect and exsolutions of goethite. P//. (C) SEM-BSE image from saddle dolomite showing edge and core (inner and outer) structures. Note the presence of pore in the transition core-edge and corrosive surface. (D) CL from saddle dolomite with a weakly luminescent edge, dark red color, and core with strong orange to reddish-orange luminescence. (E) CL spectrum. (F) 3D  $\mu$ CT image where it is possible to observe the presence of pores (reddish portions) associated with saddle dolomite. Shiny parts correspond to goethite.

## Overcoming Challenges Associated with Microscopy Image Acquisition of Geopolymers

Maria D. M. Paiva<sup>1</sup>, Otávio F. M. Gomes<sup>2\*</sup>, Carla R. Moreira<sup>3</sup>, Mauricio M. Paiva<sup>3</sup>, Raphael V. Curti<sup>4</sup>  
Braulio S. Archanjo<sup>5</sup>, Reiner Neumann<sup>2</sup>, Romildo D. Toledo Filho<sup>1</sup>

<sup>1</sup> UFRJ, ninanatal@gmail.com , toledo@coc.ufrj.br , <sup>2\*</sup> CETEM, ogomes@gmail.com ,  
rneumann@cetem.gov.br , <sup>3</sup> INT, carla.ramos@int.br , mauricio.paiva@int.gov.br ,  
<sup>4</sup> INMETRO, rvcurti-prometro@inmetro.gov.br , bsarchanjo@inmetro.gov.br

Scanning electron microscopy (SEM) is a well established technique usually employed as a complementary tool to confirm the morphology and microstructure of materials. There are, from conventional to ultra-high technological microscopes, that enable images acquisition of a wide range of materials. Nanostructured ceramics, such as geopolymers, have inherent characteristics that make SEM image acquisition difficult, such as high porosity, demanding long times to reach optimum vacuum conditions, in order to obtain SEM images at the nanometric scale. Ceramics materials also exhibit insulating characteristics, independently if a solid or powder is used, charging at the sample surface that can induce to a distorted morphology and wrong microstructure interpretation [1]. Geopolymers are inorganic polymers composed of silicate and aluminate tetrahedra linked by shared oxygen atoms and stabilized by cations such as Na<sup>+</sup> or K<sup>+</sup>, and can be designed to replace Portland cement in oil well cementing operations. When synthesized at room temperature, they are composed of a dense and predominantly amorphous matrix, leaving a homogeneous footprint at macro and lower nanoscales. So, there is a scale range, from sub-micro to nano, where the geopolymer morphology and nanostructure are a challenge to characterize due to their intrinsic porosity and small agglomerated matrix particles [2, 3]. This work presents typical geopolymer SEM images obtained from different electron microscopes: **SEM-FEG JEOL JSM-7100TF**, **SEM-FIB FEI HELIOS Nanolab DualBeam G3 CX** and Zeiss **FIB-HIM Orion NanoFab** Helium ion microscope, using distinct sample preparations (fractured, flat solid and powder) and acquisition techniques, as summarized on Figure 1. The aim of this study is to highlight the main challenges and limitations observed in each case, and discuss approaches adopted to mitigate them. Micrographs acquisitions from solid and powder samples without metallization, using SEM-FEG, SEM-FIB and FIB-HIM microscopes, were difficult due to the surface charging and damage caused by electron beam interaction with the sample surface [4]. Three available types of sputtering were assessed: a 20 nm Au, 5 nm Pt-Pd and a higher one with about 15 nm of Pt, followed by painting the supported sample edges with silver tint. In both cases, the metallization seems to mask the morphology and the porous nanostructure of the material. Best results were achieved without metallizing powder geopolymeric samples, investigating them over a carbon tape and acquiring images in a HIM, equipped with a secondary electron detector and operated at 30 kV accelerating voltage. An electron flood gun was used in order to neutralize surface charging, as the samples have insulating characteristics.

[1] Nikolov, A. et al. *Case Studies in Construction Materials*. 2017; 6:198-205.

[2] Kriven, W.M. Geopolymer-based composites. In *Comprehensive Composite Materials II*; Oxford Academic Press: Oxford, UK, 2018; Vol 5, pp. 269–280.

[3] Paiva, M.D.M. et al.. *Journal of Petroleum Science and Engineering*. 2018; 169:748-759.

[4] Kim, K.H. et al. *Materials Transactions*. 2010; 51:1080-1083.



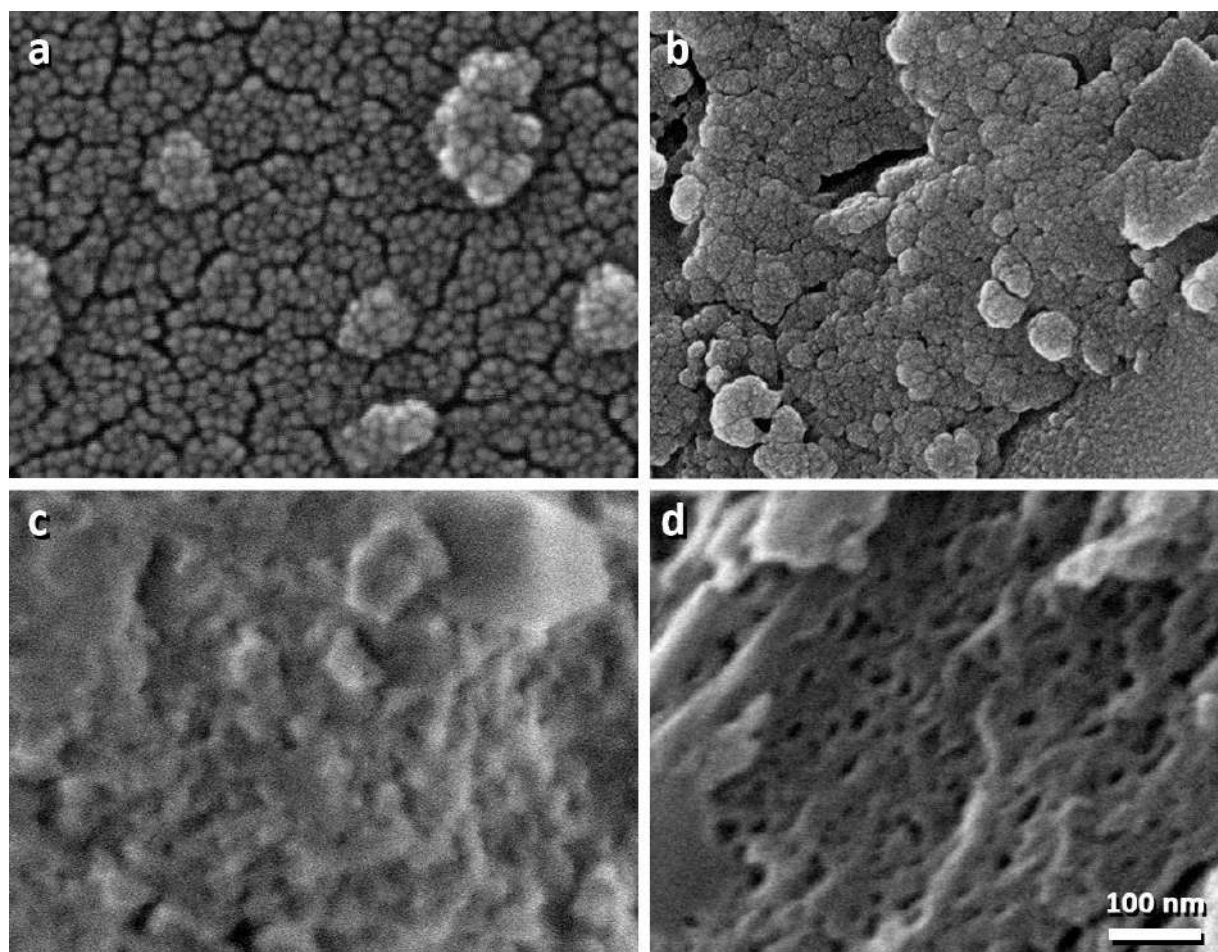


Figure 1 – Surface of a porous geopolymer using different imaging techniques and sample preparations: a) Sample with 20 nm Au conductive coating in a SEM-FEG, b) Sample with 15 nm Pd conductive coating in a SEM-FIB, c) Sample with 5 nm Pt-Pd conductive coating in a SEM-FEG and d) Sample free of coating in a FIB-HIM. All images are at the same scale.

## Scanning Electron Microscopy - Assistant Technique In The Preparation Of Fluorescence Carbon Dots On Silica Gel

Albina Mikhralieva<sup>1</sup>, Volodymyr Zaitsev<sup>1</sup>, and Michael Nazarkovsky<sup>1\*</sup>

<sup>1</sup>. Chemistry Department, Pontifical Catholic University of Rio de Janeiro, 225 Marquês de São Vicente Str., 22435-900 Rio de Janeiro, RJ, Brazil (nazarkovsky\_m@esp.puc-rio.br)

Carbon Dots (CDs) are luminescent nanoparticles with size smaller than 10 nm [1]. CDs have been successfully used for different purposes, such as analytical sensing, bio-imaging, drug delivery and photocatalysis. However, the low quantum yield (QY of less than 10%) might limit their optical applications in practice. Surface functionalization of CDs with different chemical groups may enhance the photoluminescence. Doping with heteroatoms as nitrogen, in particular, has shown a great potential to improve significantly the quantum yield of CDs up to 80% [2]. Until now, structure, composition and photo-physics of CDs are not fully understood. Carbon source and synthesis conditions are crucial criteria of fabrication of carbon dots. Several synthesis approaches have been applied to obtain CDs and they can be divided into two groups “top-down” and “bottom-up” [3]. Not all these methods can assure high reproducibility and scale-controlled final product. A possible key to obtain a homogeneous material is to employ a porous and thermal-resistant nanoreactor able to confine the growth and shape of carbon nanoparticles. For this reason, in the present work combination of a traditional preparation method of CDs with pyrolysis of citric acid (CA) in a size-limiting reactor was used to overcome these difficulties. Nanoporous silica gel is a suitable material to achieve that since it has a monomodal pore size distribution varying in the range from 2 to 15 nm and has high thermal and chemical stability. As the morphology of silica matrix cannot be seen by the naked eye, scanning electron microscopy (SEM) technique is required to observe surface behavior of our products.

Occurrence of CDs in silica matrix was provided by conventional pyrolysis of adsorbed CA through molecular dehydration of CA and further carbonization. The complete adsorption of CA from aqueous solution by silica gel (SiO<sub>2</sub>@CA) under selected experimental conditions was observed. However, to ensure the removal of the CA excess from interparticle space, the samples of SiO<sub>2</sub>@CA were washed out with diethyl ether. After drying under vacuum, the non-washed SiO<sub>2</sub>@CA produced compact glued agglomerate, while the SiO<sub>2</sub>@CA washed in ether has turned to be as a loose powder as pure silica gel. The SEM images confirm difference in SiO<sub>2</sub>@CA particles, depending on the post-treatment procedure. Small crystals of CA can be clear seen on as-prepared SiO<sub>2</sub>@CA (Figure 1a), while surface of ether-washed samples is clean (Figure 1b). These data prove that removing of CA excess from the particle surface, before thermal treatment, is essential to prepare better quality CDs using nanoreactors.

The SEM instrumentality enables selecting an improved stage of the sample preparation for the SiO<sub>2</sub>@CA composites to prevent formation of graphitized CDs product on outer part of silica.

[1] S. Zhu, et al., Nano Res. 8 (2015) 355.

[2] S. Zhu, et al., Angew. Chemie - Int. Ed. 52 (2013) 3953.

[3] L. Bao, et al., Adv. Mater. 23 (2011) 5801.

[4] This research was supported by CNPq, project PQ-2018 306992/2018-3 (Brazil).

[5] The microscopy study was performed at LABNANO, CBPF (Rio de Janeiro, Brazil).

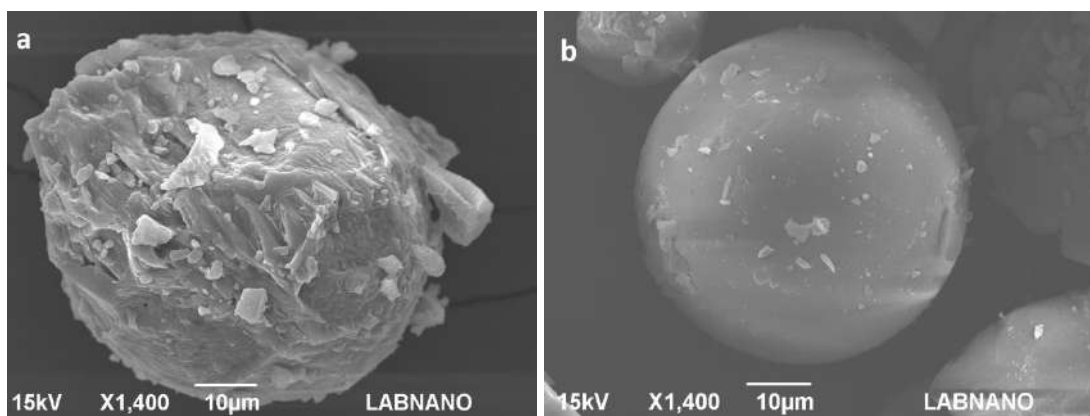


**Fig. 1.** The SEM images of citric acid-containing as-prepared (a) and washed in ether (b) silica gel sample.

## Titanium Inner Coating Of Narrow Alumina Tubes By DC Magnetron Sputtering

Osmar Roberto Bagnato<sup>1,3\*</sup>, Rafael Defavari<sup>1</sup>, Fernanda Regina Francisco<sup>1</sup>, Daniel Yukio Kakizaki<sup>1</sup>, Felipe Eduardo Manoel<sup>1</sup>, Patricia Mendonca Pimentel<sup>2</sup>, Roberta Martins da Costa Bianchi<sup>3</sup>

<sup>1</sup>. Laboratório Nacional de Luz Síncrotron, Grupo de Materiais, Campinas - Brasil.  
Email para correspondência: [rafael.defavari@lnls.br](mailto:rafael.defavari@lnls.br); <sup>2</sup> UFERSA, <sup>3</sup> USF.

Titanium films were deposited on alumina 96% narrow tubes via DC magnetron sputtering. These tubes will be used as vacuum chambers on the new Brazilian synchrotron accelerator Sirius, and its metallic coating will have an important role liberating static charges during the electron beam travel [1]. Elliptical inner shapes with 9,5mm gap and 500mm long alumina tubes were successfully coated using argon plasma and a 2mm diameter Ti wire as cathod by DC magnetron sputtering. The final resistance of the tube was monitored during the process in order to achieve its required electrical property, and the samples have been investigated by Scanning Electron Microscopy (SEM JEOL 5900LV / FEI Quanta 650 FEG) to determine film thickness along the inner section and length of the tube. Different thickness of Ti layer were observed at different points across the perimeter of the chamber. In this contribution, we present the results of a development aimed at coating these narrow and long ceramic vacuum chambers with a uniform surface resistivity across the length by a dedicated DC magnetron sputtering configuration.

### References:

[1] A.R.D. Rodrigues et al., "Sirius light source status report", in 9th International Particle Accelerator Conference (IPAC 2018), Vancouver, BC, Canada, paper THXGBD4, pp. 2886-2889.

### Acknowledgements:

Laboratório Nacional de Nanotecnologia, Rafael Molena Seraphim, Ângelo Luiz Gobbi.



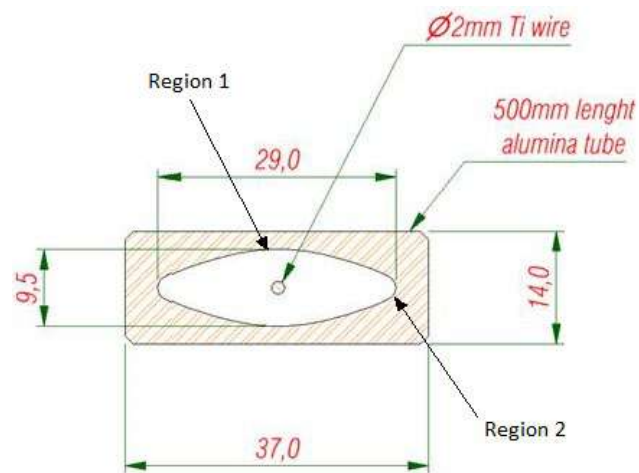


Figure 1. Cross section of the alumina tube - cathode / substrate schematics (dimensions in mm)

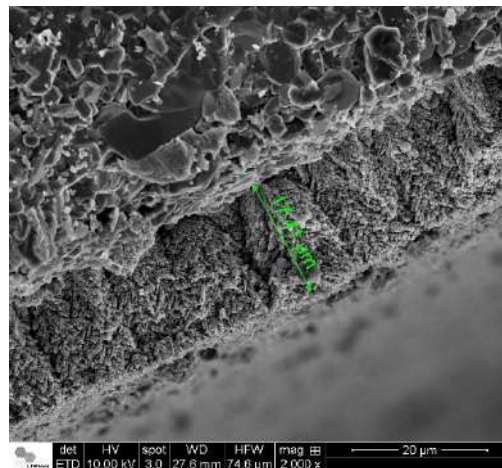


Figure 2. SEM image of Ti layer on alumina substrate measured at region 1.

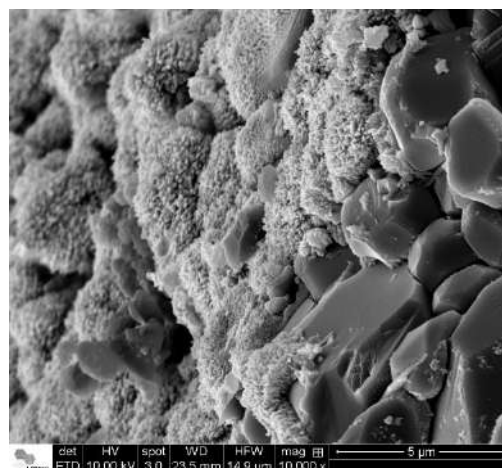


Figure 3. SEM image of Ti layer on alumina substrate at region 2.

## Comparative study of surface treatments in polytetrafluoroethylene (PTFE) for application in Guided Bone Regeneration

Paula Anastácia Moraes Cairo Gomes<sup>1\*</sup>, Emília dos Santos Monteiro<sup>1</sup>, Francielly Moura de Souza Soares<sup>1</sup>, Luíza Braga dos Santos<sup>1</sup> and Carlos Nelson Elias<sup>1</sup>.

<sup>1</sup>. Instituto Militar de Engenharia, Ciências dos Materiais/IME, Rio de Janeiro, Brazil.

The membranes are classified as absorbable and non-absorbable in Guided Bone Regeneration (ROG). Cellulose and e-PTFE (expanded polytetrafluoroethylene) membranes classified as non-absorbable are the most used in these regenerative procedures. The ideal membrane must be inert, mechanically resistant, biocompatible, semipermeable, sterilizable, non-allergenic or carcinogenic. If one of these characteristics is not present in the membrane, the regeneration of the peri-implant defects can be compromised [1,2]. In order to improve mechanical properties, biocompatibility and durability modifications have been made to membranes [4]. Polytetrafluoroethylene (PTFE) is a widely studied polymer in the biomedical and engineering field to be used as biomaterial [3]. The influence of roughness and heterogeneities on solid surfaces has been the origin of several studies during the last years [4,5,6]. The following study was developed in order to investigate the changes in the surface of the material. In this context, it is important to investigate the modification caused by treatments with argon plasma (Ar) and ultraviolet (UV) [2]. For example, such plasma treatment may offer other means that control surface modification and alter PTFE properties [3]. Polytetrafluoroethylene (PTFE) samples were treated by two exposure techniques: plasma with non-polymerizable argon gas (Ar); and ultraviolet (UV) radiation. The objective was to investigate the effects of the treatments on the surface properties of the substrate, to verify the variation of the roughness and influence on the properties of the material. The roughness parameters were quantified in the Zygo model NEW VIEW 7100 3D rugosimeter and morphologically analyzed by the FEI Quanta FEG250 scanning electron microscope (SEM). As a result, characterizations have shown that only the plasma surface treatment technique alters the surface characteristics of PTFE.

## REFERÊNCIAS

- [1], L. Gauer.; M. Takemoto; D. Camila, Guided bone regeneration associated with expanded polytetrafluoroethylene membrane (ptfe-e). Journal Article, vol. 3, n. 2, p. 60-67, (2015).
- [2] L. Campos, E. Sipes, Laparoscopic hernia repair: use of a fenestrated PTFE graft with endoclips. Surg Laparosc Endosc. 3 (1): 35-8, (1993).
- [3] S.M. Jakus, A. Shapiro, C.D. Hall, Biologic and synthetic graft use in pelvic surgery: a review. Obstet Gynecol Surv. 63 (4): 253-66, (2008).
- [4] M. Cruz, C.C. Reis, V.C. Silva Use of Allumina® (Al<sub>2</sub>O<sub>3</sub>) as a biological filter in guided tissue regeneration. Odontol Mod. V18, N5, 20p. (1991).
- [5] A.L.R. Pires, A.C Bierhalz, M.M. Moraes Biomaterials: Types, Applications, And Market. Chem. Nova, 38 (7): 957-971 (2015).
- [6] Y. Zhang, X. Zhang, B. Shi, &, R.J. Miron (2013). Membranes for guided tissue and bone regeneration. Annals of Oral & Maxillofacial Surgery, 1 (1), 10p (2013).

PÁGINA 2

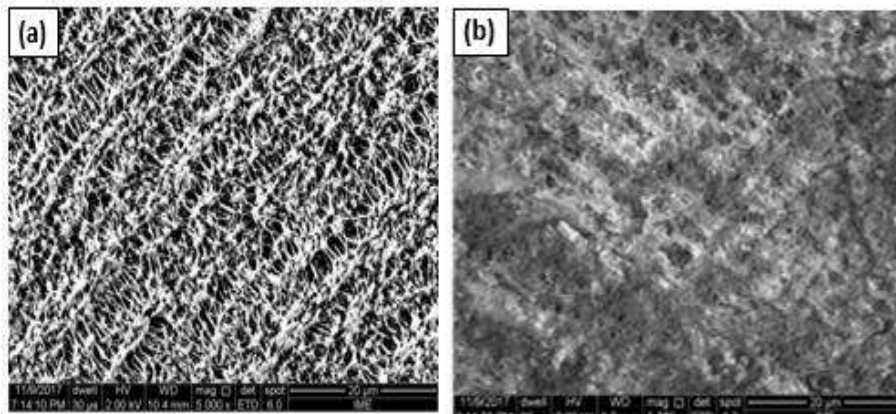


Figure 1. Scanning Electron Microscopy e-PTFE sample: (a) No treatment 5000X, (b) After Plasma Etching 5000X.

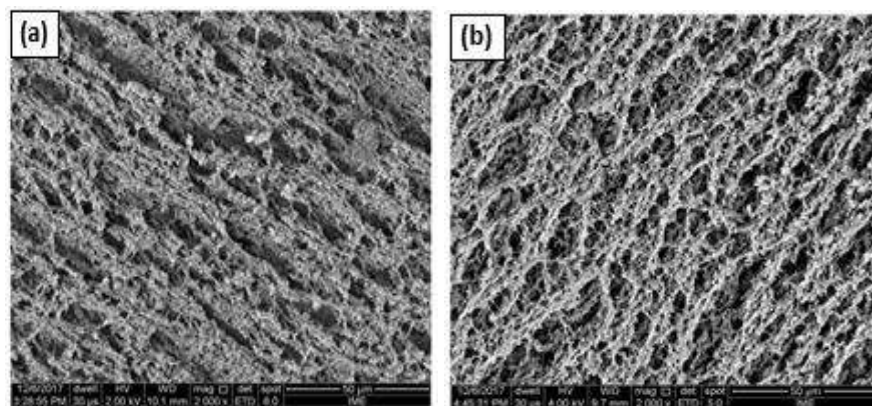


Figure 2. Scanning Electron Microscopy e-PTFE sample: (a) No treatment 5000X, (b) After UV treatment 5000X.

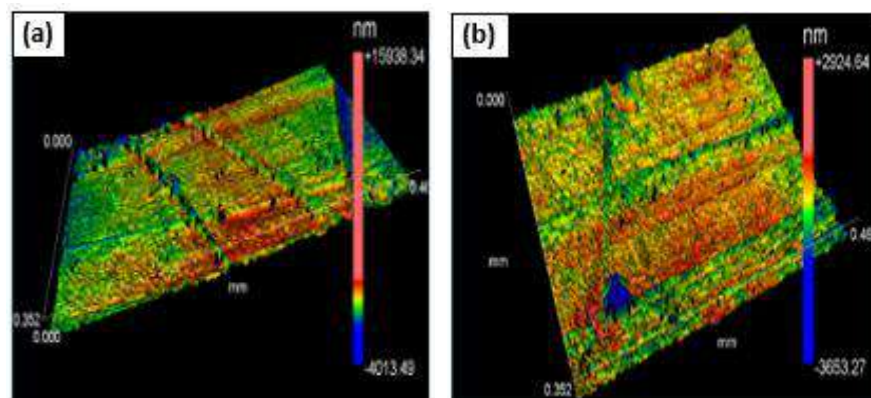


Figure 3. PTFE morphology obtained in the Zygo roughness meter of the surfaces. (a) After plasma etching and (b) After UV treatment.

**Table 1** Results of roughness tests..

Surface	Roughness ( $\mu\text{m}$ )	
No treatment	0,3001	1,0002
After UV	0,3152	1,1031
After plasma	1,0002	2,7351

## Gunshot Residue Particles from Brazilian Ammunition Have Morphological Variation

Renata Carvalho Silva<sup>1\*</sup>, Jean de Oliveira Santos<sup>2</sup> and André Luis Martins de Souza<sup>3</sup>

<sup>1,2,3</sup> Directory of Metrology applied to Life Sciences, National Institute of Metrology, Quality and Technology, Dimav/Inmetro, Rio de Janeiro, Brazil. E-mail: rcavalho@inmetro.gov.br

The detection of gunshot residue (GSR) particles on the shooter's hands and vestments presents great value to criminal expertise. GSR is the name given to the complex mixture of organic and inorganic particles generated by a combination of high temperature and high pressure conditions during firearm discharge [1], originating from the firearm, its ammunition and the combustion products. Lead (Pb), barium (Ba) and antimony (Sb), when found combined in the same particle, are markers used for unequivocal GSR detection. Their diameters vary from 0.1 to 50  $\mu\text{m}$  and they are mostly of spherical morphology. The gold-standard technique for detection of these particles is scanning electron microscopy with dispersive energy spectroscopy (SEM/EDS). Particles (collect by the Brazilian Civil Police with carbon tape-lift-techniques) were analyzed using a Quanta FEG 450 SEM (FEI Company, USA) and EDS (EDAX Genesis, USA). Detection and classification were held by the automated system GSR-Magnum 5.1 (FEI Company, USA). For this, the material was scanned using backscattered electrons to detect particles glowing above a determined contrast level. Then, X-ray spectra of all detected particles were acquired and classified based on their elemental composition in order to distinguish GSR related particles from the environmental ones. The automated scan was then followed by a manual analysis, in which the operator rejects or confirms the particles detected by the automated system based on composition and morphology. In order to evaluate the performance of GSR-Magnum 5.1 analysis, a certified reference material containing a specified distribution of synthetic particles of the most common GSR elements (Pb, Ba and Sb) was used. SEM images of all identified and confirmed GSR particles were then acquired. According to Kara et al [2], GSR particles are classified as regular spheres, spheroids or irregular spheres, which are correlated to their chemical composition. However, we observed other morphological characteristics of GSR particles from Brazilian ammunition and classified them into six categories (Figure 1): 1A. moon-like – the presence of micro holes spread all over the particle's surface; 1B. Meteor-like – structures similar to craters with multi focal Ba nanospheres on the particle surface; 1C. quartz ball-like – Pb, Sb and Ba elements merged in the particle; 1D. earth-like – well defined distribution of the 03 elements over the particle; 1E. lymphocyte-like – high Sb content and the presence of debris (probably from skin cells) on the particle's surface; 1F. deformed particles, possibly originated from outdated ammunition or even due to explosion. Typical GSR particle composition is presented in Figure 2. Further studies on Brazilian ammunition are necessary to understand the correlation between GSR particle's composition and morphology. This information is relevant to evaluate the performance of manual analysis avoiding possibly misidentification of GSR particles by the operator.

[1] O. Dalby et al., Forensic Sci. 55 (2010) 924–943.

[2] I. Kara et al., J Forensic Sci. 60 (2015) 4.

[3] This research was supported by FINEP (Brazil).



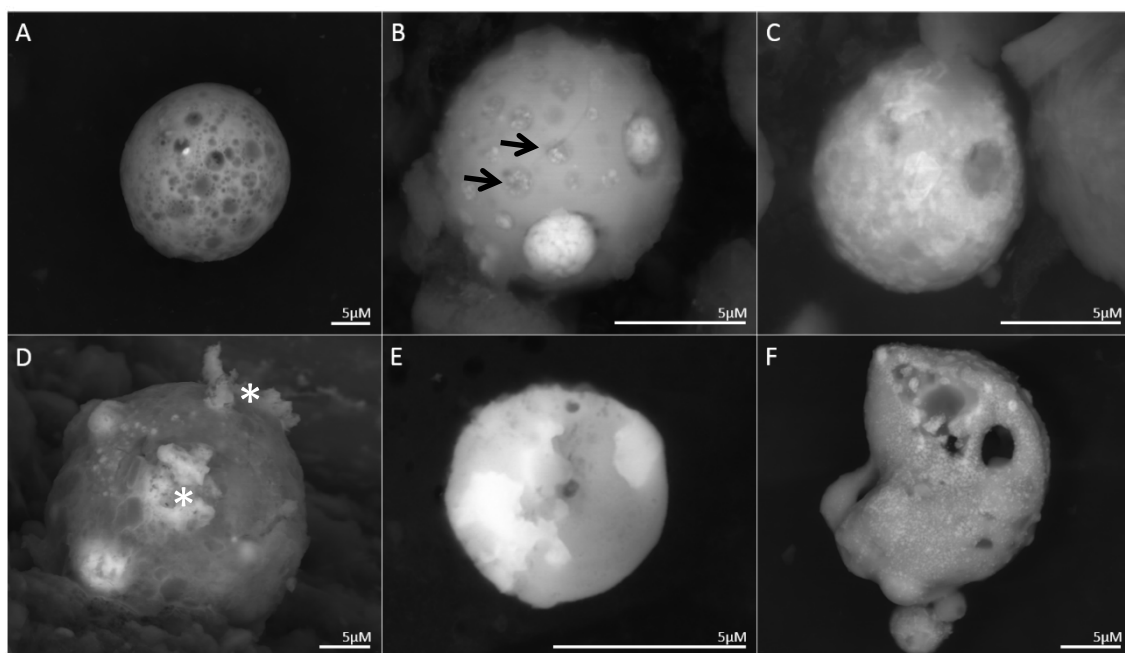


**Figure 1:** SEM Micrograph of GSR particles from Brazilian ammunition. A. The particle surface has structures similar to micro holes. B. Presence of structures similar to craters (arrows) with bright spheres of Ba in the GSR surface. C. Structure similar to a Quartz ball due to Pb, Sb and Ba elements merged in the particle; D. Structure similar to a lymphocyte. Note some debris in the particle surface (\*) E. well defined distribution of the 03 elements over the particle. F. deformed/broken GSR particle.

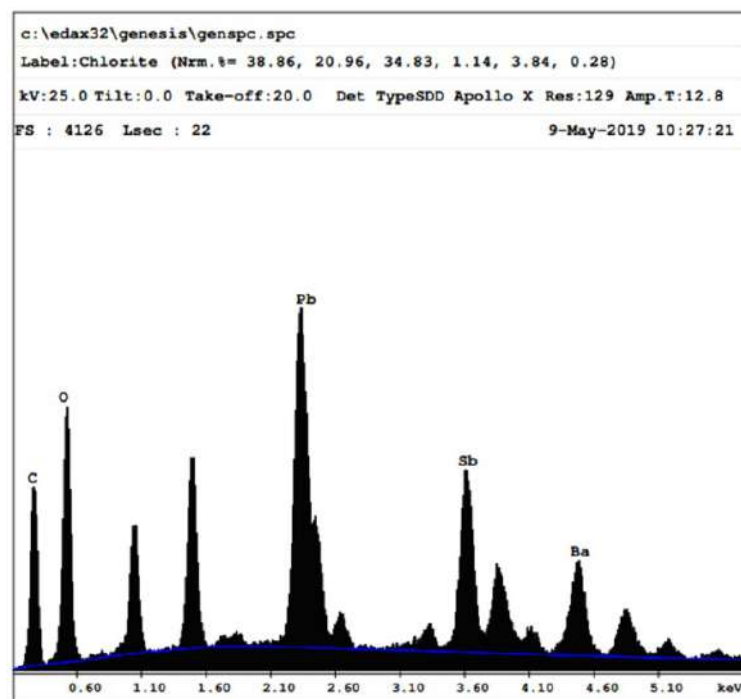


**Figure 2:** EDS spectrum of an “unique” GSR particle.

## Synthesis and characterization of Fe<sub>3</sub>O<sub>4</sub>@SiO<sub>2</sub> core-shell magnetic microparticles

Vanessa Cezar Ribas<sup>1</sup>, Jacqueline Arguello<sup>1\*</sup> and Vladimir Lavayen<sup>1</sup>

<sup>1</sup> Universidade Federal do Rio Grande do Sul, Instituto de Química, Porto Alegre, Brasil.

\* jacqueline.arguello@ufrgs.br

Magnetic nanoparticles, such as magnetite (Fe<sub>3</sub>O<sub>4</sub> NPs), are still actively investigated due to their high potential technological application [1]. However, these materials are susceptible to slow oxidation by atmospheric oxygen, as well as being relatively unstable and poorly dispersed in aqueous media. The formation of core-shell structures is a useful method to overcome such disadvantages; the shell usually composed of polymers, metal nanoparticles, or silica. This work reports the synthesis of Fe<sub>3</sub>O<sub>4</sub> NPs by precipitation of ferrous hydroxide followed by partial oxidation to magnetite. Subsequent, core-shell sphere structures (Fe<sub>3</sub>O<sub>4</sub>@SiO<sub>2</sub>) were obtained through a modified Stöber method [2]. Both materials, Fe<sub>3</sub>O<sub>4</sub> NPs and Fe<sub>3</sub>O<sub>4</sub>@SiO<sub>2</sub>, were characterized by scanning electron microscopy (SEM), transmission electron microscopy (TEM), X-ray powder diffraction (XRD), Infrared spectroscopy (FT-IR), and magnetic susceptibility measures. The SEM and TEM images, depicted in Fig. 1, reveal the formation of Fe<sub>3</sub>O<sub>4</sub> nanoparticles with octahedral morphology with an average size of 235 nm, while the silica-coated nanoparticles adopted spherical shape with an average size of 693 nm. XRD and FT-IR analysis also confirmed the functionalization of Fe<sub>3</sub>O<sub>4</sub> NPs, data presented in Fig. 2. The peak positions and relative intensities are consistent with the planes (220), (311), (222), (400), (422), (511), (440), (620), (533), (622) and (444), of magnetite (JCPDS 19-0629). Besides the magnetite diffraction pattern, the Fe<sub>3</sub>O<sub>4</sub>@SiO<sub>2</sub> exhibits a wide band corresponding to amorphous silica in the range of 20-27°. The FTIR spectra exhibit the Si-O-Si asymmetric stretching vibration at 1020-1100 cm<sup>-1</sup>. Finally, the magnetic susceptibilities were measured; the saturation magnetization values of Fe<sub>3</sub>O<sub>4</sub>@SiO<sub>2</sub> (12,5 emu/g) are lower than that of Fe<sub>3</sub>O<sub>4</sub> NPs (81,0 emu/g), because of the thick shells coated on magnetic nanoparticles.

[1] Y. Hou et al., Chem. Commun. 47 (2011) 5130.

[2] T. Herricks et al., Chem. Phys. Lett. 401 (2004) 19.

[3] E. Bohn et al., J. Colloid Interface Sci. 26 (1968) 62.

[4] M. Ogawa et al., J. Mater. Sci. 42 (2007) 5299.

This research was supported by CNPq (Brazil), INCTBio, PROPESQ-UFRGS, CMM-UFRGS.

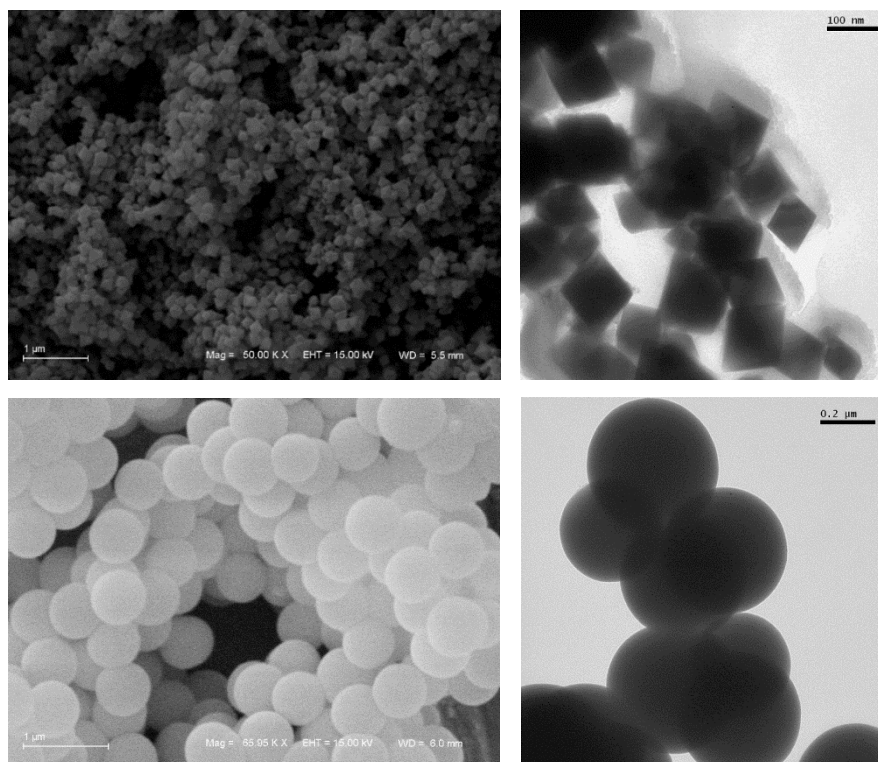


**Fig. 1.** SEM images, on the left, and TEM images, on the right, of  $\text{Fe}_3\text{O}_4$  and  $\text{Fe}_3\text{O}_4@\text{SiO}_2$ .

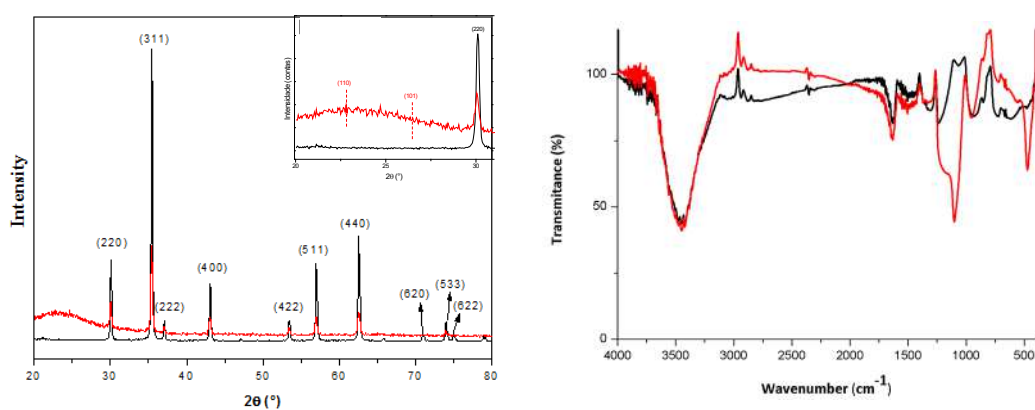


**Fig. 2.** Diffractograms, on the left, and FT-IR spectra, on the right, of  $\text{Fe}_3\text{O}_4$  (black line) and  $\text{Fe}_3\text{O}_4@\text{SiO}_2$  (red line).

## Using scanning electron microscopy to evaluate the compatibilizing effect of modified graphene oxide on poly(3-hydroxybutyrate-*co*-3-hydroxyvalerate)/poly(ethylene-*co*-vinyl acetate) blend

Willian H. Ferreira<sup>1\*</sup>, Camila A. Silva<sup>1</sup> and Cristina T. Andrade<sup>1</sup>

<sup>1</sup>Instituto de Macromoléculas Professora Eloisa Mano, Federal University of Rio de Janeiro, RJ, Brazil \* (whermogenes@ima.ufrj.br)

The environmental impact associated with petroleum-based plastics has motivated the development of bioplastics to replace these materials in at least some applications. Poly(3-hydroxybutyrate-*co*-3-hydroxyvalerate) (PHBV) is one of the most common polyhydroxyalkanoates (PHAs) copolymers produced from renewable resources by bacterial fermentation process [1]. It is well known that PHBV is stiff and brittle because of its relatively high crystallinity and significant secondary crystallization that occurs after processing and aging [2]. Poly(ethylene-*co*-vinyl acetate) (EVA) consists of a thermoplastic elastomeric copolymer. Blends based on PHBV and EVA have been developed to improve the mechanical properties of PHBV, aiming to improve its tenacity. However, this polymer pair is immiscible, and the compatibilization is the primary difficulty to be overcome. The compatibility of PHBV/EVA may be partially improved with the increase of vinyl acetate content in the EVA phase [2-3]. Nanoparticles have been used to inhibit coalescence of dispersed phase droplets in immiscible polymer blends [4]. Graphene oxide (GO) is a two-dimensional sheet consisting of sp<sup>2</sup>-hybridized carbon atoms, obtained from oxidation of graphite. The presence of oxygenated groups on the GO surface allows the coupling of molecules with different functional groups resulting in GO analogues, which can act as a compatibilizer for an immiscible polymer blend [5]. In this work, GO was functionalized with an esterified fatty acid (FA) leading to GO-FA. The main objective was to evaluate the GO-FA tensoactive properties on this blend, based on the simultaneous interaction of oxygen-containing groups, on the basal plane and edges of GO sheets, with PHBV and the aliphatic of FA with EVA. The GO-FA, at 0.5 and 1.0 mass%, was incorporated to PHBV (PHB Industrial, SP, Brazil) and EVA with 40% of vinyl acetate content (Sigma-Aldrich, SP, Brazil) using a Coperion ZSK 18 (Werner & Pfleiderer GmbH & Co. KG, Stuttgart, Germany) co-rotating twin-screw extruder, with L/D ratio of 40 at 170°C. The structure and crystallinity of the injection-molded neat PHBV/EVA 1:1 blend and this same blend with the incorporation of GO-FA at 0.5% and 1.0% were investigated by X-ray diffraction (XRD), Fig. 1a. For GO-FA, the broad reflection at 16.5° (2θ) corresponds to the *d*-spacing between sheets of 0.6 nm. For the PHBV/EVA/GO-FA samples this GO-FA reflection was not detected. This result indicates that a high level of dispersion of GO-FA sheets was achieved because of the good interaction of this filler with both phases. For the neat blend, the reflections at 13.3° and 17.2° (2θ) are attributed to crystalline PHBV planes. With the incorporation of GO-FA at 1.0%, the intensity of these reflections was decreased probably by the increase in compatibility, promoted by the nanofiller, in the amorphous phase of the polymeric components. The morphology of the cross-section of the cryofractured surfaces was visualized by scanning electron microscopy (SEM) in Fig. 1b-d. The neat blend showed dispersed phase consisting of EVA spherical domains, embedded in the PHBV matrix. For the blend with the incorporation of GO-FA, the size of dispersed phase was significantly reduced with the increase of nanofiller content. This behavior suggested that GO-FA sheets promoted the extensive breakup of the dispersed phase and prevented the coalescence of the droplets. Specifically, the sample with 1.0% of GO-FA showed high



interfacial adhesion between PHBV and EVA. This result evidenced the compatibilizing effect of the nanofiller and corroborated the increase in the amorphous halo observed in the diffractograms. GO-FA presented tensoactive properties by the increased adhesion between PHBV and EVA phases, as showed by SEM.

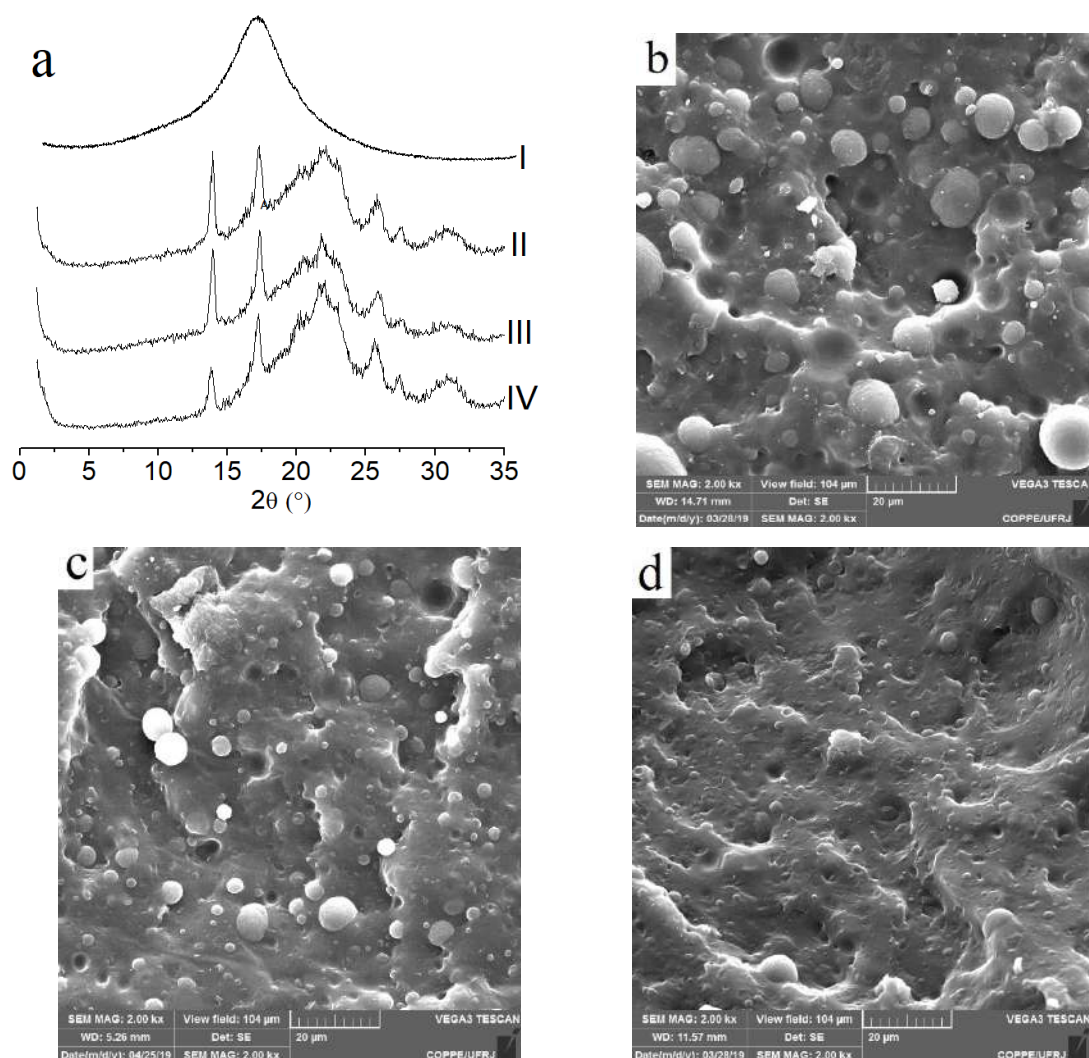


Figure 1: Diffractograms (a) and SEM (b) images obtained for the materials.

## REFERÊNCIAS

- [1] M. G. A. Vieira, M. A. Silva, Lu. O. Santos, M. M. Beppu. *Eur. Polym. J.*, 47 (2008), 254.
- [2] B. Laycock, P. Halley, S. Pratt, A. Werker, P. Lant. *Prog. Polym. Sci.* 39 (2014) 397.
- [3] S. H. El-Taweel, M. Khater. *J. Macrom. Sci., Part B: Physics*, 54 (2015) 1225
- [4] M. S. Luna, G. Filippone. *Eur. Polym. J.*, 79 (2016), 198.
- [5] W.H. Ferreira, K. Dahmouche, C.T. Andrade. *Polym Comp.* 40 (2019) E1131.

This research was supported by Fundação de Amparo à Pesquisa do Estado do Rio de Janeiro (FAPERJ) (Grant N° E-202.417/2017).

## Antibacterial Films On Jarina Seeds Obtained By Plasma Jet Activation Of Copaiba Oil

Yuri Ferreira da Silva<sup>1\*</sup>, Vanessa de Moura Queiroz<sup>1</sup>, Natália Mayumi Andrade Yoshihara<sup>2</sup>, Braulio Soares Archanjo<sup>2</sup>, Renata Nunes Oliveira<sup>3</sup> and Renata Antoun Simão<sup>1</sup>

<sup>1</sup>. Department of Metallurgical and Materials Engineering, UFRJ, Rio de Janeiro, Brazil

<sup>2</sup>. Materials Metrology Division, INMETRO, Rio de Janeiro, Brazil

<sup>3</sup>. Department of Materials Engineering, UFRRJ, Rio de Janeiro, Brazil

\*Email: yuri@metalmat.ufrj.br

The seeds from the jarina palms (*Phytelephas macrocarpa* Ruiz & Pav.), native of the Amazon, have been employed as a raw material for high jewelry pieces regarded as sustainable alternatives to ivory due to their similar appearance upon polishing. However, their chemical composition based in mannan, a linear polysaccharide constituted by  $\beta$ -d-mannose units, makes them vulnerable to micro-organisms which can provoke color and weight changes as well as skin allergies that can affect its credibility as organic gem [1]. Antimicrobial films have been obtained by plasma enhanced chemical vapor deposition (PECVD) using plant secondary metabolites such as essential oils and extracts [2]. Copaiba oil stands out among Brazilian oil-resins due to its antimicrobial, anti-inflammatory and wound healing properties [3]. In this context, the aim of this work was to produce antibacterial coatings on jarina seeds by copaiba oil activation using an atmospheric air cold plasma jet. To this end, disk shaped jarina samples had their surfaces coated with copaiba oil by spray and were exposed to an atmospheric air plasma jet for activation. Plasma treated samples, with no oil, have also been produced in order to assess the surface modification. After treatment, samples were sonicated for 15 min in an ultrasound bath and stored in desiccator for 24 h before characterization by FTIR and water contact angle. Afterwards, the samples were exposed to a *S. aureus* cell culture for 24 h and subjected to fixation by glutaraldehyde and dehydration in ethanol diluted solutions. In order to evaluate bacterial adhesion on treated surfaces, samples were coated with gold and analyzed by SEM. As a result, untreated samples allowed the formation of a surface multilayer biofilm, while air plasma treated samples presented no bacterial layering, indicating higher surface affinity attributed to extractives migration and polymerization [4]. These results are related to sample wettability [2]. *S. aureus*, a moderately hydrophilic bacteria ( $\sim 70^\circ$ ), is more compatible to plasma treated sample ( $\sim 78,9^\circ$ ) in comparison to control ( $\sim 31,5^\circ$ ), resulting in uniform dispersion over the surface, forming a single layer. On the other hand, copaiba film coated samples, in spite of presenting a similar water contact angle ( $\sim 81,9^\circ$ ), presented less bacterial accumulation, confirming its antibacterial activity associated with film chemical composition. FTIR results showed that plasma treated samples presented an increase in carboxylic acid peaks ( $1743\text{ cm}^{-1}$ ) in comparison to control due to presence of extractives [4], while copaiba film coated sample presented higher intensity carboxylic acid and ketone peaks ( $1693\text{ cm}^{-1}$ ), indicating retention of copaiba oil antimicrobial functional groups after plasma exposure [3].

[1] Y. Chu et al., Sci. Rep. 5 (2015) 14387.

[2] A. Al-Jumaili et al., Nanomaterials 7 (2017) 270.

[3] J. G. O. Pinheiro et al., Int. J. Mol. Sci. 18 (2017) 2388.

[4] X. Q. Wang et al., Sci. Rep. 7 (2017) 5601.

[5] J. Zigon, Holzforschung 72 (2017) 11.

[6] This research was supported by CNPq (Brazil).

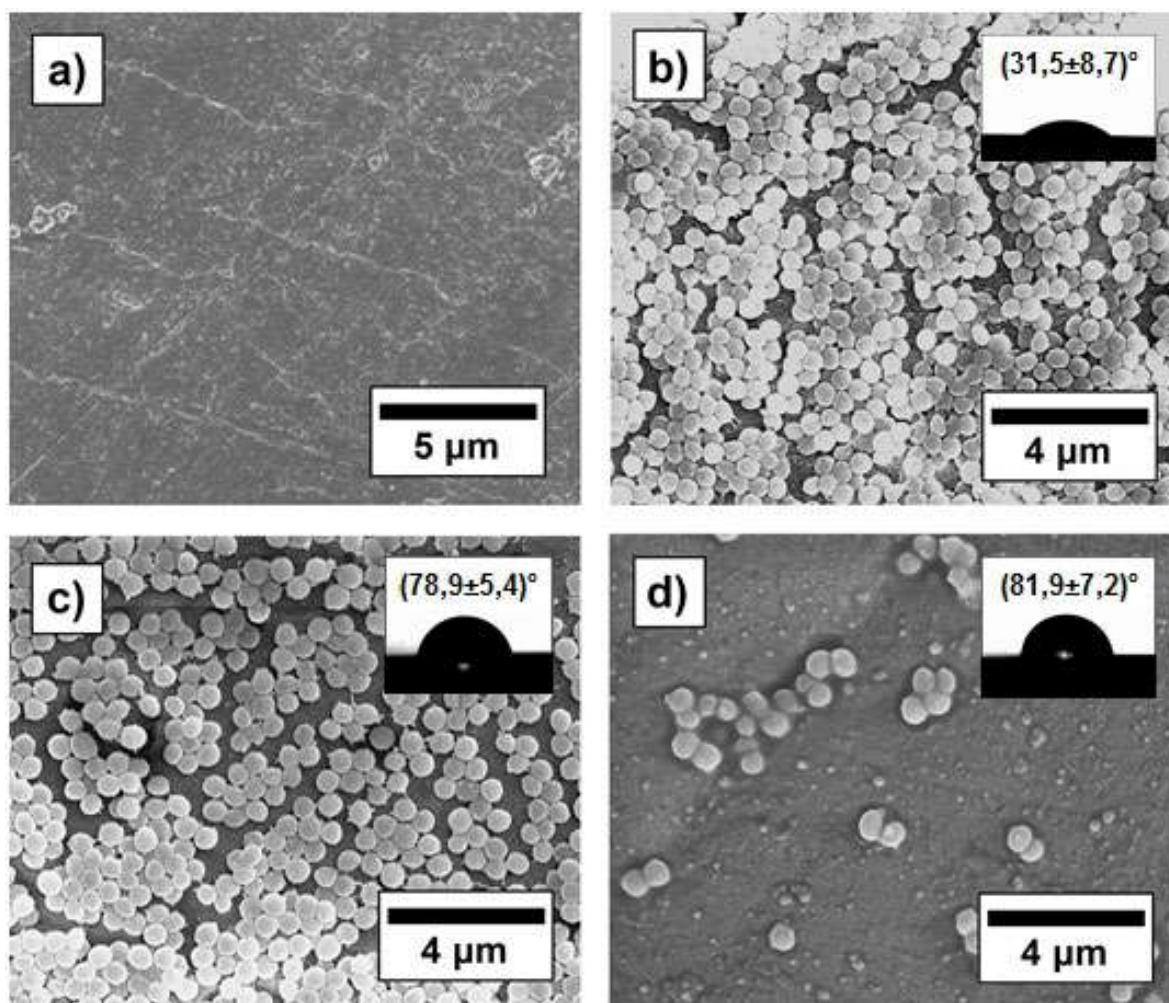


Figure 1 – SEM images and water contact angle results for negative control (a), untreated sample / positive control (b), air plasma treated surface (c) and copaiba film obtained by plasma jet activation (d). Magnifications: 16,000 x (a) and 15,000 x (b, c and d).

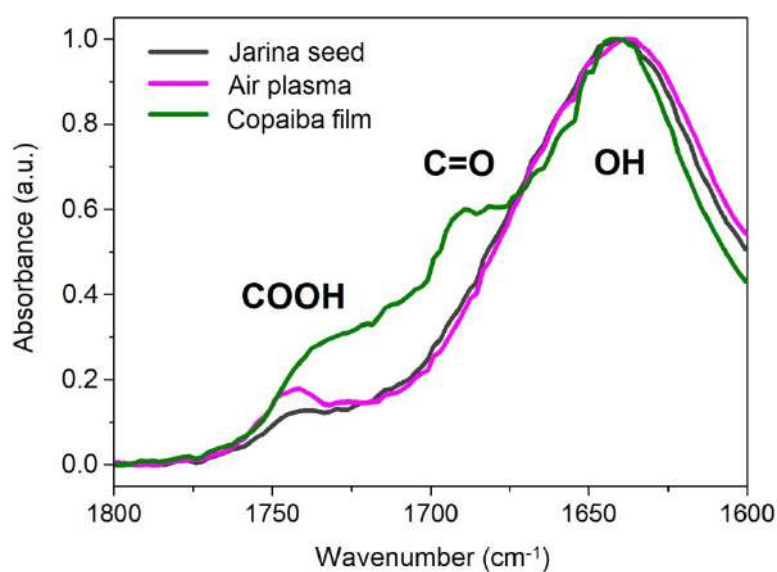


Figure 2 – FTIR spectra (1800 to 1600  $\text{cm}^{-1}$  region) for jarina seed, air plasma treated sample and copaiba oil film coated sample.

## Enhancing Manufacturing Process of Probes for Near-Field Optical Microscopy

B. S. de Oliveira<sup>1\*</sup>, T. L. Vasconcelos<sup>1</sup>, B. S. Archanjo<sup>1</sup>, C. A. Achete<sup>1</sup>.

<sup>1</sup> Instituto Nacional de Metrologia, Qualidade e Tecnologia (INMETRO), Divisão de Metrologia de Materiais (Dimat), Duque de Caxias - Brasil.

E-mail: bsoliveira@inmetro.gov.br

Raman spectroscopy is widely used for chemical and structural analysis of carbon-based materials, such as: biological samples, graphene and carbon nanotubes. However, spatial resolution achieved on conventional optical systems is limited to approximately 200 nm due to diffraction effects when visible incident light is used. On the other hand, tip-enhanced Raman spectroscopy (TERS) is a new technique capable to achieve spatial resolution beyond the diffraction limit by utilizing the near-field information through the use of a special AFM probe which acts as an optical nanoantenna [1,2]. Therefore, TERS has great capacity to properly characterize nanomaterials, such as on: carbon nanostructures [3], DNA [4]; single molecules [5]; localized optical effects generated by structural defects in WSe<sub>2</sub> [6]; and graphene defects [7]. In this configuration, the TERS probe is a metallic nanostructure that provides localized surface plasmon resonance (LSPR) with resonance wavelength in the visible spectral range, and thus configuring an optical nanoantenna [8]. Different types of methodologies have already been developed for the manufacture of TERS nanoantennas, however none of these manufacturing methodologies demonstrate reproducibility on its optical efficiency and high spatial resolution. Consequently, they do not present reliability regarding its use as TERS probes [8]. Thus, the level of reproducibility in the manufacture of these probes is the key factor to TERS technique became a routinely technique to be applied on nanomaterials characterization. To solve this problem, this work aims to improve the manufacturing process by optimized a new type of probe called plasmon-tunable tip pyramid (PTTP) [9]. Basically, the PTTP probe is composed of a gold nanopyramidal structure connected to the segmented body of a micropyramid gold probe fabricated through a lithography process and therefore compatible to large mass fabrication. This morphological configuration of the probe allows the generation of LSPR monopole modes and consequently a unprecedented high signal enhancement related to the efficient use of the near field information [9]. Thus, the microfabrication process of these probes is innovative and capable of generating reproducible and optically efficient probes with high yield. The microfabrication of PTTP probes consists of the manufacture of pyramidal like cavities on silicon substrate through the lithographic process, which is used as the PTTP probe template. This lithographic process consists in exposing specific regions of the silicon through the focused ion beam (FIB). Then, the exposed silicon passes through the process that is known as anisotropic etching of silicon. This anisotropic corrosion provides the formation of cavities with pyramidal shape. The cavity is used as template for the TERS probe thought few additional steps. The substrate is coated with a gold film and finally the probe is template stripped from the cavity ending with the mounted pyramidal shaped TERS probe. The purpose of



producing a substrate with cavities with pyramidal shape and then coating it with a metallic film is to employ it as a template, a negative structure of the final TERS gold probe (Figure 1). In this work, we applied electron microscopy to study and optimize each process step focusing in the characterization of the pyramidal cavities, on the substrate, its cleaning and bottom size measurements (Figure 2). This study helped us to improve and control the fabrication parameters that lead to a higher probe quality and thus better TERS image near-field/far-field contrast and resolution.

#### REFERÊNCIAS:

- [1] B. S. Yeo, J. Stadler, T. Schmid, R. Zenobi, and W. Zhang, “Tip-enhanced Raman Spectroscopy - Its status, challenges and future directions,” *Chem. Phys. Lett.*, vol. 472, no. 1–3, pp. 1–13, 2009.
- [2] L. G. Cançado, A. Hartschuh, and L. Novotny, “Tip-enhanced Raman spectroscopy of carbon nanotubes,” *J. Raman Spectrosc.*, vol. 40, no. 10, pp. 1420–1426, 2009.
- [3] Z. J. Lapin, R. Beams, L. G. Cançado, and L. Novotny, “Near-field Raman spectroscopy of nanocarbon materials,” *Faraday Discuss.*, vol. 184, pp. 193–206, 2015.
- [4] S. Najjar *et al.*, “Tip-Enhanced Raman Spectroscopy of Combed Double-Stranded DNA Bundles,” *J. Phys. Chem. C*, vol. 118, no. 2, pp. 1174–1181, Jan. 2014.
- [5] R. Zhang *et al.*, “Chemical mapping of a single molecule by plasmon-enhanced Raman scattering,” *Nature*, vol. 498, p. 82, Jun. 2013.
- [6] K.-D. Park, O. Khatib, V. Kravtsov, G. Clark, X. Xu, and M. B. Raschke, “Hybrid Tip-Enhanced Nanospectroscopy and Nanoimaging of Monolayer WSe<sub>2</sub> with Local Strain Control,” *Nano Lett.*, vol. 16, no. 4, pp. 2621–2627, Apr. 2016.
- [7] R. Beams, L. G. Cançado, and L. Novotny, “Raman characterization of defects and dopants in graphene,” *J. Phys. Condens. Matter*, vol. 27, no. 8, p. 83002, 2015.
- [8] T. L. Vasconcelos *et al.*, “Tuning Localized Surface Plasmon Resonance in Scanning Near-Field Optical Microscopy Probes,” *ACS Nano*, vol. 9, no. 6, pp. 6297–6304, 2015.
- [9] T. L. Vasconcelos *et al.*, “Plasmon-Tunable Tip Pyramids: Monopole Nanoantennas for Near-Field Scanning Optical Microscopy,” *Adv. Opt. Mater.*, vol. 6, no. 20, pp. 1–6, 2018.

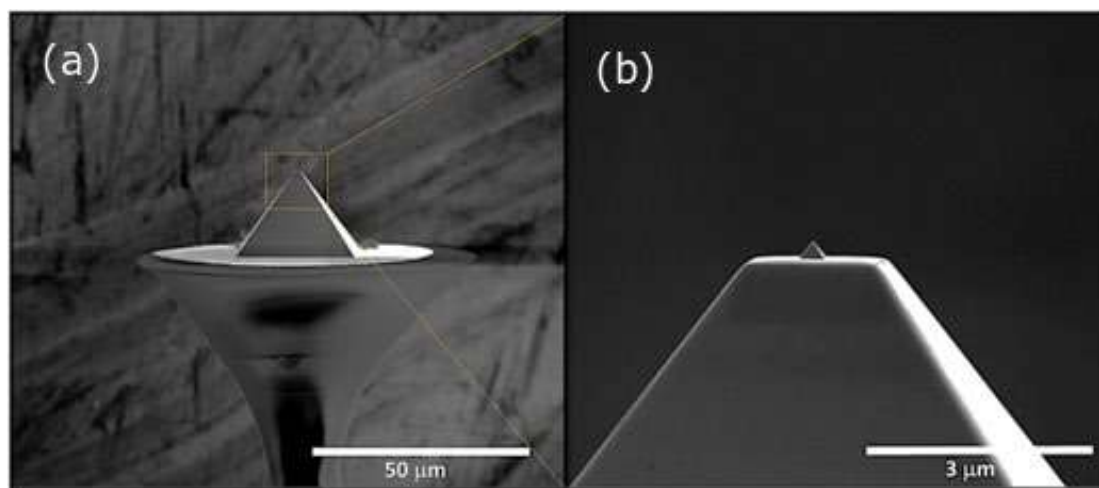


Figure 1 - SEM image of the probe after extraction of the silicon template. On the left (a) we visualize the probe completely and the replication of the pyramidal cavity of the template. On the right (b) we have the structure highlighted in (a), the apex with nanometric dimensions that allows the signal increase in the TERS system.

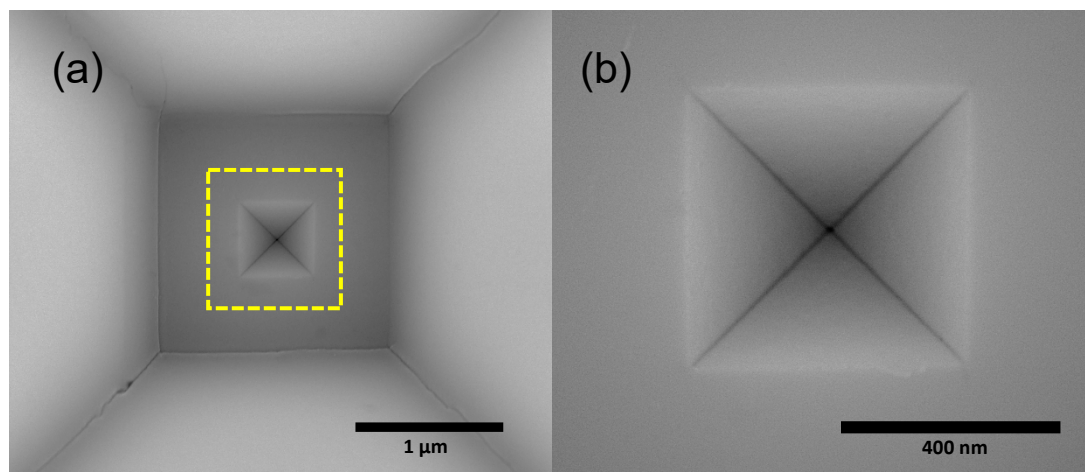


Figure 2 - Characterization of the bottoms of the wells by SEM to verify the production quality of the silicon forms. In (a) we verify the morphology of the bottom of the cavities and their cleaning. In part (b), we observe the highlighted area of figure (a). Besides, we check the cleanliness, the morphology and the apex size of the future probe.

## Thickness Measurement of thin HfO<sub>2</sub> films via transmission electron microscopy

Senna A. C.<sup>1\*</sup>, Archanjo S. B.<sup>1</sup>, Damasceno C. J.<sup>1</sup>, Araujo R. J.<sup>1</sup> and Achete A. C.<sup>1</sup>

<sup>1</sup>Instituto Nacional de Metrologia, Qualidade e Tecnologia, Diretoria de Metrologia Científica, Divisão de Metrologia de Materiais, Duque de Caxias, RJ, 25250-020 - Brasil.

Scientific and industrial metrology provides tools for the technological growth and innovation of the country, promoting the competitiveness of industries and the safety of consumers by creating a favorable environment for the development of the scientific and industrial sector. Not least, nanotechnology is a field in full development due to the large number of applications it has generated demand for more accurate measurement techniques and globally accepted standards. Therefore, progress in the field of nanometrology is needed, where precise control of object dimensions is essential and brings new challenges because of the small dimensions involved. From this perspective, quantitative measurements are one of the critical parameters to demonstrate that a particular product or process meets a required specification on the nanometer scale. In recent years, the scaling of complementary metal oxide semiconductor (CMOS) transistors has led to the silicon dioxide layer used as a gate dielectric becoming so thin that its leakage current is too large. Therefore, it is necessary to replace conventional thin layers of SiO<sub>2</sub> by higher dielectric constant materials such as hafnium oxide and hafnium silicate [1] in modern electronics. In this work, the determination of the thickness of the HfO<sub>2</sub> films was performed using a set of electron microscopy techniques, including Dual Beam platform, equipped with a scanning electron microscope (SEM) and focused ion beam (FIB), transmission electron microscope. It is important to note that there is a need to have a well prepared thin lamella and have it aligned along right zone axis in order to obtain reliable and accurate results.

### REFERENCES

- [1] J. Robertson, Eur. Phys. J. Appl. Phys. 28, 265–291(2004).

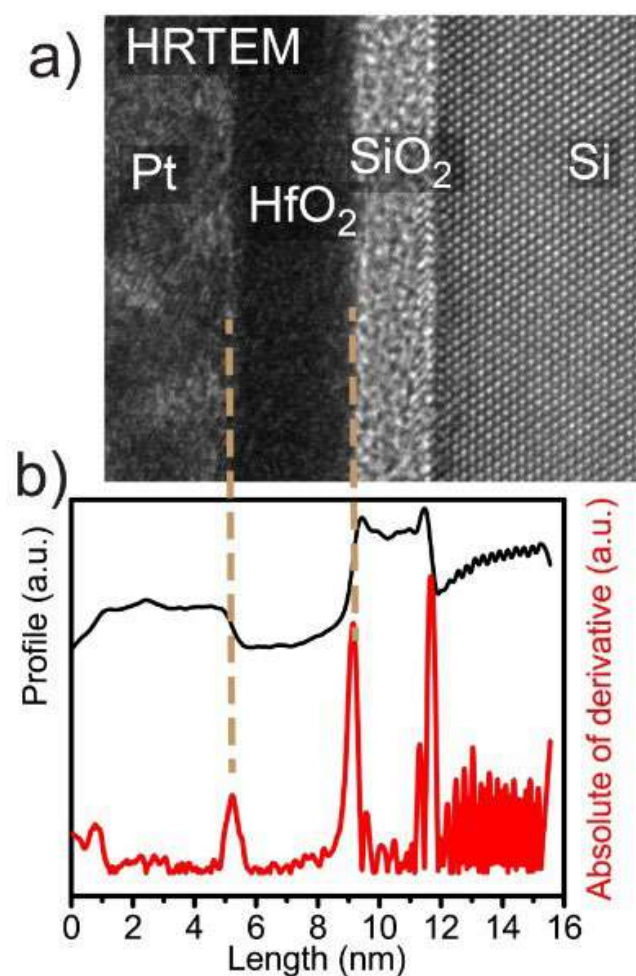


Figure 1. Cross section of the 4 nm HfO<sub>2</sub> film. a) HRTEM image showing the sample layers including the Pt protecting layer. b) In black, on top, the contrast profile of the cross section is shown. In red, below, the absolute of the derivative from the profile is seen. The dashed yellow lines were drawn as guidance to the eyes to the interfaces of the HfO<sub>2</sub> film.



## **Comparison Of Welded Steel Joints S355NL By FCAW With National And Imported Tubular Wire**

Camila Fagundes de Paula Guedes<sup>1\*</sup>, Gláucio Soares da Fonseca<sup>2</sup>, Gabrielle Cristine Lemos Duarte Freitas and Lucas Rosate Leite dos Santos<sup>3</sup>

<sup>1</sup>. Graduate Program on Metallurgical Engineering, Federal Fluminense University, Volta Redonda, Brasil. camilafagu4@hotmail.com

<sup>2</sup>. Federal Fluminense University, Mechanical Engineer Department, Graduate Program on Metallurgical Engineering - Volta Redonda, Brasil.

<sup>3</sup>. Graduate in Metallurgical Engineering, Federal Fluminense University, Volta Redonda, Brasil.

Structural steels are steels with good industrial applicability, as they have good mechanical strength and easy weldability. The applications are focused on several areas such as: naval, petrochemical, pipelines, civil construction among others. The imported tubular wire has already been used in the welding processes of the internal assembly of a submarine, a comparative study between imported and domestic wire would be of great value for comparison of properties [1, 2]. The objective of the present work was to characterize the structural microstructure of S355NL grade structural steel welded by the FCAW (flux cored arc welding) process with national tubular wire, in order to analyze its micrographs and macrographs, as well as the mechanical and corrosion properties. To obtain the results were carried out metallographic tests, mechanical tests such as traction, hardness and impact in order to obtain the analogy between consumables. The microstructure of S355 steel is known as ferritic-pearlitic [3]. The imported tubular wire comes from French origin and has already been used in the processes of welding the internal part in the assembly of a submarine, and this process of welding with the imported material has already been approved due to good quality in general, however this import makes high manufacturing costs and slow waiting for arrival of the imported product. In this way, to develop national manufacturers in the area of consumables, the possibility arose to develop consumables that similarly maintained microstructural properties, mechanical and physical in relation to imported, that is, in order to provide reliability and good quality welds. For the samples of national and imported consumables (Sample A and B) it was observed that there was a homogeneous distribution in the strands, and there was no discontinuity in the welded region, as seen in Figure 1 and 2. In Figure 3, we have the micrograph of the S355NL base material with 200x. The micrograph presents ferritic grains and perlite.

Acknowledgment,

All coordination of Graduate Program on Metallurgical Engineering (PPGEM) for the support.

[1] FOUTOURA, B.F.C.; ABILIO, M.P.J; CORREIA, J.A.F.O; SILVA, A.L.L; MATOS, R.; REBELO, C.; SILVA, L.S. Comparação da resistência a fadiga entre o aço S355 e o aço de alta resistência S690. Universidade de Coimbra, 2010.

[2] FIGUERÔA, D.W.; Influencia do teor de CO<sub>2</sub> e do metal de adição na soldagem híbrida laser-GMAW em aço estrutural grau S355. Programa de Pós Graduação em Engenharia Mecânica, 2015.

[3] GOLI-UGLU, E.A.; The manufacturing processes of heavy plates up to 150mm from structural steel microalloyed with vanadium, ISSN, 45(8), 2015.

[4] TU, H.; SCHMAUDER, S.; WEBER, U.; Numerical study of electron beam welded butt joints the GNT model. Institute for Materials Testing. IMWF. 2012.

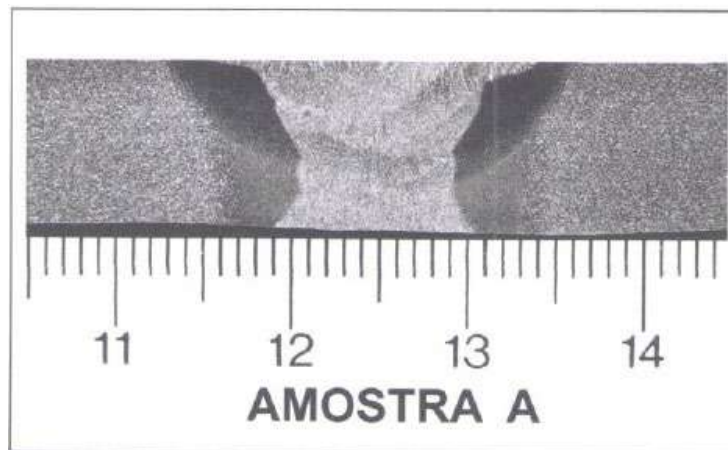


Figure 1 - Macrostructure of Sample A, with 5x, 8% nital attack.

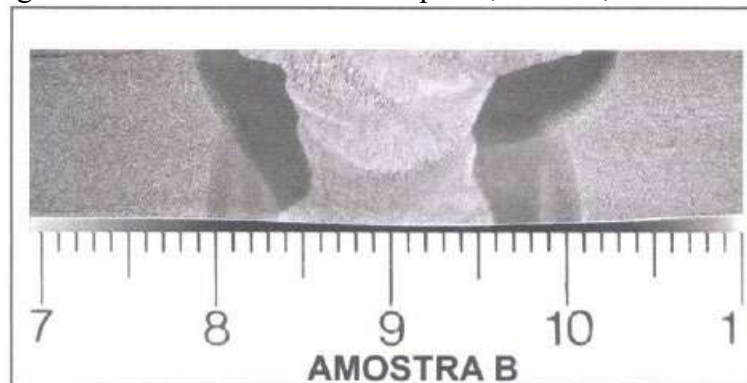


Figure 2 - Macrostructure of Sample B, with 5x, 8% nital attack.

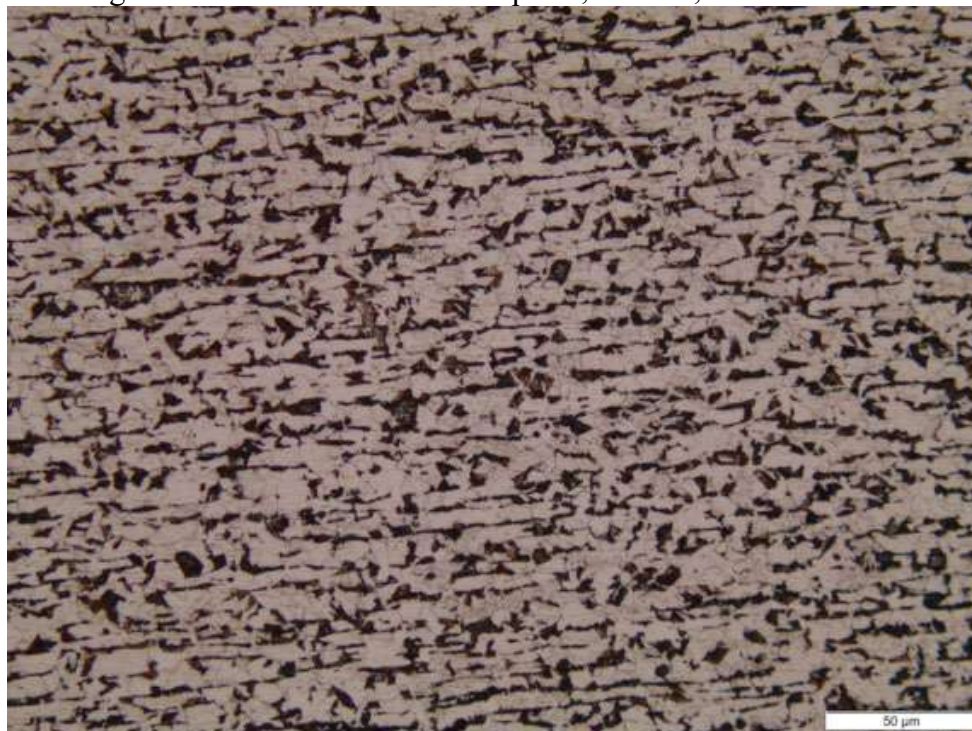


Figure 3 - Microstructure of base metal steel S355NL, with 200x, 3% nital attack.

## **An Alternative of Laser Profilometry Technique to Characterization of Morphology and Roughness of a Nanofilm from TiO<sub>2</sub>-KOH Over an Aluminium Substrate.**

Gabriel Vinicius Assai Vaz<sup>1\*</sup>, Bruno Fernando Gianelli<sup>1</sup>, Gabriel Nogueira Rodrigues<sup>1</sup> and Livia Sottovia<sup>2</sup>

<sup>1</sup>. Instituto Federal de Educação, Ciência e Tecnologia de São Paulo, Laboratório de Materiais, Itapetininga, Brasil, assaigabriel@gmail.com.

<sup>2</sup>. Universidade Estadual Paulista “Júlio de Mesquita Filho” – Unesp, Sorocaba, Brasil

The roughness surface characterization is from extreme importance for several fundamentals of engineering, such as tribological aspects, dimensional accuracy, fault analysis, among others. The roughness parameters can be analyzed in two or three dimensions, the method of 2D analysis had its greatest application for more than half a century, but recently it has lost space for the 3D surfaces analysis, carrying important information about the materials topography and applications in science and engineering [1-3]. The objective of this work is to perform a study on the morphology and roughness of a nanofilm based on potassium hydroxide (3 g / L KOH) and titanium dioxide (10 g / L TiO<sub>2</sub>) on an aluminum substrate (PEO) using 450V for 20 minutes with a frequency of 300 Hz, this study aims to compare the results obtained from a 3D Laser Scanning Microscopy (LSM) - model VK-X200 from Keyence and a low-cost alternative, an optical microscope coupled to an extensometer. The operation principle of LSM starts by capturing the height information based on the reflected light intensity of the sample, its lens scans the Z-axis, and at the same time, the software stores the data to reproduce the 3D image, immediately after the objective lens is driven in the direction of the Z-axis and the scanning process is repeated to obtain the intensity of the reflected light at the Z-axis position of each point. The system records the height information and reflects the light intensity by assuming that the position of the focal point on the Z-axis is located where the reflected light intensity is higher, thus making possible to extract an image with full focus and together the height information from the sample. While the low cost technique was based on a Zeiss Axio Lab A1 optical microscope coupled with an extensometer, which has a transducer functionality capable of micrometrically measuring the steps performed between the images recorded on the Z-axis, the images are captured in a gradual way with 2µm steps from the lowest valley to the highest peak of the sample. Right after was realized the focal composition from the recorded images, using the software of public domain ImageJ, being the composition procedure also based on the intensity of reflected light, which the region with greater intensity means that it is in focus in that point of the table offset on Z-axis, which it was possible to obtain the surface morphology from the sample. Subsequently a fine-tuning was performed on Gwyddion v5.1 software, also in the public domain, which provided roughness information.



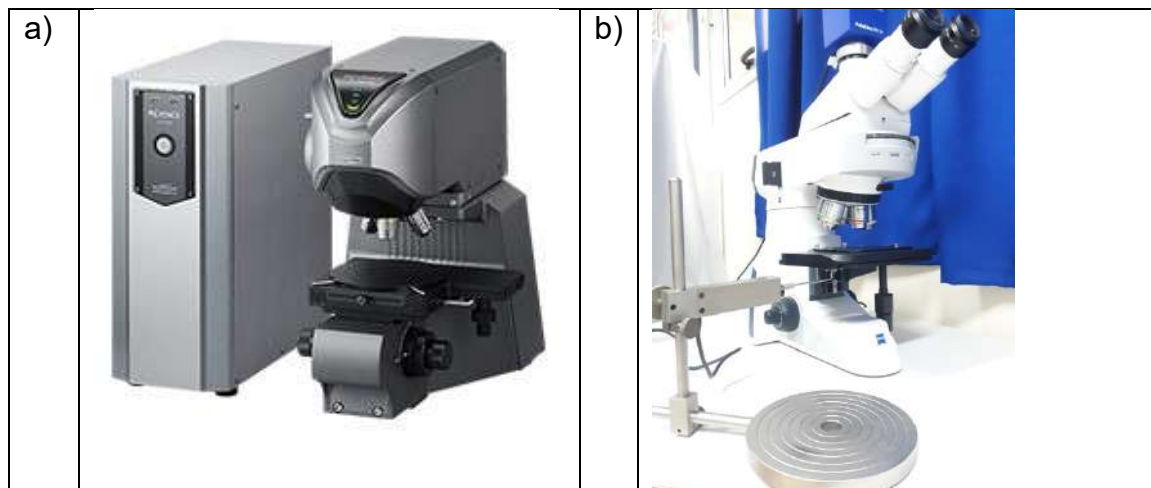


Figure 1. a) 3D Laser Scanning Microscopy – model VK-X200 (Keyence). b) Configuration of the low cost alternative.

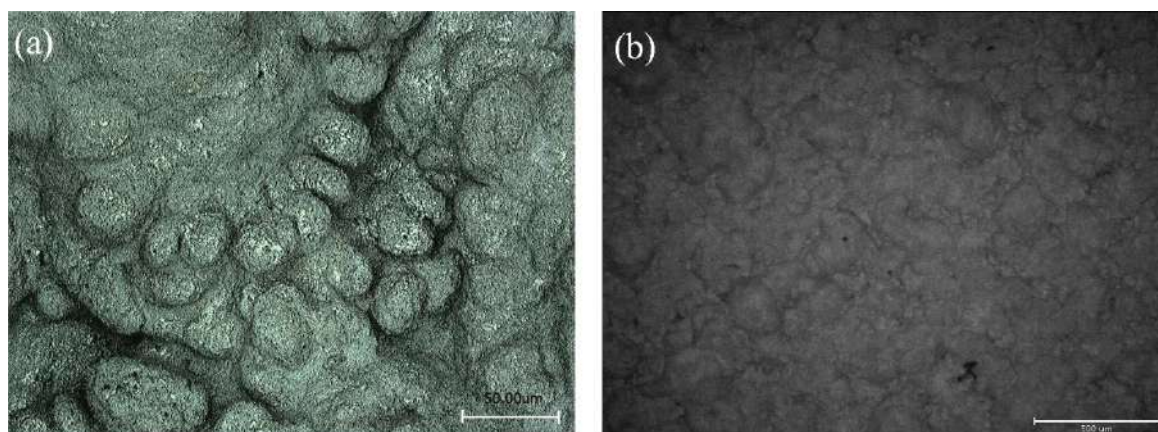


Figure 2. a) Morphology of the sample using 3D LSM. b) Morphology of the sample using the low cost alternative.

Table 1. Comparison of RMS roughness ( $R_q$ ) and Mean roughness ( $R_a$ ) between LSM and the Low cost alternative.

LSM		Error	Low cost alternative	
$R_q$ ( $\mu\text{m}$ )	23,38	7,37%	$R_q$ ( $\mu\text{m}$ )	25,24
$R_a$ ( $\mu\text{m}$ )	18,65	8,67%	$R_a$ ( $\mu\text{m}$ )	20,42

## REFERENCES

- [1] GADELMAWLA, E. S. et al. Roughness parameters. **Journal of materials processing Technology**, v. 123, n. 1, p. 133-145, 2002.
- [2] KUBIAK, K. J.; LISKIEWICZ, T. W.; MATHIA, T. G. Surface morphology in engineering applications: Influence of roughness on sliding and wear in dry fretting. **Tribology International**, v. 44, n. 11, p. 1427-1432, 2011.
- [3] GUO, K. W. Effect of polishing parameters on morphology of DF2 (AISI-O1) steel surface polished by Nd: YAG laser. **Surface Engineering**, v. 25, n. 3, p. 187-195, 2009.



## Recognition of the Phase Penetration Index in Iron Ore Sample Using Computer Vision and Machine Learning

Karen Soares Augusto<sup>1\*</sup>, Julio César Álvarez Iglesias<sup>1</sup>, Sidnei Paciornik<sup>1</sup> and Alei Leite Alcantara Domingues<sup>2</sup>

<sup>1</sup> Dept. of Chemical and Materials Engineering (DEQM), PUC-Rio, Rio de Janeiro, Brazil

<sup>2</sup> CTF/VALE, Nova Lima, Minas Gerais, Brazil

\*saugustokaren@gmail.com

Iron ore agglomeration processes, such as pelletizing and sintering, aim at obtaining products with appropriate size, shape and mechanical strength to feed the reduction furnaces in the primary iron production. The choice of one of these processes will depend on a series of factors that involve the physical-chemical characteristics and volume of the raw material, operational costs and others. In order to evaluate the quality of the reaction between the iron ore and gangue, which happens in the sintering process (and also, to a certain extent during pelletizing), a specimen, that will melt, is placed on top of an iron ore briquette sample. As the temperature increases, the liquid phase generated by the upper specimen penetrates into the sample. The goal of the present work is to delimit and measure, by image analysis, the penetration of the liquid phase in the briquette. The images, acquired by optical microscopy, were provided by Vale. Considering that the region reached by the liquid has distinct texture characteristics from the original briquette, a methodology based on semantic segmentation was proposed to identify the penetrating phase. The image processing was performed within the public domain software FIJI [1], using an available plugin called Trainable Weka Segmentation [2]. Approximately 10 regions of interest of each phase of 9 images were used for the training. Training features used were Gaussian Blur, Hessian, Membrane projections, Sobel filter and Difference of Gaussians. The classifier was the Fast Random Forest [3]. The generated model was tested in complete images of these same samples. The methodology was successful in the discrimination phase, allowing us to obtain the area fraction and depth measurements in the penetration profile of the liquid phase along the sample, as shown in Figure 1-B. It is important to emphasize that in order to measure the length of each line, they are considered connected. Once the routine is fully developed and robust, it will be routinely used by CTF/Vale.

### REFERENCES

- [1] Fiji: an open-source platform for biological-image analysis. *Nature Methods*. 9 (2012).
- [2] Trainable Weka Segmentation: a machine learning tool for microscopy pixel classification. *Bioinformatics*. 33 (2017).
- [3] Random Forests. *Machine Learning*, 45 (2001).
- [3] This research was supported by CNPq, CAPES and FAPERJ.

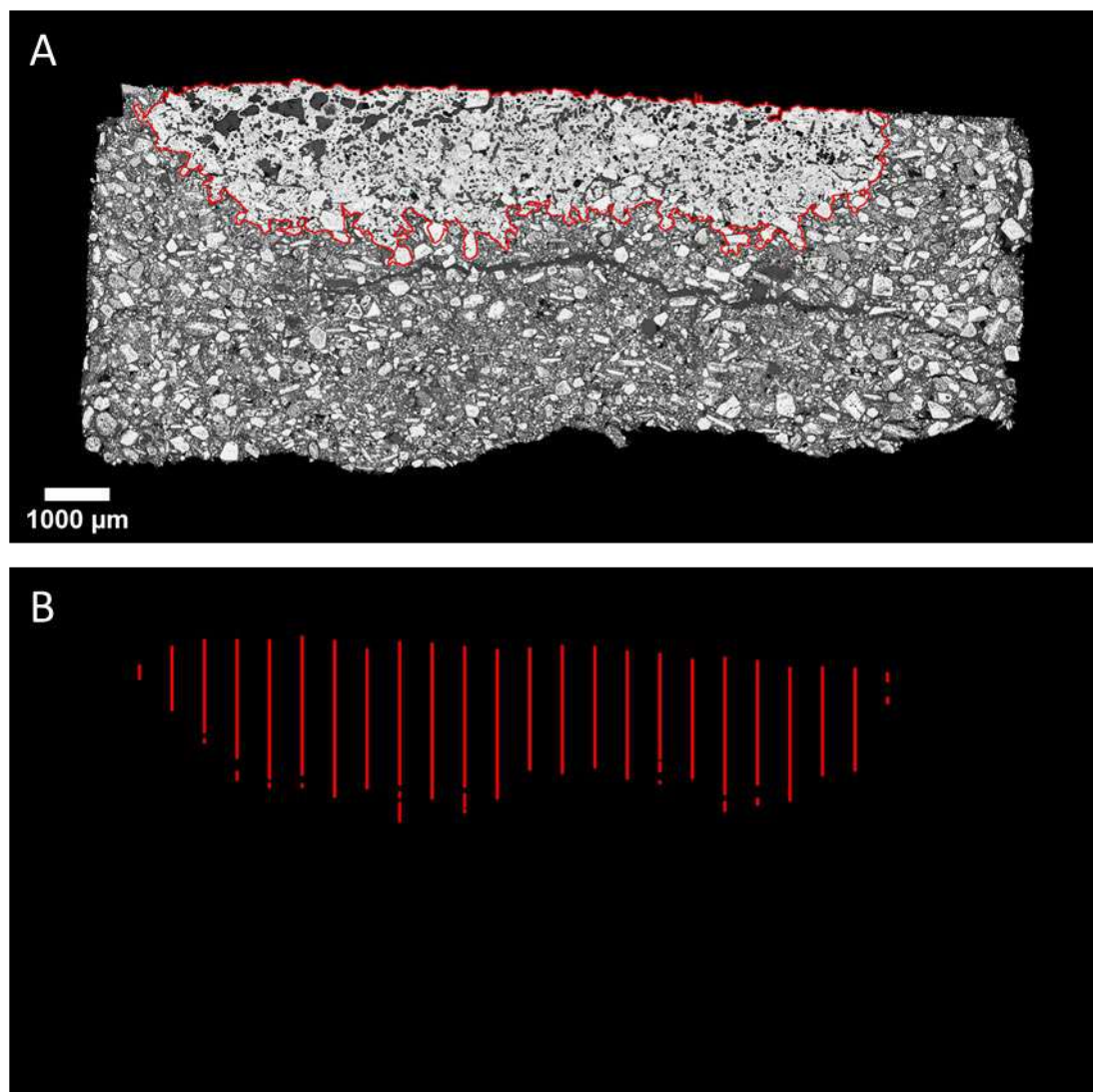


Figure 1 – A) Original image with penetrating phase discriminated in red;  
B) Liquid phase penetration profile.

Table 1 – Area fraction and depth measurements of the detected phase

Penetrating Phase		
Area Fraction (%)		27,37
Depth ( $\mu\text{m}$ )	Minimum	1705
	Maximum	3893
	Average	3194
	Mode	3545

## Exposure to 17 $\alpha$ -ethinylestradiol during development period alters the folliculogenesis and the frequency of interstitial gland on the ovary of senile gerbils (*Meriones unguiculatus*)

Vinícius Gonçalves de Souza<sup>1</sup>, Laura Borges Bandeira<sup>1</sup>, Nátaly Caroline Silva e Souza<sup>1</sup>, Tracy Martina Martins Marques<sup>1</sup>, Sebastião Roberto Taboga<sup>2</sup> and Ana Paula da Silva Perez<sup>3\*</sup>

<sup>1</sup>. Medicine Course, Federal University of Goiás (UFG), Jataí, GO, Brazil.

<sup>2</sup>. Department of Biology of São Paulo State University (IBILCE/UNESP), São José do Rio Preto, SP, Brazil.

<sup>3</sup>. Medicine Course, Postgraduate Program in Animal Bioscience, Federal University of Goiás (UFG), Jataí, GO, Brazil.

\*paulabio\_perez@yahoo.com.br

17 $\alpha$ -ethinylestradiol (EE), component of oral contraceptive, acts as endocrine disruptor. The exposure to EE promote several changes in ovary's mammals [1,2]. The aim this study was analyze the effects of the exposure to EE during development period on the ovary of senile gerbils (*Meriones unguiculatus*). For this, females gerbils were exposed to 15  $\mu$ g/kg/day of EE during the prenatal period (EE/PRE group), puberty (EE/PUB) and the both periods (EE/PRE-PUB). In the control group, the females were not treated. Animals were killed (n=4) after 12 months (CEUA/UNESP, 020/09). Testosterone and 17 $\beta$ -estradiol levels were taken by ELISA kits. The ovaries of the experimental groups were submitted to histological processing and stained with Hematoxylin and Eosin (HE) and Periodic Acid Schiff (PAS). The ovarian follicles were counted and classified in primordial, unilaminar and multilaminar primary, secondary and mature. The interstitial gland was identified and submitted to stereological analysis. The statistical analysis was performed using the analysis of variance (ANOVA) and Tukey's test. In the EE/PUB and EE/PRE-PUB group, observed an increased in the primordial follicles quantity. The numbers of pre-antral follicles (primary and secondary) decreased in EE/PRE and EE/PUB groups, while the EE/PUB presented less multilaminar primary follicle when compared to control groups. Primordial follicles are formed in the last half of fetal life and neonatal period in mice, while the folliculogenesis occurs during the puberty and sexual life [1]. The estradiol hormone is important during the antral folliculogenesis and ovulation, while no have substantial function during pre-antral folliculogenesis. However, our results suggest that the exposure to EE during development periods affects the pre-antral folliculogenesis, reducing the number of developing follicles during aging. The serological analysis shows a significant increase in the estradiol levels of the EE/PRE and EE/PUB groups. Whereas the testosterone levels were higher in the EE/PUB group when compared to control group. The stereological analysis of interstitial gland revealed a significant increase in the EE/PUB and EE/PRE-PUB groups compared to control group. This data also higher between the EE/PUB and EE/PRE-PUB groups. This gland presents a role important in steroid synthesis [3]. Thus, we concluded that exposure to EE during development period promotes disruption in folliculogenesis, hyperplasia of the interstitial gland and consequential changes in the steroidogenic function during aging.

[1] H. Zhang et al., Biol Reprod. 95 (4) (2016) 78.

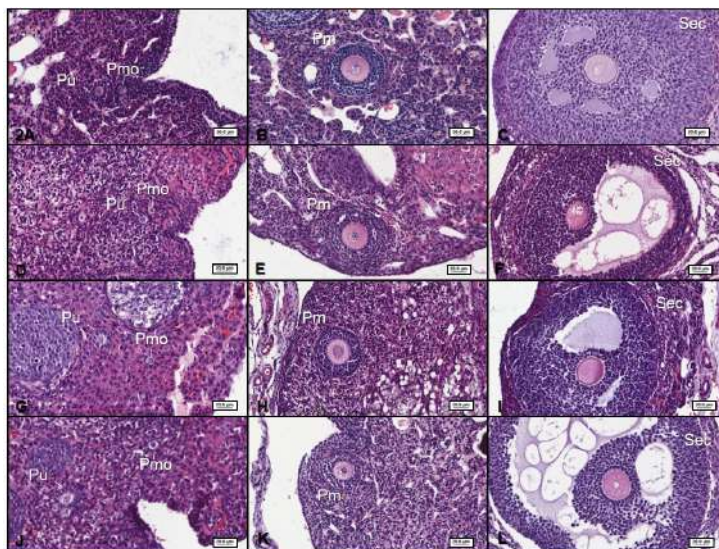
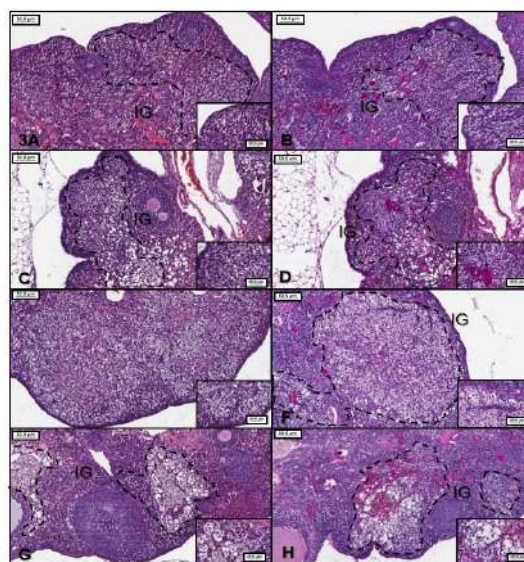
[2] H. Zhang et al. Toxicol Lett., 276 (2017) 92.

[3] M. M. Awad et al. Reprod Domest Anim., 53 (4) (2018) 872.

**Table 1. Ovarian follicle quantity, stereological analysis of interstitial gland and serological data of the experimental groups.**

Parameters	Control	EE/PRE	EE/PUB	EE/PRE-PUB
<b>Primordial follicles</b>	2.54 <sup>a</sup> ± 2.69	3.20 <sup>a,b</sup> ± 2.23	4.91 <sup>b,c</sup> ± 2.94	7.20 <sup>c</sup> ± 5.70
<b>Unilaminar primary follicles</b>	3.74 <sup>a,c</sup> ± 3.24	1.89 <sup>b</sup> ± 1.69	2.61 <sup>a,b</sup> ± 2.21	4.54 <sup>c</sup> ± 2.79
<b>Multilaminar primary follicles</b>	2.74 <sup>a</sup> ± 1.58	0.89 <sup>b</sup> ± 0.80	1.67 <sup>b</sup> ± 1.71	1.72 <sup>b</sup> ± 1.67
<b>Secondary follicles</b>	0.31 <sup>a</sup> ± 0.58	0.17 <sup>a,b</sup> ± 0.45	0.03 <sup>b</sup> ± 0.17	0.47 <sup>a,b</sup> ± 0.08
<b>Mature follicles</b>	0.00 ± 0.00	0.00 ± 0.00	0.16 ± 0.57	0.05 ± 0.22
<b>Interstitial gland (%)</b>	6.82 <sup>a</sup> ± 11.19	8.15 <sup>a</sup> ± 14.07	23.04 <sup>b</sup> ± 15.45	16.74 <sup>c</sup> ± 17.31
<b>Testosterone levels (ng/ml)</b>	1.01 <sup>a</sup> ± 0.18	1.45 <sup>a,b</sup> ± 0.25	3.24 <sup>b</sup> ± 0.19	1.46 <sup>a,b</sup> ± 0.56
<b>Estradiol levels (pg/ml)</b>	7.95 <sup>a</sup> ± 2.20	21.23 <sup>b</sup> ± 3.56	19.90 <sup>b</sup> ± 5.70	13.40 <sup>a,b</sup> ± 1.49

Value expressed as mean ± standard deviation. Superscript letters (<sup>a,b,c</sup>) indicate significant statistically differences among experimental groups (n=4).

**Figure 2.** Histological sections from ovary of experimental groups stained by Hematoxylin-Eosina (HE). Control: A-C. EE/PRE Group: D – F. EE/PUB Group: G – I. EE/PRE-PUB Group: J – L. Primordial (Pmo), primary unilaminar (Pu), primary multilaminar (Pm) and Secondary (Sec).**Figure 3.** Histological sections from ovarian interstitial gland of experimental group stained by Hematoxylin-Eosina (HE) and Periodic Acid Schiff (PAS). Control: A (HE), B (PAS). EE/PRE Group: C (HE), D (PAS). EE/PUB Group: E (HE), F (PAS). EE/PRE-PUB Group: G (HE), H (PAS). Interstitial Gland (IG).



## Plasmonic Nanoparticles as Nanosensors for Indirect Measurement of the Substrate Refractive Index

Erika L. Butthers<sup>1\*</sup>, Thiago L. Vasconcelos<sup>2</sup> and Braulio S. Archanjo<sup>2</sup>

<sup>1</sup> Universidade Federal do Rio de Janeiro, Campus Duque de Caxias, Duque de Caxias, RJ-Brazil. E-mail: erikabutthers@gmail.com

<sup>2</sup> Instituto de Metrologia, Qualidade e Tecnologia (Inmetro), Divisão de Metrologia de Materiais (Dimat), RJ-Brazil

Localized surface plasmon resonance (LSPR) is a collective oscillation of conduction electrons resonating on the surface of subwavelength metal nanostructures [1]. A remarkable characteristic of it is that the resonance energy is spectrally discrete (related to their electric dipole modes) and can be tuned by changing the size, shape of the host nanostructure, as well as by changing the medium optical properties. Among several technology applications for using LSPR on metal nanoparticles, the usage of them as nanobiosensors through measuring the nanoparticles scattering spectrum maxima due to changes of the medium optical properties has drawn special attention. In this work, we applied simulations tools to study the changes in LSPR spectrum of gold nanorods as consequence of its medium optical properties changes. Through the implementation of the finite element method in the study of plasmonic nanoparticles with a MATLAB<sup>®</sup> toolbox called MNPBEM [2], it was possible to track changes in the optical response of gold nanoparticles of different shape and medium. The simulations were performed for gold nanorods with 15 nm of width and three different lengths (50 nm, 60 nm and 100 nm), covered with a thin layer of carbon with six distinct thicknesses (1 nm, 2 nm, 3 nm, 4 nm and 5 nm), including no cover at all (Fig. 1a). Each rod was illuminated with the electromagnetic wave polarization along both the long and short rod axes direction. Another simulation was done to investigate the response of the nanoparticles laid on different substrates with four refractive indexes (Fig. 1b). One goal of this study is to predict and apply gold nanorods (Fig. 2) to indirectly measure the refractive index of a dragonfly wing core [3], analyzing the light scattering of the nanoparticles in contact with the material. The wing core is composed of distinct intercalated nanolayers (~100 nm of thickness) of chitin and chitosan with different refractive index, what lead to interference effect and beautiful reddish and greenish colors. The first simulations results showed that the wavelength of the scattering spectral maximum is redshifted and its intensity decreases as the carbon cover layer get thicker. Regarding its uses as refractive index sensors, the simulations showed that the variation of the substrate refractive index from 1.5 to 1.8 leads to a relative high redshift ( $\Delta\lambda_{\max} \sim 15$  nm) on the scattering spectral maxima, which is sufficient for experimental tests on the real wing.

### REFERENCES

- [1] T.L. Vasconcelos, B.S. Archanjo, L.G. Cançado, et al., ACS Nano 9 (2015) 6297.
- [2] U. Hohenester and A. Trügler, Comp. Phys. Commun. 183 (2012) 370.
- [3] W.W. Valeriano, Cores Estruturais da Asa da Libélula *Chalcopterix rutilans*, Dissertação, Departamento de Física da UFMG, Belo Horizonte, (2015).
- [4] This research was supported by CNPq (Brazil) and Inmetro (Brazil).

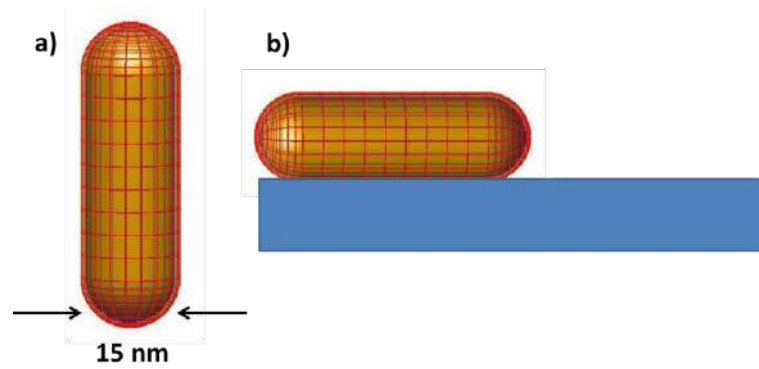


Figure 1: Objects simulated: (a) Gold nanorod (yellow) with a carbon cover (orange).  
(b) The same nanorod over the dielectric substrate.

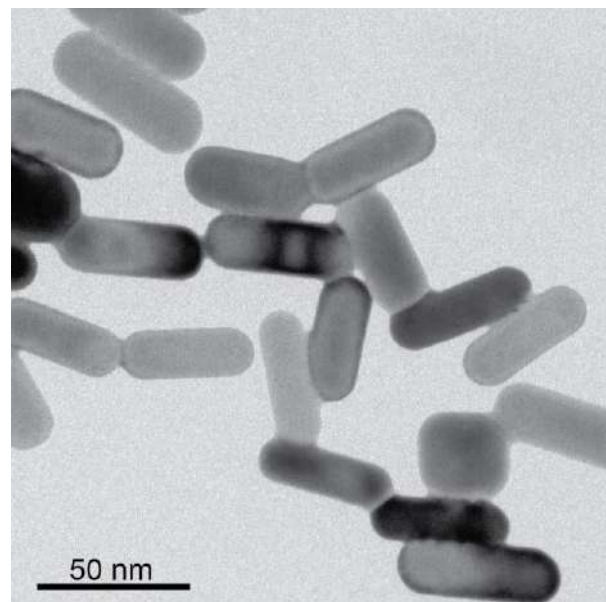


Figure 2: Transmission electron microscopy image of gold nanorods, which will be used in the experimental part of this work.

## Magnetic Arrays made by Lithography from Targets of Pressed Fe<sub>3</sub>O<sub>4</sub> Nanoparticles

Geronimo Perez<sup>1</sup>, Elisa Maria Baggio Saitovich<sup>2</sup>, Bráulio Soares Archanjo<sup>1</sup>, Ivan Guillermo Solorzano-naranjo<sup>3</sup>

<sup>1</sup>. Materials Metrology Division/Instituto Nacional de Metrologia, Duque de Caxias, Brazil.

<sup>2</sup>. Experimental Physics Coordination/Centro Brasileiro de Pesquisas Físicas, Rio de Janeiro, Brazil.

<sup>3</sup>. Materials Engineering Department/Pontificia Universidade Católica, Rio de Janeiro, Brazil.

The semi-metallic Fe<sub>3</sub>O<sub>4</sub> films have attracted interest by the characteristic of combining a 100% spin polarization with a high Curie temperature [1] and have a relatively high conductivity [1]. These have been of great interest due to the properties of spin in an insulating material, therefore, are candidates for spintronic applications [2], such as magnetoresistive devices or magnetic tunneling junctions [1, 3]. Magnetite thin films were produced using the sputtering RF (radio frequency source) deposition system. The thin films were deposited on a silicon substrates. The formation of the magnetite after the deposition was confirmed by x-ray (XRD) diffraction and vibrating sample magnetometer (VSM). The magnetite films presented a magnetic saturation near 85 emu/cm<sup>3</sup> at longitudinal direction (easy magnetization direction). The targets to sputtering were produced by compression of magnetite nanoparticles previously produced by chemical method of co-precipitation from mixing of iron salts and ammonium hydroxide. Figure 1 shows TEM micrograph of magnetite nanoparticles: (a) selected area electron diffraction pattern, (b) multi beam, (c) HRTEM of a particle. Periodic arrays of circles and squares were produced by electron beam lithography combined with sputtering deposition and lift-off process. The first step was the preparation of the resist, polymethylmethacrylate (PMMA) film, of 250 nm thick by spin coat method on silicon substrate. At the second step, this sample was drawn by electron beam and later, immersed into acetone solution for some seconds to remove the material affected by the beam to produce the mask of the arrays. Then, the magnetite film was deposited onto the lithographed sample by RF sputtering. Finally the sample was immersed in acetone until all the PMMA film has been lifted-off. The film thickness, shape, size and separation between the figures which comprise standards lithographed can influence the ease with which the mask is withdrawn from PMMA. Scanning electron microscopy (SEM), atomic force microscopy (AFM) and magnetic force microscopy (MFM) images provide additional information. The AFM provides good topography and thickness information.

### References:

- [1] H. Takahashi, *et al*, J Appl Phys, 2003,93: 8029-8031.
- [2] X. L. Tang, *et al*, Journal of Solid State Chemistry 179 (2006) 1618–1622.
- [3] K. I. Aoshima and S. X. Wang, J. Appl. Phys. 93 (2003) 7954.
- [4] This research was supported by CNPq (Brazil).

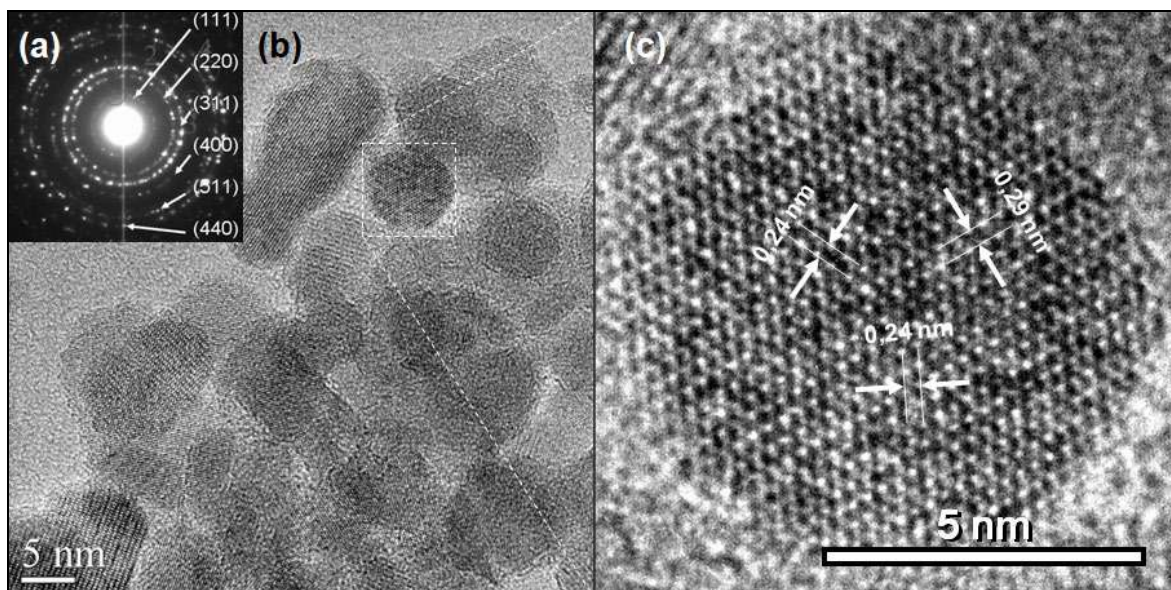


Figure 1 - TEM micrograph of magnetite nanoparticles: (a) selected area electron diffraction pattern, (b) multi beam, (c) HRTEM of a particle.

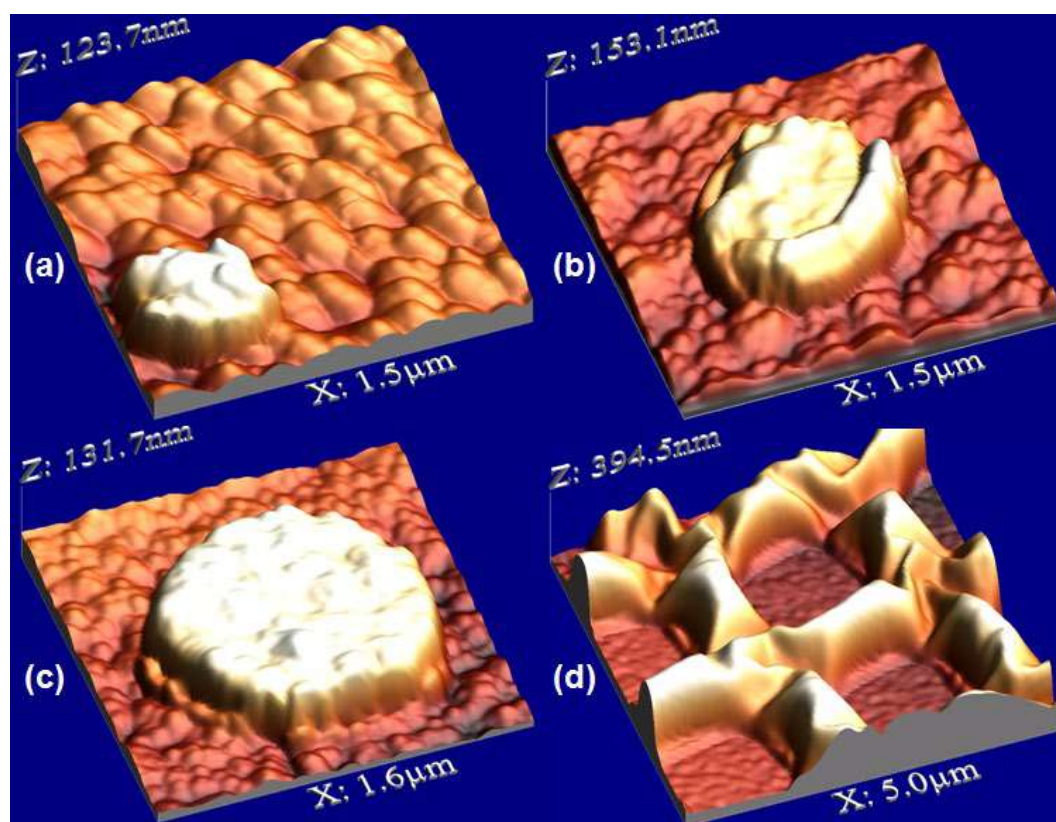


Figure 2. AFM images of the shapes corresponding to different arrays: (a) 250 nm circles, (b) 500 nm circles, (c) 1  $\mu$ m circles, (d) 1  $\mu$ m squares.



## Optical and structural properties of Co-doped ZnO nanoparticles

Marianne R. de Freitas<sup>1</sup>, Ney Mattoso<sup>2\*</sup>

<sup>1</sup> PIPE/UFPR, Curitiba-PR, Brazil.

<sup>2</sup> Department of Physics/UFPR, Curitiba -PR, Brazil.

Zinc oxide (ZnO) is one of the most studied materials due to its semiconductor properties and in the biomedical area as a bactericidal agent [1,2]. However, there are few studies on the characterization of nanoparticles (NPs) of ZnO doped with transition metals. This work presents the results on the influence of cobalt (Co) doping in different percentages in ZnO nanoparticles. These nanoparticles were synthesized by sol-gel method using zinc acetate and cobalt acetate in aqueous solutions and mono ethylene glycol as stabilizing agent. The following percentages of Co: 1, 2, 5, 10 and 20% (moles of Co/moles of Zn) were used. After drying the samples were calcinated to 400 °C for 1 hour. The morphology of NPs was evaluated by TEM (JEOL JEM 1200 EX-II) The structure was analyzed by SAED in the same equipment. Co incorporation in NPs was determined by EDS (Oxford with an X-Max 80 SDD detector) in SEM (TESCAN VEGA3 LMU). The optical properties were studied by CL (Gatan Mono CL4 Plus) in SEM (JEOL JSM 6360-LV). Morphologically, no alterations in the average particle size were observed, however, a development of NPs agglomeration was observed with the increase in the incorporation of Co. Structurally no alterations were observed in the electron diffraction pattern of the ZnO, Only one extra plane (0.2063 nm) was observed, which was interpreted with an expansion of the ZnO plane (102) (0.1911 nm). The results of EDS revealed that only half of the Co ions in solution are incorporated into the ZnO nanoparticles. The CL measurements show that in the sample with 1% nominal Co presents a very similar emission to the pure ZnO in the green region. With 2% nominal the emission becomes a greenish-yellow. In the 5% nominal composition there is a emission reduction but there are still some NPs emitting in blue. A lilac emission is observed for few particles in the composition of 10% nominal. In the composition of 20% nominal emission is even more reduced but were found emitting in yellow. In conclusion we observed the success in the production of NPs of ZnO doped with Co. These NPs have a luminescent emission strongly dependent on the amount of Co incorporated due to the generation of punctual structural defects. These results show that they are interesting for the manufacture of optoelectronic devices and as bactericidal agents activated with photons in the visible spectrum.

### References:

- [1] K. Omri et al., *Ceram. Int.* 42 (2016) 8940.
- [2] G. Vijayaprasath et al., *Mater. Res. Bull.* 76 (2016) 48.

### Acknowledgements:

CNPq, LABNANO/UFPR, Centro de Microscopia Eletrônica da UFPR.

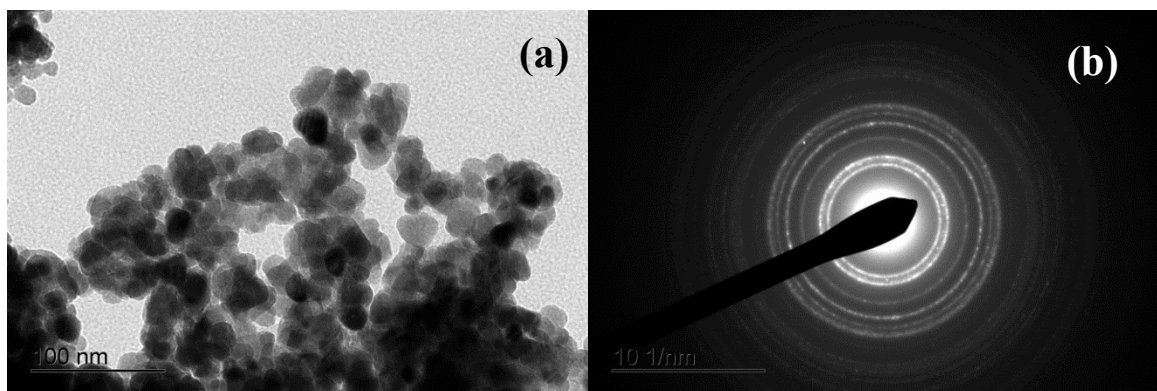


Figure 1-(a) electromicrography of ZnO nanoparticles doped with 2% nominal Co, (b) SAED of the same area of (a).

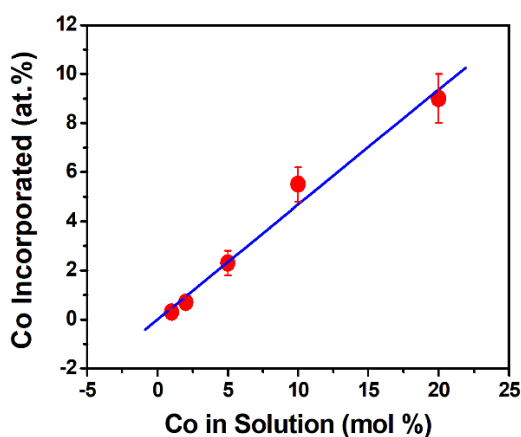


Figure 2 – EDS results showing the relationship between cobalto acetate in solution with Co incorporated in ZnO nanoparticles.

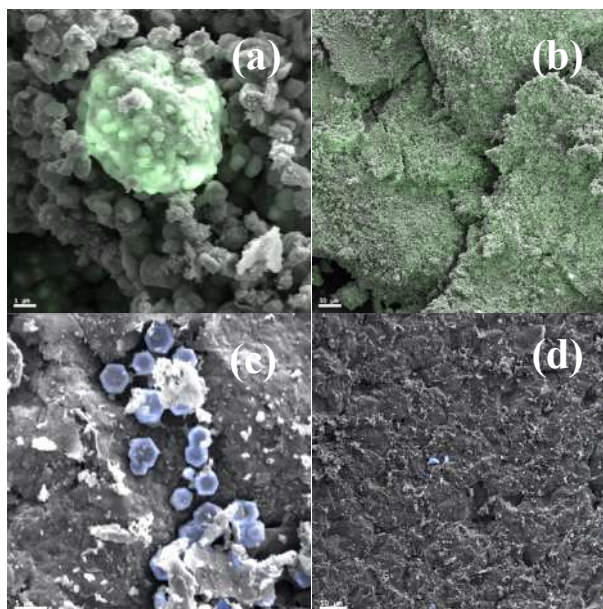


Figure 3-Superimposed CL images with SEM images. (a) 1% nominal Co with magnification of 5 kX, (b) 1% nominal Co with magnification of 150 X, (c) 10% nominal Co with magnification of 2 kX, (d) 10% nominal Co with magnification of 150 X.

## **Comparative Study between Comminutions Made in Conventional Ball Mill, Attritor Mill and Planetary Mill Aiming to Obtain Submicrometric / Nanometric Particles of Iron Oxide**

Ronilson de Carvalho Martins<sup>1\*</sup> and Antônio José Oliveira Cabral<sup>2</sup>

<sup>1</sup>Mechanical Engineering /UFF, Volta Redonda, Brasil.

E-mail: ronilsoncmartins@id.uff.br

<sup>2</sup> Mechanical Engineering/UFF, Volta Redonda, Brasil.

E-mail: ajoc@metal.eeimvr.uff.br

The focus of this work is on particle size analysis of iron oxide ( $\text{Fe}_2\text{O}_3$ ), from the industry, more specifically the URA from Companhia Siderúrgica Nacional (CSN), with the objective of particles with a final size below  $1\ \mu\text{m}$  for application in the manufacture of magnetic ferrite for end use in magnetic motors, widely discussed in the literature in recent years. For this purpose, an experimental study was carried out by means of comminution of said oxide using three types of mills: conventional ball mill (low energy), attritor mill (high energy) and planetary mill (high energy). The comminution efficiency was analyzed in all the processes by analyzing the milling time and particle size. It is noteworthy that this work aims to develop a low cost magnetic ferrite via commercial route. In figure 1 it is verified that after 24 hours of comminution in conventional ball mill the particle has a narrow particle size distribution with a mean size of  $0.50\ \mu\text{m}$ . For a longer comminution time (48 h) in the ball mill, figure 2, the same narrow particle size distribution is observed, with particles having an average size of  $0.23\ \mu\text{m}$ . In the comminution carried out in an attritor mill with 1 hour of milling, (figure 3), the high efficiency of the mill is observed in rapidly reducing the particle size, since a significant part of the particles are below  $1\ \mu\text{m}$ . After 3 hours of comminution in the attritor mill, figure 4, little evolution is observed in the reduction of the particle size in relation to the time of 1 hour. With 7 hours of milling in the attrition mill, figure 5, there are still observed particles which have not suffered a reduction of the particle size so intense, thereby demonstrating that it does not lend itself to effectively producing a uniform size distribution of particle, even over time (24 hours), according to figure 6. An agglomeration of particles is observed in all the MEVs, be it in the ball mill as well as in the attritor mill. Aímola et al (2017) and Cabral (2001) explain this fact. In the respective works of the mentioned authors, it is possible to verify that the false increase of the particle size is proportional to the time of comminution due to the effect of agglomeration between the particles. Cabral (2001) analyzed the comminution of iron oxide using a planetary mill and obtained after 1 hour and 15 min of comminution particles in the size of  $0.38\ \mu\text{m}$ , with high uniformity and only 5% of them greater than  $1\ \mu\text{m}$ . Similar suit for longer times. It is concluded in this work that although the conventional ball mill needs more time to commence the iron oxide (24 hours), it has a narrow particle size distribution and below  $1\ \mu\text{m}$ . In comparison to the three mills, the conventional ball mill is the most suitable for industrial application, either by the uniform product obtained therefrom or by the amount of material produced. The planetary mill presents a greater efficiency than the attritor mill for comminution and a narrow granulometric distribution, similar to the conventional ball mill, but for times greater than 1h and 15 minutes it tends to agglomerate the particles due to the process of mechanical allowing, mainly in the grinding dry. In this work, with a view to industrial reproducibility at low cost, conventional ball mill was used to reduce the iron oxide content.



## AGRADECIMENTOS

The authors are grateful for the collaboration of the UFF with the availability of the MEV Equipment to characterize the respective material.

## REFERÊNCIAS

A.J.O Cabral et al., Prep. Oxido Ferro subm. Aplic. Cer. magn. 5 (2001)  
T.J. Aímola, E.C. Paris, Moagem de Ox. Zinco em Moinho Atritor (2017).

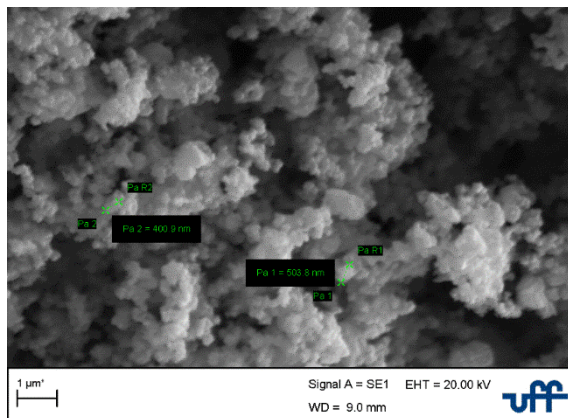


Figure 01. Iron oxide (conventional ball mill) after 24 hours. Increase of 20380 x

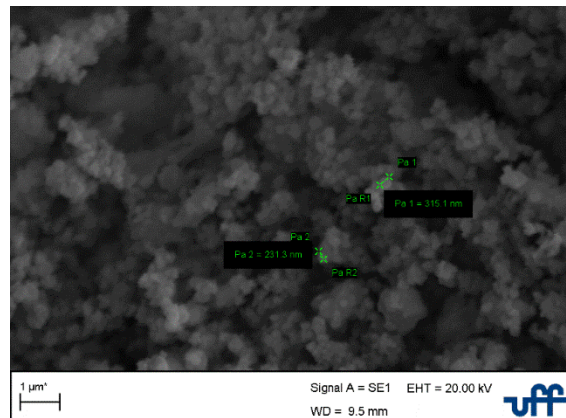


Figure 02. Iron oxide (conventional ball mill) after 48 hours. Increase of 20380 x

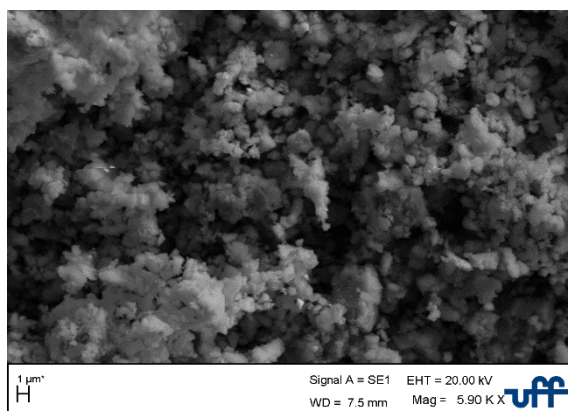


Figure 03. Iron oxide (attritor mill) after 1 hour. Increase of 5900x.

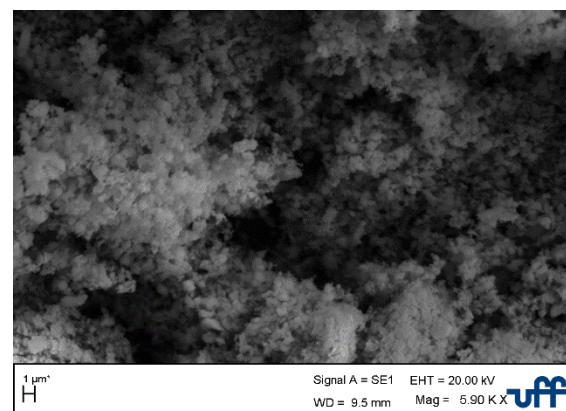


Figure 04. Iron oxide (attritor mill) after 3 hours. Increase of 5900x.

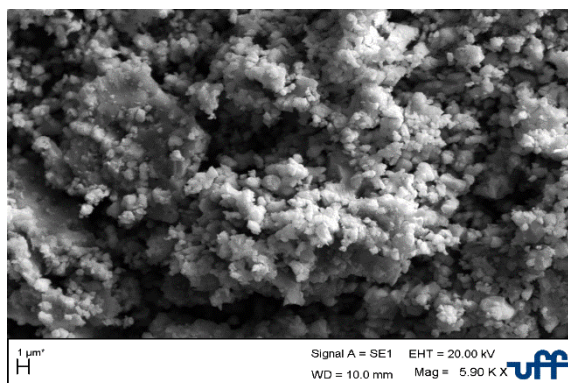


Figure 05. Iron oxide (attritor mill) after 7 hours. Increase of 5900x.

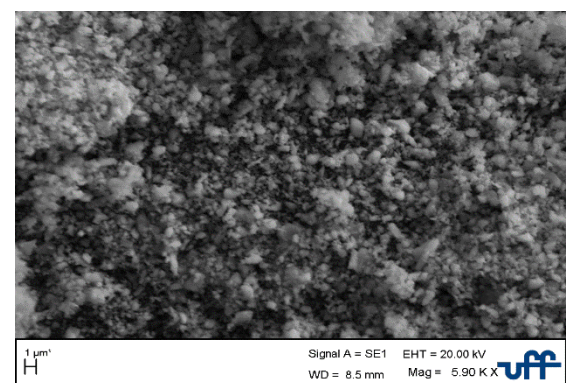


Figure 06. Iron oxide (attritor mill) after 24 hours. Increase of 5900x.



## Evaluation of Images Before and After Asphalt Binder Indentations Generated In AFM

Thaísa Ferreira Macedo<sup>1\*</sup>, Renata Antoun Simão<sup>2</sup>, Francisco Thiago Sacramento  
Aragão<sup>3</sup>, Leni Figueiredo Mathias Leite<sup>4</sup>

<sup>1</sup>. UFRJ, Department of Civil Engineering, Rio de Janeiro-RJ, Brasil,  
thaisa\_197@hotmail.com

<sup>2</sup>. UFRJ, Department of Materials and Metallurgy, Rio de Janeiro-RJ, Brasil,  
renata@metalmat.ufrj.br

<sup>3</sup>. UFRJ, Department of Civil Engineering, Rio de Janeiro-RJ, Brasil,  
fthiago@coc.ufrj.br

<sup>4</sup>. UFRJ, Department of Civil Engineering, Rio de Janeiro-RJ, Brasil,  
lenimathias@yahoo.com.br

### ABSTRACT

The present work aims to verify differences and/or similarities in the images generated before and after nanoindentations in asphalt binders with different load levels with the use of an atomic force microscope (AFM). Prior to the generation of the binder samples, this material was heated in an oven at 140°C and then placed on a glass plate which was rotated in a spin coater, followed the procedure proposed by Macedo et al., (2018) [1]. After a period of 24h, it were generated images of topography and phase contrast, with size 10 x 10  $\mu\text{m}^2$ , using the AFM, it showed Figures 1a and 1b [2], respectively, before the nanoindentation, showing well-defined asphalt binder microstructures. Then, force curves of different magnitudes ranging from 20 to 100 nN (for instance, the Figure 2) were applied in the different phases or microstructures (black bee, white bee, perifase and parafase). New images of topography and phase contrast were generated after the nanoindentation tests (or force curves). In some points in the paraphase, perifase and white bee where were applied forces of 70 nN and 100 nN it was possible to observe in the topography and phase contrast images (Figures 3a and 3b [2]) many changes occurred in the microstructure, that is, the bees practically disappeared. This may have been due to the levels of loading and the realization of several nanoindentations besides the molecular formation of each microstructure presented and with different mechanical behaviors. The results show that the images after the nanoindentations underwent changes and the microstructures were modified, probably, due to the proximity between each force curve, applied force intensity and material composition. Therefore, it was possible to conclude that the AFM is a tool for the identification of detailed microstructural characteristics of asphalt binder constituents and verification of the mechanical properties of microstructural constituents. In addition, it was found that the microstructural constituents of the binder behaved as linear viscoelastic material, since their mechanical responses varied with the loading time. The mechanical properties of the microstructural components of the binders are probably related to the chemical characteristics of these components.

[1] T. F. Macedo et al., Rev. Transportes. V 26, n3, (2018) 1616.

[2] T. F. Macedo M.A. Thesis, UFRJ, Rio de Janeiro-RJ, Brazil, 2018.

[3] This research was supported by CAPES and FAPERJ (Brazil).

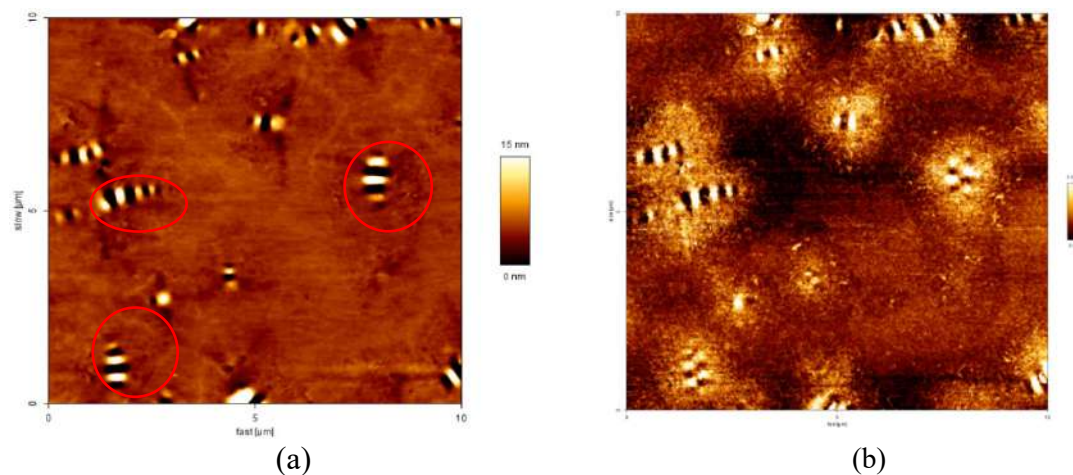


Figure 1 - Images of topography and phase contrast of the binder: (a) and (b) before the nanoindentation tests, respectively [2].

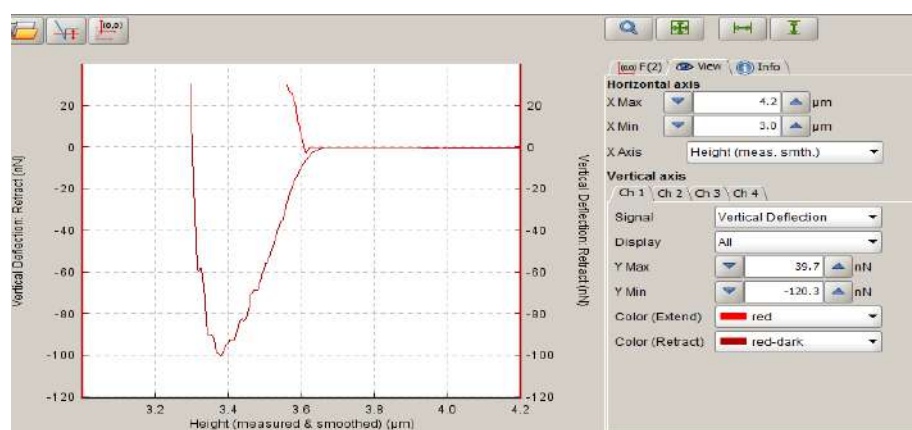


Figure 2 - Force curve obtained with the AFM, by the JPK program [2].

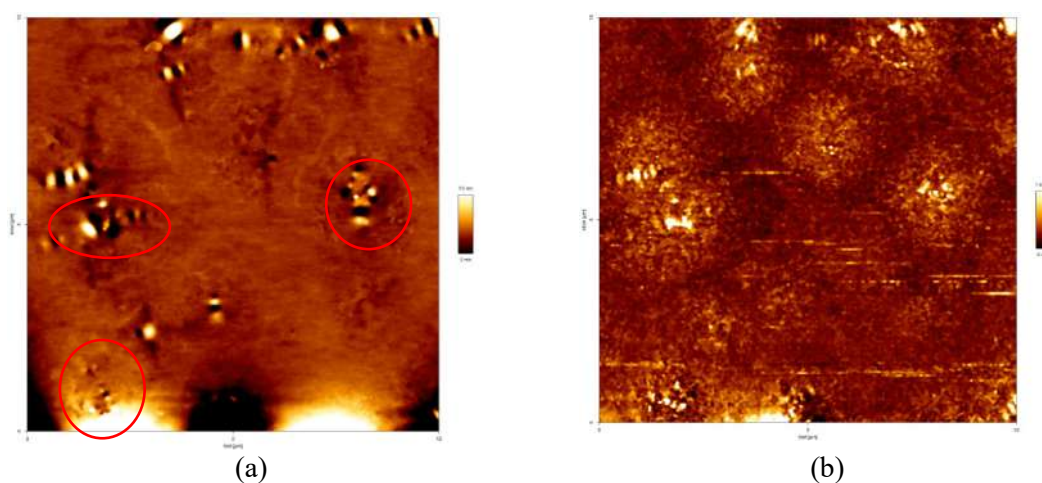


Figure 3 - Images of topography and phase contrast of the binder: (a) and (b) after the nanoindentation tests, respectively [2].

## Analysis of Cracks and Coating in Iron Ore Pellets through Digital Image Processing

Thalita Dias Pinheiro Caldas<sup>1\*</sup>, Karen Soares Augusto<sup>1</sup>, Julio Cesar Alvarez Iglesias<sup>1</sup>,  
Sidnei Paciornik<sup>1</sup> and Alei Leite Alcantara Domingues<sup>2</sup>

<sup>1</sup>. Department of Chemical and Materials Engineering, Catholic University of Rio de Janeiro (DEQM-PUC-Rio), Rio de Janeiro, Brazil.

<sup>2</sup>. CTF/VALE, Nova Lima, Minas Gerais, Brazil.

\*[yeshuathalita@gmail.com](mailto:yeshuathalita@gmail.com)

Iron ore pellets are produced by the agglomeration of fines resulting from the mining process, which cannot be used directly in steel production reduction reactors because they hamper the flow of essential charge into the furnaces [1]. In pelletizing stages, specifically in those where the pellets are exposed to compressive stresses or sudden changes in temperature, the formation of cracks occurs, which would impair both their mechanical strength and their performance in reactors [2]. Besides the formation of cracks, the formation of clusters of pellets during the reduction process is another factor that compromises the efficiency of the reactors. In order to minimize this cluster effect, the pellets are covered with an inhibitor coating which acts to attenuate possible formations of iron bridges between them [3]. Thus, characterizing the cracks and the region occupied by the coating, both of which can be observed on the surface, is important for the quality control of the pellets [4]. Through a partnership between the Research Group in Digital Microscopy and Image Analysis (MicDigi) of PUC-Rio and the company VALE, the present study sought to develop a methodology for characterizing the surface of iron ore pellets. The samples were provided by the company ready for acquisition of the images, which was performed from a Zeiss Discovery V8 stereoscope. Despite the challenge of performing a 2D characterization of an approximately spherical object, image acquisition by keeping the sample on a support, which is under development, proved to be feasible, avoiding problems of overlapping regions and allowing to cover the full surface of the pellet. Image processing/analysis was performed with the FIJI/ImageJ free software [5]. The procedure is automated, providing measurements of crack local thickness and total fractured area and of total/relative coating area.

### REFERENCES

- [1] J.M. Mourão, Aspectos Conceituais Relativos à Pelotização de Minérios de Ferro, (2017) 12-18.
- [2] H.O. Simões et al., Criação de Algoritmo para Análise de Imagens de Trincas e da Pelota Queimada e Correlação de seus Parâmetros com a Resistência Física do Material. 45° Seminário de Redução de Minério de Ferro e Materiais-primas. (2015) 961-969.
- [3] A.M.G. Bailon et al., Determinação de Metodologia para Avaliação das Causas de Colagem em Reatores de Redução Direta. 12° Seminário Brasileiro de Minério de Ferro. (2015) 1152-1159.
- [4] J. Sterneland et al., The use of coated pellets in optimising the blast furnace operation. ISIJ International. 43 (2003) 26-35.
- [5] C.T. Rueden et al., "ImageJ2: ImageJ for the next generation of scientific image data", BMC Bioinformatics. (2017).
- [6] This research was supported by CNPq, CAPES and FAPERJ.

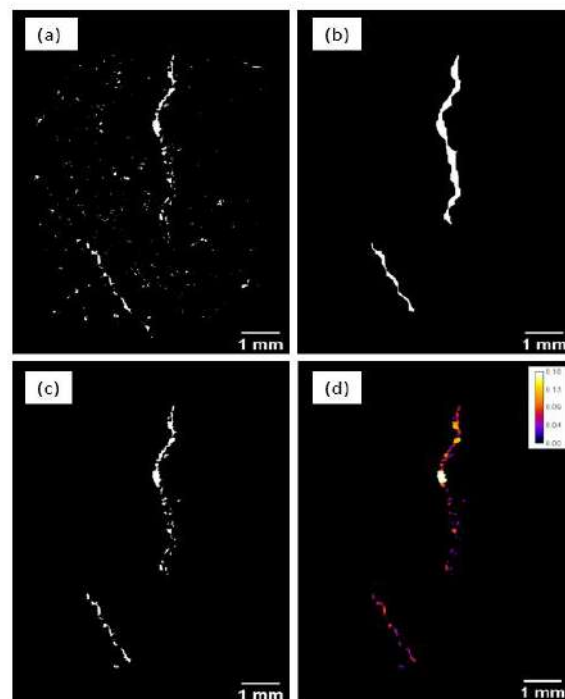


Figure 1 - Cracks in iron ore pellets: a) Segmented cracks containing spurious objects. b) Cracks after morphological operations for the elimination of spurious objects. c) Intersection between (a) and (b) to obtain the area occupied only by cracks. d) Map of local thickness of cracks analyzed.

Table 1 - Extraction of attributes of the cracks shown in Figure 1.

Crack	Length (mm)	Average Thickness (mm)	Area Fraction (%)
1	5.79	0.048	0.50
2	2.57	0.050	

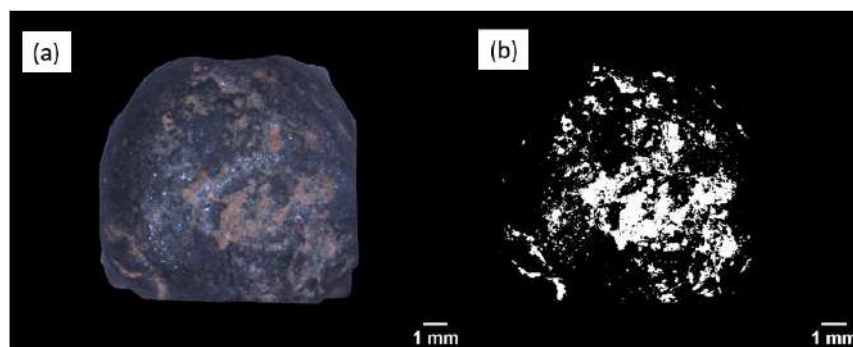


Figure 2 - Coating in iron ore pellets: A) Pellet region with selected coating. B) Coating detected by digital image processing.

Table 2 - Area fraction occupied by coating on the pellet, calculated from Figure 2b.

Area Fraction (%)
7.27



# Columnar grain growth of $\text{Co}_2\text{FeAl}$ thin films for applications in spintronics

**S. Adnan Raza, B. G. Silva, Cilene Labre, D. E. González-Chávez, M. A. Correa, R. L. Sommer**

*Centro Brasileiro de Pesquisas Físicas, Rio de Janeiro/RJ, 22290-180, Brasil*

**Email:** [adnanphy@cbpf.br](mailto:adnanphy@cbpf.br)

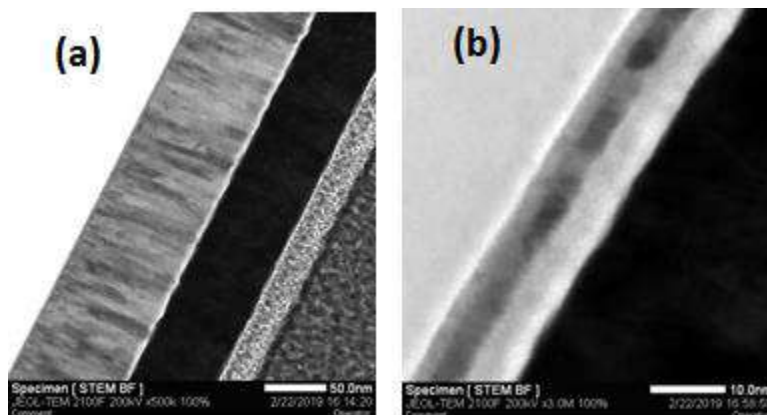
**Keywords:** Ferromagnetic resonance FMR, Magnetization dynamics, Gilbert damping, ferromagnetic films

$\text{Co}_2\text{FeAl}$  is considered to be one of the most promising materials for ultrahigh density recording applications. To achieve high density, the film media needs to be granular in nature, of small and uniform sized grains with a nonmagnetic phase at the grain boundaries [1,2,3].

The Gilbert damping depends on the type of grain growth. Low-damping magnetic materials are highly desirable for high frequency, and full Heusler compounds in this respect provide interesting properties. Here, we present a study of the magnetic dynamics of  $\text{Co}_2\text{FeAl}$  films with a Gilbert damping constant as low as  $3.1 \times 10^{-4}$  for thickness of 100 nm. The in-plane as well as out-of-plan ferromagnetic resonance (FMR) were measured on different thicknesses of  $\text{Co}_2\text{FeAl}$  films grown on Si(100), all samples were capped with a 5 nm thick Ti layer. The thickness dependencies of the magnetic anisotropy and inhomogeneous broadening of the line width are good indicators of crystal quality and magnetic uniformity. The damping parameter is investigated as a function of thickness using broad-band ferromagnetic resonance (VNA-FMR). We found that the saturated magnetic damping constant  $\alpha_0$  decreasing continuously with the  $\text{Co}_2\text{FeAl}$  thickness  $t_{\text{CFA}}$ . Furthermore, the structural investigation of these films was performed by X-ray diffraction, AFM, selected area electron diffraction (SAED) and HR-TEM. The columnar grains were observed for 100 nm thick films (Fig. a), while an island grains were observed for 5 nm thick films (Fig. b). It was found that the type of growth for CFA could influence the damping.

## References:

- [1] Xiong L L and Adeyeye A O *Appl. Phys. Lett.* **108** 262401 (2016)
- [2] Godsell J F, Kulkarni S, O'Donnell T and Roy S *J. Appl. Phys.* **107** 033907 (2010)
- [3] Liu X M, Ding J, Kakazei G N and Adeyeye A O *Appl. Phys. Lett.* **103** 062401 (2013)



## Use of hollow-cone and centered dark field TEM for characterization of size and morphology of TiO<sub>2</sub> nanorods produced from titanate nanotubes

Anderson de Farias Pereira<sup>1\*</sup>, Sidnei Paciornik<sup>2</sup> and Paula Mendes Jardim<sup>1</sup>

<sup>1</sup> Department of Metallurgical and Materials Engineering, Federal University of Rio de Janeiro, COPPE/UFRJ, Rio de Janeiro, Brazil.

<sup>2</sup> Department of Chemical and Materials Engineering, Pontifical Catholic University of Rio de Janeiro – PUC-Rio, Rio de Janeiro, RJ, Brazil

e-mail: [afpereira@metalmat.ufrj.br](mailto:afpereira@metalmat.ufrj.br)

TiO<sub>2</sub>-anatase nanorods produced by heat treatment of hydrogen titanate nanotubes (TTNT) at 550°C are found to present good catalytic and photocatalytic [1] performance when compared to its counterpart with equilibrium morphology. This study aims to evaluate morphology evolution of such nanorods with heat-treating temperature. For this purpose, TiO<sub>2</sub>-anatase nanoparticles were produced by heat treating TTNT at 550°C (NR550), 650°C (NR650) and 750°C (NR750). X-Ray Diffraction (XRD) was used for the characterization of the constituent phases of each sample and Transmission Electron Microscopy (TEM) for the evaluation of the size and morphology distribution for the TiO<sub>2</sub> nanoparticles produced at varying heat treatment temperature. TEM images were acquired in an S/TEM Tecnai G20 FEG 200kV and consisted of bright (BF) and dark-field (DF) images (produced by TiO<sub>2</sub>-anatase's (101) diffracted beams selected by the objective aperture – centered DF – and by the integration through the entire diffraction ring in a hollow-cone DF mode, as described in [2,3]). Following acquisition, DF images were submitted to an image processing semi-automatized routine using Fiji-ImageJ v.1.52c for determination of the dimensions (Feret's diameter and Min Feret's diameter) and shape (aspect ratio) of the objects. The use of dark-field images was preferred for image processing because of their simplest contrast information compared to the bright field ones, enabling observation of individual particles within agglomerates. XRD results showed that all the samples are crystalline and composed mainly of TiO<sub>2</sub>-anatase, which agrees with the expected for titanate nanotubes treated at 550°C [1,4]. Small amount of TiO<sub>2</sub>-rutile was observed for the sample treated at 750°C (NR750). Figure 1 presents a typical hollow-cone dark field image for each of the samples and Figure 2 shows the histograms and cumulative distributions of particle's length, width and aspect ratio for the samples NR550, NR650 and NR750. It is observed that the distribution of particle's length and width were very similar for the samples NR550 and NR650, with average size of 35.5 and 34.6 nm, respectively, while for sample NR750, the curves were clearly shifted to greater values of particle size (69.4 nm). In terms of the aspect ratio, the histograms show signs of a bimodal distribution (Figure 2 (e,f)) for the samples NR550 and NR650, indicating the presence of a mixture of nanoparticles and nanorods as well as a decrease in aspect ratio as heat treatment temperature is increased: NR550 presented 55% of particles with aspect ratio greater than 2, as compared to 35% for NR650 and 8%

### References :

- [1] M. de Abreu et al., Open Chemistry, 10 (4) (2012) 1183.
- [2] B. Yao et al., Micron, 42 (1) (2011) 29.
- [3] D.B. Williams and C.B. Carter, Transmission Electron Microscopy, Springer, Boston, 2009.
- [4] E. Morgado et al., Solid State Sciences, 8 (8) (2006) 888.
- [5] This research was supported by CNPq (Brazil). We are also grateful to CENABIO/UFRJ for allowing the use of their electron microscopy facilities in this study.

for NR750. As a general conclusion, the increase in heat treatment temperature of TTNT lead to the reduction in the fraction of nanorods and the increase in the average nanoparticle's size. The employment of the dark-field technique was efficient in allowing the observation of TiO<sub>2</sub> nanoparticles within agglomerates.

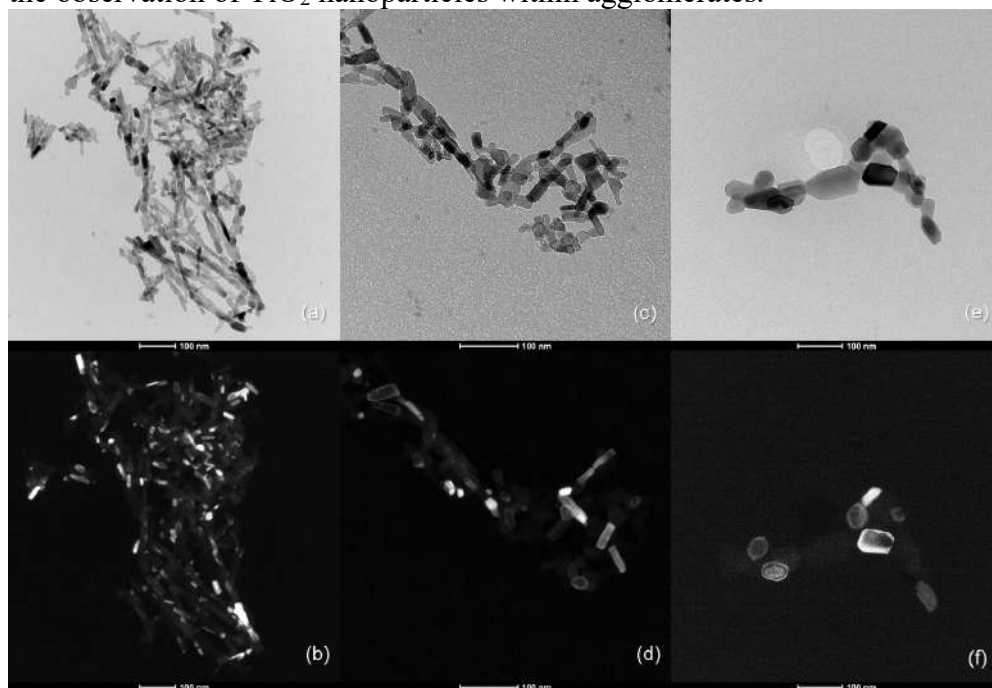


Figure 1 – Bright-field (top) and Hollow-cone Dark-field (bottom) TEM images of the samples NR550 (a, b), NR650 (c, d) and NR750 (e, f).

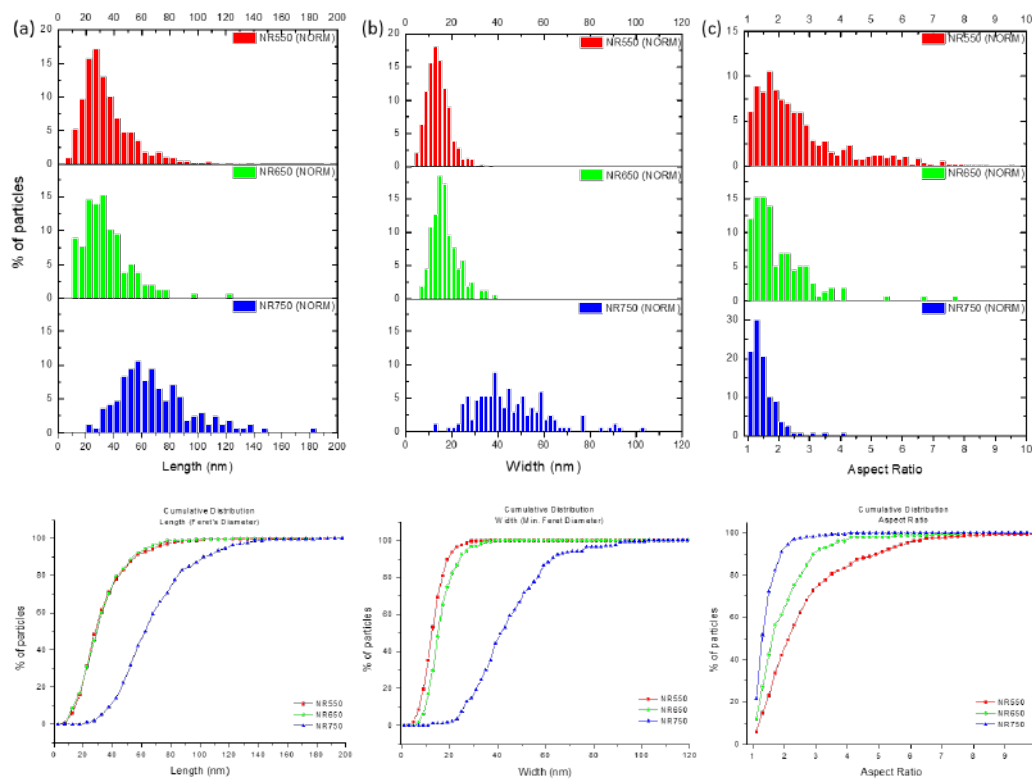


Figure 2 – Comparative Histogram (top) and accumulated distribution (bottom) of particle's length (a), width (b) and aspect ratio (c) obtained from TEM analysis of samples NR550, NR650 and NR750.

## Synthesis Of Fe-Fe<sub>3</sub>O<sub>4</sub>@SiO<sub>2</sub> Nanoparticles For Nanomedicine Applications

Bianca Galeano-Villar<sup>1\*</sup>, Richard Caraballo-Vivas<sup>1</sup>, Raquel Checca<sup>1</sup>, Priscilla Finotelli<sup>2</sup>, and Flávio Garcia<sup>1</sup>

<sup>1</sup>. Departamento de Matéria Condensada, Física Aplicada e Nanociência. Centro Brasileiro de Pesquisas Físicas. Rio de Janeiro, Brasil.

<sup>2</sup>. Departamento de Produtos Naturais e alimentos, Faculdade de Farmácia. Universidade Federal do Rio de Janeiro. Rio de Janeiro, Brasil.

\*e-mail: biancagaleano@cbpf.br

### ABSTRACT

The nanomedicine, which consist in the application of nanotechnology in medicine, allows the exploration of exciting new treatment and diagnosis techniques, such as magnetic hyperthermia, drug delivery, magnetic resonance imaging [1]. In this work a new class of magnetic nanoparticles with a ring shape morphology are studied. These particles have magnetic vortex behavior and are named Vortex Iron Oxide Nanoparticles (VIP), whose chemical composition is given by a core of iron and a shell of magnetite. The synthesis of this nanoparticles is carried out in three steps: first, hematite nanorings ( $\alpha$ -Fe<sub>2</sub>O<sub>3</sub>), are prepared via hydrothermal method, following the procedure reported by Jia *et al.* [2]. Sodium phosphate, sodium sulfate and ferric chloride are mixed in the necessary concentrations, transported to an autoclave and annealed at 220°C during 48h. The obtained red powder is washed and dried several times. The second step consists in reducing hematite nanoparticles to iron-iron oxide (Fe-Fe<sub>3</sub>O<sub>4</sub>), to this purpose the red powder is annealed during 1,5h at 400°C under H<sub>2</sub>/Ar (10%) 70ml/min flux atmosphere. In the third step, the Fe-Fe<sub>3</sub>O<sub>4</sub> particles are coated with silica (SiO<sub>2</sub>) using the modified Stober method, which consist in the dispersion of Fe-Fe<sub>3</sub>O<sub>4</sub> nanoparticles into a solution containing water, ethanol and ammonia hydroxide. Under violent mechanical agitation TEOS (tetraethyl orthosilicate) is added drop by drop. Afterward, the agitation is maintained during 24h. The final product is washed using magnetic separation and dried at room temperature, the resultant powder is called Fe-Fe<sub>3</sub>O<sub>4</sub>@SiO<sub>2</sub>. X-ray diffraction reveal the crystallinity of the  $\alpha$ -Fe<sub>2</sub>O<sub>3</sub> and Fe-Fe<sub>3</sub>O<sub>4</sub> particles. EDS mapping before the recovering process shows the presence of iron and oxygen elements; additionally, after that process silicon element can be found, which indicates the efficiency of such process. TEM images show the presence of the amorphous silica layer. These results indicate that we obtained a new class of Fe-Fe<sub>3</sub>O<sub>4</sub>@SiO<sub>2</sub> with ring morphology that can be used in nanomedicine due to the presence of a well known biocompatible layer and easily functionalized [3].

### REFERÊNCIAS

- [1] Wahajuddin & Arora, S. Superparamagnetic iron oxide nanoparticles: magnetic nanoplatforms as drug carriers. *Int. J. Nanomedicine* **7**, 3445–71 (2012).
- [2] Jia, C. C. *et al.* Large-scale synthesis of single-crystalline iron oxide magnetic nanorings. *J. Am. Chem. Soc.* **130**, 16968–77 (2008).
- [3] Vivero-Escoto, J. L., Slowing, I. I., Trewyn, B. G. & Lin, V. S.-Y. Mesoporous silica nanoparticles for intracellular controlled drug delivery. *Small* **6**, 1952–67 (2010).
- This research was supported by CAPES (Brazil). The authors acknowledge to LABNANO-CBPF



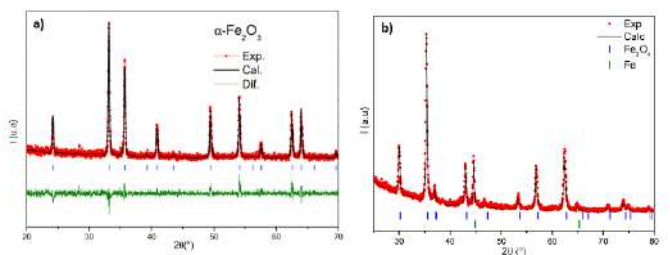


Figure 1: X-ray diffraction of a)  $\alpha$ -Fe<sub>2</sub>O<sub>3</sub> and b) Fe-Fe<sub>3</sub>O<sub>4</sub> particles.

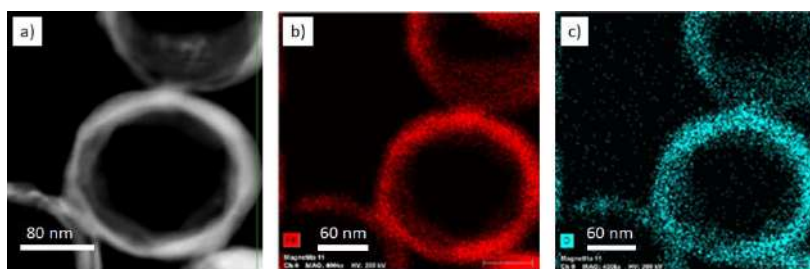


Figure 2: a) STEM image of Fe-Fe<sub>3</sub>O<sub>4</sub> nanoring, EDS maps for b) Fe and c) O elements

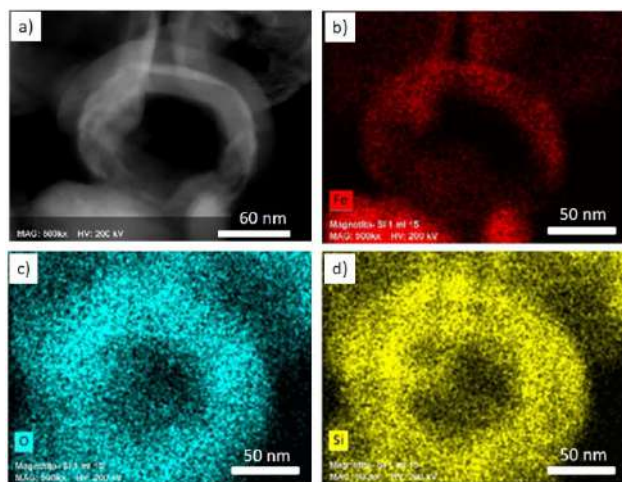


Figure 3: a) STEM image of Fe-Fe<sub>3</sub>O<sub>4</sub>@SiO<sub>2</sub> nanoring, EDS maps for b) Fe, c) O and d) Si elements.

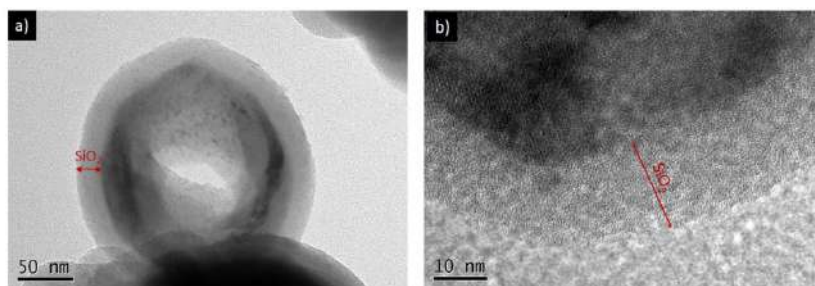


Figure 5: a) TEM image of Fe-Fe<sub>3</sub>O<sub>4</sub>@SiO<sub>2</sub> nanoring indicates the covering layer, b) HRTEM image showing the amorphous silica.

## Imaging chiral spin textures in Pt/Co/Pt multilayers by using Lorentz Transmission Electron Microscopy

C. Labre<sup>1</sup>, R. Dutra<sup>1,2</sup>, R. P. Loreto<sup>1</sup>, B. G. Silva<sup>1</sup>, D. E. Gonzalez-Chavez<sup>1</sup> and R. L. Sommer<sup>1</sup>

<sup>1</sup> Centro Brasileiro de Pesquisas Físicas, Rio de Janeiro, Brazil.

<sup>2</sup> Centro Técnico-Científico, Pontifícia Universidade Católica do Rio de Janeiro (PUC-Rio), Rio de Janeiro, Brazil.

Magnetic skyrmions are nanometer-sized topological defects presenting swirling chiral spin textures and are promising candidates for the next generation of spintronic devices due to their small size, topologically protected structure, and functionality towards the development of room temperature magnetic devices [1]. Lorentz transmission electron microscopy (LTEM) has emerged as a powerful tool for the characterization of sub-micron size magnetic features, such as magnetic domains and magnetic domain walls [2]. In comparison with other techniques such as Kerr microscopy and X-ray methods, which are limited by spatial resolution, L-TEM has a better spatial resolution and larger scattering cross-section for electrons compared to X-rays [3]. In this work, we investigated the formation of chiral spin textures in Pt/Co/Pt multilayers with Lorentz transmission electron microscopy (LTEM). Magnetic multilayers [Pt (1 nm)/Co (*t*)/Pt (1 nm)]x15 were grown onto Si<sub>3</sub>N<sub>4</sub> membrane windows by magnetron sputtering as shown in Figure 1a and 1b. The magnetization reversal as a function of magnetic field was acquired by using an alternating gradient field magnetometer (AGFM). These parameters emerge as a source for the skyrmions (Figure 1c and 1d) stability indicating that the combination of higher PMA and low *M<sub>s</sub>* may allow their formation at zero field [4,5]. Figure 1 shows the LTEM image of magnetic domains structure for the sample with Cobalt thickness of 1 nm where the magnetic domains are present. Below 1 nm of Cobalt, the magnetic domains nucleate into skyrmions. Micromagnetic simulations were also performed using the Mumax<sup>3</sup> GPU-accelerated program. The magnetic anisotropy *K*<sub>eff</sub>, magnetization saturation *M<sub>s</sub>*, and Dzyaloshinskii-Moriya value *D* were modified to understand their impact on the skyrmions stability. The authors thank Labnano/CBPF for technical support and CNPq, Capes and FACC for financial support.

### References

- [1] Pollard, Shawn D., *et al.* "Observation of stable Néel skyrmions in cobalt/palladium multilayers with Lorentz transmission electron microscopy." *Nature communications* 8 (2017): 14761.
- [2] Volkov, V. V., and Y. Zhu. "Lorentz phase microscopy of magnetic materials." *Ultramicroscopy* 98.2-4 (2004): 271-281.
- [3] Pollard, S. D., *et al.* "Direct dynamic imaging of non-adiabatic spin torque effects." *Nature communications* 3 (2012): 1028.

- [4] Brandão, J., *et al.* "Observation of magnetic skyrmions in unpatterned symmetric multilayers at room temperature and zero magnetic field." *Scientific reports* 9 (2019).
- [5] Peng, L C., *et al* "Lorentz transmission electron microscopy studies on topological magnetic domains." *Chin. Phys. B* 27, 6 (2018) 066802.
- [6] Kézsmárki, I. *et al.*, Néel-type skyrmion lattice with confined orientation in the polar magnetic semiconductor GaV4S8. *Nature Materials* 14 (2015) 1116.

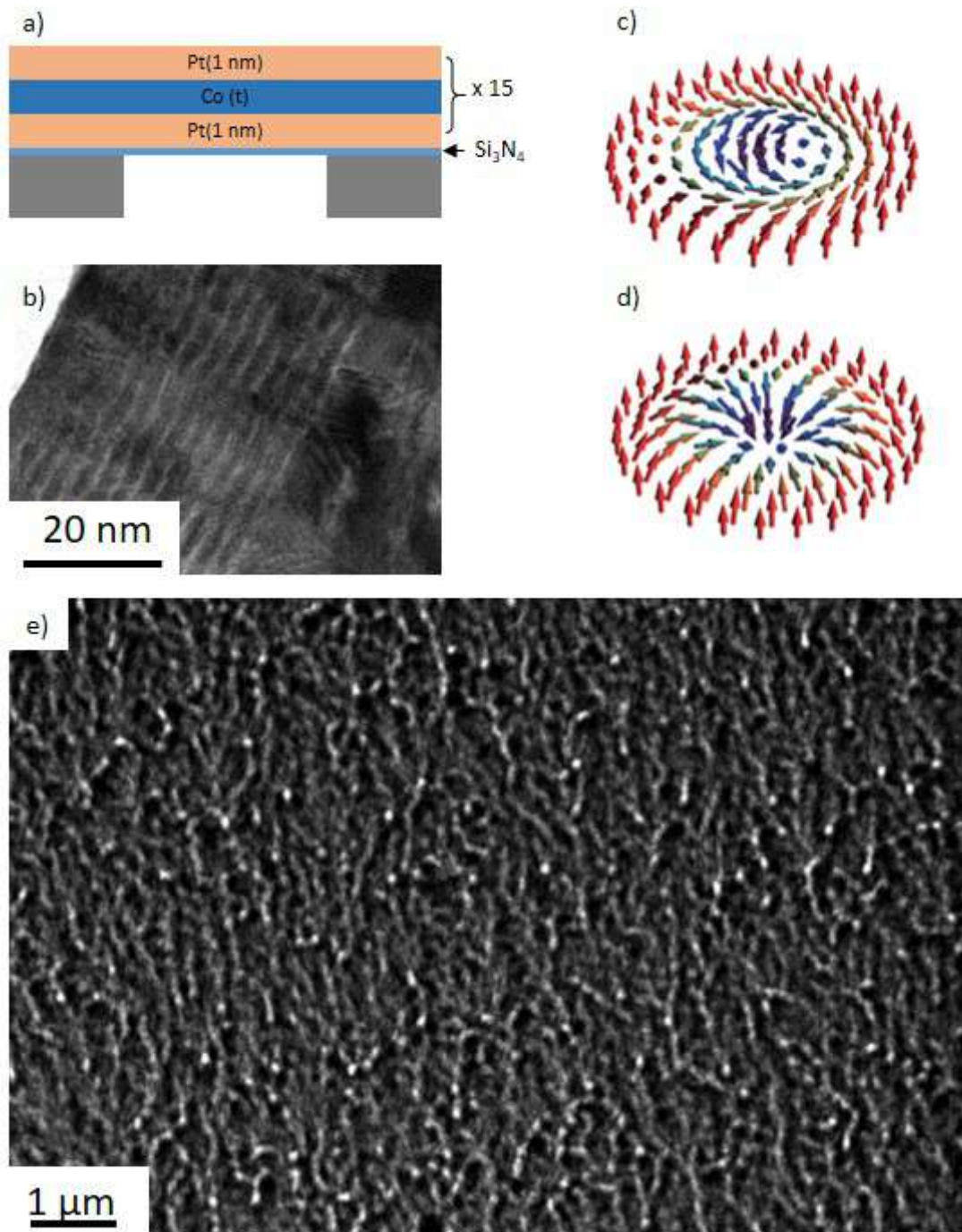


Figure 1 – (a) Schematics of the Pt/Co/Pt trilayer grown on silicon nitride membrane. (b) Cross-sectional HRTEM image of multilayers. (c) Bloch and (d) Néel skyrmions [6]. (e) LTEM image of the magnetic domains on the 1 nm thick Cobalt sample.

## Microstructural characterization of the amorphous and nanocrystalline $\text{Fe}_{68}\text{Cr}_8\text{Mo}_4\text{Nb}_4\text{B}_{16}$ alloy

D.D. Coimbra<sup>1,2\*</sup>, W. Wolf<sup>3</sup>, F.H.P. de Almeida<sup>2</sup>, A.M. Jorge Jr.<sup>1</sup>, G. Zepon<sup>1</sup>, W.J. Botta<sup>1</sup>

1. Universidade Federal de São Carlos, Departamento de Engenharia de Materiais, São Carlos, SP, Brasil
2. Programa de Pós-Graduação em Ciência e Engenharia de Materiais, Departamento de Engenharia de Materiais, São Carlos, SP, Brasil
3. Universidade Federal de Minas Gerais, Departamento de Engenharia Metalúrgica e de Materiais, Belo Horizonte, MG, Brasil

Recently it has been observed by our group that Fe-based glassy alloys can be formed by B addition in the range of 16-18 at% in the multicomponent Fe-Cr-Mo-Nb-B system. This system, which can be classified as a pseudo high entropy type, is of great interest due to the possibility of better ductility in comparison with almost all other Fe-based glassy alloys, which have higher contents of metalloid elements. The multicomponent Fe-based alloys with low B contents may exhibit useful engineering properties even in partially and fully crystallized state. The presence of nano-scale multicomponent borides in the microstructure can improve the mechanical properties, such as increasing the Vickers hardness and wear resistance with only minor deterioration of the corrosion resistance. In the present work, we report the detailed structural characterization of the amorphous and nanocrystalline  $\text{Fe}_{68}\text{Cr}_8\text{Mo}_4\text{Nb}_4\text{B}_{16}$  alloy. A master alloy was produced in an arc-melt apparatus, using a mixture of pure elements. This alloy was then rapid solidified in a melt-spinning apparatus resulting in 30  $\mu\text{m}$  thick amorphous ribbons. TEM sample preparation was carried out by ion milling in a Gatan PIPS - Model 691. The microstructural characterization of the alloy was performed under all conditions, amorphous, partially crystallized and fully crystallized, using X-ray diffraction, DSC, TEM with EDS and EELS. Figure 1 shows a STEM bright and dark field images (Figures 1 (a) and (b)) and the electron diffraction pattern of the melt-spun ribbon (Figure 1 (c)) confirming the fully amorphous character of the  $\text{Fe}_{68}\text{Cr}_8\text{Mo}_4\text{Nb}_4\text{B}_{16}$  alloy. Figure 2 shows a TEM dark field image of partially crystallized sample (in (a) TEM dark field image; (b) SAED pattern indicating the crystalline and amorphous phase, Figure 3 shows STEM bright and dark field images of the fully crystallized ribbon. Figures 3 (a) and (b) shows a bright and dark field images, respectively, and Figures 3 (c) the corresponding electron diffraction pattern. The results of electron energy loss spectroscopy (EELS), not shown here, confirm the presence of borides among the nanocrystalline phases in the fully crystallized sample. Detailed EDS composition shown in Figure 4 indicated that crystallization does not deplete Cr from the matrix, which can have important consequences for corrosion resistance of the partially crystallized alloy.



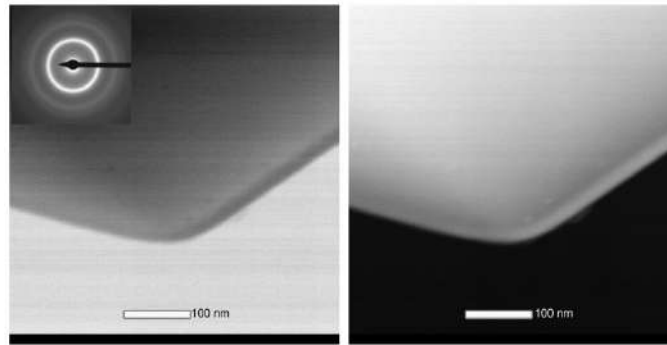


Figure 1. TEM image, bright field, dark field and selected-area electron diffraction pattern of amorphous ribbon.

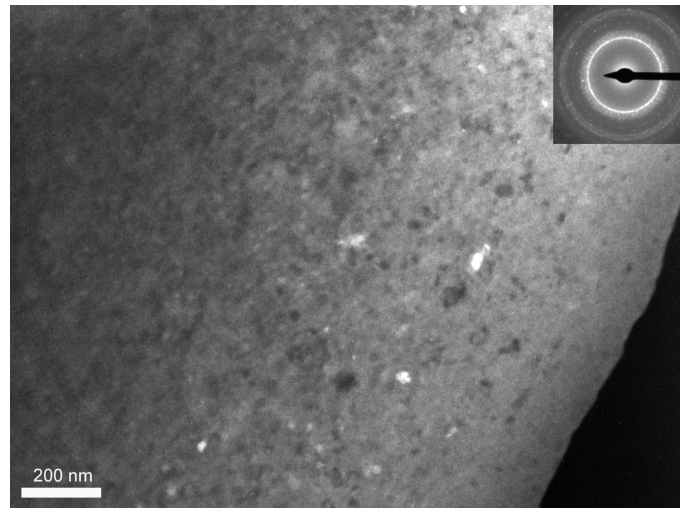


Figure 2. Sample partially crystallized; Dark field image and SAED.

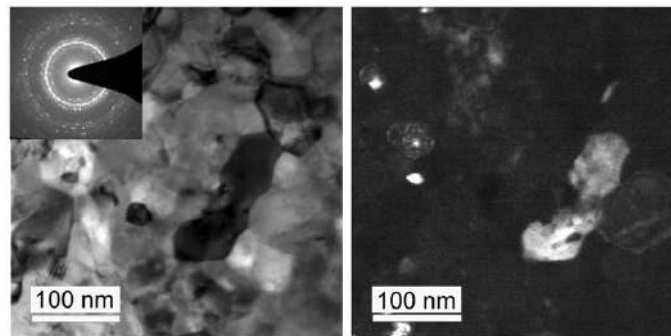


Figure 3. TEM image, bright field, dark field and selected-area electron diffraction pattern of fully crystallized sample.

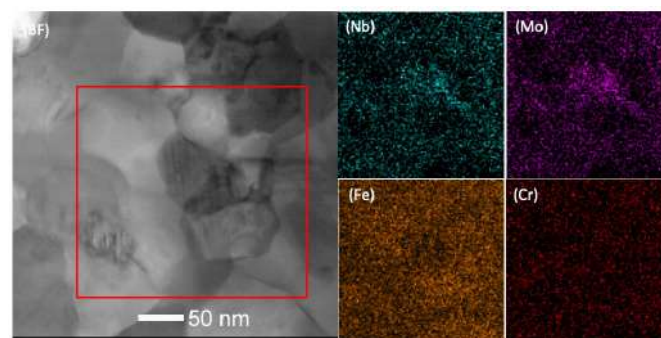


Figure 4. TEM bright field image and EDS mapping.

## Process of Deoxidation of Superalloy Nanoparticles Through the Use of Sucrose and L-Ascorbic Acid as Additives in the Process of Chemical Co-Reduction by Borohydride

Fabio Muchenski<sup>1\*</sup>, Aline Tanabe<sup>2</sup> and Ney Mattoso<sup>3</sup>

<sup>1</sup>. Universidade Federal do Paraná, PIPE/IFC campus São Bento do Sul, Curitiba, Brasil.

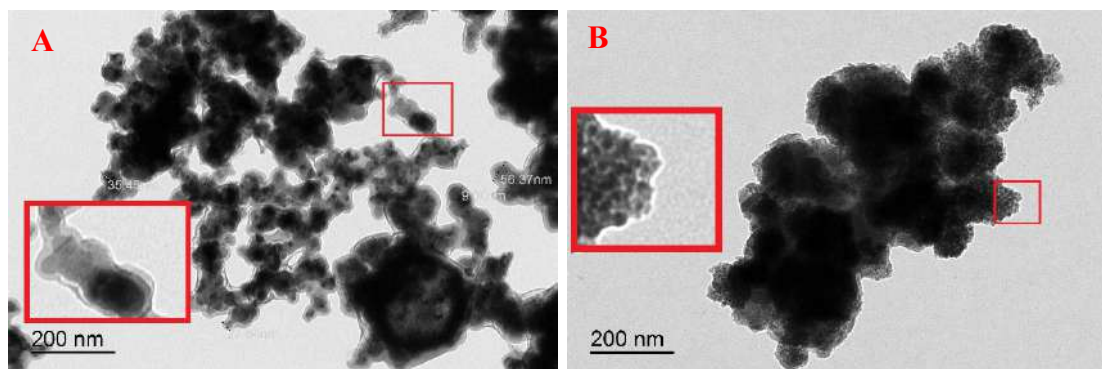
<sup>2</sup>. Universidade Federal do Paraná, PIPE, Curitiba, Brasil.

<sup>3</sup>. Universidade Federal do Paraná, Departamento de Física, Curitiba, Brasil.

Nowadays, there are many applications for nanoparticles. To mention a few that, there are applications in the area of food, health, environment, among others. Nanoparticles can be used to food conservation, drug delivery, help to identify diseases and act in treatment of these [2,4,6]. Of course, for each application there is a type of nanoparticle. Thus, they are composed of different chemical elements. In this work, will be present the chemical synthesis by co-reduction as a method to obtain metallic and magnetic nanoparticles of the superalloy alloy ( $\text{Ni}_{80}\text{Fe}_{15}\text{Mo}_5$ ), as well as morphological and compositional characterization, comparing the use of different additives during the synthesis process. Chemical synthesis by co-reduction allows to obtain relative control of size and shape of nanoparticles in general [3,5]. Were carried out a comparison among some additives used by researches of this group. Were investigated  $\text{HOC}(\text{COONa})(\text{CH}_2\text{COONa})_2 \cdot 2\text{H}_2\text{O}$  (sodium citrate),  $\text{C}_{12}\text{H}_{22}\text{O}_{11}$  (saccharose), o  $\text{C}_6\text{H}_8\text{O}_6$  (L-ascorbic acid), IGEPAL<sup>®</sup> CO-520,  $\text{CH}_3(\text{CH}_2)_{15}\text{N}(\text{Br})(\text{CH}_3)_3$  (Cetyltrimethylammonium bromide),  $[\text{C}_6\text{H}_7\text{O}_2(\text{OH})_2\text{OCH}_2\text{COONa}]_n$  (Sodium carboxymethylcellulose), mixed with  $\text{NiCl}_2 \cdot 6\text{H}_2\text{O}$  (Nickel chloride hexahydrate),  $\text{FeCl}_2 \cdot 4\text{H}_2\text{O}$  (Iron chloride tetrahydrate) e  $\text{Na}_2\text{MoO}_4 \cdot 2\text{H}_2\text{O}$  (Sodium molybdate dihydrate). In all solutions were added  $\text{NaBH}_4$  as reducing agente. For morphological e compositional characterization were used a Transmission Electron Microcopy (TEM), JEOL, model JEM 1200EX-II and a Scanning Electron Microscopy (SEM), TESCAN VEGA3 LMU, respectively. Were performed na extensive series of tests with each one of additives or a combination of these. Initially, the combination of sucrose and L-ascorbic acid showed to be more promising in the morphological aspect. From the micrographs, it was verified that there was a persistent formation of oxides during the synthesis process when using the citrate and also with the great majority of the additives used in this work. Sodium citrate was shown to be important in the dispersion process of the nanoparticles, since it performed a pre-reduction and delayed the final reduction process promoted by the borohydride [1]. However, it was not possible to avoid the appearance of oxides. During the tests, it was found that sucrose together with L-ascorbic acid not only provided adequate morphology (particles ranging in size from 100 nm to 200 nm) but also considerably reduced the presence of oxides surrounding the particles. In the micrograph presented in figure 1A it is possible to verify an apparent oxide layer nanoparticles with citrate. In figure 1B it is possible to verify the reduction / elimination of the oxide layer in the nanoparticles with sucrose and L-ascorbic acid. It is estimated that the oxide layer, when used sodium citrate, was approximately 9 nm. Figure 2A shows a micrograph obtained on the TESCAN VEGA3 LMU equipment of a part of the area used to perform EDS (Electron Dispersive Spectroscopy) analysis, in order to verify the atomic percentages of the elements Ni, Fe and Mo present in the nanoparticles and, 2B, a

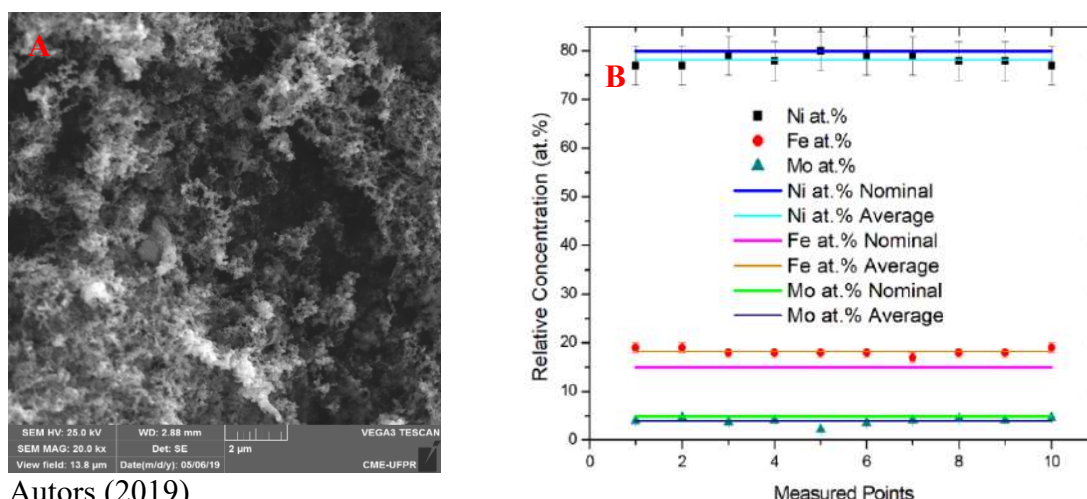
graph with the obtained results. 10 points distributed over the material placed on a plate were analyzed.<sup>1</sup>

Figure 1 - transmission micrographs obtained by JEOL / JEM 1200EX-II. In 1A sample containing sodium citrate and in 1B containing sucrose and L-ascorbic acid. Magnification of 20,000 times. In red box a zoom of selection area to show oxidation level.



Autors (2018, 2019).

Figure 2 - scanning micrograph obtained by TESCAN VEGA3 LMU, magnification of 20,000 times in 2A and in 2B, graph with percentages obtained by EDS.



Autors (2019)

## REFERENCES

- [1] A. Tanabe. Síntese e caracterização de nanopartículas pelo método químico de precipitação por co-redução. UFPR, Curitiba, 2018.
- [2] Benelli, G.; Caselli, A.; Canale, A. Journal of King Saud University - Science, 29 (4) (2016) 424.
- [3] P. B. de C. Gaiotto, Ensaios no processo de eletrodeposição a liga magnética Supermalloy, UFPR, Curitiba, 2007.
- [4] Leeper, N. J.; Park, S.; Smith, B. R. JACC: Basic to Translational Science. 2 (2017) 98.
- [5] S. Majidi, F. Z. Sehrig, S. M. Farkhani, M. S. Goloujeh, and A. Akbarzadeh, J. Artif. Cells, Nanomedicine, Biotechnol. 44 (2016) 722.
- [6] K. Pathakoti, M. Manubolu, H.-M. Hwang. Journal of Food and Drug Analysis, 25

<sup>1</sup> E-mail addresses: fabio.muchenski@ifc.edu.br

## **Radiation Effect on Morphology of Magnetite Nanoparticles Synthesized by Electron Beam Irradiation**

Flavio K. Tominaga\*, Raynara M. S. Jacovone, Rafael H. L. Garcia, Flávia R. O Silva  
and Solange K. Sakata

Instituto de Pesquisas Energéticas e Nucleares (IPEN/CNEN), São Paulo, Brazil.  
fktominaga@ipen.br

**ABSTRACT:** Magnetite nanoparticles (MNP) are widely explored in several applications such as drug carrier [1], medical diagnostics and cancer treatment [2], and magnetic resonance imaging [3].  $\text{Fe}_3\text{O}_4$  nanoparticles present advantages as biocompatibility, biodegradability, low toxicity and facile synthesis [2]. Properties of these nanoparticles are dependent on the size and morphology [4]. The synthesis of magnetite via chemical methods is commonly used due to the low cost of production, high performance, simplicity, high efficiency and manipulation of size [5]. Electron Beam Irradiation (EBI) has been proved as an alternately sustainable process for synthesis of magnetic nanoparticles [6]. In this present work, the effect of irradiation on morphology of magnetite nanoparticles at different doses was evaluated. MNP were synthesized by Electron Beam Irradiation, using  $\text{FeSO}_4 \cdot 7\text{H}_2\text{O}$  as precursor in alkaline medium. The samples were irradiation in an Electron Beam Accelerators at doses of 20, 40 and 80 kGy and dose rate of 10.01 kGy/s. The characterization was performed by X-ray diffraction (XDR) and Transmission Electron Microscopy (TEM). XDR patterns demonstrated several characteristic diffraction peaks at  $30.1^\circ$ ,  $35.7^\circ$ ,  $43.3^\circ$ ,  $53.8^\circ$ ,  $57.2^\circ$  and  $62.6^\circ$ , which were ascribed respectively, to the (220), (311), (400), (422), (511) and (440), crystalline planes of  $\text{Fe}_3\text{O}_4$ , correspondent to the standard XDR data for the cubic phase with a face-centered cubic (fcc) structure (JCPDS 01-074-1910) [7]. TEM images demonstrated agglomeration of the magnetic nanoparticle synthesis in all applied doses, since no stabilizer were used. For all studied doses, most of MNP presented spherical shape with slight alterations of morphologies. In conclusion, EBI is a fast, simple and efficient method for synthesis of MNP, inducing few changes on MNP morphology.

### References

- [1] V. Arora et al. *Mat. Sci. Eng. R*, 80 (2017).
- [2] R. A. Revia et al. *Mater. Today*, 19 (2016).
- [3] Z. R. Stephen et al. *Mater. Today*, 14 (2011).
- [4] K. Parekh et al. *AIP Publishing* (2018).
- [5] A. Ali et al. *Nanotechnol Sci Appl*, 9 (2016).
- [6] M. GOTIĆ et al. *Mater Res Bull*, 44 (2009).
- [7] B. Mu et al. *Sci Rep-UK*, 7 (2017).
- [8] This research was supported by Instituto de Pesquisas Energéticas e Nucleares (IPEN/CNEN-SP), Universidade de São Paulo (USP) and Conselho Nacional de Desenvolvimento Científico e Tecnológico (CNPq) (Brazil).



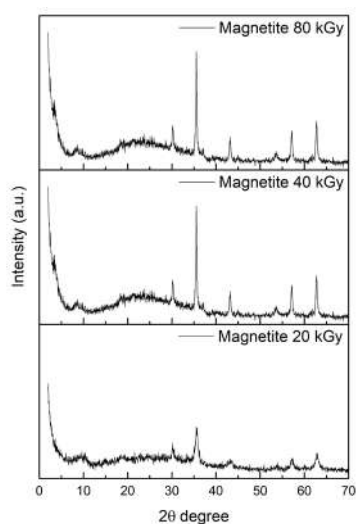


Figure 1 – XRD pattern of magnetite nanoparticles irradiated at 20, 40 and 80 kGy by EBI.

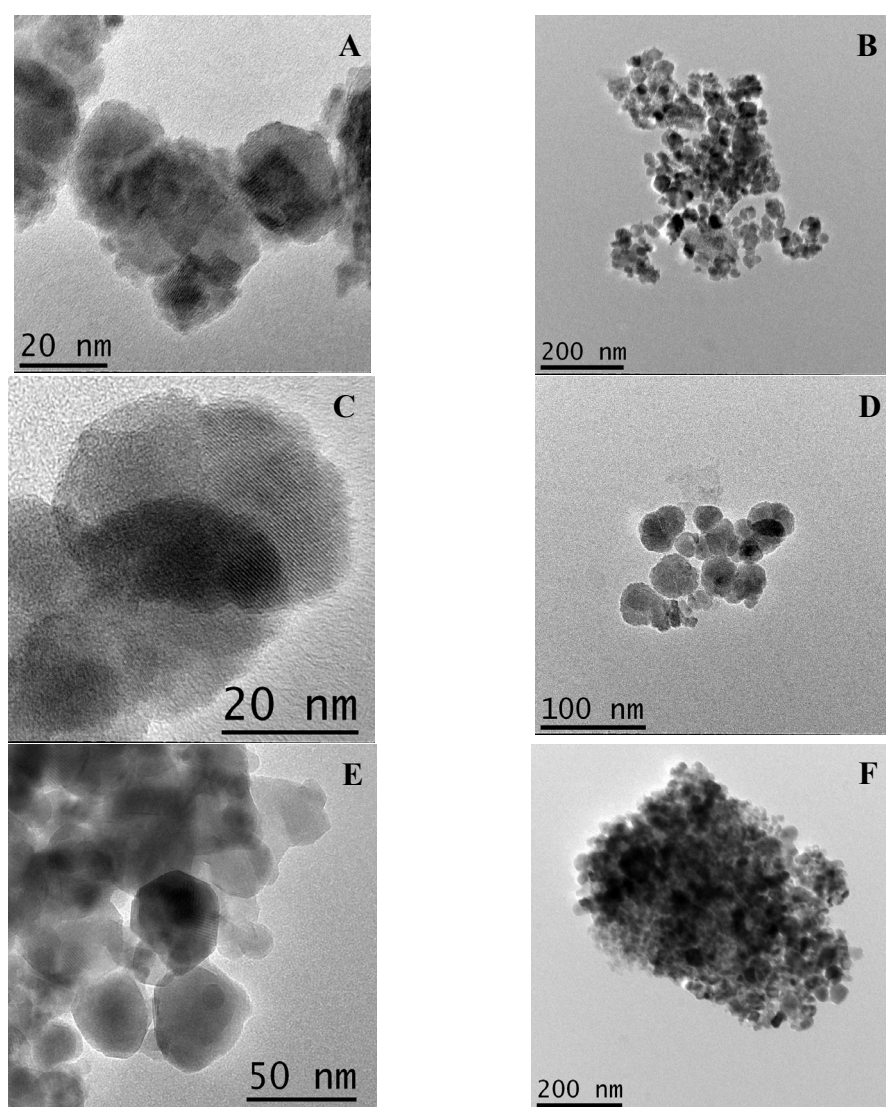


Figure 2 – TEM images of MNP irradiated at (A,B) 20 kGy, (C,D) 40 kGy and (E,F) 80 kGy.

## In situ-TEM of Calcium Phosphate Crystallization and Growth in aqueous medium

Gisele M.L. Dalmônico<sup>1\*</sup>, Dris ihiawakrim<sup>3</sup>, Nathaly Ortiz<sup>3</sup>, Ovidiu Ersen<sup>3</sup>, Marcos Farina<sup>2</sup>, Alexandre M. Rossi<sup>1</sup>, André L. Rossi<sup>1</sup>

<sup>1</sup>Brazilian Center for Physics Research, Rio de Janeiro, Brazil

<sup>2</sup>Institute of Biomedical Sciences, Federal University of Rio de Janeiro, Brazil

<sup>3</sup>Institut de Physique et Chimie des Matériaux de Strasbourg (IPCMS), UMR 7504 CNRS – Université de Strasbourg, 23 rue du Loess, 67034 Strasbourg Cedex 2, France  
[gisele@cbpf.br](mailto:gisele@cbpf.br)

Calcium phosphates are widely investigated for the study of biomineralization processes and for the development of new biomaterials. Recent studies showed that the crystallization of hydroxyapatite (HA) in aqueous medium occurs by steps: briefly, pre-nucleation clusters aggregate to form amorphous spheres that grow and crystallize into hydroxyapatite [1]. In situ TEM is a novel technique that allows to follow in real time the reaction inside the TEM and thus to visualize the formation of calcium phosphates, since the first mineral depositions and the presence of intermediate precursor phases. In this work in situ-TEM was performed in static conditions (closed volume maintaining original solution). The synthesis was performed using  $\text{Ca}(\text{OH})_2$  and  $(\text{PO}_4)^{3-}$  as precursors in aqueous medium and then dropped in a specific microchip for liquid in situ-TEM (Protochips liquid cell carrier-Poseidon Select 550). Previously to synthesis, the microchip was washed successively in acetone, methanol and ethanol, to remove the protective coating. The experiments were performed in a 200 kV JEOL 2100F/Cs(S) TEM. Movies were recorded at 3 frames per second in TEM and STEM modes. During the assay, it was possible to verify the presence/appearance of different nanoparticle with specific morphologies as shown in figure 1. In order to identify their elemental composition, energy dispersive X ray analysis (EDX) was performed. It was found that particles around 100nm were related to  $\text{Ca}(\text{OH})_2$  (Figure 1a), one of the precursors used in the synthesis. Smaller particles ( $\sim 10\text{nm}$ ) formed after 20 min were CaP (figure 1b). These spherical nano-particles agglomerate with time (figure 1c). Finally, the characteristic needle-like morphology of HA, was observed after 3,5 h of synthesis (figure 1d). In this preliminary essay, it was not possible to visualize all the steps of HA crystallization in only 1 video, but the morphologies observed were similar to those found in the previous studies of HA formation using cryo-TEM [1, 2]. New studies are underway by our group to uncover details of the beginning of calcium phosphates mineralization using this promising and unique methodology for nanoscience research.

### REFERENCES

- [1] Habraken, Wouter J.E.M., Jinhui Tao, Laura J. Brylka, Heiner Friedrich, Luca Bertinetti, Anna S. Schenk, Andreas Verch, et al. 2013. *Nature Communications* 4. <https://doi.org/10.1038/ncomms2490>.
- [2] Wang, Xiaoyue, Jie Yang, Carmen M Andrei, Leyla Soleymani, and Kathryn Grandfield. 2018. <https://doi.org/10.1038/s42004-018-0081-4>.

### ACKNOWLEDGMENTS

Institut de Physique et Chimie des Matériaux de Strasbourg (IPCMS) in France and the Brazilian agencies FAPERJ and CNPq.

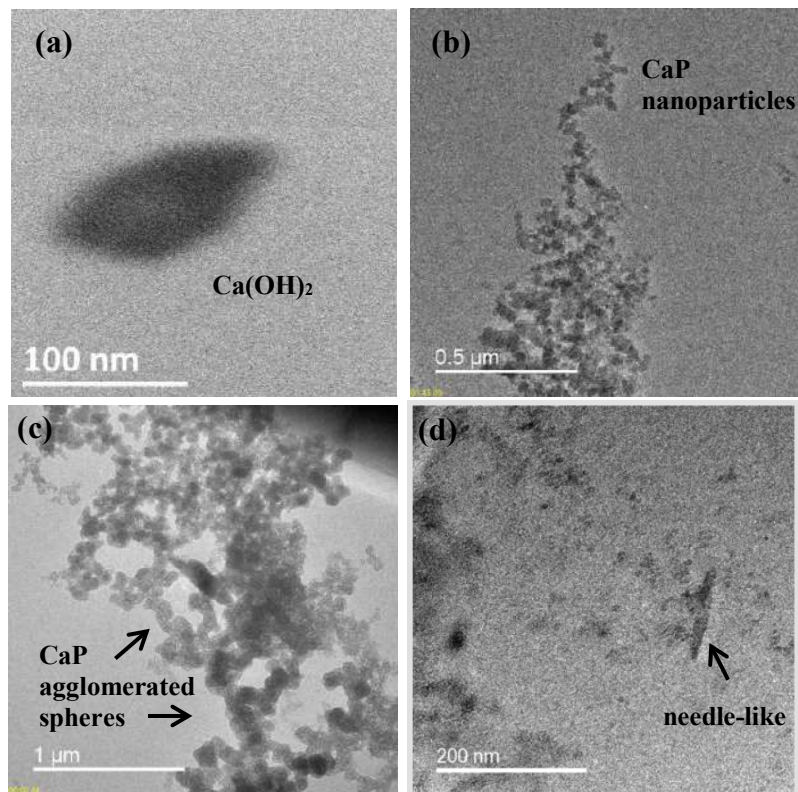


**Figure 1. *In situ*-TEM: (a)  $\text{Ca(OH)}_2$  (0 min), (b) CaP nanoparticles (20min), (c) CaP agglomerated spheres (1,5h) (d) needle-like (3,5 h).**



## **Multiuser Laboratory of Nanoscience and Nanotechnology For The Development Of The Brazilian Science**

H. Coelho-Júnior<sup>1\*</sup>, C. Labre<sup>1</sup>, J. E. V. Amarante<sup>2</sup>, A. L. Rossi<sup>1</sup>, and R. L. Sommer<sup>1</sup>

<sup>1</sup>Centro Brasileiro de Pesquisas Físicas, Coordenação de Matéria Condensada, Física Aplicada e Nanociência, 22.290-180 Rio de Janeiro-RJ, Brazil.

<sup>2</sup>Universidade Federal Fluminense, Centro de Ciências Médicas, Faculdade de Odontologia, 28.625-650 Nova Friburgo-RJ, Brazil.

\*Corresponding author e-mail address: horaciocoelhojunior@gmail.com

The Multiuser Laboratory of Nanoscience and Nanotechnology (LABNANO) is integrated to the Brazilian Center for Research in Physics (CBPF) in Rio de Janeiro City. This laboratory is one of the strategic laboratories of the Ministry of Science, Technology, Innovation and Telecommunications (MCTIC) from the Brazilian govern, in the ambit of the Brazilian Nanotechnology Initiative (IBN) and of the National System for Nanotechnology (SisNano). The LABNANO is a multiuser equipment center that serves the entire local scientific community and external users, providing training and assistance for user, which also includes a variety of sample preparations techniques for Electron Microscopy. Additionally, a complete structure for micro and nano manufacturing is available including a cleanroom environment and a Raith e-Line lithography system. Our facilities include several Electron Microscopes: a Scanning Electron Microscope (SEM) JEOL JSM-6510, Field Emission Scanning Electron Microscope (FEG-SEM) JEOL 7100FT, Field Emission Transmission Electron Microscope (FEG-TEM) JEOL JEM-2100F, and a Focused Ion Beam Scanning Electron Microscopy (FIB-SEM) TESCAN LYRA3. These microscopes offer capabilities to high quality image acquisition accomplished of analytical characterization. Mainly for this reason, LABNANO is one of the most requested laboratories for support research in nanoscience and nanotechnology in Brazil. Figure 1 shows the percent of users per institution that developed research using LABANANO/CBPF facilities, where only 20% are internal users from CBPF, agreeing with the policies of the laboratory that establishes that the available time can be dedicated to internal researches from CBPF, but mostly for external users. This operational organization promote the LABNANO/CBPF as being one of the more efficient and complete multiuser centers funded by Brazilian research agencies.

Acknowledgments: FAPERJ, FINEP, LABNANO/CBPF/MCTIC, CNPq, Capes.



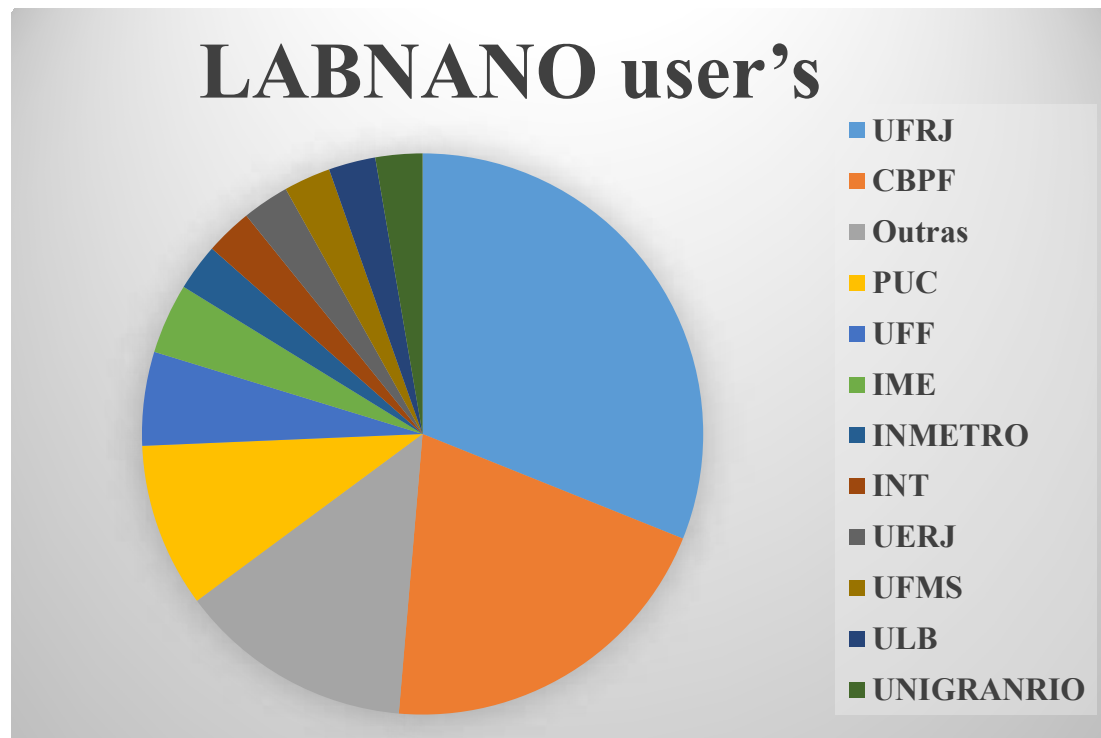


Figure 1 – Graphic of the percent of users from LABANANO/CBPF and their respective institutions.

## Combustion Synthesis and AEM Characterization of $\text{FeAl}_2\text{O}_4$ Spinel

Jesana Moura<sup>1\*</sup>; Cilene Labre<sup>2</sup>; Julio Spadotto<sup>1</sup>; Eduardo Brocchi<sup>1</sup> and Guillermo Solórzano<sup>1</sup>

<sup>1</sup> Department of Chemical and Materials Engineering - PUC-Rio, Rio de Janeiro - RJ- Brazil.

<sup>2</sup> Brazilian Center for Physical Research (CBPF), Rio de Janeiro - RJ- Brazil.

\* [jesana\\_moura@hotmail.com](mailto:jesana_moura@hotmail.com)

In recent years, there is increasing interest in multifunctional ceramic materials, arising from both intriguing fundamental properties and potential applications. Spinel with general formula  $\text{AB}_2\text{O}_4$  [1,2] and FCC structure is typical of such interest. Several synthesis methods for these materials have been proposed, including co-precipitation, sol-gel, and combustion reaction synthesis. The last is particularly convenient because of its low costs, high-reaction speed, and also energy efficient as the reaction release energy, which is contrary to other techniques mentioned [3]. We have chosen to synthesize and characterize  $\text{FeAl}_2\text{O}_4$  spinel because of its magnetic properties and wide possibility of applications. In the present study, the reaction combustion synthesis methods for obtaining  $\text{FeAl}_2\text{O}_4$  has been used starting with a solution of hydrated iron and aluminum nitrites under two conditions: with and without urea as combustion source. Such solutions were heated up to 500 °C until ignition occurred, burning and the production of a solid products in a powder form. The final synthesis product has been characterized in terms of structure and compositional by means of X-ray diffraction (DRX - Panalytical), and Analytical Electron Microscopy (AEM): scanning electron microscopy (SEM JEOL 7100F) and scanning and transmission electron microscopy (TEM/STEM – JEOL 2100F), aiming at phase identification of the solid product as well as detailed morphological characterization. Figure 1 shows a diffractogram, Figure 1a, and two SEM images, Figure 1b and 1c, of a sample produced without urea. The diffractogram corresponds to a single-phase material with typical structure of iron oxide ( $\text{Fe}_2\text{O}_3$ ) (JCPDF 00-013-0534). In this condition, the sample displays limited crystallinity with low intensities peaks. There is no indication of aluminum in this sample. Figure 1b and 1c are secondary-electrons (SE) and backscattered electron (BSE) images corresponding which corroborate the nature of a single phase material with a granular structure and grains size in the order of 40 to 50 nm. On the other hand, as show in Figure 2a the X-ray diffractogram of a sample produced with a urea as fuel (sample 01) displays well defined peaks allowing to index prominent crystallographic planes in this compound identified as  $\text{FeAl}_2\text{O}_4$  (JCPDF 01-089-1686). SEM images both under SE and BSE signals shows the solid agglomerated products as single-phase material with particle/grain size in the same order as in the sample 00. TEM observations of a sample 00 showing in Figure 3 in both BF and CDF image conditions corroborate mostly amorphous product although with some crystalline particles. Figure 4 is a montage of TEM/STEM images with corresponding diffraction patterns and elemental mapping. While TEM confirms the nature of crystalline aggregates with particle size as before mentioned in the order 40-50 nm before mentioned, the STEM images with lower diffraction contrast as compared to TEM still reveals the same morphological and particle size distribution however are quite unique in confirming the XED elemental mapping of Al, Fe, and O that the final product is a single phase spinel [4].

### REFERENCES

- [1] J. Ilona, et al. EUR J MINERAL. 29, (2017) 63–72.
- [2] D.P. Dutta, et al. Materials Science and Engineering B 176, (2011) 177–180.
- [3] M. Azam et al. Materials Today: Proceedings 2, (2015) 5150 – 5154.
- [4] The authors are grateful to the LabNano/CBPF and CAPES (Brazil).

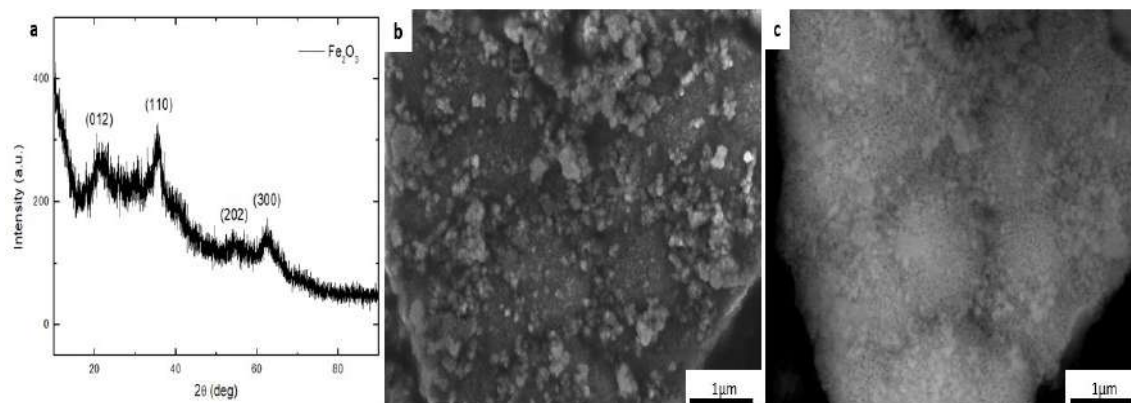


Figure 1 - (a) X-ray diffractogram of sample 00; (b) SE and (c) BSE SEM image of sample 00.

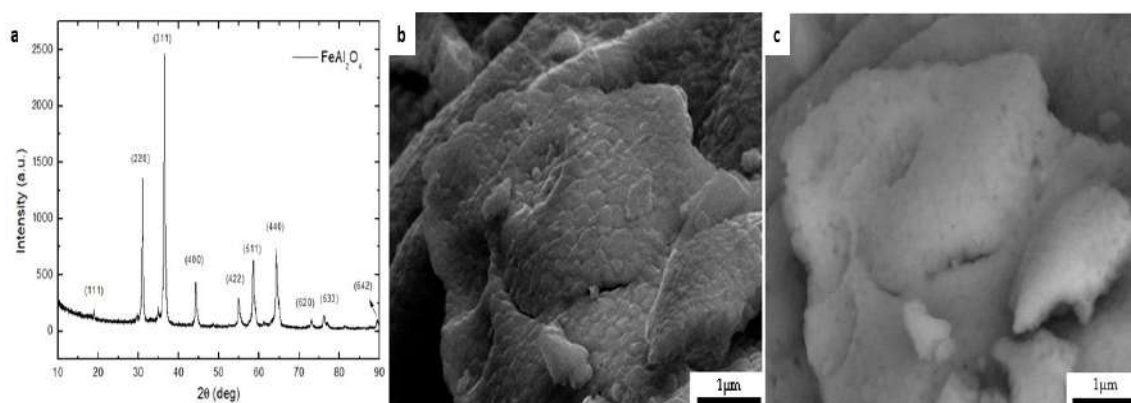


Figure 2 - (a) X-ray diffractogram of sample 01; (b) SE and (c) BSE images of sample 01.

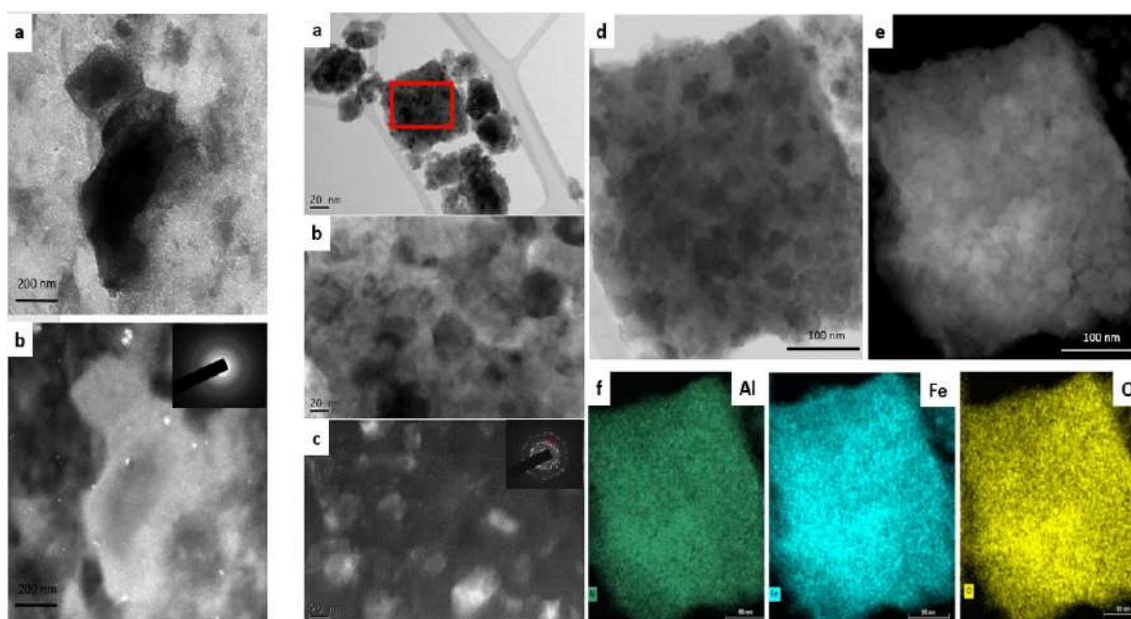


Figure 3 - (a) Bright-field (BF) TEM image of sample 00. (b) dark-field (DF) TEM image of sample 00.

Figure 4 - (a) BF-TEM image of sample 01; (b) and (c) BF/DF-TEM images obtained from box area in (a) and corresponding diffraction pattern; (d) and (e) BF/DF STEM images of the same particle shown in (a); (f) corresponding XED elemental maps of Al, Fe, and O.

## Structural and Morphological Studies of ZnO Nanosheets Using Graphene Oxide as Template.

Lunz J.N.<sup>1\*</sup>, Santana C.A.<sup>1</sup>, Vasconcelos T.L.<sup>1</sup>, Archanjo B.S.<sup>1</sup> and Achete C.A.<sup>1</sup>

<sup>1</sup>. Instituto Nacional de Metrologia, Qualidade e Tecnologia, Diretoria de Metrologia Científica, Divisão de Metrologia de Materiais, Duque de Caxias, Xerém, RJ, 25250-020 – Brasil.

\* jnlunz@colaborador.inmetro.gov.br

The quest for different zinc oxide (ZnO) morphologies keep scientists captivated to develop new synthesis routes for ZnO, based on their promising characteristics. Nanosheets of metal oxides, material in initial research phase, as well as graphene oxide (GO), present a versatile potential of application in varied fields of the economy due its distinct physical and chemical properties; which stimulates the constant development of research and technology<sup>[1]</sup>. Zinc oxide is an important intrinsic semiconductor with a direct 3.37 eV band gap, high exciton binding energy (60 meV) and good electron mobility. It decomposes at atmospheric pressure and temperatures above 2070 K. It has optical, electrical, physical and mechanical activity<sup>[2]</sup>. It easily crystalizes and in nanoparticle form its crystal structure changes<sup>[3]</sup>. The crystalline structure in the hexagonal form (wurtzite) presents lattice parameters:  $a = b = 0.3249$  nm and  $c = 0.5206$  nm, consisting of zinc atoms ( $\text{Zn}^{2+}$ ) and oxygen ( $\text{O}^{2-}$ ) coordinates tetrahedrally, arranged alternately layer by layer along  $c$  axis, with polar surfaces of equal and opposite charges of  $+$  (0001) for  $\text{Zn}^{+2}$  and  $-$  (0001) for  $\text{O}^{2-}$  <sup>[4]</sup>. The system was synthesized by a one-pot controlled precipitation methodology in alkaline medium and at room temperature, with zinc acetate and ethanol P.A in the presence of GO as template. The detailed study of ZnO/GO microstructural evolution was performed by Helium Ion Microscopy (HIM), and Transmission Electron Microscopy (TEM), in the conventional and scanning modes (STEM). Compositional analyzes were conducted by energy dispersive x-ray spectroscopy in STEM-EDS mode. HIM images of the ZnO/GO samples without thermal treatment (see Fig. 1), show the presence of thin layered GO sheets, however no evidence of effective interaction between GO and ZnO nanosheets were observed. The presence of GO in the synthesis did not alter the ZnO format; therefore, the implementation of GO as template is promising. TEM/STEM images (see Fig. 2) show agglomeration of several monocrystals, where it is observed well-defined and faceted particles, proving the efficiency of the synthesis and the thermal treatment performed. The result of the electron diffraction in the TEM mode operation, confirmed the presence of monocrystalline nanoparticles. EDS spectra (Fig. 3) obtained in the region of interest demonstrates the formation of ZnO. The results exhibit an interesting behavior of the material, however the thermal treatment is responsible to densify it, losing the nanosheet shape. Therefore the need to further investigation in order to fulfil its potential application is required.

### REFERENCES:

- [1] P. Raizada et al. Materials Science for Energy Technologies, (2019).
- [2] C. Mayrinck et al. Revista Virtual de Química, 6 (2014) 1185 – 1204.
- [3] T. Chiang et al. Solar Energy Materials and Solar Cells, 95 (2011), 740-744.
- [4] P. Gao et al. Process Journal of Physical Chemistry B, 108 (2004), 7534-7537.
- [5] The authors acknowledge the financial support from the Brazilian Agencies CNPq and FAPERJ.



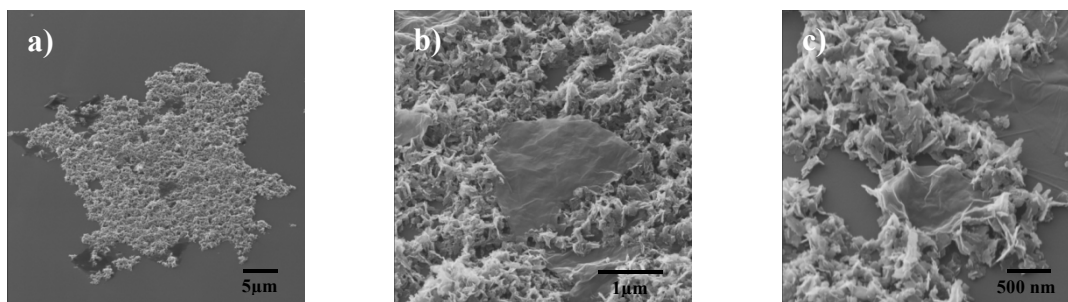


Fig. 1. HIM images of ZnO/GO without thermal treatment with field of view of: a) 45 microns; b) 6,5 microns; c) 3,5 microns;

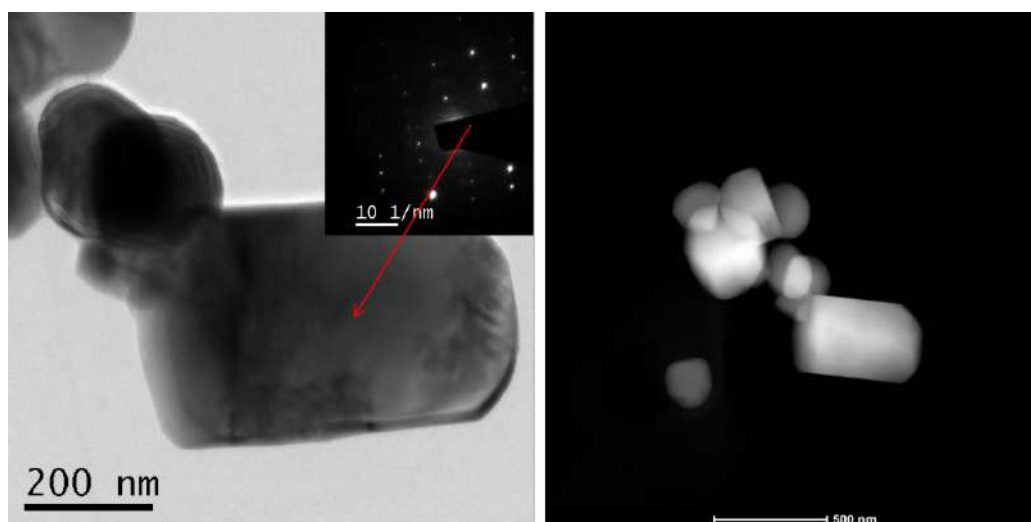


Fig. 2. TEM-STEM micrographs of ZnO/GO after thermal treatment at 800°C in different regions and magnifications with respective diffraction pattern indicated. Microscope FEG-TITAM 80-300, operated at 300 KV.

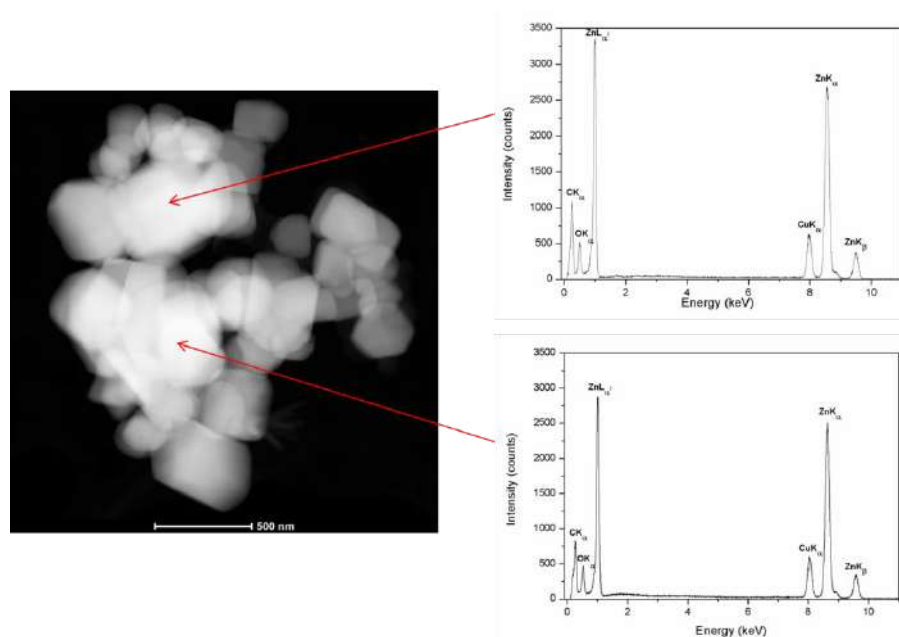


Fig. 3. STEM-EDS: a) region 1 EDS spectrum and b) region 2 EDS spectrum; c) image obtained in STEM mode. Microscope FEG-TITAM 80-300, operated at 300 KV.

## Study of Small Alloy (AuAg) Nanoparticle Structure using Pair Distribution Function (PDF) derived from Precession Electron Diffraction (PED)

Leonardo M. Corrêa\*, Murilo H. M. Moreira, Varlei Rodrigues and Daniel Ugarte

Dept. Applied Physics, Inst. Physics ‘Gleb Wataghin’, UNICAMP, Campinas SP, Brazil

\*lmcorre@ifi.unicamp.br

Nanoparticles (NP) are of great technological interest due to their unique chemical and physical properties. Transmission electron microscopy allows a detailed characterization of NPs; but a deep study also requires ensemble characterization techniques (ex. X-ray diffraction). However, even in a modern synchrotron NP samples of several milligrams may be necessary. The use of electron diffraction approaches may reduce sample mass by several orders of magnitude due to the stronger electrons-matter interaction. This stronger interaction leads to dynamical diffraction that renders rather difficult the understanding of diffraction intensities. The use of real space Pair Distribution Function (PDF) derived from X-Ray diffraction has been shown as a powerful method to understand and, even refine, the structure of NP systems [1]. Here, we analyze the use of PDF based on electron diffraction patterns of NP obtained using Precession Electron Diffraction (PED) [2]. Diffraction intensities derived from PED are quasi-kinematical allowing us to use much simpler and conventional X-ray approaches to process and interpret diffraction data. Our NP samples ( $\text{Ag}_{0.30}\text{Au}_{0.70}$ ) were generated in a home-built molecular beam cluster source [3] deposited on a thin a-C film (Fig. 1). Experiments were performed at room temperature using a TECNAI G2 200KV microscope, equipped PED system Nanomegas ASTAR and an axial CCD Camera (LCE-DEMa-UFSCar). PDF derivation and structure refinement were realized using a home-made developed software (see Figs. 2 & 3), which includes: i) correction of geometrical aberrations in the diffraction pattern; ii) simultaneous subtraction of carbon support and scattering background; iii) simulation of NP diffracted intensities using the Debye scattering equation. PDF profiles were compared with different simulated NP patterns (FCC, twinned FCC, icosahedral and decahedral); refinement of the NP diameter was also performed. The best fits ( $R \sim 50\%$ , no-PED patterns) correspond to twinned and decahedral NPs; the residue improves significantly by using PED ( $R \sim 40\%$ ). The derived NP diameter ( $\sim 2.5$  nm) is much smaller than the NP sample mean diameter ( $\sim 5.8$  nm). This suggests that NPs generated in the cluster source are formed by the aggregation of smaller NP during flight. Recent studies indicate that significant improvement of PED-based PDF structural refinement can be obtained by using a LN2 sample holder [4]; work is under progress to test this approach.

### REFERENCES

- [1] T. Egami and S.J.L. Billinge, *Underneath the Bragg peaks: Structural Analysis of Complex Materials*, Elsevier, Oxford UK, 2003. J
- [2] P. A. Midgley, A. S. Eggeman, *IUCrJ*, 2 (2015) 126.
- [3] A. D. Tavares de Sá, et al, *J. Vac. Sci. Technol. B*, 32 (2014) 061804.
- [4] M.M. Hoque, et al., unpublished.
- [5] We are grateful to D. Coimbra for assistance during PED work; we acknowledge financial support from CAPES, CNPQ and FAPESP.

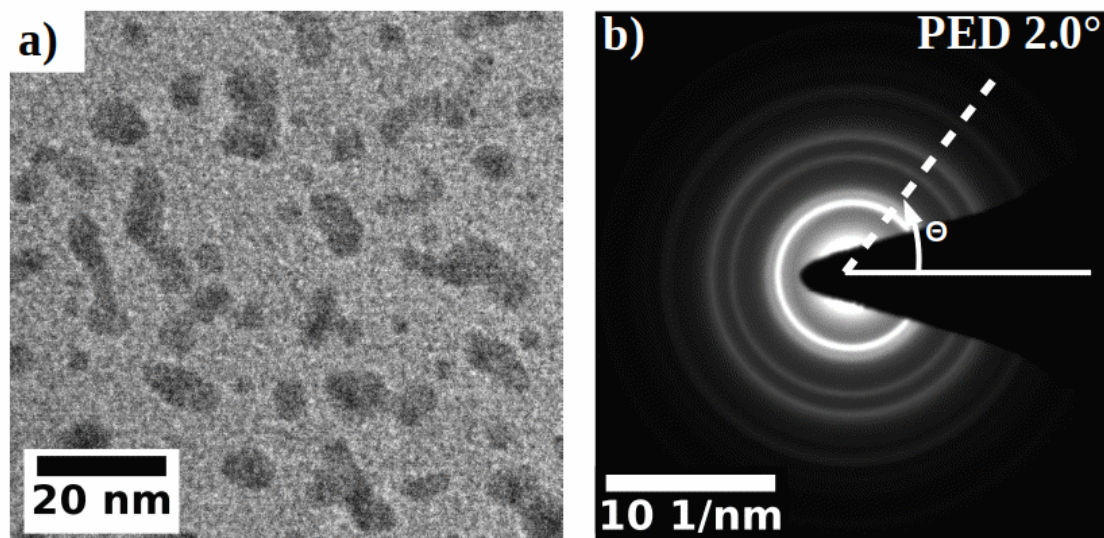


Figure 1. a) TEM image of NP sample. b) Selected Area Diffraction (SAD) pattern using 2.0 degrees PED. Dashed line indicate a radial profile line, solid line is the reference axis.

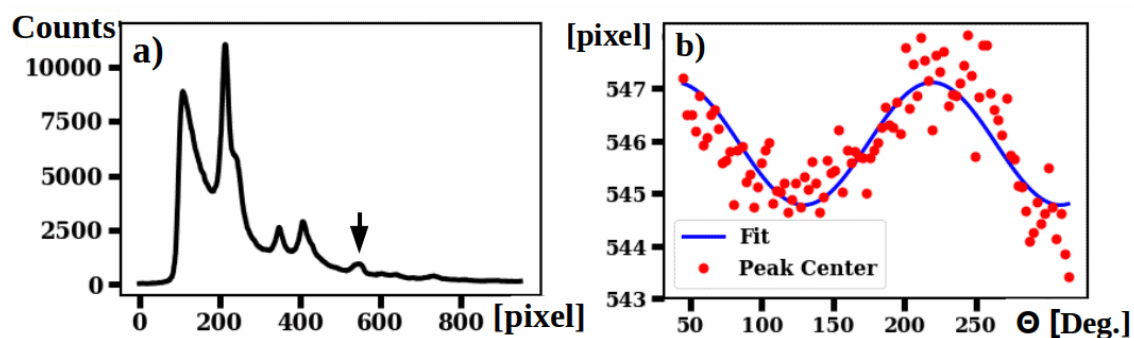


Figure 2. a) Typical radial profile extracted from the PED-SAD, the arrow indicates a peak used to map geometrical distortion as a function of azimuthal angle (b).

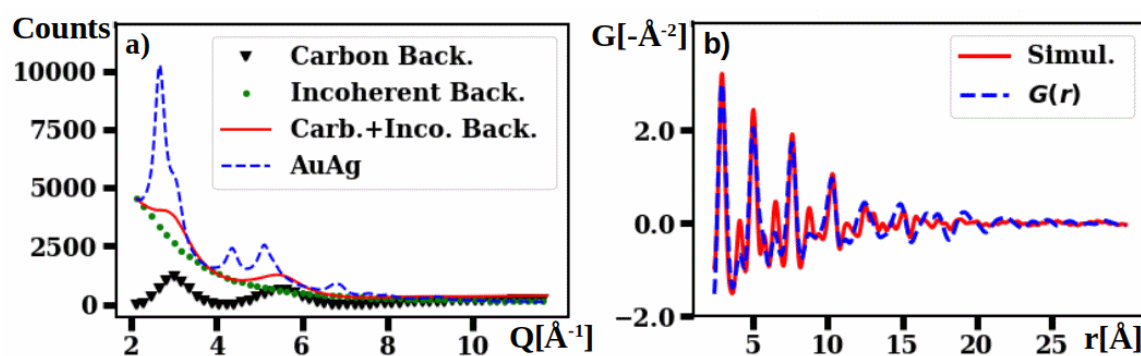


Figure 3. a) PED-SAD azimuthally integrated pattern and background subtraction components. b) Experimental real space reduced PDF ( $G(r)$ ) and simulated curve for a decahedral particle.

## Microstructure and superconductivity in Bi/Ni nanoparticles/thin-film hybrid systems prepared by pulsed laser deposition

L.Y. Liu<sup>1,2\*</sup>, Y. T. Xing<sup>3</sup>, I. L.C. Merino<sup>1</sup>, E. Baggio-Saitovitch<sup>1</sup>, D. F. Franceschini<sup>3</sup>,  
and I. G. Solórzano<sup>2</sup>

<sup>1</sup> COMAN, Centro Brasileiro de Pesquisas Físicas, Rio de Janeiro 22290-180, Brasil

<sup>2</sup> DEQM, Pontifícia Universidade Católica do Rio de Janeiro, Rio de Janeiro, Brasil

<sup>3</sup> Instituto de Física, Universidade Federal Fluminense, Niterói 24210-346, Brasil

\*lyliu.xing@gmail.com

Superconductivity in Bi-Ni bi-layer system attracted great attention because both of the Ni and crystalline Bi are non-superconducting above 5 mK and no agreement has been made for the interpretation [1]. One of the explanations is the formation of NiBi<sub>3</sub> phase in this system during the sample preparation [2]. Diffusion of Ni and Bi atoms is highly involved in this process [3]. Considering that the diffusion of nanoparticles are much more difficult than the single atoms depositing on top of thin films, we prepared hybrid systems with Bi layer and Ni nanoparticles on top, or Ni layers with Bi nanoparticles on top by pulsed laser deposition (PLD) and studied the superconductivity properties. The thin film layer was deposited in vacuum and the nanoparticle layer was deposited in Ar atmosphere with pressure of 1 mbar. Most importantly, the nanoparticles have been formed before they reach the substrate, which is placed 35 mm far from the target. The morphology and microstructure of the Ni and Bi nanoparticles have been studied by means of high resolution transmission electron microscopy (HRTEM) under diffraction and phase contrast modes. Fig.1 and Fig. 2 show representative TEM images of the Ni and Bi nanoparticles produced by PLD. The electric transport results (as shown in Fig. 3) show that with deposition of the same amount of materials, Bi\_nanoparticles/Ni\_thin-film system always has better superconducting properties than Bi\_thin-film/Ni\_nanoparticles system. This confirmed that the diffusion process played an important role in the superconductivity in Bi/Ni system [4].

### References:

- [1] Moodera, et al. Superconducting phases of Bi and Ga induced by deposition on a Ni sublayer. *Physical Review B*, 42(1):179, 1990.
- [2] Siva, et al. Spontaneous formation of superconducting NiBi<sub>3</sub> phase in Ni-Bi bilayer films. *Journal of Applied Physics*, 117(8):083902, 2015.
- [3] L.Y. Liu, et al. Superconductivity in Bi/Ni bilayer system: Clear role of superconducting phases found at Bi/Ni interface. *Physical Review Materials* 2, 014601, 2018.
- [4] This research was sponsored by CAPES, CNPq and FAPERJ (Brazil). The authors thank LaMAR/CAIPE at UFF, LABNANO at CBPF for the use of their facilities.



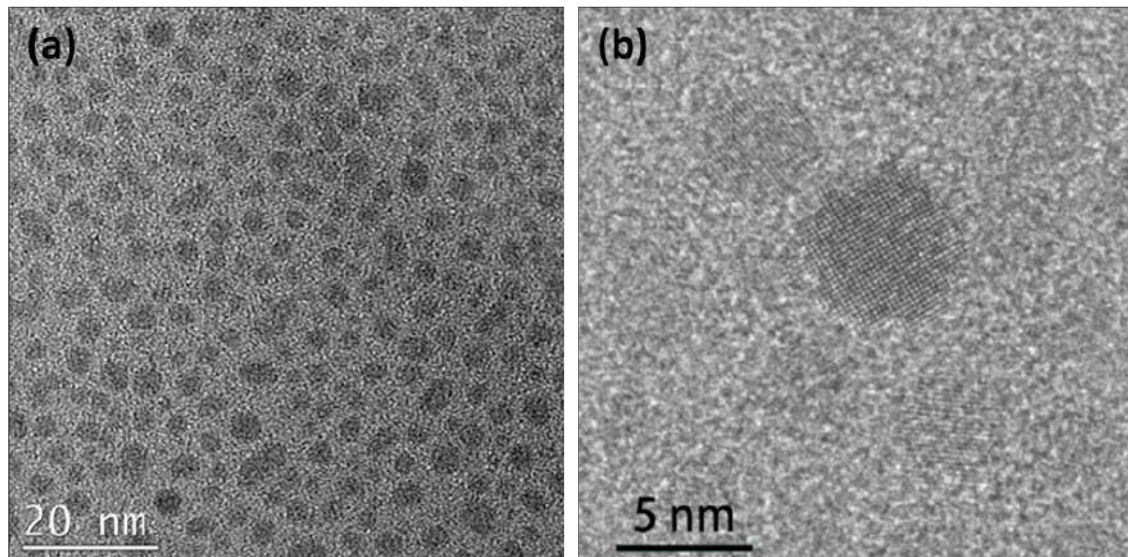


Figure 1. (a) Low magnification image of Ni nanoparticles, and (b) HRTEM image of Ni nanoparticles.

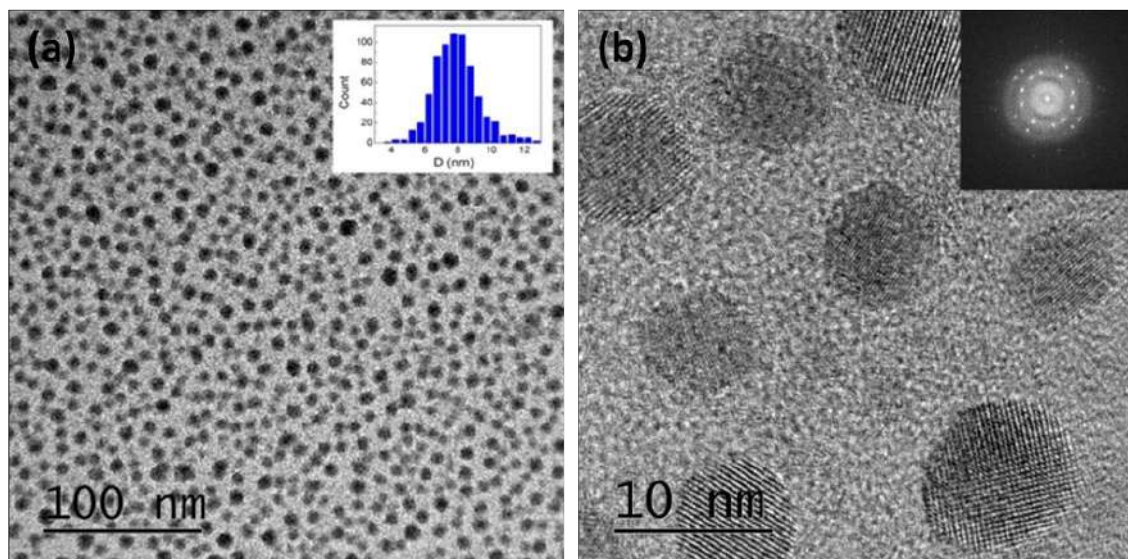


Figure 2. (a) Low magnification image of Bi nanoparticles. Inset shows the size distribution of the particles, and (b) HRTEM image of Bi nanoparticles. Inset: FFT of the image.

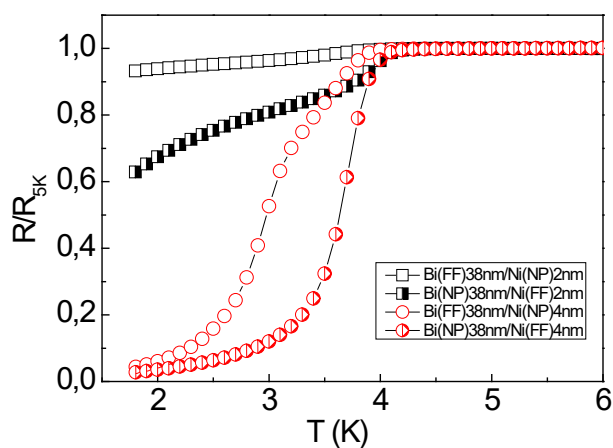


Figure 3. Normalized resistivity as a function of temperature for Bi/Ni nanoparticles/thin-film hybrid systems.

## Synthesis and Characterization of Polymeric Nanoparticles Functionalized for Drug Delivery Applied on Osteoporosis Treatment

Mariana Moreira Longuinho<sup>1,2\*</sup>, André Linhares Rossi<sup>2</sup> and Marcos Farina<sup>3</sup>

<sup>1</sup> Institute of Biophysics Carlos Chagas Filho, Federal University of Rio de Janeiro, Rio de Janeiro, Brazil,

<sup>2</sup> Condensed Material, Applied Physics and Nanoscience Coordination, Brazilian Center for Physics Research, Rio de Janeiro, Brazil,

<sup>3</sup> Institute of Biomedical Sciences, Federal University of Rio de Janeiro, Rio de Janeiro, Brazil.

\*mariana.longuinho@gmail.com

Osteoporosis is a chronic, systemic and metabolic disease unleashed by the imbalance of the bone resorption by osteoclast and bone formation by osteoblast, resulting in progressive reduction of bone density, increasing the risk of fractures and deterioration of bone tissue microstructure [1], [2]. Osteoporosis is a major cause of morbidity and mortality in the elderly, being one of the major public health problems [1], [3]. Even though a variety of drugs for osteoporosis therapy are available, the benefits for long-term treatment are still limited. Sometimes the drug of choice has no activity in the patient, the expected effect takes time to occur, it is toxic in long term, or the therapy is interrupted after a certain time, without the expected efficiency [3], [4]. Observing these problems and the relevance of the disease in the population, especially the elderly, new approaches are needed, in order to improve the therapy, aiming to optimize dose/effect ratios and decrease side effects. The present project aims to produce and characterize a nanoparticulate system using alginate as wall material and L-aspartic acid to functionalize the system, since this molecule has high affinity to the hard tissue. The system will be applied to encapsulate drugs used in osteoporosis therapy such as alendronate. Nanoparticles (NP) were synthesized by cation-induced gelification using strontium as divalent cation. Strontium was chosen as ion of choice for the cross-link because of its similarity with calcium and its double function, inhibiting bone resorption and increasing bone formation already confirmed when linked with ranelic acid [5]. To attach the L-aspartic acid on the NP, the pH of the reactional medium was adjusted to 10 so that the positive charge could be guaranteed. NP were analyzed by size using dynamic light scattering (90Plus/Bi-MAS, Brookhaven Instruments) and morphology by transmission electron microscopy (JEOL-2100F). Both NP had similar mean size (Non-functionalized NP = 400.04 nm ± 19.52 and functionalized NP = 427.96 nm ± 46.45). By TEM and EDS, both NP showed micro agglomerates with electron dense nanospheres rich in strontium (Figures 1 and 2). In functionalized NP the regions rich in strontium contained also nitrogen that can be associated with the link of both ions with the hydroxyl groups of alginate (Figure 2). These results show that the presence of L-aspartic acid did not influence the NP morphology and size. However, the synthesis will be repeated changing the concentration of each component to obtain the optimum size of 200 nm which is described as the best size to reach bone tissue from blood circulation.

### REFERENCES

- [1] P. Mora-Raimundo, M. Manzano, and M. Vallet-Regí, *AIMS Bioengineering* 4 (2017) 259.
- [2] C. Ruosi *et al.*, *J. Osteoporos. Phys. Act.* 3 (2015) 1.

- [3] E. M. Lewiecki, *Nat. Rev. Rheumatol.* 7 (2011) 631.
- [4] J. S. Chen and P. N. Sambrook, *Nat. Publ. Gr.* 8 (2011) 81.
- [5] W. Querido, A. L. Rossi, and M. Farina, *Micron* 80, (2016) 122.
- [6] This research was supported by CNPq (Brazil).

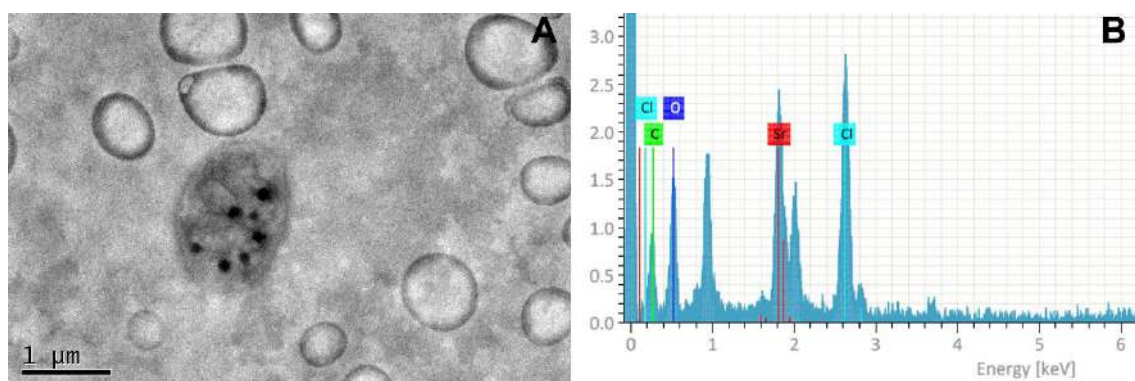


**Figure 1:** A: Micrograph obtained by TEM of non-functionalized NP sample. B: EDS spectrum referred to the electron dense spheres in A.

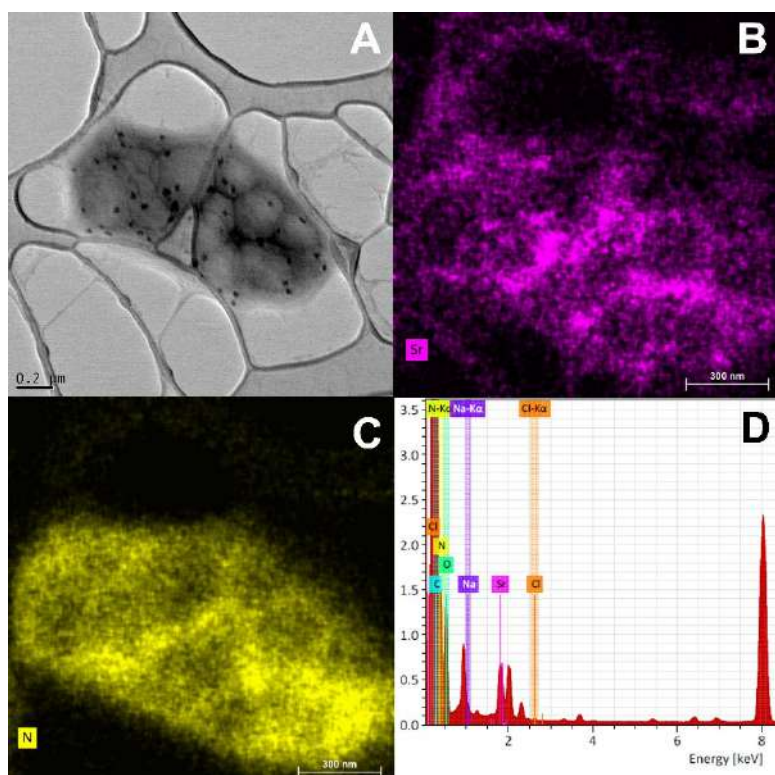


**Figure 2:** A: Micrograph obtained by STEM of functionalized NP sample. B: EDS map of strontium of A. C: EDS map of nitrogen of A. D: EDS spectrum of the mappings made from image A.



## Transmission Electron Microscopy For The Characterization of Hydroxyapatite Nanostructure From Hen's Eggshell

Marla Karolyne dos Santos Horta<sup>1\*</sup>, Francisco José Moura<sup>1</sup>, Marilza Sampaio Aguilar<sup>2</sup>, José Brant de Campos<sup>3</sup>, Vitor Santos Ramos<sup>3</sup>, Suzana Bottega Peripolli<sup>3</sup>, Maria Isabel Navarro<sup>4</sup>, Bráulio Soares Archanjo<sup>4</sup> and Adilson Claudio Quizunda<sup>3</sup>

<sup>1</sup> Pontifícia Universidade Católica do Rio de Janeiro, Departamento de Engenharia Química e de Materiais/Instituto, Rio de Janeiro, Brasil.

<sup>2</sup> Universidade Estácio de Sá, Departamento de Química, Rio de Janeiro, Brasil. <sup>3</sup> Universidade do Estado do Rio de Janeiro, Departamento de Engenharia Mecânica, Rio de Janeiro, Brasil

<sup>4</sup> Instituto Nacional de Metrologia, Qualidade e Tecnologia, Divisão de Metrologia de Materiais, Rio de Janeiro, Brasil

\*marla.horta@hotmail.com

Due to its composition (calcium carbonate- $\text{CaCO}_3$ ), the chicken eggshell is a promising source for calcium phosphates compounds synthesis, such as hydroxyapatite (HAP) [1-2], a biomaterial widely used for technological applications in materials science, engineering and medical areas. The HAP have a chemical similarity to bones and teeth exhibiting excellent biocompatibility making it an ideal candidate for orthopedic and dental implants or components of implants [3]. In this work, nanohydroxyapatite powders were successfully synthesized from chicken eggshells and characterized by transmission electron microscopy (TEM) to elucidate the effect of synthesis conditions in the characteristics of the material obtained since its biocompatibility is related and can vary according to morphology, size, composition. The calcium carbonate (eggshell) was converted into CaO which was hydrolyzed to form  $\text{Ca}(\text{OH})_2$  and then was react with phosphoric acid. The reaction was given at room temperature under constant stirring and then the sample was calcined at  $600^\circ\text{C}/2\text{h}$ . Scanning electron microscopy is a very complete technique in comparison to scanning electron microscopy (SEM) as it allows simultaneous analysis of morphology, crystallography and chemical composition of the materials. And due to the great magnifications it can achieve is a more appropriate technique to work with nanostructured material. Detailed observations and analysis were conducted by transmission electron microscopy (TEM) in a probe corrected FEI-Titan 80-300 instrument working at 300 kV. The samples were analyzed by high-resolution TEM (HRTEM), electron diffraction pattern (DP), scanning transmission electron microscopy using a high annular dark field detector (STEM-HAADF) and energy dispersive X-ray spectroscopy (EDXS). A TEM image of a large nanoparticles agglomerate is presented in Fig. 1a. The nanoparticles have a morphology rods like with size smaller than 50nm. The Fig. 1b shows the electron diffraction patterns obtained from HAP which is presented as being of a material polycrystalline with indexed plans corresponding to HAP (Tab 1). Diffracted planes crystals were comparable with 2 intense HAP peaks found by X-ray diffraction (DRX) equal to  $32.902^\circ$  and  $32.196^\circ$  (data not shown) and for comparison with PDF#09-0432. The EDS analysis confirms the chemical composition of the sample presenting peaks in the spectrum exclusively of P, O and Ca (Fig 2b). Some results are still being analyzed and discussed so that further consideration can be given to the work.

### References

[1] E. M. RIVERA, et al., Materials Letters. No. 41, pg. 128-134, 1999.



- [2] D. A. OLIVEIRA, et al., Key elements for a sustainable world: energy, water and climate change, São Paulo, 2009.
- [3] A. FIHRI, et al., Coordination Chemistry Reviews, v. 347, p. 48-76, 2017.

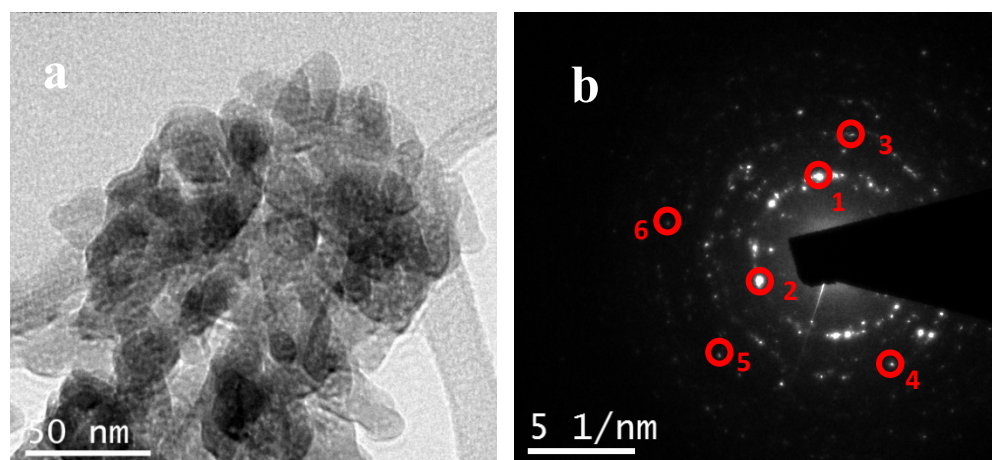


Fig 1. TEM image of HAP nanoparticles (1a) with the respective electron diffraction pattern (1b) (DP).

PDF#09-0432			Diffraction pattern	
d (Å)	2 theta	h l k	Spot	d (nm)
2.720	32.902	300	1	0.2717
2.778	32.196	112	2	0.2764
1.78	51.283	410	3	0.1787
1.754	52.1	402	4	0.1760
1.433	65.031	511	5	0.1427
1.28	73.995	423	6	0.1281

Tab. 1. Diffraction pattern of the literature and those obtained in the analysis.

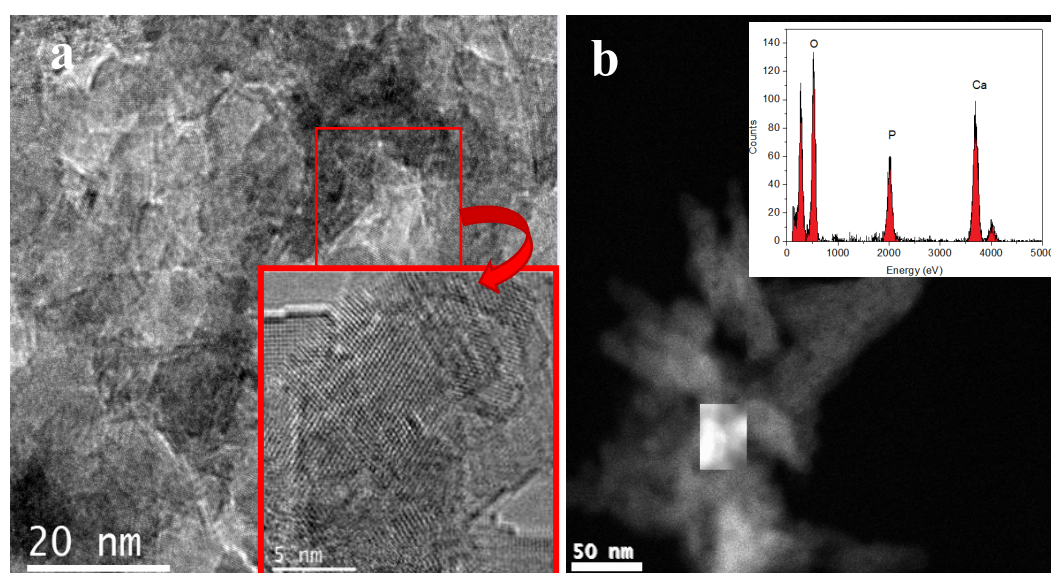


Fig 2. HRTEM image of HAP (2a) and dark field STEM image with energy dispersive X-ray spectroscopy results (2b).

## Development of an antibacterial composite of calcium silicate incorporated with silver for applications in the area of bone engineering

Natália Yoshihara<sup>1\*</sup>, Abner Figueiredo<sup>1</sup>, Kelly Castro<sup>1</sup>, Ana Ribeiro<sup>2</sup>, Bráulio Archanjo<sup>1</sup>, Carlos Achete<sup>1</sup>

<sup>1</sup>. Instituto Nacional de Metrologia, Qualidade e Tecnologia – Divisão de Materiais, Duque de Caxias. Brasil.

<sup>2</sup>. Universidade do Grande Rio, Programa de Pós-Graduação em Biomedicina Translacional, Duque de Caxias. Brasil.

Calcium silicate ceramics (CaSiO<sub>3</sub>) have been investigated for bone regeneration purpose due to its high bioactivity and high hydroxyapatite formation. Incorporating specific metallic ions into the structure of biomaterials for bone regeneration is an approach that aims to optimize the process of bone healing, as well as offer greater bioactivity, antibacterial effect, among others deficient or absent properties [1]. Silver nanoparticles have been extensively studied in the biomedical area because of their antimicrobial properties. The toxicity of silver is known, but may be reduced upon incorporation into an inorganic substance [2]. In this study, calcium silicates hydrated (CSH) as well as silver incorporated CSH (CSH-Ag) powder were prepared by chemical precipitation modified with in situ Ag incorporation for bone regeneration applications. The materials were characterized by scanning electron microscopy operated in transmission mode (TSEM), X-ray photoelectron spectroscopy (XPS), X-Ray Fluorescence (XRF) and X-ray diffraction (XRD). The in vitro bioactivity was evaluated through incubation in simulated body fluid solution (SBF) as recommended by ISO 23317:2007 standard. The antibacterial effects were tested on gram-negative bacterium *Pseudomonas aeruginosa* and a gram-positive bacterium *Staphylococcus aureus* resistant to antibiotics. The viability of CSH-Ag as biomaterial for bone regeneration applications, was investigated through cytotoxicity and cell adhesion on human osteoblast cells. Results showed the presence of silver nanoparticles homogeneously spread all over the CSH-Ag, in addition no significant changes were detected in the morphology and crystal structure in all Ag incorporated samples. All samples showed bioactivity and interestingly CSH-Ag presented similar bioactivity to the pure CSH. CSH-Ag showed promising antibacterial activities. The viability will be more investigated in lower concentrations of incorporation.

### REFERÊNCIAS

Siga os modelos abaixo para inserir as referências:

- [1] Siyu Ni, Jiang Chang. In vitro degradation, bioactivity and cytocompatibility of calcium silicate, dimagnesium silicate and tricalcium phosphate bioceramics. *Journal of Biomaterials Applications*, vol 24, 2009.
- [2] Wei Jiao, *RSC Advances*, 6 (2016) 112931.

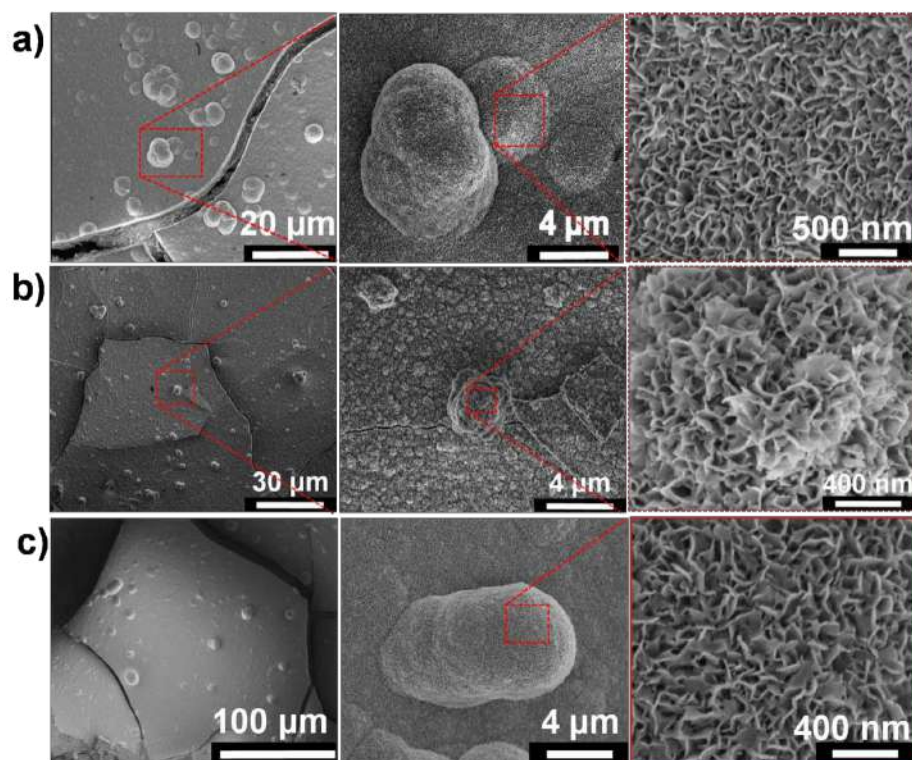


Figure 1: Bioactivity assay. Growth of apatite after 14 days in SBF solution. a) Micrographs obtained by SEM of a) pure calcium silicate, b) calcium silicate incorporated with 1% Ag and c) calcium silicate incorporated with 10% Ag.

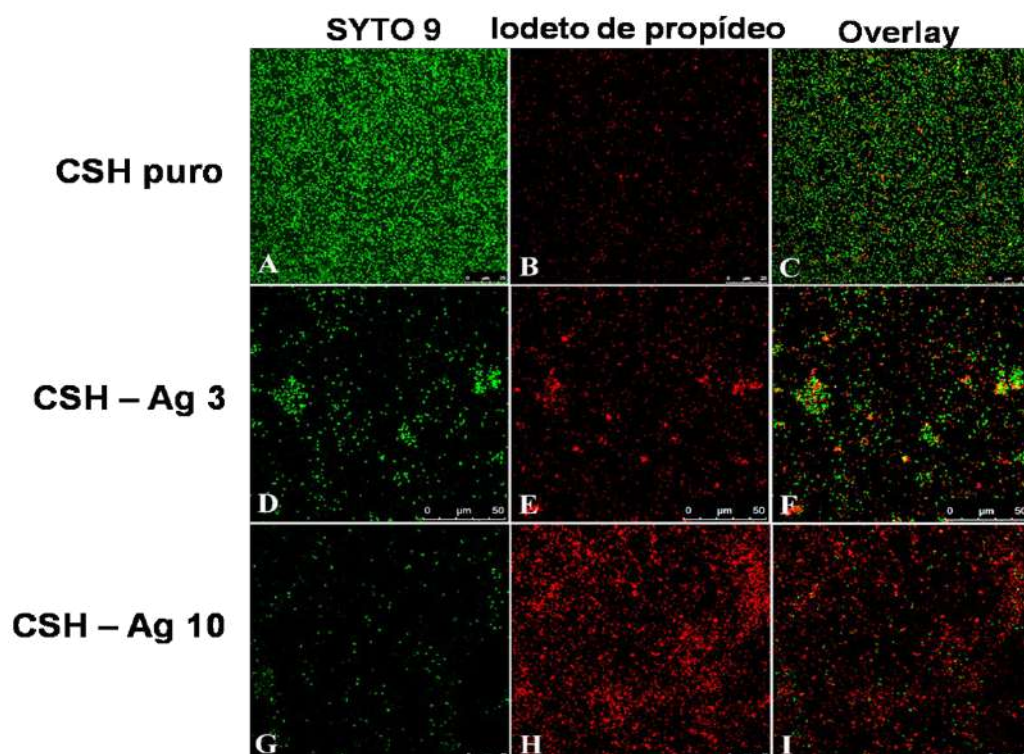


Figure 2: Cell viability of calcium silicate incorporated with different concentrations of silver. The cells of quadrants (a), (d) and (g) exhibit green fluorescence, characteristic of SYTO 9 dye, which acts only on viable cells. The quadrants (b), (e) and (h) exhibit red fluorescence stained with propidium iodide, which marks only the dead cells. The quadrants (c), (f) and (i) show the overlay of living and dead cells.



## Stability in Culture Media for Antimicrobial Assays of Reduced Gold Nanoparticles with Extract of *Punica granatum* L.

Natane Aparecida de Oliveira <sup>1\*</sup>, Marco Cesar Cunegundes Guimarães <sup>2</sup>

<sup>1\*</sup>. Programa de Pós Graduação em Biotecnologia, Universidade Federal do Espírito Santo (UFES), Vitória, Brasil. E-mail: [natane.a.oliveira@gmail.com](mailto:natane.a.oliveira@gmail.com),

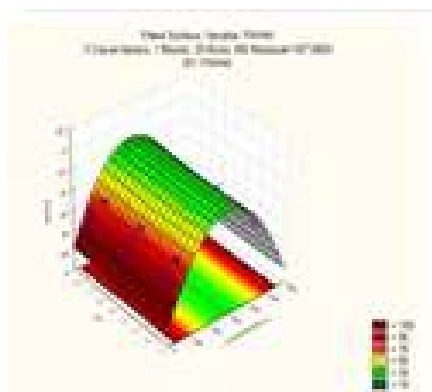
<sup>2</sup>. Laboratório de Ultraestrutura Celular Carlos Alberto Redins (LUCCAR), Departamento de Morfologia, Universidade Federal do Espírito Santo (UFES), Vitória, Brasil.

The present study purpose to evaluate the stability of gold nanoparticles reduced with extract of pomegranate (*Punica granatum* L.) through the test of resuspension in bacterial culture media (Mueller Hinton Broth and Mueller Hinton Broth cation adjusted). For the synthesis of nanoparticles reduced with pomegranate extract, we used the complete factorial planning, with two levels (-1, 1) and five variables (pH, concentration, rotation, concentration of the extract and temperature) (adapted [1]), totaling 32 experiments. The response variables were analyzed full width at half maximum (FWHM), maximum absorbance, area under the curve and maximum  $\lambda$ , obtained by the spectrum of Uv-Vis with microscopy in the wavelength range between 250 to 800 nm. From the significant response variables obtained by factorial outlined the experimental conditions for the optimization process based on the central composite experimental design being used three levels (-1, 0, 1) and three variables (pH, temperature and concentration of the extract). The response variable presented in this summary is the full width at half maximum (FWHM). This response was selected to represent the material synthesized more monodisperse, being the optimal condition for this factor obtained by response surface methodology (RSM) (Graph 1) and the values of the variables at the optimal point shown in the following table. After the optimization of synthesis, the gold nanoparticles reduced with pomegranate extract were subjected to the resuspension to evaluate the stability of coloide forward to the culture media used for antimicrobial sensitivity tests (Mueller Hinton Broth and Mueller Hinton Broth adjusted). Thus, the pellets were resuspended in different weather conditions (5, 10 and 20 minutes) and speed (6,000 rpm and 8,000 rpm 10,000 RPM 12,000 RPM and 14,000 rpm). The pellets were resuspended in their respective culture media (1.5 mL). The stability of coloide was evaluated by the spectrum of Uv-Vis with microscopy between 250 to 800 nm, where they are compared to the variations of bandwidth to half height (FWHM), maximum absorbance, area under the curve and maximum  $\lambda$  in relation to control (Table 1 and 2). It can be concluded that by means of factorial design was able to control the synthesis of nanoparticles, being the optimal point of synthesis found with pH values of 3,0335; 62,4373°C temperature and concentration at a ratio of 2,95:5 (extract: solution). Regarding the stability of coloide, we observed that the nanoparticles have great stability compared to culture media were analyzed, no major changes somewhat larger in the stability of the nanoparticles re-suspended in Mueller Hinton Broth with adjustment of cations, thus the material obtained by this route of synthesis shows himself able to be used in antimicrobial sensitivity tests.



## REFERENCES

- [1] R. S VALOTTO. Caracterização e avaliação da estabilidade de nanopartículas De ouro sintetizadas com casca de romã (*Punica granatum L.*), Vitória, 2018.
- [2] This research was supported by CNPq (Brazil), CAPES, FAPES and FINEP.



Graph 1: Graph surface response of optimization

Mueller Hinton				
Respostas				
CONDIÇÕES	FWHM	Abs. máxima	$\lambda$ máximo	Área
CONTROLE	52,12879	0,27533	527	14,76217
5 min 6000 rpm	52,74013	0,28001	527	15,28459
5 min 8000 rpm	57,52859	0,37688	529	23,0507
5 min 10000 rpm	59,8806	0,2554	526	15,54667
5 min 12000 rpm	61,15406	0,25939	529	16,04659
5 min 14 000 rpm	59,58807	0,25297	529	16,04659
10 min 6000 rpm	54,58558	0,22635	528	12,59896
10 min 8000 rpm	56,50459	0,2357	529	13,63601
10 min 10000 rpm	65,59182	0,22796	530	14,82966
10 min 12000 rpm	57,85937	0,24475	529	14,59932
10 min 14000 rpm	58,45711	0,24965	529	14,8697
20 min 6000 rpm	52,97747	0,21509	526	11,73414
20 min 8000 rpm	55,94545	0,25903	527	15,02122
20 min 10000 rpm	62,08333	0,25222	529	15,89056
20 min 12000 rpm	155,4982	0,20319	544	30,07162
20 min 14000 rpm	69,57489	0,23091	532	16,03174

Table 1: responses in the resuspension with Mueller Hinton Both

Mueller Hinton cátion ajustado				
Respostas				
CONDIÇÕES	FWHM	Abs. máxima	$\lambda$ máximo	Área abaixo da curva
CONTROLE	52,12879	0,27533	527	17,12987
5 min 6000 rpm	68,84539	0,23717	529	15,28459
5 min 8000 rpm	68,94127	0,77985	526	55,74464
5 min 10000 rpm	59,21664	0,30561	527	18,55503
5 min 12000 rpm	70,53368	0,28836	533	20,12988
5 min 14 000 rpm	63,25006	0,28977	529	18,5167
10 min 6000 rpm	60,89323	0,26224	530	16,32621
10 min 8000 rpm	57,67456	0,28943	528	17,17087
10 min 10000 rpm	65,59182	0,23385	528	14,58444
10 min 12000 rpm	64,77892	0,26188	530	17,0925
10 min 14000 rpm	69,09115	0,28387	532	19,85472
20 min 6000 rpm	57,32999	0,31849	527	18,8569
20 min 8000 rpm	60,41817	0,30155	530	18,5336
20 min 10000 rpm	63,94275	0,23189	531	15,02036
20 min 12000 rpm	65,70136	0,27636	532	18,33577
20 min 14000 rpm	67,23726	0,2177	532	14,62794

Table 2: responses in the resuspension test Mueller Hinton Both cation ajusted

## Resuspension And Flocculation Analysis Of Gold Nanoparticles Synthesized With Pomegranate Peel (*Punica granatum* L.)

Rafaela S. Valotto<sup>1\*</sup>, Flávio C. Monteiro<sup>1</sup>, Wanderson J. Keijok<sup>1</sup> and Marco C. C. Guimarães<sup>1</sup>

<sup>1</sup>. Morphology Department, Federal University of Espírito Santo (UFES), Vitória, Espírito Santo, Brazil. \*E-mail: rafavalotto@gmail.com.

Nanotechnology is characterized by the study of nanometric scale materials (10<sup>-9</sup> meters) and is an emerging science all around the world. One of the ways of manufacturing nanomaterials, especially nanoparticles (NP's), is by the synthesis method [1]. In this procedure, an oxireduction reaction forms the NP's by reducing the metal in its ionic form from the use of a reducing agent. In the green synthesis area, this reducing agent is, for the most part, of vegetable origin [2]. In this case, for the formation of gold nanoparticles (AuNP's), the reducing agent used is pomegranate peel (*Punica granatum* L.) tea, since it has a high level of antioxidant activity [3]. In order to evaluate the stability of AuNP's, the colloid was submitted to flocculation assays with ionic activity varying between 0,05 mM – 200 mM (Figure 1A), and pH between 1 and 13 (Figure 1B). These nanoparticles showed to be stable at high concentration of ions and at pH range of 1 to 9. Once checked that this nanoparticles are stable, they were centrifuged and resuspended on ultrapure water (Figure 2A), dimetilsulfoxide (DMSO) (Figure 2B), phosphate-saline buffer (PBS) (Figure 3) and ethyl alcohol. Formed nanoparticles were characterized through the UV-Vis spectrophotometer, Transmission Electron Microscopy (Figure 4), Infrared spectroscopy and Raman spectroscopy. It was not possible to resuspend the NP's in ethyl alcohol, once the colloid has flocculated and precipitated. The resuspension of DMSO and PBS have modify the characteristics of  $\lambda_{max}$  and half-bandwidth length (FWHM) which indicate colloid agglomeration, not being possible the application of AuNP's reduced by pomegranate in these aqueous environments without loss of its physicochemical properties.

### REFERENCES

- [1] K. N. Thakkar, S. S. Mhatre, R. Y. Parikh, Nanomedicine: Nanotechnology, Biology and Medicine. 6 (2010) 257.
- [2] I. Hussain et al., Biotechnol. Lett. 38 (2016) 545.
- [3] N. Ahmad, S. Sharma, R. Rai, Advanced Materials Letters. 3 (2012) 1

This research was supported by UFES (Brazil). Thanks to LUCCAR, LABIOM and LABPETRO/UFES for analysis support.

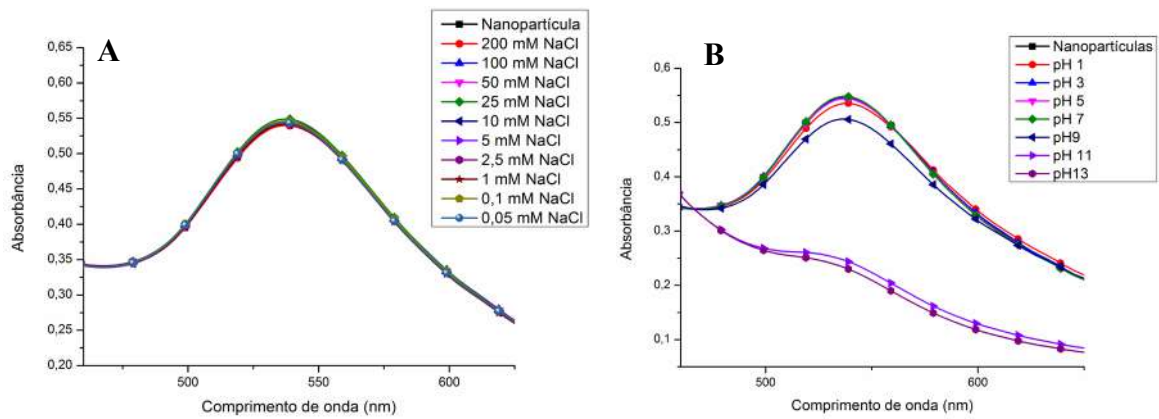


**Figure 1.** AuNP's UV-Vis spectrometry in different saline concentrations (A) and in different pHs (B).

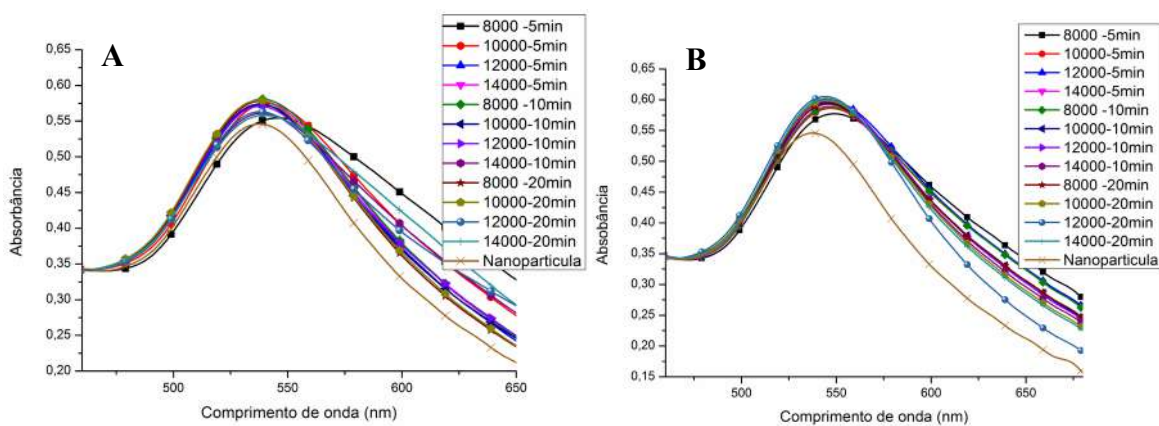


**Figure 2.** AuNP's UV-Vis spectrometry resuspension in ultrapure water (A) and in DMSO (B).

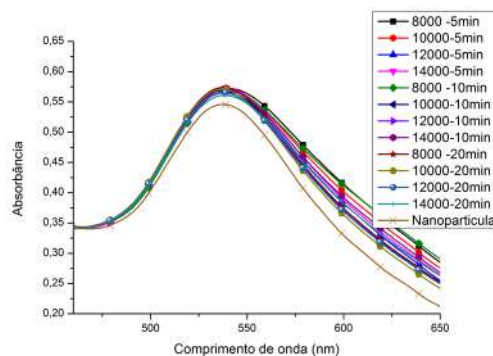


**Figure 3.** AuNP's UV-Vis spectrometry resuspension in PBS.

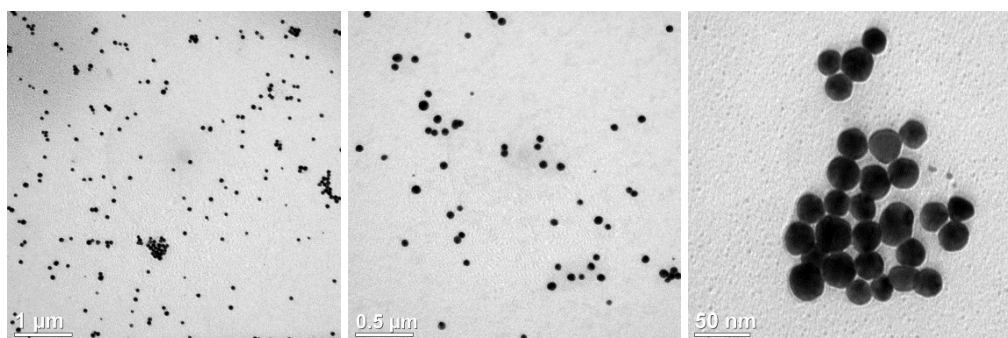


**Figure 4.** AuNP's TEM images.

## **Analysis of gold nanoparticles reduced with *Virola oleifera* resin and their stability in different microbiological growth mediuns to possible applies antimicrobial evaluations.**

Rafaella de Resende Marques<sup>1\*</sup>, Marco Cesar Cunegundes Guimarães<sup>1</sup>

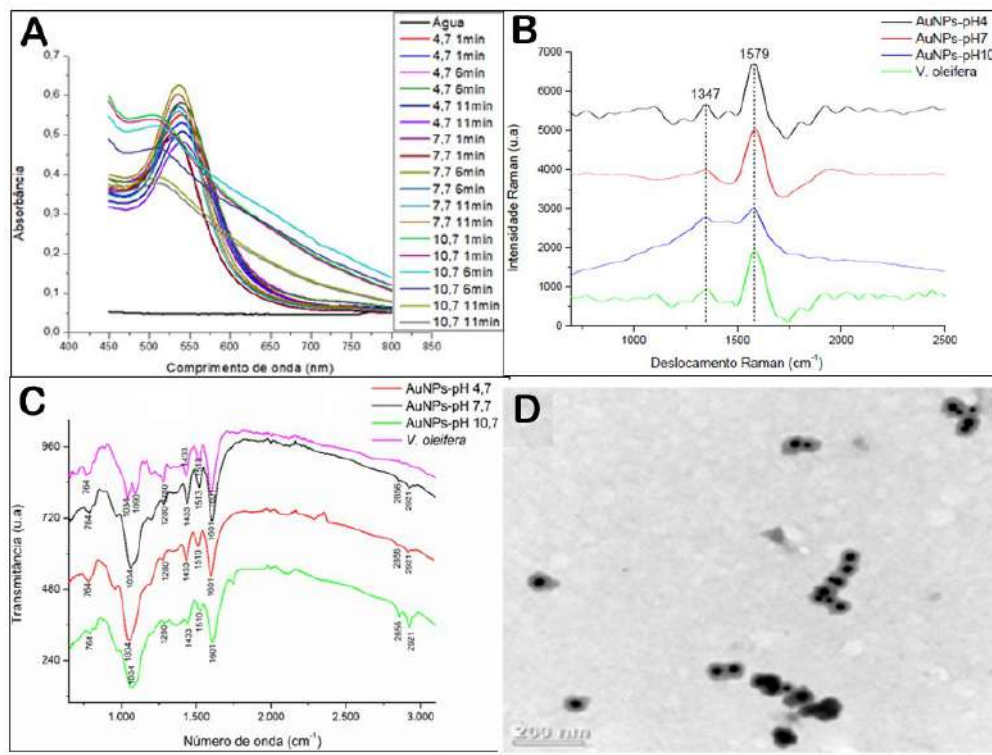
<sup>1</sup>. Laboratório de Ultraescultura Celular Carlos Alberto R (LUCCAR), Departamento de Morfologia, Universidade Federal do Espírito Santo (UFES), Vitória-ES.

The objective of present work is analysis of gold nanoparticles reduced with *Virola oleifera* resin and their stability in different microbiological growth mediuns to applies in evaluation of antimicrobial activities. The presente nanomaterial is a sustentable material included in green synthesis nanomaterial, and has diferents physical features and them, results in efficient reactivity. The first stage of present work was sinthesys in diferent conditions (pH and Temperature) to view the best nanoparticles sinthesys. It has been analyzed to Ultraviolet-visible spectroscopy (UV-Vis). The second stage, the nanoparticles synthesized has been performed with transmission electron microscopy analyzes (TEM), Raman and infra-red (IR). After UV-Vis analyses, the best synthesis are selected to ressuspended tests in microbiological growth mediuns: Mueller Hinton broth (MH) and Mueller Hinton cation ajusted broth (MH+) to analyses their stability. The tests has done in diferentes conditions of gyration and time. The solutions has been analyzed to UV-Vis, too. In experiments of synthesis, the best nanoparticles were synthesized on pH 7,7 and 6 (six) minutes because it has the most concentration and the same size and dispersal between their. The results are represented on Picture 1. The nanoparticles hadn't modify their results of absorbance (Abs. e  $\lambda$  máx.), size and dispersal (full width at half maximum - FWHM) when are ressuspended in diferent microbiological growth médiuns. The Picture 2 shows the organization of results. In conclusion with the founded results, gold nanoparticles reduced with *Virola oleifera* resin has great stability in microbiological growth mediuns and can be applied in evaluation of antimicrobial activities.

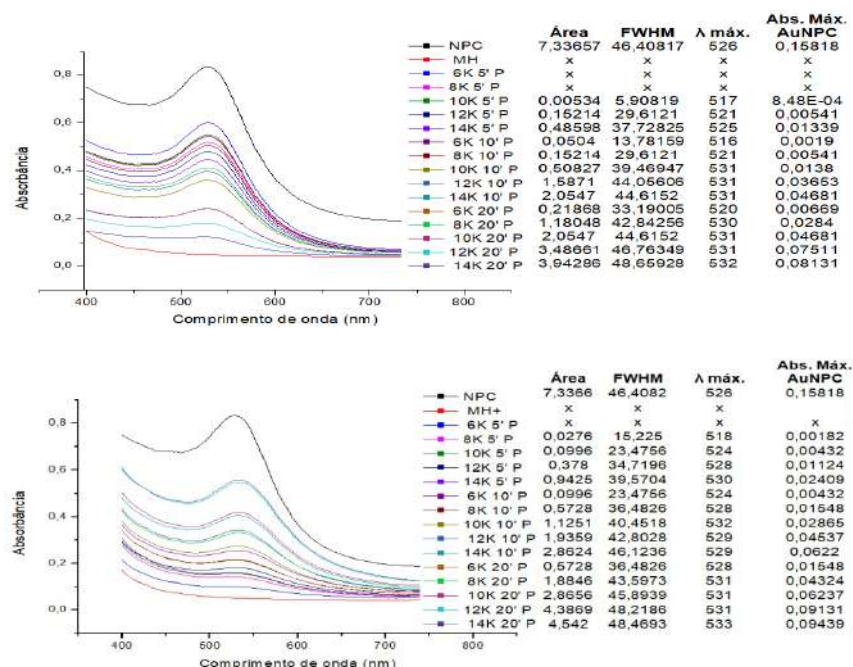
### REFERÊNCIAS

- [1] L. A. A. Contreras. Proposição de uma rota de síntese verde de nanopartículas de ouro reduzidas com resina de *virola oleifera* através do planejamento fatorial , 2017.
- [2] C. Kindel. Atividade antimicrobiana e antibiofilme da epigalocatequina galato em *Staphylococcus aureus*. Vitória, 2018.





Picture 1: results of synthesis of gold nanoparticle reduced with *Virola oleifera* resin from UV=Vis (A) and das caracterizações indifferents pHs from Raman (B), Infra-red (C) and MET (D). Fonte: author and Contreras (2017).



Picture 2: results os (ressuspensões) from UV-Vis in Mueller Hinton broth (MH) (up) and Mueller Hinton cation ajusted broth (MH+) (down) in differents conditions gyration/time with numbers. Fonte: author.

## **Synthesis, characterization and stability analysis of reduced gold nanoparticles with epigallocatechin 3-gallate in microbiological growth medium mueller hinton and cation adjusted**

Sady Roberto Rodriguez Avila<sup>1</sup>, Gisele Pereira Diniz Schuenck<sup>1</sup> Marco Cesar Cunegundes Guimarães<sup>1\*</sup>

<sup>1</sup>. Department of Morphology, Health Sciences Center, Federal University of Espírito Santo (UFES) Vitoria, Brazil

The objective of this work is to analyze the physicochemical properties of nanoparticles (NPs) synthesized with epigallocatechin 3-gallate (EGCG) and their behavior in a culture medium to test their antibacterial activity. EGCG is a phytochemical of green tea with the ability to reduce and stabilize metal matrices, when coupled to the surface also offers certain biological properties in conjunction with reduced gold. The project begins with the screening and optimization of the variables that influence the synthesis, in this case the most significant in the process were concentration of the extract and pH, determining values of 0.17 mg / ml and 7.2 corresponding for each one; in this way stable nanoparticles can be obtained over time, without aggregation and with a considerable concentration; to evaluate this the NPs were analyzed by UV-Vis spectrophotometry. The characterization analyzed the size and shape by transmission electron microscopy (MET) obtaining discoid (mostly non-spherical) NPs with low aggregation and with a uniform size of 14.54 nm. Surface analysis involved infrared spectroscopy (FT-IR) and Raman spectroscopy, the results showed the presence of the chemical groups of EGCG and the complexes that form with the metallic gold suggesting that the catechin effectively adhered to the gold surface, Figure 1 show the main results of synthesis and characterization. The resuspension test was performed with Mueller Hinton and Mueller Hinton Cation Adjusted broth (MH +) and the readings were realized on the UV / Vis spectrophotometer. Comparing with a control and using parameters related to the concentration (maximum Absorbance) and dispersion (FWHM and  $\lambda_{max}$ ) of these NPs, the results showed that the best behavior in the medium mueller hinton was found when NPs were rotated at 14,000 rpm for 20 minutes and in mueller hinton cation adjusted was 12,000 rpm for 20 minutes, in both conditions, the plasmon band remains intact and well defined similar to control, indicating good stability and higher concentration of NPs in this culture medium (Figure 2) this indicates that NPs are related to such culture media, this mean that they manage to keep certain properties out of their original solvent (water). Therefore, an optimal route for the synthesis of reduced gold nanoparticles with EGCG can be reported, demonstrating a good degree of stability in a bacterial culture medium, therefore the biological and structural properties together with this favorable behavior make them ideal for testing antimicrobial with several references. and clinical strains.

### REFERENCES

- [1] Gisele. P. D. S. Síntese e caracterização físico-química de nanopartículas de ouro usando epigallocatequina-3-galato (EGCG), 2018.
- [2] Carina. K. Atividade antimicrobiana e antibiofilme da epigallocatequina galato em *Staphylococcus aureus*. Vitória, 2018.

ACKNOWLEDGEMENT: to God, to my Dad, my family, friends, partner, teacher Marco, Honduras and LUCCAR.

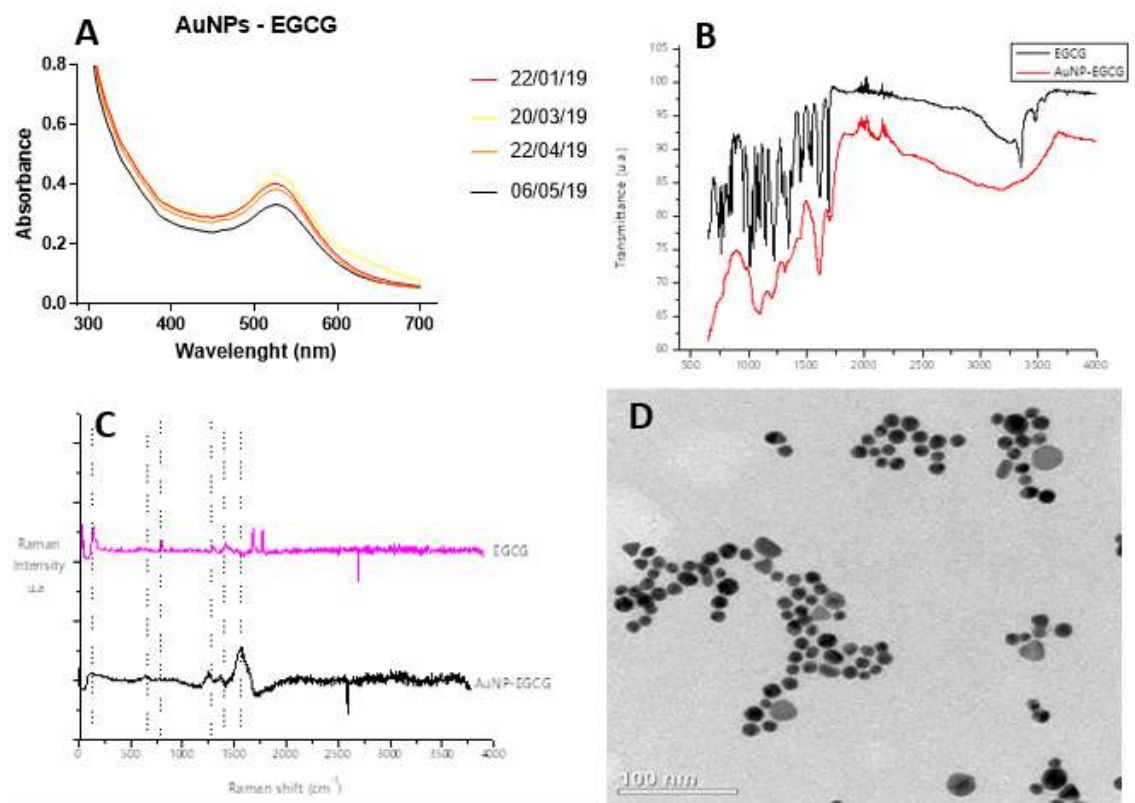


Figure 1: (A) Synthesis' Graph of NPs with readings made on different dates, showing their stability (B) Infrared Spectrum (IF-TR) of EGCG and EGCG Reduced NPs (C) Raman Spectrum of EGCG and EGCG Reduced NPs (D) MET image. Source: author and Gisele (2018).

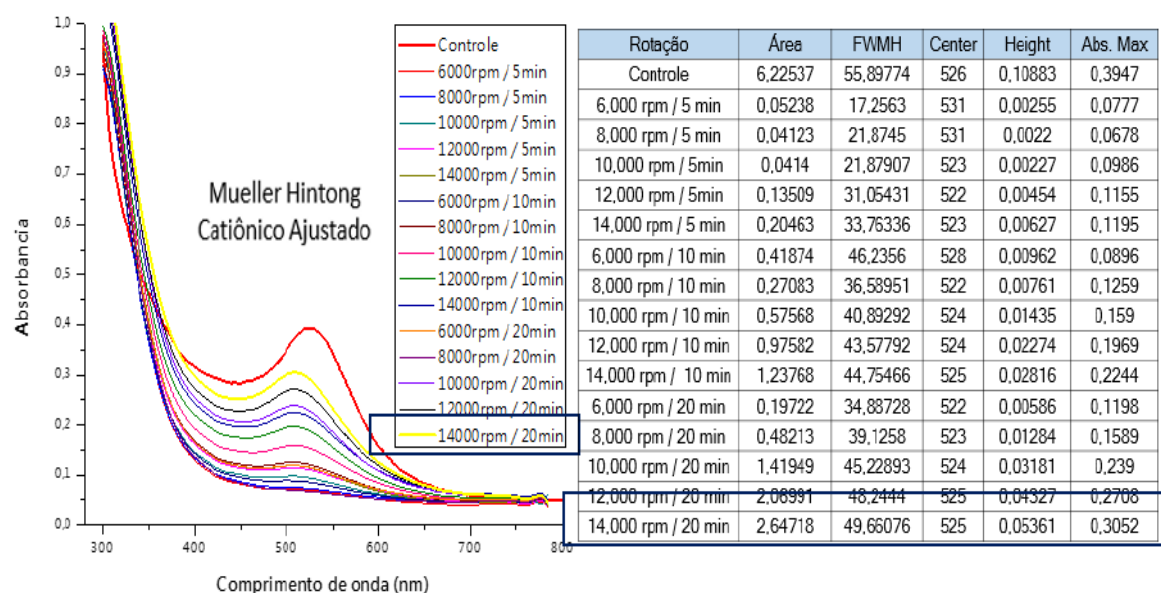


Figure 2: Results of the UV-VIS scan readings of the resuspensions in the Mueller Hinton cation medium adjusted at different rotation / time conditions along with the comparative analytical data table. This will be the culture medium to perform the antimicrobial tests. Source: author.

## Hybrid hydrogels of self-assembled fluorenylmethoxycarbonyl diphenylalanine as biomaterial matrix

Sandra Valeria Vassiliades<sup>1</sup>, Karina A. B. Arguello<sup>1</sup>, Andréa M. Aguilar<sup>2</sup>, Iseli L. Nantes-Cardoso<sup>1</sup>, Francesca Giuntini<sup>3</sup>, Wendel A. Alves<sup>1\*</sup>

[\\*wendel.alves@ufabc.edu.br](mailto:wendel.alves@ufabc.edu.br)

- <sup>1</sup>. Centro de Ciências Naturais e Humanas, Universidade Federal do ABC, Santo André, SP, Brazil;  
<sup>2</sup>. Departamento de Química, Instituto de Ciências Ambientais, Químicas e Farmacêuticas, Universidade Federal de São Paulo, Diadema, SP, Brazil;  
<sup>3</sup>. School of Pharmacy and Biomolecular Sciences, Liverpool John Moores University, Liverpool, United Kingdom.

Hydrogels formed by the self-assembly of low molecular weight gelators (LMWGs) attracted considerable interest because of their potential for application as biomaterials for biosensing, tissue engineering, regenerative medicine, and drug delivery [1]. The *N*- $\alpha$ -protected dipeptide fluorenylmethoxycarbonyl-diphenylalanine (FmocFF – **1**, Figure 1) is a compound part of a family of small peptide hydrogels that form supramolecular assemblies with tunable mechanical and electrochemical properties [2]. As the  $\pi$ -stack type interactions of the rings present in the Fmoc protective group aid in the formation and stabilization of the hydrogel, we propose in this work the preparation of *N*- $\alpha$ -protected diphenylalanine with porphyrin rings (Fig. 1), with different substituents in the meso position, and investigate the morphological and optical properties of the hydrogels formed by the mixture of Fmoc-FF and porphyrin-FF, and their applicability as the new biomaterial for cell growth. Porphyrin compounds **2-4** were prepared according to standard synthetic procedures (Fig. 2) [3]. The hydrogels were made with a mixture of organic solvent and water in a ratio of 0.5:9.5 (DMSO:H<sub>2</sub>O), respectively. Five hydrogel concentrations were prepared with the porphyrin-FF varying in 0.5, 5, 10, 20, and 30%. The prepared samples were characterized by absorption and fluorescence spectroscopy (Fig. 3a-c), and it is possible to observe that the optical properties of the porphyrins are not affected by their dispersion in the matrix. The increase in porphyrin concentration leads to a decrease in fluorescence to compound **2** and **3**, while compound **4** has an increase in intensity indicated that aggregation of **4** is less dependent of the concentration. Scanning electron microscopy analysis shows that the Fmoc-FF hydrogel is composed of long wires with no apparent branching (Fig. 3a-b). The samples containing porphyrins (Fig. 3c-f) show small branching along the fiber, at all concentrations observed, these branches did not see the formation of crosslinking, thus it is possible to expect that the hydrogels formed with porphyrin-FF have lower mechanical resistance. At the present moment, the compounds of interest **2-4** were prepared in overall yields of 6%, 5% and 3.5% for **2**, **3** and **4**, respectively, and the dispersion did not suppress the optical properties of the porphyrin-FF within the hydrogel matrix. It is possible to observe from the SEM analysis that hydrophilic samples containing porphyrin-FF have no significant difference between them, but different from the Fmoc-FF hydrogel.

- [1] D. M. Ryan and B. L. Nilsson, *Polym. Chem.* **2012**, 3, 18.  
 [2] D. J. Adams, *Macromol. Biosci.* **2011**, 11, 160.  
 [3] J. S. Lindsey, *et al.*, *J. Org. Chem.*, **1987**, 52, 827–836; K. E. Borbas, *et al.*, *Bioconjug. Chem.*, **2006**, 3, 638–653; R. Moumne, *et al.*, *J. Org. Chem.*, **2006**, 8, 3332–3334.

Acknowledgments: **FAPESP, CAPES, CNPq, LNLS, LNNano, and INCTBio.**



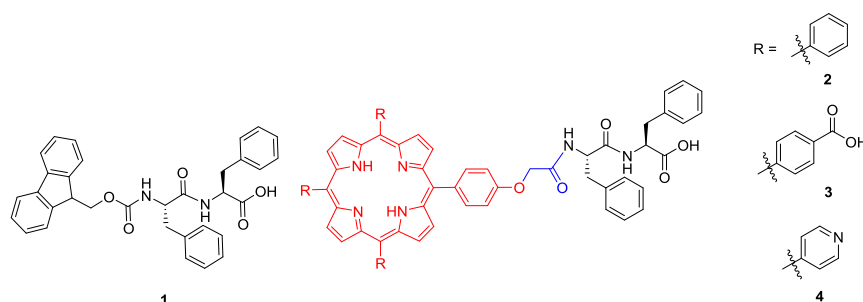


**Figure 1:** Structure of Fmoc-FF (**1**) and porphyrin-FF (**2-4**)

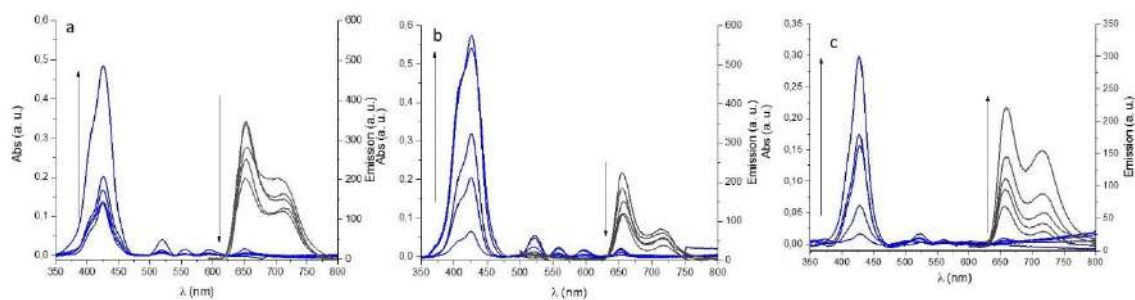


**Figure 2:** Absorption and fluorescence, quartz cuvette 1 mm: panel a) compound **2** (fluorescence 419 nm); panel b) compound **3** (fluorescence 422 nm); panel c) compound **4** (fluorescence 420 nm), in water at room temperature.

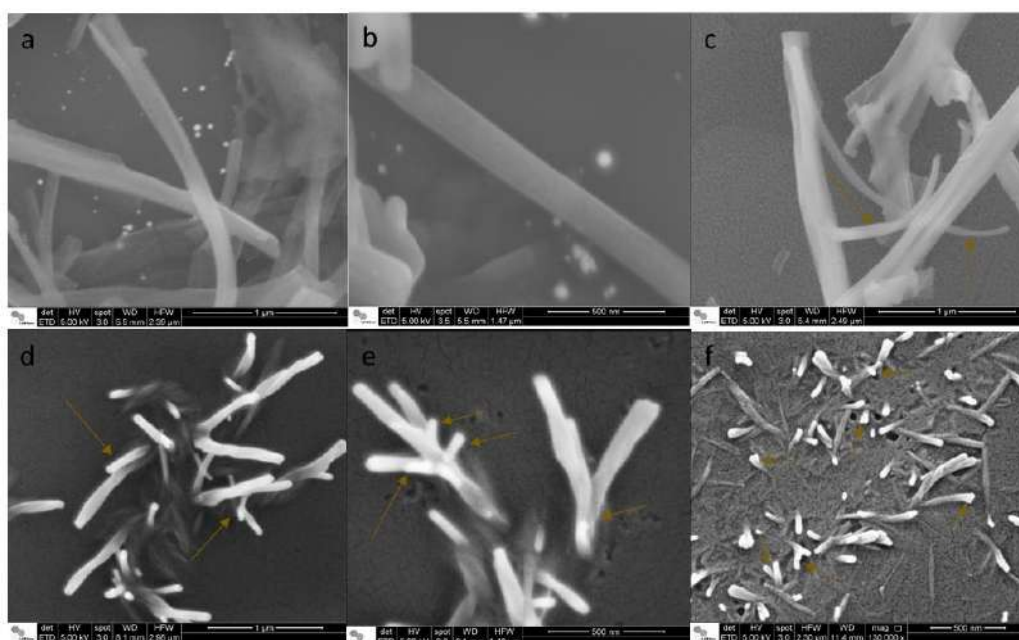


**Figure 3:** SEM images from hydrogels at 10% of porphyrin-FF: panel a and b) Fmoc-FF; panel c) compound **2**; panel d and e) compound **3**; panel f) compound **4**.

## Analysis of Precipitates of a *Maraging* 350 Steel Undergoing Thermomechanical Treatments

Simone Izabel Vieira de Santana <sup>1\*</sup>, Luiz Paulo Brandao <sup>1</sup>

<sup>1</sup>. Section of Materials Engineering, Military Engineering Institute - IME, Rio de Janeiro, RJ, Brazil.

In this work, precipitates formed in a *maraging* steel 350, subjected to thermomechanical treatments, were identified and analyzed by dark field images, which is an essential condition for the identification of the precipitates. *Maraging* steels have high alloy content, high fracture toughness and ultra-high mechanical strength. In these materials, the mechanical properties are derived from a very low carbon martensitic microstructure with body centered cubic crystalline structure (BCC) associated with precipitates of intermetallic compounds formed in the heat treatment of aging [1]. The near absence of carbon, together with other alloying elements, promotes special characteristics to the *maraging* steels. The high nickel content allows the formation of martensite by solubilization heat treatment followed by cooling to room temperature. After such processes, the material can then undergo considerable increase in mechanical strength through aging treatment, without significant distortions or dimensional changes. The primary objective of the treatment is to generate a uniform distribution of intermetallic precipitates in the martensitic matrix, providing high mechanical strength and fracture toughness [2]. The stable precipitates are formed by  $\text{Ni}_3(\text{Ti}, \text{Mo})$  and  $\text{Fe}_2\text{Mo}$ , being formed by nucleation and growth processes. For the development of this work, samples of the *maraging* steel 350 were deformed by cold rolling with a 60% reduction and afterwards subjected to the aging treatment at the temperature of 510 °C for 8 h which produced distribution of the aforementioned precipitates. The material used was provided by Villares Metals SA, with the chemical composition in percentage by weight: Ni (18,15), Co (11,98), Mo (5,02), Ti (1,297), C (0,003) and Fe (balance). Transmission electron microscopy (TEM) analyzes were performed on the sample, which had its

---

\* [simoneizabel@ime.eb.br](mailto:simoneizabel@ime.eb.br)

### References

- [1] K. Rohrbach, M. Schimidt. *Maraging* steels. In: ASM Handbook, v. 1, Properties and selection: irons, steels, and high-performance alloys. Materials Park, Russell Township: ASM International Handbook Committee; 1993. p. 1869-1887.
- [2] L.G. Carvalho et al. A dilatometric study of the phase transformations in 300 and 350 *maraging* steels during continuous heating rates. Materials Research-Ibero-American Journal of Materials. 2013; 16: 740-744.
- [3] D.B. Williams, C.B. Carter. Transmission Electron Microscopy, New York: Ed. Plenum, 1996.
- [4] U.K. Viswanathan et al. Precipitation hardening in 350-grade *maraging*-steel, Metallurgical Transactions A24(1993), pp.2429-2442.

### Acknowledgment

The authors thank the company Villares Metals S.A. for supplying the material evaluated in this work.

mechanically reduced thickness followed by electrolytic polishing in a solution containing 60% methanol, 34% n-butanol and 6% perchloric acid at a temperature of - 30 °C. TEM analyzes were performed using a JEOL JEM-2010 HRTEM equipment with an acceleration voltage of 200 kV. The 60% laminated sample, subjected to a time of 8 h at aging and at 510 °C showed the images of figure 1. The phase present in the observed area is martensitic  $[001]_M$ , which is obtained from the analysis of the angles measured between the planes  $(1\bar{1}0)_M$  and  $(\bar{2}00)_M$  seen in figure 1 (d) [3]. The spot 2 of figure 1(d) is related to the diffraction lattice of the  $Ni_3(Ti, Mo)$  precipitates, which can be seen by dark field in figure 1(b) as fine needle (like traces of the white circle). Transmission microscopy analyzes (diffraction patterns and dark field images) of cold and aged cold rolled *maraging* steel 350 showed the coexistence of the martensitic crystalline structure of the studied material with the crystalline structure of precipitates, which can be identified by the diffraction patterns and which function as hardeners of the martensitic matrix.

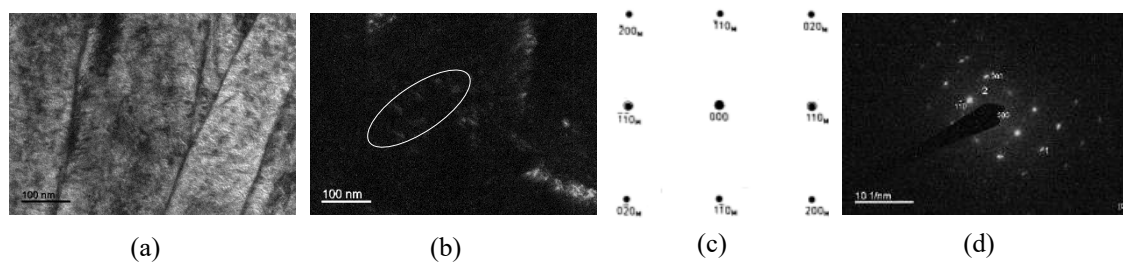


**Figure 1.** *Maraging* steel 350 60% laminate and aged for 8 h at 510 °C. (a) MET image, (b) dark field image of spot 2 of (d), (c) diffraction pattern model (adapted from VISWANATHAN [4]) and (d) diffraction pattern showing spots of matrix and two precipitates.



## **Formation of Nanocrystalline Borides in Superduplex Steels with Boron Additions Processed by Rapid Solidification**

José Eduardo Berger<sup>1</sup>, Vitor Anibal do Sacramento Mendes<sup>1</sup>, Claudio Shyinti Kiminami<sup>1</sup>, Claudemiro Bolfarini<sup>1</sup>, Alberto Moreira Jorge Junior<sup>1</sup>, Walter Jose Botta<sup>1,\*</sup>

<sup>1</sup>Department of Materials Engineering, Federal University of São Carlos, 13565-905, Brazil

\*corresponding author: wjbotta@ufscar.br

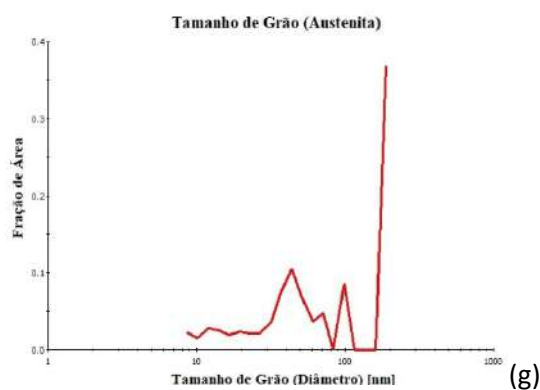
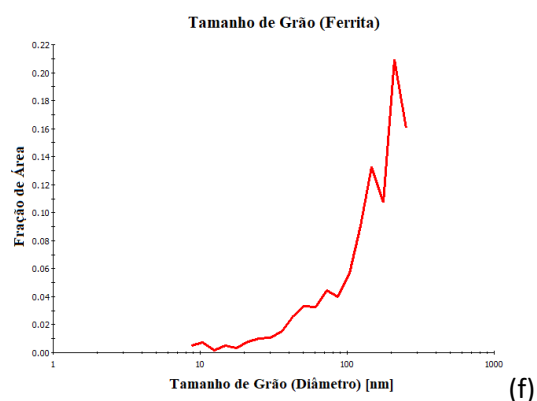
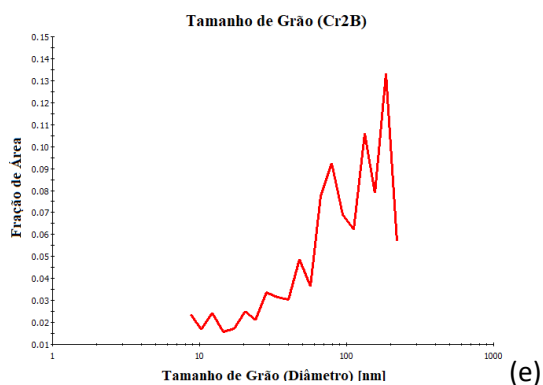
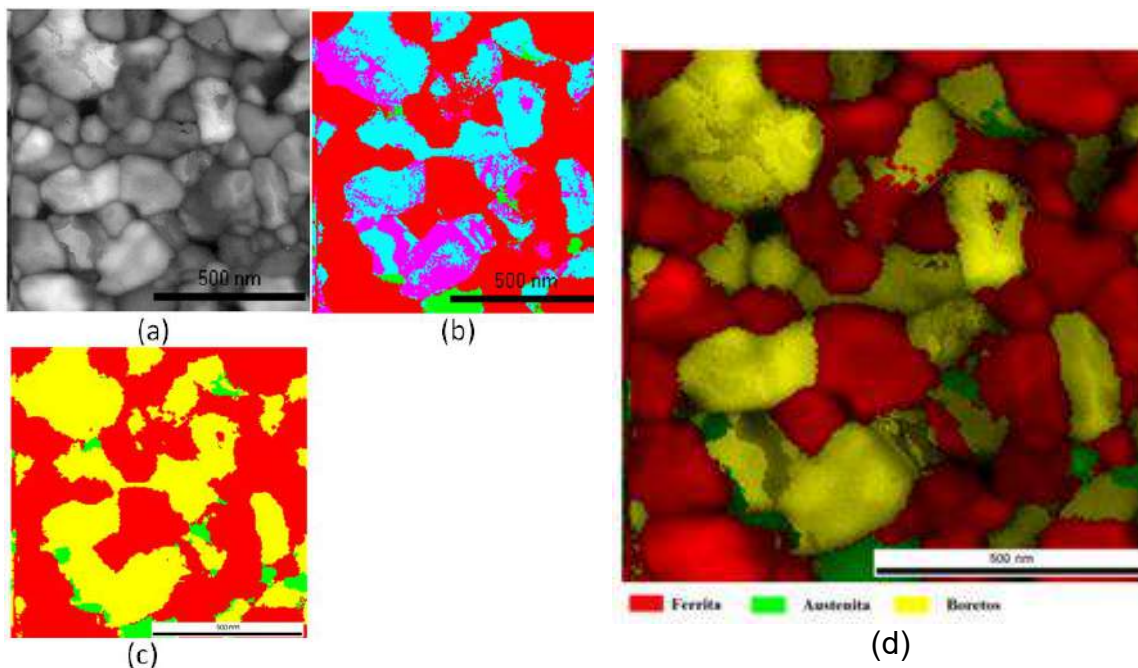
Protective coatings of pipelines used in the oil industry are expected to present an ideal combination of high corrosion and wear resistance. Such properties linked to low cost, and general good mechanical properties, far superior to conventional materials, make the Fe-Cr-Ni-B system alloys with partially amorphous structures a very attractive material for such an application. Successful elaboration and design of an alloy providing specific characteristics and properties depend on an in-depth knowledge of each system alloy composition, including the formation of possible phases and structures, consequences and limitations of the microstructure in its specific use. The present work aims to present part of an extensive study of a mapping of characteristics, trends, and behavior of the Fe-Cr-Ni-B system alloys. Such study involved thermodynamic simulations, a series of alloys elaboration that could incorporate a broad range of compositions of possible interest, in such a way to record patterns and tendencies of crystals and structures' formation, correlating them with the final properties of the alloy. The alloys were produced in the form of ribbons in melt-spinning equipment. Vacuum heat treatments were used for partial and total crystallization of amorphous alloys, allowing evaluating structural changes of crystalline phases. This work will then present a partial result of the Fe-26Cr-2.5Ni-4.5B alloy heat treated at 600 °C, which was studied by transmission electron microscopy and Automated Crystal Orientation Mapping (ACOM) in nanoprobe mode enabling orientation/phase maps with a spatial resolution of about 1 nm. Such results reveal that partially amorphous alloys contain both the superduplex stainless structure and boride particles.

### **Acknowledgments**

The authors are grateful to FAPESP under the grant number FAPESP Thematic # 2013/05987-8. The authors thank the Laboratory of Structural Characterization (LCE/DEMa/UFSCar) for using their facilities.



## Results:



Ferrite: 58% - 32,6 nm  
Austenite: 4,2% - 18,7 nm  
 $(\text{Cr,Fe})_2\text{B}$ : 38% - 18,7 nm

Results obtained by MET ASTAR from the Fe-26Cr-2.5Ni-4.5B tape sample, treated at 600°C. (a) IQ, (b) phases considering the borides  $\text{Fe}_2\text{B}$  and  $\text{Cr}_2\text{B}$ , (c) considering only the  $\text{Cr}_2\text{B}$  boride, (d) complete phase mapping. Grains size distribution of (e) boride, (f) ferrite, (g) austenite.

## Study Osseointegration at Coating SiC With and Without TiO<sub>2</sub> in Substrat SS316L.

Angela A. Vieira<sup>1</sup>, Bruno H. Godoi<sup>1</sup>, Carlos D.G.O. Moraes<sup>1</sup>, Amanda L.G. Albuquerque<sup>1</sup>, Silvelene A. Silva<sup>2</sup>, Getúlio de Vasconcelos<sup>2</sup>, Lucia Vieira<sup>1</sup>, Cristina Pacheco-Soares<sup>1</sup>, Newton S. Silva<sup>1\*</sup>

<sup>1</sup>Universidade do Vale do Paraíba - UNIVAP, São José dos Campos - SP, Brazil

<sup>2</sup>Instituto de Estudos Avançados, São José dos Campos - SP, Brazil  
nsoares@univap.br

Stainless Steel 316L (SS316L) is the most accessible raw material used for prosthesis due to its low cost, manufacturability, and reasonable corrosion resistance [1,2]. However, this material contains cobalt, chromium, and nickel, these elements, when applied over a long time as implantable material, are aggressive for the biological environment, under almost of concentration they are carcinogenic and can inhibit the repair of damaged DNA [3]. In order to improve the lifetime of the metallic prosthesis, coatings with good tribocorrosion performance [4], a high level of adherence [5] and biocompatibility [6], has been extensively studied. Some SiC coatings have been studied for biomedical applications because of their mechanical and physicochemical properties, such as high hardness, biocompatibility, resistance to corrosion and wear [7,8]. One of the techniques used to produce coating is laser cladding. This technique is based on the dispersion of the precursor powder of the coating on the substrate followed by its irradiation with the CO<sub>2</sub> laser, which creates a strong metallurgical bonding between the coating and the substrate [9]. In this work, The SiC-TiO<sub>2</sub> coating was produced and characterised for the first time. SiC and SiC-TiO<sub>2</sub> powders were used to produce a melting by laser cladding over Stainless Steel 316L (SS316L). TiO<sub>2</sub> nanoparticles in the anatase phase were used, in order to improve surface coating properties like osseointegration for a dental implant, hardness and resistance to the corrosion. In order to analyze the adhesion morphology of the cells on SiC and SiC-TiO<sub>2</sub> films, the MG63 osteoblastic cells were seeded on the samples during 24 h. After this, the cell spreading on the samples were examined by Scanning Electron Microscopy (SEM - ZEISS EVO MA10). Cell morphology is shown in Fig. 1. We observed the MG63 osteoblastic cells elongated, flattened with microvilli and/or cell prolongations on their surface. The presence of elongated and adherent cells demonstrated very good adhesion and good spreading of the osteoblastic cells on the SiC (1A) and SiC-TiO<sub>2</sub> (1B) coatings.

- [1] A.-S. Loir et al. *Appl. Surf. Sci.* 247 (2005), 225–231.
- [2] S. A. Naghibi et al. *Mater. Chem. Phys.* 148 (2014), 614–623.
- [3] A. Sargeant and T. Goswami *Mater. Des.* 28 (2007), 155–171.
- [4] R. J. K. Wood *J. Phys. D. Appl. Phys.* 40 (2007), 5502–5521.
- [5] L. Vieira et al. *Surface Coatings Technology* 260 (2014), 205–213.
- [6] F.Z. Cui et al. *Surface Coatings Technology* 131 (2000), 481–487.
- [7] W. Daves et al. *Thin Solid Films* 519 (2011), 5892–5898.
- [8] R. Pessoa et al. *Mater. Sci. Semicond. Process.* 29 (2015), 56–68.
- [9] A. Contin et al. *Diam. Relat. Mater.* 65 (2016), 105–114.

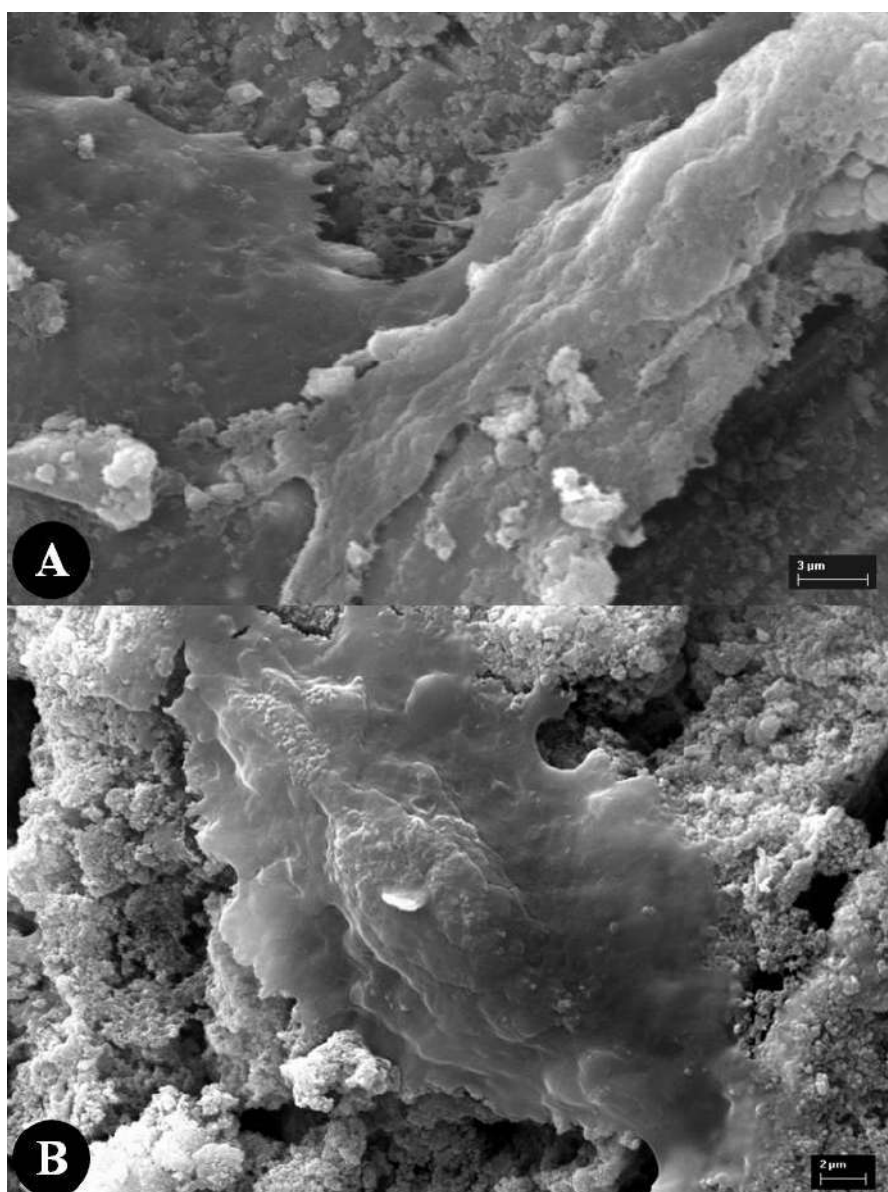


Figure 01 – SEM images of MG63 osteoblastic cells spreading on a SiC (1A) and SiC-TiO<sub>2</sub> (1B) films. 3000X

## **Mechanically Induced Phase Transformation in the biocompatible Ti-13Nb-13Zr Alloy Processed By High-Pressure Torsion**

Diego Alfonso Godoy Pérez<sup>1,2</sup>, Vitor Anibal do Sacramento Mendes<sup>1</sup>, Jean-Claude Lepretre<sup>2</sup>, Virginie Roche<sup>2</sup>, Claudemiro Bolfarini<sup>1</sup>, Walter Jose Botta<sup>1,2</sup>, Alberto Moreira Jorge Junior<sup>1,2\*</sup>

<sup>1</sup>Department of Materials Engineering, Federal University of São Carlos, 13565-905, Brazil

<sup>2</sup>Grenoble Alpes University, CNRS, LEPMI, F-38000 Grenoble, France

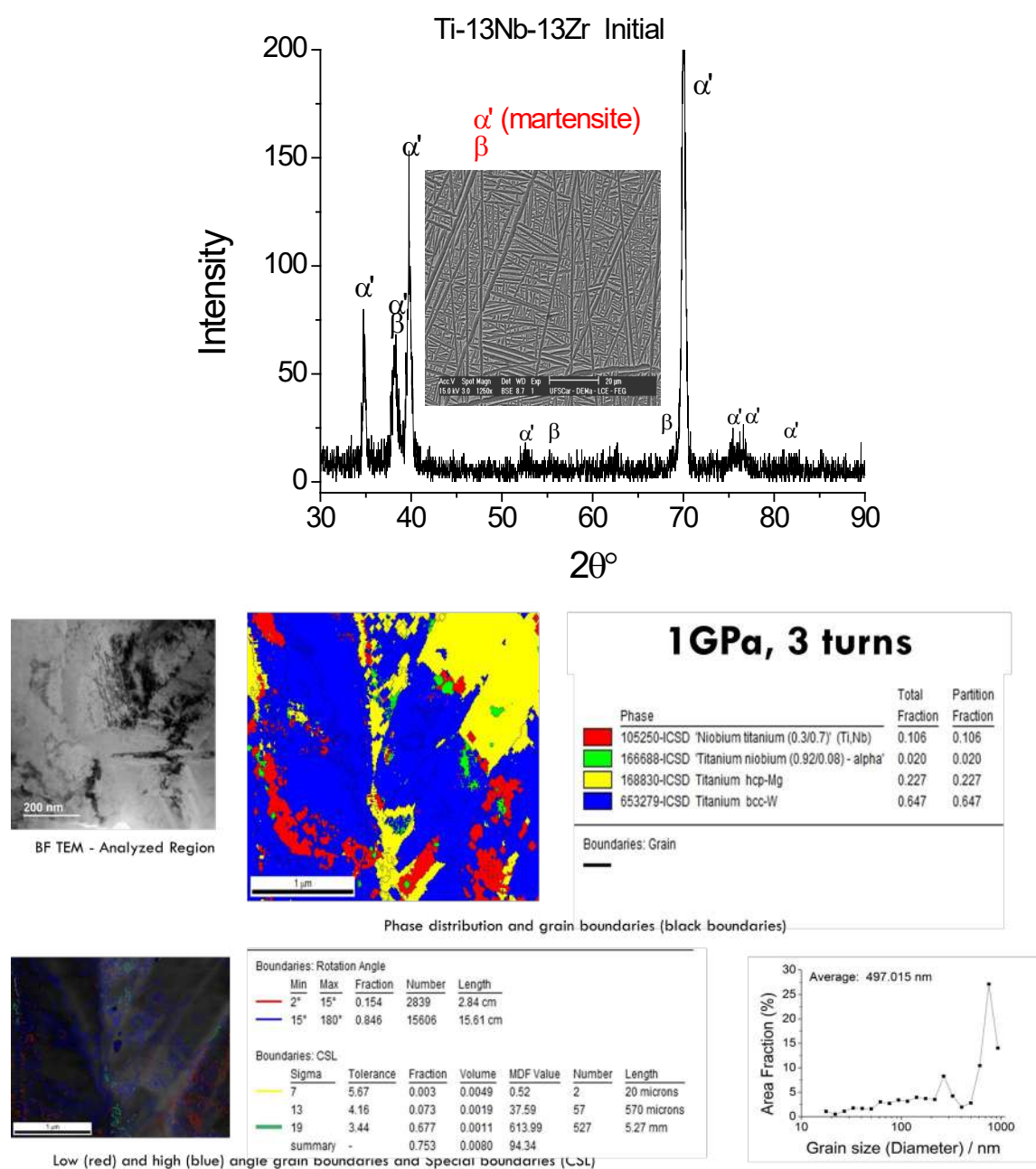
\*corresponding author: [jorge.moreira@dema.ufscar.br](mailto:jorge.moreira@dema.ufscar.br)

The passive biomedical devices currently in use (prostheses, implants) have satisfactory performance in many cases, but they are, with few exceptions, at best, inert about the body. However, in many cases, the body reacts to the device insertion, by developing inflammation, allergic responses, and necrosis, which may lead to rejection, imposing their replacement. This may occur at relatively short time (e.g., inflammatory processes) or long term (e.g., stress shielding effect, which leads to bone resorption, and loss of implant fixation). To minimize stress-shielding effects and allow bone rebuilding, a low stiffness (as close as possible to that of natural bone) provides good load transfer to the bone, which stimulates new bone formation. Some of these drawbacks can be solved with the use of Ti and Ti alloys, which present excellent corrosion resistance and remarkable specific strength, free- allergic problems and the maximum biocompatibility when compared with other competing biomaterials (for instance, stainless steel, Co-Cr alloys, ceramics, polymers, and composite materials). More recently, ultrafine-grained (UFG) Ti-materials have been developed by severe plastic deformation (SPD) processing. Such UFG materials have superior properties than their coarse-grained counterparts, and also, improvements in wear resistance and the combination of high strength and good ductility at room temperature have been observed in the SPD processed alloys. However, most commercially used Ti-based implant alloys exhibit considerably higher Young Moduli (E) compared to human bones and the resulting stress shielding effect results in bone resorption. The  $\beta$ -Ti phase, whose E is well below that of the equilibrium  $\alpha$ - and  $\omega$ -phases and closer to the human bone, can be retained with increasing content of  $\beta$  stabilizing elements such as Mo, Ta, and Nb. Nevertheless, to obtain such a phase is not a simple task, involving extensive thermomechanical processing followed by heat treatment, which, in fact, will lead to further grain growth. This work presents the possibility of obtaining near beta titanium alloy induced by deformation with ultrafine grains produced by severe plastic deformation using High-Pressure Torsion.

### **Acknowledgments**

The authors are grateful to the French Committee for the Evaluation of Academic and Scientific Cooperation with Brazil (COFECUB) and the Brazilian CAPES (Process number #88887.137755/2017-00) for funding the bilateral cooperation, and also FAPESP under the grant number for the partial funding. FAPESP Thematic # 2013/05987-8. The authors thank the Laboratory of Structural Characterization (LCE/DEMa/UFSCar) for using their facilities. AMJJ would like to acknowledge the CNPq (Brazil) under grant #301429/2017-0.



**Results:****Summary**

This abstract presents results of the processing of the Ti-13Nb-13 Zr alloy by high-pressure torsion (HPT) using 1 GPa of pressure and applying 3 turns. However, in the complete work, the load was varied, keeping the number of turns constant. Samples were microstructurally characterized by X-ray diffraction (XRD), scanning electron microscopy (SEM) and transmission (TEM). The initial condition was a microstructure composed by the phases hcp  $\alpha'$  and small amounts of the bcc  $\beta$ , whose grain size was  $\sim 500 \mu\text{m}$ . HPT deformation of the Ti-13Nb-13Zr alloy resulted in considerable grain refinement. Grain sizes went down to less than  $1 \mu\text{m}$ , which includes the as-processed material within the category of ultrafine-grained materials. Phase transformation induced by deformation was observed, in some cases  $\alpha'$  to  $\beta$  and in other  $\alpha'$  to  $\omega$ , which is not linear with the increase of the load. However, undoubtedly, by increasing the load to 4.5 GPa and 6 GPa  $\alpha'$  to  $\omega$  is prone to occur.

## Factorial Planning Of Directed Biosynthesis Of Gold Nanoparticles Reduced And Stabilized With *Coffea Arabica*.

Wanderson Juvencio Keijok<sup>1, +</sup>, Rayssa Helena Arruda Pereira<sup>1, +</sup>, Adilson Ribeiro Prado<sup>2</sup>, André Romero da Silva<sup>3</sup>, Josimar Ribeiro<sup>4</sup>, Jairo Pinto de Oliveira<sup>1</sup>, and Marco Cesar Cunegundes Guimarães<sup>1, \*</sup>

<sup>1</sup>Federal University of Espírito Santo, Department of Morphological Sciences, Vitória, Brazil

<sup>2</sup>Federal Institute of Espírito Santo, Department of chemistry, Serra, Brazil

<sup>3</sup>Federal Institute of Espírito Santo, Department of chemistry, Aracruz, Brazil

<sup>4</sup>Federal University of Espírito Santo, Department of chemistry, Vitória, Brazil

<sup>+</sup>these authors contributed equally to this work

\*marco.guimaraes@ufes.br

The use of plant extracts for the reduction, stabilization and functionalization of metallic nanoparticles has been extensively explored, however the great majority of the works do not bring reproducible protocols of synthesis and the discussions about the main mechanisms that affect the control of the synthesis are in most exploited. The study was carried out with the objective of making the synthesis of gold nanoparticles a controlled and reproducible process. For that, several conditions to obtain the extract were performed as a function of the antioxidant activity. In addition, a fractional factorial design ( $2^{5-1}$ ) was performed to evaluate the variables that interfere in the yield of the synthesis of green gold nanoparticles using the *Coffea arabica* extract. The process was optimized through a complete factorial design ( $3^2$ ) with the probing of output variables, namely: full width at half maximum, Maximum Absorbance and maximum lambda size. The suitability of the model was duly verified and the predicted values were confirmed for synthesis yield after experimental analysis. We obtained stable nanoparticles (Zeta Potential, UV-vis and Dynamic Light Scattering), monodisperse and quasi-spherical (Transmission electron microscopy), which presented Fourier-transform infrared spectroscopy and Raman spectroscopy and defined the crystal structure diffraction), proving that the plant extract acted as a reducing, stabilizing and potentially functionalizing agent for the synthesized nanostructures. The images obtained by transmission electron microscopy also confirmed the presence of the vegetal extract on the metallic surface. The factorial planning employed is a potential source of information for a controlled and reproducible synthesis, allowing new possibilities of application in several fields.

**Keywords:** *Coffea arabica*, Nanoparticles, Synthesis, Factorial design and Antioxidant.

[1] M. A. BOLES et al, The surface science of nanocrystals. Nature Materials, v. 15, n. 2, p. 141–153, 2016.

[2] O. V. KHARISSOVA et al, The greener synthesis of nanoparticles. Trends in Biotechnology, v. 31, n. 4, p. 240–248, 2013.

This research was supported by CNPq (Brazil), Ministry of Science and Technology (MCTI/FINEP/CT-INFRA grant PROINFRA 01/2006) and Technology and Foundation Support Research and Innovation of Espírito Santo. This work used the equipment facilities at the Laboratory of Cellular Ultrastructure Carlos Alberto Redins and the Laboratory of Biomolecular Analysis (LABIOM) at Federal University of Espírito Santo.

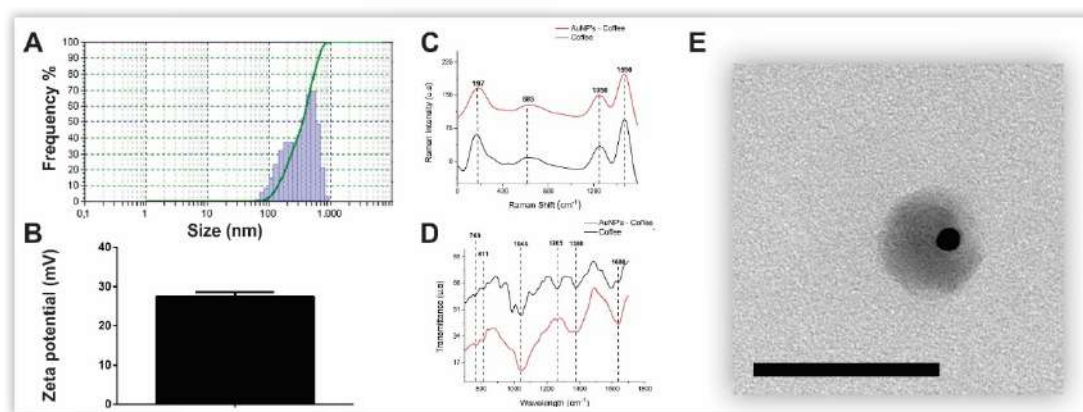


**Figure 1.** Nanoparticle DLS graph as a function of size frequency (A); Zeta potential of optimal conditions for synthesis dispersion (B); Comparison of the Raman spectra of the extract *Coffea arabica* and AuNPs (C); FTIR spectra of the extract *Coffea arabica* and AuNPs (D); Images obtained after the material was stained with uranyl acetate, it is possible to observe the presence of the extract around particles, confirming the DLS response; scale bar 100 nm (E).

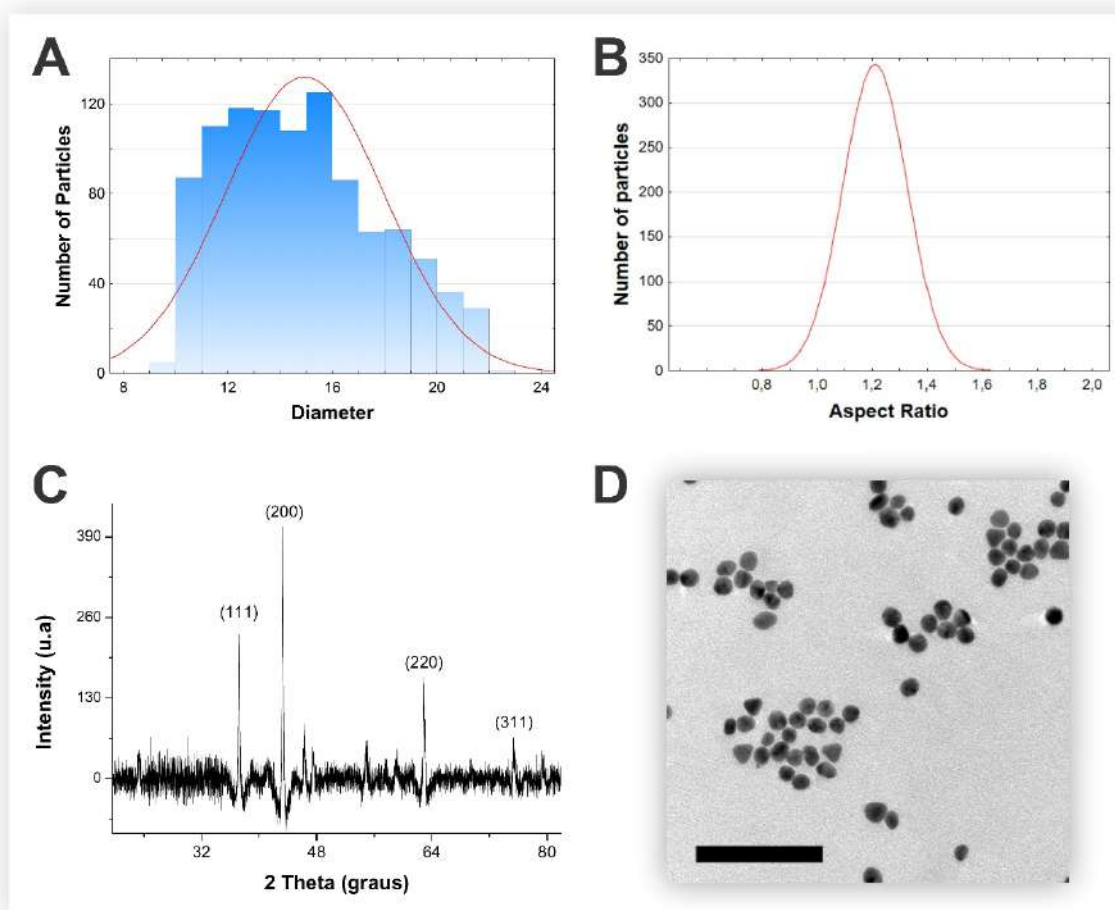


**Figure 2.** Histogram showing the Gaussian distribution of diameter (A) and aspect ratio of 1000 particles obtained from images made by transmission electron microscopy (B); X-ray diffractogram of AuNPs (C); Images obtained by transmission electron microscopy; scale bar 100 nm (D).

## The Relationship Between Perpendicular Magnetic Anisotropy (PMA) of (CoFe/Pt)<sub>5</sub> Multilayers and the Crystallinity of the Buffer Layer

Wesller G. Schmidt<sup>1</sup>, Luis E. Fernandez Outon<sup>2</sup>, Maximiliano Delany Martins<sup>3</sup>

1 Centro de Microscopia da UFMG, Belo Horizonte, Brasil, [wesller@ufmg.br](mailto:wesller@ufmg.br)

2 Departamento de Física da UFMG, Belo Horizonte, Brasil

3 Centro de Desenvolvimento da Tecnologia Nuclear (CDTN), Belo Horizonte, Brasil

Monocrystalline and isovolumetric ferromagnetic materials exhibit intrinsic "easy" and "hard" directions of magnetization, i.e. the energy required to magnetize them depends on the direction of the field applied relative to the crystalline axes. The easy axis being defined as the direction that requires the lowest energy to archive saturation magnetization, and the hard axis being the direction that requires the highest energy. Such anisotropy knowns as magnetocrystalline anisotropy, is of paramount technological importance, as as well as from fundamental point of view [1]. The mangetic anisotropy of non-isovolumetric magnetic materials is strongly influenced by influenced by shape anisotropy. When one of their dimensions is reduced towards 2D proportions, shape anisotropy dominates over magnetocrystalline anisotropy, and the easy axis of magnetization lies in plane. However, as the thickness approaches a few atomic layers (hyperfine films) [2-4], the easy axis of magnetization changes from in-plane to a perpendicular to the plane direction [1,5], achieving perpendicular magnetic anisotropy (PMA). Although the relation of PMA with interfaces and surfaces was already studied by Néel in 1954, the physical origin of this effect is still controversial, being related to several factors [7]. In this work the perpendicular magnetic anisotropy (PMA) of Pt/[Co<sub>60</sub>Fe<sub>40</sub>/Pt]<sub>5</sub> multilayered systems was investigated as a function of the growth rate of the Pt buffer layer, and the effect of this parameter on the anisotropy energy constant ( $K_u$ ), the crystallinity and texture of CoFe/Pt multilayer (figure 1). TEM experimental analyses allowed establishing a relation between the value of  $K_u$  and the crystallinity of the deposited materials. These results contribute to improving the scientific understanding of the processes that involve the appearance of perpendicular magnetic anisotropy in hyperfine films.

1. R. Sbiaa et al. **Journal of Applied Physics**, n. 107, 2010.
2. Tae Young Lee, Y. C. W. D. S. S. H. L. **Journal of Applied Physics** , n. 114, p. 173909-1 173909-6, 2013.
3. G. Winkler, A. K. A. C. D. L. A. S. H. P. O. **Journal of Applied Physics** , v. 117, 2015.
4. A Zarefy, L. L. R. L. H. C. J.-M. L. B. **Journal of Physics D: Applied Physics**, Maio 2013.
5. Dieny, B.; Chshiev, M. **Reviews of Modern Physics**, Volume 89, April–June 2017, junho 2017.
7. A. V. Davydenko. **Physical Review B**, v. 95, p. 064430 , Fevereiro 2017.



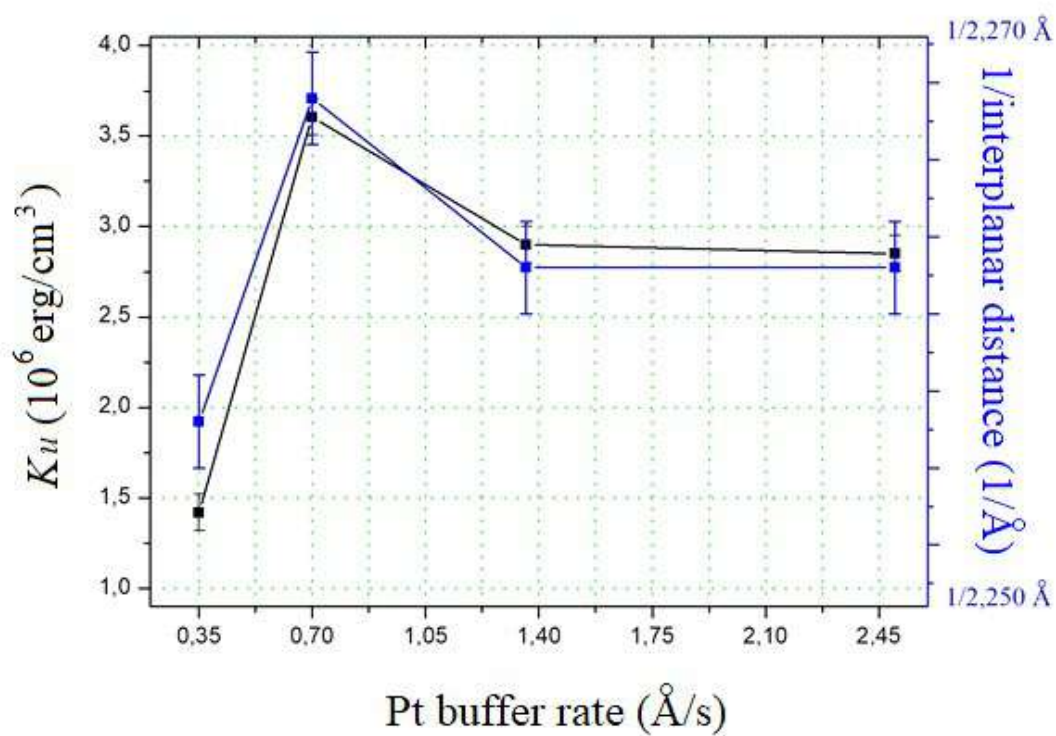
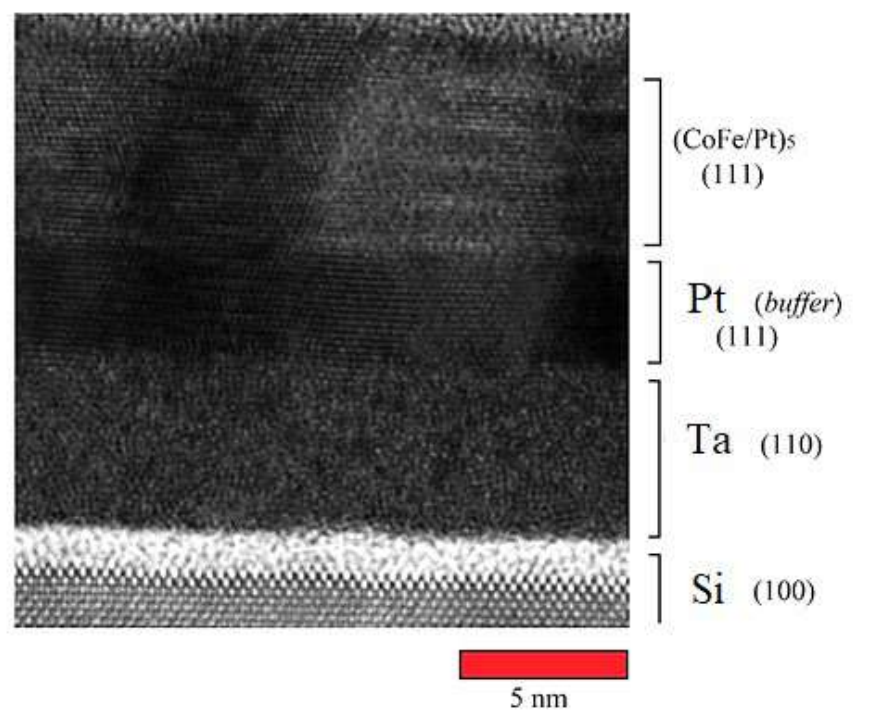


Figure 1: Relationship between Pt buffer interplanar distance and anisotropy constant ( $K_u$ )

## **A Microstructural Study on Different Phases in a Heat Treated AISI-SAE 430 Ferritic Stainless Steel by SEM/EDS/EBSD**

Cássio Barboa<sup>1\*</sup>, Rachel Pereira Carneiro da Cunha<sup>2</sup> and Arthur Costa Gonzaga<sup>3</sup>

<sup>1</sup>. Instituto Nacional de Tecnologia (INT), DIEMP/LACPM, Rio de Janeiro, Brasil.

<sup>2</sup>. Instituto Nacional de Tecnologia (INT), DIEMP/LACPM, Rio de Janeiro, Brasil.

<sup>3</sup> Instituto Nacional de Tecnologia (INT), DIEMP/LACPM, Rio de Janeiro, Brasil.

**ABSTRACT:** Stainless steels are Fe-Cr or Fe-Cr-Ni alloys which were developed in the first decades of the 20<sup>th</sup> century with the purpose of attaining excellent properties for several applications, such as very good corrosion resistance combined with good strength. According to their type of microstructure, they can be classified in five main groups; ferritic, austenitic, martensitic, duplex and precipitation hardened (PH). Furthermore, according to the different contents of the elements of their chemical composition, they are designed by numbers in a classification system determined by AISI-SAE: American Institute of Steel and Iron (AISI) and Society of Automotive Engineers (SAE). In this system, a 17 % Cr ferritic stainless steel was analyzed to obtain necessary knowledge about high temperature phenomena: service conditions and heat treatments [1-2].

**EXPERIMENTAL METHODS:** A 430 stainless steel rolled sheet was heat treated at 1000°C for 3 hours in a muffle furnace and then cooled inside it. Sample: metallographic preparation: cutting, mounting, grinding (100 to 1200 mesh), polishing (diamond paste: 6 µm, 3 µm, 1 µm and colloidal silica: 0.2 µm), etching: Vilella: 5ml HCl, 1 g picric acid 100 ml H<sub>2</sub>O: SEM: Field emission gun: Quanta FEG 450, 20 kV, EDS (X-Ray energy dispersive spectroscopy) and EBSD ("Electron Back Scattering Diffraction) [3-4].

### **CONCLUSIONS:**

- Annealing caused significant grain growth, mainly when time is longer (2 to 3 h), and also caused the precipitation of carbide particles, mainly cementite (Fe<sub>3</sub>C), but also chromium carbide (Cr<sub>23</sub>C<sub>6</sub>) on the grain boundaries of the ferritic matrix.
- Although a small fraction of austenite (0.3 %) has been observed, this material is almost entirely ferritic (99.2 %).

### **REFERENCES:**

- [1] - A.L.V. Costa e Silva and P. R. Mei, Aços e Ligas Especiais, Editora Edgard Blücher, São Paulo, 2006.
- [2] M. Alizadeh-Sh, S.P.H. Marashi, M. Pouranvari, Materials and Design, 56 (2014) 258.
- [3] J.I. Goldstein et al., Scanning Electron Microscopy and X-ray Microanalysis, Plenum, New York, 1992.
- [4] This research was supported by CNPq and FAPERJ (Brazil), acknowledgements also to R.O. Centeno and R.A.Vinhosa for metallographic samples preparation.



## RESULTS:

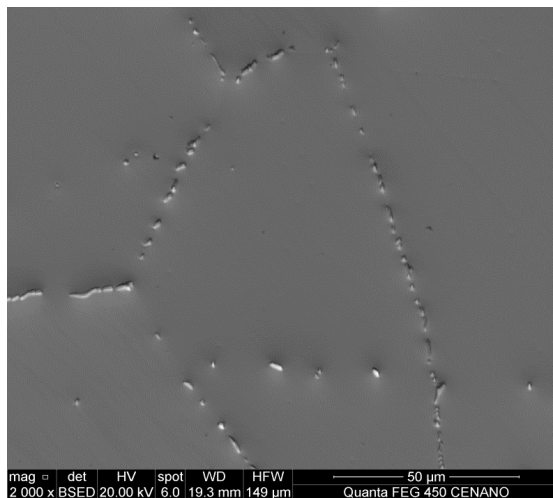


Figure 1 – SEM image: elongated particles on grain boundaries of AISI 430 stainless steel annealed at 1000°C for 3 h.

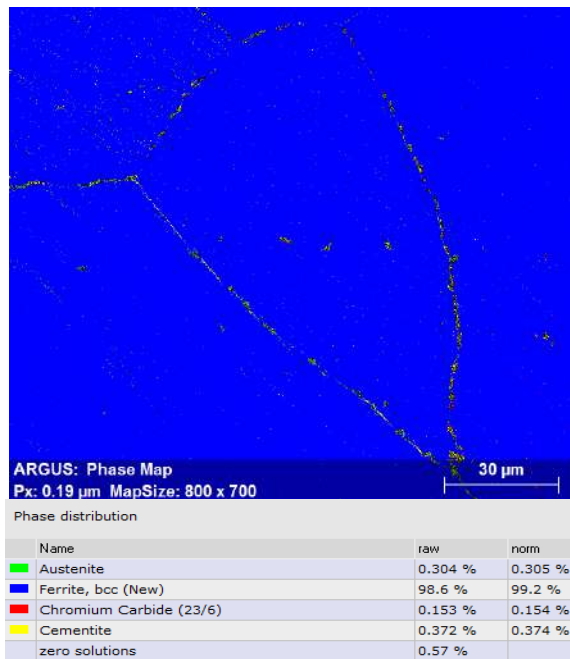


Figure 2 - EBSD map: elongated particles on grain boundaries of AISI 430 stainless steel annealed at 1000°C for 3 h.

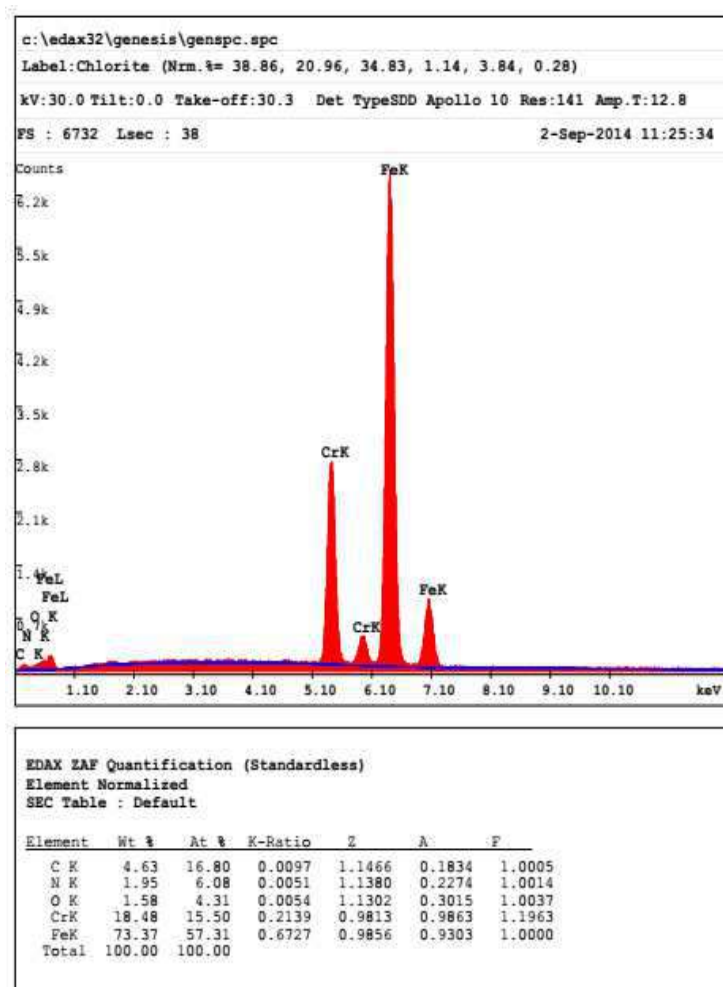


Figure 3 – EDS spectrum: elongated particles on the grain boundaries of 3 h annealed at 1000°C.

## Characterization of Oxides Formed in Stainless Steels Welded Joints by EBSD Technique

Leandro G. de Oliveira<sup>1</sup>, Marcelo A. N. Beltrão<sup>1</sup>, Plinio H.R Pecly<sup>2</sup>, Leonardo P. Carvalho<sup>2</sup> Suzana B. Peripolli<sup>1</sup>

<sup>1</sup>. Instituto SENAI de Tecnologia Solda (IST Solda) - Firjan, Rio de Janeiro, Brazil

<sup>2</sup>. SEQUI Petrobras, Rio de Janeiro, Brazil

Stainless steel is the given name to the steels family which are corrosion resistant, with a minimum of 10,5% chromium content by mass. When this chromium is exposed to oxygen, a very thin film of chromium oxide  $\text{Cr}_2\text{O}_3$  is formed, protecting the metal against the corrosive attack. However, during the welding, due to the high temperatures, the oxidation process is facilitated, promoting the formation of additional oxides besides  $\text{Cr}_2\text{O}_3$ . It is well known from the literature [1-3] that the welding purging process has a large effect on the corrosion resistance, so that near fusion line, the material experiences a range of temperature which the oxide formed has lower percentage of chromium and higher iron content, which is detrimental to the anti-corrosive properties of the stainless steels. Therefore, it is important that the oxides formed during the welding purging process should be characterized in order to quantify the corrosion resistance decreasing of these materials. The aim of this work was to determine and quantify the oxides formed in weld root at weld metal and HAZ (heat-affected zone) welded joint regions during the welding process using EBSD technique. However, in order to facilitate the formation of the oxides, the purging process was not employed during the welding process. For the oxides characterization, the detector  $e^-$  Flash model from Bruker connected to a scanning electron microscope (SEM), Quanta 450 model from FEI Company was employed. The base materials used in this work were three Schedule 40 stainless steels pipes (6.02mm of wall thickness): AISI 316L, UNS S32205 (duplex) and UNS S32750 (superduplex) steels. The methodology of the analysis consists, for the first step, of mounting, grinding and polishing processes in order to obtain a well-polished surface. After polishing stage, the entire non-conducting sample region was first recovered by silver ink in order to be analyzed. The EBSD evaluations were carried out in the center of the weld root at weld metal region. For HAZ cases, the evaluations were done at 0.5mm from the fusion line. EBSD results at weld metal regions of AISI 316L, UNS S32205 and UNS S32750 steels indicated mostly the formation of chromite ( $\text{FeCr}_2\text{O}_4$ ). Magnetite ( $\text{Fe}_3\text{O}_4$ ), eskolaite ( $\text{Cr}_2\text{O}_3$ ) and hematite ( $\text{Fe}_2\text{O}_3$ ) were also detected but in lower quantity. The HAZ results showed low quantity of chromite and magnetite. Eskolaite and hematite were found in higher quantity. The results also revealed that the EBSD technique is a powerful tool to be employed in order to characterize the oxide formation in the welded joints.

[1] Turner, S., Robinson, F. P. A., The Effect of the Surface Oxides Produced during Welding on the Corrosion Resistance of Stainless Steels. *Corrosion*, Vol. 45, No. 9, pp. 710-716.

[2] Hinds, G., Wickström, L., Turnbull, A., Influence of Weld Preparation Procedure and Heat Tinting on Sulfide Stress Corrosion Cracking of Duplex Stainless Steel. *In: NACE International Conference & Expo*, 2015.

[3] Taban, E., Kaluc, E., Aykan, T. S., Effect of the Purging Gas on Properties of 304H GTA Welds. *Welding Research*, Vol. 93, pp. 124s-130s, 2014.

The authors would like to thank Petrobras for the financial and technical support.



Table 1 – Quantification results of the identified phases by EBSD technique.

Base Material	AISI 316L		UNS S32205		UNS S32750	
Phase name	Welding Metal (%)	HAZ (%)	Welding Metal (%)	HAZ (%)	Welding Metal (%)	HAZ (%)
Eskolaite	0,031	1,08	0,025	3,97	2,87	1,84
Hematite	0,004	1,32	0,024	5,28	1,97	2,83
Austenite	73,5	94,8	63,4	45,7	30,6	41,6
Chromite	24,7	0,711	31,1	14,6	16,2	4,07
Magnetite	1,82	2,06	1,15	4,59	29,0	20,9

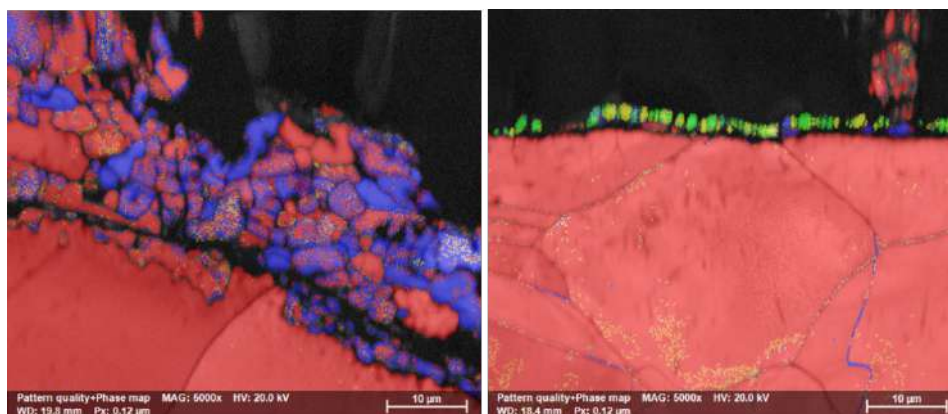


Figure 1 – EBSD image of weld root: weld metal region (left side) and HAZ region (right side). AISI 316L steel welded joint.

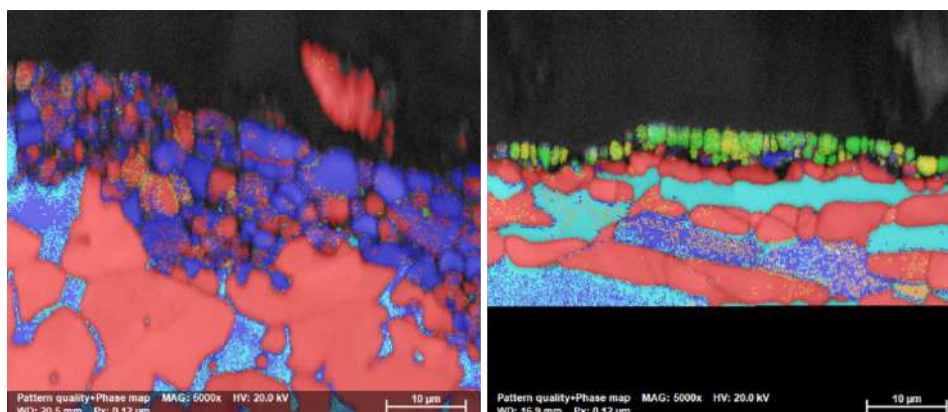


Figure 2 – EBSD image of weld root: weld metal region (left side) and HAZ region (right side). UNS S32205 steel welded joint.

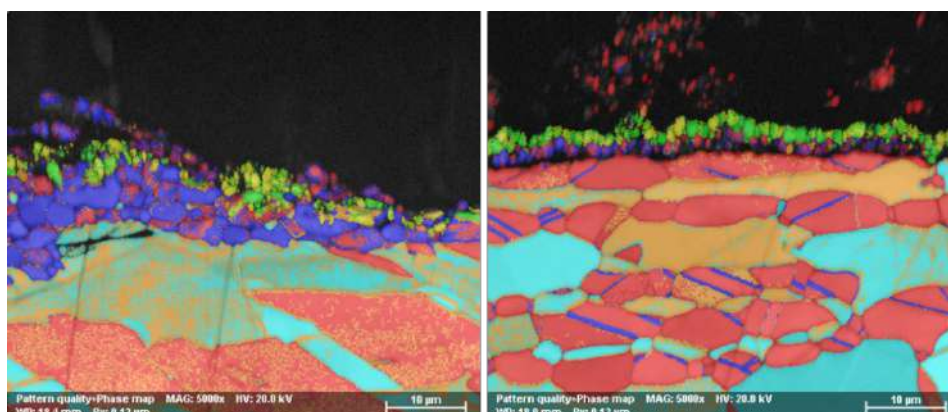


Figure 3 – EBSD image of weld root: weld metal region (left side) and HAZ region (right side). UNS S32750 steel welded joint.



## Evaluating the Microstructure of C-Mn Steel Weld Deposits

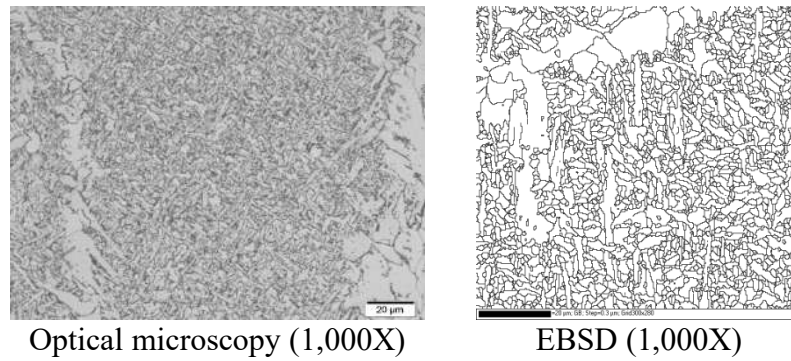
Jorge C.F. Jorge<sup>1</sup>, Matheus Campolina Mendes<sup>2\*</sup>, Luis Felipe G. Souza<sup>3</sup>, Leonardo S. Araújo<sup>4</sup>, Ivani S. Bott<sup>5</sup>, Glyn M. Evans<sup>6</sup>

- <sup>1</sup> Departamento de Engenharia Mecânica, CEFET/RJ, jorgecfjorge@gmail.com
- <sup>2</sup> Departamento de Engenharia Mecânica, CEFET/RJ, campolinamendes@gmail.com
- <sup>3</sup> Departamento de Engenharia Mecânica, CEFET/RJ, lfgs59@gmail.com
- <sup>4</sup> Departamento de Metalurgia e Materiais, UFRJ, leonardo.sales@gmail.com
- <sup>5</sup> Departamento de Engenharia Química e de Materiais, PUC-Rio, ivanibott@gmail.com
- <sup>6</sup> Consultant, United Kingdom, gmevans@globalnet.co.uk

As recommended by the International Institute of Welding (IIW), the characterization of the microstructure of a C-Mn steel weld metal was performed by optical microscopy (OM) [1]. However, the addition of specific elements such as titanium can promote refinement of the microstructure, making OM unsuitable even for low alloyed weld metals [2], since the separation of the microstructural constituents becomes more challenging even at magnification higher than that recommended by the IIW (Figure 1). For multi-pass welds, due to the influence of several other parameters interacting, such as the ratio of the reheated region, amount of acicular ferrite and the presence of martensite-austenite constituents (MA), the microstructure definition by OM can be even more difficult. Electron Back Scattering Diffraction (EBSD) has been considered as an alternative technique [3,4] to supply this OM deficiency. In this respect, it can be seen in Figure 2 the strong influence of the reheating on the microstructure of C-Mn-Ti weld deposits. Besides recrystallization, significant changes along the thickness can be observed. As all these factors are essential when considering the mechanical properties of weld metals, the application of complementary techniques can add information and help to minimize microstructure misinterpretation. Comparative analysis (Figure 1) reinforce the above statement, where the high definition provided by EBSD technique especially regarding the grain boundaries, is beneficial to separate acicular ferrite and bainite (ferrite with the second phase). However, the low carbon content, usually encountered in C-Mn and High Strength Steel weld metals, make the precise distinction between the main constituents very difficult by EBSD technique [5,6]. Besides, the presence of MA constituent and its decomposition due to reheating, a significant contributing factor to the impact toughness, is more easily detected by SEM analysis (Figure 2), making this last technique more adequate for this task. Therefore the present authors believe the association of SEM and EBSD techniques are the best methodology to study C-Mn steel weld metals when a refined microstructure is present.

## REFERENCES

- [1] IIW, IIW Doc. No.IX-1533-88, 1988.
- [2] G.M. Evans, Weld. J. 71(1992) 447s.
- [3] S.L. Shrestha et al., Ultramicroscopy 137 (2014) 40.
- [4] M. Díaz-Fuentes et al., Met. Mat. Trans. A 34A (2003) 2505.
- [5] D.J. Abson, Sci. Tech. Weld. Join. 23(2018) 635.
- [6] B.K. Narayanan et al., Sci. Tech. Weld. Join. 16(2011) 12.



Optical microscopy (1,000X) EBSD (1,000X)  
Figure 1. Microstructure of the columnar region of a C-Mn steel weld deposit containing 28 ppm Ti (Basic composition: 0.07C, 1.50Mn, 0.4Si [2]).

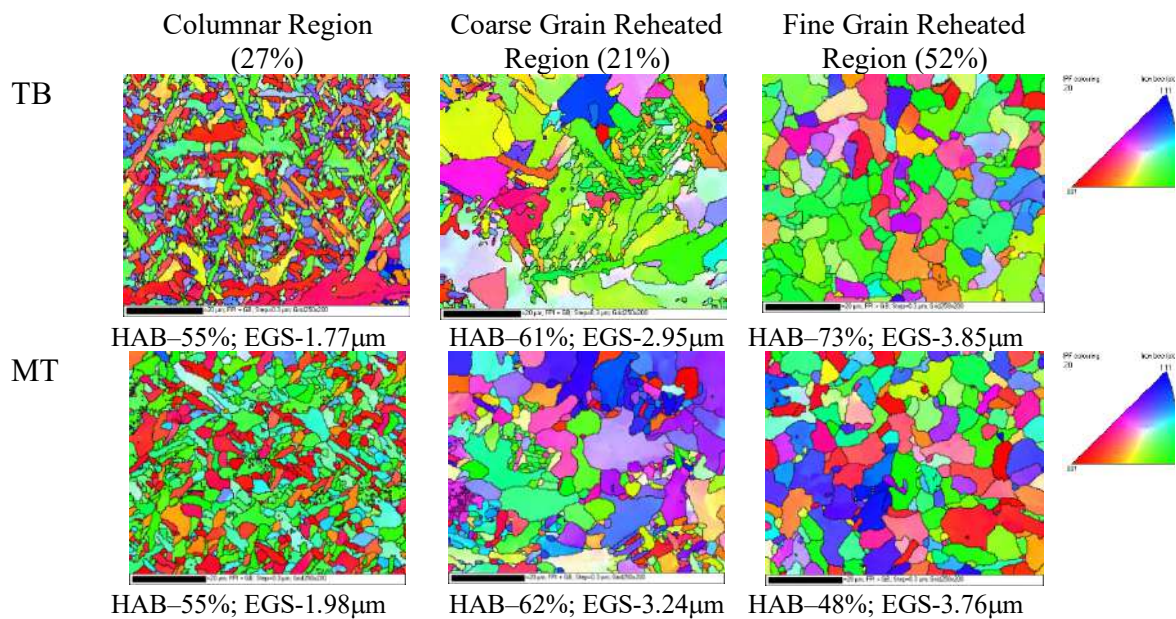


Figure 2. Influence of reheating on the characteristics of a weld metal (EBSD) (1,500X).  
Where: TB – Top Bead; MT – Mid-Thickness,  
HAB – High Angle Boundaries; EGS – Effective Grain Size.

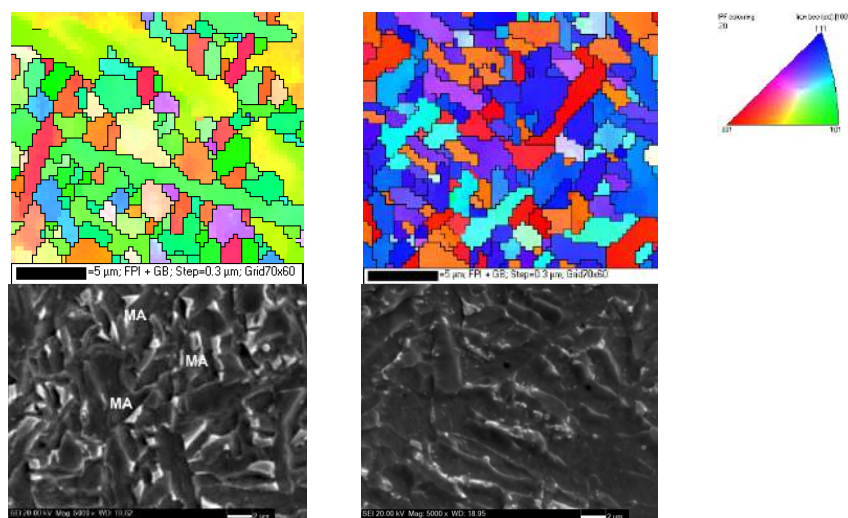


Figure 3. Aspects of the microstructure occurring at the columnar region of a weld metal containing 28 ppm Ti [2], when observed by SEM and EBSD. (5,000X).



## Evaluating the Microstructure of Steel Weld Deposits.

### Part 2: High Strength Steels.

Jorge C.F. Jorge<sup>1</sup>, Matheus Campolina Mendes<sup>2\*</sup>, Luis Felipe G. Souza<sup>3</sup>,  
Leonardo S. Araújo<sup>4</sup>, Ivani S. Bott<sup>5</sup>

- <sup>1</sup>. Departamento de Engenharia Mecânica, CEFET/RJ, jorgecfjorge@gmail.com
- <sup>2</sup>. Departamento de Engenharia Mecânica, CEFET/RJ, campolinamendes@gmail.com
- <sup>3</sup>. Departamento de Engenharia Mecânica, CEFET/RJ, lfgs59@gmail.com
- <sup>4</sup>. Departamento de Metalurgia e Materiais, UFRJ, leonardo.sales@gmail.com
- <sup>5</sup>. Departamento de Engenharia Química e de Materiais, PUC-Rio, ivanibott@gmail.com

High strength steel weld metals microstructural characterization has always been a challenge for the last decades since Optical Microscopy (OM) is unable to resolve the refined microstructures [1], as observed in Figure 1. The presence of martensite (M) and bainite (B) can better be observed due to the higher resolution of the Scanning Electron Microscopy (SEM) and has been extensively applied as a helpful complementary technique to clarify the constituents present in higher strength steel weld metals [1,2]

Weld metals of the class 600-700 MPa, have a microstructure composed by a mixture of primary ferrite, ferrite with second phase and acicular ferrite (Figure 2). The evaluation of the impact toughness requires a detailed quantitative analysis of the microstructure, where the determination of the amount of acicular ferrite is crucial due to its strong influence on the impact toughness [3,4].

As stated by Abson [4], weld metals obtained by modern welding consumables can produce fine bainite colonies similar to the lath size observed for acicular ferrite, and there is a risk of some confusion between these constituents. Metallographic examination performed by OM does not allow to see these microstructures even at higher magnification [5] and, consequently, it is not possible to correlate the microstructure with the Charpy-V results.

Electron Back Scattering Diffraction (EBSD) can reveal grain boundaries (Figure 2c) more clearly and simultaneously supply significant contribution as the quantitative measurements of the microstructural constituents. It can also provide other relevant information to the impact toughness (Figure 3), such as grain boundary characteristic distribution. However, the incidence of inclusions and MA constituents, which are also extremely relevant to the mechanical properties [6,7], isn't clearly identified by EBSD being better characterized using a secondary electrons signal on SEM. Therefore, as also indicated for C-Mn steel weld metals, the association of SEM and EBSD techniques is the best methodology to the characterization of microstructures of high strength steel weld metals.

#### REFERENCES

- [1] J.C.F. JORGE et al., J. Mater. Res. Tech. 8 (2019) 561.
- [2] A.J.C. Gomes, Dissertação M.Sc, CEFET-RJ (2018).
- [3] D. Loder et al., J. Mater. Sci. Res. 6 (2017) 24.
- [4] D.J. Abson, Sci. Tech. Weld. Join. 23(2018) 635.
- [5] G. Thewlis, Mater. Sci. Tech. 20 (2004) 143.
- [6] R. Pamnani et al., J. Manuf. Proc. 21(2016) 75.
- [7] J.C.F. Jorge et al., IIW-DOC-II-A-243-18 (2018) 1.



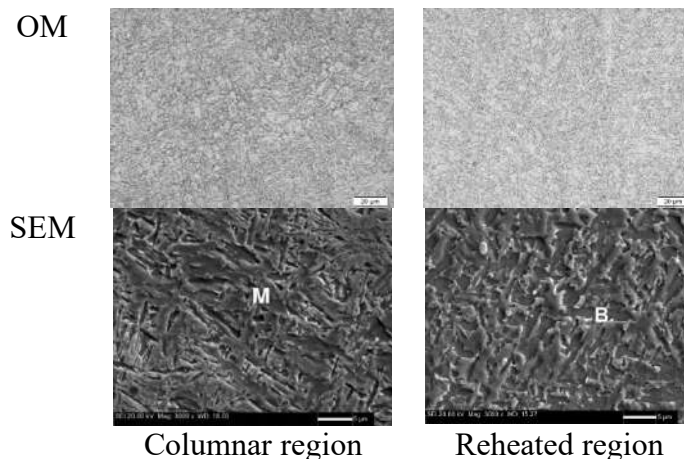


Figure 1. Microstructure observed in a high strength steel weld metal deposited by Shielded Metal Arc Welding Process. Etchant: nital 2%.  
Basic composition: 0.08C, 1.9Mn, 3.0Ni, 0.4Mo, 0.3Cr [2].

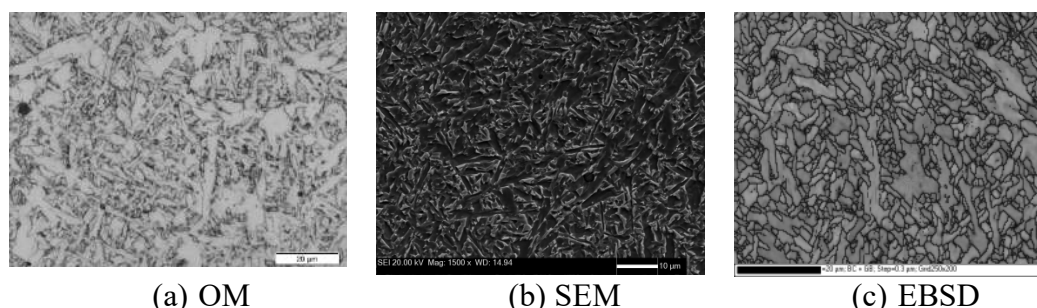


Figure 2. Microstructure of a weld metal of the class 690 MPa deposited by Metal Cored Arc Welding Process (MCAW). Basic composition: 0.13C, 1.4Mn, 1.6Ni, 0.5Mo, 0.1Cr.

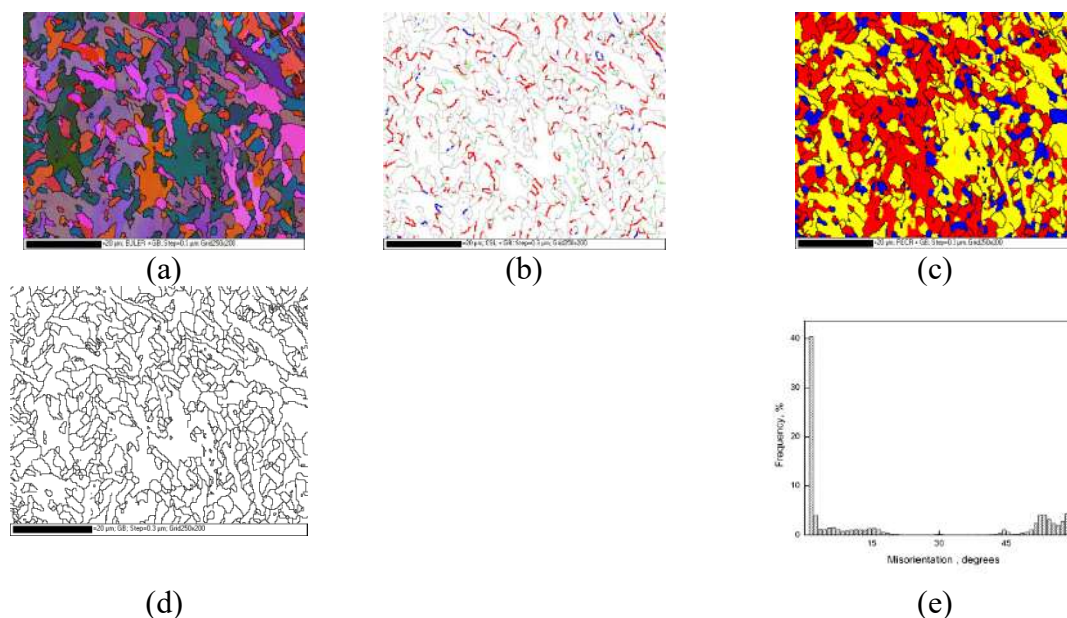


Figure 3. Some information provided by EBSD analysis.  
(a) All Euler Map; (b) CSL Map; (c) Deformation Map ;  
(d) Grain Boundary map; (e) Misorientation distribution profile.



## **The use of 3D Misorientation spaces in the study of phase transformation of iron oxides: a case study of Carajás Iron Formations' oxide assembly using EBSD data.**

Victor Mota e Nogueira<sup>1\*</sup>, Paola Ferreira Barbosa<sup>1</sup>, Sathish Mayanna<sup>2</sup>, Adalene Moreira Silva<sup>1</sup>, Catarina Labouré Bemfica Toledo<sup>1</sup>, Luciano Mozer de Assis<sup>3</sup> and Matheus Costa Bracioli<sup>1</sup>.

<sup>1</sup>. Universidade de Brasília (UnB), Instituto de Geociências, Brasília, Brazil.

<sup>2</sup>. German Research Center for Geoscience, Dept. of Geochemistry, Potsdam, Germany.

<sup>3</sup>. Exploração Mineral de Ferrosos, Vale S.A., Nova Lima, Brazil.

Martite grains composed of hematite, goethite and magnetite are the most common constituents of the iron formations called jaspilite in the Serra Norte - N4WS deposit of iron ore in the Carajás Mineral Province. In this study, natural phase transformation between the minerals magnetite-hematite-goethite is described in detail and in pairs (magnetite-hematite and hematite-goethite) by the use of 3D Neo-Eulerian misorientation spaces proposed in [1]. During progressive oxidation and reduction of iron oxides, the cubic, trigonal and orthorhombic lattices of the three iron oxides are linked by specific topotactic relations, being the hematite with its trigonal lattice, in most cases, the intermediate phase in natural systems. These relations can be studied and better visualized with the use of misorientation experimental data obtained by EBSD techniques. EBSD measurements were carried out on a FEI Quanta 3D Dual Beam FEG equipped with an EDAX-OIM electron backscatter diffraction system and analysis were performed in the MATLAB toolbox MTEX with scripts provided in [1] and complementary images were processed in Channel 5.0 software's Tango. An accelerating voltage of 20kV, beam current of 4.0 nA and working distance of 15mm were used with no carbon coating. The SEM stage was controlled manually to the selected areas where the three phases coexist and forescattering electron images were generated. The results of grain boundary misorientation between magnetite-hematite and hematite-goethite were generated and plotted in reduced fundamental zones of axis-angle ( $\nu = \omega$ ) representation. The phase transformation between magnetite and hematite is represented by a fundamental zone combination of the symmetries 432 and 32 ( $a/2$ ) and two clusters can be observed, both related to a high density of misorientation angles close to 55°. Hematite-goethite transition is represented by the fundamental zone  $f/2$  determined by the symmetries 32 and 222 combination. Just one cluster is observed in the coincidental zone and it is related to a high density of low misorientation angles, close to zero, between hematite and goethite grains. Both results are in consonance with theoretical studies [2][3] and orientation data represented by inverted pole figures and pole figures done in previous studies [4][5], which shows parallelism between the planes (111) and (0001) for the magnetite-hematite transformation, respectively, and between (0001) and (001) planes in the transition of hematite to goethite. Thereby, this same parallelism is best seen and represented by 3D Misorientation spaces with the use of the same experimental data used before for orientation analysis. All misorientation clusters described in both coincidental fundamental zones are related to the expected rotation angles necessary for its transformation and indicates that topotactic transitions between magnetite-hematite-goethite are the biggest contribution to the crystallographic texture in martite grains of the iron formations of the N4WS deposit.

- [1] R. Krakow et al., Proceedings of the Royal Society A (2007) 473.  
[2] Y. Cuenec & A. Lecerf, Solid State Science 7 (2005) 520.  
[3] L. Lagoeiro, Journal of Metamorphic Geology 16 (3) (1998) 415.  
[4] P. F. Barbosa & L. Lagoeiro, American Mineralogist 95 (2009) 118.  
[5] P. F. Barbosa et al., Microsc. Microanal. 17 (Suppl. 2) (2011) 408.  
[6] This research was supported by CNPq, CAPES, Vale S.A. and The German Research Center for Geoscience (GFZ).

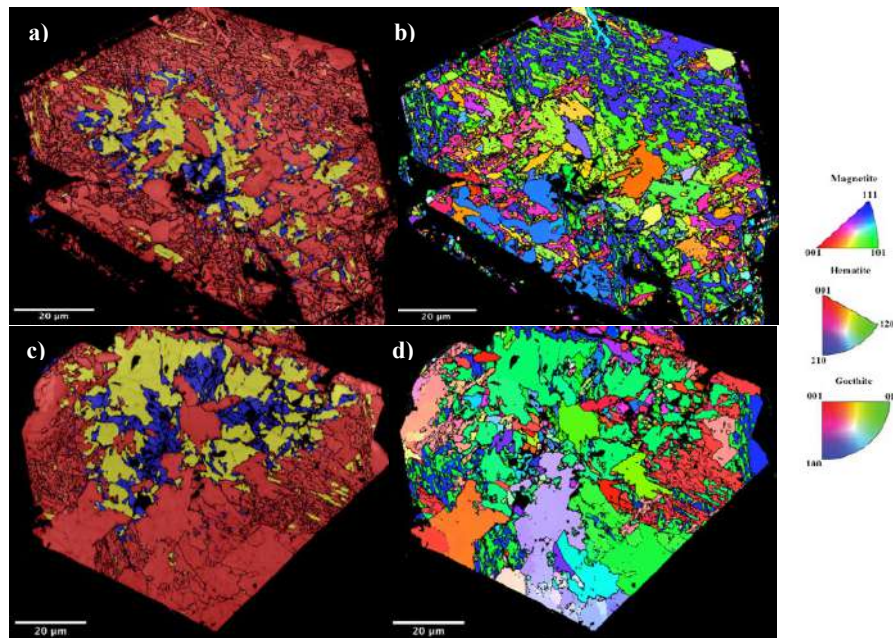


Figure 1: a) Grain I Phase Map - Hematite in red, magnetite in yellow and goethite in blue; b) Grain I Inverted Pole Figure (IPF) in z direction; c) Grain II Phase Map - Hematite in red, magnetite in yellow and goethite in blue; Grain II Inverted Pole Figure (IPF) in z direction;

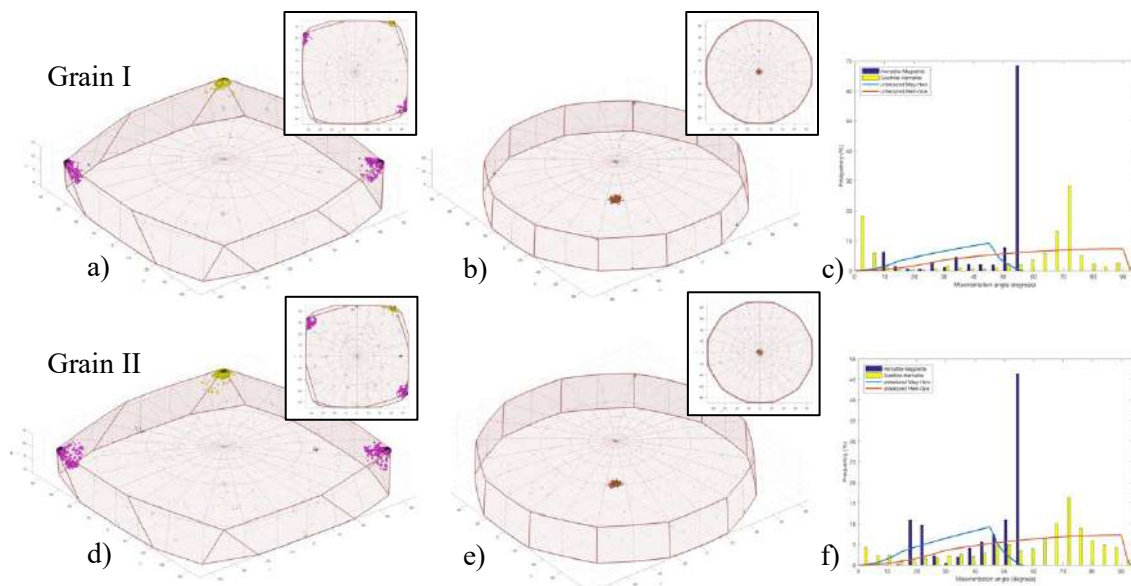


Figure 2: a) Grain I – 3D misorientation distribution of magnetite-hematite boundary in the fundamental zone a/2 (432-32); b) Grain I – 3D misorientation distribution of hematite-goethite boundary in the fundamental zone f/2 (32-222); c) Grain I - Misorientation angle distribution d) Grain II – 3D misorientation distribution of magnetite-hematite boundary in the fundamental zone a/2 (432-32); e) Grain II – 3D misorientation distribution of hematite-goethite boundary in the fundamental zone f/2 (32-222); f) Grain II - Misorientation angle distribution.



## **Micro-Raman spectroscopy and Electron probe micro-analyzer techniques applied to the gemological study and identification of Paraíba tourmaline liddicoatite.**

Victor Mota e Nogueira<sup>1\*</sup>, Nelson Fava<sup>2</sup>, Camilla Vasconcelos Kafino<sup>2</sup>, Erich Adam Moreira Lima<sup>2</sup>, Paola Ferreira Barbosa<sup>1</sup> and Matheus Costa Bracioli<sup>1</sup>.

<sup>1</sup> Universidade de Brasília (UnB), Instituto de Geociências, Brasília, Brazil.

<sup>2</sup> Departamento de Polícia Federal – Área de Perícias de Meio Ambiente (APMA).

With the discovery of Paraíba tourmaline (Cuprian elbaite species) in the Mina da Batalha in 1987, near to the city of São José da Batalha, Paraíba - Brazil, the Paraíba Tourmaline was introduced in the gemological market. For a long time, the occurrence of such gem was restricted to the region of the states of Paraíba and Rio Grande do Norte. Recently, occurrences of gemological elbaite species also enriched in copper have also been found in Nigeria and Mozambique, in the Edeko and Alto Lingonha mines, respectively [1]. The introduction of new producing mines in Africa in the early 2000s drove the need for a better study of the origin of these gems. But a variety of Paraíba tourmaline with a more calcic composition than those already known began to be offered in the market, being identified as liddicoatite and of unknown provenance [2]. These gemstones, that probably underwent to some treatment, call the attention of researchers around the world due to their mineralogical differences from the previous classic Paraíba tourmaline already known until then and some peculiarities referring to the Raman spectrum and mineral chemistry.

Micro-Raman analysis were carried out on a Horiba Explora and the spectra obtained were used in order to characterize this new variety of tourmaline now abundant in the market and easily identify such species from other elbaite tourmaline. Microprobe analysis in which the chemical differences of the samples were evidenced were obtained through electronic microprobe (EPMA) and carried out on a JEOL JXA 8200 and JXA 8230. The samples were provided by the National Institute of Criminalistics (INC), part of the Federal Police Department, and analyzed in partnership with the University of Brasília (UnB) and The Regional Center for the Technological Developing and Innovation (CRTI).

The variations in the Raman spectra in wavelengths 780 nm and 532 nm, their characterization and comparison with spectra of Brazilian gemological species are of fundamental importance for the gemological study of treated and natural materials and may become an important method of verification and characterization of these gemstones, so far not officially proposed in the literature. These liddicoatite tourmalines in question have on average 3.46% of CaO in their structure and 0,21% of CuO and a strong anomaly of fluorescence interference in the Raman spectrum (780nm) between  $895\text{cm}^{-1}$  and  $1915\text{cm}^{-1}$  in all samples analyzed. This interference is not seen in analysis using 532nm wavelength laser. Whilst Brazilian specimens from São José da Batalha showed much lower average content of CaO (0,23%) and higher average values of CuO (0,23%). No fluorescence or anomaly is identified in both Raman spectra of Brazilian specimens, showing regular elbaite tourmaline structure.

[1] A. Abduriyim et al., *Gems and Gemology* 4 (2006) 4-21.

[2] Y. Katsurada & Z. Sun, *Gems and Gemology* 53 (2017).



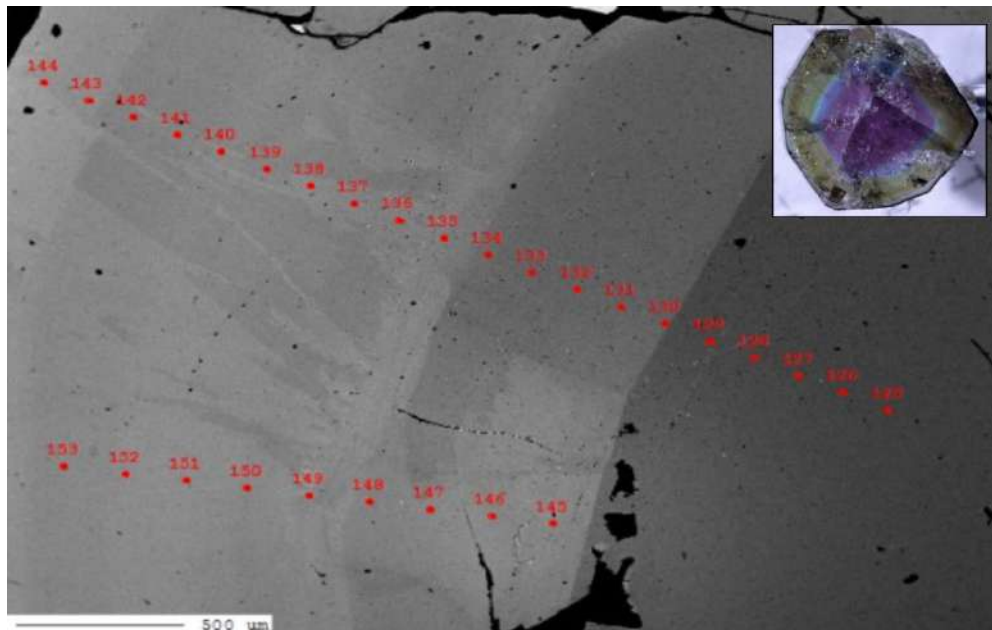


Figure 1: BSE image showing EPMA analysis points in rough tourmaline elbaite (Mina da Batalha).

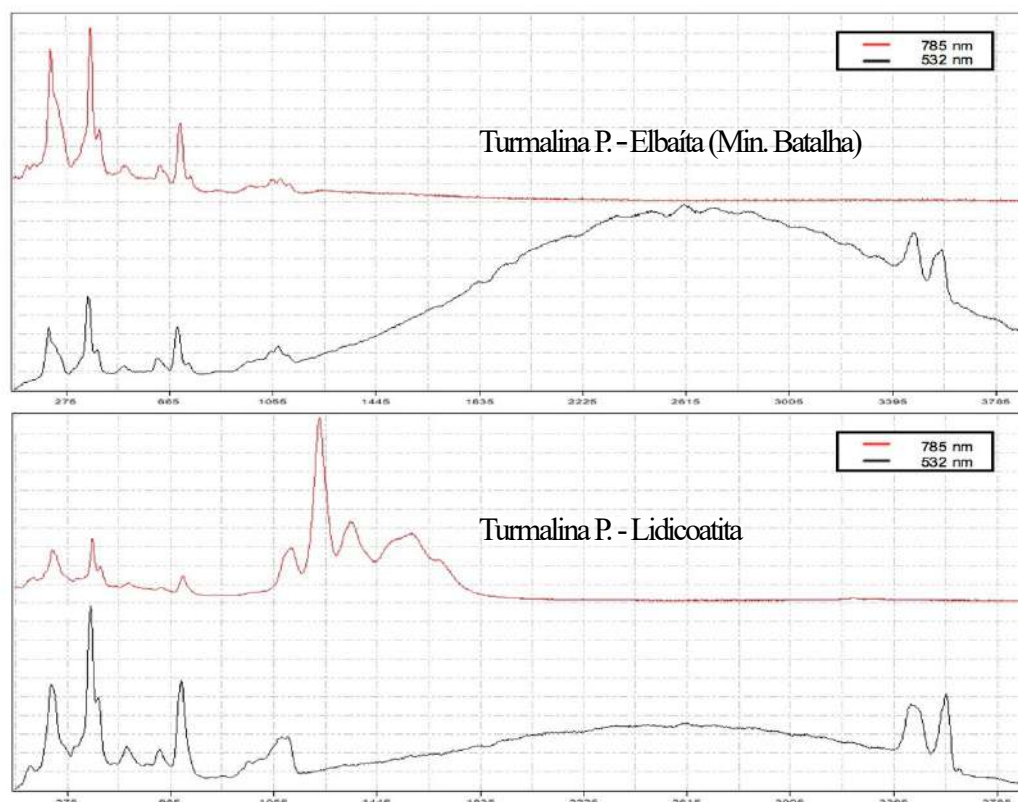


Figure 2: Micro-Raman spectra (785nm and 532nm) of Paraíba tourmaline elbaite from the Mina da Batalha and liddicoatite Paraíba Tourmaline of unknown provenance.

## Microstructure evaluation and lamellae spacing of the cementite from the HSLA steel DIN 38MnSiVS5 over different cooling process.

Bruno Fernando Gianelli<sup>1</sup>, Gabriel Nogueira Rodrigues<sup>1</sup> and Mario Luiz Nunes Silva<sup>1</sup>

<sup>1</sup>- Instituto Federal de Educação, Ciência e Tecnologia de São Paulo, Laboratório de Materiais, Itapetininga, Brasil, assaigabriel@gmail.com.

Micro alloyed steels are steels with small amounts of alloying elements (nano precipitates), the main ones being V, Ti and Nb. For this work, the use of DIN 38MnSiVS5 steel (vanadium- micro linked) (Table 1) was chosen because it is increasingly used in the automotive industry, as it provides a great saving of time and energy, since it does not require further heat treatment [2].

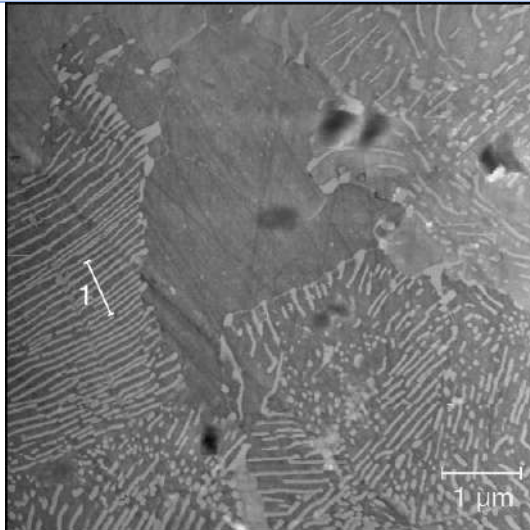
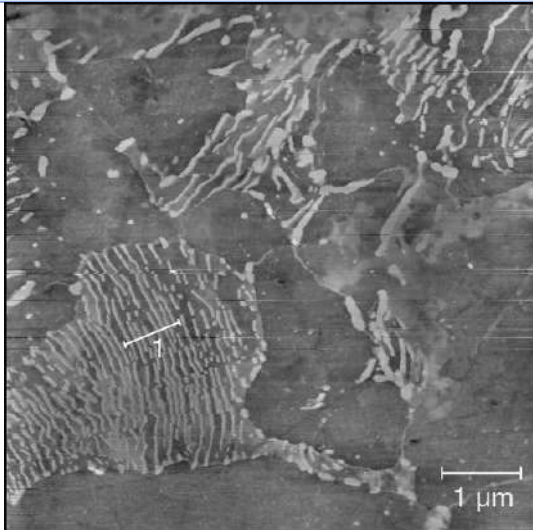
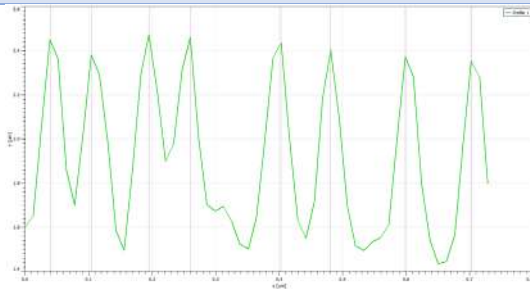
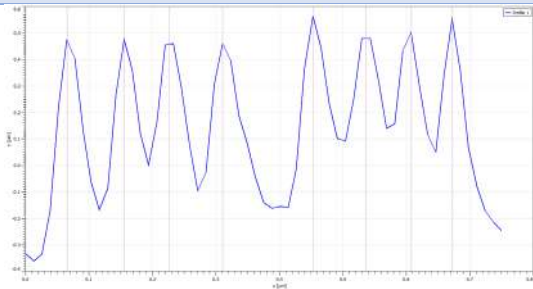
C	Si	Mn	P	S	Cr	Mo	V	N
0,34	0,15	1,20	< 0,025	0,020	< 0,30	< 0,08	0,08	0,01
0,41	0,80	1,60		0,060			0,20	0,02

The presence of vanadium as a chemical element into its composition facilitates the refinement of the ferrite grain. This process occurs due to the austenite conditioning during the material processing, which leads to ferrite nucleation sites maximization. Taking into account the nitrogen high solubility in the ferritic grains and the low solubility of the vanadium, an increase of the nitrogen concentration will make the kinetics of vanadium nitride precipitation faster, reducing the size of these precipitates, resulting in a smaller spacing between the particles and improving their physical properties, such as hardness, formability and tensile strength [1; 3]. It is known that the heat treatment and the rates of plastic deformation from micro-alloyed steels influence over its microstructure, and consequently the mechanical properties, being hardness one of the main affected characteristics, due to the spacing variation of the cementite lamellae into the pearlite matrix [3]. The objective of this work is to correlate the hardness of a heated DIN 38MnSiVS5 steel in a furnace at 1000°C for 10 minutes, being sample 1 (A1) cooled inside the furnace with the door closed and sample 2 (A2) with the furnace door open. Samples with 10 x 10 x 5 mm were used, sanded, polished and attacked with Nital 2.0%, after which a SHIMADZU SPM 9700 atomic force microscope was used at the non-contact mode for data collection and the open source software, GWYDDION v2.51 for lamellar spacing processing, the hardness was characterized by an EMCOTEST DURAVISION 20 G5 Hardness Tester, with a Vickers indenter with a force of 1 Kgf.

### REFERENCES

- [1] RENTERÍA-BORJA, L. et al. Atomic force microscopy applied to the quantification of nano-precipitates in thermo-mechanically treated microalloyed steels. **Materials Characterization**, v. 69, p. 9-15, 2012.
- [2] SILVA, M. L. N.; PIRES, G. H.; BUTTON, S. T. Damage evolution during cross wedge rolling of steel DIN 38MnSiVS5. **Procedia Engineering**, v. 10, p. 752-757, 2011.
- [3] ZHAO, Jingwei; JIANG, Zhengyi. Thermomechanical processing of advanced high strength steels. **Progress in Materials Science**, 2018.



Furnace door closed		Furnace door opened	
AFM topography image			
			
Profiles from cementite lamellae spacing			
			
Average cementite spacing (nm)			
94,86 ± 22,98		86,71 ± 16,73	
Average Hardness Vickers (HV1)			
201 ± 3,2		216 ± 4,3	

## Raman Spectroscopy on Twisted Bilayer Graphene Engineered by Atomic Force Microscopy

Camila Machado França<sup>1</sup>, Clara Muniz de Almeida<sup>2</sup> and Mônica de Mesquita Lacerda<sup>3\*</sup>

<sup>1</sup> Universidade Federal do Rio de Janeiro, Campus UFRJ - Duque de Caxias, Duque de Caxias, Brazil.

<sup>2</sup> Instituto Nacional de Metrologia, Qualidade e Tecnologia, Divisão de Metrologia de Materiais, Duque de Caxias, Brazil.

<sup>3</sup> Universidade Federal do Rio de Janeiro, Campus UFRJ - Duque de Caxias, Duque de Caxias, Brazil. \*monica\_lacerda@xerem.ufrj.br

Graphene has been studied for over a decade with great development on large-scale preparation and full characterization of electrical, thermal and mechanical properties. Raman spectroscopy (RS) is an important technique to study carbonaceous materials, mainly graphene due to its scattered resonant signal [1]. RS is also used to determine the rotation angle of twisted bilayer graphene (tBLG) and to check the role of atomic deformation induced by the fold. In this work, graphene was prepared by mechanical exfoliation of graphite flakes, was folded by atomic force microscopy (AFM) and analyzed by RS at 532 nm wavelength. Figure 1 shows optical image of monolayer graphene before folding (Fig. 1a) and its Raman spectrum (Fig. 1b), which presents typical G and 2D bands. Folded graphene presents also D-like and rotational (R) bands due to rotational mismatch between layers. Figure 2 shows three AFM images at different instant of time during folding procedure. The main folding in this work presents a mismatch angle of 27 degrees and was inferred by knowing R band position [2]. Another difference between monolayer and folded graphene is the existence of G band splitting, known as G' band in the literature [3]. It has been reported as being related to inactive infrared mode in twisted multilayer samples as 1+3 (monolayer on top of trilayer) [4]. We address the problem by analyzing the folded (1+1 - monolayer on top of monolayer) sample at different positions and at different incident laser power in order to study the role played by induced stress as a consequence of forced bond stretching at folded sample border. The results of this study aims to elucidate the origin of G' band in tBLG, which could be used as parameters for quality assessment of device based on graphene.

### REFERENCES

- [1] M. S Dresselhaus, Phil. Trans. R. Soc., 368, (2010) 5355.
- [2] V. Carozo, Physical Review, 88 (2013) 085401.
- [3] M. Huang, PNAS, 106, (2009), 18.
- [4] J. B. Wu, Nat. Commun., 5 (2014) 5309.

### ACKNOWLEDGEMENTS

Camila França acknowledges to Fundação de Amparo à Pesquisa do Estado do Rio de Janeiro (FAPERJ) for her scholarship. We thanks to Divisão de Metrologia em Materiais (Dimat) of Inmetro for laboratorial support.



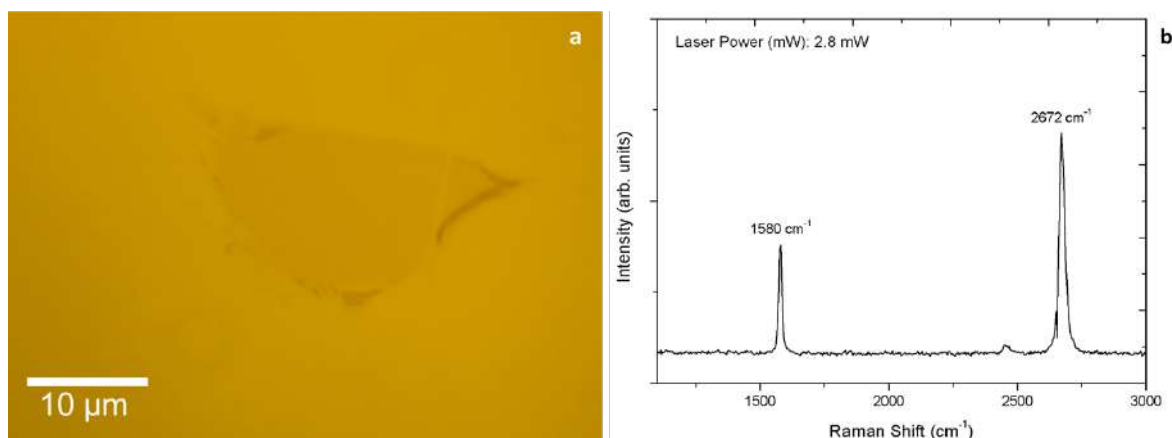


Figure 1. **a)** Optical microscopy image of monolayer graphene on Si/SiO<sub>2</sub> substrate before folding. **b)** Raman spectrum of monolayer graphene showing the G peak at 1580 cm<sup>-1</sup> and 2D band at 2672 cm<sup>-1</sup>.

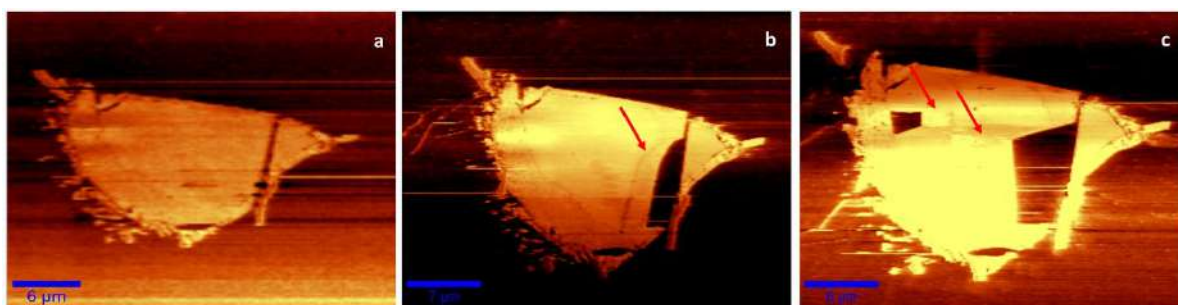


Figure 2. Lateral force images obtained by AFM. **a)** monolayer graphene before scanned, **b)** monolayer graphene after be scanned, with one folding and **c)** monolayer graphene after be scanned with two foldings (showing by arrows).

## Raman Characterizations of Low Cost Electrochemical Sensor Made with Recycled PET and Graphite

Deonir Agustini<sup>1,2\*</sup>, Luis Gustavo de Matos dos Santos<sup>1</sup>, Márcio Fernando Bergamini<sup>2</sup>,  
Luiz Humberto Marcolino-Junior<sup>2</sup>

<sup>1</sup> Centro de Microscopia Eletrônica (CME), Setor de Ciências Biológicas, Universidade Federal do Paraná (UFPR), CEP 81.530-000, Curitiba-PR, Brazil.

<sup>2</sup> Laboratório de Sensores Eletroquímicos (LabSense), Departamento de Química, Universidade Federal do Paraná (UFPR), CEP 81.531-980, Curitiba-PR, Brazil.

\* Corresponding author: [deonir@ufpr.br](mailto:deonir@ufpr.br)

Polyethylene terephthalate (PET) is chemically stable polyester widely used in the world, which can be recycled and reused in the construction of new products, such as in the manufacture of low cost electrochemical sensors. For this purpose, the incorporation of a conductive material into PET is necessary, like graphite, which is a cheap carbon allotrope with a high melting point ( $> 3500^{\circ}\text{C}$ ) [1]. However, due to the size of the graphite particles and their elemental composition similar to PET, the monitoring of the effectiveness of the mixture is not conclusive by the traditional optical and electronic techniques of analysis, thus requiring specific techniques, such as Raman spectroscopy. Here, we present the different options of Raman spectroscopy to evaluate and develop an electrochemical sensor constructed with recycled PET and graphite. The mixing of the materials was done at  $250^{\circ}\text{C}$  and the sensor was molded into a heated aluminum piece with a center hole of 3.5 mm diameter, where the mixture and a copper connector were added. The electroactive area of the sensor (3.5 mm section) was delimited with insulating tape. The effect of heating in the graphite and PET was evaluated by thermal analysis with obtaining Raman spectra between 25 and  $300^{\circ}\text{C}$ . No change in graphite or PET degradation (Fig. 1A) were observed, only a change in the semi-crystalline to the amorphous phase of the polymer [2], as indicated by the gradual disappearance of the vibrational band at  $1098\text{ cm}^{-1}$  (Fig. 1B). Thus, with these observations, and to avoid a greater proximity to the melting point of PET ( $280^{\circ}\text{C}$ ), when the degradation process of the polymer begins [3], the temperature of  $250^{\circ}\text{C}$  was selected for mixing and construction of the electrodes. The proportion of PET and graphite used in the mixture was evaluated by Raman mapping. To the electrodes with 30% and 40% of graphite, a large amount of small regions with absence of graphite was observed. On the electrodes with 60% and 70% of graphite, there was a good distribution of this material, but due to the smaller amount of PET, the electrodes became brittle. In this way, the mixture with 50% of graphite was chosen for the construction of the sensors, since it presented a good mechanical resistance and a good homogeneity of the materials, as shown in Fig. 2A-C obtained through Raman mapping ( $280 \times 280\text{ }\mu\text{m}$ ) of the electrode surface, using the options of topography correction (True Surface) and Large Area and in Fig. 2D-E, with the evaluation of the internal distribution of the materials through Raman mapping in  $110\text{ }\mu\text{m}$  depth. Finally, the electrochemical characterizations confirmed a good response of the developed sensor, with the cyclic voltammetry (CV) profile (Fig. 3A) obtained in ascorbic acid (AA) solution showing the oxidation process of this compound (in 0.24 V) in comparison with the CV made in supporting electrolyte. An analytical curve for AA between 40.0 and  $600.0\text{ }\mu\text{mol L}^{-1}$  was constructed by chronoamperometry (Fig. 3B), where a linear response was observed in the studied range (Fig. 3C). In addition, the sensor was evaluated in the determination of AA present in effervescent tablets, with the quantification being done by standard addition

method. A correlation of 98.95% was obtained between the AA value calculated by the electrochemical measurements with the proposed electrode and the value described in the drug label. Therefore, Raman characterizations have proved to be effective and fundamental for the evaluation and development of a low-cost electrochemical sensor with recycled PET and graphite.

### References:

- [1] N. D. Orekhov et al., *Carbon*, **87** (2015), 358-364.
- [2] P. Rizzo et al., *Macromol. Chem. Phys.*, **219** (2018), 1700362.
- [3] F. Awaja et al., *European Polymer Journal*, **41** (2005), 1453-1477.

### Acknowledgments:

Centro de Microscopia Eletrônica of the Universidade Federal do Paraná.

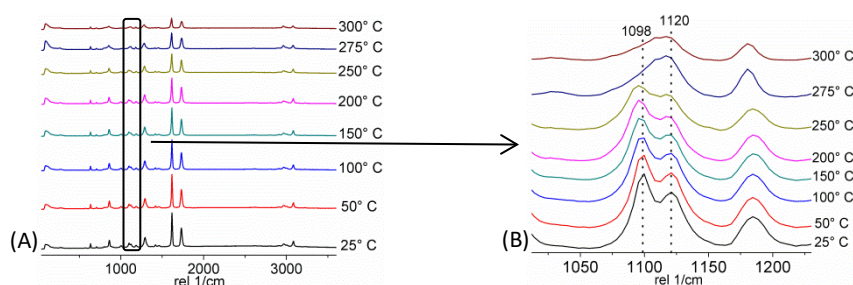


**Fig. 1** - Raman spectra obtained between 25 and 300 °C for (A) PET. (B) Detail of the region around the bands 1098 and 1120 cm<sup>-1</sup>.

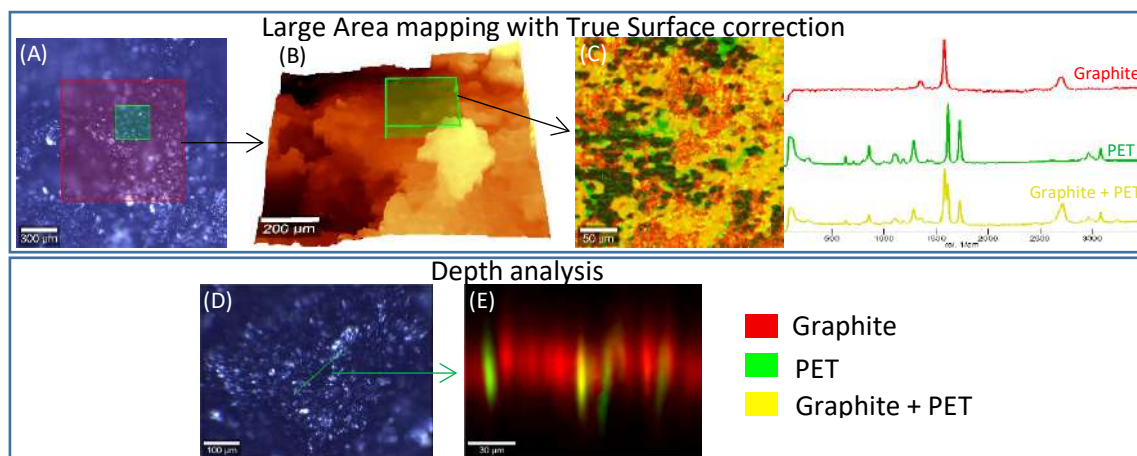


**Fig. 2** - Analyses of the PET mixture with graphite: (A) Optical image, (B) surface of the material obtained with the True Surface tool, (C) Raman mapping in Large Area with the indication of the spectra corresponding to each color. (D) Optical image and (E) Raman mapping in depth. Line length: 150 µm.

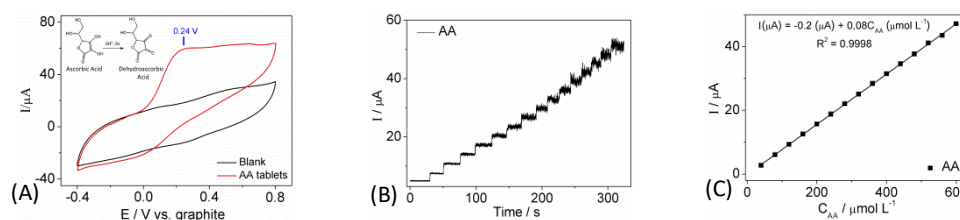


**Fig. 3** - (A) CV obtained in the absence (blank) and presence of 1.0 mmol L<sup>-1</sup> AA. (B) Analytical curve obtained by chronoamperometry for AA between 40.0 and 600.0 µmol L<sup>-1</sup>. (C) Calibration curve constructed with the current values measured in B.

## **Interface Analysis of ASME SA516-70 / Inconel 625 Bimetal Plate Obtained by Explosion Welding Employing Atomic Force Microscopy**

Gabriel Nogueira Rodrigues<sup>1\*</sup>, Tamires de Souza Nossa<sup>2</sup> and Bruno Fernando Gianelli<sup>3</sup>

<sup>1\*</sup>Discente, Engenharia Mecânica/Instituto Federal de Educação, Ciência e Tecnologia de São Paulo, Itapetininga - SP, Brasil – [nogueiragabrieltr@gmail.com](mailto:nogueiragabrieltr@gmail.com)

<sup>2</sup>Docente, Engenharia Mecânica/Instituto Federal de Educação, Ciência e Tecnologia de São Paulo, Itapetininga - SP, Brasil.

<sup>3</sup>Docente, Engenharia Mecânica/Instituto Federal de Educação, Ciência e Tecnologia de São Paulo, Itapetininga - SP, Brasil.

Explosion welding is a process capable of uniformly bonding different metal alloys over a large area. The detonation of an explosive material causes a violent collision between the plates to be bounded, this collision is responsible for the welding of the pieces. Over the years, the parameters improvement grant the uplift of the welding and allowed the union of several different kinds of alloys, a fact uncommon in other welding processes. Given that important metallurgical phenomena, that has process influence, occur in the micrometric and nanoscale, the microscopic analysis is a relevant characterization to these materials. The literature review constantly presents studies involving Transmission Electron Microscopy [1],[3], but this technique demands a high degree of quality on samples preparation and a high equipment cost, difficulting to replicate the studies. Characterization using Scanning Electron Microscopy are also frequently found, however, such ones has focus on micrometric scale analyzes. The present work aimed to analyze the bimetal plate interface, ASME SA516-70 / Inconel 625, using Atomic Force Microscopy, a technique that has a lower degree of difficulty in the preparation of samples and resolution of nanometric order [2], to study the maximum plastic deformation region caused by the explosion. Samples were cut and inlay for metallographic preparation, which consisted of sanding using water grit, from #100 to #2400, and polishing with synthetic diamond paste of 3, 1 and  $\frac{1}{4}$   $\mu\text{m}$ . After preparation, the samples were chemically attacked using 2% solution of nitric acid in alcohol for 5 seconds. Atomic force microscopy was performed using the non-contact mode into a Shimadzu-SPM 9700 microscope, with the tips Nanosensors type PPP-NCHR-50, and the image processing was made at Gwyddion v5.1 software, with 1D FFT correction, to remove data noises. Was observed an area of approximately 1  $\mu\text{m}$  where the morphology and the roughness have significant alteration in comparison to the neighboring regions, being able to defined as the maximum plastic deformation region, due to the fact that the residual tension present in the interface of the welding, facilitates the chemical attack, distinguishing itself from the neighboring regions that do not have the same level of residual tension. Different chemical attack parameters will be employed in future works in order to study the microstructural behavior of the interface.

### **REFERENCES**

- [1] CHU, Qiaoling et al. Experimental and numerical investigation of microstructure and mechanical behavior of titanium/steel interfaces prepared by explosive welding. *Materials Science and Engineering: A*, v. 689, p. 323-331, 2017.
- [2] EATON, Peter; WEST, Paul. *Atomic force microscopy*. Oxford university press, 2010.
- [3] GREENBERG, B. A. et al. The problem of intermixing of metals possessing no mutual solubility upon explosion welding (Cu-Ta, Fe-Ag, Al-Ta). *Materials characterization*, v. 75, p. 51-62, 2013.



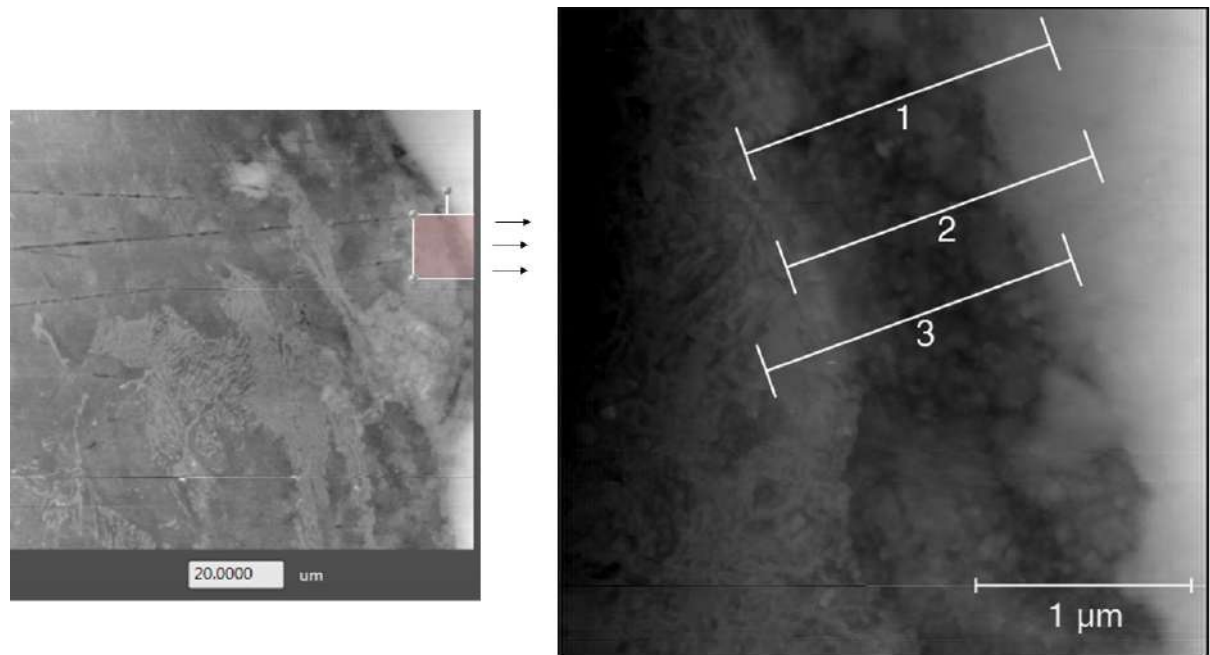


Figure 1: 20x20  $\mu\text{m}$  analysis (left) and 3x3  $\mu\text{m}$  analysis focused on the transition between metals (right).

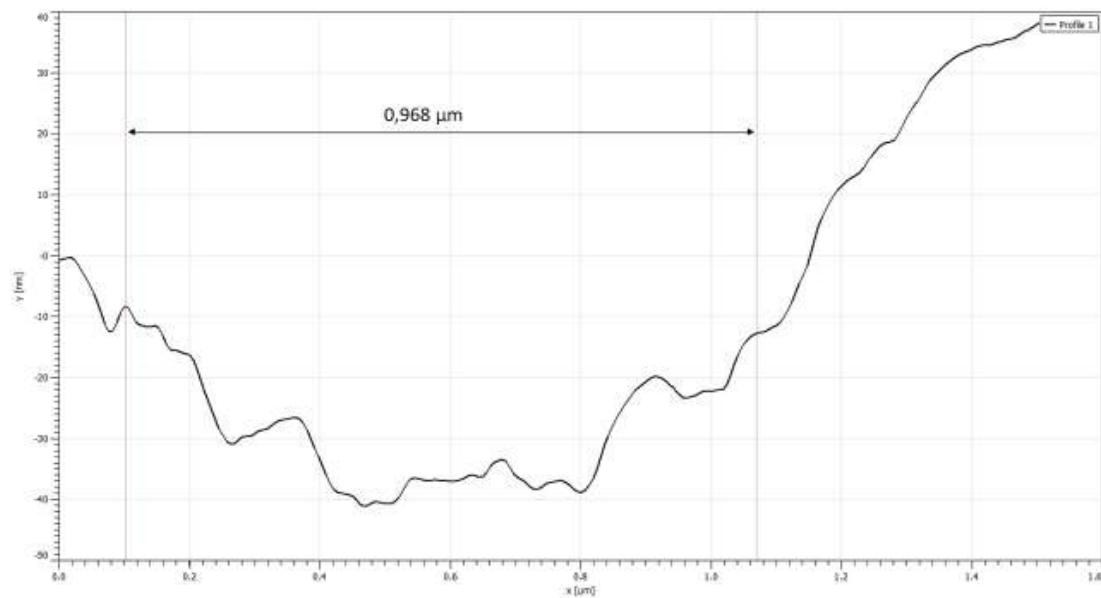


Figure 2: Variation of the roughness along the line 1 drawn in the image of 3x3  $\mu\text{m}$

Line	Distance between the roughness transition ( $\mu\text{m}$ )
1	0,968
2	0,944
3	0,975

Table 1: Distance between the roughness transition of the lines drawn in the 3x3  $\mu\text{m}$  image.

## Control of the Electromechanical Properties of Transition Metal Dicalcogenides

Maurício V. Bessa<sup>1\*#</sup>, Wellington D. de Freitas<sup>1</sup>, Natalia Neme<sup>1</sup>, Mário S. de C. Mazzoni<sup>2</sup>, Matheus J. de S. Matos<sup>1</sup>, Bernardo Ruegger A. Neves<sup>2</sup>, Ana Paula M. Barboza<sup>1</sup>

<sup>1</sup> Departamento de Física, Universidade Federal de Ouro Preto. Ouro Preto, BR.

<sup>2</sup> Departamento de Física, Universidade Federal de Minas Gerais. Belo Horizonte, BR.

\*Centro de Microscopia Universidade Federal de Minas Gerais. Belo Horizonte, BR.

#Corresponding author e-mail: [mauriciobessa@outlook.com](mailto:mauriciobessa@outlook.com)

Two-dimensional transition metal dichalcogenides (TMDs) are an emerging class of materials with exquisite properties that make them highly attractive for fundamental studies of novel physical phenomena and for applications ranging from nanoelectronics and nanophotonics [1]. TMDs are semiconductors of the type  $\text{MX}_2$ , where M is a transition metal atom (such as Mo or W) and X is a chalcogen atom (such as S, Se or Te), provide a promising alternative. This work investigates some electromechanical properties of TMDs using Scanning Probe Microscopy techniques and first principles calculations, based on the Density Functional Theory (DFT) formalism. Theoretical calculations predict that the approximation of the TMDs layers, or hydrogenation of these materials, could lead to the reduction of their energy gap. We performed Electric Force Microscopy (EFM) measurements on single and few-layer in different TMDs to investigate this gap closure. EFM is a dual-pass technique: during the first pass, the AFM topography image is recorded in intermittent-contact mode. Then, the probe is retracted from the surface by a vertical shift, a DC bias is applied between tip and sample and scanning is repeated following a path similar to the original topographical one, but vertically shifted. The shifts  $\Delta\omega$  on the cantilever oscillation frequency can occur either due to variations of the tip-sample capacitance or to local changes of the sample charge distribution, which are, then, acquired to form the EFM image. We observe a compression-induced charging increase of bilayer and few-layers of TMDs. The results show that there are two transition mechanisms: the first occurs at low forces ( $F < 200$  nN) and its magnitude is reduced by the partial evaporation of the water layer. The second transition occurs at higher forces ( $F > 400$  nN) (Figure 1). Figure 2 resumes the experimental results.

[1] S. Manzeli,, D. Ovchinnikov, D. Pasquier, O. V. Yazyev, A. Kis, Nature Reviews Materials. 2 (2017) 17033.

#### Acknowledgement

We acknowledge financial support from the Brazilian agencies FAPEMIG and CAPES. Luiz Gustavo P. Martins (MIT – Cambridge, USA) and Ingrid Barcelos (LNLS – Campinas, BR) acknowledge by providing the sample.

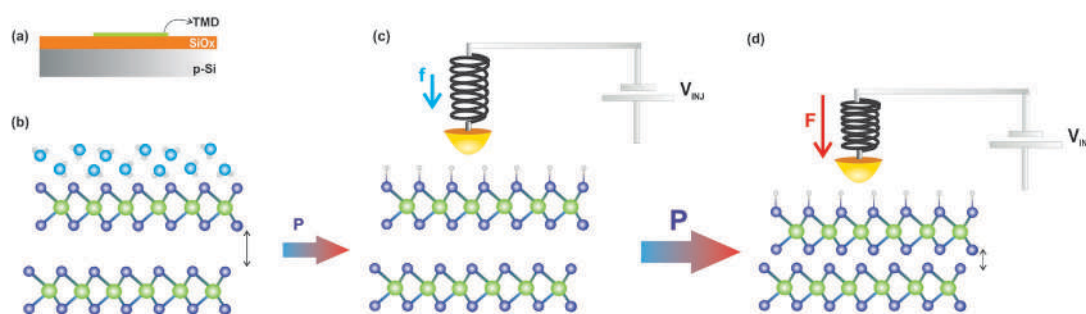


Figure 1 – Schematic representation of the experimental setup

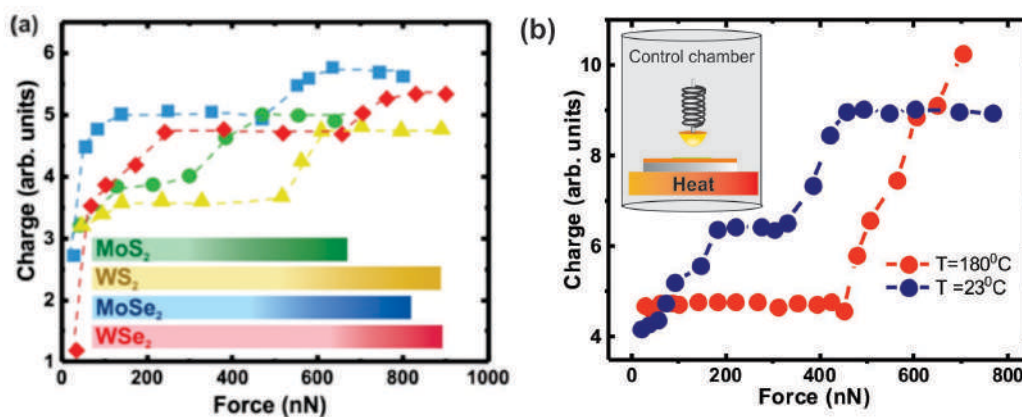


Figure 2 – (a) The effect compressive force in the different TMDs. (b) Temperature effect.



## **Development Of Chitosan-Coated Liposomes For Octylmethoxycinnamate Encapsulation Applied In Sunscreen Formulations**

Natália Ruben Castro<sup>1\*</sup>, Cristal dos Santos Cerqueira Pinto<sup>1</sup>, Cláudia Regina Elias Mansur<sup>1</sup>

<sup>1</sup> Universidade Federal do Rio de Janeiro, Instituto de Macromoléculas, RJ, Brazil

\*e-mail: nataliacastro@ima.ufrj.br

Nanotechnology has great importance in the development of new drugs and cosmetic formulations, since nanomaterials can act as carriers promoting the controlled release of active substances [1]. In cosmetics, these nanocarriers act as protection for the encapsulated active, avoiding possible irritations caused by direct contact with the skin, and, specifically in photoprotectors, contribute to the improvement of sunscreens photostability, skin permeation control and increase the efficacy of these products [2]. Liposomes are a promising alternative to carry different actives and are advantageous for biocompatibility and low toxicity, however, the low stability can lead to leakage of the encapsulated active [3]. For this reason, the objective of this work was to develop and characterize liposomes coated by the cationic polymer of chitosan to encapsulate octylmethoxynamate, aiming to obtain systems with good stability and potential for application in a photoprotective formulation. First, different liposomal systems were developed by the pre-dispersion method, from the active mixture with a pre-dispersion of phosphatidylcholine, polysorbate (tween®) 80 and trishydroxymethylaminomethane buffer solution (pH 6.8) under magnetic stirring. The composition and stability of the vesicles were evaluated by Dynamic Light Scattering (DLS) and Scanning Electron Microscopy (SEM). The effect of the incorporation of surfactant (Tween® 80) at different concentrations was evaluated, in which reduction of vesicle size was observed with increasing surfactant concentration. The best stability system was selected and proceeded to the coating step, in which the liposomal dispersion was poured into chitosan solution and kept under stirring. The results indicated the obtaining of the coated liposomes with good stability and the efficiency in the encapsulation of the active, with potential to compose a photoprotective formulation, aiming at future studies of permeation.

### **REFERENCES**

- [1] Bajwa SZ, Munawar A, Khan WS. Pharm Bioprocess. 5(2), 11–5 (2017).
- [2] Sebaaly C, Charcosset C, Stainmesse S, Fessi H, Greige-Gerges H. Carbohydr Polym. 138, 75–85 (2016).
- [3] Coutinho C, Santos E, Mansur C. Journal of Nanoscience and Nanotechnology. 15, 1–10 (2015).
- [4] This research was supported by CAPES (Finance Code 001), CNPq and Faperj (Brazil).



## **Different Samples Preparation Method for Electron Microscopy Assisting the Comprehension of Vanadium Nanostructures. What can be seen inside the particle?**

Carla Ramos Moreira\*, Bruna B. Pozes and Andréa M. Duarte de Farias

INT-National Institut of Technology/CENANO-Nanotechnology Characterization Center, Rio de Janeiro, Brazil; \*carla.ramos@int.gov.br

Because of their unique properties, nanostructured catalysts represent an immense potential for application in industrial and laboratory processes and can make catalytic systems more efficient. Electron microscopy represents a crucial tool in understanding and monitoring the formation of these structures. The sample preparation step is extremely important and varies according to the chemical composition and morphology of the sample. In this context, different methodologies were used with vanadium microspheres (ME) samples to establish protocols and obtain necessary information for mapping the interior of the nanostructures: hollow microspheres, massive microspheres, core-shell microspheres and flower-like microspheres. It is interesting to note that, although well published, it is not easy to find full details about the catalytic behavior of these structures. Samples were analyzed by electron microscopy at CENANO/INT using both a Field Emission Gun Scanning Electron Microscope (SEM-FIB) operating from 5-30kV, equipped with an ion beam FEI/Thermo Fischer Helios Nanolab Dual Beam G3 GX; and a Field Emission Gun Transmission Electron Microscope (TEM) operating at 200kV FEI/ThermoFischer Tecnai G2 F30. The sample preparation consisted of some different comparative procedures: 1) support the sample (dispersed or powder) in a holey carbon covered Cu; 2) polishing procedure; 3) fractured at very lower temperatures; 4) embedded sample in Spurr's resin followed by sectioning in ultra-thin sections (range: 80-100 nm) in an ultramicrotome (PT-PC/ RMC Boeckeler) using a diamond knife; and 5) FIB. The micrographs obtained by dispersing the sample in isopropyl alcohol produce agglomerated particles despite the sonication step and therefore resulted in lack of transparency to the transmitted electron beam, making MET analysis difficult. Without the use of solvent, direct dispersion of the sample in the microscopy grid revealed finer and dispersed particles, enabling TEM analyses. However, to observe the inner side of spherical particles, these methodologies did not provide adequate results, pointing to sample preparation through ultramicrotomy or FIB sectioning. Considering the cutting with the ion beam and refining, the preparation using SEM-FIB could be very laborious. According to the literature, it is possible to perform a simpler cut using SEM-FIB [1], however, it is necessary to protect with Pt, otherwise the microspheres can be damaged, mainly inside it. Also, during the cut, part of the sample can be dragged by the beam towards the void parts of the spheres, misleading observation. Ultramicrotomy showed great potential in processing these  $V_2O_5$  microspheres. The ultra-thin sections resulting from the cross-section of a resin-embedded sample, allowed the observation of some hidden characteristics of the sample core. So far, these were unknown details, the unveiling of this data offers the opportunity of studying especially the inner face of the microspheres, including the core-shell nucleus that present vanadium nanoparticles on the surface or flower-like structures inside it.

### **REFERÊNCIAS**

- [1] L. Barner et al., J. Polymer Sci.: Part A: Polymer Chem. 42 (2004) 5067.

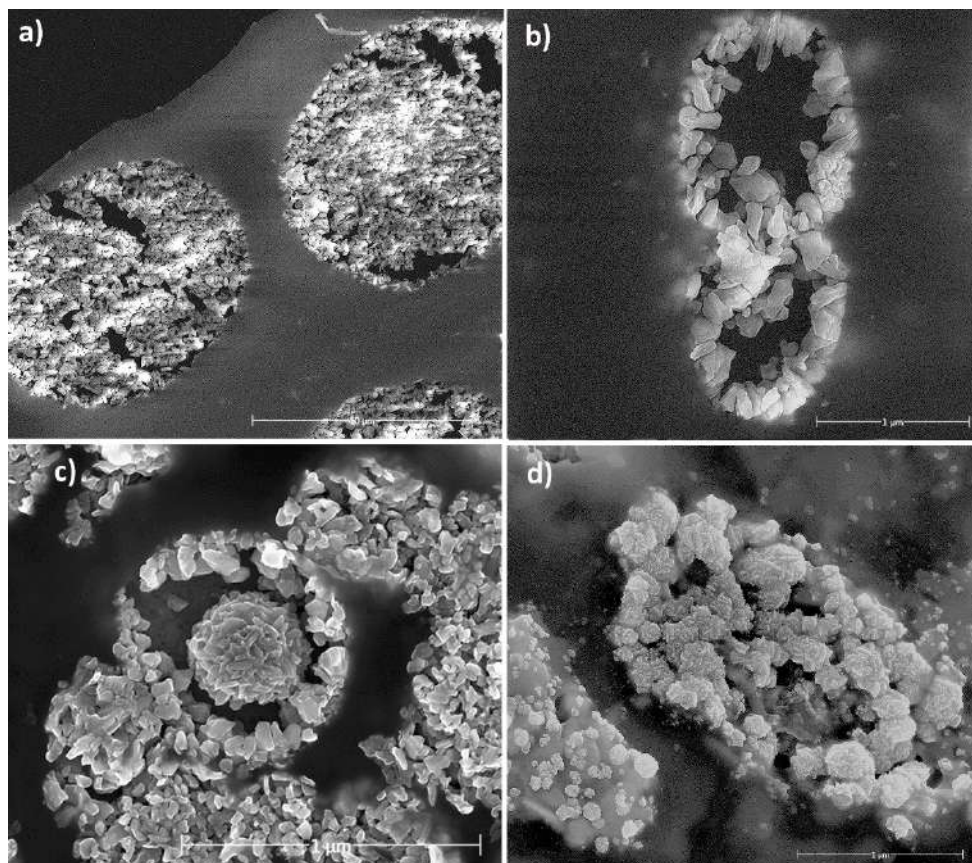


Figure 1 – SEM micrographs of the cross-sections of different synthesized  $\text{V}_2\text{O}_5$  microspheres unveiling their interior: a) massive, b) hollow, c) core-shell and d) flower-like. The scale bar of (a) is 10  $\mu\text{m}$ . The scale bars of (b)-(d) are 1  $\mu\text{m}$ .

## Design of ZnO structures: growth and formation mechanism determined from the correlation of morphological, structural, vibrational and optical properties

M. Montero-Muñoz<sup>1\*</sup>, J. E. Ramos-Ibarra<sup>1-2</sup>, Cecibel M. L. Felix<sup>3</sup>, G. E. Marques<sup>4</sup>, M. D. Teodoro<sup>4</sup>, J. A. H. Coaquira<sup>1</sup>.

<sup>1</sup>. Institute of Physics, University of Brasilia, 70910-900 Brasília - DF, Brazil

<sup>2</sup>. University Center Estácio Brasília, 72035-509 Brasília – DF, Brazil

<sup>3</sup>. Institute of Biological Sciences, University of Brasilia, 70910-900 Brasília - DF, Brazil

<sup>4</sup>. Department of Physics, Federal University of São Carlos, 13565-905 São Carlos- SP, Brazil

### ABSTRACT

Nanostructured systems show novel electrical, optical and chemical properties, which are notoriously different from their bulk counterpart. Among the nanostructured systems, zinc oxide (ZnO) has been of interest due to the wide band gap energy ( $E_g \sim 3.4$  eV), large exciton energy at room temperature ( $\sim 60$  meV) and good electrical properties which could be used in a wide range of applications, such as sensors, solar cells and photodegradation of organic pollutants[1-3]. Several approaches have been developed to prepare ZnO powders, such as sol-gel, microemulsion, thermal decomposition of organic precursor, spray pyrolysis, electrodeposition, ultrasonic, microwave-assisted techniques, chemical vapor deposition, hydrothermal and precipitation methods, obtaining different properties, morphologies and sizes.

In this work, a shape-selective preparation method was used to obtain highly crystalline ZnO rod-, needle-, nut- and donut-like structures with distinct morphologies, particle sizes, and surface areas. We study nucleation and growth mechanism of those structures and the influence of physicochemical parameters—such as the synthesis-solvent and the pH condition of the solution—on the morphology and the structural and optical properties. Our results indicate that the needle- and rod-like morphologies are established due to the crystal growth direction and the occurrence of crystalline defects, such as oxygen vacancies and interstitial Zn located at the surface. A clear correlation between the growth rate along the c-axis and surface defects was also established. Based on the experimental results, growth mechanisms for the formation of ZnO structures were proposed, Fig.1. We believe this synthesis method will be readily adopted in realizing different shapes for various materials and for specific applications.

**Keywords:** ZnO structures, ZnO synthesis, morphology control, shape control, growth mechanisms.

1. Teke, A. et al. *Physical Review B* **2004**, 70 (19), 195207.
2. Zhang et al. *Journal of Catalysis* **2015**, 331, 57-62.
3. Montero-Muñoz, M. et al. *Applied Surface Science* **2018**, 448, 646-654.



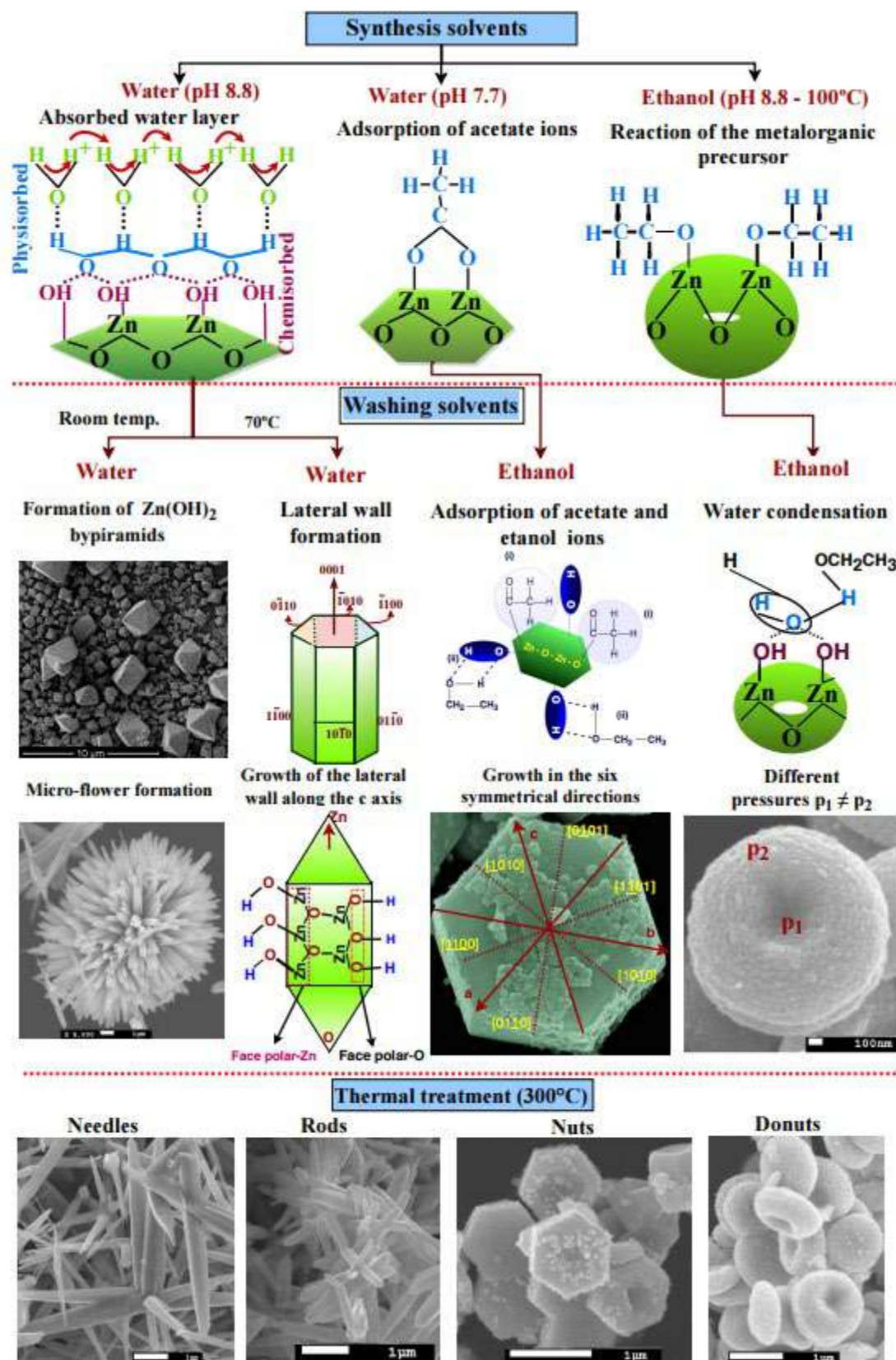


Figure 1. Schematic representation of the growth mechanisms of zinc oxide nanostructures using different synthesis solvents and washing agents.



## Synthesis of Supported Nickel Catalysts in Yttria-Modified by Alumina Characterized by Electron Microscopy for H<sub>2</sub> Generation

Lídia O.O. da Costa<sup>1\*</sup>, Vanderson V. Gonçalves<sup>1-2</sup>, Eduardo J. N. Souza<sup>2</sup>,

Marcos A. Silva<sup>3</sup>, Carla R. Moreira<sup>1</sup> and Fábio B. Noronha<sup>1</sup>

\* lidiaaloazem@gmail.com

<sup>1</sup>. Instituto Nacional de Tecnologia, Rio de Janeiro, Brasil

<sup>2</sup>. Universidade Federal Fluminense/ Engenharia Química, Rio de Janeiro, Brasil

<sup>3</sup>. Universidade Federal do Rio de Janeiro/ COPPE/PEQ-NUCAT, Rio de Janeiro, Brasil

Ni-based catalysts are more widely studied due to its high activity and low cost for conversion reactions of ethanol to hydrogen. A previous contribution was found by TEM/HRTEM/FFT, in the nickel catalyst supported in yttrium oxide, obtained by calcination of nitrates at high temperatures, the phase NiY<sub>3</sub>. It was verified by the TPR analyse that this phase was not reducible and led to low catalyst activity [2]. In this contribution, nickel catalysts were prepared supported in yttria modified by alumina in (2YAL) molar ratio. Two methodologies were adopted: .co-precipitation of the nitrate solutions with excess ammonium hydroxide solution being 12 the final pH of the solution and the support obtained by the precipitation of the nitrates solutions with control of pH, 8-7, aiming that nickel precipitation occurs in the isoelectric point (pi) of yttria. The supports were impregnated to have 15% Ni. The objective of this contribution was to control the formation of the metallic phase and the particular metallic size of the nickel, in order to reduce the catalytic deactivation. Electron microscopy was associated with other techniques to characterize Ni/2YAl\_pH12, Ni/2YAl\_ pH 8, Ni/2YA\_ pH 7. The formation of the crystallographic phases present in the reduced catalyst was started by the XRD analyses, where the characteristic lines of Y<sub>2</sub>O<sub>3</sub> and Ni were found for all catalysts, seeing that Ni-2YAL\_pH 8 presented more crystalline than the others.. Fig. 1 a. TPR analysis for Ni\_2YAl\_pH12, two regions were identified referring to the presence of phases NiO and Ni/Al<sub>2</sub>O<sub>4</sub> reducible at high temperatures. The particle size of nickel of Ni-2YAl\_pH 12 was obtained through the TEM images, Fig.1b, it was calculated the average particle diameter 3,3 nm agreeing with the results of XRD. However, for the Ni-2YALpH 7 the images presented a small contrast being difficult to find particles of nickel in yttria by this mode of operation, Figura 2a. HRTEM/FFT images of Ni-2YALpH 7 shows the presence Al<sub>2</sub>O<sub>3</sub> and a particle with darker contrast of Yttrium, Fig 2b. The reaction residues were analyzed by SEM/FEG showing the presence of filamentous carbon, Fig.3a. For SEM/ STEM the nickel metal particle was located in the residue of

the reaction Fig 3b. Our results suggest that the pH of the precipitation does not change significantly the size of nickel particle, but favors nickel precipitation in yttria, justifying the best performance of Ni/2YALpH 8 in ethanol conversion to  $H_2$  (not shown).

## REFERENCES

- [1] L.V.Mattos et al., Chemical Reviews. 112 (2012) 4094.  
[2] L.O.O.Costa et al., Characterization of Yttrium supported nickel catalysts by TEM/HRTEM used the reaction of hydrogen generation, In Anais in XXIII Congresso da Sociedade de Microscopia e Microanalise, 2011.

Acknowledgements :The authors thank the CNPq and Capes the financial support and LABNANO for the used the TEM

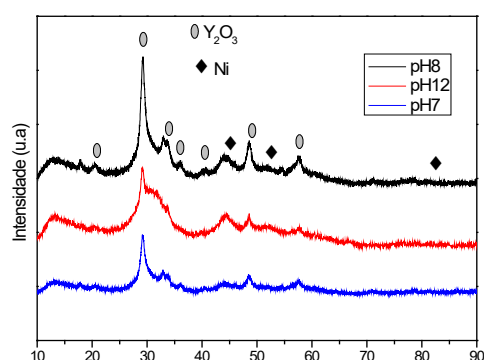


Figure 1 XRD of the catalysts

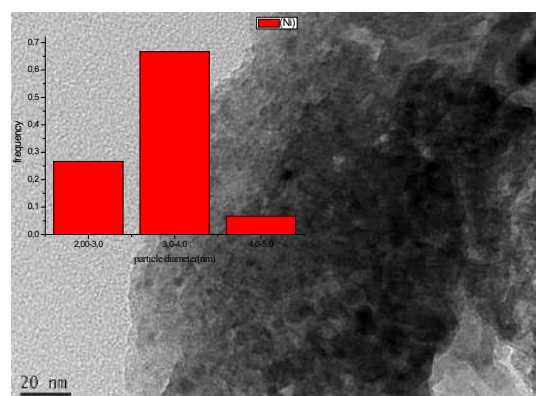


Figure 2 TEM Image of the/2YAL\_pH 12

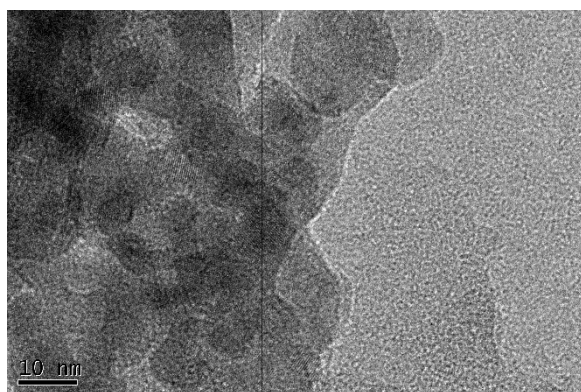
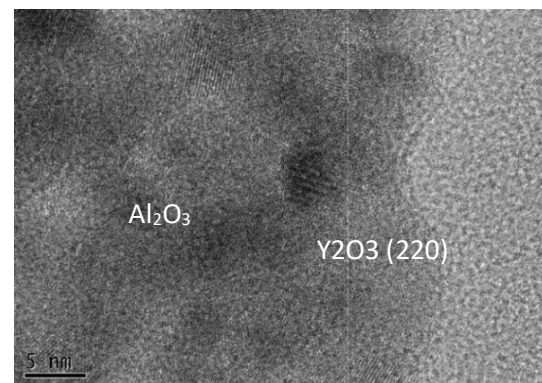


Fig 3 Ni/2YAL pH 7 a)- TEM image



b) HRTEM image

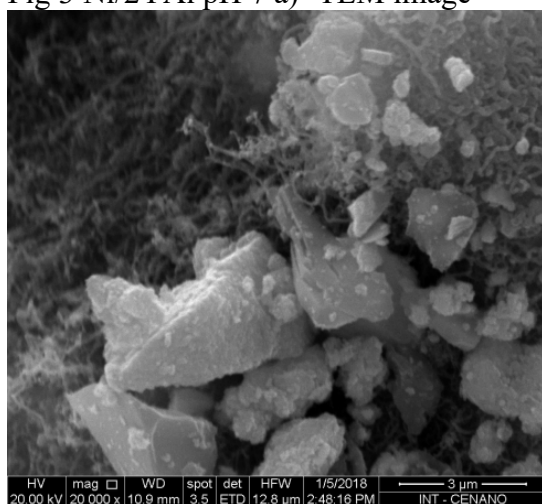


Fig. 3 Residues: a) SEM -image Ni/2YALpH 8



b) SEM-STEM -Image Ni/ 2YAL pH 7

## S(TEM) Preliminary Characterization of a Cs-P-V-W-O Mixed Pyrochlore Oxide.

Yordy E. Licea<sup>1\*</sup>, Jacques Werckmann<sup>2</sup>, Jean G. Eon<sup>1</sup>

<sup>1</sup> Instituto de Química, Departamento de Química Inorgânica/Universidade Federal do Rio de Janeiro, Rio de Janeiro, Brasil. \*ylicea@iq.ufrj.br

<sup>2</sup> Centro Brasileiro de Pesquisas Físicas, Rio de Janeiro, Brasil

The pyrochlore oxides have been studied for years due to their magnetic, electric and catalytic properties. As a matter of fact, they have several technological applications as fuel cell electrodes, superconductors and catalysis [1]. In this work a new composition of a bronze pyrochlore structure has been obtained from a thermal treatment of a previous hydrothermal synthesized precursor. This method has an energetic economic advantage over the usual high-temperature solid reaction for the synthesis of this material, even more, it is promising in the further control of particle distribution and morphology, which is fundamental in catalysis. The XRD pattern match the ICSD 18091 solved for the CsVWO<sub>6</sub> and IR spectrum also shows the typical band in the structural region (~400-1200 cm<sup>-1</sup>). The crystal structure has the pyrochlore cubic phase (space group Fd-3m) and S(TEM), see Figure 1, has proved the homogeneous distribution of metal in the structure studied. The SADP, Figure 1D, of the selected region is typical of polynanocrystals. In fact they are situated in a rod-like structure which in turns forms a rectangular base prism (Figure 1 A.)

This is a disordered structure since tungsten and vanadium atoms could have different occupancy in the same crystallographic sites, however, the P atoms position in the crystallographic structure of the compound synthesized in this study is still under analysis. It seems not to correspond to the already reported monophosphate tungsten bronzes A<sub>x</sub>(PO<sub>2</sub>)<sub>4</sub>(WO<sub>3</sub>)<sub>2m</sub>, or diphosphates tungsten bronzes A<sub>x</sub>(P<sub>2</sub>O<sub>4</sub>)<sub>2</sub>(WO<sub>3</sub>)<sub>2m</sub> where P occupies different position depending on *m* [2]. Indeed, the V and P forms lost of different compounds that have also interesting properties.

It is clear that doing a HR-S(TEM) and also taken EELS spectrum to better study the P symmetry and coordination is critical at this stage of the study.

## REFERÊNCIAS

- [1] F. Polo-Garzon et al., J. Catal. 340 (2016) 196.
- [2] P. Roussel et al., Acta Cryst. B57 (2001) 603.
- [3] The authors acknowledge o LABNANO/CBPF and CNPq for the support.

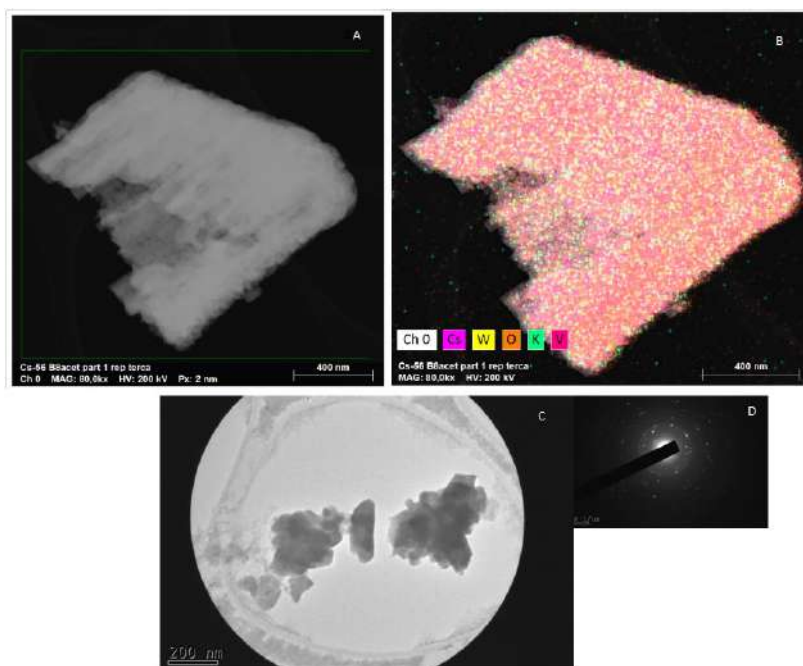


Figure1. S(TEM) Image of a pyrochlore Cs-P-V-W-O fragment (A) and it EDS mapping (B). A selected area (C) and its SADP (D)



## SEM and TEM Characterization of Titanium Oxides Recovery from Tailing of Magnetite Concentration

Aimée M. Valente<sup>1\*</sup>, Eduardo A. Brocchi<sup>2</sup> and Guillermo Solórzano<sup>2</sup>

<sup>1</sup>. Department of Chemical Engineering/ Amazonas State University, Manaus, Brazil.

<sup>2</sup>. Department of Chemical and Materials Engineering/ PUC-Rio, Rio de Janeiro, Brazil.

\* Corresponding author: aimee.valente@gmail.com

Brazil is one of the world producers of materials containing vanadium in the form of its most common oxide,  $V_2O_5$ , which occurs in association with magnetite [1]. Its industrial production process has as its first step the concentration of this mineral, where a large amount of tailings is generated. Materials with these characteristics can provide a source for the recovery of titanium by chemical processes that enable the selective separation of its constituents [2,3]. In order to become part of these residues a commercial product, present project becomes to characterize the material received, process it to make possible the Ti concentration, in the form of  $TiO_2$ , by increasing the initial content, between 5 and 15%, to marketable levels. The received material characterized by scanning electron microscopy (SEM Hitachi TM3000), and diffraction x-ray (DR-X Bruker AXS, model D8-Discover), to identify the morphology, structure and chemical aggregation of the residue by systematic analysis of representative samples. The final product was also characterized by SEM, DR-X and besides with transmission electron microscopy (TEM/STEM – JEOL 2100F), once the SEM results showed grains significant size reduction. The received material was then treated with sodium carbonate at kiln and after lixiviated with water then with diluted HCl to obtain a final product, expected to be some titanium oxide. The SEM images for received material reveal distinct grains morphologies and different phases in a single grain, as shown in Figure 1a. DR-X analysis of this material reveal presence of ilmenite, anatase and rutile, besides other complexes as tremolite and clinocllore IIb-2, shown in Figure 2a. Knowing the results from DR-X, using EDS was possible identify most part of the sample particles as multifaceted silicates containing low amounts of titanium and ilmenite grains. After processing the initial sample, results of SEM showed reducing of particle size, Figure 1b, when compared by EDS. Results indicated titanium and calcium concentrate increased as well as iron, aluminum and magnesium concentrate decreased, shown in Figure 3, Figure 4a and Figure 4b. DR-X results confirmed the presence mostly of titanium and calcium, Figure 2b, as perovskite ( $CaTiO_3$ ) as only crystalline product. TEM analysis, showed amorphous particles around 3  $\mu m$ , Figure 5a and 5b, and crystalline particles around 200 nm, mutlicrystalline, Figure 5c and 5d, and monocrystalline, Figure 5e and 5f. Comparing all results characterization of final product, it can be assumed that the other elements detected (mainly Fe, Al, Si) formed amorphous phases in the final product. The production of titanium oxides from tailing of magnetite concentrate is possible, although initial suspicions that silicon removal is the principal challenge were confirmed for the chosen process [4].

### REFERENCES

- [1] Departamento Nacional de Produção Mineral, SMB. 36 (2016).
- [2] G. Alkan et al., A mineralogical assessment on residues after acidic leaching of bauxite residue (red mud) for titanium recovery, 7 (Metals) (2017) 458.
- [3] F. Habashi, Handbook of Extractive Metallurgy II. Wiley-VCH, Weinham, 1997.

[4] The authors are grateful to Labnano- CBPF for access to the laboratories and to CNPq (Brazil) for financial support.

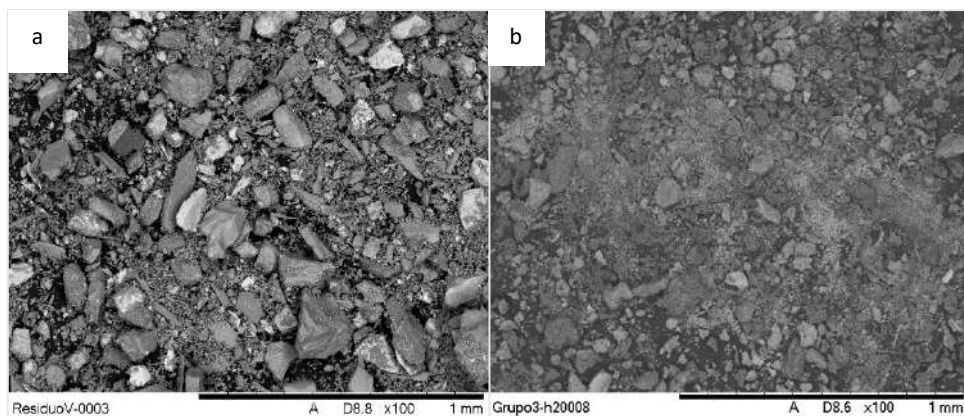


Figure 2 – SE image of a large area (a) material received and (b) final product.

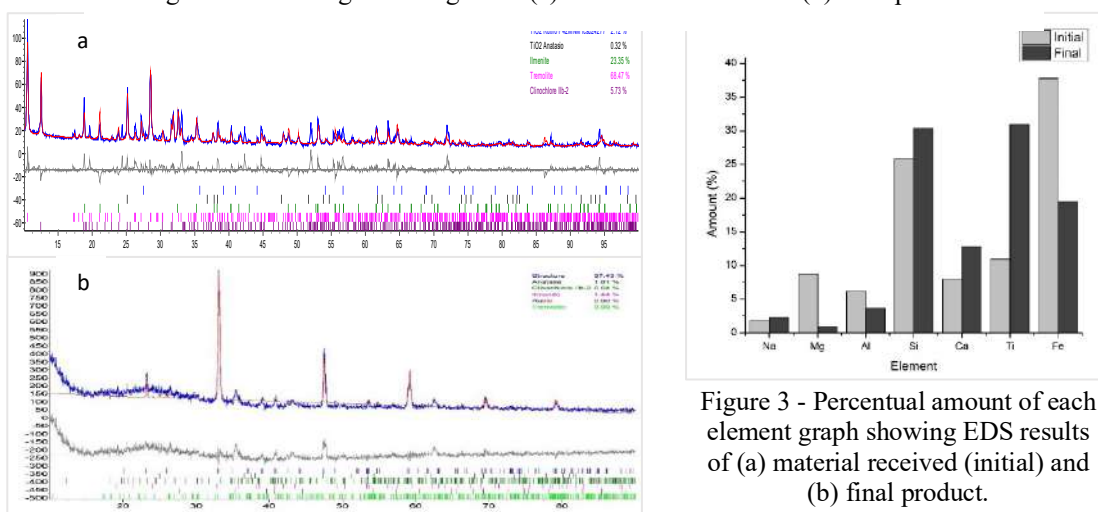


Figure 3 - Percentual amount of each element graph showing EDS results of (a) material received (initial) and (b) final product.

Figure 1 –X-ray diffractograms of (a) material as received and (b) final product.

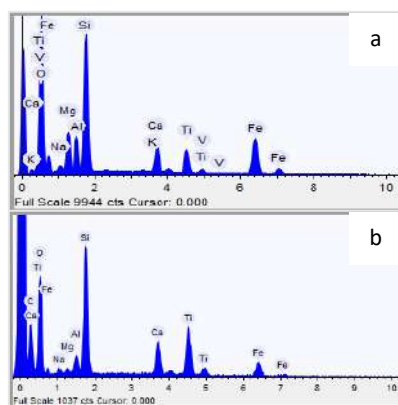


Figure 4 – EDS spectrums of (a) material received and (b) final product.

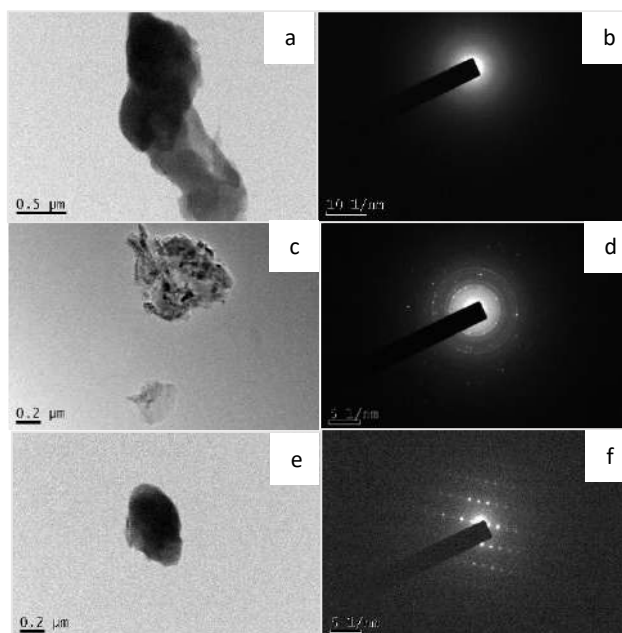


Figure 5 – MET images of (a) an amorphous particle, (c) a multicrystalline particle and (e) monocrystalline particle, and its respectively diffraction patterns, (b) amorphous particle, (d) multicrystalline particle and (f) monocrystalline particles.

## Grain Refinement and Residual Stress in an ASTM 201LN Austenitic Stainless Steel Cold Rolled and Reversion Annealed

Camila Oliveira Souza<sup>1</sup> and Andersan dos Santos Paula<sup>2\*</sup>

<sup>1</sup>. Seção de Engenharia de Materiais (SE-8), Programa de Pós-graduação em Ciência dos Materiais (PPGCM), Instituto Militar de Engenharia (IME), Rio de Janeiro – RJ, Brazil

\* andersan@ime.eb.br

Austenitic stainless steels are present in structural applications due to their high corrosion resistance, high performance when subjected to high temperatures, excellent ductility and weldability. In 300 serie steels, these properties are attributed to the introduction of nickel that stabilizes the austenitic structure, making it possible to obtain a material with different characteristics. Used in structural applications, 200 series austenitic stainless steels are the result of a partial replacement of nickel by manganese, aiming at a lower cost. The corrosion resistance of these alloys is lower than that of 300 series steels [1]. According to the chemical composition of austenitic stainless steels, they may exhibit a peculiar characteristic: stress or strain induced phase transformation. This effect is targeted because it gives the steel mechanical properties such as high strength, ductility and toughness [2]. This phenomenon is called TRIP (Transformation Induced Plasticity) effect. In cold working conditions, in which the material is plastically deformed generating the TRIP effect, the homogeneous deformation belonging to the austenitic phase results in the martensitic transformation. Therefore, the volumetric fraction of transformed martensite increases with increasing deformation [3]. In the last decade, there has been considerable attention in the development of ultrafine (submicron or nanometric) structures in order to obtain a combination of high strength and good ductility for applications in light structures [4]. In order to obtain this grain refinement, initially the martensitic transformation is promoted by means of a severe cold rolling and then the material is subjected to a heat treatment of annealing, which will reverse the martensite induced by austenite plasticity, which will result in a significant decrease in grain size. The study interest was motivated by recent results found in the literature, highlighting the works of REZAEI, MOALLEMI et al. and HAMADA [4-6]. Thus, a hot rolled and annealed at 1050 °C 201LN austenitic stainless steel was subjected to cold rolling with 8 reduction passes (10% reduction per pass) and annealed for 750 °C reversal for 15 minutes, in pilot scale, with the objective to observe grain refinement and residual stress after complete reversal [7]. Based on scanning electron microscopy analyzes, using backscattered electron detectors (BSED) and backscattered electron diffraction (EBSD), it was possible to show a significant grain refinement and presence of residual stresses distinctly in austenitic grains recovered from of the deformed austenite ( $\gamma_{\text{def}}$ ) and in the austenitic grains reverted from the martensite ( $\alpha'$ ) formed by TRIP effect.

### REFERÊNCIAS

- [1] OUTOKUMPU; Handbook of stainless steel (2013)18.
- [2] T. Iawamoto et al., Elsevier Science 40 (1998) 173.
- [3] B. Petit, International Journal of Plasticity 23 (2007) 323.
- [4] A. Rezaei, Mater. Sci. Eng. A 528 (2011) 5025.
- [5] M. Moallemi et al., Materials Letters 89 (2012) 22.
- [6] A.S. Hamada et al., Mater. Sci. Eng. A 628 (2015) 154.
- [7] This research was supported by CNPq (Brazil) using steel donated by APERAM South America.



Table 1: 201LN Austenitic Stainless Steel Chemical Composition (%wt) donated by APERAM South America.

C	Mn	Si	P	S	Cr	Ni	Mo	Al	Cu
0.0300	6.9078	0.3088	0.0381	0.0009	17.0043	4.0093	0.0188	0.0034	0.0239
Co	V	Nb	Pb	B	Ti	Sn	W	N	-
0.0463	0.0428	0.0224	0.0073	0.0006	0.0058	0.0029	0.0117	0.2000	-

Table 2: Martensite Quantification (%) from Ferritoscope probe.

Hot Rolled and Annealed at 1050 °C (As received)	Cold Rolled	Reversion Annealed (750 °C / 15 minutes)
0.12	27.32 ± 0.37	0.12

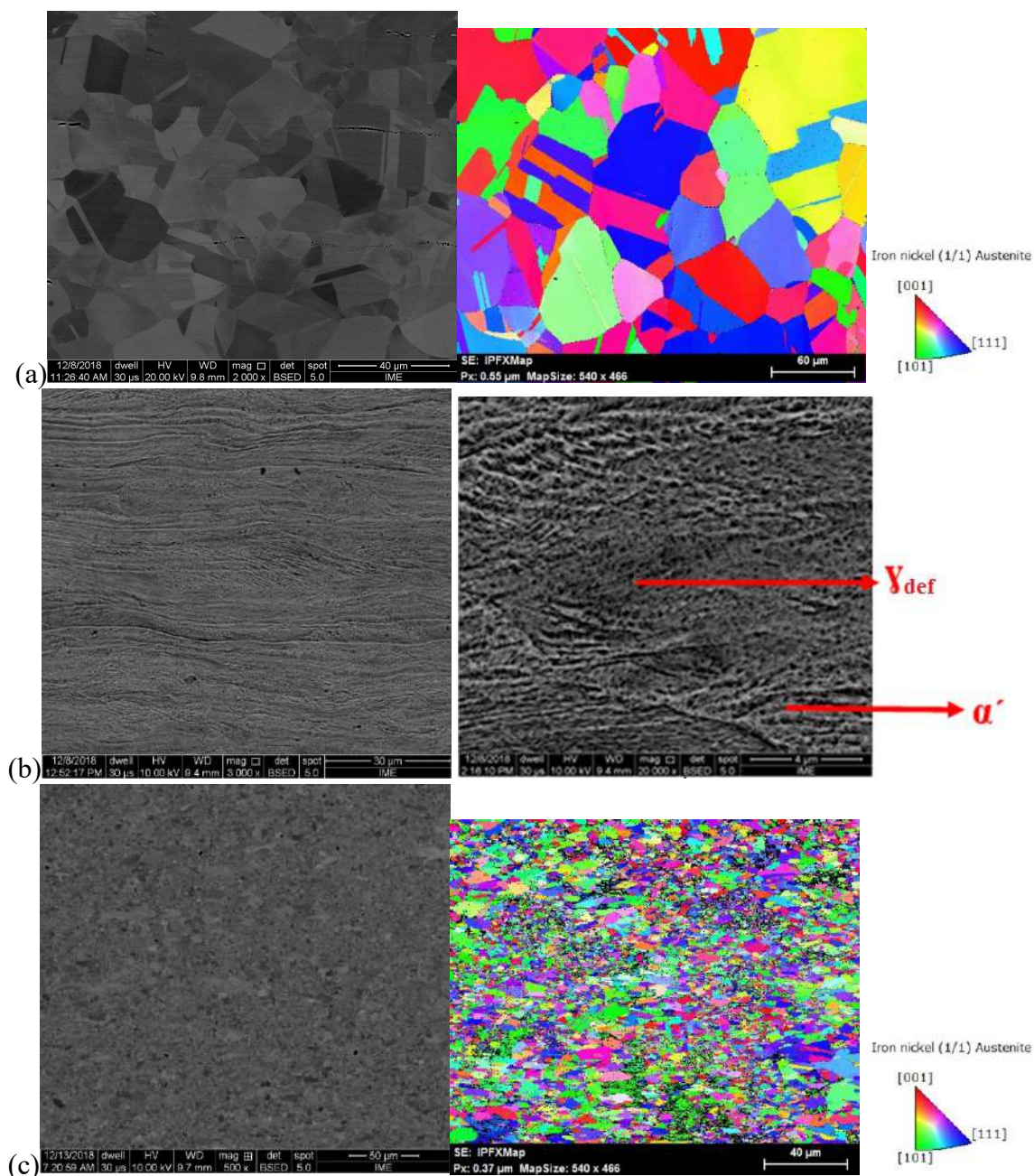


Figure: Scanning Electron Microscopy analyses associated to BSED and EBSD data from (a) hot rolled and annealed at 1050 °C – as received, (b) cold rolled and (c) reversion annealed at 750 °C / 15 minutes.



## Cryogenic Sample Preparation for Cryo-TEM of Metals by Ion Milling

Ricardo Sanson Namur<sup>1</sup>, Jefferson Bettini<sup>2</sup> and Osvaldo Mitsuyuki Cintho<sup>1\*</sup>

<sup>1</sup> Universidade Estadual de Ponta Grossa. Departamento de Engenharia de Materiais, Ponta Grossa, PR – Brazil.

<sup>2</sup> Centro Nacional de Pesquisa em Energia e Materiais (CNPEM), Laboratório Nacional de Nanotecnologia (LNNano), Campinas, SP – Brazil.

\* omcintho@uepg.br

Processing of metals by cryogenic plastic deformation is a well-known method for producing highly refined microstructures and promoting mechanical properties improvements, such as strength and ductility. The accumulation of crystallographic defects due to the partial suppression of dynamic recovery at very low temperatures is the main mechanism that explains this behavior [1-2]. Although many studies were performed to characterize cryogenic deformed metals, such studies were performed at room temperature, which may lead to the loss of information regarding the structure and substructure of defects due to the recovery and recrystallization of metals. In this context, a route for ion milling cryogenic preparation of transmission electron microscopy (TEM) samples of bulk cryogenic deformed metals is proposed for the investigation and precise characterization of these materials. Initially, a precision cut-off machine was adapted for cryogenic cutting of samples, as displayed in Figure 1. Instead of lubricant, liquid nitrogen (LN) was used and the sample was kept underneath LN during the cutting. Foils of approximately 80  $\mu\text{m}$  were obtained by this process. After cutting the sample, a thin disk ( $\varnothing$  3mm) was obtained from the foil by using a toll for disk punching (Figure 2). To avoid heating, the punching of the foil was performed underneath LN. The disk obtained was then transferred to a sample holder for ion milling. Once again, this transfer was performed underneath LN, as displayed in Figure 3. By using a Gatan Precision Ion Polishing System (model 691) with the support for a cold stage (Figure 4), the sample was then thinned until a small hole was obtained for the analysis of its borders. Finally, the insertion of the sample into the microscope was performed by the use of a Gatan 626 single tilt liquid nitrogen cryo-transfer holder. The cryogenic TEM sample preparation of a bulk cryogenic deformed metal by ion milling was performed successfully. The development and future improvements in this technique may allow the better understanding of several phenomena involved in the cryogenic deformation of metals.

[1] D.C.C. Magalhães, et al, J Mater Sci 52 (2017) 7466

[2] Y.L. Gong, et al, Mater Sci Eng A 583 (2013) 199

The authors acknowledge the Centro Nacional de Pesquisa em Energia e Materiais (CNPEM) and the Laboratório Nacional de Nanotecnologia (LNNano) for providing the infrastructure for the execution of this research. Ricardo Sanson Namur acknowledges CAPES for the scholarship.



Figure 1: Cut-off machine adapted to operate cryogenically. At the right, the copper sample was being cut underneath LN. Foils of approximately 80  $\mu\text{m}$  were obtained



Figure 2: Disk punching tool used for obtaining a  $\varnothing$  3mm thin disk from the thin foil.

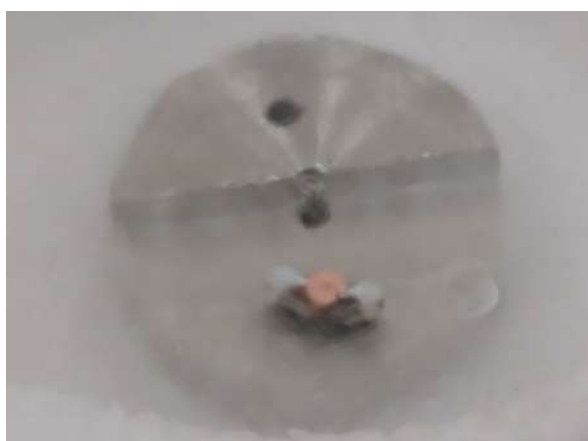


Figure 3: Disk transferred to the Ion milling sample holder. Image blur is observed because the transfer was performed underneath LN.



Figure 4: Gatan Precision Ion Polishing System (model 691) with a cold stage used for thinning the sample until a small hole was obtained.

## Cryogenic Sample Preparation for Cryo-TEM of Metals by Cryo-Ultramicrotomy

Ricardo Sanson Namur<sup>1</sup>, Jefferson Bettini<sup>2</sup> and Osvaldo Mitsuyuki Cintho<sup>1\*</sup>

<sup>1</sup>. Universidade Estadual de Ponta Grossa. Departamento de Engenharia de Materiais, Ponta Grossa, PR – Brazil.

<sup>2</sup>. Centro Nacional de Pesquisa em Energia e Materiais (CNPEM), Laboratório Nacional de Nanotecnologia (LNNano), Campinas, SP – Brazil.

\* omcintho@uepg.br

Processing of metals at cryogenic temperatures (~77 K) is a well-known development that may improve mechanical properties, as strength and/or ductility. The partial suppression of dynamic recovery at very low temperatures leads with the accumulation of crystallographic defects, which can be associated to the strength/ductility gains [1]. Many investigations were performed to understand and explain the mechanisms involved in the cryogenic deformation of metals and the obtaining of ultrafine-grained and nanostructured materials by this method [2]. Nevertheless, the analysis of these materials was performed after substantial heating of the sample, i.e. at room temperature. By raising the temperature, important information about the structure and substructures of defects was possibly lost due to the recovery and recrystallization of these metals. Thus, in this work, the authors propose a method for the cryogenic sample preparation of bulk cryogenic deformed metal samples by cryo-ultramicrotomy. Thin strips (100  $\mu\text{m}$ ) were obtained by many steps of cryo-rolling of a bulk specimen of commercially pure copper. These copper strips were cut into small parts in the shape of triangles and then attached to an ultramicrotome sample holder. The cutting of the strips and the attachment was performed underneath liquid nitrogen (LN) to avoid the heating of the samples, as displayed in Figure 1. The sample holder was attached to the cryo-ultramicrotome (RMC PowerTome XL) after its cooling until about -150°C (Figure 2). The obtaining of the ultra-thin slices was performed carefully to avoid heating and the excessive formation of ice, as displayed in Figure 3. Also, in Figure 3, TEM grids and a TEM grid holder can be seen inside the cryogenic chamber of the cryo-ultramicrotome for the thermal stabilization and the capture of the ultra-thin slices obtained directly into the grids. To insert these samples into the TEM a Gatan 626 single tilt liquid nitrogen cryo-transfer holder was used, as can be seen in Figure 4. The obtaining of ultra-thin slices for TEM analysis by cryo-ultramicrotomy was performed successfully. The development and future improvements in this technique may allow a better understanding of several phenomena involved in the cryogenic deformation of metals.

[1] D.C.C. Magalhães, et al, J Mater Sci 52 (2017) 7466

[2] Y.L. Gong, et al, Mater Sci Eng A 583 (2013) 199

The authors acknowledge the Centro Nacional de Pesquisa em Energia e Materiais (CNPEM) and the Laboratório Nacional de Nanotecnologia (LNNano) for providing the infrastructure for the execution of this research. Ricardo Sanson Namur acknowledges CAPES for the scholarship.



Figure 1: Cryo-rolled strip of copper attached to the cryo-ultramicrotome sample holder. Image blur due to liquid nitrogen.



Figure 2: Cryo-ultramicrotome RMC PowerTome XL and its temperature controller indicating that a cryogenic temperature was achieved.



Figure 3: Cryo-ultramicrotome chamber with details on the diamond knife, sample holder with the copper strip attached and TEM grids for thermal stabilization.



Figure 4: Details on the cryogenic transfer system for placing the grids into the TEM sample holder



E.C. GONÇALVES  
EDITOR CIENTÍFICO